AWARD NUMBER: W81XWH-15-1-0303

TITLE: Primary Blast Injury Criteria for Animal/Human TBI Models using Field Validated Shock Tubes

PRINCIPAL INVESTIGATOR: Dr. Namas Chandra

RECIPIENT: New Jersey Institute of Technology
323 Martin Luther King Jr Blvd
Newark NJ 07102-1824

REPORT DATE: November 2020

TYPE OF REPORT: Final

PREPARED FOR: U.S. Army Medical Research and Materiel Command
Fort Detrick, Maryland 21702-5012

DISTRIBUTION STATEMENT: Approved for Public Release;
Distribution Unlimited

The views, opinions and/or findings contained in this report are those of the author(s) and should not be construed as an official Department of the Army position, policy or decision unless so designated by other documentation.

REPORT DOCUMENTATION PAGE

Form Approved
OMB No. 0704-0188

Public reporting burden for this collection of information is estimated to average 1 hour per response, including the time for reviewing instructions, searching existing data sources, gathering and maintaining the data needed, and completing and reviewing this collection of information. Send comments regarding this burden estimate or any other aspect of this collection of information, including suggestions for reducing this burden to Department of Defense, Washington Headquarters Services, Directorate for Information Operations and Reports (0704-0188), 1215 Jefferson Davis Highway, Suite 1204, Arlington, VA 22202-4302. Respondents should be aware that notwithstanding any other provision of law, no person shall be subject to any penalty for failing to comply with a collection of information if it does not display a currently valid OMB control number. **PLEASE DO NOT RETURN YOUR FORM TO THE ABOVE ADDRESS.**

1. REPORT DATE	2. REPORT TYPE	3. DATES COVERED
NOVEMBER 2020	Final	15 Aug 2015 – 14 Aug 2020

4. TITLE AND SUBTITLE
Primary Blast Injury Criteria for Animal/Human TBI Models using Field Validated Shock Tubes

5a. CONTRACT NUMBER
W81XWH-15-1-0303

5b. GRANT NUMBER
14059001

5c. PROGRAM ELEMENT NUMBER

6. AUTHOR(S)
Namas Chandra, Maciej Skotak, KV Rama Rao

E-Mail: namas.chandra@njit.edu

5d. PROJECT NUMBER

5e. TASK NUMBER

5f. WORK UNIT NUMBER

7. PERFORMING ORGANIZATION NAME(S) AND ADDRESS(ES)

New Jersey Institute of Technology
323 Martin Luther King Jr Blvd
Newark NJ 07102-1824

8. PERFORMING ORGANIZATION REPORT NUMBER

9. SPONSORING / MONITORING AGENCY NAME(S) AND ADDRESS(ES)

U.S. Army Medical Research and Materiel Command
Fort Detrick, Maryland 21702-5012

10. SPONSOR/MONITOR'S ACRONYM(S)

11. SPONSOR/MONITOR'S REPORT NUMBER(S)

12. DISTRIBUTION / AVAILABILITY STATEMENT

Approved for Public Release, Distribution Unlimited

13. SUPPLEMENTARY NOTES

14. ABSTRACT

In the four specific aims and the 13 tasks, we advanced the knowledge of how blast causes neurotrauma using animal and human cadaveric models by combining experimental and computational methods. In Specific Aim 1, we developed dose-response (pressure-injury) curves for rodent models in the range of 10-350 kPa blast overpressure range and identified the pressure ranges for mild, moderate, and severe TBI. In Specific Aim 2, we identified that increase in oxidative stress, breakage of blood-brain barrier and neuroinflammation are the main biological mechanisms of injury. We identified that neuroinflammation is initiated by both innate microglia as well as infiltrating monocytes; other injury mechanisms persist over time inducing not only acute but chronic effects. In Specific Aim 3, we demonstrated that both blast overpressure and impulse (independently and together) determine the injury severity and symptom progression. Through direct measurements of both blast overpressure and impulse in live animals, we showed that impulse plays a key role in determining both injury initiation and progression. It is not the current practice to report impulse in the blast data and our research shows that both overpressure and impulse should be reported for proper characterization of blast. In the last Specific Aim 4, we tested five human cadaveric heads under comparable shock loadings and measured pressure/impulse at various points in the simulated brain regions. These data were then compared to values that causes injury in animal models. By combining rodent and human data, a transfer function is established which shows that humans have a higher tolerance for injury at all injury severities for given external shock loading. The overarching contribution of this research is that we identified the ranges of blast overpressure and impulse that cause mild, moderate, severe, and lethal TBI. Using animal-human cadaver transfer function, for the first time we have determined the possible blast overpressure and impulse ranges that is likely to cause various TBI injury severity levels in warfighters based on experimental and computational methods.

15. SUBJECT TERMS
Blast Induced Neurotrauma, Blast TBI, Primary blast brain injury, Blast overpressure, Impulse, Intracranial Pressure, Pressure measurement, Finite element numerical models.

16. SECURITY CLASSIFICATION OF:			17. LIMITATION OF ABSTRACT	18. NUMBER OF PAGES	19a. NAME OF RESPONSIBLE PERSON
a. REPORT	b. ABSTRACT	c. THIS PAGE			USAMRMC
U	U	U	UU	713	19b. TELEPHONE NUMBER *(include area code)*

Table of Contents

1. INTRODUCTION 12
2. ACOMPLISHMENTS 13
Task 1. Evaluate mortality rates 14
Task 2. Determine the Biomechanical Loading of the Rat Brain During Simulated Blast 21
Task 3. Numerical Simulation of Brain Injury 22
Task 4. Evaluate the Lung Injuries Caused by Blast Exposure 42
Task 5. Assess Extent of Oxidative/Nitrosative Stress, BBB damage and Neuroinflammation ..44
Task 6. Examine plasma membrane permeability using fluorescent tracers 63
Task 7. Evaluate alterations in brain proteome after primary blast exposure 64
Task 8. Establish Master Impulse Dose-Response Curve at Three Blast Overpressures 65
Task 9. Examine the changes in protein expression due to changes in blast impulse 24 hours after primary blast exposure 68
Task 10. Determine Alterations of Loading in the Rat Brain Caused by Changes in Impulse 72
Task 11. Identify Cross-Species Mild-To-Moderate bTBI via Numerical Simulations 84
Task 12. Comprehensive Characterization of Blast Loading in cephalic PMHS model 114
Task 13. Devise Transfer Function Correlating Rat and Human BOP Conditions 131
References 140
3. IMPACT 144
4. CHANGES/PROBLEMS 145
5. PRODUCTS 146
6. SPECIAL REPORTING REQUIREMENTS 148
7. APPENDICES 148

List of Figures

S. No	Figure Name	Page No
1	The 9-inch square cross section shock tube at CIBM^3, NJIT	14
2	The representative incident shock wave profiles generated using helium as a driver gas and Mylar membrane (thickness of 1.016 mm), with accompanying secondary reflected shock and under pressure waves are presented	15
3	Peak overpressure inside of the shock tube as a function of sensor location and membrane thickness	16
4	The relationship between Mylar membrane thickness and BOP in the test section of the shock tube (T4 sensor)	16
5	Calculated shock wave velocities at different sensor locations as a function of BOPs generated using Mylar membranes with thicknesses of: A) 0.02", B) 0.04", and C) 0.06"	17
6	The ratios of peak overpressure between incident and reflected shock wave measured at different locations inside of the shock tube as a function of sensor location and blast intensity	18
7	The logistic regression dose-response model for rats exposed to single blast with intensity in the range of 60-450 kPa peak overpressure (left) and corresponding impulse (90-780 Pa·s, right)	19
8	Lung injury scores for rats exposed to a single blast	20
9	Blast induced bradycardia as a function of peak overpressure (A) and impulse (B)	21
10	Representative pressure profiles measured by incident (loading), intracranial and carotid artery sensors (response) implanted in a rat exposed to 130 kPa of nominal blast intensity	21
11	Sequence of finite element modelling is presented	23
12	A. Input value (incident pressure), B. Unfiltered result at the hippocampus, C. Filtered using Butterworth filter at 2.5 kHz, and D. Comparison of filtered and unfiltered values	25
13	Differential loading of the brain caused by geometry of the rat's head and animal orientation with respect to incident shock wave	26
14	The internal segmentation of the rat Lagrangian model as observed with a mid-sagittal cut	27
15	A lateral depiction of the input conditions used to simulate shock loading on the Lagrangian rat head. The shock tube Eulerian mesh is shown in grey	28
16	Input pressure profiles used in the simulation of the shock wave	29
17	A temporal pressure map, reported as a multiple of the incident overpressure, of the mid-sagittal cut of a rat brain over the course of a 100 kPa shock wave	30
18	A temporal pressure map, reported as a multiple of the incident overpressure, of the mid-sagittal cut of a rat brain over the course of a 130 kPa shock wave	31
19	A temporal pressure map, reported as a multiple of the incident overpressure, of the mid-sagittal cut of a rat brain over the course of a 190 kPa shock wave	31
20	A temporal von Mises stress map, given in kPa, of the mid-sagittal cut of a rat brain over the course of a 100 kPa shock wave	32
21	A temporal von Mises stress map, given in kPa, of the mid-sagittal cut of a rat brain over the course of a 130 kPa shock wave	33
22	A temporal von Mises stress map, given in kPa, of the mid-sagittal cut of a rat brain over the course of a 190 kPa shock wave	33

23	A temporal maximum principal logarithmic strain map of the mid-sagittal cut of a rat brain over the course of a 100 kPa shock wave	34
24	A temporal maximum principal logarithmic strain map of the mid-sagittal cut of a rat brain over the course of a 130 kPa shock wave	35
25	A temporal maximum principal logarithmic strain map of the mid-sagittal cut of a rat brain over the course of a 190 kPa shock wave	35
26	The sensor locations taken from micro-CT scans of the rat head	36
27	A depiction of the sensor location within test specimen 1 with a cranial, lateral, and isometric view	37
28	A depiction of the sensor location within test specimen 2 with a cranial, lateral, and isometric view	37
29	A depiction of the sensor location within test specimen 3 with a cranial, lateral, and isometric view	37
30	A depiction of the sensor location within test specimen 4 with a cranial, lateral, and isometric view	38
31	A depiction of the sensor location within test specimen 5 with a cranial, lateral, and isometric view	38
32	A depiction of the sensor location within test specimen 6 with a cranial, lateral, and isometric view	39
33	A depiction of the sensor location within test specimen 7 with a cranial, lateral, and isometric view	39
34	A depiction of the sensor location within test specimen 8 with a cranial, lateral, and isometric view	40
35	A depiction of the sensor location within test specimen 9 with a cranial, lateral, and isometric view	40
36	The transformed and normalized intracranial pressure, von Mises stress, and the maximum principal logarithmic strains at the left, anterior sensor location (A) and the right, posterior sensor location (B)	41
37	Histological evaluation of blast injured lung tissue via H&E staining (20x (top) and 4x (bottom) magnification).	42
38	Lung injury scores for rats exposed to a single blast	43
39	Mild TBI range of blast-wave exposure induces NADPH oxidase 1 (NOX1), inducible nitric oxide synthase (iNOS), 4-hydroxynonenal (4HNE) and 3-nitrotyrosine (3NT) expression in rat brain microvessels	44
40	Oxidative/nitrosative damage of capillaries impaired BBB integrity by disrupting the tight junction proteins.	45
41	The neuronal damage marker leakage into serum is facilitated by BBB disruption	46
42	Immunoblot analyses showing increased protein expression of NOX1 and NOX2 isoforms in cerebrum and cerebellum 4 hours after moderate bTBI.	47
43	Fluorescence intensities (red channel) of NOX1 in hippocampus from control (A) and blast-injury (B) and NOX2 intensities from control (C) and Blast-injury (D) animals	47
44	NOX1 shows greater co-localization in neurons (A-D) than astrocytes (E-H) or microglia (I-L). Cerebellum displays increased NOX1 expression in neurons than other neural cell	49
45	Primary blast increases superoxide levels in different brain regions	50
46	Assessment of BBB permeability using extravasation of sodium fluorescein (NaFl) and Evans blue (EB).	50
47	Extravasation of Evan's blue (EB, red) and sodium fluorescein (NaFl, Green) in frontal cortex of control and injured animals at different time points after injury	51
48	Changes in Iba1 protein expression in hippocampus of animals 7 days after injury displays a strong tendency of increase compared to controls	52
49	Western blots of MMP 9 (right panel) and tight junction proteins Occludin and Claudin-5 and respective quantitation	52

50	ELISA results for whole brain lysates for MMP-3 and MMP-9	53
51	Fluorescent images of Evans blue extravasation. Images show 10x macro-shots as well as zoomed in 40x images in representative regions in the frontal cortex (A), striatum (B), somatosensory barrel-field cortex (C), hippocampus (D), thalamus (E) and cerebellum (F), 15 minutes following 180 kPa blast exposure.	54
52	ELISA results for S100β in blood serum	54
53	Immunohistochemistry in frontal cortex for endothelial cell marker (RECA-1) and monocyte marker (CCR2) at four hours post-exposure for control (A) and moderate (180 kPa BOP) blast (B)	56
54	ELISA results for tight junction proteins occludin and claudin-5, respectively in brain (A & B) and blood serum (C & D)	56
55	Fluorescent images of Iba (microglia) and RECA (rat endothelial cells) expression in the frontal cortex in control (A) and 4 hours of moderate blast in small (B) medium (C) and large (D) blood vessels.	57
56	Colocalization of NOX-1 (red) and RECA-1 (green) in vascular endothelial cells in the frontal cortex	57
57	DHE stain to observe superoxide concentration in the frontal cortex	58
58	ELISA results for matrix metalloproteinases. A & B show results for MMP-3 and 9, respectively, in control and blast groups	59
59	Fluorescent images of Evans blue extravasation	59
60	ELISA results for GFAP concentration in blood plasma	60
61	ELISA results for albumin concentration in CSF and blood plasma, as presented as a ratio between the two	60
62	ELISA results for IL-1β and TNF-α in hippocampus and thalamus lysates in animals exposed to moderate blast (180 kPa)	61
63	Lucifer Yellow positive cells in the frontal cortex of brain in rats exposed to a single blast with 180 kPa peak overpressure (left, middle) versus control (right)	62
64	Top 20 of identified canonical pathways by QIAGEN IPA (top), and schematic representation of electron transport chain complexes involved in the oxidative phosphorylation and mitochondrial dysfunction pathways (bottom)	63
65	The effect of the baseline drift on the quality of the recorded shock wave profiles	64
66	The effect of static electricity on the peak overpressure (A) and impulse (B)	64
67	The BOP-impulse calibration	65
68	The two dose-response curves developed for short (A) and long (B) duration impulse using a cohort of 150 animals	66
69	Levels of glial fibrillary acidic protein (GFAP) a marker of astrocytes in plasma samples obtained from animals of control, immediately and 4 hours after blast injury (180 kPa).	67
70	Levels of synaptophysin and PSD-95, markers of pre-and-post synaptic vesicles as a function of different BOPs	67
71	The volcano plots of the proteins identified in the brains of rats exposed to 180 kPa with low- (330 Pa·s) and high-impulse (720 Pa·s)	68
72	The comparative analysis of the canonical pathways identified by proteomic analysis of the cerebelli of rats exposed to a single shock wave with 180 kPa and impulse of 330 Pa·s (short-impulse) and 720 Pa·s (long-impulse)	69
73	The verification of the proteomic data via Western blot	70
74	An example of the excessive distortion caused by numerical instabilities	71
75	A lateral depiction of the input conditions used to simulate shock loading on the Lagrangian rat head	71
76	Input pressure profile used in the simulation of the shock wave for the CEL method and the ConWep method	72
77	Verification of the simulated reflected pressures loading the Lagrangian system at the element shown (right, inset).	73
78	A depiction of the surface excluded from interaction with the incident wave	73

79	Comparison of the simulated and experimental ICP profiles in the left and right hemispheres of a rodent exposed to a low impulse 130 kPa shock wave	74
80	A comparison of (A) the loading incident pressure-time waveforms used in this work with (B-C) experimental waveforms for (B) 130 kPa, (C) 180 kPa, and (D) 230 kPa	75
81	A comparison of the ICPs experimentally measured in the left (top) and right (bottom) hemispheres with simulated ICPs at the same locations	76
82	A comparison of the ICP in the midsagittal plane of a rat brain	77
83	A comparison of the ICP in the midsagittal plane of a rat brain	77
84	A comparison of the ICP in the midsagittal plane of a rat brain	78
85	A comparison of the von Mises stress in the midsagittal plane of a rat brain	79
86	A comparison of the von Mises stress in the midsagittal plane of a rat brain	79
87	A comparison of the von Mises stress in the midsagittal plane of a rat brain	80
88	A comparison of the logarithmic strain in the midsagittal plane of a rat brain	80
89	A comparison of the logarithmic strain in the midsagittal plane of a rat brain	81
90	A comparison of the logarithmic strain in the midsagittal plane of a rat brain	81
91	The biomechanical loading evaluation – the impulse effect	82
92	Two orientations were considered in this work	83
93	The geometrical model of the surrogate head surrogate mounted on a Hybrid III neck in the lateral (left) and isometric (right) views	83
94	The loading pressure profile used in the simulation of a 130 kPa shock wave	84
95	A frontal, lateral, and isometric view of the RED surrogate head form model	84
96	The geometry of the shock tube was based on the shock tube with a 28 in square cross section	85
97	A comparison of the experimental (black) and simulated (red) maximum reflected pressures (left) and the impulses (right) for a frontal (top) and lateral blast (bottom)	86
98	The temporal evolution of the surface reflected pressures in a frontal blast	87
99	The temporal evolution of the surface reflected pressures in a lateral blast	87
100	The reflected pressures (normalized with respect to the incident wave of 130 kPa) from over the course of 0.55 μs (Δt = 30 μs) shows the shock wave's interaction with the head surrogate in a shock	88
101	A segmented human head with nine segmented geometries	88
102	Mesh convergence of the quadratic models	89
103	Rat with two ICP pressure sensors implanted in the brain and affixed to the skull and strain gauges attached at the lambda and bregma points (inset).	91
104	The preparation of the surrogate rat head model	92
105	The preparation of the surrogate rat head model	93
106	Representative profiles of the intracranial pressure (A, C, E) and strain (B, D, F) recorded at the nominal BOP of: 70 kPa (A, B), 130 kPa (C, D), and 180 kPa (E, F)	94
107	Representative profiles of the intracranial pressure (A, C, E) and strain (B, D, F) recorded at the nominal BOP of: 70 kPa (A, B), 130 kPa (C, D), and 180 kPa (E, F)	95
108	Representative profiles of the intracranial pressure (A, C, E) and strain (B, D, F) recorded at the nominal BOP of: 70 kPa (A, B), 130 kPa (C, D), and 180 kPa (E, F)	96
109	The quantification of the incident and intracranial pressure (sensor embedded in the left hemisphere) waveforms in blast exposures performed at 70 kPa nominal shockwave intensity	97
110	The quantification of the incident and intracranial pressure (sensor embedded in the left hemisphere) waveforms in blast exposures performed at 130 kPa nominal shockwave intensity	98
111	The quantification of the incident and intracranial pressure (sensor embedded in the left hemisphere) waveforms in blast exposures performed at 180 kPa nominal shockwave intensity	99
112	The quantification of the incident and intracranial pressure (sensor embedded in the right hemisphere) waveforms in blast exposures performed at 70 kPa nominal shockwave intensity	100

113	The quantification of the incident and intracranial pressure (sensor embedded in the right hemisphere) waveforms in blast exposures performed at 180 kPa nominal shockwave intensity	101
114	The micro CT reconstruction of the rat head illustrating the sensor locations (A) used in the FEM simulations of the intracranial pressure changes at different incident peak overpressure: B) 15 kPa, C) 30 kPa and D) 70 kPa	103
115	The temporal ICP profiles obtained from the finite element simulations using a shock wave with the nominal duration of 4 ms and intensities of: A) 100 kPa, B) 140 kPa, C) 180 kPa and D) 210 kPa BOP	104
116	The relationship between ICP as a function of incident shock wave intensity obtained from numerical modeling	105
117	The relationship between ICP as a function of incident shock wave intensities obtained experimentally	105
118	The temporal snapshots of the midsagittal plane of the brain illustrating the evolution of: A) intracranial pressure, B) logarithmic strain, and C) von Mises stress, for the incident shock wave with 15 kPa peak overpressure and 4 ms duration	106
119	The temporal snapshots of the midsagittal plane of the brain illustrating the evolution of: A) intracranial pressure, B) logarithmic strain, and C) von Mises stress, for the incident shock wave with 30 kPa peak overpressure and 4 ms duration	107
120	The temporal snapshots of the midsagittal plane of the brain illustrating the evolution of: A) intracranial pressure, B) logarithmic strain, and C) von Mises stress, for the incident shock wave with 70 kPa peak overpressure and 4 ms duration	108
121	The temporal snapshots of the midsagittal plane of the brain illustrating the evolution of: A) intracranial pressure, B) logarithmic strain, and C) von Mises stress, for the incident shock wave with 100 kPa peak overpressure and 4 ms duration	109
122	The temporal snapshots of the midsagittal plane of the brain illustrating the evolution of: A) intracranial pressure, B) logarithmic strain, and C) von Mises stress, for the incident shock wave with 140 kPa peak overpressure and 4 ms duration	110
123	The temporal snapshots of the midsagittal plane of the brain illustrating the evolution of: A) intracranial pressure, B) logarithmic strain, and C) von Mises stress, for the incident shock wave with 180 kPa peak overpressure and 4 ms duration	111
124	The temporal snapshots of the midsagittal plane of the brain illustrating the evolution of: A) intracranial pressure, B) logarithmic strain, and C) von Mises stress, for the incident shock wave with 210 kPa peak overpressure and 4 ms duration	112
125	The 3D models of the specimens 1 and 2 reconstructed using the DICOM images obtained from the CT scans	113
126	The 3D models of the specimens 3, 4 and 5 reconstructed using the DICOM images obtained from the CT scans	114
127	The sensor locations obtained from the sagittal plane projections of the CT scans performed after the shock tube experiments for the following cephalic PMHS: A. P190395, B. P190500, C. P192868, and D. P192693	116
128	The representative overpressure-time histories collected for the specimen P190395 at nominal shock wave intensity of: A) 70 kPa, B) 70 kPa (long impulse), C) 130 kPa and D) 180 kPa	118
129	The quantification of the: A) peak overpressure, B) duration, C) impulse and D) rise time of incident and five ICP waveforms recorded for the specimen P190395 at nominal shock wave intensity of 70 kPa	118
130	The quantification of the: A) peak overpressure, B) duration, C) impulse and D) rise time of incident and five ICP waveforms recorded for the specimen P190395 at nominal shock wave intensity of 70 kPa, with the long duration impulse	119
131	The quantification of the: A) peak overpressure, B) duration, C) impulse and D) rise time of incident and five ICP waveforms recorded for the specimen P190395 at nominal shock wave intensity of 130 kPa	119

132	The quantification of the: A) peak overpressure, B) duration, C) impulse and D) rise time of incident and five ICP waveforms recorded for the specimen P190395 at nominal shock wave intensity of 180 kPa	120
133	The representative overpressure-time histories collected for the specimen P190500 at nominal shock wave intensity of: A) 70 kPa, B) 70 kPa (long impulse), C) 130 kPa and D) 180 kPa	120
134	The quantification of the: A) peak overpressure, B) duration, C) impulse and D) rise time of incident and five ICP waveforms recorded for the specimen P190500 at nominal shock wave intensity of 70 kPa	121
135	The quantification of the: A) peak overpressure, B) duration, C) impulse and D) rise time of incident and five ICP waveforms recorded for the specimen P190500 at nominal shock wave intensity of 70 kPa, with the long duration impulse	121
136	The quantification of the: A) peak overpressure, B) duration, C) impulse and D) rise time of incident and five ICP waveforms recorded for the specimen P190500 at nominal shock wave intensity of 130 kPa	122
137	The quantification of the: A) peak overpressure, B) duration, C) impulse and D) rise time of incident and five ICP waveforms recorded for the specimen P190500 at nominal shock wave intensity of 180 kPa	122
138	The representative overpressure-time histories collected for the specimen S192693 at nominal shock wave intensity of: A) 70 kPa, B) 70 kPa (long impulse), C) 130 kPa and D) 180 kPa	123
139	The quantification of the: A) peak overpressure, B) duration, C) impulse and D) rise time of incident and five ICP waveforms recorded for the specimen S192693 at nominal shock wave intensity of 70 kPa	123
140	The quantification of the: A) peak overpressure, B) duration, C) impulse and D) rise time of incident and five ICP waveforms recorded for the specimen S192693 at nominal shock wave intensity of 70 kPa, with the long duration impulse	124
141	The quantification of the: A) peak overpressure, B) duration, C) impulse and D) rise time of incident and five ICP waveforms recorded for the specimen S192693 at nominal shock wave intensity of 130 kPa	124
142	The quantification of the: A) peak overpressure, B) duration, C) impulse and D) rise time of incident and five ICP waveforms recorded for the specimen S192693 at nominal shock wave intensity of 180 kPa	125
143	The representative overpressure-time histories collected for the specimen S192868 at nominal shock wave intensity of: A) 70 kPa, B) 70 kPa (long impulse), C) 130 kPa and D) 180 kPa	125
144	The quantification of the: A) peak overpressure, B) duration, C) impulse and D) rise time of incident and five ICP waveforms recorded for the specimen S192868 at nominal shock wave intensity of 70 kPa	126
145	The quantification of the: A) peak overpressure, B) duration, C) impulse and D) rise time of incident and five ICP waveforms recorded for the specimen S192868 at nominal shock wave intensity of 70 kPa, with the long duration impulse	126
146	The quantification of the: A) peak overpressure, B) duration, C) impulse and D) rise time of incident and five ICP waveforms recorded for the specimen S192868 at nominal shock wave intensity of 130 kPa	127
147	The quantification of the: A) peak overpressure, B) duration, C) impulse and D) rise time of incident and five ICP waveforms recorded for the specimen S192868 at nominal shock wave intensity of 180 kPa	127
148	The summary of the quantification of the peak overpressure for all four PMHS included in the analysis. The specimen was exposed to a single shock wave with nominal intensity of: A) 70 kPa, B) 70 kPa (long duration), C) 130 kPa and D) 180 kPa	128
149	The summary of the quantification of the rise time for all four PMHS included in the analysis. The specimen was exposed to a single shock wave with nominal intensity of: A) 70 kPa, B) 70 kPa (long duration), C) 130 kPa and D) 180 kPa	128

150	The summary of the quantification of the impulse for all four PMHS included in the analysis. The specimen was exposed to a single shock wave with nominal intensity of: A) 70 kPa, B) 70 kPa (long duration), C) 130 kPa and D) 180 kPa	129
151	The summary of the quantification of the duration for all four PMHS included in the analysis. The specimen was exposed to a single shock wave with nominal intensity of: A) 70 kPa, B) 70 kPa (long duration), C) 130 kPa and D) 180 kPa	129
152	The linear regression of the peak ICP data (5 in. sensor) as a function of peak incident overpressure	131
153	The linear regression of the peak intracranial ICI data (5 in. sensor) as a function of peak incident overpressure	131
154	The linear regression of the peak ICP data (4 in. sensor) as a function of peak incident overpressure	132
155	The linear regression of the peak intracranial ICI data (4 in. sensor) as a function of peak incident overpressure	132
156	The linear regression of the peak ICP data (3 in. sensor) as a function of peak incident overpressure	133
157	The linear regression of the peak intracranial ICP data (3 in. sensor) as a function of peak incident overpressure	133
158	The linear regression of the peak ICP data (2 in. sensor) as a function of peak incident overpressure	134
159	The linear regression of the peak intracranial ICP data (2 in. sensor) as a function of peak incident overpressure	134
160	The linear regression of the peak ICP data (1 in. sensor) as a function of peak incident overpressure	135
161	The linear regression of the peak intracranial ICP data (2 in. sensor) as a function of peak incident overpressure	135
162	The overview of linear regression curves for rat (left and right ICP sensors) and PMHS (five ICP sensors)	136
163	The overview of the linear regression curves for rat (left and right ICP sensors) and PMHS (five ICP sensors)	136
164	The inter specimen scaling laws were developed using peak overpressure (A) and impulse (B) experimental values	137

List of Tables

Table No	Table Name	Page No
1	Material properties used in the numerical simulation of shock	31
2	The time points from which the simulation output was sampled	32
3	The loading conditions, or simulated parameters, selected to best replicate the experimental test configurations, referred to as the target parameters	75
4	Material properties used in the numerical simulation of shock	84
5	The constitutive material models and material parameters used in the convergence study	102
6	The characteristics of the PMHS specimen used in the study	115

1. INTRODUCTION

This final report is a comprehensive report of all the five years of the project. The project was originally scheduled for four years and was extended for one additional year with no cost extension. We made the following hypotheses in the project.

1. Blast overpressure and impulse independently affect the mortality rates and neuro-pathophysiology in rats; they trigger different bio-chemical responses over time and across various brain regions
2. Intracranial pressure in the acute phase (during the blast exposure) is determined by the peak overpressure (p*) and impulse (I*) of the blast
3. While intracranial pressure due to the same blast may vary due to anatomy of the species, injury to a brain is directly correlated with the resulting intracranial pressure (not the incident blast) and independent of species (i. e. rat versus human)

We formulated four Specific Aims. They are

Specific Aim 1: Establish a ***master*** dose response curve using a field validated blast injury animal model. This curve will map the probability of 24-hour survival over a wide range of field-relevant blast over pressures.

Specific Aim 1 comprises three tasks: (1) evaluate mortality rates, (2) determine biomechanical loading, (3) numerical simulation of brain injury.

Specific Aim 2: Determine the pathologies associated with primary blast exposure corresponding to mild- to- moderate TBI. Using the survival probability dose curve, we will identify the blast parameters associated with 50-75-100% survival for detailed pathological and proteomic analysis.

Specific Aim 2 comprises four tasks: (4) evaluate lung injuries, (5) assess injury mechanisms, (6) examine plasma membrane damage, (7) evaluate alterations in brain proteome.

Specific Aim 3: Examine the effect of blast *impulse* on the ***master*** dose response curve. Experimental measures will be used to determine the relationship between both blast parameters and the resulting change in intracranial pressure.

Specific Aim 3 comprises three tasks: (8) establish impulse dose-response curve, (9) examine changes in protein expressions, (10) determine alterations of loading in the rat brain due to impulse.

Specific Aim 4: Establish a human brain injury criterion (hBIC) for blast TBI based on experiments on live animal models and human cadaveric (PMHS) heads. The correlation will be based on the hypothesis that at the tissue level, injury is determined purely by the state of mechanical loading on similar tissues regardless of species.

Specific Aim 4 comprises of three tasks: (11) identify cross-species TBI loading via numerical simulations, (12) characterization of blast loading of post-mortem human head model, and (13) Formulate transfer function to correlate rat and human blast overpressure conditions.

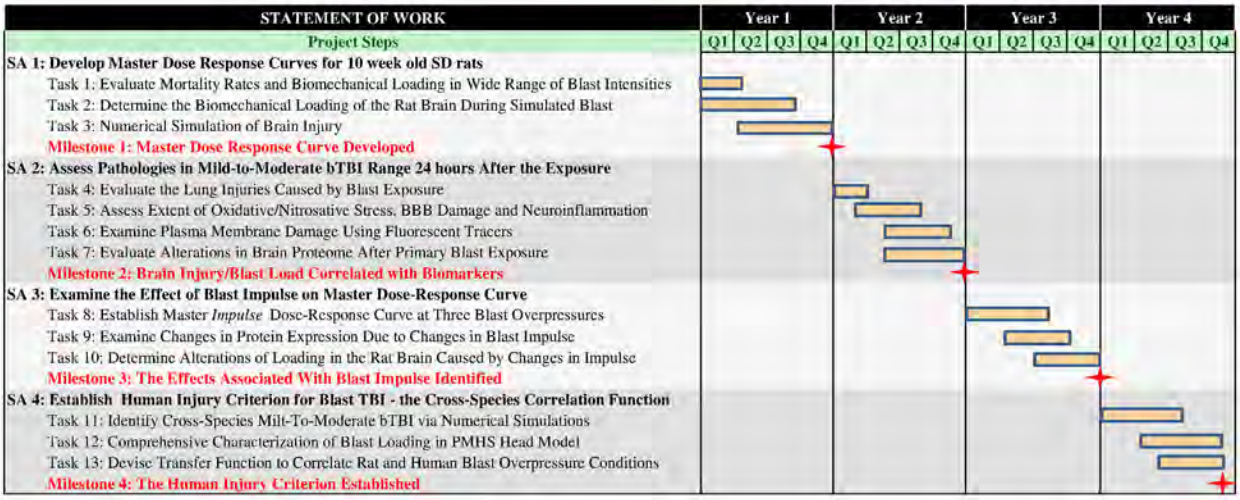
In the section on accomplishments, we outline the details of how we accomplished each aim. Our main outcome of this project was to *establish a brain injury criterion for the human brain exposed to a primary blast*.

KEYWORDS

Blast Induced Neurotrauma, Blast TBI, Primary blast brain injury, Blast overpressure, Impulse, Intracranial Pressure, Pressure measurement, Brain surrogate, Ballistic gelatin, Finite element numerical models.

2. ACOMPLISHMENTS

Major Goals of the Project (Statement of Work with Timeline):



Specific Aim 1: Establish a ***master*** dose response curve using a field validated blast injury animal model. This curve will map the probability of 24-hour survival over a wide range of field-relevant blast over pressures.
Specific Aim 1 comprises three tasks: (1) evaluate mortality rates, (2) determine biomechanical loading, (3) numerical simulation of brain injury

Task 1. Evaluate mortality rates

1.1 Calibration of 9-inch square cross section shock tube

We have performed comprehensive calibration of the 9-inches square cross section shock tube. This shock tube is a vital piece of equipment for successful completion of majority of research tasks planned within the framework of this award.

The new 9-inch square cross section shock tube was constructed based on patented design,[1] which was adapted by US Army and other laboratories performing similar research. The device is in the Shock Wave Testing Facility in the Center of Injury Biomechanics, Materials and Medicine (CIBM^3) in GITC building on NJIT campus. This new device which implements some additional modifications compared to original design[1-5] and it is more than likely due to manufacturing process some parts critical for shock tube operation are different, which might influence its performance. Thus, it was necessary to perform comprehensive calibration to establish a basic set of working parameters. For this purpose, we performed several tests to answer questions regarding the range of blast overpressure intensities and conditions in the test section.

The 9" square cross section shock tube has a modular design with the following characteristics: 1) adjustable volume breech, 2) variable length transition section, 3) the 6 meter long test section, equipped with bullet-proof glass windows for high speed video observation of the specimen during the shock wave exposure, and 4) the reflector end-plate (fig. 1). We used helium as a driver gas, and it was fed into the breech, separated from the main body of the shock tube with Mylar membranes of three thicknesses: 20, 40 and 60 mil (1 mil is 0.001 inch). The pressure inside of the breech is continuously monitored using a WIKA A-10 sensor (0-5000 psi range) and the burst pressure was recorded for all tests.



Fig. 1. The 9-inch square cross section shock tube at CIBM^3, NJIT. View from the back-illustrating reflector end plate, test section and distribution of sensors along the shock tube.

Measurement of the incident overpressure shock wave and secondary waves was realized by a series of pressure sensors distributed along the shock tube (fig. 2A, 2C). Custom made LabView program running on in-house built data acquisition system based on National Instruments PXI-6133 S Series

multifunction DAQ modules and PXIe-1082 PCI Express chassis was used for this purpose. Pressure sensors used in our experiments were PCB Piezotronics (Depew, NY) model 134A24. All data were recorded at 1.0 MHz sampling frequency and the typical acquisition time was 200 milliseconds.

This study was designed as two factor experimental design, 4 x 3. Two experimental variables investigated in this study were: 1) the distance between the reflector plate and the end of the shock tube (four levels) and 2) shock wave intensity (three levels). The distance between the reflector plate and the end of the shock tube was adjusted as shown in Fig. 2B. Four different lengths were used: 1) 0.625", 2) 2" and 3) 4", and 4) open end. The shock wave intensity (peak overpressure) was controlled by adjusting the thickness of Mylar membranes sandwiched between the breech and expansion section. The thickness was adjusted by stacking individual membranes with thickness of 0.01 inches. In this study we used three membrane thicknesses (0.02, 0.04, and 0.06 inches). All tests were performed using single fixed breech length of 21.6875 in, and were repeated six times for each combination of experimental covariates.

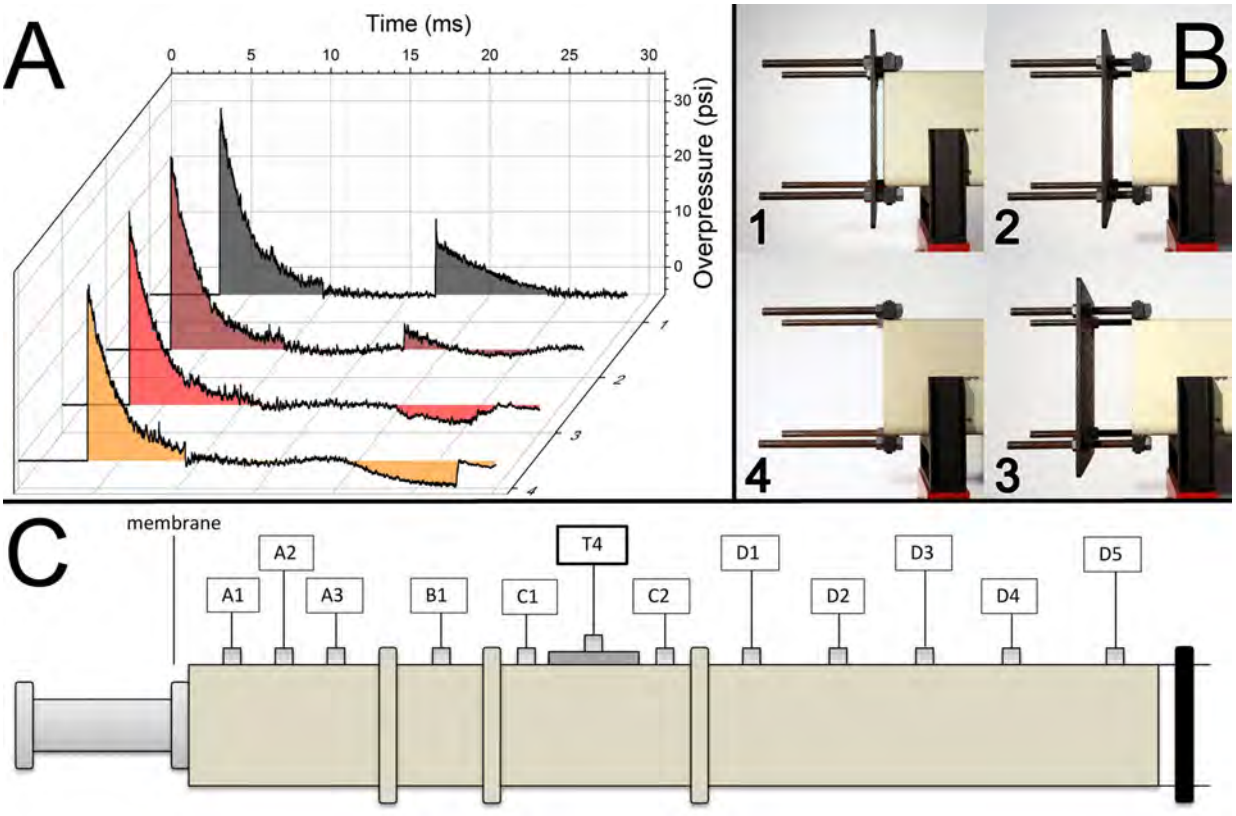


Fig. 2. The representative incident shock wave profiles generated using helium as a driver gas and Mylar membrane (thickness of 1.016 mm), with accompanying secondary reflected shock and underpressure waves are presented (A). The profile of the secondary wave depends on the gap between the end plate reflector and the exit of the shock tube (B): 1. 0.625-inch, 2. 2-inch, 3. 4-inch, and 4. open end. C. Schematics of the 9-inch square cross section shock tube with the pressure sensor locations. Typically sensors B1, C1, T4, C2, D2 and D4 were used in our experiments to track the shock wave profile evolution along the entire length of the shock tube.

1.2 Blast Overpressure

Peak blast overpressures (BOP) for different membrane thicknesses and back plate conditions are presented in fig. 3. BOP increased with membrane thickness and shows a direct correlation with the burst pressure (the maximum pressure measured in the breech at the time of membrane rupture). The variations between the measured BOP in experiments where the same membrane thicknesses were used are relatively small for all four back plate conditions, as evidenced by narrow standard deviation values (fig. 3A-C). The peak overpressure independently on the sensor location is a linear function of the burst pressure (fig. 4). The variations of the maximum burst pressure can be attributed to sample-to-sample differences in Mylar membrane mechanical properties, typical for this class of commercially available materials. The variation in burst pressure increases with Mylar membrane thickness (i.e. number of membranes), as evidenced by increasing standard deviation (fig. 4), but these variations don't translate into similar variation degree of BOP. The general observed trend is that the peak BOP decreases as the shock wave travels down the tube, and the end plate configuration has no effect on the peak BOP, with an exception of peak overpressures recorded at sensor locations C1 and T4, which differences are not statistically significant ($p > 0.05$, fig. 3D).

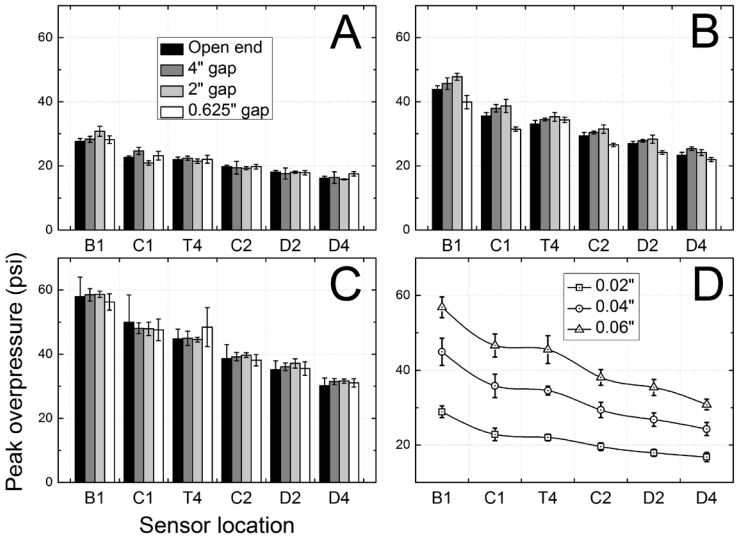


Fig. 3. Peak overpressure inside of the shock tube as a function of sensor location and membrane thickness: A) 0.02", B) 0.04", and C) 0.06". Peak overpressure values averaged among experiments preformed using the same Mylar membrane thickness (D): differences of average BOPs for sensors C1 and T4 are not statistically significant ($p > 0.05$) in respective test groups.

Using this graph, we calculated the relationship between the BOP and the thickness of Mylar membrane (fig. 4). In this case the second order polynomial was fitted to the experimental data. Established relationship will be used to calculate necessary thickness of Mylar membrane to achieve specific BOP in the test section (sensor T4).

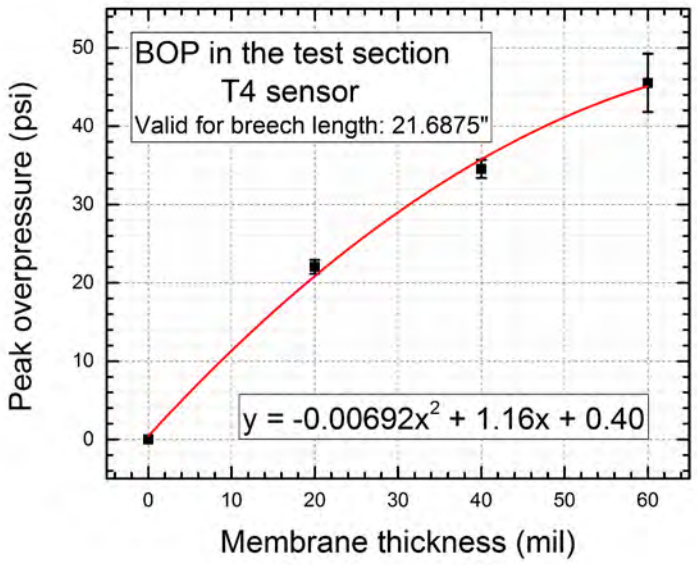


Fig. 4. The relationship between Mylar membrane thickness and BOP in the test section of the shock tube (T4 sensor).

1.3 Incident Shock Wave Velocities

The calculated values of the velocity of the shock front, traveling in the shock tube are presented in figure 5. The shockwave velocities increase with the thickness of the Mylar membrane, but just as in the case of peak BOPs there appears to be virtually no difference between the shock velocities for varying back plate conditions. For all three Mylar membrane thicknesses used in these experiments the general observed trend is that the shock wave velocity decreases with the distance travelled in the shock tube: 540 to 500 m/s (deceleration: 16.4 $m \cdot s^{-2}$, fig. 5A), 630 to 570 m/s (22.9 $m \cdot s^{-2}$, fig. 5B) and 680 to 620 m/s (23.3 $m \cdot s^{-2}$, fig. 5C), for the membrane thickness of 0.02, 0.04 and 0.06 inches, respectively. It is also clear that the shock wave velocity variation is higher the closer to the breech is the measurement location. The pooled data for all measurements shows narrow standard deviations for the velocities for all sensor locations after the test section sensor T4 (C2, D2 and D4). The velocities remain unchanged until shock wave reaches sensor D2 ($p < 0.005$, power: >0.95 with respect to velocities at T4 and C2) for all three tested membrane thicknesses (fig. 5D).

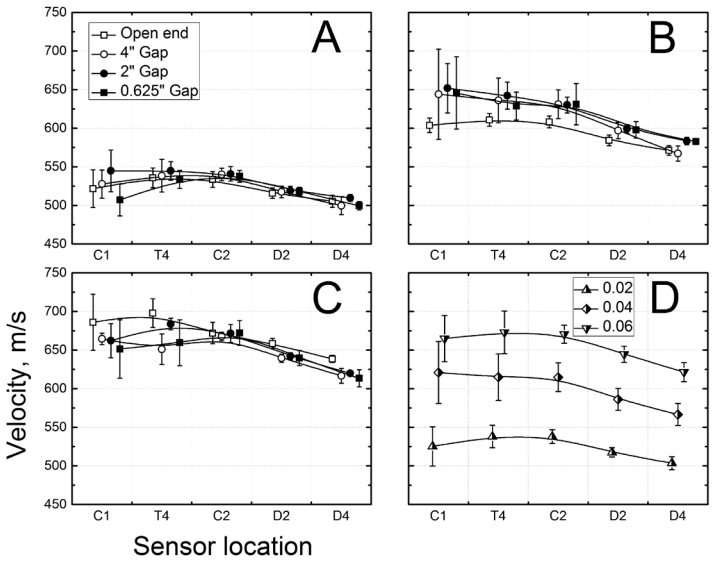


Fig. 5. Calculated shock wave velocities at different sensor locations as a function of BOPs generated using Mylar membranes with thicknesses of: A) 0.02", B) 0.04", and C) 0.06". Shock wave velocities were averaged for all experiments preformed using the same Mylar membrane thickness (D). Individual data points were horizontally shifted for clarity of presentation. The B1 sensor was used as a reference for all calculations.

1.4 Quantification of secondary over- (positive) and under-pressure (negative) waves

We also performed quantification of the secondary reflected waves, over- and under-pressure waves, since these have pronounced effect on the loading of the test subject (in the test section at the T4 sensor location, fig. 6). This quantification is expressed as the ratio of peak (or valley) of secondary reflected waves over peak incident primary wave (BOP) at specific sensor location. Without a back plate, the under-pressure wave that was generated had a peak minimum within 35% to 45% of the intensity of the original shock wave in the test section (as measured at T4

location). This means that the test subject (i.e. animal model) is being loaded with the original shock wave, and then shortly thereafter also by under-pressure wave, coming from the opposite direction. Implementing a back plate 4 inches away from the mouth of the shock tube decreases the under-pressure ratio by about 20% in the test section. Bringing the plate two inches closer eliminates the observed under-pressure waves but causes a secondary reflected shock wave to travel back into the shock tube. At this configuration, the test subject is exposed to the original shock wave plus the additional reflection wave, with intensity of merely 10-15% of the original shock front, coming from the opposite direction. When the plate-to-shock tube gap is further decreased to 0.625 inches, the peak overpressure of incident to reflected shock wave ratio in the test section increases to 30-40% of the original shock front BOP. These tests indicate 2-inch end plate gap is acceptable for further testing since only very weak reflected shock wave (only approximately 10% intensity of the original wave) reaches the test section. Using these tests, we can calculate the optimal end plate gap, which in this case is 2.8 inches. In this configuration there are no reflected secondary waves in the test section.

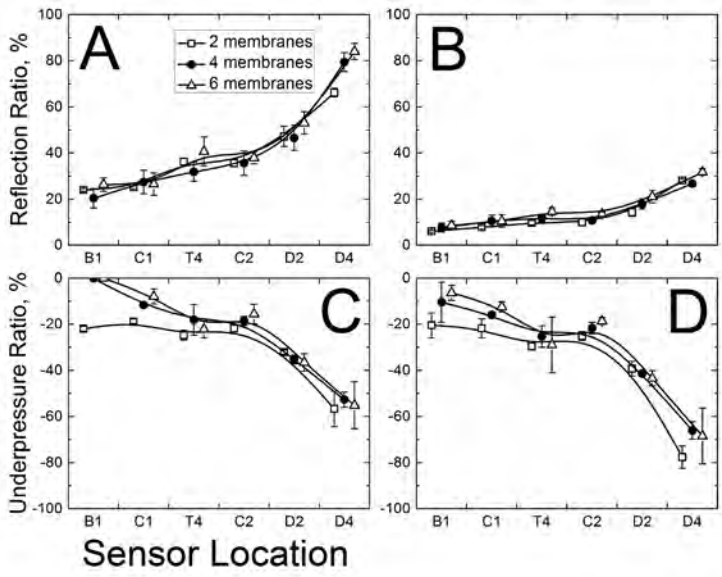


Fig. 6. The ratios of peak overpressure between incident and reflected shock wave measured at different locations inside of the shock tube as a function of sensor location and blast intensity: A) 0.625" gap, B) 2" gap between end of the shock tube and reflector plate. The ratios between incident peak overpressure and "peak" reflected underpressure for blasts generated when the gap between the end of the shock tube and reflector plate was 4" (C) and with open end (D). The data points were horizontally shifted for clarity of presentation.

1.5 Dose-response logistic regression model

All the test animals were in a prone position with a head restrained and thus no artifacts associated with uncontrolled head acceleration were present in this bTBI model, as demonstrated elsewhere.[6] The net movement of the specimen did not exceed 3 mm as determined by analysis of captured high speed video. We exposed 13 rats per discrete incident peak overpressure to develop a dose-response linear regression model for predicted mortality rate (PMR) as a function of BOP and corresponding impulse values (fig. 7). We did not observe any mortality of animals exposed to blast intensity lower than 170 kPa (fig. 7, left) or impulse 300 Pa·s (fig. 7, right). However, mortality rate gradually increased from 170 kPa to 300 kPa, and mortality rate was 100% above 300 kPa (or 500 Pa·s impulse). These accounted for an immediate loss (not delayed deaths, i.e. animals were removed from the shock tube in less than a minute after the shock wave exposure) of 45 rats as a consequence of shock wave exposure, consistent with our previous work.[6, 7] The insets in fig. 7 present receiver operating characteristic (ROC) curves for respective logistic regression fits with the following areas under ROC curves: 0.878 (left) and 0.882 (right), for BOP and impulse, respectively. Analysis from these models indicated good predictive power of

mortality rate using peak overpressure and impulse as metrics to gauge injury risk under primary blast. The McFadden pseudo-R^2 values of 0.389 and 0.412 were obtained for fits using peak overpressure and impulse as independent variables, respectively. These values indicate a highly satisfactory quality of fit.

The logistic regression models were developed and evaluated using Systat 13.0 software (Systat Software, Inc., San Jose, CA). Dose-response models for heart rate and pulmonary injury were fitted with Origin 9.0 software (OriginLab Corp., Northampton, MA) using dose-response function:

$$y = A_1 + (A_2 - A_1)/(1 + 10^{(\log x_0 - x)p}) \quad (1)$$

Where A_1, A_2 are asymptotes, $log\ x_0$ is an inflection point, and p is a slope value.

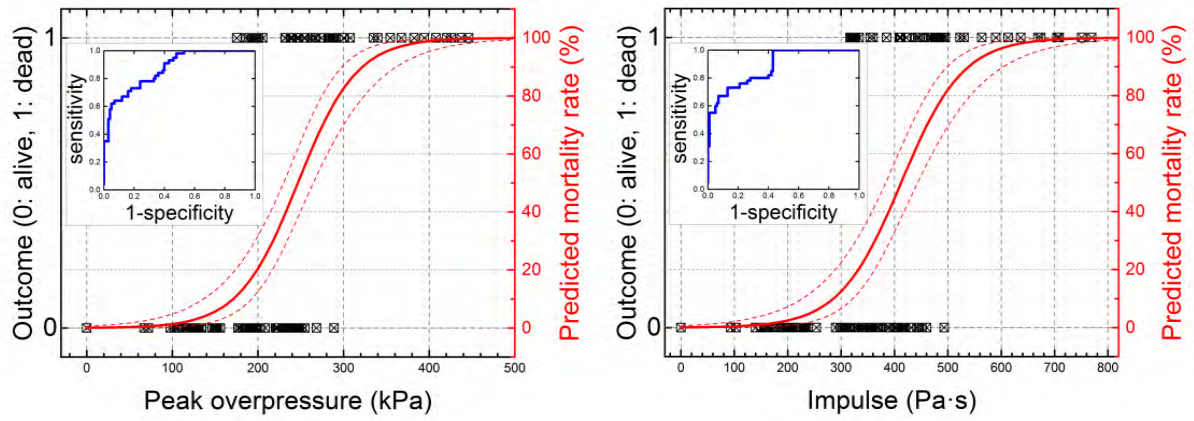


Figure 7. The logistic regression dose-response model for rats exposed to single blast with intensity in the range of 60-450 kPa peak overpressure (left) and corresponding impulse (90-780 Pa·s, right). The insets present receiver operating characteristic (ROC) curves for respective logistic regression fits with areas under ROC curves: 0.88 and 0.88. McFadden R^2 = 0.39 and 0.41, for fits using peak overpressure and impulse as independent variables, respectively. Dashed lines indicate confidence intervals of the model.

1.6 Primary blast impacts mild pulmonary injury

Animals tested in prone position have their abdomen partially protected from the blast wave by the aluminum holder used in our experiments.[6] The observed levels of pulmonary injury expressed using Yelveton's scoring system[8] revealed a low level of injury (fig. 8 A, B). However, we observed an increasing trend of injury score with increasing peak overpressure and impulse. We observed only a few cases where pathological score exceeded 21 for the blast strength higher than 300 kPa BOP with high standard deviations (fig. 8 C). A score of 21 is considered as a cut-off threshold for mild pulmonary injury.[8] The pathological score at 50% PMR (at 260 kPa) was found to be less than 10, while the score was less than 4 in the 60 - 190 kPa range. Moreover, there are six animals which died because of blast exposure and had no lung injury (score of zero, fig. 8C, D). These results suggested minimal pulmonary injuries and thus, we conclude lung injury is not a viable indicator of PMR.

1.7 Blast induced bradycardia

We evaluated the functional changes in the heart rate, blood oxygen saturation (spO_2) and perfusion index in the 60-250 kPa peak overpressure range over period of 30 minutes before and after blast exposure. We found that the onset of bradycardia occurred immediately after the blast exposure even at 60 kPa (fig. 9, p=0.01, power: 0.85 vs control). The values of the differential

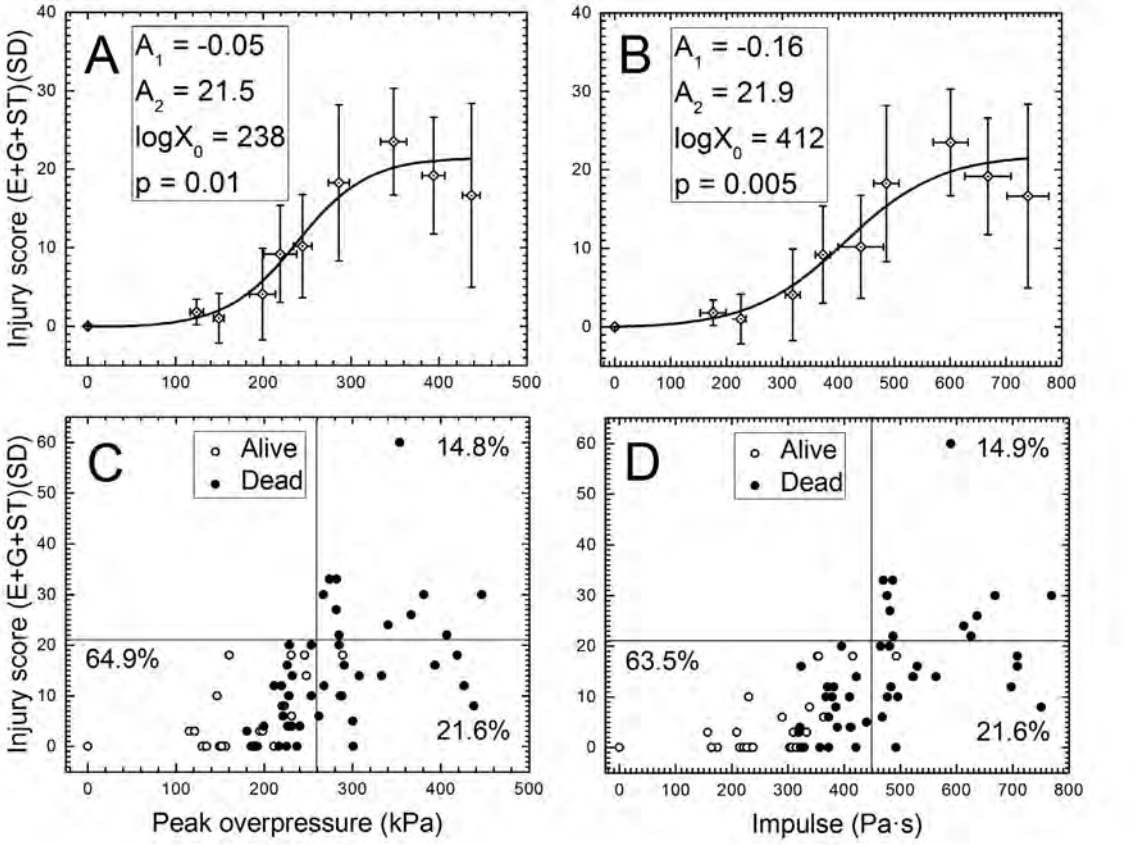


Figure 8. Lung injury scores for rats exposed to a single blast. The dose-response model was used to fit the IS as a function of peak overpressure (A, C) and impulse (B, D). The scattergrams (C, D) illustrate individual scores and their distribution among the cohort of 75 rats evaluated in this test. The value of 21 is the upper limit of the slight lung injury level as defined by Yelverton. The vertical lines (peak overpressure of 260 kPa (C), or impulse of 450 Pa·s (D)) correspond to 50% predicted mortality rate according to the dose-response model in fig. 1. There are six animals which died after the blast and had no apparent lung injuries (score of zero).

average heart rates (ΔHR) decreased gradually with increase in blast intensity: -29±10 (60 kPa), -26±20 (100 kPa), -43±26 (130 kPa), -62±21 (190 kPa), -62±43 (230 kPa) and -62±24 (250 kPa) bpm. These data were modeled using a simple dose-response function to quantify the characteristics of ΔHR as a function of two blast parameters, the peak overpressure and the impulse. This mathematical modeling generated asymptotic values of A_1 and A_2: -13.9 and -59.5 (for peak overpressure, fig. 9 A), and -12.7 and -67.1 (for impulse, fig. 9 B), respectively. The calculated inflection points ($\log(x_0)$) are 109.3 kPa and 186.9 Pa·s for both blast parameters (fig. 9). The control group was not correlated with any of the blast exposure groups ($p < 0.05$).

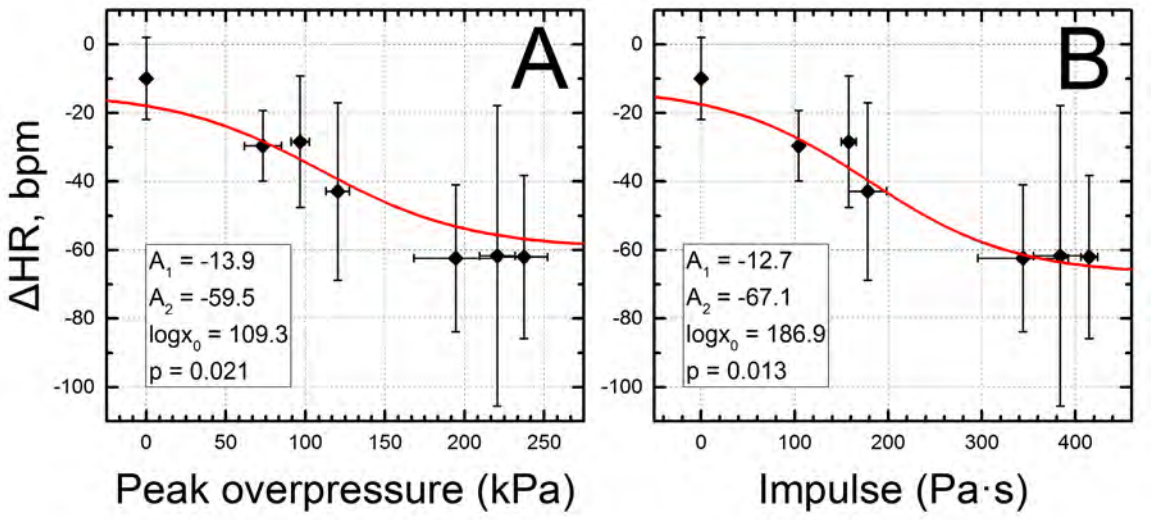


Figure 9. Blast induced bradycardia as a function of peak overpressure (A) and impulse (B). In both cases, the dose-response function (1) was used to model the pathological response and resulting parameters are listed in respective insets in both figures. All blast exposed groups have statistically significant heart rate decrease versus control ($p < 0.05$).

Task 2. Determine the Biomechanical Loading of the Rat Brain During Simulated Blast

2.1 Intracranial pressure measurements

Correlation of intracranial pressure during blast exposure and brain injury mechanisms is ongoing research topic where many important questions are awaiting to be appropriately addressed. Particularly, due to limited number of studies very little experimental evidence is available in the literature correlating specific brain pathologies with ICP fluctuations. To date most of the experimental work was performed using numerical models and direct ICP pressure measurements. These studies give only limited insight into BINT associated with ICP fluctuations. The contribution to brain injury associated exclusively with skull flexures is a difficult research task aggravated by simultaneous occurrence of other injury factors contributing to increase of ICP during blast exposure.

Experiments performed in our laboratory at University of Nebraska-Lincoln preformed on 10 weeks old Sprague Dawley rats exposed to five discrete blast intensities (130, 190, 220, 250 and 290 kPa peak overpressure) resulted in peak incident-to-ICP ratios in the range of 1.5 to 1.3 for

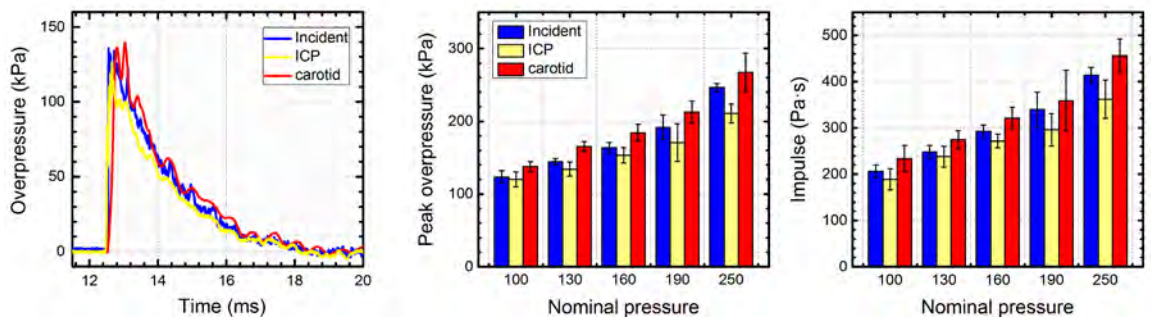


Figure 10. Representative pressure profiles measured by incident (loading), intracranial and carotid artery sensors (response) implanted in a rat exposed to 130 kPa of nominal blast intensity. Biomechanical loading was performed at 5 blast overpressures in the 100 to 250 kPa range and peak overpressure (middle panel) and impulse (right panel) were quantified.

lower and higher peak overpressures (see: Skotak et. al., J. Neurotrauma, 2013, 30, 1147-1160). The FFT analysis of ICP profiles indicated the oscillations have harmonic characteristics, with low (5-10 kHz) and high frequency component (10-20 kHz). The high frequency oscillations were linked to observed mortality (animals exposed to 190, 250 and 290 kPa BOP) and we have also observed the maximum ICP frequency increases with increasing blast intensity: 13 kHz (190 kPa), 16 kHz (250 kPa) and 19 kHz (290 kPa).
However, our measurements performed on a cohort of 6 animals indicate ICP-to-incident pressure ratio is less than 1, which is a strong contradiction of what has been reported in the literature to date (fig. 10). Most likely the methodology differences are responsible for observed discrepancies. We have initiated use of miniature Millar SPR-671 sensors which are only 0.5 mm OD and typically are suitable for measurements of arterial blood pressure. These sensors have robust construction and easily withstand blast exposure, which was confirmed during our experiments. Currently we are performing implantation of sensors using live animals and this might be a contributing factor responsible for observed differences. The sensor size and mounting strategy might also play important role. In the past the sensor was mounted in the forehead, which is not ideal location considering biofidelity of the measurement, i.e. when the skull structure is affected by craniotomy and application of the cement to keep sensor cannula in place, one would expect the pressure transmission of the head to be quite different than when skull and skin layer remain intact. It is also hard to avoid relative motion of the sensor with respect to skull using this strategy, although it might be a general drawback of any sensor implantation methodology due to specificity of blast experimentation. There is always a minute head displacement independently how well the restrain system is designed and performed.

Task 3. Numerical Simulation of Brain Injury

3.1 Rat head and shock tube models

High resolution MRI and CT datasets of a male Sprague Dawley rat were used in combination to generate a three-dimensional rat head model. Separate T2-weighted MRI scans for muscle and skin, and brain, along with a CT scan for skull and bones were used to achieve proper contrast and segmentation of various tissues (i.e. muscle, skin, brain, skull, and bones). Brain MRI consisted of an isotropic resolution of 256 x 256 x 256 pixels, for a field of view of 30 mm in all three directions. MRI for muscle and skin has an anisotropic resolution of 512 x 512 x 256, for a field of view of 30, 30 and 50 mm, respectively. The three datasets where overlapped, registered, segmented and triangulated using Avzio 6.2. The triangulated surface mesh was imported to Hypermesh, and a volume mesh consisting of 10-node tetrahedron element was generated from the imported mesh. The generated interface is shared between the brain, skin, and skull regions, which are treated as Lagrangian elements. The model is then imported to Abaqus 6.13 and inserted into the shock tube model. The generation and propagation of blast waves are modeled in the shock tube environment. The air inside the tube, in which the blast wave propagates, is modeled with Eulerian elements. The size of the tube corresponds to the physical dimensions of the shock tube used in experiments, with the cross section 229 x 229 mm. The tube was subjected to biased meshing (mesh size varying from 100mm to 5mm), with the highest density of fine meshes in the region encompassing the rat head (the test section) and coarse mesh elsewhere, to reduce the total number of elements in the model, without sacrificing accuracy.

3.2 Loading, Interface, and Boundary Conditions

The rat head model is subjected to the blast wave from the frontal direction. A complete model of the shock tube, with the driver, transition and extension section, reproducing the burst, expansion and development of the blast wave would be time consuming and computationally taxing, thus less efficient for this research task. Hence, a partial model with experimentally measured pressure-time profile is used as the pressure boundary condition as well as the input, with the numerical model including only downstream flow field including test specimen section of the shock tube.

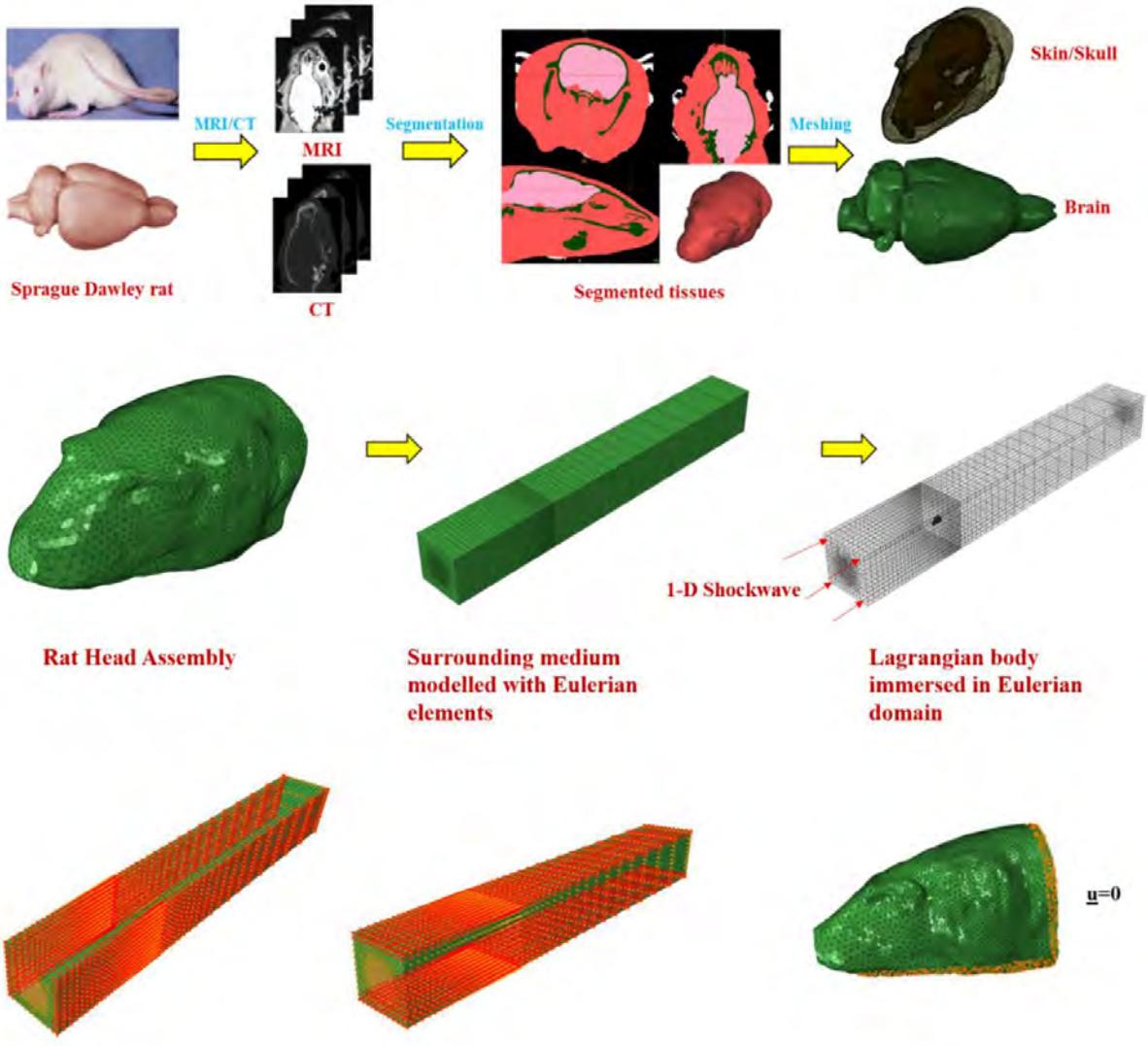


Figure.11. Sequence of finite element modelling is presented: 1) MRI/CT scans are overlapped, registered, segmented and triangulated using Avizo 6.0, 2) triangulated surface mesh is imported to Hypermesh to generate 3D mesh with 10-node tetrahedron Lagrangian elements, and 3) model is then imported to Abaqus and assembled with the Eulerian shock tube. Numerical boundary conditions are set for the shock tube along with displacement constrained within the axis, and rat model with displacement constrained in all three linear directions (x, y and z).

Except for the face on which the pressure is acting, velocity perpendicular to all other remaining faces of the shock tube is kept at zero, to avoid leaking of air from the shock tube. This

configuration also maintains a planar shock front travelling in the longitudinal direction with no lateral flow. The interface between all components (skin, skull and brain) of the rat head was modelled as tied (i.e. no tangential and sliding) contact. The nodes on the bottom and rear faces of the rat head is constrained in all degrees of freedom.
An enhanced immersed boundary method is used to provide the coupling between the Eulerian and the Lagrangian domains. Here, the Lagrangian region resides fully or partially within the Eulerian region and provides *no-flow* boundary conditions to the fluid in the direction normal to the local surface. Further, the Eulerian region provides the pressure boundary conditions to the Lagrangian region. Thus, a combination of fixed Eulerian mesh and solid-fluid interface modeling through the enhanced immersed boundary method allows for the concurrent simulations of the formation and propagation of a primary blast wave in a fluid medium and accounts for the effects of both fluid-structure interaction and structural deformations once the blast wave encounters a solid. The interactions (contact conditions) between Eulerian (containing air and a propagating blast wave) and Lagrangian regions are defined using 'general contact' feature (card) in Abaqus. In general, contact constraints are enforced through the penalty method with finite sliding contact formulation. Various contact property models are available in general contact. In the present work, frictionless tangential sliding with hard contact is used as the contact property model (figure 11).

3.3 Solution Scheme

The finite element model is solved using the nonlinear transient dynamic procedure with the Euler-Lagrangian coupling method (Abaqus 6.13). In this procedure, the governing partial differential equations for the conservation of momentum, mass and energy along with the material constitutive equations and the equations defining the initial and boundary conditions are solved simultaneously.
Conservation of mass (continuity equation):

$$\rho \frac{\partial v_i}{\partial x_i} + \frac{\partial \rho}{\partial t} + v \cdot \nabla \rho = 0 \qquad (1.5)$$

Conservation of momentum (equation of motion):

$$\frac{\partial \sigma_{ij}}{\partial x_j} + \rho b_i = \rho a_i \qquad (1.6)$$

Conservation of energy (energy equation):

$$\rho \frac{\partial e}{\partial t} + v \cdot \nabla e = \sigma_{ij} \frac{\partial v_i}{\partial x_j} - \frac{\partial q_i}{\partial x_i} + \rho q_S \qquad (1.7)$$

where, ρ is density, x, v and a are displacement, velocity and acceleration of a particle respectively, σ is Cauchy stress, b is body force, e is internal energy per unit mass, q is heat flow per unit area and q_S is rate of heat input per unit mass by external sources.

In Eulerian-Lagrangian method, the whole model is solved (i.e. both Eulerian and Lagrangian domains) with the same Lagrangian equations. The notion of a material (solid or fluid) is introduced when specific constitutive assumptions are made. The choice of a constitutive law for a solid or a fluid reduces the equation of motion appropriately (e.g., compressible Navier-Stokes equation, Euler equations etc.). For the Eulerian domain in the model the results are simply mapped back to the original mesh with extensions to allow multiple materials and to support the Eulerian transport phase for Eulerian elements. Eulerian framework allows for the modeling of highly

dynamic events (e.g. shock) which would otherwise induce heavy mesh distortion. In Abaqus, the Eulerian time increment algorithm is based on an operator split of the governing equations, resulting in a traditional Lagrangian phase followed by an Eulerian, or transport phase. This formulation is known as "Lagrange-plus-remap." During the Lagrangian phase of the time increment nodes are assumed to be temporarily fixed within the material, and elements deform with the material.

3.4 Model validation

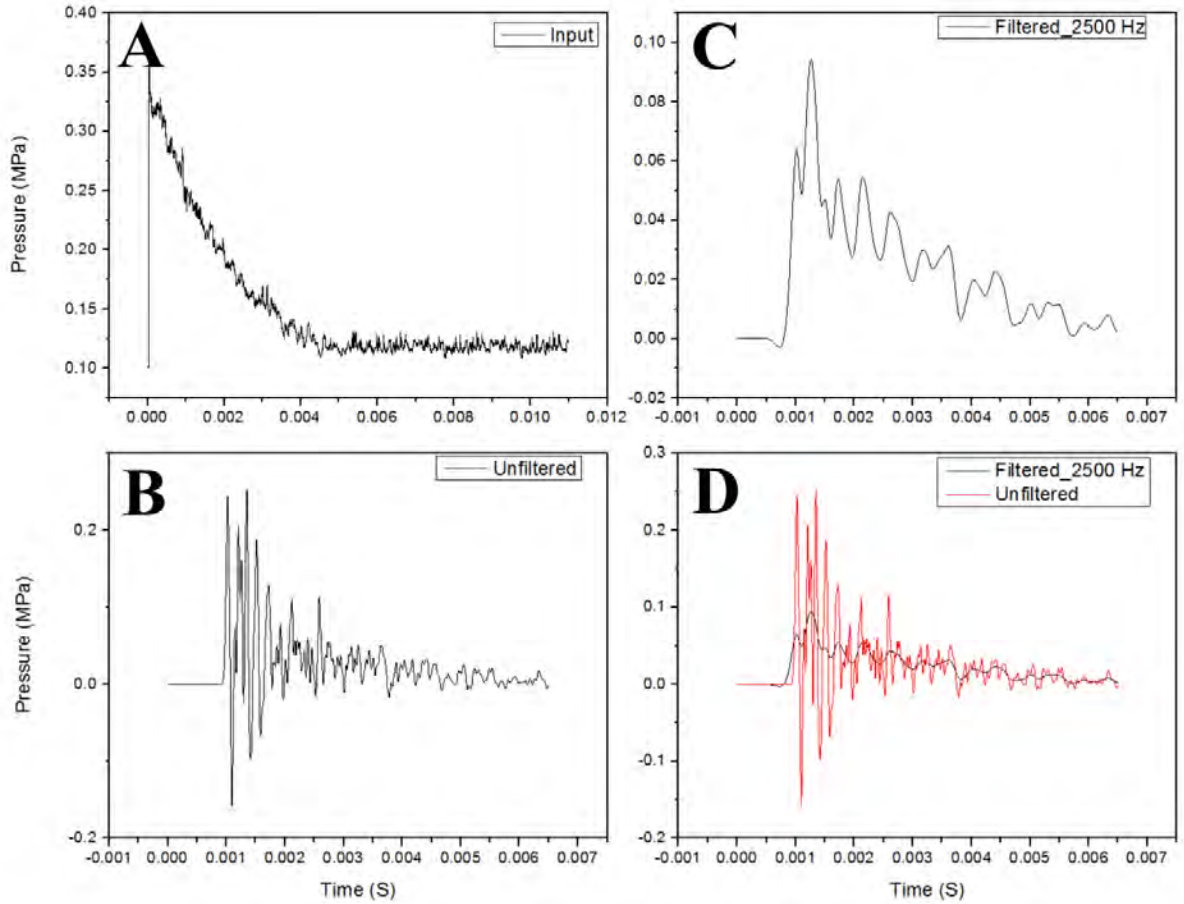


Figure.12. A. Input value (incident pressure), B. Unfiltered result at the hippocampus, C. Filtered using Butterworth filter at 2.5 kHz, and D. Comparison of filtered and unfiltered values.

Results of simulations will require further refinement, since excessive oscillations were observed within the pressure profiles obtained from the hippocampus region (fig. 12). The existence of the oscillations may be due to variation between the geometries of the Lagrangian vs the Eulerian domain, leading to inaccurate transfer of the blast wave from the air into the rat head. In order to eliminate the oscillations, the Butterworth filter was applied, which led to the peak pressure falling by half. Variation of mesh size (5 mm to 1 mm) made the oscillations higher. Also, literature was used to obtain alternate material properties for the skin, skull and brain, which was used for simulations. These modifications had no effect on the results of repeated simulations.

3.5 Wave transmission pathways

Numerical model allowed us to identify loading pathways in the rat brain during the blast exposure. As the blast wave impinges the rat, the wave first interacts with the snout and undergoes diffraction, where it bends and converges towards the eye socket (pathway 1) and on top of the skull (pathway 2). The surface pressure loading along pathways 1 and 2 are transmitted to the rat brain, which start converging towards each other in the region of bregma, lambda and midline

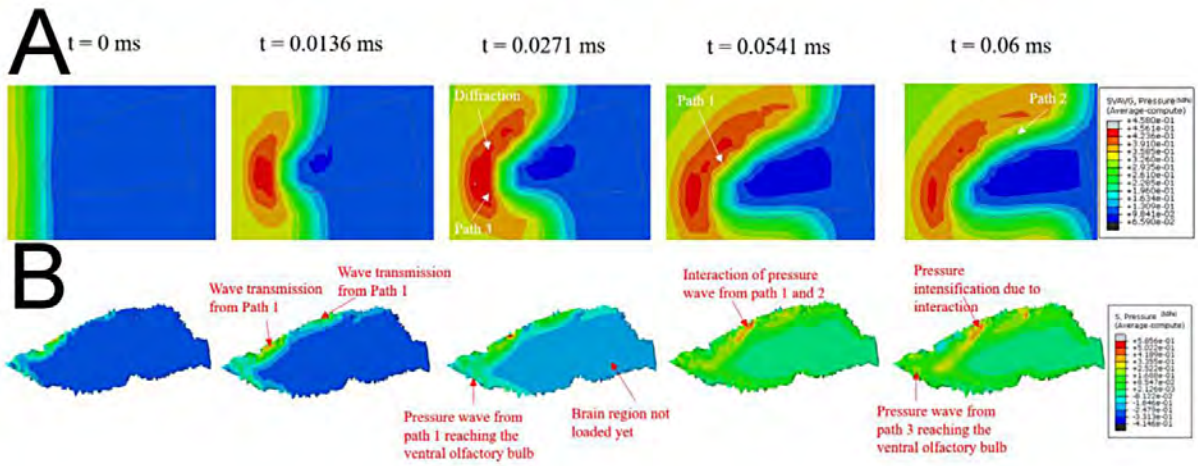


Figure.13: Differential loading of the brain caused by geometry of the rat's head and animal orientation with respect to incident shock wave: A. Pressure contour plots outside the rat head, B. Corresponding pressures inside the brain.

sutures. The loading through the snout (pathway 3) does not reach the brain before the transmitted pressure wave from pathways 1 and 2 completely load the brain (figure 13).

Rat Lagrangian Model

A geometrical model of a ten-week old Sprague Dawley rat was generated by combining a magnetic resonance image (MRI) of a rat head, a micro-computed tomography (micro-CT) scan of the rat skull, and a geometrical representation of the rat body. The micro-CT scan of the rat skull was taken at a resolution of 35.6 µm (SkyScan 1275, Bruker microCT, Kontich Belgium) and was segmented into a solid mask (Simpleware ScanIP, Synopsys, Exeter, United Kingdom). The segmented mask was then imported with the MRI DICOM and co-registered. As different specimens were used, three-dimensional scaling was conducted to ensure accurate co-registration. The MRI images facilitated the segmentation of the soft tissues, which include the skin, brain, and the dura mater. A geometrical model representing the average dimensions of a 50th percentile rat body was combined with the segmented masks[9]. For simplicity, the geometrical model of the rat body was simulated as a skin material and did not have internal segmentation. The model is shown in Figure 14.

The model was meshed using a 10-node modified tetrahedral biased mesh, with an average minimum edge length of 0.75 mm and average maximum edge length of 1.25 mm at the regions of interest (Simpleware FE, Synopsys, Exeter, United Kingdom). This mesh density was selected based on the results of a convergence study, which highlighted that increasing the mesh density did not result in a substantial improvement in pressure predictions (defined to be a 5% change). Material properties used to approximate the mechanical response of the rat head tissues are included in Table 1.

Shock Tube Eulerian Model

A three-dimensional geometrical model was generated of the nine-inch shock tube, simulating a portion of the test region that was 3.3 m in length. The shock tube was modeled as a 8-node

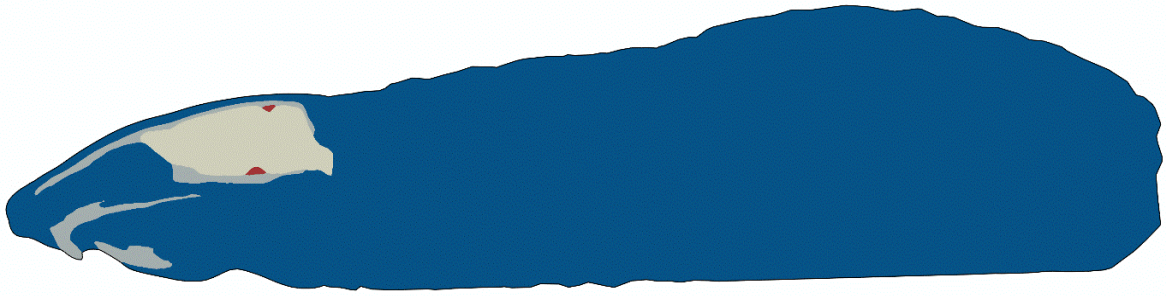


Figure .14. The internal segmentation of the rat Lagrangian model as observed with a mid-sagittal cut. The skin is depicted in blue, the skull in grey, the dura mater in red, and the brain in beige.

hexahedral Eulerian mesh with reduced integration and hourglass control with a minimum average mesh seed length of 6 mm at the region of interest (Abaqus/CAE, Dassault Systems, Vélizy-Villacoublay, France). The region of interest was 0.6 m in length which, when assembled, contained the full extent of the Lagrangian rat model. The air within the shock tube model was simulated as an equation of state at with ambient conditions (an air density of 1.225 kg/m^3 at 291 K) using the parameters in Table 1.

Table 1 Material properties used in the numerical simulation of shock.

	Linear Elastic			
	Elastic Modulus		Poisson's Ratio	
Skull[10, 11]	9500 MPa		0.3	
Soft Tissue[12]	16.7 MPa		0.42	
Dura[10]	20.0 MPa		0.45	
	Linear Viscoelastic			
	Long-Term Bulk Modulus	Poisson's Ratio	Shear Modulus	Relaxation Time Constant
Brain[13]	2.19 GPa	0.4999	1.05 MPa	0.02 s
	Ideal Gas Equation of State			
	Gas Constant		Specific Heat	
Air	287 J kg^{-1} K^{-1}		1010 J kg^{-1} K^{-1}	

Shock Simulation

The Lagrangian rat head was positioned within the Eulerian shock tube mesh so that it was in the center of the shock tube at the test section in a prone position. The entire body of the rat model was fixed in all rotational and translational degrees of freedom, to mirror the experimental methods of strapping down the rat body. The two domains were allowed to interact using Eulerian-Lagrangian contact. The Eulerian volume fraction was used to assign the elements which were filled with air, partially filled with air, or void of Eulerian material. This initial condition was based upon the surface generated at the interface between the Lagrangian part and the Eulerian material, as defined using an enhanced immersion boundary method. An initial step of 25 ms was conducted

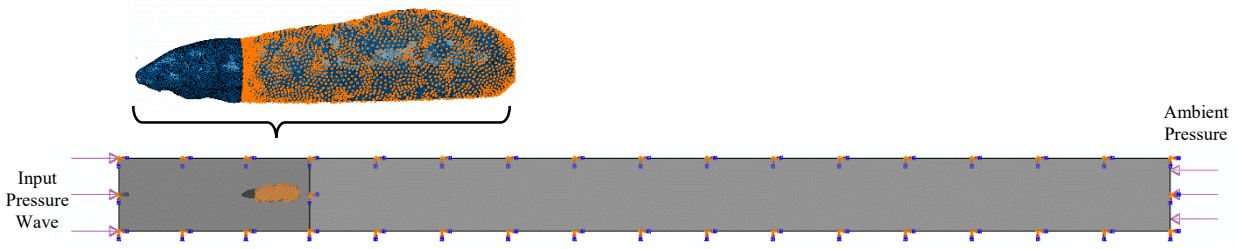


Figure .15. A lateral depiction of the input conditions used to simulate shock loading on the Lagrangian rat head. The shock tube Eulerian mesh is shown in grey. Pink arrows show the pressure loading locations. The left face, the opening of the shock tube model, is loaded with the pressure profiles shown in Figure 3. The right face is loaded with a constant pressure equivalent to the ambient pressure conditions. The orange and blue arrows indicate that a face is constrained in all degrees of freedom. This boundary condition was applied to the rat body, as shown in the above enlarged depiction of the Lagrangian model, and the walls of the Eulerian instance.

to initialize the system and to resolve this boundary condition, allowing the system to reach homeostasis (Abaqus/Explicit). During this step, the shock tube walls and the shock tube opening were constrained against all translational degrees of freedom. The exit of the shock tube experienced a distributed pressure load equal to ambient pressure (102.3 kPa).

At the end of this step, an explicit dynamic analysis was conducted to simulate the shock. These boundary conditions are summarized in Figure 15. The shock tube opening was subjected to a time-varying pressure load. This pressure load was calculated from the experimental pressure measurements taken at the location of the simulated shock tube opening. Eight pressure measurements were taken for each overpressure (four animals and two blasts per animal). The signals were normalized for arrival time and the mean profile was taken. To ensure that the simulation was not affected by experimental variability, experimental consistency was examined.

The average input pressure profiles used are depicted in Figure 16 with one standard deviation. As in the previous step, the translational degrees of freedom of the shock tube walls were constrained and the exit of the shock tube was subjected to a pressure load equal to ambient pressure.

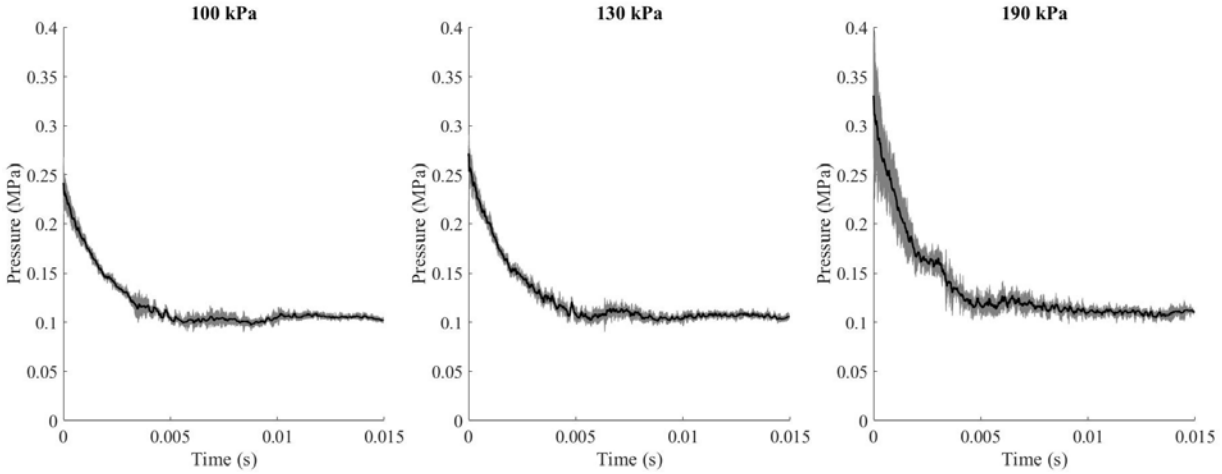


Figure .16. Input pressure profiles used in the simulation of the shock wave. The mean pressures are depicted in black and the standard deviation is included in grey.

Field variables were sampled from the solution at a variable sampling rate. This was done to ensure that adequate resolution was obtained in the solutions. The sampling rates is described in Table 2. From these points, it was found that the shock wave hit the rat head at 0.818, 0.807, and 0.780 ms, for the 100, 130, and 190 kPa blasts, respectively.

Table 2 The time points from which the simulation output was sampled.

Step:	Start Time (Step)	End Time (Step)	Start Time (Total)	End Time (Total)	Sampling Rate
Initialization	0 ms	25 ms	0 ms	25 ms	800 Hz
Shock	0 ms	0.78 ms	25 ms	25.78 ms	5 kHz
	0.78 ms	0.98 ms	25.78 ms	25.98 ms	1 MHz
	0.98 ms	5 ms	25.98 ms	30 ms	100 kHz
	5 ms	88.25 ms	30 ms	113.25 ms	10 kHz

Pressure Maps

The pressure within the rat brain was mapped temporally in Figures 4-6. To give perspective on the magnitude of the observed intracranial pressures, pressure values are reported as a multiplicative factor to the blast overpressure. For the lowest blast overpressure simulated, 100 kPa, the maximum pressures observed were on the order of three times higher than the blast overpressure (a maximum pressure of 300 kPa, Figure 17). The pressure begins to develop in the anterior region of the brain, beginning in the olfactory bulb, 64 μs, 51 μs, and 54 μs after the wave begins interacting with the headform for the 100, 130, and 190 kPa blast. This generates a pressure wave which traverses the brain which is of a lower magnitude, closer to the value of the incident waveform, indicated by a multiplier value of 1. This waveform traverses the brain very uniformly, followed by an underpressure in the anterior brain. The locations which see the highest intracranial pressures occurred in the brainstem in all blast overpressures. These high pressures are observed, in each case, over 1 ms after the shock wave has passed over the specimen. This location of interest, posterior to the cerebellum in the brain stem, is the location in which the brainstem passes through

the foramen magnum. It was found that the pressure is transmitted through the skull and loads the brainstem with an additional pressure wave. Additionally, it can be observed that the pressure wave results in an oscillatory pressure. The pressure wave develops shortly after the shock wave interacts with the specimen, can be observed to decay approximately around 3-4 ms after the shock wave interacts with the specimen, and then increase again after 12.5 ms.

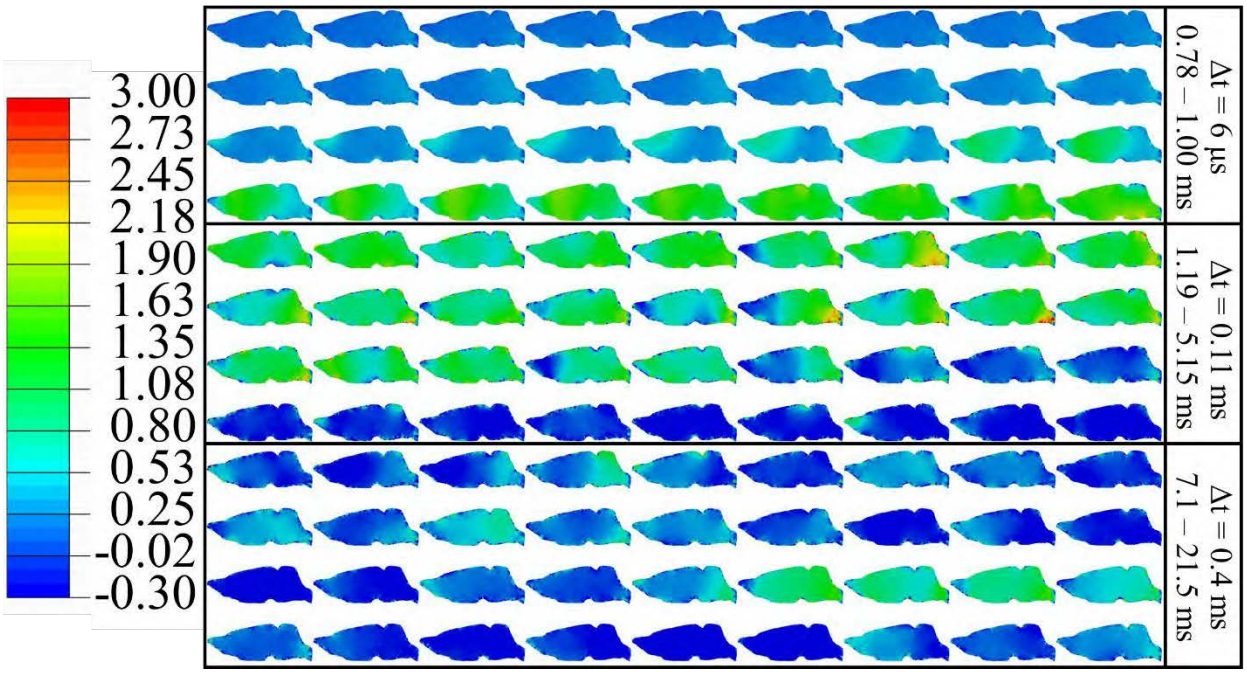


Figure .17. A temporal pressure map, reported as a multiple of the incident overpressure, of the mid-sagittal cut of a rat brain over the course of a 100 kPa shock wave. The earliest time point is in the upper left corner and time progresses at the time step Δt, moving left to right from the top to the bottom.

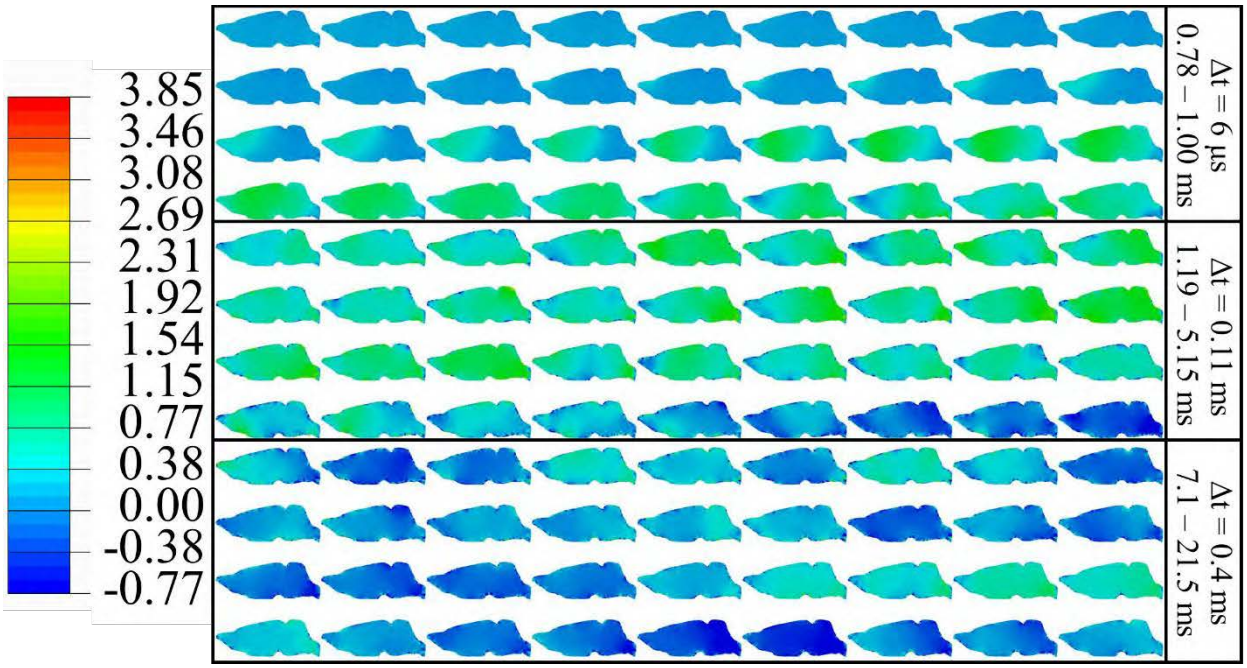


Figure .18. A temporal pressure map, reported as a multiple of the incident overpressure, of the mid-sagittal cut of a rat brain over the course of a 130 kPa shock wave. The earliest time point is in the upper left corner and time progresses at the time step Δt, moving left to right from the top to the bottom.

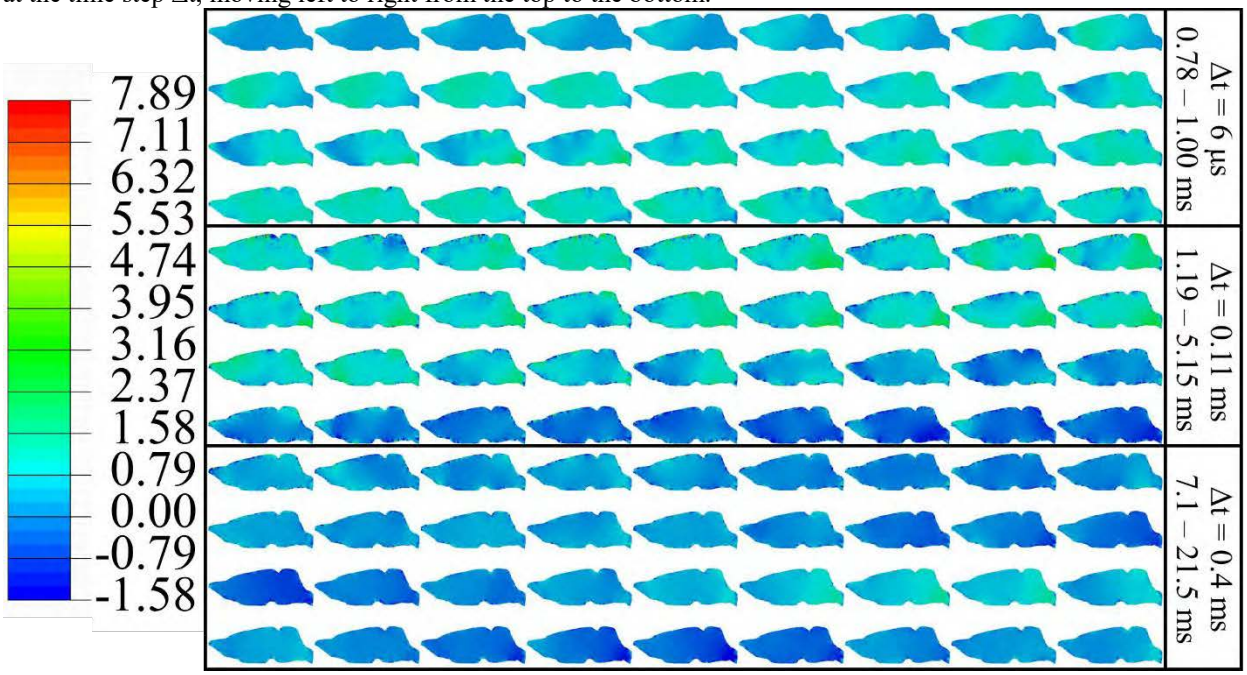


Figure .19. A temporal pressure map, reported as a multiple of the incident overpressure, of the mid-sagittal cut of a rat brain over the course of a 190 kPa shock wave. The earliest time point is in the upper left corner and time progresses at the time step Δt, moving left to right from the top to the bottom.

Stress Distribution

Figures 7-9 detail the temporal evolution of the von Mises stress in the mid-sagittal plane of a rat head for a 100, 130, and 190 kPa shock wave, respectively. The von Mises stress is reported in values of kPa. When comparing the spatial variation of the von Mises stress with the pressure waves in Figures 4-6, it is apparent that the von Mises stress is more diffuse and is of a lower magnitude than that of the pressure wave. The initial pressure wave does not appear to significantly induce a von Mises stress and peak von Mises stresses are not observed until the time point in which the pressure wave passes through the skull and loads the brainstem through the foramen magnum. Additionally, the von Mises stresses develop more at the periphery of the brain, converging toward the center of the brain. This supports the hypothesis that the skull is loading the brain with additional pressures and stresses. The development of the von Mises stresses in the brain appears to occur around the same time point as the pressure decay. However, this does not appear to have any correlation with the secondary increase in pressure observed in Figures 17-19. The magnitudes of the maximum von Mises stresses were not found to scale linearly with blast overpressure. When normalized with respect to the incident pressure wave, the maximum von Mises stresses for a 100, 130, and 190 kPa overpressure are 1.20, 1.46, and 1.58, respectively. These peak von Mises stresses appears to be greater on the ventral side of the brainstem.

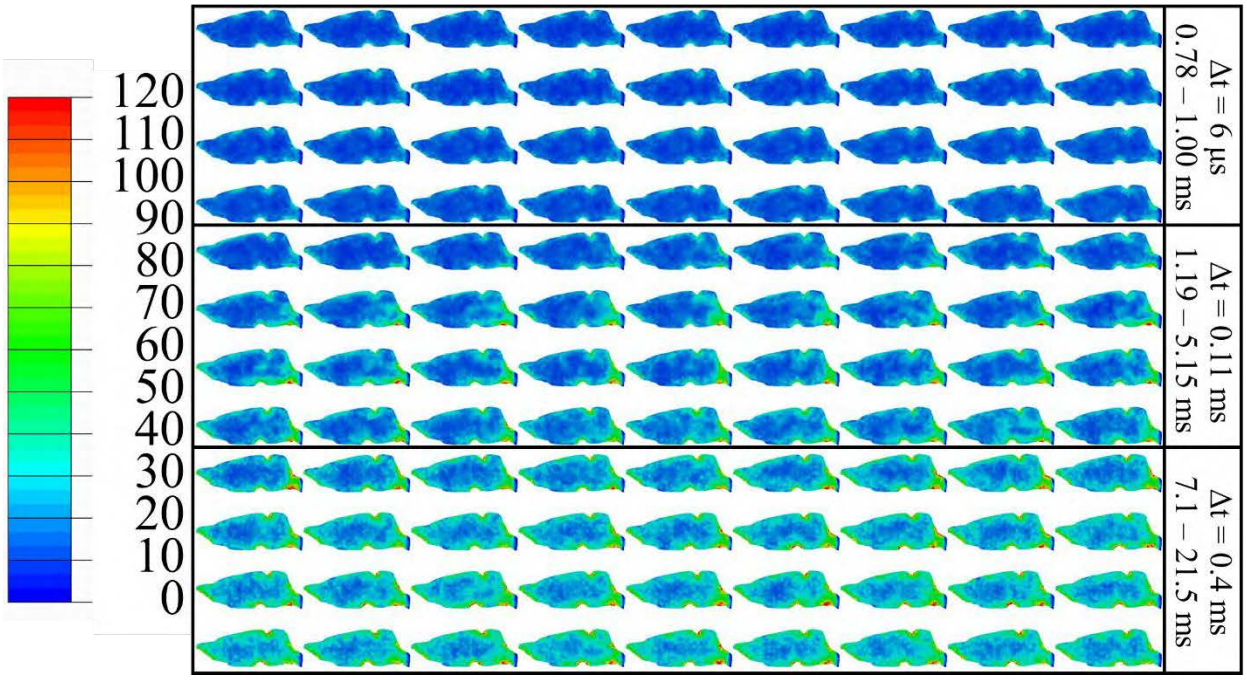


Figure .20. A temporal von Mises stress map, given in kPa, of the mid-sagittal cut of a rat brain over the course of a 100 kPa shock wave. The earliest time point is in the upper left corner and time progresses at the time step Δt, moving left to right from the top to the bottom.

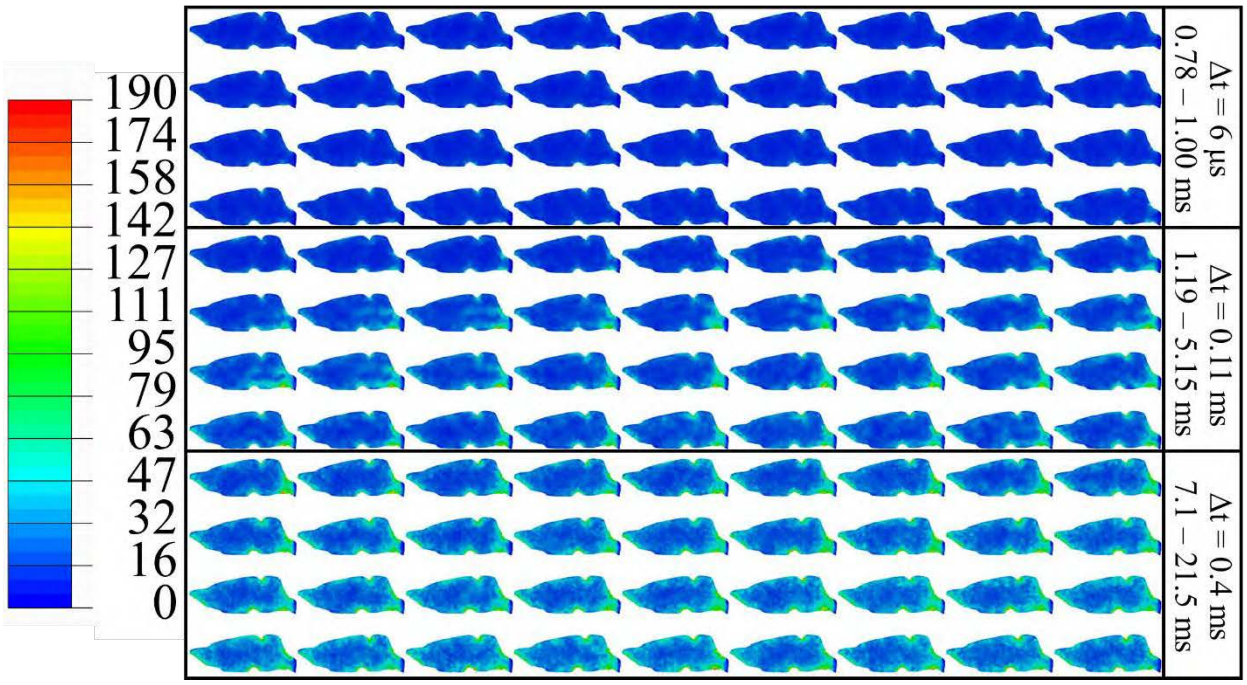


Figure.21. A temporal von Mises stress map, given in kPa, of the mid-sagittal cut of a rat brain over the course of a 130 kPa shock wave. The earliest time point is in the upper left corner and time progresses at the time step Δt, moving left to right from the top to the bottom.

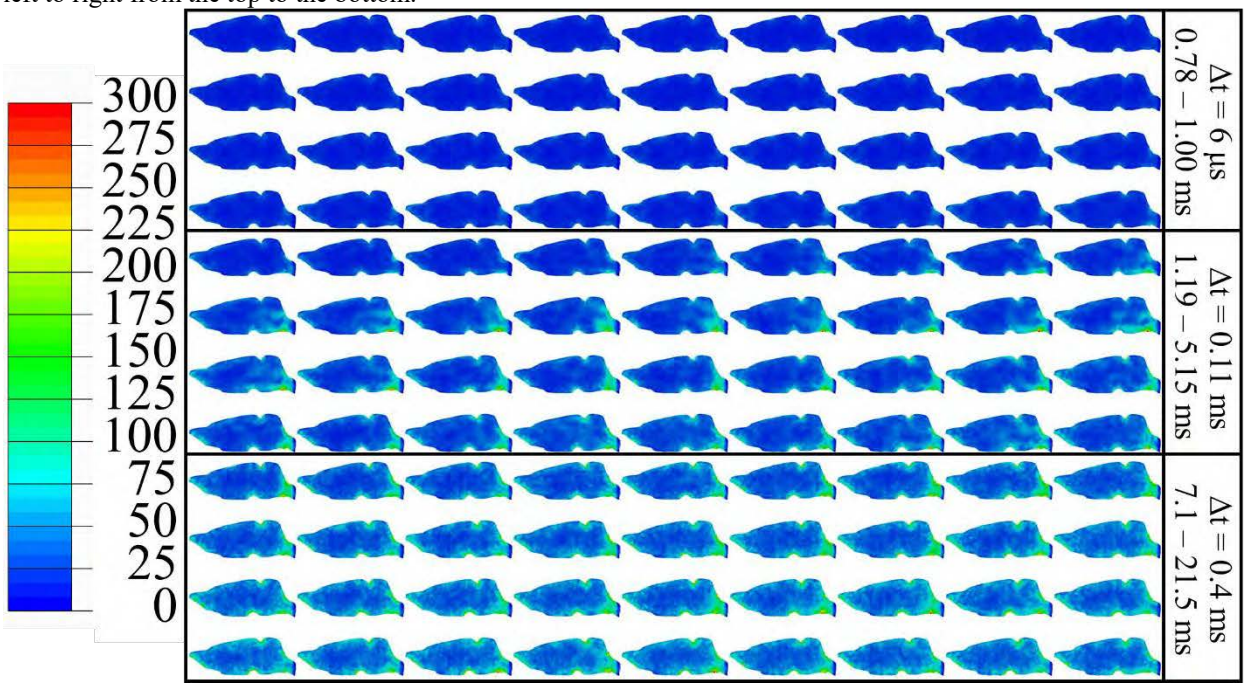


Figure.22. A temporal von Mises stress map, given in kPa, of the mid-sagittal cut of a rat brain over the course of a 190 kPa shock wave. The earliest time point is in the upper left corner and time progresses at the time step Δt, moving left to right from the top to the bottom.

Strain Distribution

The temporal evolution of the maximum principal logarithmic strain in the mid-sagittal section of the rat brain is reported in Figures 23-25 for a 100, 130, and 190 kPa blast overpressure. When comparing the appearance of the strain maps with the pressure wave maps and the von Mises stress maps, it is apparent that the strain map more closely matches the diffuse nature of the von Mises stress. The pressure wave causes no notable strains to develop and the maximum strains were also observed at the posterior brainstem. It can be observed that the strains appear to be more pronounced on the ventral side of the brainstem, as seen in Figures 20-22 with the von Mises stresses. Additionally, the pattern of strain development closely follows that observed with the von Mises stresses. The strain pattern does not appear to be influenced by the passing of the initial pressure wave. The initial development of strains within the brain appear to occur shortly after the pressure wave begins to decay, but no apparent correlation is observed with the secondary pressure increase. The magnitude of the maximum logarithmic strain was found to increase with increased blast overpressure.

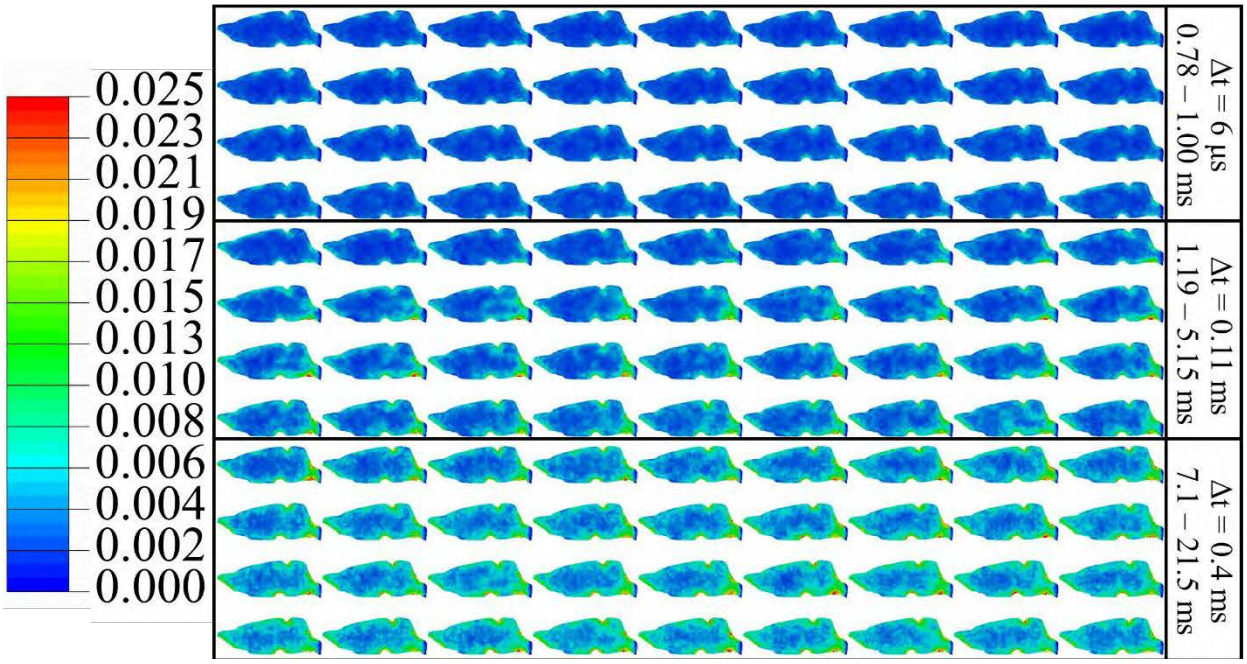


Figure.23. A temporal maximum principal logarithmic strain map of the mid-sagittal cut of a rat brain over the course of a 100 kPa shock wave. The earliest time point is in the upper left corner and time progresses at the time step Δt, moving left to right from the top to the bottom.

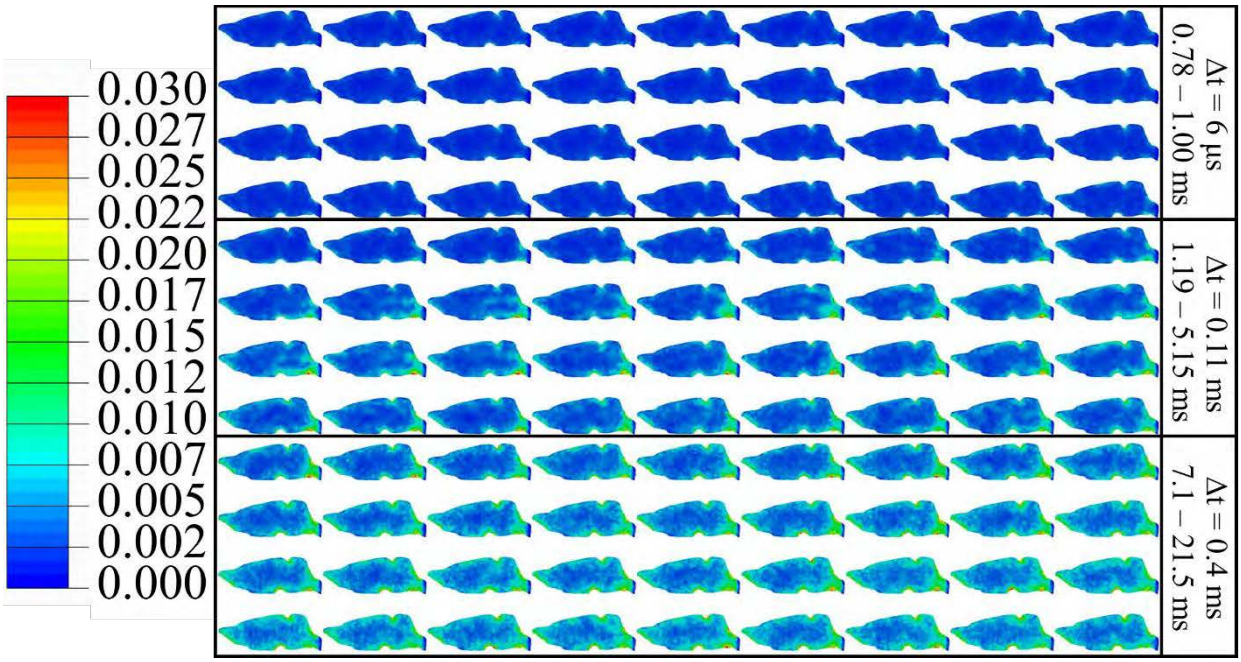


Figure.24. A temporal maximum principal logarithmic strain map of the mid-sagittal cut of a rat brain over the course of a 130 kPa shock wave. The earliest time point is in the upper left corner and time progresses at the time step Δt, moving left to right from the top to the bottom.

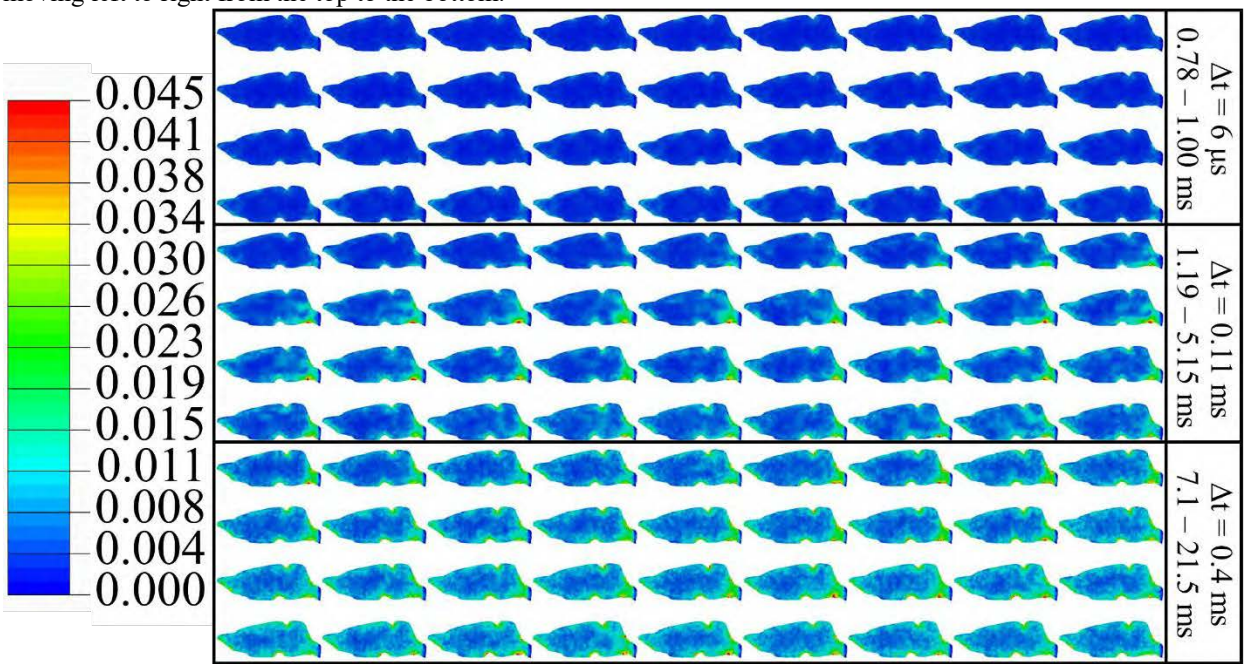


Figure.25. A temporal maximum principal logarithmic strain map of the mid-sagittal cut of a rat brain over the course of a 190 kPa shock wave. The earliest time point is in the upper left corner and time progresses at the time step Δt, moving left to right from the top to the bottom.

Reconstruction of Sensor Locations

To support model validation efforts, the locations of the ICP sensors were ascertained using micro-CT. After shock exposure and sacrifice, the test subjects were preserved in 4% paraformaldehyde for later imaging. The scans were taken with an image pixel size of 32.5 μm (SkyScan 1275, Bruker microCT), reconstructed (NRecon Reconstruction, Brucker microCT), and segmented into a solid mask (Simpleware ScanIP, Synopsys). These locations were scaled with respect to size of the cranial cavity and compared between the nine specimens. This highlighted the reproducibility of the experimental protocol. These locations were then selected to be the regions of interest from the simulation results when examining the local intracranial pressures, von Mises stresses, and the maximum principal logarithmic strains. The scaled sensor locations for the left, anterior and right, posterior sensors are included in Figure 26. It was observed that consistent spacing was maintained between the left, anterior and right, posterior sensors for all test subjects. The reconstructed images are included in Figures 27-35.

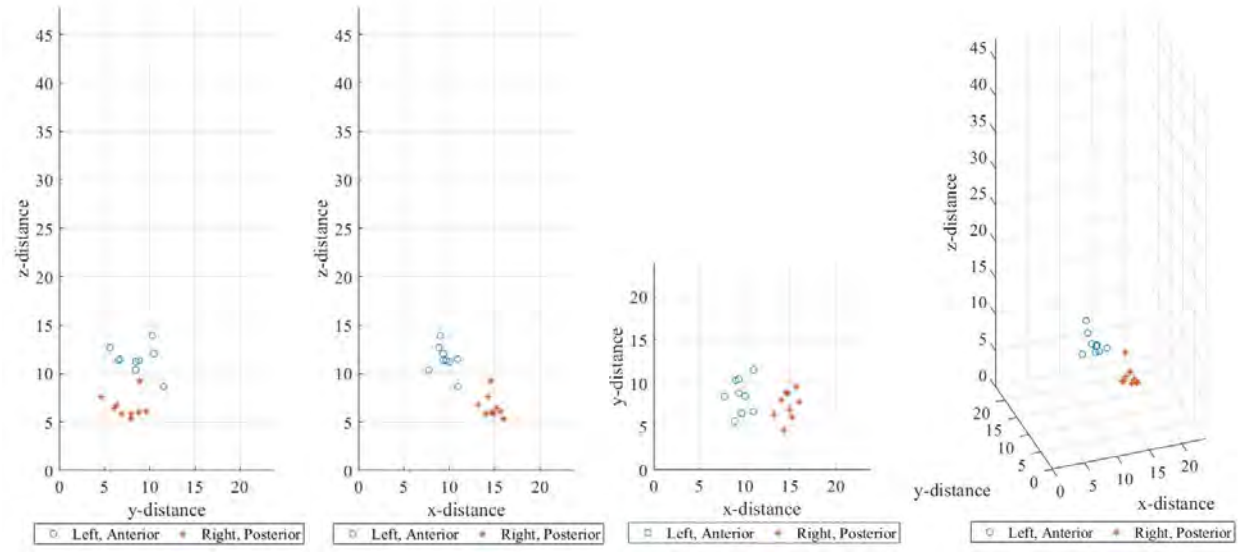


Figure .26. The sensor locations taken from micro-CT scans of the rat head. The field of view and the sensor locations are normalized to the dimensions the average skull size. Values of x-, y-, and z- distance are in mm.

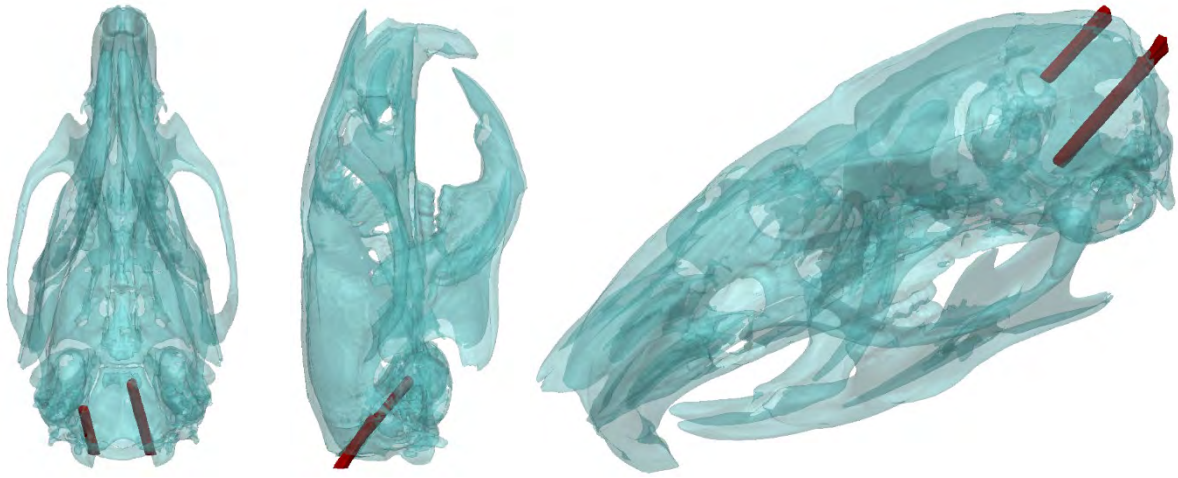


Figure.27. A depiction of the sensor location within test specimen 1 with a cranial, lateral, and isometric view. The skull is shown in blue and the cannulas are shown in red. This specimen was used in Task 2.



Figure.28. A depiction of the sensor location within test specimen 2 with a cranial, lateral, and isometric view. The skull is shown in blue and the cannulas are shown in red. This specimen was used in Task 2.

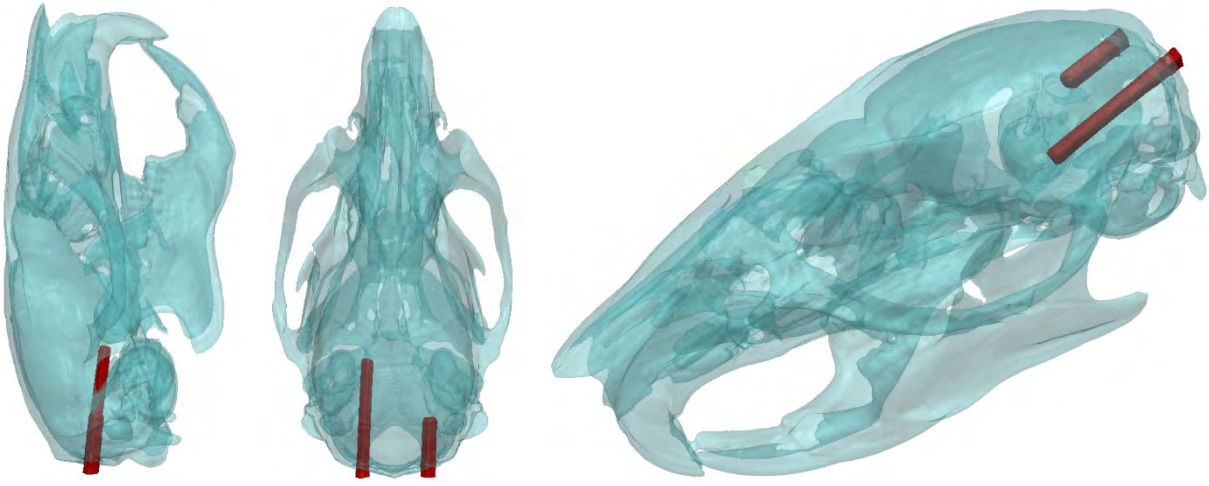


Figure.29. A depiction of the sensor location within test specimen 3 with a cranial, lateral, and isometric view. The skull is shown in blue and the cannulas are shown in red. This specimen was used in Task 2.

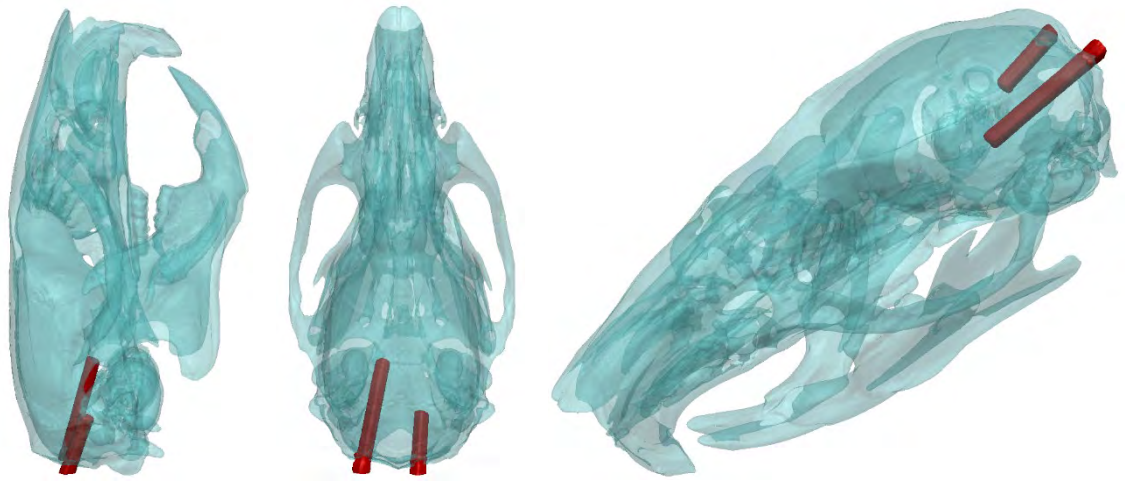


Figure.30. A depiction of the sensor location within test specimen 4 with a cranial, lateral, and isometric view. The skull is shown in blue and the cannulas are shown in red. This specimen was used in Task 2.

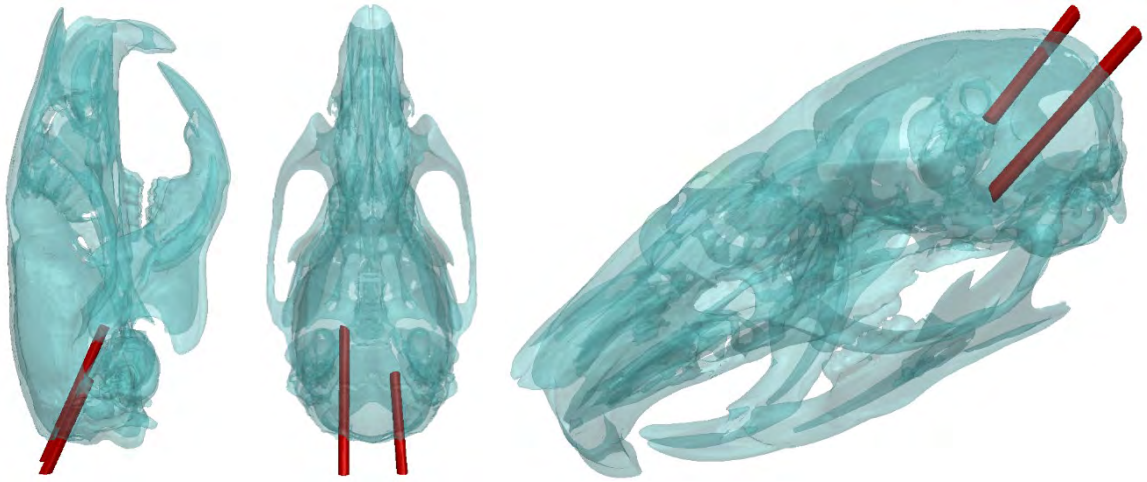


Figure.31. A depiction of the sensor location within test specimen 5 with a cranial, lateral, and isometric view. The skull is shown in blue and the cannulas are shown in red. This specimen was used in Task 8.

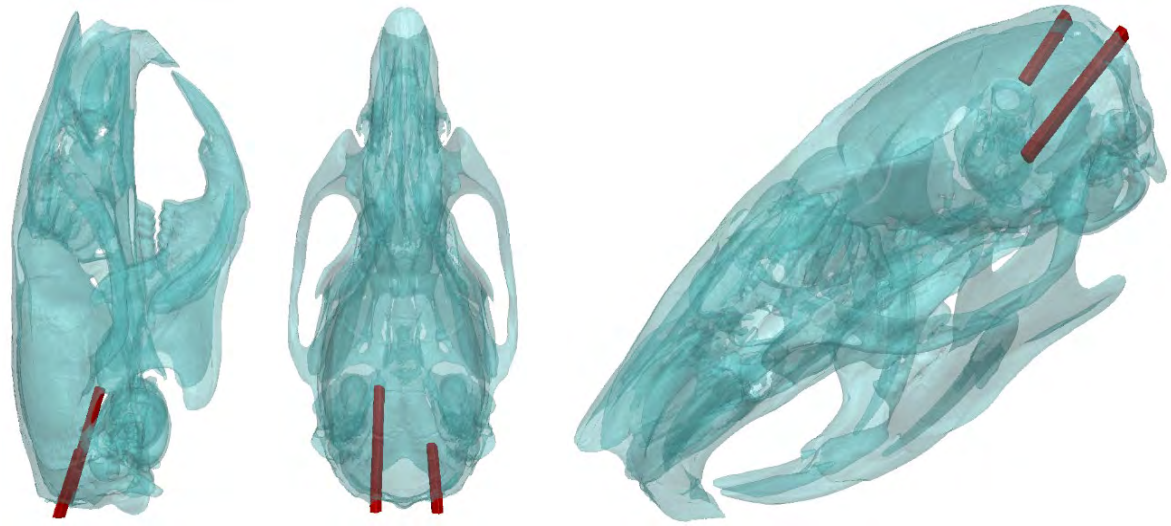


Figure.32. A depiction of the sensor location within test specimen 6 with a cranial, lateral, and isometric view. The skull is shown in blue and the cannulas are shown in red. This specimen was used in Task 8.

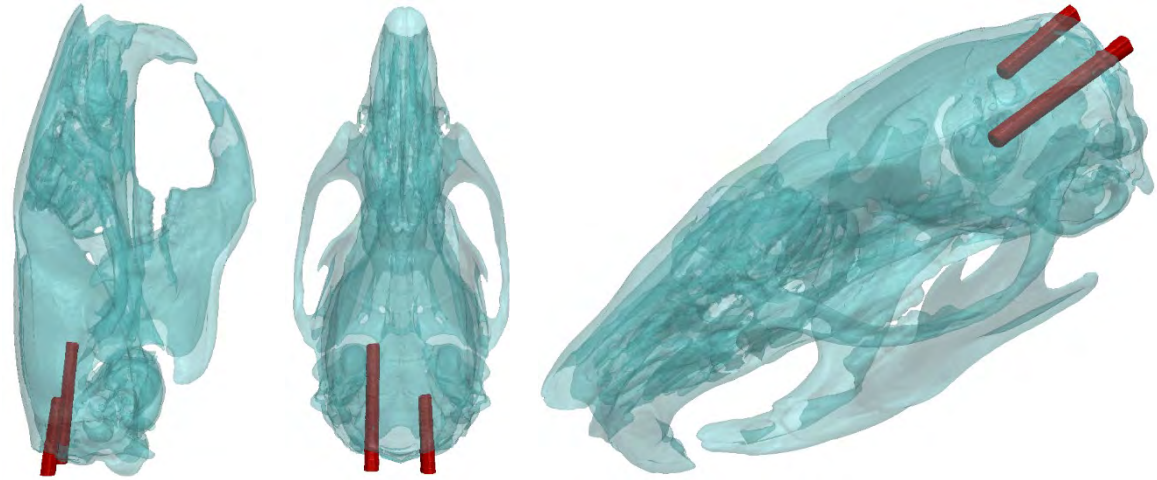


Figure.33. A depiction of the sensor location within test specimen 7 with a cranial, lateral, and isometric view. The skull is shown in blue and the cannulas are shown in red. This specimen was used in Task 8.

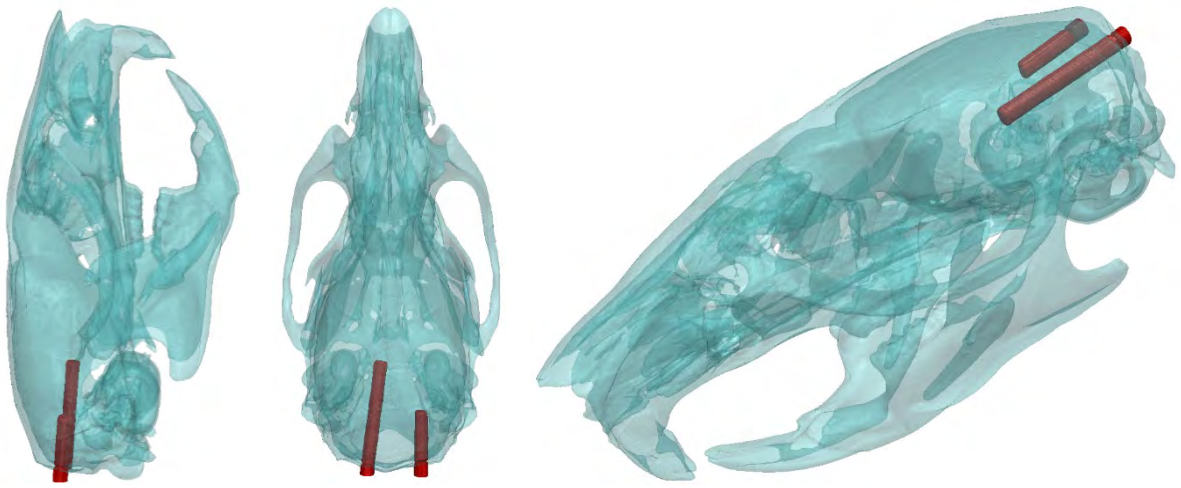


Figure.34. A depiction of the sensor location within test specimen 8 with a cranial, lateral, and isometric view. The skull is shown in blue and the cannulas are shown in red. This specimen was used in Task 8.

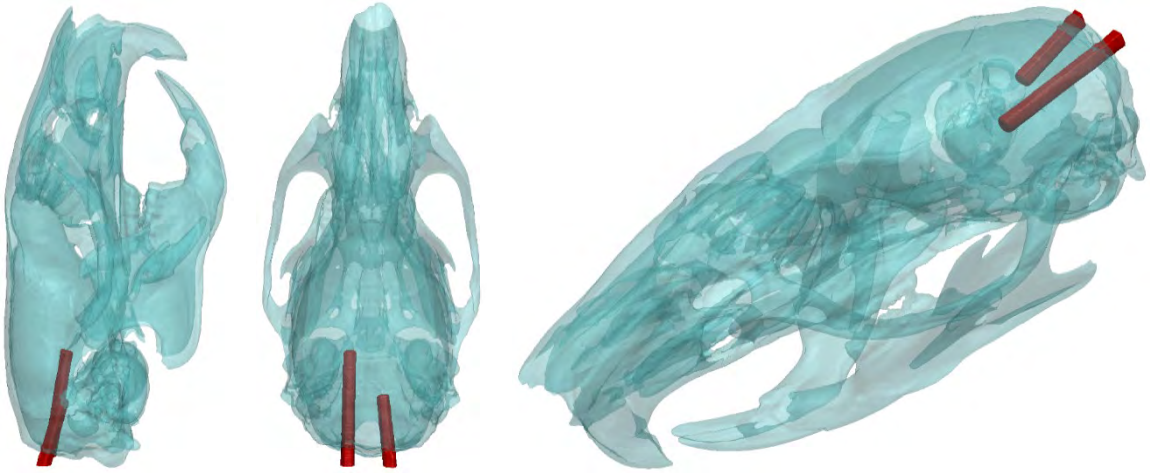


Figure.35. A depiction of the sensor location within test specimen 9 with a cranial, lateral, and isometric view. The skull is shown in blue and the cannulas are shown in red. This specimen was used in numerical simulations planned in the Task 8.

Temporal Relationship Between Mechanical Injury Markers

To compare the temporal evolution of the press, stress, and strain patterns in the rat brain, the normalized pressure, stress, and strain profiles were compared for the 190 kPa blast. Two locations were selected to compare, which correspond with the experimental ICP sensor locations. These locations, A and B, were selected to be the nodes which are closest to the sensor locations identified from micro-CT reconstruction of the rat skull/cannula complex. Location A was the sensor in the anterior left hemisphere and location B was the sensor in the posterior right hemisphere. The field variable outputs were plotted together, transformed to begin at zero when the shock loading step begins (t = 25 ms) and normalized with respect to the maximum value. This comparison is shown in Figure 36. It can be observed that the von Mises stress and the maximum principal logarithmic strain develop in the more anterior location earlier. Additionally, the increase of the von Mises stress and the logarithmic strain appears to coincide with the decrease of the intracranial pressure.

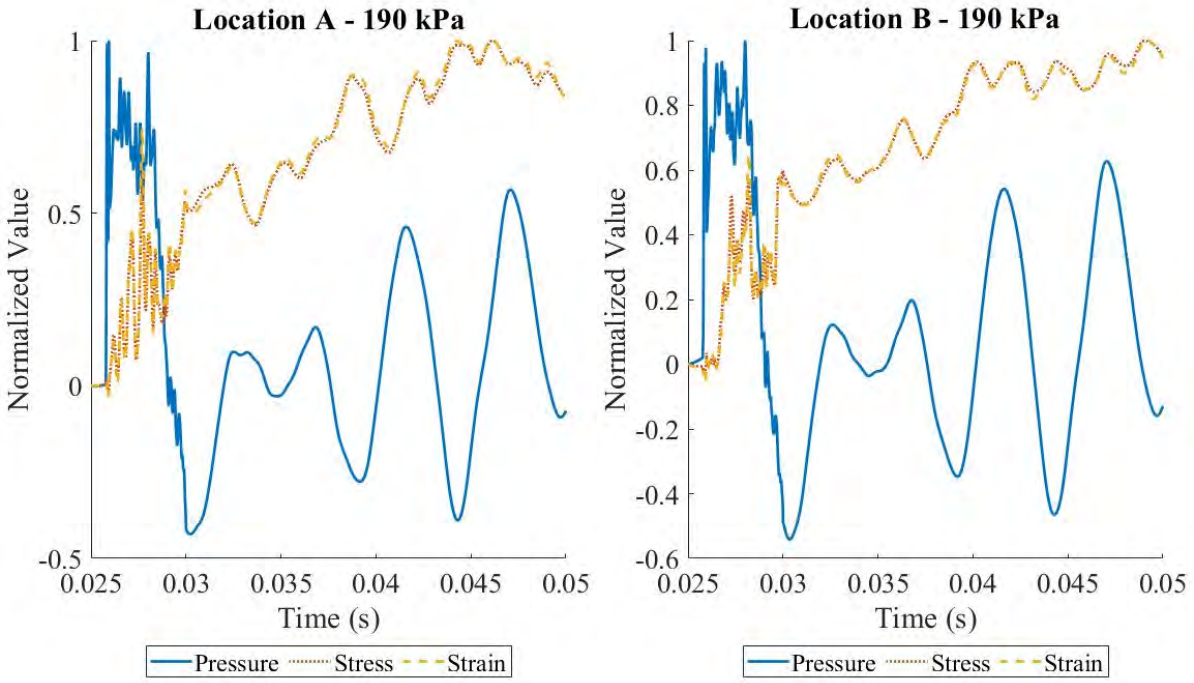


Figure.36. The transformed and normalized intracranial pressure, von Mises stress, and the maximum principal logarithmic strains at the left, anterior sensor location (A) and the right, posterior sensor location (B).

Task 4. Evaluate the Lung Injuries Caused by Blast Exposure

Animals tested in prone position have their abdomen partially protected from the blast wave by the aluminum holder used in our experiments.[6, 14] Extracted lungs has visible signs of hemorrhage, especially at higher blast overpressures, and were assessed via histology (fig. 37). Quantification of the lung injury was performed and the observed levels of pulmonary injury

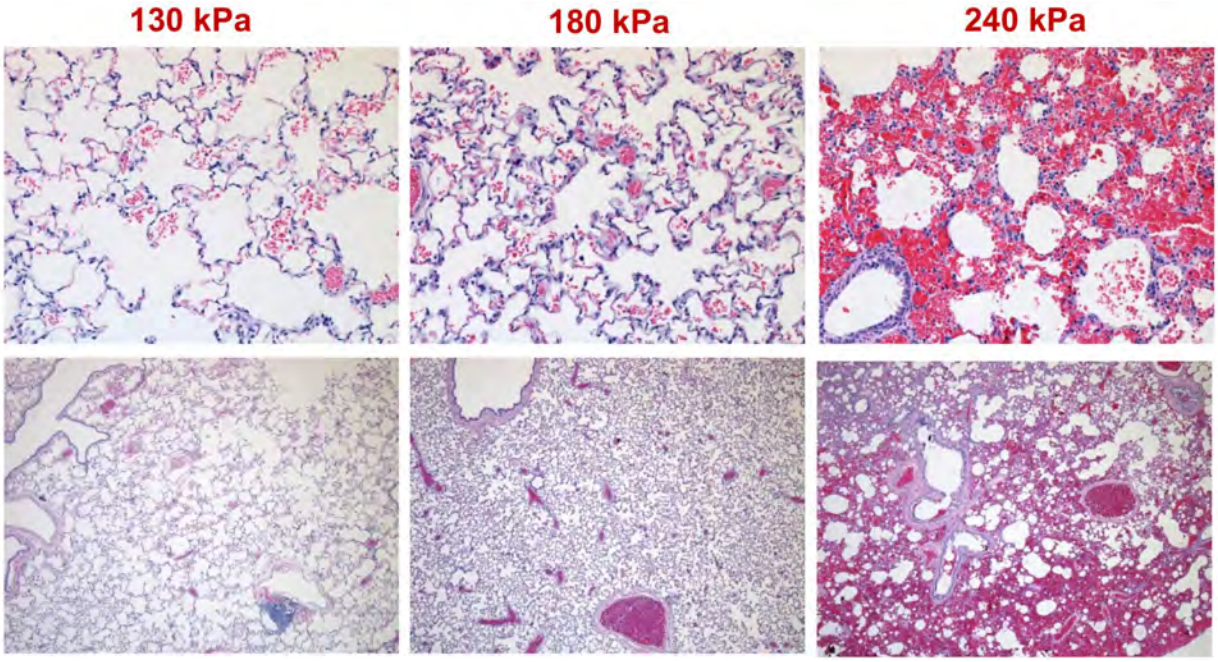


Figure.37. Histological evaluation of blast injured lung tissue via H&E staining (20x (top) and 4x (bottom) magnification). Three sections of lung are examined: the right cranial, right caudal, and left middle lung lobes. **130 kPa:** Multifocal, small groups of alveoli are partially filled with very small pools of acute hemorrhage. **180 kPa:** Minimal, multifocal pools of acute hemorrhage characterized by partial filling of small groups of alveoli by blood. **240 kPa:** Mild multifocal pools of acute hemorrhage which partially fill alveoli. The hemorrhage in this lung is more severe than the other three rats examined and in a few foci, the hemorrhage is slightly more extensive and fills medium-sized groups of alveoli. The largest foci of hemorrhage are between 1-2 mm in length.

expressed using Yelveton's scoring system[8] revealed a low level of injury (fig. 38). However, we observed an increasing trend of injury score with increasing peak overpressure and impulse. We observed only a few cases where pathological score exceeded 21 for the blast strength higher than 300 kPa BOP with high standard deviations (fig. 38C). A score of 21 is considered as a cut-off threshold for mild pulmonary injury.[8] The pathological score at 50% Predicted Mortality Rate (PMR)[14] (at 260 kPa) was found to be less than 10, while the score was less than 4 in the 60 - 190 kPa range. Moreover, there are six animals which died as a result of blast exposure and had no lung injury (score of zero, fig. 38C, D). These results suggested minimal pulmonary injuries and thus, we conclude lung injury is not a viable indicator of PMR.

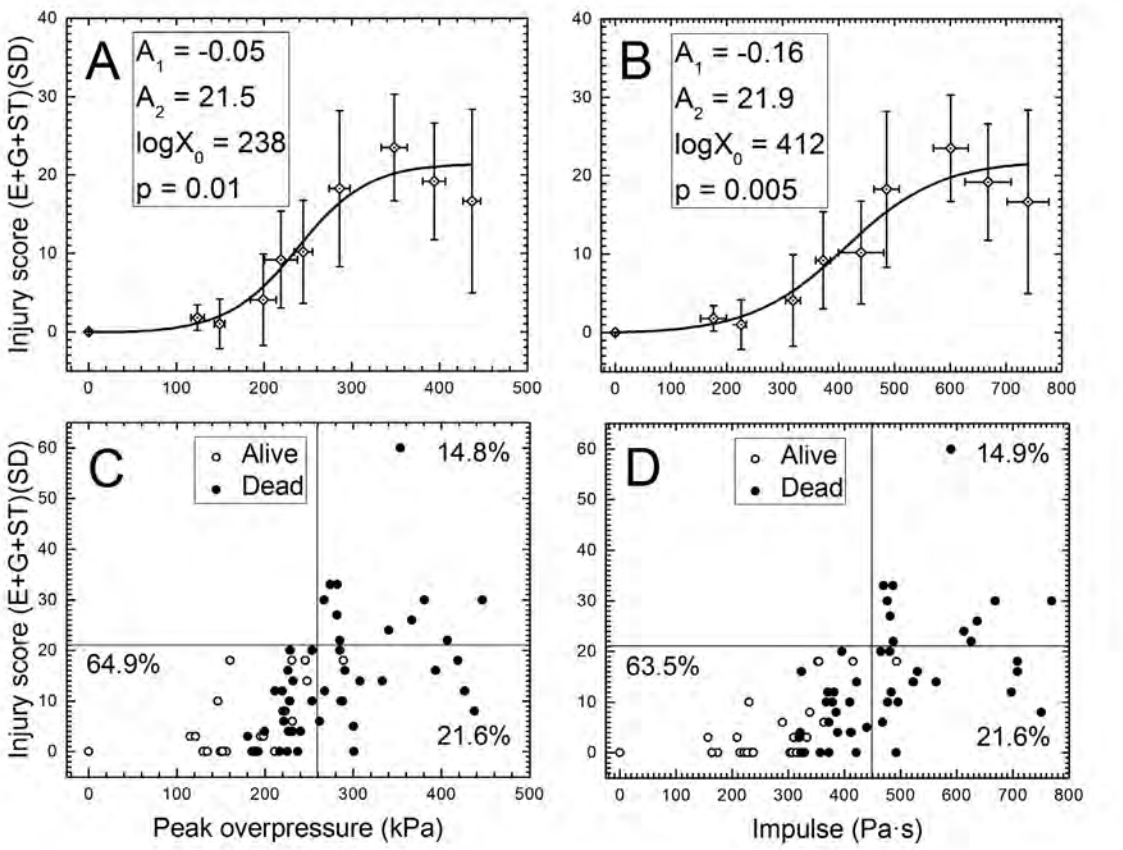


Figure.38. Lung injury scores for rats exposed to a single blast. The dose-response model was used to fit the IS as a function of peak overpressure (A, C) and impulse (B, D). The scattergrams (C, D) illustrate individual scores and their distribution among the cohort of 75 rats evaluated in this test. The value of 21 is the upper limit of the slight lung injury level as defined by Yelverton. The vertical lines (peak overpressure of 260 kPa (C), or impulse of 450 Pa·s (D)) correspond to 50% predicted mortality rate according to the dose-response model in fig. 37. There are six animals which died after the blast and had no apparent lung injuries (score of zero).

Task 5. Assess Extent of Oxidative/Nitrosative Stress, BBB damage and Neuroinflammation

5.1 Induction of oxidative/nitrosative stress markers

Using our logistic regression risk injury model, we defined the upper level of mTBI at 145 kPa

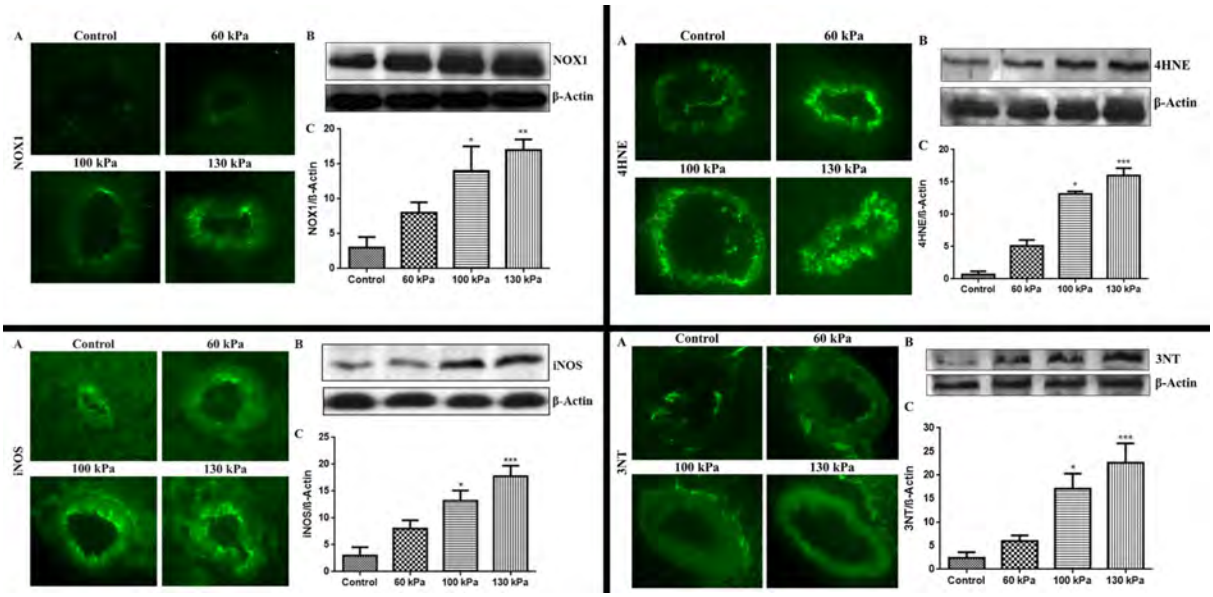


Figure 39. Mild TBI range of blast-wave exposure induces NADPH oxidase 1 (NOX1), inducible nitric oxide synthase (iNOS), 4-hydroxynonenal (4HNE) and 3-nitrotyrosine (3NT) expression in rat brain microvessels. (A) A representative of immunofluorescent staining of specific marker as indicated on the Y-axis in intact microvessels of brain cross sections from rats subjected to a single exposure to 60, 100, or 130 kPa peak overpressure, and control. (B) Corresponding Western blot specific marker (as indicated on the Y-axis) and housekeeping protein, β-actin. (C) The quantification of the results of the immunoreactive fluorescence intensities. Values are mean ± SEM (n = 4) with p-value ≤ 0.01 compared with control.

BOP as 5% PMR. We examined the oxidative/nitrosative injury and the BBB integrity in the range of 60 kPa to 130 kPa peak overpressures and determined lower threshold of mTBI at 80 kPa. These markers were evaluated 24 hours after the injury, at a time point which proved in our previous study to yield their maximum levels in analogous bTBI model[15]. We first evaluated the induction of free radical generating enzymes NADPH oxidase (NOX1) and inducible nitric oxide synthase (iNOS) in the brain capillary cross section tissues. We found that blast-wave exposure significantly up-regulated the induction of NOX1 with 100 kPa (p= 0.02) and 130 kPa (p= 0.001) BOP (fig. 39, left upper panel). Similarly, iNOS expression was increased at 130 kPa BOP (p= 0.0005) and at 100 kPa BOP (p=0.04) (fig. 39, left lower panel). Induction of NOX1 and iNOS produces superoxide and nitric oxide respectively, which will also react together to form peroxynitrite, a more reactive free radical. The oxidative/nitrosative damage is a post-oxidant production event. Proteins adducted with 4-hydroxynonenal (4HNE, oxidative stress marker) or 3-nitrotyrosine (3NT, nitrosative stress marker) are used for assessing the extent of injury in the tissue. In parallel with the induction of NOX1 and iNOS enzymes, we found that the level of oxidative damage signature 4HNE (fig. 39, right upper panel) is increased in mTBI range exposure with 100 kPa (p= 0.05) and 130 kPa (p= 0.0004). Similarly, 3NT (fig. 39, right lower panel) was found to be increased with the mTBI range exposure (100 kPa BOP, p= 0.04 and 130 kPa BOP, p= 0.002).

5.2 Disruption of the BBB integrity

The capillary oxidative/nitrosative damage might lead to BBB disruption, and thus we evaluated the alterations of tight junction (TJ) proteins claudin-5, occludin and zonula occluden 1 (ZO-1). TJ proteins are the primary functional barrier biomolecules of the BBB. A reduction in TJ protein levels or disruption of the architectural structure of any TJ protein is expected to impair BBB integrity, thereby enhances the chance of immune cell infiltration into the brain for initiation of neuroinflammation.

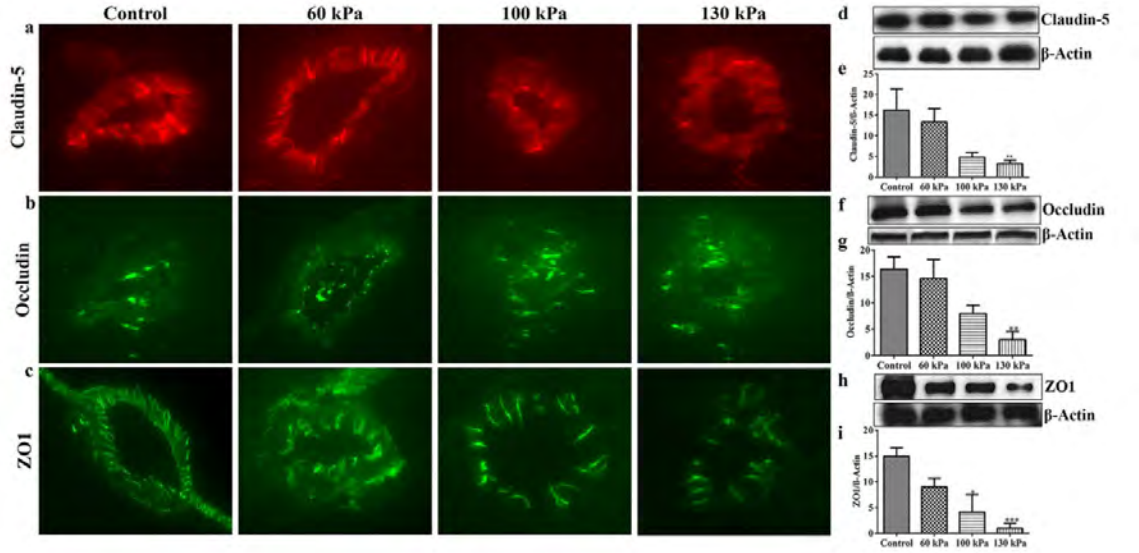


Figure 40. Oxidative/nitrosative damage of capillaries impaired BBB integrity by disrupting the tight junction proteins. (A). A representative of immunofluorescent staining of TJ protein Claudin-5 (a), Occludin (b), and zonula occluden 1 (ZO-1, c) in capillaries of whole brain cross-sections in control and blast exposed animals. (B). Corresponding Western blot and bar graphs showing the quantification of respective immunoreactive fluorescence intensity of Claudin-5 (d, e), Occludin (f, g), and zonula occluden 1 (h, i). Values are mean ± SEM, (n = 4), and asterisk indicates each blast intensity compared with control where level of statistical significance was achieved ($p < 0.05$).

Interestingly, our results showed that mTBI range of blast-wave exposure decreased the levels of claudin-5 (130 kPa, $p = 0.001$) (fig.40 a, d, e), occludin (130 kPa, $p= 0.002$) (fig. 40b, f, g) and ZO-1 (100 kPa, $p = 0.03$; 130 kPa, $p = 0.0007$) (fig. 40 c, h, i) proteins in brain tissue sections. These data suggest possible leakiness of the BBB and it might result in neuronal inflammation around the perivascular region of the brain.

5.3 Assessment of BBB leakage

To assess this BBB leakiness and neuronal injury, we examined the leaking out of neuronal-specific enolase (NSE) into the blood samples of tissues exposed at BOP of 60, 100 and 130 kPa versus control animals. In agreement with a decrease in BBB integrity, we observed elevation of NSE levels in blood samples exposed to blast compared with controls (fig. 41). The glycolytic enzyme enolase is a dimeric isoenzyme and also known as neuronspecific enolase (NSE-aa, ag and gg), as these isoenzymes were initially detected in neurons and neuronendocrine cells. However, in other pathological conditions such as small cell lung cancer and neuroblastoma, NSE exhibits a signatory value in disease detection and progression. In the absence of such pathological status or stimuli, as in our experimental setup, NSE detection in plasma samples establishes BBB leakage in primary bTBI.

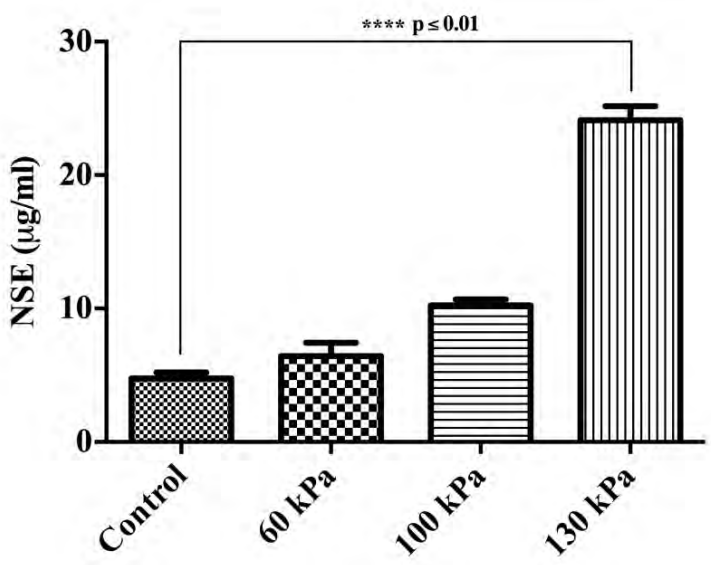


Figure. 41. The neuronal damage marker leakage into serum is facilitated by BBB disruption. ELISA results show the levels of neuronal specific enolase (NSE) in rat blood serum collected from a single blast exposure at 60, 100 and 130 kPa. Blood samples were collected at the time of sacrifice after 24-hour post blast exposure. Values are mean ± SEM, n=4. Statistical significance ($p < 0.01$) compared with control was observed at130 kPa as the lowest blast intensity.

5.4 A single blast induces cell-type dependent increase in NADPH oxidase isoforms

We have performed characterization of the spatial variations and cellular distribution of NADPH oxidase 1 (NOX), a superoxide (a free radical) producing enzyme in different vulnerable brain regions (Frontal cortex, Striatum, Somatosensory barrel cortex, hippocampus and thalamus) at moderate blast-over pressure (180 kPa) at 4 hours post-exposure.

The NADPH oxidase (NOX) is a multi-subunit enzyme that catalyzes the reduction of molecular oxygen and oxidation of NADPH to generate superoxide radicals ($O_2^{\bullet -}$). Extensive experimental evidence suggests NOX plays a significant role in the pathophysiology of various forms of TBI. While studies establish a primary role of NOX1 in the pathophysiology of various forms of TBI,[15-18] no studies have been performed on the brain spatial and temporal resolution of NOX family of enzymes and their role in the pathophysiology of bTBI. The rationale and hypothesis of our study include that bTBI has a unique pathophysiology (in this instance, oxidative stress) in that the propagation of the shock waves in bTBI and associated blast over pressure uniformly distribute and affect the whole brain. However, pathophysiological outcomes (e.g., NOX changes) in

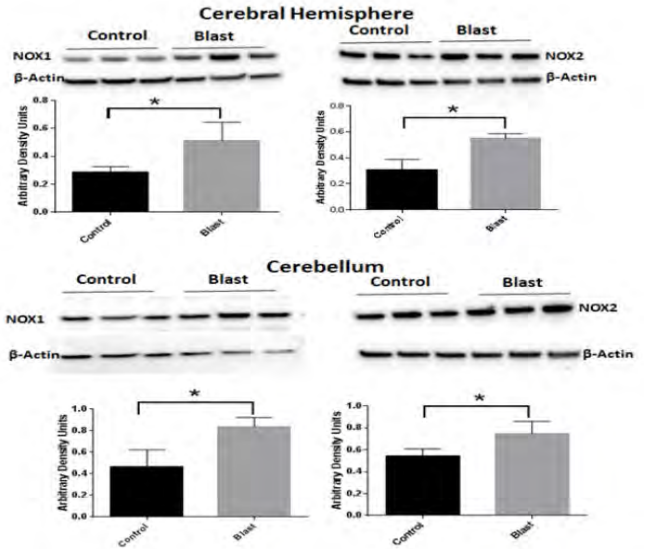


Figure.42. Immunoblot analyses showing increased protein expression of NOX1 and NOX2 isoforms in cerebrum and

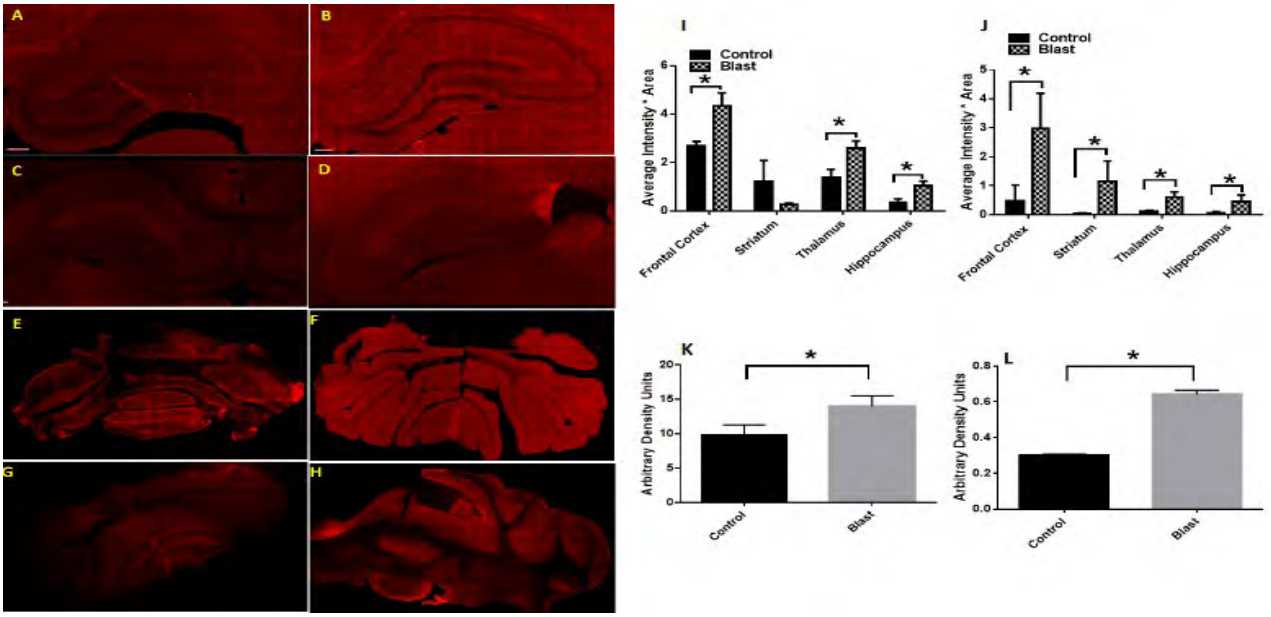


Figure .43. Fluorescence intensities (red channel) of NOX1 in hippocampus from control (A) and blast-injury (B) and NOX2 intensities from control (C) and Blast-injury (D) animals. Cerebellum also displays a greater increase in both isoforms of NOX in injured animals (F, H) compared to controls (E, G).

response to bTBI depend on the differential vulnerability of neural cell types in various brain structures.

Immunoblot analysis of NOX1 and NOX2 in the whole cerebral hemisphere showed a significant increase (87%, and 52%, respectively, $p<0.05$) (Figure 42). In order to assess the diffusive nature of primary blast (shockwave) in the posterior region of the brain, NOX1 and NOX2 protein levels were also determined in cerebellum, and we found that similar to cerebral hemisphere, cerebellar levels of NOX1and NOX2 protein were significantly increased (60% and 40%, respectively,

$p<0.05$) (Figure 42). Different brain regions displayed a differential response in NOX isoform expression. NOX1 levels in the frontal cortex (FC) showed a 49% increase; hippocampus (HC) showed the highest degree of increase (107%) followed by thalamus displaying a 90% increase (Figure 43). The regional variations in the levels of NOX2 are slightly different from that of NOX1. NOX2 levels were highest in frontal cortex (>2 fold) followed by striatum and hippocampus showed the lowest increase (Figure 43).

5.5 Different neural cell types display differential vulnerability to oxidative damage

Cellular vulnerability to oxidative damage (NOX isoform expression) was examined in astrocytes, neurons and microglia by double immunofluorescence staining. Interestingly, neurons display highest amount of the increase in NOX1expression in hippocampus and thalamus and to a lesser extent in the frontal cortex as compared to astrocytes (Figure 44). Primary blast caused diffused pathological changes in not only perpendicular (deeper brain structures, hippocampus, and thalamus) but also the injury spread laterally to the cerebellum. The total tissue levels of NOX1 in the cerebellum not only increased, but this increase was highest in neurons (Figure 44).Such higher increase in NOX expression in neurons indicate that these cells are at higher risk for oxidative damage compared to other neural cells (astrocytes and microglia). Further, greater increased NOX expression in hippocampus and cerebellum also correlate with the known fact that these regions contain highest density of neurons compared to other brain regions.

5.6 Primary blast increases superoxide production in vulnerable brain regions

Superoxide in brain is produced by variety of sources including mitochondrial oxidative phosphorylation as well as by NOX enzymes in the plasma membrane, which are ubiquitously expressed in different brain cells. We measured *in vivo* levels of superoxide by injecting rats with dihydroethidium (DHE) (10 µmol/kg weight) which when reacts with superoxide becomes hydroethidium. The fluorescence levels of hydroethidium in different brain regions were measured 4 h after blast injury by capturing images using Leica Aperio Versa 1000 fluorescent microscope and slide scanner. The fluorescent intensities were quantitated by using AreaQuant FL algorithm.

5.7 Different brain regions show different degree of changes in superoxide production in a NOX-dependent manner

Quantitative measurements of DHE immunofluorescence in different brain regions displayed variability in its increase. Thus, frontal cortex (FC) showed a 2-fold increase; hippocampus and thalamus showed a highest degree of four-to-six fold increase (Figure 44). Interestingly, increased superoxide production observed following blast is derived from the increased NOX levels since apocynin a specific inhibitor of NOX activity, 30 min prior to blast injury completely inhibited the increase in the superoxide levels (Figure 45).

Overall, these data strongly indicate that primary blast results in uniformly diffused propagation

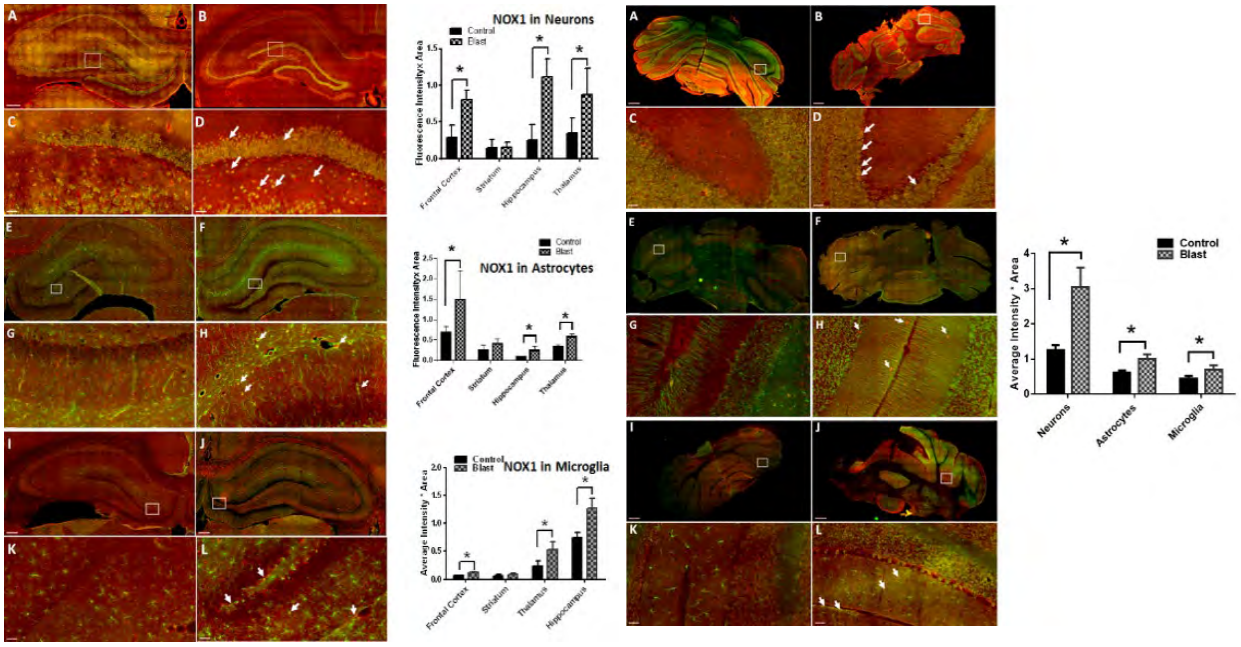


Figure 44. Left panel: NOX1 shows greater co-localization in neurons (A-D) than astrocytes (E-H) or microglia (I-L). **Right panel:** Cerebellum displays increased NOX1 expression in neurons than other neural cell. Representative merged images showing the co-localization of NOX1 with NeuN (A-D), GFAP (E-H) and Iba1 (I-L) in cerebellum indicating the neuronal, astrocytic and microglia localization respectively of NOX1 from control (A&C; E&G; I&K) and blast-injury (B&D; F&H; J&L) animals. Majority of NOX1 is localized in neurons compared to astrocytes and microglia express lowest amount of NOX1. *, $p < 0.01$-0.05.

of shockwave throughout the brain structures, however, oxidative damage exerts a differential effect on different brain regions wherein hippocampus and cerebellum higher vulnerability. Further, neurons are far more vulnerable to oxidative damage compared to other neural cells, which indicates that neurons are at higher risk during blast injury.

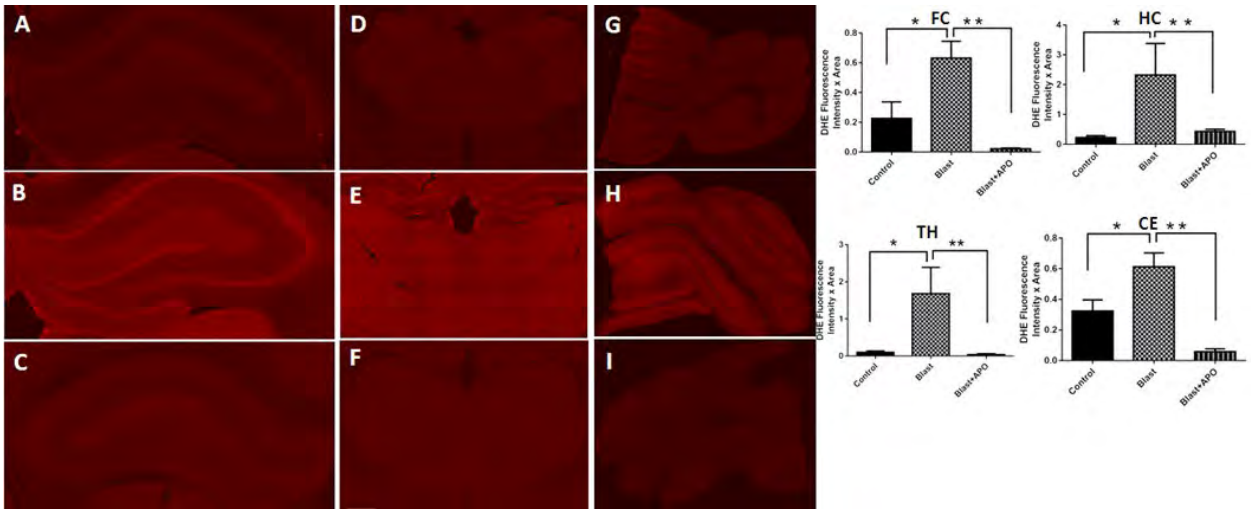


Figure 45 Primary blast increases superoxide levels in different brain regions. Fluorescent intensities (red) of DHE (dye that recognizes superoxide production) in different brain regions of control and blast-injury animals: Hippocampus [Control (A), blast-injury (B) and blast+ Apocynin (C)], thalamus [Control (D) and blast-injury (E) and blast + apocynin (F)] and cerebellum [Control (G) and blast-injury (H) and blast + apocynin (I)]. Quantification of florescence intensities in different brain regions show a striking increase in DHE fluorescence in hippocampus of blast-injured animals compared to controls (J) indicating highest level of superoxide production in hippocampus. Note that a pretreatment with apocynin (APO), an inhibitor of NOX activation completely blocked the DHE fluorescence increase indicating that the superoxide increase is mediated by activation of NOX. *, $p<0.01$-0.05.

5.8 Temporal and Spatial Effects of Blast Overpressure on the Blood-Brain Barrier in Traumatic Brain Injury

The blood-brain barrier is a semi-permeable membrane that separates the brain from the circulatory system. The BBB is dynamically modulated by cellular interactions between endothelial cells and the tight junctions that join them, pericytes, and astrocytes amongst other. Damage to the BBB is one of the most frequently investigated mechanisms of injury in TBI and has been commonly used as an assay to determine the degree and extent of injury. We investigated changes in BBB function at different levels, which include assessment of capillary leakage using extravasation of fluorescent dyes of different molecular size. These studies have been carried out at moderate blast intensity (180 kPa) at 0, 4 and 24 hours after injury (fig. 46).

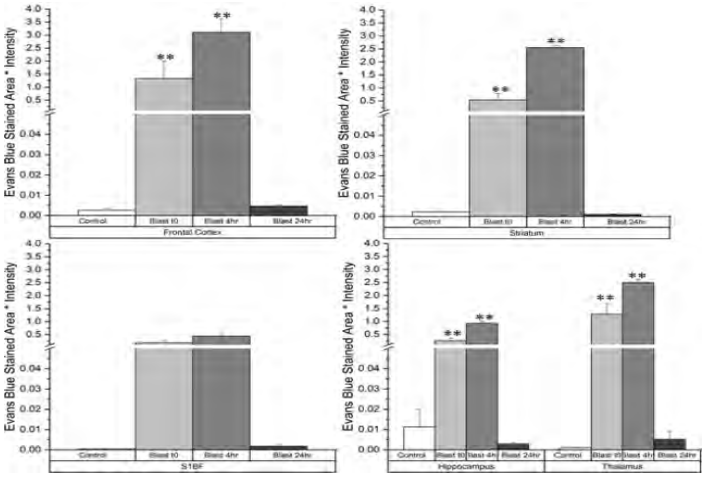


Figure.46. Assessment of BBB permeability using extravasation of sodium fluorescein (NaFl) and Evans blue (EB). There was highest extravasation of both NaFl and EB at 4 h post injury and frontal cortex (FC) displays highest degree of extravasation. Note that the extravasation of these dyes is restored at 24 h indicating the resealing/repair process occurring at this time point.

5.9 Primary blast induces breakdown of the blood-brain barrier

Extravasation of both sodium fluorescein and Evans blue was observed in all selected regions of the brain with differentially in six different regions investigated in this study, implying a degree of spatial vulnerability in different regions of the brain. In each region, statistically significant difference in the levels of both extravasated dyes was observed. The most robust changes occurred in the frontal cortex and striatum, while minimal to no statistically significant extravasation was observed in the cerebellum, which aligns well with previous results. In every region analyzed, there is at least a tenfold difference for dyes compared to controls in the acute time (~15 minutes).

5.10 For a given region, BBB permeability varies as a function of time post-injury

Groups of rats were sacrificed at specified times post-injury (15minutes, 4 hours, and 24 hours) in order to determine the time-course for blood-brain barrier permeability following blast. While the amount of extravasation was significant for both sodium fluorescein and Evans blue immediately after blast, there was an even greater increase in tracer penetration four hours following the blast exposure (Figure 47). Interestingly, extravasation levels drop at 24 hours, which implicate a possible resealing mechanism following mild blast. The differences between the amount of extravasated dye in 24-hour group and controls were not statistically significant.

Overall, these data strongly indicate that primary blast causes a direct mechanical injury to brain vasculature resulting in increased BBB permeability immediately after blast and peak over by 4 h. Interestingly, beyond 4 hours time scale it appears that there is a resealing/repair process occurring.

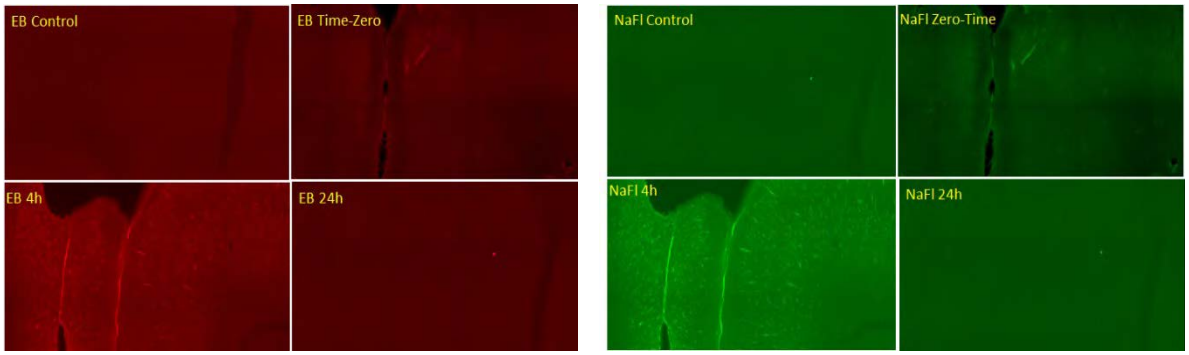


Figure .47. Extravasation of Evan's blue (EB, red) and sodium fluorescein (NaFl, Green) in frontal cortex of control and injured animals at different time points after injury. Note a robust extravasation of both the dyes at 4h after injury indicating peak of BBB permeability. Interesting to note that by 24 h post-injury the level of extravasation restored to that of control indicating a resealing/repair process occurring at 24 hours post injury.

5.11 Mechanisms of neuroinflammation following blast injury

Microglial activation and subsequent induction of neuroinflammatory mechanisms is one of the hallmarks of TBI. Such inflammatory mechanisms trigger the synthesis and secretion of various proinflammatory cytokines including TNF-α and IL-1β which exert an autocrine effect on microglia to further activate them or exert a paracrine effect on other cell such as cerebral endothelial cells, neurons and astrocytes to propagate further brain damage. Here we examined microglial activation in animals at different time points after exposure to moderate blast injury (180 kPa, data not shown).

5.12 Blast TBI changes the profile of microglial activation marker protein Iba1

The protein level of Iba1 showed a strong trend towards an increase in hippocampus 7 days after injury but not at the earlier time point (24h) (Figure 48). Other brain regions including thalamus and cerebellum did not display changes in Iba1 level (data not shown). These results suggest that microglial activation is relatively a late stage phenomenon in blast injury and such changes are region-dependent.

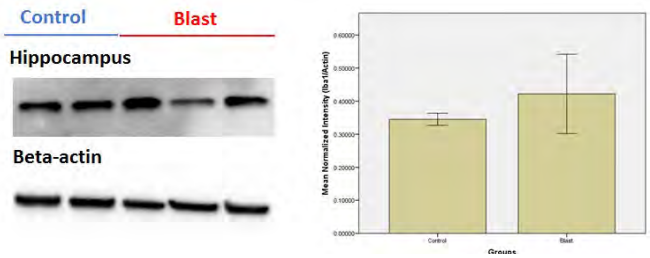


Figure.48. Changes in Iba1 protein expression in hippocampus of animals 7 days after injury displays a strong tendency of increase compared to controls.

5.13 Changes in the protein expression of matrix metalloproteinases that contribute to BBB permeability changes in bTBI

A continuation of work on the spatial and temporal changes in the BBB permeability in rats subjected to different blast over pressures (70, 180, 240 kPa) examined changes in the matrix metalloproteinases (MMPs). MMPs, also called matrixins, comprise a family of enzymes that cleave protein substrates based on a conserved mechanism involving activation of a site-bound water molecule by a Zn^{2+} ion, and their activation may contribute to BBB permeability. There are several MMPs present in brain among which MMP-3 and MMP-9 are the most dominant. MMPs have been linked to BBB disruption since these proteases once released into the extracellular matrix degrade tight junction proteins which act as anchor between the two capillary endothelial cells to prevent the leakage of the barrier between blood and brain.

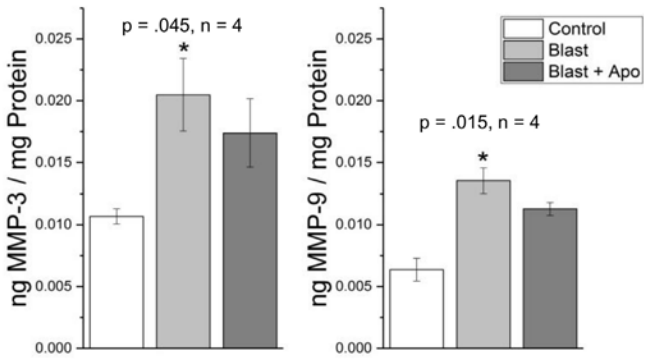


Figure.50. ELISA results for whole brain lysates for MMP-3 and MMP-9 (n=4). Statistically significant increases in blast groups were seen compared to controls (p = 0.045 and 0.015, respectively).

5.14 Protein levels of MMP9 significantly increase in moderate blast as a function of time and such increase correlate with the reduction in tight junction proteins

Quantitative measurements by Western blots of MMP9 in

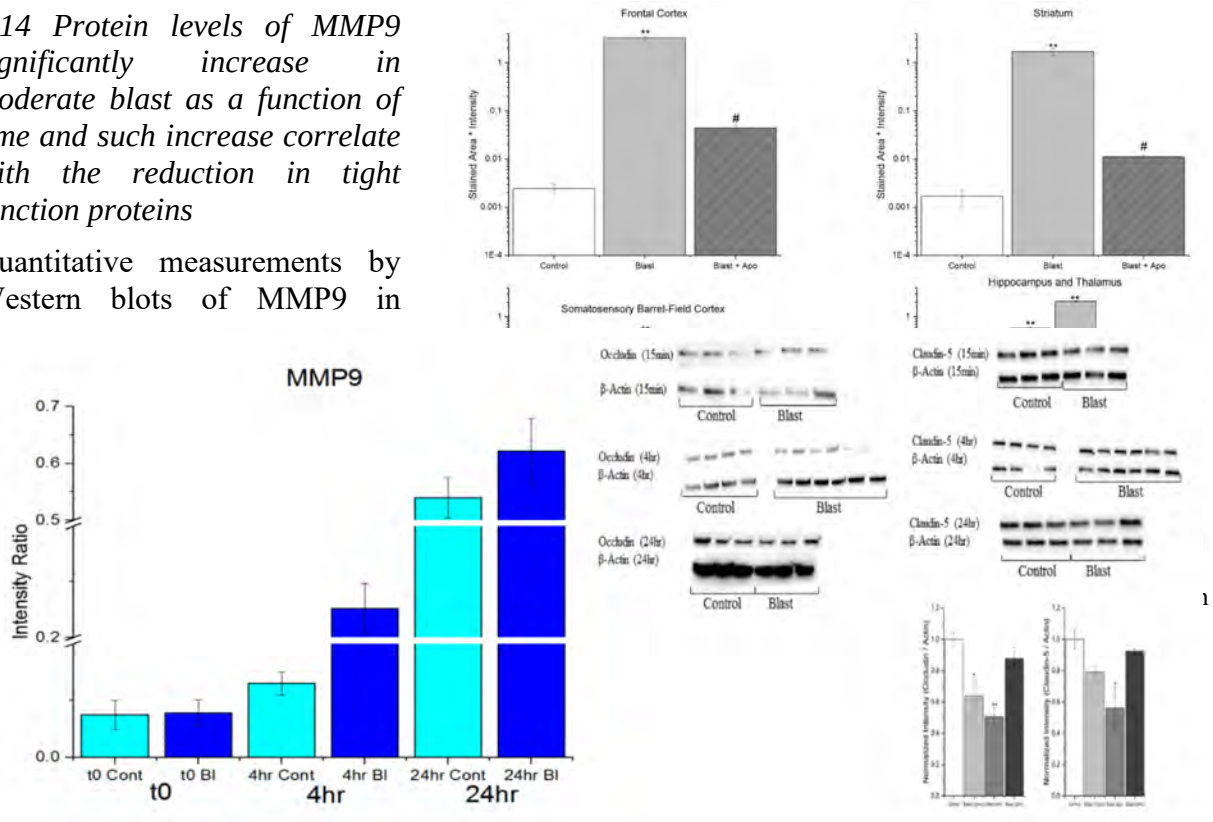


Figure.49. Western blots of MMP 9 (right panel) and tight junction proteins Occludin and Claudin-5 and respective quantitations. Proteins taken from control and blast (180 kPa BOP) cerebral brain homogenates fifteen minutes, four, and 24 four hours post-exposure and compared with levels of β-actin housekeeping protein. [*] indicates a difference in intensity. compared with control with a statistical significance of $p < 0.05$, [**] indicates

homogenates prepared from cerebral hemispheres from rats subjected to moderate blast at 180 kPa showed a progressive increase in its expression. Immediately following blast (t_0) there was no change in the expression of MMP9, whereas 4h post injury there was a significant increase, which persisted up to 24 h (Figure 49). Noteworthy that the increase in MMP 9 expression inversely correlated with the reduction in the protein levels of tight junction proteins claudin 5 and occludin (Figure 49), suggesting that the degradation of tight junction proteins following blast may be mediated by MMP9, which could ultimately result in the BBB permeability. We conducted ELISAs for both MMP-9 and MMP-3 (figure 50), which have been implicated in the breakdown of the BBB and are present on neurovascular endothelial cells for control, injured, and injured groups treated with apocynin. It is important to note that in the case of both MMPs studied, apocynin treated groups did not show statistically significant differences from blast groups ($p > 0.05$), although it does seem as though there is a tendency towards decrease. This may indicate that upregulation of MMPs is not mediated by NOX (oxidative stress), but it is a response to some other mechanism, or a process disturbing the homeostasis in the brain parenchyma like influx of exogenous proteins after the BBB damage.

5.15 Oxidative stress resulting from NADPH oxidase (NOX) activation contributes to BBB permeability

We have identified that blast injury results in oxidative stress mainly via the activation of NADPH oxidase (NOX), a superoxide producing enzymes in different brain regions (figure 51). Oxidative stress has been implicated as a secondary mechanism in BBB disruption in various blunt TBI as well as in other neurological disorders including stroke, meningitis and HIV infections. We examined the efficacy of apocynin, an antioxidant as well as agent that inhibits the activation of NOX on the extravasation of Evan's blue (EB) as measures of BBB permeability. Rats subjected to moderate blast resulted in BBB disruption as indicated by extensive extravasation of EB (Figure 27) across different brain regions. Interesting that frontal cortex displayed maximum extravasation compared to other brain regions. Treatment of rats with apocynin 30 µM (i.p. injection) 30 min before blast injury showed a significant reduction in EB extravasation 4 h post-injury across all the brain regions. These results strongly suggest that oxidative stress likely resulting by the activation of NOX contributes to BBB disruption. ELISA analysis of S100β, an astrocytic calcium-binding protein, on blood serum samples for animals exposed to moderate blast (180 kPa) at 4 and

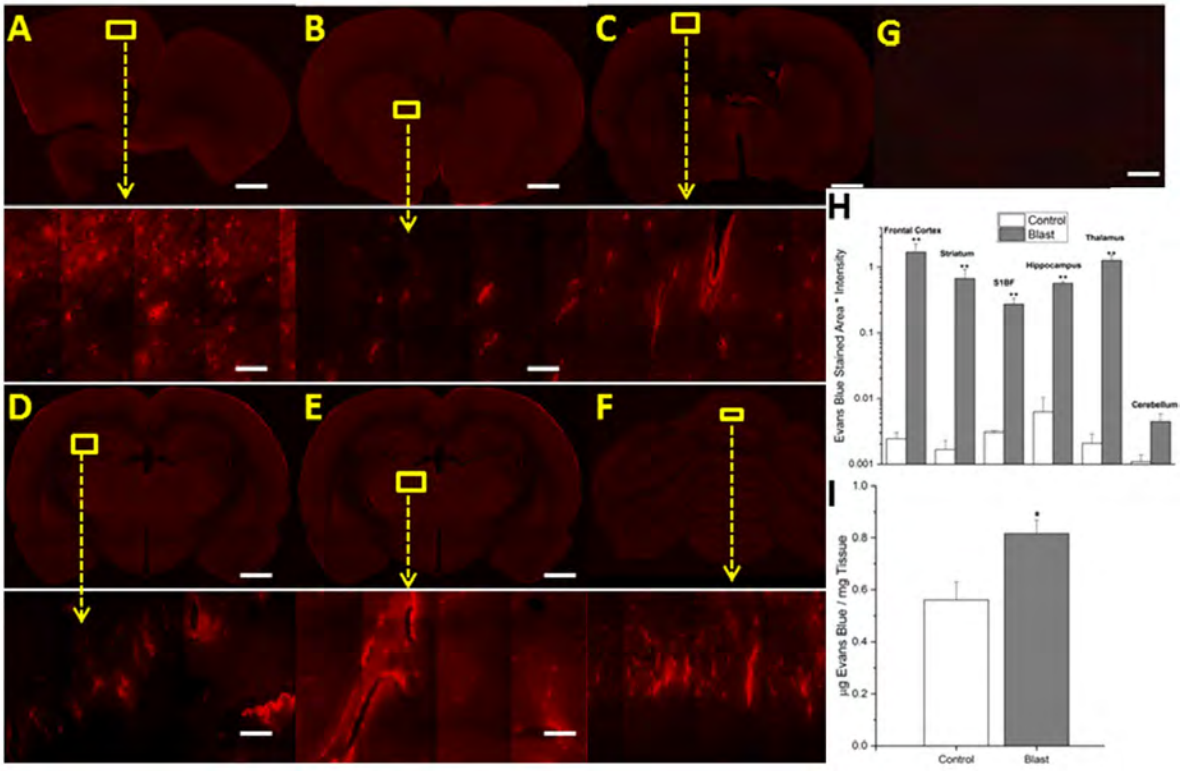


Figure.51. Fluorescent images of Evans blue extravasation. Images show 10x macro-shots as well as zoomed in 40x images in representative regions in the frontal cortex (**A**), striatum (**B**), somatosensory barrel-field cortex (**C**), hippocampus (**D**), thalamus (**E**) and cerebellum (**F**), 15 minutes following 180 kPa blast exposure. Control images were dramatically enhanced, yet still show limited visibility, due to the absence of extravasated dye. Frontal cortex was taken as a representative control image (**G**). Quantitation of extravasation is shown using a semilog plot to capture the differences (**H**). Absorption spectrophotometry results of Evans blue in control and injured rats (n = 5) (**I**). *Indicates a difference in intensity compared with control with a statistical significance of $p < 0.05$, **Indicates $p < 0.01$. Scale bar = 1 mm in coronal sections and 50 µm in 40x images.

24 hours post injury (figure 52) corroborate these findings. Immunohistochemistry was also done to determine the presence of monocytes in brain parenchyma in the frontal cortex, four hours after blast. Fluorescent co-stain for RECA-1 (endothelial cell marker) and CCR-2 (monocyte marker)

was conducted for control and blast groups, qualitatively demonstrating increased presence of monocytes in the brain (fig. 53). These results clearly demonstrate a multiple mode of increased permeability of the BBB.

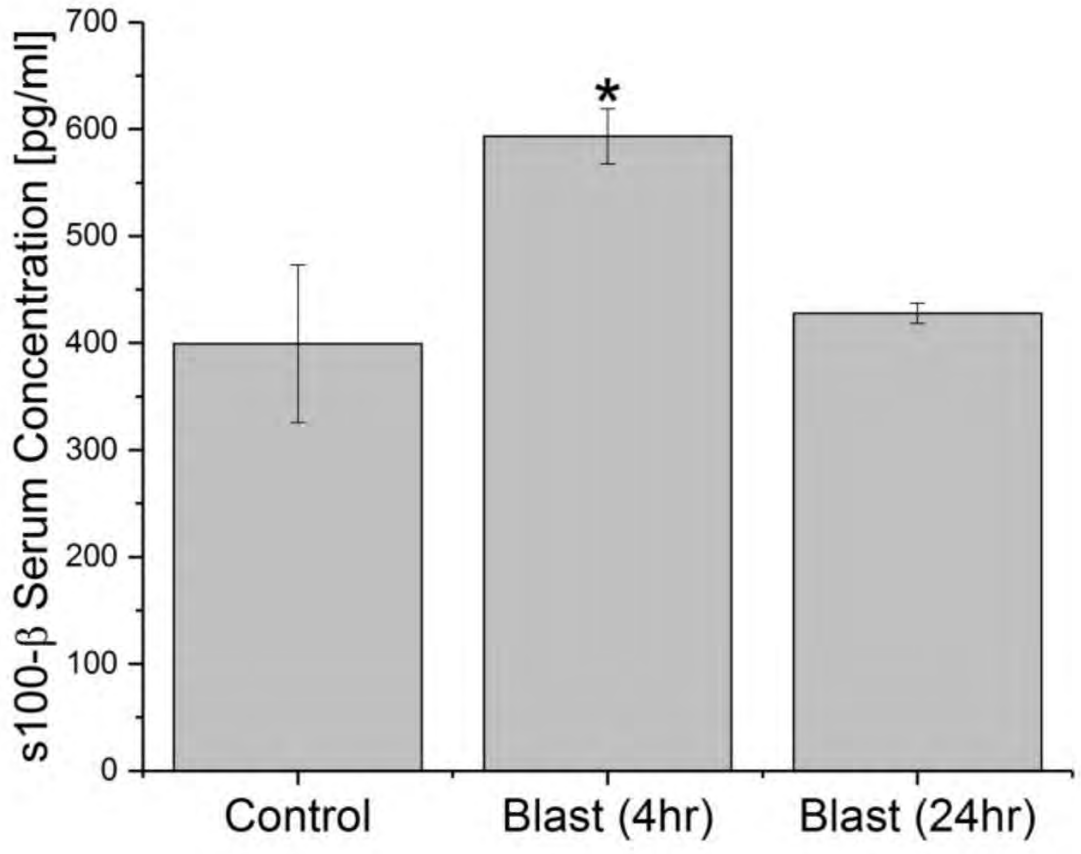


Figure.52. ELISA results for S100β in blood serum (n = 3). Statistically significant increase from control was seen in the blast groups four hours post injury ($p=0.037$), before returning to control values in 24 hours ($p > 0.05$).

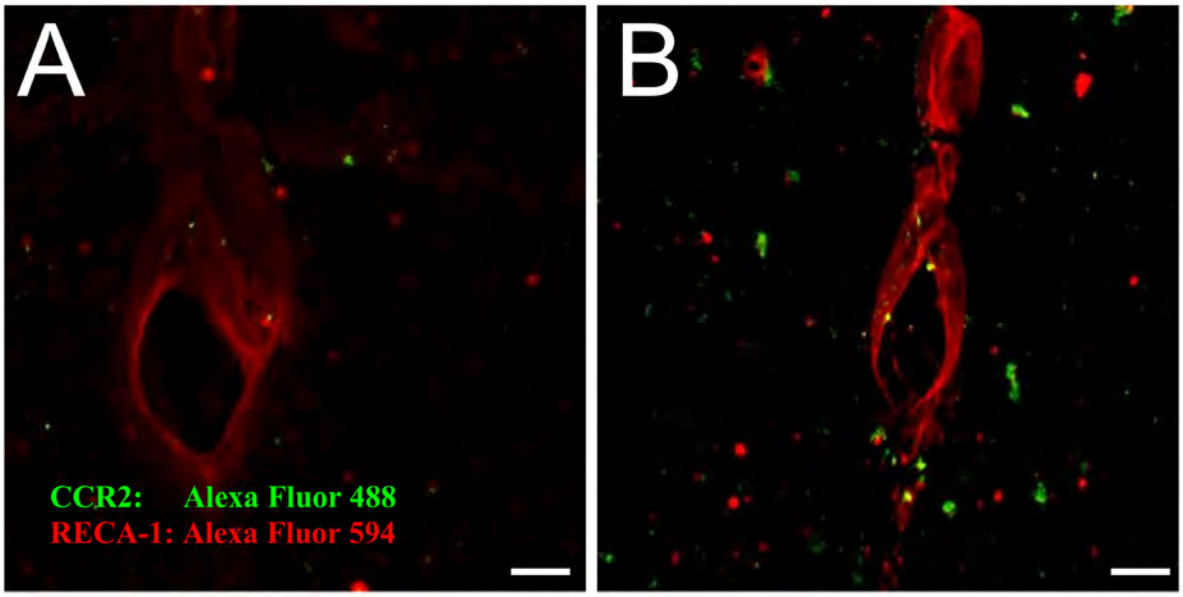


Figure.53. Immunohistochemistry in frontal cortex for endothelial cell marker (RECA-1) and monocyte marker (CCR2) at four hours post-exposure for control (A) and moderate (180 kPa BOP) blast (B). Scale bar equals 50μm.

Finally, to confirm our hypothesis that the tight junction proteins were indeed dislodged following the blast, an analysis via ELISA was conducted on brain lysates and serum samples for two tight-junction proteins, occludin and claudin-5 (figure 54). These results corroborate our early hypothesis; after the tight junctions are dislodged from their complexes on endothelial cells, they are taken up by circulation. However, by 24 hours, all the tight junction proteins that were taken up by the serum were excreted or otherwise removed from circulation.

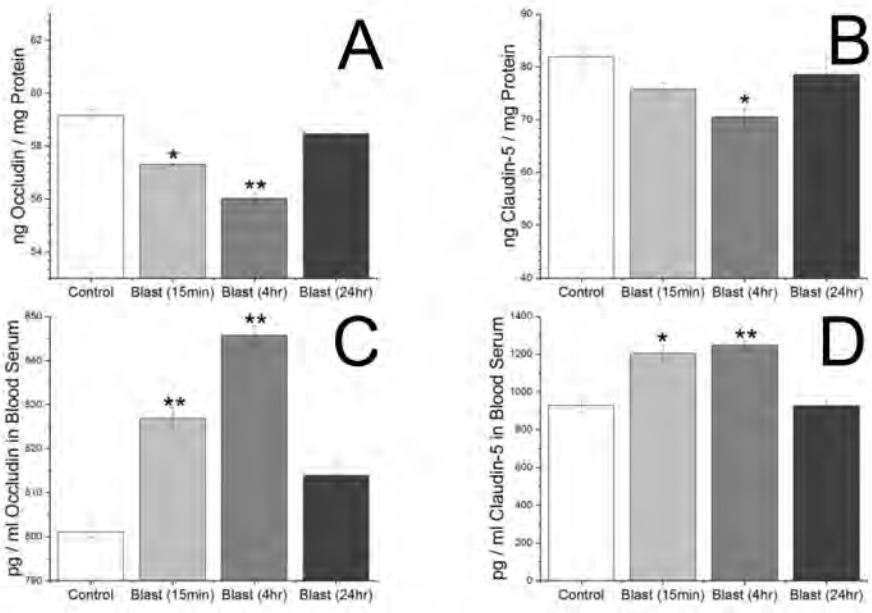


Figure.54. ELISA results for tight junction proteins occludin and claudin-5, respectively in brain (A & B) and blood serum (C & D). Assay conducted for blast (180 kPa BOP) samples fifteen minutes, four, and twenty-four hours post-exposure and compared with controls. [*] indicates a difference in intensity compared with control with a statistical significance of $p < 0.05$, [**] indicates $p < 0.01$.

5.16 Activation of microglia following blast TBI

The microglial activation is a frequent sequela in animals exposed to blast. We found that in control animals (fig. 55A), microglia appear to be in their resting state (fully ramified) with their processes probing their microenvironment. Under normal physiological conditions these cells are evenly distributed throughout the brain. However, 4 hours following blast exposure microglia begin to migrate towards the blood vessel and activate, with apparent changes in morphology (amoeboid shape). This response is likely due to components of the blood entering the brain parenchyma through the compromised BBB. Once detected by the microglia, the cells activate and begin clearing the foreign material by phagocytosis. In figures 55B-D one can observe that microglia respond to blood vessels of all sizes indicating that BBB of arteries, arterioles and capillaries are all compromised. At 7 days following blast, microglia remain in their active state surrounding the blood vessels. The number of activated microglia surrounding each blood vessel decreased compared to the 4-hour time point. This may be due to the sealing of the BBB, which prevents additional foreign material from

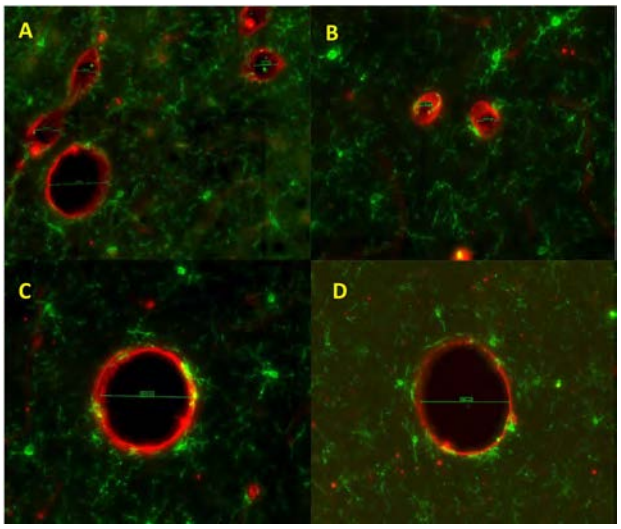


Figure.55. Fluorescent images of Iba (microglia) and RECA (rat endothelial cells) expression in the frontal cortex in control (A) and 4 hours of moderate blast in small (B) medium (C) and large (D) blood vessels. Note the change in microglia morphology surrounding the vessels of the blast group.

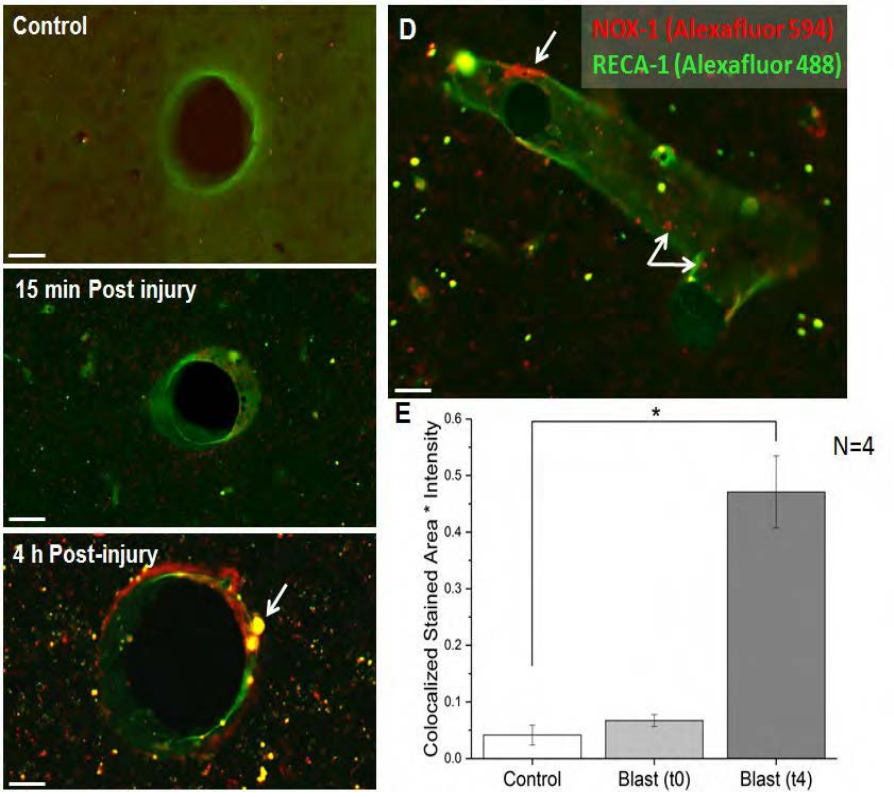


Figure.56. Colocalization of NOX-1 (red) and RECA-1 (green) in vascular endothelial cells in the frontal cortex. Control: little NOX-1 in vascular endothelial cells with an increase in colocalization fifteen minutes following blast. At four hours, there is a significant upregulation of NOX-1 in endothelial cells: yellow is indicating an overlap of NOX-1 and RECA-1. D. NOX-1 upregulation across the length of the vessel lumen (arrows). Quantitation of the colocalization shows a significant increase in blast groups, $p < 0.05$.

entering the brain parenchyma. At this later time point, all the microglia surrounding large vessels return to their resting ramified state. This was not observed for small and medium vessels where microglia remained in their activated

5.17 NOX1 is upregulated in neurovascular endothelial cells

Previous studies in this laboratory identified increased levels of NOX1 and NOX2 in neurons, astrocytes, and microglia following moderate blast injury (180 kPa) across the cerebral hemisphere and cerebellum. In the present study, we examined the levels of NOX1 in brain endothelial cells in the frontal cortex in vascular endothelial cells. The double immunofluorescence for NOX1 and RECA-1 (endothelial cell marker) showed a significant increase in amount of colocalization following moderate blast (Fig. 56). Fifteen minutes post-exposure, a statistically insignificant increase in colocalized NOX1 compared to controls was observed. Four hours after blast, which previous work from this group has shown as the peak time for BBB permeability following blast injury, we observed a robust increase (ten-fold) in NOX1 concentration in vascular endothelial cells.

5.18 Apocynin significantly reduces superoxide production following blast injury

Several groups have demonstrated that activation of NOX results in increased superoxide production. After demonstrating the increase in NOX1 concentration in neurovasculature in the frontal cortex, we sought to determine if this results in an increase of superoxide production. *In-vivo* levels of superoxide were measured using DHE and we observed a clear increase in superoxide produced in the frontal cortex, which corroborated well with the upregulation of NOX1 (Fig. 57). Differences between control and blast groups and blast and treatment groups were found to be statistically significant.

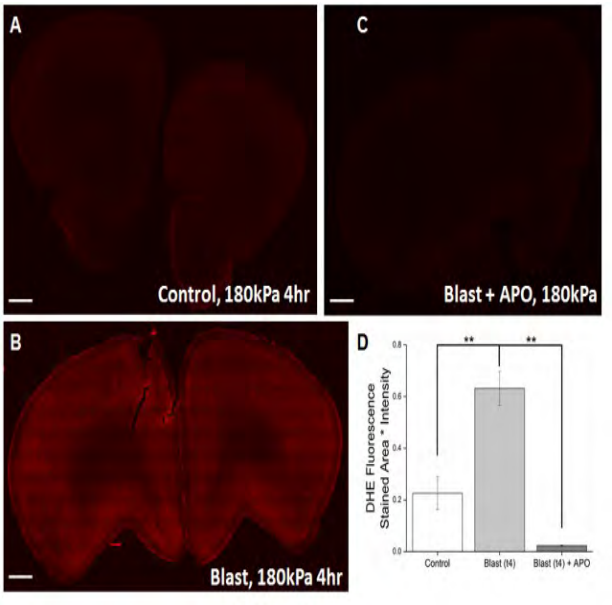


Figure.57. DHE stain to observe superoxide concentration in the frontal cortex: A control (basal level of superoxide). B superoxide increase 4 hours following blast exposure, C. return to basal levels with pretreatment of apocynin. D quantitation of DHE fluorescence intensity for the three groups. [**] $p < 0.01$.

5.19 Apocynin significantly reduces tight junction degradation following blast injury

To determine the degree of BBB breakdown following blast injury, ELISA was conducted for tight junction proteins occludin and claudin-5 for control, blast, and blast + apocynin groups (Fig. 58). Occludin decreased by 20.31% four hours post-blast compared to controls but barely changed in animals treated with apocynin. The difference between the blast group and the treatment group was also significant. Claudin-5 decreased by 12.40% four hours post-blast compared to controls, but like occludin, displayed only a negligible decrease in the treatment group. The difference between blast and treatment groups was statistically significant.

5.20 Apocynin significantly decreases blood-brain barrier permeability following blast injury

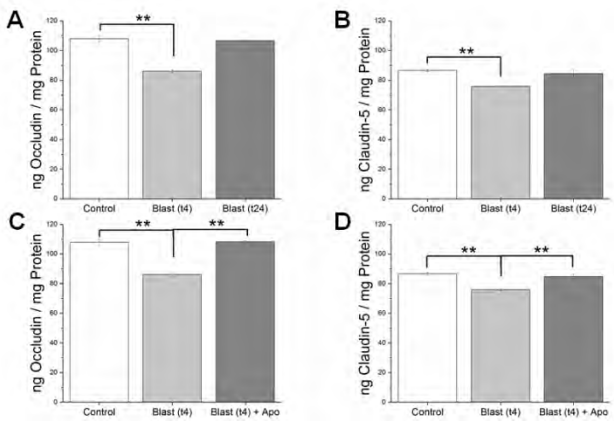


Figure.58. ELISA results for matrix metalloproteinases. A & B show results for MMP-3 and 9, respectively, in control and blast groups. Levels of MMPs were taken four and 24 hours after exposure and compared against controls. C & D show results for MMP-3&9, respectively, in control, blast, and treatment groups. [*] indicates a difference in intensity with a statistical significance of $p < 0.05$, [**] indicates $p < 0.01$

The extent of extravasation was evaluated in the frontal cortex at both fifteen minutes and four hours post-blast injury (Fig. 59). Our group previously displayed that extravasation of Evans blue was significant at both times post-moderate blast injury and our current results support that. Significant extravasation was observed in both injured and treatment groups at the acute stage, with no statistically significant difference between them. EB presence in the brain parenchyma increased by 1300-fold four hours following moderate blast over the control in the frontal cortex and over the blast + apocynin group (75-fold, $p < 0.01$). There was no statistically significant difference between the control group and the treated group. Four animals were used per group in this phase of the study.

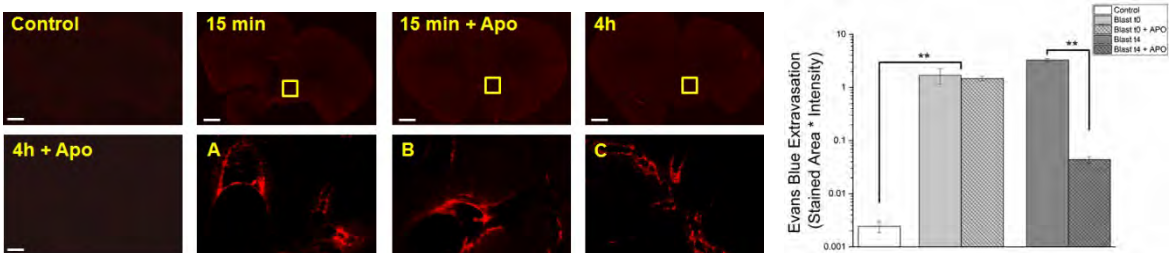


Figure 59. Fluorescent images of Evans blue extravasation. Images show frontal cortex from control animal, with almost no observable extravasation of leakage, Sections from 180kPa BOP, acutely (15 minutes) show significant leakage, apocynin treatment completely blocked EB extravasation. 4 h post-exposure showed greater leakage than 15m post injury A, B, C show zoomed in, 20x images from images. Quantitation of extravasation intensity shows a statistical significance of $p < 0.01$.

5.21 Moderate blast induces translocation of glial fibrillary acidic protein into the blood stream

Concentration of GFAP, an astrocyte specific protein in brain (which is not present in blood under normal conditions) in the blood plasma was determined via ELISA (Fig. 60). Statistically significant increase in GFAP concentration was seen compared to controls in both blast and treatment groups 15 minutes after injury, but no difference between blast and treatment group. At four hours post-blast, there is a further increase in GFAP concentration in blood plasma, but with apocynin, the values drop back to control levels. Intergroup comparison reveals a statistically significant difference between blast and treatment groups four hours after injury.

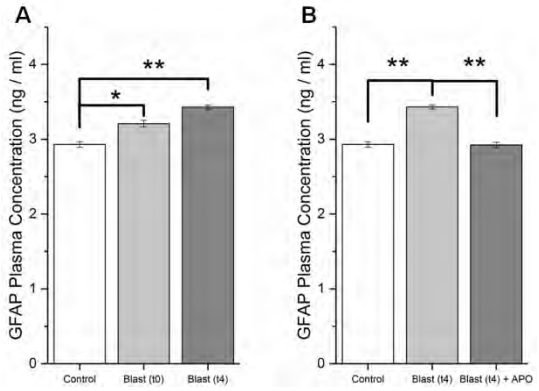


Figure.60. ELISA results for GFAP concentration in blood plasma. A compares control levels with levels 15 minutes and 4 hours following blast and B compares control levels with levels 4 hours following blast with and without apocynin pretreatment. [*] indicates a difference in intensity with a statistical significance of $p < 0.05$. [**] indicates $p < 0.01$.

5.22 CSF-Plasma ratio of albumin increases following moderate blast injury

To determine the ratio of albumin in the CSF (which should be negligible in normal conditions) and blood plasma, another ELISA was conducted on both samples (Fig. 61). While an increase in the CSF-Plasma albumin ratio was observed acutely (fifteen minutes post-blast) for both blast and treatment groups, statistical significance was not achieved in either. Four hours following blast, a statistically significant increase over control was observed in the injured group. Comparison between blast and treatment group at this point also revealed statistically significant difference. These studies together strongly suggest that NOX-derived oxidative stress plays a major role in BBB disruption following moderate blast injury.

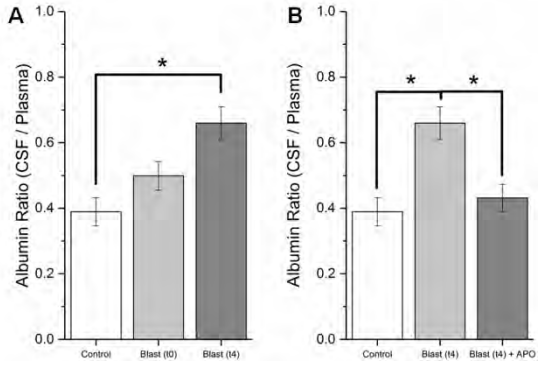


Figure.61. ELISA results for albumin concentration in CSF and blood plasma, as presented as a ratio between the two. A compares control levels with levels 15 minutes and 4 hours following blast and B compares control levels with levels 4 hours following blast with and without apocynin pretreatment. [*] indicates a difference in intensity with a statistical significance of $p < 0.05$.

5.23 Moderate blast increases the production of proinflammatory cytokines

In the previous progress report, we reported that microglial activation occurred in animals exposed to moderate blast (180 kPa). One event associated with microglial activation is increased production of proinflammatory cytokines. Here we examined the temporal profiles of two proinflammatory cytokines TNF-α and IL-1β in homogenates from hippocampus and thalamus brain regions found to me more vulnerable to blast injury. Levels of IL-1β moderately increased 4h post injury and declined to control levels by 24h, however showed a progressive increase at 7- and 15-days post-injury (Figure 62) in hippocampus. Thalamus showed much robust increase in

IL-1β production compared to hippocampus but showed a similar time course of increase as that of hippocampus. Like IL-1β, levels of TNF-α also showed a biphasic response of increase in both hippocampus and thalamus (Fig. 62). These results indicate that moderate blast increases the production of proinflammatory cytokines and such increase is likely mediated by activation of microglia.

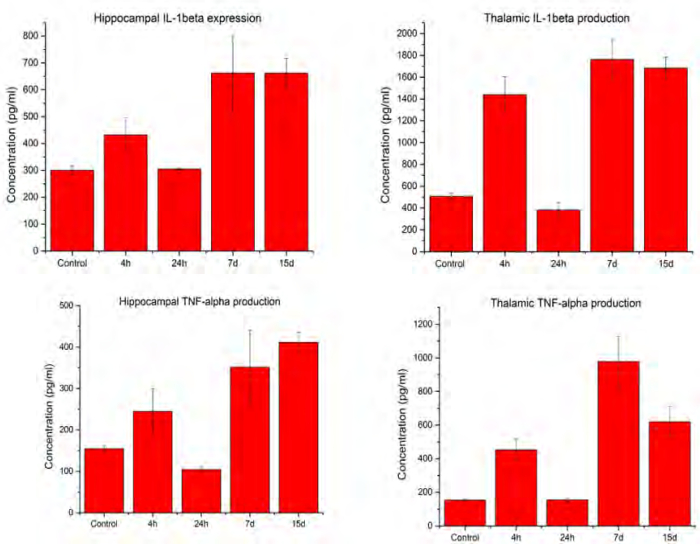


Figure.62. ELISA results for IL-1β and TNF-α in hippocampus and thalamus lysates in animals exposed to moderate blast (180 kPa).

Task 6. Examine plasma membrane permeability using fluorescent tracers

In the current work, we evaluated alterations in cell plasmalemmal permeability following blast exposure using a shock tube at two peak overpressures (180 kPa and 240 kPa) and a single time point post-injury (30 min). Animals were sacrificed using transcardial perfusion, brains extracted and sectioned on a vibratome into 50 micrometer thick slices. We assessed the patterns of neural cells acutely permeabilized due to blast based on neuroanatomical locale, phenotype, and extent of damage. We hypothesized that blast shockwave directly elicits biophysical plasmalemmal disruptions in specific neural cellular populations that are dependent on brain region. We found that blast exposure caused immediate increases in cell membrane permeability predominantly in the cortical region. We have noticed a large numbers of Lucifer Yellow positive (LY+) cells in

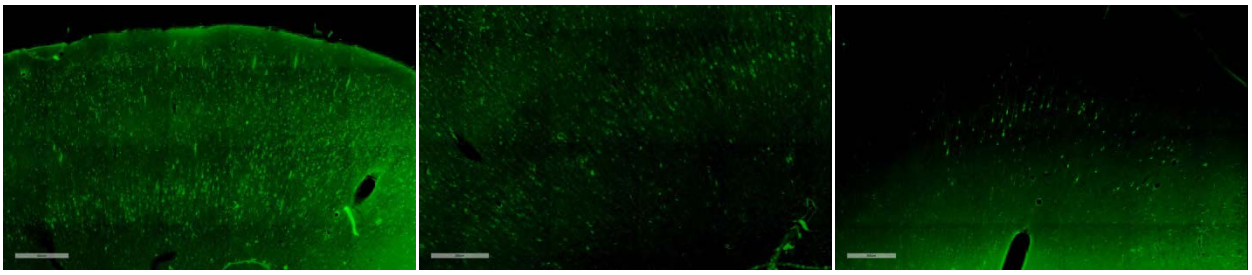


Figure 63 Lucifer Yellow positive cells in the frontal cortex of brain in rats exposed to a single blast with 180 kPa peak overpressure (left, middle) versus control (right).

both contralateral and ipsilateral regions with respect to injection site (fig. 63). However, further optimization of the injection protocol is necessary to limit the number of LY+ cells present in the ipsilateral side of the brain, i.e. near the injection site.

Task 7. Evaluate alterations in brain proteome after primary blast exposure

7.1 Advantages of Proteomics

Proteomics offers unique insight into etiology of brain injury by providing unbiased information about large dataset of proteins involved in variety of cellular processes. Simultaneous label free fingerprinting readily available with an aid of bioinformatics data mining backed by differential expression information allows identification of major biochemical pathways involved. These attractive traits perfectly suited for cross-sectional characterization were exploited in this work to demonstrate largely unexplored fundamental attributes of blast TBI (bTBI) in hippocampus.
Ten weeks old Sprague Dawley rats were exposed to single blast at 130 kPa intensity and sacrificed 24 hours post exposure. Brains were homogenized and thirty micrograms of proteins from each sample were subjected to separation followed by digestion. Peptides were labeled by 8-plex iTRAQ labeling, combined, separated by high pH Reverse-phase Liquid Chromatography (RPLC) and further analyzed by RPLC-MS/MS on Q Exactive™ Hybrid Quadrupole-Orbitrap mass-spec. Protein identification: mass spectra were searched against Uniprot rat database via Mascot 2.4 search engine on Proteome Discovery 1.4 platform. Differential cortical and hippocampal proteome analysis in blast exposed rats (n = 4) identified: 1) 4621 proteins (hippocampus: 35 upregulated and 25 downregulated, $p<0.05$), and 2) 4991 proteins (hippocampus: 219 upregulated and 29 downregulated, $p<0.05$). Further analysis revealed there are two major canonical pathways involved in pathology of blast TBI: 1) oxidative phosphorylation and 2) mitochondrial dysfunction. These pathways include changes in mitochondrial electron transport chain and respiratory chain proteins: 1) cytochrome c oxidase (6 fragments), 2) NADH: ubiquinone (16 fragments), 3) ATP

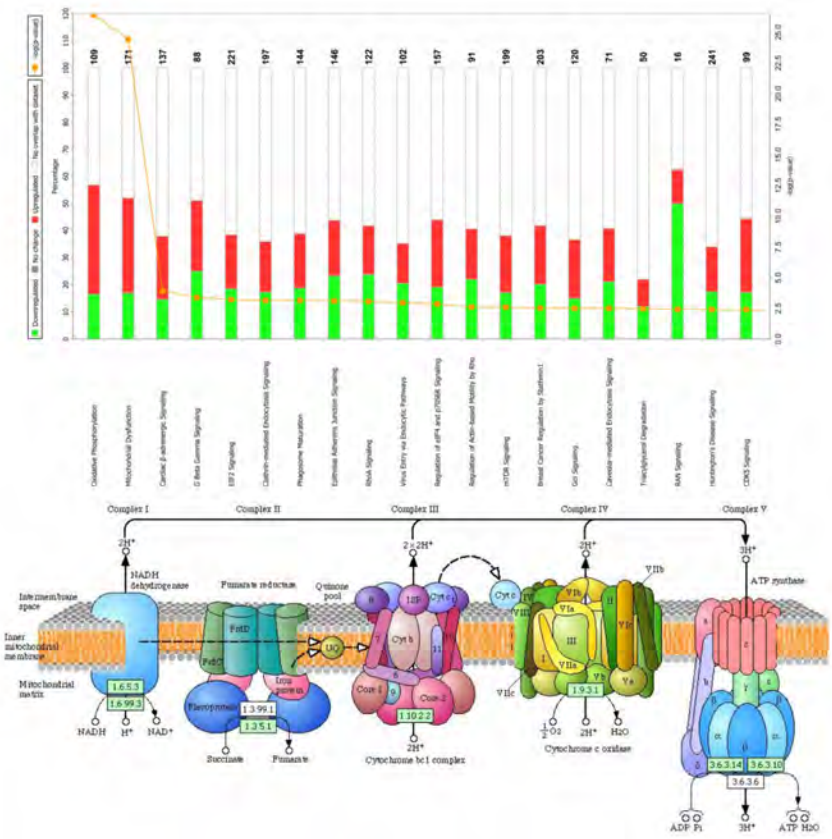


Figure 64. Top 20 of identified canonical pathways by QIAGEN IPA (top), and schematic representation of electron transport chain complexes involved in the oxidative phosphorylation and mitochondrial dysfunction pathways (bottom).

synthase (H+) (5 fragments), 4) NADH dehydrogenase (2 fragments) and ubiquinol-cytochrome c complex (2 fragments). These proteins were mostly upregulated suggesting rapid activation of repair mechanism merely 24 hours post injury. Overall pathway analysis identified total of 70+ canonical pathways (fig. 64) potential for etiological, therapeutic and diagnostic applications.

Task 8. Establish Master Impulse Dose-Response Curve at Three Blast Overpressures

8.1 The effect of the electrostatic charges on the pressure profile and impulse

We performed a set of experiments where incident pressure was measured and pressure sensors (PCB 134A24) were used in protected and unprotected configuration. Tests were performed at a single nominal shock wave intensity (130 kPa), and the effect of the static electricity along the shock tube was evaluated. Measurements were repeated four times and shock wave evolution was monitored using six pressure sensors (fig. 65, for details of the experimental setup see figures 1 in references [19] and [20]). The quantification of the BOP and impulse was performed to capture the effect of static electricity on the signal quality in the unprotected mode. It turns out that pressure profiles recorded using unprotected sensors result in impulse values with values lower by 30-50% (figure 66).

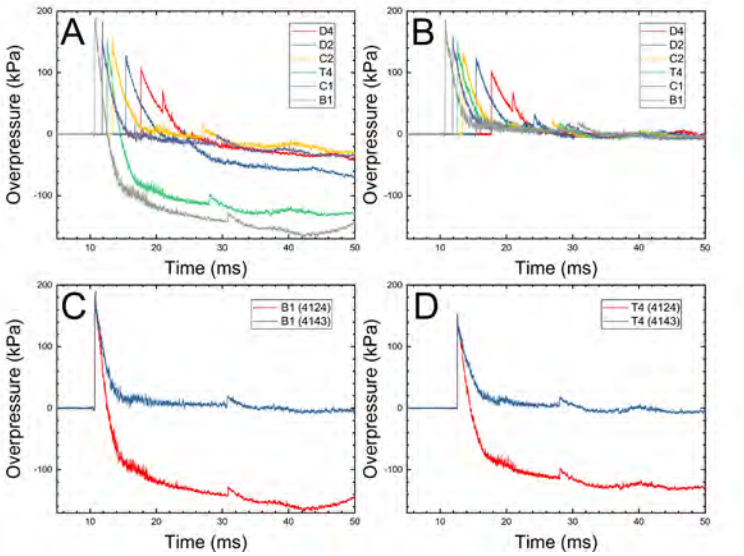


Figure.65. The effect of the baseline drift on the quality of the recorded shock wave profiles. The same set of sensors was tested in the unprotected (A) and protected (B) configurations. The comparison of individual pressure-time traces for sensors B1 (C) and T4 (D) is presented. It is evident there is severe signal degradation which will results in underestimation of the duration and impulse values.

8.2 Calibration of the shock tube to control the impulse at three blast overpressures

The control over shock wave profile characteristics is one of the many recent advances from our laboratory, a feature which, to our knowledge, was not demonstrated in any other published work

to date. Considering the deleterious effects of the static electricity on the impulse we had to perform a set of experiments to re-calibrate the operational parameters of the 9-inch shock tube and establish a set of experimental conditions to select the location in the shock tube where the shock wave profile has the same peak overpressure and increasing duration (impulse).

We used helium and nitrogen as driver gases, three operational breech

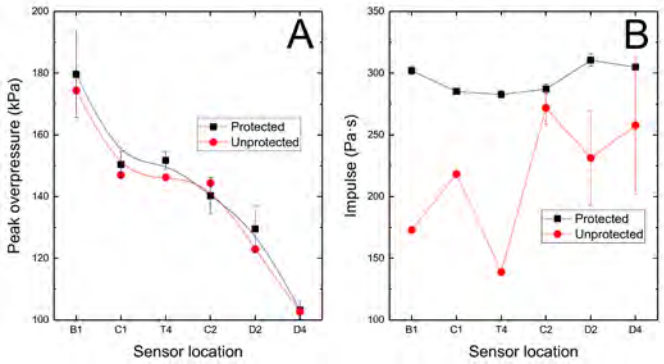


Figure.66. The effect of static electricity on the peak overpressure (A) and impulse (B). Tests were performed at a nominal blast intensity of 130 kPa. The peak overpressure is unaffected, while pressure histories recorded using unprotected pressure sensors result in diminished impulse values.

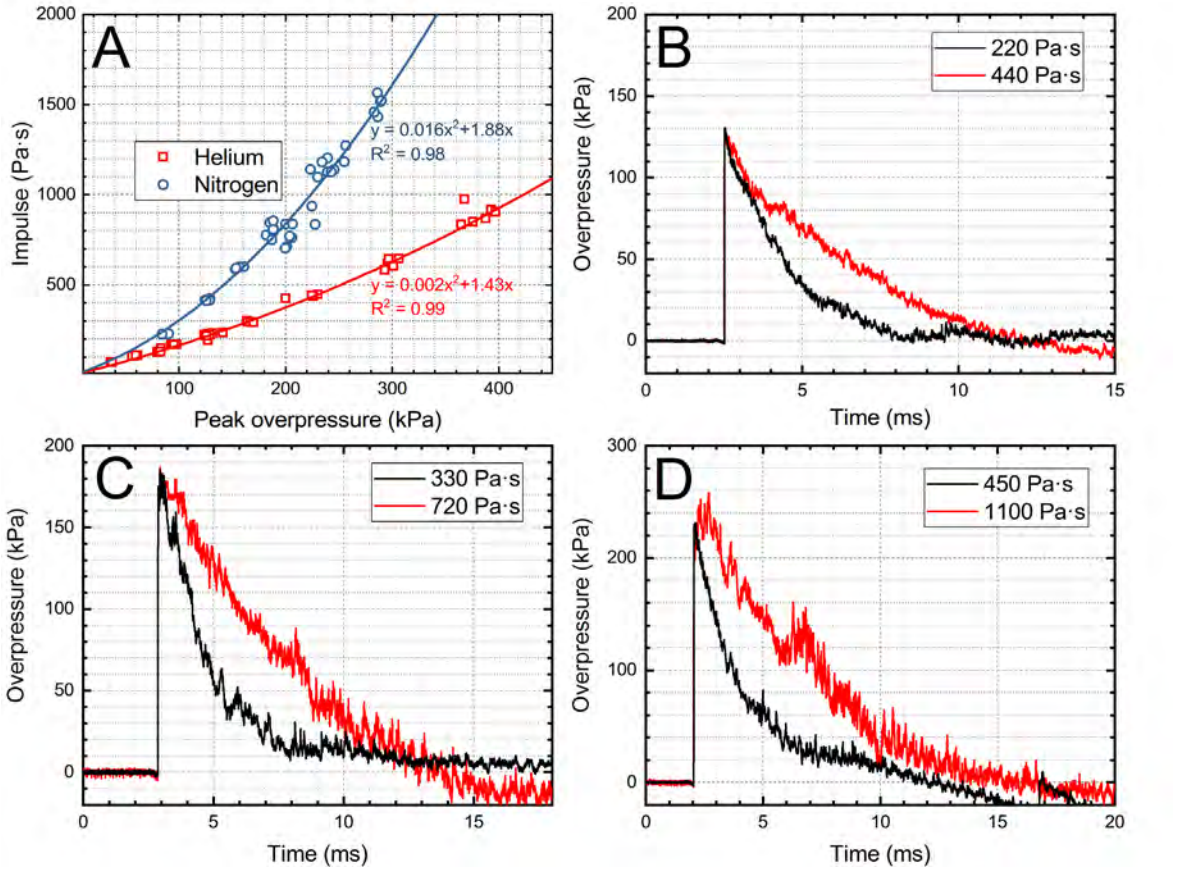


Figure. 67. The BOP-impulse calibration. A. Two calibration curves for helium and nitrogen used as a basis for the development of the master impulse dose-response curves and BOP-impulse selection for biochemical and biomechanical evaluation. Representative curves illustrating controlled variable impulse at three nominal BOPs: B. 130 kPa, C. 180 kPa and D. 230 kPa.

configurations and four membrane thicknesses and repeated four times, for a total of 96 tests (2 x 3 x 4 x 4 = 96). Shock wave profile evolution was monitored by 6 pressure sensors distributed along the shock tube, and total of 576 profiles were generated (96 x 6 = 576). The data analysis consisted of quantification of four characteristics of the shock wave: 1) peak overpressure, 2) rise

time, 3) duration and 4) impulse. The evaluation of time domain parameters (rise time and duration) included reading: 1) the time at 10% and 90% of the pressure increase of the shock front (for the rise time) and 2) onset of the pressure increase and intersection of the pressure decay with neutral (baseline) pressure (for the duration). The data points were fitted with two polynomial functions to establish low impulse and high impulse curves (figure 67) with the following six nominal BOP-impulse combinations selected for further tests: 1) 130 kPa-220 Pa·s, 2) 130 kPa-440 Pa·s, 3) 180 kPa-330 Pa·s, 4) 180 kPa-720 Pa·s, 5) 230 kPa-450 Pa·s, and 6) 230 kPa-1100 Pa·s.

8.3 Master impulse dose-response curves

The final step in the process of dose-response curves generation was the exposure of 150 animals to a single shock wave with precisely known peak overpressure and impulse values obtained from shock tube calibration experiments. The results are presented in figure 44. It is obvious that mortality rates for long duration impulse are shifted towards lower peak overpressures (figure

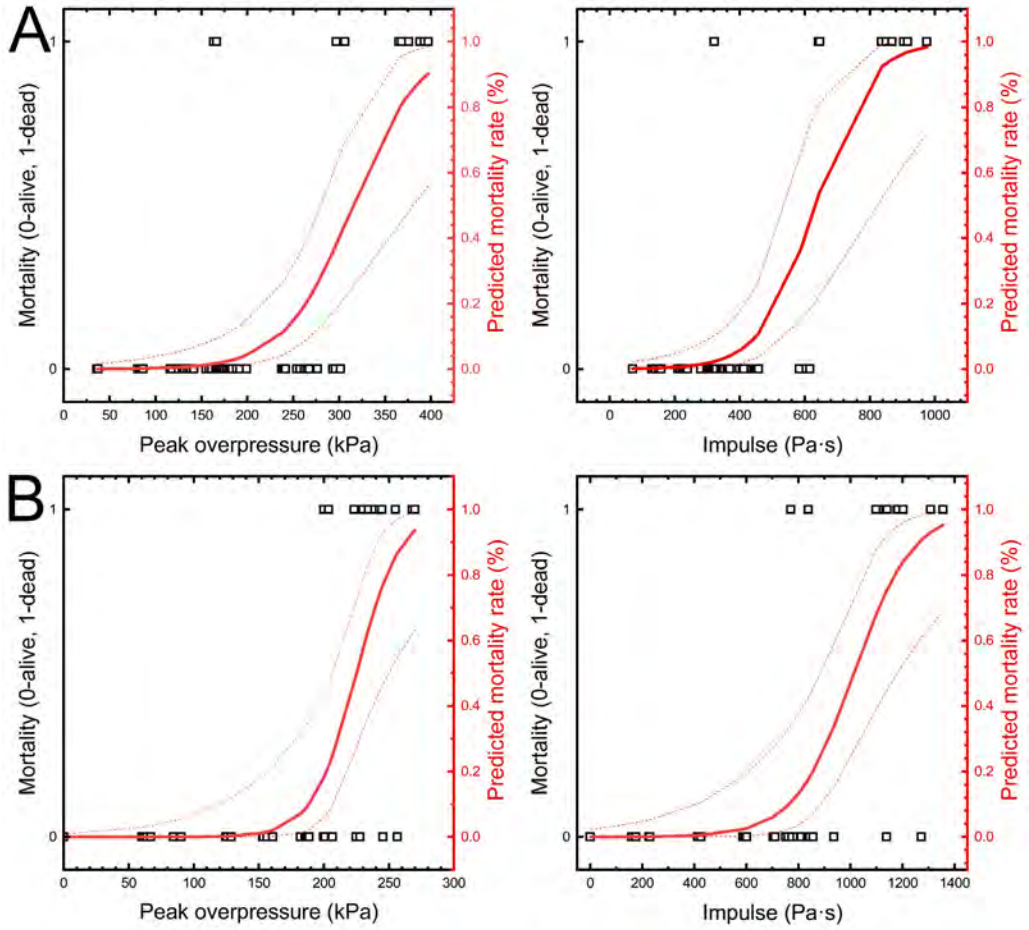


Figure .68. The two dose-response curves developed for short (A) and long (B) duration impulse using a cohort of 150 animals. Rats were exposed to a single shock wave with predefined characteristics, based on the two calibration curves (see fig. 43), and 24-hour survival was evaluated (0-alive, 1-dead). The data were fitted using binary logistic regression for BOP and impulse as mortality predictors. For long duration impulse (B) the shift towards lower BOPs is apparent.

68B): the 10%-90% predicted mortality rate (PMR) function are in the 230-400 kPa (figure 68A) and 190-260 kPa (figure 68B) peak overpressure for short and long impulse, respectively

Task 9. Examine the changes in protein expression due to changes in blast impulse 24 hours after primary blast exposure

In this ongoing study as part of Specific Aim 3 we performed biomarker identification and examined by ELISA the levels of glial fibrillary acidic protein (GFAP), an astrocyte marker that is released into blood stream after astrocyte end feet damage. Blood samples were collected from control and animals exposed to moderate blast (180 kPa, immediately and 4 hours after injury) and levels of GFAP were examined by quantitative ELISA. Blast injury caused significant increase in plasma levels of GFAP immediately following blast and continued to show elevation until 4 hours after blast injury (Figure 69). These results not only indicate evidence of blood brain barrier breakdown following blast, but also that astrocytes undergo cellular (plasma membrane) damage following blast injury.

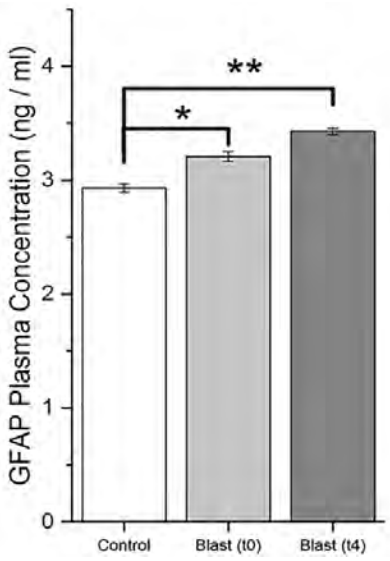


Figure. 69. Levels of glial fibrillary acidic protein (GFAP) a marker of astrocytes in plasma samples obtained from animals of control, immediately and 4 hours after blast injury (180 kPa).

As part of proteomic analysis to identify different protein biomarkers following changes in blast impulse, we performed studies initially screening the levels of neuronal synaptic vesicle markers synaptophysin and post-synaptic density protein of 95 kDa (PSD-95), markers of pre-and-post synapses in hippocampus of animals exposed to 2 BOPs (180 kPa and 240 kPa) and 24 hours after injury. Accordingly, lysates from hippocampus were used to determine the protein levels of synaptophysin (marker of presynaptic vesicles) and PSD95 (marker of post-synaptic vesicles) by

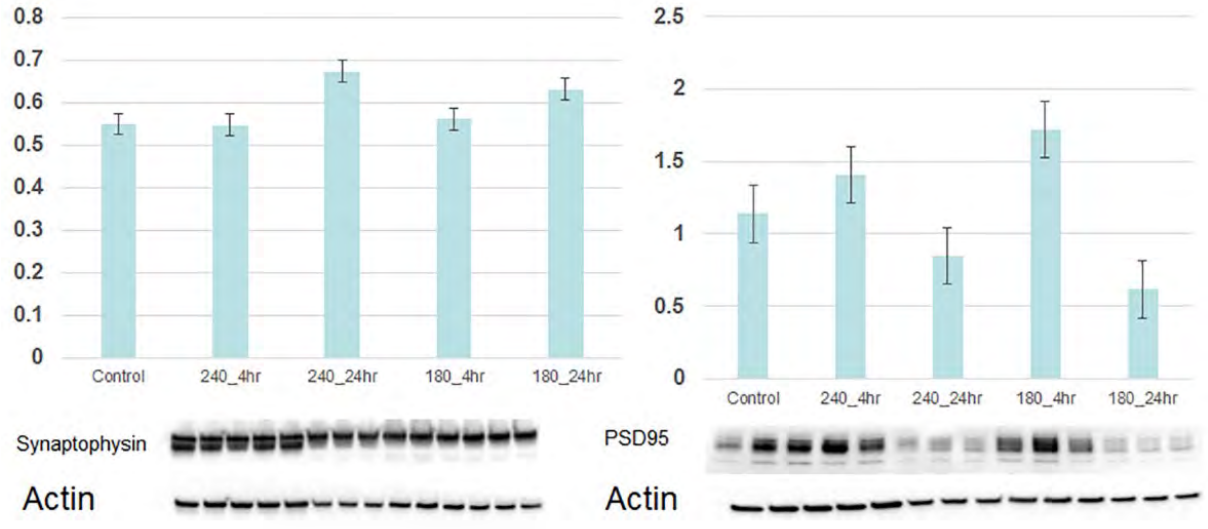


Figure.70. Levels of synaptophysin and PSD-95, markers of pre-and-post synaptic vesicles as a function of different BOPs. Note that there is an inverse correlation of changes between synaptophysin and PSD-95 24 hours post injury at 180 and 240 kPa.

immunoblot analysis. Results show differential changes in synaptophysin and PSD-95 as a function of different blast overpressures, in that synaptophysin protein levels showed strong tendency of increase at 24h post injury at both BOPs (180 and 240 kPa). However, PSD-95 protein levels show an increase as early as 4 h post injury, but their levels significantly reduced 24 hours after blast (Figure 70). These data strongly suggest: 1) blast injury causes post-synaptic vesicle protein changes earlier than pre-synaptic vesicle proteins and that while there appears to be an inverse correlation between pre-and-post synaptic vesicle protein changes 24 hours post-injury. Further studies are being carried out investigating proteomic analysis of synaptic vesicle changes following changes in blast impulse.

9.1 Examine Changes in Protein Expression Due to Changes in Blast Impulse

The proteomic analysis revealed the total number of identified proteins is 3638 and 3363 for 330 and 720 Pa·s, respectively. The volcano plots for the low and high impulse are presented in figure 1. The statistical significance threshold was set at p = 0.05 ($-\log_{10}$(p-value) = 1.3). It is evident that for the low impulse there are total of 238 proteins (upregulated: 112, downregulated: 126) which reached or exceeded the threshold, while for the high impulse group there are 435 proteins (upregulated: 99, downregulated: 336). The upregulated proteins number changed relatively small (13) while the number of downregulated proteins is higher for the high impulse group by 210 (figure 71). Moreover, the ratio of the upregulated to downregulated number of proteins is 0.8 and 0.5, for low and high impulse groups, respectively.

The network analysis revealed that the most dominant canonical pathway is oxidative

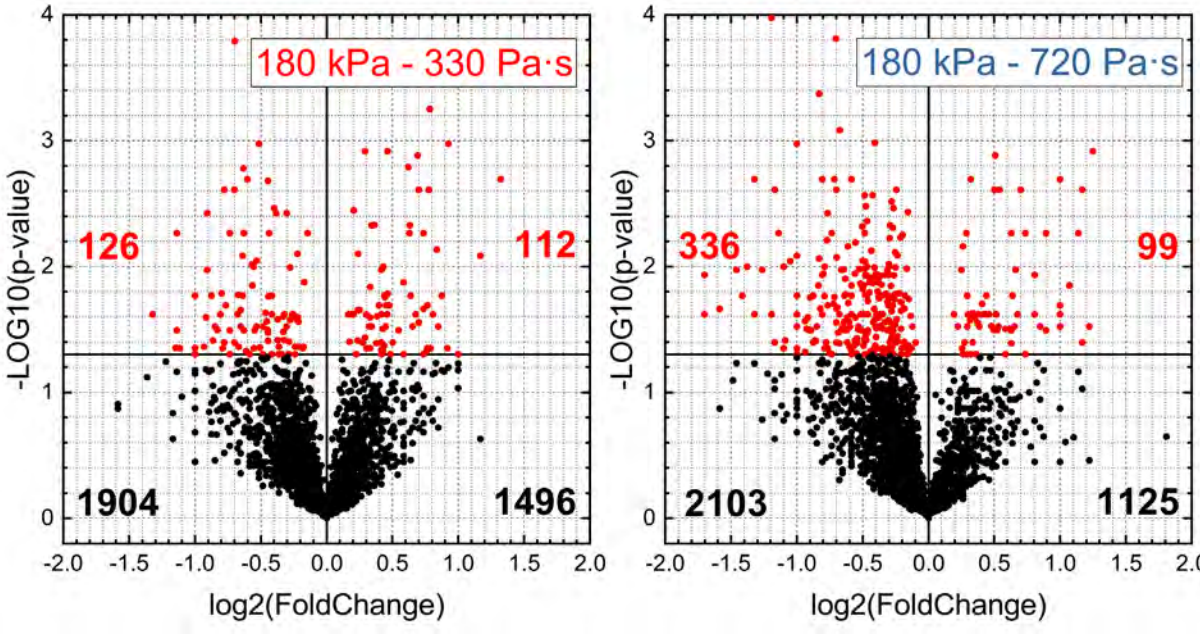


Figure. 72. The volcano plots of the proteins identified in the brains of rats exposed to 180 kPa with low- (330 Pa·s) and high-impulse (720 Pa·s). The number of upregulated proteins is 112 and 99 for low- and high-impulse groups, respectively, while the number of downregulated proteins is 126 and 336 in these respective data sets.

phosphorylation (OXPHOS) in both cases (fig. 2). Additionally, there are 15 pathways which are activated in the high impulse (720 Pa·s) group only (absolute z-score of 2 or more, fig. 72), while only OXPHOS is in an activated state in the low energy impulse (330 Pa·s). The Western blot was

performed on three proteins in the isolated cerebellar fractions: 1) Synaptophysin, postsynaptic density protein 95 kDa and ATP synthase-coupling factor 6 (Syp, PSD95 and ATP5j, respectively, fig. 73). Changes or lack of thereof observed in the expression of these proteins confirm the results of mass-spec protein characterization.

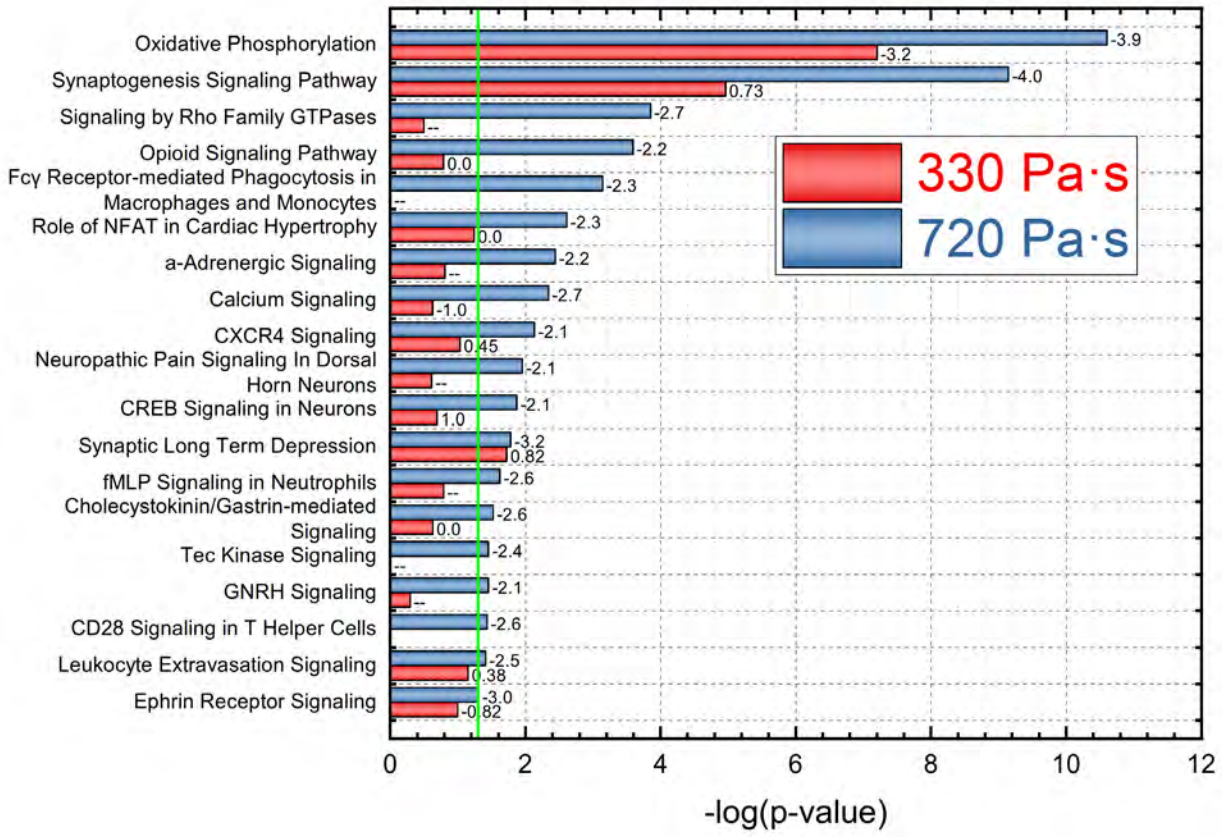


Figure 73 The comparative analysis of the canonical pathways identified by proteomic analysis of the cerebelli of rats exposed to a single shock wave with 180 kPa and impulse of 330 Pa·s (short-impulse) and 720 Pa·s (long-impulse). The z-score filtering was performed on identified canonical pathways, and only pathways with absolute score of 2 were included in the analysis for the short-impulse group. This filter left only "Oxidative phosphorylation" pathway in the short-impulse group, while the remaining pathways are presented for comparison.

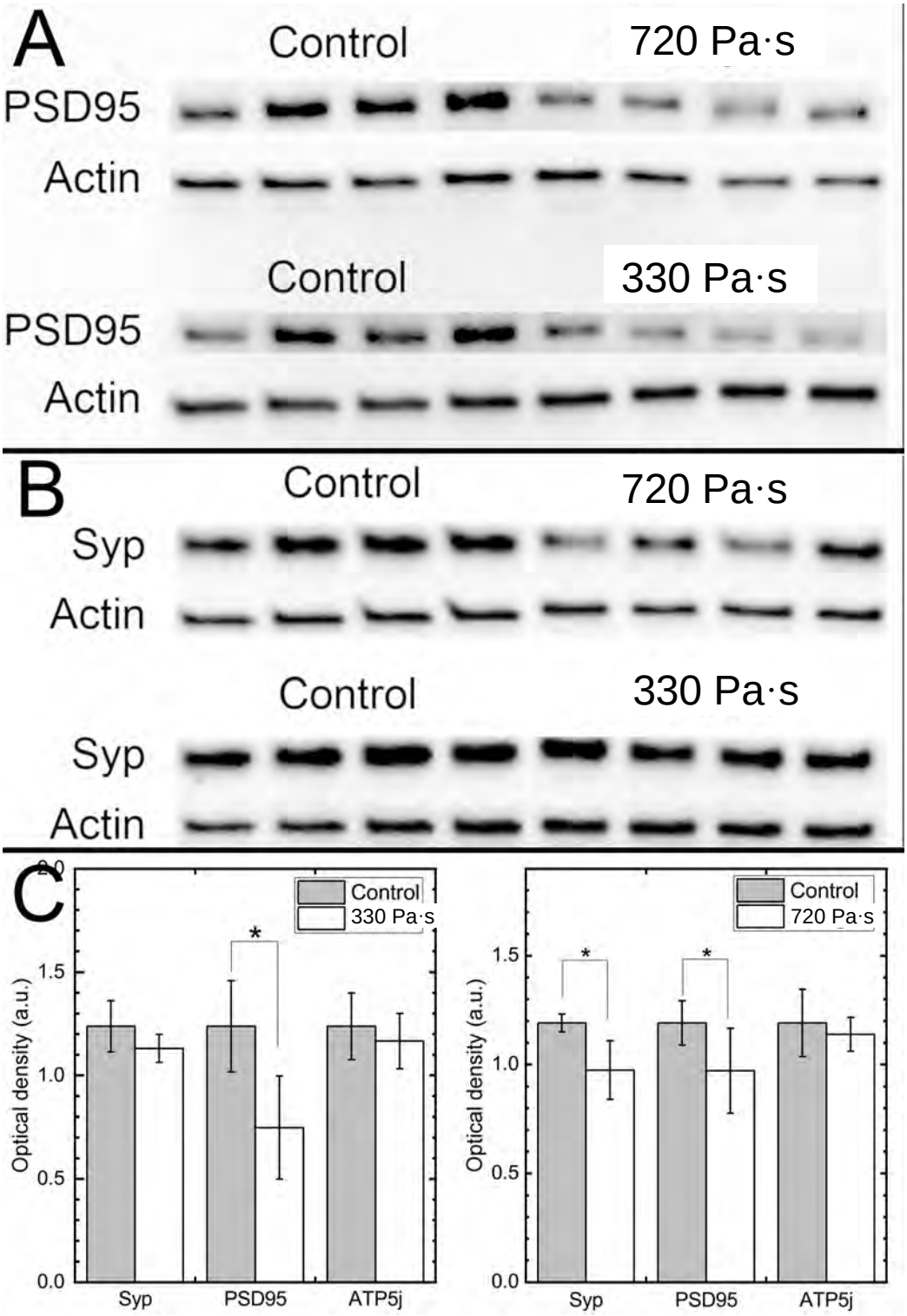


Figure 74 The verification of the proteomic data via Western blot. Synaptophysin (Syp), postsynaptic density protein 95 kDa (PSD95), and ATP synthase-coupling factor 6 (ATP5j) were used. A, B: Western blot and quantification results (C) are presented. Actin was used as a housekeeping protein and the level of statistical significance is set at p = 0.05. Groups where statistical significance threshold was reached are marked with asterisk.

Task 10. Determine Alterations of Loading in the Rat Brain Caused by Changes in Impulse

Initial work into the simulation of high and low impulse exposures. Modeling the high energy high impulse conditions (180 kPa, 720 Pa·s; 240 kPa, 1100 Pa·s) resulted in numerical instabilities impeding the ability of the solutions to converge. These instabilities manifested themselves in single node excessive distortions indicative of volumetric locking of the solution (figure 74). A lack of confidence in the quality of the simulation results at higher energy exposures encouraged the investigation of additional analysis techniques. Therefore, a comparison of shock wave modeling via the previously used coupled Eulerian-Lagrangian (CEL) methods and the Conventional Weapons Effects (CONWEP) incident wave interaction method.

10.1 Coupled Eulerian-Lagrangian Method

This method of shock wave simulation has been discussed at length for the purpose of computationally generating shock waves [19, 21, 22]. In short, the shock tube system is comprised of two interacting domains. One domain, the Eulerian domain, is ideal for the simulation of air flow and shock waves. This domain allows material to freely flow through the domain, enabling the simulation of large deformation loading events. A Eulerian mesh was chosen to represent the air contained within the shock tube (fig. 75). The second domain, the Lagrangian domain, is optimal for the simulation of solid mechanics. In a Lagrangian domain, the mesh is tied to the material and both systems deform together. This domain was selected for the simulation of the rat body and brain.

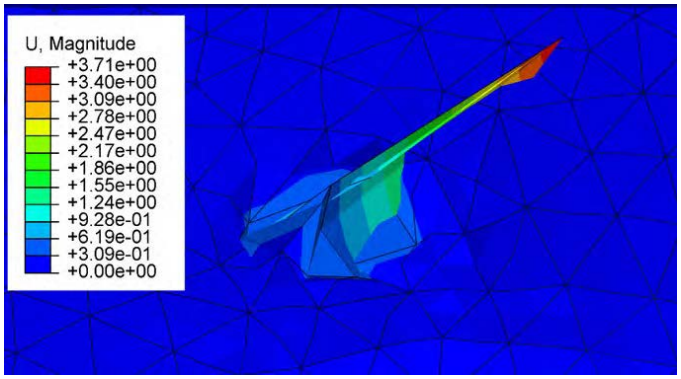


Figure 75. An example of the excessive distortion caused by numerical instabilities. The unscaled deformed variable of displacement magnitude, U, is displayed in the units of millimeter. The location shown is on the top of the cranium in a corner node shared between elements which meet the Abaqus minimum mesh quality metrics. This deformation behavior was observed to occur in the preloading period, when the system is brought up to ambient pressure, before the arrival of the 180 kPa long duration shock wave.

The Lagrangian domain is immersed in the Eulerian domain and the two systems contact each other. As air cannot occupy the same space as the rat, the Eulerian domain is filled with air in all elements which do not contain the Lagrangian rat model. Elements which are partially filled with the Lagrangian system are partially filled with air. This is calculated for every solution iteration as the

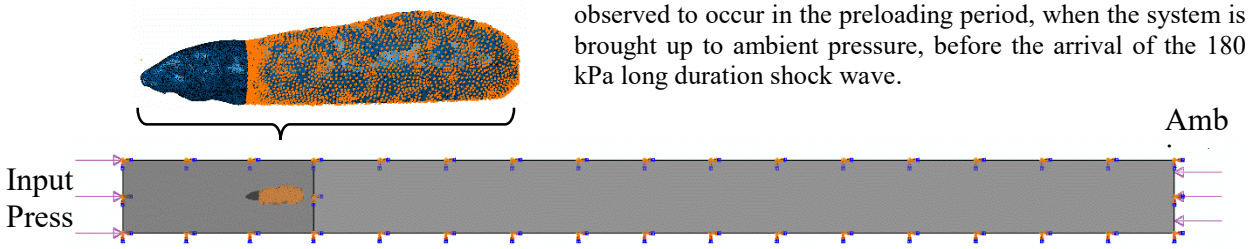


Figure 76. A lateral depiction of the input conditions used to simulate shock loading on the Lagrangian rat head. The shock tube Eulerian mesh is shown in grey. Pink arrows show the pressure loading locations. The left face, the opening of the shock tube model, is loaded with the pressure profiles shown in Figure 3. The right face is loaded with a constant pressure equivalent to the ambient pressure conditions. The orange and blue arrows indicate that a face is constrained in all degrees of freedom. This boundary condition was applied to the rat body, as shown in the above enlarged depiction of the Lagrangian model, and the walls of the Eulerian instance.

finite element (FE) solver calculates the boundary between the two domains. The material within the Eulerian domain is constrained to flow around and interact with the Lagrangian domain without passing through it. The energy contained within the Eulerian domain, resulting from the pressure-time amplitude applied to the system to simulate a shock wave exposure, is transmitted through this contact definition to the Lagrangian domain and this constitutes the mechanism of shock wave loading the CEL method.

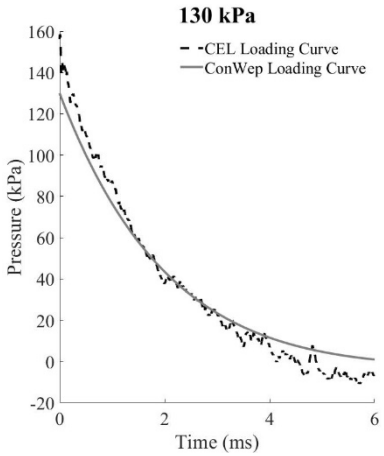


Figure 77. Input pressure profile used in the simulation of the shock wave for the CEL method and the ConWep method.

10.2 CONWEP Incident Wave Interaction

This technique has been used in the literature to simulate an idealized free-field air blast, and is implemented directly within Abaqus 6.13-4 (Dessault Systems Simulia Corp., Providence, Rhode Island, USA) [23]. In this method, the CONWEP program uses theory and empirical data to output the incident pressure, reflected pressure, and shock velocity of a free-field spherical shock front resulting from user inputs. It is a collection from the US Army standard TM-5-855-1 [24]. The user can input two of any of the following parameters: stand-off distance, charge weight, incident pressure, or reflected pressure. This will result in the calculation of the non-specified parameters, as well as the arrival time, positive phase duration, incident and reflected impulses, and other parameters. The CONWEP Program is directly integrated with the Abaqus solver through the definition of an incident wave property. The empirical data from the CONWEP output is used to create a pressure load which interacts with prescribed surfaces on the Lagrangian model.

10.3 Comparison of Output Results

A 130 kPa, 220 Pa·s loading event was simulated using both analysis techniques. This loading event was selected as it was the highest energy (i.e. impulse) simulation in which observable effects of numerical instability were not observed in the CEL modeling technique. For the CEL event, the simulation set-up is shown in figure 75 and the loading event is shown in figure 76. This model was identical to the results reported in the 2018 Annual Report.

The CONWEP program was used to determine the stand-off distance and charge weight necessary for a 130 kPa, 220 Pa·s shockwave. This was determined to be a 22.24 kg TNT charge located 6.76 m away from the specimen. The CONWEP-generated incident pressure profile is shown in fig. 76. A reference point was placed at the specified stand-off distance and the incident wave originated from that point. The incident wave was allowed to interact with all exposed surfaces of the model, excluding the belly of the animal, which experimentally would be in contact with the aluminum bed (figure 77,78). The nodes which were excluded from the incident wave interaction were fixed in all translational degrees of freedom. These boundary conditions were selected based upon the results of the a parametric study. This set of boundary conditions resulted in minimal motion of the rodent head without over-constraining the system. The motion of the rodent model was confirmed to be visually similar to the motion overserved experimentally in high-speed video of the exposures.

First, the loading pattern of the CONWEP method was confirmed. The analytical CONWEP predicted and simulated reflected pressure at an element which was nearly perpendicular to the

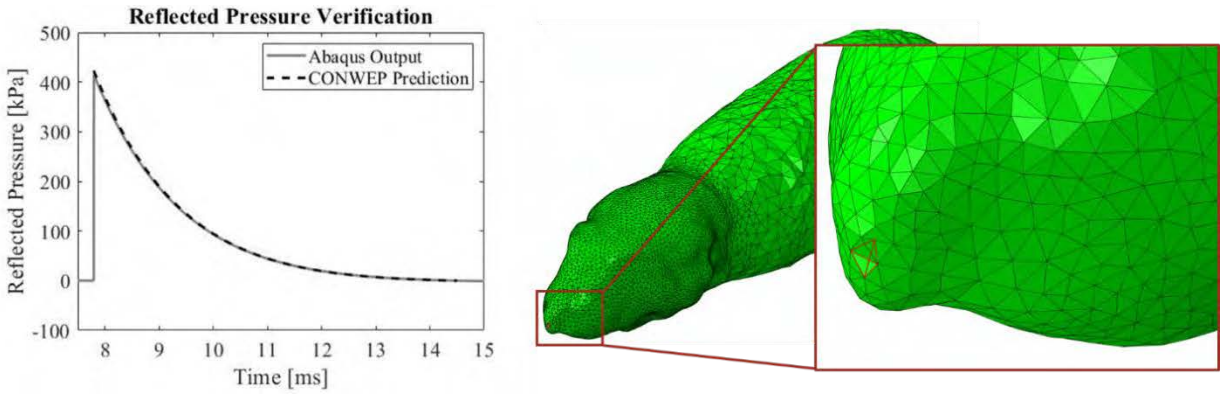


Figure 78. Verification of the simulated reflected pressures loading the Lagrangian system at the element shown (right, inset).

interacting incident waveform. The element location is shown in figure 77. It was confirmed that the peak reflected pressures and the decay profile were nearly identical. A small difference was observed, with the peak simulated reflected pressure 2.15% lower than the ideal value. This small error can be attributed to the violation of two reflected pressure assumptions, an ideal angle of incidence and an unyielding surface. This comparison confirmed that the CONWEP incident wave was interacting accurately with the Lagrangian instance.

Next, the output of the CONWEP incident wave model was compared with the output of the previously reported CEL model. Using techniques described in [21], the simulations were compared with experimental measurements of ICP at two locations. Briefly, the micro-computed tomography was used to localize the measurement location. After shock exposure and sacrifice, the experimental test subjects were preserved in 4% paraformaldehyde. The scans were taken with an image pixel size of 32.5 μm (SkyScan 1275, Bruker microCT), reconstructed (NRecon Reconstruction, Brucker microCT), and segmented into solid masks of the skull and the cannulas (Simpleware ScanIP, Synopsys). The location of the pressure sensors was then found for each specimen. Scaling was performed to match the size of the cranial cavities.

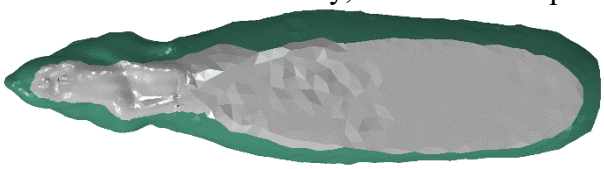


Figure 79. A depiction of the surface excluded from interaction with the incident wave.

The simulation output was examined at the nodes closest to the sensor locations. The ICPs were normalized with respect to arrival time (figure 79). The results highlight that the CONWEP simulation shows an improved match with the experimental results. Based on the positive validation of the CONWEP incident wave loading solution scheme, the long impulse, high energy simulations were conducted with the new modeling technique.

10.4 Effect of Shock Wave Impulse on Brain Mechanical Loading

A FE model of a ten-week old Sprague Dawley rat was used to investigate the influence of pressure impulse on the ICP, von Mises stress, and logarithmic strain within the brain. Three nominal overpressures were simulated with a normal and an increased impulse. Overpressures were simulated using the CONWEP incident wave loading procedure in Abaqus, which was previously extensively validated in our previous report. Charge weights and stand-off distances for the loading procedures were selected to match peak overpressure and impulse. As the decay rate of the CONWEP loading procedure is limited, this resulted in simulated loading conditions of substantially longer duration signals, as detailed in Table 3. A comparison between the overpressure at the stand-off location is presented in figure 80.

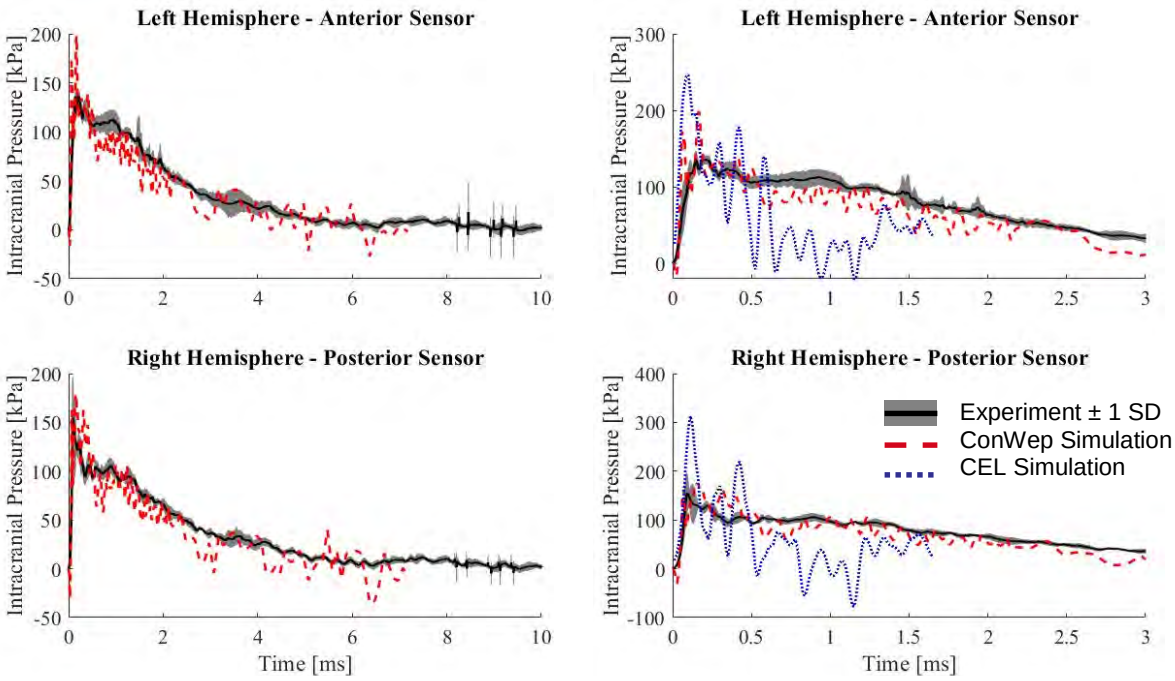


Figure 710. Comparison of the simulated and experimental ICP profiles in the left and right hemispheres of a rodent exposed to a low impulse 130 kPa shock wave. The experimental values are depicted as a mean (n=4) value in black and a band showing one standard deviation away from the mean in gray. Good agreement is observed between the ConWep simulation outputs and the experimental data.

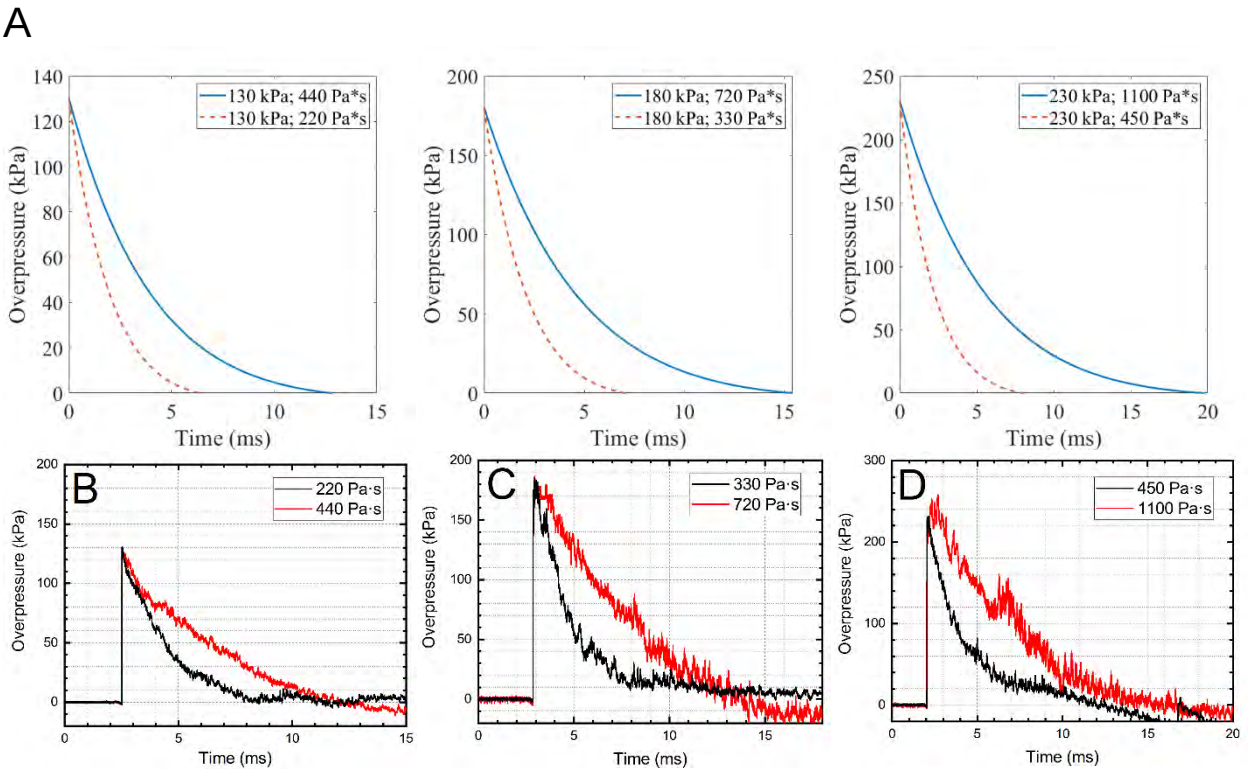


Figure 11. A comparison of (A) the loading incident pressure-time waveforms used in this work with (B-C) experimental waveforms for (B) 130 kPa, (C) 180 kPa, and (D) 230 kPa.

The rodent FE model was oriented in the prone position and the incident wave was permitted to load the rodent model on all surfaces not obstructed experimentally by the animal holder. This excluded interactions with the under surface of the rat body, as detailed in Figure 78. The charge was initiated at a source point placed at the stand-off distance detailed in Table 3. The solution was record using a variable time step in order to best resolve the rise time of the ICP and to minimize solution size. Prior to arrival of the shock front, four frames were sampled to ensure health of the solution. For 0.2 ms the solution was sampled at a sampling frequency of 1MHz. Following the sharp rise, a high sampling frequency was used to sample the exponential decay. This region, 2 ms in duration, was sampled at a frequency of 100 kHz. The remaining portion of the simulated time was sampled at a frequency of 1 kHz.

Table 3. The loading conditions, or simulated parameters, selected to best replicate the experimental test configurations, referred to as the target parameters. BOP = Blast Overpressure

Target		Simulated				
BOP (kPa)	Impulse (Pa·s)	BOP (kPa)	Impulse (Pa·s)	Duration (ms)	Charge Wt. (kg TNT)	Distance (m)
130	440	130	440	12.8	178.3	13.53
130	220	130	219.9	6.39	22.24	6.76
180	720	180	720.3	15.4	525.7	16.72
180	330	180	329.9	7.06	50.54	7.66
230	1100	230	1110	19.8	1427	20.9
230	450	230	449.8	8.00	94.97	8.47

10.5 Model Validation

Simulated ICPs were compared with experimentally measured values to validate the simulations. The locations of the pressure sensors were verified using micro-computed tomographic reconstruction of the locations of the stainless-steel cannulas. Co-localization and morphological scaling of the reconstructed skulls identified the nodes closest to the pressure sensors. The ICPs were compared and are included in Figure 81A-F. The close match between experimental measurements and simulated pressures validated the simulations, enabling further analysis. Following validation, a temporal map of the ICPs, von Mises stress, and logarithmic strain was developed for each simulation in the midsagittal plane of the rat brain.

10.6 Intracranial Pressure

The spatio-temporal pattern of ICPs remains conserved between the high and low impulse loading. When comparing the ICPs between the high and low impulse, it is apparent that the ICP remains

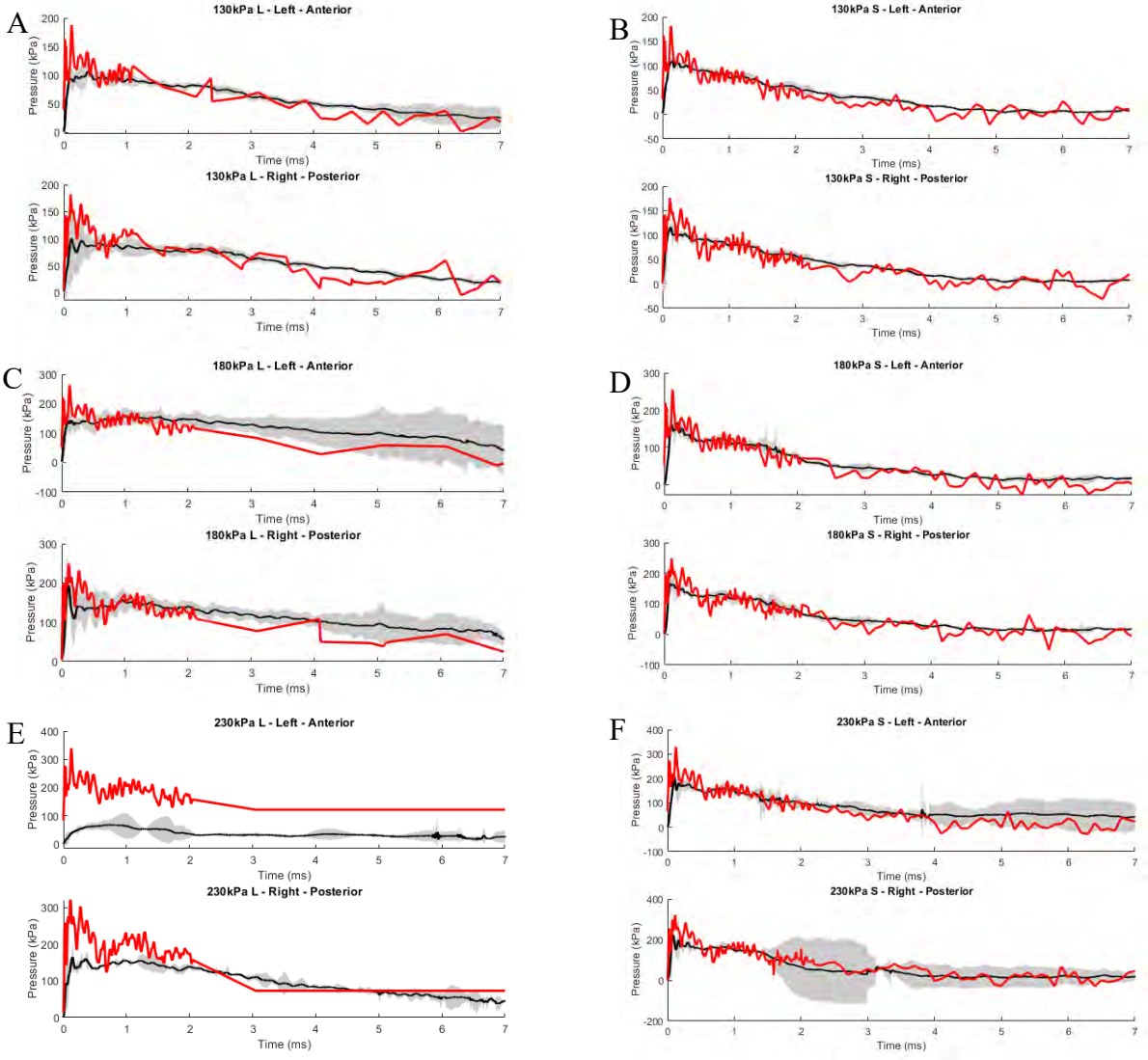


Figure 12. A comparison of the ICPs experimentally measured in the left (top) and right (bottom) hemispheres with simulated ICPs at the same locations.

elevated for a longer period. This is apparent when comparing the last time points presented in Figures 82-84. The short impulse exposures show a relaxation of the ICPs.

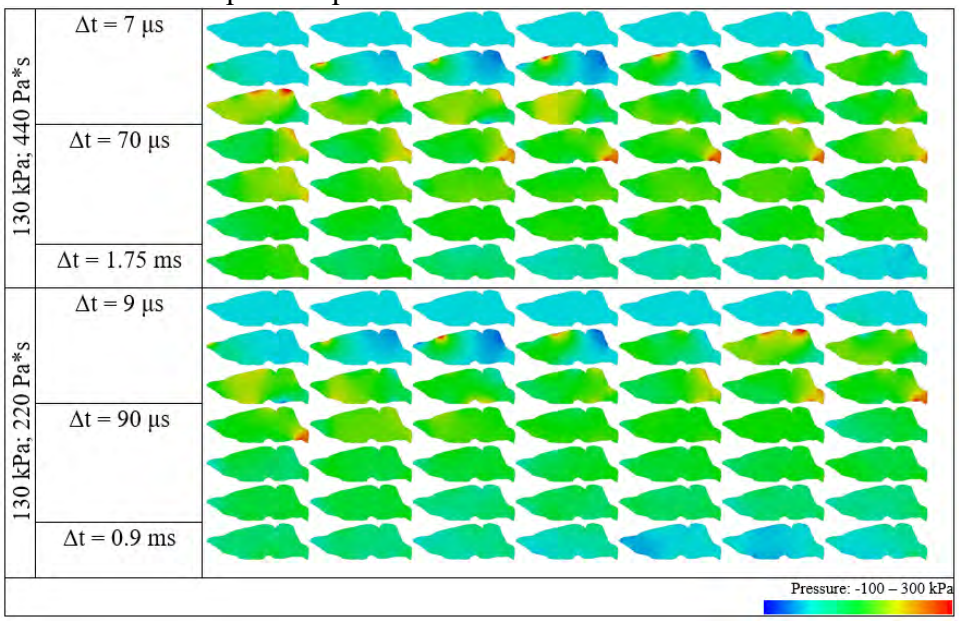


Figure 13. A comparison of the ICP in the midsagittal plane of a rat brain. Colors denote high and low pressures within the range specified.

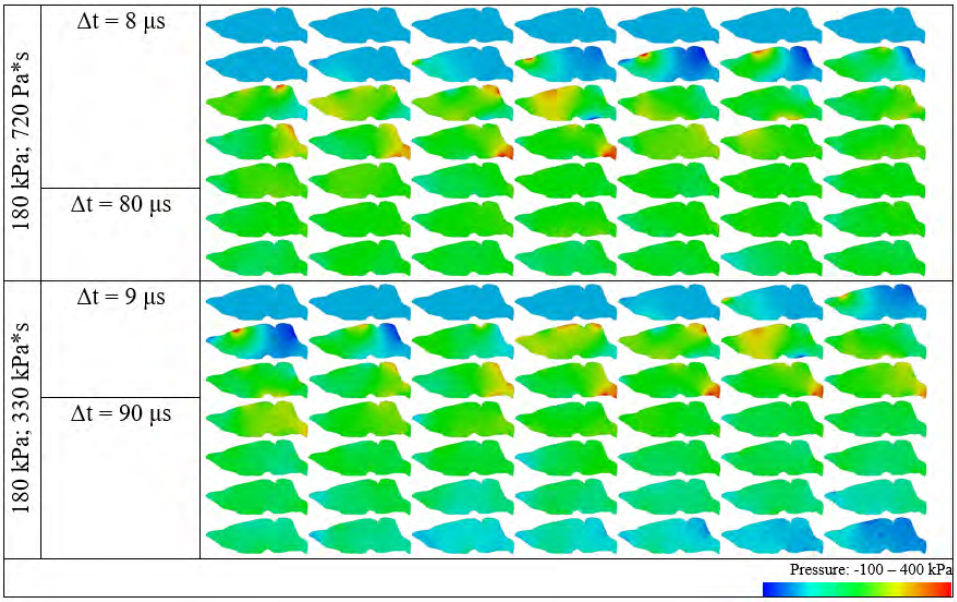


Figure 14. A comparison of the ICP in the midsagittal plane of a rat brain. Colors denote high and low pressures within the range specified.

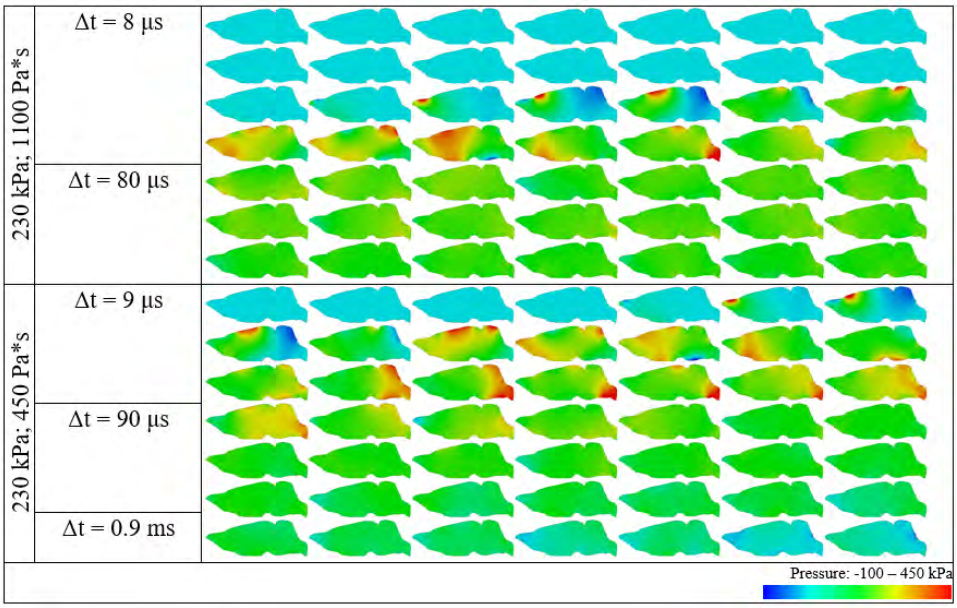


Figure 15. A comparison of the ICP in the midsagittal plane of a rat brain. Colors denote high and low pressures within the range specified.

10.7 Von Mises Stress

The von Mises stress was observed to be slower to develop in the high impulse simulations. This could indicate a slower dissipation of the internal stresses, paralleling the patterns of the ICPs. In general, the development of internal stresses is delayed following the arrival of the shock front. Therefore, the decay of these internal stresses is theorized to occur over a longer period of time as well. In Figures 85-87, it can be observed that the time-course of stress development for the high impulse simulations appears to follow that of the low impulse simulations. Longer simulations times, investigating the recovery of the system, would be necessary to provide insight into the dissipation of the built-up energy. However, it appears to be that the internal stress remains elevated within the system following blast exposure. Additionally, the pattern of von Mises stresses appears to be conserved between the high and low impulse simulations.

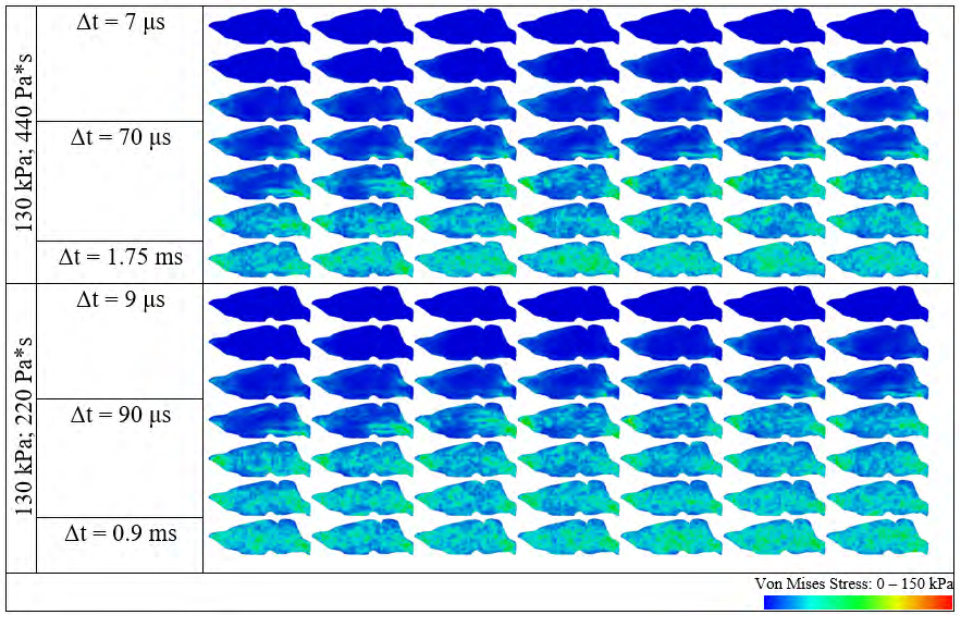


Figure 16. A comparison of the von Mises stress in the midsagittal plane of a rat brain. Colors denote high and low stresses within the range specified.

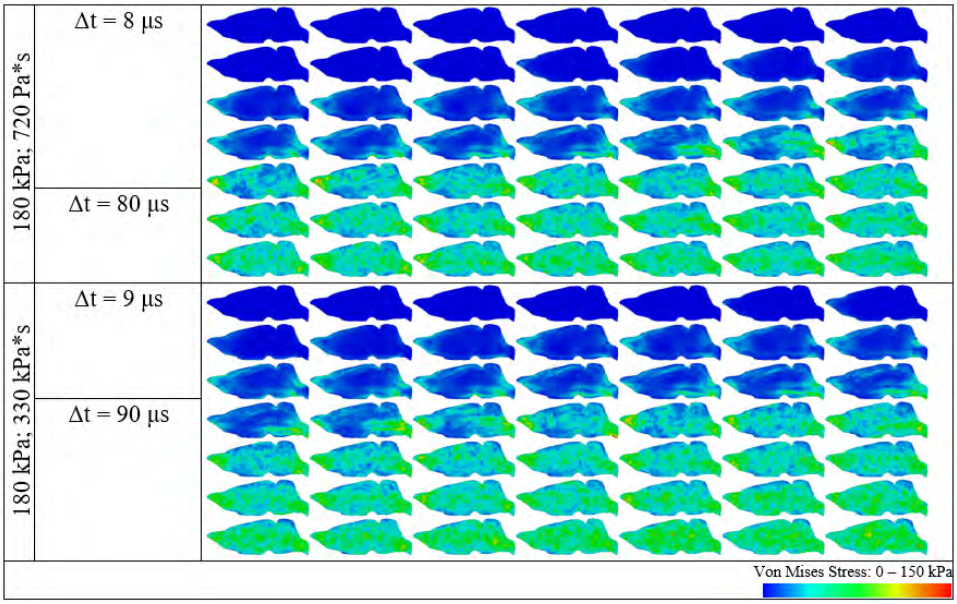


Figure 17. A comparison of the von Mises stress in the midsagittal plane of a rat brain. Colors denote high and low stresses within the range specified.

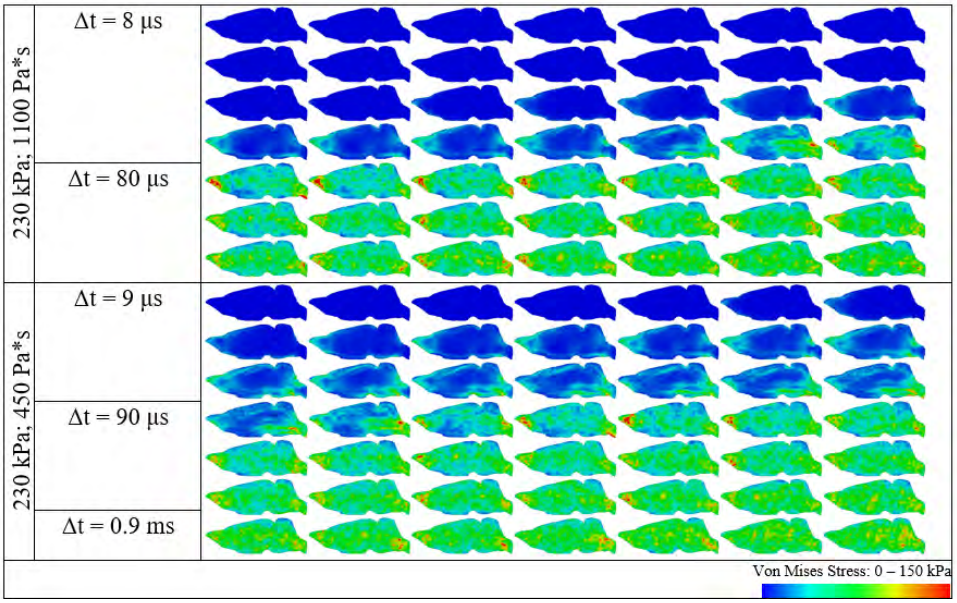


Figure 18. A comparison of the von Mises stress in the midsagittal plane of a rat brain. Colors denote high and low stresses within the range specified.

10.8 Logarithmic Strain

The strain within the brain appears to follow a similar pattern to that of the von Mises stress. Again, the development of strain appears to be delayed in high impulse loading conditions. The strain is slower to develop and remains elevated over the time investigated. The pattern of strain development remains conserved between the high and low impulse simulations (figures 88-90).

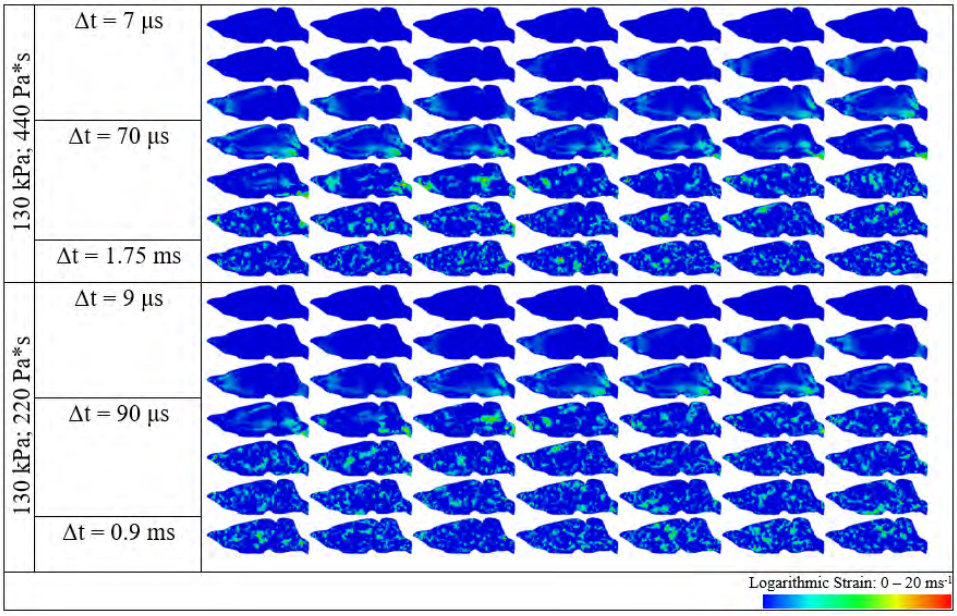


Figure 19. A comparison of the logarithmic strain in the midsagittal plane of a rat brain. Colors denote high and low strains within the range specified.

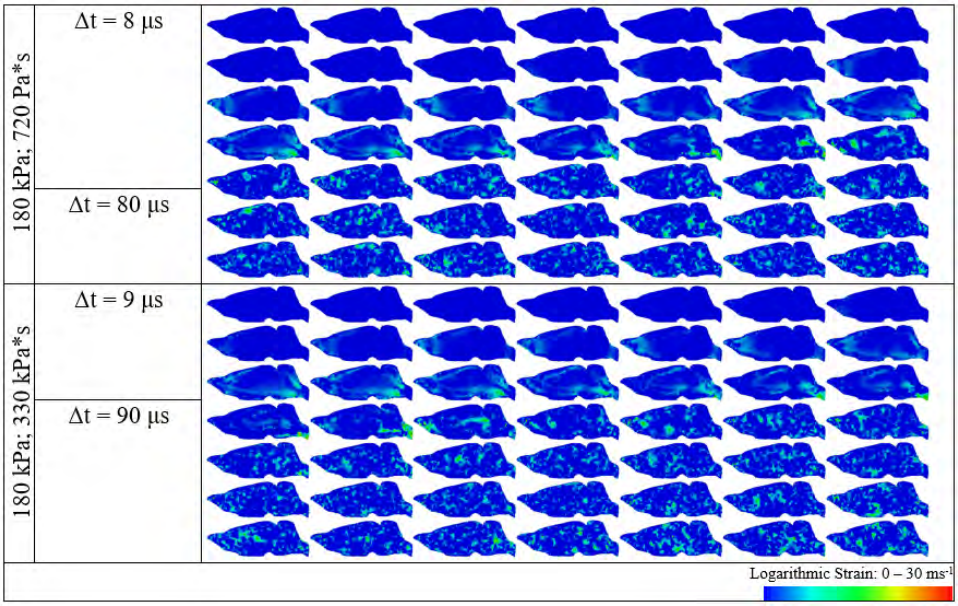


Figure 20. A comparison of the logarithmic strain in the midsagittal plane of a rat brain. Colors denote high and low strains within the range specified.

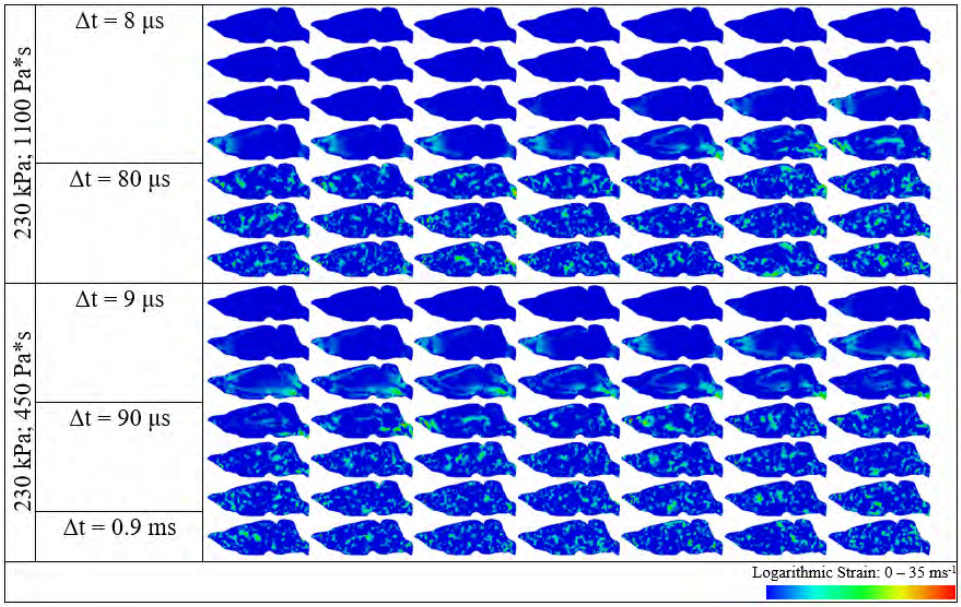


Figure 21. A comparison of the logarithmic strain in the midsagittal plane of a rat brain. Colors denote high and low strains within the range specified.

We performed biomechanical loading evaluation on rats implanted with three sensors: two in the brain and a single sensor in the carotid artery (Figure 91). The measurements were performed at

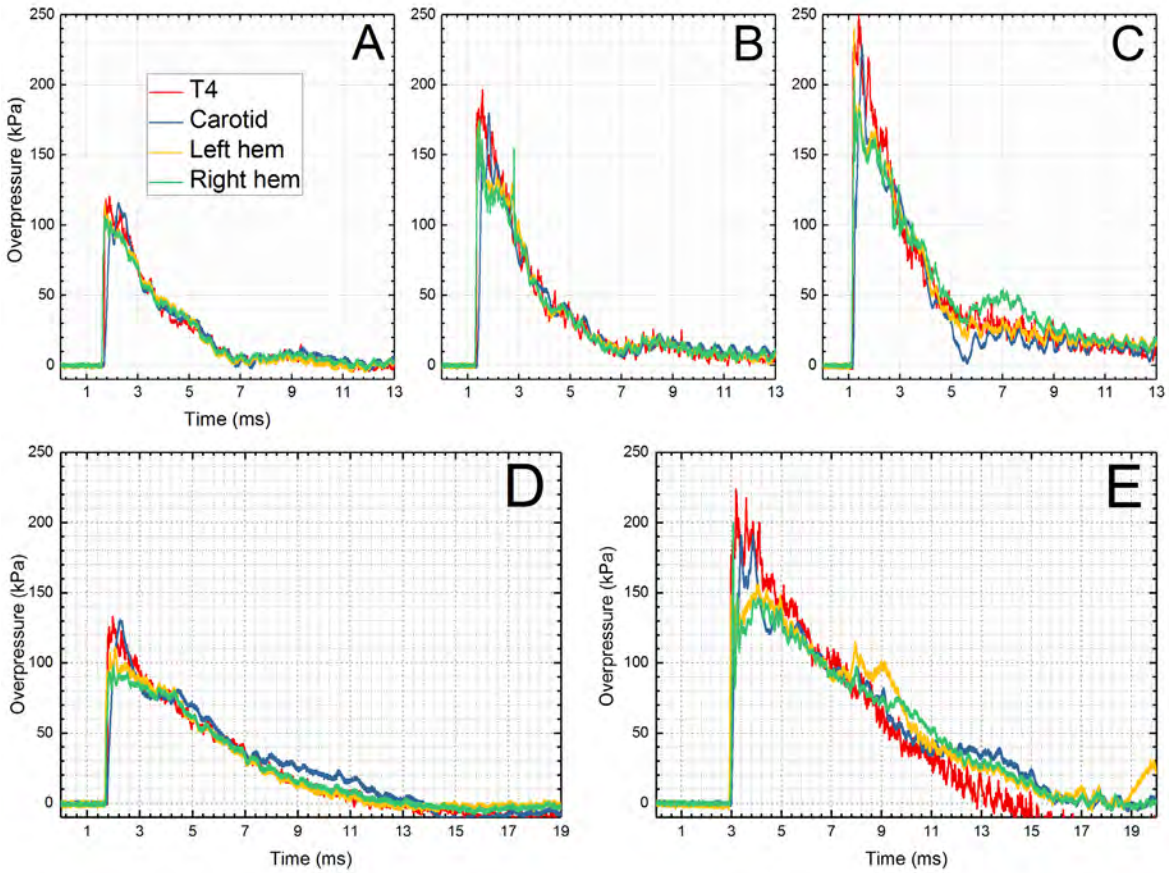


Figure 91. The biomechanical loading evaluation – the impulse effect. Double ICP and carotid artery pressure sensors were used to measure the pressures of rats exposed to the "low impulse" (with nominal BOP of: A. 130, B. 180, and C. 230 kPa) or "high impulse" (nominal BOP: D. 130 kPa, and E. 180 kPa). The durations in each group are illustrated.

three nominal BOPs: 130, 180 and 230 kPa with variable shock wave impulse (Figure 91). The heads of rats were imaged using micro-CT scanner to establish precise location of the cannulas where pressure sensors were implanted. This information will be used in the development of the refined numerical model of the rat's head under shock wave loading conditions. The parametric studies of the material properties were completed, and manuscript submitted to AMBE journal (currently under review). With the conclusion of Task 3 and Task 8, work has begun to apply the computational model and analysis techniques used to examine the effect of changing impulse. Six simulations are underway for this task, simulating low impulse blasts at overpressures of 130, 180, 230 kPa at low and high impulse values. The simulations have been constructed in an identical manner as those reported in Task 3. The waveforms which are being used for these simulations are included in Figure 91D and E. Precluding unforeseen numerical solution instabilities or simulation artifacts resulting from the higher energy waveforms, results are anticipated to be completed for the Q1 Quarterly Report for Year 4.

Task 11. Identify Cross-Species Mild-To-Moderate bTBI via Numerical Simulations

The excessive oscillations observed using the original modeling techniques prompted a review of the model assumptions and simulation inputs for the previously developed FE model of the human head [25]. As the work presented in Task 10 concluded that the loading procedure contributed to the excessive observed oscillations, the loading methodologies were tested for the human head model as well. First, the loading methodology was selected through a comparison of surface reflected pressures on an experimental and simulated headform model. Next, a biofidelic FE model of a human head was developed and converged.

11.1 Surrogate Headform Experimental Data Collection

A head surrogate was mounted to a Hybrid III neck surrogate and exposed to shock waves within a field-validated shock tube. The surrogate was exposed to a mild-intensity shock wave (130 kPa) at two orientations: (1) where the shock wave was traveling from anterior to posterior, called a frontal blast, and (2) where the shock wave was traveling laterally, called a lateral blast (figure 92). Surface pressures were recorded at ten regions of interest on the surface of the head (figure 93). The surface-measured reflected pressures were used as validation criteria for a numerical model of the experimental setup, comparing the peak reflected pressures and the impulse of the pressure-time profiles.

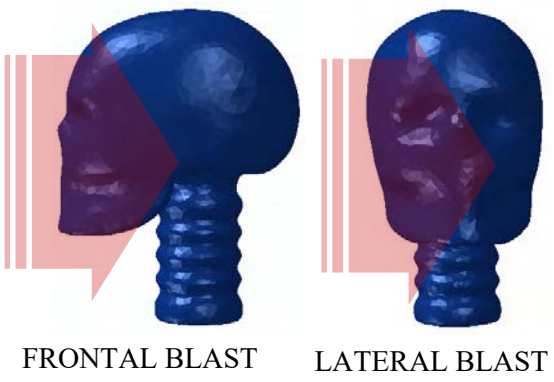


Figure 92. Two orientations were considered in this work. These were where the shock wave, depicted with a red arrow, moved anterior to posterior, termed a frontal blast, (left) and right to left, termed a lateral blast (right).

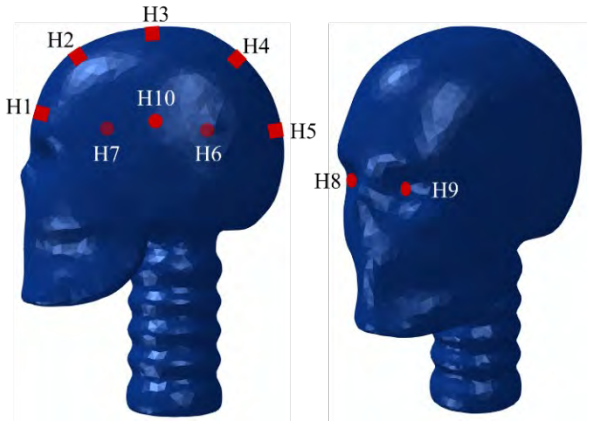


Figure 93. The geometrical model of the surrogate head surrogate mounted on a Hybrid III neck in the lateral (left) and isometric (right) views. The head surrogate was assumed to be a rigid shell. The five mid-sagittal sensors (H1-H5) were located along the midline, with the circumferential sensors (H6-H10) examining the right side (H6, H7), eye cavities (H8, H9), and left side (H10).

Shock Tube Eulerian Model. A geometrical model of the 28-inch shock tube was generated which consisted of a driven region, 6.7 m in length, and the 1.4x1.4x1.8 m^3 catch tank. This geometry was meshed using a linear, reduced order, hexahedral Eulerian mesh with hourglass control. A convergence study was conducted to establish the minimum mesh seed density required to match incident pressure profiles at the test section and the reflected surface pressures. A minimum mesh seed length at the testing location was found to be 13 mm, resulting in a Eulerian domain of approximately 740,000 elements. As described in Task 3, the air was modeled to be in ambient conditions (an air density of 1.2 kg/m^3 at 292 K) using the values included in Table 4.

Table 4. Material properties used in the numerical simulation of shock.

Ideal Gas Equation of State		
	Gas Constant	Specific Heat
Air	287 J kg^{-1} K^{-1}	1010 J kg^{-1} K^{-1}

11.2 Surrogate Headform Lagrangian Model

A geometrical model of the RED headform and Hybrid III neck were reconstructed from a series of photographs using ReCap Pro 2018 (Autodesk, Inc. San Rafael, CA) and meshed using Simpleware CAD and FE (Synopsys). As an initial investigation into the model assumptions necessary to match surface reflected pressures, the surrogate headform was first assumed to be a discrete rigid body. The geometry of the headform was meshed with two -dimensional linear triangular elements into a three-dimensional shell. The Lagrangian mesh can be seen in figure 95.



Figure 95. A frontal, lateral, and isometric view of the RED surrogate head form model. The model is a three-dimensional discrete rigid body consisting of a linear, triangular shell mesh.

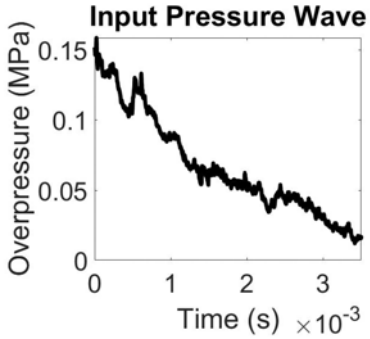


Figure 94. The loading pressure profile used in the simulation of a 130 kPa shock wave. The input pressure wave was experimentally taken at the same location.

11.3 Coupled-Eulerian Lagrangian Shock Simulation



Figure 96. The geometry of the shock tube was based on the shock tube with a 28 in square cross section. The Lagrangian headform is shown at the test section. The colors reflect the Eulerian volume fraction, with red denoting elements which are 100% air and blue denoting the elements which are 100% void.

The headform was positioned within the large shock tube 1.3 m downstream from the opening of the shock tube. Two simulations were conducted, with the headform oriented so that a frontal and lateral blast were simulated. The node which governed the motion of the Lagrangian discrete rigid body was constrained with all translational and rotational degrees of freedom. As was established in Task 3, the simulation was accomplished in two steps. First, the initial pressures equilibrated for a time period of 100 ms. In this step, all translational degrees of freedom were fixed along the shock tube walls and at the shock tube opening. This step allowed for the establishment of the

Eulerian material surfaces, establishing the location of the boundary between the Eulerian and Lagrangian instances. The space within the Lagrangian instance was said to be void of material and the space external to the Lagrangian instance consisted of ambient air. In the second step, a shock was simulated and propagated down the length of the shock tube for 14 ms. As, at this time, only the surface pressures were of interest, the time scale of the simulation was much shorter than that used in Tasks 3 and 10. The loading amplitude, depicted in Figure 94, was experimentally taken from the sensor at the same location. It constituted a simulated overpressure of 130 kPa. Surface reflected pressures were sampled from the simulation at times of interest at a sampling frequency of 100 kHz. The loading and boundary conditions are summarized in Figure 96.

11.4 Coupled-Eulerian Lagrangian Reflected Pressure Validation

The surface reflected pressures were compared between experimental sensor measurements and the corresponding locations on the Lagrangian model. The maximum reflected pressure and the impulse of the pressure sensors were compared for a frontal and lateral blast, shown in Figure 97. The impulses were calculated over a set time (0.5 ms) to eliminate signal artifacts. The lateral blast had lower reflected pressures and impulse values than the frontal blast, corroborated by observations seen in figure 26. The simulation tended to accurately predict the peak reflected pressures and overpredict the impulses for the frontal (5.82±13.5% and 45.5±38.4%, respectively) and lateral blasts (-5.92±20.9% and 66.9±18.1%, respectively).

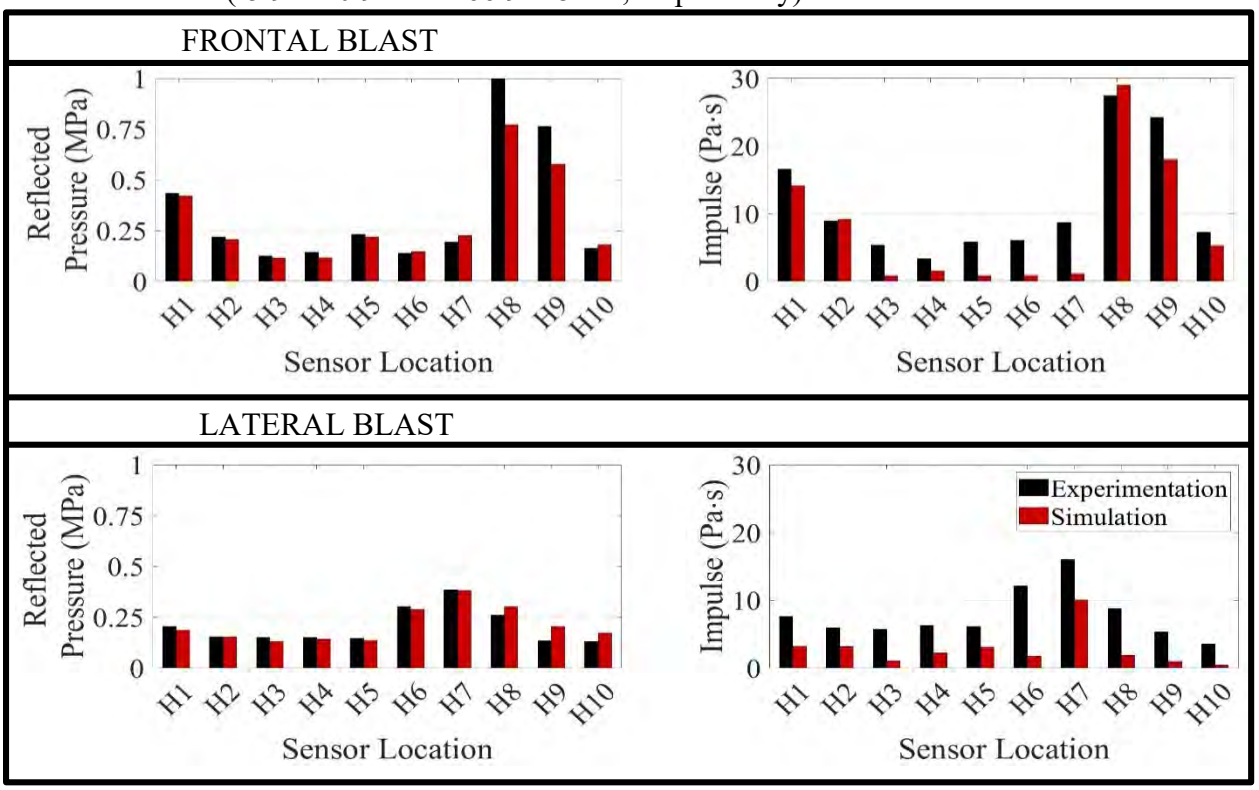


Figure 97. A comparison of the experimental (black) and simulated (red) maximum reflected pressures (left) and the impulses (right) for a frontal (top) and lateral blast (bottom).

The pressure profiles were compared at the sensor locations to validate the shape of the reflected surface pressures. These are summarized in figures 98 and 99. In general, a similar shape is observed. It is apparent that the impulse of the pressure-time profiles is greater in the simulation than that observed experimentally. This is theorized to be due to the rigid body assumption. As the

surface is not compliant, able to deform to the applied pressure load, higher impulse values are seen. However, when comparing the pressure profiles with the impulses calculated and reported in figure 26, opposite trends are observed. This highlights that the simulated pressure profiles have a longer rise time than the experimentally measured surface pressures. This is thought to also be an artifact of the rigid body assumption and of the modeling paradigm.

FRONTAL BLAST

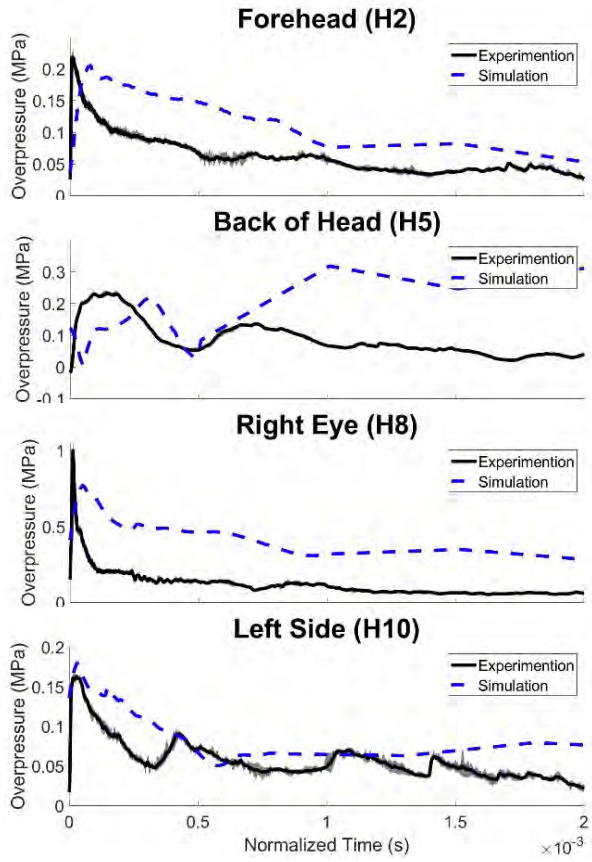


Figure 98. The temporal evolution of the surface reflected pressures in a frontal blast. The mean experimental measurement (black, range shaded in grey) is compared to the simulated profile (blue, dashed). All waveforms are normalized with arrival time to facilitate comparison.

LATERAL BLAST

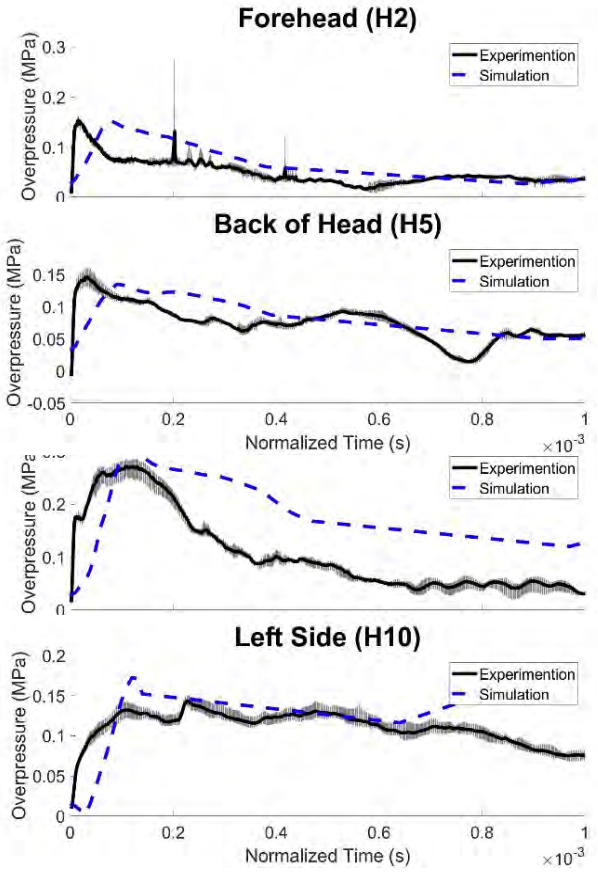


Figure 99. The temporal evolution of the surface reflected pressures in a lateral blast. The mean experimental measurement (black, range shaded in grey) is compared to the simulated profile (blue, dashed). All waveforms are normalized with arrival time to facilitate comparison.

Additionally, the temporal and spatial evolution of the surface reflected pressures were compared for a frontal and lateral blast in figure 100. To give perspective on the magnitude of the reflected pressures, the pressures are reported as normalized with respect to the incident wave (130 kPa). When comparing a frontal blast and a lateral blast, the locations of peak observed pressures differ. In a frontal blast, peak contact stresses are observed at the nose, the eye cavities, and along the jawline. In a lateral blast, the presented surface is smoother, resulting in a more even pressure distribution. The anomalous peak reflected pressures seen at the jawline of the head surrogate appeared during the consolidation of the air pressure in the shock tube and can be observed prior to the arrival of the shock wave. This highlights that they are likely an artifact of the simulation. The converged mesh density of 13 mm exceeds the thickness of the head surrogate geometry at

this location and, therefore, the boundaries of the Eulerian domain are likely affecting the quality of the reflected pressure predictions. However, as the air behind the jawline is not an accurate representation of the human head, this artifact will not be observed in simulations with a full human head.

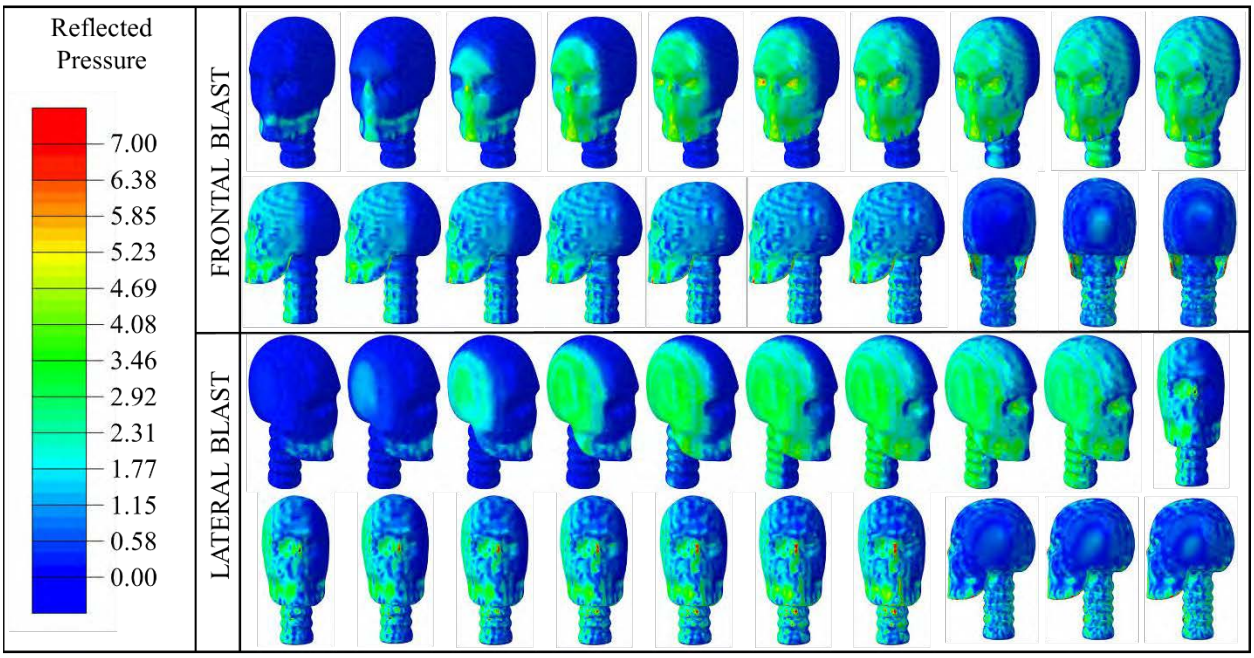


Figure 100. The reflected pressures (normalized with respect to the incident wave of 130 kPa) from over the course of 0.55 μs (Δt = 30 μs) shows the shock wave's interaction with the head surrogate in a shock.

A computational model of the loading and boundary conditions was validated against shock tube experimentation with a surrogate head model. With confidence, we can now simulate how a shock wave interacts with the geometry of a human head. This gives confidence into the simulation assumptions and bridges the gap that precludes the creation of FE models depicting the internal complexity of the human brain. We now have confidence that loading and boundary conditions within the simulation accurately reflect the experimental testing conditions. Pressure maps indicate that the highest loads are seen in the eye cavities and at the nose, implicating the importance of the face shape on generating an accurate simulated load.

11.5 Anatomically Accurate Human Head Geometry

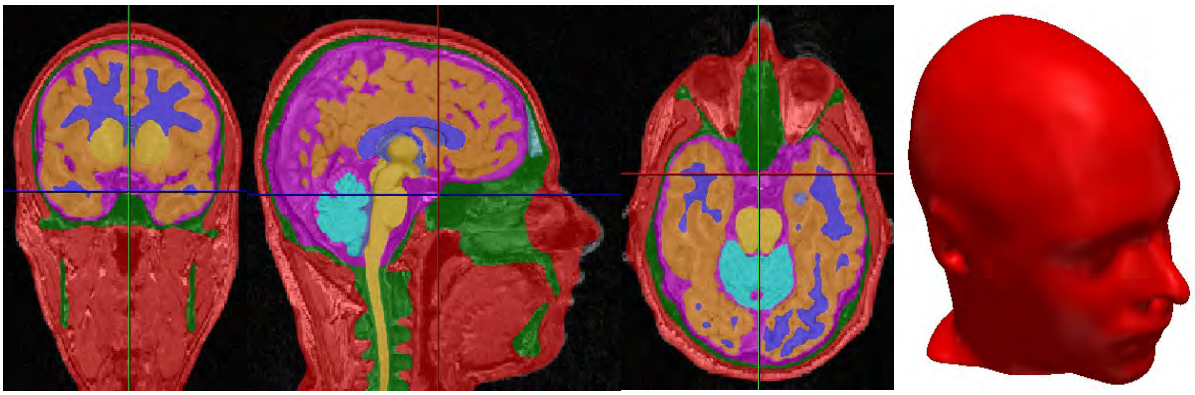


Figure 101. A segmented human head with nine segmented geometries.

Additional work has been conducted to generate a human head geometry with internal geometries segmented. A T1 MRI of a healthy 22-year-old male was obtained from the McConnell Brain Imaging Centre [26-29] and was segmented (Simpleware ScanIP, Synopsys). This model was segmented into the skin/soft tissues, skull and vertebrae, sinuses, dura, cerebral white matter, cerebral grey matter, brain stem, ventricles, and cerebellum. This model was meshed with several mesh refinements to commence initial mesh convergence. The segmented model is shown in Figure 101.

11.6 Human Head Model Convergence

Although nine internal geometries were segmented, initial applications of this model necessitate a close match between the model and the upcoming PMHS experiments. Therefore, further model development was conducted on a model which contained three segmented geometries, a homogeneous brain, the skull, and the skin/soft tissue. The simplification of approximating the brain as a homogeneous material was made to better replicate the experimental procedure of replacing the rapidly lysing brain tissue with a gelatin brain analogue. These tissues were modeled with the material properties included in Table 5.

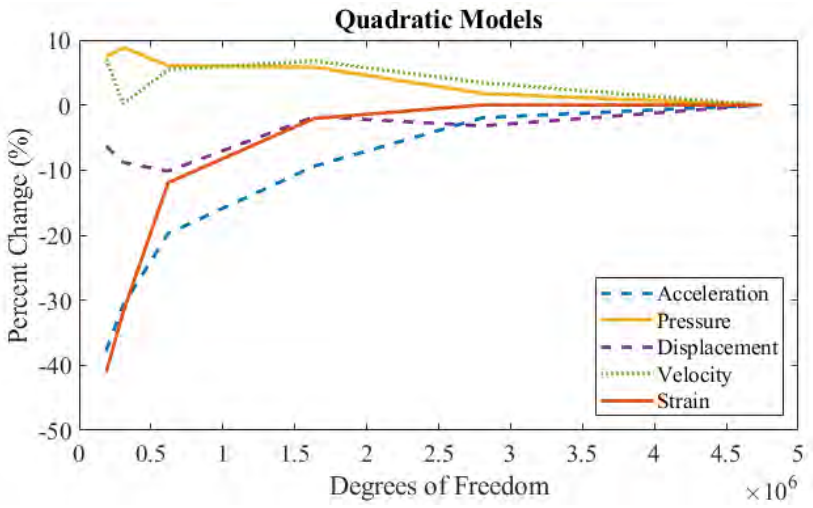


Figure 2202. Mesh convergence of the quadratic models. The percent change of the field variables was calculated with respect to the densest model, which was assumed to be the converged, ideal values. Convergence was deemed acceptable when all field variables were less than 10% different between the converged values.

This geometry was then meshed with seven mesh densities and two element orders (linear and quadratic) to converge the mesh. Solutions were converged for the pressure, maximum principal strain, displacement, velocity, and acceleration. The models were loaded with a 130 kPa, 220 Pa·s blast wave using the CONWEP loading procedure previously described. While the linear models

offered a noisy solution, with evidence of volumetric locking, the quadratic models were found to converge at 2.8M degrees of freedom (935k elements) as shown in Figure 102.

Table 5. The constitutive material models and material parameters used in the convergence study. ρ = density; $E_{(0)}$ = (instantaneous) elastic modulus; ν = Poisson's ratio; G_1 = dimensionless one-term Prony shear relaxation modulus ratio; β_1 = the relaxation time constant.

Tissue Constitutive Material Model	Material Parameters [30]
Soft Tissue Linear Elastic	$\rho = 1200$ kg/mm^3 E = 16.7 MPa $\nu = 0.42$
Bone Linear Elastic	$\rho = 4740$ kg/mm^3 E = 8 GPa $\nu = 0.22$
Brain Linear One-Term Prony Viscoelastic	$\rho = 1040$ kg/mm^3 $E_0 = 123$ kPa $\nu = 0.4996$ $G_1 = 0.81$ $\beta_1 = 200$ s

11.7 Experimental validation of brain material properties via ICP and strain measurements

Alive animals

Four 10-week-old male Sprague Dawley rats (Charles River Laboratories) weighing between 300-350 g were used in accordance with protocols approved by Rutgers-Newark Institutional Animal Care and Use Committee (IACUC). Animals were housed at 22 °C with free access to food and water in a 12-hour dark-light cycle. Before the blast, surgeries were performed to implant two cannulas with Millar 2F (SPR-407) catheter pressure sensors inside the rat brain on in each hemisphere of the brain, as shown in figure 103. The left cannula places the sensor 11 mm deep from the base of the skull; while the right cannula places the sensor 6 mm deep. Two strain gauges were also be fixed to the skull of the rat at the Lambda and Bregma locations. The skin flap is then pulled over the strain gauges limiting direct exposure to shock (details of the instrumentation are presented in the figure 103).

11.8 Postmortem animal with brain surrogate

Four postmortem 10-week-old male Sprague Dawley rats weighing between 300-350 g were used. Rats were sacrificed using exposure to carbon dioxide and brains were surgically removed via an opening in the occipital bone. The cranial cavity was thoroughly cleaned and filled with 10% and 20% porcine gelatin. Subsequently, the surgeries were performed to implant cannulas for two Millar 2F (SPR-407) catheter pressure sensors inside the brain surrogate (10% or 20% gelatin in water). Two strain gauges were also attached at the lambda and bregma locations on the skull. The skin flap was then pulled over the strain gauges limiting their direct exposure to shock. It should be noted that aside from the brain of the rat, the skull and other tissues were kept as intact as possible.

11.9 Surrogate rat head model preparation

Rat skulls were purchased from The Bone Room, LLC (Los Alamitos, CA). These skulls were filled with either 10% or 20% porcine gelatin dissolved in deionized water, similarly to the method used for the postmortem rat brain surrogate model (fig. 104). A negative mold of a rat head (based on the MRI and micro CT imaging) was prepared using CAD software Pro/Engineer Wildfire 5.0 (PCT, Boston, MA) and 3D printed using acrylonitrile butadiene styrene (ABS) plastic. The skull was placed in the mold (fig. 105), to create the external layer mimicking the flesh made of 20% porcine gelatin, 5% professional grade ballistic gel, or 10% professional grade ballistic gel depending on the test. Before the skull is submerged in the mold, holes were drilled into the skull and cannulas were fixed for the pressure sensors (fig. 104). In addition, two strain gauges were fixed to the Lambda and Bregma regions of the skull.

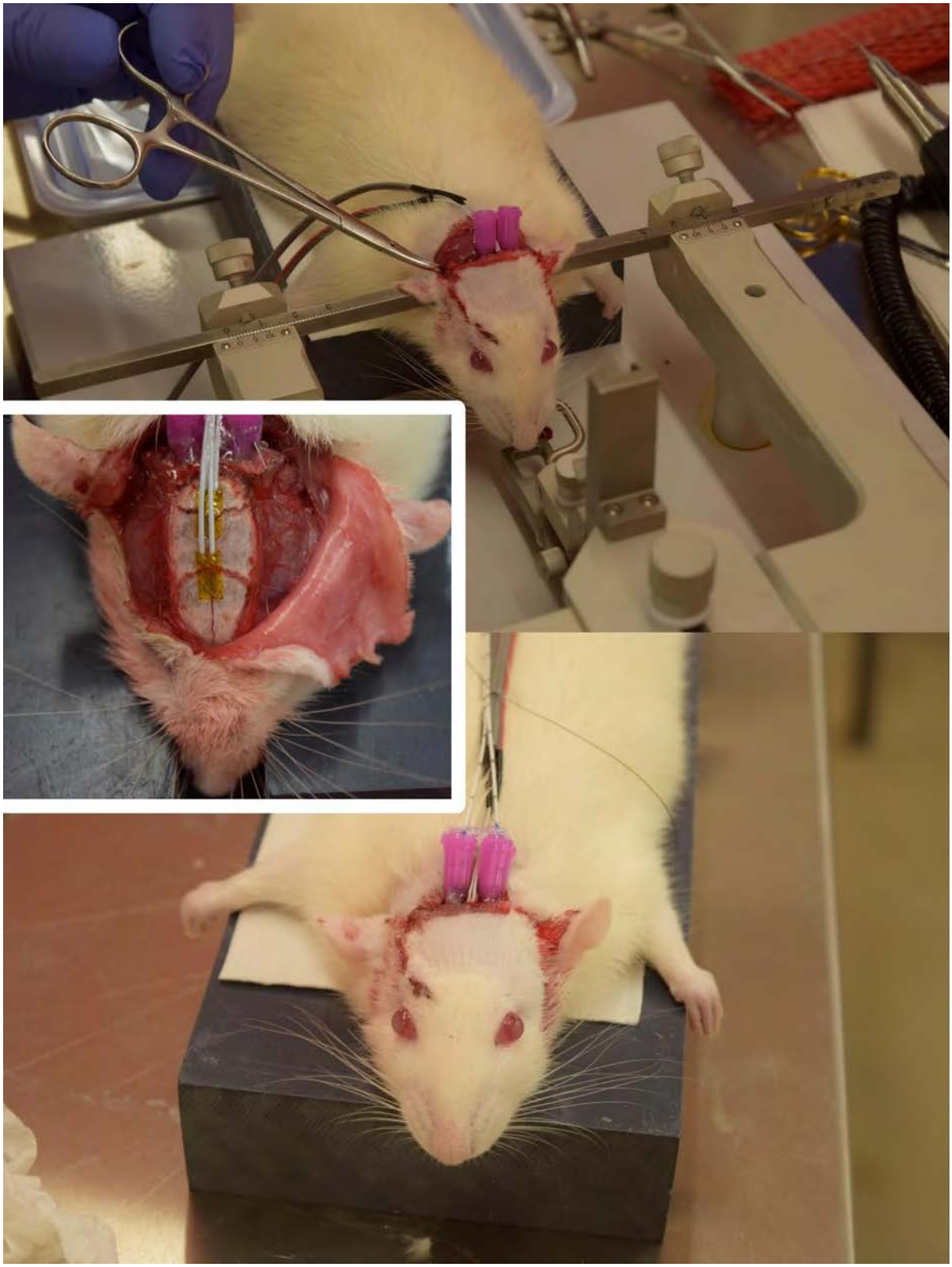


Figure 103 Rat with two ICP pressure sensors implanted in the brain and affixed to the skull and strain gauges attached at the lambda and bregma points (inset).



Figure 104 The preparation of the surrogate rat head model. The intracranial cavity if filled with 20% gelatin in water solution and allowed to gel. The rat skull is then instrumented with two strain gauges and cannulas to house the miniature pressure sensors for ICP measurements.

11.10 Shock Wave Exposure

All specimens were exposed to three discrete incident overpressures of 70, 130, 180 kPa. Helium was used as the driver gas in all tests to provide shock wave durations of approximately 4-5 milliseconds. Live rats and semi-surrogates were placed on the holder in the test section of the shock tube similarly to our previous studies [14, 31-33]. The body wrapping prevents unwanted head and body movement that may cause motion artifacts in the pressure profiles. Full surrogates were attached to the holder. Intracranial pressure (ICP) measurements were taken as well as incident overpressure measurements throughout the length of the shock tube. Pressure measurements were recorded at 1.0 MHz for a duration of 50 milliseconds. Strain measurements were recorded using NI-cDAQ9188 strain gauge system. Strain gauges were set in a Quarter Bridge set up with a 350Ω reference resistor. Strains were recorded at 50,000 samples per second, using the NI-cDAQ9188, for an acquisition time 50 milliseconds.

11.11 Experimental data

We performed shock wave exposure using live rats, postmortem rats with the brain replaced with 10% and 20% gelatin in water, and surrogate rat head model where we used a rat skull and 20% gelatin in water as brain, flesh and skin surrogate. The 10% synthetic ballistic gelatin was used as additional brain surrogate material in this comparison. All specimens were instrumented with two miniature pressure sensors to measure the intracranial pressure (ICP) and two strain gauges attached on the bregma and lambda. The exposures at 70, 130, and 180 kPa BOP were repeated four times (n = 4) for each test condition, and three specimen per group were used (n = 3) for the

total of 144 tests (4 x 3 x 3 x 4 = 144). The response of different brain models measured as ICP characteristics and strain response was of primary interest and will be used for informed brain

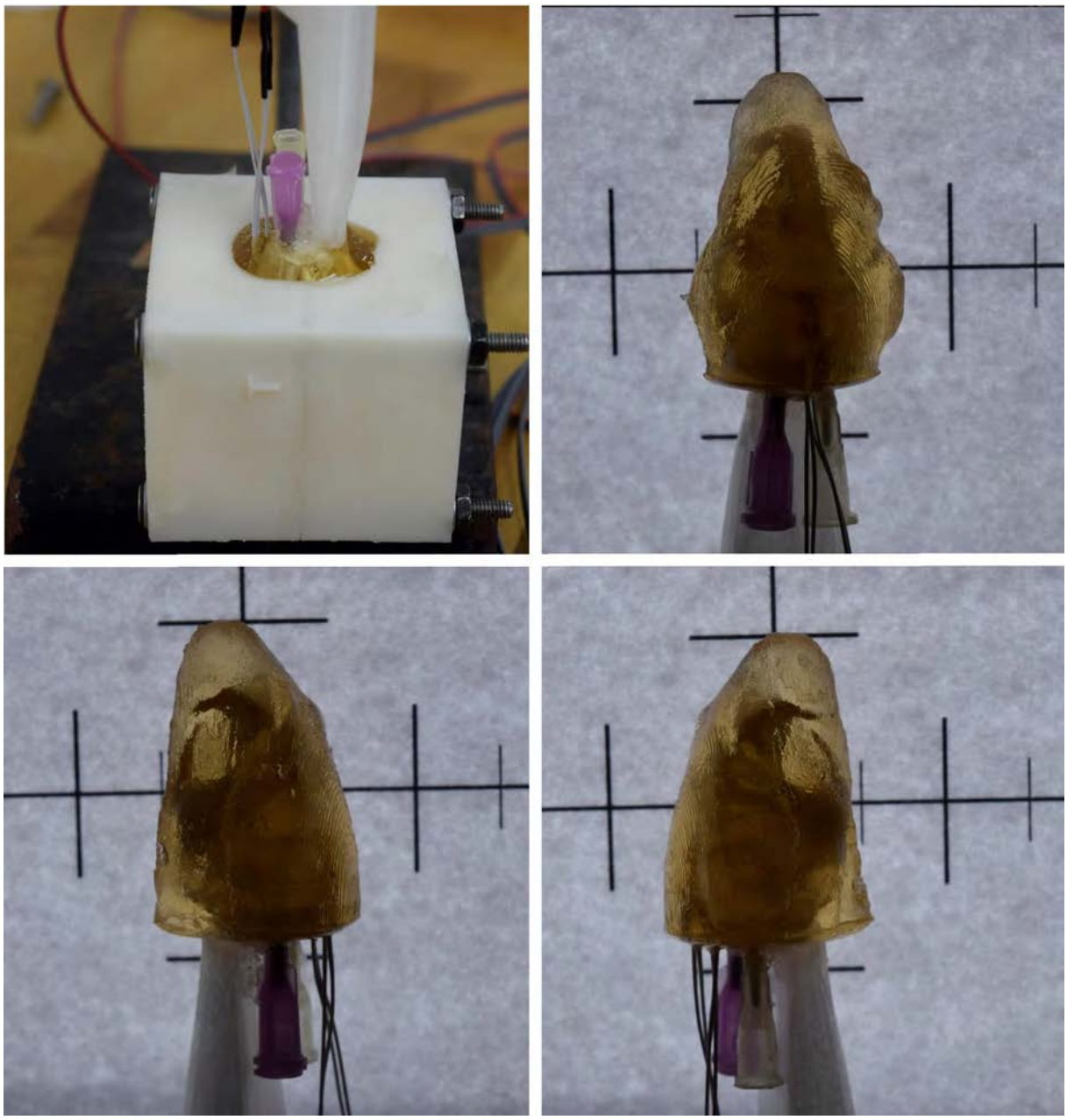


Figure 105 The preparation of the surrogate rat head model. The skull was filled with the gelatin in water solution and instrumented with the two ICP sensors and two strain gauges. Then it was inserted into the mold and the void space was filled with hot 20% gelatin in water solution and left to cool down and jellify. The pictures of the model were taken using a digital camera and in-house built lightbox to visualize the separation between the skull and the outline of the gelatin layer.

material selection in the studies with PMHS and to guide the development of interspecies scaling laws. The data collected using live animals are used as a reference (fig. 106), and two response measures will be compared: 1) the intracranial pressure at two locations, and 2) the skull response measured in the bregma and lambda points. It is obvious that the ICP profiles closely resemble the

incident pressure (denoted as T4 in figure 106, and subsequent figures), which was previously reported by our research group as well as others [6, 34]. The strain measured during shock wave loading increases proportionally with the incident BOP, and rather complex waveforms indicating periodic compression-tension loading were recorded. Similar trends are observed in all other three models tested (figures 106-108). The only exception of the general trend is relatively high peak strain values noted for the model where the brain surrogate is 10% gelatin in water gel.

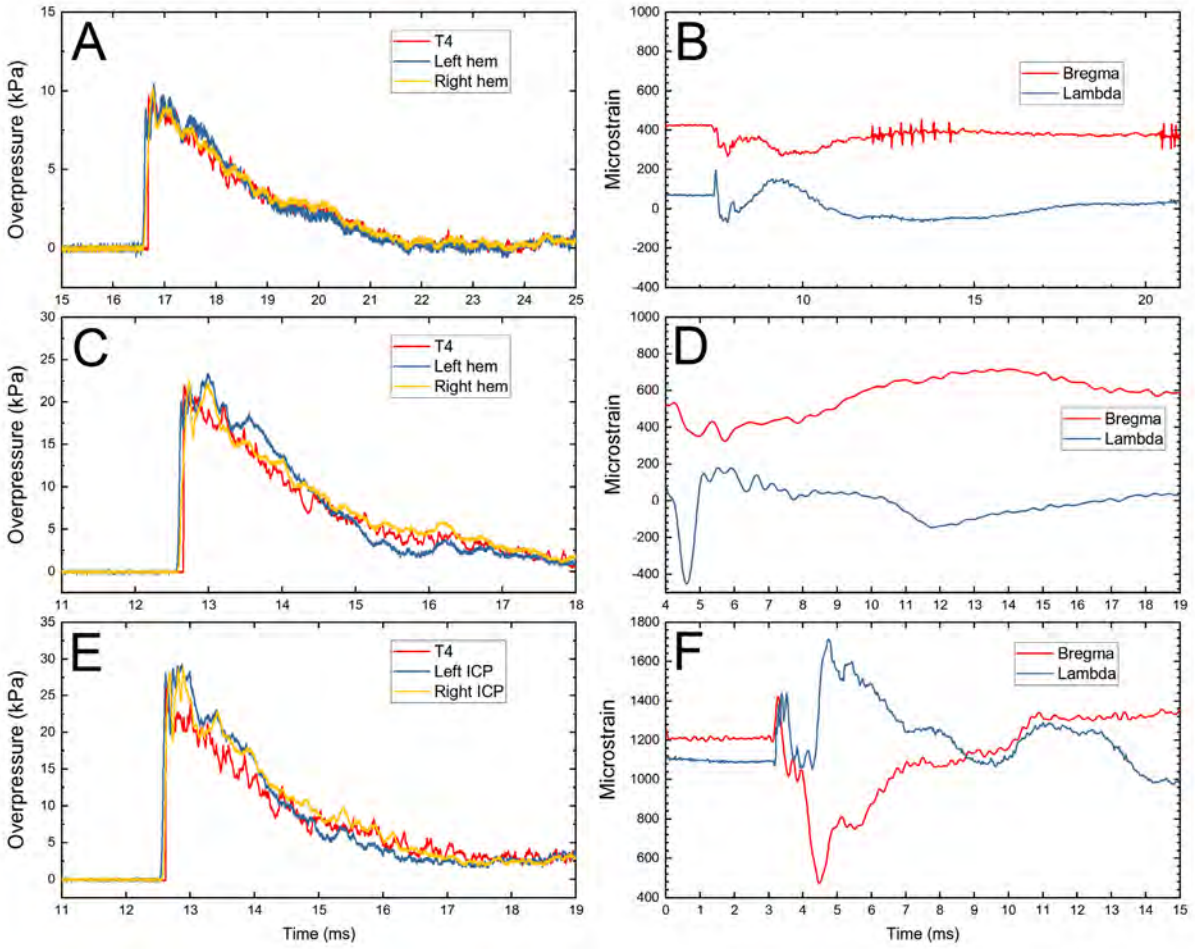


Figure 106 Representative profiles of the intracranial pressure (A, C, E) and strain (B, D, F) recorded at the nominal BOP of: 70 kPa (A, B), 130 kPa (C, D), and 180 kPa (E, F). Live rats were used in these experiments.

11.12 Quantification of the surrogate ICP experimental data

We evaluated the response, measured as ICP profile, of two different types of 'ballistic gelatin': 1) gelatin from the natural source, and 2) commercially available synthetic gelatin. The semi-surrogate and full-surrogate models were prepared; semi surrogate was a rat with a brain replaced with 10% or 20% gelatin in water gel, and full-surrogate models used the rat skull and had skin, flesh and the brain prepared using 10% and 20% gelatin in water, or 10% synthetic gelatin. Both types of models were subjected to a shock wave loading at three different nominal intensities (70, 130 and 180 kPa) and ICP waveforms were recorded. Subsequently, we quantified peak

overpressure, rise time, duration and impulse (fig. 109-113), and based on these metrics the brain surrogate material with the characteristics closely resembling the brain response was selected for further testing (20% gelatin in water). This kind of rigorous material validation for blast testing was not performed previously, to the best of our knowledge.

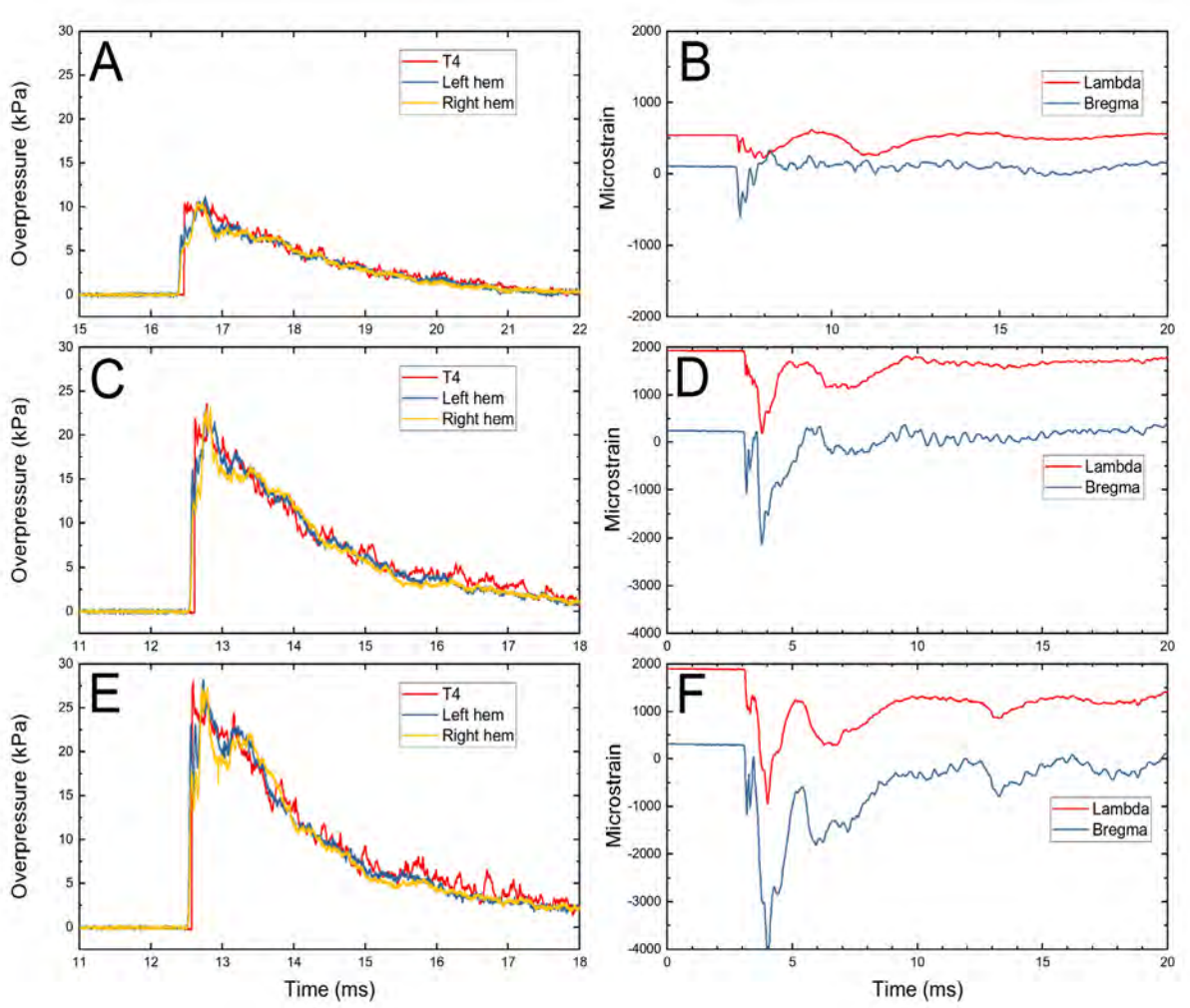


Figure 107 Representative profiles of the intracranial pressure (A, C, E) and strain (B, D, F) recorded at the nominal BOP of: 70 kPa (A, B), 130 kPa (C, D), and 180 kPa (E, F). Postmortem rats with the brain replaced with 10% gelatin were used in these experiments. It is noticeable the peak microstrain values measures at bregma and lambda increased 2-4-fold compared to live animals, while the intracranial pressures remained largely unchanged following the same trends observed in ICP profiles recorded in live animals (Fig 106).

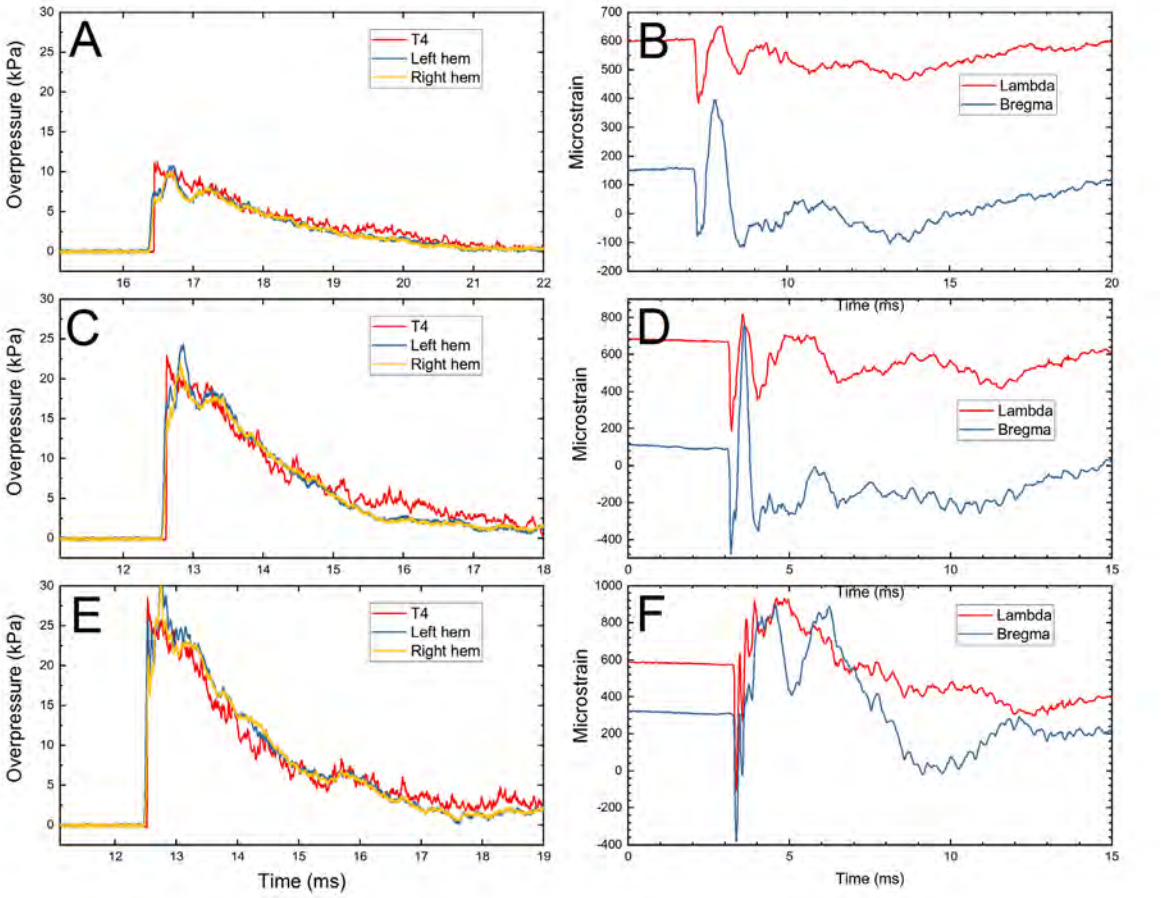


Figure 108 Representative profiles of the intracranial pressure (A, C, E) and strain (B, D, F) recorded at the nominal BOP of: 70 kPa (A, B), 130 kPa (C, D), and 180 kPa (E, F). Postmortem rats with the brain replaced with 20% gelatin were used in these experiments. It is noticeable the peak microstrain values measures at bregma and lambda have similar magnitude to these recorded in live animals. Similarity with other experiments is noticeable: the intracranial pressures remained largely unchanged following the same trends observed in ICP profiles recorded in live animals (Fig 106) and postmortem rats with 10% gelatin in water gel deposited in the intracranial cavity (Fig 107).

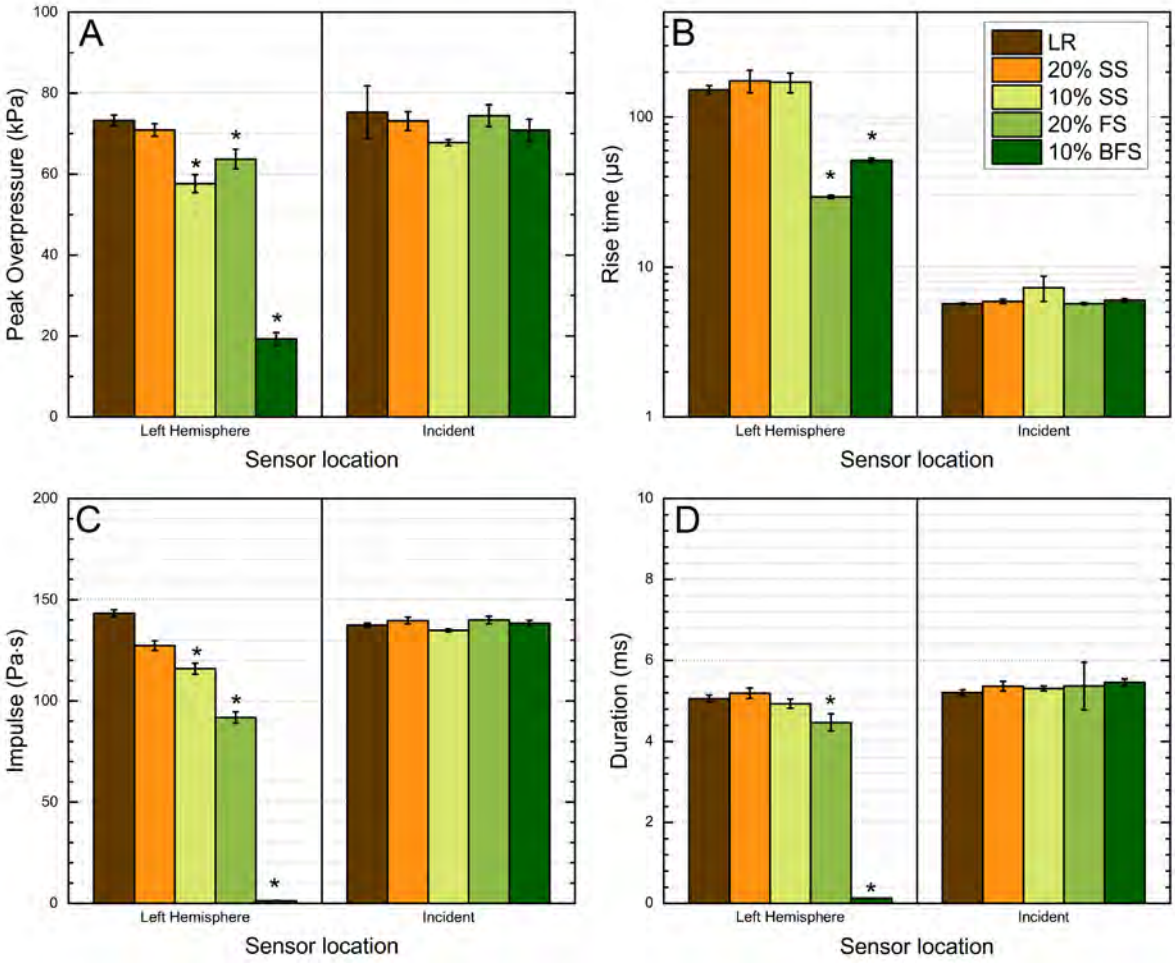


Figure 109 The quantification of the incident and intracranial pressure (sensor embedded in the left hemisphere) waveforms in blast exposures performed at 70 kPa nominal shockwave intensity. Four waveform characteristics: A. peak overpressure, B. rise time, C. impulse, and D. duration were quantified and compared with live rat (LR). Statistical significance is marked with asterisk ($p < 0.05$). Legend: LR – live rat, 20% SS – brain replaced with 20% gelatin in water (semi-surrogate), 10% SS – brain replaced with 10% gelatin in water (semi-surrogate), 20% FS – brain, skin and flesh made of 20% gelatin in water (full-surrogate), 10% FS – brain replaced with 10% synthetic ballistic gelatin (full-surrogate).

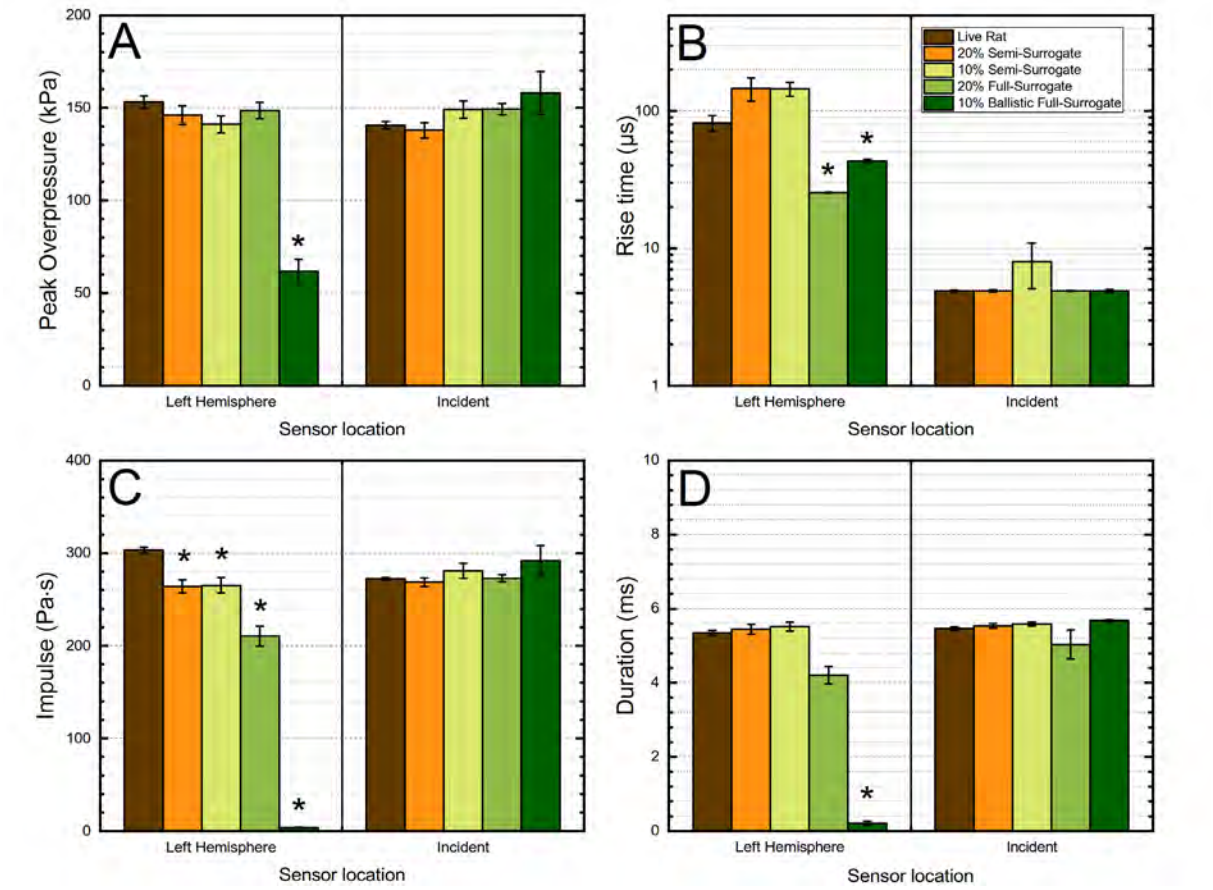


Figure 110 The quantification of the incident and intracranial pressure (sensor embedded in the left hemisphere) waveforms in blast exposures performed at 130 kPa nominal shockwave intensity. Four waveform characteristics: A. peak overpressure, B. rise time, C. impulse, and D. duration were quantified and compared with live rat (LR). Statistical significance is marked with asterisk ($p < 0.05$). Legend: LR – live rat, 20% SS – brain replaced with 20% gelatin in water (semi-surrogate), 10% SS – brain replaced with 10% gelatin in water (semi-surrogate), 20% FS – brain, skin and flesh made of 20% gelatin in water (full-surrogate), 10% FS – brain replaced with 10% synthetic ballistic gelatin (full-surrogate).

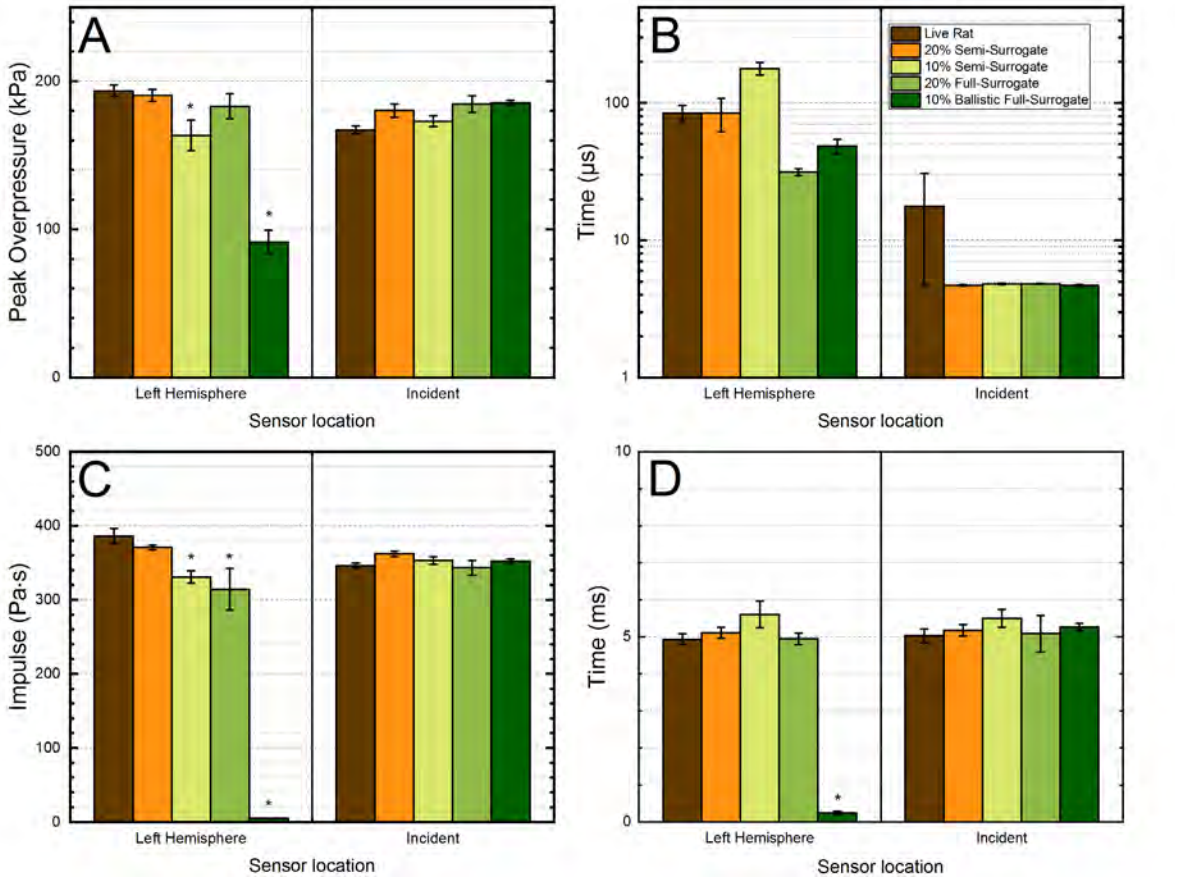


Figure 111 The quantification of the incident and intracranial pressure (sensor embedded in the left hemisphere) waveforms in blast exposures performed at 180 kPa nominal shockwave intensity. Four waveform characteristics: A. peak overpressure, B. rise time, C. impulse, and D. duration were quantified and compared with live rat (LR). Statistical significance is marked with asterisk ($p < 0.05$). Legend: LR – live rat, 20% SS – brain replaced with 20% gelatin in water (semi-surrogate), 10% SS – brain replaced with 10% gelatin in water (semi-surrogate), 20% FS – brain, skin and flesh made of 20% gelatin in water (full-surrogate), 10% FS – brain replaced with 10% synthetic ballistic gelatin (full-surrogate).

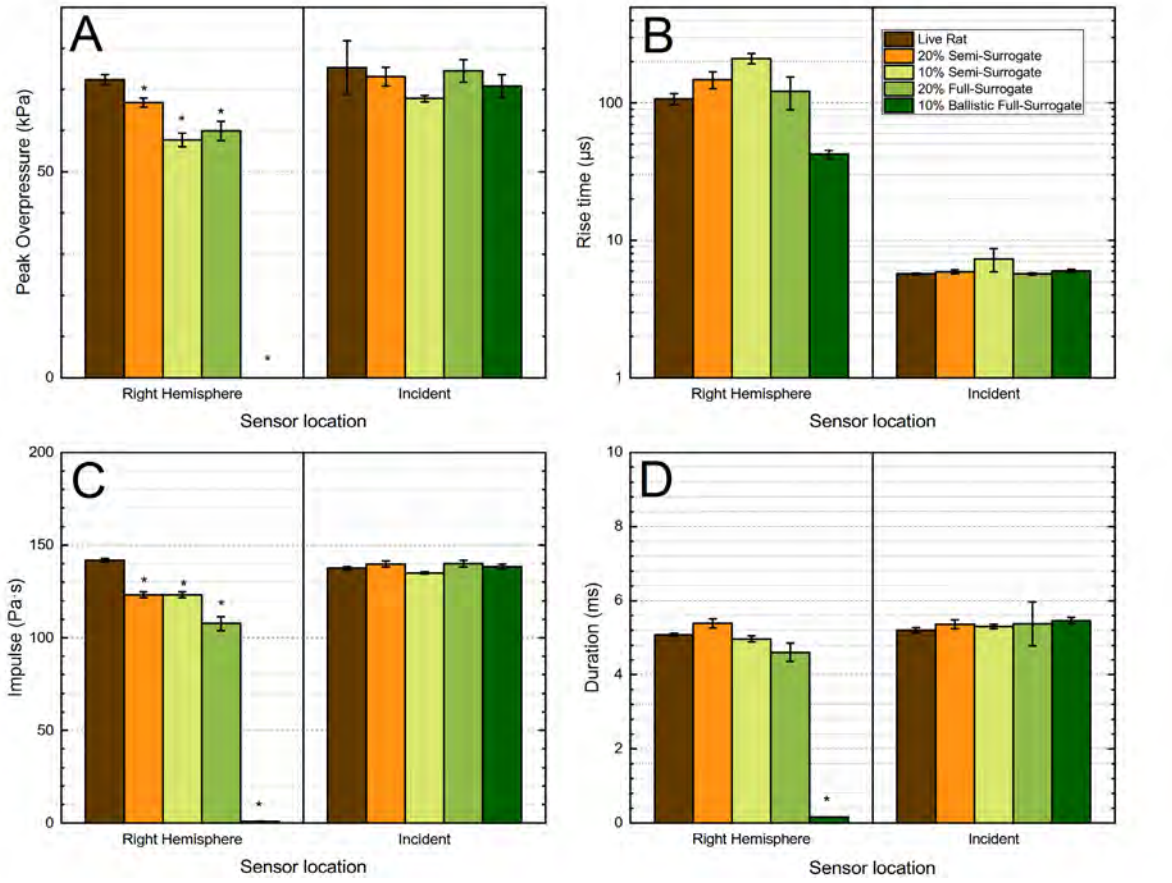


Figure 112 The quantification of the incident and intracranial pressure (sensor embedded in the right hemisphere) waveforms in blast exposures performed at 70 kPa nominal shockwave intensity. Four waveform characteristics: A. peak overpressure, B. rise time, C. impulse, and D. duration were quantified and compared with live rat (LR). Statistical significance is marked with asterisk ($p < 0.05$). Legend: LR – live rat, 20% SS – brain replaced with 20% gelatin in water (semi-surrogate), 10% SS – brain replaced with 10% gelatin in water (semi-surrogate), 20% FS – brain, skin and flesh made of 20% gelatin in water (full-surrogate), 10% FS – brain replaced with 10% synthetic ballistic gelatin (full-surrogate).

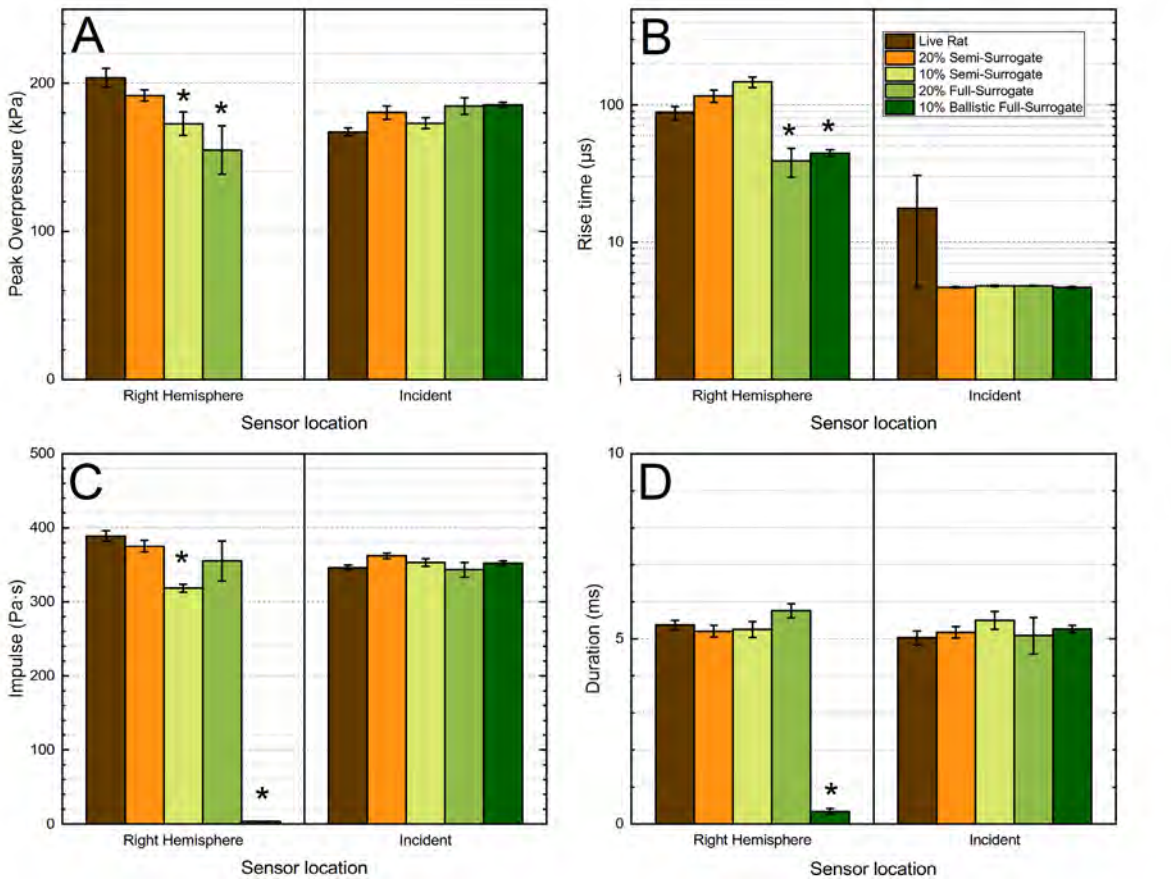


Figure 113 The quantification of the incident and intracranial pressure (sensor embedded in the right hemisphere) waveforms in blast exposures performed at 180 kPa nominal shockwave intensity. Four waveform characteristics: A. peak overpressure, B. rise time, C. impulse, and D. duration were quantified and compared with live rat (LR). Statistical significance is marked with asterisk ($p < 0.05$). Legend: LR – live rat, 20% SS – brain replaced with 20% gelatin in water (semi-surrogate), 10% SS – brain replaced with 10% gelatin in water (semi-surrogate), 20% FS – brain, skin and flesh made of 20% gelatin in water (full-surrogate), 10% FS – brain replaced with 10% synthetic ballistic gelatin (full-surrogate).

11.13 Intracranial pressure, stress and strain comparison using validated finite element model of a rat head exposed to a broad range of shock wave intensities

A finite element model of a ten-week old Sprague Dawley rat was used to investigate the influence of various levels of the incident pressure (15, 30, 70, 100, 140, 180 and 210 kPa BOP) and duration (4, 7, 10 and 13 ms) on the intracranial pressure, von Mises stress, and logarithmic strain within the brain. Three nominal overpressures were simulated with a normal impulse by varying the shock wave duration. Overpressures were simulated using the CONWEP incident wave loading procedure in Abaqus, which was previously extensively validated in our previous reports. Charge weights and stand-off distances for the loading procedures were selected to match peak overpressure and duration (impulse).

The rodent finite element model was oriented in the prone position and the incident wave was permitted to load the rodent model on all surfaces not obstructed experimentally by the animal holder (see previous reports for the details). The solution was recorded using a variable time step to best resolve the rise time of the intracranial pressure and to minimize solution time, which typically was 36 hours per simulation. Prior to arrival of the shock front, four frames were sampled to ensure health of the solution: at the early stages the solution was sampled at a sampling frequency of 1 MHz. Following the sharp rise, an adequate sampling frequency was used to sample the exponential decay, i.e. the initial decay region, 2 ms in duration, was sampled at a frequency of 100 kHz, while the remaining portion of the simulations were sampled at a frequency of 1 kHz. Then the temporal evolution of the intracranial pressure (ICP) was extracted at the locations of the pressure sensors established based on the micro CT scans with the implanted cannulas (fig. 114A). The temporal evolution of the intracranial pressure was then extracted for all combinations of the peak overpressure and impulse (duration) studied (fig. 114 and 115). Then the ICP peak overpressure and impulse values obtained experimentally and these from computational model were extracted and modeled using linear regression method (fig. 116 and 117). It would appear these two approaches produce comparable results, based on the obtained fitting parameters and statistical descriptors of these tests, for a shock wave family with 4 ms duration. Similar results were observed for the remaining three shock wave families with the nominal durations of 7, 10 and 13 ms for the rat ICP.

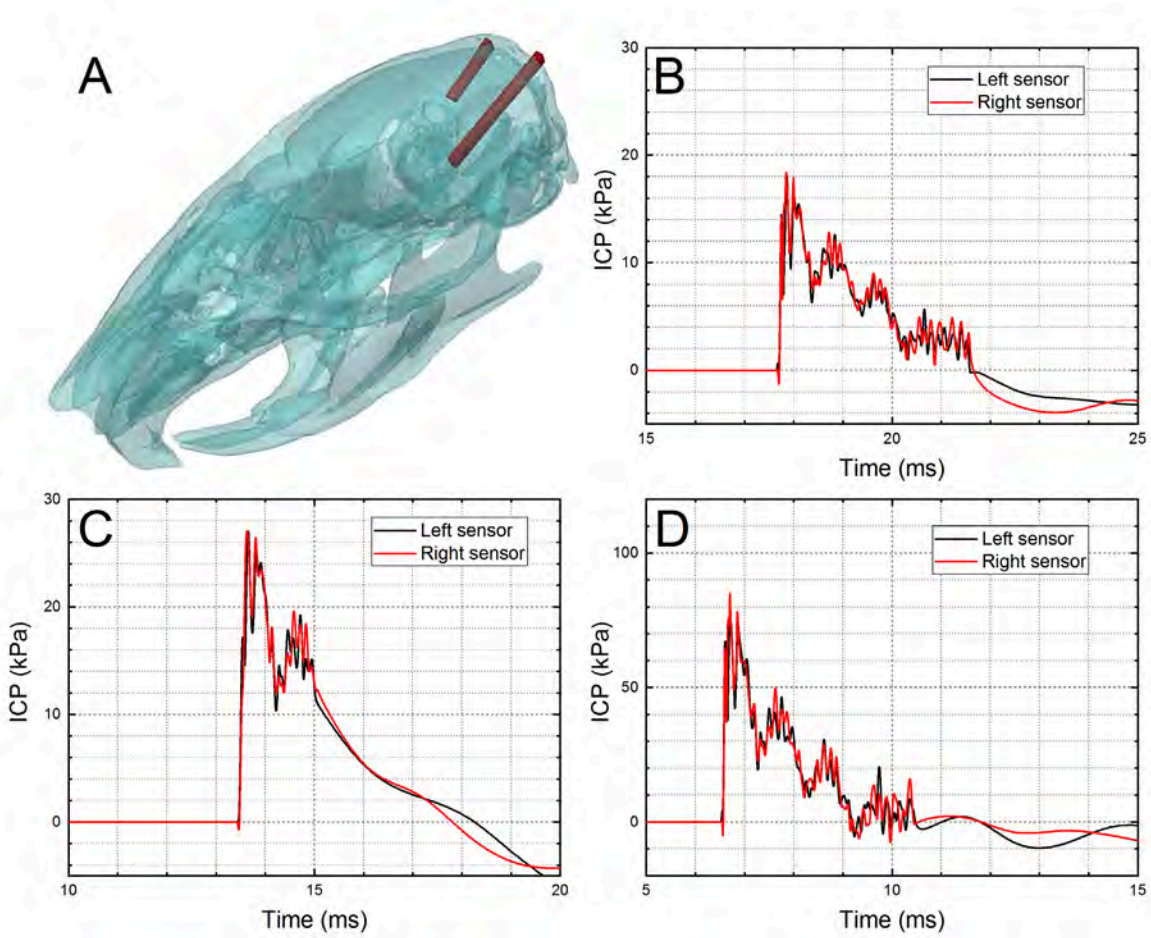


Figure 2414 The micro CT reconstruction of the rat head illustrating the sensor locations (A) used in the FEM simulations of the intracranial pressure changes at different incident peak overpressure: B) 15 kPa, C) 30 kPa and D) 70 kPa. The temporal evolution of the ICP traces is illustrated.

A temporal map of the intracranial pressures, von Mises stress, and logarithmic strain was developed for each simulation in the midsagittal plane of the rat brain (figures 118-124). The spatiotemporal pattern of intracranial pressures remains conserved between the respective loading conditions. When comparing the intracranial pressures between seven different intensities of the family shock waves with 4 ms duration, it is apparent that the intracranial pressure remains elevated for a longer time than used in our simulations (28 ms). This is apparent when comparing the last time points presented in Figures 118-124. This effect is independent on the nominal shock wave intensity as evidenced by the temporal strain and stress dissipation patterns.

The von Mises stress was observed to be slower to develop in the simulations which used lower intensity shock waves. This could indicate a slower dissipation of the internal stresses, paralleling the patterns of the intracranial pressures. In general, the development of internal stresses is delayed following the arrival of the shock front. In Figures 120-124, it can be observed that the time-course of stress development for the high intensity simulations appears to follow that of the low intensity simulations. Longer simulations times, investigating the recovery of the system, would be necessary to provide insight into the dissipation of the built-up energy. However, it appears to be that the internal stress remains elevated within the system for far longer times following blast exposure. Additionally, the pattern of von Mises stresses appears to be conserved between the high

and low intensity simulations, but these assumptions must be rigorously verified using unbiased methods.

The strain within the brain appears to follow a similar pattern to that of the von Mises stress. Again, the development of strain appears to be delayed in high intensity loading conditions. The strain is slower to develop and remains elevated over the time investigated. It would appear, that the pattern of strain development remains conserved between the high and low intensity simulations.

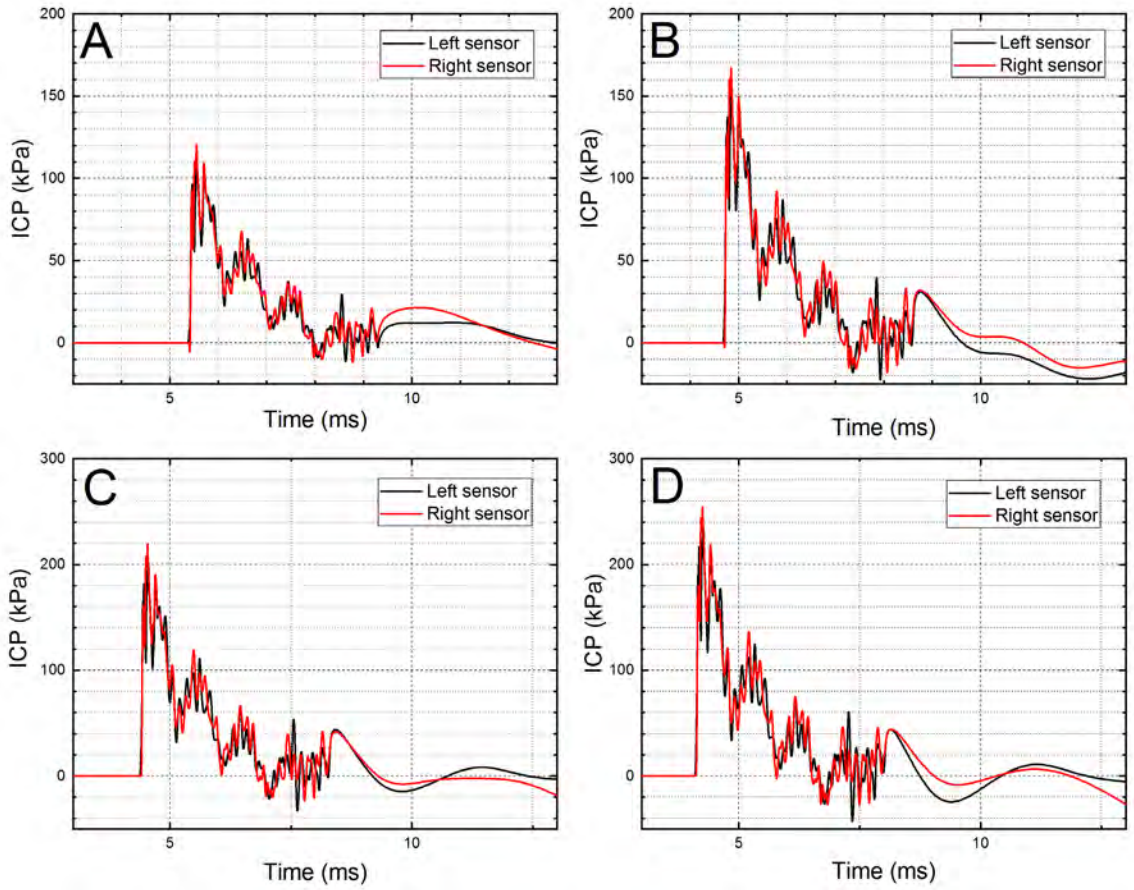


Figure 115 The temporal ICP profiles obtained from the finite element simulations using a shock wave with the nominal duration of 4 ms and intensities of: A) 100 kPa, B) 140 kPa, C) 180 kPa and D) 210 kPa BOP.

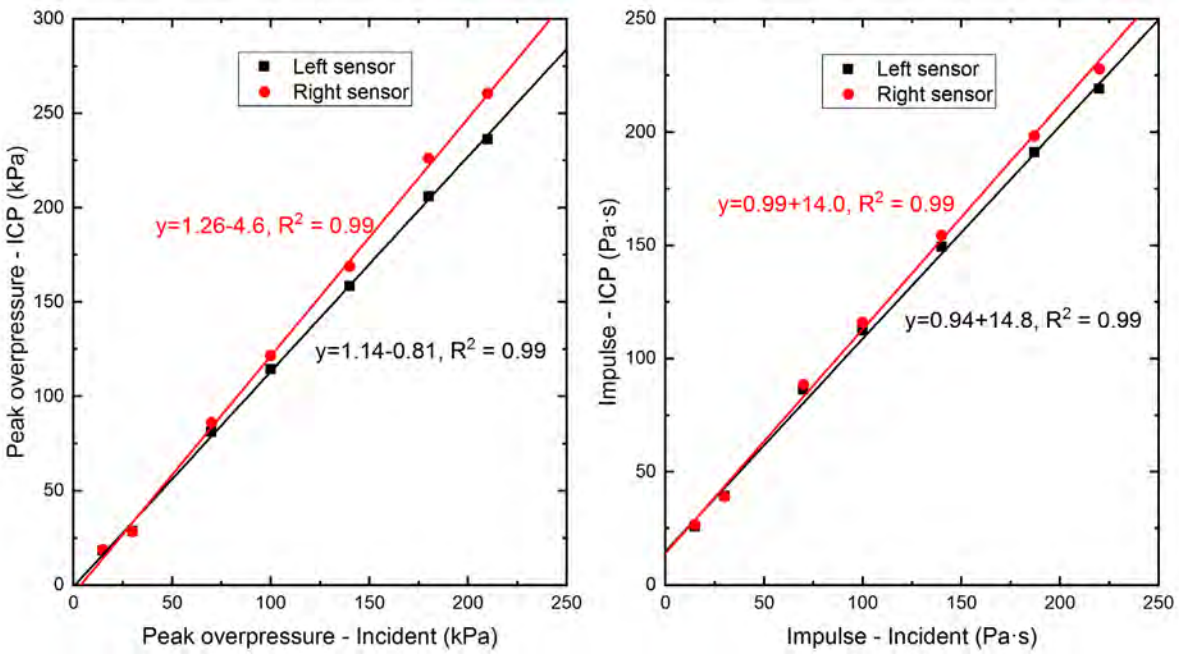


Figure 116 The relationship between ICP as a function of incident shock wave intensity obtained from numerical modeling. The correlations between: A) peak overpressure, and B) impulse are presented for a for a family of shock waves with 4 ms duration.

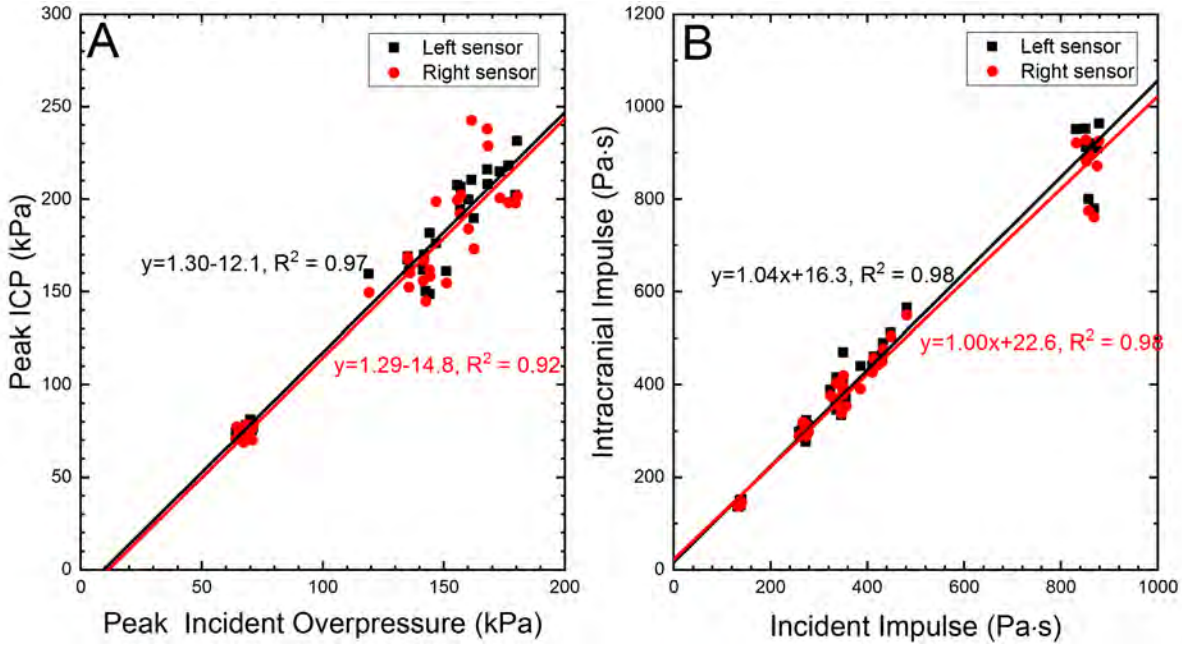


Figure 117 The relationship between ICP as a function of incident shock wave intensities obtained experimentally. The correlations between: A) peak overpressure, and B) impulse are presented.

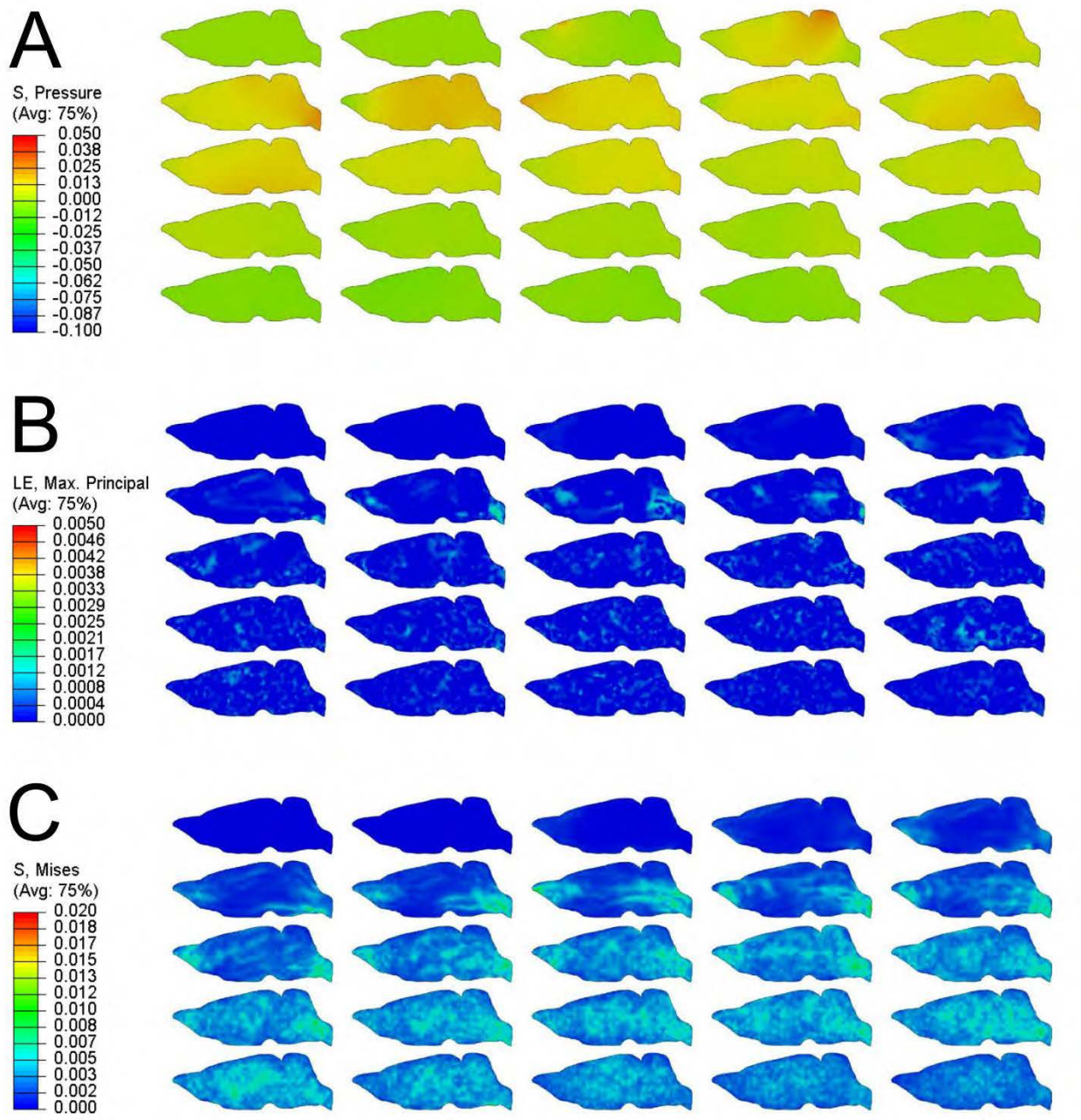


Figure 118 The temporal snapshots of the midsagittal plane of the brain illustrating the evolution of: A) intracranial pressure, B) logarithmic strain, and C) von Mises stress, for the incident shock wave with 15 kPa peak overpressure and 4 ms duration. The time separation between snapshots is as follows: 0.04 (first and second row), 0.4 ms (third and fourth row) and 4.0 ms (fifth row).

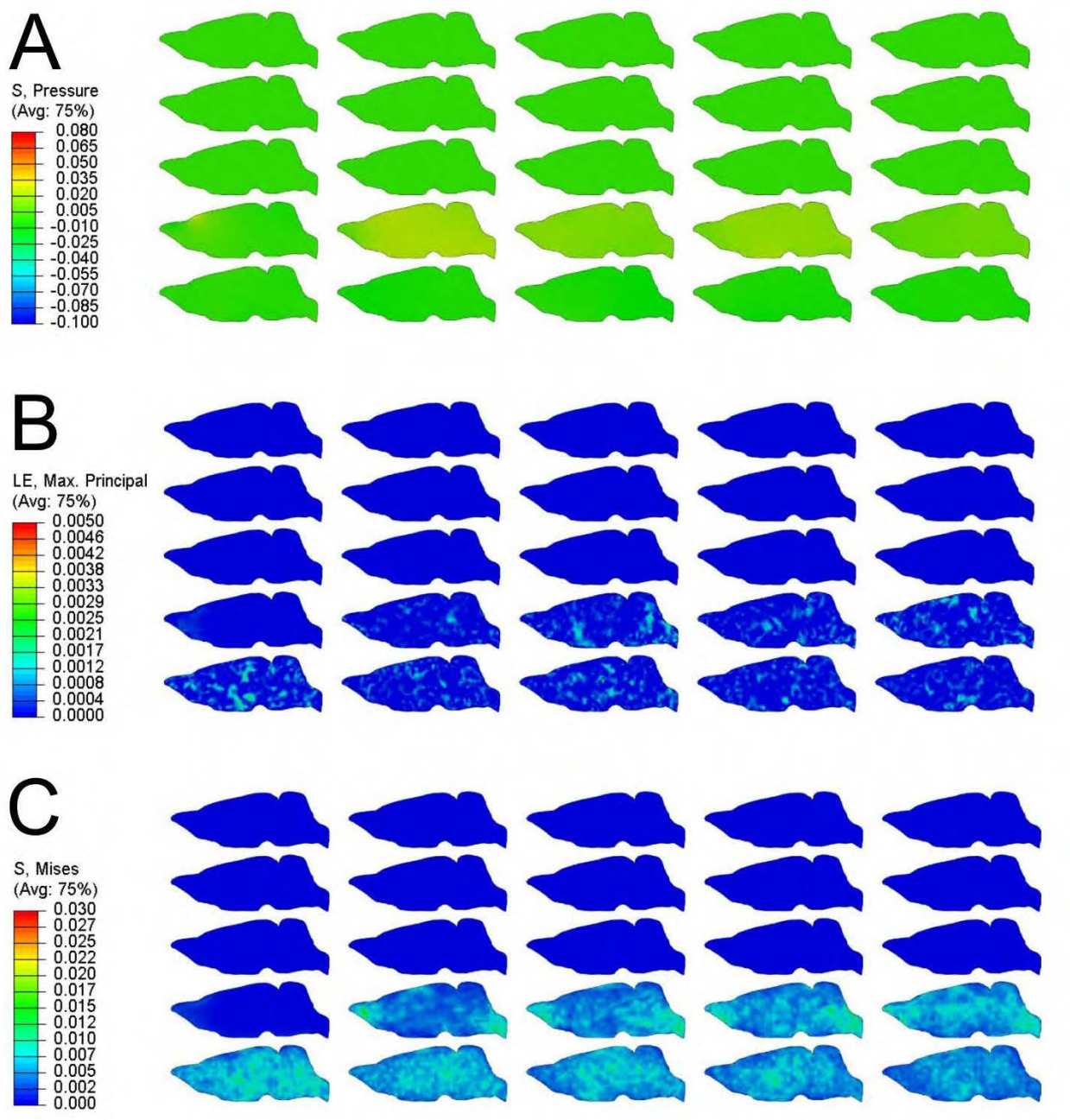


Figure 119 The temporal snapshots of the midsagittal plane of the brain illustrating the evolution of: A) intracranial pressure, B) logarithmic strain, and C) von Mises stress, for the incident shock wave with 30 kPa peak overpressure and 4 ms duration. The time separation between snapshots is as follows: 0.04 (first and second row), 0.4 ms (third and fourth row) and 4.0 ms (fifth row).

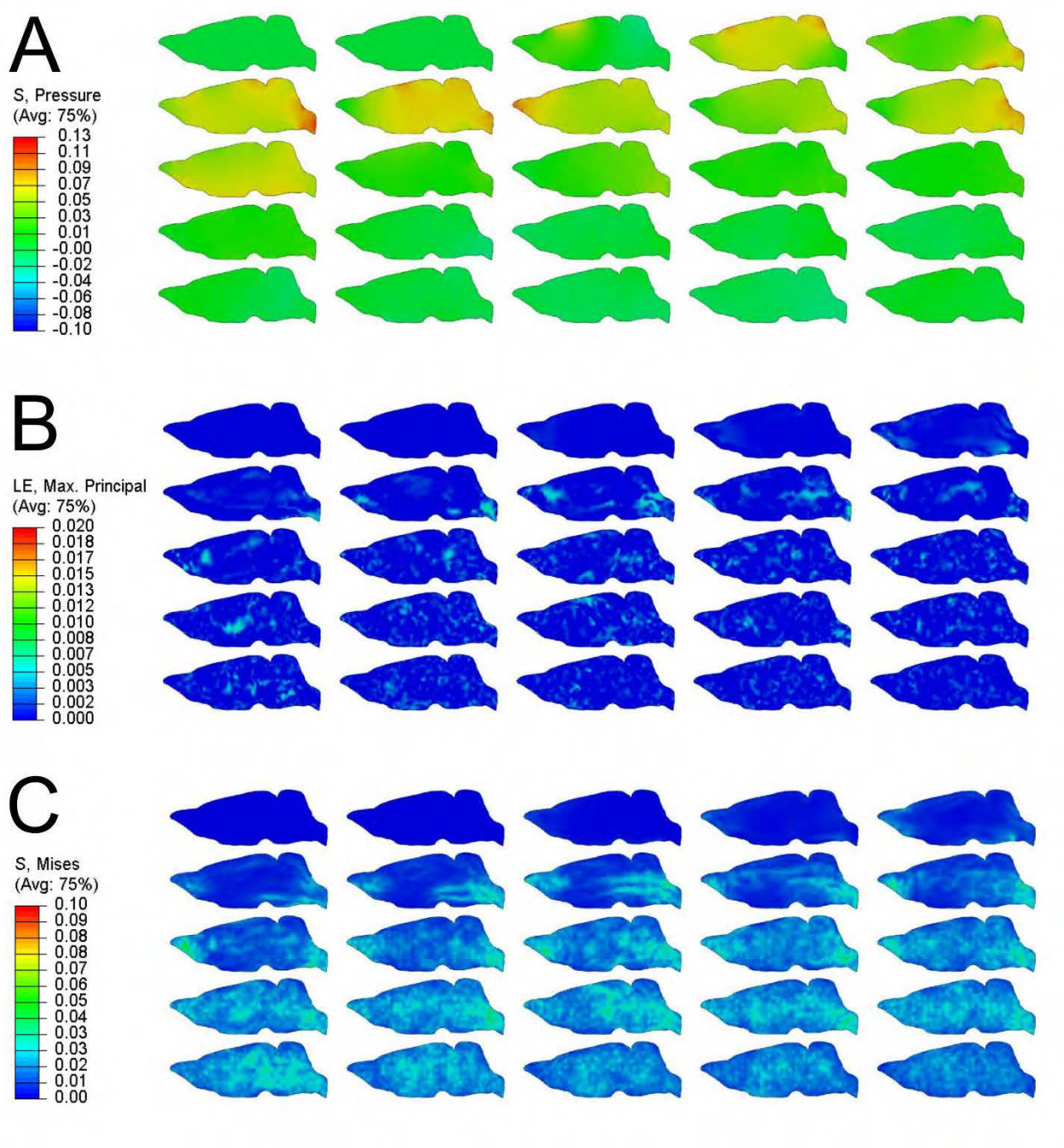


Figure 120 The temporal snapshots of the midsagittal plane of the brain illustrating the evolution of: A) intracranial pressure, B) logarithmic strain, and C) von Mises stress, for the incident shock wave with 70 kPa peak overpressure and 4 ms duration. The time separation between snapshots is as follows: 0.04 (first and second row), 0.4 ms (third and fourth row) and 4.0 ms (fifth row).

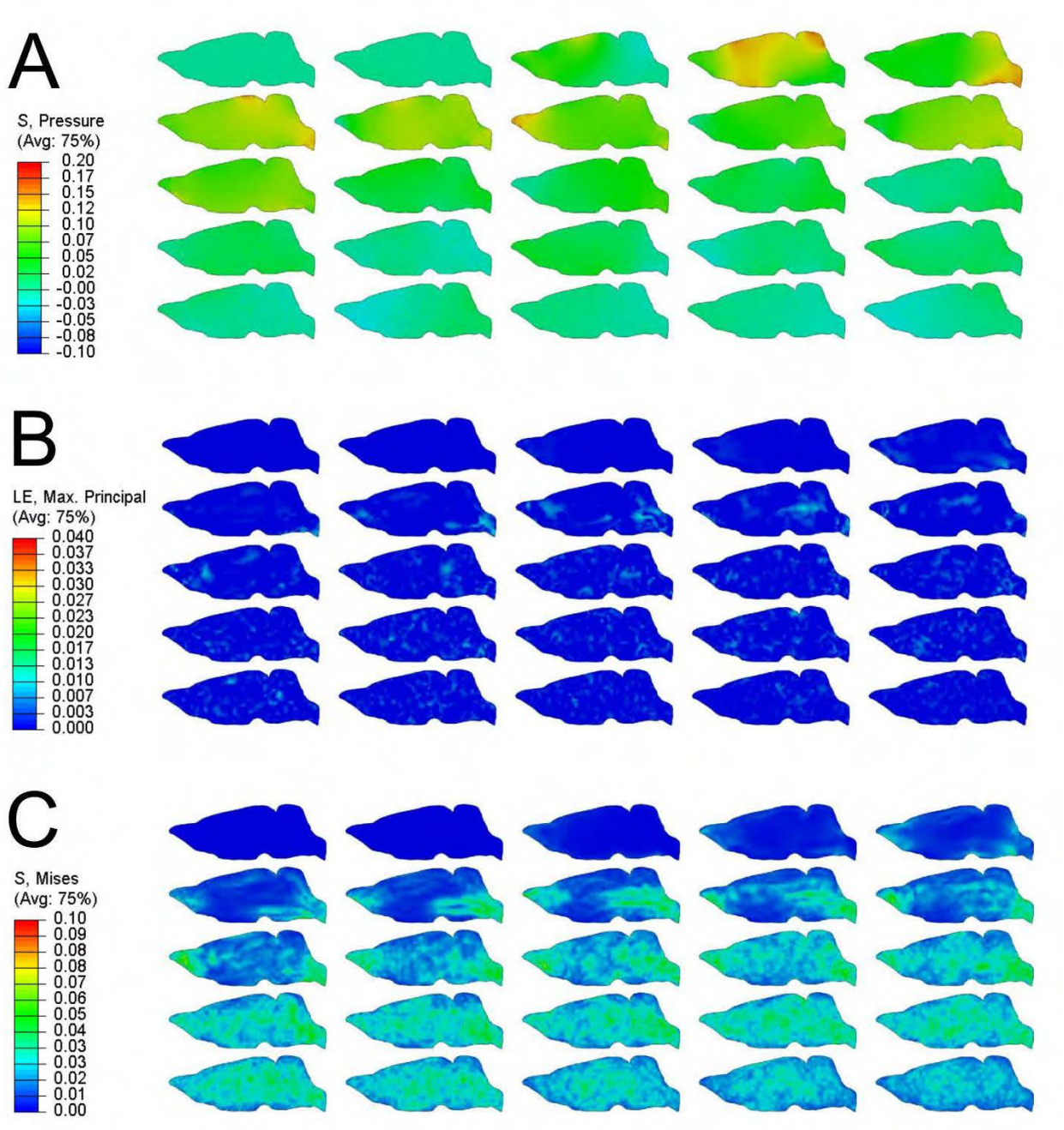


Figure 121 The temporal snapshots of the midsagittal plane of the brain illustrating the evolution of: A) intracranial pressure, B) logarithmic strain, and C) von Mises stress, for the incident shock wave with 100 kPa peak overpressure and 4 ms duration. The time separation between snapshots is as follows: 0.04 (first and second row), 0.4 ms (third and fourth row) and 4.0 ms (fifth row).

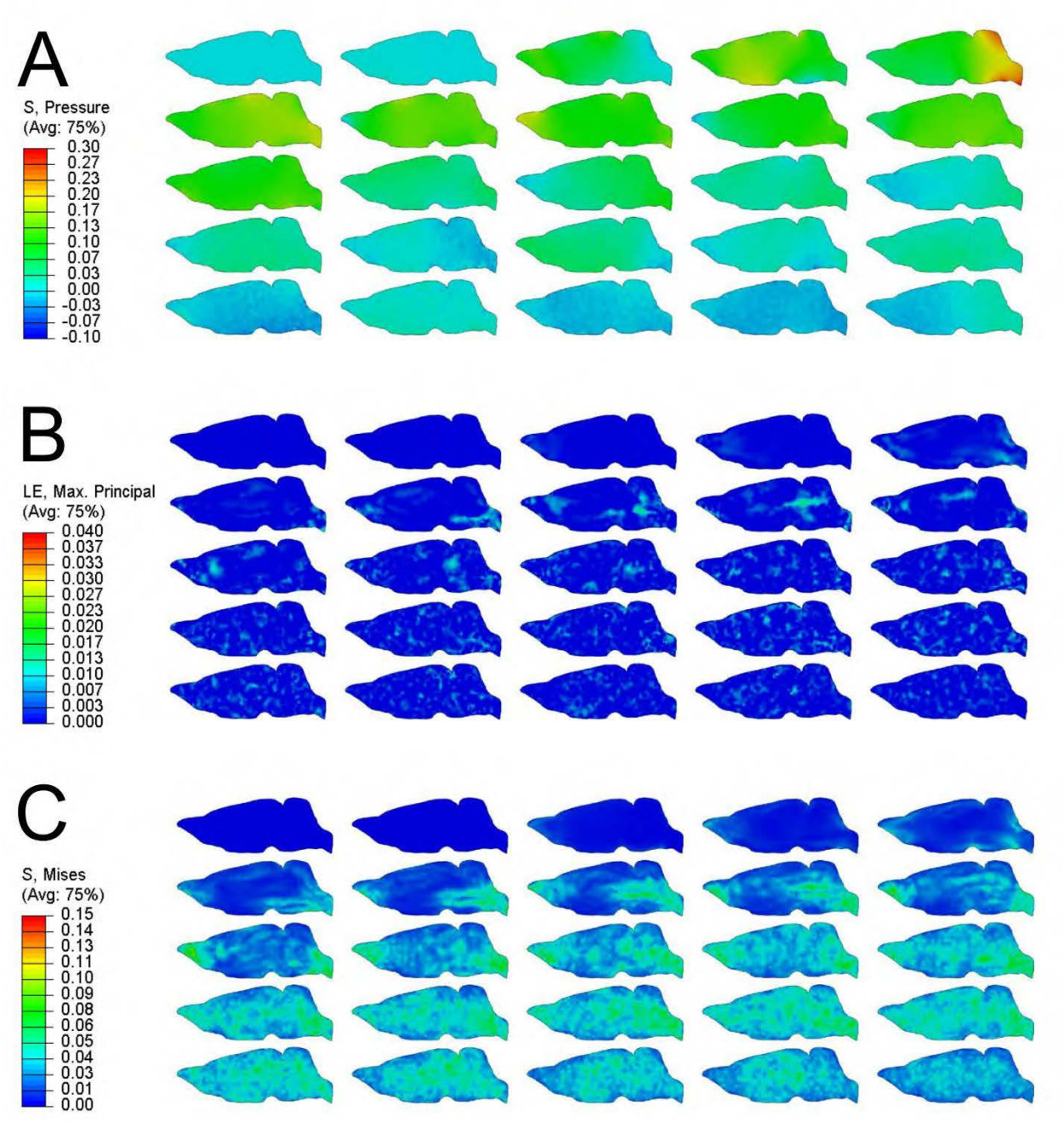


Figure 122 The temporal snapshots of the midsagittal plane of the brain illustrating the evolution of: A) intracranial pressure, B) logarithmic strain, and C) von Mises stress, for the incident shock wave with 140 kPa peak overpressure and 4 ms duration. The time separation between snapshots is as follows: 0.04 (first and second row), 0.4 ms (third and fourth row) and 4.0 ms (fifth row).

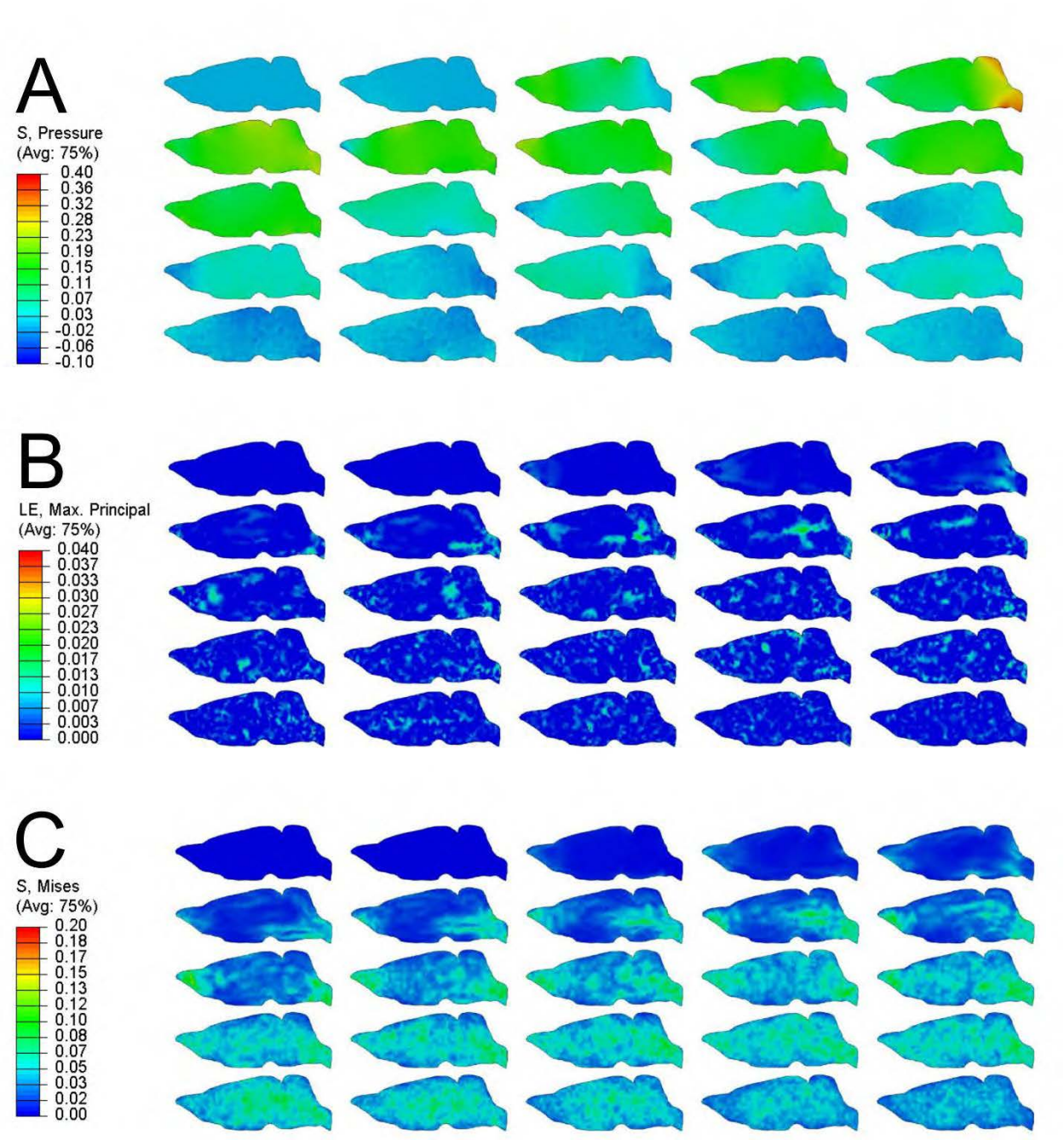


Figure 123 The temporal snapshots of the midsagittal plane of the brain illustrating the evolution of: A) intracranial pressure, B) logarithmic strain, and C) von Mises stress, for the incident shock wave with 180 kPa peak overpressure and 4 ms duration. The time separation between snapshots is as follows: 0.04 (first and second row), 0.4 ms (third and fourth row) and 4.0 ms (fifth row).

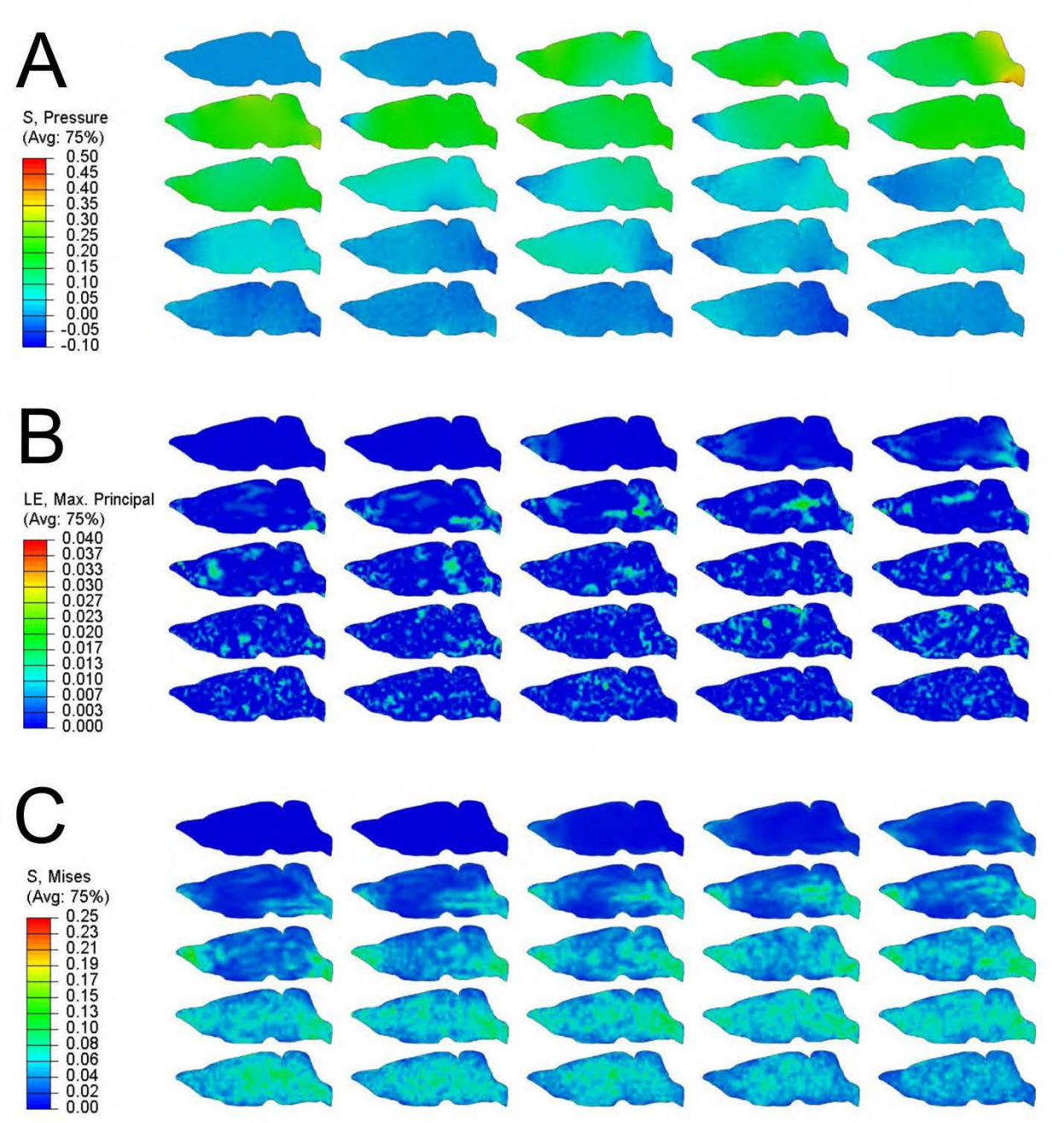


Figure 124 The temporal snapshots of the midsagittal plane of the brain illustrating the evolution of: A) intracranial pressure, B) logarithmic strain, and C) von Mises stress, for the incident shock wave with 210 kPa peak overpressure and 4 ms duration. The time separation between snapshots is as follows: 0.04 (first and second row), 0.4 ms (third and fourth row) and 4.0 ms (fifth row).

Task 12. Comprehensive Characterization of Blast Loading in cephalic PMHS model

The experiments within the scope of this task were conducted using 5 specimens. We have received the computer tomography (CT) scans from the vendor, reconstructed the DICOM images into the 3D models and evaluated the quality and structural integrity of the cranium. All five specimen are deemed suitable for the shock tube testing based on this evaluation (fig 125,126).

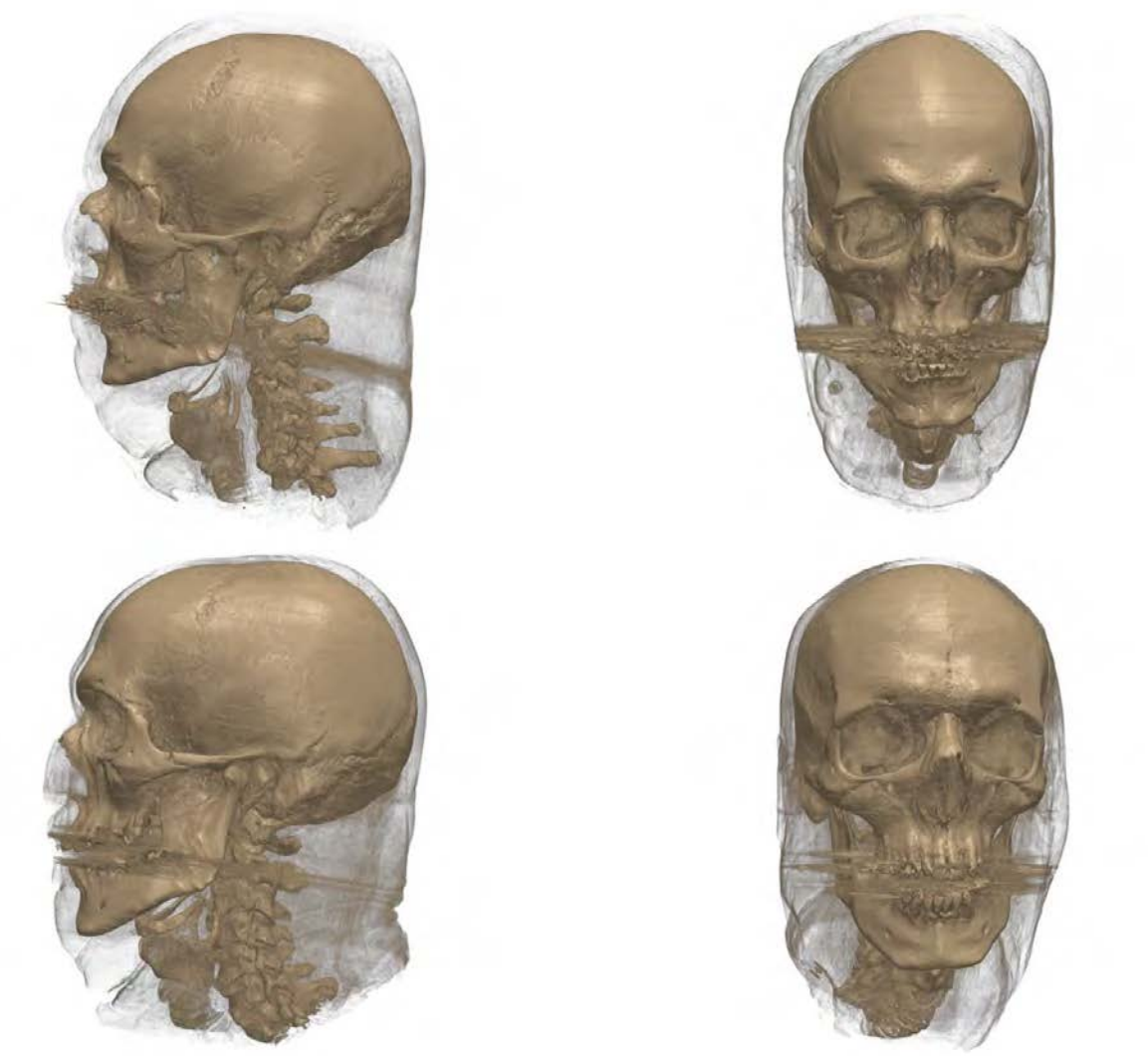


Figure 255 The 3D models of the specimens 1 and 2 reconstructed using the DICOM images obtained from the CT scans.



Figure 126 The 3D models of the specimens 3, 4 and 5 reconstructed using the DICOM images obtained from the CT scans.

12.1 Shock Wave Exposure

All specimens were exposed to three discrete incident overpressures of 70, 130, 180 kPa. Helium was used as the driver gas in all tests to provide shock wave durations of approximately 4-5 milliseconds. These shock wave exposures followed the same protocol established for human surrogate specimen testing performed previously and published recently [35, 36]. We also performed the long duration impulse exposures of the specimen; in which case the shock wave characteristics were configured to be 70 kPa peak overpressure and 7-8 ms duration. These experiments were designed to explore the effects of the shock wave duration on the ICP response in a specimen with human geometry, and to the best of our knowledge were not performed previously.

The cephalic PMHS was defrosted for at least 24 hours, the content of the intracranial cavity removed, and void space filled with the hot 20% gelatin in water solution via the occipital opening. The gelatin was allowed to cool down for approximately 2 hours. In the next step, the neck bone was removed, and the mounting plate was attached to the base of the skull. The ICP sensor mounting hub was attached to the back of the skull using two screws (fig. 127), and the cannulas were driven in the intracranial cavity and secured with the standard HPLC 10-32 Fingertight PEEK fittings. The sensors used for ICP measurements were Millar SPR-524 (3.5 F), which were inserted into the cannulas and airtight sealed on the back end using agarose gel and fixed with Superglue to avoid the sensor displacement during the tests. We used five different lengths of the cannulas: 1, 2, 3, 4, and 5 inches. The sensors were inserted in the cannulas and we made sure the sensing element was extended outside of the cannula and in the contact with the gelatin gel. Subsequently, the four strain gauges were attached on the skull, front to back along the sagittal suture in the 90° intervals, i.e. to match the location of the surface pressure sensor locations H1 to H4 in the experiments with human surrogate headform (for the details see reference [35]). The instrumented specimen was mounted in the shock tube using the Hybrid III neck and exposed to a set of n= 16 shock waves. After the experiments, the specimen was transferred to the prep room and the sensors were carefully removed. The cannulas were retained for the post-exposure CT scanning, which was performed by the vendor supplying the PMHS, to discover the precise location of the sensors (fig. 127).

Intracranial pressure (ICP) measurements were taken as well as incident overpressure measurements throughout the length of the shock tube. Pressure measurements were recorded at 1.0 MHz for a duration of 50 milliseconds. Strain measurements were recorded using NI-cDAQ9188 strain gauge system. Strain gauges were set in a Quarter Bridge set up with a 350Ω reference resistor. Strains were recorded at 50,000 samples per second, using the NI-cDAQ9188, for an acquisition time of 50 milliseconds. As standard practice and quality control [6, 14, 19, 20, 35], high-speed videos were recorded at 5,000 frames per second (fps) for all experiments.

Table 6. The characteristics of the PMHS specimen used in the study.

Specimen ID	Age	Height, in	Weight, lb.	BMI	Cause of Death
P190500	58	72	160	21.7	Metastatic Lung Cancer
P190395	57	68	202	30.7	Neuromuscular Diseases, Anoxic Brain Injury, PEA Arrest
S192668	65	79	210	23.6	Pulseless Electrical Activity, Pulmonary Hypertense
S192693	61	73	280	36.9	Cardiac Shock, NSTEMI

S192868	65	78	220	33.4	Cardiopulmonary Arrest; Ischemic Stroke

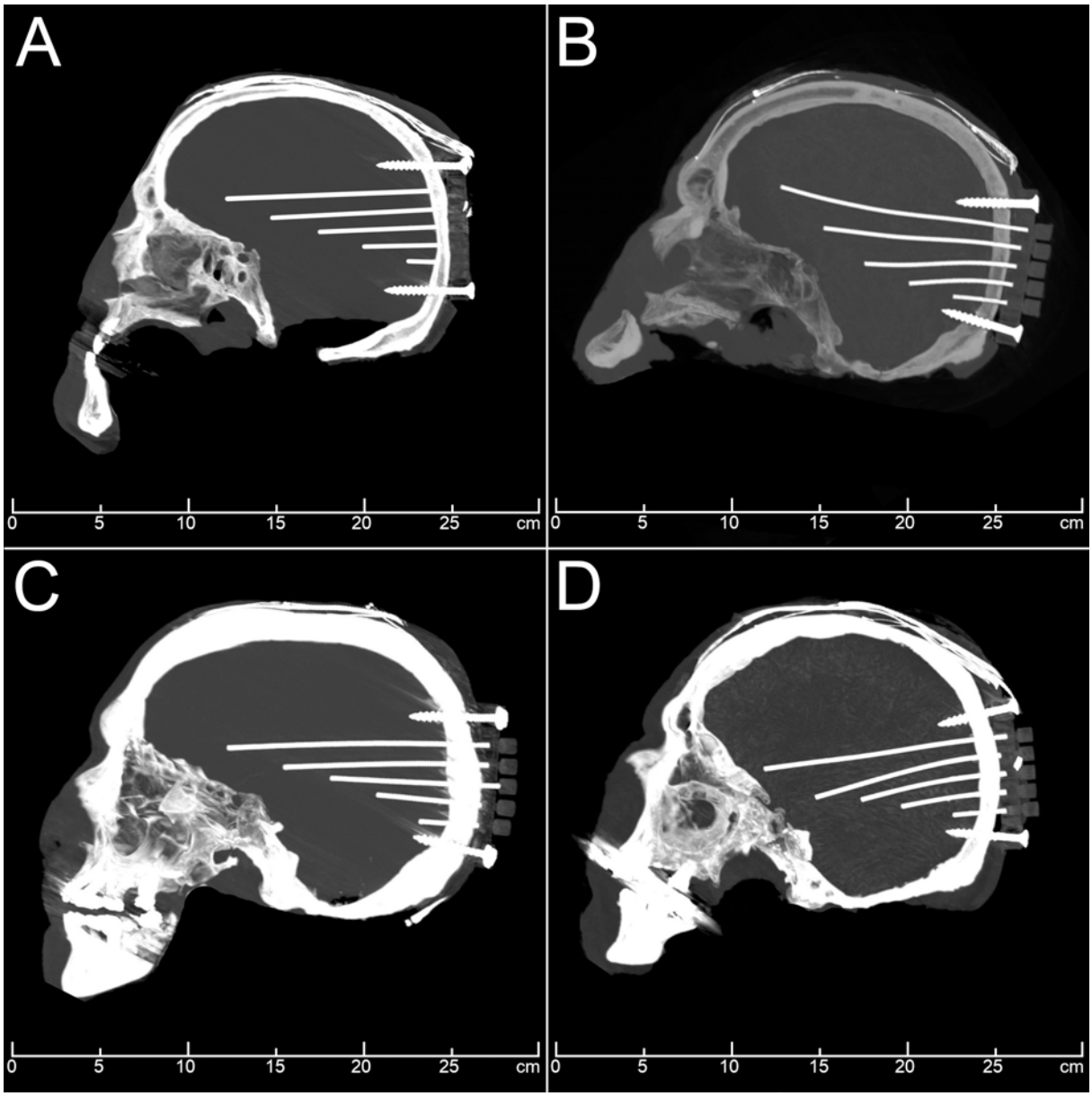


Figure 127 The sensor locations obtained from the sagittal plane projections of the CT scans performed after the shock tube experiments for the following cephalic PMHS: A. P190395, B. P190500, C. P192868, and D. P192693. The specimen P192688 is not presented for brevity. The positions of the five sensors projecting into the intracranial cavity are illustrated. The lengths the cannulas used in these experiments were 1 to 5 inches, top to bottom, respectively.

12.2 Data analysis

The total number of shock wave exposures per individual specimen was 16. The ICP waveforms were imported into Origin 2019 Pro and four waveform characteristics (peak overpressure, impulse, duration and rise time) were quantified and tabulated (table 6). The results are presented for each specimen in the following order: a) a representative sample of the experimental waveforms, b) quantification of the results (four figures). The results obtained for the specimen number P190395 (figures 128-132), P190500 (figures 133-137), S192693 (figures 138-142) and S192868 (figures 143-147) are presented. The data recorded for the specimen S192668 were excluded from the analysis, considering it was used as a testbed to optimize the procedures of data collection.

Upon conclusion of the analysis, the data for all four cephalic PMHS were collated and analyzed for consistency and repeatability (figures 148-151). It appears the exposure conditions were characterized by excellent repeatability between test shots, based on the narrow standard deviations and virtually no changes seen in the average values for specific specimen at all shock wave intensities. There is some degree in variation between ICP characteristics recorded for different specimen, but these variations are likely due to the anatomical differences between specimen and deviations in the sensor locations.

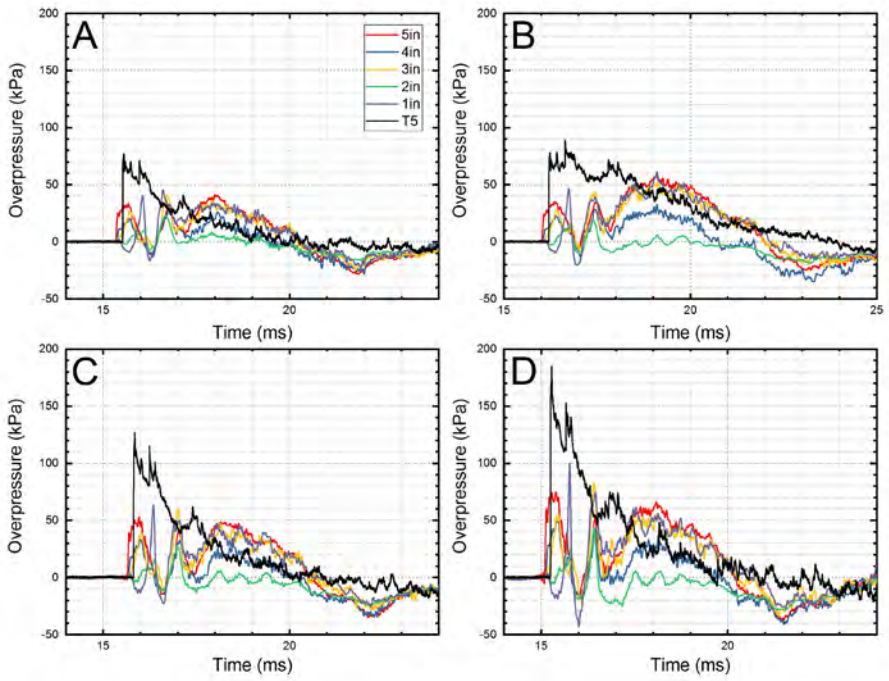


Figure 128 The representative overpressure-time histories collected for the specimen P190395 at nominal shock wave intensity of: A) 70 kPa, B) 70 kPa (long impulse), C) 130 kPa and D) 180 kPa.

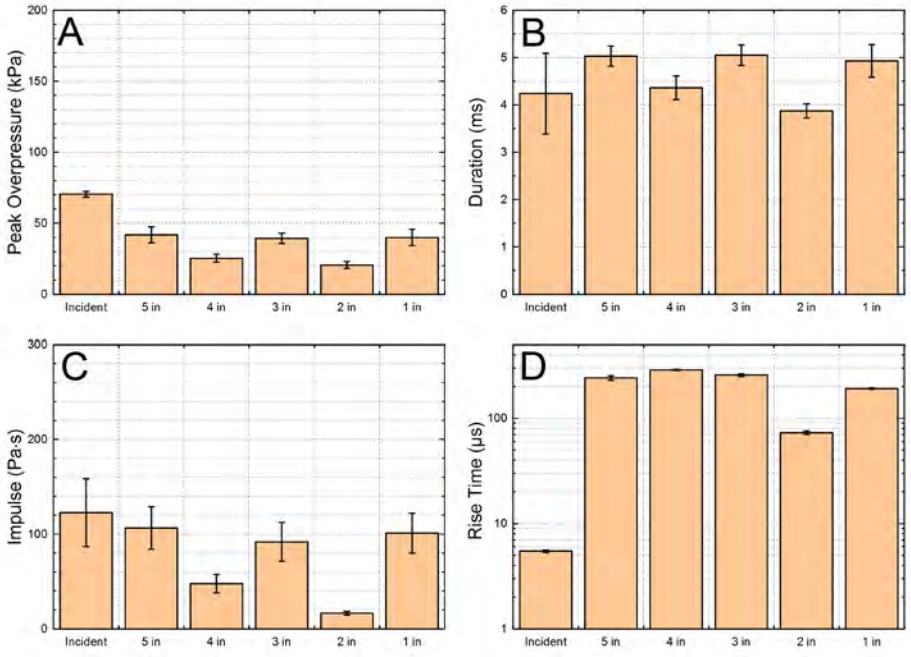


Figure 129 The quantification of the: A) peak overpressure, B) duration, C) impulse and D) rise time of incident and five ICP waveforms recorded for the specimen P190395 at nominal shock wave intensity of 70 kPa (n = 4).

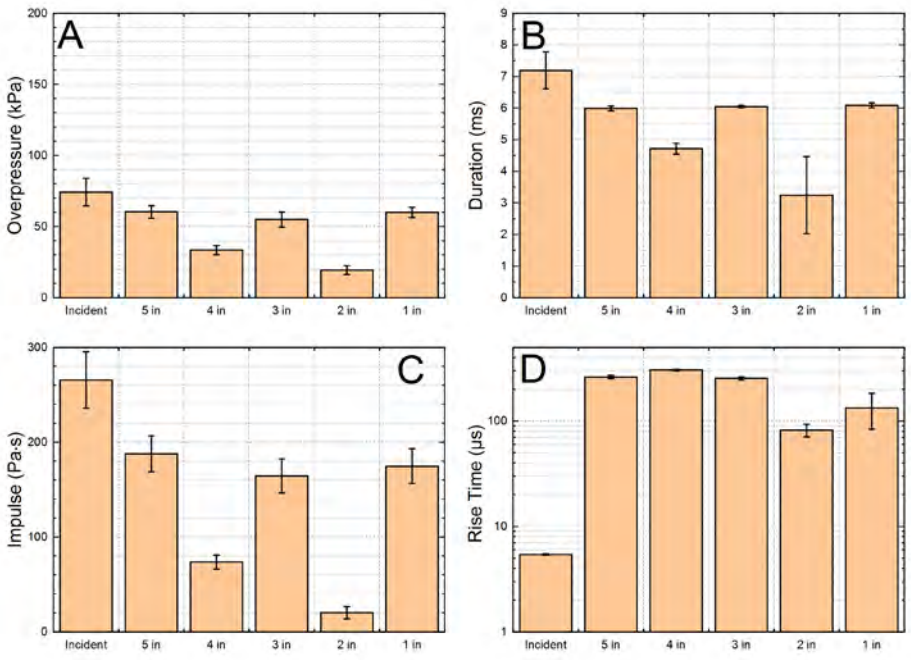


Figure 130 The quantification of the: A) peak overpressure, B) duration, C) impulse and D) rise time of incident and five ICP waveforms recorded for the specimen P190395 at nominal shock wave intensity of 70 kPa, with the long duration impulse (n = 4).

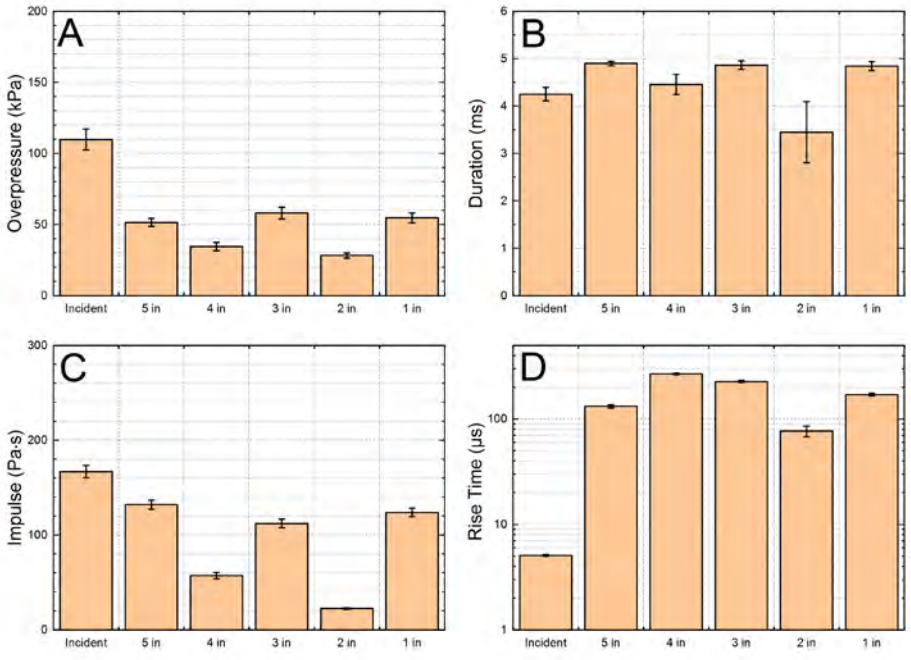


Figure 131 The quantification of the: A) peak overpressure, B) duration, C) impulse and D) rise time of incident and five ICP waveforms recorded for the specimen P190395 at nominal shock wave intensity of 130 kPa (n = 4).

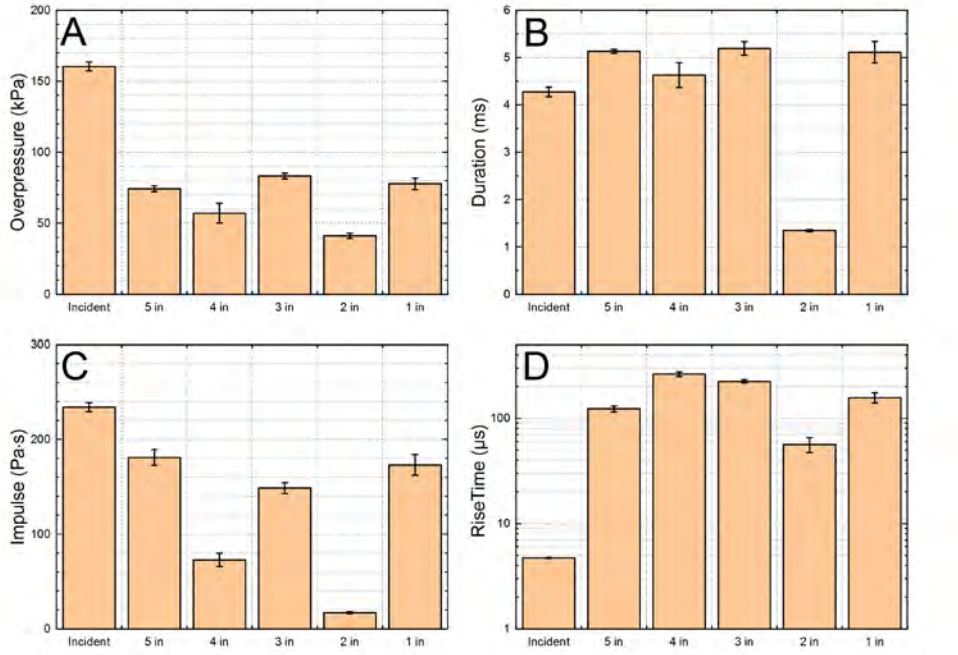


Figure 132 The quantification of the: A) peak overpressure, B) duration, C) impulse and D) rise time of incident and five ICP waveforms recorded for the specimen P190395 at nominal shock wave intensity of 180 kPa (n = 4).

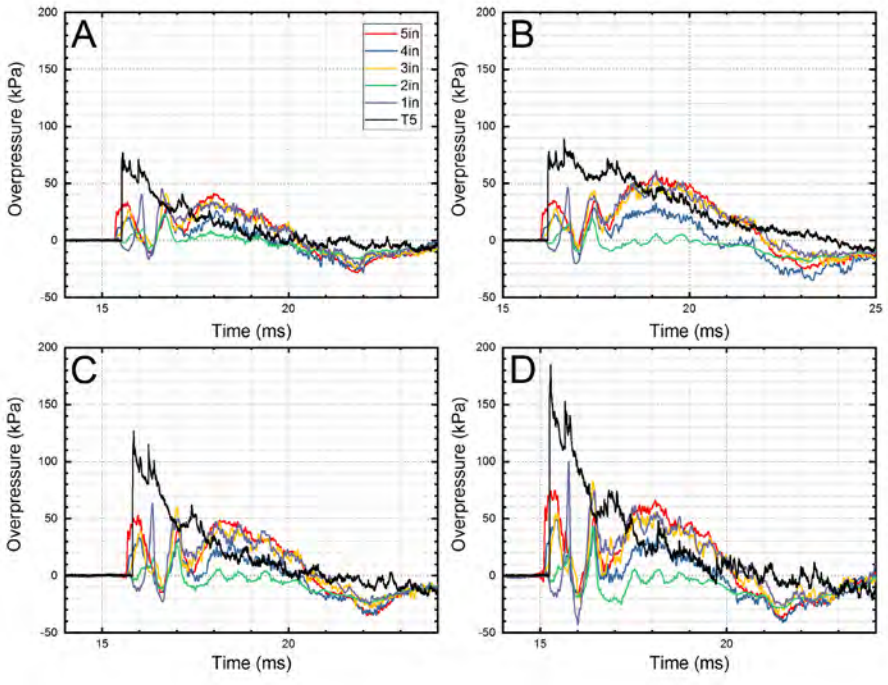


Figure 133 The representative overpressure-time histories collected for the specimen P190500 at nominal shock wave intensity of: A) 70 kPa, B) 70 kPa (long impulse), C) 130 kPa and D) 180 kPa.

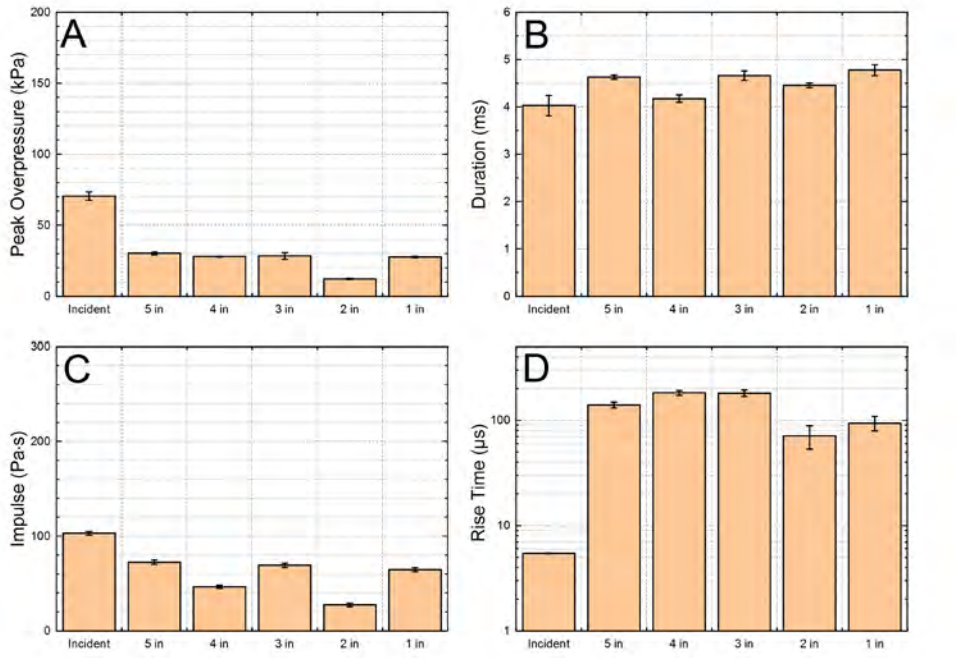


Figure 134 The quantification of the: A) peak overpressure, B) duration, C) impulse and D) rise time of incident and five ICP waveforms recorded for the specimen P190500 at nominal shock wave intensity of 70 kPa (n = 4).

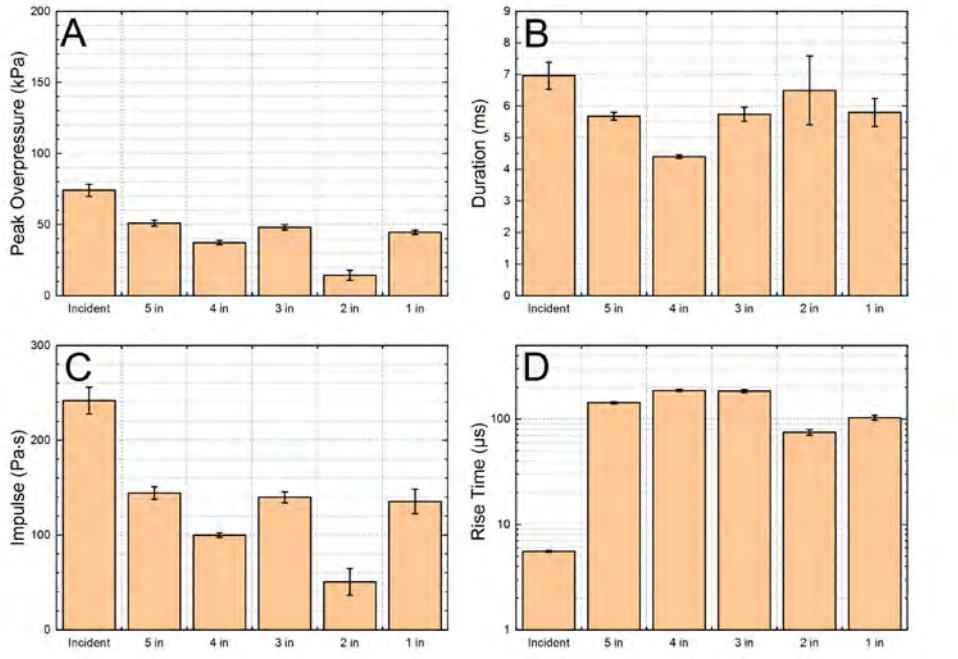


Figure 135 The quantification of the: A) peak overpressure, B) duration, C) impulse and D) rise time of incident and five ICP waveforms recorded for the specimen P190500 at nominal shock wave intensity of 70 kPa, with the long duration impulse (n = 4).

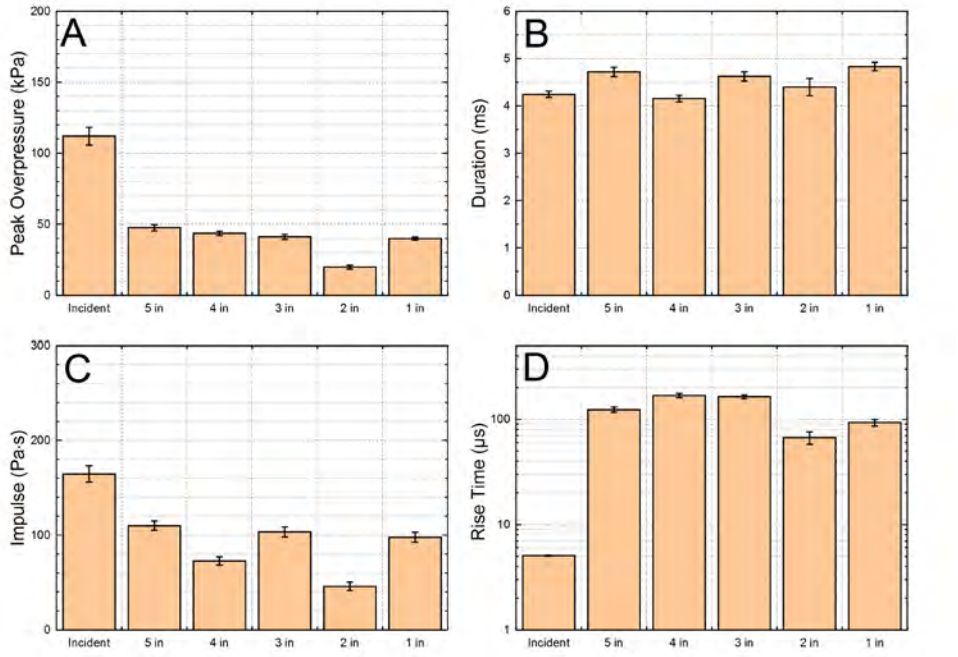


Figure 136 The quantification of the: A) peak overpressure, B) duration, C) impulse and D) rise time of incident and five ICP waveforms recorded for the specimen P190500 at nominal shock wave intensity of 130 kPa (n = 4).

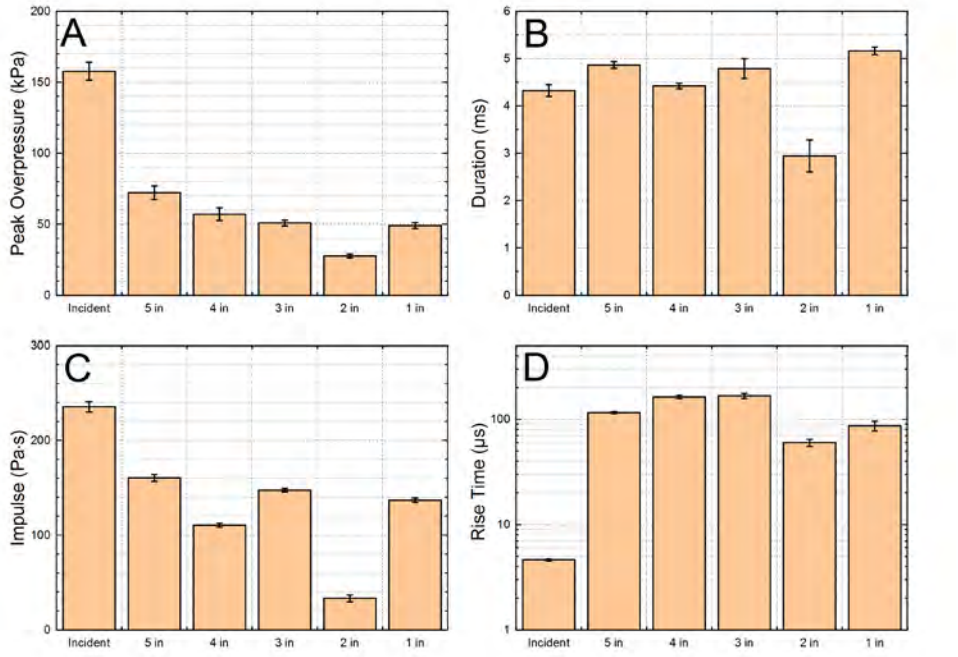


Figure 137 The quantification of the: A) peak overpressure, B) duration, C) impulse and D) rise time of incident and five ICP waveforms recorded for the specimen P190500 at nominal shock wave intensity of 180 kPa (n = 4).

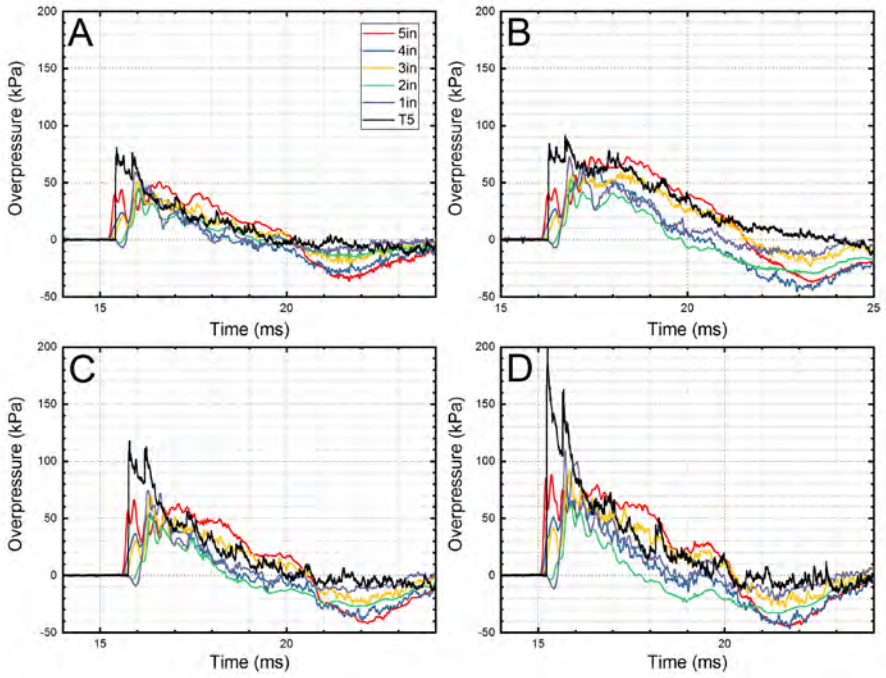


Figure 138 The representative overpressure-time histories collected for the specimen S192693 at nominal shock wave intensity of: A) 70 kPa, B) 70 kPa (long impulse), C) 130 kPa and D) 180 kPa.

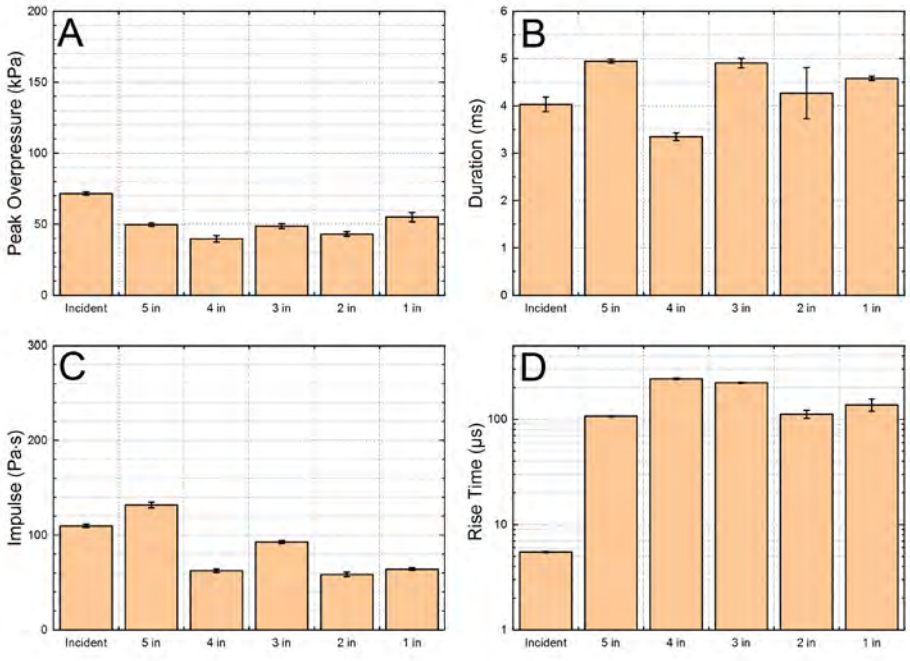


Figure 139 The quantification of the: A) peak overpressure, B) duration, C) impulse and D) rise time of incident and five ICP waveforms recorded for the specimen S192693 at nominal shock wave intensity of 70 kPa (n = 4).

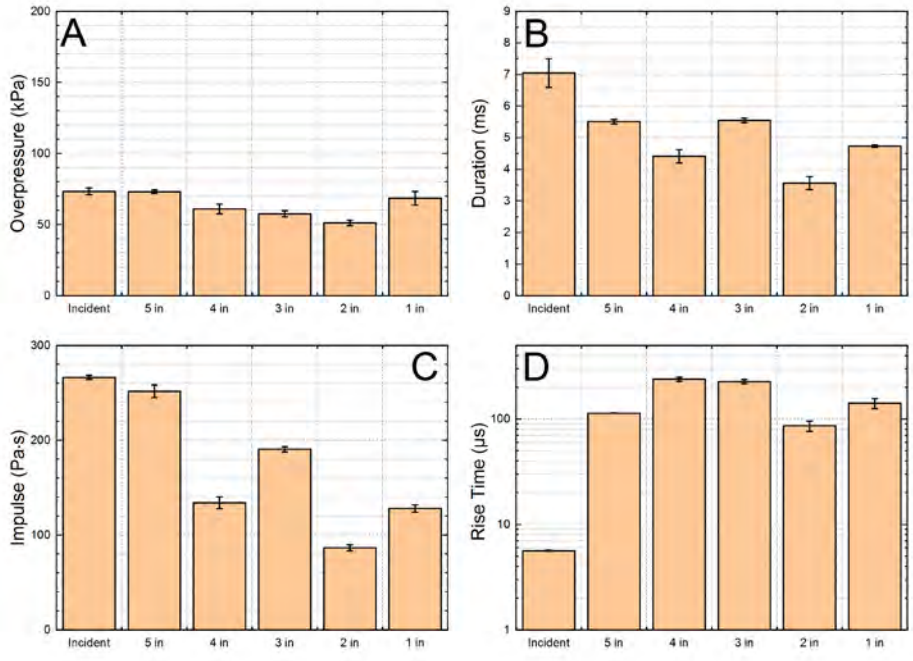


Figure 140 The quantification of the: A) peak overpressure, B) duration, C) impulse and D) rise time of incident and five ICP waveforms recorded for the specimen S192693 at nominal shock wave intensity of 70 kPa, with the long duration impulse (n = 4).

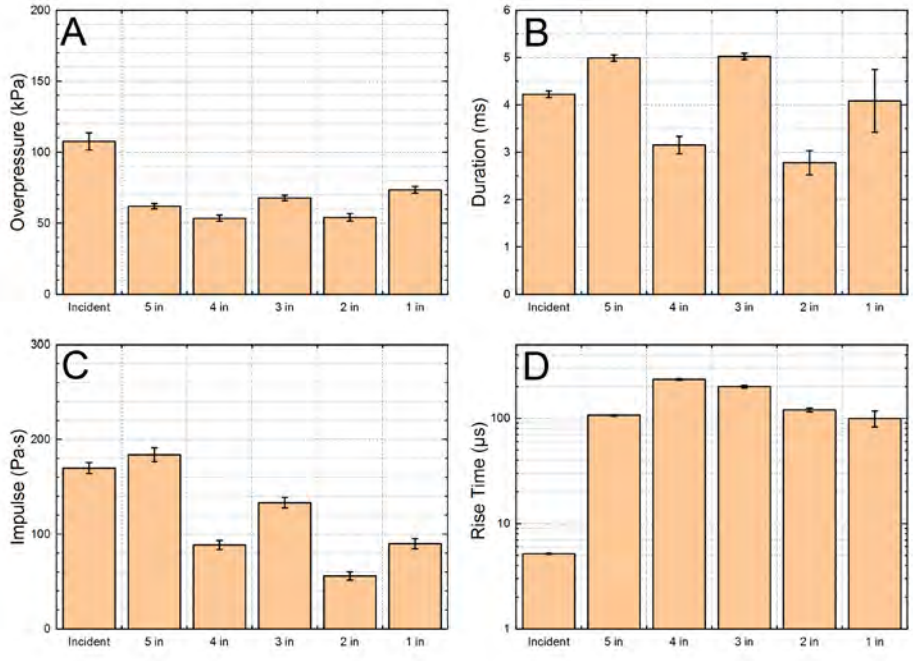


Figure 141 The quantification of the: A) peak overpressure, B) duration, C) impulse and D) rise time of incident and five ICP waveforms recorded for the specimen S192693 at nominal shock wave intensity of 130 kPa (n = 4).

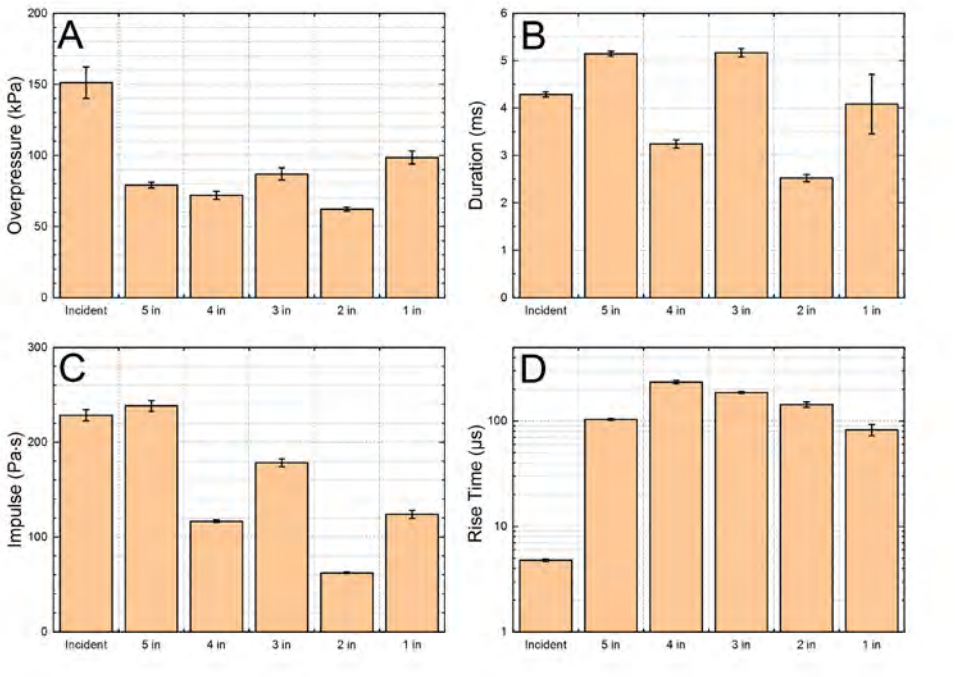


Figure 142 The quantification of the: A) peak overpressure, B) duration, C) impulse and D) rise time of incident and five ICP waveforms recorded for the specimen S192693 at nominal shock wave intensity of 180 kPa (n = 4).

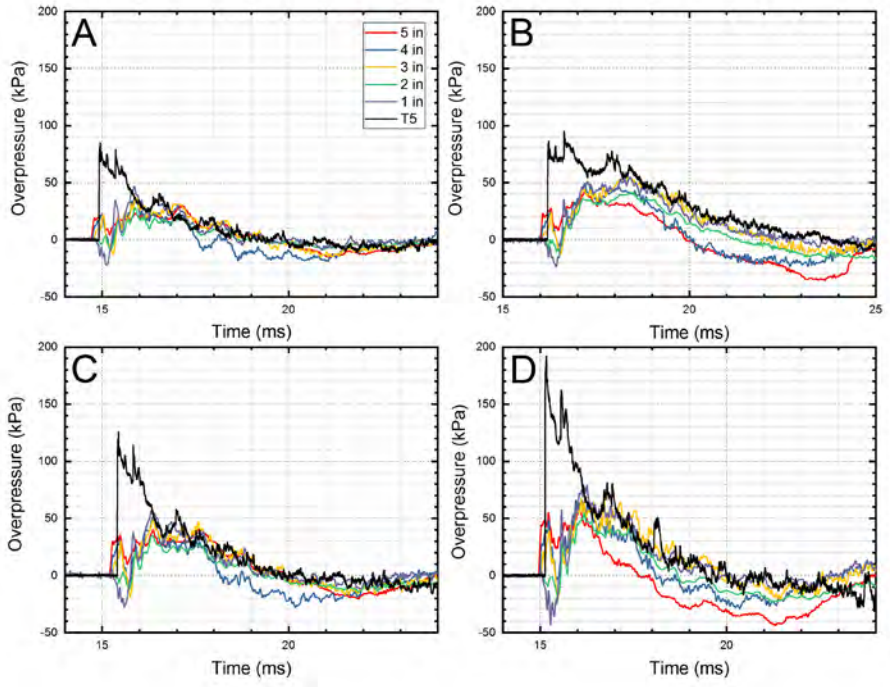


Figure 143 The representative overpressure-time histories collected for the specimen S192868 at nominal shock wave intensity of: A) 70 kPa, B) 70 kPa (long impulse), C) 130 kPa and D) 180 kPa.

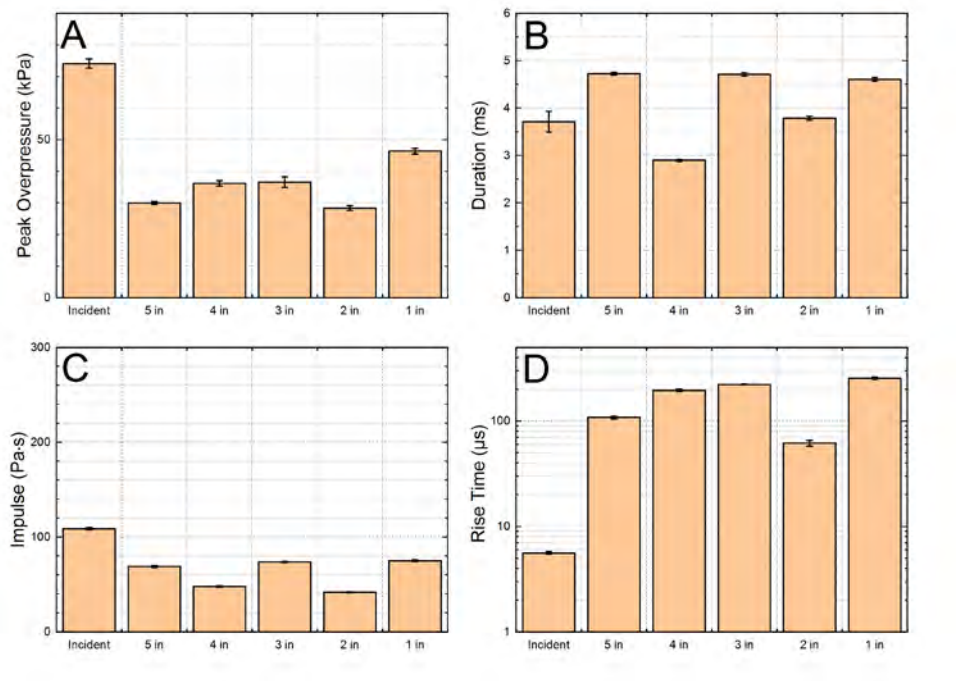


Figure 144 The quantification of the: A) peak overpressure, B) duration, C) impulse and D) rise time of incident and five ICP waveforms recorded for the specimen S192868 at nominal shock wave intensity of 70 kPa (n = 4).

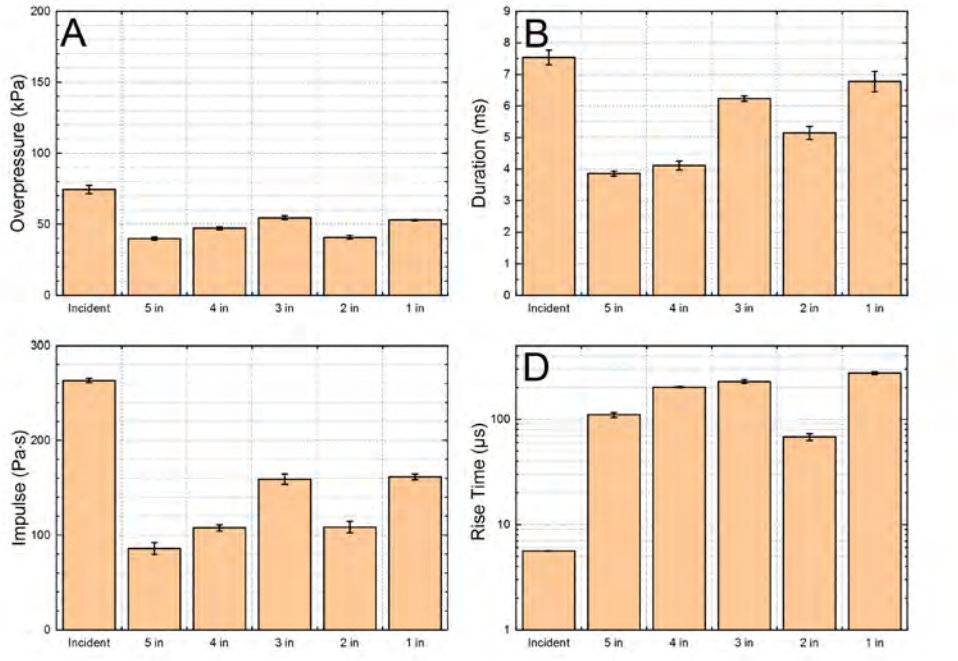


Figure 145 The quantification of the: A) peak overpressure, B) duration, C) impulse and D) rise time of incident and five ICP waveforms recorded for the specimen S192868 at nominal shock wave intensity of 70 kPa, with the long duration impulse (n = 4).

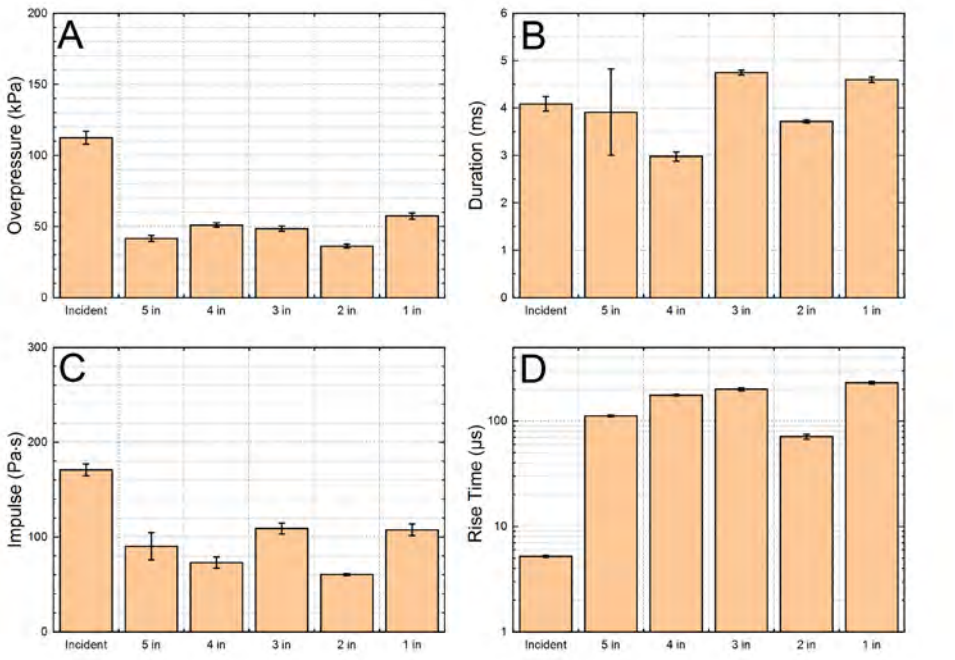


Figure 146 The quantification of the: A) peak overpressure, B) duration, C) impulse and D) rise time of incident and five ICP waveforms recorded for the specimen S192868 at nominal shock wave intensity of 130 kPa (n = 4).

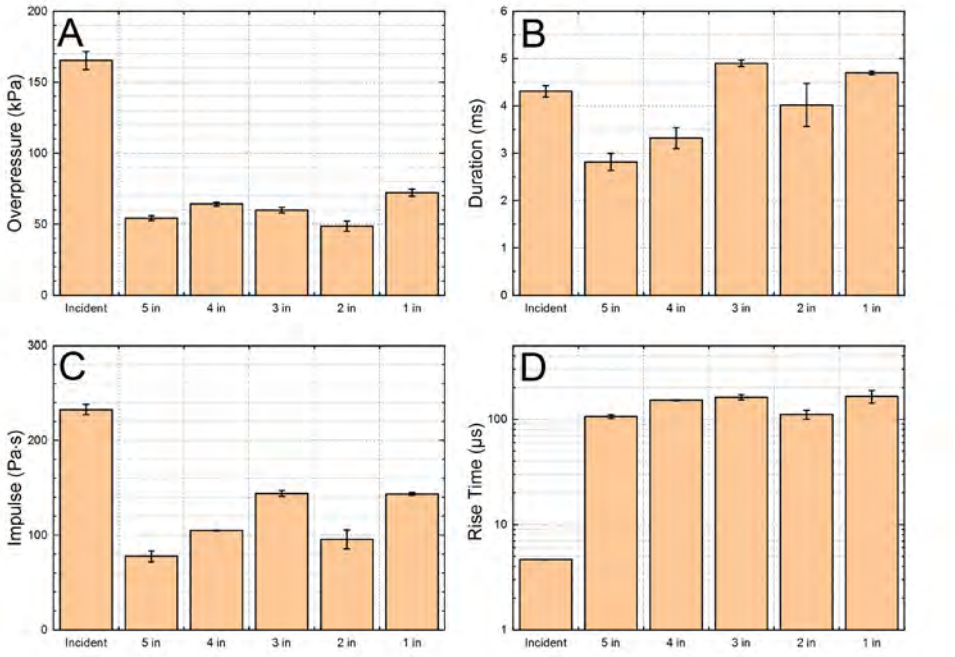


Figure 147 The quantification of the: A) peak overpressure, B) duration, C) impulse and D) rise time of incident and five ICP waveforms recorded for the specimen S192868 at nominal shock wave intensity of 180 kPa (n = 4).

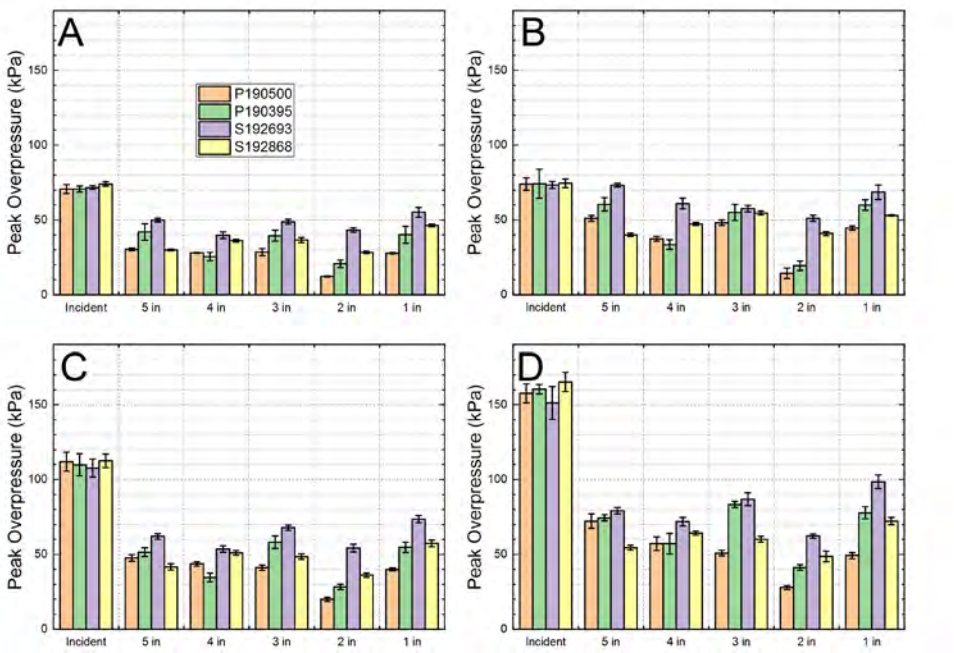


Figure 148 The summary of the quantification of the peak overpressure for all four PMHS included in the analysis. The specimen was exposed to a single shock wave with nominal intensity of: A) 70 kPa, B) 70 kPa (long duration), C) 130 kPa and D) 180 kPa.

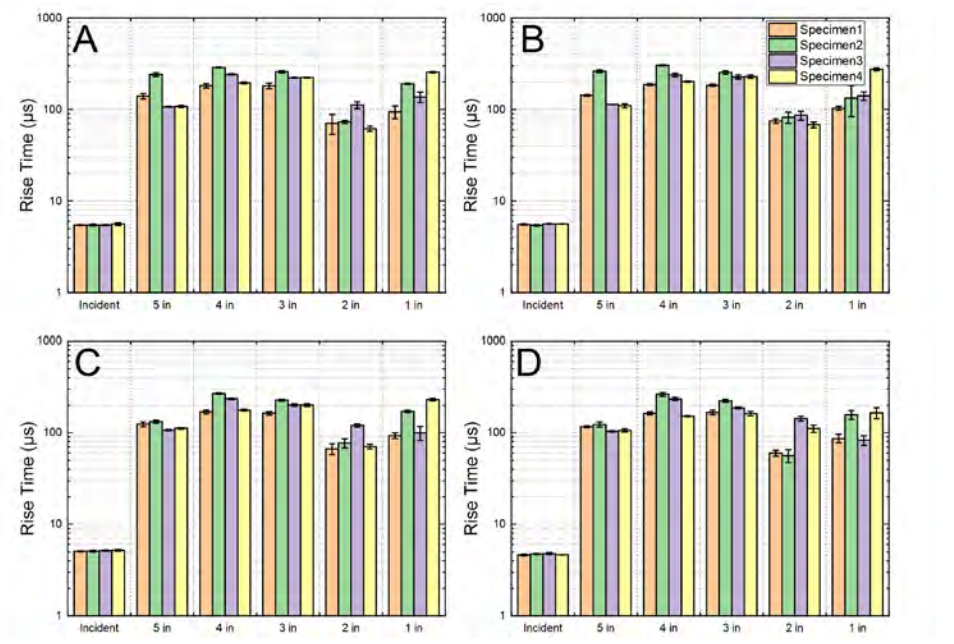


Figure 149 The summary of the quantification of the rise time for all four PMHS included in the analysis. The specimen was exposed to a single shock wave with nominal intensity of: A) 70 kPa, B) 70 kPa (long duration), C) 130 kPa and D) 180 kPa.

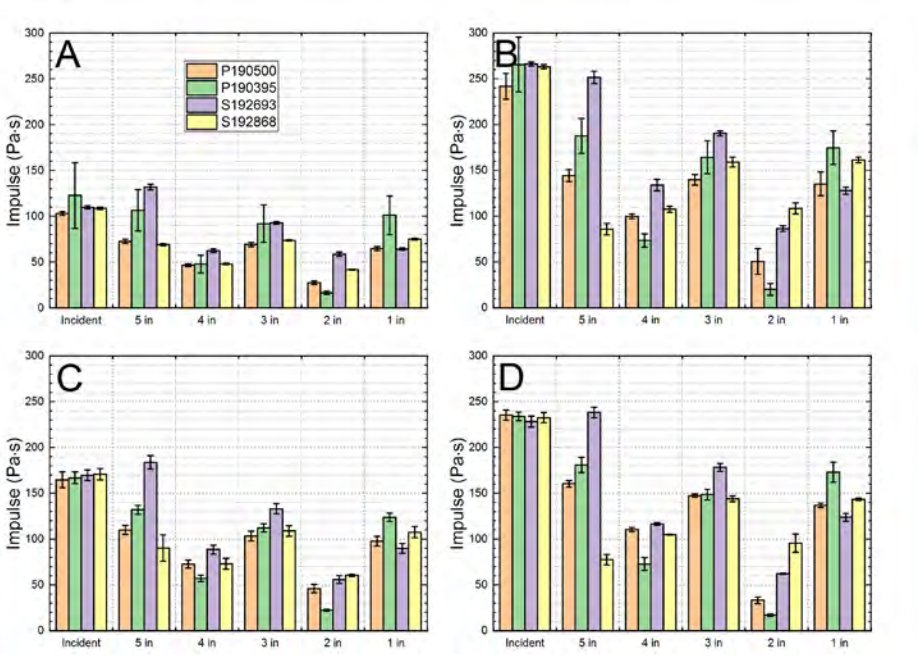


Figure 150 The summary of the quantification of the impulse for all four PMHS included in the analysis. The specimen was exposed to a single shock wave with nominal intensity of: A) 70 kPa, B) 70 kPa (long duration), C) 130 kPa and D) 180 kPa.

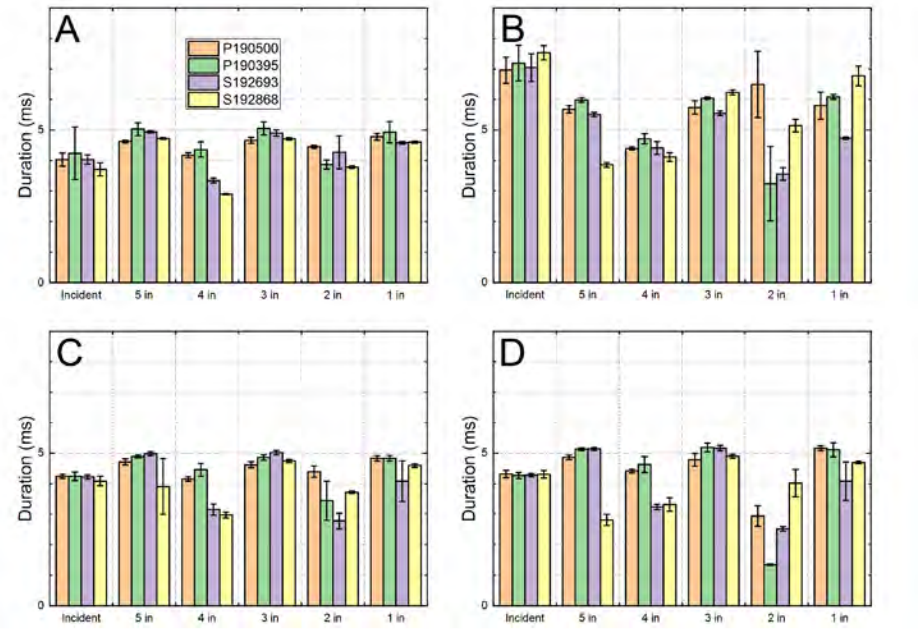


Figure 151 The summary of the quantification of the duration for all four PMHS included in the analysis. The specimen was exposed to a single shock wave with nominal intensity of: A) 70 kPa, B) 70 kPa (long duration), C) 130 kPa and D) 180 kPa.

Task 13. Devise Transfer Function Correlating Rat and Human BOP Conditions

13.1 PMHS experiments and data analysis

All specimens were exposed to three discrete incident overpressures of 70, 130, 180 kPa. These shock wave exposures followed the same protocol established for human surrogate specimen testing performed previously and published recently [35, 36]. We also performed the long duration impulse exposures of the specimen; in which case the shock wave characteristics were configured to be 70 kPa peak overpressure and 7-8 millisecond duration. These experiments were not included in the development of interspecies scaling functions.

For PMHS experiments five different lengths of the cannulas were used, ranging from 1 to 5 inches (fig. 127). The locations of the sensors were confirmed by reconstructing the CT scans. Intracranial and incident pressure measurements were imported into Origin 2019 Pro and four waveform characteristics (peak overpressure, impulse, duration and rise time) were quantified and tabulated. The peak ICP and intracranial impulse for each specimen were plotted as a function of incident peak overpressure and impulse, respectively (fig. 152-161). The regression analysis was performed on all individual datasets, which yielded 10 equations. The linear regression equations for peak overpressure and impulse were plotted (fig. 162, 163) and compared the corresponding rat data. It is evident that the rat plots have similar slope, but there is some degree of variability among PMHS plots, especially for the impulse (fig. 163). Thus, for the development of the scaling between PMHS and rat data, the plots with the highest peak ICP or intracranial impulse (i.e., the highest slope values) at specific incident BOPs were selected. The ratio of the PMHS to rat data was then plotted and an exponential decay fit was performed, which yielded two equations (fig. 164). These equations are rat-to-human scaling laws binding the peak intracranial pressure and impulse with the incident peak overpressure and impulse:

$$y = 7.17e^{\frac{-x}{12.28}} + 0.66e^{\frac{-x}{57.1}} + 0.32,\ R^2=0.99 \quad (1)$$

$$y = 1.8e^{\frac{-x}{31.03}} + 0.27e^{\frac{-x}{199.8}} + 0.587,\ R^2=0.99 \quad (2)$$

These scaling laws are applicable in the 50-200 kPa and 100-1000 Pa·s incident peak overpressure and impulse, respectively. The following figures illustrate the application of the above two equations.

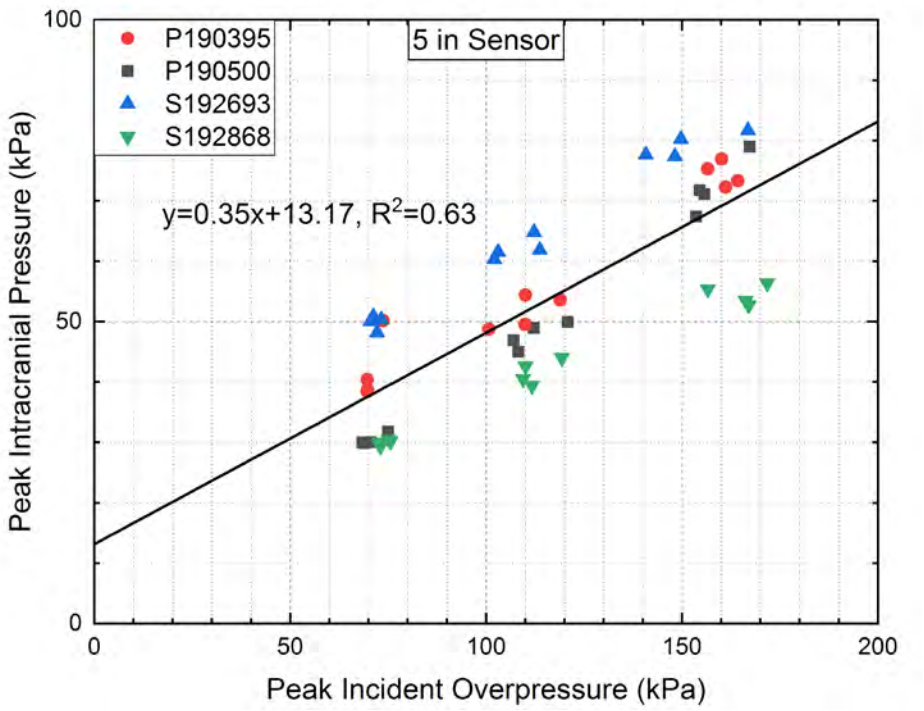


Figure 152 The linear regression of the peak ICP data (5 in. sensor) as a function of peak incident overpressure. The data were collected using four PMHS specimen at three nominal shockwave intensities: 70, 130 and 180 kPa. The regression equation and coefficient of determination, R^2 are presented.

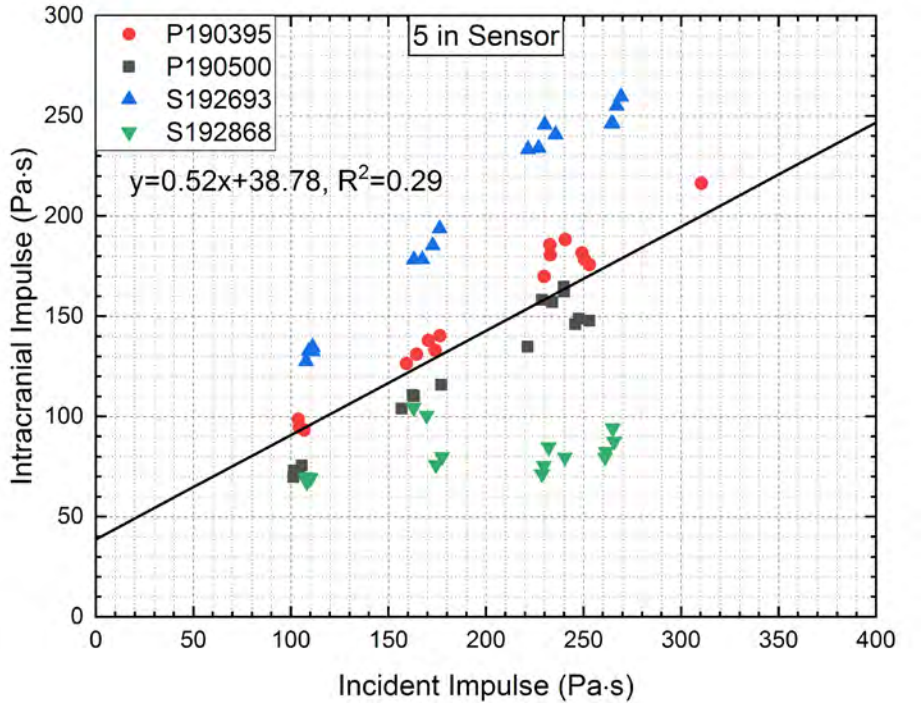


Figure 153 The linear regression of the peak intracranial ICI data (5 in. sensor) as a function of peak incident overpressure. The data were collected using four PMHS specimen at three nominal shockwave intensities: 70, 130 and 180 kPa. The regression equation and coefficient of determination, R^2 are presented.

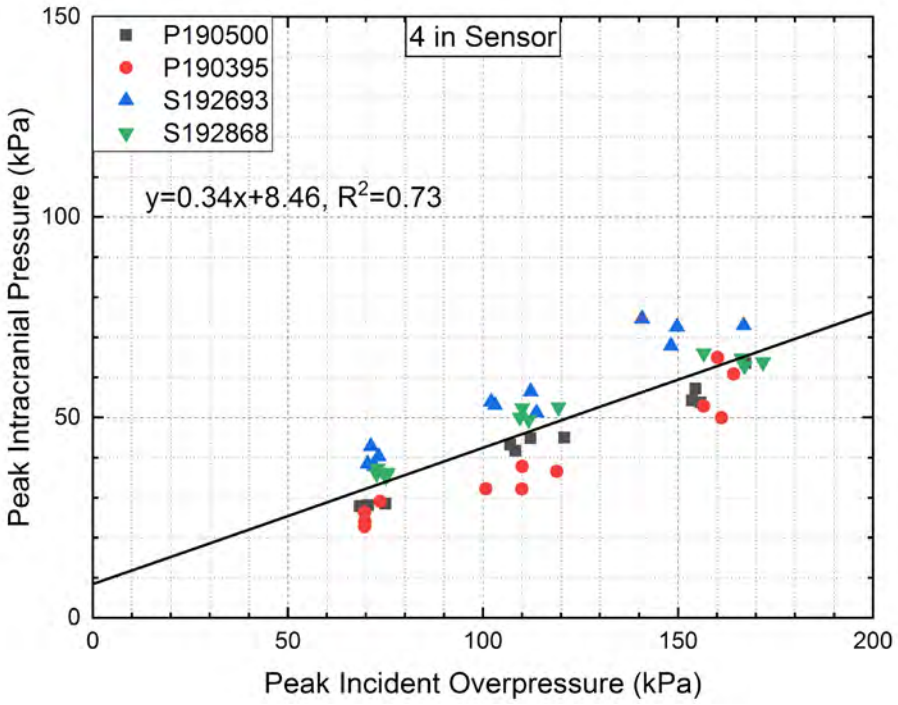


Figure 154 The linear regression of the peak ICP data (4 in. sensor) as a function of peak incident overpressure. The data were collected using four PMHS specimen at three nominal shockwave intensities: 70, 130 and 180 kPa. The regression equation and coefficient of determination, R^2 are presented.

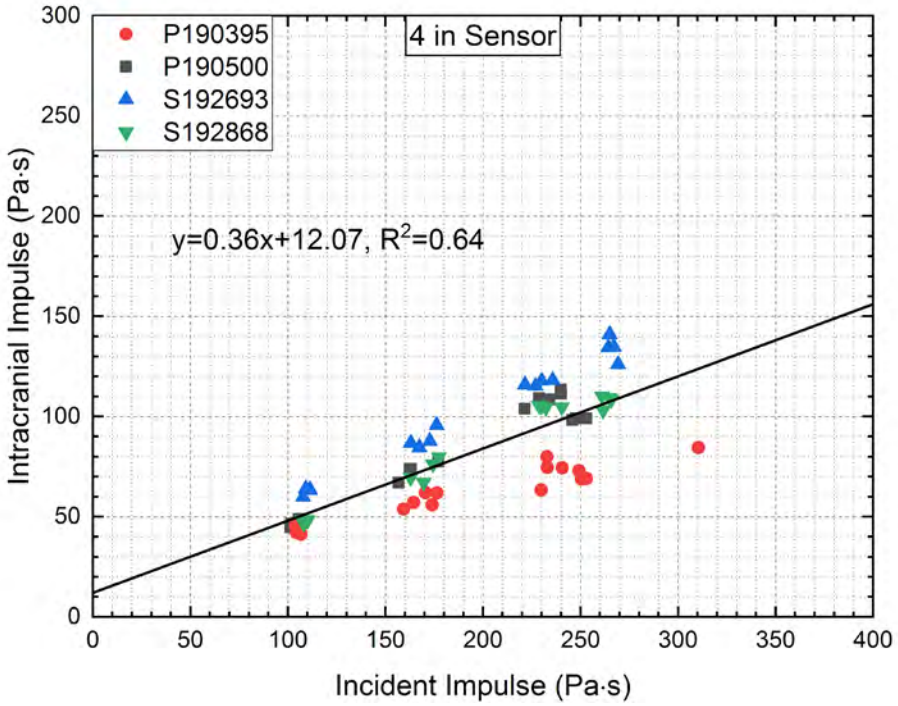


Figure 155 The linear regression of the peak intracranial ICI data (4 in. sensor) as a function of peak incident overpressure. The data were collected using four PMHS specimen at three nominal shockwave intensities: 70, 130 and 180 kPa. The regression equation and coefficient of determination, R^2 are presented.

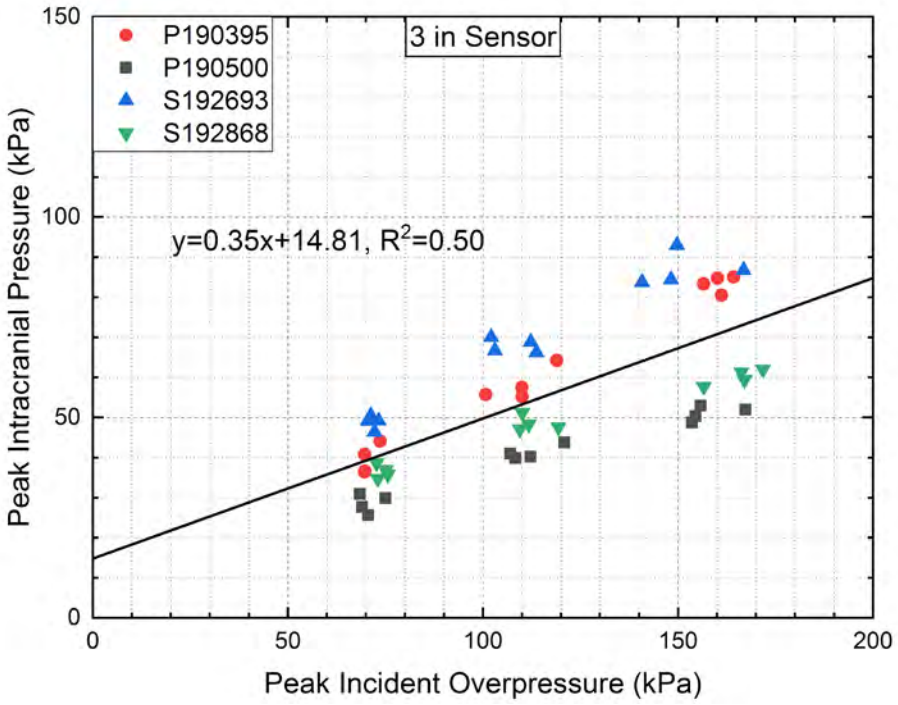


Figure 156 The linear regression of the peak ICP data (3 in. sensor) as a function of peak incident overpressure. The data were collected using four PMHS specimen at three nominal shockwave intensities: 70, 130 and 180 kPa. The regression equation and coefficient of determination, R^2 are presented.

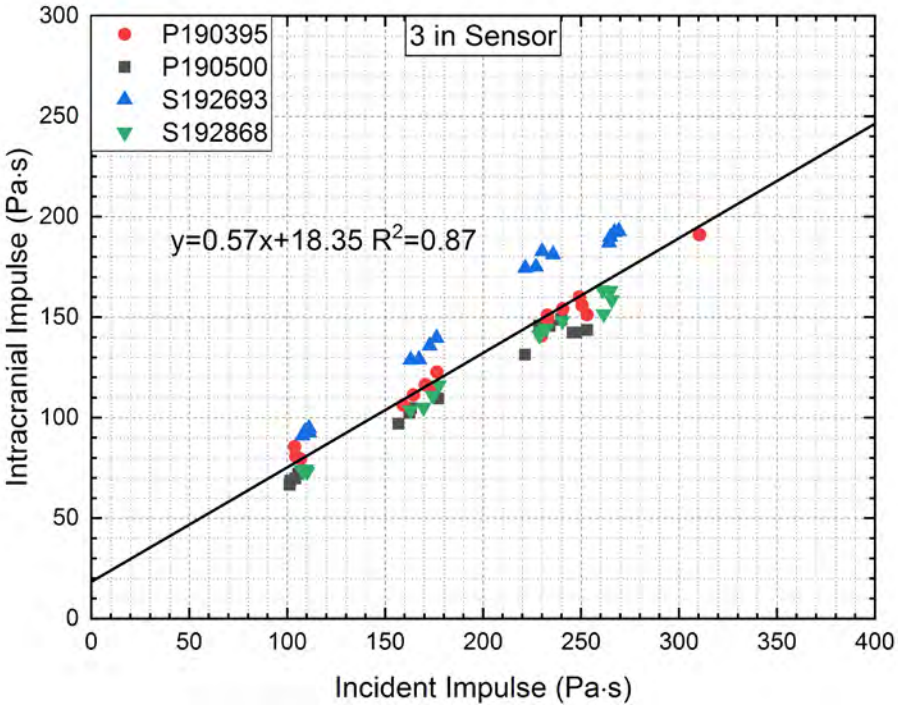


Figure 157 The linear regression of the peak intracranial ICP data (3 in. sensor) as a function of peak incident overpressure. The data were collected using four PMHS specimen at three nominal shockwave intensities: 70, 130 and 180 kPa. The regression equation and coefficient of determination, R^2 are presented.

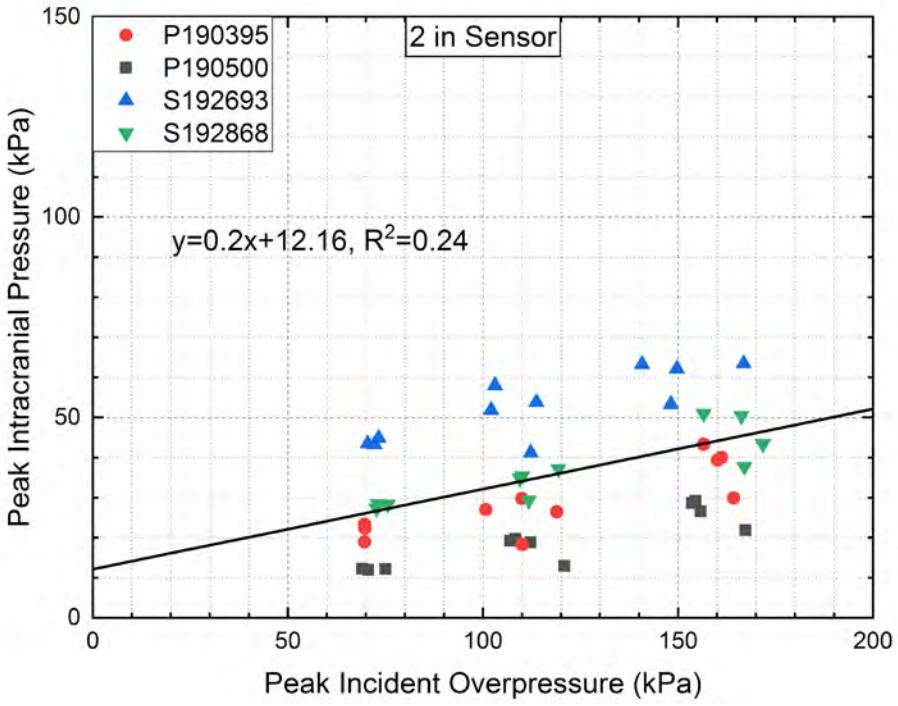


Figure 158 The linear regression of the peak ICP data (2 in. sensor) as a function of peak incident overpressure. The data were collected using four PMHS specimen at three nominal shockwave intensities: 70, 130 and 180 kPa. The regression equation and coefficient of determination, R^2 are presented.

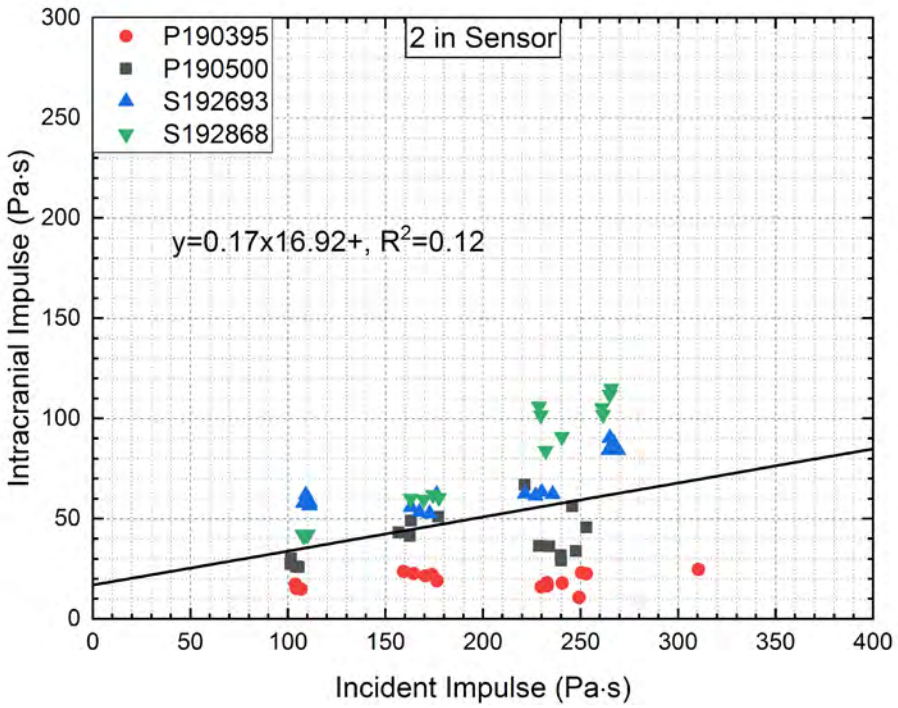


Figure 159 The linear regression of the peak intracranial ICP data (2 in. sensor) as a function of peak incident overpressure. The data were collected using four PMHS specimen at three nominal shockwave intensities: 70, 130 and 180 kPa. The regression equation and coefficient of determination, R^2 are presented.

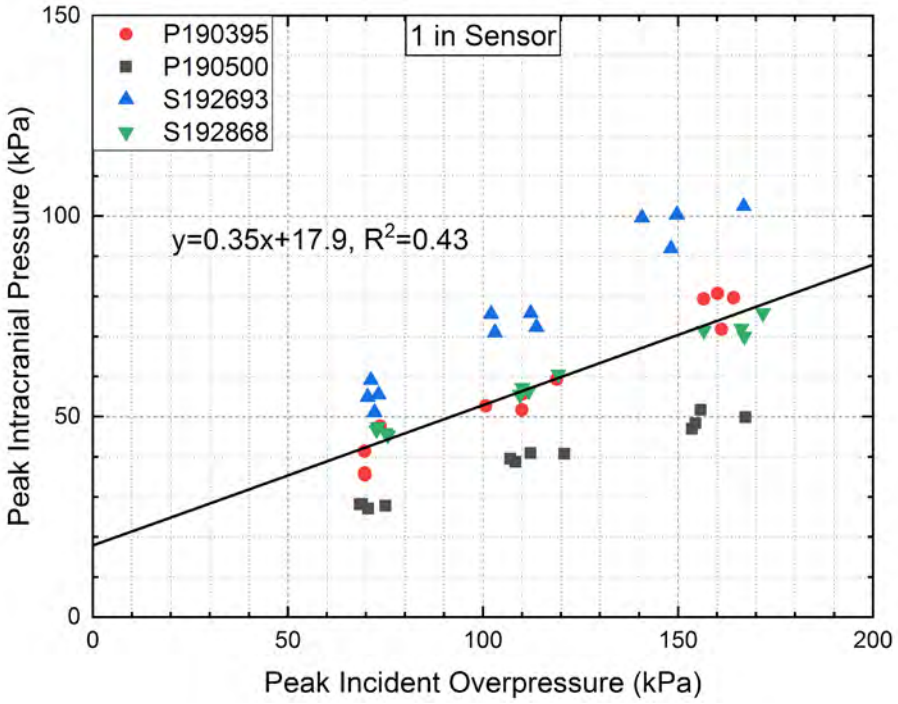


Figure 160 The linear regression of the peak ICP data (1 in. sensor) as a function of peak incident overpressure. The data were collected using four PMHS specimen at three nominal shockwave intensities: 70, 130 and 180 kPa. The regression equation and coefficient of determination, R^2 are presented.

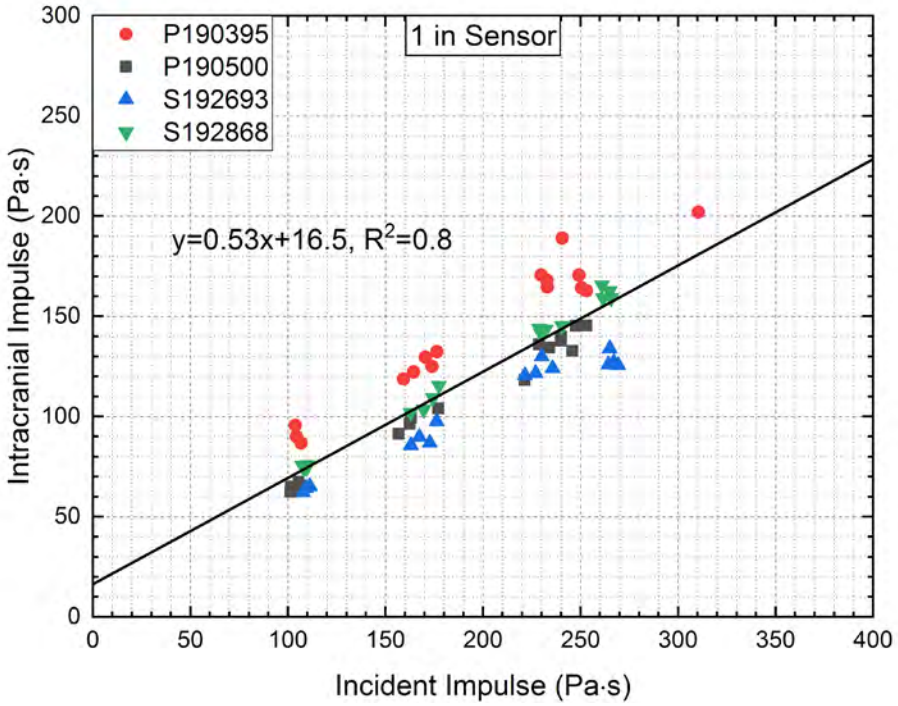


Figure 161 The linear regression of the peak intracranial ICP data (2 in. sensor) as a function of peak incident overpressure. The data were collected using four PMHS specimen at three nominal shockwave intensities: 70, 130 and 180 kPa. The regression equation and coefficient of determination, R^2 are presented.

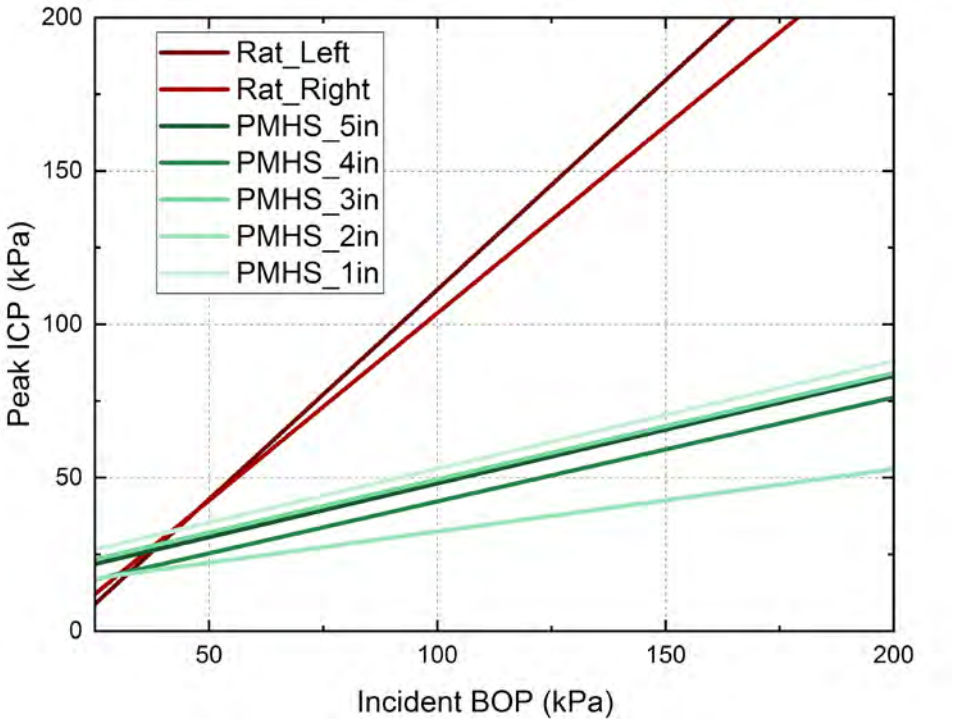


Figure 162 The overview of linear regression curves for rat (left and right ICP sensors) and PMHS (five ICP sensors). The analyses were performed using peak incident and peak intracranial overpressure values.

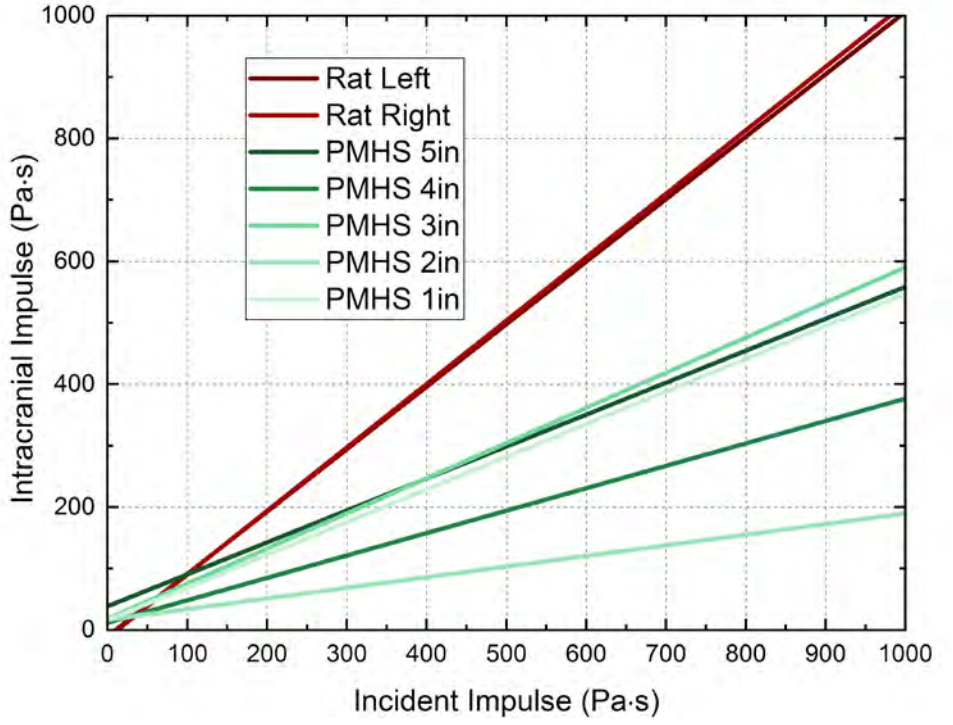


Figure 163 The overview of the linear regression curves for rat (left and right ICP sensors) and PMHS (five ICP sensors). The analyses were performed using incident and intracranial impulse values.

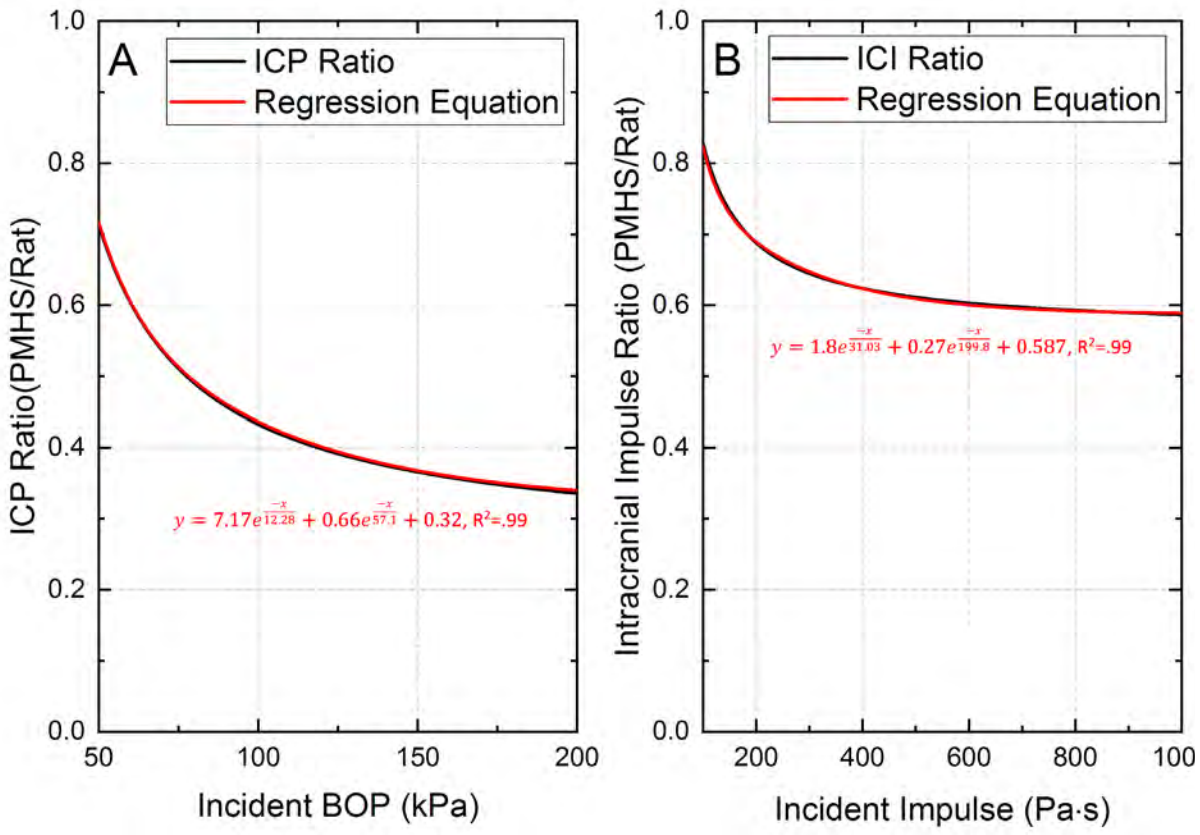


Figure 164 The inter specimen scaling laws were developed using peak overpressure (A) and impulse (B) experimental values. The PMHS/rat ratios were calculated from linear regression equations. The exponential decay function was subsequently used to model ratios of the peak ICP and intracranial impulse. These scaling laws are applicable in the 50-200 kPa and 100-1000 Pa·s incident peak overpressure and impulse, respectively.

What opportunities for training and professional development has the project?

A group of undergraduate students participated in projects developed as sub-sections of the project, or directly related to the research objectives of the project. Undergraduate students worked in the capacity of 20 hours per week under the supervision of graduate students, laboratory technicians, and senior research staff. Many students also volunteered to learn laboratory techniques under the supervision of graduate students and senior scientific staff throughout the five years. Many of them were supported in summers through grants administered by NJIT. Students gained practical knowledge of the techniques used in the characterization of blast TBI: 1) computer simulations: 1) development of 3D models and hands on experience with FEM software, 2) shock tube experimentation, pressure and strain measurements, as well as data analysis techniques used in these research areas. The comprehensive list is presented in the appendix.

References

1. Holmberg A, Chandra N, Feng R, inventorsControlling the shape of the shock wave profile in a blast facility, U.S. Provisional patent application no. 615423542011.
2. Sundaramurthy A, Alai A, Ganpule S, Holmberg A, Plougonven E, Chandra N. Blast-induced biomechanical loading of the rat: an experimental and anatomically accurate computational blast injury model. J Neurotrauma. 2012;29(13):2352-64. Epub 2012/05/25. doi: 10.1089/neu.2012.2413. PubMed PMID: 22620716.
3. Skotak M, Wang F, Alai A, Holmberg A, Harris S, Switzer Iii RC, et al. Rat injury model under controlled field-relevant primary blast conditions: Acute response to a wide range of peak overpressures. J Neurotrauma. 2013. Epub 2013/02/01. doi: 10.1089/neu.2012.2652. PubMed PMID: 23362798.
4. Ganpule S, Gu L, Alai A, Chandra N. Role of helmet in the mechanics of shock wave propagation under blast loading conditions. Comput Methods Biomech Biomed Engin. 2012;15(11):1233-44. Epub 2011/08/03. doi: 10.1080/10255842.2011.597353. PubMed PMID: 21806412.
5. Ganpule S, Alai A, Plougonven E, Chandra N. Mechanics of blast loading on the head models in the study of traumatic brain injury using experimental and computational approaches. Biomech Model Mechanobiol. 2012. Epub 2012/07/27. doi: 10.1007/s10237-012-0421-8. PubMed PMID: 22832705.
6. Skotak M, Wang F, Alai A, Holmberg A, Harris S, Switzer RC, et al. Rat injury model under controlled field-relevant primary blast conditions: acute response to a wide range of peak overpressures. Journal of neurotrauma. 2013;30(13):1147-60. doi: 10.1089/neu.2012.2652. PubMed PMID: 23362798; PubMed Central PMCID: PMC3700437.
7. Chandra N, Skotak M, Wang F, Ganpule S, Haorah J, editors. Do Primary Blast-Shock Waves Cause Mild TBI? Experimental Evidence Based on Animal Models and Human Cadaveric Heads. J Neurotrauma; 2013.
8. Yelveton JT. Pathology scoring system for blast injuries. J Trauma. 1996;40(3 Suppl):S111-5. Epub 1996/03/01. PubMed PMID: 8606390.
9. Misistia A. Rodent testing device surrogate for shockwave blast testing: New Jersey Institute of Technology; 2015.
10. Baumgartner D, Lamy M, Willinger R, Choquet P, Goetz C, Constatinesco A, et al. Finite element analysis of traumatic brain injuries mechanisms in the rat. IRCOBI Conference2009. p. 97-108.
11. Hua Y, Akula P, Kelso M, Gu L. Characterization of Closed Head Impact Injury in Rat. Biomed Research International. 2015;2015. doi: 10.1155/2015/272976.
12. Gadd CW, Nahum AM, Schneider DC, Madeira RG. Tolerance and properties of superficial soft tissues in situ. SAE Technical Paper, 1970 0148-7191.
13. Gefen A, Gefen N, Zhu QL, Raghupathi R, Margulies SS. Age-dependent changes in material properties of the brain and braincase of the rat. Journal of Neurotrauma. 2003;20(11):1163-77. doi: 10.1089/089771503770802853. PubMed PMID: WOS:000186784600002.
14. Mishra V, Skotak M, Schuetz H, Heller A, Haorah J, Chandra N. Primary blast causes mild, moderate, severe and lethal TBI with increasing blast overpressures: Experimental rat injury model. Scientific reports. 2016;6:26992.
15. Abdul-Muneer PM, Schuetz H, Wang F, Skotak M, Jones J, Gorantla S, et al. Induction of oxidative and nitrosative damage leads to cerebrovascular inflammation in an animal model of

mild traumatic brain injury induced by primary blast. Free Radic Biol Med. 2013;60:282-91. doi: 10.1016/j.freeradbiomed.2013.02.029. PubMed PMID: 23466554; PubMed Central PMCID: PMC4007171.
16. Cooney SJ, Bermudez-Sabogal SL, Byrnes KR. Cellular and temporal expression of NADPH oxidase (NOX) isotypes after brain injury. Journal of neuroinflammation. 2013;10(1):917.
17. Lu X-Y, Wang H-D, Xu J-G, Ding K, Li T. NADPH oxidase inhibition improves neurological outcome in experimental traumatic brain injury. Neurochemistry International. 2014;69:14-9. doi: https://doi.org/10.1016/j.neuint.2014.02.006.
18. Choi BY, Jang BG, Kim JH, Lee BE, Sohn M, Song HK, et al. Prevention of traumatic brain injury-induced neuronal death by inhibition of NADPH oxidase activation. Brain research. 2012;1481:49-58.
19. Kuriakose M, Skotak M, Misistia A, Kahali S, Sundaramurthy A, Chandra N. Tailoring the Blast Exposure Conditions in the Shock Tube for Generating Pure, Primary Shock Waves: The End Plate Facilitates Elimination of Secondary Loading of the Specimen. PLoS One. 2016;11(9):e0161597. Epub 2016/09/08. doi: 10.1371/journal.pone.0161597. PubMed PMID: 27603017; PubMed Central PMCID: PMCPMC5014318.
20. Skotak M, Alay E, Chandra N. On the accurate Determination of shock Wave Time-Pressure Profile in the experimental Models of Blast-induced neurotrauma. Frontiers in neurology. 2018;9:52.
21. Townsend MT, Alay E, Skotak M, Chandra N. Effect of Tissue Material Properties in Blast Loading: Coupled Experimentation and Finite Element Simulation. Annals of Biomedical Engineering. 2018:1-14. doi: 10.1007/s10439-018-02178-w.
22. Sundaramurthy A, Chandra N. A parametric approach to shape field-relevant blast wave profiles in compressed-gas-driven shock tube. Front Neurol. 2014;5:253. Epub 2014/12/19. doi: 10.3389/fneur.2014.00253. PubMed PMID: 25520701; PubMed Central PMCID: PMCPMC4251450.
23. Garimella HT, Kraft RH, Przekwas AJ. Do blast induced skull flexures result in axonal deformation? PLoS One. 2018:1-24. Epub March 16, 2018. doi: https://doi.org/10.1371/journal.pone.0190881.
24. Design and Analysis of Heardened Structures to Conventional Weapons Effects. 1986 Edition ed1986. p. 1-258.
25. Skotak M, Chandra N. Primary Blast Injury Criteria for Animal/Human TBI Models using Field Validated Shock Tubes. New Jersey Institute of Technology: New Jersey Institute of Technology, Newark, NJ, 07102, 2016 W81XWH-15-1-0303 Contract No.: AD1033280.
26. Cocosco CC, Kollokian V, Kwan RK-S, Evans AC. BrainWeb: Online Interface to a 3D MRI Simulated Brain Database. NeuroImage. 1997;5(4):S425.
27. Cocosco CC, Kollokian V, Kwan RK-S, Evans AC, editors. BrainWeb: Online Interface to a 3D MRI Simulated Brain Database. Proceedings of 3-rd International Conference on Functional Mapping of the Human Brain; 1997; Copenhagen.
28. Collins DL, Zijdenbos AP, Kollokian V, Sled JG, Kabani NJ, Holmes CJ, et al. Design and construction of a realistic digital brain phantom. IEEE Transactions on Medical Imaging. 1998;17(3):463-8. doi: 10.1109/42.712135.
29. Kwan RK-S, Evans AC, Pike GB. MRI simulation-based evaluation of image-processing and classification methods. IEEE Transactions on Medical Imaging. 1999;18(11):1085-97.

30. Cotton RT, Pearce CW, Young PG, Kota N, Leung AC, Bagchi A, et al. Development of a geometrically accurate and adaptable finite element head model for impact simulation: the Naval Research Laboratory-Simpleware Head Model. Comput Methods Biomech Biomed Engin. 2016;19(1):101-13. Epub 2015/01/08. doi: 10.1080/10255842.2014.994118. PubMed PMID: 25563692.
31. Kuriakose M, Rao KVR, Younger D, Chandra N. Temporal and spatial effects of blast overpressure on blood-brain barrier permeability in traumatic brain injury. Scientific reports. 2018;8(1):8681.
32. Kuriakose M, Younger D, Ravula AR, Alay E, Rama Rao KV, Chandra N. Synergistic Role of Oxidative Stress and Blood-Brain Barrier Permeability as Injury Mechanisms in the Acute Pathophysiology of Blast-induced Neurotrauma. Scientific Reports. 2019;9(1):7717. doi: 10.1038/s41598-019-44147-w.
33. Rama Rao KV, Iring S, Younger D, Kuriakose M, Skotak M, Alay E, et al. A Single Primary Blast-Induced Traumatic Brain Injury in a Rodent Model Causes Cell-Type Dependent Increase in Nicotinamide Adenine Dinucleotide Phosphate Oxidase Isoforms in Vulnerable Brain Regions. Journal of neurotrauma. 2018.
34. Leonardi AD, Bir CA, Ritzel DV, VandeVord PJ. Intracranial pressure increases during exposure to a shock wave. Journal of neurotrauma. 2011;28(1):85-94. Epub 2010/11/26. doi: 10.1089/neu.2010.1324. PubMed PMID: 21091267.
35. Skotak M, Alay E, Zheng JQ, Halls V, Chandra N. Effective testing of personal protective equipment in blast loading conditions in shock tube: Comparison of three different testing locations. PLoS One. 2018;13(6):e0198968. Epub 2018/06/13. doi: 10.1371/journal.pone.0198968. PubMed PMID: 29894521; PubMed Central PMCID: PMCPMC5997325.
36. Sundaramurthy A, Skotak M, Alay E, Unnikrishnan G, Mao H, Duan X, et al. Assessment of the Effectiveness of Combat Eyewear Protection Against Blast Overpressure. J Biomech Eng. 2018;140(7). Epub 2018/04/21. doi: 10.1115/1.4039823. PubMed PMID: 29677280.

What opportunities for training and professional development has the project provided?

A group of undergraduate and graduate students participated directly related to the research objectives of the project. 3 graduate students and 1 master's student were awarded degrees working on this project. Many undergraduate students worked in the capacity of 20 hours per week under the supervision of graduate students, laboratory technicians, and senior research staff. Many students also volunteered to learn laboratory techniques under the supervision of graduate students and senior scientific staff throughout the five years. Many of them were supported in summers through grants administered by NJIT. Students gained practical knowledge of the techniques used in the characterization of blast TBI: 1) computer simulations: 1) development of 3D models and hands on experience with FEM software, 2) biochemistry and molecular biology: brain sectioning, immunostaining, and Western blot, and 3) shock tube experimentation, pressure and strain measurements, as well as analytical techniques used in these research areas.

The list of students who participated in the program is given in Appendix (See Appendix G)

Among of this group undergraduate students participating in the research projects were awarded NJIT Provost Undergraduate Research and Innovation (7 students) and Albert Dorman Honors College (3 students) Scholarships to conduct individual research projects during the Summer semester. (See Appendix G)

How were the results disseminated to communities of interest?

- Manuscripts/Publications: (see appendix A-F for a complete list)
- Conference presentations; (see appendix A-F for a complete list)

What do you plan to do during the next reporting period to accomplish the goals?

The project is completed and achieved all stated goals

3. IMPACT

What was the impact on the development of the principal discipline(s) of the project?

1. We demonstrated for the first time that the impulse effect has measurable outcomes in the brains of exposed animals. The analysis of brain proteome of animal models exposed to a single shock wave with variable impulse was completed and validated. The proteomics samples collected from brains of the two injury groups (short- and long-duration impulse, 180 kPa BOP, 330 and 720 Pa·s, respectively) and control were analyzed. We also performed verification of the proteomic data via Western blot using three proteins (Synaptophysin (Syp), Postsynaptic Density Protein 95 kDa (PSD95), and ATP synthase-coupling factor 6 (ATP5j)). Western blot confirmed the expression patterns observed in the proteomic data. A pathway analysis on proteomic data indicates a large set of differentially expressed proteins in the long-impulse group compared to its short counterpart. Among these the downregulated proteins dominated in the long-duration impulse dataset by a margin of 210. This study also for the first time examined the brain region-specific and temporal changes on oxidative stress, blood brain barrier permeability changes in a well validated shock tube.
2. The methodology to validate a brain surrogate material, which will be used in the experiments with cephalic postmortem human specimen (PMHS), was developed. Similar material validation was not performed previously, to the best of our knowledge. We evaluated the response, measured as ICP profile, of two different types of 'ballistic gelatin': 1) gelatin from the natural source, and 2) commercially available synthetic gelatin. The semi-surrogate and full-surrogate models were prepared; semi surrogate was a rat with a brain replaced with 10% or 20% gelatin in water gel, and full-surrogate models used the rat skull and had skin, flesh and the brain prepared using 10% and 20% gelatin in water, or 10% synthetic gelatin. Both types of models were subjected to a shock wave loading at three different nominal intensities (70, 130 and 180 kPa) and ICP waveforms were recorded. Subsequently, we quantified peak overpressure, rise

What was the impact on technology transfer?

Nothing to Report

What was the impact on other disciplines?

Nothing to Report

What was the impact on society beyond science and technology?

Nothing to Report

4. CHANGES/PROBLEMS

The Project Director/Principal Investigator (PD/PI) is reminded that the recipient organization is required to obtain prior written approval from the awarding agency Grants Officer whenever there are significant changes in the project or its direction. If not previously reported in writing, provide the following additional information or state, "Nothing to Report," if applicable:

Changes in approach and reasons for change

Nothing to Report

Actual or anticipated problems or delays and actions or plans to resolve them
Describe problems or delays encountered during the reporting period and actions or plans to resolve them.

Nothing to Report

Changes that had a significant impact on expenditures
Describe changes during the reporting period that may have had a significant impact on expenditures, for example, delays in hiring staff or favorable developments that enable meeting objectives at less cost than anticipated.

Nothing to Report

Significant changes in use or care of human subjects, vertebrate animals, biohazards, and/or select agents
Describe significant deviations, unexpected outcomes, or changes in approved protocols for the use or care of human subjects, vertebrate animals, biohazards, and/or select agents during the reporting period. If required, were these changes approved by the applicable institution committee (or equivalent) and reported to the agency? Also specify the applicable Institutional Review Board/Institutional Animal Care and Use Committee approval dates.

Significant changes in use or care of human subjects

Nothing to Report

Significant changes in use or care of vertebrate animals.

Nothing to Report

Significant changes in use of biohazards and/or select agents

Nothing to Report

5. PRODUCTS

List any products resulting from the project during the reporting period. If there is nothing to report under a particular item, state "Nothing to Report."

- ***Publications, conference papers, and presentations***

Report only the major publication(s) resulting from the work under this award.
Journal publications (all published):

See complete list in Appendix A-F

Books or other non-periodical, one-time publications.

See complete list in Appendix A-F

Other publications, conference papers, and presentations.
See Complete list in Appendix A-F

- Website(s) or other Internet site(s)

List the URL for any Internet site(s) that disseminates the results of the research activities. A short description of each site should be provided. It is not necessary to include the publications already specified above in this section.

http://news.njit.edu/institute-brain-and-neuroscience-research-meeting-challenges-understanding-and-healing/
As part of the inauguration of the Institute for Brain and Neuroscience Research, Raj Gupta, deputy director and senior science advisor for the U.S. Department of Defense Blast Injury Research Program Coordinating Office, Colonel Sidney R. Hinds II and Namas Chandra, IBNR co-director, discussed promising research that will be advanced by the new institute with NJIT faculty and students. Commenting on the relationship between NJIT and the Department of Defense, Gupta said that NJIT researchers have a special understanding of the needs of U.S. service members with regard to brain injuries, and a commitment to collaborative work essential for both new insights into basic physiological mechanisms and better treatment.

https://www.youtube.com/watch?v=l-AZmJn_kCs
Highlights of multi-disciplinary activities involving the brain injury due to blast and blunt loadings.

Technologies or techniques
Identify technologies or techniques that resulted from the research activities. In addition to a description of the technologies or techniques, describe how they will be shared.

Nothing to Report

Inventions, patent applications, and/or licenses
Identify inventions, patent applications with date, and/or licenses that have resulted from the research. State whether an application is provisional or non-provisional and indicate the application number. Submission of this information as part of an interim research performance progress report is not a substitute for any other invention reporting required under the terms and conditions of an award.

Nothing to Report

Other Products

Nothing to Report

Has there been a change in the active other support of the PD/PI(s) or senior/key personnel since the last reporting period?
If there is nothing significant to report during this reporting period, state "Nothing to Report."

If the active support has changed for the PD/PI(s) or senior/key personnel, then describe what the change has been. Changes may occur, for example, if a previously active grant has closed and/or if a previously pending grant is now active. Annotate this information so it is clear what has changed from the previous submission. Submission of other support information is not necessary for pending changes or for changes in the level of effort for active support reported previously. The awarding agency may require prior written approval if a change in active other support significantly impacts the effort on the project that is the subject of the project report.

Nothing to Report

What other organizations were involved as partners?

Blast Injury Coordinating office was involved in some parts of the research as a part of US-India PA # US-IN-A-16-0002. There were multiple participants from US and India in this PA.

6. SPECIAL REPORTING REQUIREMENTS

COLLABORATIVE AWARDS: For collaborative awards, independent reports are required from BOTH the Initiating PI and the Collaborating/Partnering PI. A duplicative report is acceptable; however, tasks shall be clearly marked with the responsible PI and research site. A report shall be submitted to **https://ers.amedd.army.mil** for each unique award.

QUAD CHARTS: If applicable, the Quad Chart (available on https://www.usamraa.army.mil) should be updated and submitted with attachments.

7. APPENDICES

See below Appendices A-G

Appendix A. List of publications in peer reviewed journals

2020

1. A. Aravind, A.R. Ravula, N. Chandra and BJ Pfister, "Behavioral deficits in animal models of blast traumatic brain injury, **Frontiers in Neurology,** https://doi.org/10.3389/fneur.2020.00990, (2020), [20-1]

2. E. Alay, M. Skotak, S. Chandrasekaran, J. Ziner, N. Chandra, *"Variations of Constitutive Properties of the Fluid Elicit Divergent Vibrational and Pressure Response Under Shock Wave Loading",* **Journal of Biomechanical Engineering, (**2020), [20-2].

3. A. Aravind, J. Kosty, N. Chandra, B.J. Pfister, *"Blast exposure predisposes the brain to increased neurological deficits in a model of blast plus blunt traumatic brain",* **Experimental Neurology, 332**, (2020), [20-3].

4. M. Murugan, A. Ravula, A. Gandhi, G. Vegunta, S Mukkamala, W. Mujib, N. Chandra, *"Chemokine signaling mediated monocyte infiltration affects anxiety-like behavior following blast injury",* **Brain, Behavior and Immunity, 88**, 340-352**,** (2020), [20-4].

5. P. Rana, K.V. Rama Rao, A. Ravula, R. Trivedi, M. D'Souza, A.K. Singh, R.K. Gupta, N. Chandra, *"Oxidative stress contributes to cerebral metabolomic profile changes in animal model of blast-induced traumatic brain injury",* **Metabolomics, 16**, 3, 1-12, (2020), [20-5].

6. S. Kahali, M. Townsend, M. M. Nguyen, J. Kim, E Alay, N. Chandra, *"The evolution of secondary flow phenomena and their effect on primary shock conditions in shock tubes: Experimental and numerical model",* **Plos One, 15 (1),** e0227125**,** (2020), [20-6].

2019

7. M. Kuriakose, D. Younger, A. R. Ravula, E. Alay, K.V. Rama Rao, N. Chandra, *"Synergistic role of oxidative stress and blood-brain barrier permeability as injury mechanisms in the acute pathophysiology of blast-induced neurotrauma",* **Nature- Scientific Reports,** 9 (1), 7717**,** (2019), [19-7]

8. X. Ma, A. Aravind, B.J. Pfister, N. Chandra and J. Haorah, *"Animal models of traumatic brain injury and assessment of injury severity",* **Molecular Neurobiology,** https://doi.org/10.1007/s12035-018-1454-5, 1-14, (2019), [19-8].

9. M. T. Townsend, E. Alay, M. Skotak, N. Chandra, *"Effect of tissue material properties in blast loading: coupled experimentation and finite element simulation",* **Annals of Biomedical Engineering,** ABME-D-18-0051, 1-14**,** (2019), [19-9].

10. D. Younger, M. Murugan, K.V. Rama Rao, L.J. Wu, N. Chandra, *"Microglia Receptors in Animal Models of Traumatic Brain Injury",* **Molecular Neurobiology,** MOLN-D-18-00916R1, 1-27**,** (2019), [19-10].

11. M. Skotak, M.T. Townsend, K.V. Rama Rao, N. Chandra, "A comprehensive review of experimental rodent models of repeated blast TBI", **Frontiers in Neurology,** 10:1015, DOI: 10.3389/fneur.2019.01015, (2019), [19-11].

12. B. Swietek, M. Skotak, N. Chandra, B.F. Pfister, "*Characterization of a controlled shock wave delivered by a pneumatic table-top gas driven shock tube*", **Review of Scientific Instruments**, 90 (7), 075116 (2019), [19-12].

2018

13. G. Ordek, A. S. Asan, E. Centinkaya, M. Skotak, K.V. Rama Rao, N. Chandra, M. Sahin,*"Electrophysiological correlates of blast-wave induced cerebellar injury",* **Nature- Scientific Reports,** 8 (1), 13633**,** (2018), [18-13]

14. M. Skotak, E. Alay, J.Q. Zheng, V. Halls, N. Chandra, *"Effective testing of personal protective equipment in blast loading conditions in shock tube: comparison of three different testing locations",* **PloS one,** 13 (6), e018968**,** (2018), [18-14]

15. M. Skotak, E. Alay, N. Chandra, "*On the accurate determination of shock wave time-pressure profile in the experimental models of blast induced neurotrauma*", **Frontiers in Neurology,** 9, 52, (2018), [18-15]

16. A. Sundaramurthy, M. Skotak, E. Alay, G. Unnikrishnan, H. Mao, X. Duan, S. T. Williams, T. H. Harding, N. Chandra, and J. Reifman, "*Assessment of the effectiveness of combat eyewear protection against blast overpressure*", **Journal of Biomechanical Engineering**, 140, 071003-1-12, (2018), [18-16]

17. K.V. Rama Rao, S. Iring, D. Younger, M. Kuriakose, M. Skotak, E. Alay, R. K. Gupta, N. Chandra, "*A single primary blast-induced traumatic brain injury in rodent model causes cell-type dependent increase in NADPH oxidase isoforms in vulnerable brain regions"*, **Journal of Neurotrauma,** 35,1-14, (2018), [18-17]

18. M. Kuriakose, K.V. Rama Rao, D. Younger, N. Chandra. *"Temporal and Spatial Effects of Blast Overpressure on Blood-Brain Barrier Permeability in Traumatic Brain Injury."* **Nature-Scientific Reports,** 8(1), 8681, (2018), [18-18]

19. Daniel E Bonder, Carolyn E Keating, N. Chandra, D Kacy Cullen, BJ Pfister, "Modeling Traumatic Brain Injury In Vitro", **Preclinical and Clinical Methods in Brain Trauma Research**, 37-69, (2018), [18-19]

2017

20. E. Alay, M. Skotak, A. Misistia, N. Chandra, "*Dynamic loads on human and animal surrogates at different test locations in compressed gas driven shock tubes",* **Shock Waves**, 28, 51-62, (2017), [17-20]

21. N. Chandra, A. Sundaramurthy, R.K. Gupta, *"Validation of laboratory animal and surrogate human models in the primary blast injury studies",* **Journal of Military Medicine**, 182, 3/4:105, (2017), [17-21].

2016

22. M. Kuriakose, Skotak, M, Misistia, A, Kahali S, Sundaramurthy A, Chandra N *"Tailoring the Blast Exposure Conditions in the Shock Tube for Generating Pure, Primary Shock Waves: The End Plate Facilitates Elimination of Secondary Loading of the Specimen."* **PLoS ONE** 11(9): e0161597. doi:10.1371/journal.pone.0161597, (2016), [16-22]

23. V. Mishra, M. Skotak, H. Schuetz, A. Heller, J. Haorah, N. Chandra, *"Primary blast causes mild, moderate, severe and lethal TBI with increasing blast overpressures: Experimental rat injury model,"* **Nature-Scientific Reports**, **6**, 26992, (2016), [16-23]

24. S. Ganpule, R. Salzar, B. Perry and N. Chandra, *"Role of helmets in blast mitigation: insights from experiments on PMHS surrogate,"* **International Journal of Experimental and Computational Biomechanics**, (2016), [16-24]

25. Y Qiu, Y Wang, Y Xu, N Chandra, J Haorah, B Hubbi, BJ Pfister, X Liu, *Quantitative optical coherence elastography based on fiber-optic probe for in situ measurement of tissue mechanical properties*, **Biomedical optics express** 7 (2), 688-700, (2016), [16-25].

26. Y. Qiu, F.R. Zaki, N. Chandra, S. Chester and X. Liu, "Nonlinear characterization of elasticity using quantitative optical coherence elastography," **Biomedical Optics Express**, 7 (11), 4702-4710 (2016), [16-26].

2015

27. PM Abdul-Muneer, BJ Pfister, J Haorah, N Chandra, *Role of matrix metalloproteinases in the pathogenesis of traumatic brain injury*, **Molecular neurobiology**, 1-18, (2015), [15-27].

28. A. Sundaramurthy and Namas Chandra, *A parametric approach to shape field relevant blast wave profiles in compressed gas-driven shock tube*, **Frontiers in Neurology**, 1-17, (2015), [15-28].

Appendix B

Book Chapter

- Acute Pathophysiology of Blast Injury-From Biomechanics to Experiments and Computations: Implications on Head and Polytrauma, Chapter 18, 196-253, Brain Neurotrauma: Molecular, Neuropsychological and Rehabilitation Aspects, Ed. Firas H. Kobeissy, (2015) [15-B1].

- M. Skotak, M.T. Townsend, E. Alay and N. Chandra, The effect of geometrical factors on the surface pressure distribution on a human phantom model following shock exposure: A computational and experimental study, An online publication, DOI: 10.5772/intechopen.88809, (2019), [19-B2]s

Appendix C

Conference Presentations

- Military Health Sciences Research Symposium, Kissimmee, FL, August 19-22, 2019:
    - Molly Townsend, Namas Chandra, "On the Development of Inter-Species Mechanical Injury Thresholds in Sub-Clinical Blast Exposures: A Numerical and Experimental Approach", MHSRS-19-01951
    - Maciej Skotak, Eren Alay, Rama Rao V. Kakulavarapu, Namas Chandra "The effect of impulse on brain pathology in an animal blast TBI model: a telltale case study for occupational low-level blast human studies?", MHSRS-19-01892
- 4th International Forum on Blast Injury Countermeasures, McLean, VA, May 8-10, 2019:
    - Namas Chandra, "Tutorial: Synergistic interaction of oxidative stress, blood-brain barrier breakage and neuroinflammation in the pathogenesis of blast TBI"
    - Madhuvika Murugan, Namas Chandra, "Role of resident microglia and circulating monocytes in chronic neuroinflammation and behavioral outcomes in a mouse model of blast-induced traumatic brain injury"
    - Molly Townsend, Namas Chandra, "Investigation of blast-induced traumatic brain injury thresholds and mechanisms using a rodent finite element model"
- 16th International Symposium on Computer Methods in Biomechanics and Biomedical Engineering and the 4th Conference on Imaging and Visualization, New York City, NY, August 14-16, 2019:
    - Molly Townsend, Namas Chandra, "Mechanical injury thresholds and mechanisms for a rodent finite element model of blast-induced traumatic brain injury" (801)
    - Rahul Shah, Molly Townsend, Namas Chandra, "Evaluating the Effect of Skull and Brian Stiffness on Shock Wave Propagation in a Rodent Finite Element Model" (949)

- National Neurotrauma Society Annual Meeting, Snowbird, UT, July 7-12, 2017:
    - Namas Chandra, KV RamaRao, Stephanie Iring, Daniel Younger, Aswati Aravind, Bryan Pfister, Maciej Skotak, "Blast-Induced Traumatic Brain Injury Displays a Unique Pattern of Spatial Neuropathology" (B02-05)
    - Rama Rao Kakulavarapu, Stephanie Iring, Daniel Younger, Maciej Skotak, Namas Chandra, "Activation of NLRP3 Inflammasome and its Impact on Cerebral Autophagy Mechanisms in Severe Blast-Induced Traumatic Brain Injury" (B02-13)
    - Maciej Skotak, Bogumila Swietek, Lin Yan, Tong Liu, Hong Li, Vijayalakshmi Santhakumar, Namas Chandra, "Identification of Pathological Changes in Hippocampus Induced by A Single Blast Via Differential Proteomics and Pathway Analysis" (B02-16)
- Military Health Science Research Symposium, Kissimmee, FL, August 27-30, 2017:
    - Daniel Younger, Matthew Kuriakose, Venkata Kakulavarapu, Stephanie Iring, Namas Chandra, "Blast-induced Traumatic Brain Injury Displays a Unique Pattern of Spatial Resolution of Brain NADPH oxidase", MHSRS-17-1238
    - Matthew Kuriakose, Venkata Kakulavarapu, Namas Chandra, "Temporal and spatial considerations of blood-brain barrier dysfunction following blast-induced traumatic brain injury as a function of blast overpressure", MHSRS-17-1240
    - M. Skotak, B. Swietek, L. Yan, T. Liu, H. Li, V. Santhakumar, and Namas Chandra, "Identification of pathological changes in hippocampus induced by a single blast via differential proteomics and pathway analysis", MHSRS-17-1416
- Second Japan-US Technical Information Exchange Forum on Blast Injury (JUFBI 2017)
    - Namas Chandra, Blast-induced traumatic brain injury displays a unique pattern of neuropathology (invited talk)
    - Namas Chandra, Blast shock tube and animal research (Tutorial)
- National Neurotrauma Society Annual Meeting, Snowbird, UT, July 7-12, 2017:
    - Namas Chandra, KV RamaRao, Stephanie Iring, Daniel Younger, Aswati Aravind, Bryan Pfister, Maciej Skotak, "Blast-Induced Traumatic Brain Injury Displays a Unique Pattern of Spatial Neuropathology" (B02-05)
    - Rama Rao Kakulavarapu, Stephanie Iring, Daniel Younger, Maciej Skotak, Namas Chandra, "Activation of NLRP3 Inflammasome and its Impact on Cerebral Autophagy Mechanisms in Severe Blast-Induced Traumatic Brain Injury" (B02-13)
    - Maciej Skotak, Bogumila Swietek, Lin Yan, Tong Liu, Hong Li, Vijayalakshmi Santhakumar, Namas Chandra, "Identification of Pathological Changes in Hippocampus Induced by A Single Blast Via Differential Proteomics And Pathway Analysis" (B02-16)
- Military Health Science Research Symposium, Kissimmee, FL, August 27-30, 2017:
    - Daniel Younger, Matthew Kuriakose, Venkata Kakulavarapu, Stephanie Iring, Namas Chandra, "Blast-induced Traumatic Brain Injury Displays a Unique Pattern of Spatial Resolution of Brain NADPH oxidase", MHSRS-17-1238
    - Matthew Kuriakose, Venkata Kakulavarapu, Namas Chandra, "Temporal and spatial considerations of blood-brain barrier dysfunction following blast-induced traumatic brain injury as a function of blast overpressure", MHSRS-17-1240
    - M. Skotak, B. Swietek, L. Yan, T. Liu, H. Li, V. Santhakumar, and Namas Chandra, "Identification of pathological changes in hippocampus induced by a single blast via differential proteomics and pathway analysis", MHSRS-17-1416
- Northeast Bioengineering Conference, Newark, NJ, March 31-April 2, 2017:
    - D. Younger, M. Kuriakose, V. Kakulavarapu, S. Iring, N. Chandra, "Spatial Resolution of Brain NADPH Oxidase-1 in Traumatic Brain Injury"
    - A. Aravind, M. Long, A. Fitzsimmons, N. Chandra, V. Santhakumar, K. Pang, B. Pfister, "Characterization of Cumulative Subconcussive Exposures of Blunt and Blast Injury"
- National Neurotrauma Society Meeting, Lexington, KY, June 26-29, 2016:
    - Daniel~~.~~ Younger, M.A.M. Peringady, D. Halder, N. Prasad, N. Chandra, Pathophysiological Changes Due to Blast Induced Neurotrauma Is Affected by Animal Orientation (J. Neurotrauma, 2016, pp. A87-A87)
    - Bogumila~~.~~ Swenson, C. Miao, N. Chandra, B. Pfister, The Spatial and Temporal Deformation Pattern of The Brain from Blunt Trauma (J. Neurotrauma, 2016, pp. A22-A22)

- Sudeepto. Kahali, M. Kuriakose, M. Skotak, E. Alay, A. Misistia, N. Chandra, Artifact-Free Loading Conditions In Compressed Gas Driven Shock Tube With End Plate: Focus In Primary Blast Injury Animal Models (J. Neurotrauma, 2016, pp. A93-A93)
- G. Ordek, M. Skotak, N. Chandra, M. Sahin, Electrophysiological Assessment of Blast-Induced Injury in The Rat Cerebellum (J. Neurotrauma, 2016, pp. A40-A41)

- Eren Alay, Maciej Skotak, Anthony Misistia, Namas Chandra, Protection effectiveness against blast overpressure-role of shield-specimen geometric mismatch and gap-filler material properties (J. Neurotrauma, 2016, pp. A24-A24).
- Sudeepto Kahali, Matthew Kuriakose, Maciej Skotak, Eren Alay, Anthony Misistia, Namas Chandra, Artifact-free loading conditions in compressed gas driven shock tube with end plate: focus in primary blast injury animal models properties (J. Neurotrauma, 2016, pp. A24-A24)

- Matthew Kuriakose, Namas Chandra, Experimental investigation of cavitation as a mechanism of primary blast-induced traumatic brain injury (J. Neurotrauma, 2016, pp. A24-A24)

- Gokhan Ordek, Maciej Skotak, Namas Chandra and Mesut Sahin, Electrophysiological patterns of the cerebellum injury with subdural recordings, Nanosymposium, 484-10, Society for Neuroscience, Nov. 15, 2016.

- Bogumile Swenson, Chen MS, Namas Chandra, Bryan Pfister, The spatial and temporal deformation pattern of the brain from blunt trauma, Military Health Systems Research Symposium, MSHRS2016, Orlando, Florida, June 26-29, 2016.

- C.Q. Wu, Y. Chen, and Namas. Chandra. On Development and Optimization of Computing Workflows for Big Data Analytics in Brain Injury Research. In Proceedings of the NSF Workshop on Data Science, Learning, and Applications to Biomedical & Health Sciences, New York Academy of Sciences, January 7-8, 2016 (DLSA-BHS16)

- Namas. Chandra, Bryan. Pfister, James. Haorah and Maciej. Skotak, Animal model of dose-dependent primary blast induced traumatic brain injury, Military Health Systems Research Symposium, MSHRS2015, Fort Lauderdale, Florida, 18 August 2016.

- Abdul-Muneer. Peringady, Mathew Long Conte AA, Chandra. N, Pfister BJ, Ca^{2+} influx in mild stretch neuronal injury causes caspase-1 dependent neuroinflammation and cell death, Biomedical Engineering Society 2015 Annual Meeting, Track: Neural Engineering, Tampa, Florida, (2015).

Appendix D

INVITED COLLOQUIMS

Blast overpressure vs. survival dose-response response for primary blast brain injury animal models in a wide range of field-relevant shock pressures, Department of Aeronautical Engineering, Embry-Riddle Aeronautical University, 8 October 2015.

1 Effect of blast overpressure on blast induced neurotrauma-experimental evidence, U. S. Naval Research Laboratory, 5 August 2015.
2 Experimental and computational approaches to explore the mechanisms of blast induced brain injuries, DRDO-Suffield, Medicine Hat, Alberta, Canada, 10 June 2015.
3 Blast overpressure vs. survival dose-response response for primary blast brain injury animal models in a wide range of field-relevant shock pressures, Invited NATO meeting on blast injuries, Stockholm, Sweden, 12 May 2015

4 Blast-shock waves from explosions cause traumatic brain injury (TBI): Experimental and computational evidence, Department of Mechanical Engineering, Florida State University, Florida, 17 April 2015
5 Blast-shock waves from explosions cause traumatic brain injury (TBI): Experimental and computational evidence, Department of Mechanical Engineering, Indian Institute of Technology, New Delhi, India, 6 April 2015

Appendix E

POST-DOCTORAL RESEARCHERS SUPERVISED

1 Dr. V. Perumal, Nanotechnology based therapeutics for brain injury, 2019-present
2 Dr. M. Murugan, Neuropathology of Brain Injury, 2017 – 2019
3 Dr. M. Townsend, Computational Biomechanics of Brain Injury, 2017 – 2019.

RESEARCH FACULTY CONTRIBUTED TO THE PROJECT

4 Dr. K.V. Rama Rao, Neuro-biochemistry of brain injury-2016-present
5 Dr. M. Skotak, Biochemisty of neuronal cells, 2011-2015.
6 Dr. P.M. Abdul-Muneer, Neurobiology of cellular injury in animal models, 2014-2016

Appendix F

What individuals have worked on the project?
Provide the following information for: (1) PDs/PIs; and (2) each person who has worked at least one-person month per year on the project during the reporting period, regardless of the source of compensation (a person month equals approximately 160 hours of effort). If information is unchanged from a previous submission, provide the name only and indicate "no change."

Name: Namas Chandra
Project Role: PI/PD
Researcher Identifier:
Nearest person month worked: 15.0
Contribution to Project: Supervision of project, design of the research, data interpretation

Name: Bryan Pfister
Project Role: Co-PI
Researcher Identifier:
Nearest person month worked: 8.0
Contribution to Project: Co-Supervision of project, data interpretation

Name: Sunil Dhar
Project Role: Statistician
Researcher Identifier:
Nearest person month worked: 1.0
Contribution to Project: Provide Statistical analysis

Name: Maciej Skotak
Project Role: Research Scientist
Researcher Identifier: 0000-0003-2584-7294
Nearest person month worked: 40
Contribution to Project: Exposure of animals, sensor implantation, data analysis (pressure quantification), shock tube experimentation, proteomics, submission IACUC and ACURO documents, PMHS instrumentation, manuscript and report preparation, supervision of students & staff

Name: RamaRao Venkata Kakulavarapu
Project Role: Research Scientist
Researcher Identifier:
Nearest person month worked: 29
Contribution to Project: Overseeing western blot, histological analysis biochemistry analysis, supervision of students and staff, manuscript and report preparation

Name: Molly Townsend
Project Role: Research Scientist
Researcher Identifier:
Nearest person month worked: 20
Contribution to Project: Development of the 3D human and rat model, validation of numerical simulations, Shock tube numerical simulations, data analysis, supervision of students, manuscript preparation

Name: Venkatesan Perumal
Project Role: Research Scientist
Researcher Identifier:
Nearest person month worked: 11
Contribution to Project: Histological analysis biochemistry analysis, supervision of students and staff

Name: Monuel Aulov
Project Role: Laboratory/Project Manager
Researcher Identifier:
Nearest person month worked: 40
Contribution to Project: Assistance with ordering of animals, shock tube supplies, sensor order, PMHS PPE review and set-up, supervision of undergraduate and graduate students as well as researchers, custody of IACUC documentation, report preparation, sf425 financial report preparation and submissions in Ebrap

Name: Eren Alay
Project Role: Laboratory technician
Researcher Identifier:
Nearest person month worked: 28
Contribution to Project: Assistance with exposure of animals, shock wave experimentation and sensor implantation, sensor calibration and instrumentation maintenance as well as Western blot, data analysis and quantification

Name: Anthony Misistia
Project Role: Graduate Student
Researcher Identifier:
Nearest person month worked: 4
Contribution to Project: Assistance with exposure of animals and sensor implantation, RTD development, CAD development, data analysis

Name: Stephanie Iring
Project Role: Laboratory technician (biochemistry)
Researcher Identifier:
Nearest person month worked: 6
Contribution to Project: Western blot, staining of brain sections

Name: Arun Ravula
Project Role: Graduate student
Researcher Identifier:
Nearest person month worked: 8
Contribution to Project: ELISA, Western blot, Biochemical analysis, staining of brain sections

Name: Matthew Kuriakose
Project Role: Graduate student
Researcher Identifier:
Nearest person month worked: 24
Contribution to Project: Western blot, sectioning of brain sections, data quantification, Assistance with shock wave experimentation, exposure of animals, biochemistry work, data analysis, manuscript preparation

Name: Daniel Younger
Project Role: Graduate student
Researcher Identifier:
Nearest person month worked: 18
Contribution to Project: Assistance with shock wave experimentation, exposure of animals, biochemistry work, data analysis, Western blot, sectioning of brain sections, data quantification, manuscript preparation

Name: Sudeepto Kahali
Project Role: Graduate student
Researcher Identifier:
Nearest person month worked: 8
Contribution to Project: Development of rat model, numerical simulations

Name: Jose Rodriguez
Project Role: Graduate student
Researcher Identifier:
Nearest person month worked: 12
Contribution to Project: Shock tube experimentation, ICP and strain measurements, data analysis, PMHS instrumentation, supervision of undergraduate students, manuscript preparation

Name: Mohamed Eraky
Project Role: Graduate student
Researcher Identifier:
Nearest person month worked: 3
Contribution to Project: Refinement of the FEM methods for rat and human models, data analysis

Name: Madison Taylor
Project Role: Undergraduate student
Researcher Identifier:
Nearest person month worked: 3
Contribution to Project: Western blot, sectioning of brain sections, data quantification

Name: Smit Shah
Project Role: Graduate student
Researcher Identifier:
Nearest person month worked: 3
Contribution to Project: Western blot, sectioning of brain sections, data quantification

Name: Debanjan Haldar
Project Role: Undergraduate student
Researcher Identifier:
Nearest person month worked: 2
Contribution to Project: Western blot, sectioning of brain sections, data quantification

Name: Ryan Rattazzi
Project Role: Undergraduate student
Researcher Identifier:
Nearest person month worked: 2
Contribution to Project: Assistance with shock tube experiments, data analysis

Name: George Fahmy
Project Role: Undergraduate student
Researcher Identifier:
Nearest person month worked: 1
Contribution to Project: Assistance with shock tube experiments, data analysis

Name: Supriya Iyer
Project Role: Undergraduate student
Researcher Identifier:
Nearest person month worked: 12
Contribution to Project: Shock tube experiments, model preparation, data analysis

Name: Thinuri Fernando
Project Role: Undergraduate student
Researcher Identifier:
Nearest person month worked: 12
Contribution to Project: Shock tube experiments, model preparation, data analysis

Name: Zenit Winfield
Project Role: Undergraduate student
Researcher Identifier:
Nearest person month worked: 6
Contribution to Project: Shock tube experiments, model preparation, data analysis

Name: Rahul Shah
Project Role: Undergraduate student
Researcher Identifier:
Nearest person month worked: 4
Contribution to Project: Numerical simulations of the rodent model

Name: Aayush Verma
Project Role: Undergraduate student
Researcher Identifier:
Nearest person month worked: 4
Contribution to Project: Numerical simulations of the human head model

Name: Neel Amin
Project Role: Undergraduate Student
Researcher Identifier:
Nearest person month worked: 9
Contribution to Project: Assistance with data analysis, videos and pictures of experiments, rat model simulation

Appendix A –Publication Cover #1
2020

Authors: A. Aravind, A.R. Ravula, N. Chandra and BJ Pfister

Title: "*Behavioral deficits in animal models of blast traumatic brain injury*"

Journal Publication: Frontiers in Neurology,
https://doi.org/10.3389/fneur.2020.00990, (2020), [20-1]

frontiers in Neurology

REVIEW
published: 04 September 2020
doi: 10.3389/fneur.2020.00990

Behavioral Deficits in Animal Models of Blast Traumatic Brain Injury

Aswati Aravind, Arun Reddy Ravula, Namas Chandra and Bryan J. Pfister**

Department of Biomedical Engineering, Center for Injury Biomechanics, Materials and Medicine, New Jersey Institute of Technology, Newark, NJ, United States

Blast exposure has been identified to be the most common cause for traumatic brain injury (TBI) in soldiers. Over the years, rodent models to mimic blast exposures and the behavioral outcomes observed in veterans have been developed extensively. However, blast tube design and varying experimental parameters lead to inconsistencies in the behavioral outcomes reported across research laboratories. This review aims to curate the behavioral outcomes reported in rodent models of blast TBI using shockwave tubes or open field detonations between the years 2008–2019 and highlight the important experimental parameters that affect behavioral outcome. Further, we discuss the role of various design parameters of the blast tube that can affect the nature of blast exposure experienced by the rodents. Finally, we assess the most common behavioral tests done to measure cognitive, motor, anxiety, auditory, and fear conditioning deficits in blast TBI (bTBI) and discuss the advantages and disadvantages of these tests.

Keywords: blast TBI, behavior deficits, cognitive deficits, anxiety and depression, motor deficits, auditory deficits, fear conditioning

OPEN ACCESS

Edited by:
Denes V. Agoston, Karolinska Institutet (KI), Sweden

Reviewed by:
Samar Abdelhady, Faculty of Medicine, Alexandria University, Egypt
Alana Conti, Wayne State University, United States

****Correspondence:***
Namas Chandra
namas.chandra@njit.edu
Bryan J. Pfister
bryan.j.pfister@njit.edu

Specialty section:
This article was submitted to Neurotrauma, a section of the journal Frontiers in Neurology

Received: *18 March 2020*
Accepted: *29 July 2020*
Published: *04 September 2020*

Citation:
Aravind A, Ravula AR, Chandra N and Pfister BJ (2020) Behavioral Deficits in Animal Models of Blast Traumatic Brain Injury. Front. Neurol. 11:990. doi: 10.3389/fneur.2020.00990

INTRODUCTION

Traumatic Brain Injury (TBI) is one of the most prevalent causes for disability and a reduced quality of life among military personnel. About 380,000 military personnel have been diagnosed with TBI since 2000 according to the Defense and Veterans Brain Injury Center (DVBIC) (1). Of these, more than 50% of combat TBI are reported to occur due to blast exposures (2). Most of the soldiers with blast TBI (bTBI) develop cognitive, behavioral and psychological deficits such as PTSD, attention deficits, headaches, anxiety, depression, memory loss, suicidal ideation, tinnitus and vestibular deficiencies (3–6). The etiology of these deficits following a blast injury is unclear. One of the major challenges over the years of bTBI research has been to design a blast injury model in rodents that mimics the primary blast wave and correlates to the clinical outcome of human TBI.

Blast loading is typically classified into four categories: (1) Primary effect caused by the blast wave propagating through the skull and brain, (2) Secondary effects caused by the penetration of shrapnel, (3) Tertiary effects caused by the blast wind resulting in impact or acceleration-deceleration injuries and (4) Quaternary effects caused by toxic gases from the blast exposure (7). The primary effect of a blast exposure caused by the propagation of the blast wave through the brain has been the main area of focus in the area of blast induced neurotrauma. Linking blast exposure mechanics to the behavioral outcome is crucial in validating rodent blast models in order to the study the underlying cellular mechanisms and to further drug development, as exposure level determines injury severity and hence the mechanisms. Shock tubes have been designed to induce bTBI in rodent models since 2007 (8). Several variants of shock tube models have been used in the past 10 years to study behavioral outcome of bTBI in

rodent models. A recent review from our group has listed the types of shock tubes used in bTBI with some of the geometric, process and test parameters (9). The variations in those parameters result in inconsistent findings of behavioral outcome (9).

The objective of this review is (1) to outline and evaluate the behavioral tests currently being used in bTBI (2) to summarize the parameters used in testing and the deficits observed in rodents subjected to blast injury between 2008 and 2019. (3) to highlight the crucial features in the blast testing that can lead to the variability in behavioral deficits seen throughout the bTBI literature.

OVERVIEW OF BLAST APPARATUS IN RODENT MODELS

The major criterion for a blast tube is to reproduce the biomechanical loading of an open field blast exposure and mimic the clinical outcome observed in TBI patients. A blast overpressure wave propagates as a sharp positive pressure rise compressing the surrounding medium of air or water moving radially outward followed by a negative under pressure wave before returning to baseline or ambient pressure values. The primary blast pressure wave generated in open field explosions has been best described by the Friedlander waveform (10). Pressure waves of explosions in confined spaces are more complex due to reflection of the wave from objects, ground, diffraction, and interaction with the incident shockwave. Most shock tubes used to study rodent models of bTBI have attempted to recreate the Friedlander waveform in order to allow for better reproducibility and comparison across laboratories (10, 11).

One of the most direct forms of bTBI exposure in rodent models has been subjecting the animals to open field blast explosions using TNT or other explosives. This model helps to mimic real life blast exposures containing the primary, reflected waveforms and blast wind. The open field explosions expose the rodents to primary, secondary, tertiary, and quaternary effects of the blast. As a result, these models are associated with higher mortality and diÿ culty in controlling the clinical outcome in the animals. Open field experiments also require large number of explosives to generate the desired blast pressures when compared to recreating the same blast pressures in shock tubes (12–14). In the 1950s, Clemedson and Criborn (15), proposed a cone shaped shock tube using pentaerythritol tetranitrate (PETN) explosives as a blast injury model for rats. The rats were placed 1 m away from the source of detonation and were fixed with the help of metallic nets to limit the tertiary effects of the blast. This, however, does not limit the effects of reflective wave on the rodent head. This model also did not negate the quaternary effects of the blast but required less explosives than the open field experiments to produce the desired blast overpressure (8, 11, 13, 15).

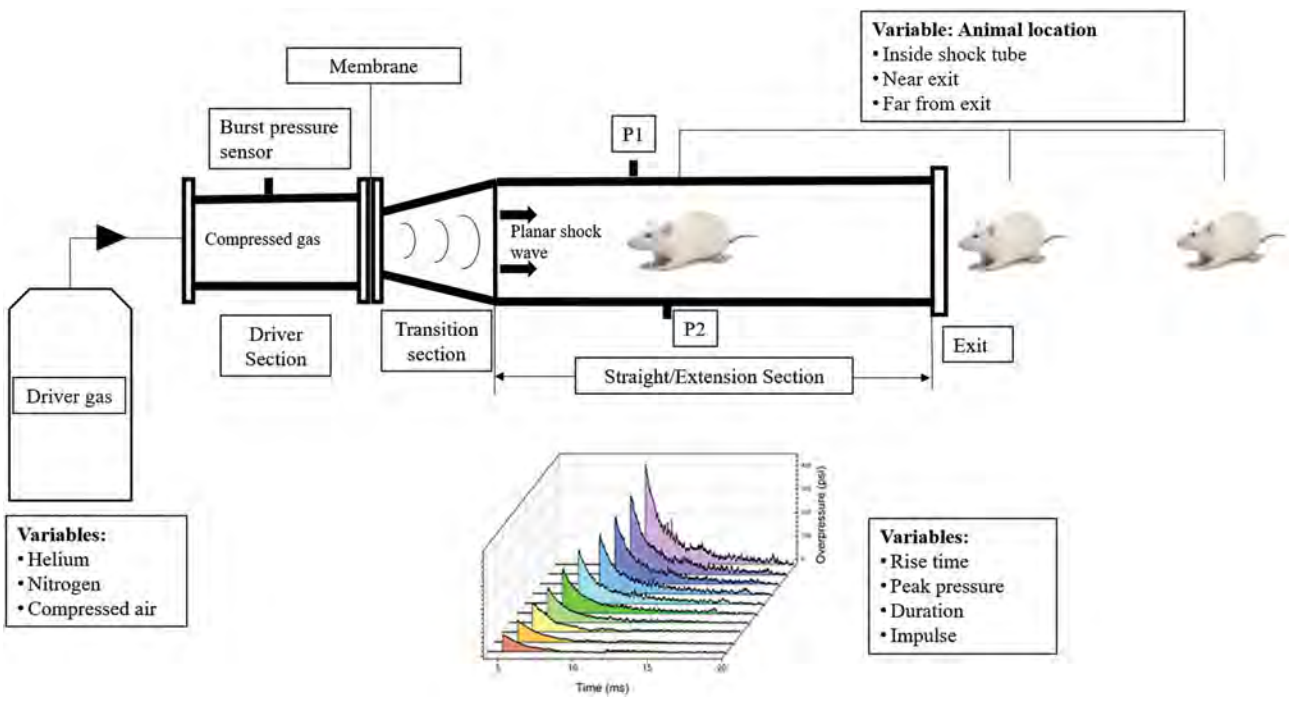


FIGURE 1 | Variability in the design and process variables of the shock tube and its effect on shock wave profile, bTBI injury and behavior in animal models. The compressed gas and number of membranes used affect the incident pressure generated in shock tubes. The geometry of the shock tube, presence or absence of a transition section affect variables of the shockwave profile such as rise time, peak pressure, duration, and impulse. The animal locations inside, near exit and far from exit of the blast tube play a role in the injury severity and behavioral outcomes. P1 and P2 represent the side on blast pressure measurement sensors.

In order to study the effects of the primary blast wave, shockwave tubes using compressed gases that disrupt membranes in order to produce a planar Friedlander waveform have been used (10, 16). Such shock tubes typically contain a driver section that is filled with a compressed gas usually helium, nitrogen or compressed air separated by membranes from the transition and extension section, where the animal is placed, followed by an end plate as shown in **Figure 1**. The compressed gases fill the driver section leading to the disruption of the membranes. The rapidly expanding gas propagates as a planar shock wave front down the test section. The number, thickness of the membranes and length of the test section controls the intensity, duration, and impulse of the blast overpressure wave produced. Several variations of these models are currently in use for investigating bTBI in rodents (10, 17–19).

Some shock tube variations that can alter behavioral outcomes include position of the animal in the blast tube, orientation of the animal, use of head restraint, end conditions of the blast tube (open vs. closed) and length of the blast tube (20). The animal's position in the blast tube plays a crucial role in determining the type of blast injury it is exposed to. Several studies have shown that animal placement at the exit of the blast tube leads to significant changes of the incident pressure waveform from the ideal Friedlander waveform (10, 21). At the outer edges of the blast tube near the exit end, an expansion wave is created that decreases the peak pressure and impulse of the blast overpressure wave, exposing the rat brain to a subsonic jet wind resulting in an acceleration-deceleration induced tertiary blast injury. The animals that were constrained and placed at the exit end of the blast tube experienced high amounts of compression pressure in the head and neck regions (10, 21–24).

Another criterion that is crucial in the design of the blast tube is the closed or open exit end of shock tubes. A closed ended shock tube results in the propagation of a reflected wave back into the shock tube when the incident pressure wave reaches the end of the tube. This results in the rodent being exposed to a complex blast waveform with the gases unable to dissipate from the blast tube. An open-ended shock tube, on the other hand, results in the formation of an expansion wave at the end of the shock tube which propagates back into the tube (25). Kuriakose et al., indicated that an end plate reflector placed at an optimum distance to the exit of the blast tube can reduce the reflective waveforms and thereby prevent secondary loading (7). Absence of head restraint during the blast exposure also results in tertiary effects of blast leading to increased behavioral deficits (18, 26). The blast overpressure waves decays over the length of the blast tube. The optimal placement of the animal in the blast tube would be where the Friedlander wave is fully formed (10, 27). The amplitude of the incident blast overpressure wave is also critical in determining the severity in terms of mild, moderate or severe TBI. Previous work in our lab has classified the severity of bTBI overpressure wave based on animal mortality and presence of oxidative markers (28). Due to different blast models used across labs, varying lengths of blast tube and thereby incident blast overpressures corresponding to mild, moderate, and severe bTBI have been reported in literature (28–31).

BEHAVIORAL DEFICITS IN BLAST TBI

Cognitive Deficits

Cognitive deficits have been reported in patients with mild TBI which often resolve in 6 months while moderate and severe TBI cause long term deficits including dementia or other neurodegenerative disorders (32). Soldiers exposed to bTBI have been diagnosed with retrograde or anterograde amnesia and decreased executive function (33, 34). Cognitive deficits, however, have been more associated with blunt TBI than with a primary blast exposure (32). In a study by Barnes et al., it was reported that older veterans diagnosed with a TBI were associated with a 60% increase in the risk of developing dementia over a period of 9 years (35).

bTBI in animal models have been reported to affect prefrontal and hippocampal regions involved in cognition (36). Recognition memory in rodents following bTBI has been evaluated using the novel object recognition test while spatial working memory has been studied using Morris water maze (MWM), Barnes maze and Y maze tests. Novel object recognition test (NOR) measures deficits in both the perirhinal cortex which plays a major role in object recognition and the parahippocampal region involved with visual object recognition memory. NOR measures the ability of the rodent to recognize novelty and is measured by the difference in time spent by the animal in exploring a novel object when compared to a familiar object. The main advantage of the NOR test is its simplicity and lack of training or habituation required prior to conducting the test. The NOR test can also be modified to study short or long term memory deficits by increasing or decreasing the retention time before introducing a novel object (37, 38).

Allocentric spatial memory involving the hippocampus and entorhinal cortex has been studied using several maze tests with the most popular form of assessment being the Morris Water Maze test (39). The other alternatives heavily used in the blast literature have been the Barnes Maze, radial arm maze and Y maze tests. Morris water maze tests the ability of a rodent to use spatial visual cues to identify the location of a rescue platform submerged in water. Place cells present in the hippocampus and entorhinal cortex have been identified to have increased firing rates when the rodent nears the submerged platform location in the MWM test (40). Further, lesions in the hippocampus have been identified to eliminate water maze learning (41).

The Barnes Maze test is similar to the MWM in identifying hippocampal related deficits in cognition. Barnes maze test consists of a circular platform with evenly spaced holes around the circumference with an escape platform placed under one of these holes. The presence of brightly lit open space, use of an aversive sound or blowing air above the maze are some of the methods used to motivate the rats to seek the escape platform (20, 39). The advantage of the Barnes maze test over MWM is that it does not induce the stress of swimming in the animals as measured by the increased plasma cortisone levels in the rats post MWM test (42).

The Y maze test is also used to measure deficits in the hippocampus and the prefrontal cortex and can be used to measure the spatial working and reference memory. The Y maze

consists of 3 arms, 120° to each other. Similar to the RA, the number of entries to each arm is measured with greater alternation in the arms indicating good working memory. An alternative to this approach is closing one of the arms during training and measuring the spatial reference memory of the rats to visit the novel unvisited arm during the testing phase. Recognizing the previously visited arms with spatial cues and increased visits to the novel arm indicates intact hippocampal function (43).

Findings of cognitive deficits recorded by researchers across different models of shockwave tubes and blast pressures are summarized in **Table 1**. Literature review was done using advanced search in Google Scholar for articles with all of the words "rodents, shockwave tube, cognitive memory deficit" and the exact phrase "blast TBI," between the years 2008–2019. Studies generating blast TBI conditions using open field detonations or shockwave tubes were only incorporated in this review.

Based on observations from **Table 1**, deficits in object recognition memory has been consistently reported in bTBI using the novel object recognition test. Deficits in recognition memory are reported in mild blast exposures of 74–129 kPa and last from 7 days up to 33 weeks following bTBI. Interestingly, Sajja et al. (64), did not observe novel object recognition deficits on day 3 following blast but the animals were observed to develop the deficits on day 7 post injury. This could indicate that the recognition memory deficit in bTBI is not immediate but occurs over time.

Spatial working memory deficits have not been consistently reported across bTBI models. Some factors that contribute to the difference in outcome are the positioning of the animal in the blast tube, blast pressures exposed, use of head restraint and the overall design of the blast tube. Working memory deficits measured by Y maze test has been reported only in animals subjected to open detonations and the duration of deficits directly correlate with the distance from the detonation source (12). Similarly, Barnes maze test has only been reported in literature for injured animals without head restraint or animals kept outside the exit end of the blast tube. These deficits were observed in low bTBI pressures and lasted up to 11 days post blast. Memory deficits in open detonation experiments persisted for a month (58). The working memory deficits in Barnes maze were resolved when animals were provided with head restraint (26). Most deficits that lasted weeks post injury observed in the Morris Water maze test also involves animals placed at the exit end of the blast tube. When the animals are placed inside the blast tube only transient deficits observed at 24 or 48 h post injury were observed (17, 18).

Anxiety and Depression

Veterans diagnosed with bTBI also report developing anxiety and depression disorders over time. In a sample population of veterans exposed to bTBI, it was identified that 50% of individuals exposed to bTBI developed anxiety disorders, 88% developed depression and 60% showed Post Traumatic Stress Disorder (PTSD) traits (68). Treating military personnel with PTSD and depression has been estimated to cost ∼$6.2 billion in the first 2 years post deployment (69).

Depression is a complex mental illness which causes persistent feeling of sadness and loss of interest which affects person's quality of life negatively. Severe post-concussive symptoms such as headache, blurred vision, dizziness, and memory impairment manifests due to depression following TBI. Depression following TBI causes disturbances in neuronal circuits such as frontal lobe -basal ganglia circuits and anterior ascending monoaminergic pathways (70, 71). The forced swim test is one of the popular behavior tasks successfully used for assessing depression behavior. Mice or rats are placed in an inescapable transparent tank that is filled with water and their escape related mobility behavior is measured in order to evaluate depression. Increased time spent immobile in the tank correlates with depression traits such as behavioral despair and disengagement from stress coping (72). Can et al. (72), Slattery et al. (73), and Yankelevitch-Yahav et al. (74) have provided detailed protocols for the test parameters for forced swim test for rats and mice (72–74).

Anxiety is a psychological, physiological and behavioral state induced in animal or humans by a threat to well-being. Anxiety is characterized by an increased arousal, expectancy, autonomic and neuroendocrinal activation which results in manifestation of specific pattern of behaviors such as exploration, feeding, flight or defensive behavior to the specific stimulus (75). Anxiety behavior is regulated by forebrain and hindbrain regions involving the septo-hippocampal system, entorhinal cortex, medial prefrontal cortex, basolateral amygdaloid complex, and midbrain raphe system (76–80).

Anxiety in rodent models of bTBI has been evaluated using tests such as the elevated plus maze (EPM), open field test, elevated zero maze and light/dark box tests as described in **Table 2**. The EPM test is widely used to study anxiety and has been used to identify deficits in regions such as the limbic regions, hippocampus, amygdala and dorsal raphe nucleus (31, 47, 48, 56, 83, 90). Briefly, rats or mice are placed at the junction of the four arms of the maze, two of which are closed by walls and two are open. The animal is placed facing an open arm and the time spent or number of entries in the open or closed arms of the maze is recorded. The time spent in the closed arms correlates to anxiety, since the animal lacks the drive to explore the open arm that is less safe. The elevated zero maze works on a similar principle as the elevated plus maze with closed and open arms. The elevated zero maze is circular with alternating open and closed arms.

The open field test (OFT) assesses the animal's locomotor activity, exploratory behavior and anxiety. Briefly, the test involves placing the animal in a square, rectangle or circular box with set spacing requirements as described by Gould et al. (91), Seibenhener et al. (92), and recording the animal's exploratory behavior (19, 46, 91, 92). Two factors are known to influence anxiety-like behavior in the open field. The first is the social isolation resulting from the physical separation from cage mates when performing the test. The second is the stress/aversion created by the brightly lit, unprotected, novel test environment (92). Rodents exposed to the novel experimental arena typically spend greater time exploring the periphery rather than the center area. This tendency of animals in known as thigmotaxis. Mice

TABLE 1 | Summary of experimental variable and cognitive deficits observed in rodent models of blast TBI.

Behavior test	Animals	Position of animal	Head restrained	Gas used in blast tube	Blast pressure	Duration of deficits	References
Morris Water Maze (MWM)	Wistar Rats (230–330 g)	0.25 m from expansion compartment facing the blast wind	Yes	Compressed air.	10 and 30 kPa at 4–6 ms	Up to day 2 for both 10 and 30 kPa exposure groups	(44, 45)
	Sprague-Dawley (SD) rats	39 and 17 cm outside shock tube opening, 40° and 20° lateral to shock tube axis respectively	Yes	Helium	100 and 450 kPa reflected peak overpressure	Up to 30 days for both groups	(46)
	SD rats (250–350 g)	Transverse prone position across the mouth of the blast tube.	Yes. Chest protection with rat head exposed	Compressed air	114, 126, and 147 kPa	Days 8 and 9	(30)
	SD rats (225–250 g)	Supine position with the blast wave generator nozzle above the animal's head.	Yes, chest shielded with 2 mm lead plate	Nitrogen	80 Psi	Up to day 13–15 post blast.	(31)
	Male SD rats (150–200 g)	265 mm from the exploding wire with head facing impact	No; movement restricted	Exploding wire technique to generate small scale blast waves	95 kPa for 0.189 ms	No deficits from 8 to 11 days post blast. In the reversal phase test deficits were observed on days 13–15	(47)
	Male SD rats (250 g)	1.09 m inside the shock tube facing impact	No information	Compressed helium	97, 117, 153 kPa	Deficits for 117 and 153 kPa were observed at 48 h but not at 3, 6, or 72 h post blast	(17)
	SD rats (289 ± 21 g)	17 cm from the opening of the tube at an angle of 18° to shock tube axis with the sagittal plane of rat head perpendicular to the radial axis of shock tube.	Yes	Helium	450 kPa for 0.4 ms	No deficits observed up to 60 days post blast	(48)
	Long Evans hooded (LE) rats (250–350 g; 10–12 weeks of age)	18 inches inside the shock tube. Animals were placed both facing and sideways to the blast.	Yes	Compressed air	36.45 ± 2.32 kPa, with a mean duration of 3.78 ± 0.09 ms. One blast every day for 12 days over 2.5 weeks	Significant deficits 24 h. post the last blast impact	(49)
	LE rats (250–350 g, 10 weeks old)	30 cm inside the shock tube with head facing the blast exposure	Yes	Compressed air	74.5 kPa for 3 days	No memory deficits at 9 weeks post blast	(50)
	LE rats (250–300 g)	18 inches inside the shock tube. Animals were placed both frontal and sideways to the BOP	Yes	Compressed air	Repeated 36.6 kPa for 12 days	24 h after blast animals exposed at a frontal orientation showed slower acquisition memory at the 2nd and 3rd trial of the MWM test.	(18)
	SD rats (250–300 g)	4 cm from the blast cone	Minimal spatial movement of head	Compressed Nitrogen	80 Psi	Days 5 and 6 post blast	(51)
	C57BL/6 mice (2–3 months, 20–24 g)	Not mentioned	Not mentioned	Compressed air	321.2 ± 4.01 kPa at 50.29 ± 1.86	Up to 8 weeks post blast	(52)

(Continued)

TABLE 1 | Continued

Behavior test	Animals	Position of animal	Head restrained	Gas used in blast tube	Blast pressure	Duration of deficits	References
	SD rats (60–70 days)	503 cm from the bursting membrane and 112 cm from the open end of the driven cylinder	Yes, with no earplugs. Head restraint not mentioned	Helium	14 Psi	No deficits 5 weeks post blast.	(53)
	SD rats (6-month-old)	Placed outside with right side of the skull facing the pressure wave	No	Nitrogen	50 Psi in 1 ms	At 3 weeks post blast	(54)
Barnes maze	Heterozygous *WldS* mice (8-week-old)	10 cm from Mylar membrane, with the left side of head facing the blast	No	Compressed air	27 kPa	On day 11 post blast	(55)
	C57BL/6 Mice (2.5 months)	0.56 m inside open exit of shock tube	Both with and without head restraint	Compressed gas	77 ± 2 kPag	Up to 5 days (Deficits were resolved when mice heads were restrained during blast)	(26)
	SD Rats (∼300g)	Transverse prone position across the mouth of the blast tube.	Yes, with chest protection	Compressed air	20.6 ± 3 psi	Days 10 and 11 in test session 1 (conducted between 10 and 15 days post injury) and all days of test session II (between 47 and 51 days post injury)	(56)
	SD rats (300–330 g)	Transverse prone position across the mouth of the blast tube.	Yes. Chest protection with rat head exposed	Compressed air	138 kPa single or 5 blasts	No significant deficits up to day 21 post blast	(19)
	SD Rats (∼300 g)	Transverse prone position across the mouth of the blast tube.	Yes, with chest protection and head exposed	Compressed air	20.63 psi. Animals were placed in normal or environmentally enriched housing post blast	Animals in normal housing had deficits on day 16, 18 and days 67–71 post impact. Blast animals in enriched housing had no deficits.	(57)
	C57BL/6J mice (2-month-old)	Prone position 3-m distance away from the source with the head longitudinally aligned to the shockwave propagation	No	C4 explosives	∼46.6 kPa	23–29 days post injury in the 3 m blast group	(58)
Eight arm radial maze	LE rats(250–350 g, 10 weeks old)	30 cm inside the shock tube with head facing the blast exposure	Yes	Compressed air	74.5 kPa for 3 days	No deficits at 10–23 weeks post blast	(50)
Y Maze	ICR Mice (30–40 g)	7 m from open detonation source	No	500 g TNT	17.2 kPa Shockwave and reflected wave	No deficits	(59)
	ICR Mice (25–30 g)	4 and 7 m away from detonation source	No	500 g TNT	Shockwave and reflected wave 2.5Psi or 5.5 Psi	At 7 day in the 2.5 Psi group. 7 and 30 days in the 5.5 Psi group animals.	(12)
Novel Object Recognition (NOR)	ICR mice (25–30 g)	4 and 7 m away from detonation source	No	500 g TNT	Shockwave and reflected wave 2.5 or 5.5 Psi	7 and 30 days after blast exposure for 2.5 and 5.5 Psi blasts.	(12)

(Continued)

TABLE 1 | Continued

Behavior test	Animals	Position of animal	Head restrained	Gas used in blast tube	Blast pressure	Duration of deficits	References
	ICR Mice (30–40 g)	7 m from open detonation source	No	500g TNT	17.2 kPa Shockwave and reflected wave	Up to 14 days	(59)
	ICR mice (30–40 g)	7m from detonation source, placed 'side on' to the blast source.	No	500g of TNT	17.23 kPa	Deficits observed on days 7 and 14 post blast	(60)
	SD Rats (250 g)	Rostral cephalic orientation facing the shockwave inside the tube	Not mentioned	Compressed helium	129.23 ± 3.01 kPa for 2.5 ms	2 weeks	(61)
	LE rats (250–350 g, 10–12 weeks old)	Head facing the shockwave exposure	Yes	Compressed air	One 74.5 kPa exposure for 3 consecutive days	Between weeks 11–17 post blast	(62)
	SD rats (200–250 g)	Prone position 20 cm from the end of the tube facing the blast wave	No	Compressed air	74 kPa	2 weeks post blast impact.	(63)
	SD rats (250 g)	1.09 m from open end of the blast tube in a rostral cephalic position	No information on head restraint	Helium	117 kPa at 2.5 ms	Significant deficits at 1- and 3-months post impact	(36)
	SD rats (250 g)	1.09 m from open end of the blast tube in a rostral cephalic position	No information on head restraint	Helium	117 kPa at 2.5 ms	At 7 days post blast but not at 3 days.	(64)
	LE rats (250 g−350 g; 10 weeks of age)	Head facing the blast exposure	Yes	Compressed air	74.5 kPa	At 33 weeks post blast	(65)
Spatial Object Recognition (SOR)	Adult C57BL/6 mice (12–16 weeks)	1 cm outside exit end of blast tube facing head front.	Both head restrained and unrestrained	Helium	Mild blast of 215 ± 13 kPa, 46 ± 5kPa * ms impulse or moderate blast of 415 ± 41 kPa, 148 ± 12 kPa * ms impulse	Both blast groups showed deficits 5 days post blast. No difference was observed between mild vs. moderate blast or head restrained vs. unrestrained group.	(66)
Active avoidance test	Male C57/Bl6 mice (3–4 months; 25.22 ± 1.96 g)	Supine position 53 cm from driven section opening	Yes	Helium	Rupture pressure of 183 kPa(mild) or 213 kPa (moderate)	Mild blast animals showed deficits up to day 21 post blast but not on day 30. Moderate blast had deficits till day 30.	(16)
	Wistar rats (220–250 g)	Not mentioned	Not mentioned	Compressed air	338.9 ± 9.1 kPa at 52 ms	Up to 5 days	(29)
Passive avoidance task	LE rats (250–300 g)	18 inches inside the shock tube, in both frontal and sideways orientation to the blast	Yes	Compressed air	36.6, 74.5, and 116.7 kPa	Up to 24 hrs. in the 116.7 kPa in sideways orientation and 74.5 kPa frontal orientation when animals were trained after blast exposure	(18)
	ICR Mice (30–40 g)	7 m from open detonation source	No	500 g TNT	17.2 kPa Shockwave and reflected wave	No deficits	(59)
Visual- cue discrimination	SD rats	17 cm from the end of the shock tube	Yes	Helium	450 kPa over 80 kPa*ms	24 h post injury	(67)

TABLE 2 | Summary of experimental variables and anxiety and depression related behavior test outcomes in bTBI.

Behavior test	Rodent used	Position of animal	Animal restrained	Gas used in blast tube	Blast pressure	Duration of deficits	References
Elevated Plus Maze (EPM)	ICR mice (30–40 g)	7 m away from detonation source	No	500 g TNT	17.2 kPa Shockwave and reflected wave	No deficits observed at day 7	(59)
	SD rats (∼300 g)	Transverse prone position across the mouth of the blast tube.	Yes, with chest protection	Compressed air	20.6±3 psi	No deficits at 9 days but deficits were observed 46 days post blast.	(56)
	SD rats	39 and 17 cm outside shock tube opening, 40 and 20° lateral to shock tube axis, respectively	Yes	Helium	100 and 450 kPa reflected peak overpressure	No deficits at 4 days or 30 days post impact	(46)
	Male SD rats (150–200 g)	265 mm from the exploding wire with head facing impact	No	Exploding wire technique to generate small scale blast waves	95 kPa for 0.189 ms	At days 38 and 62 post blast	(47)
	SD rats (225–250 g)	Supine position with the blast wave generator nozzle right above the animal's head.	Yes, chest shielded with 2 mm lead plate	Nitrogen	80 Psi	Deficits at day 9 but no deficits at days 22 and 48 post blast.	(31)
	Male Wistar rats (408.3 ± 93 g)	Right side of the front cortex is aligned to the impact	Yes	A lithotripsy machine fired 5 shockwave pulses with 60 Hz frequency	∼50 MPa	Significant deficits post blast impact	(81)
	SD rats (289 ± 21 g)	17 cm from the exit of the tube at an angle of 18° to shock tube axis with the sagittal plane of rat head perpendicular to the radial axis of shock tube.	Yes	Helium	450 kPa for 0.4 ms	At 60 days but not at 30 days	(48)
	ICR mice (30–40 g)	7 m from detonation source. Animals were placed 'side on' to the blast source.	No	500g of TNT	17.23 kPa	No deficits were observed on days 7 and 14 post blast	(60)
	SD rats (∼300 g)	Transverse prone position across the mouth of the blast tube.	Yes, with chest protection and head exposed	Compressed air	20.63 psi	At days 15 and 44 post blast but not on day 66.	(57)
	SD rats (245–265 g)	Transverse prone position across the mouth of the blast tube.	Yes, with chest protection and head exposed	Compressed air	20.63 psi	Inconclusive	(82)
	Male and naturally cycling female C57BL/6J mice (7–9 weeks of age)	Prone position facing blast exposure	Yes	Compressed air	15.74 Psi	At 6 days post blast in male mice. Female mice had deficits that did not reach significance.	(83)
	LE rats (250 g−350 g; 10 weeks of age)	Head facing the blast exposure	Yes	Compressed air	74.5 kPa	At 30 weeks post blast	(65)
	SD rats (60–70 days)	503 cm from the bursting membrane and 112 cm from the open end of the driven cylinder	Not mentioned	Helium	14 Psi	At 5 weeks post blast.	(53)
Staircase test	ICR Mice (25–30 g)	4 and 7 m away from detonation source	No	500 g TNT	Shockwave and reflected wave 2.5Psi or 5.5 Psi	Up to 30 days for both groups of animals	(12)

(Continued)

TABLE 2 | Continued

Behavior test	Rodent used	Position of animal	Animal restrained	Gas used in blast tube	Blast Pressure	Duration of deficits	References
Elevated Zero Maze	Adult C57BL/6 mice (12–16 weeks)	1 cm outside exit end of blast tube facing head front.	both head restrained and unrestrained	Helium	Mild blast of 215 ± 13 kPa, 46 ± 5 kPa * ms impulse or moderate blast of 415 ± 41 kPa, 148 ± 12 kPa * ms impulse	No significant deficits in both blast groups vs. sham 24 h post blast.	(66)
	LE rats (250–350 g, 10 weeks old)	30 cm inside the shock tube with head facing the blast exposure	Yes	Compressed air	74.5 kPa for 3 days	At 24 weeks post blast.	(50)
	LE rats (250–350 g, 10–12 weeks old)	Head facing the shockwave exposure	Yes	Compressed air	One 74.5 kPa exposure for 3 consecutive days	At week 11 post blast.	(62)
	LE rats (250–350 g)	18 inches inside the shock tube, both facing and sideways to the blast	Yes	Compressed air	74.5 kPa for 3 days	3 rats had deficits while 9 did not at 3 weeks post injury. 9 unaffected and 4 affected rats at 6-month timepoint.	(84)
Open Field test (OFT)	Adult C57BL/6 mice (12–16 weeks)	1 cm outside exit end of blast tube facing head front.	Both head restrained and unrestrained	Helium	Mild blast of 215 ± 13 kPa, 46 ± 5kPa * ms impulse or moderate blast of 415 ± 41 kPa, 148 ± 12 kPa * ms impulse	At day 4 post blast	(66)
	C57BL/6J mice (2-month-old)	Prone position 3, 4, and 7 m away from the source with mice head longitudinally aligned to the shockwave propagation	No	C4 explosives	∼46.6 kPa, ∼31.9 kPa and ∼19.6 kPa corresponding to 3, 4, and 7 m distances from source.	At 6 days post injury in the 3 m blast group	(58)
	SD rats (215–300 g)	73 cm inside the shock tube in an antero- posterior axis with head perpendicular to the shockwave	Yes	Compressed air	3 blasts of 40 Psi; each blast was administered at an interval of 14 days	At days 1 and 7 post blast	(85)
	SD rats (300 g)	19 cm from the nozzle opening at an angle of 21° from the vertical axis of the shock tube.	Not mentioned	Nitrogen gas	28 kPa	At 3 days post impact	(86)
	SD rats (300–330 g)	Transverse prone position across the mouth of the blast tube.	Yes. Chest protection with rat head exposed	Compressed air	138 kPa single or 5 blasts	Significant deficits on day 1. No deficits were observed on day 16	(19)
	Male and naturally cycling female C57BL/6J mice (7–9 weeks of age)	Prone position facing blast exposure	Yes	Compressed air	15.74 Psi	No deficits	(83)
	Male C57/Bl6 mice (3–4 months; 25.22 ± 1.96 g)	Supine position 53 cm from driven section opening	Yes	Helium	Rupture pressure of 183 kPa(mild) or 213 kPa (moderate)	Moderate blast rats had deficits up to 30 days. Mild injury rats had deficits up to 10 days. Freezing response was observed in mild rats up to 30 days.	(16)
	SD rats (325 g)	Prone position with the right side of the thorax facing the shock wave	Not mentioned	Helium	28.49 ± 1.5 Psi in 2.475 ± 0.16 ms	Significant deficits 6-days post blast	(87)

(Continued)

TABLE 2 | Continued

Behavior test	Rodent used	Position of animal	Animal restrained	Gas used in blast tube	Blast Pressure	Duration of deficits	References
Forced Swim test	Male SD rats (150–200 g)	265 mm from the exploding wire with head facing impact	No	Exploding wire technique to generate small scale blast waves	95 kPa for 0.189 ms	No deficits were observed	(47)
	Male SD rats (290–320 g, 10–12 weeks)	1 m from the charge in a transverse prone position	Yes	Swedish army plastic explosive containing explosive m/46, 86% pentaerythritol tetranitrate and mineral oil	550 kPa in 0.2 ms	Decreased immobility in blast animals that may be due to Hyperarousal 24 h post blast. No deficits at 14- or 35-days post blast	(88)
	SD rats (6-month-old)	Placed outside with right side of the skull facing the pressure wave	No	Nitrogen	50 Psi in 1 ms	At 72 h post blast	(54)
Light/dark box emergence test	LE rats (250–350 g, 10–12 weeks old)	Head facing the shockwave exposure	Yes	Compressed air	One 74.5 kPa exposure for 3 consecutive days	At week 11 post blast	(62)
	SD rats (300g)	19 cm from the nozzle opening at an angle of 21° from the vertical axis of the shock tube.	Not mentioned	Nitrogen gas	28 kPa	Up to 9 days	(86)
	LE rats (250 g−350 g; 10 weeks of age)	Head facing the blast exposure	Yes	Compressed air	74.5 kPa	At 29 weeks post blast	(65)
	Male SD rats 250-300g	Rostral cephalic orientation toward shock wave	Not mentioned	Compressed helium	10,14, 24 psi	At 7 days post blast in the 10 & 14 psi group.	(89)
	SD rats (250 g)	1.09 m from open end of the blast tube in a rostral cephalic position	Yes. No information on head restraint	Helium	117 kPa at 2.5 ms	Significantly decreased time 1- and 3-months post blast to enter dark box but no difference in time spent or number of transitions	(36)
	C57BL/6J mice (2–month-old)	Prone position 3, 4, and 7 m distances away from the source with the head longitudinally aligned to the shockwave propagation	No	C4 explosives	∼46.6 kPa, ∼31.9 kPa and ∼19.6 kPa corresponding to 3, 4, and 7 m distances from source.	5 days post injury in the 3 m blast group	(58)
	LE rats (250–350 g)	18 inches inside the shock tube, both facing and sideways to the blast	Yes	Compressed air	74.5 kPa for 3 days	Two animals developed deficits while 6 animals showed no deficits, 3 weeks post injury. At 6 months post injury, 9 animals were unaffected while 3 animals showed deficits.	(84)
Acoustic Startle	Male SD rats (150–200 g)	265 mm from the exploding wire with head facing impact	No head restrained; movement restricted	Exploding wire technique to generate small scale blast waves	95 kPa for 0.189 ms	At days 38 and 62 post impact.	(47)
Predator Scent Challenge (open field and light /dark emergence test)	LE rats (250–350 g, 10 weeks old)	30 cm inside the shock tube with head facing the blast exposure	Yes	Compressed air	74.5 kPa for 3 days	At 3 days in open field test and at 7 days in light/dark emergence task post exposure to predator scent	(50)

or rats exploring more time at periphery of the arena than the center represents anxious behavior. Besides exploratory activity other anxiety behaviors such as grooming, rearing and defecation can be recorded in OFT task.

The light/dark box test consists of a dark box which represents the "safe area," a light box which represents the aversive environment and utilizes the rodent's innate aversion to light and exploratory behavior to measure anxiety. The animal is habituated in a dark room and placed in the center of the light box and recorded. The time taken by the animal to explore and reach the dark box is measured. Animals with anxiety are generally observed to take more time to reach the dark box than control animals. This test has been identified to be more effective when done in the dark or night cycle of rodents as their plasma corticosterone levels which are higher in their dark cycle play a significant role in their exploratory behavior (93).

One of the major pitfalls involved in anxiety testing is habituation. Testing done over multiple timepoints leads to habituation of the new/aversive environment leading to a decline in the exploratory behavior of the rats. The weight of the animals and motor deficits have also been identified to play a negative role in their exploratory behavior (37, 73, 90).

Table 2 summarizes the work done in literature regarding anxiety and depression behavior testing in rodents subjected to bTBI. Literature review was done using advanced search in Google Scholar with keywords "rodents, shockwave tube, anxiety, depression" and the exact phrase "blast TBI," between the years 2008-2019. In most published works in **Table 2**, bTBI has been correlated with positive anxiety deficits in rodents.

Anxiety measured by the elevated plus maze, light/dark emergence test were identified in most studies at chronic timepoints of 7, 15 days post bTBI resulting in long term deficits irrespective of animal location in the blast tube (36, 48, 56, 65). However, no deficits were observed in animals placed 7 m away from detonation source in open field explosions (59, 60). Animals exposed to multiple blasts analyzed with the elevated zero maze were identified with deficits that lasted months post exposure. Deficits in the open field test were observed 1–7 days post injury in animals placed outside the blast tube (66, 85). Chronic deficits lasting a month have not been reported with the open field test except in a study involving moderate bTBI overpressure (16). These results implicate the importance of experimental parameters and choice of behavior tests in measuring deficits following bTBI.

Fear Conditioning

PTSD and bTBI have symptoms that often overlap with each other. These include attention deficits, irritability, increased startle response, sleep disturbance, emotional numbness and anger (94, 95). However, there is also increasing evidence indicating the development of chronic PTSD as a result of secondary neuronal damage following a bTBI (96–98). PTSD is known to manifest in the following stages: an individual is first exposed or witness to a life-threatening situation leading to re-experiencing symptoms such as nightmares and sense of reliving the trauma. This then leads to active avoidance of the trauma, inability to recall the trauma, emotional numbing resulting in irritability, insomnia, hyper vigilance, or an increased startle response (95). PTSD is associated with medial and orbitofrontal cortices, amygdala, and hippocampal regions of the brain (97). Fear conditioning is one of the tests that is used to measure PTSD traits in rodent models of bTBI. Contextual and cued fear conditioning test involve the amygdala, hippocampus, frontal, and cingulate cortex brain regions (99).

Contextual and cued fear conditioning is done by training the rodent in a chamber (context) and providing a conditional stimulus (CS) typically an aversive noise followed by an unconditioned stimulus (US) such as a foot shock. The pairing of the CS- US generates the freezing behavior in rats. When this pairing is repeated, the animal creates a stronger negative association to the testing environment and the auditory cue. This then generates a freezing response when the animal is returned either to the testing chamber or on hearing the auditory cue. The contextual fear memory is tested by placing the rat in the same chamber and measuring the freezing behavior in the animal without the presence of the CS or US. In order to test the cued conditioning, the animal is placed in a different chamber and its freezing response to the CS is now measured. This enables to differentiate the freezing effect observed due to the context and the CS (50, 99).

Table 3 summarizes the fear conditioning tests done in bTBI literature using Google scholar and keywords "shockwave tube," "rodents," "fear conditioning," and the exact phrase "blast TBI" between the years 2008–2019. Most of the published studies in bTBI measuring fear conditioning post bTBI were carried out with repetitive low-level blasts and have consistently reported an increase in freezing or cued fear response following bTBI. The duration of deficits have been reported from 1 to 25 weeks post blast. Fear conditioning deficits measured in a single blast exposure by Perez Gracia et al. (65), were observed 3 weeks post injury further implicating the long-term consequence of blast exposure on fear conditioning (65). These results indicate the development of PTSD related deficits following bTBI in rodent models.

Motor Deficits

Veterans diagnosed with bTBI have been known to manifest balance and vestibular motor co-ordination issues with symptoms ranging from dizziness, vertigo, postural instability and impaired tandem gait (101–103). Further, balance deficits are found to be amplified in veterans with a combined diagnosis of TBI and amnesia or PTSD (104). Balance and gait disorders in rodent bTBI models are measured using staircase test, ladder test, rotarod, and beam balance test as described in **Table 4**. Additionally, anxiety assessment apparatus such as elevated plus maze and open field test have also been used to measure locomotor deficits in rodents.

The Rotarod test originally described by Dunham and Miya is often used for testing the neurological effects of drugs or trauma on the motor coordination of rodents (50, 108–110). The apparatus consists of a rotating rod of constant or accelerating speed on which the rodent is placed and variables such as the time and the speed of rotation for the animal to fall from the apparatus is noted and evaluated for motor deficits. The Rotarod

TABLE 3 | Fear conditioning behavioral testing in bTBI.

Behavior test	Rodent used	Position of animal	Head restraint	Gas used in blast tube	Blast Pressure	Duration of deficits	References
Fear conditioning	SD Rats 325 g	Head facing blast impact placed inside the blast tube	Yes	Compressed air	Three 74.5 kPa, 4.8 ms exposures, one each day	Significant reduction conditioned fear suppression one-week post impact	(100)
Cued and contextual fear conditioning	LE rats (250–350 g, 10 weeks old)	30 cm inside the shock tube with head facing the blast exposure	Yes	Compressed air	74.5 kPa for 3 days	Significant freezing in cued testing 25 weeks post impact	(50)
	LE rats (250–350 g, 10–12 weeks old)	Head facing the shockwave exposure	Yes	Compressed air	One 74.5 kPa exposure for 3 consecutive days	Between weeks 11–17 post blast	(62)
	LE rats (250 g–350 g; 10 weeks of age)	Head facing the blast exposure	Yes	Compressed air	74.5kPa	Cued fear response was significantly enhanced at 35 weeks post blast.	(65)
	LE rats (250–350 g)	18 inches inside the shock tube, both facing and sideways to the blast	Yes	Compressed air	74.5 kPa for 3 days	8 rats did not develop deficits, 4 rats developed deficits 3 weeks post injury.	(84)
Grimace scale	Male and naturally cycling female C57BL/6J mice (7– 9 weeks of age)	Prone position facing blast exposure	Yes	Compressed air	15.74 Psi	No deficits 6 days post blast	(83)

apparatus was identified to be more sensitive in identifying motor deficits in mild TBI than the beam balance or beam walk test (108). The disadvantages of this model are that the deficits observed in the rotarod test can also be influenced by endurance and motor learning in the animals. Motor learning refers to the rodent's ability to develop a strategy to remain on the rotating rod rather than as a result of improved locomotor skills (111, 112). Stress has also been identified to play a role in rotarod deficits (113).

The beam walk, ladder rung tests measure the fine motor skills of the rat unlike the gross motor skills assessed by the rotarod test (99). The beam walk or beam balance apparatus consists of a narrow-elevated beam that the rodent is made to walk on from one end to the other. The number of foot faults of the rodent is measured to assess its motor performance. The advantages of the test are the low cost, the relative ease of setup and very little motor learning associated with recovery of function. However, the weight of the animal can affect their performance on this apparatus. Beam walking test is more suited to identify deficits in moderate and severe TBI than in mild TBI (112). The ladder rung test, similar to the beam balance test, measures the foot faults of rodents as they walk across a horizontal ladder to reach a platform on the other side. The ladder rung test, additionally, allows to assess the grasping ability and motor deficits in each limb of the rodent. The diÿ culty of the test can be varied by altering the distance between the rungs. An irregular pattern of rung placement for each trial prevents familiarity and learning in the rodents (114). One disadvantage of the beam walk and ladder rung tests is the manual assessment of foot fault scoring which can be tedious and may differ from one individual to another. Anxiety tests such as open field test has also been utilized to study locomotor deficits. Ambulation, latency and rearing of the rodents can be assessed through these tests in addition to anxiety and depression traits (92).

Table 4 summarizes literature review done using Google scholar and keywords "shockwave," "rodents," "motor deficits," and the exact phrase "blast TBI" between the years 2008–2019. Motor deficits, similar to the spatial working memory deficits, have not been consistently reported in bTBI. Most of the deficits observed following bTBI were in animals placed at the exit end of the blast tube implicating the role of reflective pressures and tertiary loading of the blast (30, 46, 86). Majority of the studies with animals located inside the blast tube have reported no motor deficits (17, 18, 50). However, animals located inside the blast tube subjected to multiple blasts have been identified to develop motor deficits (107).

Auditory Deficits

Blast TBI has been well-associated with tinnitus and hearing loss deficits in the veteran population (115–117). In a study done by Oleksiak et al. (118), with a sample population of veterans with mild TBI, 76% of veterans were associated with tinnitus while 60% developed hearing loss. About 92.5% of personnel exposed to blast TBI reported some form of hearing loss (118). Blast exposure can cause both peripheral and central auditory system damage by rupture of the tympanic membrane, ossicular disruption, structural damage of inner and outer hair cells and impairment of central auditory processing (CAP). Blast related auditory deficits include CAP deficits, peripheral hearing loss, tinnitus, and vestibular deficits. Tinnitus is defined as head or ear noise that lasts 5 min or longer while CAP deficits causes diÿ culty in hearing background noises, speech perception, sound localization, and lateralization (4).

TABLE 4 | Summary of experimental variables and motor deficit outcomes in bTBI.

Behavior test	Rodent used	Position of animal	Head restraint	Gas used in blast tube	Blast pressure	Duration of deficits	References
Staircase test	ICR Mice (25–30 g)	4 and 7 m away from detonation source	No (animals were fixed in position with plastic net)	500 g TNT	Shockwave and reflected wave 2.5 Psi or 5.5 Psi	Up to 7 days only in the 2.5 Psi group. No deficits were observed at 30 days for both groups	(12)
Ladder test	Male SD rats (250g)	1.09 m inside the shock tube facing impact	Yes. No information on head restraint	Compressed helium	97, 117, 153 kPa	No deficits were observed at 3, 6, 48 or 72h post blast	(17)
Beam walk task	SD rats (250–350 g)	Transverse prone position across the mouth of the blast tube.	Yes	Compressed air	114, 126, and 147 kPa	Up to 3 days	(30)
	SD rats (200–250 g)	Prone position 20cm from the end of the tube facing the blast wave	No	Compressed air	74 kPa	No deficits up to 14 days post blast.	(63)
Beam walk/ Beam balance test	Adult male SD (350-480g)	Transverse prone position with the head perpendicular to the direction of the shockwave.	Yes	Compressed air	135 ±12.4 kPa with a mean duration of 3.50 ±0.063 ms	No significant deficits 1–5 days post blast.	(105)
Photo beam walk	Male SD 350 g rats	Outside the blast tube with the right side of head perpendicular to the blast front.	No	Compressed nitrogen gas.	Reflected pressures of 31.47, 50.72, and 72.05 in <3 ms	At 24 h for all blast groups	(106)
Beam balance test	LE rats (250–−300 g)	18 inches inside the shock tube, both facing and sideways to the blast	Yes	Compressed air	36.6, 74.5, and 116.7 kPa	No deficits in the 36.6 and 74.5 kPa rats in both orientations. The rats in frontal orientation at 116.7 kPa showed significant deficits at 30 min which resolved by 2 h. Side-oriented rats had deficits at 30 min and 2 h that was resolved by 6 h	(18)
	Male Wistar rats (408.3 ± 93g)	Right side of the front cortex is aligned to the impact	Yes	Lithotripsy machine fired 5 shockwave pulses with 60 Hz frequency	n/a	Up to 7 days post impact	(81)
	Heterozygous *WldS* mice (8-week-old)	10 cm from Mylar membrane with the left side of head facing the blast	No	Compressed air	27kPa	Day 28 post blast	(55)
Rotarod test	Male C57/Bl6 mice (3–4 months; 25.22 ± 1.96 g)	Supine position, 53 cm from driven section opening	Yes	Helium	Rupture pressure of 183kPa(mild) or 213 kPa (moderate)	Up to day 14 but not on days 21 and 30 in both groups	(16)
	Male C57BL/6J mice (8–10 weeks old; 22–26 g)	2.5 feet inside the open end of the expansion chamber, perpendicular to the direction of the shock wave	Yes	Compressed air	Two 20.6 Psi blasts separated by a min and a third blast 30 min later	Significant deficits in single and repetitive blast animals at 10 rpm, 2 and 24 h post blast. At 20 rpm, single blast animals had deficits up to 72 h and multiple impact animals up to 120 h.	(107)
	Adult C57BL/6 mice (12–16 weeks)	1 cm outside exit end of blast tube facing head front.	Experiments were conducted with both head restrained and unrestrained	Helium	Mild blast of 215 ± 13 kPa, 46 ± 5kPa * ms impulse or moderate blast of 415 ± 41 kPa, 148 ± 12 kPa * ms impulse	No deficits in both groups of blast animals up to 3 days post blast	(66)

(Continued)

TABLE 4 | Continued

Behavior test	Rodent used	Position of animal	Head restraint	Gas used in blast tube	Blast pressure	Duration of deficits	References
	LE rats (250–350 g, 10 weeks old)	30 cm inside the shock tube with head facing the blast exposure	Yes	Compressed air	74.5 kPa for 3 days	No motor deficits were observed in rotarod at 8 weeks post blast.	(50)
	SD rats (300 g)	At 19 cm from the nozzle opening at an angle of 21° from the vertical axis of the shock tube.	Not mentioned	Nitrogen gas	28 kPa	Up to 9 days post blast	(86)
	SD rats (200–250 g)	Prone position 20 cm from the end of the tube facing the blast wave	No	Compressed air	74 kPa	No deficits up to 14 days post blast.	(63)
	Male Wistar rats (408.3 ± 93g)	Right side of the front cortex is aligned to the impact	Yes	A lithotripsy machine fired 5 shockwave pulses with 6o Hz frequency	n/a	Up to 7 days post impact	(81)
Open Field Test (OFT)	SD rats	39 and 17 cm outside shock tube opening, 40 and 20° lateral to shock tube axis, respectively	yes	Helium	100 and 450 kPa reflected peak overpressure	At 4 days and 30 days post impact in both blast groups	(46)
	SD rats (∼300 g)	Transverse prone position across the mouth of the blast tube.	Yes, with chest protection and head exposed	Compressed air	20.6 ± 3 psi	Higher resting times at day 45 post injury.	(56)
	Adult C57BL/6 mice (12–16 weeks)	1 cm outside exit end of blast tube facing head front.	Experiments were conducted with both head restrained and unrestrained	Helium	Mild blast of 215 ± 13 kPa, 46 ± 5 kPa * ms impulse or moderate blast of 415 ± 41 kPa, 148 ± 12 kPa * ms impulse	At day 4 post blast in both groups.	(66)
	C57BL/6J mice (2-month-old)	Prone position 3, 4, and 7 m distances away from the source with the head longitudinally aligned to the shockwave propagation	No	C4 explosives	∼46.6 kPa, ∼31.9 kPa and ∼19.6 kPa corresponding to 3, 4, and 7 m distances from source.	At 3 days post injury in the 3, 4, and 7 m blast group	(58)
	LE rats (250–350 g, 10 weeks old)	30 cm inside the shock tube with head facing the blast exposure	Yes	Compressed air	74.5 kPa for 3 days	No motor deficits at 7 weeks post blast.	(50)
	LE rats (250–350 g, 10–12 weeks old)	Head facing the shockwave exposure	Yes	Compressed air	One 74.5 kPa exposure for 3 consecutive days	No deficits 11 weeks post blast	(62)
	SD rats (300–330 g)	Transverse prone position across the mouth of the blast tube.	Yes. Chest protection with rat head exposed	Compressed air	138 kPa single or 5 blasts	At day 1 but not on day 16 in multiple impact group.	(19)
	C57BL/6 Mice (2.5 months)	0.56 m inside open exit of shock tube	Both with and without head restraint	Compressed gas	77 ± 2 kPag	No deficits	(26)
	LE rats (250 g−350 g; 10 weeks of age)	Head facing the blast exposure	Yes	Compressed air	74.5kPa	At 28 weeks post blast	(65)
Elevated plus maze	SD rats (∼300 g)	Transverse prone position across the mouth of the blast tube.	Yes with chest protection and head exposed	Compressed air	20.63 psi	At day 44 post blast but not at days 15 or 66.	(57)
	SD rats (245–265 g)	Transverse prone position across the mouth of the blast tube.	Yes, with chest protection and head exposed	Compressed air	20.63 psi	Immediately after blast.	(82)

Auditory deficits in bTBI rodent models have been evaluated using acoustic startle response (ASR) and various modifications of the test to include prepulse inhibition for identifying hearing loss and gap detection deficits for evaluating tinnitus. The acoustic startle response is described as a rapid contraction of facial and skeletal muscles in response to a loud and unexpected auditory stimulus usually 80 dB above the auditory threshold for a rat (119). The acoustic signaling pathway consists of the auditory nerve, the ventral cochlear nucleus, the cochlear root neurons, the caudal pontine reticular nucleus (PnC), spinal interneurons and finally the motor neurons which produce the startle response (119–121). The PnC neurons, specifically, play a crucial role in the startle response elicited (122, 123).

The acoustic startle experiments are generally conducted in a chamber mounted with a platform containing an accelerometer or other voltage motion sensors to assess the startle response in rats. Briefly, the test involves acclimatizing rats to background noise (65–68 dB) before introducing the animal to increasing intensity of the startle stimuli. The startle amplitude of rats is then measured as an output function of the startle intensity provided. For the prepulse inhibition, a sound of lower intensity than the startle stimulus is presented before the startle stimuli. This prepulse stimulus provided in anticipation of the startle stimulus is expected to lower the startle amplitude in control subjects but not in subjects with hearing loss (124). A modification of this paradigm is the gap prepulse inhibition which has recently gained prominence in evaluating tinnitus in human and animal models. The gap prepulse inhibition involves a gap trial in which a silent gap is provided prior to the startle stimuli. Since subjects with tinnitus are expected to fail to hear the silent gap, there would be no reduction in startle amplitude in the gap trials when compared to control subjects. The gap detection is measured as the ratio between the magnitude of the startle stimulus presented alone without a gap trial and trials in which a gap preceded the startle stimulus (125).

The main advantage of the acoustic startle test is since it measures the reflex of the rodent, there is no training involved prior to conducting the test. However, there is considerable variability in the experimental protocol and data interpretation for the gap detection experiments across laboratories. One of the major discrepancies is in comparing the "no gap" vs. "gap trials" of individual rats and determining the presence of tinnitus than comparing the overall performance across groups. Since it is possible that only a percentage of blast exposed rats may develop tinnitus, it would be beneficial to compare individual rat performances than performances across groups (125). Further, there has been contradicting evidence in the assumption that subjects with tinnitus would "fill in" the silent gap trial (126, 127). However, there is significant evidence to support that the gap detection ratio measured is affected in rats with tinnitus (127, 128).

Blast induced tinnitus and hearing loss investigations done in rodent models are summarized in **Table 5** using Google Scholar and keywords such as "blast TBI," "rodents," "hearing loss," "tinnitus," and the exact phrase "blast TBI" between the years 2008–2019. Most of the studies at different blast overpressures observe consistent findings of hearing loss and tinnitus in blast exposed animals indicating the prevalence of auditory deficits in bTBI and the eÿ cacy of the behavioral test.

SUMMARY AND DISCUSSION

The primary effects of blast TBI have been replicated and studied in rodent models by many researchers. We have attempted in this review to summarize the various behavioral models used to study common behavioral outcomes of blast TBI such as cognition, anxiety, depression, PTSD, motor, and auditory deficits. The advantages and shortcomings of the tests most commonly used in literature have been summarized in **Table 6**.

Cognitive deficits in blast induced TBI have been studied using spatial memory tasks such as Morris Water maze, Y maze, Barnes Maze, and object recognition tasks such as the novel object recognition test. From **Table 1**, it can be inferred that animals exposed to the reflective blast pressure or blast wind manifest spatial memory deficits. In the studies where the animals were placed inside the blast tube, a few researchers observed deficits with Morris Water Maze test at 24 h post impact but not at longer timepoints. No cognitive deficit was observed with the eight arm radial maze. Multiple blast studies done with the Morris Water Maze test also indicated similar transient deficits at 24 h but not at later timepoints (49, 50). Studies done with animals placed outside the blast tube, on the other hand, consistently reported cognitive deficits lasting for weeks indicating these animals may be receiving a higher severity of TBI (30, 31, 57). Investigations of bTBI with animals placed outside the shock tube have demonstrated that the animals are not only subject to the pure effects of a primary blast wave but can be subject to the reflective pressures and blast wind (10, 22). Similarly, spatial memory deficits were also observed to last for weeks or months in animals subject to open field detonations (12, 58). Stemper et al. (48), reported no cognitive deficits up to 60 days post impact when animals were placed at an angle to the opening of the blast tube to minimize the blast wind effects (48). These results indicate that chronic spatial memory deficits observed due to a blast impact are not majorly manifested due to the primary blast wave and could be a result of the secondary or tertiary effects of a blast impact. This was further demonstrated by Goldstein et al. (26), when spatial memory deficits were observed in animals subject to bTBI without head restraint but not in animals with head restraint (26). Thus, it is possible that the spatial memory deficits are more likely to be produced due to tertiary effect of head and body motion and not primary loading effect when the animal is relatively motionless. However, this hypothesis has not been carefully tested.

Object recognition memory, however, measured by the novel object recognition test showed consistent deficits in animals placed both inside and outside the blast pressure tube indicating that primary blast pressure does alter the recognition memory in rodents. Interestingly, spatial object recognition deficits were not affected by the presence or absence of head

TABLE 5 | Auditory deficits in bTBI.

Behavior test	Rodent used	Position of animal	Head restraint	Gas used in blast tube	Blast pressure	Duration of deficits	References
Prepulse inhibition (PPI) and acoustic startle	LE rats (250–350 g, 10–12 weeks old)	Head facing the shockwave exposure	Yes	Compressed air	One 74.5 kPa exposure for 3 consecutive days	Significant increase in PPI in blast animals between weeks 11–17 post blast	(62)
	SD Rats (225–250 g)	Supine position with the blast wave generator nozzle right above the animal's head.	Yes, chest shielded with 2 mm lead plate	Nitrogen	80 Psi	Decreased startle amplitude response 2 weeks post blast but no effects of PPI	(31)
	LE rats (250–350 g, 10 weeks old)	30 cm inside the shock tube with head facing the blast exposure	Yes	Compressed air	74.5 kPa for 3 days	Increased acoustic startle 24 weeks post blast but had no change in PPI	(50)
	LE rats (250 g−350 g; 10 weeks of age)	Head facing the blast exposure	Yes	Compressed air	74.5 kPa	Enhanced PPI at 34-week post blast	(65)
Gap detection (GAP), acoustic startle reflex and PPI	SD Rats (70–80 days)	1.09 m from open end of blast tube in a rostral cephalic orientation	Yes, with one ear occluded. No information on head restraint	Helium	150 kPa for 10ms	Tinnitus positive rats had impaired GAP ratios 24 h, a month and 3 months post blast. PPI ratios were increased only at the 24 h time point. All blast rats had decreased startle force at 24 h, 1 month, and 3-month, time points.	(129)
	SD rats (110 days old, 250-300g)	109 cm inside the open end of the blast tube in a rostro-cephalic orientation to the blast wave	Not mentioned. Right ear was occluded with an earplug.	Helium	3 blast exposures of 22 psi 5 min apart.	Hearing loss and tinnitus up to 7 weeks post blast	(128)
GAP and PPI testing.	Long Evans rats (60–70 days old)	44 inches from open end of tube in a prone position with head facing blast	No earplugs. Head restraint not mentioned	Helium	95 kPa for 10 ms	Tinnitus observed at 24 h and at certain frequencies on day 14. The GAP deficits recovered by day 28. PPI deficits pertained at particular frequencies up to day 90.	(130)
	SD rats (60–70 days)	503 cm from the bursting membrane and 112 cm from the open end of the driven cylinder	Yes, with no earplugs. Head restraint not mentioned	Helium	14 Psi	8 out of 13 rats developed tinnitus,	(53)

Behavioral tests to measure hearing loss and tinnitus in bTBI rodent models.

restraint unlike the spatial working memory deficits (66). This further supports that primary blast loading affects recognition memory while the effects of tertiary loading may affect the working memory. Fear based learning tests such as the active avoidance test which is associated with deficits in the basal forebrain also showed deficiencies following the primary blast injury (18, 29, 131).

Anxiety due to bTBI has most commonly been studied using elevated plus maze, zero maze, open field test and light/dark box emergence tests. In **Table 2**, most of the anxiety deficits measured by these tests are seen to be manifested at chronic timepoints with the quickest onset being 4 days post blast in the OFT test and not as immediate deficits post blast exposure. Most of the studies using EPM were done with the animals placed at the mouth of the blast tube manifesting chronic anxiety deficits. However, studies by Perez-Garcia et al. (120), and Russell et al. (83), have also demonstrated chronic anxiety deficits in animals subjected to bTBI placed inside the shock tube (65, 83). Statz et al. (84), subjected rats to a repetitive mild blast TBI of 74.5 kPa over 3 consecutive days and found that a part of the blast cohort, but not all animals, manifested anxiety measured by elevated zero maze, light/dark emergence test and fear conditioning, 3 weeks and 6 months post blast impact (84). Increased anxiety behavior at 24 hrs to 3 days post blast exposure was observed in the open field test only when the animals were placed at the exit end of the blast tube or were subjected to multiple blast exposures over days (19, 54, 66, 85, 86). EPM and light /dark emergence tests showed long term deficits of anxiety following bTBI and may be more accurate tests for anxiety. Open field tests are also dependent on exploratory behavior of rodents but deficits in this model

TABLE 6 | Behavior tests used in blast TBI with their advantages and disadvantages.

Behavioral tests	Advantages	Disadvantages
Cognition:		
• Morris Water Maze	Fear of water serves as a good motivator, minimal training required, most rodents learn to perform the test.	Induces stress in animals. Depressed animals can exhibit "floating" behavior that can affect results
• Barnes Maze	Does not induce stress in animals	Lack of motivation may result in poor performance.
• Y Maze	Simplicity and lack of training	Stress can affect results observed
• Novel Object Recognition	Simple setup, no training required and less stressful	Inconsistent exploration of the novel object amongst animals of the same group.
• Active avoidance test	Less time required for testing	Rodent results within same group can be inconsistent.
Anxiety and depression:		
• Elevated Plus Maze • Elevated Zero Maze	Simplicity of testing, no training required.	Testing at multiple timepoints results in habituation and false positive results. Locomotor deficits can also affect results.
• Open Field Test	Simplicity of testing, no training required.	Locomotor deficits affects results. Weight of animals can affect their exploratory behavior.
• Light/dark box emergence test	Quick and easy to use, no prior training required.	Locomotor deficits can affect results. The lit side of the test has to be sufficiently aversive to the rodents to avoid false positive results.
• Forced Swim Test	Ease of testing and analysis.	Locomotor deficits have to be considered to prevent false positive results.
Fear conditioning:		
• Cued and contextual fear conditioning	Motor deficits do not affect the results as the test involves passive learning.	The strain and phenotype of rodents have to be taken into consideration for the cue and aversive conditioning levels.
Motor deficits:		
• Beam Walk/Beam Balance Test	Low cost, relative ease of setup, very little motor learning associated with recovery function.	Weight of the animal may affect results. Manual assessment of foot fault scoring can be tedious and produce inconsistent results. Factors such as age, weight of the animals, lack of motivation affects results. Recovery of function observed can be influenced by endurance and motor learning in animals.
• Rotarod	Highly reproducible results	Training of animals is required to reduce stress and to segregate rodents capable of performing on the rotarod.
Auditory deficits:		
• Acoustic startle	No prior training as it measures the reflex of the animal.	Variability in data interpretation across labs.

were observed only at early timepoints of few days post blast and no deficits were observed at chronic timepoints of a month post blast.

Increased fear conditioning has been observed in blast animals at chronic time points from single blast or multiple blast exposure (**Table 3**). Interestingly, a decrease in fear conditioning was observed in repetitive bTBI in a study by Genovese et al. (100). Auditory deficits that could play a role suppressing the ability to hear the aversive cue and thereby the performance of the animals in the fear conditioning test were negated as there were no auditory deficits observed in the prepulse inhibition test. However, in this study conditioned suppression was measured and not the fear conditioning. Conditioned suppression is the reduction of the conditioned response to a positive stimulus, which in this study was a lever press to obtain food when the aversive stimulus was presented. Hence, the conditioned suppression parameter measured in this study might produce different results than the typical fear conditioning measured in other studies (100). Whether conditioned fear and conditioned suppression are correlated or different remains disputable and hence the results may still indicate deficits to the conditioned fear in the blast animals (100, 132–134).

Motor deficits following bTBI were measured by Rotarod, beam walk/balance tests, elevated plus maze and open field tests. Motor deficits in bTBI showed a similar trend to the cognitive deficits, with increased deficits in animals exposed to the reflective pressures, placed at the mouth of the blast tube or placed inside an open-ended shockwave tube. Most of the studies with animals placed inside the tube indicated little to no motor deficits.

Auditory deficits in blast TBI have been measured using the acoustic startle test with prepulse inhibition for identifying hearing loss and gap detection deficits for evaluating tinnitus. bTBI induced hearing loss and tinnitus have consistently been reported as chronic deficits. However, some studies report only a part of the cohort undergoing blast to be associated with hearing deficits and tinnitus (**Table 5**). It is critical to make this distinction between animals with and without auditory deficits within the injury group to avoid possible dilution of results.

Overall, it is observed from **Tables 1**–**5**, that the blast pressures used in most studies investigating behavioral deficits of bTBI are mild blasts ranging from 70 to 153 kPa. The most consistently reported chronic behavioral deficits following primary blast TBI in literature between the years 2008–2019 were anxiety, auditory deficits, recognition memory deficits, and fear conditioning often observed between a week to 1-month post blast exposure. This indicates that exposure to primary mild bTBI can lead to persistent anxiety, auditory, fear conditioning and recognition memory deficits. Additionally, animal location in the blast tube did not play a significant role in the development of these deficits. Spatial working memory and motor deficits following bTBI, on the other hand, depend heavily on experimental parameters. Exposure to a primary blast wave where the animal is kept inside the shock tube seemed to cause only transient effects on

working memory measured by the Morris Water maze lasting 24 h post injury while exposure to tertiary effects of blast, reflective pressure wave leads to long lasting deficits. Similarly, motor deficits in a primary blast exposure causes little to no deficits while manifesting long term deficiencies in open field experiments and in studies where animals are placed at the exit end of the blast tube. This suggests that the primary blast wave exposure has a significant role in the manifestation of recognition memory deficits, auditory, fear conditioning and anxiety deficits while tertiary effects of loading experienced by the animal placed outside the blast tube may have a role in the manifestation of spatial working memory and motor deficits. Thus, position of the animal in the blast tube and use of head restraint plays a significant role in bTBI behavioral deficits and have to be considered while studying the effects of a primary blast wave.

AUTHOR CONTRIBUTIONS

AA carried out the literature research, acquisition of data for the tables, and prepared the manuscript. AR aided in data acquisition for the tables and wrote the subheading Anxiety and Depression in the manuscript. NC and BP procured funding, supervised, provided critical revisions, and edited the manuscript. All authors contributed to the article and approved the submitted version.

FUNDING

This work was funded by New Jersey Commission on Brain Injury Research [grant no. CBIR16PIL021] and U.S. Army Medical Research and Materiel Command [grant no. 14059001 and W81XWH-15-1-0303].

REFERENCES

1. *DoD Worldwide Numbers for TBI*. Available online at: https://dvbic.dcoe.mil/dod-worldwide-numbers-tbi (accessed June 19, 2019).
2. Butler D, Buono J, Erdtmann F, Reid, P. *Traumatic brain injury and the military health system in Systems Engineering to Improve Traumatic Brain Injury Care in the Military Health System: Workshop Summary*. (2009) National Academies Press.
3. Lindquist LK, Love HC, Elbogen EB. Traumatic brain injury in iraq and afghanistan veterans: new results from a national random sample study. *J Neuropsychiatry Clin Neurosci.* (2017) 29:254–9. doi: 10.1176/appi.neuropsych.16050100
4. Fausti SA, Wilmington DJ, Gallun FJ, Myers PJ, Henry JA. Auditory and vestibular dysfunction associated with blast-related traumatic brain injury. *J Rehabil Res Dev.* (2009) 46:797–810. doi: 10.1682/JRRD.2008.09.0118
5. Scherer MR, Schubert MC. Traumatic brain injury and vestibular pathology as a comorbidity after blast exposure. *Phys Ther.* (2009) 89:980–92. doi: 10.2522/ptj.20080353
6. Trudeau DL, Anderson J, Hansen LM, Shagalov DN, Schmoller J, Nugent S, et al. Findings of mild traumatic brain injury in combat veterans with PTSD and a history of blast concussion. *J Neuropsychiatry Clin Neurosci.* (1998) 10:308–13. doi: 10.1176/jnp.10.3.308
7. Kuriakose M, Skotak M, Misistia A, Kahali S, Sundaramurthy A, Chandra N. Tailoring the blast exposure conditions in the shock tube for generating pure, primary shock waves: the end plate facilitates elimination of secondary loading of the specimen. *PLoS ONE.* (2016) 11:e0161597. doi: 10.1371/journal.pone.0161597
8. Chen Y, Constantini S. Caveats for using shock tube in blast-induced traumatic brain injury research. *Front Neurol.* (2013) 4:117. doi: 10.3389/fneur.2013.00117
9. Kahali S, Townsend M, Mendez Nguyen M, Kim J, Alay E, Skotak M, et al. The evolution of secondary flow phenomena and their effect on primary shock conditions in shock tubes: experimentation and numerical model. *PLoS ONE.* (2020) 15:e0227125. doi: 10.1371/journal.pone.0227125
10. Sundaramurthy A, Alai A, Ganpule S, Holmberg A, Plougonven E, Chandra N. Blast-induced biomechanical loading of the rat: an experimental and anatomically accurate computational blast injury model. *J Neurotrauma.* (2012) 29:2352–64. doi: 10.1089/neu.2012.2413
11. Ning YL, Zhou YG. Shock tubes and blast injury modeling. *Chin J Traumatol.* (2015) 18:187–93. doi: 10.1016/j.cjtee.2015.04.005
12. Rubovitch V, Ten-Bosch M, Zohar O, Harrison CR, Tempel-Brami C, Stein E, et al. A mouse model of blast-induced mild traumatic brain injury. *Exp Neurol.* (2011) 232:280–9. doi: 10.1016/j.expneurol.2011.09.018
13. Risling M, Davidsson J. Experimental animal models for studies on the mechanisms of blast-induced neurotrauma. *Front Neurol.* (2012) 3:30. doi: 10.3389/fneur.2012.00030
14. Kovacs SK, Leonessa F, Ling GS. Blast TBI models, neuropathology, and implications for seizure risk. *Front Neurol.* (2014) 5:47. doi: 10.3389/fneur.2014.00047
15. Clemedson CJ, Criborn CO. A detonation chamber for physiological blast research. *J Aviat Med.* (1955) 26:373–81.
16. Cernak I, Merkle AC, Koliatsos VE, Bilik JM, Luong QT, Mahota TM, et al. The pathobiology of blast injuries and blast-induced neurotrauma as identified using a new experimental model of injury in mice. *Neurobiol Dis.* (2011) 41:538–51. doi: 10.1016/j.nbd.2010.10.025
17. Vandevord PJ, Bolander R, Sajja VS, Hay K, Bir CA. Mild neurotrauma indicates a range-specific pressure response to low level shock wave exposure. *Ann Biomed Eng.* (2012) 40:227–36. doi: 10.1007/s10439-011-0420-4
18. Ahlers ST, Vasserman-Stokes E, Shaughness MC, Hall AA, Shear DA, Chavko M, et al. Assessment of the effects of acute and repeated exposure to blast overpressure in rodents: toward a greater understanding of blast and the potential ramifications for injury in humans exposed to blast. *Front Neurol.* (2012) 3:32. doi: 10.3389/fneur.2012.00032
19. Kamnaksh A, Kwon SK, Kovesdi E, Ahmed F, Barry ES, Grunberg NE, et al. Neurobehavioral, cellular, and molecular consequences of single and multiple mild blast exposure. *Electrophoresis.* (2012) 33:3680–92. doi: 10.1002/elps.201200319
20. Pitts MW. Barnes maze procedure for spatial learning and memory in mice. *Bio Protoc.* (2018). 8:e2744. doi: 10.21769/BioProtoc.2744
21. Gullotti DM, Beamer M, Panzer MB, Chen YC, Patel TP, Yu A, et al. Significant head accelerations can influence immediate neurological impairments in a murine model of blast-induced traumatic brain injury. *J Biomech Eng.* (2014) 136:091004. doi: 10.1115/1.4027873
22. Svetlov SI, Prima V, Kirk DR, Gutierrez H, Curley KC, Hayes RL, et al. Morphologic and biochemical characterization of brain injury in a model of controlled blast overpressure exposure. *J Trauma.* (2010) 69:795–804. doi: 10.1097/TA.0b013e3181bbd885
23. Chang K-S, Kim J-K. Numerical investigation of inviscid shock wave dynamics in an expansion tube. *Shock Waves.* (1995) 5:33–45. doi: 10.1007/BF02425034
24. Haselbacher AC, Balachandar S, Kieffer S. Open-ended shock tube flows: influence of pressure ratio and diaphragm position. *AIAA J.* (2007) 45:1917–29. doi: 10.2514/1.23081
25. Bass CR, Panzer MB, Rafaels KA, Wood G, Shridharani J, Capehart B. Brain injuries from blast. *Ann Biomed Eng.* (2012) 40:185–202. doi: 10.1007/s10439-011-0424-0
26. Goldstein LE, Fisher AM, Tagge CA, Zhang XL, Velisek L, Sullivan JA, et al. Chronic traumatic encephalopathy in blast-exposed military veterans and a blast neurotrauma mouse model. *Sci Transl Med.* (2012) 4:134ra60. doi: 10.1016/j.jalz.2012.05.592
27. Chandra N, Ganpule S, Kleinschmit N, Feng R, Holmberg A, Sundaramurthy A, et al. Evolution of blast wave profiles in simulated air blasts:

experiment and computational modeling. *Shock Waves.* (2012) 22:403–15. doi: 10.1007/s00193-012-0399-2
28. Mishra V, Skotak M, Schuetz H, Heller A, Haorah J, Chandra N. Primary blast causes mild, moderate, severe and lethal TBI with increasing blast overpressures: experimental rat injury model. *Sci Rep.* (2016) 6:26992. doi: 10.1038/srep26992
29. Cernak I, Wang Z, Jiang J, Bian X, Savic J. Cognitive deficits following blast injury-induced neurotrauma: possible involvement of nitric oxide. *Brain Injury.* (2001) 15:593–612. doi: 10.1080/02699050010009559
30. Long JB, Bentley TL, Wessner KA, Cerone C, Sweeney S, Bauman RA. Blast overpressure in rats: recreating a battlefield injury in the laboratory. *J Neurotrauma.* (2009) 26:827–40. doi: 10.1089/neu.2008.0748
31. Awwad HO, Gonzalez LP, Tompkins P, Lerner M, Brackett DJ, Awasthi V, et al. Blast overpressure waves induce transient anxiety and regional changes in cerebral glucose metabolism and delayed hyperarousal in rats. *Front Neurol.* (2015) 6:132. doi: 10.3389/fneur.2015.00132
32. Elder GA. Update on TBI and cognitive impairment in military veterans. *Curr Neurol Neurosci Rep.* (2015) 15:68. doi: 10.1007/s11910-015-0591-8
33. Taber KH, Warden DL, Hurley RA. Blast-related traumatic brain injury: what is known? *J Neuropsychiatry Clin Neurosci.* (2006) 18:141–5. doi: 10.1176/jnp.2006.18.2.141
34. Hicks RR, Fertig SJ, Desrocher RE, Koroshetz WJ, Pancrazio JJ. Neurological effects of blast injury. *J Trauma.* (2010) 68:1257–63. doi: 10.1097/TA.0b013e3181d8956d
35. Barnes DE, Kaup A, Kirby KA, Byers AL, Diaz-Arrastia R, Yaffe K. Traumatic brain injury and risk of dementia in older veterans. *Neurology.* (2014) 83:312–9. doi: 10.1212/WNL.0000000000000616
36. Sajja VSSS, Hubbard WB, Hall CS, Ghoddoussi F, Galloway MP, et al. Enduring deficits in memory and neuronal pathology after blast-induced traumatic brain injury. *Scient Rep.* (2015) 5:15075. doi: 10.1038/srep15075
37. Antunes M, Biala G. The novel object recognition memory: neurobiology, test procedure, its modifications. *Cogn Process.* (2012) 13:93–110. doi: 10.1007/s10339-011-0430-z
38. Cohen SJ, Stackman RW Jr. Assessing rodent hippocampal involvement in the novel object recognition task. A review. *Behav Brain Res.* (2015) 285:105–17. doi: 10.1016/j.bbr.2014.08.002
39. Vorhees CV, Williams MT. Assessing spatial learning and memory in rodents. *ILAR J.* (2014) 55:310–32. doi: 10.1093/ilar/ilu013
40. Hollup SA, Molden S, Donnett JG, Moser MB, Moser EI. Accumulation of hippocampal place fields at the goal location in an annular watermaze task. *J Neurosci.* (2001) 21:1635–44. doi: 10.1523/JNEUROSCI.21-05-01635.2001
41. Logue SF, Paylor R, Wehner JM. Hippocampal lesions cause learning deficits in inbred mice in the Morris water maze and conditioned-fear task. *Behav Neurosci.* (1997) 111:104–13. doi: 10.1037/0735-7044.111.1.104
42. Harrison FE, Hosseini AH, McDonald MP. Endogenous anxiety and stress responses in water maze and Barnes maze spatial memory tasks. *Behav Brain Res.* (2009) 198:247–51. doi: 10.1016/j.bbr.2008.10.015
43. Kraeuter AK, Guest PC, Sarnyai Z. The Y-maze for assessment of spatial working and reference memory in mice. *Methods Mol Biol.* (2019) 1916:105–11. doi: 10.1007/978-1-4939-8994-2_10
44. Saljo A, Svensson B, Mayorga M, Hamberger A, Bolouri H. Low-level blasts raise intracranial pressure and impair cognitive function in rats. *J Neurotrauma.* (2009) 26:1345–52. doi: 10.1089/neu.2008.0856
45. Saljo A, Bolouri H, Mayorga M, Svensson B, Hamberger A. Low-level blast raises intracranial pressure and impairs cognitive function in rats: prophylaxis with processed cereal feed. *J Neurotrauma.* (2010) 27:383–9. doi: 10.1089/neu.2009.1053
46. Budde MD, Shah A, McCrea M, Cullinan WE, Pintar FA, Stemper BD. Primary blast traumatic brain injury in the rat: relating diffusion tensor imaging and behavior. *Front Neurol.* (2013) 4:154. doi: 10.3389/fneur.2013.00154
47. Zuckerman A, Ram O, Ifergane G, Matar MA, Sagi R, Ostfeld I, et al. Controlled low-pressure blast-wave exposure causes distinct behavioral and morphological responses modelling mild traumatic brain injury, post-traumatic stress disorder, and comorbid mild traumatic brain injury-post-traumatic stress disorder. *J Neurotrauma.* (2017) 34:145–64. doi: 10.1089/neu.2015.4310
48. Stemper BD, Shah AS, Budde MD, Olsen CM, Glavaski-Joksimovic A, Kurpad SN, et al. Behavioral outcomes differ between rotational acceleration and blast mechanisms of mild traumatic brain injury. *Front Neurol.* (2016) 7:31. doi: 10.3389/fneur.2016.00031
49. Hall AA, Mendoza MI, Zhou H, Shaughness M, Maudlin-Jeronimo E, McCarron RM, et al. Repeated low intensity blast exposure is associated with damaged endothelial glycocalyx and downstream behavioral deficits. *Front Behav Neurosci.* (2017) 11:104. doi: 10.3389/fnbeh.2017.00104
50. Elder GA, Dorr NP, De Gasperi R, Gama Sosa MA, Shaughness MC, Maudlin-Jeronimo E, et al. Blast exposure induces post-traumatic stress disorder-related traits in a rat model of mild traumatic brain injury. *J Neurotrauma.* (2012) 29:2564–75. doi: 10.1089/neu.2012.2510
51. Tompkins P, Tesiram Y, Lerner M, Gonzalez LP, Lightfoot S, Rabb CH, et al. Brain injury: neuro-inflammation, cognitive deficit, and magnetic resonance imaging in a model of blast induced traumatic brain injury. *J Neurotrauma.* (2013) 30:1888–97. doi: 10.1089/neu.2012.2674
52. Ning YL, Yang N, Chen X, Zhao ZA, Zhang XZ, Chen XY, et al. Chronic caffeine exposure attenuates blast-induced memory deficit in mice. *Chin J Traumatol.* (2015) 18:204–11. doi: 10.1016/j.cjtee.2015.10.003
53. Ouyang J, Pace E, Lepczyk L, Kaufman M, Zhang J, Perrine SA, et al. Blast-induced tinnitus and elevated central auditory and limbic activity in rats: a manganese-enhanced MRI and behavioral study. *Sci Rep.* (2017) 7:4852. doi: 10.1038/s41598-017-04941-w
54. Lucke-Wold BP, Logsdon AF, Turner RC, Huber JD, Rosen CL. Endoplasmic reticulum stress modulation as a target for ameliorating effects of blast induced traumatic brain injury. *J Neurotrauma.* (2017) 34:S62–S70. doi: 10.1089/neu.2016.4680
55. Yin TC, Voorhees JR, Genova RM, Davis KC, Madison AM, Britt JK, et al. Acute axonal degeneration drives development of cognitive, motor, and visual deficits after blast-mediated traumatic brain injury in mice. *eNeuro.* (2016) 3. doi: 10.1523/ENEURO.0220-16.2016
56. Kovesdi E, Kamnaksh A, Wingo D, Ahmed F, Grunberg NE, Long JB, et al. Acute minocycline treatment mitigates the symptoms of mild blast-induced traumatic brain injury. *Front Neurol.* (2012) 3:111. doi: 10.3389/fneur.2012.00111
57. Kovesdi E, Gyorgy AB, Kwon SK, Wingo DL, Kamnaksh A, Long JB, et al. The effect of enriched environment on the outcome of traumatic brain injury; a behavioral, proteomics, histological study. *Front Neurosci.* (2011) 5:42. doi: 10.3389/fnins.2011.00042
58. Song H, Konan LM, Cui J, Johnson CE, Langenderfer M, Grant D, et al. Ultrastructural brain abnormalities and associated behavioral changes in mice after low-intensity blast exposure. *Behav Brain Res.* (2018) 347:148–57. doi: 10.1016/j.bbr.2018.03.007
59. Tweedie D, Rachmany L, Rubovitch V, Zhang Y, Becker KG, Perez E, et al. Changes in mouse cognition and hippocampal gene expression observed in a mild physical- and blast-traumatic brain injury. *Neurobiol Dis.* (2013) 54:1–11. doi: 10.1016/j.nbd.2013.02.006
60. Tweedie D, Rachmany L, Rubovitch V, Li Y, Holloway HW, Lehrmann E, et al. Blast traumatic brain injury-induced cognitive deficits are attenuated by preinjury or postinjury treatment with the glucagon-like peptide-1 receptor agonist, exendin-4. *Alzheimers Dement.* (2016) 12:34–48. doi: 10.1016/j.jalz.2015.07.489
61. Cho HJ, Sajja VS, Vandevord PJ, Lee YW. Blast induces oxidative stress, inflammation, neuronal loss and subsequent short-term memory impairment in rats. *Neuroscience.* (2013) 253:9–20. doi: 10.1016/j.neuroscience.2013.08.037
62. Perez-Garcia G, De Gasperi R, Gama Sosa MA, Perez GM, Otero-Pagan A, Tschiffely A, et al. PTSD-related behavioral traits in a rat model of blast-induced mTBI are reversed by the mGluR2/3 receptor antagonist BCI-838. *eNeuro.* (2018) 5. doi: 10.1523/ENEURO.0357-17.2018
63. Baalman KL, Cotton RJ, Rasband SN, Rasband MN. Blast wave exposure impairs memory and decreases axon initial segment length. *J Neurotr.* (2013) 30:741–51. doi: 10.1089/neu.2012.2478
64. Sajja VS, Perrine SA, Ghoddoussi F, Hall CS, Galloway MP, VandeVord PJ. Blast neurotrauma impairs working memory and disrupts prefrontal myo-inositol levels in rats. *Mol Cell Neurosci.* (2014) 59:119–26. doi: 10.1016/j.mcn.2014.02.004

65. Perez-Garcia G, Gama Sosa MA, De Gasperi R, Lashof-Sullivan M, Maudlin-Jeronimo E, Stone JR, et al. Chronic post-traumatic stress disorder-related traits in a rat model of low-level blast exposure. *Behav Brain Res.* (2018) 340:117–25. doi: 10.1016/j.bbr.2016.09.061
66. Beamer M, Tummala SR, Gullotti D, Kopil C, Gorka S, Ted A, et al. Primary blast injury causes cognitive impairments and hippocampal circuit alterations. *Exp Neurol.* (2016) 283(Pt A):16–28. doi: 10.1016/j.expneurol.2016.05.025
67. Muelbl MJ, Slaker ML, Shah AS, Nawarawong NN, Gerndt CH, Budde MD, et al. Effects of mild blast traumatic brain injury on cognitive- and addiction-related behaviors. *Sci Rep.* (2018) 8:9941. doi: 10.1038/s41598-018-28062-0
68. Collen J, Orr N, Lettieri CJ, Carter K, Holley AB. Sleep disturbances among soldiers with combat-related traumatic brain injury. *Chest.* (2012) 142:622–30. doi: 10.1378/chest.11-1603
69. Rosenfeld JV, Ford NL. Bomb blast, mild traumatic brain injury and psychiatric morbidity: a review. *Injury.* (2010) 41:437–43. doi: 10.1016/j.injury.2009.11.018
70. Fann JR, Hart T, Schomer KG. Treatment for depression after traumatic brain injury: a systematic review. *J Neurotr.* (2009) 26:2383–402. doi: 10.1089/neu.2009.1091
71. Rosenthal M, Christensen BK, Ross TP. Depression following traumatic brain injury. *Arch Phys Med Rehabil.* (1998) 79:90–103. doi: 10.1016/S0003-9993(98)90215-5
72. Can A, Dao DT, Arad M, Terrillion CE, Piantadosi SC, Gould TD. The mouse forced swim test. *JoVE*. (2012) 2012:e3638. doi: 10.3791/3638
73. Slattery DA, Cryan JF. Using the rat forced swim test to assess antidepressant-like activity in rodents. *Nat Protoc.* (2012) 7:1009–14. doi: 10.1038/nprot.2012.044
74. Yankelevitch-Yahav R, Franko M, Huly A, Doron R. The forced swim test as a model of depressive-like behavior. *J Vis Exp*. (2015) 52587. doi: 10.3791/52587
75. Steimer T, Animal models of anxiety disorders in rats and mice: some conceptual issues. *Dialog Clin Neurosci.* (2011) 13:495–506.
76. Hale MW, Hay-Schmidt A, Mikkelsen JD, Poulsen B, Shekhar A, Lowry CA. Exposure to an open-field arena increases c-Fos expression in a distributed anxiety-related system projecting to the basolateral amygdaloid complex. *Neuroscience.* (2008) 155:659–72. doi: 10.1016/j.neuroscience.2008.05.054
77. Gray JA. Précis of The neuropsychology of anxiety: an enquiry into the functions of the septo-hippocampal system. *Behav Brain Sci*. (1982) 5:469–84. doi: 10.1017/S0140525X00013066
78. Duncan GE, Knapp DJ, Breese GR. Neuroanatomical characterization of Fos induction in rat behavioral models of anxiety. *Brain Res.* (1996) 713:79–91. doi: 10.1016/0006-8993(95)01486-1
79. Campbell BM, Merchant KM. Serotonin 2C receptors within the basolateral amygdala induce acute fear-like responses in an open-field environment. *Brain Res.* (2003) 993:1–9. doi: 10.1016/S0006-8993(03)03384-5
80. Abrams JK, Johnson PL, Hay-Schmidt A, Mikkelsen JD, Shekhar A, Lowry CA. Serotonergic systems associated with arousal and vigilance behaviors following administration of anxiogenic drugs. *Neuroscience.* (2005) 133:983–97. doi: 10.1016/j.neuroscience.2005.03.025
81. Divani AA, Murphy AJ, Meints J, Sadeghi-Bazargani H, Nordberg J, Monga M, et al. A novel preclinical model of moderate primary blast-induced traumatic brain injury. *J Neurotrauma.* (2015) 32:1109–16. doi: 10.1089/neu.2014.3686
82. Kamnaksh A, Kovesdi E, Kwon SK, Wingo D, Ahmed F, Grunberg NE, et al. Factors affecting blast traumatic brain injury. *J Neurotrauma.* (2011) 28:2145–53. doi: 10.1089/neu.2011.1983
83. Russell AL, Handa RJ, Wu TJ. Sex-dependent effects of mild blast-induced traumatic brain injury on corticotropin-releasing factor receptor gene expression: potential link to anxiety-like behaviors. *Neuroscience.* (2018) 392:1–12. doi: 10.1016/j.neuroscience.2018.09.014
84. Statz JK, Ciarlone SL, Goodrich JA, McCarron RM, Walker PB, Norris JN, et al. Affective profiling for anxiety-like behavior in a rodent model of mTBI. *Behav Brain Res.* (2019) 368:111895. doi: 10.1016/j.bbr.2019.04.009
85. Huang E, Ngo M, Yee S, Held L, Norman K, Scremin AM, et al. Repeated blast exposure alters open field behavior recorded under low illumination. *Brain Res.* (2013) 1529:125–33. doi: 10.1016/j.brainres.2013.06.042
86. Park E, Eisen R, Kinio A, Baker AJ. Electrophysiological white matter dysfunction and association with neurobehavioral deficits following low-level primary blast trauma. *Neurobiol Dis.* (2013) 52:150–9. doi: 10.1016/j.nbd.2012.12.002
87. Hubbard WB, Lashof-Sullivan M, Greenberg S, Norris C, Eck J, Lavik E, et al. Hemostatic nanoparticles increase survival, mitigate neuropathology and alleviate anxiety in a rodent blast trauma model. *Sci Rep.* (2018) 8:10622. doi: 10.1038/s41598-018-28848-2
88. Kawa L, Arborelius UP, Yoshitake T, Kehr J, Hokfelt T, Risling M, et al. Neurotransmitter systems in a mild blast traumatic brain injury model: catecholamines and serotonin. *J Neurotrauma.* (2015) 32:1190–9. doi: 10.1089/neu.2014.3669
89. Sajja VSSS, Hubbard WB, VandeVord PJ. Subacute oxidative stress and glial reactivity in the amygdala are associated with increased anxiety following blast neurotrauma. *Shock (Augusta, Ga.).* (2015) 44 (Suppl. 1):71–8. doi: 10.1097/SHK.0000000000000311
90. Walf AA, Frye CA. The use of the elevated plus maze as an assay of anxiety-related behavior in rodents. *Nat Prot.* (2007) 2:322–8. doi: 10.1038/nprot.2007.44
91. Gould TD, Dao DT, Kovacsics CE. *The Open Field Test, in Mood and Anxiety Related Phenotypes in Mice.* New York, NY: Springer. (2009). p. 1–20. doi: 10.1007/978-1-60761-303-9_1
92. Seibenhener ML, Wooten MC. Use of the Open Field Maze to measure locomotor and anxiety-like behavior in mice. *J Vis Exp*. (2015) 2015:e52434. doi: 10.3791/52434
93. Bourin M, Hascoet M. The mouse light/dark box test. *Eur J Pharmacol.* (2003) 463:55–65. doi: 10.1016/S0014-2999(03)01274-3
94. Chen Y, Huang W. Non-impact, blast-induced mild TBI and PTSD: concepts and caveats. *Brain Inj.* (2011) 25:641–50. doi: 10.3109/02699052.2011.580313
95. Bryant R, Post-traumatic stress disorder vs traumatic brain injury. *Dialogues Clin Neurosci.* (2011) 13:251–62.
96. Sinz EH, Kochanek PM, Dixon CE, R.Clark SB, Carcillo JA, Schiding JK, et al. Inducible nitric oxide synthase is an endogenous neuroprotectant after traumatic brain injury in rats and mice. *J Clin Invest.* (1999) 104:647–56. doi: 10.1172/JCI6670
97. McAllister TW, Neurobiological consequences of traumatic brain injury. *Dialogues Clin Neurosci.* (2011) 13:287–300. doi: 10.1176/appi.books.9781585624201.js15
98. Schneiderman AI, Braver ER, Kang HK. Understanding sequelae of injury mechanisms and mild traumatic brain injury incurred during the conflicts in Iraq and Afghanistan: persistent postconcussive symptoms and posttraumatic stress disorder. *Am J Epidemiol.* (2008) 167:1446–52. doi: 10.1093/aje/kwn068
99. Curzon P, Rustay NR, Browman KE. Cued and contextual fear conditioning for rodents. In: Buccafusco JJ, editor. *Methods of Behavior Analysis in Neuroscience. Chapter 2.* Boca Raton, FL: CRC Press/Taylor & Francis (2009).
100. Genovese RF, Simmons LP, Ahlers ST, Maudlin-Jeronimo E, Dave JR, Boutte AM. Effect of mild TBI from repeated blast overpressure on the expression and extinction of conditioned fear in rats. *Neuroscience.* (2013) 254:120–9. doi: 10.1016/j.neuroscience.2013.09.021
101. Gattu R, Akin FW, Cacace AT, Hall CD, Murnane OD, Haacke EM. Vestibular, balance, microvascular and white matter neuroimaging characteristics of blast injuries and mild traumatic brain injury: Four case reports. *Brain Inj.* (2016) 30:1501–14. doi: 10.1080/02699052.2016.1219056
102. Akin FW, Murnane OD. Head injury and blast exposure: vestibular consequences. *Otolaryngol Clin North Am.* (2011) 44:323–34, viii. doi: 10.1016/j.otc.2011.01.005
103. Vanderploeg RD, Curtiss G, Luis CA, Salazar AM. Long-term morbidities following self-reported mild traumatic brain injury. *J Clin Exp Neuropsychol.* (2007) 29:585–98. doi: 10.1080/13803390600826587
104. Wares JR, Hoke KW, Walker W, Franke LM, Cifu DX, Carne W, et al. Characterizing effects of mild traumatic brain injury and posttraumatic stress disorder on balance impairments in blast-exposed servicemembers and Veterans using computerized posturography. *J Rehabil Res Dev.* (2015) 52:591–603. doi: 10.1682/JRRD.2014.08.0197
105. Rodriguez UA, Zeng Y, Deyo D, Parsley MA, Hawkins BE, Prough DS, et al. Effects of mild blast traumatic brain injury on cerebral vascular,

histopathological, and behavioral outcomes in rats. *J Neurotrauma.* (2018) 35:375–92. doi: 10.1089/neu.2017.5256
106. Turner RC, Naser ZJ, Logsdon AF, DiPasquale KH, Jackson GJ, Robson MJ, et al. Modeling clinically relevant blast parameters based on scaling principles produces functional & histological deficits in rats. *Exp Neurol.* (2013) 248:520–9. doi: 10.1016/j.expneurol.2013.07.008
107. Wang Y, Wei YL, Oguntayo S, Wilkins W, Arun P, Valiyaveettil M, et al. Tightly coupled repetitive blast-induced traumatic brain injury: development and characterization in mice. *J Neurotr.* (2011) 28:2171–83. doi: 10.1089/neu.2011.1990
108. Hamm RJ, Pike BR, O'Dell DM, Lyeth BG, Jenkins LW. The rotarod test: an evaluation of its effectiveness in assessing motor deficits following traumatic brain injury. *J Neurotr.* (1994) 11:187–96. doi: 10.1089/neu.1994.11.187
109. Dunham NW, Miya TS. A note on a simple apparatus for detecting neurological deficit in rats and mice. *J Am Pharm Assoc Am Pharm Assoc.* (1957) 46:208–9. doi: 10.1002/jps.3030460322
110. Pearl J, Stander H, McKean DB. Effects of analgesics and other drugs on mice in phenylquinone and rotarod tests. *J Pharmacol Exp Ther.* (1969) 167:9–13.
111. Buitrago MM, Schulz JB, Dichgans J, Luft AR. Short and long-term motor skill learning in an accelerated rotarod training paradigm. *Neurobiol Learn Mem.* (2004) 81:211–6. doi: 10.1016/j.nlm.2004.01.001
112. Scott D, Saatman KE. *Cognitive and Motor Function Assessments in Rodent Models of Traumatic Brain Injury, in Pre-Clinical and Clinical Methods in Brain Trauma Research*. Springer. (2018). p. 139–54. doi: 10.1007/978-1-4939-8564-7_9
113. Mizoguchi K, Yuzurihara M, Ishige A, Sasaki H, Tabira T. Chronic stress impairs rotarod performance in rats: implications for depressive state. *Pharmacol Biochem Behav.* (2002) 71:79–84. doi: 10.1016/S0091-3057(01)00636-0
114. Metz GA, Whishaw IQ. The ladder rung walking task: a scoring system and its practical application. *J Vis Exp.* (2009) 1204. doi: 10.3791/1204
115. Yurgil KA, Clifford RE, Risbrough VB, Geyer MA, Huang M, Barkauskas DA, et al. Prospective associations between traumatic brain injury and postdeployment tinnitus in active-duty marines. *J Head Trauma Rehabil.* (2016) 31:30–9. doi: 10.1097/HTR.0000000000000117
116. Clifford RE, Baker D, Risbrough VB, Huang M, Yurgil KA. Impact of TBI, PTSD, and hearing loss on tinnitus progression in a US marine cohort. *Mil Med.* (2019) 184:839–46. doi: 10.1093/milmed/usz016
117. Swan AA, Nelson JT, Swiger B, Jaramillo CA, Eapen BC, Packer M, et al. Prevalence of hearing loss and tinnitus in Iraq and Afghanistan Veterans: A Chronic Effects of Neurotrauma Consortium study. *Hear Res.* (2017) 349:4–12. doi: 10.1016/j.heares.2017.01.013
118. Oleksiak M, Smith BM, St Andre JR, Caughlan CM, Steiner M. Audiological issues and hearing loss among Veterans with mild traumatic brain injury. *J Rehabil Res Dev.* (2012) 49:995–1004. doi: 10.1682/JRRD.2011.01.0001
119. Koch M, Schnitzler HU. The acoustic startle response in rats–circuits mediating evocation, inhibition and potentiation. *Behav Brain Res.* (1997) 89:35–49. doi: 10.1016/S0166-4328(97)02296-1
120. Fitch RH, Threlkeld SW, McClure MM, Peiffer AM. Use of a modified prepulse inhibition paradigm to assess complex auditory discrimination in rodents. *Brain Res Bull.* (2008) 76:1–7. doi: 10.1016/j.brainresbull.2007.07.013
121. Davis M, Gendelman DS, Tischler MD, Gendelman PM. A primary acoustic startle circuit: lesion and stimulation studies. *J Neurosci.* (1982) 2:791–805. doi: 10.1523/JNEUROSCI.02-06-00791.1982
122. Krase W, Koch M, Schnitzler HU. Glutamate antagonists in the reticular formation reduce the acoustic startle response. *Neuroreport.* (1993) 4:13–6. doi: 10.1097/00001756-199301000-00003
123. Koch M, Lingenhohl K, Pilz PK. Loss of the acoustic startle response following neurotoxic lesions of the caudal pontine reticular formation: possible role of giant neurons. *Neuroscience.* (1992) 49:617–25. doi: 10.1016/0306-4522(92)90231-P
124. Valsamis B, Schmid S. Habituation and prepulse inhibition of acoustic startle in rodents. *J Vis Exp.* (2011) 2011:e3446. doi: 10.3791/3446
125. Galazyuk A, Hebert S. Gap-prepulse inhibition of the acoustic startle Reflex (GPIAS) for tinnitus assessment: current status and future directions. *Front Neurol.* (2015) 6:88. doi: 10.3389/fneur.2015.00088
126. Campolo J, Lobarinas E, Salvi R. Does tinnitus "fill in" the silent gaps? *Noise Health.* (2013) 15:398–405. doi: 10.4103/1463-1741.121232
127. Fournier P, Hebert S. Gap detection deficits in humans with tinnitus as assessed with the acoustic startle paradigm: does tinnitus fill in the gap? *Hear Res.* (2013) 295:16–23. doi: 10.1016/j.heares.2012.05.011
128. Mahmood G, Mei Z, Hojjat H, Pace E, Kallakuri S, Zhang JS. Therapeutic effect of sildenafil on blast-induced tinnitus and auditory impairment. *Neuroscience.* (2014) 269:367–82. doi: 10.1016/j.neuroscience.2014.03.020
129. Luo H, Pace E, Zhang XG, Zhang JS. Blast-induced tinnitus and spontaneous firing changes in the rat dorsal cochlear nucleus. *J Neurosc Res.* (2014) 92:1466–77. doi: 10.1002/jnr.23424
130. Mao JC, Pace E, Pierozynski P, Kou Z, Shen Y, VandeVord P, et al. Blast-induced tinnitus and hearing loss in rats: behavioral and imaging assays. *J Neurotrauma.* (2012) 29:430–44. doi: 10.1089/neu.2011.1934
131. Miyamoto M, Shintani M, Nagaoka A, Nagawa Y. Lesioning of the rat basal forebrain leads to memory impairments in passive and active avoidance tasks. *Brain Res.* (1985) 328:97–104. doi: 10.1016/0006-8993(85)91327-7
132. Pickens CL, Navarre BM, Nair SG. Incubation of conditioned fear in the conditioned suppression model in rats: role of food-restriction conditions, length of conditioned stimulus, generality to conditioned freezing. *Neuroscience.* (2010) 169:1501–10. doi: 10.1016/j.neuroscience.2010.06.036
133. McDannald MA. Contributions of the amygdala central nucleus and ventrolateral periaqueductal grey to freezing and instrumental suppression in Pavlovian fear conditioning. *Behav Brain Res.* (2010) 211:111–7. doi: 10.1016/j.bbr.2010.03.020
134. Amorapanth P, Nader K, LeDoux JE. Lesions of periaqueductal gray dissociate-conditioned freezing from conditioned suppression behavior in rats. *Learn Mem.* (1999) 6:491–9. doi: 10.1101/lm.6.5.491

Conflict of Interest: The authors declare that the research was conducted in the absence of any commercial or financial relationships that could be construed as a potential conflict of interest.

Copyright © 2020 Aravind, Ravula, Chandra and Pfister. This is an open-access article distributed under the terms of the Creative Commons Attribution License (CC BY). The use, distribution or reproduction in other forums is permitted, provided the original author(s) and the copyright owner(s) are credited and that the original publication in this journal is cited, in accordance with accepted academic practice. No use, distribution or reproduction is permitted which does not comply with these terms.

Appendix A –Publication Cover #2
2020

Authors: E. Alay, M. Skotak, S, Chandrasekaran, J. Ziner, N. Chandra

Title: *"Variations of Constitutive Properties of the Fluid Elicit Divergent Vibrational and Pressure Response Under Shock Wave Loading"*

Journal Publication: Journal of Biomechanical Engineering, (2020), [20-2]

Journal of Biomechanical Engineering. Received July 17, 2019;
Accepted manuscript posted July 20, 2020. doi:10.1115/1.4047841
Copyright (c) 2020 by ASME

Check for updates

Variations in constitutive properties of the fluid elicit divergent vibrational and pressure response under shock wave loading

Eren Alay[1#], Maciej Skotak[1,2#*], Subhalakshmi Chandrasekeran[1], Jonathan Ziner[1], and Namas Chandra[1*]

[1]Department of Biomedical Engineering, New Jersey Institute of Technology, Newark, NJ 07102-1982, USA

[2]current address: Blast Induced Neurotrauma, Walter Reed Army Institute of Research, Silver Spring, MD 20910

[#] EA and MS are joint primary authors

[*] Correspondence should be addressed to Drs. Maciej Skotak and Namas Chandra, Department of Biomedical Engineering, New Jersey Institute of Technology, Newark, NJ 07102-1982, USA. Telephone: +1 973-596-6080, Fax: +1 973-596-5222, E-mail: maciej.skotak@njit.edu, namas.chandra@njit.edu

Keywords: shock wave, shock tube, blast overpressure, reflected pressure, wavelet transform, time series analysis

Downloaded from https://asmedigitalcollection.asme.org/biomechanical/article-pdf/doi/10.1115/1.4047841/6550945/bio-19-1359.pdf by New Jersey Institute Of Technology user on 21 July 2020

Journal of Biomechanical Engineering. Received July 17, 2019;
Accepted manuscript posted July 20, 2020. doi:10.1115/1.4047841
Copyright (c) 2020 by ASME

Abstract

We performed a characterization of the shock wave loading on the response of the specimen representing a simplified head model. A polycarbonate cylinder (2-inch outer diameter, wall thickness: 0.06 or 0.12-inch) was filled with two fluids: pure deionized water and 40% glycerol in water, which differ only slightly in their constitutive material properties. These two fluids were selected to represent the CSF and cerebral blood, using their high strain rate viscosity as a primary selection criterion. The model specimen was exposed to a single shock wave with two nominal intensities: 70 and 130 kPa overpressure. The response of the model was measured using three strain gauges and three pressure sensors, one mounted on the front face of the cylinder and two embedded in the cylinder to measure the pressure inside of the fluid.

We noted several discriminant characteristics in the collected data, which indicate that the type of fluid is strongly influencing the response. The vibrations of the cylinder walls are strongly correlated with the fluid kind. The similarity analysis via the Pearson coefficient indicated that the pressure waveforms in the fluid are only moderately correlated, and these results were further corroborated by Euclidean distance analysis. Continuous wavelet transform of pressure waveforms revealed that the frequency response is strongly correlated with the properties of the fluid. The observed differences in strain and pressure modalities stem from relatively small differences in the properties of the fluids employed in this study.

Downloaded from https://asmedigitalcollection.asme.org/biomechanical/article-pdf/doi/10.1115/1.4047841/6550945/bio-19-1359.pdf by New Jersey Institute Of Technology user on 21 July 2020

Journal of Biomechanical Engineering. Received July 17, 2019;
Accepted manuscript posted July 20, 2020. doi:10.1115/1.4047841
Copyright (c) 2020 by ASME

1. Introduction

The mechanistic aspects of blast traumatic brain injury (bTBI) remain elusive despite decades of research, invigorated in the last two decades by the large number of mild traumatic brain injury TBI (mTBI) cases among veterans returning from the active war zones [1, 2]. The primary blast injuries are caused by shock wave propagation into the brain, and several mechanisms (direct transmission, acceleration, thoracic surge, skull flexures, and cavitation), have been proposed as responsible for the mechanical tissue injury [1]. In the controlled laboratory environment, the evaluation of the biomechanical loading imposed by the shock wave is typically achieved via measurements of surface and intracranial pressure, as well as surface (skull) strain [3]. Depending on the model size of the specimen, a single (for rodents) [3-5], or multiple (for a large animal, cadaveric specimen, or human phantom models) sensors are used [6-9]. The complexity of the recorded waveforms usually increases with the increase in size and the shape complexity of the specimen. For rodents, the recorded intracranial pressure (ICP) waveforms resemble the incident shock wave, irrespectively of the location of the sensing element within the brain parenchyma [10]. For large animal [11, 12], or human head surrogates, the ICP signal is characterized by a highly complex waveform with multiple peaks and periodic pressure fluctuations [7, 13, 14]. There is also substantial heterogeneity in the pressure waveform depending on the location of the sensor. One of the discriminating factors for large animal and human ICP under blast exposure is also a presence of the negative phase, which might induce cavitation [11, 15, 16]. Experimental methods offer only limited insight into the deformation of the brain, tissue strain levels, and shear and stress wave propagation and their spatiotemporal development. This kind of detail can only be accurately determined using numerical methods [17]. However, efforts to reproduce experimental measures using numerical models are hindered by the selection of suitable material models and availability

Downloaded from https://asmedigitalcollection.asme.org/biomechanical/article-pdf/doi/10.1115/1.4047841/6550945/bio-19-1359.pdf by New Jersey Institute Of Technology user on 21 July 2020

Journal of Biomechanical Engineering. Received July 17, 2019;
Accepted manuscript posted July 20, 2020. doi:10.1115/1.4047841
Copyright (c) 2020 by ASME

of constitutive properties of the brain [18, 19]. Especially the experimental characterization of the properties of the brain in a wide range of frequencies is a challenging task, owing to the variability of the brain properties between species and other hard to control variables like brain freshness, or simply improvements in the measurement methodology (see the discussion and fig. 3 in ref. [20] for details).

Accurate values for material properties of the anatomical brain structures are necessary to develop reliable numerical models [21]. We performed a parametric study on how the values of bulk and shear moduli affect the ICP and maximum principal strain measured in two locations and using experimental data as a benchmark [21]. Both, the time-independent (linear elastic [22], Ogden hyperelastic [23]) and time-dependent (one- and three-term Prony series [24]) mathematical models of the brain material properties were used in this evaluation. We noted that the ICP and strain were correlated with the long-term bulk and shear moduli ($p < 0.0001$), with an 80 MPa effective bulk modulus value matching best with experimental measurements. However, considering only ICP can be measured experimentally, there are no existing methods to directly measure tissue strain and stress levels with a high temporal and spatial resolution at high loading rates associated with shock wave loading. Thus, the alternative experimental measurements supporting the validation of numerical models are necessary [18]. An obvious choice to fill this need is a skull strain measurement, which is straightforward and can be implemented into an experimental design with relative ease [8, 13]. Alternatively, models with simplified geometry and material properties can be used to study the response of the structure under high loading rates for validation, but a full potential of these is yet to be realized.

In this contribution, we demonstrate that two fluids with relatively small differences in their constitutive properties induce significant differences in the strain and pressure response when

Downloaded from https://asmedigitalcollection.asme.org/biomechanical/article-pdf/doi/10.1115/1.4047841/6550945/bio-19-1359.pdf by New Jersey Institute Of Technology user on 21 July 2020

Journal of Biomechanical Engineering. Received July 17, 2019;
Accepted manuscript posted July 20, 2020. doi:10.1115/1.4047841
Copyright (c) 2020 by ASME

subjected to different intensity shock wave loading. Relatively small differences in the material properties of the fluid inside polycarbonate container elicit a different vibrational response of the polycarbonate shell in our simplified head model. It, in turn, creates significant differences in the pressure profiles measured inside of the fluid in two locations. The rudimentary quantification of the pressure waveforms characteristics is not sufficient to account for observed changes, and we applied advanced similarity time series and time-frequency analytical techniques to discern the differences.

2. Experimental

2.1 The shock tube

The 9-inch, square cross-section shock tube located at the Center for Injury Biomechanics, Materials and Medicine (New Jersey Institute of Technology) was used in this work to generate shock waves. The device consists of four principal components: 1) breech with adjustable volume, 2) transition section with variable geometry, 3) the 6 m long test section, with laminated glass windows to facilitate high-speed video monitoring of the specimen during tests, and 4) reflector end-plate. The shock tube was comprehensively described and characterized in previous publications [25-28]. In this study, the specimen was placed in the observation deck in a freely moving configuration. We used compressed helium (99.999%, Airgas, Oakland, NJ) as the driver gas and circular Mylar membranes (Grafix, Cleveland, OH) of various thickness arrangements to generate a single planar shock wave with two nominal discrete peak overpressures of 70 and 130 kPa in the test section. All tests were conducted at normal temperature and pressure.

2.2 Specimen preparation, instrumentation, pressure and strain measurements

Downloaded from https://asmedigitalcollection.asme.org/biomechanical/article-pdf/doi/10.1115/1.4047841/6550945/bio-19-1359.pdf by New Jersey Institute Of Technology user on 21 July 2020

Journal of Biomechanical Engineering. Received July 17, 2019;
Accepted manuscript posted July 20, 2020. doi:10.1115/1.4047841
Copyright (c) 2020 by ASME

A transparent polycarbonate (PC) cylinder with 2-inches outer diameter and the height of 7-inches is used to typify the skull in this simplified head surrogate. The acoustic impedance of polycarbonate and skull have similar values, and thus, polycarbonate has been chosen as the representative material of the skull [29]. Two different uniform wall thicknesses (0.06" and 0.12") were selected. The cylinder is cut to a size of 7 inches to fit it in between the railings of the slider plates inside the test section of the shock tube (fig. 1A). The slider plates are designed with the stopper screws inside of the rails for the stationary and moving (in the direction of the shock front propagation) cylinder test scenarios. The cylinder is capped on either end using polycarbonate caps to prevent any fluid leakage during shock loading. The PC cylinder was instrumented with two XCL-100 series miniature leadless pressure transducers (Kulite Semiconductor Products, Inc., Leonia, NJ), one LE-125 series thin line surface pressure transducer (Kulite Semiconductor Products, Inc., Leonia, NJ) and three pre-wired, 350 Ω single-axis strain gages (OMEGA Engineering). The two XCL-100 sensors were positioned parallel facing the shock wave to measure transmitted pressure inside the fluid-filled cylinder. The LE-125 surface pressure sensor was mounted on the front wall of the cylinder using the same facing direction with other pressure transducers to measure the reflected pressure. Single-axis strain gauges are positioned along the mid-horizontal plane of the PC cylinder and mounted on the three sides: front, back, and left side in 90º intervals to measure the strain reflecting the deformation of the cylinder under shock loading conditions (fig. 1). All pressure transducer and strain gage leads were routed through the backside of the cylinder and bundled with electrical tape.

The incident overpressure of the shock waves was measured using a high-frequency pressure transducer model 134A24 (PCB Piezotronics, Inc., Depew, NY), which was located 106-inches away from the breech and 9-inches ahead of the PC cylinder. Distribution of the incident pressure

Downloaded from https://asmedigitalcollection.asme.org/biomechanical/article-pdf/doi/10.1115/1.4047841/6550945/bio-19-1359.pdf by New Jersey Institute Of Technology user on 21 July 2020

Journal of Biomechanical Engineering. Received July 17, 2019;
Accepted manuscript posted July 20, 2020. doi:10.1115/1.4047841
Copyright (c) 2020 by ASME

sensor locations along the shock tube and detailed information about the measurement presented in previous work [30].

Pressure waveforms were acquired using NI PXIe-6366 DAQ device at 1 MHz sampling rate, while the strain measurements were recorded at 50 kHz via NI 9237 simultaneous bridge module mounted in the cDAQ-9188 chassis. The PC cylinder was filled with two different fluids: 1) deionized (DI) water, and 2) 40% (v/v) glycerol in deionized water solution. These two biofluids with different properties are used to simulate central nervous system components, the cerebrospinal fluid (CSF), and blood. Deionized (DI) water is used to simulate the CSF as the properties of these compounds, density, sound velocity, and acoustic impedance, match closely (Table 1). Similarly, the selection of blood surrogate was also made using these criteria. The replication of the properties of the complex biofluid like the blood using a mixture of pure fluids is more challenging. Thus, we also included the viscosity in the surrogate fluid inclusion criteria since it can be easily measured in the laboratory. The viscosity of different solutions of glycerol in water (10%-40% v/v range) was measured at room temperature and compared with the literature (Table 1). The viscosity of glycerol in water is not a linear function [31], and for further testing, the 40% glycerol-water solution was selected, because, at room temperature, it closely matches the viscosity of blood at body temperature (3.2 mPa·s) at rates above 100 s^{-1} [32-34].

2.3 Experimental design and statistical analysis

The study was comprised of three experimental variables 1) shock wave intensity at two levels: 70 and 130 kPa (n = 2), 2) the type of fluid, deionized water, and 40% glycerol in deionized water solution (n = 2), and 3) wall thickness of the PC cylinder, 0.06" and 0.12" (n = 2). The experiments were repeated four times (n = 4) with each combination of the experimental variables for a total number of 32 tests (N = 2 x 2 x 2 x 4 = 32).

Downloaded from https://asmedigitalcollection.asme.org/biomechanical/article-pdf/doi/10.1115/1.4047841/6550945/bio-19-1359.pdf by New Jersey Institute Of Technology user on 21 July 2020

Journal of Biomechanical Engineering. Received July 17, 2019;
Accepted manuscript posted July 20, 2020. doi:10.1115/1.4047841
Copyright (c) 2020 by ASME

2.4 Data analysis

Before analysis, the pressure data from the sensors mounted on the cylinder (denoted as reflected, bottom, and top in fig. 1) were averaged and normalized in the time domain (fig. 2). The onset of the reflected pressure increase was used as a reference, and we used 100 data points before, and 20000 data points after the rise of reflected pressure for further analysis. The total number of 20100 samples was used, which corresponds to the 20.1 ms time window. The strain gauge data didn't require any specific pre-processing, and the entire 50 ms time window was considered for the analysis.

2.4.1 Time-domain analysis

The quantification of the basic characteristic parameters for all pressure and strain waveforms, peak overpressure and peak strain, and the impulse (integral of the pressure in the time domain) were performed using Origin 2017 software (OriginLab Corp., Northampton, MA), and the data are presented in figure 3. The amplitude values for three strain gauges were quantified and compared between different experimental conditions (fig. 4).

Several data mining methods utilizing tools written in Python 3.7.1 programming language were used for the comparison of the complex pressure-time series and to reveal the existing relationships (correlation and similarity) within the experimental data recorded by the reflected pressure sensor and the two sensors embedded in the cylinder.

2.4.2 Pearson correlation

The Pearson correlation test was conducted using pressure data obtained from cylinder mounted sensors (fig. 5). The Pearson's coefficient, r, was used as a measure of the correlation strength

Downloaded from https://asmedigitalcollection.asme.org/biomechanical/article-pdf/doi/10.1115/1.4047841/6550945/bio-19-1359.pdf by New Jersey Institute Of Technology user on 21 July 2020

Journal of Biomechanical Engineering. Received July 17, 2019;
Accepted manuscript posted July 20, 2020. doi:10.1115/1.4047841
Copyright (c) 2020 by ASME

between complex pressure waveforms normalized in the time domain and was computed using the following formula:

$$r = \rho(x, \mathrm{y}) = \frac{\sum(x_i - \overline{x})\,(y_i - \overline{y})}{\sqrt{\sum(x_i - \overline{x})^2 \sum(y_i - \overline{y})^2}} \quad (1)$$

The Pearson coefficient values range from -1 to 1, and negative values indicate a negative correlation between variables, i.e., the values in one dataset decrease, while the values of the other one increase). The positive r value means that there is a positive correlation between variables, and the two datasets closely match each other. The closer the r-value is to 1, the closer two data sets match each other or are strongly correlated. We used a "corr" function, which is a part of the pandas open-source Python programming language library, https://pandas.pydata.org/) to compute a pairwise correlation. To visualize the Pearson's correlation coefficients, we used a "heatmap" function from a seaborn library (https://seaborn.pydata.org/).

2.4.3 Euclidean distance

Euclidean distance between the corresponding data points of the two datasets was calculated using equation (2), and based on these calculations; the distance matrix was created (fig. 6). This distance metric used to calculate the distance between two data points on a plane. It is implemented explicitly using the mathematical formula stated in equation 2.

$$d(T, S) = \sqrt{\sum_{i=1}^{n} (T_i - S_i)^2} \quad (2)$$

2.4.4 Cluster analysis

Downloaded from https://asmedigitalcollection.asme.org/biomechanical/article-pdf/doi/10.1115/1.4047841/6550945/bio-19-1359.pdf by New Jersey Institute Of Technology user on 21 July 2020

Journal of Biomechanical Engineering. Received July 17, 2019;
Accepted manuscript posted July 20, 2020. doi:10.1115/1.4047841
Copyright (c) 2020 by ASME

Cluster analysis was also conducted using the "cluster map" function available in the seaborn library. The output of this analysis is a tree diagram called a dendrogram, which is combined with a corresponding heat map (fig. 7). The horizontal axis outlines the clusters generated using the Euclidean distance metric, which uses normalized pressure data, i.e., in each data set, the minimum value was identified, subtracted, and divided by the maximum value. The z-axis of the dendrogram delineates how (dis)similar the clusters are or how far the distance between the clusters.

2.5 Frequency domain analysis (Fourier Transform)

The pressure and strain time-series signal were transformed into the frequency domain using the built-in Fast-Fourier Transform (FFT) module in the Origin 2017 software. Eminent frequency components embedded in the data were extracted. The amplitude and peak frequencies of the bands identified in the signal were quantified tabulated and analyzed (fig. 4).

2.6 Time-frequency analysis (Wavelet transform)

We performed a continuous wavelet transform (CWT) to decompose pressure signals into time and frequency using MATLAB. The transform is performed at 1 MHz sampling frequency using a 'bump' analytic wavelet. Scalograms of the pressure magnitude as a function of time and frequency for all averaged pressure-time profiles are generated and exported as the TIFF images (fig. 9, and figures S4-S8 in the Supporting information).

Subsequently, all 24 scalogram images are used in the image (dis)similarity analysis. In the first step, the mean squared error (MSE) is computed using the following mathematical formula (Eqn. 3):

Downloaded from https://asmedigitalcollection.asme.org/biomechanical/article-pdf/doi/10.1115/1.4047841/6550945/bio-19-1359.pdf by New Jersey Institute Of Technology user on 21 July 2020

Journal of Biomechanical Engineering. Received July 17, 2019;
Accepted manuscript posted July 20, 2020. doi:10.1115/1.4047841
Copyright (c) 2020 by ASME

$$d_{MSE} = \frac{1}{n \times m} \sum_{i=0}^{m-1} \sum_{j=0}^{n-1} [I(i,j) - K(i,j)]^2 \quad (3)$$

Then, the distance and histogram specific functions are applied to the images utilizing SciPy, a Python-based ecosystem, and OpenCV, an open-source computer vision and machine learning software that can support Python, respectively. The heatmap illustrating results of the CWT images analysis (fig. 9), was obtained using modified code snippets [35, 36].

3. Results and Discussion

The polycarbonate cylinder instrumented with three pressure sensors and three strain gauges (fig. 1) was exposed to a single shock wave with two nominal intensities, 70 and 130 kPa [29]. We tested the effect of the fluid (deionized water and 40% glycerol in water) on the vibrational characteristics of the PC (measured as strain in three locations, fig. 1B) and pressure variation inside of the cylinder (measured in two locations inside of the cylinder, fig. 1B). The example of the raw experimental pressure and strain data are presented in figures 1C and 1D, respectively.

It is worth to set the stage for further discussion and presentation of the data, with a paragraph of general remarks. Most of the presented analysis revolves around the vibrational response of the system. The vibrating cylinder walls (a relaxation upon the initial shock wave impact) are the source of the extended pressure fluctuations inside of the cylinder. In the absence of vibrations of the cylinder wall the attenuation of the pressure due to the acoustic impedance would be a decisive factor. If this mechanism were true, we'd expect to see an attenuated pressure profile resembling the incident shock wave profile. However, it is not what we have observed in any of our experiments. There are no signs of decay in both wall thickness configurations resembling incident

Downloaded from https://asmedigitalcollection.asme.org/biomechanical/article-pdf/doi/10.1115/1.4047841/6550945/bio-19-1359.pdf by New Jersey Institute Of Technology user on 21 July 2020

Journal of Biomechanical Engineering. Received July 17, 2019;
Accepted manuscript posted July 20, 2020. doi:10.1115/1.4047841
Copyright (c) 2020 by ASME

shock wave decay. On the contrary, the pressure pulses extend for approx. 20 ms (fig. 2), that is 4 times longer than the duration of the shock wave.

3.1 Pressure data analysis

The representative pressure profiles recorded by the incident, cylinder mounted (reflected, top and bottom) sensors are presented in fig. 2. The raw pressure traces are average and standard deviation of four repetitions for the PC cylinder with two wall thicknesses: 0.06" (fig. 2A) and 0.12" (fig. 2B). It is evident that the incident and reflected pressures (two top panels in fig. 3A and 3B) are highly repeatable, i.e., characterized by narrow standard deviation values. On the other hand, a higher degree of variability is apparent in the pressure traces recorded by both sensors measuring the pressure inside of the cylinder (two bottom panels in fig. 2).

The quantification of the characteristics of the recorded pressure signals, peak overpressure and impulse, revealed that the exposure conditions are highly repeatable (fig. 3). There are no statistically significant differences reported by the incident and reflected pressure sensors for both peak overpressure and impulse. Similar to results observed by our group and others, the peak overpressure and impulse scale with shock wave intensity [5, 37]. However, the peak overpressure and impulse values obtained for the sensors reporting pressure inside of the cylinder revealed that this kind of analysis applied to complex waveforms is not sensitive to determine the differences between various combinations of shell thickness, fluid type, and exposure intensity. The majority of the observed differences are caused by negative pressure fluctuations (fig. 3).

3.2 Strain data analysis

The time-domain analysis of strain measurements gives more detailed insight into the response of the PC cylinder under the shock loading compared to pressure data. The front and back strain

Downloaded from https://asmedigitalcollection.asme.org/biomechanical/article-pdf/doi/10.1115/1.4047841/6550945/bio-19-1359.pdf by New Jersey Institute Of Technology user on 21 July 2020

Journal of Biomechanical Engineering. Received July 17, 2019;
Accepted manuscript posted July 20, 2020. doi:10.1115/1.4047841
Copyright (c) 2020 by ASME

gauges report initially negative strain, while side strain gauge reports positive strain. It indicates in the initial phase of shock wave loading, the front and back of the cylinder are under compressive, while the side is in under tensile loading. The PC shell oscillations are gradually extinguished and last for approx. 20 milliseconds (dig. 4A). We quantified the peak amplitude values, and these are proportional to the nominal shock wave intensity and wall thickness (fig. 4B). At higher shock wave intensity, the strain amplitudes are higher, and increasing the wall thickness decreases the amplitudes for the front gauge (cylinder wall is under compression and direct loading of the shock wave).

Interestingly, the side strain gauges, reported increased values when the thick wall cylinder was used. It can be hypothesized that the deformation of the more rigid thick-wall cylinder is more uniform than its thin wall counterpart, and this effect is responsible for the observed strain increase. The type of the fluid inside of the cylinder doesn't seem to have any measurable effect on the peak strain.

The frequency-domain analysis of the strain waveforms revealed there are four main bands in the signal (fig. 4C), and these frequencies roughly correspond to the 1^{st} (420 Hz), 2^{nd} (840 Hz), 4^{th} (1720 Hz) and 6^{th} (2500 Hz, for 0.06-inch wall thickness), or 8^{th} (3400 Hz, for 0.12-inch wall thickness) harmonics. We performed the peak frequencies quantification in the FFT spectra, and this analysis revealed that the type of fluid is strongly influencing the vibrational response of the cylinder (fig. 4D). The largest number of frequency differences were noted for the second (~800 Hz) and the fourth (2.5-3.5 kHz) bands. For the same shell thickness water filling results in a higher vibrational frequencies, as reported by all three strain gauges, e.g., 840 Hz (water) vs. 800 Hz (40% glycerol), 825 Hz (water) vs. 790 Hz (40% glycerol), and 840 Hz (water) vs. 800 Hz (40% glycerol) for FRONT, SIDE, and BACK gauges, respectively (fig. 4D, 0.06-inch wall thickness).

Downloaded from https://asmedigitalcollection.asme.org/biomechanical/article-pdf/doi/10.1115/1.4047841/6550945/bio-19-1359.pdf by New Jersey Institute Of Technology user on 21 July 2020

Journal of Biomechanical Engineering. Received July 17, 2019;
Accepted manuscript posted July 20, 2020. doi:10.1115/1.4047841
Copyright (c) 2020 by ASME

Similar effects are also observed in the other three frequency bands. Moreover, with increasing wall thickness, there is a noticeable frequency downshift from 800 Hz towards 600 Hz for the second component. However, the opposite trend is observed for the fourth frequency band, where increasing the wall thickness increases the vibration frequency from 2.5 kHz to 3.6 kHz.

The analysis of the strain FFT spectra indicates that the maxima of the first two bands (420 and 840 Hz) for the thin-wall have much higher amplitudes compared to thick-wall tests. The amplitude of the second band is a dominant feature of all spectra irrespectively of the wall thickness (except 70 kPa thin cylinder side strain measurements). These results underline that shock loading imposed on the thin wall cylinder causes more substantial (higher amplitude) vibrations in the low-frequency range. For the thick-wall cylinder, the lower amplitude-higher frequency is a preferred vibrational mode, which is well illustrated by the higher amplitude values for bands in the 4^{th} harmonics frequency range (1700-1800 Hz), which become more prominent at 130 kPa (fig. S1B).

3.3 Timeseries data analysis

The raw pressure time-series data (Fig. 2) are complex and typical for surrogate models [8]. The complexity of the signal makes basic quantification of the peak pressure and impulse less sensitive as discriminant metrics between different experimental groups [38]. We decided to resort to a few data mining methods to extract the similarity information from the time series data collected at various experimental conditions. Pearson correlation was computed to evaluate the strength of the correlation among pressure time-series recorded by the reflected pressure sensor, as well as the two sensors used to measure pressures inside of the cylinder. It is evident in Figure 5 only positive correlation values are present among the pressure-time profiles. The correlation coefficients above 0.89 for all the reflected pressure time profiles suggest that all these pressure-time profiles are

Downloaded from https://asmedigitalcollection.asme.org/biomechanical/article-pdf/doi/10.1115/1.4047841/6550945/bio-19-1359.pdf by New Jersey Institute Of Technology user on 21 July 2020

Journal of Biomechanical Engineering. Received July 17, 2019;
Accepted manuscript posted July 20, 2020. doi:10.1115/1.4047841
Copyright (c) 2020 by ASME

highly correlated. The first step in the data processing to calculate the correlations is normalization, which results in highly correlated ($r > 0.89$) reflected pressure groups for both 70 and 130 kPa, i.e., despite these two have very different magnitudes. It means the algorithm compares the temporal fluctuation of the normalized pressure, and that was the goal of this test.

These results also indicate that there is an excellent repeatability in our experiments. Likewise, top and bottom pressure waveforms inside fluid media among the same experimental groups are highly correlated with each other (these data are distributed on the diagonal in fig. 5). There is a relatively high correlation between thick-wall cylinder groups, marked as E-F and G-H in fig. 5 in the right bottom corner, where r varies from 0.56 to 0.79. It indicates that the response of the thick wall cylinder is similar regardless of the fluid type and shock wave intensity. However, it leaves some room for differences between these samples, as demonstrated by other analysis results (vide infra).

Somewhat weaker correlations are identified for the thin wall experiments, between groups A-B and C-D, in the upper left corner of the diagram in fig. 5, i.e., only 4 out of 6 top-bottom sensor correlation coefficients exceed 0.5. The signals recorded at 130 kPa are characterized by the highest r coefficient values (0.67 to 0.78 and belong to groups C and D). Conversely, the weakest correlations are observed between groups A-D and E-H, which indicates that the experimental profiles for the thin and thick cylinder at both nominal blast intensities possess different temporal characteristics. More importantly, the comparison between experiments where the type of fluid was the only variable, which was altered, revealed the correlations between respective pressure time-series have values below 0.8, i.e. A-B (70 kPa-0.06") = 0.38-0.52, C-D (70 kPa-0.12") = 0.67-0.78, E-F (130 kPa-0.06") = 0.72-0.79, and G-H (130 kPa-0.12") = 0.56-0.70. These results suggest that the properties of the fluid influence the modality of the pressure response.

Downloaded from https://asmedigitalcollection.asme.org/biomechanical/article-pdf/doi/10.1115/1.4047841/6550945/bio-19-1359.pdf by New Jersey Institute Of Technology user on 21 July 2020

Journal of Biomechanical Engineering. Received July 17, 2019;
Accepted manuscript posted July 20, 2020. doi:10.1115/1.4047841
Copyright (c) 2020 by ASME

Furthermore, similarity or distance measures are useful tools to compare time series and to unravel the convoluted information embedded in the signal (the 2D matrix), or image (the 3D matrix) [39-41]. For this reason, we selected the Euclidean distance, which is one of the most frequently used methods [42, 43]. With the aid of the Euclidean metric, a standardized heat map was generated to visualize the detailed structure of the pressure-time profiles (Figure 6). Unlike the Pearson correlation (fig. 5), the Euclidean distance method doesn't have the normalization term and thus compares the absolute distance differences between respective data points. It is not surprising that the reflected pressure groups (G), which had high Pearson correlation coefficients irrespectively on the shock wave intensity, in this test are separated according to the exposure conditions. For example, all test datasets which belong to the 70 kPa group have Euclidean distance values of less than 515, irrespectively of the wall thickness and fluid type (fig. 6). The same is not valid for the 130 kPa group, where the reflected pressure waveform appears to be affected by the kind of fluid and wall thickness, e.g., C-D: 1990 (G vs. W at 130 kPa, 0.06"), C-G: 1147 (W at 130 kPa, 0.06" vs 0.12"), C-H: 1293 (G vs. W at 130 kPa, 0.06" vs. 0.12"), and G-H: 481 (G vs. W at 130 kPa, 0.12").

The effect of fluid type on the Euclidean distance score can be illustrated by the comparison of respective top and bottom sensor groups at two nominal shock wave intensities (marked with red squares in fig. 6). At 70 kPa for 0.06" wall thickness (A-B groups in fig. 6) the scores are in the range of 2339-2808, while for 0.12" wall thickness, they are in the 1654 to 2300 range (E-F groups in fig. 6). At 130 kPa nominal shock wave intensity, the scores scale proportionally (2929-4153 for 0.06" and 3290-4014 for 0.12" wall thickness). It indicates the differences between pressure profiles measured inside of the cylinder using two different fluids increase with shock wave intensity irrespectively of the wall thickness. Moreover, the wall thickness effect (comparison of

Downloaded from https://asmedigitalcollection.asme.org/biomechanical/article-pdf/doi/10.1115/1.4047841/6550945/bio-19-1359.pdf by New Jersey Institute Of Technology user on 21 July 2020

Journal of Biomechanical Engineering. Received July 17, 2019;
Accepted manuscript posted July 20, 2020. doi:10.1115/1.4047841
Copyright (c) 2020 by ASME

0.06" vs. 0.12") can be evaluated using the following comparison groups. At 70 kPa for water, the scores are in the 2203-3078 range (A-E groups), while for 40% glycerol, the scores are in the 2623-3456 (B-F groups), while at 130 kPa for water, the scores are in the 4421-5922 range (C-G groups), while for 40% glycerol, the scores are in the 5102-6529 (D-H groups). It would appear that in this classification, the pressure profiles appear more dissimilar when 40% of glycerol in water was used.

The cluster analysis was performed to discover the relationships between experimental datasets collected at different conditions. The data is displayed in the form of a heat map where each row represents the time, and each column represents the normalized pressure (Figure 7). In the dendrogram on the top of the heat map, the respective experimental groups are clustered according to their hierarchy, i.e., the most similar pressure time-series are clustered first. Due to similarities of the pressure waveform profiles, all reflected pressure measurements are grouped and separated from the remaining two groups. Overall, the pressure measurements are grouped according to their 'class': the reflected pressure (R), or the wall thickness of the cylinder (denoted with -12 and -06 suffix in fig. 7).

Interestingly, irrespectively on the experimental conditions, there was no mixed-mode clustering for pressure time-series recorded by the top and bottom sensors. The closest similarity was always computed for the pressure sensors which belong to the same experimental group (denoted as T or B, for top and bottom, respectively, fig. 7). For the thin wall (0.06"), the next level of clustering was the incident pressure intensity, either 70 or 130 kPa (denoted as 70- and 130- prefix, fig. 7).

3.4 Wavelet transform

The raw average pressure data were transformed into the wavelet domain to determine the frequency distribution as a function of time at specific experimental conditions: nominal shock

Downloaded from https://asmedigitalcollection.asme.org/biomechanical/article-pdf/doi/10.1115/1.4047841/6550945/bio-19-1359.pdf by New Jersey Institute Of Technology user on 21 July 2020

Journal of Biomechanical Engineering. Received July 17, 2019;
Accepted manuscript posted July 20, 2020. doi:10.1115/1.4047841
Copyright (c) 2020 by ASME

wave intensity, fluid type, and wall thickness (fig. 8, figures S4-S8 in supporting information). We used Matlab implementation of the CWT to decompose the time domain pressure signal into time, and frequency-resolved components to gain insight into the intricate features in the data [44]. A representative CWTs for four different combinations of wall thickness and fluid type obtained at 130 kPa nominal shock wave intensity, is presented in fig. 8. The shock wave loading results in a shift towards higher frequencies for thick wall cylinder (fig. 8B, 8D), and the vibrations decay faster compared to its thin wall counterpart (fig. 8A, 8C). Specifically, the band at approx. 500 Hz is absent in the scalograms of the thick wall cylinder (fig. 8B, 8D), which is a dominant feature in the thin wall cylinder data and extends for 15 milliseconds, depending on the fluid type. Compared to a scenario when pure deionized water was used, the 40% glycerol in water results in a more complex scalogram: the band at approx. 500 Hz lasts longer (20 ms vs. 15 ms for water), and there are two additional bands that were identified at 300 Hz and 2,400 Hz (fig. 8A and 8C). Similarly, for the thick wall cylinder, there is a strong band at 750 Hz (fig. 8D), which is not present in the scalogram for pure water (fig. 8B). These characteristics were also identified in the scalograms for pressure waveforms recorded at lower shock wave intensity (70 kPa) and the top sensor (see Figures S5, S6, and S8 in the supporting information).

To distinguish differences in the CWT scalograms, the (dis)similarity analysis was performed using pixel-wise and histogram comparison via mean-squared error (MSE) metrics (fig. 9). It was done to corroborate a semi-qualitative analysis based on respective CWT scalograms. The higher the score, the more dissimilar wavelet scalograms are: it is obvious that the reflected pressure scalograms for 70 and 130 kPa are the most dissimilar (scores higher than 300, fig. 9A). Interestingly, the effect of the fluid type is demonstrated even by the sensor mounted on the outside of the cylinder and measuring the reflected pressure (red squares in fig. 9A). Similarly, the analysis

Downloaded from https://asmedigitalcollection.asme.org/biomechanical/article-pdf/doi/10.1115/1.4047841/6550945/bio-19-1359.pdf by New Jersey Institute Of Technology user on 21 July 2020

Journal of Biomechanical Engineering. Received July 17, 2019;
Accepted manuscript posted July 20, 2020. doi:10.1115/1.4047841
Copyright (c) 2020 by ASME

of scalograms for sensors reporting the pressure inside of the PC reveals the most considerable dissimilarity was computed for groups at incident shock wave of 70 and 130 kPa (e.g., D-A and D-B in fig. 9B, where the scores exceed the 50% total scale of 750). The red 2x2 squares outline the comparison of dissimilarity between test groups with different fluid type at 70 kPa: 1) B-A for 70 kPa: 173-283, 2) F-E for 70 kPa: 129-426, for wall thickness of 0.06" and 0.12", respectively, and 130 kPa: 3) D-C for 130 kPa: 288-543, and 4) H-G for 70 kPa: 270-411 for wall thickness of 0.06" and 0.12", respectively. These results, in an unbiased way, further corroborate that the fluids with constitutive properties which vary to a relatively small degree elicit a divergent vibrational response on the shell (as illustrated by reflected pressure analysis), which then translates into variable time-frequency response in the fluid.

4. Conclusions

We performed a characterization of the response of the model system to a shock wave loading. A 2-inch diameter PC cylinder with two wall thicknesses (0.06" and 0.12") was filled with two fluids: pure deionized water and 40% glycerol in water and exposed to two shock waves with nominal intensities of 70 kPa and 130 kPa. The response of the model was measured using a set of three strain gauges and three pressure sensors, one mounted on the front face of the cylinder and two embedded in the cylinder to measure the pressure inside of the fluid. The governing mechanism responsible for the pressure complexity inside of the cylinder is a relaxation of the cylinder walls upon initial impact by the shock wave. The vibrating walls act as a source of secondary pressure waves and their superposition, considering the duration of the pressure traces exceeds by a factor of five the duration of the shock wave (approx. 20 ms for the TOP and BOTTOM sensors vs 4 ms for the incident shock wave, fig. 2). The extended duration of the internal pressure alone suggests that other mechanisms (e.g., direct transmission) are less likely to explain experimental data.

Downloaded from https://asmedigitalcollection.asme.org/biomechanical/article-pdf/doi/10.1115/1.4047841/6550945/bio-19-1359.pdf by New Jersey Institute Of Technology user on 21 July 2020

Journal of Biomechanical Engineering. Received July 17, 2019;
Accepted manuscript posted July 20, 2020. doi:10.1115/1.4047841
Copyright (c) 2020 by ASME

We noted several discriminant characteristics in the collected data: the frequency of the second harmonic band in the strain signal (700-900 Hz, a dominant band in the spectrum) is strongly correlated with the type of fluid. In general, the liquid with higher acoustic impedance (40% glycerol) results in a decreased vibrational frequency, compared to water. The Pearson correlation analysis indicated that the pressure waveforms in the cylinder under shock wave loading are only moderately correlated and that the properties of the fluid influence the modality of the pressure response. These results were further corroborated by Euclidean distance analysis. Using continuous wavelet transform on pressure waveforms, we identified that the frequency response is strongly correlated with the properties of the fluid in the cylinder. It is noteworthy to underline, the observed differences in pressure modality stem from relatively small differences in the constitutive properties of the two fluids employed in this study.

5. Acknowledgments

This work was supported by the Office of Naval Research award number N00014-15-1-2637.

Downloaded from https://asmedigitalcollection.asme.org/biomechanical/article-pdf/doi/10.1115/1.4047841/6550945/bio-19-1359.pdf by New Jersey Institute Of Technology user on 21 July 2020

Journal of Biomechanical Engineering. Received July 17, 2019;
Accepted manuscript posted July 20, 2020. doi:10.1115/1.4047841
Copyright (c) 2020 by ASME

Table 1 Properties of the biological tissues and fluids, and their respective surrogates used in the study. The viscosity of glycerol in water solutions was measured at 20 ºC.

Material	Density, $kg \cdot m^{-3}$	Speed of sound, $m \cdot s^{-1}$	Acoustic impedance $kg \cdot m^{-2} \cdot s^{-1} \times 10^6$	Viscosity, mPa·s
CSF[a]	995	1510	1.50	1.00
Water	1000	1450	1.45	1.00
Blood[b]	1060	1570	1.61	3.20
10% glycerol in water[c]	1050 (1022.1)	1575	1.40	1.30 (1.31)
20% glycerol in water[c]	1100 (1046.9)	1615	1.60	1.94 (1.76)
40% glycerol in water[c]	1125 (1099.3)	1730	1.90	3.80 (3.72)
Skull[d]	1710	2250	3.85	–
Polycarbonate	1197	2286	2.74	–

a) Taken from ref. [45]

b) See Table 1 in ref. [46]

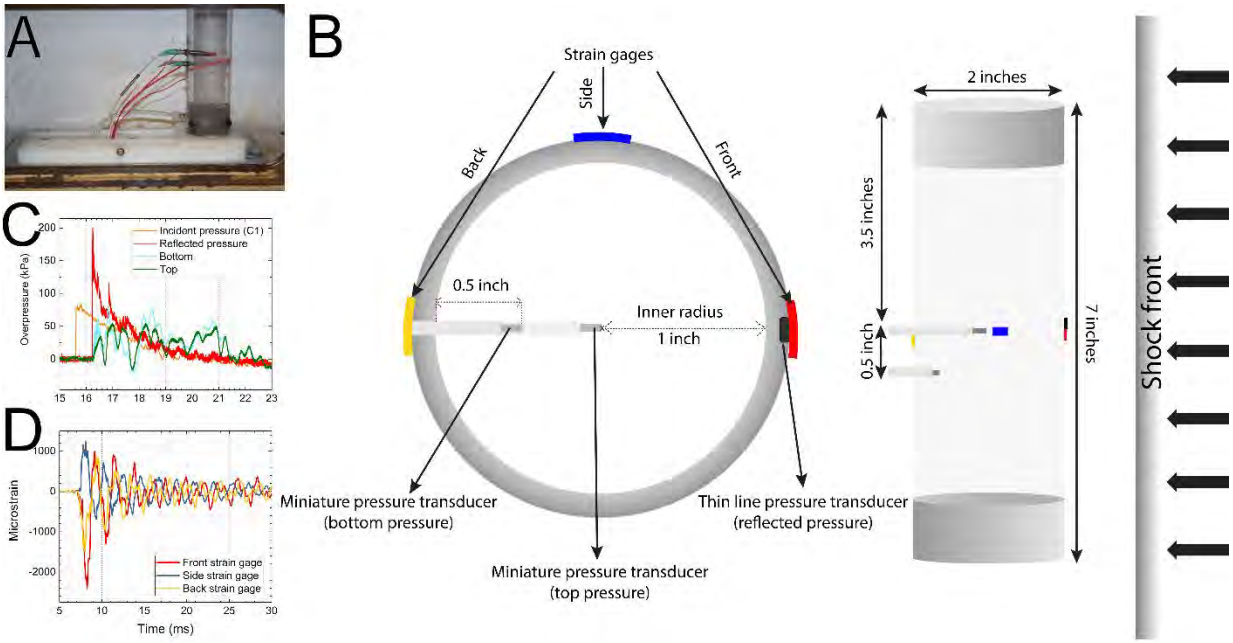
c) See figure 7 and table 1 in the ref. [47]. In parentheses values taken from ref. [31].

d) Taken from ref. [48]

Downloaded from https://asmedigitalcollection.asme.org/biomechanical/article-pdf/doi/10.1115/1.4047841/6550945/bio-19-1359.pdf by New Jersey Institute Of Technology user on 21 July 2020

Journal of Biomechanical Engineering. Received July 17, 2019;
Accepted manuscript posted July 20, 2020. doi:10.1115/1.4047841
Copyright (c) 2020 by ASME

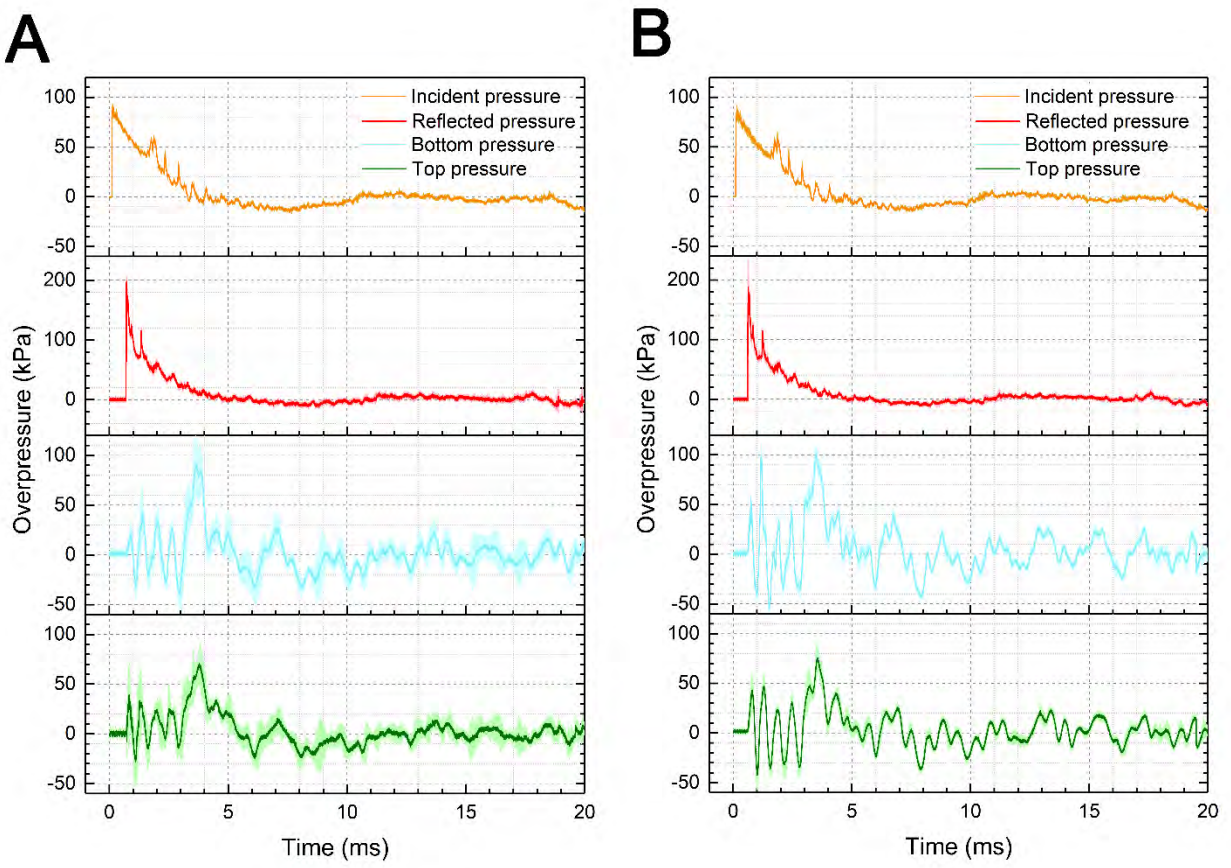
Figure 1 Representative image of the instrumented polycarbonate cylinder mounted inside the shock tube (A). The schematic of the cylinder instrumentation (B): the top and side view illustrate the location of the pressure sensors and strain gauges with respect to the direction of the shock wave propagation. Representative pressure-time (C) and strain (D) profiles are presented.



Downloaded from https://asmedigitalcollection.asme.org/biomechanical/article-pdf/doi/10.1115/1.4047841/6550945/bio-19-1359.pdf by New Jersey Institute Of Technology user on 21 July 2020

Journal of Biomechanical Engineering. Received July 17, 2019;
Accepted manuscript posted July 20, 2020. doi:10.1115/1.4047841
Copyright (c) 2020 by ASME

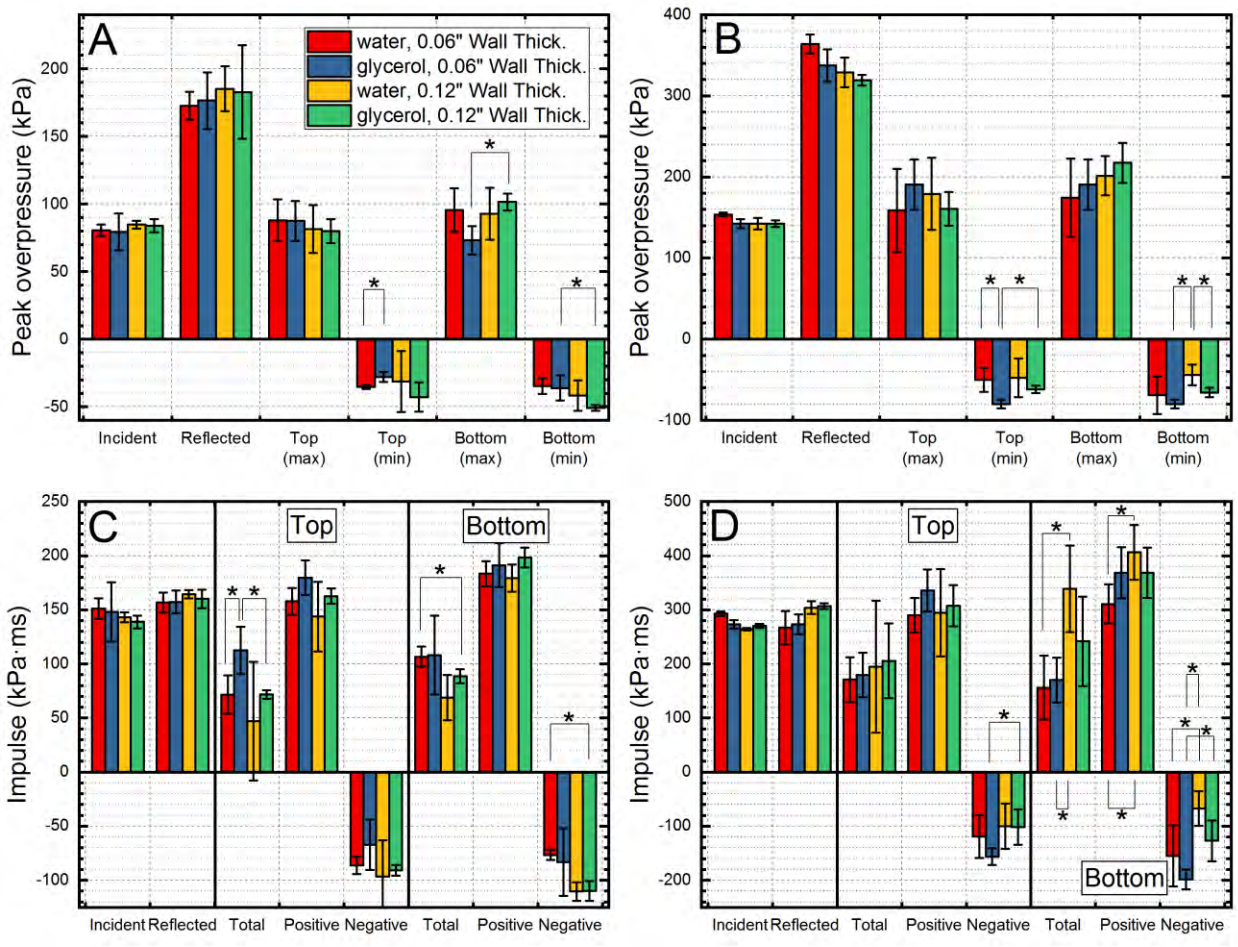
Figure 2 Representative pressure-time profiles recorded using a PC cylinder with 0.12" wall thickness and exposed to the shock wave with a nominal intensity of 70 kPa overpressure. The waveforms reported by the incident, reflected, bottom and top sensors are presented for the cylinder filled with: A) deionized water, and B) 40% glycerol in water solution. Data are normalized in the time domain and presented as an average and standard deviation.



Downloaded from https://asmedigitalcollection.asme.org/biomechanical/article-pdf/doi/10.1115/1.4047841/6550945/bio-19-1359.pdf by New Jersey Institute Of Technology user on 21 July 2020

Journal of Biomechanical Engineering. Received July 17, 2019;
Accepted manuscript posted July 20, 2020. doi:10.1115/1.4047841
Copyright (c) 2020 by ASME

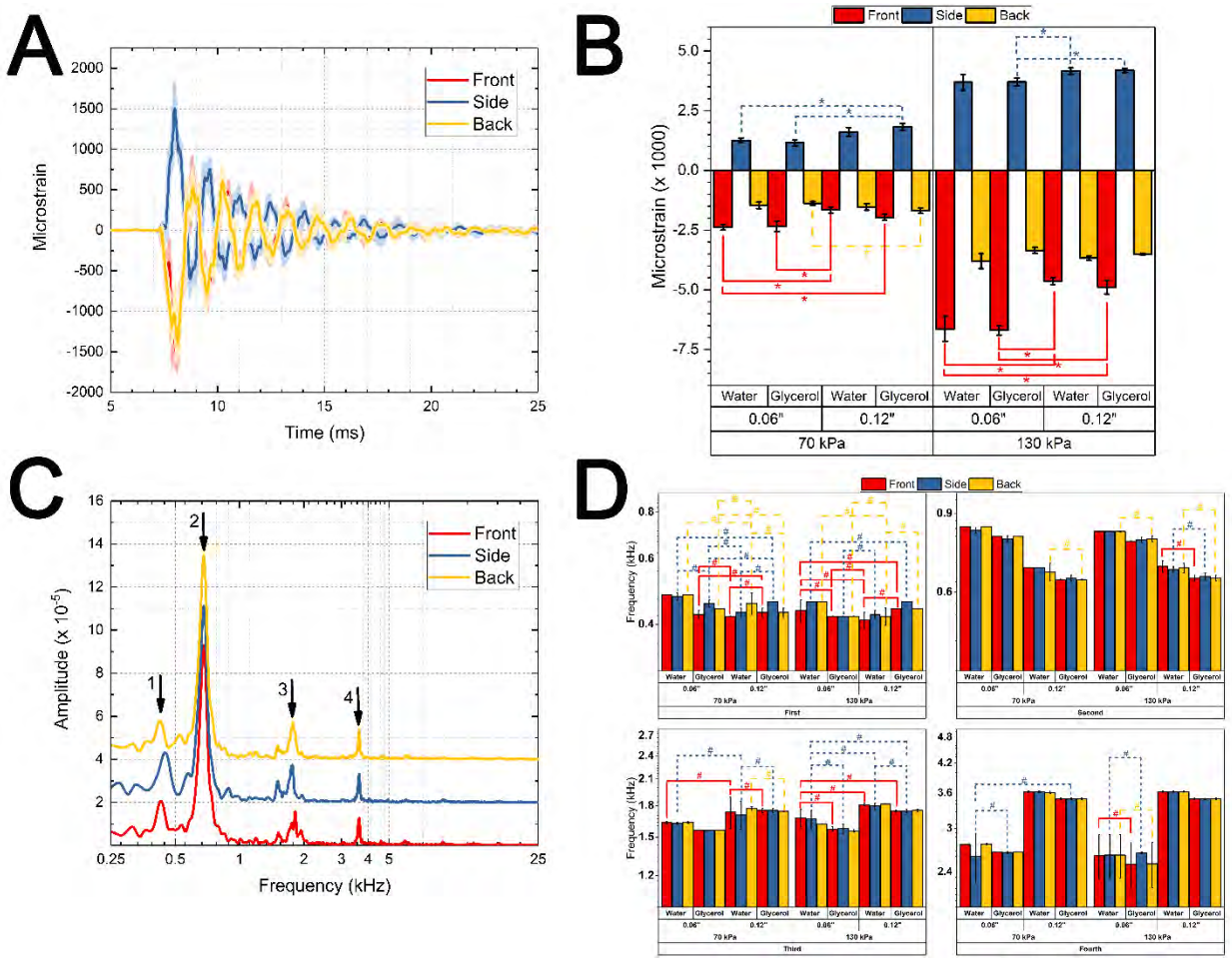
Figure 3 The quantification of the pressure waveform characteristics: the peak overpressure (A, C) and impulse (B, D) for exposures at nominal shock wave intensities of 70 kPa (A, B) and 130 kPa (C, D). The data for the incident, reflected, top, and bottom sensors are presented. Pairs marked with an asterisk indicate $p < 0.05$.



Downloaded from https://asmedigitalcollection.asme.org/biomechanical/article-pdf/doi/10.1115/1.4047841/6550945/bio-19-1359.pdf by New Jersey Institute Of Technology user on 21 July 2020

Journal of Biomechanical Engineering. Received July 17, 2019;
Accepted manuscript posted July 20, 2020. doi:10.1115/1.4047841
Copyright (c) 2020 by ASME

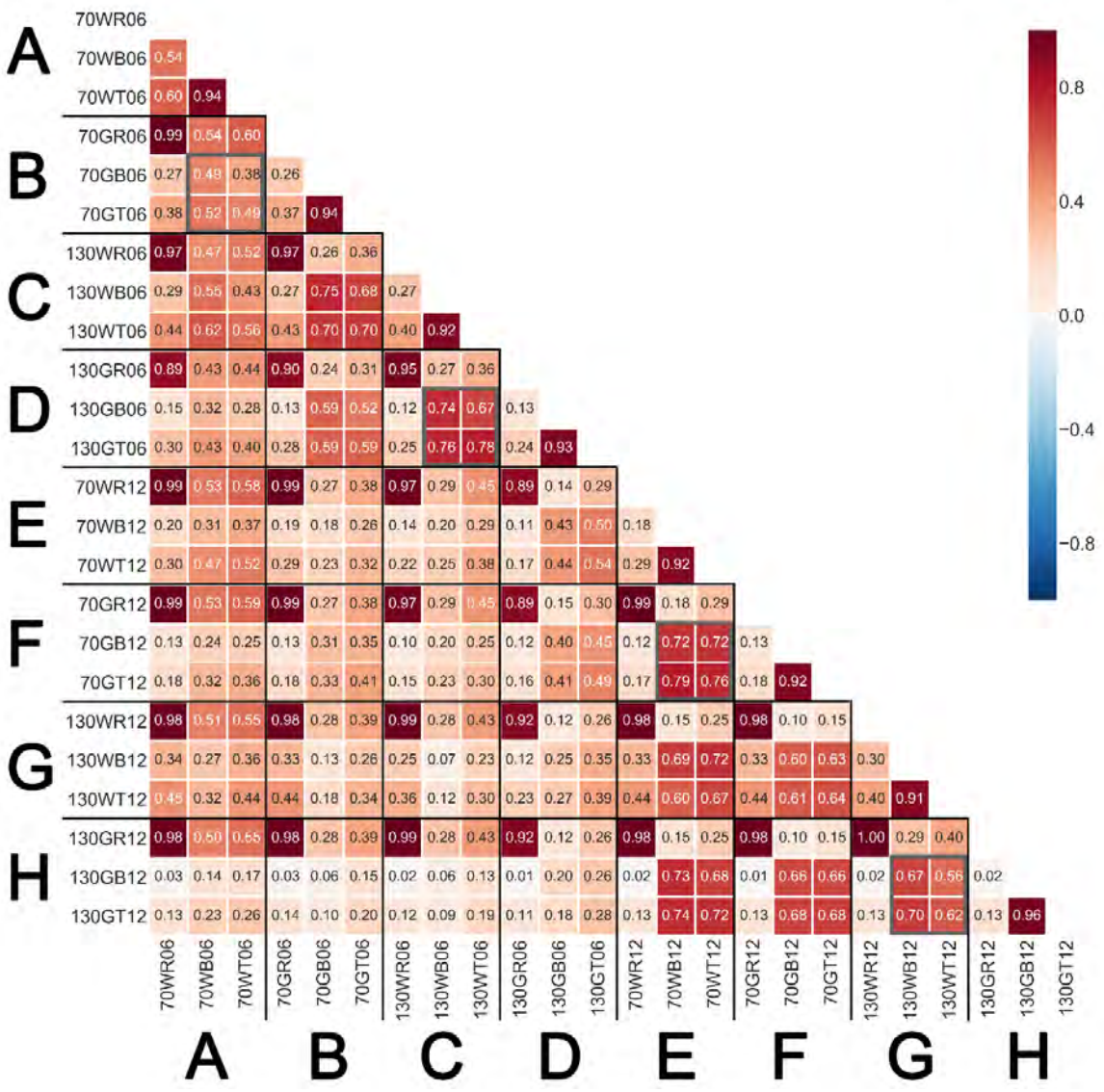
Figure 4 The analysis of the strain gauge signals: A) Representative average profiles recorded by three strain gauges (70 kPa, 0.12" wall thickness, 40% glycerol), B) the quantification of the peak strain, C) representative FFT spectrum of the strain gauge signal indicating four major frequency bands, and D) quantification of the peak frequencies extracted from the strain gauge FFT spectra (n = 4). Data are presented as mean ± standard deviation. The asterisk (*) in B indicates groups where statistical significance was established ($p < 0.00625$) while the hashtag (#) in D indicates groups where a threshold of statistical significance was not met ($p > 0.00625$).



Downloaded from https://asmedigitalcollection.asme.org/biomechanical/article-pdf/doi/10.1115/1.4047841/6550945/bio-19-1359.pdf by New Jersey Institute Of Technology user on 21 July 2020

Journal of Biomechanical Engineering. Received July 17, 2019;
Accepted manuscript posted July 20, 2020. doi:10.1115/1.4047841
Copyright (c) 2020 by ASME

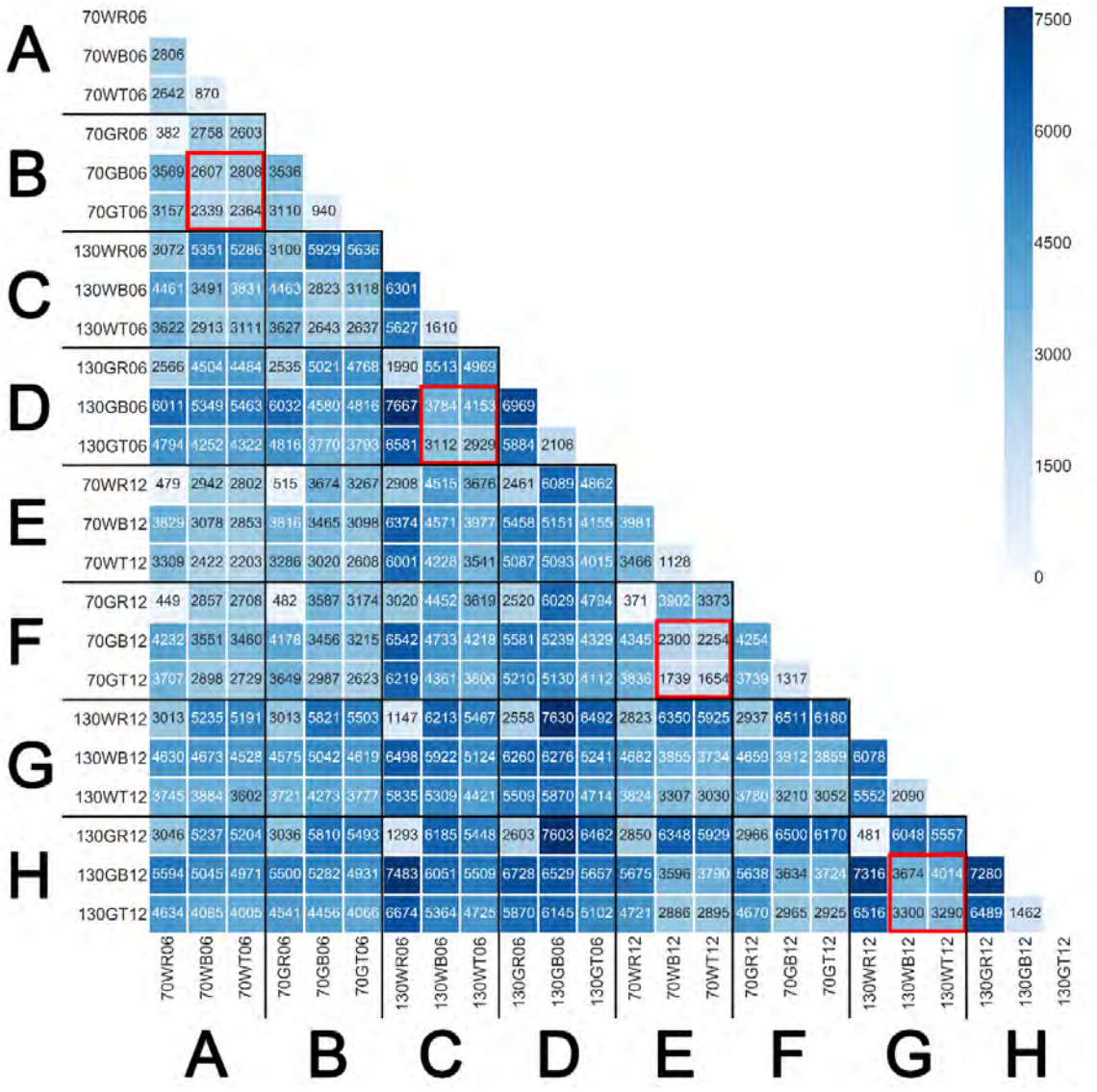
Figure 5 The heat map of Pearson's correlation coefficients between three variables: the averaged reflected (R), bottom (B), and top (T) pressure waveforms acquired at 70 and 130 kPa nominal shock wave intensities (denoted as 70 and 130) for both cylinder wall thicknesses (denoted as 06 and 12, for 0.06-inch and 0.12-inch wall thickness, respectively), and two types of fluids: water (W) and 40% glycerol in water (G). The data are grouped using wall thickness and shock wave intensity as the two primary factors. The 2x2 grey squares outline the correlation coefficients between the top and bottom pressure sensors only for group comparison between two fluids used in these experiments.



Downloaded from https://asmedigitalcollection.asme.org/biomechanical/article-pdf/doi/10.1115/1.4047841/6550945/bio-19-1359.pdf by New Jersey Institute Of Technology user on 21 July 2020

Journal of Biomechanical Engineering. Received July 17, 2019;
Accepted manuscript posted July 20, 2020. doi:10.1115/1.4047841
Copyright (c) 2020 by ASME

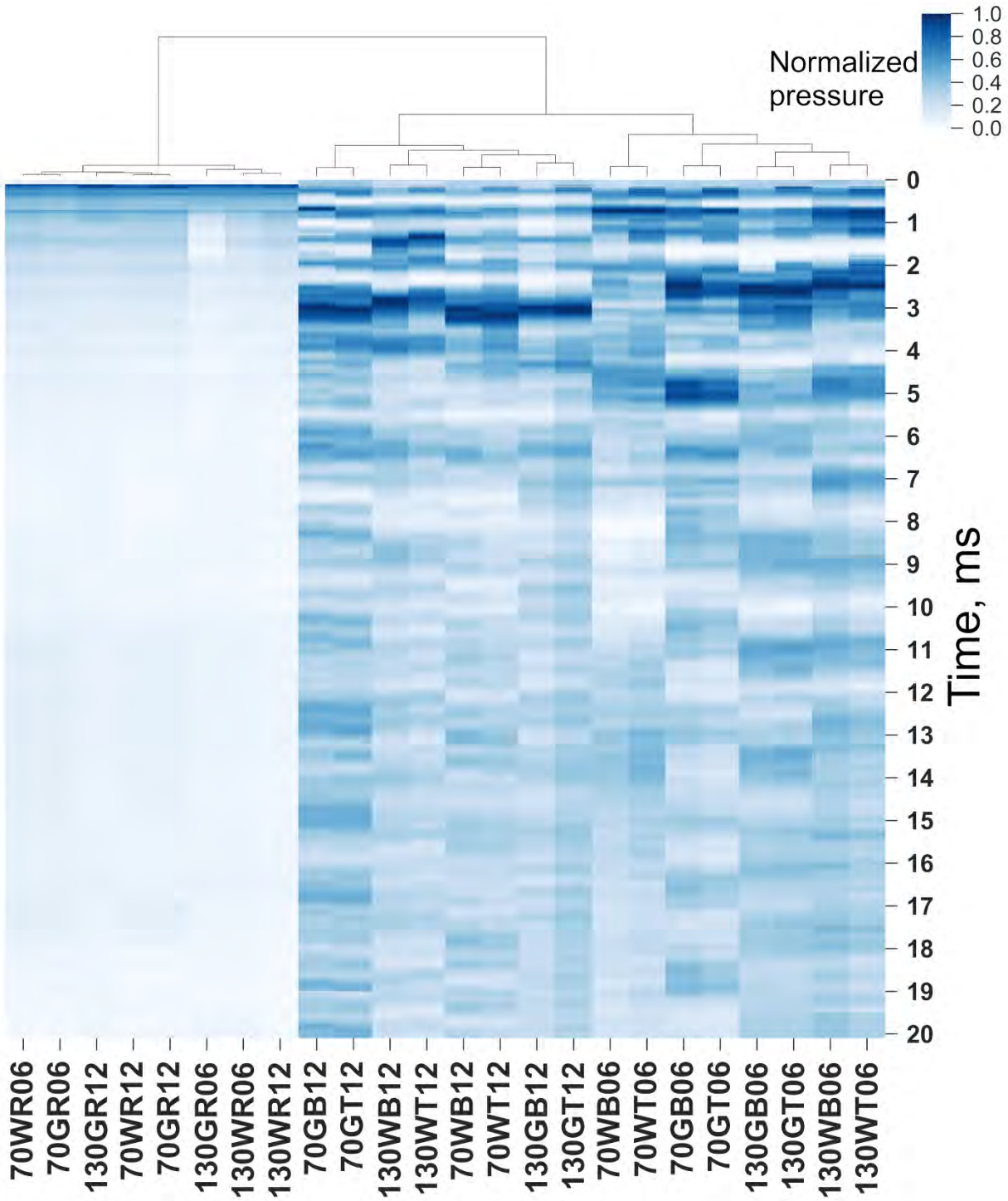
Figure 6 The heatmap of the Euclidean distance matrix between the averaged reflected (R), bottom (B), and top (T) pressure waveforms acquired at 70 and 130 kPa nominal shock wave intensities for both wall thicknesses (denoted as 06 and 12, for 0.06-inch and 0.12-inch wall thickness, respectively), and two types of fluids: water (W) and 40% glycerol in water (G). The same grouping on the correlation map applied to this one also. The 2x2 red squares indicate the correlations between the top and bottom pressure sensors only for group comparison between two fluids used in these experiments.



Downloaded from https://asmedigitalcollection.asme.org/biomechanical/article-pdf/doi/10.1115/1.4047841/6550945/bio-19-1359.pdf by New Jersey Institute Of Technology user on 21 July 2020

Journal of Biomechanical Engineering. Received July 17, 2019;
Accepted manuscript posted July 20, 2020. doi:10.1115/1.4047841
Copyright (c) 2020 by ASME

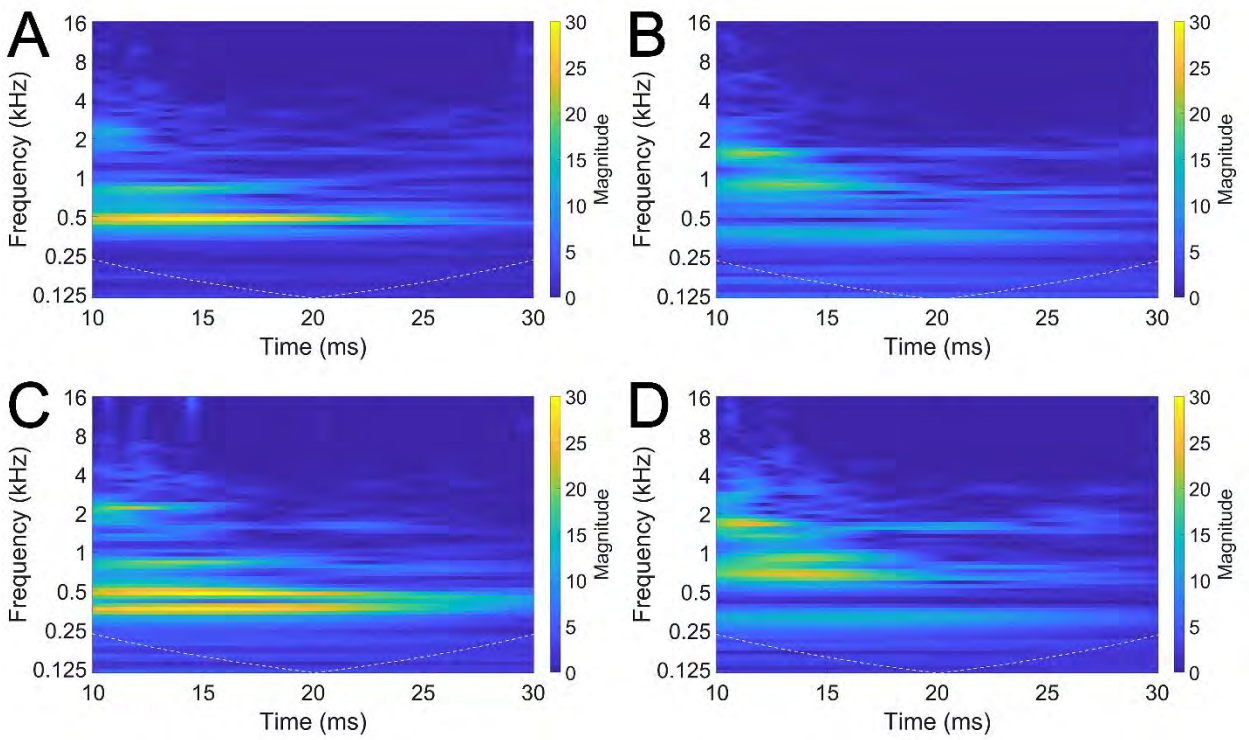
Figure 7 Standardized cluster map of the recorded pressure profiles to visualize the structure of the data. The data are labeled using the same code as in figures 5 and 6.



Downloaded from https://asmedigitalcollection.asme.org/biomechanical/article-pdf/doi/10.1115/1.4047841/6550945/bio-19-1359.pdf by New Jersey Institute Of Technology user on 21 July 2020

Journal of Biomechanical Engineering. Received July 17, 2019;
Accepted manuscript posted July 20, 2020. doi:10.1115/1.4047841
Copyright (c) 2020 by ASME

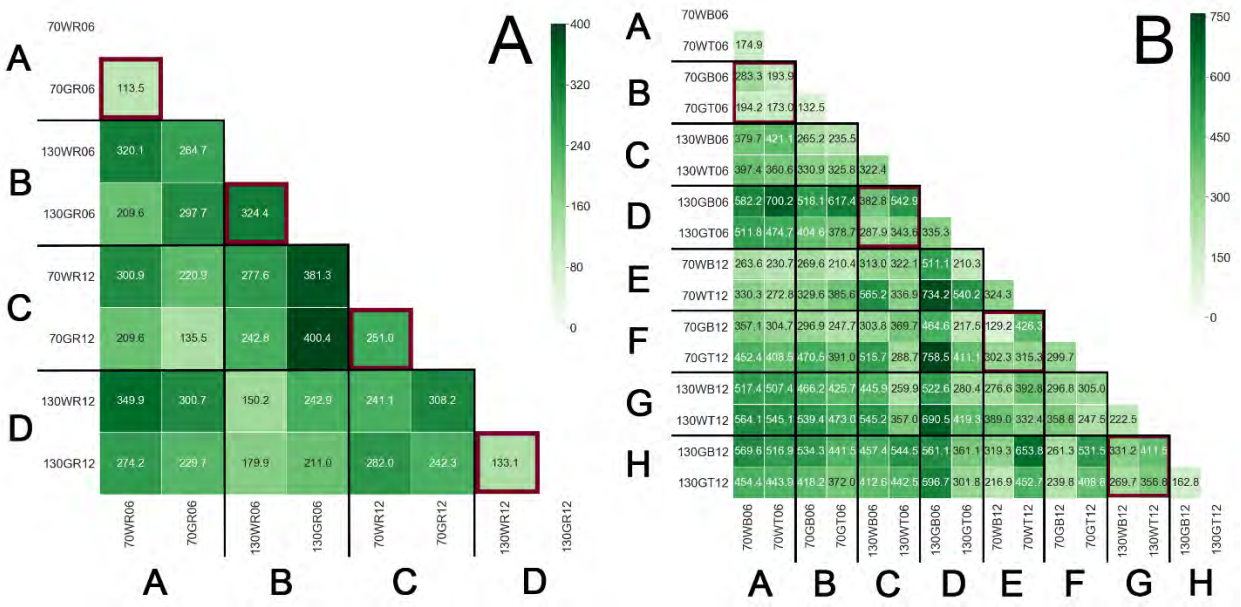
Figure 8 The CWT scalograms of averaged *bottom* pressure sensor waveforms obtained at *130 kPa* nominal shock wave intensity for the following fluid-wall thickness combinations: A) water-0.06", B) water-0.12", C) 40% glycerol in water-0.06", D) 40% glycerol in water-0.12".



Downloaded from https://asmedigitalcollection.asme.org/biomechanical/article-pdf/doi/10.1115/1.4047841/6550945/bio-19-1359.pdf by New Jersey Institute Of Technology user on 21 July 2020

Journal of Biomechanical Engineering. Received July 17, 2019;
Accepted manuscript posted July 20, 2020. doi:10.1115/1.4047841
Copyright (c) 2020 by ASME

Figure 9 Extraction of the (dis)similarity information from continuous wavelet transform scalogram images for: A) reflected pressure only, and B) top and bottom pressure waveforms. The algorithm based on the mean squared error (MSE) is employed for pixel-wise image comparison. The red squares indicate the between fluid comparison.



Downloaded from https://asmedigitalcollection.asme.org/biomechanical/article-pdf/doi/10.1115/1.4047841/6550945/bio-19-1359.pdf by New Jersey Institute Of Technology user on 21 July 2020

Journal of Biomechanical Engineering. Received July 17, 2019;
Accepted manuscript posted July 20, 2020. doi:10.1115/1.4047841
Copyright (c) 2020 by ASME

6. References

1. Gupta RK, Przekwas A. Mathematical models of blast-induced TBI: current status, challenges, and prospects. Frontiers in neurology. 2013;4:59.
2. Warden D. Military TBI during the Iraq and Afghanistan wars. The Journal of head trauma rehabilitation. 2006;21(5):398-402.
3. Leonardi AD, Bir CA, Ritzel DV, VandeVord PJ. Intracranial pressure increases during exposure to a shock wave. J Neurotrauma. 2011;28(1):85-94. Epub 2010/11/26. doi: 10.1089/neu.2010.1324. PubMed PMID: 21091267.
4. Bolander R, Mathie B, Bir C, Ritzel D, VandeVord P. Skull flexure as a contributing factor in the mechanism of injury in the rat when exposed to a shock wave. Annals of biomedical engineering. 2011;39(10):2550.
5. Skotak M, Wang F, Alai A, Holmberg A, Harris S, Switzer RC, et al. Rat injury model under controlled field-relevant primary blast conditions: acute response to a wide range of peak overpressures. Journal of neurotrauma. 2013;30(13):1147-60.
6. Zhu F, Wagner C, Leonardi ADC, Jin X, VandeVord P, Chou C, et al. Using a gel/plastic surrogate to study the biomechanical response of the head under air shock loading: a combined experimental and numerical investigation. Biomechanics and modeling in mechanobiology. 2012;11(3-4):341-53.
7. Hua Y, Kumar Akula P, Gu L, Berg J, Nelson CA. Experimental and Numerical Investigation of the Mechanism of Blast Wave Transmission Through a Surrogate Head. 2014;9(3):031010. doi: 10.1115/1.4026156.
8. Mediavilla Varas J, Philippens M, Meijer SR, van den Berg AC, Sibma PC, van Bree JL, et al. Physics of IED Blast Shock Tube Simulations for mTBI Research. Front Neurol. 2011;2:58. Epub 2011/10/01. doi: 10.3389/fneur.2011.00058. PubMed PMID: 21960984; PubMed Central PMCID: PMCPMC3177142.
9. Ganpule S, Salzar R, Perry B, Chandra N. Role of helmets in blast mitigation: insights from experiments on PMHS surrogate. International Journal of Experimental and Computational Biomechanics. 2016;4(1):13-31.
10. Tan X, Przekwas AJ, Long JB, editors. Validations of virtual animal model for investigation of shock/blast wave TBI. ASME 2013 International Mechanical Engineering Congress and Exposition; 2013: American Society of Mechanical Engineers.
11. Shridharani JK, Wood GW, Panzer MB, Capehart BP, Nyein MK, Radovitzky RA, et al. Porcine Head Response to Blast. 2012;3. doi: 10.3389/fneur.2012.00070.
12. Zhu F, Skelton P, Chou CC, Mao H, Yang KH, King AI. Biomechanical responses of a pig head under blast loading: a computational simulation. International journal for numerical methods in biomedical engineering. 2013;29(3):392-407.
13. Moss WC, King MJ, Blackman EG. Skull flexure from blast waves: a mechanism for brain injury with implications for helmet design. Physical review letters. 2009;103(10):108702.
14. Tan XG, Przekwas AJ, Gupta RK. Computational modeling of blast wave interaction with a human body and assessment of traumatic brain injury. Shock Waves. 2017;27(6):889-904. doi: 10.1007/s00193-017-0740-x.
15. Goeller J, Wardlaw A, Treichler D, O'Bruba J, Weiss G. Investigation of cavitation as a possible damage mechanism in blast-induced traumatic brain injury. Journal of neurotrauma. 2012;29(10):1970-81.

Downloaded from https://asmedigitalcollection.asme.org/biomechanical/article-pdf/doi/10.1115/1.4047841/6550945/bio-19-1359.pdf by New Jersey Institute Of Technology user on 21 July 2020

Journal of Biomechanical Engineering. Received July 17, 2019;
Accepted manuscript posted July 20, 2020. doi:10.1115/1.4047841
Copyright (c) 2020 by ASME

16. Panzer MB, Myers BS, Capehart BP, Bass CR. Development of a finite element model for blast brain injury and the effects of CSF cavitation. Annals of biomedical engineering. 2012;40(7):1530-44.
17. Zhang L, Makwana R, Sharma S. Brain Response to Primary Blast Wave Using Validated Finite Element Models of Human Head and Advanced Combat Helmet. Frontiers in Neurology. 2013;4. doi: 10.3389/fneur.2013.00088.
18. Petr K, Bondi MW, Ward SR, Frank LR. On Sources of Error in Finite Element Simulations of Blast Effects in the Human Brain. 2012;7(3):031008. doi: 10.1115/1.4006143.
19. Singh D, Cronin DS, Haladuick TN. Head and brain response to blast using sagittal and transverse finite element models. International journal for numerical methods in biomedical engineering. 2014;30(4):470-89.
20. Meaney DF, Morrison B, Dale Bass C. The Mechanics of Traumatic Brain Injury: A Review of What We Know and What We Need to Know for Reducing Its Societal Burden. 2014;136(2):021008. doi: 10.1115/1.4026364.
21. Townsend MT, Alay E, Skotak M, Chandra N. Effect of Tissue Material Properties in Blast Loading: Coupled Experimentation and Finite Element Simulation. Ann Biomed Eng. 2018. Epub 2018/12/14. doi: 10.1007/s10439-018-02178-w. PubMed PMID: 30523466.
22. Zhu F, Mao H, Leonardi ADC, Wagner C, Chou CC, Jin X, et al. Development of an FE model of the rat head subjected to air shock loading. SAE Technical Paper, 2010.
23. Elkin BS, Ilankovan A, Morrison B. Age-dependent regional mechanical properties of the rat hippocampus and cortex. Journal of biomechanical engineering. 2010;132(1):011010.
24. Mendis K, Stalnaker R, Advani S. A constitutive relationship for large deformation finite element modeling of brain tissue. Journal of Biomechanical Engineering. 1995;117(3):279-85.
25. Chandra N, Ganpule S, Kleinschmit NN, Feng R, Holmberg AD, Sundaramurthy A, et al. Evolution of blast wave profiles in simulated air blasts: experiment and computational modeling. Shock Waves. 2012;22(5):403-15. doi: 10.1007/s00193-012-0399-2.
26. Ganpule S, Alai A, Plougonven E, Chandra N. Mechanics of blast loading on the head models in the study of traumatic brain injury using experimental and computational approaches. Biomechanics and Modeling in Mechanobiology. 2013;12(3):511-31. doi: 10.1007/s10237-012-0421-8.
27. Kuriakose M, Skotak M, Misistia A, Kahali S, Sundaramurthy A, Chandra N. Tailoring the Blast Exposure Conditions in the Shock Tube for Generating Pure, Primary Shock Waves: The End Plate Facilitates Elimination of Secondary Loading of the Specimen. PLoS One. 2016;11(9):e0161597. Epub 2016/09/08. doi: 10.1371/journal.pone.0161597. PubMed PMID: 27603017; PubMed Central PMCID: PMCPMC5014318.
28. Sundaramurthy A, Alai A, Ganpule S, Holmberg A, Plougonven E, Chandra N. Blast-Induced Biomechanical Loading of the Rat: An Experimental and Anatomically Accurate Computational Blast Injury Model. Journal of Neurotrauma. 2012;29(13):2352-64. doi: 10.1089/neu.2012.2413. PubMed PMID: 22620716.
29. Selvan V, Ganpule S, Kleinschmit N, Chandra N. Blast Wave Loading Pathways in Heterogeneous Material Systems–Experimental and Numerical Approaches. Journal of Biomechanical Engineering. 2013;135(6):061002--14. doi: 10.1115/1.4024132.
30. Skotak M, Alay E, Chandra N. On the Accurate Determination of Shock Wave Time-Pressure Profile in the Experimental Models of Blast-Induced Neurotrauma. Frontiers in Neurology. 2018;9(52). doi: 10.3389/fneur.2018.00052.

Downloaded from https://asmedigitalcollection.asme.org/biomechanical/article-pdf/doi/10.1115/1.4047841/6550945/bio-19-1359.pdf by New Jersey Institute Of Technology user on 21 July 2020

Accepted manuscript. Not copyedited.

Journal of Biomechanical Engineering. Received July 17, 2019;
Accepted manuscript posted July 20, 2020. doi:10.1115/1.4047841
Copyright (c) 2020 by ASME

31. Miner CS, and N. N. Dalton. Physical Properties of Glycerine and Its Solutions Hydrocarbon Processing: Gulf Publishing Company. 1967.
32. Segur JB, Oberstar HE. Viscosity of glycerol and its aqueous solutions. Industrial & Engineering Chemistry. 1951;43(9):2117-20.
33. Windberger U, Bartholovitsch A, Plasenzotti R, Korak K, Heinze G. Whole blood viscosity, plasma viscosity and erythrocyte aggregation in nine mammalian species: reference values and comparison of data. Experimental physiology. 2003;88(3):431-40.
34. Valant AZ, Žiberna L, Papaharilaou Y, Anayiotos A, Georgiou GC. The influence of temperature on rheological properties of blood mixtures with different volume expanders—implications in numerical arterial hemodynamics simulations. Rheologica acta. 2011;50(4):389-402.
35. Rosebrock A. How-To: 3 Ways to Compare Histograms using OpenCV and Python 2014 [4/25/2019]. Available from: https://www.pyimagesearch.com/2014/07/14/3-ways-compare-histograms-using-opencv-python/.
36. Rosebrock A. How-To: Python Compare Two Images 2014 [4/25/2019]. Available from: https://www.pyimagesearch.com/2014/09/15/python-compare-two-images/.
37. Feng K, Zhang L, Jin X, Chen C, Kallakuri S, Saif T, et al. Biomechanical Responses of the Brain in Swine Subject to Free-Field Blasts. Front Neurol. 2016;7:179. Epub 2016/11/09. doi: 10.3389/fneur.2016.00179. PubMed PMID: 27822197; PubMed Central PMCID: PMCPMC5075707.
38. Skotak M, Alay E, Zheng JQ, Halls V, Chandra N. Effective testing of personal protective equipment in blast loading conditions in shock tube: Comparison of three different testing locations. PLoS One. 2018;13(6):e0198968. Epub 2018/06/13. doi: 10.1371/journal.pone.0198968. PubMed PMID: 29894521; PubMed Central PMCID: PMCPMC5997325.
39. Fukunaga K. Introduction to statistical pattern recognition (2nd ed.): Academic Press Professional, Inc.; 1990. 592 p.
40. Jain AK, Dubes RC. Algorithms for clustering data: Prentice-Hall, Inc.; 1988. 320 p.
41. Palubinskas G. Image similarity/distance measures: what is really behind MSE and SSIM? International Journal of Image and Data Fusion. 2017;8(1):32-53. doi: 10.1080/19479832.2016.1273259.
42. Carmelo C, Placido M, Marco A, Andrea C, Alfredo P. Similarity Measures and Dimensionality Reduction Techniques for Time Series Data Mining. 2012. doi: 10.5772/49941.
43. Berthold MR, Höppner F. On Clustering Time Series Using Euclidean Distance and Pearson Correlation. arXiv e-prints [Internet]. 2016 January 01, 2016. Available from: https://ui.adsabs.harvard.edu/\#abs/2016arXiv160102213B.
44. Murtagh F, Starck J-L. Wavelets and Multiscale Transform in Astronomical Image Processing. In: Abello J, Pardalos PM, Resende MGC, editors. Handbook of Massive Data Sets. Boston, MA: Springer US; 2002. p. 473-500.
45. Palaniappan L, Velusamy V. Ultrasonic study of human cerebrospinal fluid. 2004.
46. Baumgartner RW. Handbook on neurovascular ultrasound: Karger Medical and Scientific Publishers; 2006.
47. Kim M-s, Kim J-Y, Noh S-C, Choi H-H. Thermal characteristics of non-biological vessel phantoms for treatment of varicose veins using high-intensity focused ultrasound. PloS one. 2017;12(4).

Downloaded from https://asmedigitalcollection.asme.org/biomechanical/article-pdf/doi/10.1115/1.4047841/6550945/bio-19-1359.pdf by New Jersey Institute Of Technology user on 21 July 2020

Journal of Biomechanical Engineering. Received July 17, 2019;
Accepted manuscript posted July 20, 2020. doi:10.1115/1.4047841
Copyright (c) 2020 by ASME

48. Pichardo S, Sin VW, Hynynen K. Multi-frequency characterization of the speed of sound and attenuation coefficient for longitudinal transmission of freshly excised human skulls. Physics in Medicine & Biology. 2010;56(1):219.

Downloaded from https://asmedigitalcollection.asme.org/biomechanical/article-pdf/doi/10.1115/1.4047841/6550945/bio-19-1359.pdf by New Jersey Institute Of Technology user on 21 July 2020

Appendix A –Publication Cover #3
2020

Authors: A. Aravind, J. Kosty, N. Chandra, BJ Pfister

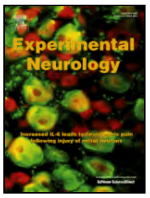
Title: *"Blast exposure predisposes the brain to increased neurological deficits in a model of blast plus blunt traumatic brain"*

Journal Publication: Experimental Neurology, 332, (2020), [20-3]

Contents lists available at ScienceDirect

Experimental Neurology

journal homepage: http://ees.elsevier.com



Research paper

Blast exposure predisposes the brain to increased neurological deficits in a model of blast plus blunt traumatic brain injury

Aswati Aravind, Julianna Kosty, Namas Chandra, Bryan J. Pfister *

Center for Injury Biomechanics, Materials and Medicine, Department of Biomedical Engineering, New Jersey Institute of Technology, 323 Dr M.L.K. Jr. Blvd, Newark, NJ 07102, USA

ARTICLE INFO

Keywords
Blast TBI
Fluid percussion injury
Blast plus injury
Neurodegeneration
Cognitive deficits
Motor deficits
Ventricular enlargement
Neuronal loss
RIP1

ABSTRACT

Soldiers are often exposed to more than one traumatic brain injury (TBI) over the course of their service. In recent years, more attention has been drawn to the increased risk of neurological deficits caused by the 'blast plus' polytrauma, which typically is a blast trauma combined with other forms of TBI. In this study, we investigated the behavioral and neuronal deficits resulting from a blast plus injury involving a mild-moderate blast followed by a mild blunt trauma using the fluid percussion injury model. We identified that the blast injury predisposed the brain to increased cognitive deficits, chronic ventricular enlargement, increased neurodegeneration at acute time points and chronic neuronal loss. Interestingly, a single blast and single blunt injury differed in their onset and manifestation of cognitive and regional neuronal loss. We also identified the presence of cleaved RIP1 from caspase 8 mediated apoptosis in the blunt injury while the blast injury did not activate immediate apoptosis but led to decreased hilar neuronal survival over time.

1. Introduction

In the past 18 years approximately 380,000 cases of traumatic brain injury (TBI) have been reported in US military personnel. TBI numbers are typically classified based on trauma severity amongst which 97% of cases have been classified as mild or moderate. The type or number of head traumas, however, are generally not reported (DoD Worldwide Numbers for TBI, n.d.). Studies have shown that soldiers evacuated from the field for TBI have rarely been due to a single blast exposure. During the course of their service it is more common for soldiers to be exposed to multiple TBIs caused by either blasts or blunt trauma from falls, routine trainings and motor vehicle crashes (Maguen et al., 2012). A more common group has been referred to as 'blast plus' where an exposure to blast precedes a subsequent TBI by another mechanism, most often a blunt trauma (MacDonald et al., 2014; Lange et al., 2012).

Blast and blunt trauma differ greatly in three ways: 1) the mode of biomechanical loading, 2) the spatial distribution of the loading, and 3) the temporal aspect of the loading. Spatially, primary blast waves cause a diffuse loading to the brain whereas blunt injuries can be either focal or diffuse or both at the site of injury (Sundaramurthy et al., 2012; Dixon et al., 1987; Rama Rao et al., 2018). Temporally, the duration of the blast wave is several orders of magnitude shorter than a blunt injury (Sundaramurthy et al., 2012; Thompson et al., 2005). Though these injury mechanisms vary in the blast and blunt impact, veteran studies in patients with TBI have failed to reach a consensus whether blast and blunt trauma differ in their clinical outcomes (Petrie et al., 2014; Mendez et al., 2013; Mac Donald et al., 2011; Kontos et al., 2013; Dretsch et al., 2015; Hoffer et al., 2009). As a result, no distinction is made in the treatment of blast or blunt TBI.

Investigations on repetitive blasts or blunt injuries have shown increased neuropathological and behavioral deficits (Nichols et al., 2016; Meabon et al., 2016; Shultz et al., 2012; Aungst et al., 2014). This leads to our hypothesis that injury from a single primary blast wave predisposes the brain to exacerbated injury outcomes from an additional TBI. While several models have considered repetitive blast and repetitive blunt injuries, a model considering the 'blast plus' (i.e., a blast and blunt trauma) has yet to be considered experimentally.

In this effort, we studied the effect of a blast plus trauma (a mild-moderate blast followed by a mild blunt fluid percussion injury) on cognitive and motor functions, acute neurodegeneration, chronic neuronal loss and morphological changes in a rodent brain. The injury severity of mild, moderate or severe is based on the intensity of blast overpressure in the case of blast, and fluid pressure in the case of blunt injury (Mishra et al., 2016; Hamm et al., 1992; Hamm et al., 1994). We hypothesize that a single mild-moderate blast injury predisposes the brain to increased neuronal deficits and associated neuronal loss upon a subsequent mild blunt injury.

* Corresponding author.
E-mail address: pfister@njit.edu (B.J. Pfister)

https://doi.org/10.1016/j.expneurol.2020.113378
Received 30 December 2019; Received in revised form 20 May 2020; Accepted 8 June 2020
Available online xxx
0014-4886/© 2020.

Acute neurodegeneration and apoptosis has been reported in hilar region of fluid percussion injury (Keane et al., 2001; Conti et al., 1998; Sato et al., 2001; Neuberger et al., 2014; Hellmich et al., 2007). Additionally, necroptosis or programmed necrosis has also been identified as a potential mechanism of cell death in the cortex of FPI animals (Liu et al., 2018; Ma et al., 2019a). We attempt to study the role of RIP1, a key marker involved in both necroptosis and apoptosis cell death pathways, in hippocampal neuronal loss at acute timepoints following the single blast, blunt and blast plus injuries. In addition to histopathological effects in this work, we also attempt to distinguish a single blast and a single blunt injury in terms of the onset of behavioral deficits and neuronal loss.

2. Materials and methods

2.1. Animals

A total of 76, 10-week-old male Sprague Dawley rats (Charles River Laboratories) weighing between 300 and 380 g were used for all experiments in this study using protocols approved by the Rutgers University Institutional Animal Care and Use Committee (IACUC). The animals were housed at 22 °C with ad libitum access to food and water in a 12-h light/dark cycle-maintained facility. Groups of animals subjected to single blast (n = 13), blast sham (n = 10), single blunt (n = 18), blunt sham (n = 11), blast plus (n = 18) and blast plus sham (n = 6) injuries were generated for this study as described below. The animals were closely monitored following surgery and injury. Rats were euthanized by transcardial perfusion at 4 h post blunt injury for measure of acute neurodegeneration and apoptosis markers or at post injury day (PID) 34 for quantification of long-term neuronal survival and ventricular enlargement area mapping (Fig. 1). All PIDs mentioned in this study are with respect to the blunt injury. Since the blast injury was carried out 24 h. prior to the blunt injury in the blast plus animals, all timepoints for the single blast injury are 24 h + PID mentioned here [Fig. 1].

The deficits of a blast plus injury produced by a combination of mild-moderate blast and mild blunt injury are investigated in this study. A blast exposure of 180 kPa overpressure has previously been characterized to produce a mild-moderate response with respect to oxidative stress, blood brain barrier disruption and activation of inflammatory cytokines at acute time points (Rama Rao et al., 2018; Kuriakose et al., 2018; Kuriakose et al., 2019; Skotak et al., 2013). The mild blunt injury was carried out at 1.6–1.9 atm which has been described as a mild FPI injury (Hamm et al., 1992; Hamm et al., 1994). FPI injuries ranging between 2.0 and 2.2 atm have consistently been classified as moderate TBI (Chen et al., 2014; Neuberger et al., 2017; Korgaonkar et al., 2020; Hamm et al., 1993). In a previous study by Hylin et al. (2013), mild lateral fluid percussion injury at 1.0 atm did not result in cognitive, motor deficits or visible neuronal loss. Animals injured at 1.5 atm showed motor and cognitive deficits but no neuronal loss (Hylin et al., 2013). Rats injured at 1.6–1.8 atm using the FPI model have been identified to develop cognitive deficits measured by the Morris Water Maze and motor deficits measured by the Rotarod test (Hamm et al., 1992; Hamm et al., 1994). The objective of this work was to induce mild behavioral and neuronal deficits from the FPI injury to elucidate if the prior blast injury interacted with the blunt injury to exacerbate the deficits observed in the blast plus injury.

2.2. Blast injury

Blast injury was carried out using a shock tube at the Center of Injury Biomechanics, Material and Medicine at New Jersey Institute of Technology as described previously (Sundaramurthy et al., 2012; Mishra et al., 2016; Kuriakose et al., 2016). Briefly, a 9-in. cross section shock tube was used with helium gas to rupture mylar membranes generating a 180 kPa planar shockwave that travels through the test section where the animal is placed 2.8 m from the driver section. The 180 kPa blast pressure in our shockwave tube has been characterized to produce mild- moderate TBI (Mishra et al., 2016). For blast exposure, rats were anaesthetized with 5% isoflurane for 3 min. The animals were then quickly removed from isoflurane, placed on an aerodynamic aluminum riser in the prone position, and restrained with a cotton wrap to restrict its movement. Importantly, the restraint prevents the rat head from moving during exposure, ensuring that the brain is only exposed to the primary blast wave and not affected by additional tertiary (inertial) biomechanical loading. Sham blast animals were anaesthetized, placed next to the shock tube and exposed to the noise of the blast without receiving a blast exposure.

2.3. Blunt injury

In this study, we use the term blunt injury to refer to rats injured with the fluid percussion injury device (Amscien Instruments, Inc.). The animals were anaesthetized by an intraperitoneal injection of ketamine and xylazine (10:1 (100 mg/10 mg/kg), 0.1 mL/100 g) and a 3 mm diameter craniectomy was performed to expose the site of injury (−3 mm bregma, 3.5 mm lateral to the sagittal suture). A 3 mm plastic luer lock needle hub was attached with cyanoacrylate adhesive above the craniectomy site as per established protocol (Wahab et al., 2015). A mild FPI of 1.6–1.9 atm delivered 24 h following the surgery. The animals were anaesthetized using 5% isoflurane for 3 min, hooked to the FPI device and the injury was delivered when a toe pinch response was elicited from the animal. Sham blunt animals underwent the craniectomy procedure, anesthesia with 5% isoflurane 24 h later and were hooked to the FPI device but did not receive an injury.

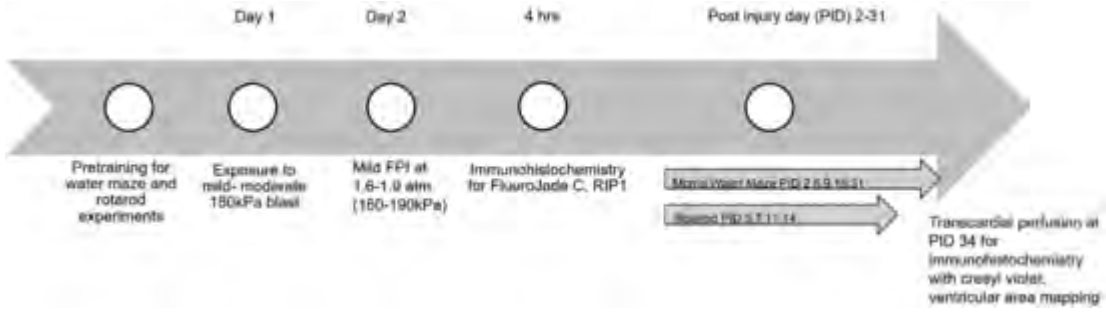


Fig. 1. Timeline for behavioral experiments for the injured animals. Single blast animals were injured on day 1. For the single blunt animals, craniectomy was performed on day 1 and injury was performed on day 2. The blast plus injured animals were exposed to the blast injury followed by craniectomy on day 1 and were subjected to the blunt injury on day 2. Post injury day 1 (PID1) begins the day after the blunt injury and 2 days after the blast injury. Thus, single blast animals have an additional 24 h added to the PIDs mentioned in this study as no procedure was done on these animals on day 2. This has been done to evaluate the deficits in a single blast animal at the time points corresponding to the blast plus injury animal.

2.4. Blast plus injury

The combined blast and blunt injury group will be referred to as the *blast plus* injury group. The animals receiving blast plus injuries were: 1) exposed to a 180 kPa blast, 2) immediately anaesthetized with ketamine/xylazine (10:1 (100 mg/10 mg/kg), 0.1 mL/100 g) intraperitonially and underwent craniectomy as described above, and 3) after 24 h, animals underwent a FPI of 1.6–1.9 atm as described above. Animals were first exposed to the blast since the craniectomy could potentially compromise the protection provided by the skull to the blast exposure. Blast plus sham animals were generated by exposing the animals to the blast followed by the procedures for the sham blunt animals to negate any contributions of anesthesia and craniectomy to the development of neurological or functional deficits.

2.5. Physiological measures

Physiological measures such as apnea, righting reflex, weight loss at 24 h and percent weight gain at PID 34 were measured for all groups of animals generated. Sham and FPI animals were disconnected from the injury device and immediately placed in the supine position and observed for apnea and righting reflex. The time taken by the animal for its first breath was noted as the time of apnea. The righting reflex was the time taken by the animals to right themselves from the supine to prone position. These measures could not be carried out for the blast injury as the animals gained consciousness even before being removed from the shock tube. All animals were weighed before surgery or injury and on PID 1 to evaluate the percentage of weight lost post injury.

2.6. Spatial working memory

Spatial working memory was examined using the Morris water maze (MWM) to test the ability of the rat to remember the location of a submerged platform using distal cues. The MWM consisted of a 6 ft diameter, 2 ft deep tank with a 10 cm diameter, 30 cm high clear plexiglass platform (Stoelting, Inc., 60,030). Four distal cues were present on each of the walls surrounding the apparatus that were kept constant throughout the experiment. The tank was divided into 3 quadrants using the Anymaze software (San Diego Instruments) with each quadrant containing 2 possible platform locations.

The rats were pretrained for 2 days, a baseline measure was conducted prior to surgery or injury, and tests conducted on PID 2, 6, 9, 16 and 31. Pretraining occurred over three trials each day using one platform location in each quadrant. For the baseline and post injury time points, 6 trials were conducted for each platform location. Each trial has a fixed predetermined entry point in a quadrant different than the one the platform was placed in. All trials comprised of 3 phases: 1) A 'sample' phase for 60 s where the animal is introduced into the water maze and allowed to find the escape platform. 2) A retention phase for 20 s in which the animal is left on the platform to familiarize the location of the escape platform with the help of spatial cues. 3) A 'choice' phase conducted a min after the retention phase, also for 60 s, where the animal is placed in the same entry location as the sample phase. A 30 min inter trial period is maintained for each rat. The path efficiency, latency to platform and mean speed of the animals for the 'choice' phase are analyzed and compared between groups using the Anymaze software.

$$\text{Path efficiency} = \frac{\text{Shortest distance between the entry location and platform}}{\text{Total distance travelled by the rat}}$$

A path efficiency close to 1 indicates higher efficiency in finding the platform while lower values indicate decreasing efficiency.

2.7. Sensorimotor deficits

Sensorimotor function was assessed using the Rota Rod test (Harvard Apparatus, model 76–0772). The rats were trained over 4 days with an acceleration from 4 to 30 rpm over 3 min. Baseline performance was evaluated a day prior to craniectomy or blast injury depending on the injury group and post-injury performance were evaluated at time points 3, 7, 11- and 14-days. To measure performance, three trials were conducted at each time point and the trial was terminated when the animal fell from the rod or after 3 min. The mean duration for the rat to fall from the Rota Rod apparatus and the average rpm at the time of fall over the 3 trials were noted. The timeline for the behavior experiments are shown in Fig. 1.

2.8. Immunohistochemistry

FluoroJade C staining for acute neurodegeneration and immunostaining for the necroptosis marker, RIP1, and was carried out at 4 h post blunt injury. Cresyl violet staining for quantifying surviving neurons was carried out at PID 34. Rats were anaesthetized with ketamine and xylazine (10:1 (100 mg/10 mg/kg), 0.1 mL/100 g) and were transcardially perfused with 1× phosphate buffered saline (PBS) and 4% paraformaldehyde (PFA) at 4 h and PID 34. The rat brains were isolated and stored at 4 °C in 4% PFA fixative for 24 h., following which the brains were placed in 30% sucrose for cryopreservation for 2 days. Only sections ipsilateral to the blunt injury were examined. Brain tissue sections were generated using a cryostat (Leica Biosystems) and mounted on superfrost glass slides (Thermofisher Scientific) and used for immunohistochemical analysis.

Forty μm sections from 4 h time point (n = 3, 6 sections per rat) were stained with Fluoro-Jade C to quantify the acute induction of neurodegeneration as described in prior publications (Neuberger et al., 2014; Gupta et al., 2012). The slides were immersed with 100% ethanol for 3 min, followed by 70% ethanol (1 min) and distilled water (1 min). The slides were then incubated with 0.006% potassium permanganate for 15 min, washed in distilled water for a minute and immersed in 0.001% Fluoro-Jade C (Sigma Aldrich) for 30 min. The slides were finally washed three times in distilled water (1 min) and submerged in xylene twice for 2 min before being air dried and cover slipped with DPX (Sigma Aldrich). Quantification was performed using every tenth section between −2.68 mm to −4.80 mm bregma for neurodegeneration in the ipsilateral hilus and between −2.68 to −3.68 mm bregma for the neurodegeneration in the sensorimotor region. Unbiased neuronal counts were performed using the Optical Fractionator probe of Stereo Investigator V.10.02 (MBF Bioscience), an Olympus BX51 microscope and a × 40 objective. The hilus and sensorimotor regions were outlined by a contour at ×10 objective. Sampling parameters were set at ×40, counting frame 50 × 50 μm, dissector height 25 μm, and top guard zone 2 μm. Approximately 100 sites per contour were sampled using randomized systematic sampling protocols. The number of stained neurons were calculated by the Stereo Investigator as described in previous literature (West et al., 1991; Golub et al., 2015; Olesen et al., 2017; Grady et al., 2003). Data was plotted as the total number of stained neurons estimated by the Stereo Investigator.

Coronal hippocampal sections at 40 μm thickness were collected from rats (n = 6; 6 sections per rat) at PID 34 to quantify long term neuronal survival using cresyl violet staining. Briefly, the slides are immersed in distilled water for 30 s followed by 30 s immersions in 100%, 90%, 70% and 30% ethanol. The slides are then further washed with distilled water for 30 s following which the slides are immersed in cresyl violet solution for 1 min. The slides are then washed in distilled water three times for 30 s and dehydrated by 30 s immersions in 30%, 70%, 90 and 100% ethanol. Finally, the slides are immersed in xylene

for 3 min, air dried and mounted with coverslips using DPX mountant (Sigma Aldrich). The number of surviving neurons were quantified using every tenth section between −2.68 mm to −4.80 mm bregma using the Stereo Investigator software as described above. Sampling parameters used were ×40 objective, counting frame 100 × 100 μm, dissector height 25 μm, and top guard zone 5 μm. Approximately 40 sites per contour were sampled using randomized systematic sampling protocols. Total number of neurons estimated by the Stereo Investigator software were plotted.

Immunostaining was carried out to identify the presence of the necroptosis and apoptosis marker RIP1 at 4 h post blunt injury. Here, 20 μm coronal hippocampal tissue sections from sham, single blast, single blunt and blast plus animals were sectioned on the cryostat and mounted on glass slides as described above. The tissues were placed in ice cold methanol for 10 min at −20 °C, washed with 10 mM PBS, blocked with 10% donkey serum at room temperature for 1 h following which the slides were incubated with primary RIP1(Abcam, Ab106393) and NeuN (Abcam, Ab104224) antibodies. The sections were washed with PBS with 0.3% triton solutions the following day and incubated with secondary antibodies, donkey-antimouse Alexafluor 488 for NeuN and donkey-antirabbit Alexafluor 594 for RIP1.

2.9. Western blot

Western blot was carried out on single blast, single blunt, blast plus and sham animals at 4 h to study the expression of RIP1 in the hippocampus. Briefly, rats were sacrificed and perfused with 1× PBS following which rat brains were excised and the ipsilateral hippocampus was dissected. The hippocampal tissue was then homogenized in ice cold RIPA buffer (Sigma Aldrich) with protease inhibitors (Thermo Fisher Scientific) using a sonicator. Samples were then centrifuged at 14000 *g* at 4 °C. 20 μg of protein was loaded into 4–15% SDS-PAGE gradient gels (Bio-rad Laboratories) to separate the proteins based on their molecular weight. The gel was then transferred to a polyvinylidene difluoride (PVDF) membrane using the Trans-Blot Turbo™ RTA Mini PVDF Transfer Kit (Bio-rad Laboratories). The membranes were then blocked with 5% milk dissolved in Tris-Buffered saline containing 0.1% Tween-20 (TBS-T) for an hr following which the membrane was incubated overnight with the RIP1 antibody (1:500, Cell Signaling Technologies). The membranes were then washed with TBS-T, incubated for an hr with the corresponding HRP conjugated secondary antibody and developed using Western Pico Chemiluminescence Substrate (Thermo Scientific) on Chemi Doc Imaging System (Bio Rad Laboratories). The bands were analyzed using ImageJ software.

2.10. Ventricular enlargement area mapping

The brain sections stained with cresyl violet as described above were digitized using Leica Aperio Versa 200 fluorescent microscope and slide scanner (Leica Biosystems, Inc). Every fifth section between −3.64 mm to −4.80 mm bregma were mounted on superfrost slides (Thermofisher Scientific) and mapped for ipsilateral ventricular area at 20× magnification using the Aperio Imagescope software (Leica Biosystems, Inc). The mean ipsilateral ventricular area mapped for each group of rats was plotted.

2.11. Statistical analysis

Statistical analysis was carried out using the SPSS software (IBM, version 23). Physiological measures were analyzed using ANOVA and Tukey's HSD post hoc. The MWM and Rota Rod experiments were analyzed using mixed ANOVA followed by factorial ANOVA or Brown-forsythe at each time point and post hoc tests using pairwise *t*-tests with Bonferroni correction (α adjusted to 0.008) or Games Howell respectively. Neuronal counts obtained from cresyl violet staining and the ipsilateral ventricular area were assessed statistically by using a 2 × 2 factorial ANOVA and pairwise *t*-tests with Bonferroni correction (α adjusted to 0.008) as post hoc. The neuronal counts obtained from Fluoro-Jade staining were analyzed using one-way ANOVA and Tukey's post hoc. Statistical differences where considered significant when $p < .05$. Immunoblot OD values were evaluated using one-way ANOVA followed by post hoc tests using pairwise t-tests with Bonferroni correction (α adjusted to 0.01).

3. Results

Ten-week-old Sprague Dawley rats were subjected to a single blunt, a single blast or a blast plus injury. Additionally, sham groups of sham blast, sham blunt and animals subjected to the blast and the craniectomy surgery (blast plus sham) were generated. Perfused rat brains subjected to blunt injury were observed to have blood collected under the dura while this was not observed in the single blast brains owing to the difference in open vs. closed head nature of injury [Fig. 2A]. At 34 days post injury, brains of all injured groups did not show the presence of necrotic tissue or contusions [Fig. 2B].

3.1. Blunt and blast plus injury results in similar physiological outcomes

Apnea, righting reflex and weight loss were found to be similar in the blunt and blast plus injured animals and significantly different from the shams [Fig. 3]. Righting reflex and apnea in the blast cohort could not be measured as the animals gained consciousness few seconds after injury and before being removed from the harness within the shock tube apparatus. Weight loss on PID1 was not significantly different in the blunt and the blast plus injury group (7.69 ± 2.22% and 7.89 ± 2.28% respectively) while blast animals had a slight weight loss of 1.78 ± 0.6%. All cohorts of animals, however, were observed to attain similar percentages of weight gain at PID34 when compared to their pre-injury weights.



Fig. 2. Perfused rat brains subjected to single and blast plus injury at 4 h and 34 days post injury. (A) From left to right: sham, blast, blunt and blast plus injured perfused rat brains at 4 h. (B) From left to right: sham, blast, blunt and blast plus injured perfused rat brains 34 days post injury. The animals subjected to single blunt and blast plus injury had blood collected under the dura at 4 h. Brains of all injury groups at PID 34 showed no contusion or necrotic tissue at the site of injury.

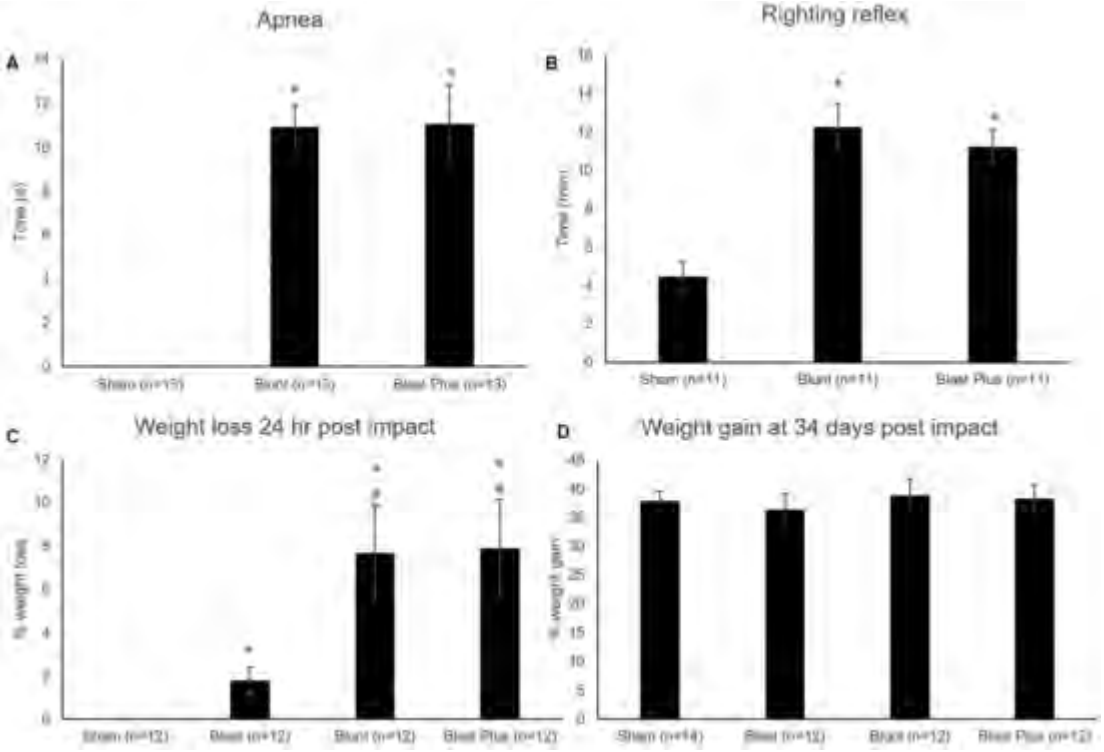


Fig. 3. Physiological measures across experimental groups. Blunt and blast plus injury animals show similar scores of righting reflex (A), apnea (B) and weight loss at PID1 (C). Blast animals had apnea and loss of consciousness times which could not be monitored. D. All groups had similar weight gain at the time of euthanasia (pid34). All values are mean ± SE., * denotes $p < .05$ vs sham, # denotes $p < .05$ vs. blast.

3.2. Blast injury elevated the acute cognitive impairment in the blast plus injured animals

Cognitive function was assessed using the Morris Water Maze test at PID 2,6,9,16 and 31. Sham groups for each injury- sham blast ($n = 6$), sham blunt ($n = 9$) and sham blast plus ($n = 6$) were generated to assess for any effects of anesthesia or surgery in the development of cognitive deficits. Sham blast and sham blunt animals did not differ statistically in their path efficiencies and were combined into one sham group. Similarly, single blast and blast plus sham groups were also combined as the blast group since they showed no statistical difference (Fig. S.1).

Blast injured rats did not develop cognitive deficits in the MWM and performed similar to the sham animals, Fig. 4. Blunt and blast plus animals, however, developed memory deficits that improved over time. Statistical analysis was carried using a 2 × 2 × 5 mixed ANOVA that indicated a significant effect of time points ($F(4,192) = 10.348$, $p < .01$, $\eta^2 = 0.177$) and an interaction of time points and blunt injury ($F(4,192) = 6.391$, $p < .01$, $\eta^2 = 0.118$). A 2 × 2 factorial ANOVA was then carried out to determine the main and interaction effects of the blast and blunt injury at each time point. At PID2, there was a significant effect of interaction of blast and blunt injury ($F(1,48) = 4.925$, $p = .031$, $\eta^2 = 0.093$) for the path efficiency scores. Post hoc analysis with Bonferroni test indicated that at PID2, the blast plus animals had significantly lower path efficiency ($t(22) = 4.104$, $p < .001$) and greater latency to reach the platform ($t(22) = 2.89$, $p = .008$) when compared to the single blunt or single blast injured animals [Fig. 4,B and D].

The mean speed of the animals did not vary across groups Fig. 4,C. This indicated that the motor function of the rats required for the swimming test were not affected and did not contribute to the decreased latency or path efficiency observed. The blast plus animals, thus, showed significant decline of cognitive function at PID2 when compared to sham and single injury animals. The blast plus injured animals and the single blunt injured animals showed similar recovery of cognitive function at later time points.

3.3. Blast injury did not exacerbate sensorimotor deficits in the blast plus injury

Blast injured animals did not manifest motor deficits on the Rota Rod and performed similar to sham animals. Statistical analysis with 2 X 2 X 4 mixed ANOVA showed significant main effect of time points, blunt injury and interaction effects of time points and blunt injury. Further analysis at each time point with Brown-Forsythe and Games Howell post hoc test indicated single blunt and blast plus injured animals showed reduced performance on PID 3 and PID 7 ($p < .05$) which improved over time. There was no significant difference between the single blunt and blast plus injured animals [Fig. 5]. Accordingly, the blast injury did not exacerbate motor deficits in the blast plus injury.

3.4. Blast injury exacerbated the acute hilar neurodegeneration and chronic neuronal loss in the blast plus injured animals

Neurodegeneration in the hilar region was assessed with Fluoro-Jade labeling ($n = 3$, 6 sections per rat) 4 h post injury in blunt and blast plus injured animals and 24 h post injury for the single blast group. The hippocampus was chosen as the region of interest since water maze deficits have been closely linked to neuronal loss in the hippocampus (Hicks et al., 1993; Broadbent et al., 2006). Specifically, hilar neuronal loss following FPI has been well correlated to memory deficits observed in the animals (Hicks et al., 1993). As expected, single blunt injured animals had Fluoro-Jade labeled neurons in the hippocampus as is common in the FPI model [Fig. 6]. Interestingly, blast animals had an absence of neuronal degeneration and was similar to

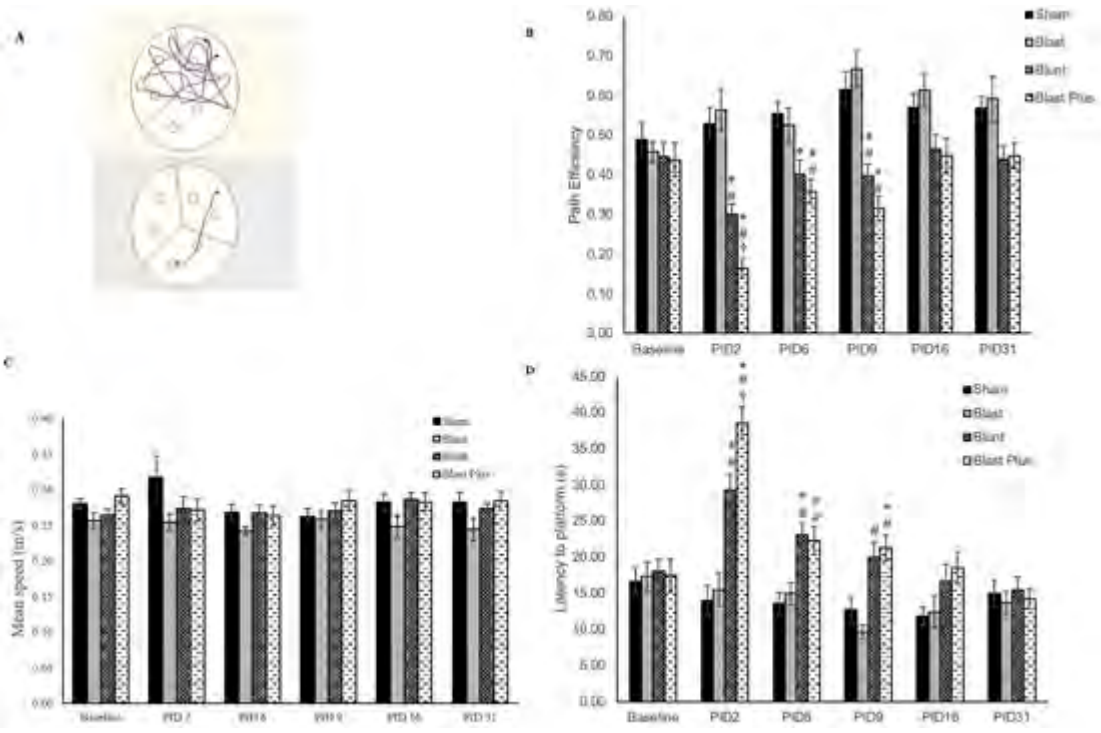


Fig. 4. Cognitive performance measured by Morris Water Maze. (A) Track plot of animal during the sample and choice phase indicating 'learning' of platform location in the choice phase. (B) Path efficiency measured across post injury days 2,6,9,16 and 31 across injury groups. Blunt and blast plus injury animals show significant deficits on PID 2 that improve with time. Blast and sham animals show no cognitive deficits. (C) Mean speed of the animals measured during the water maze task show no significant differences between groups. (D) Latency to platform at PID 2 shows increased duration required by blunt and blast plus injury animals to reach the platform compared to sham and blast animals. All values represent mean ± SE. * denotes $p < .008$ vs. sham, # denotes $p < .008$ vs. blast, † denotes $p < .008$ vs. blunt.

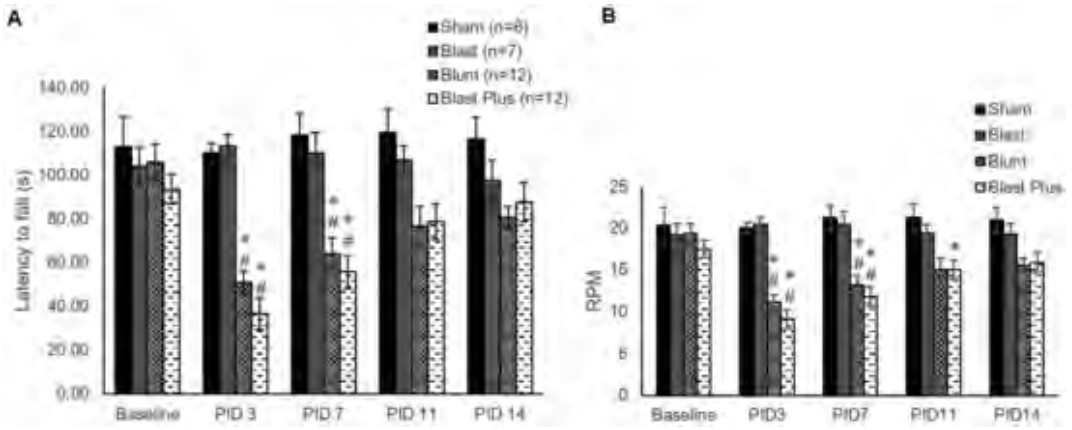


Fig. 5. Motor deficits measured by Rota Rod. (A) Time taken by the animals to fall from the Rota rod apparatus, (B) Speed in RPM of the Rota rod at the time of fall. Sham and blast animals did not show motor deficits while the blunt and blast plus injury animals showed significant deficits at PID3 and 7 that improved over time. There was no significant difference in time taken to fall between blunt and blast plus injury group animals. The values are all mean ± SE. * denotes $p < .008$ vs. sham, # denotes $p < .008$ vs. blast.

sham animals [Fig. 6A, B]. Blast injury, however, predisposed animals to additional neurodegeneration in the blast plus injured animals with positive Fluoro-Jade labeling significantly greater than single blunt injured animals ($f(3,11) = 37.262$, $p < .01$) [Fig. 6E]. Neurodegeneration was also observed in the CA2-CA3 region but was not quantified in this study.

Neuronal survival in the hilus region 34 days post injury was measured using stereology counting of cresyl violet stained hippocampal sections [Fig. 7]. A significant main effect of blast ($f(1,20) = 66.249$, $p < .01$), blunt injury ($f(1,20) = 38.268$, $p < .01$) was observed without an interaction of blast and blunt injury ($f(1,20) = 2.909$, 0.104) as observed on assessment with factorial ANOVA ($p < .05$) indicating that both injuries had an additive effect on the cell loss observed in the blast plus injury group. Post hoc pairwise *t*-tests with Bonferroni correction (α adjusted to 0.008), identified that both the blast and blunt injury groups had significantly lower neuronal numbers than the sham ($p < .008$). Additionally, the blast plus injury group showed significantly lower neuronal numbers than the sham, single blunt or single blast injured animals ($p < .008$). Interestingly, this indicates that the blast injured animals result in a similar reduction in surviving neurons as the blunt injured animals despite the absence of acute neurodegeneration as assessed by Fluoro-Jade above.

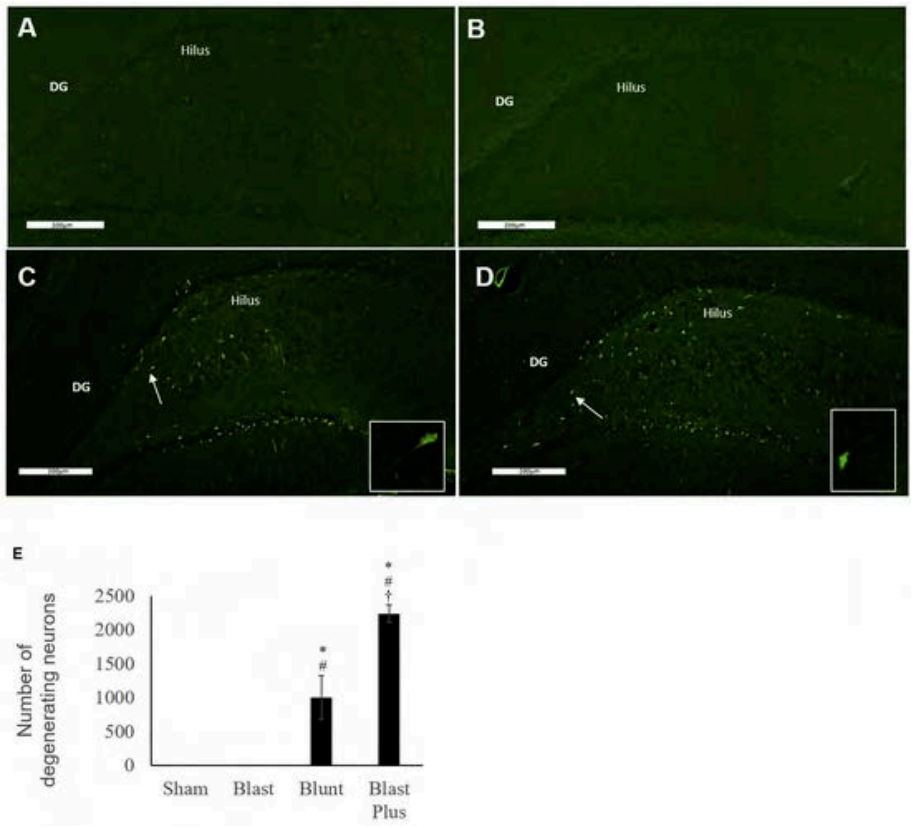


Fig. 6. Histopathology of degenerating hilar neurons 4 h post injury. Fluoro-Jade stained ipsilateral hippocampus of (A) Sham, (B) Blast, (C) Blunt, (D) Blast + Blunt. (C) and (D) have insets of individual neurons in the hilus at 20×. Both Sham and Blast animals had no Fluoro-Jade staining. (E) Number of degenerating neurons in injured animals assessed by stereology. The values are mean ± SE, $n = 3$. *denotes p < .05 ($p = .024$) vs. blunt.

3.5. Blast plus animals showed similar neurodegeneration in the sensorimotor cortex as the single blunt animals

Sensorimotor cortex has been implicated in motor deficits following FPI (Sato et al., 2001; Peterson et al., 2015). Accordingly, coronal sections from injured animals were evaluated for neurodegeneration in the sensorimotor cortex 4 h post injury using Fluoro-Jade C staining. Presence of degenerating neurons was observed in the sensorimotor cortex of both the single blunt and blast plus injured animals ($n = 3$, 6 sections per rat) but there was no significant difference between the groups ($p = .321$)

[Fig. 8,E]. No neurodegeneration in the sensorimotor cortex was observed in the sham or blast injured animals.

3.6. Blast plus injured animals had increased ventricular enlargement at PID34

Gross observation of sections mounted for nissl staining indicated a large cavity in the ipsilateral ventricle compared to the contralateral ventricle in all blast plus injured animals. Ventricular enlargement, however, was observed in only 40% of the single blunt injured animals. Enlarged ventricles were not found in blast injured or sham animals. The ventricle enlargement in the blast plus injured animals were found to decrease in size on moving from posterior to anterior planes of the brain. On analysis with a 2 × 2 factorial ANOVA, it was identified that there was a significant interaction effect of the blast and blunt injury indicating a synergistic effect of the single injuries on the increased ventricular enlargement area in the blast plus animals ($f(1,16) = 14.221$, $p = .002$, $\eta^2 = 0.471$). Post hoc analysis with Bonferroni correction identified that the blast plus animals had significant ventricular enlargement compared to sham ($t(4.102) = 10.651$, $p < .001$), blunt ($t(8) = 3.842$, $p = .005$) and blast animals ($t(4.213) = 10.467$, $p < .001$) [Fig. 9,G]. The area of cortex surrounding the ventricle region was also identified to have considerable cortical thinning [Fig. 9,F].

3.7. Caspase 8 cleaved RIP1 fragment was found in the ipsilateral hippocampus of single blunt and blast plus animals

Ipsilateral hilar regions of sham, single blunt, single blast and blast plus injured animals ($n = 3$) were stained for the presence of NeuN and RIP1, an early marker of apoptosis and necroptosis at 4 h post FPI. Co-localization of NeuN and RIP1 in hilar neurons was identified in single blast, single blunt and blast plus injured animals. [Fig. 10A]. Further quantification by immunoblot using isolated ipsilateral hippocampi indicated a decrease in expression of full length RIP1(78KDa) and significant increase in a caspase 8 mediated cleaved RIP1 (~37KDa) fragment in the single blunt and blast plus animals compared to sham [Fig. 10B]. The single blast injured showed similar full length RIP1 expression as sham and a slight increase in the cleaved RIP1 in the immunoblot, but this did not resolve to significance.

4. Discussion

TBI in soldiers is rarely the result of a single blast exposure but more commonly due to exposures to multiple TBIs caused by either blasts or blunt trauma from falls and motor vehicle crashes (Maguen et al., 2012). A frequent head injury is the 'blast plus' where an exposure to blast precedes a blunt trauma and has been associated with an increased risk of cognitive deficits and PTSD (MacDonald et al.,

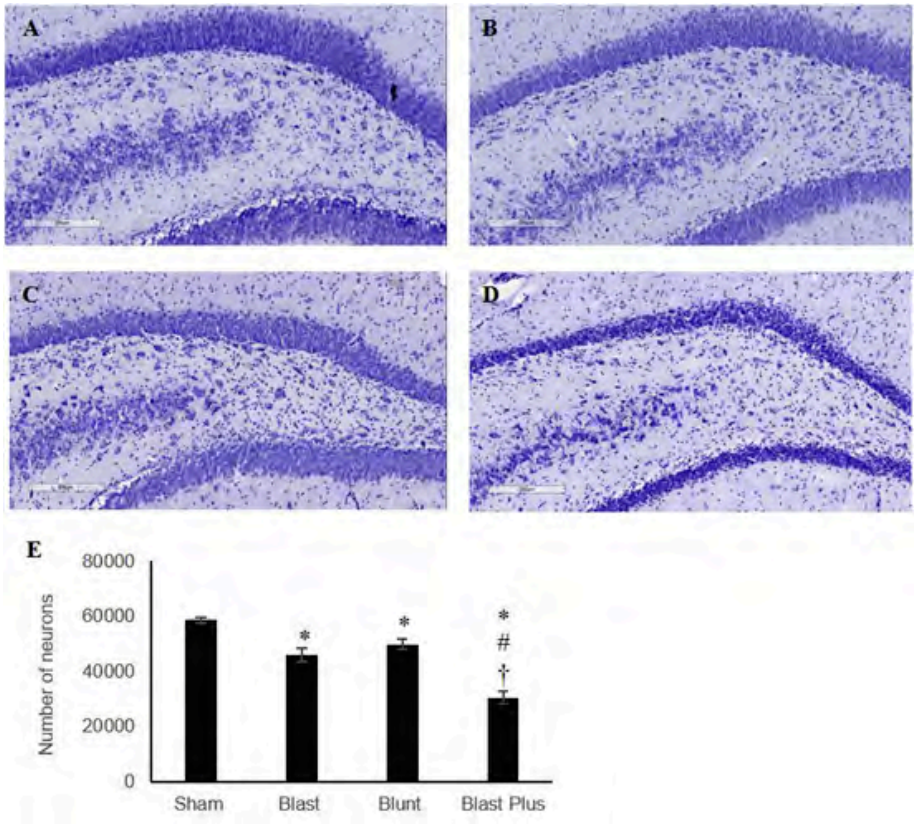


Fig. 7. Neuronal survival measured by cresyl violet staining. Cresyl violet staining in ipsilateral hilus of (A) Sham, (B) Blast, (C) Blunt, (D) Blast + Blunt animals. (E) Stereological counts of surviving neurons at 34 days post injury. All injured groups had lower neuronal survival when compared to sham. Blast plus injuries led to fewer survivng neruons than single injuries. All values are in mean ± SE., $n = 6$. * denotes $p < .008$ vs. sham, # denotes $p < .008$ vs. blast, † denotes $p < .008$ vs. blunt. (For interpretation of the references to colour in this figure legend, the reader is referred to the web version of this article.)

2014; Lange et al., 2012; Kontos et al., 2013). In this study we proposed to identify the increased susceptibility to neurological deficits due to a blast impact in a model of blast plus TBI. To our knowledge, this study is the first attempt to replicate the blast plus injury in a rodent model.

In order to characterize enhanced deficits in the blast plus TBI model, we began by establishing the pathological and behavioral differences observed between a single mild blunt (160-190 kPa) and a single mild-moderate blast (180 kPa) injury. The 180 kPa has been previously characterized by mortality rate and presence of oxidative stress markers to be a mild-moderate blast injury (Mishra et al., 2016; Skotak et al., 2013). Similarly, 1.6–1.9 atm fluid percussion injury has been characterized to be a mild impact that results in mild behavioral and neuronal deficits (Hamm et al., 1992; Hamm et al., 1994). These results were then compared to the blast plus injury (mild-moderate blast TBI and a mild blunt injury), to establish that a blast injury predisposes the rodent brain to increased cognitive deficits, acute and chronic hilar neuronal loss, long-term ventricular enlargement and cortical thinning. Our results also indicate that a single blast and single blunt injury vary in the onset of behavioral deficits and neuronal loss in the rodent model.

In this study, we demonstrate for the first time that a single mild-moderate blast injury and a single blunt impact differ in the onset of acute neurodegeneration but ultimately result in similar chronic neuronal loss. Significantly, the blast impact did not result in cognitive deficits despite the hilar neuronal loss observed at later time points. Our single blunt injury served as a positive control with expected cognitive and motor deficits that improved over time and neurodegeneration evaluated at 4 h post injury (Ma et al., 2019b; Fujimoto et al., 2004). While blast injury itself did not produce acute neurodegeneration or behavioral deficits, the exacerbated deficits in the blast plus injury indicated that the mild-moderate blast trauma predisposed the brain to adverse outcomes from additional injury. Here we observed a significant increase in cognitive deficits at PID 2, increased hilar neuronal loss both at immediate and long-term time points, and ventricular enlargement not seen in the single injuries. These results suggest that though the single blast injury does not result in overt cognitive or motor deficits, it does increase the vulnerability of the hippocampus to increased deficits from a second injury.

4.1. Blast injury predisposes the brain to increased cognitive deficits from a second blunt injury

Mild-moderate blast or blunt TBI in veterans has been associated with decreased long term cognitive and motor function, attention deficits, PTSD, anxiety and depression (Lange et al., 2012; Kontos et al., 2013; Clark et al., 2018; Trudeau et al., 1998; Heitger et al., 2006; Swick et al., 2012). Blunt TBI in rodents has been well characterized by the pendulum fluid percussion injury model and has been demonstrated to replicate human TBI clinical outcomes (Thompson et al., 2005; Hamm et al., 1994; Ma et al., 2019b; Shultz et al., 2011). Following FPI, cognitive and motor deficits are commonly studied using Morris water maze and Rota-Rod experiment (Hamm et al., 1994; Fujimoto et al., 2004; Floyd et al., 2002; Smith et al., 1991). FPI with a percussion of 1.0 atm has been compared to produce similar behavioral and pathological outcomes to that of human concussion studies (Hylin et al., 2013). Fluid percussion injury at 1.0 atm in the rat has been reported to not produce cognitive or motor deficits whereas 1.2 atm and 1.5 atm results in cognitive deficits that last 24 h and 5 days respectively without neuronal loss (Hylin et al., 2013;

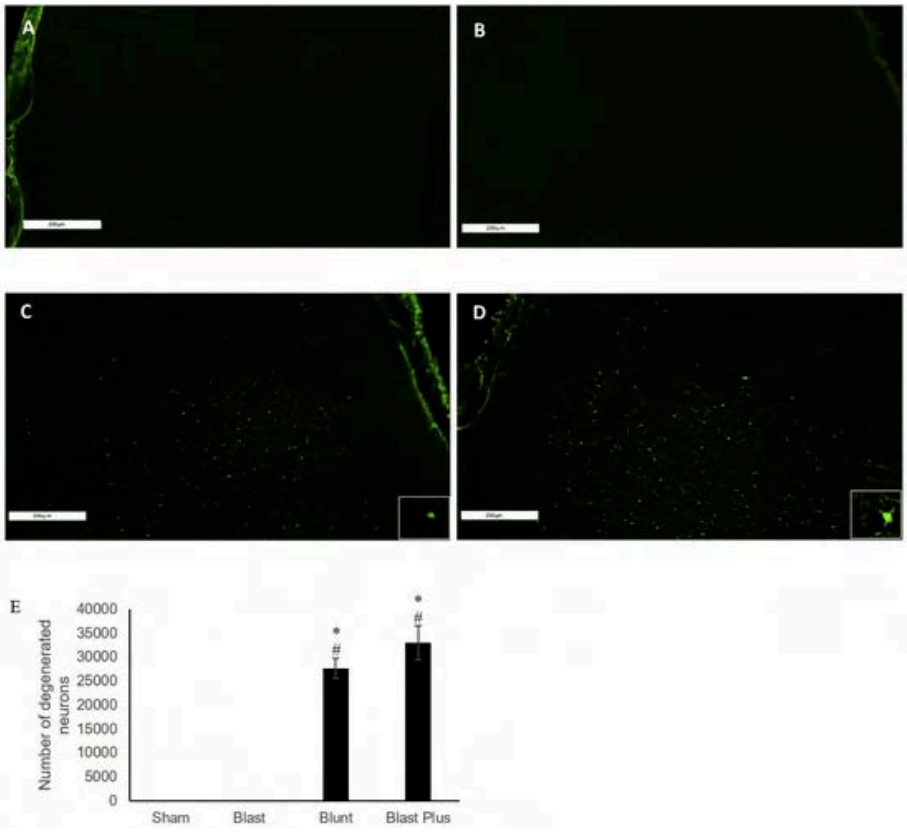


Fig. 8. Neurodegeneration in the sensorimotor cortex 4 h post injury. Fluoro-Jade staining in the ipsilateral somatosensory cortex of (A) Sham, (B) Blast, (C) Blunt, (D) Blast plus animals. (C) and (D) have insets of magnified neurons at 20×. Degenerating neurons were observed in both the blunt and blast plus injured animals, but the number of degenerated neurons did not vary significantly from each other between both groups (E). The values are represented as mean ± SE, n = 3. * denotes $p < .05$ vs. sham, # denotes $p < .05$ vs. blast.

Shultz et al., 2011). In this study, we used FPI with percussions of 1.6–1.9 atm to produce a TBI with loss of consciousness, cognitive and motor deficits that were reversible within 7–9 days and low levels of neurodegeneration. The selection of lower end of blunt injury severity was deliberately made to study how a previous blast injury can predispose the brain and make it additionally vulnerable even to a lower level blunt injury.

Animals exposed to a single 180 kPa primary blast overpressure wave did not produce cognitive or motor deficits. Cognitive deficits reported in rodent blast TBI literature, however, have been inconsistent (Vandevord et al., 2012; Stemper et al., 2016; Tompkins et al., 2013; Lucke-Wold et al., 2017; Ouyang et al., 2017). Blast TBI studies where rodents were placed outside the exit end of the tube facing the blast wave have reported spatial working memory deficits measured by MWM (Long et al., 2009; Awwad et al., 2015). Indeed, the location of the animal exposure has been shown to play a significant role in altering the biomechanical loading experienced by the rodent brain (Sundaramurthy et al., 2012). Animals placed outside the shock tube are exposed to reflective pressure waves and blast wind in addition to the primary blast overpressure loading (Sundaramurthy et al., 2012; Svetlov et al., 2010). In this study, the animal is placed prone to the blast overpressure wave at an optimal location inside the shock tube that has been characterized previously to ensure the exposure of the rodent brain to the peak incident pressure while minimizing the effect of blast wind and reflective pressure waves (Sundaramurthy et al., 2012).

The development of cognitive deficits from primary blast may also be related to the age of the animals and time point of cognitive assessment using the MWM. In a study by Vandevord et al. (2012), adolescent rats placed inside the shock tube and subjected to 153 kPa blast developed cognitive deficits in the MWM at 48 h post injury but not at 3, 6 or 72 h time points indicating a very transient deficit which resolves by the 72 h time point. Additionally, neurodegeneration was found in the hilar region which could indicate a higher severity of injury than observed in the adult blast animals used in this study (Vandevord et al., 2012). Adolescent animals have been previously implicated to develop increased neurodegeneration and cognitive deficits when compared to adult animals exposed to TBI (Guilhaume-Correa et al., 2020). In our study, the earliest time point measured after the single blast injury group was 3 days in order to match the timing of the blast plus injury model, Fig. 1. Accordingly, there may be a possibility of transient cognitive deficits within the 72 h post blast that this study did not identify.

While cognitive deficits were not found in the blast injured animals, increased deficits were found in the blast plus injury animals. Similar transient cognitive deficit at 24 h has been reported from repetitive blast TBI using MWM but not at chronic timepoints (Ahlers et al., 2012; Elder et al., 2012a). The blast plus injury animals in this study showed increased cognitive deficits only at the earliest time point and recovered similar to the single blunt injury animals with no prolonged cognitive deficits or increased time of recovery. This indicates that though a single blast may not result in measurable cognitive deficits, the blast does worsen acute cognitive outcome from a secondary blunt injury.

The single blast animals in this study did not produce sensorimotor deficits as assessed by the Rota-Rod test while the single FPI and blast plus animals had similar motor deficits at PID 3 and 6. Accordingly, the blast exposure did not have an effect in the motor deficits of the blast plus injury animals. Motor deficits measured in single and multiple low-level blast exposures using Rota-Rod or beam balance test in shock-

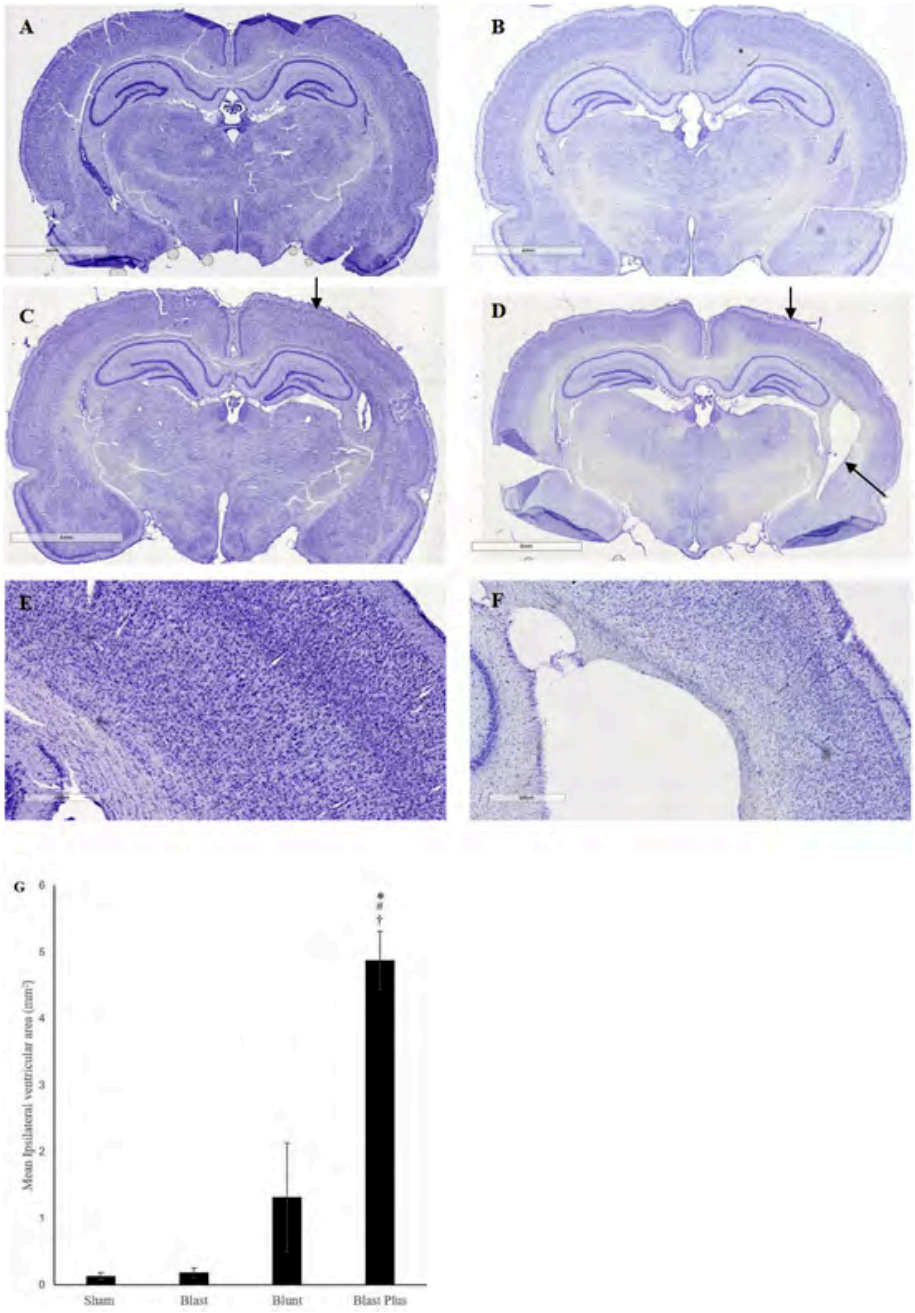


Fig. 9. Ventricular enlargement at 34 days post FPI in (A) Sham, (B) Blast, (C) Blunt, (D) Blast + Blunt animals. The vertical arrows indicate the FPI injury site. Increased ventricular area was observed in the blast plus injury animals 34 days post FPI (D). No ventricular enlargement was observed in either sham (A) or blast (B) animals. Sixty percent of animals subjected to a single FPI injury did not manifest increased ventricular area 34 days post injury (C). (E) Cortex of a sham animal at 4× . (F) Cortex of a blast plus injury animal at 4× indicating cortical thinning and apparent cell loss. (F) Ipsilateral ventricular area measured for sham, single blast, single blunt and blast plus animals. Animals subjected to the blast plus injury had significantly larger area of ventricle enlargement than single injury or sham animals. $n = 5$. * denotes $p < .008$ vs. sham, # denotes $p < .008$ vs blast, † denotes $p < .008$ vs. blunt.

wave tubes with similar animal placement and orientation as our apparatus have also failed to indicate significant deficits (Ahlers et al., 2012; Elder et al., 2012b; Baalman et al., 2013).

The type of anesthesia used and its confounding effects on neuronal outcome has been reported previously (Rowe et al., 2013). In this work, both the blast and the blunt cohort received similar anesthesia regimen of 5% isoflurane, 3 min prior to injury. For the FPI craniectomy, however, ketamine/xylazine (10:1) was used. Fluid percussion studies done under intraperitoneal injections of ketamine, an NMDA antagonist, have been previously reported to cause neuroprotective effects against cognitive deficits (Smith et al., 1993). The blunt injury was carried out 24 h post craniectomy to allow for the animal to recover from surgery and effects of ketamine/xylazine anesthesia as described in previous studies (Dixon et al., 1987). In the Morris Water Maze test, in order to identify the effects of anesthesia and craniectomy, we generated sham blast, sham blunt and blast plus sham groups. No differences were observed in the cognitive scores of the sham blast vs. sham blunt or the single blunt and blast plus sham animals. However, since the single blast animals did not develop any cognitive deficits, it was difficult to assess if the ketamine/xylazine had any neuroprotective effect following the blast injury in the blast plus sham animals. The blast plus animals in this study developed increased cognitive and neuronal deficits. It is possible that the ketamine could

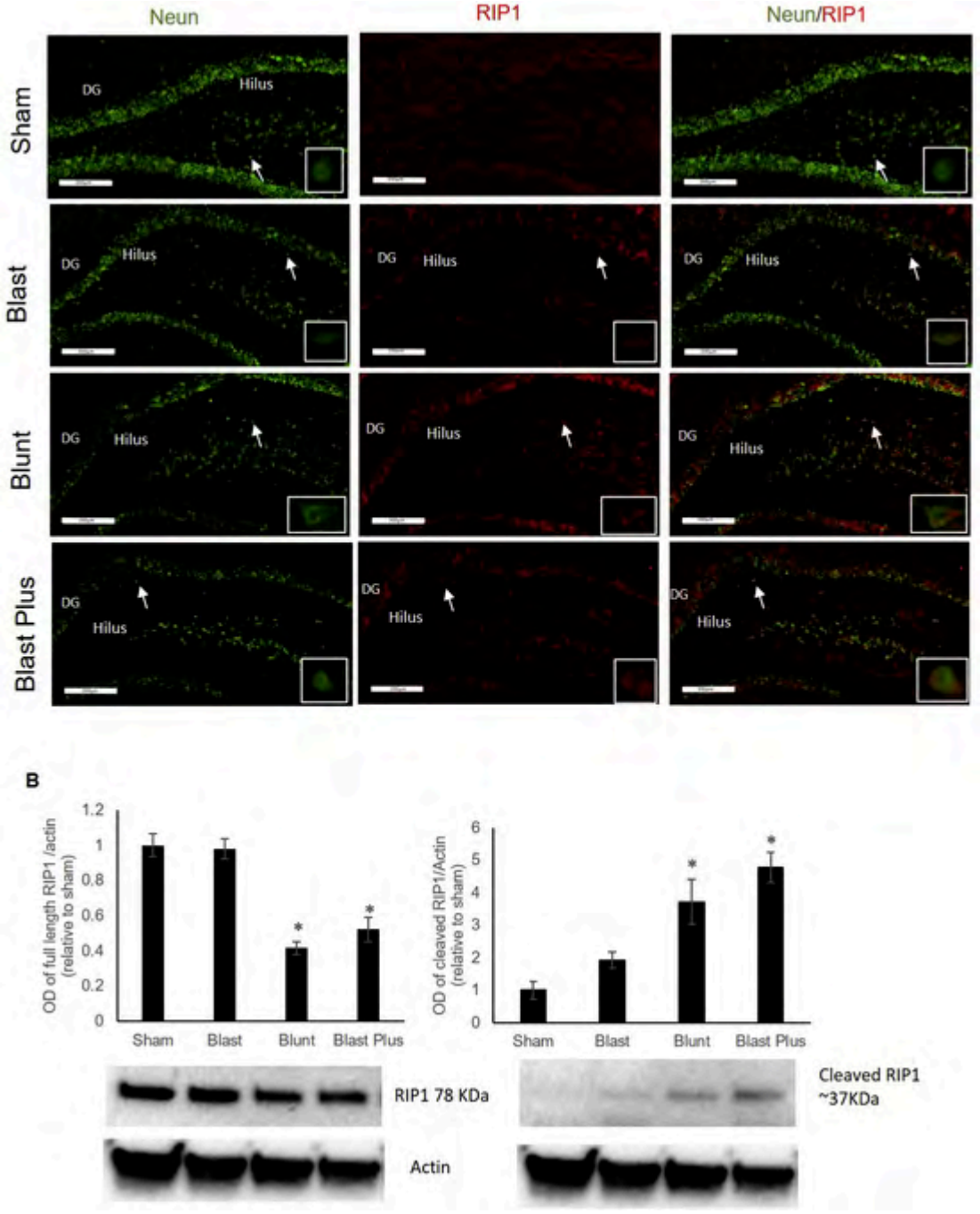


Fig. 10. Expression pattern of RIP1 in the ipsilateral hilar neurons. (A) Expression of RIP1 co-localized with NeuN in the hilar neurons of Sham, Blast, Blunt and Blast plus animals. Increased expression of RIP1 in neurons were observed in all injured groups when compared to sham. (B) Quantification of RIP1 expression in the hippocampus indicated a decreased expression of full-length RIP 1 in single blunt and blast plus groups with a corresponding increase in the caspase 8 cleaved fragment of RIP1 indicating activation of caspase 8 mediated apoptosis in these blunt exposed animals. * denotes $p < .01$ compared to sham.

have provided protection against the initial blast injury and reduced the exacerbation effects on the subsequent blunt injury.

4.2. Blast and blunt injury vary in the onset and progression of neuronal loss

The presence of degenerating neurons has consistently been reported in the ipsilateral hippocampus and sensorimotor cortex regions following FPI injury (Sato et al., 2001; Neuberger et al., 2014; Hicks et al., 1993). The single blunt FPI injury in this study produced neurodegeneration consistent with these studies. Blast TBI outcome in rodent models is heavily dependent on experimental parameters that have widely varied in literature. Previous work from our group and others have indicated the importance of animal positioning in the shock tube, use of head restraint and the positioning of the end plate in the varying the type of loading experienced by the animal and thereby in TBI outcome (Sundaramurthy et al., 2012; Kuriakose et al., 2016). As a result, there is inconsistent reporting of neurodegeneration and behavioral outcome in blast TBI. Our shock tube has been designed to generate the primary loading of the blast overpressure while minimizing effect of reflective waves or tertiary loading. Previous results from our group using silver staining has also indicated an absence of

neurodegeneration in the hippocampal region. Vandevord et al. (2012), using similar shock tube as our group has indicated neurodegeneration as early as 6 h in the hilar region (Vandevord et al., 2012). However, adolescent rats were used in this study compared to the adult rats used in this study. Previous work by Guilhaume-Correa et al. (2020), has shown increased neurodegeneration in adolescent animals compared to adult rodents subjected to TBI (Guilhaume-Correa et al., 2020). However, the significantly increased neurodegeneration observed at 4 h in the blast plus injury animals indicate that the blast exposure causes damage to hippocampal neurons and increases vulnerability to increased neurodegeneration upon a second trauma. While expected neurodegeneration in the sensorimotor cortex was found in the blunt injured animals, the results did not show an increase in neurodegeneration in the blast plus injured animals. Motor deficits are found to accompany increased neurodegeneration and cell death in the sensorimotor cortex (Sato et al., 2001; Peterson et al., 2015; Bramlett et al., 1999; Bhowmick et al., 2018). Since no motor deficits were found in relation to the blast injury, we did not pursue further study of the sensorimotor cortex.

In the ipsilateral hilus of the hippocampus, both a single mild-moderate blast injury and blunt injury with the FPI model leads to similar loss in neuronal numbers and significantly decreased neuronal survival in the blast plus injured animals. These findings are important because it deviates from the TBI literature in two ways. First, the absence of Fluoro-Jade labeling at 24 h in the blast injury is in contrast to FPI where neurodegeneration correlates with neuronal loss (Sato et al., 2001). This suggests that there is a progressive loss of neurons by potentially different mechanisms from blast injury. Second, the neuronal loss in the blast and blast plus animals does not correlate with increased long-term cognitive deficits. Cognitive deficits in rodents subjected to FPI have been related to axonal degeneration, synaptic dysfunction and cell death in the hippocampus (Neuberger et al., 2014). Interestingly the blast animals showed no cognitive deficits in the MWM despite loss of neurons. The additive neuronal loss in the blast plus animals implicates an increased risk to additional cognitive decline. The blunt and blast plus animals, however, recovered to the same performance levels in the water maze. It is possible that the increased performance may have been a result of neuroplasticity occurring during a slower progressive loss of neurons and providing the animals with cognitive activity of testing procedures done at various post injury time points (Griesbach et al., 2007; Wogensen et al., 2015).

The presence of chronic hilar neuronal loss in single blast injury signifies that secondary mechanisms propagates cell loss much differently than in the single blunt injury. Studies by Kuriakose et al. (2018), and Rama Rao et al. (2018), have indicated the hippocampus as a region of vulnerability to increased oxidative and blood brain barrier damage post 180 kPa blast injury (Rama Rao et al., 2018; Kuriakose et al., 2018). Hippocampal neurons were identified to have an increased production of Nicotinamide Adenine Dinucleotide Phosphate Oxidase (NOX) and superoxide production as early as 4 h post mild-moderate blast injury (Rama Rao et al., 2018). Blood brain barrier disruption in the hippocampus and monocyte infiltration into the brain has also been observed 4 h post blast injury. This blood brain barrier breach was, however, reversed at 24 h (Kuriakose et al., 2018). Monocyte infiltration and leakage of blood borne substances into the brain can in turn trigger inflammatory responses. These pro-inflammatory events in a blast injured brain may have a role in the increased susceptibility of the blast plus animals to hilar neurodegeneration at 4 h and cognitive deficits at PID2. Inflammation induced cell death mechanisms such as death receptor mediated pathways could be triggered downstream to further play a role in the progressive cell death observed in the hippocampal neurons.

Receptor interacting protein (RIP1) has been identified to be a highly regulated protein that can be involved in both the extrinsic apoptotic and the necroptotic pathway (Degterev et al., 2008; Ofengeim and Yuan, 2013). Inflammatory cytokines such as tumor necrosis factor alpha (TNF-α) have been identified to be elevated post blast and FPI injury (Elder et al., 2015; Dalle Lucca, 2012; Vitarbo et al., 2004). Activation of TNF receptors can lead to the formation of complex IIA which contains RIP1, FAS-associated protein with a death domain (FADD) and caspase 8 (Ofengeim and Yuan, 2013). TNF induced apoptosis has also been associated with the caspase 8 cleavage of RIP1 at Asp324 in humans and Asp325 in mice (Lin et al., 1999; Kim et al., 2000; Zhang et al., 2015). Inhibition of caspase 8 or FADD leads to RIP1 mediated necroptosis via binding to RIP3 and the formation of complex IIb (Degterev et al., 2008; Ofengeim and Yuan, 2013; Dhuriya and Sharma, 2018). Cleavage of RIP1 by caspase 8 during extrinsic apoptosis has been implicated as a mechanism to prevent RIP1 mediated necroptosis (Declercq et al., 2009).

In this study, we identified increased expression of RIP1 in hippocampal neuronal cells from single blunt and blast plus injury at the 4 h time point. Single blast animals also stained positive for RIP1, 24 h post injury but the expression levels in dentate gyrus neurons were less prominent compared to the single blunt and blast plus injury groups. We also identified increased expression of caspase 8 cleaved RIP1 fragment in the single blunt and blast plus groups and a decrease in full length RIP1 fragment indicating that FPI triggered caspase 8 activation and extrinsic apoptotic pathway at 4 h post injury. Positive Fluoro-Jade staining in the hippocampal neurons as early as 3 h post FPI and positive caspase 3 and TUNEL expression in the hippocampus 72 h post FPI has been previously reported and supports the results observed in this work (Keane et al., 2001; Sato et al., 2001; Rink et al., 1995). Our results also correspond with a study by Liu et al. (2016), which indicated the activation of necroptosis in the cortex but not in the hippocampus 6 h post FPI (Liu et al., 2016).

The activation of caspase 8 in the hilus and RIP1 cleavage may contribute to the increased neurodegeneration observed in the blunt and blast plus animals. The blast animals showed a slight increase expression of RIP1 cleaved fragment but did not show a depletion of the full length RIP1. This suggests that there is no immediate extrinsic apoptosis activated in the blast animals, however, the slight cleavage of RIP1 observed could have a role in the exacerbated neurodegeneration counts in the blast plus animals. Other active inflammatory mechanisms in the blast injury as a result of blood brain barrier disruption could also contribute to the increased vulnerability of the hippocampal neurons observed in the blast plus animals and requires further research.

4.3. Blast plus injury mimics post traumatic hydrocephalus observed in blunt injury of increased severity

Enlargement of the lateral ventricles also known as ventriculomegaly or post traumatic hydrocephalus (PTH) is a condition that has been associated with moderate or severe closed head human TBI. PTH may develop early or in chronic stages after a TBI insult and has been reported in approximately 44% of individuals with severe head trauma (Zhao et al., 2014). Although the mechanism of PTH remains unclear, ventricular enlargement has been attributed to degeneration of white matter surrounding the lateral ventricles, diffuse axonal injury and hypoxic- ischemic trauma (Poca et al., 2005; Meyers et al., 1983; Yoon et al., 2018). Moderate to severe insults by the fluid percussion injury model has resulted in similar observations of increased ventricular volume. Bramlett et al. (1997), reported increased ventricular area in moderate TBI (2.0–2.38 atm) injured FPI rats eight weeks post injury (Bramlett et al., 1997). In a study by Pierce et al. (1998), rats subjected to severe injury of 2.7–3.1 atm were found to develop a cortical cavity by 2–6 months post injury, eventually spreading to the lateral

ventricle and resulting in ventriculomegaly a year post FPI (Pierce et al., 1998).

In this study, only 40% of animals subjected to the mild blunt injury developed slightly enlarged ventricles. However, in blast plus injury substantial chronic ventricular enlargement in all animals were observed to a level observed in more severe FPI animals (> 2.0 atm) (Bramlett et al., 1997; Pierce et al., 1998; Smith et al., 1997; Vink et al., 2001). Blast plus animals also showed significant cortical thinning similar to observations reported in moderate FPI animals at chronic time points (Bramlett et al., 1997). This further suggests that secondary mechanisms of damage in the blast plus trauma persist despite recovery of behavioral deficits by PID2. It has been suggested by Meyers et al. (1983), that ventricular enlargement at acute timepoints is associated with an obstruction to the cerebrospinal fluid while long term ventricular enlargement is associated more with a hypoxic-ischemic insult (Meyers et al., 1983). In the blast plus injured animals, ventricular enlargement was not observed at 4 h but was observed at 34 days post injury. Since these were the only two timepoints that were evaluated in this study, further work is required in establishing if this was an acute or a long-term impairment. Additionally, the mechanisms leading to ventricular enlargement is still unknown and would require future studies to understand the ventricular enlargement observed in higher severity fluid percussion injury and the mechanism of the blast injury in exacerbating the ventricular area observed in the blast plus injured animals.

5. Summary and future directions

In this work, we attempted to identify the effect of a mild-moderate blast wave exposure in increasing the vulnerability of the hippocampus and sensorimotor regions of the brain to a subsequent mild blunt injury. We identified that the blast injury predisposed the hippocampus to increased neurodegeneration leading to chronic neuronal loss and cognitive deficits that recovered with time. In the sensorimotor cortex, the blast did not lead to increased neurodegeneration or motor deficits but resulted in chronic ventricular enlargement resulting in cortical thinning. The blast plus injured animals had almost 50% hilar neuronal loss compared to sham animals despite recovery of cognitive function.

Further, we compared a single mild-moderate blast injury and a mild blunt injury and identified that both injuries differed in their temporal behavioral and pathological outcomes. A single mild-moderate blast did not cause hilar or sensorimotor neurodegeneration, activate extrinsic apoptosis in the hilus at early time points or develop cognitive or motor deficits. However, the blast injury did develop neuronal loss at later time points indicating the presence of secondary mechanisms following a blast leading to neuronal loss. A mild blunt injury, on the other hand, led to immediate neurodegeneration in the hippocampal and sensorimotor regions with cognitive, motor deficits that developed at early time points and recovered over time. Blunt injury also led to activation of caspase 8 activation in the hippocampus at 4 h post impact. Blunt injury, thus, resulted in immediate events that results in neurodegeneration and behavioral deficits while the blast impact developed neuronal loss over time. This result indicates that cell death mechanisms involved in both injuries could be different and are activated at varied time points despite resulting in similar neuronal loss numbers over time. Our future direction is to explore the role of death receptor and inflammasome triggered cell death pathways to elucidate the mechanisms leading to the chronic hilar neuronal loss in the blast and blunt injury. The increased time window after the blast injury for the onset of neuronal loss may provide increased avenues for therapeutic intervention.

The main objective of this study was to understand whether a prior blast predisposed the brain to exacerbated injury outcome on a second blunt injury. Most soldiers subjected to a mild-moderate primary loading of blast are rarely evacuated and may develop behavioral and physical symptoms, but the onset and severity of these symptoms may be staggered and can occur months if not years post the primary exposure. This leads to an underdiagnosis of mild-moderate blast TBI and an increased risk of deficits on exposure to a second TBI (Buck, 2011). Repetitive blast or blunt injury have been studied in rodent models and has been found to increase the deficits caused by a single TBI (Meabon et al., 2016; Shultz et al., 2012; Mouzon et al., 2012; Wang et al., 2011). In these repetitive studies of blast or blunt injury, each injury subjected is identical in terms of magnitude, duration and loading conditions. However, in the blast plus injury model studied in this work, the blast and blunt injury vary in their temporal, spatial loading, onset and propagation of behavioral and cellular deficits. Thus, the deficits observed in the blast plus injury model in this study is unique to the biomechanical loading conditions of the single blast and blunt injury and would be different from the deficits observed in two mild-moderate blasts or two mild blunt injuries studied.

This study establishes the increased risk caused by the primary effect of the blast wave that may not result in overt deficits by itself but exacerbates the behavioral outcome and neuronal loss on a second trauma 24 h post blast. In our study, the blast and the blunt injury were separated by 24 h in order to allow for the animals to recover from the craniectomy surgery. Repetitive low- level blast studies in rodent models subjected to 3 blasts separated by 24 h have also demonstrated increased risk of neurological impairment (Meabon et al., 2016; Perez-Garcia et al., 2018; Skotak et al., 2019). A second scenario is exposure to blast resulting in a blunt TBI due to a fall. This scenario correlates to the tertiary effect of a blast loading that causes an additional acceleration-deceleration effect on the brain. In rodent models of blast TBI with no head restraint, the additional acceleration forces on the brain have been reported to increase memory deficits, neurological impairments and decrease survivability (Goldstein et al., 2012; Gullotti et al., 2014). Blast plus injuries could also be a potential reason for the lack of difference in clinical outcome of blast and blunt TBI observed in veteran population. This work demonstrates an increased susceptibility to TBI 24 h post blast TBI. We also observe a delayed onset of neuronal loss in blast TBI. Future work is needed to determine the time of onset and mechanism of neuronal loss following a single blast TBI to determine the time window of increased susceptibility to TBI post blast injury.

Author contributions

Aswati Aravind: Investigation, Project administration, Formal analysis, Writing- original draft preparation. Julianna Kosty: Investigation, Formal analysis. Namas Chandra: Resources, Supervision, Writing- review and editing. Bryan J Pfister: Resources, Conceptualization, Supervision, Funding acquisition, Writing- review and editing.

Declaration of Competing Interest

The authors declare that they have no known competing financial interests or personal relationships that could have appeared to influence the work reported in this paper.

Acknowledgements

This work was funded by New Jersey Commission on Brain Injury Research [grant no. CBIR16PIL021] and U.S. Army Medical Research and Materiel Command [grant no. 14059001, W81XWH-15-1-0303]. The authors gratefully acknowledge the assistance of Dr. Kevin Pang (Veterans Admin. Medical Center, Rutgers University) for his valuable insights and guidance in setting up the behavioral experiments and in statistical analysis. We thank Dr. James Haorah (New Jersey Institute of Technology) for use of the fluid percussion injury device. We also thank Matthew Long, Eren Alay, Jose Rodriguez, Xiaotang Ma and

Mike Dolegiewitz for their assistance in performing blast and blunt injuries.

Appendix A. Supplementary data

Supplementary data to this article can be found online at https://doi.org/10.1016/j.expneurol.2020.113378.

References

Ahlers, S T, Vasserman-Stokes, E, Shaughness, M C, Hall, A A, Shear, D A, Chavko, M, McCarron, R M, Stone, J R, 2012. Assessment of the effects of acute and repeated exposure to blast overpressure in rodents: toward a greater understanding of blast and the potential ramifications for injury in humans exposed to blast. Front. Neurol. 3, 32. doi:10.3389/fneur.2012.00032.

Aungst, S L, Kabadi, S V, Thompson, S M, Stoica, B A, Faden, A I, 2014. Repeated mild traumatic brain injury causes chronic neuroinflammation, changes in hippocampal synaptic plasticity, and associated cognitive deficits. J. Cereb. Blood Flow Metab. 34 (7), 1223–1232. doi:10.1038/jcbfm.2014.75.

Awwad, H O, Gonzalez, L P, Tompkins, P, Lerner, M, Brackett, D J, Awasthi, V, Standifer, K M, 2015. Blast overpressure waves induce transient anxiety and regional changes in cerebral glucose metabolism and delayed hyperarousal in rats. Front. Neurol. 6, 132. doi:10.3389/fneur.2015.00132.

Baalman, K L, Cotton, R J, Rasband, S N, Rasband, M N, 2013. Blast wave exposure impairs memory and decreases axon initial segment length. J. Neurotrauma 30 (9), 741–751. doi:10.1089/neu.2012.2478.

Bhowmick, S, D'Mello, V, Ponery, N, Abdul-Muneer, P M, 2018. Neurodegeneration and Sensorimotor Deficits in the Mouse Model of Traumatic Brain Injury. Brain Sci 8(1). doi:10.3390/brainsci8010011.

Bramlett, H M, Dietrich, W D, Green, E J, Busto, R, 1997. Chronic histopathological consequences of fluid-percussion brain injury in rats: effects of post-traumatic hypothermia. Acta Neuropathol. 93 (2), 190–199. doi:10.1007/s004010050602.

Bramlett, H M, Dietrich, W D, Green, E J, 1999. Secondary hypoxia following moderate fluid percussion brain injury in rats exacerbates sensorimotor and cognitive deficits. J. Neurotrauma 16 (11), 1035–1047. doi:10.1089/neu.1999.16.1035.

Broadbent, N J, Squire, L R, Clark, R E, 2006. Reversible hippocampal lesions disrupt water maze performance during both recent and remote memory tests. Learn. Mem. 13 (2), 187–191. doi:10.1101/lm.134706.

Buck, P W, 2011. Mild traumatic brain injury: a silent epidemic in our practices. Health Soc. Work 36 (4), 299–302. doi:10.1093/hsw/36.4.299.

Chen, X, Zhao, Z, Chai, Y, Luo, L, Jiang, R, Zhang, J, 2014. The incidence of critical-illness-related-corticosteroid-insufficiency is associated with severity of traumatic brain injury in adult rats. J. Neurol. Sci. 342 (1–2), 93–100. doi:10.1016/j.jns.2014.04.032.

Clark, A L, Merritt, V C, Bigler, E D, Bangen, K J, Werhane, M, Sorg, S F, Bondi, M W, Schiehser, D M, Delano-Wood, L, 2018. Blast-exposed veterans with mild traumatic brain injury show greater frontal cortical thinning and poorer executive functioning. Front. Neurol. 9, 873. doi:10.3389/fneur.2018.00873.

Conti, A C, Raghupathi, R, Trojanowski, J Q, McIntosh, T K, 1998. Experimental brain injury induces regionally distinct apoptosis during the acute and delayed post-traumatic period. J. Neurosci. 18 (15), 5663–5672.

Dalle Lucca, J J, 2012. M. Chavko, M.a. Dubick, S. Adeeb, M.J. Falabella, J.L. slack, R. McCarron, and Y. Li, *Blast-induced moderate neurotrauma (BINT) elicits early complement activation and tumor necrosis factor alpha (TNFalpha) release in a rat brain.* J. Neurol. Sci. 318 (1–2), 146–154. doi:10.1016/j.jns.2012.02.002.

Declercq, W, Vanden Berghe, T, Vandenabeele, P, 2009. RIP kinases at the crossroads of cell death and survival. Cell 138 (2), 229–232. doi:10.1016/j.cell.2009.07.006.

Degterev, A, Hitomi, J, Germscheid, M, Ch'en, I L, Korkina, O, Teng, X, Abbott, D, Cuny, G D, Yuan, C, Wagner, G, Hedrick, S M, Gerber, S A, Lugovskoy, A, Yuan, J, 2008. Identification of RIP1 kinase as a specific cellular target of necrostatins. Nat. Chem. Biol. 4 (5), 313–321. doi:10.1038/nchembio.83.

Dhuriya, Y K, Sharma, D, 2018. Necroptosis: a regulated inflammatory mode of cell death. J. Neuroinflammation 15 (1), 199. doi:10.1186/s12974-018-1235-0.

Dixon, C E, Lyeth, B G, Povlishock, J T, Findling, R L, Hamm, R J, Marmarou, A, Young, H F, Hayes, R L, 1987. A fluid percussion model of experimental brain injury in the rat. J. Neurosurg. 67 (1), 110–119. doi:10.3171/jns.1987.67.1.0110.

DoD Worldwide Numbers for TBI [cited 2019 7/19/2019]. Available from:https://dvbic.dcoe.mil/dod-worldwide-numbers-tbi

Dretsch, M N, Kelly, M P, Coldren, R L, Parish, R V, Russell, M L, 2015. No significant acute and subacute differences between blast and blunt concussions across multiple neurocognitive measures and symptoms in deployed soldiers. J. Neurotrauma 32 (16), 1217–1222. doi:10.1089/neu.2014.3637.

Elder, G A, Dorr, N P, De Gasperi, R, Gama Sosa, M A, Shaughness, M C, Maudlin-Jeronimo, E, Hall, A A, McCarron, R M, Ahlers, S T, 2012. Blast Exposure Induces Post-Traumatic Stress Disorder-Related Traits in a Rat Model of Mild Traumatic Brain Injury. 29(16). pp. 2564–2575. doi:10.1089/neu.2012.2510.

Elder, G A, Dorr, N P, De Gasperi, R, Sosa, M A G, Shaughness, M C, Maudlin-Jeronimo, E, Hall, A A, McCarron, R M, Ahlers, S T, 2012. Blast exposure induces post-traumatic stress disorder-related traits in a rat model of mild traumatic brain injury. J. Neurotrauma 29 (16), 2564–2575. doi:10.1089/neu.2012.2510.

Elder, G A, Gama Sosa, M A, De Gasperi, R, Stone, J R, Dickstein, D L, Haghighi, F, Hof, P R, Ahlers, S T, 2015. Vascular and inflammatory factors in the pathophysiology of blast-induced brain injury. Front. Neurol. 6, 48. doi:10.3389/fneur.2015.00048.

Floyd, C L, Golden, K M, Black, R T, Hamm, R J, Lyeth, B G, 2002. Craniectomy position affects Morris water maze performance and hippocampal cell loss after parasagittal fluid percussion. J. Neurotrauma 19 (3), 303–316. doi:10.1089/089771502753594873.

Fujimoto, S T, Longhi, L, Saatman, K E, Conte, V, Stocchetti, N, McIntosh, T K, 2004. Motor and cognitive function evaluation following experimental traumatic brain injury. Neurosci. Biobehav. Rev. 28 (4), 365–378. doi:10.1016/j.neubiorev.2004.06.002.

Goldstein, L E, Fisher, A M, Tagge, C A, Zhang, X L, Velisek, L, Sullivan, J A, Upreti, C, Kracht, J M, Ericsson, M, Wojnarowicz, M W, Goletiani, C J, Maglakelidze, G M, Casey, N, Moncaster, J A, Minaeva, O, Moir, R D, Nowinski, C J, Stern, R A, Cantu, R C, Geiling, J, Blusztajn, J K, Wolozin, B L, Ikezu, T, Stein, T D, Budson, A E, Kowall, N W, Chargin, D, Sharon, A, Saman, S, Hall, G F, Moss, W C, Cleveland, R O, Tanzi, R E, Stanton, P K, McKee, A C, 2012. Chronic traumatic encephalopathy in blast-exposed military veterans and a blast neurotrauma mouse model. Sci. Transl. Med. 4 (134), 134ra60. doi:10.1126/scitranslmed.3003716.

Golub, V M, Brewer, J, Wu, X, Kuruba, R, Short, J, Manchi, M, Swonke, M, Younus, I, Reddy, D S, 2015. Neurostereology protocol for unbiased quantification of neuronal injury and neurodegeneration. Front. Aging Neurosci. 7, 196. doi:10.3389/fnagi.2015.00196.

Grady, M S, Charleston, J S, Maris, D, Witgen, B M, Lifshitz, J, 2003. Neuronal and glial cell number in the hippocampus after experimental traumatic brain injury: analysis by stereological estimation. J. Neurotrauma 20 (10), 929–941. doi:10.1089/089771503770195786.

Griesbach, G S, Gomez-Pinilla, F, Hovda, D A, 2007. Time window for voluntary exercise-induced increases in hippocampal neuroplasticity molecules after traumatic brain injury is severity dependent. J. Neurotrauma 24 (7), 1161–1171. doi:10.1089/neu.2006.0255.

Guilhaume-Correa, F, Cansler, S M, Shalosky, E M, Goodman, M D, Evanson, N K, 2020. Greater neurodegeneration and behavioral deficits after single closed head traumatic brain injury in adolescent versus adult male mice. J. Neurosci. Res. 98 (3), 557–570. doi:10.1002/jnr.24535.

Gullotti, D M, Beamer, M, Panzer, M B, Chen, Y C, Patel, T P, Yu, A, Jaumard, N, Winkelstein, B, Bass, C R, Morrison, B, Meaney, D F, 2014. Significant head accelerations can influence immediate neurological impairments in a murine model of blast-induced traumatic brain injury. J. Biomech. Eng. 136 (9), 091004. doi:10.1115/1.4027873.

Gupta, A, Elgammal, F S, Proddutur, A, Shah, S, Santhakumar, V, 2012. Decrease in tonic inhibition contributes to increase in dentate semilunar granule cell excitability after brain injury. J. Neurosci. 32 (7), 2523–2537. doi:10.1523/JNEUROSCI.4141-11.2012.

Hamm, R J, White-Gbadebo, D M, Lyeth, B G, Jenkins, L W, Hayes, R L, 1992. The effect of age on motor and cognitive deficits after traumatic brain injury in rats. Neurosurgery 31 (6), 1072–1077 discussion 1078. https://doi.org/10.1227/00006123-199212000-00013.

Hamm, R J, Lyeth, B G, Jenkins, L W, O'Dell, D M, Pike, B R, 1993. Selective cognitive impairment following traumatic brain injury in rats. Behav. Brain Res. 59 (1–2), 169–173. doi:10.1016/0166-4328(93)90164-l.

Hamm, R J, Pike, B R, O'Dell, D M, Lyeth, B G, Jenkins, L W, 1994. The Rotarod test: an evaluation of its effectiveness in assessing motor deficits following traumatic brain injury. J. Neurotrauma 11 (2), 187–196. doi:10.1089/neu.1994.11.187.

Heitger, M H, Jones, R D, Dalrymple-Alford, J C, Frampton, C M, Ardagh, M W, Anderson, T J, 2006. Motor deficits and recovery during the first year following mild closed head injury. Brain Inj. 20 (8), 807–824. doi:10.1080/02699050600676354.

Hellmich, H L, Eidson, K A, Capra, B A, Garcia, J M, Boone, D R, Hawkins, B E, Uchida, T, Dewitt, D S, Prough, D S, 2007. Injured Fluoro-jade-positive hippocampal neurons contain high levels of zinc after traumatic brain injury. Brain Res. 1127 (1), 119–126. doi:10.1016/j.brainres.2006.09.094.

Hicks, R R, Smith, D H, Lowenstein, D H, Saint Marie, R, McIntosh, T K, 1993. Mild experimental brain injury in the rat induces cognitive deficits associated with regional neuronal loss in the hippocampus. J. Neurotrauma 10 (4), 405–414. doi:10.1089/neu.1993.10.405.

Hoffer, M E, Donaldson, C, Gottshall, K R, Balaban, C, Balough, B J, 2009. Blunt and blast head trauma: different entities. Int Tinnitus J 15 (2), 115–118.

Hylin, M J, Orsi, S A, Zhao, J, Bockhorst, K, Perez, A, Moore, A N, Dash, P K, 2013. Behavioral and histopathological alterations resulting from mild fluid percussion injury. J. Neurotrauma 30 (9), 702–715. doi:10.1089/neu.2012.2630.

Keane, R W, Kraydieh, S, Lotocki, G, Alonso, O F, Aldana, P, Dietrich, W D, 2001. Apoptotic and antiapoptotic mechanisms after traumatic brain injury. J. Cereb. Blood Flow Metab. 21 (10), 1189–1198. doi:10.1097/00004647-200110000-00007.

Kim, J W, Choi, E J, Joe, C O, 2000. Activation of death-inducing signaling complex (DISC) by pro-apoptotic C-terminal fragment of RIP. Oncogene 19 (39), 4491–4499. doi:10.1038/sj.onc.1203796.

Kontos, A P, Kotwal, R S, Elbin, R J, Lutz, R H, Forsten, R D, Benson, P J, Guskiewicz, K M, 2013. Residual effects of combat-related mild traumatic brain injury. J. Neurotrauma 30 (8), 680–686. doi:10.1089/neu.2012.2506.

Korgaonkar, A A, Li, Y, Sekhar, D, Subramanian, D, Guevarra, J, Swietek, B, Pallottie, A, Singh, S, Kella, K, Elkabes, S, Santhakumar, V, 2020. Toll-like receptor 4 signaling in neurons enhances calcium-permeable alpha-Amino-3-Hydroxy-5-Methyl-4-Isoxazolepropionic acid receptor currents and drives post-traumatic Epileptogenesis. Ann. Neurol. 87 (4), 497–515. doi:10.1002/ana.25698.

Kuriakose, M, Skotak, M, Misistia, A, Kahali, S, Sundaramurthy, A, Chandra, N, 2016. Tailoring the blast exposure conditions in the shock tube for generating pure, primary shock waves: the end plate facilitates elimination of secondary loading of the specimen. PLoS One 11 (9), e0161597. doi:10.1371/journal.pone.0161597.

Kuriakose, M, Rama Rao, K V, Younger, D, Chandra, N, 2018. Temporal and spatial effects of blast overpressure on blood-brain barrier permeability in traumatic brain injury. Sci. Rep. 8 (1), 8681. doi:10.1038/s41598-018-26813-7.

Kuriakose, M, Younger, D, Ravula, A R, Alay, E, Rama Rao, K V, Chandra, N, 2019. Synergistic role of oxidative stress and blood-brain barrier permeability as injury mechanisms in the acute pathophysiology of blast-induced Neurotrauma. Sci. Rep. 9 (1), 7717. doi:10.1038/s41598-019-44147-w.

Lange, R T, Pancholi, S, Brickell, T A, Sakura, S, Bhagwat, A, Merritt, V, French, L M, 2012. Neuropsychological outcome from blast versus non-blast: mild traumatic brain injury in U.S. military service members. J. Int. Neuropsychol. Soc. 18 (3), 595–605. doi:10.1017/S1355617712000239.

Lin, Y, Devin, A, Rodriguez, Y, Liu, Z G, 1999. Cleavage of the death domain kinase RIP by caspase-8 prompts TNF-induced apoptosis. Genes Dev. 13 (19), 2514–2526. doi:10.1101/gad.13.19.2514.

Liu, T, Zhao, D X, Cui, H, Chen, L, Bao, Y H, Wang, Y, Jiang, J Y, 2016. Therapeutic hypothermia attenuates tissue damage and cytokine expression after traumatic brain injury by inhibiting necroptosis in the rat. Sci. Rep. 6, 24547. doi:10.1038/srep24547.

Liu, W, Chen, Y, Meng, J, Wu, M, Bi, F, Chang, C, Li, H, Zhang, L, 2018. Ablation of caspase-1 protects against TBI-induced pyroptosis in vitro and in vivo. J. Neuroinflammation 15 (1), 48. doi:10.1186/s12974-018-1083-y.

Long, J B, Bentley, T L, Wessner, K A, Cerone, C, Sweeney, S, Bauman, R A, 2009. Blast overpressure in rats: recreating a battlefield injury in the laboratory. J. Neurotrauma 26 (6), 827–840. doi:10.1089/neu.2008.0748.

Lucke-Wold, B P, Logsdon, A F, Turner, R C, Huber, J D, Rosen, C L, 2017. Endoplasmic reticulum stress modulation as a target for ameliorating effects of blast induced traumatic brain injury. J. Neurotrauma 34 (S1), S62–S70. doi:10.1089/neu.2016.4680.

Ma, X, Cheng, Y, Garcia, R, Haorah, J, 2019. Hemorrhage Associated Mechanisms of Neuroinflammation in Experimental Traumatic Brain Injury. J. NeuroImmune Pharmacol.. doi:10.1007/s11481-019-09882-x.

Ma, X, Aravind, A, Pfister, B J, Chandra, N, Haorah, J, 2019. Animal models of traumatic brain injury and assessment of injury severity. Mol. Neurobiol. 56 (8), 5332–5345. doi:10.1007/s12035-018-1454-5.

Mac Donald, C L, Johnson, A M, Cooper, D, Nelson, E C, Werner, N J, Shimony, J S, Snyder, A Z, Raichle, M E, Witherow, J R, Fang, R, Flaherty, S F, Brody, D L, 2011. Detection of blast-related traumatic brain injury in U.S. military personnel. N. Engl. J. Med. 364 (22), 2091–2100. doi:10.1056/NEJMoa1008069.

MacDonald, C L, Johnson, A M, Nelson, E C, Werner, N J, Fang, R, Flaherty, S F, Brody, D L, 2014. Functional status after blast-plus-impact complex concussive traumatic brain injury in evacuated United States military personnel. J. Neurotrauma 31 (10), 889–898. doi:10.1089/neu.2013.3173.

Maguen, S, Madden, E, Lau, K M, Seal, K, 2012. The impact of head injury mechanism on mental health symptoms in veterans: do number and type of exposures matter? J. Trauma. Stress. 25 (1), 3–9. doi:10.1002/jts.21669.

Meabon, J S, Huber, B R, Cross, D J, Richards, T L, Minoshima, S, Pagulayan, K F, Li, G, Meeker, K D, Kraemer, B C, Petrie, E C, Raskind, M A, Peskind, E R, Cook, D G, 2016. Repetitive blast exposure in mice and combat veterans causes persistent cerebellar dysfunction. Sci. Transl. Med. 8 (321) p. 321ra6. doi:10.1126/scitranslmed.aaa9585.

Mendez, M F, Owens, E M, Reza Berenji, G, Peppers, D C, Liang, L J, Licht, E A, 2013. Mild traumatic brain injury from primary blast vs. blunt forces: post-concussion consequences and functional neuroimaging. NeuroRehabilitation 32 (2), 397–407. doi:10.3233/NRE-130861.

Meyers, C A, Levin, H S, Eisenberg, H M, Guinto, F C, 1983. Early versus late lateral ventricular enlargement following closed head injury. J. Neurol. Neurosurg. Psychiatry 46 (12), 1092–1097. doi:10.1136/jnnp.46.12.1092.

Mishra, V, Skotak, M, Schuetz, H, Heller, A, Haorah, J, Chandra, N, 2016. Primary blast causes mild, moderate, severe and lethal TBI with increasing blast overpressures: experimental rat injury model. Sci. Rep. 6, 26992. doi:10.1038/srep26992.

Mouzon, B, Chaytow, H, Crynen, G, Bachmeier, C, Stewart, J, Mullan, M, Stewart, W, Crawford, F, 2012. Repetitive mild traumatic brain injury in a mouse model produces learning and memory deficits accompanied by histological changes. J. Neurotrauma 29 (18), 2761–2773. doi:10.1089/neu.2012.2498.

Neuberger, E J, Wahab, R A, Jayakumar, A, Pfister, B J, Santhakumar, V, 2014. Distinct effect of impact rise times on immediate and early neuropathology after brain injury in juvenile rats. J. Neurosci. Res. 92 (10), 1350–1361. doi:10.1002/jnr.23401.

Neuberger, E J, Swietek, B, Corrubia, L, Prasanna, A, Santhakumar, V, 2017. Enhanced dentate neurogenesis after brain injury undermines Long-term neurogenic potential and promotes seizure susceptibility. Stem Cell Reports 9 (3), 972–984. doi:10.1016/j.stemcr.2017.07.015.

Nichols, J N, Deshane, A S, Niedzielko, T L, Smith, C D, Floyd, C L, 2016. Greater neurobehavioral deficits occur in adult mice after repeated, as compared to single, mild traumatic brain injury (mTBI). Behav. Brain Res. 298 (Pt B), 111–124. doi:10.1016/j.bbr.2015.10.052.

Ofengeim, D, Yuan, J, 2013. Regulation of RIP1 kinase signalling at the crossroads of inflammation and cell death. Nat. Rev. Mol. Cell Biol. 14 (11), 727–736. doi:10.1038/nrm3683.

Olesen, M V, Needham, E K, Pakkenberg, B, 2017. The optical fractionator technique to estimate cell numbers in a rat model of electroconvulsive therapy. J. Vis. Exp. 125. doi:10.3791/55737.

Ouyang, J, Pace, E, Lepczyk, L, Kaufman, M, Zhang, J, Perrine, S A, Zhang, J, 2017. Blast-induced tinnitus and elevated central auditory and limbic activity in rats: a manganese-enhanced MRI and behavioral study. Sci. Rep. 7 (1), 4852. doi:10.1038/s41598-017-04941-w.

Perez-Garcia, G, De Gasperi, R, Gama Sosa, M A, Perez, G M, Otero-Pagan, A, Tschiffely, A, McCarron, R M, Ahlers, S T, Elder, G A, Gandy, S, 2018. PTSD-Related Behavioral Traits in a Rat Model of Blast-Induced mTBI Are Reversed by the mGluR2/3 Receptor Antagonist BCI-838. eNeuro 5(1). doi:10.1523/ENEURO.0357-17.2018.

Peterson, T C, Maass, W R, Anderson, J R, Anderson, G D, Hoane, M R, 2015. A behavioral and histological comparison of fluid percussion injury and controlled cortical impact injury to the rat sensorimotor cortex. Behav. Brain Res. 294, 254–263. doi:10.1016/j.bbr.2015.08.007.

Petrie, E C, Cross, D J, Yarnykh, V L, Richards, T, Martin, N M, Pagulayan, K, Hoff, D, Hart, K, Mayer, C, Tarabochia, M, Raskind, M A, Minoshima, S, Peskind, E R, 2014. Neuroimaging, behavioral, and psychological sequelae of repetitive combined blast/impact mild traumatic brain injury in Iraq and Afghanistan war veterans. J. Neurotrauma 31 (5), 425–436. doi:10.1089/neu.2013.2952.

Pierce, J E, Smith, D H, Trojanowski, J Q, McIntosh, T K, 1998. Enduring cognitive, neurobehavioral and histopathological changes persist for up to one year following severe experimental brain injury in rats. Neuroscience 87 (2), 359–369. doi:10.1016/s0306-4522(98)00142-0.

Poca, M A, Sahuquillo, J, Mataro, M, Benejam, B, Arikan, F, Baguena, M, 2005. Ventricular enlargement after moderate or severe head injury: a frequent and neglected problem. J. Neurotrauma 22 (11), 1303–1310. doi:10.1089/neu.2005.22.1303.

Rama Rao, K V, Iring, S, Younger, D, Kuriakose, M, Skotak, M, Alay, E, Gupta, R K, Chandra, N, 2018. A Single Primary Blast-Induced Traumatic Brain Injury in a Rodent Model Causes Cell-Type Dependent Increase in Nicotinamide Adenine Dinucleotide Phosphate Oxidase Isoforms in Vulnerable Brain Regions. J. Neurotrauma 35 (17), 2077–2090. doi:10.1089/neu.2017.5358.

Rink, A, Fung, K M, Trojanowski, J Q, Lee, V M, Neugebauer, E, McIntosh, T K, 1995. Evidence of apoptotic cell death after experimental traumatic brain injury in the rat. Am. J. Pathol. 147 (6), 1575–1583.

Rowe, R K, Harrison, J L, Thomas, T C, Pauly, J R, Adelson, P D, Lifshitz, J, 2013. Using anesthetics and analgesics in experimental traumatic brain injury. Lab Anim (NY) 42 (8), 286–291. doi:10.1038/laban.257.

Sato, M, Chang, E, Igarashi, T, Noble, L J, 2001. Neuronal injury and loss after traumatic brain injury: time course and regional variability. Brain Res. 917 (1), 45–54. doi:10.1016/s0006-8993(01)02905-5.

Shultz, S R, MacFabe, D F, Foley, K A, Taylor, R, Cain, D P, 2011. A single mild fluid percussion injury induces short-term behavioral and neuropathological changes in the Long-Evans rat: support for an animal model of concussion. Behav. Brain Res. 224 (2), 326–335. doi:10.1016/j.bbr.2011.06.012.

Shultz, S R, Bao, F, Omana, V, Chiu, C, Brown, A, Cain, D P, 2012. Repeated mild lateral fluid percussion brain injury in the rat causes cumulative long-term behavioral impairments, neuroinflammation, and cortical loss in an animal model of repeated concussion. J. Neurotrauma 29 (2), 281–294. doi:10.1089/neu.2011.2123.

Skotak, M, Wang, F, Alai, A, Holmberg, A, Harris, S, Switzer, R C, Chandra, N, 2013. Rat injury model under controlled field-relevant primary blast conditions: acute response to a wide range of peak overpressures. J. Neurotrauma 30 (13), 1147–1160. doi:10.1089/neu.2012.2652.

Skotak, M, Townsend, M T, Ramarao, K V, Chandra, N, 2019. A comprehensive review of experimental rodent models of repeated blast TBI. Front. Neurol. 10, 1015. doi:10.3389/fneur.2019.01015.

Smith, D H, Okiyama, K, Thomas, M J, Claussen, B, McIntosh, T K, 1991. Evaluation of memory dysfunction following experimental brain injury using the Morris water maze. J. Neurotrauma 8 (4), 259–269. doi:10.1089/neu.1991.8.259.

Smith, D H, Okiyama, K, Gennarelli, T A, McIntosh, T K, 1993. Magnesium and ketamine attenuate cognitive dysfunction following experimental brain injury. Neurosci. Lett. 157 (2), 211–214. doi:10.1016/0304-3940(93)90739-8.

Smith, D H, Chen, X H, Pierce, J E, Wolf, J A, Trojanowski, J Q, Graham, D I, McIntosh, T K, 1997. Progressive atrophy and neuron death for one year following brain trauma in the rat. J. Neurotrauma 14 (10), 715–727. doi:10.1089/neu.1997.14.715.

Stemper, B D, Shah, A S, Budde, M D, Olsen, C M, Glavaski-Joksimovic, A, Kurpad, S N, McCrea, M, Pintar, F A, 2016. Behavioral outcomes differ between rotational acceleration and blast mechanisms of mild traumatic brain injury. Front. Neurol. 7, 31. doi:10.3389/fneur.2016.00031.

Sundaramurthy, A, Alai, A, Ganpule, S, Holmberg, A, Plougonven, E, Chandra, N, 2012. Blast-induced biomechanical loading of the rat: an experimental and anatomically accurate computational blast injury model. J. Neurotrauma 29 (13), 2352–2364. doi:10.1089/neu.2012.2413.

Svetlov, S I, Prima, V, Kirk, D R, Gutierrez, H, Curley, K C, Hayes, R L, Wang, K K, 2010. Morphologic and biochemical characterization of brain injury in a model of controlled blast overpressure exposure. J. Trauma 69 (4), 795–804. doi:10.1097/TA.0b013e3181bbd885.

Swick, D, Honzel, N, Larsen, J, Ashley, V, Justus, T, 2012. Impaired response inhibition in veterans with post-traumatic stress disorder and mild traumatic brain injury. J. Int. Neuropsychol. Soc. 18 (5), 917–926. doi:10.1017/S1355617712000458.

Thompson, H J, Lifshitz, J, Marklund, N, Grady, M S, Graham, D I, Hovda, D A, McIntosh, T K, 2005. Lateral fluid percussion brain injury: a 15-year review and evaluation. J. Neurotrauma 22 (1), 42–75. doi:10.1089/neu.2005.22.42.

Tompkins, P, Tesiram, Y, Lerner, M, Gonzalez, L P, Lightfoot, S, Rabb, C H, Brackett, D J, 2013. Brain injury: neuro-inflammation, cognitive deficit, and magnetic resonance imaging in a model of blast induced traumatic brain injury. J. Neurotrauma 30 (22), 1888–1897. doi:10.1089/neu.2012.2674.

Trudeau, D L, Anderson, J, Hansen, L M, Shagalov, D N, Schmoller, J, Nugent, S, Barton, S, 1998. Findings of mild traumatic brain injury in combat veterans with PTSD and a history of blast concussion. J. Neuropsychiatr. Clin. Neurosci. 10 (3), 308–313. doi:10.1176/jnp.10.3.308.

Vandevord, P J, Bolander, R, Sajja, V S, Hay, K, Bir, C A, 2012. Mild neurotrauma indicates a range-specific pressure response to low level shock wave exposure. Ann. Biomed. Eng. 40 (1), 227–236. doi:10.1007/s10439-011-0420-4.

Vink, R, Mullins, P G, Temple, M D, Bao, W, Faden, A I, 2001. Small shifts in craniotomy position in the lateral fluid percussion injury model are associated with differential lesion development. J. Neurotrauma 18 (8), 839–847. doi:10.1089/089771501316919201.

Vitarbo, E A, Chatzipanteli, K, Kinoshita, K, Truettner, J S, Alonso, O F, Dietrich, W D, 2004. Tumor necrosis factor alpha expression and protein levels after fluid percussion injury in rats: the effect of injury severity and brain temperature. Neurosurgery 55 (2), 416–424 discussion 424-5. https://doi.org/10.1227/01.neu.0000130036.52521.2c.

Wahab, R A, Neuberger, E J, Lyeth, B G, Santhakumar, V, Pfister, B J, 2015. Fluid percussion injury device for the precise control of injury parameters. J. Neurosci. Methods 248, 16–26. doi:10.1016/j.jneumeth.2015.03.010.

Wang, Y, Wei, Y L, Oguntayo, S, Wilkins, W, Arun, P, Valiyaveettil, M, Song, J, Long, J B, Nambiar, M P, 2011. Tightly coupled repetitive blast-induced traumatic brain injury: development and characterization in mice. J. Neurotrauma 28 (10), 2171–2183. doi:10.1089/neu.2011.1990.

West, M J, Slomianka, L, Gundersen, H J, 1991. Unbiased stereological estimation of the total number of neurons in thesubdivisions of the rat hippocampus using the optical fractionator. Anat. Rec. 231 (4), 482–497. doi:10.1002/ar.1092310411.

Wogensen, E, Mala, H, Mogensen, J, 2015. The effects of exercise on cognitive recovery after acquired brain injury in animal models: a systematic review. Neural Plast 2015, 830871. doi:10.1155/2015/830871.

Yoon, J E, Lee, C Y, Sin, E G, Song, J, Kim, H W, 2018. Clinical Feature and Outcomes of Secondary Hydrocephalus Caused by Head Trauma. Korean J Neurotrauma 14 (2), 86–92. doi:10.13004/kjnt.2018.14.2.86.

Zhang, L, Blackwell, K, Workman, L M, Chen, S, Pope, M R, Janz, S, Habelhah, H, 2015. RIP1 cleavage in the kinase domain regulates TRAIL-induced NF-kappaB activation and lymphoma survival. Mol. Cell. Biol. 35 (19), 3324–3338. doi:10.1128/MCB.00692-15.

Zhao, J, Chen, Z, Xi, G, Keep, R F, Hua, Y, 2014. Deferoxamine attenuates acute hydrocephalus after traumatic brain injury in rats. Transl. Stroke Res. 5 (5), 586–594. doi:10.1007/s12975-014-0353-y.

Appendix A –Publication Cover #4
2020

Authors: M. Murugan, A. Ravula, A. Gandhi, G. Vegunta, S Mukkamala, W. Mujib, N. Chandra

Title: "*Chemokine signaling mediated monocyte infiltration affects anxiety-like behavior following blast injury*"

Journal Publication: Brain, Behavior and Immunity, 88, 340-352**,** (2020), [20-4]

Brain, Behavior, and Immunity xxx (xxxx) xxx–xxx

Contents lists available at ScienceDirect

Brain, Behavior, and Immunity

journal homepage: www.elsevier.com/locate/ybrbi

Chemokine signaling mediated monocyte infiltration affects anxiety-like behavior following blast injury

Madhuvika Murugan, Arunreddy Ravula, Ajay Gandhi, Geetasravya Vegunta, Sushni Mukkamalla, Waleed Mujib, Namas Chandra*

Department of Biomedical Engineering, Center for Injury Biomechanics Materials and Medicine, New Jersey Institute of Technology, Newark, NJ 07102, United States

ARTICLE INFO

Keywords:
Blast
Brain injury
Microglia
Monocyte infiltration
Chemokine
CCL2-CCR2 signaling

ABSTRACT

The activation of resident microglia and infiltrated monocytes are known potent mediators of chronic neuroinflammation following traumatic brain injury (TBI). In this study, we use a mouse model of blast-induced TBI (bTBI) to investigate whether microglia and monocytes contribute to the neuroinflammatory and behavioral consequences of bTBI. Eight-ten week old mice were subject to moderate TBI (180 kPa) in a shock tube. Using double transgenic $CCR2^{RFP/+}$: $CX3CR1^{GFP/+}$ mice, we were able to note that in addition to resident Cx3CR1+ microglia, infiltrating CCR2+ monocytes also contributed to the expanding macrophage population that was observed after bTBI. The microglia activation and monocyte infiltration occurred as early as 4 h and lasted up to 30d after blast exposure, suggesting chronic inflammation. The infiltration of monocytes may be partly mediated by chemokine CCL2-CCR2 signaling axis and compromised blood brain barrier permeability. Hence, bTBI-induced infiltration of monocytes and production of IL-1β were prevented in mice lacking CCR2 (CCR2 KO). Finally, this study showed that interference of monocyte infiltration using CCR2 KO, ameliorated the chronic effects of bTBI such as anxiety-like behavior and short-term memory decline. Taken together, these data suggest that bTBI leads to activation of both resident microglia and infiltrated monocytes. The infiltration of monocytes was partly mediated by CCL2-CCR2 signaling, which in turn contributes to increased production of IL-1β leading to behavioral deficits after bTBI. Furthermore, bTBI induced behavioral outcomes were reduced by targeting CCL2-CCR2 signaling, highlighting the significance of this signaling axis in bTBI pathology.

1. Introduction

Blast-induced traumatic brain injury (bTBI) is a signature wound among military personnel exposed to improvised explosive devices, particularly affecting the returning veterans from Iraq and Afghanistan (Bell, 2009). Brain injuries can be caused by blunt impact, ballistic penetration, blast shockwaves or a combination thereof. Unlike other brain injury mechanisms, the primary injury of bTBI is caused by high-pressure shock wave from an explosion/detonation that traverses the skull and causes physical injury to the brain tissue. We recently showed that blast exposure leads to increased blood-brain barrier (BBB) permeability as a function of increased shock wave pressure in an exposure-dependent manner (Kuriakose et al., 2018). The acute changes in BBB following blast exposures are attributed to shock wave induced physical damage to blood vessels and is associated with a significant reduction in the occurrence of tight junction proteins in the brain (Kuriakose et al., 2018; Rama Rao, 2018; Abdul-Muneer, 2013). At the same time, there is an increase in oxidative stress mediated damage in neurons, astrocytes and microglia (Rama Rao, 2018; Abdul-Muneer, 2013). Recent studies also suggest that blast-mediated disruption of blood vessels and oxidative stress lead to microglia activation/accumulation (Huber, 2016; Readnower, 2010). However, it is unclear whether microglia activation occurs because of direct mechanical disruption or whether it is a result of secondary injury mechanisms following bTBI.

The degree of microglia/macrophage accumulation after bTBI is strongly correlated with severity of blast induced brain injury and inflammation (Huber, 2016). Human post-mortem studies show accumulation of microglia, a key mediator of inflammation, even after several years following TBI (Gentleman, 2004; Ramlackhansingh, 2011). In non-blast models of TBI, injury has been shown to activate resident microglia, as well as recruit peripheral monocytes to the site of injury (Nimmerjahn et al., 2005; Roth, 2014; Shechter, 2009; London, 2011). Although there is evidence of microglia accumulation in bTBI

* Corresponding author at: Dept. of Biomedical engineering, Center for Injury Biomechanics Materials and Medicine, New Jersey Institute of Technology, 111 Lock Street, Room105 CHEN bldg, Newark, NJ 07102, United States.
E-mail address: namas.chandra@njit.edu (N. Chandra).

https://doi.org/10.1016/j.bbi.2020.03.029
Received 16 August 2019; Received in revised form 27 March 2020; Accepted 28 March 2020
0889-1591/ © 2020 Elsevier Inc. All rights reserved.

ARTICLE IN PRESS

Table 1
Number of GFP + microglia and RFP + monocytes per field of view in different brain regions at 0, 0.167 (or 4 h), 1 (or 24 h), 3, 7 and 30 days following bTBI. All comparisons were made against the sham group. *p < 0.05, **p < 0.01, ***p < 0.001. Student's *t*-test. (n = 5).

Number of GFP + resident microglia							
Region	Day following bTBI	0 (Sham)	0.167 (4 h)	1	3	7	30
PFC	Mean ± SEM	71.67 ± 4.86	115.33 ± 3.611	107.17 ± 2.74	116.33 ± 3.07	114.67 ± 9.96	86.37 ± 17.09
	p value		2.89 E-05	8.22 E-05	1.52 E-05	0.003	0.437
Striatum	Mean ± SEM	99.67 ± 7.40	118.67 ± 5.19	98.51 ± 5.90	114.83 ± 6.41	94.67 ± 6.68	77.5 ± 4.76
	p value		0.061	0.904	0.152	0.626	0.030
CC	Mean ± SEM	45.67 ± 4.63	115.5 ± 5.45	77.50 ± 4.51	103.17 ± 5.02	77.83 ± 3.52	66.83 ± 3.82
	p value		1.97 E-06	0.0006	7.52E-06	0.0003	0.06
Cortex	Mean ± SEM	74.83 ± 6.23	92.67 ± 2.56	101.11 ± 4.16	84.5 ± 6.43	83.67 ± 4.42	91.5 ± 4.33
	p value		0.024	0.006	0.305	0.275	0.053
CA1	Mean ± SEM	79 ± 2.79	105 ± 5.65	90 ± 1.73	92.5 ± 4.98	90.5 ± 2.32	101.5 ± 1.23
	p value		0.002	0.007	0.039	0.009	2.39E-05
CA3	Mean ± SEM	71.17 ± 5.19	71.4 ± 4.92	75.2 ± 6.23	62 ± 3.93	83.4 ± 3.44	77.2 ± 4.004
	p value		0.845	0.954	0.369	0.164	0.228
Hilus	Mean ± SEM	76 ± 5.31	98.5 ± 4.01	78.83 ± 8.54	79 ± 4.51	73.83 ± 3.75	93.83 ± 7.13
	p value		0.007	0.783	0.675	0.745	0.072
Number of RFP + infiltrating monocytes							
Region	Day following bTBI	0 (Sham)	0.167 (4 h)	1	3	7	30
PFC	Mean ± SEM	0.00 ± 0.00	23 ± 5.68	6.33 ± 1.25	1.67 ± 0.42	1.5 ± 0.5	11.17 ± 2.89
	p value	0.00	0.002	0.0005	0.002	0.013	0.003
Striatum	Mean ± SEM	0.00 ± 0.00	6.5 ± 1.23	4.5 ± 2.33	1.67 ± 0.80	1.5 ± 0.5	1.83 ± 0.79
	p value	0.00	0.0003	0.082	0.064	0.013	0.043
CC	Mean ± SEM	0.00 ± 0.00	4.33 ± 1.28	3 ± 1.59	1.5 ± 0.34	2.67 ± 0.21	2.67 ± 0.71
	p value	0.00	0.007	0.088	0.001	0.015	0.003
Cortex	Mean ± SEM	0.00 ± 0.00	17.33 ± 3.62	2 ± 0.36	1.17 ± 0.48	0.83 ± 0.40	5.5 ± 0.81
	p value	0.00	0.0007	0.0002	0.034	0.579	0.00004
CA1	Mean ± SEM	0.00 ± 0.00	13 ± 0.85	1.5 ± 0.42	1.17 ± 0.48	1.67 ± 0.42	6.33 ± 1.23
	p value	0.00	3.11602E-08	0.005	0.034	0.002	0.0004
CA3	Mean ± SEM	0.00 ± 0.00	12.2 ± 3.21	0.8 ± 0.37	0.2 ± 0.2	3.4 ± 1.6	2.8 ± 1.46
	p value	0.00	0.0007	0.021	0.341	0.023	0.069
Hilus	Mean ± SEM	0.00 ± 0.00	9.17 ± 4.02	1.67 ± 0.61	0 ± 0	2.17 ± 0.54	2.33 ± 0.71
	p value	0.00	0.046	0.02	0	0.002	0.008

(Kaur, 1995), whether it is sourced by local microgliosis alone, or supplemented by infiltration of peripheral monocytes remains to be investigated. Further, the pathway(s) responsible for such infiltration remains poorly understood.

CCL2 is a chemokine released by injured neurons, microglia and astrocytes that attracts CCR2 receptor expressing cells such as peripheral monocytes. CCL2-CCR2 signaling has been implicated in the infiltration of monocytes and production of inflammatory cytokines such as IL-1β in neurological conditions including impact injury, epilepsy and Alzheimer's disease (Hsieh, 2014; Gyoneva, 2015; Semple et al., 2010; Tian, 2017; Severini, 2014; Chen, 2003). However, little is known about the significance of CCL2-CCR2 signaling in infiltration of monocytes, inflammation and behavioral outcomes after bTBI. Interestingly, mice lacking CCR2 showed reduced infiltrated monocytes, improved neuronal survival and greater spatial learning and memory after controlled cortical impact injury (Hsieh, 2014).

The most important implication of bTBI are the behavioral and functional symptoms such as anxiety, sleep disorders and post-traumatic epilepsy that continue to persist long after the time of exposure to blast in bTBI (O'Neil, 2017; Nelson et al., 2015; Petrie, 2014; Kovacs et al., 2014). Since, inflammation is also implicated in the pathogenesis of behavioral deficits (Yang, 2016; Salim, 2011), we hypothesize that *monocyte/macrophage infiltration and microglia activation may synergistically contribute to inflammation and subsequent behavioral deficits after bTBI.* Here we investigate the degree of resident microglia activation and monocyte infiltration following moderate bTBI using a double transgenic ($CCR2^{RFP/+}$: $CX3CR1^{GFP/+}$) mice line. We further test the relative contribution of the two-macrophage populations to bTBI. To this end, transgenic mice lacking CCR2 (CCR2 KO) were used to prevent the infiltration of monocytes to test the effect on IL-1β expression and consequent neurobehavioral outcomes. This study would provide a novel perspective on whether infiltrating monocytes and the CCL2-CCR2 signaling axis contribute significantly to bTBI pathology and neurological outcomes; if true, then the results pave the way of targeting this pathway for the treatment of bTBI. Further, these results are expected to yield insights into the same critical question in other types of TBI/neuropathologies in which monocyte infiltration and CCL2-CCR2 signaling are implicated.

2. Materials and methods

Animals: $CCR2^{RFP/+}$: $CX3CR1^{GFP/+}$, $CCR2^{RFP/+}$ and $CCR2^{RFP/RFP}$ (CCR2 KO) genotypes of mice (both male and female) were used in this study. $CX3CR1^{GFP/GFP}$ and $CCR2^{RFP/RFP}$ lines were obtained from the Jackson Laboratory and bred in our animal facility. $CCR2^{RFP/+}$: $CX3CR1^{GFP/+}$ line was established by crossing $CX3CR1^{GFP/GFP}$ mice with $CCR2^{RFP/RFP}$ mice, resulting in microglia selectively labeled with GFP (Jung, 2000) and peripheral monocytes labeled with RFP (Saederup, 2017). Note that all mice were on a B6.129 strain background. Animals were used in accordance with institutional guidelines, as approved by the Institutional Animal Care and Use Committee (IACUC) at Rutgers University and New Jersey Institute of Technology. Power analysis was conducted a priori to achieve a power of 80% to detect differences of < 5% in quantitative measures (sham versus bTBI) ($\sigma = 0.05$, $\alpha = 0.05$). The sample size was to be: n = 5 mice for histological quantification and n = 10 mice for behavioral assays.

Blast Injury Model: Eight-ten week old mice (both male and female) were subjected to a single shock wave with peak overpressure 180 kPa in a 6 m long shock tube with 9-inch square cross-section to induce a moderate bTBI (Kuriakose, 2016; Mishra, 2016). Mice were anesthetized with 3% isoflurane before mounting them horizontally inside the test chamber located 2.8 m from the point where the shockwave will be generated at one end of the tube and 3.05 m from its exit. The pressure waveform was recorded using PCB Piezotronics sensors model 134A24

(Depew, NY) at 1.0 MHz sampling frequency for a duration of 100 ms. Sham animals were placed outside the shocktube and received anesthesia and noise exposure without the shockwave loading. For calculating the dose response curve of blast overpressure in terms of mortality rate, the mice were subject to various overpressures – 70 kPa, 130 kPa, 180 kPa, 240 kPa, 320 kPa and 350 kPa. A minimum of 5 mice were used per dose and the actual experimental overpressure values for each mouse is noted in Supplemental Fig. 1. The predicted mortality rate (PMR) and classification of injury severity were performed as described previously (Mishra, 2016).

Slice electrophysiology: Whole cell patch-clamp recordings were made on GFP + microglia from cortical slices (50 μm deep) in sham and at 1d after bTBI. Recording electrodes (4–5 MΩ) contained a K-based internal solution composed of (in mM): 120 K-gluconate, 5 NaCl, 1 MgCl2, 0.5 EGTA, 10 Na2Phosphocreatine, and 10 HEPES (pH 7.2; 280–300 mOsmol. The membrane potential was held at − 60 mV for microglia. Data were amplified and filtered at 2 kHz by a patch-clamp amplifier (Multiclamp 700B), digitalized (DIGIDATA 1440A), stored, and analyzed by pCLAMP (Molecular Devices, Union City, CA).The intrinsic membrane properties of microglia and monocytes are listed in Table 1. Data were discarded when the input resistance changed > 20% during recording. The voltage ramp test was performed from −100 to 100 mV in 500 ms. For electrophysiology, a minimum of three cells from at least three different mice from the same litter were randomly selected for recording per condition.

Immunostaining: In order to evaluate whether microglia activation and monocyte infiltration are attenuated in CCR2KO mice, we performed double-immunofluorescence studies of Iba1 and RFP to detect microglia and to enhance RFP labeling in monocytes, respectively. Briefly, 24 h post-injury, both sham and bTBI animals were transcardially perfused with phosphate buffered saline (PBS) followed by 4% paraformaldehyde (PFA). After perfusion, the brains were post-fixed in PFA overnight and moved to 30% sucrose. Coronal sections (30 μm) were cut using a Leica vibratome and stored in-80 ˚C until used for immunostaining. The tissue sections were blocked with 10% donkey serum at room temperature for 1 h in PBS containing 0.03% Triton and incubated overnight in a cocktail of primary antibodies (anti-Iba-1 and anti-RFP). For staining performed in tissue from $CCR2^{RFP/+}$: $CX3CR1^{GFP/+}$ mice, only anti-RFP primary and corresponding secondary antibody was used. Following washing with PBS-T, the sections were incubated in corresponding secondary antibody with fluorescent tag for 1hr. The sections were then mounted with coverslips and allowed to dry. Images were acquired using the Leica Confocal microscope with 40x magnification with an image matrix of 1024 × 1024 pixel. Analysis of microgliosis in various brain regions were performed on specific stereological planes as follows: Prefrontal cortex (PFC) [bregma + (2.2 to 2.6 mm)], striatum and corpus callosum [bregma ± (0.2 mm)], cortex and hippocampus [bregma − (2.6 to 3.0 mm)]. Manual morphological analysis was carried out using FIJI software. Confocal images were collected from 30 μm thick tissue with 20 slices taken every 1.5 μm. The maximum intensity projection image was subjected to a threshold to create a binary mask and skeletal images that were manually constructed to represent the spatial structure of cell bodies and microglia processes (Heindl, 2018). Shoenen ramification index (RI) was calculated (number of end branches/number of primary branches) and collected for each cell. The number of microglia/monocytes, the soma size, microglia process length and ramification index were quantified by two independent blinded observers and averaged. For each animal, a minimum of 10 cells were analyzed per imaging region (between 10 and 20 cells depending on the number of detectable cells in a Z-stack due to variable cell numbers in the analyzed locations).

Evans Blue Quantification: The quantification of Evans blue entering brain tissue was used to evaluate the degree of BBB permeability following blast exposure. Six $CCR2^{RFP/+}$: $CX3CR1^{GFP/+}$ mice were subject to blast (180 kPa) or sham conditions at 0 h, administered tail vein injections of EB (4% solution in saline, single bolus of 2 ml/kg body weight of mice) at 22 h under deep ketamine/xylazine anesthesia. Since the half-life of EB was previously determined to be 256 ± 139 m (William, 1982) and to further ensure uniform dye distribution, the blood was collected from the left atrium at 2 h after EB injection and centrifuged at 10,000 × *g* for 20 m at 4 ˚C to separate serum from blood cells. The concentration of EB in the blood serum was measured using fluorescence spectroscopy (620 nm/680 nm) and plotted against a standard curve (0.025–1000 μg/ml) using a method described previously (Wang and Lai, 2014). The serum EB level was used to validate efficiency of tail vein injection and control for unsuccessful EB delivery. The animals used in this study had serum EB levels in the range 150–220 μg/ml. Immediately following blood collection, each mouse was thoroughly perfused with PBS to get rid of remaining dye. The perfused brain tissue was collected and placed in 4% paraformaldehyde. After 24 h, the brains were changed to 30% sucrose for up to 48 h and sectioned into 60 μm thick sections for confocal imaging. The brain regions including prefrontal cortex (PFC), striatum and corpus callosum, cortex and hippocampus at stereotaxic planes described above. The Z-stack (30 μm) images were obtained using a Leica Confocal microscope for microglia (GFP-green), monocytes (RFP-red) and Evans blue (EB-blue) at excitation wavelengths (488 nm, 530 nm and 620 nm) and emission peaks at 510 nm, 590 nm and 680 nm, respectively. Sequential scanning mode was used to prevent spectral bleeding. The average intensity of green, red and blue was measured for each field of view was done in maximum projection images obtained from at least 3 random field of views per animal per brain region using RGB plugin of Image J/ FIJI (NIH software).

Western blotting: To quantify the levels of RFP, animals were transcardially perfused with sterile PBS, brains extracted, and PFC dissected from different experimental groups at 24 h after Sham/ bTBI. Mice with CCR2 het and CCR2 KO genotypes were used for this experiment. Each sample was separately homogenized in cell lysis buffer. The total protein concentration was determined by BCA assay. For each lane, 50 μg of proteins was loaded and separated by SDS-PAGE. After the transfer, the blots were incubated overnight at 4 ˚C with Anti-RFP primary antibody. The blots were then washed, incubated with HRP-conjugated secondary antibody, and developed in an enhanced chemiluminescent solution. Specific bands were evaluated by apparent molecular size. Finally, images was be captured using an Odyssey Fc Imaging System and the intensity of the selected bands was analyzed using National Institutes of Health ImageJ (FIJI) software.

ELISA for IL-1 β: Enzyme-linked Immunosorbent Assay (ELISA) was performed to quantify the concentration of IL-1β in the PFC of sham and blast exposed mice of WT and CCR2 KO genotype. The assay was performed according to the manufacturer's instructions (Abcam ab197742). Briefly, 200 μg/50 μL of total protein extract (as obtained for western blotting) or 50 μL of standard was added to each well of the pre-coated plate. This was followed by 50 μL of antibody cocktail and incubation for 1 h in room temperature on a shaker set to 400 rpm. Each well was washed 3× with 350 μL wash buffer. Substrate (100 μL) of was added to each well and incubated for 10 m in dark on a plate shaker set to 400 rpm. Finally, 100 μL of stop solution was added and the optical density was noted at 450 nm using a plate reader (Molecular Devices, SpectraMax i3).

Behavioral Assays: *Elevated Plus Maze:* This is a test used to determine anxiety-like behavior at 1d and 30d after bTBI. The animals are typically placed in a plus-shaped maze with 26 in. long arms: two open and two closed arms. The entire apparatus is elevated 15 in. above the ground. Mice were placed at the center junction of the maze facing an open arm and given 5 min to explore. The number of entries into each arm, the time spent in each arm, and the total distance traveled in the maze (and in each individual arm) was tracked using the video camera positioned over the maze and analyzed using ANYMaze software. The software tracked the center point of the mouse body, and mice were considered to have entered an arm when their center point crossed into

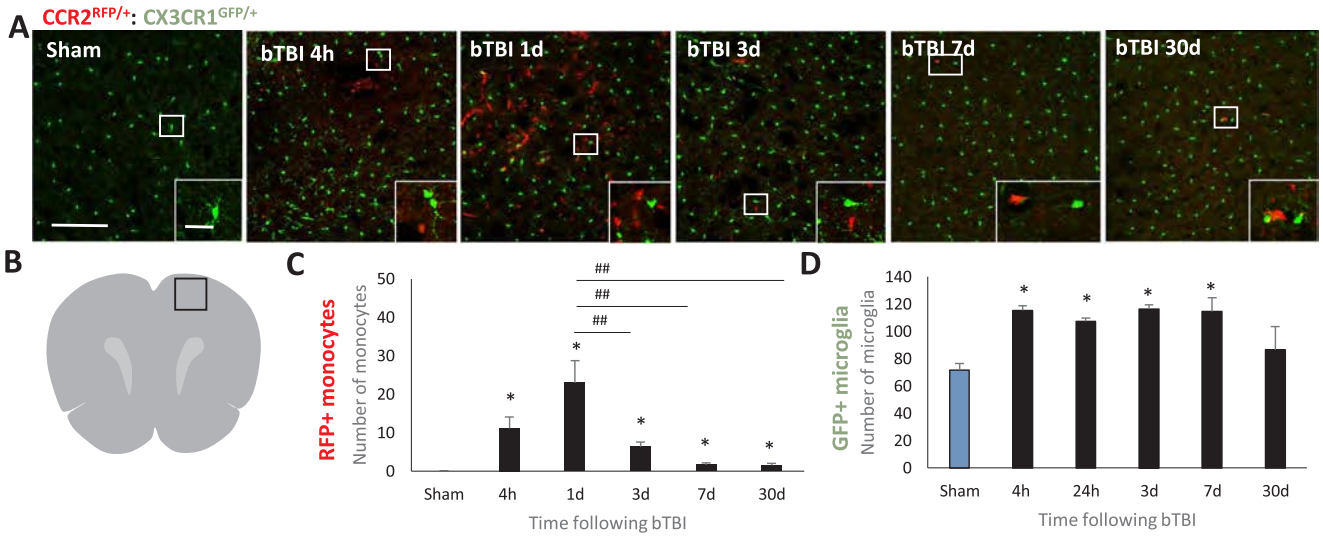


Fig. 1. Microglia activation and monocyte infiltration after moderate bTBI. **A**. Representative confocal images of prefrontal cortex in sham, 4 h, 1d, 3d, 7d and 30d following moderate bTBI in $CCR2^{RFP/+}$:$CX3CR1^{GFP/+}$ mice. Inset shows higher magnification image of cells within the highlighted box area. **B**. Schematic showing coronal plane and location in which analysis was performed. **C-D**. Bar graphs showing number of $CCR2^{RFP/+}$ monocytes and $CX3CR1^{GFP/+}$ microglia at various time points after bTBI. Scale bar: 100 μm and 20 μm for lower and higher magnification images, respectively. n = 5 for each time point. One-way ANOVA with Bonferroni correction for multiple comparisons. *p < 0.05, comparisons were made against the sham group. ## p < 0.01, comparisons showing changes with time.

the arm. The amount of time spent in the closed versus open arm was used as a measure of anxiety-like behavior.

Novel object recognition: To determine whether bTBI caused changes to the cognitive function, novel object recognition test was used at 7d and 29d after blast exposure. Briefly, each mouse was allowed to acclimatize in the testing chamber for 5 mins 1d prior to the testing. On the day of testing, each mouse was subject to a 10-min acquisition trial, during which the mouse was placed in an open field/test chamber in presence of two identical objects. On completion of 10 min of exploration (familiarization stage), the mouse was returned to its cage for 1 h. The mouse was then placed back in the box and introduced to the familiar object and a novel object for another 5 min (test stage). The total time spent exploring each of the two objects was recorded. Each test cohort was divided into even and odd groups and exposed to the novel object in symmetrically identical, yet diagonally opposite locations to avoid any location-specific preferences. A discrimination index for the novel object is used to measure recognition memory and is defined as the ratio of difference in time spent with the novel object (t_{novel}) and familiar object ($t_{familiar}$) to the total exploration time (t_{total}). Discrimination Index = $[(t_{novel}\text{-}t_{familiar})/(t_{total})]$, where $t_{total} = t_{familiar} + t_{novel}$.

Open Field Assay: The open field test was used to detect gross-motor ability and exploratory behavior. Mice were left in an empty open field box equipped with a video camera (50 × 50 cm) for a period of 10 min. The mice were tracked by ANYMaze software and the overall distance travelled by the mice and the time spent in the center of the field versus the corners were measured for each group. The boundary of the corners were set as squares of area 100 cm^2. Since multiple behavioral assays cannot be conducted in the same animal on the same day, we performed the tests on different days. Also, we minimized the experiments to 2-time points per animal per assay (1 acute time point and 1 chronic time point). For all behavioral studies, note that WT mice and $CCR2^{RFP/RFP}$ (CCR2 KO) mice lacking both copies of CCR2 were used.

Statistical Analysis: We validated the normal distribution of all data through the Shapiro-Wilk test. Independent Student's *t*-test was performed to ascertain statistical significance in the IL-1β ELISA and western blot. We performed one-way ANOVA with Bonferroni correction for multiple comparisons to confirm the statistical significance of temporal changes in morphological characterization of microglia/monocytes after blast injury. We performed two-way ANOVA with post hoc Tukey test for multiple comparisons for behavioral assays and certain immunostaining data. This allowed us to test the significant effect of bTBI (sham versus injury) and genotype (WT versus CCR2 KO) (2x2 set up) on the experimental outcome and to investigate any possible interaction between the variables. In bar graphs, data are presented as mean ± standard error of the mean (SEM). In box whisker plots center line represents median, cross mark indicates mean value, box limits represent the upper and lower quartiles, whiskers represent highest and lowest observations and each point represents a data value including outliers. Differences between means were assessed at the probability level of P ≤ 0.05, 0.01, and 0.001. Statistical analysis was performed using the SPSS (IBM SPSS statistics 20, NY).

3. Results

3.1. bTBI induced microgliosis is composed of microglia and monocytes

Accumulating evidence suggests that microglia activation and accumulation follows bTBI. However, the time course, source and mechanism underlying microglia/macrophage activation following moderate bTBI remains unclear. First, we established a dose response curve to correlate blast overpressure (BOP) with injury severity based on mortality in a mice model (Supplementary Fig. 1). We set a BOP of 154 kPa as upper mild TBI threshold (5% predicted mortality rate (PMR)), the percentage was set based on our previous work performed in rats (Mishra, 2016). Further, we determined 154–210 kPa and 210–248 kPa levels as moderate and severe TBI based on 35%, and 70% PMR, respectively, while BOP above 248 kPa was determined to be lethal (100% PMR). In order to deliver a moderate blast injury, we chose 180 kPa for the rest of the study. We then investigated microglial activation and monocytes infiltration following moderate bTBI using $CCR2^{RFP/+}$: $CX3CR1^{GFP/+}$ mice in which CCR2 monocytes and CX3CR1 microglia are labeled by RFP (red) and GFP (green), respectively (Fig. 1). We note that blast-induced microgliosis consists of both local increase microglia numbers, as well as, monocyte infiltration (Fig. 1). We observed ramified GFP-positive resting microglia but not RFP-positive macrophages in the brain of $CCR2^{RFP/+}$:$CX3CR1^{GFP/+}$ mice under normal conditions. However, in mice after bTBI, we identified

the accumulation of RFP-positive cells, which are presumably infiltrated CCR2-positive macrophages in the prefrontral cortex. The infiltration occurred as early as 4 h, peaked at 24 h and continued to last up to 30d after bTBI. (Fig. 1**A, 1C**). Since CCR2 expression may be downregulated in mature macrophages, we estimated the number of CD169 + monocytes/ macrophages to confirm the significant occurrence of infiltrated monocytes at 1d and 30d after bTBI (Supplementary Fig. 1B). Moreover, we observe that the number of microglia significantly increased within 4 h following bTBI and lasted up to 7d (Fig. 1**A, 1D**). Though the number of microglia remained higher at 30d post bTBI compared to the sham, the increase was not statistically significant (Fig. 1**D**). There was no significant recovery/reduction in microglia numbers with time (4 h versus 24 h, 3d, 7d, 30d) indicating that the increase in microglia numbers persisted from acute to chronic phase. On the other hand, monocyte numbers compared to peak at 1d showed significant recovery/reduction indicating clearance or decreased infiltration.

Quantification of resident microglia and infiltrated monocytes in the brain shows spatial and temporally distinct pattern (Supplementary Fig. 2). It also consistently shows that there is an increase in microglia number at 4 h, a transient dip at 1d and a steady increase in microglia numbers at 3d, 7d and 30d (Supplementary Fig. 2B). It is interesting to note that the number of microglia returned to sham levels in most brain regions except the striatum- where the microglia numbers were significantly reduced and in CA1- where the numbers were significantly increased compared to sham (Table 1), suggesting the existence of chronic microglia activation. In the case of infiltrated monocytes, we noted a peak in infiltration at1d after bTBI in all brain regions that was analyzed (Supplemental Fig. 2C). However, only a few infiltrated monocytes were detectable by 7d and 30d after bTBI (Table 1).

3.2. bTBI causes chronic activation of resident microglia and infiltrating monocytes

In addition to microglia numbers, the morphological changes to microglia structure such as soma size, process length and ramification, are key features of microglia activation. Hence, we characterized the morphological changes in PFC microglia after bTBI (Fig. 2). To this end, we performed skeletal construction of microglia structures (Fig. 2**A-B**). Interestingly, the soma of RFP+ monocytes in the neuronal parenchyma increased in size with time, suggesting that the blood-borne monocytes may be evolving within the neuronal parenchyma post-infiltration (Fig. 2**C**). We also confirmed that the soma size of GFP+ microglia significantly increased at all time points suggesting that bTBI induced chronic microglia activation, with recovery noted at 7d and 30d (Fig. 2**D**). This was accompanied by a decrease in process length at 4 h, 1d, and 3d, with recovery seen at 7d and 30d (Fig. 2**E**). Although, we note a recovery in process length, the Shoenen ramification index remains significantly lower than the sham levels at 4 h, 1d, 3d, 7d and 30d (Fig. 2**F**). Taken together, our results suggest that both activated microglia, as well as infiltrated monocytes remain in the neuronal parenchyma at chronic time points and may synergistically contribute to inflammation after bTBI.

In addition to the morphological analysis, we performed whole cell patch clamp recordings to test the functional activation of microglia by measuring their membrane currents from live brain slices in sham and 1d after bTBI (Supplementary Fig. 3). We noted increased outward K currents in microglia at 1d after bTBI compared to the linear current–voltage relationship that was observed in sham microglia (Supplementary Fig. 3A-B), suggesting a mild activated state, However, there were no significant differences in the cell capacitance and membrane potential of microglia in sham and bTBI conditions (Supplementary Fig. 3C-D).

3.3. Chemokine CCL2-CCR2 signaling mediates monocyte infiltration and IL-1β production

CCL2 is a chemokine released by injured neurons, microglia and astrocytes that attracts CCR2 receptor expressing cells such as monocytes. CCL2-CCR2 signaling has been implicated in the infiltration of monocytes and production of inflammatory cytokines such as IL-1β in neurological conditions such as epilepsy and Alzheimer's disease (Hsieh, 2014; Gyoneva, 2015; Semple et al., 2010; Tian, 2017; Severini, 2014; Chen, 2003). However, little is known about the functional significance of CCL2-CCR2 signaling in brain injury. We recently reported an increase in chemokine CCL2 in the prefrontal cortex following bTBI[2].

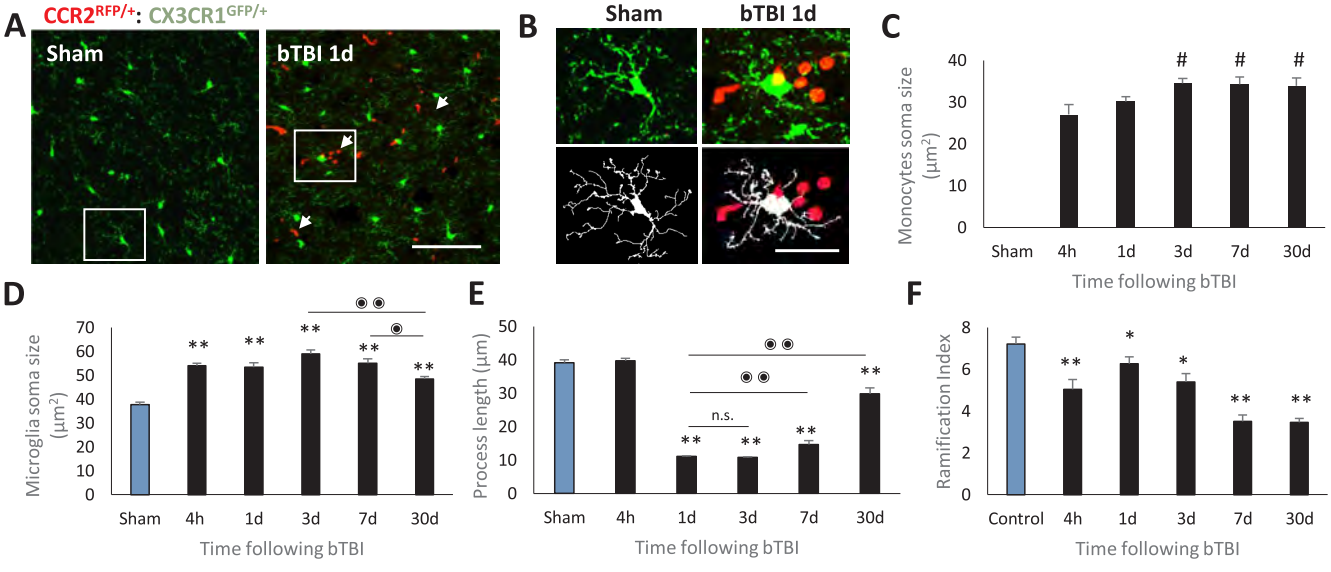


Fig. 2. Morphological characterization of microglia and monocytes. **A**. Confocal images of prefrontal cortex in sham and 1d following moderate bTBI in CCR2$^{RFP/+}$:CX3CR1$^{GFP/+}$ mice. **B**. Higher magnification images of cells shown in box in (**A**) and their respective skeletal constructions depicting microglia (white) and monocytes (red). **C-D**. Bar graphs showing soma size of CCR2$^{RFP/+}$ monocytes and CX3CR1$^{GFP/+}$ microglia at various time points after bTBI. **E-F**. Bar graph showing microglia process length and ramification index in sham and bTBI groups. Scale bar: 100 μm and 20 μm for lower and higher magnification images, respectively. n = 5 for each time point. Student's *t*-test. *p < 0.05, **p < 0.01, ***p < 0.001.*comparison with microglia sham group. #comparison with monocytes at 4 h. ◉ comparisons for recovery with time. (For interpretation of the references to colour in this figure legend, the reader is referred to the web version of this article.)

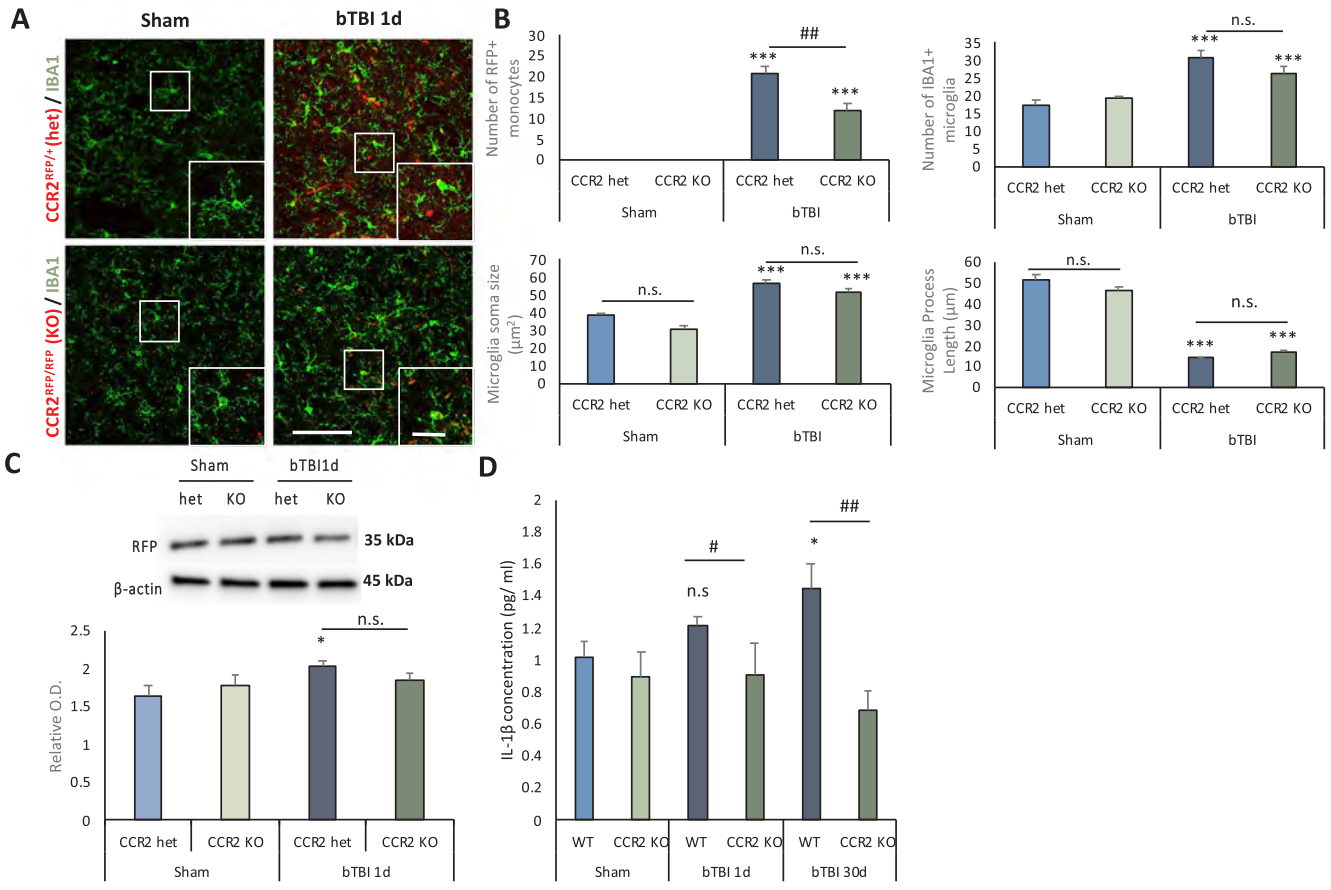


Fig. 3. CCL2-CCR2 mediates monocyte infiltration after bTBI. **A.** Representative images showing IBA1 positive microglia and RFP + monocytes in sham and 1d after moderate bTBI in $CCR2^{RFP/+}$ (CCR2 het) and $CCR2^{RFP/RFP}$ (CCR2 KO) mice. **B.** The bar graph represents number of IBA1 + microglia, number of RFP + monocytes, microglia soma size and process length in sham and bTBI groups in CCR2 het and CCR2KO groups. Scale bar: 100 μm and 20 μm for lower and higher magnification images, respectively. n = 5, Two-way ANOVA was used with Tukey HSD test. ***$p < 0.001$. * Comparison made against representative sham group. $^{\#\#}p < 0.01$, # Represents comparisons made between blast groups of WT and CCR2 KO. **C.** Immunoblots of RFP and β-actin, and analysis of relative optical density are shown. n = 3, Two-way ANOVA was used with Tukey HSD test. *$p < 0.05$, n.s. – not significant. **D.** Bar graph shows IL-1β expression in WT and CCR2KO mice from Sham, 1d bTBI and 30d bTBI. n = 6, *$p < 0.05$ comparison between bTBI and respective genotypic sham. #$p < 0.05$, ##$p < 0.01$, comparison between WT and CCR2KO. n.s. – no significance. Two-way ANOVA was used with Tukey HSD test.

Hence, we surmised that CCL2-CCR2 signaling may participate in the pathology of TBI-related events such as monocyte infiltration, inflammation and hence neurobehavioral deficits.

In order to determine whether mechanical damage to the BBB or CCL2-CCR2 signaling contributes to the infiltration of monocytes into the brain after bTBI, we used transgenic mice lacking CCR2 receptor. Our results show that the increase in CCR2 + monocytes at 1d after bTBI was partially prevented in CCR2 KO compared to the CCR2 het (Fig. 3**A-B**). A two-way ANOVA was conducted to examine the effect of bTBI and CCR2 genotype on monocyte infiltration. A significant interaction between the effects of bTBI and CCR2 genotype on monocyte numbers was noted, $F(1, 16) = 18.69$, $p < 0.001$. Simple main effects analysis showed that both bTBI ($p < 0.0001$) and genotype ($p = 0.001$) significantly affected monocyte numbers. Post-hoc Tukey test for multiple comparisons showed significant difference in monocyte numbers between CCR2 het and CCR2 KO at 1d after bTBI (##, $p < 0.01$). While these results suggest a role for CCL2-CCR2 signaling in blast-mediated monocyte infiltration, it does not rule out biomechanical damage to the BBB as one of the causes for the infiltration. In order to investigate the link between monocyte infiltration/microglia activation and BBB permeability, we quantified the number of monocytes and microglia, respectively and correlated it with the intensity of Evan's blue permeation into various brain regions at 1d after bTBI. Our results suggest that bTBI-mediated infiltration of monocytes into the PFC, cortex and CA1 correlated with intensity of Evan's blue, an indicator of increased BBB permeability (Supplementary Fig. 4A, 4C). This correlation was however not as prominent in brain regions such as CA3, CC and hilus (Supplementary Fig. 4C). Further, the peak increase in BBB permeability was noted at 4 h after bTBI and recovered to sham levels by 1d in mice (data not shown), similar to our previous report on rats[2]. Taken together, we believe that monocyte infiltration is mediated independently by the passive entry via disrupted BBB and/or CCL2-CCR2 signaling. This is a novel and pertinent finding since preserving the BBB integrity does not ensure prevention of inflammatory monocytes. Hence, treatment strategies for bTBI have to be designed accordingly.

Interestingly, the number of microglia, microglia soma size and process length remained unaffected in CCR2KO (Fig. 3**B**) nor did it correlate with the intensity of Evan's blue dye (Supplementary Fig. 4B) in the PFC at 1d after bTBI. Individual two-way ANOVA analysis showed no interaction between effects of bTBI and CCR2 genotype on the following parameters: microglia numbers [$F(1,16) = 3.95$, $p = 0.0642$], soma size [$F(1,150) = 1.62$, $p = 0.2051$] and process length [$F(1,476) = 3.6$, $p = 0.0584$]. However, simple main effects analysis showed that bTBI had a significant effect on microglia numbers (***,$p < 0.0001$), microglia soma size (***, $p < 0.0001$) and microglia process length (***, $p < 0.001$), whereas, CCR2 genotype did not affect either microglia numbers ($p = 0.461$), soma size

(p = 0.0918) or process length (p = 0.5544) (Fig. 3**B**). This suggests that in the acute phase, change in microglia number, soma size and process length may be independent of monocyte infiltration and BBB permeability after bTBI. Western blot data further confirmed that CCRKO prevented blast-induced increase in RFP expression at 1d following bTBI (Fig. 3**C**). Two-way ANOVA statistics: overall effect of bTBI [F(1,10) = 5.14, p = 0.0.0468] and CCR2 genotype [F(1,10) = 3.14, p = 0.1068] on CCR2-RFP expression. No interaction was noted between the variables bTBI and genotype [F(1,10) = 0.8, p = 0.3921]. Post-hoc Tukey test for multiple comparisons showed significant increase in RFP expression at 1d after bTBI in CCR2 het but not in CCR2KO group (*, p < 0.05) (Fig. 3**C**). Moreover, we noted that increase in IL-1β expression at 30d but not at 1d after bTBI, was reduced in CCR2KO mice (Fig. 3**D**). Two-way ANOVA statistics: overall effect of bTBI [F(1,24) = 0.29, p = 0.7493] and CCR2 genotype [F (1,24) = 8.64, p = 0.00716] on IL-1β expression. No interaction was noted between the variables bTBI (sham, bTBI 1d and bTBI 30d) and genotype (F(1,24) = 1.39, p = 0.24996). Post-hoc Tukey test for multiple comparisons showed significant difference in IL-1β expression between WT mice and CCR2 KO at 1d (#, p < 0.05) and at 30d (##,p < 0.01) after bTBI, The increase in IL-1β at 30d WT (*,p < 0.05) needs to be cautiously interpreted since the overall effect of bTBI was found to be insignificant based on ANOVA statistics. **(**Fig. 3**D)**. This provides evidence that CCL2-CCR2 signaling may significantly contribute to the release of proinflammatory cytokine IL-1β.

3.4. CCR2 receptor deficiency prevented bTBI induced anxiety-like behavior

To examine whether CCL2-CCR2 signaling was involved in bTBI-induced anxiety-like behavior, we tested WT and CCR2 KO mice in the elevated plus maze at 1d and 30d after bTBI (Fig. 4**A)**. We found that WT mice exposed to blast spent significantly longer periods in the closed arm compared to the sham at 30d after exposure (Fig. 4**B-C**). Individual two-way ANOVA statistics at each time point show significant overall effect of bTBI on time spent in the closed arm at 1d [F (1,38) = 37.79, p < 0.0001] and 30d [F(1,38) = 8.65, p = 0.0055] after exposure and genotype (WT vs. CCR2KO) had overall significant effect on time spent in the closed arm at 1d [F(1,38) = 8.79, p = 0.0052] and 30d [F(1,38) = 6.96, p = 0.012] after exposure. Post-hoc Tukey test for multiple comparisons showed that CCRKO mice experienced significantly lesser time in the closed arm or reduced anxiety-like behavior and 30d (##, p < 0.001) but not at 1d after bTBI compared to their respective WT groups (Fig. 4**B-C**). Two-way ANOVA statistics for each time point show insignificant overall effect of bTBI and CCR2 genotype on total distance travelled and total arm entries at both 1d and 30d after bTBI **(**Fig. 4**D,E)**. Total distance travelled: 1d Sham vs. bTBI: [F(1,38) = 0.08, p = 0.7788]; 30d Sham vs. bTBI: [F (1,38) = 1.04, p = 0.3142], 1d WT vs.CCR2KO: [F(1,38) = 0.45, p = 0.5063]; 30d WT vs. CCR2KO: [F(1,38) = 2.63, p = 0.1131]. Total arm entries: 1d Sham vs. bTBI: [F(1,38) = 3.5, p = 0.0691]; 30d Sham vs. bTBI: [F(1,38) = 2.23, p = 0.1436], 1d WT vs.CCR2KO: [F (1,38) = 0.09, p = 0.7658]; 30d WT vs. CCR2KO: [F(1,38) = 0.05, p = 0.8242]. In other words, all experimental groups of mice travelled similar distances in the maze (Fig. 4**D**) and had a similar number of total arm entries in the maze (Fig. 4**E**), confirming that the total exploratory behavior remained unchanged regardless of bTBI or genotype. Taken together, our data shows that the anxiety-like behavior in WT blast was significantly higher than in CCR2KO blast at 30d suggesting that CCL2-CCR2 signaling may be involved in chronic maintenance of bTBI-induced anxiety-like behavior.

3.5. CCR2 receptor deficiency prevented bTBI induced short-term memory deficits

To test whether bTBI had any effect on short-term memory, we performed novel object recognition test at 7d and 29d after bTBI. The test mice were allowed to familiarize with two identical objects for 10 m and their ability to identify a novel object (replacing a familiar object) was tested in an hour for 5 m (Fig. 5**A**). We found that WT mice exposed to blast were unable to discriminate a novel from a familiar object at both 7d and 29d after bTBI (Fig. 5**B-C**). Individual two-way ANOVA statistics at each time point show significant overall effect of bTBI on discrimination index at 7d [F(1,38) = 15.89, p = 0.0003] and 29d [F(1,38) = 7.78, p = 0.0082] after exposure, whereas genotype (WT vs. CCR2KO) had overall insignificant effect on time spent in the closed arm at 1d [F(1,38) = 0.35, p = 0.5576] and 30d [F (1,38) = 2.29, p = 0.1385] after exposure. Post-hoc Tukey test for multiple comparisons showed that CCRKO mice experienced significantly increased discrimination index or improved short-term memory at 29d (##, p < 0.01) but not at 7d after bTBI compared to their respective WT groups (Fig. 4**B-C**). In other words, the discrimination index/short term memory was partially rescued in CCR2KO at the 29d time point but had no effect at 7d after blast exposure (Fig. 5**B-C**). This data suggests that CCL2-CCR2 signaling may be implicated in chronic but not acute alterations in short-term memory. Two-way ANOVA statistics for each time point show insignificant overall effect of bTBI and CCR2 genotype on time spent exploring novel object alone and total exploration time at both 7d and 29d after bTBI **(**Fig. 4**D,E)**. Time spent exploring novel object: 7d Sham vs. bTBI: [F (1,38) = 1.69, p = 0.2014]; 29d Sham vs. bTBI: [F(1,38) = 0.99, p = 0.326], 7d WT vs.CCR2KO: [F(1,38) = 1.82, p = 0.1852]; 29d WT vs. CCR2KO: [F(1,38) = 3.86, p = 0.0568]. Total exploration time: 7d Sham vs. bTBI: [F(1,38) = 0.39, p = 0.536]; 29d Sham vs. bTBI: [F (1,38) = 3.45, p = 0.071], 7d WT vs.CCR2KO: [F(1,38) = 3.31, p = 0.0767]; 29d WT vs. CCR2KO: [F(1,38) = 0.38, p = 0.5413]. Although there was a trend, there was no significant difference in time spent in the novel object alone (Fig. 5**D**). Due to the comparable total exploration time among the various experimental groups (Fig. 5**E**), the significance in discrimination index indicates that mice exposed to blast were unable to discriminate the novel object from a familiar object at both 7d and 29d after initial insult.

3.6. bTBI had no effect on gross motor-behavior or exploratory behavior

We tested gross-motor and exploratory behavior in WT and CCR2 KO mice at 4d and 28d after bTBI using the open field assay (Fig. 6**A**). We found no difference between groups in time spent in the corner zone (Fig. 6**B-C**), time spent in the center zone (Fig. 6**D**) or total distance travelled in the maze (Fig. 6**E**). Two-way ANOVA statistics for each time point show insignificant overall effect of bTBI and CCR2 genotype on time spent in corner zone, time spent in center zone and total distance travelled at both 4d and 28d after bTBI **(**Fig. 6**C-E)**. Time spent in corner zone: 4d Sham vs. bTBI: [F(1,38) = 1.8, p = 0.1877]; 28d Sham vs. bTBI: [F(1,38) = 0.42, p = 0.5208], 4d WT vs.CCR2KO: [F (1,38) = 0.75, p = 0.3919]; 28d WT vs. CCR2KO: [F(1,38) = 0.31, p = 0.5809]. Time spent in center zone: 4d Sham vs. bTBI: [F (1,38) = 0.06, p = 0.8078]; 28d Sham vs. bTBI: [F(1,38) = 1.72, p = 0.1976], 4d WT vs.CCR2KO: [F(1,38) = 3.5, p = 0.0691]; 28d WT vs. CCR2KO: [F(1,38) = 0.85, p = 0.3624]. Total distance travelled: 4d Sham vs. bTBI: [F(1,38) = 0.93, p = 0.341]; 28d Sham vs. bTBI: [F (1,38) = 1.77, p = 0.1913], 4d WT vs.CCR2KO: [F(1,38) = 0.81, p = 0.3738]; 28d WT vs. CCR2KO: [F(1,38) = 0.54, p = 0.4669]. In addition to demonstrating locomotory behavior, open field test is also used to measure anxiety. Although our results show that bTBI causes anxiety-like behavior based on elevated plus maze test, we do not observe these effects in open field test. Such discrepancies have been previously noted and is thought to be due to the different anxiogenic properties tested by the two methods and represents the multidimensional structure of mouse anxiety-related behavior (Carola et al., 2002). In conclusion, our results suggest that bTBI did not have a significant effect on motor/exploratory behavior. These findings rule out the possibility of a motor deficit and further strengthens our results

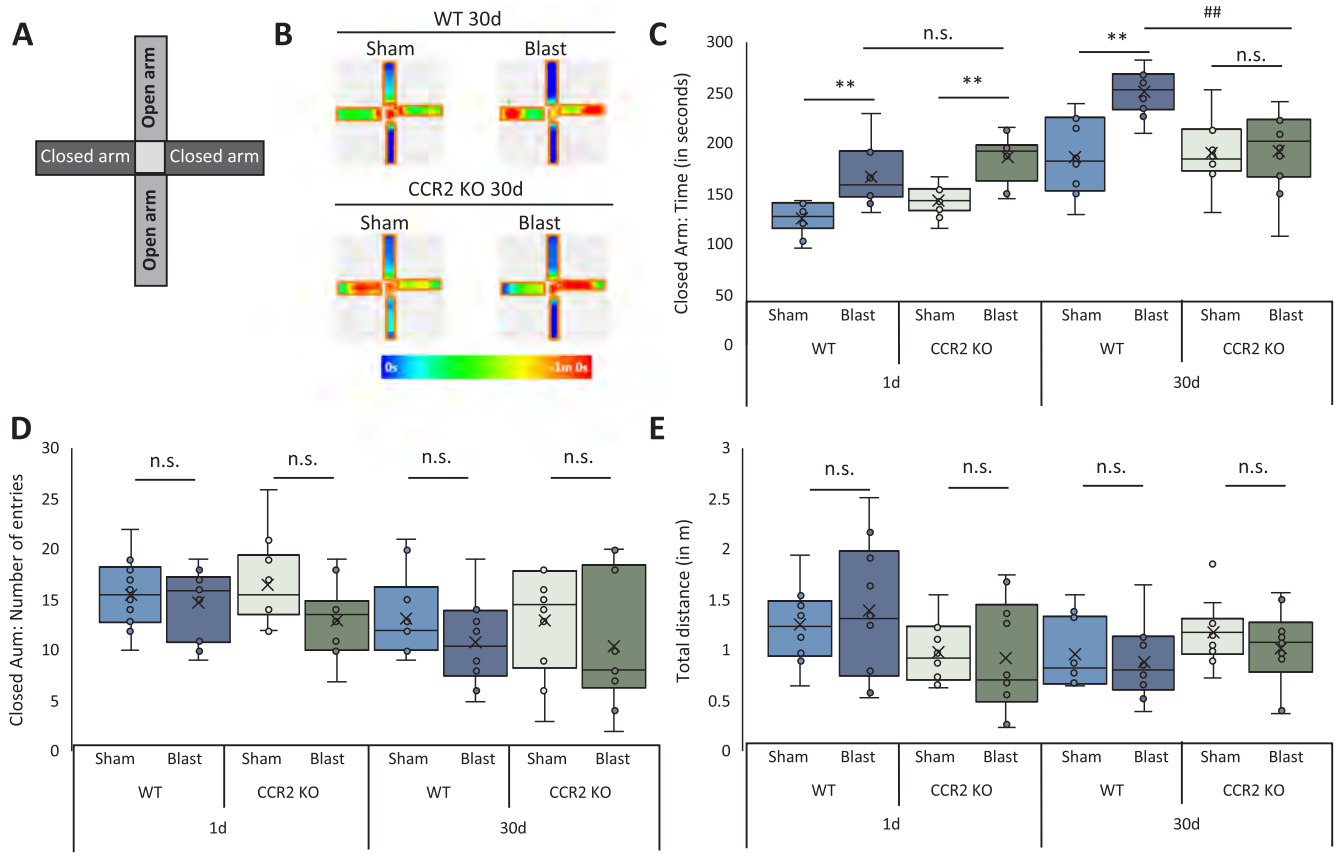


Fig. 4. Increased anxiety-like behavior after brain injury. **A**. Schematic showing elevated plus maze used to test anxiety-like behavior in mice. **B**. Representative heat maps showing time spent in the closed arm of the elevated plus maze by sham and 30d bTBI group in WT and CCR2 KO genotypes. Note that mice exposed to blast spend considerable time in the closed arm as noted in the heat maps. **C-E**. Box and whisker plot showing time spent in closed arm (**C**), number of entries into the closed arm (**D**) and total distance travelled (**E**) in sham and blast groups in WT and CCR2 KO ($CCR2^{RFP/RFP}$) at 1d and 30 after bTBI. **p < 0.01. *Represents comparisons made between sham and blast groups (within genotype) for each time point. ##p < 0.01. # Represents comparisons made between blast groups of WT and CCR2 KO. Note the # values for comparisons between sham groups were insignificant (> 0.05). Individual two-way ANOVA was used with Tukey HSD test for each time point. WT sham and blast (n = 10), CCR2 KO sham (n = 10), CCR2 KO blast (n = 12).

from elevated plus maze and novel object recognition.

4. Discussion

Using double transgenic mice model, we identified robust microglia activation and monocyte infiltration with distinct spatiotemporal patterns following moderate bTBI. The current study delineates the peak temporal window for bTBI mediated microglia activation versus monocyte infiltration based on morphological properties and the occurrence of infiltrated CCR2+ cells, respectively. We further show that chemokine CCL2-CCR2 signaling significantly contributed to monocyte infiltration after injury, as evidenced by reduced monocyte in CCR2 KO mice. More importantly, CCR2 KO mice demonstrate reduced anxiety-like behavior and improved short-term memory compared to wildtype (WT) mice after bTBI. Production of proinflammatory cytokine IL-1β may be a potential mechanism by which CCL2-CCR2 signaling mediates behavioral deficits after bTBI (Fig. 7).

Accumulation of microglia/macrophages is noted in several models of animal TBI as well as in human TBI (Ramlackhansingh, 2011; Donat et al., 2017; Johnson, 2013). In this study, we show that bTBI resulted in microglia activation and monocyte infiltration in various regions confirming the global effect that blast exposure has on the brain. This is in line with previous works that have shown a highly diffuse effect of blast injury including disruptions in BBB (Kuriakose et al., 2018; Rama Rao, 2018), oxidative stress (Rama Rao, 2018) and axonal injury (Zhang, 2018), that traverses the prefrontal cortex all the way to the cerebellum. The spatial variation in microglia activation after bTBI may be due to regional differences in mechanical loading and/or the intrinsic property of the tissue (Younger et al., 2018). Despite the limited studies on mechanical signaling in microglia, mechanical stimuli have been shown to affect microglia proliferation, activation and chemotaxis (Bollmann, 2015; Navone, 2018). The response of microglia to injury may also depend on the intrinsic property of the tissue such as blood vessel distribution (Navone, 2018), neuronal vulnerability within the region (Goodrich, 2016; Przekwas et al., 2016) and/or microglial heterogeneity itself (Hammond, 2019).

Although, microglia/macrophage accumulation was previously reported in a blast model of brain injury (Huber, 2016), the cellular source of the macrophages remain uninvestigated. Studies delineating resident microglia from blood-borne macrophages have employed poorly developed techniques such as irradiation chimerism and parabiosis, with controversial and misinterpreted results (Ajami et al., 2011; Ajami et al., 2007; Ransohoff, 2007). Here, we used $CCR2^{RFP/+}$: $CX3CR1^{GFP/+}$ double transgenic mice to establish that both resident Cx3CR1+ microglia and CCR2+ monocytes contributed to the expanded macrophage population following bTBI.

Microglia activation based on morphological changes occurred in two phases following blast: the acute increase at 4 h, and chronic activation that starts at 3d lasting up to 30 d. We also note a slight increase in outward potassium currents suggestive of functional activation of microglia at 1d after bTBI. Similar changes in microglia membrane properties have been noted in conditions of neuropathic pain and epilepsy and is associated with microglia activation (Peng et al., 2016; Feng and Muruga, 2019). We have previously shown that

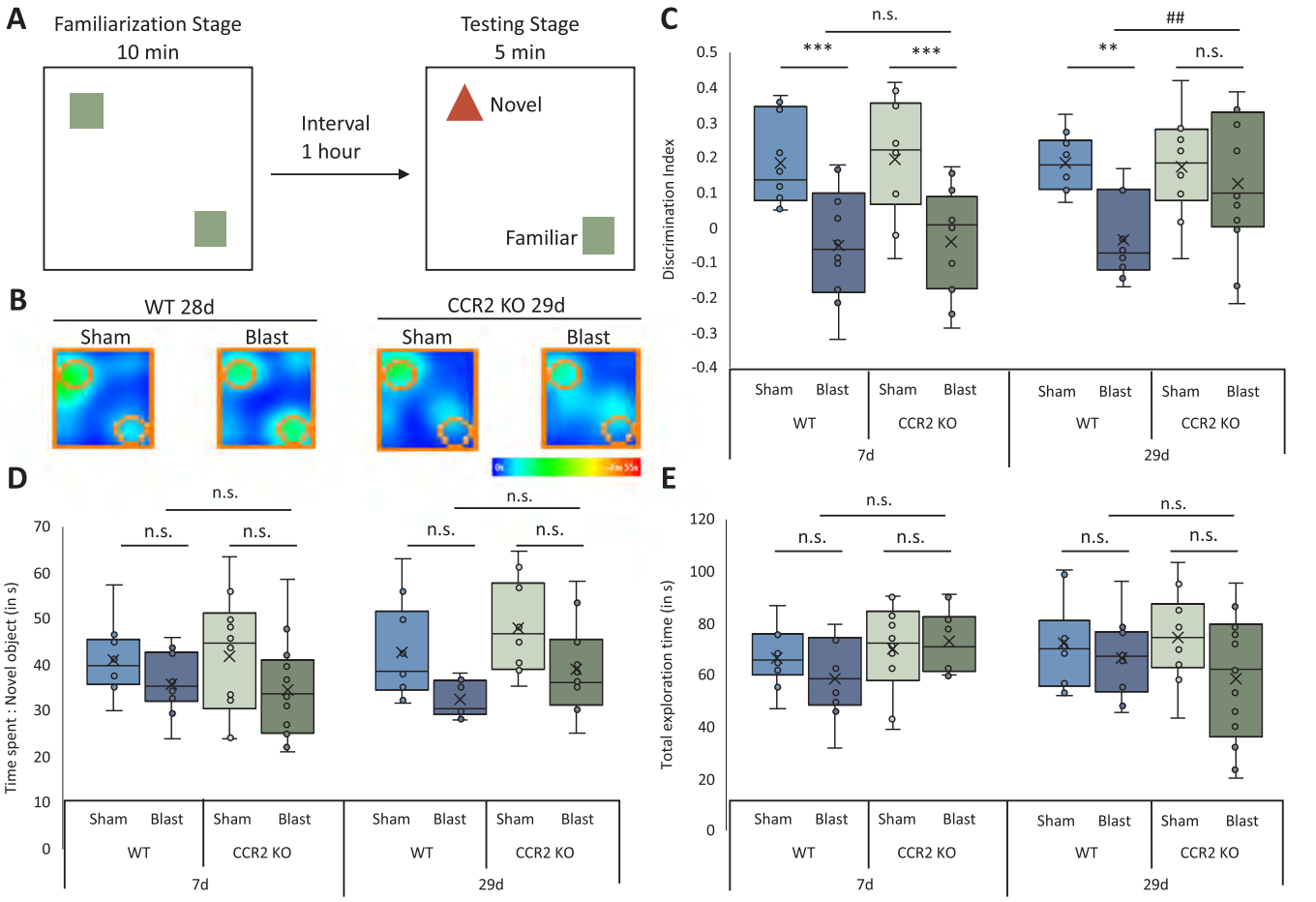


Fig. 5. Decline in short-term memory after brain injury. **A.** Schematic showing Novel Object Recognition (NOR) test paradigm used to measure short-term memory in mice. **B.** Representative heat maps showing time spent mice near the familiar versus novel object during a 5 mins testing phase in sham and 29d bTBI group from WT and CCR2 KO genotypes. **C-E** Box and whisker shows discrimination index for ability to differentiate a novel object from a familiar object (**C**), time spent exploring novel object (**D**) and total exploration time (**E**) in sham and blast groups in WT and CCR2 KO mice at 7d and 29 d after bTBI. $^{**}p < 0.01$, $^{***}p < 0.001$. * Represents comparisons made between sham and blast groups (within genotype) for each time point. $^{\#\#}p < 0.01$. # Represents comparisons made between blast groups of WT and CCR2 KO. Note that comparisons made between WT and CCR2 KO within shams and blast groups proved to be insignificant. Also, there was no significant recovery in discrimination index (1d vs. 30d) in either WT blast and CCR2 KO blast animals. Individual two-way ANOVA was used with Tukey HSD test for each time point. WT sham and blast (n = 10), CCR2 KO sham (n = 10), CCR2 KO blast (n = 12). Note that for analysis, time spent interacting with the novel object was taken into account.

direct biomechanical loading of the primary blast itself is capable of causing disruption to BBB as early as 15 min following blast exposure (Kuriakose et al., 2018). Further, the reported timeline of BBB damage following bTBI correlates with the biphasic activation of microglia noted here, suggesting that microglia activation might be closely associated to vascular leakage. Another recent study reported similar changes in microglia morphology/activation as early as 45 m following blast exposure (15 psi) and noted them to be closely associated with vascular disruptions further strengthening our findings (Huber, 2016).

Moreover, we note that monocyte infiltration starts at 4 h, peaked at 24 h and continues to survive in the neuronal parenchyma until 30d, following the initial blast exposure. Unlike microglia with low-turnover rate (Ajami et al., 2007; Lawson et al., 1992), monocytes exhibit rapid turnover (van Furth and Cohn, 1968) suggesting that monocyte infiltration continues even at chronic time points following blast exposure. However, the increase in soma size indicates that the infiltrated monocytes morphologically transform into macrophages in the neuronal tissue. Taken together, it is unclear whether the monocytes infiltration is continuous or if infiltrated monocytes are capable of surviving/evolving in the neuronal tissue and this aspect needs to be investigated.

4.1. CCL2-CCR2 signaling mediates bTBI-induced monocyte infiltration

The chemokine CCL2, also known as monocyte chemoattractant protein (MCP), is elevated in patients following TBI (Semple et al., 2010). We previously showed that the expression of chemokine CCL2 is increased in the PFC at 4 h after bTBI (Kuriakose et al., 2018). The chemokine in turn attracts CCR2-expressing cells such as blood-borne monocytes to infiltrate the neuronal tissue. Given the strong association between BBB damage and oxidative stress in our rat model of bTBI (Rama Rao, 2018), we hypothesized that monocyte infiltration in our TBI model to be likely mediated by BBB leakage. To our surprise, we note that the infiltration of monocytes was reduced in CCR2 KO mice suggesting that the infiltration was at least partly dependent on CCL2-CCR2 signaling. Our data shows that at least in vascular-rich areas such as the prefrontal cortex, the number of infiltrated monocytes correlated with the increased BBB leakage. Taken together, it seems likely that both increased BBB permeability and CCL2-CCR2 signaling mediated mechanisms play key roles in monocyte infiltration after bTBI. Pre-injury depletion of monocytes increased BBB permeability after TBI indicating that peripheral monocytes are required for BBB repair (Aertker, 2019; Hua et al., 2015). However, the role of monocytes in BBB integrity and repair in bTBI model needs to be elucidated.

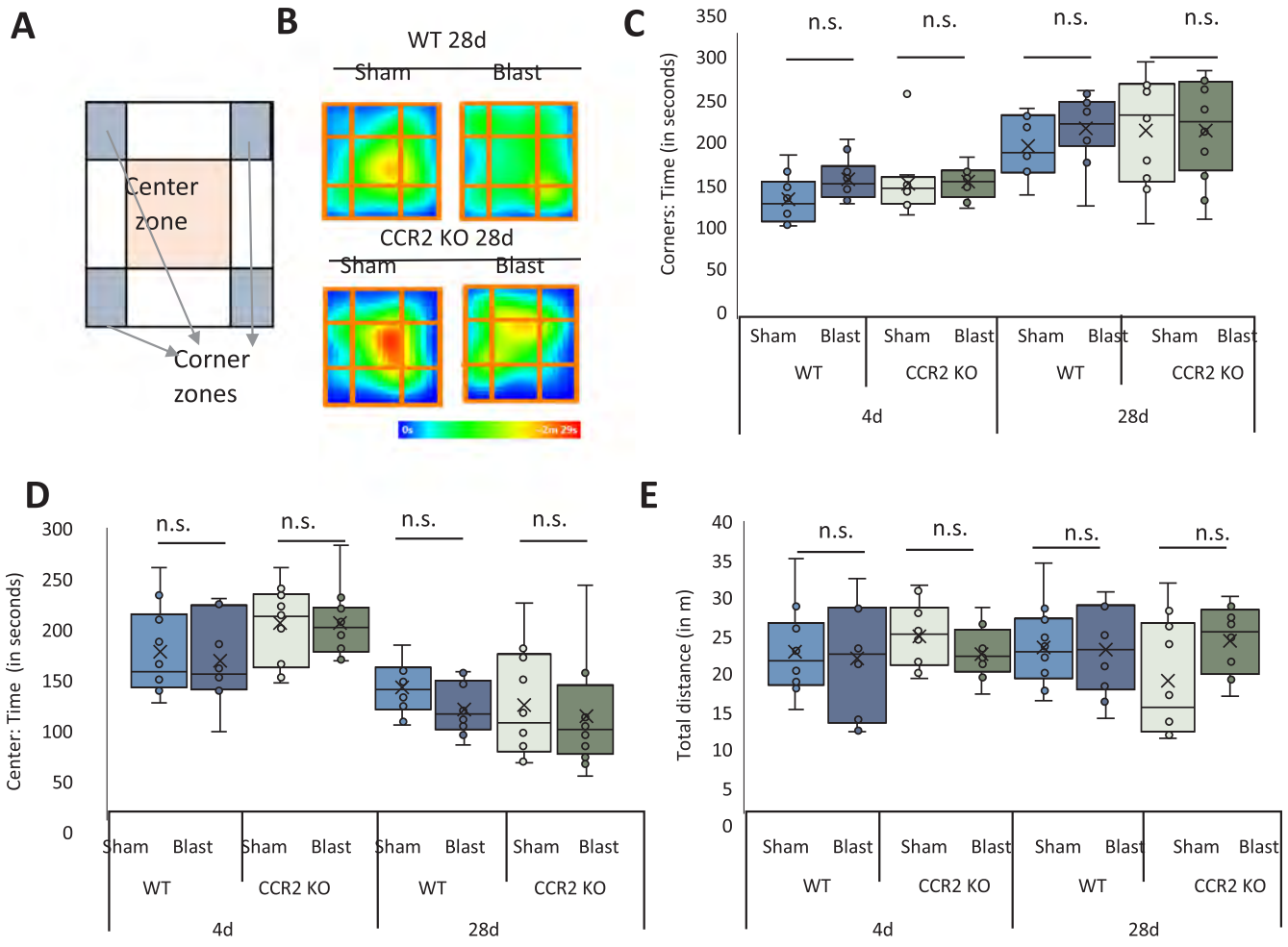


Fig. 6. Motor performance is maintained after blast exposure. **A**. Schematic showing open field test arena with center and corner zones. **B**. Representative heat maps showing time spent by mice in the center versus corner zones of the open field assay by sham and 28d bTBI group from WT and CCR2 KO genotypes. **C-E**. Box and whisker plots shows time spent in the corner zones (**C**), time spent in center zone (**D**) and total distance explored (**E**) by sham and blast exposed groups from WT and CCR2 KO genotypes at 4d and 28d after bTBI. No significant differences were noted in comparisons between respective sham versus bTBI or WT versus KO conditions for time spent in the corner/center zone(s) and total distance travelled in the open field arena. Individual two-way ANOVA was used with Tukey HSD test for each time point. WT sham and blast (n = 10), CCR2 KO sham (n = 10), CCR2 KO blast (n = 12).

4.2. Distinct role of microglia and monocytes in inflammation

Activated microglia/macrophages is thought to mediate chronic neuroinflammation after moderate bTBI. Infiltrating cells in TBI were confirmed to be of monocyte-origin and the maturation state of these cells was dependent on the severity of TBI (Trahanas et al., 2015). Accumulating evidence suggests that infiltrating monocyte-derived macrophages and resident microglia work synergistically, yet distinctly in promoting inflammation in various neuropathological conditions (Roth, 2014; Peng et al., 2016). Hence, investigating the relationship between infiltrating monocytes and microglia is key to understanding and treating neuroinflammation. Here, we note that deficiency in CCR2 prevented the chronic increase in production of IL-1β. Similar increase in IL-1β was shown to be mediated by CCL2-CCR2 signaling via phosphorylation of signal transducer and activator of transcription 3 (STAT3) after kainic acid-induced seizures (Tian, 2017). Although monocyte numbers peak at 1d, there is no corresponding increase in IL-1β, suggesting that CCR2 signaling may mediate IL-1β production through indirect mechanisms at chronic time points. Hence, further investigation on the expression levels of a repertoire of cytokines/chemokines is essential to fully comprehend the extent and cellular origin of inflammatory response following bTBI.

4.3. CCL2-CCR2 signaling in behavioral changes

Chronic inflammation has been increasingly implicated in behavioral changes that occur after bTBI (Sajja, 2014; Muelbl, 2018; Hoffman, 2017). Here, we report an increase in anxiety-like behavior and short-term memory decline in both and acute and chronic time points following bTBI. This is in line with previous studies that have observed anxiety, depression-like behavior and memory deficits in animal models following exposure to blast overpressurr (Sajja, 2014; Beamer, 2016). PTSD-related behavioral traits including anxiety, fear-related behaviors as well as long-term recognition memory were noted at 11–17 weeks from blast exposure (Perez-Garcia, et al., 2018). Similar behavioral outcomes including poor performance in executive functions was observed in blast-exposed veterans with mild TBI (Clark, 2018). These studies along with our findings reiterate the existence of chronic behavioral outcomes following blast exposure and the need for timely therapeutic intervention.

We then went on to investigate whether the infiltrated monocytes/CCL2-CCR2 signaling is implicated in behavioral alterations observed after bTBI. We note that CCR2 deficiency rescued bTBI-induced behavioral deficits, suggesting that monocyte infiltration is an important effector of behavioral outcomes in mice exposed to blast. Hseieh et al showed a similar prevention in monocyte infiltration and functional

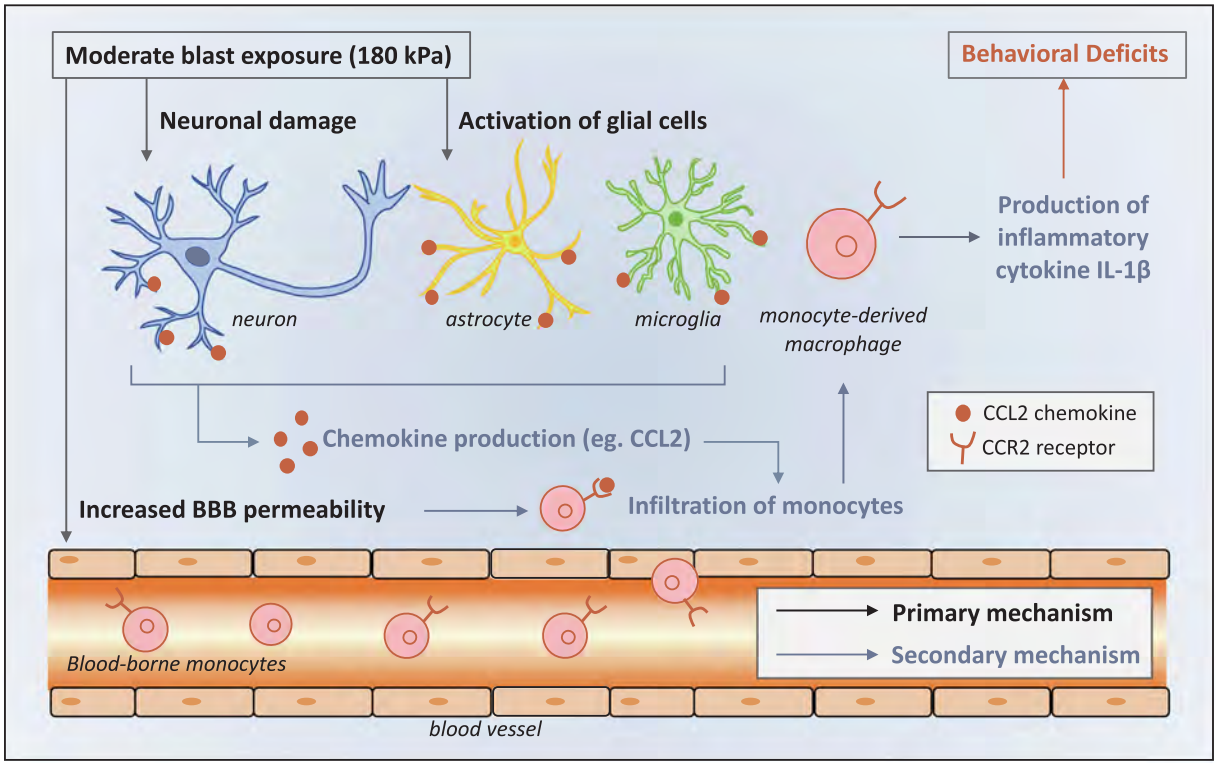


Fig. 7. Schematic illustration depicting sequence of events following moderate blast-induced traumatic brain injury (bTBI). bTBI induces activation of resident microglia (1) and infiltration of blood-borne monocytes expressing CCR2 receptor (2). Chemokine CCL2 secreted by microglia, astrocytes, neurons may attract CCR2+ monocytes causing them to infiltrate the neuronal parenchyma (3). Infiltrated monocytes together with resident activated microglia may contribute to the release of proinflammatory cytokines such as IL-1β (4), eventually leading to behavioral deficits such as increased anxiety-like behavior and reduced short term memory (5) following bTBI.

recovery in CCR2 KO mice following controlled cortical impact injury (Hsieh, 2014). Interestingly, antagonism of CCR2+ macrophages with CCC872, a novel Phase I CCR2 selective antagonist and EVT901, a novel antagonist of p75NTR reduced infiltration of pro-inflammatory monocytes and spared behavioral function after TBI (Lee, 2016; Morganti, 2015). The CCL2-CCR2 dependent changes in behavior may also be associated with IL-1β increase, which is known to alter neuronal activity and promote depression-like behavior (Norman, 2010). In line with our study, another study showed that microglia selectively expressed CCL2 resulting in the recruitment of IL-1β producing monocytes and caused stress-induced anxiety in a mice model of repeated social defeat (McKim, 2018). Despite the reduction in chronic IL-1β production and improvements in bTBI-induced behavioral outcomes, CCR2 deficiency did not alter acute microglia activation or acute behavioral deficits because monocyte infiltration is highest at 1d. Hence, the effects of blocking CCL2-CCR2 signaling may not have a significant immediate effect on the inflammatory microenvironment and therefore the acute behavioral deficits.

Recent studies have shown that immune cells such as microglia and T-lymphocytes act differently in male versus female mice resulting in variance in pain sensitivity (Sorge, 2015; Nissen, 2017). Further, mild bTBI was shown to cause sex specific changes in production of stress-induced serum corticosterone levels (Russell, 2018). We did not note sex differences in bTBI induced behavioral deficits such as anxiety-like behavior and short-term memory decline, although this data has to be interpreted with caution due to the small sample size (Supplementary Fig. 5). Overall, our study highlights the need to investigate sex specific changes at both cellular and behavioral-levels, which is often overlooked in bTBI studies.

In this study, the effects of CCR2 is used to describe the receptors expressed predominantly by monocytes/macrophages (Saederup, 2017). However, there is some evidence to show that microglia (Zhang, 2007) and a few neuronal populations (Fan et al., 2007; Tran et al., 2007) may express the receptor at certain conditions. Hence, the behavioral and phenotypic changes noted here might be a result of glial/neuronal response to bTBI. Recent work using unbiased bioinformatics approach identified a robust set of markers to discriminate resident microglia from infiltrating monocytes (Haage, 2019), which needs to be employed in future studies that delineate the two macrophage subpopulations.

In conclusion, we show that resident microglia and infiltrated monocytes distinctly contribute to bTBI-mediated pathology. Most importantly, CCL2-CCR2 signaling axis is a significant mediator and a potential therapeutic target for achieving improved neurobehavioral outcomes in TBI.

Acknowledgements

This work was supported by New Jersey Commission on Brain Injury Research (CBIR16IRG017, CBIR17PIL020, CBIR20IRG011) and USAMRMC (W81XWH-15-1-0303). Eren Alay and Jose Rodriguez were involved in maintenance and running of the shock tube used for blast injuries. We thank Vijayalakshmi Santhakumar for sharing the electrophysiology equipment and resources.

Author contributions

M.M., conceived and planned the experiments. M.M., A.R., A.G., G.V., W.M. and S.M. carried out the experiments. M.M., and N.C. contributed to the interpretation of the results. M.M. took the lead in writing the manuscript. All authors provided critical feedback and helped shape the research, analysis and manuscript.

Appendix A. Supplementary data

Supplementary data to this article can be found online at https://doi.org/10.1016/j.bbi.2020.03.029.

References

Bell, R.S., et al., 2009. Military traumatic brain and spinal column injury: a 5-year study of the impact blast and other military grade weaponry on the central nervous system. J. Trauma 66, S104–S111. https://doi.org/10.1097/TA.0b013e31819d88c8.

Kuriakose, M., Rama Rao, K.V., Younger, D., Chandra, N., 2018. Temporal and spatial effects of blast overpressure on blood-brain barrier permeability in traumatic brain injury. Sci. Rep. 8, 8681. https://doi.org/10.1038/s41598-018-26813-7.

Rama Rao, K.V., et al., 2018. A single primary blast-induced traumatic brain injury in a rodent model causes cell-type dependent increase in nicotinamide adenine dinucleotide phosphate oxidase isoforms in vulnerable brain regions. J. Neurotrauma 35, 2077–2090. https://doi.org/10.1089/neu.2017.5358.

Abdul-Muneer, P.M., et al., 2013. Induction of oxidative and nitrosative damage leads to cerebrovascular inflammation in an animal model of mild traumatic brain injury induced by primary blast. Free Radic. Biol. Med. 60, 282–291. https://doi.org/10.1016/j.freeradbiomed.2013.02.029.

Huber, B.R., et al., 2016. Blast exposure causes dynamic microglial/macrophage responses and microdomains of brain microvessel dysfunction. Neuroscience 319, 206–220. https://doi.org/10.1016/j.neuroscience.2016.01.022.

Readnower, R.D., et al., 2010. Increase in blood-brain barrier permeability, oxidative stress, and activated microglia in a rat model of blast-induced traumatic brain injury. J. Neurosci. Res. 88, 3530–3539. https://doi.org/10.1002/jnr.22510.

Gentleman, S.M., et al., 2004. Long-term intracerebral inflammatory response after traumatic brain injury. Forensic Sci. Int. 146, 97–104. https://doi.org/10.1016/j.forsciint.2004.06.027.

Ramlackhansingh, A.F., et al., 2011. Inflammation after trauma: microglial activation and traumatic brain injury. Ann. Neurol. 70, 374–383. https://doi.org/10.1002/ana.22455.

Nimmerjahn, A., Kirchhoff, F., Helmchen, F., 2005. Resting microglial cells are highly dynamic surveillants of brain parenchyma in vivo. Science 308, 1314–1318. https://doi.org/10.1126/science.1110647.

Roth, T.L., et al., 2014. Transcranial amelioration of inflammation and cell death after brain injury. Nature 505, 223–228. https://doi.org/10.1038/nature12808.

Shechter, R., et al., 2009. Infiltrating blood-derived macrophages are vital cells playing an anti-inflammatory role in recovery from spinal cord injury in mice. PLoS Med. 6, e1000113. https://doi.org/10.1371/journal.pmed.1000113.

London, A., et al., 2011. Neuroprotection and progenitor cell renewal in the injured adult murine retina requires healing monocyte-derived macrophages. J. Exp. Med. 208, 23–39. https://doi.org/10.1084/jem.20101202.

Kaur, C., et al., 1995. The response of neurons and microglia to blast injury in the rat brain. Neuropathol. Appl. Neurobiol. 21, 369–377.

Hsieh, C.L., et al., 2014. CCR2 deficiency impairs macrophage infiltration and improves cognitive function after traumatic brain injury. J. Neurotrauma 31, 1677–1688. https://doi.org/10.1089/neu.2013.3252.

Gyoneva, S., et al., 2015. Ccr2 deletion dissociates cavity size and tau pathology after mild traumatic brain injury. J. Neuroinflamm. 12, 228. https://doi.org/10.1186/s12974-015-0443-0.

Semple, B.D., Bye, N., Rancan, M., Ziebell, J.M., Morganti-Kossmann, M.C., 2010. Role of CCL2 (MCP-1) in traumatic brain injury (TBI): evidence from severe TBI patients and CCL2-/- mice. J. Cereb. Blood Flow Metab. 30, 769–782. https://doi.org/10.1038/jcbfm.2009.262.

Tian, D.S., et al., 2017. Chemokine CCL2-CCR2 signaling induces neuronal cell death via STAT3 activation and IL-1beta production after status epilepticus. J. Neurosci. 37, 7878–7892. https://doi.org/10.1523/JNEUROSCI.0315-17.2017.

Severini, C., et al., 2014. Bindarit, inhibitor of CCL2 synthesis, protects neurons against amyloid-beta-induced toxicity. J. Alzheimers Dis. 38, 281–293. https://doi.org/10.3233/JAD-131070.

Chen, Y., et al., 2003. Overexpression of monocyte chemoattractant protein 1 in the brain exacerbates ischemic brain injury and is associated with recruitment of inflammatory cells. J. Cereb. Blood Flow Metab. 23, 748–755. https://doi.org/10.1097/01.WCB.0000071885.63724.20.

O'Neil, M.E., et al., 2017. Postconcussion symptoms reported by Operation Enduring Freedom/Operation Iraqi Freedom veterans with and without blast exposure, mild traumatic brain injury, and posttraumatic stress disorder. J. Clin. Exp. Neuropsychol. 39, 449–458. https://doi.org/10.1080/13803395.2016.1232699.

Nelson, N.W., Davenport, N.D., Sponheim, S.R., Anderson, C.R., in Brain Neurotrauma: Molecular, Neuropsychological, and Rehabilitation Aspects Frontiers in Neuroengineering (ed F. H. Kobeissy) (2015).

Petrie, E.C., et al., 2014. Neuroimaging, behavioral, and psychological sequelae of repetitive combined blast/impact mild traumatic brain injury in Iraq and Afghanistan war veterans. J. Neurotrauma 31, 425–436. https://doi.org/10.1089/neu.2013.2952.

Kovacs, S.K., Leonessa, F., Ling, G.S., 2014. Blast TBI models, neuropathology, and implications for seizure risk. Front. Neurol. 5, 47. https://doi.org/10.3389/fneur.2014.00047.

Yang, L., et al., 2016. Systemic inflammation induces anxiety disorder through CXCL12/CXCR4 pathway. Brain Behav. Immun. 56, 352–362. https://doi.org/10.1016/j.bbi.2016.03.001.

Salim, S., et al., 2011. Potential contribution of oxidative stress and inflammation to anxiety and hypertension. Brain Res. 1404, 63–71. https://doi.org/10.1016/j.brainres.2011.06.024.

Jung, S., et al., 2000. Analysis of fractalkine receptor CX(3)CR1 function by targeted deletion and green fluorescent protein reporter gene insertion. Mol. Cell. Biol. 20, 4106–4114.

Saederup, N., et al., 2017. Correction: selective chemokine receptor usage by central nervous system myeloid cells in CCR2-Red fluorescent protein knock-in mice. PLoS ONE 12, e0176931. https://doi.org/10.1371/journal.pone.0176931.

Kuriakose, M., et al., 2016. Tailoring the blast exposure conditions in the shock tube for generating pure, primary shock waves: the end plate facilitates elimination of secondary loading of the specimen. PLoS ONE 11, e0161597. https://doi.org/10.1371/journal.pone.0161597.

Mishra, V., et al., 2016. Primary blast causes mild, moderate, severe and lethal TBI with increasing blast overpressures: experimental rat injury model. Sci. Rep. 6, 26992. https://doi.org/10.1038/srep26992.

Heindl, S., et al., 2018. Automated morphological analysis of microglia after stroke. Front. Cell. Neurosci. 12, 106. https://doi.org/10.3389/fncel.2018.00106.

William, R.S.R., Hubbard, W., Denise Schehel-Geiger. Indocyanine Green (ICG) and Evans Blue: Comparative Study of Plasma Volume Measurement. U.S. Army Research Institute of Environmental Medicine (1982).

Wang, H.L., Lai, T.W., 2014. Optimization of Evans blue quantitation in limited rat tissue samples. Sci. Rep. 4, 6588. https://doi.org/10.1038/srep06588.

Carola, V., D'Olimpio, F., Brunamonti, E., Mangia, F., Renzi, P., Evaluation of the elevated plus-maze and open-field tests for the assessment of anxiety-related behaviour in inbred mice. Behav. Brain Res., 134, 1-2, doi: 10.1016/S0166-4328(01)00452-1 (2002).

Donat, C.K., Scott, G., Gentleman, S.M., Sastre, M., 2017. Microglial activation in traumatic brain injury. Front. Aging Neurosci. 9, 208. https://doi.org/10.3389/fnagi.2017.00208.

Johnson, V.E., et al., 2013. Inflammation and white matter degeneration persist for years after a single traumatic brain injury. Brain 136, 28–42. https://doi.org/10.1093/brain/aws322.

Zhang, J.H., et al., 2018. Establishment of a novel rat model of blast-related diffuse axonal injury. Exp. Ther. Med. 16, 93–102. https://doi.org/10.3892/etm.2018.6146.

Younger, D., Murugan, M., Rama Rao, K.V., Wu, L.J., Chandra, N., 2018. Microglia receptors in animal models of traumatic brain injury. Mol. Neurobiol. https://doi.org/10.1007/s12035-018-1428-7.

Bollmann, L., et al., 2015. Microglia mechanics: immune activation alters traction forces and durotaxis. Front. Cell. Neurosci. 9, 363. https://doi.org/10.3389/fncel.2015.00363.

Navone, S.E., et al., 2018. Mechanical loading of intervertebral disc modulates microglia proliferation, activation, and chemotaxis. Osteoarthritis Cartilage 26, 978–987. https://doi.org/10.1016/j.joca.2018.04.013.

Hua, Y., Lin, S., Gu, L., 2015. Relevance of blood vessel networks in blast-induced traumatic brain injury. Comput. Math. Methods Med. 2015, 928236. https://doi.org/10.1155/2015/928236.

Goodrich, J.A., et al., 2016. Neuronal and glial changes in the brain resulting from explosive blast in an experimental model. Acta Neuropathol. Commun. 4, 124. https://doi.org/10.1186/s40478-016-0395-3.

Przekwas, A., Somayaji, M.R., Gupta, R.K., 2016. Synaptic mechanisms of blast-induced brain injury. Front. Neurol. 7, 2. https://doi.org/10.3389/fneur.2016.00002.

Hammond, T.R., et al., 2019. Single-cell RNA sequencing of microglia throughout the mouse lifespan and in the injured brain reveals complex cell-state changes. 253-271 e256. Immunity 50. https://doi.org/10.1016/j.immuni.2018.11.004.

Ajami, B., Bennett, J.L., Krieger, C., McNagny, K.M., Rossi, F.M., 2011. Infiltrating monocytes trigger EAE progression, but do not contribute to the resident microglia pool. Nat. Neurosci. 14, 1142–1149. https://doi.org/10.1038/nn.2887.

Ajami, B., Bennett, J.L., Krieger, C., Tetzlaff, W., Rossi, F.M., 2007. Local self-renewal can sustain CNS microglia maintenance and function throughout adult life. Nat. Neurosci. 10, 1538–1543. https://doi.org/10.1038/nn2014.

Ransohoff, R.M., 2007. Microgliosis: the questions shape the answers. Nat. Neurosci. 10, 1507–1509. https://doi.org/10.1038/nn1207-1507.

Peng, J., Gu, N., Zhou, L., B Eyo, U., Murugan, M., Gan, W.B., Wu, L.J., 2016. Microglia and monocytes synergistically promote the transition from acute to chronic pain after nerve injury. Nature Commun., 7, 12029.

Feng, L., Muruga, M., Bosco., D.B., Liu, Y., Peng, J., Worell, G.A., Wang, H.L., Ta, L.E., Richardson, J.R., Shen, Y., Wu, L.J., 2019. Microglial proliferation and monocyte infiltration contribute to microgliosis following status epilepticus. Glia. doi: 10.1002/glia.23616.

Lawson, L.J., Perry, V.H., Gordon, S., 1992. Turnover of resident microglia in the normal adult mouse brain. Neuroscience 48, 405–415.

van Furth, R., Cohn, Z.A., 1968. The origin and kinetics of mononuclear phagocytes. J. Exp. Med. 128, 415–435.

Aertker, B.M., et al., 2019. Pre-injury monocyte/macrophage depletion results in increased blood-brain barrier permeability after traumatic brain injury. J. Neurosci. Res. https://doi.org/10.1002/jnr.24395.

Trahanas, D.M., Cuda, C.M., Perlman, H., Schwulst, S.J., 2015. Differential activation of infiltrating monocyte-derived cells after mild and severe traumatic brain injury. Shock 43, 255–260. https://doi.org/10.1097/SHK.0000000000000291.

Sajja, V.S., et al., 2014. Blast neurotrauma impairs working memory and disrupts prefrontal myo-inositol levels in rats. Mol. Cell. Neurosci. 59, 119–126. https://doi.org/10.1016/j.mcn.2014.02.004.

Muelbl, M.J., et al., 2018. Effects of mild blast traumatic brain injury on cognitive- and addiction-related behaviors. Sci. Rep. 8, 9941. https://doi.org/10.1038/s41598-018-28062-0.

Hoffman, J.R., et al., 2017. Behavioral and inflammatory response in animals exposed to a

ARTICLE IN PRESS

low-pressure blast wave and supplemented with beta-alanine. Amino Acids 49, 871–886. https://doi.org/10.1007/s00726-017-2383-8.
Beamer, M., et al., 2016. Primary blast injury causes cognitive impairments and hippocampal circuit alterations. Exp. Neurol. 283, 16–28. https://doi.org/10.1016/j.expneurol.2016.05.025.
Perez-Garcia, G., et al., PTSD-Related Behavioral Traits in a Rat Model of Blast-Induced mTBI Are Reversed by the mGluR2/3 Receptor Antagonist BCI-838. eNeuro 5, doi: 10.1523/ENEURO.0357-17.2018 (2018).
Clark, A.L., et al., 2018. Blast-exposed veterans with mild traumatic brain injury show greater frontal cortical thinning and poorer executive functioning. Front. Neurol. 9, 873. https://doi.org/10.3389/fneur.2018.00873.
Lee, S., et al., 2016. A novel antagonist of p75NTR reduces peripheral expansion and CNS trafficking of pro-inflammatory monocytes and spares function after traumatic brain injury. J. Neuroinflammation 13, 88. https://doi.org/10.1186/s12974-016-0544-4.
Morganti, J.M., et al., 2015. CCR2 antagonism alters brain macrophage polarization and ameliorates cognitive dysfunction induced by traumatic brain injury. J. Neurosci. 35, 748–760. https://doi.org/10.1523/JNEUROSCI.2405-14.2015.
Norman, G.J., et al., 2010. Stress and IL-1beta contribute to the development of depressive-like behavior following peripheral nerve injury. Mol. Psychiatry 15, 404–414. https://doi.org/10.1038/mp.2009.91.
McKim, D.B., et al., 2018. Microglial recruitment of IL-1β-producing monocytes to brain endothelium causes stress-induced anxiety. Mol. Psychiatry 23 (6), 1421–1431. https://doi.org/10.1038/mp.2017.64.
Sorge, R.E., et al., 2015. Different immune cells mediate mechanical pain hypersensitivity in male and female mice. Nat. Neurosci. 18, 1081–1083. https://doi.org/10.1038/nn.4053.
Nissen, J.C., 2017. Microglial function across the spectrum of age and gender. Int. J. Mol. Sci. 18. https://doi.org/10.3390/ijms18030561.
Russell, A.L., et al., 2018. Differential responses of the HPA axis to mild blast traumatic brain injury in male and female mice. Endocrinology 159, 2363–2375. https://doi.org/10.1210/en.2018-00203.
Zhang, J., et al., 2007. Expression of CCR2 in both resident and bone marrow-derived microglia plays a critical role in neuropathic pain. J. Neurosci. 27, 12396–12406. https://doi.org/10.1523/JNEUROSCI.3016-07.2007.
Fan, Y., Liu, Z., Weinstein, P.R., Fike, J.R., Liu, J., 2007. Environmental enrichment enhances neurogenesis and improves functional outcome after cranial irradiation. Eur. J. Neurosci. 25, 38–46. https://doi.org/10.1111/j.1460-9568.2006.05269.x.
Tran, P.B., Banisadr, G., Ren, D., Chenn, A., Miller, R.J., 2007. Chemokine receptor expression by neural progenitor cells in neurogenic regions of mouse brain. J. Comp. Neurol. 500, 1007–1033. https://doi.org/10.1002/cne.21229.
Haage, V., et al., 2019. Comprehensive gene expression meta-analysis identifies signature genes that distinguish microglia from peripheral monocytes/macrophages in health and glioma. Acta Neuropathol. Commun. 7, 20. https://doi.org/10.1186/s40478-019-0665-y.

Appendix A –Publication Cover #5
2020

Authors: P. Rana, K.V. Rama Rao, A. Ravula, R. Trivedi, M. D'Souza, A.K. Singh, R.K. Gupta, N. Chandra

Title: *"Oxidative stress contributes to cerebral metabolomic profile changes in animal model of blast-induced traumatic brain injury"*

Journal Publication: Metabolomics, 16, 3, 1-12, (2020), [20-5]

Metabolomics (2020) 16:39
https://doi.org/10.1007/s11306-020-1649-4

ORIGINAL ARTICLE

Oxidative stress contributes to cerebral metabolomic profile changes in animal model of blast-induced traumatic brain injury

Poonam Rana[1] · Kakulavarapu V. Rama Rao[4] · Arunreddy Ravula[4] · Richa Trivedi[1] · Maria D'Souza[2] · Ajay K. Singh[1] · Raj K. Gupta[3] · Namas Chandra[3,4]

Received: 19 July 2019 / Accepted: 2 February 2020
© Springer Science+Business Media, LLC, part of Springer Nature 2020

Abstract

Introduction Blast-induced neurotrauma (BINT) has been recognized as the common mode of traumatic brain injury amongst military and civilian personnel due to an increased insurgent activity domestically and abroad. Previous studies from this laboratory have identified three major pathological events following BINT which include blood brain barrier disruption the earliest event, followed by oxidative stress and neuroinflammation as secondary events occurring a few hours following blast.

Objectives Our recent studies have also identified an increase in oxidative stress mediated by the activation of superoxide producing enzyme NADPH oxidase (NOX) in different brain regions at varying levels with neurons displaying higher oxidative stress (NOX activation) compared to any other neural cell. Since neurons have higher energy demands in brain and are more prone to oxidative damage, this study evaluated the effect of oxidative stress on blast-blast induced changes in metabolomics profiles in different brain regions.

Methods Animals were exposed to mild/moderate blast injury (180 kPa) and examined the metabolites of energy metabolism, amino acid metabolism as well as the profiles of plasma membrane metabolites in different brain regions at different time points (24 h, 3 day and 7 day) after blast using ^{1}H NMR spectroscopy. Effect of apocynin, an inhibitor of superoxide producing enzyme NADPH oxidase on cerebral metabalomics profiles was also examined.

Results Several metabolomic profile changes were observed in frontal cortex and hippocampus with concomitant decrease in energy metabolism. In addition, glutamate/glutamine and other amino acid metabolism as well as metabolites involved in plasma membrane integrity were also altered. Hippocampus appears metabolically more vulnerable than the frontal cortex. A post-treatment of animals with apocynin, an inhibitor of NOX activation significantly prevented the changes in metabolite profiles.

Conclusion Together these studies indicate that blast injury reduces both cerebral energy and neurotransmitter amino acid metabolism and that oxidative stress contributes to these processes. Thus, strategies aimed at reducing oxidative stress can have a therapeutic benefit in mitigating metabolic changes following BINT.

Keywords Apocynin · Amino acid metabolism · Blast-induced neurotrauma · Energy metabolism · Oxidative stress

1 Introduction

Traumatic brain injury (TBI) is a leading cause of morbidity and mortality worldwide. There are about 250,000 cases of TBI occurring annually in USA alone, leading to about 50,000 deaths. TBI has been broadly classified into two categories, namely blunt and blast injuries based on the type of impact occurring to the skull and the brain (de Lanerolle et al. 2015). Blast-induced TBI (bTBI) is the most prevalent form of brain injury in soldiers due to a growing use of improvised explosive devices (IED's) in armed conflicts and

Poonam Rana and Kakulavarapu V. Rama Rao have equally contributed and are co-first authors.

Electronic supplementary material The online version of this article (https://doi.org/10.1007/s11306-020-1649-4) contains supplementary material, which is available to authorized users.

✉ Raj K. Gupta
raj.k.gupta.civ@mail.mil

✉ Namas Chandra
nama.chandra@njit.edu

Extended author information available on the last page of the article

Published online: 12 March 2020

in military and civilian populations as a weapon by insurgents (Ling et al. 2013; Moore 2015).

Among the many pathological factors associated with either primary mechanical injury or secondary biochemical cascades, oxidative stress has been shown to play a major role in various models of TBI (Bayir et al. 2006; Cornelius et al. 2013). The main inducers of oxidative stress are reactive oxygen species (ROS) which include superoxide ($O_2^{\cdot -}$), hydroxyl radical ($HO^{\cdot}$), and hydrogen peroxide (H_2O_2) (Koppula et al. 2012; Lewen and Hillered 1998). ROS are normally produced in several metabolic reactions, including redox-reactions (oxidation/reduction), oxidative phosphorylation and in a normal process of electron transport chain reactions. There are a number of enzymes that produce free radicals during their catalytic reactions, which include the NADPH oxidase family, cytochrome P450 (CYP450), cyclooxygenase (COX), lipoxygenase (LOX), and xanthine oxidase (XO).

Our recent study reported neurons are more vulnerable to oxidative damage in blast TBI compared to other neural cells including astrocytes and microglia (Rama Rao et al. 2018). Additionally, among different brain regions examined, hippocampus and frontal cortex were more vulnerable which invokes the possibility that neurons in these regions are metabolically compromised (Rama Rao et al. 2018). Understanding of metabolic status of cells or tissues provides an important evidence to comprehend the mechanism of blast injury at the cellular level.

Metabolomics is one of the recent systems biology approaches that has the capability of understanding the unique insights to disease and health at both cellular and organism levels (Cheema et al. 2018a, b; Stewart and Bolt 2011). It is the complete measurement of global small molecules (metabolites) in a biological sample that serve as substrates/intermediates of biochemical pathways or as signaling molecules and is considered closest to the organism's phenotype. In traumatic brain injury, metabolomics is being widely used for establishing useful and reliable biomarkers in biofluids (Dadas et al. 2018; Fiandaca et al. 2018). However, tissue metabolomics is also important as tissue is the first place where metabolic changes takes place in response to disease or insult providing the snapshot of real biochemical processes happening at that point of time. Altered analytes in different brain regions have been associated with their corresponding pathways to obtain a global overview of their dysfunction and trying to establish a link between altered biological pathways and pathophysiological conditions (Gonzalez-Riano et al. 2016). In TBI, therefore, metabolomics can play an important role in linking primary phase of brain injury to secondary phase of injury through studying the changes in cascades of intermediary metabolic pathways. In the present study, we have assessed the metabolic responses of different brain regions in bTBI using nuclear magnetic resonance (NMR)-based metabolomics and further tried to elucidate the role of oxidative stress in bTBI using metabolomics.

2 Materials and methods

Adult (10-week old), male Sprague–Dawley rats (Charles River Laboratories) weighing between 350 ± 50 g were used in accordance with protocols approved by Rutgers University Institutional Animal Care and Use Committee (IACUC). Animals were housed at 22 °C with free access to food and water in a 12 h light–dark cycle. Animals were divided into sham, blast, and treatment groups. A total of 60 rats were used for both metabolomics and immunofluorescent studies. Animals were sacrificed 24 h, 3 days and 7 days post blast. All the methods used throughout the study were performed in accordance with protocols, guidelines, and regulations approved by Rutgers University IACUC.

2.1 Exposure to blast and apocynin treatment

Rats were exposed to a single shock wave at the New Jersey Institute of Technology (Center for Injury Biomechanics, Materials, and Medicine) in the shock tube described in previous publications (Chandra et al. 2011; Mishra et al. 2016; Rama Rao et al. 2018; Skotak and Chandra 2016). A total of 60 rats were used in the study for different experimental methods with at least 4–5 animals in each experimental group (power value of 0.8, $\alpha = 0.05$) based on a priori power analysis. Prior to blast exposure, all animals (controls, blast, blast + apocynin) were anesthetized with 5% isoflurane, released in a chamber containing 95% air and 5% CO_2, until rats were unresponsive to noxious stimulation. Apocynin (5 mg/kg, Sigma-Aldrich) was administered intraperitoneally 30 min after blast exposure. Sham animals were kept near the shock tube to expose them to noise but not any pressure shock wave. Following blast injury, animals were closely monitored for any signs of apnea, loss of motor coordination and neurological severity score (NSS) was evaluated 5 min post exposure. None of the animals included in this study displayed NSS scores that differed from sham animals. Animals were exposed to a single blast of 180 kPa peak overpressure. For immunofluorescence studies, animals were first perfused with PBS followed by 4% paraformaldehyde, whereas for tissue extraction for metabolomics study, animals were perfused with only PBS to completely clear the blood and obtain pure brain tissue. Such procedure of transcardial perfusion before isolating tissue samples were performed by several investigators (Yu et al. 2019; Li et al. 2015). brain was dissected into frontal cortex and hippocampus using rat brain tissue slicer (Zivic Instruments Inc., PA) flash frozen in liquid nitrogen and stored at – 80 °C until use.

Different tissue samples were homogenized in a solution of PBS and acetonitrile (1:1 ratio) in order to extract both hydrophilic and hydrophobic metabolites. Homogenates were centrifuged at 12,000 rpm and the supernatants were then lyophilized and stored at 80 °C until NMR analysis.

2.2 ^{1}H NMR spectroscopy of tissue extracts

The tissue extracts were reconstituted in 580 µl of deuterated water (D2O) containing 0.5 mM trimethylsilyl-2,2,3,3-tetradeutero-propionic acid (TSP) as an internal NMR chemical shift standard and transferred to 5 mm NMR tubes for NMR spectroscopy. ^{1}H NMR spectra were acquired for each sample on a Bruker 600 MHz NMR spectrometer (Bruker Biospin, Switzerland) at 300 K using 1D pulse sequence with water saturation (NOESYGPPR1D). NMR acquisition parameters included a 90° pulse, a 6 kHz spectral width, 64 transients, 64 K data points with 4 s relaxation delay. Fourier transformed spectra obtained were phase and base line corrected and calibrated using TSP with Topspin software (version 3.5, Bruker, Switzerland). The metabolites were assigned based on chemical shifts and signal multiplicity according to literature and HMDB database. Identified metabolites were then integrated, normalized with total spectral area to calculate the relative intensity in percentage. Changes in the corresponding peak areas among experimental group were further examined using one-way ANOVA with Bonferroni post hoc multiple comparison test.

2.3 PCA analysis of ^{1}H NMR spectra

In order to categorize the differences in metabolic profiles of tissue samples between TBI and control groups, an unsupervised pattern recognition method, principal component analysis (PCA) was conducted on tissue samples using SIMCA (Umetrics, Sweden). The integrated data set was log transformed, mean centered and pareto scaled before performing PCA. Score values of the principal components (PCs) were constructed to visualize the separation or clustering of different groups based on the loading values. NMR Spectroscopy was conducted at the Institute of Nuclear and Allied Sciences (INMAS) in India.

2.4 Immunofluorescence and microscopy

In order to evaluate changes in NOX1 expression immunofluorescence studies were conducted using antibody specific for NOX1. Briefly, animals were transcardially perfused with PBS and brains were fixed with 4% paraformaldehyde (PFA). Tissue section and staining procedure were done in a manner similar to that described in our previous publications (Rama Rao et al. 2018). Fixed tissues were incubated overnight at 4 °C with respective primary antibody to NOX1 (Rabbit polyclonal, Sigma-Aldrich, 1:400) and immunofluorescence was performed using Alexa Fluor 594 for NOX1. Quantification of the fluorescence intensities was performed following the method recently published by us (Rama Rao et al. 2018). Briefly, slides containing mounted coronal sections of frontal cortex were imaged at × 20 magnification using a Leica Aperio Versa 200 digital pathology scanner. Control sections were used as reference for adjusting the exposure times and gray scale balance for optimal image quality; once set, these parameters were fixed and used for image acquisition of the remainder of both control and experimental groups. To remove variability that might arise, all sections to be compared were scanned on the same day using the same established scanning protocol. For the immunostained sections, two channels were collected for each coronal section. Blue: 405 nm (DAPI) and red: 594 nm (NOX1). For quantification of fluorescent intensity, a maximum intensity threshold was also set to remove any oversaturation from excess fluorescent dye. The algorithm outputs the area of positive staining for each brain region, the average intensity of each channel, and intensity profile of each antigen.

3 Results

3.1 Metabolic changes in different brain regions post blast exposure

In order to screen the metabolite changes following blast exposure, we examined the metabolomics profiles in different brain regions at different time points (1–7 days) in animals exposed to blast. The ^{1}H NMR spectra displayed several metabolites that were altered in the brain after blast injury compared to controls. We identified about 20 metabolites in different categories that were changes following blast injury. The metabolites observed in ^{1}H NMR spectra of different regions include energy metabolism (lactate, succinate, aspartate, creatine), ketone body metabolism (acetate), osmolytes (myo-inositol, taurine), neurotransmitter amino acids (glutamine, glutamate, aspartate, GABA), amino acids (branched chain amino acids, alanine, glycine), N Acetyl aspartate (NAA) and membrane metabolites (choline, phosphotidyl choline, glycerophosphoethanol amine, ethanol amine) (Table 1). Amongst all regions, changes were more prominent in frontal cortex and hippocampus at all time points. Therefore, further analysis was carried out mainly in FC and hippocampus region.

PCA analysis of NMR spectral data was done as an initial classifier to determine whether blast exposed group could be distinguished from control group and to further identify any outlier in the data. 2D score plot based on PCA analysis of spectral data showed blast exposed group and control group

Table 1 Summary of NMR spectroscopy based blast induced metabolic changes in different brain regions compared to controls at different time points

Metabolites	Chemical shifts	Hippocampus			Frontal cortex			Striatum			Thalamus		
		Day 1	Day 3	Day 7	Day 1	Day 3	Day 7	Day 1	Day 3	Day 7	Day 1	Day 3	Day 7
Branched chain amino acid	0.94 (t), 0.96 (t), 1.04 (d), 1.33 (d), 4.12 (q),1.48 (d), 3.79 (q)	–	–	–	–	–	–	–	–	–	–	–	–
Lactate	1.33 (d), 4.10 (q)	↑*	–	–	–	–	–	–	–	–	–	–	–
Alanine	1.48 (d), 3.79 (q)	–	–	–	↑*	–	–	–	–	–	–	–	–
γ Amino butyric acid (GABA)	1.91 (M), 2.31 (ABX), 3.02 (t)	↑*	–	–	↑*	–	–	–	↓*	↓*	–	–	–
Acetate	1.92 (s)	↑*	–	–	↑*	–	–	–	–	–	–	–	–
N-Acetylaspartate (NAA)	2.03 (s), 2.51 (ABX), 2.70 (ABX)	–	–	–	–	–	–	–	–	–	–	–	–
Glutamine	2.08 (m), 2.41 (m)	↓*	–	–	↓*	↓*	–	–	–	–	–	–	–
Glutamate	2.10 (m), 2.36 (m), 2.50 (m)	↓*	–	–	↓*	↓*	↓*	–	↓*	–	–	–	–
β-Hydroxy butyrate		–	–	–	–	–	–	–	↑*	–	–	–	–
Succinate	2.43 (s)	↑*	–	–	–	–	–	–	–	–	–	–	–
Aspartate	2.63 (dd), 2.81 (dd)	↑*	–	–	↑*	↑*	–	–	–	–	–	–	–
Creatine	3.04 (s)	–	–	–	–	–	–	–	–	–	–	–	–
Ethanol amine		–	–	–	–	–	–	–	–	–	–	–	–
Choline	3.21 (s), 3.52 (m), 4.07 (m)	–	↑*	–	–	↑*	↑*	–	–	–	–	↑*	–
Glycerophospho ethanol amine (GPE)	3.23 (t)	–	–	–	–	–	–	–	↑*	–	–	–	–
Betaine	3.28 (s)	–	–	–	–	–	–	–	–	–	–	–	–
Taurine	3.25(t), 3.43 (t)	–	–	–	–	–	–	–	–	–	–	–	–
myo inositol (mI)	3.28 (t), 3.56 (dd), 3.63 (dd)	–	–	–	–	–	–	–	–	–	–	–	–
Glycine	3.61 (s)	–	–	–	–	–	–	–	–	–	–	–	–
Phosphotidyl choline	3.58 (m)	–	–	–	–	–	–	–	–	–	–	–	–

p value for the changing metabolites were assessed using ANOVA and were less than 0.05. ↑ indicates increase in the levels of selected metabolites; – no change; ↓ indicates relative decrease in level of selected metabolite

as distinct clusters in both the tissue regions at 24 h time points. Principal component-1 (PC1) and Principal component-2 (PC2) of score plot presented a total variance of 58% and 52% in hippocampus and frontal cortex region respectively. Though distinct clusters of blast-exposed and control group were observed, there seems to be a wider spread within the group. In hippocampus, two of the control data points (C5 and C7) appeared away from other data points of the group and were present near the border of Hotelling's T2 ellipse. In frontal cortex, clustering of controls and blast exposed group in PCA score plot was much better compared to score plot of hippocampus region except for one control data point (C9), which was placed outside the Hoteling's T2 ellipse. Therefore, C9 was considered as an outlier and removed from data set for further analysis (Fig. 1). List of metabolites with significant increase or decrease in metabolites based on relative integrals in different brain regions is presented in Table 1. Complete data set of relative integrals of metabolites are provided in supplementary files (Region wise table). We also observed a temporal difference in alterations in these metabolites It was observed that changes were more prominent at 24 h time point compared to day 3 and day 7 post blast exposure. Significant decrease in glutamate and glutamine was observed in both the brain regions compared to controls at 24 h time point. On the other hand, aspartate, lactate, succinate, acetate, GABA levels were elevated in blast exposed groups compared to controls at 24 h time point. Some of these metabolites showed temporal changes prominently in frontal cortex. Longitudinal changes in blast exposed group demonstrated continuous decrease in glutamate and choline till day 7 post blast exposure (Fig. 2a, b). However, significant changes at glutamine (0.003) and aspartate (0.009) was observed only till day 3. Most of the energy metabolites started restoring to control levels following 24 h time point.

3.2 NOX expression in animals exposed to moderate blast

We recently reported that animals exposed to moderate blast showed a significant increase in the levels of superoxide producing enzyme NADPH oxidase (NOX) isoforms (NOX1 and NOX2) in different brain regions as early as 4 h post injury. Noteworthy that NOX isoforms were robustly increased in neurons compared to astrocytes and microglia (Rama Rao et al. 2018) indicating that neurons are more vulnerable to oxidative damage than other neural cells in blast TBI. We now extended these studies to investigate the time course of NOX1 isoform expression to correlate changes in NOX with that of alterations in metabolomics profiles.

Results showed that both NOX1 protein levels showed a biphasic response in frontal cortex with a 77% increase acutely at 4 h post injury, which further showed a 159% increase before restoring back to that control at 7 days. Similarly, in hippocampus and thalamus there was a 66% increase at 4 h followed by 115% increase by 24 in animals exposed to blast TBI. The levels of NOX isoforms were completely restored 7 days post injury in both hippocampus and thalamus (Fig. 3a, b).

3.3 Apocynin significantly prevents region-dependent changes in brain metabolomics profiles in animals exposed to moderate blast

To implicate potential involvement of NOX-mediated oxidative stress in blast-induced alterations in the metabolomics profile, animals were exposed to moderate blast and 30 min post administration of apocynin (5 mg/kg wt i.p). In blast + apocynin treatment groups, 24 h after administration of apocynin, metabolomics profiles were

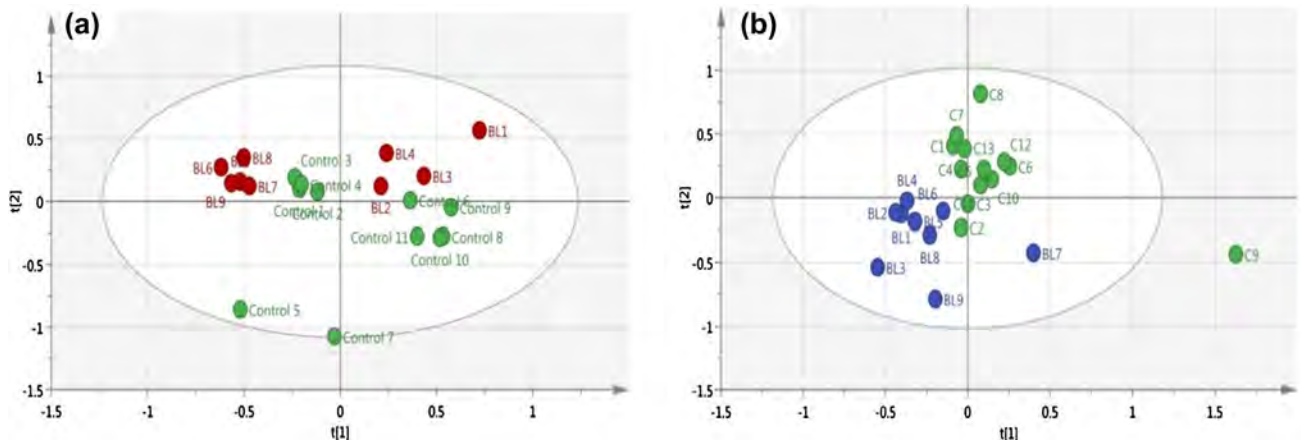


Fig. 1 PCA score plots based on ^{1}H NMR spectra of hippocampus (**a**) and frontal cortex (**b**) tissue extract from control and blast exposed group. Two PC components were calculated with explanation of 58% and 52% of total variances

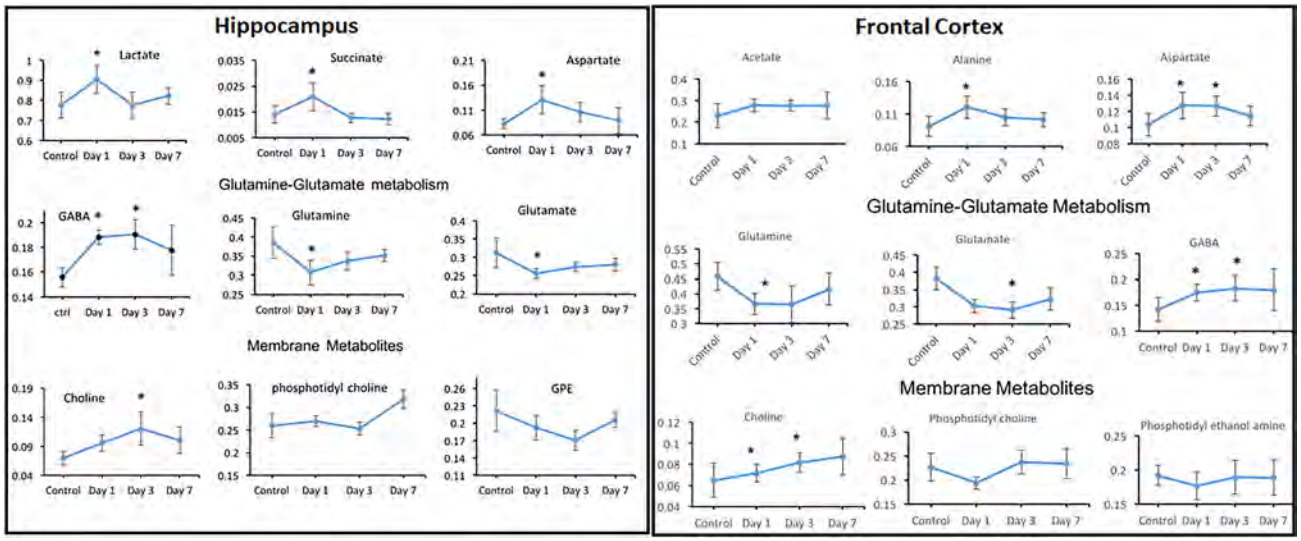


Fig. 2 Temporal changes in the levels of selected metabolites in hippocampus (**a**) and frontal cortex (**b**) tissue extracts of blast exposed groups at different time point. Data presented as relative intensity levels with respect to total spectral area ± standard deviation, with overall difference between different time points to controls(pre dose) using ANOVA and post hoc test ($p < 0.05$)

examined in frontal cortex and hippocampus. Apocynin treatment showed a significant restoration of several metabolites to that of controls in both frontal cortex and hippocampus as observed by ANOVA analysis. Decreased levels of glutamate, glutamine as well as increased aspartate alanine and branched chain amino acids were significantly corrected by apocynin (Table 2). However, apocynin treatment failed to restore the increased levels of some of the metabolites including GABA, succinate, ethanolamine and adenosine. Figure 4a, b illustrates quantitative changes in the levels of various metabolites and the effect of apocynin in frontal cortex and hippocampus 24 h post injury. The box plot of most of the metabolites levels exhibited comparable changes in apocynin treated blast exposed (BLA) group in both the regions (Fig. 4a, b). PCA analysis of hippocampus data showed that with a variance of 69%, score plot of blast exposed group was clearly separated from control groups, while apocynin treated blast exposed group (BLA) displayed overlapping with controls, indicating similarity in apocynin treated blast group and control data set. On the other hand, in frontal cortex, PCA score plot with a variance of 75% did not show separation of blast exposed and apocynin treated blast exposed group. Though multiple comparison still exhibited significant reversal of most of the metabolites. The results further assume that apocynin treatment may not be able to restore the metabolic activities to control levels in frontal cortex.

4 Discussion

This work aims to investigate the role of NOX-mediated oxidative stress as a mechanism for region-dependent changes in cerebral metabolomics profiles in blast-induced traumatic brain injury. Several metabolites of energy metabolism, amino acid metabolism as well as metabolites that contribute to membrane integrity were significantly altered by blast. Treatment of animals with apocynin that inactivates NOX and prevents subsequent increase in superoxide production, significantly prevented the alterations in several metabolites. Further, blast caused biphasic changes in the levels of NOX isoforms wherein a significant increase was observed 4 h peaking at 24 h and completely restoring back to normal reduced in 7 days post injury. Taken together the current study strongly suggests that moderate blast induces changes in several metabolites and that oxidative stress is a major mechanism for alterations in cerebral metabolomics profiles in blast TBI.

Blast wave is known to cause differential response of different brain regions on exposure. Therefore, in this study, we have investigated changes in metabolomics profile in different brain regions. The findings of the study displayed pertinent changes in hippocampus and frontal cortex regions compared to other regions studied.

Among frontal cortex and hippocampus currently analyzed, changes in several metabolites were more

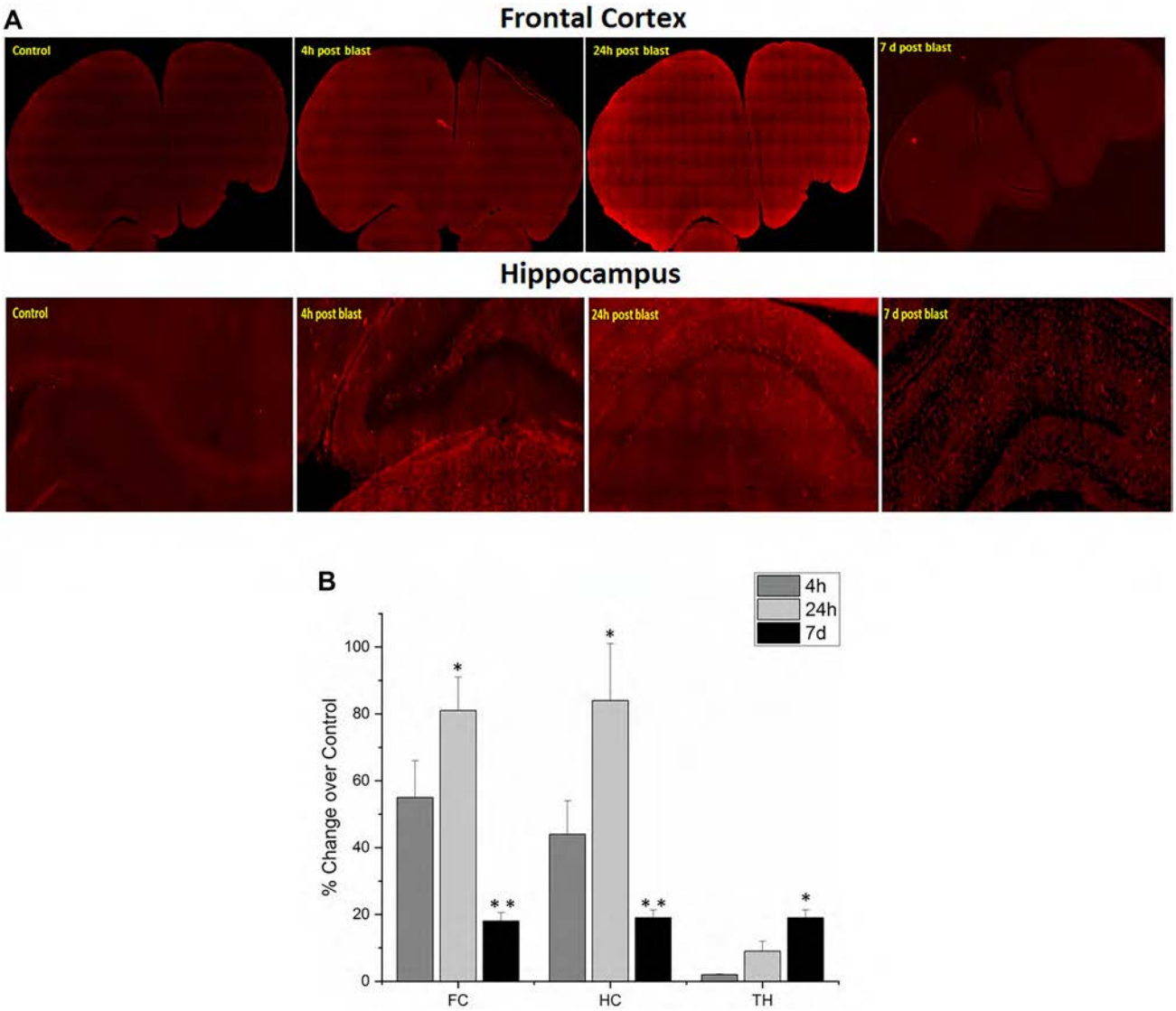


Fig. 3 Upper panel: immunofluorescence analysis of protein level of NOX1 isoform (red) showing a biphasic response in frontal cortex and hippocampus as a function of time in animals exposed to blast TBI. Note there was significant change acutely at 4 h post injury which further increased at 24 h after injury. Levels of NOX were completely restored to that control 7 days post injury. The scale bar of each image at this magnification was 300 µm. Lower panel: quantification of protein levels of NOX1 (left panel) display a biphasic response of change as a function of time in animals exposed to blast injury. % change over control at 4 h, 24 h and 7 days for frontal cortex (FC) are 77%, 159%, 9% and for hippocampus (HC) is 66,115 and 18% and for thalamus (TH) its 65, 68 and 4% for NOX-1 with overall difference between different time points to controls(pre dose) using ANOVA and post hoc Bonferroni test (*$p < 0.05$, *$p < 0.002$). N = 4–5 animals in each group

pronounced in hippocampus compared to frontal cortex at 24 h post blast exposure. This is highly possible since hippocampus has more energy metabolic demand than other brain regions and it is one of the most vulnerable regions for hypoxia in brain (Penny et al. 1974; Schmidt-Kastner 2015). In the present study significant changes were observed in the intermediates of citric acid cycle (succinate) as well as their amino acid precursors such as glutamate and aspartate, which by transamination reactions contribute to the de novo synthesis of intermediates of citric acid cycle.

Glutamate and aspartate are not only excitatory neurotransmitter amino acids but also important energy substrates which are integral components in various pathways of cerebral energy metabolism including citric acid cycle (Plaitakis and Zaganas 2001; Rodriguez-Rodriguez et al. 2013; Sokoloff 1992; Turski and Turski 1993). Reduced glutamate levels may indirectly represent changes in the

Table 2 NMR spectroscopy based metabolic changes in frontal cortex and hippocampus post blast (BL) and apocynin treated blast exposed (BLA) compared to controls at 24 h post blast exposure

Metabolites	Hippocampus		Frontal Cortex	
	BL	BLA	BL	BLA
Branched chain amino acid	↑*	–	–	–
Lactate	–	–	–	–
Alanine	–	–	↑*	–
γ Amino butyric acid (GABA)	↑*	↑*	↑*	↑*
Acetate	–	–	–	–
N-Acetylaspartate (NAA)	–	–	–	–
Glutamine	↓*	–	↓*	–
Glutamate	↓*	–	↓*	–
β-Hydroxy butyrate	–	–	–	–
Succinate	↑*	↑*	–	–
Aspartate	↑*	–	↑*	–
Creatine	–	–	–	–
Ethanol amine	–	–	↑*	↑*
Choline	–	–	–	–
Glycerophosphoethanol amine (GPE)	–	–	–	–
Betaine	–	–	–	–
Taurine	–	–	–	–
myo inositol (mI)	–	–	–	–
Glycine	–	–	–	–
Phosphotidyl choline	–	–	–	–

*p value for the changing metabolites were assessed using ANOVA and were less than 0.05. ↑ indicates increase in the levels of selected metabolites; – no change; ↓ indicates relative decrease in level of selected metabolite

levels of α-ketoglutarate, a key intermediate in the citric acid cycle since glutamate is converted to α-ketoglutarate a reaction mediated by glutamate dehydrogenase (GDH). In fact one report showed decreased GDH enzyme in mice exposed to moderate blast (Arun et al. 2013) which may interfere with the synthesis of glutamate from α-ketoglutarate. The present study showing increased levels of aspartate also reflects in the reduced glutamate levels since it is likely that aspartate aminotransferase (AST) which converts aspartate into glutamate may have been inhibited by blat injury, which could further impact on the citric acid cycle (α-ketoglutarate).

The reduction observed in glutamate levels may not only affect cerebral energy metabolism, but also impact on neurotransmission and its synaptic receptors. Decreased glutamate levels may reduce glutamatergic neurotransmission, once conditions of under availability of glutamate sets in, this can exert a feedback inhibition on the cell surface levels of their receptors including NMDA, AMPA-kainite receptors. It is noteworthy that we observed a profound reduction in the synaptic levels of NMDA-R1 receptors in hippocampus in rats exposed to mild/moderate blast (180 kPa) (data not presented).

The present study also showed significantly increased levels of succinate in hippocampus as early as 24 h post injury. Succinate is an important intermediate of citric acid cycle which is produced by conversion of α-ketoglutarate in the presence of coenzymeA to form succinylCoA a reaction catalyzed by α-ketoglutarate dehydrogenase (α-KGDH). Several studies report that increased succinate indicates marked hypoxia in tissues particularly in brain (Flores et al. 2018; Kacso et al. 2016; Tretter et al. 2016) and it is noteworthy that we observed significant increase in succinate levels predominantly in hippocampus reinforcing the possibility that blast induces adverse conditions in hippocampus, a region highly vulnerable to hypoxia. Increased succinate could represent decreased activity of succinate dehydrogenase, an important enzyme in respiratory chain function and subsequent oxidative phosphorylation, since succinate is a substrate for its activity. Taken together our results strongly indicate that moderate blast TBI causes disturbances in cerebral energy metabolism in vulnerable brain regions such as hippocampus.

While the present study indicates disturbed energy metabolism in blast TBI, we also observed increased levels of acetate in frontal cortex and hippocampus. These results indicate a compensatory upregulation of ketone metabolism in vulnerable brain regions in response to energy deprivation. Astrocytes are the major cells that produce ketone bodies in brain a process mediated by fatty acid oxidation (Amaral et al. 2010; Achanta and Rae 2017; Achanta et al. 2017). Increased production of acetate indicate that astrocytes provide energy source to neurons in blast-induced TBI. It is well known that that increased transport and utilization of non-glucose fuel in the brain occurs under conditions of hypoglycemia (Bernini et al. 2018; Prins and Giza 2006; Prins and Matsumoto 2014; Wolahan et al. 2017). Further, at cellular level, loss of energy status may lead to activation of apoptosis cascade leading to hippocampal neuronal loss and related clinical deficit.

Another group of metabolites that showed significant increase are phosphatidyl choline (PC), ethanolamine (PE). PC and PE are lipid based metabolites, also called as plasmalogens that have multiple functions including acting as reservoirs of inflammatory mediators as well as maintaining membrane fluidity (Dawaliby et al. 2016; Hinkovska-Galcheva et al. 1988; Hirata and Axelrod 1978; Wallner et al. 2018). Additionally, PC and PE are involved in energy metabolism in mammalian tissues and alterations in the ratio of PE and PC. This PE to PC ratio has been shown to increase the progression of neurological diseases including Alzheimer's disease, stroke and Parkinson's disease. Increased levels of these metabolites have shown to alter the membrane fluidity (van der Veen et al. 2017). Since

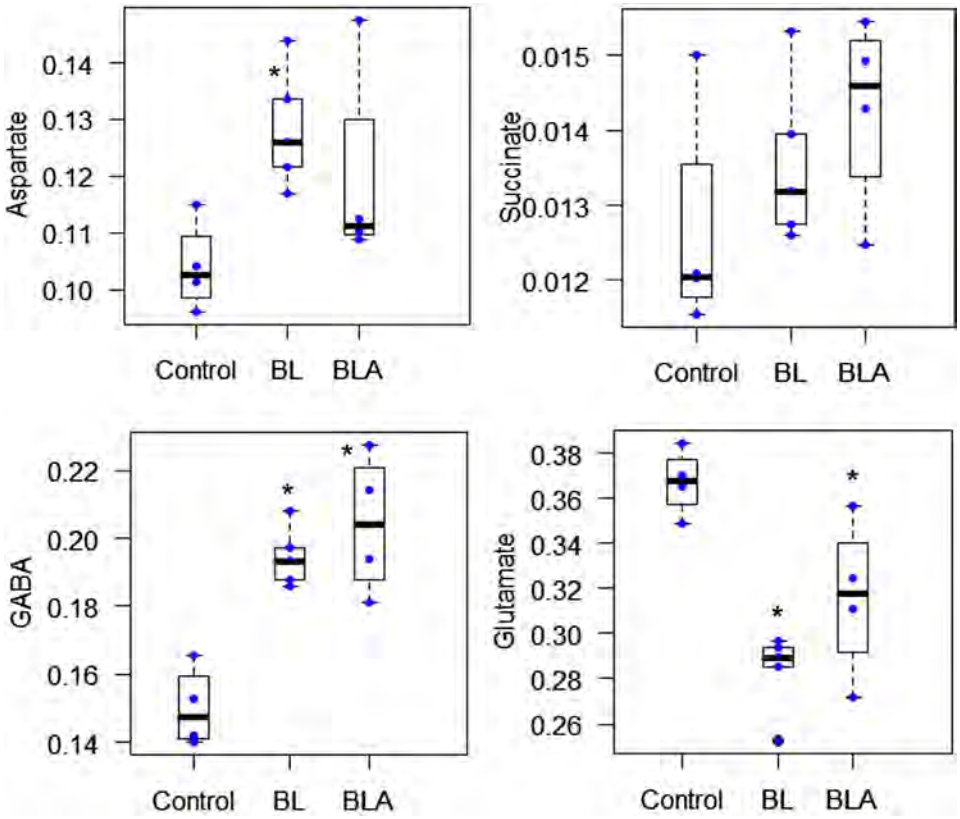


Fig. 4 Box plot of selected metabolites representing significant restoration of metabolites in apocynin treated blast exposed group (BLA) compared to control (C) and blast exposed group (BL) in hippocampus (**a**) and frontal cortex region (**b**)

shockwaves resulting from blast TBI traverse throughout the cerebral vasculature as well as brain parenchyma, mechanical damage to the plasma membrane structures are highly likely and such mechanical damage may significantly alter the plasma membrane fluidity and integrity by a mechanism likely mediated by increased levels of PC and PE. PC is known to elicit inflammation by producing inflammatory mediators and therefore, increased PC levels in brain region might reflect an elevated state of neuroinflammation.

While the precise mechanisms responsible for altered metabolomics profiles in blast TBI are not known, our recent studies strongly established oxidative stress as a leading secondary pathological event in moderate blast TBI. Exposing rats to moderate blast (180 kPa), we reported increased levels of two isoforms of superoxide producing enzyme NADPH oxidase (NOX1 and NOX2) in various brain regions including frontal cortex, striatum, hippocampus, thalamus and cerebellum (Rama Rao et al. 2018). Additionally, neurons of hippocampus displayed highest increase in NOX1 and NOX2 compared to astrocytes and microglia strongly indicating that hippocampal neurons have a higher risk for oxidative damage in blast TBI. It is interesting that the present study showed a close correlation between the time course of increased NOX expression and metabolomic profile changes in frontal cortex and hippocampus, which strongly suggests an association between increased oxidative stress and altered cerebral energy metabolic profile in blast TBI. Additionally, administration of apocynin, an inhibitor of NOX subunit assembly significantly prevented changes in various metabolite levels in frontal cortex and hippocampus 24 h post blast TBI further implicating the role of oxidative stress in metabolomics profile changes.

Several studies reported oxidative stress is a major mechanisms that significantly impacts the cerebral energy metabolism in various neurological conditions including stroke (Li et al. 2011), traumatic brain injury (Tavazzi et al. 2005) and Alzheimer's disease (Hoyer 1993). Apocynin, also called as acetovanillone is a natural plant product that belongs to vanillin group of alkaloids. Apocynin has shown beneficial effects and offer neuroprotection in conditions of traumatic brain injury (Feng et al. 2017; Song et al. 2013), stroke (Kapoor et al. 2018) and hypoxia (Hui-guo et al. 2010; Liu et al. 2013; Zhang et al. 2013). Apocynin has also been shown to improve cerebral energy metabolism in drug-induced neurotoxicity (Dang et al. 2016), Parkinson's disease (Kapoor et al. 2018) and vascular dementia (Choi et al. 2014) to name a few.

The metabolic response determined by ^{1}H MRS in our study is consistent with mitochondrial distress which might in turn be indirectly related to emergence of cognitive deficit. Moderate blast also increased the levels of superoxide producing enzyme NOX at a time point that corresponds to maximum changes occurring in cerebral metabolic changes in frontal cortex and hippocampus. A post treatment (30 min

after blast) of animals with apocynin, which prevents the assembly of various NOX subunits and renders the enzyme inactive, significantly reversing most of the trends caused by blast in various metabolites in different brain regions. These studies together indicate that oxidative stress resulting from NOX activation plays a major role in alterations in cerebral metabolic profile in blast TBI. This strong relationship between NOX-mediated oxidative stress and metabolic changes may need a thorough investigation delineating relationships between other injury mechanisms, a prerequisite for better therapeutic interventions.

Acknowledgements This work was supported by Army Medical Research and Materiel Command project *Primary Blast Injury Criteria for Animal/Human TBI Models using Field Validated Shock Tube*, Grant Number: 14059001 (PI: Namas Chandra) and Indo-U.S Joint DRDO and DoD project (US-IN-A-16–0002 on Experimental and Computational studies in Blunt and Blast induced Traumatic Injuries. PI: Raj Gupta).

Author contributions PR, KVR, RT wrote the main manuscript text, PR, KVR, AR and RT performed the experimental studies. All authors reviewed the manuscript.

Compliance with ethical standards

Conflict of interest The authors declare no conflicts of interests.

Ethics approval This study utilized rodents. All animal studies conducted in the manuscript were approved by the Newark Institute of Animal Care and Use Committee (File No. 1605A1E1019) and Animal Welfare and Ethical Review Committee at the Rutgers University.

References

Achanta, L. B., & Rae, C. D. (2017). beta-Hydroxybutyrate in the brain: One molecule, multiple mechanisms. *Neurochemical Research, 42*, 35–49. https://doi.org/10.1007/s11064-016-2099-2.

Achanta, L. B., Rowlands, B. D., Thomas, D. S., Housley, G. D., & Rae, C. D. (2017). beta-Hydroxybutyrate boosts mitochondrial and neuronal metabolism but is not preferred over glucose under activated conditions. *Neurochemical Research, 42*, 1710–1723. https://doi.org/10.1007/s11064-017-2228-6.

Amaral, A. I., Teixeira, A. P., Martens, S., Bernal, V., Sousa, M. F., & Alves, P. M. (2010). Metabolic alterations induced by ischemia in primary cultures of astrocytes: Merging 13C NMR spectroscopy and metabolic flux analysis. *Journal of Neurochemistry, 113*, 735–748. https://doi.org/10.1111/j.1471-4159.2010.06636.x.

Arun, P., et al. (2013). Acute mitochondrial dysfunction after blast exposure: Potential role of mitochondrial glutamate oxaloacetate transaminase. *Journal of Neurotrauma, 30*, 1645–1651. https://doi.org/10.1089/neu.2012.2834.

Bayir, H., Kochanek, P. M., & Kagan, V. E. (2006). Oxidative stress in immature brain after traumatic brain injury. *Developmental Neuroscience, 28*, 420–431. https://doi.org/10.1159/000094168.

Bernini, A., et al. (2018). Modulation of cerebral ketone metabolism following traumatic brain injury in humans. *Journal of Cerebral Blood Flow and Metabolism*. https://doi.org/10.1177/0271678X18808947.

Chandra, N., Holmberg, A., & Feng, R. (2011). Controlling the shape of the shock wave profile in a blast facility. U.S. provisional patent application no. 61542354.

Cheema, A. K., et al. (2018a). Proteomic changes in mouse spleen after radiation-induced injury and its modulation by gamma-tocotrienol. *Radiation Research, 190*, 449–463. https://doi.org/10.1667/RR15008.1.

Cheema, A. K., et al. (2018b). Plasma derived exosomal biomarkers of exposure to ionizing radiation in nonhuman primates. *International Journal of Molecular Sciences, 19*, 3427. https://doi.org/10.3390/ijms19113427.

Choi, D. H., et al. (2014). NADPH oxidase 1, a novel molecular source of ROS in hippocampal neuronal death in vascular dementia. *Antioxidants & Redox Signaling, 21*, 533–550. https://doi.org/10.1089/ars.2012.5129.

Cornelius, C., et al. (2013). Traumatic brain injury: Oxidative stress and neuroprotection. *Antioxidants & Redox Signaling, 19*, 836–853. https://doi.org/10.1089/ars.2012.4981.

Dadas, A., Washington, J., Diaz-Arrastia, R., & Janigro, D. (2018). Biomarkers in traumatic brain injury (TBI): A review. *Neuropsychiatric Disease and Treatment, 14*, 2989–3000. https://doi.org/10.2147/NDT.S125620.

Dang, D. K., et al. (2016). Apocynin prevents mitochondrial burdens, microglial activation, and pro-apoptosis induced by a toxic dose of methamphetamine in the striatum of mice via inhibition of p47phox activation by ERK. *Journal of Neuroinflammation, 13*, 12. https://doi.org/10.1186/s12974-016-0478-x.

Dawaliby, R., et al. (2016). Phosphatidylethanolamine is a key regulator of membrane fluidity in eukaryotic cells. *Journal of Biological Chemistry, 291*, 3658–3667. https://doi.org/10.1074/jbc.M115.706523.

de Lanerolle, N. C., Kim, J. H., & Bandak, F. A. (2015). Neuropathology of traumatic brain injury: Comparison of penetrating, nonpenetrating direct impact and explosive blast etiologies. *Seminars in Neurology, 35*, 12–19. https://doi.org/10.1055/s-0035-1544240.

Feng, Y., et al. (2017). Protective role of apocynin via suppression of neuronal autophagy and TLR4/NF-kappaB signaling pathway in a rat model of traumatic brain injury. *Neurochemical Research, 42*, 3296–3309. https://doi.org/10.1007/s11064-017-2372-z.

Fiandaca, M. S., Mapstone, M., Mehmoodi, A., Gross, T., Macciardi, F., Cheema, A., et al. (2018). Plasma metabolomic biomarkers accurately classify acute mild traumatic brain injury from controls. *PLoS ONE, 13*, 4.

Flores, R. E., et al. (2018). Mycoplasma infection and hypoxia initiate succinate accumulation and release in the VM-M3 cancer cells. *Biochimica et Biophysica Acta - Bioenergetics, 1859*, 975–983. https://doi.org/10.1016/j.bbabio.2018.03.012.

Gonzalez-Riano, C., Garcia, A., & Barbas, C. (2016). Metabolomics studies in brain tissue: A review. *Journal of Pharmaceutical and Biomedical Analysis, 130*, 141–168. https://doi.org/10.1016/j.jpba.2016.07.008.

Hinkovska-Galcheva, V., Peeva, D., Momchilova-Pankova, A., Petkova, D., & Koumanov, K. (1988). Phosphatidylcholine and phosphatidylethanolamine derivatives, membrane fluidity and changes in the lipolytic activity of ram spermatozoa plasma membranes during cryoconservation. *International Journal of Biochemistry, 20*, 867–871.

Hirata, F., & Axelrod, J. (1978). Enzymatic methylation of phosphatidylethanolamine increases erythrocyte membrane fluidity. *Nature, 275*, 219–220.

Hoyer, S. (1993). Brain oxidative energy and related metabolism, neuronal stress, and Alzheimer's disease: A speculative synthesis. *Journal of Geriatric Psychiatry and Neurology, 6*, 3–13. https://doi.org/10.1177/002383099300600101.

Hui-guo, L., Kui, L., Yan-ning, Z., & Yong-jian, X. (2010). Apocynin attenuate spatial learning deficits and oxidative responses to

intermittent hypoxia. *Sleep Medicine, 11*, 205–212. https://doi.org/10.1016/j.sleep.2009.05.015.

Kacso, G., et al. (2016). Two transgenic mouse models for beta-subunit components of succinate-CoA ligase yielding pleiotropic metabolic alterations. *The Biochemical Journal, 473*, 3463–3485. https://doi.org/10.1042/BCJ20160594.

Kapoor, M., Sharma, N., Sandhir, R., & Nehru, B. (2018). Effect of the NADPH oxidase inhibitor apocynin on ischemia-reperfusion hippocampus injury in rat brain. *Biomedicine & Pharmacotherapy, 97*, 458–472. https://doi.org/10.1016/j.biopha.2017.10.123.

Koppula, S., Kumar, H., Kim, I. S., & Choi, D. K. (2012). Reactive oxygen species and inhibitors of inflammatory enzymes, NADPH oxidase, and iNOS in experimental models of Parkinson's disease. *Mediators of Inflammation, 2012*, 823902. https://doi.org/10.1155/2012/823902.

Lewen, A., & Hillered, L. (1998). Involvement of reactive oxygen species in membrane phospholipid breakdown and energy perturbation after traumatic brain injury in the rat. *Journal of Neurotrauma, 15*, 521–530.

Li, H., Yan, Z., Zhu, J., Yang, J., & He, J. (2011). Neuroprotective effects of resveratrol on ischemic injury mediated by improving brain energy metabolism and alleviating oxidative stress in rats. *Neuropharmacology, 60*, 252–258. https://doi.org/10.1016/j.neuropharm.2010.09.005.

Li, Q., Deng, S., Ibarra, R. A., Anderson, V. E., Brunengraber, H., & Zhang, G. F. (2015). Multiple mass isotopomer tracing of acetyl-CoA metabolism in Langendorff-perfused rat hearts: Channeling of acetyl-CoA from pyruvate dehydrogenase to carnitine acetyltransferase. *Journal of Biological Chemistry, 290*, 8121–8132. https://doi.org/10.1074/jbc.M114.631549.

Ling, G. S., et al. (2013). Traumatic brain injury in modern war. *Current Opinion in Anesthesiology, 24*, 124–130.

Liu, X., et al. (2013). Effect of NADPH oxidase inhibitor apocynin on the expression of hypoxia-induced factor-1alpha and endothelin-1 in rat carotid body exposed to chronic intermittent hypoxia. *Journal of Huazhong University of Science and Technology [Medical Sciences], 33*, 178–184. https://doi.org/10.1007/s11596-013-1093-z.

Mishra, V., Skotak, M., Schuetz, H., Heller, A., Haorah, J., & Chandra, N. (2016). Primary blast causes mild, moderate, severe and lethal TBI with increasing blast overpressures: Experimental rat injury model. *Scientific Reports, 6*, 26992.

Moore, B. (2015). Blast injuries—A prehospital perspective. *Australasian Journal of Paramedicine, 4*, 1.

Penny, J. E., Kukums, J. R., Tyrer, J. H., & Eadie, M. J. (1974). Selective vulnerability of the hippocampus to hypoxia: Cytophotometric studies of enzyme activity in single neurones. *Proc Aust Assoc Neurol, 11*, 177–181.

Plaitakis, A., & Zaganas, I. (2001). Regulation of human glutamate dehydrogenases: Implications for glutamate, ammonia and energy metabolism in brain. *Journal of Neuroscience Research, 66*, 899–908. https://doi.org/10.1002/jnr.10054.

Prins, M. L., & Giza, C. C. (2006). Induction of monocarboxylate transporter 2 expression and ketone transport following traumatic brain injury in juvenile and adult rats. *Developmental Neuroscience, 28*, 447–456. https://doi.org/10.1159/000094170.

Prins, M. L., & Matsumoto, J. H. (2014). The collective therapeutic potential of cerebral ketone metabolism in traumatic brain injury. *Journal of Lipid Research, 55*, 2450–2457. https://doi.org/10.1194/jlr.R046706.

Rama Rao, K. V., et al. (2018). A single primary blast-induced traumatic brain injury in rodent model causes cell-type dependent increase in NADPH oxidase isoforms in vulnerable brain regions. *Journal of Neurotrauma*. https://doi.org/10.1089/neu.2017.5358.

Rodriguez-Rodriguez, P., Almeida, A., & Bolanos, J. P. (2013). Brain energy metabolism in glutamate-receptor activation and excitotoxicity: Role for APC/C-Cdh1 in the balance glycolysis/pentose phosphate pathway. *Neurochemistry International, 62*, 750–756. https://doi.org/10.1016/j.neuint.2013.02.005.

Schmidt-Kastner, R. (2015). Genomic approach to selective vulnerability of the hippocampus in brain ischemia-hypoxia. *Neuroscience, 309*, 259–279. https://doi.org/10.1016/j.neuroscience.2015.08.034.

Skotak, M., & Chandra, N. (2016). *Primary blast injury criteria for animal/human TBI models using field validated shock tubes* (pp. 1–28). New Jersey Institute of Technology: Newark, NJ.

Sokoloff, L. (1992). Energy metabolism and effects of energy depletion or exposure to glutamate. *Canadian Journal of Physiology and Pharmacology, 70*(Suppl), S107–S112.

Song, S. X., et al. (2013). Attenuation of brain edema and spatial learning deficits by the inhibition of NADPH oxidase activity using apocynin following diffuse traumatic brain injury in rats. *Mol Med Rep, 7*, 327–331. https://doi.org/10.3892/mmr.2012.1147.

Stewart, J. D., & Bolt, H. M. (2011). Metabolomics: Biomarkers of disease and drug toxicity. *Archives of Toxicology, 85*, 3–4. https://doi.org/10.1007/s00204-010-0635-4.

Tavazzi, B., et al. (2005). Cerebral oxidative stress and depression of energy metabolism correlate with severity of diffuse brain injury in rats. *Neurosurgery, 56*, 582–589. https://doi.org/10.1227/01.neu.0000156715.04900.e6.

Tretter, L., Patocs, A., & Chinopoulos, C. (2016). Succinate, an intermediate in metabolism, signal transduction, ROS, hypoxia, and tumorigenesis. *Biochimica et Biophysica Acta, 1857*, 1086–1101. https://doi.org/10.1016/j.bbabio.2016.03.012.

Turski, L., & Turski, W. A. (1993). Towards an understanding of the role of glutamate in neurodegenerative disorders: Energy metabolism and neuropathology. *Experientia, 49*, 1064–1072.

van der Veen, J. N., Kennelly, J. P., Wan, S., Vance, J. E., Vance, D. E., & Jacobs, R. L. (2017). The critical role of phosphatidylcholine and phosphatidylethanolamine metabolism in health and disease. *Biochimica et Biophysica Acta - Biomembranes, 1859*, 1558–1572. https://doi.org/10.1016/j.bbamem.2017.04.006.

Wallner, S., Orso, E., Grandl, M., Konovalova, T., Liebisch, G., & Schmitz, G. (2018). Phosphatidylcholine and phosphatidylethanolamine plasmalogens in lipid loaded human macrophages. *PLoS ONE, 13*, e0205706. https://doi.org/10.1371/journal.pone.0205706.

Wolahan, S. M., et al. (2017). Influence of glycemic control on endogenous circulating ketone concentrations in adults following traumatic brain injury. *Neurocritical Care, 26*, 239–246. https://doi.org/10.1007/s12028-016-0313-3.

Zhang, G. L., Dai, D. Z., Zhang, C., & Dai, Y. (2013). Apocynin and raisanberine alleviate intermittent hypoxia induced abnormal StAR and 3beta-HSD and low testosterone by suppressing endoplasmic reticulum stress and activated p66Shc in rat testes. *Reproductive Toxicology, 36*, 60–70. https://doi.org/10.1016/j.reprotox.2012.12.002.

Publisher's Note Springer Nature remains neutral with regard to jurisdictional claims in published maps and institutional affiliations.

Affiliations

Poonam Rana[1] · Kakulavarapu V. Rama Rao[4] · Arunreddy Ravula[4] · Richa Trivedi[1] · Maria D'Souza[2] · Ajay K. Singh[1] · Raj K. Gupta[3] · Namas Chandra[3,4]

[1] Metabolomics Research Facility, Division of Behavioral Neuroscience, Institute of Nuclear Medicine and Allied Sciences, Delhi, India

[2] Department of NMR, Institute of Nuclear Medicine and Allied Sciences, Delhi, India

[3] US Department of Defense Blast Injury Research Program Coordinating Office, US Army MRMC, 504 Scott Street, Fort Detrick, MD, USA

[4] Center for Injury Biomechanics, Materials and Medicine (CIBM3), Department of Biomedical Engineering, New Jersey Institute of Technology, Newark, NJ 07102-1982, USA

Appendix A –Publication Cover #6
2020

Authors: S. Kahali, M. Townsend, M. M. Nguyen, J. Kim, E Alay, N. Chandra

Title: "*The evolution of secondary flow phenomena and their effect on primary shock conditions in shock tubes: Experimental and numerical model*"

Journal Publication: Plos One, 15 (1), e0227125**,** (2020), [20-6]

,

PLOS ONE

RESEARCH ARTICLE

The evolution of secondary flow phenomena and their effect on primary shock conditions in shock tubes: Experimentation and numerical model

Sudeepto Kahali[1☯], Molly Townsend[2☯], Melissa Mendez Nguyen[2], Jeffrey Kim[2], Eren Alay[2], Maciej Skotak[2], Namas Chandra[2]*

1 Department of Mechanical Engineering, New Jersey Institute of Technology, Newark, New Jersey, United States of America, **2** Department of Biomedical Engineering, New Jersey Institute of Technology, Newark, New Jersey, United States of America

☯ These authors contributed equally to this work.
* namas.chandra@njit.edu

Check for updates

OPEN ACCESS

Citation: Kahali S, Townsend M, Mendez Nguyen M, Kim J, Alay E, Skotak M, et al. (2020) The evolution of secondary flow phenomena and their effect on primary shock conditions in shock tubes: Experimentation and numerical model. PLoS ONE 15(1): e0227125. https://doi.org/10.1371/journal.pone.0227125

Editor: Roi Gurka, Coastal Carolina University, UNITED STATES

Received: May 29, 2019

Accepted: December 12, 2019

Published: January 16, 2020

Copyright: © 2020 Kahali et al. This is an open access article distributed under the terms of the Creative Commons Attribution License, which permits unrestricted use, distribution, and reproduction in any medium, provided the original author and source are credited.

Data Availability Statement: All relevant data are within the manuscript and its Supporting Information files.

Funding: This work was funded by the United States Army Medical Research and Materiel Command under award number W81-XWH-15-1-0303. The funders had no role in study design, data collection and analysis, decision to publish, or preparation of the manuscript.

Abstract

Compressed gas-driven shock tubes are widely used for laboratory simulation of primary blasts by accurately replicating pressure profiles measured in live-fire explosions. These investigations require sound characterization of the primary blast wave, including the temporal and spatial evolution of the static and dynamic components of the blast wave. The goal of this work is to characterize the propagation of shock waves in and around the exit of a shock tube via analysis of the primary shock flow, including shock wave propagation and decay of the shock front, and secondary flow phenomena. To this end, a nine-inch shock tube and a cylindrical sensing apparatus were used to determine incident and total pressures outside of the shock tube, highlighting the presence of additional flow phenomena. Blast overpressure, impulse, shock wave arrival times, positive phase duration, and shock wave planarity were examined using a finite element model of the system. The shock wave remained planar inside of the shock tube and lost its planarity upon exiting. The peak overpressure and pressure impulse decayed rapidly upon exit from the shock tube, reducing by 92–95%. The primary flow phenomenon, or the planar shock front, is observed within the shock tube, while two distinct flow phenomena are a result of the shock wave exiting the confines of the shock tube. A vortex ring is formed as the shock wave exited the shock tube into the still, ambient air, which induces a large increase in the total pressure impulse. Additionally, a rarefaction wave was formed following shock front expansion, which traveled upstream into the shock tube, reducing the total and incident pressure impulses for approximately half of the simulated region.

Introduction

For a few centuries, the explosive blast was a threat to soldiers and civilians in armed conflicts. Only in the early days of the 20th century, technological advances in the weaponry and massive

Competing interests: The authors have declared that no competing interests exist.

deployment of artillery in the trench warfare during World War I resulted in the identification of the neurological and psychological effects of blast waves, described as the shell shock [1]. The mechanisms responsible for shell shock were poorly understood; the term was subsequently banned and replaced with post-concussive syndrome during World War II [2]. It was only a decade after WWII when systematic research to identify mechanisms responsible for blast injuries was initiated. Blast lung injury was the subject of intense experimental study at the Lovelace Foundation in Albuquerque, New Mexico from the 1950s to 1980 [3]. The research group led by Clemedson was among the first to use blast tubes to study the effect of shock waves on biological tissues [4]. Both groups used shock tubes, which had previously been used in other research fields to study detonation, combustion, ionization, supersonic, and transonic flow fields since the early 19th century [5–8]. In the last two decades, shock tubes have become a standard laboratory tool to study, the effect of shock waves on animal models, including rodents, pigs, and ferrets [9, 10]. In a broad survey of recent literature (time span: 2010–2019, S1 Table), trends can be observed in 71 experimental studies using shock tubes [11].

The survey, summarized in Fig 1, shows that in the majority of the work surveyed, the purpose of the work was to study injury pathologies in animal models (76%). In more than half of

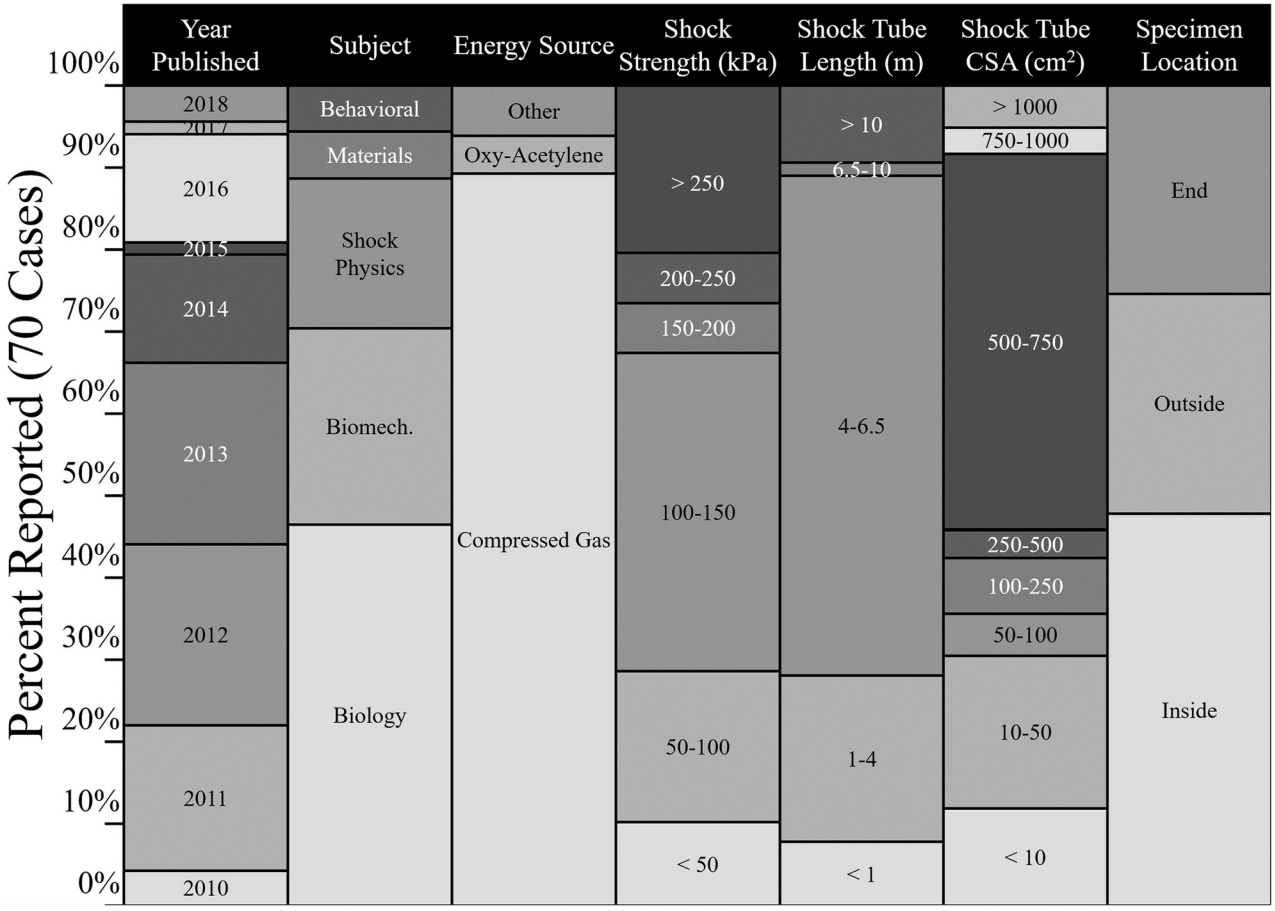


Fig 1. Summary of a recent literature survey of experiments using shock tubes. The survey analyzed 71 recent experiments, published between 2010 and 2018, which were conducted using a shock tube. The experimental subject being investigated, the energy source used to generate the shock wave, the shock strength, shock tube length, and size, and the location of specimens were identified for each study. Biomech.: Biomechanics; CSA: cross-sectional area. See S1 Table for additional details.

https://doi.org/10.1371/journal.pone.0227125.g001

the tests surveyed, the specimens (animal models, human surrogates, or animal surrogates) were tested near the exit or outside of the shock tubes. However, it is well-established that an unconfined shock front will undergo diffraction upon exit from the shock tube [11]. Free expansion of the unconstrained shock front at the exit induces a flow field which is very different from that of the inside; the flow field is affected by blast winds, air entrapment, vorticity, and rarefaction waves [12, 13]. An object placed at different locations both inside, near the exit, or outside of the shock tube is subjected to different types of loadings based on the static and dynamic components of the total pressure of the flow field.

Experimental investigation into the hydrodynamica of shock wave diffraction from an open ended shock tube utilize a variety of optical techniques to visualize the flow field. Some optical techniques include particle image velocimetry [14], holographic interferometry [15], schlieren imaging [16], smoke flow visualization [17]. These techniques capture the density or instantaneous velocities of the flow fields and are primarily used to understand and characterize the nature of exit jets, vortex rings. Increasingly, these optical techniques are coupled with numerical simulations to better describe the observable flow phenomena, enabling additional quantifiable analysis of the flow field [18]. However, despite the wealth of work performed in this field, a majority of the work conducted is conducted in shock tubes which are much smaller [11, 14, 19, 20] or much larger [21] than those conventionally used in biomedical applications. Additionally, much of the work is conducted at Mach numbers which would induce a fatal injury in animal models, precluding their usefulness for the study of mild traumatic brain injury [22–25].

In this work, we have generated shock waves at three shock strengths which have been previously shown to generate mild traumatic brain injuries in animal models [26]. For each of those conditions, we have made sixteen measurements of static and dynamic pressures in separate experiments. Additionally, we have developed a computational model to simulate the flow field produced in the shock tube experimental setup and validated the computational model against experimental measurements. Based on additional simulations, we have identified the temporal and spatial evolution of flow phenomena resulting from the free expansion of an unconstrained shock. It confirms the earlier evidence that experiments conducted outside of the shock tube do not ever reproduce the idealized flow field conditions of primary shock waves [27, 28].

Methods

Validation dataset

The shock tube used in this work has been validated to reproduce free-field explosions within the test section accurately at sensor location I3 in Fig 2 (230 x 230 mm^2 square cross-section, 6 m in length) [29, 30]. Briefly, compressed helium within a 55 cm length, 10 cm diameter chamber is separated from atmospheric-pressure air by Mylar membranes. When the pressure differential causes the membranes to burst, a shock wave is formed which travels through a 1.5 m transition region to the driven region. Shock strength is dependent upon the pressure ratio between the pressurized chamber of helium and the body of ambient air. In this work, three pressure ratios, 15.8:1, 8.7:1, and 2.5:1, were used to generate a shock wave with overpressures within the test section of the shock tube of 180, 130, and 70 kPa. These overpressures induced shock waves at the test section traveling at Mach 1.2–1.44 and at the shock tube exit at Mach 1.15–1.29. As this work seeks to study the evolution of the shock wave as a function of overpressure, the shocks will be referred to as a high, moderate, and low strength shock, respectively.

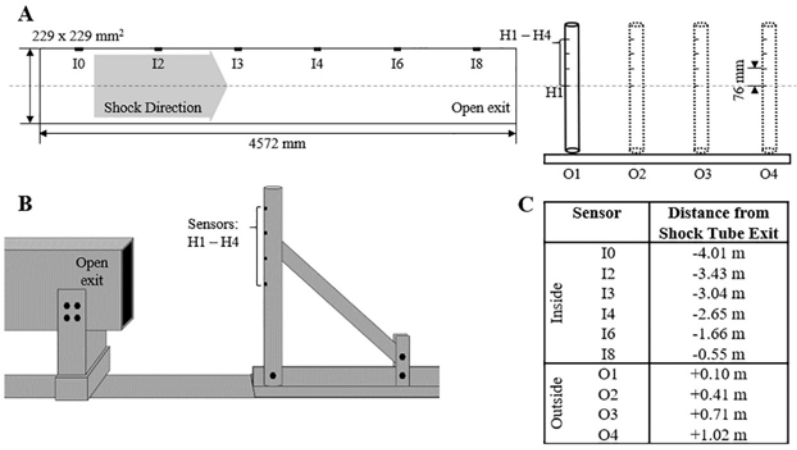


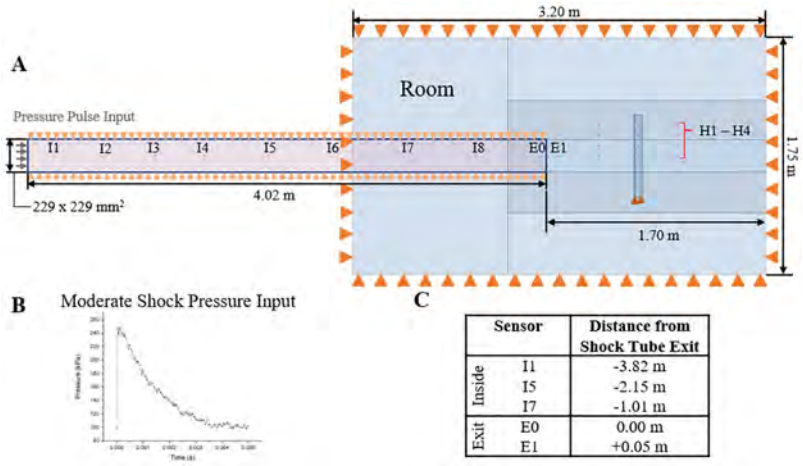
Fig 2. Schematic of the experimental setup used to create the validation dataset. (A) A shock tube with a square cross section was used in the development of the experimental dataset. Incident pressures were measured at six locations within the shock tube (I0, I2-I4, I6, and I8). Total and incident pressures were measured at four longitudinal locations outside of the shock tube (O1-O4) at four vertical heights (H1-H4). (B) A schematic representation of the experimental setup for the O1-O4 tests, with the sensing apparatus in the total pressure orientation. (C) The locations of all sensors with respect to the shock tube exit. Negative values denote upstream distances, into the shock tube, and positive values indicate downstream distances.

https://doi.org/10.1371/journal.pone.0227125.g002

Incident pressures were measured within the shock tube at six locations (Fig 2A and 2C) using flush-mounted piezoelectric pressure sensors (Model 134A24, PCB Piezoelectronics). Additional incident pressure measurements and total pressure measurements were taken outside the shock tube, in line with the longitudinal axis of the shock tube as depicted in Fig 2A. The PCB 102B06 pressure sensors were mounted in an aluminum cylinder referred to as the sensing apparatus (61 cm length, 51 mm diameter, 6.4 mm wall thickness), rigidly attached to the shock tube support structure. Four pressure sensors were placed on the upper half of the sensing apparatus at four heights (H1-H4), with the H1 sensor aligned with the longitudinal axis of the shock tube and an inter-sensor spacing of 76 mm. The sensing apparatus was positioned at four locations offset from the exit (open end) of the shock tube, at 4, 16, 28, and 40 in (100, 410, 710, and 1020 mm; O1-O4). Total pressures were measured by orienting the pressure sensors so that the longitudinal axis of the pressure sensor was parallel to the longitudinal axis of the shock tube. Although this technique explicitly measured the reflected pressures on the surface of the sensing apparatus, the reflected pressure is known to decay rapidly to the total pressure due to wave interference from rarefaction waves generated from the incident wave diffracting about the cylinder and, therefore, can be assumed to closely approximate the total pressure [31]. Incident pressures were measured by rotating the sensing apparatus 90 degrees, such that the sensors were perpendicular to the longitudinal axis of the shock tube. Additional incident pressure measurements were taken within the shock tube at six locations along the shock tube (I0, I2-I4, I6, and I8). Experiments were repeated four times (n = 4) at each measurement location (O1-O4), for each measurement type (incident and total), at the three shock strengths (high, moderate, and low).

Finite element model

The finite element method was used in this work to simulate the generation and propagation of the shock wave. A three-dimensional Eulerian model of the experimental setup was created and consisted of two continuous domains, a 4 m segment of the shock tube and a room region surrounding the exit of the shock tube (3.2 x 1.75 x 1.75 mm^3). The length of the shock tube



	Sensor	Distance from Shock Tube Exit
Inside	I1	-3.82 m
	I5	-2.15 m
	I7	-1.01 m
Exit	E0	0.00 m
	E1	+0.05 m

Fig 3. Schematic of the experimental simulation setup. (A) A depiction of the modeling domain, consisting of the sensing apparatus and the shock tube and room region with boundary conditions. Orange triangles indicate boundaries which are constrained. (B) An example of the pressure-time amplitude used to induce the moderate shock wave, which consists of the average pressure measured at sensor location I0 from Fig 1 (n = 4). (C) A table of additional sensor locations which were included in the numerical simulations. The sensor locations are reported with respect to the shock tube exit. Negative values denote upstream distances, into the shock tube, and positive values denote downstream distances.

https://doi.org/10.1371/journal.pone.0227125.g003

was selected to simulate the portion of the shock tube located downstream from the first sensor location (I0). A sensitivity analysis was conducted to identify the dimensions of a room region which optimizes computational time and solution quality, where the shock wave would not be affected by any reflections from the boundary of the room (see S1 Fig). The Eulerian domain was discretized using a biased mesh with a minimum element edge length of 8 mm at all regions of interest (see S2 Fig). To validate the simulation, a Lagrangian model of the sensing apparatus was created to match the experimental setup. Fig 3A shows the shock tube, room region, and the sensing apparatus with the testing locations used for model validation. The Lagrangian domain offered a converged solution at an ideal mesh density of 6 mm (see S3 Fig). This resulted in a system of approximately 3,600,000 Eulerian and 3,500 Lagrangian isothermal, reduced integration, linear, hexahedral elements with hourglass control. The Eulerian domain was filled with 300 K air at a density of 1.225 kg/m^3. The sensing apparatus was modeled as aluminum, approximated to be linear, elastic, and isotropic with a density, elastic modulus, and Poisson's ratio of 2700 kg/m^3, 70 GPa, and 0.33, respectively.

A typical experimental pressure-time profile collected from the sensor I0 (Fig 3B) was used to model the shock wave. Although experiments were shown to be very reliable (see S4 Fig), the pressure-time pulses of a minimum of four exposures were averaged for each shock strength to minimize the effect of any measurement artifacts. The edges of the room and shock tube were constrained against displacement normal to the edge (Fig 3A). The open exit of the shock tube was unconstrained, allowing for the unimpeded flow of the shock wave from the shock tube into the room region.

Simulations to derive the incident pressures were conducted without the sensing apparatus model in a purely Eulerian simulation. Total pressure simulations were conducted with the sensing apparatus. In the total pressure simulations, all nodes located at the bottom of the sensing apparatus were constrained in all translational and rotational degrees of freedom. The contact between the Lagrangian and Eulerian domains is based on an enhanced boundary method. Here, the void mesh of the Eulerian domain is occupied by the Lagrangian structure.

The general contact algorithm automatically tracks the interface between the domains, compensating for mesh size discrepancies to prevent the entry of Eulerian material through the Lagrangian surface. Contact constraints are enforced through the penalty method with a finite sliding contact formulation. The total pressure simulations use frictionless tangential sliding with hard contact.

All simulations were performed using Abaqus/Explicit 6.13–4 (Simulia, Dessault Systemes) in 16 threads of an 3.00 GHz Intel i7-5960X with 64GB of physical memory.

Methodology

Overall thirty-nine simulations were conducted, three incident pressure simulations, one for each shock strengths (low, moderate, and high), and thirty-six total pressure simulations at three shock strengths for twelve locations. Additional locations were identified to better map the shock tube system, including seven locations inside the shock tube (I1-I8), two locations near the exit of the shock tube (E0 and E1), and four locations outside the shock tube (O1-O4). Exact locations of the additional measurements are included in Fig 3C.

First, validation was conducted in which the shock wave pressure-time profiles were compared to the experimental measurements. The peak overpressure, impulse, duration, and general form of the total and incident pressure-time profiles were compared to ensure validation of the simulation. Upon validation, the simulation results were analyzed to identify potential flow phenomena.

Results and discussion

In the discussion below, the evolution of a shock wave at the exit of a shock tube is presented, including the discussion of how the shock wave decays in strength and induces several flow phenomena. First, the observations from the experimental measurements will be presented and the numerical simulations will be validated. Then, the numerical model, supported by experimental measurements when possible, will be used to discuss several metrics used to define the characteristics of the shock wave. First, the shock is observed to be planar within the shock tube and non-planar outside of the shock tube. The shock tube constrains the shock wave, maintaining the planarity of the wave until the shock front experiences rapid expansion into the ambient air within the room. Next, the peak pressure decays as the shock wave propagates, decreasing slowly while inside the shock tube and decreasing rapidly upon exiting the shock tube. Finally, two flow phenomena were generated from the rapid expansion of the shock front at the shock tube exit: a vortex ring and a rarefaction wave. The vortex ring propagates behind the shock wave at a slower velocity that is dependent on the shock strength. The rarefaction wave reflects into the shock tube, decreasing the positive phase duration and impulse. These metrics of the shock wave highlight the regions of the shock tube experimental setup which experience an ideal shock wave and those which interact with a vortex ring and a rarefaction wave.

Experimentally observed incident and total pressures

Experimental measurements of the shock overpressure outside the shock tube exit identified two distinct flow phenomena (Fig 4). First, the shock front arrives, characteristically observed as a rapid increase in overpressure and an exponential decay to baseline in which the reflected pressure is proportionally higher than the incident pressure reading. The reflected pressure rapidly decays to the total pressure, which remains proportionally higher than the incident pressure reading. The difference between shock front arrival time can be used to confirm the

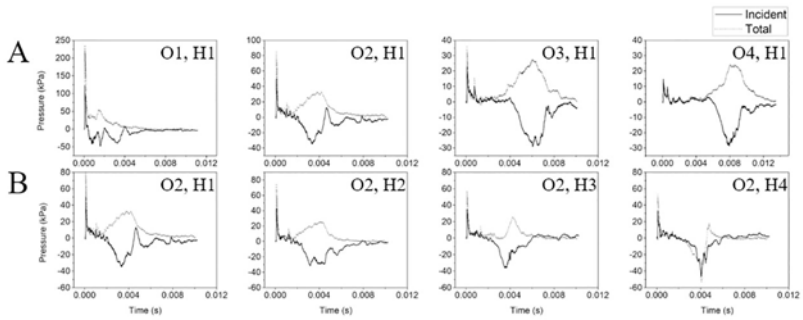


Fig 4. Measurement location along the longitudinal axis (O1-O4) and the vertical axis (H1-H4) changes the characteristics of the pressure measurements. (A) The experimentally measured total (grey) and incident (black) pressures at the four measurement locations O1-O4 at sensor location H1 highlight a reduction in the peak overpressure and a delay in the arrival of the secondary flow phenomena as the distance from the shock tube exit increases. (B) Likewise, when comparing the pressure profiles vertically (H1-H4) at a single longitudinal location, O2, shows a change in the nature of the secondary flow phenomena.

https://doi.org/10.1371/journal.pone.0227125.g004

shock velocity, which is confirmed to be higher in higher shock intensities and gradually slows as it propagates in the ambient air outside the shock tube. The peak overpressure of the shock front decreases as the distance from the shock tube exit increases. Additionally, the peak overpressure decreases with increased distance from the midline, i.e., normal to the direction of shock wave propagation. This trend is less pronounced as the distance from the shock tube exit increases.

The second distinct flow phenomenon arrives after the shock front and is characterized by a slow increase in the total pressure and decrease in the incident pressure, resulting in an incident underpressure, or pressure less than atmospheric pressure. At a distance closest to the shock tube exit, O1, the flow artifact occurs shortly after the shock passes. This artifact is observed to travel at a slower velocity than the shock front, moving at a subsonic velocity with a magnitude proportional to the shock strength. As these rarefaction waves travel at the speed of sound within the fluid behind the shock front, a subsonic velocity is observed. This flow phenomenon was observed at sensor locations H1-H3 and the highest sensor measurement location, H4, showed an underpressure in both the total and incident pressures.

A few general trends can be observed in Fig 5 by comparing the peak overpressure, positive phase durations, and the impulse at the four vertical locations (H1-H4) at the four longitudinal sensing apparatus measurement locations (O1-O4). Trends are conserved between the three shock strengths examined, differing only in magnitude (Fig 5). Peak overpressure, duration, and the magnitude of the impulse increased with shock strength. Over the duration of the pressure signal, underpressures resulted in negative impulse values in all sensor locations in the incident waveform and in the O4 total pressure measurement. Total pressure measurements exhibited higher peak overpressures and impulses in all cases. As longitudinal distance from the shock tube exit increased (O1-O4), peak overpressure and impulse decreased. There exhibited no significant change in incident pressure duration and the total pressure duration decreased with increasing longitudinal distance. As the vertical distance increased from the longitudinal axis (H1-H4), the peak overpressure decreased, with the magnitude of the reduction decreasing with longitudinal distance. Significance was not observed between the H1 and H2 sensors in the incident pressure measurement at O4. The duration of the total pressure signal increased in the off-axis locations.

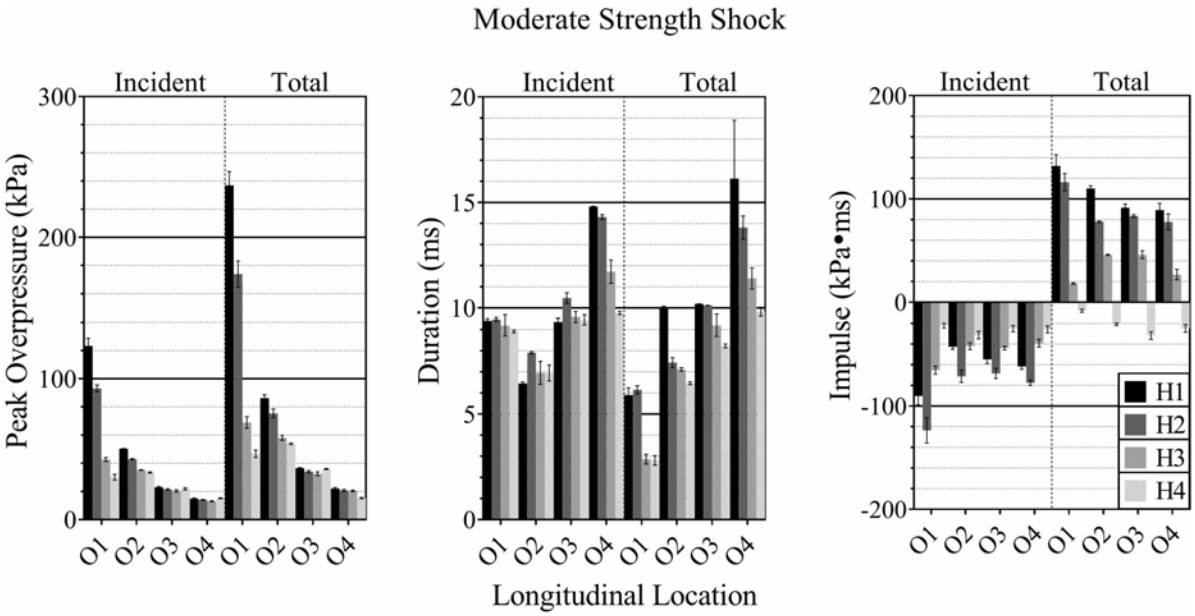


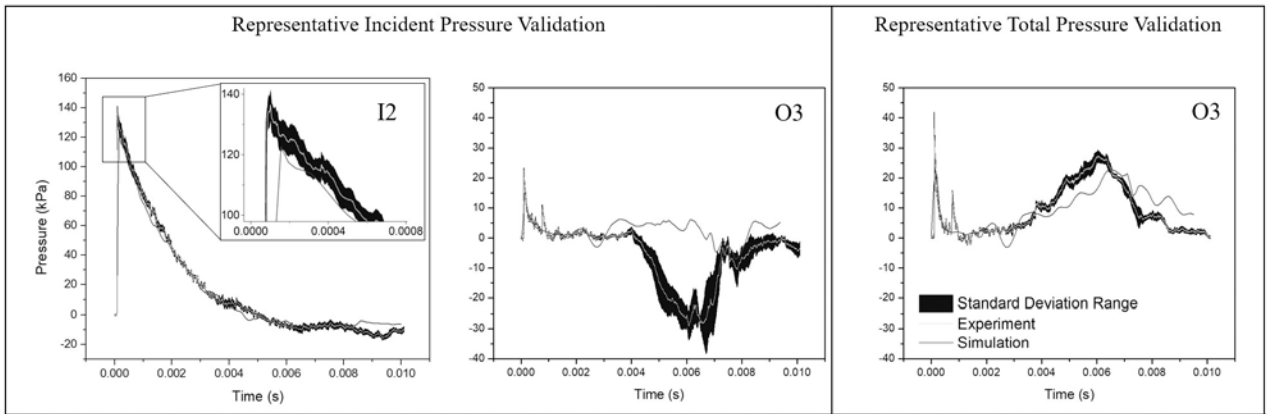
Fig 5. Pressure profile characteristics of the incident and total pressures. The peak overpressure (left), signal duration (middle), and impulse (right) of the experimentally measured incident, and total pressure pulses for the moderate-intensity shock wave showed several trends.

https://doi.org/10.1371/journal.pone.0227125.g005

Validation of computational model

The simulations were validated against the experimental datasets through a comparison of the pressure-time waveforms, the peak overpressures, impulses, rise-times, and durations. The simulations, on average, underestimated the peak overpressure and overestimated the rise time, which is attributed to a sampling rate and an element density which were not adequate to resolve the shock front location. The simulations were sampled at a frequency of 26 kHz. Experimentally, sampling frequencies of a similar range have been shown to be sufficient to resolve the peak overpressure, yet overestimate the rise time of the signal [32]. However, low sampling frequency coupled with spatial discretization reduces the ability to capture the shock front location. For the shock strengths simulated, the velocity of the shock front is 345–518 m/s (low to high strength) which would enable the shock front to traverse an 8 mm element in the range of 15.5–20.4 μs, respectively. To accurately resolve the shock front at that spatial density, a higher sampling frequency, coupled with adaptive mesh refinement techniques, would be required. However, as the accurate resolution of the rise time was not the focus of this work, additional techniques were not implemented to improve the simulation of the rise time and the idealized peak overpressure. Despite the underprediction of the peak pressure, average point-by-point percent error between the experimental and simulated pressures were under 6% for all incident pressures within the shock tube and under 12.5% for all incident and total pressure measurements taken outside of the shock tube (Fig 6). On average, the best match was observed at locations closer to the input location, I0.

Simulation results matched the impulse and duration of the shock front, but incident pressure simulations did not exhibit a negative impulse, as seen in the experimental measurements (Fig 5). Several methods of simulating the incident and total pressures were compared, indicating that the decrease in pressure was likely due to the interactions between the secondary flow phenomenon and the cylindrical sensing apparatus (S5 Fig). In general, a comparison of the



	Incident Pressure Percent Difference		Total Pressure Percent Differences (Outside Only)
	Sensors Inside Shock Tube	Sensors Outside Shock Tube	
Low Strength	5.6 ± 2.6%	10.6 ± 3.2 %	10.7 ± 3.9 %
Moderate Strength	5.2 ± 2.2%	10.7 ± 2.3%	10.4 ± 3.6%
High Strength	6.1 ± 2.4%	12.4 ± 3.1%	12.3 ± 3.6%

Fig 6. Simulation predictions compared to experimental results for the high-strength shock. The simulated pressures (grey) showed good validation with the average experimentally measured pressures (black with grey, mean, with standard deviation) for the incident (left and middle) and total (right) pressure measurements for the high strength shock. The point-by-point percent error for the shock front was under 12.5%. Average errors for interior locations (I2-I4, I6, and I8) showed the best validation.

https://doi.org/10.1371/journal.pone.0227125.g006

pressure-time waveforms revealed an excellent match, meaning that the simulation can be considered validated with conservative blast overpressure estimates.

Peak overpressure

The shock pressure ratio, defined as the ratio of the pressure within the shock front and the ambient pressure, decreased slowly as it propagated through the shock tube and rapidly upon sudden expansion into the room region (Fig 7). The rate of decay varied with shock strength, with the high strength shock pressure ratio decaying the most rapidly. The shock pressure ratio decreased within the shock tube at an average rate of 0.09, 0.19, and 0.22 for the low, moderate, and high strength shocks, respectively. The peak pressure at the shock tube exit was 30.99%, 33.33% and 34.15% of the input peak overpressure for the low, moderate, and high strength shock. These results are in line with previous findings from our group, which states

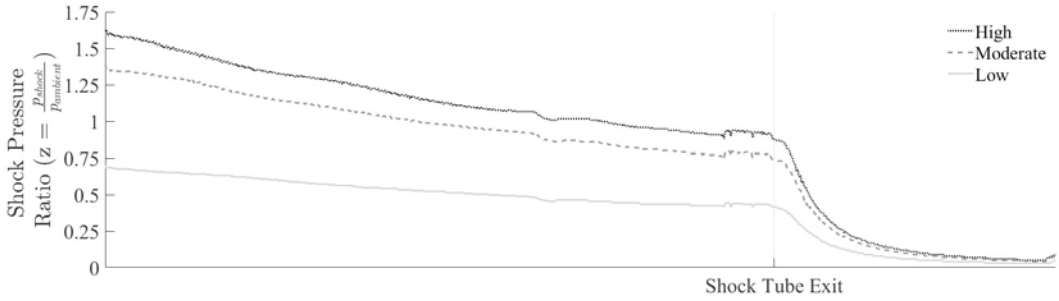


Fig 7. The shock pressure ratio along the longitudinal axis. The shock pressure ratio, z, defined as the ratio of the shock front, p_{shock}, to the ambient pressure, $p_{ambient}$, decays gradually along the shock tube and declines rapidly after expansion begins at the shock tube exit. The rate of decay within the shock tube and the following expansion was found to depend on the shock strength.

https://doi.org/10.1371/journal.pone.0227125.g007

that the peak pressure decays as the shock wave propagates down the shock tube [29, 32]. Energy loss occurs due to the expansion of the high-pressure shock front as it interacts with low-pressure upstream air, increasing the shock duration while maintaining a comparable impulse [29].

Shock wave expansion at the shock tube exit decreased the shock pressure ratio rapidly, with the average rate of decay increasing to 0.55, 1.00, and 1.19 and an average peak rate of decay of 2.65, 4.96, and 6.03 for the low, moderate, and high strength shocks, respectively. Outside of the shock tube, the pressure decayed rapidly, reducing 92.96%, 94.33%, and 94.51% for the low, moderate, and high strength shocks, respectively. This rapid decay in overpressure is consistent with an increased area of the shock front as the shock front experiences expansion into the ambient air [33]. A relationship exists between the shock strength and the area of the shock front using the function derived by Chisnell (*f(z)*) which, when multiplied by the area of the shock front (*A*), remains constant [34]. As the area of the shock front increases, the Chisnell function decreases, accordingly, and is given for a shock in diatomic air by [34]

$$f(z) = \frac{z^{\frac{5}{7}}(z-1)}{\sqrt{z+\frac{1}{6}}}\left[\frac{1+\left(1+\frac{6}{z}\right)^{-1/2}}{1-\left(1+\frac{6}{z}\right)^{-1/2}}\right]^{\sqrt{7}/2} \times \left[\frac{\left(1+\frac{6}{z}\right)^{-1/2}-7^{-1/2}}{\left(1+\frac{6}{z}\right)^{-1/2}+7^{-1/2}}\right] \times e^{\left(\sqrt{5}\tan^{-1}\left(5\sqrt{\frac{7z}{5(z+6)}}\right)\right)}. \quad (1)$$

This function is derived from the Rankine-Hugoniot equations and has been proven to accurately model symmetrical, spherical and cylindrical shocks experiencing rapid, unconfined expansion between two square or circular chambers of similar or very different cross-sectional areas[34, 35]. When used in conjunction with the area of the shock front given for a spherical shock by

$$A = 2\pi X^2 \quad (2)$$

where *X* is the longitudinal distance from the exit of the shock tube after which a critical shock is formed. It can be calculated from the shock tube diameter (*d*) and the angle of propagation (α) by

$$X = \frac{d}{2}\cot \propto . \quad (3)$$

Using a relationship between the angle of propagation and the Mach number, given by

$$\tan^2 \propto = \frac{(M^2-1)(M^2+5)}{6M^4}, \quad (4)$$

a relationship describing the loss in shock pressure ratio due to expansion can be derived. Using this theory for the conditions studied here, the rapid decay of the shock pressure ratio is explained by the increase in the area of the shock front. As the shock front area increases and continues to expand, the shock pressure ratio exponentially decays.

Shock planarity

As the simulated shock propagated through the shock tube, it remained planar. At the shock tube exit, the shock front experienced sudden, unconstrained expansion into the still ambient air. At this point, the simulation shows the shock front became less planar and expanded. As the shock front propagated, it eventually regained some planarity (Fig 8).

This simulated phenomenon was confirmed experimentally by examining the shock front arrival times at each sensor. At all longitudinal measurement locations (O1-O4), the shock wave arrived at the sensor aligned with the longitudinal axis first (H1). At the measurement



Fig 8. The planarity of the shock front is largely lost at the shock tube exit. The edge of the shock front at each time step (Δt = 38.5 μs) from t = 0–13.5 ms in the moderate strength shock in a mid-wall cut. As the shock exits the shock tube, denoted by a grey bar, the shock front loses its planar nature and expands, becoming non-planar.

https://doi.org/10.1371/journal.pone.0227125.g008

location closest to the shock tube exit, the center of the shock front remains mostly planar. When comparing the elapsed time between the shock wave arrival, little difference was observed between the two sensors closest to the longitudinal axis, H1 and H2. The arrival of the shock front at H2 was delayed an average of 2.75±0.98 μs. The shock wave curvature is apparent in the much higher arrival time delays at the sensors located farther from the midline, with H3 and H4 being delayed by 55.25±1.91 μs and 187.33±2.12 μs, respectively. This demonstrates that the shock wave is only beginning to lose planarity at this location. The curvature of the shock wave is more apparent at the O2-O4 longitudinal measurement locations, where the shock curvature is more even (Fig 9). The curvature is highest at O2, then starts decreasing to O4. The shock front arrival time delay was mostly independent of the shock strength. A slight trend was observed where a high-strength shock exhibited a slightly longer delay. This trend was most apparent at the O1 location, and the strength of the trend decreased with the distance from the shock tube exit. The shock front travels at a faster speed in the higher strength shock and, therefore, the shock front will be less planar than a low strength shock, despite there being little to no difference in the shock front arrival time delay.

These observations highlight that the shock front was behaving in line with previous experimental results of sudden shock wave expansion, further validated by the theory. Using the relationship in Eq 4, the Mach number of the shock wave as it exits the shock tube can be used to

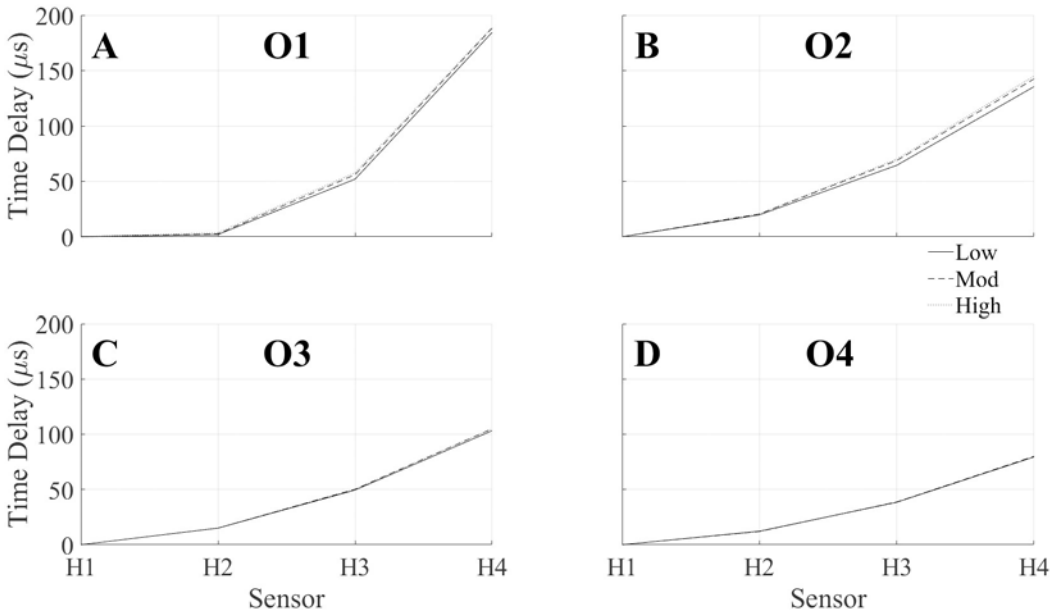


Fig 9. Experimentally observed shock curvature. The arrival times of the shock wave normalized with the shock arrival at the H1 sensor showed a curvature of the shock front at the measurement locations (A) O1, (B) O2, (C) O3, and (D) O4.

https://doi.org/10.1371/journal.pone.0227125.g009

predict the angle of propagation of the critical shock, predicting the point at which planarity of the shock front decays. The difference in the experimentally measured arrival times of the shock front between the I8 and O1 and the distance between those measurement locations were used to calculate the shock velocity (v) and the Mach number, using the relationship

$$M = \frac{v}{c}, \tag{5}$$

where the speed of sound, c, was assumed to be 343 m/s. At the measurement location O1, the angles of propagation for the shock strengths investigated in this study are 69.5, 62.9, and 61.8 mm for the low, moderate, and high strength shocks, respectively. This indicates that the limits of the planar area fall between the H1 and H2 sensors (76.2 mm) for all three shock strengths at the O1 location, as demonstrated by a lack of curvature seen in Fig 9A. The point of contact, or the point in which the shock loses the original planar shock front, occurs between 222–374 mm for the shock strengths examined in this study. Therefore, by the O2 longitudinal measurement location, the shock front no longer retains any planarity and decays completely, referred to as a "critical shock". As the shock expands into the ambient air, the shock undergoes diffraction and expands freely around the sharp edge of the shock tube exit. This shock front which undergoes diffraction interacts with the planar shock front, causing the planar front to decay into a critical shock. This interaction creates an expansion wave which propagates longitudinally upstream into the shock tube [33]. The expansion wave, or rarefaction wave, will be described in detail later.

Following the complete decay of the planar shock front into a critical shock, the critical shock front was observed in the simulations to propagate at a much lower strength and, eventually, become more planar in nature. This is theorized to be due to the initial uneven expansion of the wave into a critical shock and due to interactions of the shock front with the boundaries of the room region. As the cross-section of the shock tube investigated here is not of a circular diameter, the planar region will decay in a non-axisymmetric manner. The narrower cross section at the mid-wall of the shock tube will have a smaller planar area than the widest cross-section, at a diagonal cut. The non-axisymmetric decay will cause the behavior of the critical shock to deviate from the ideal behavior of a spherical shock. Additionally, as the critical shock continues to expand, the increase in the shock area will eventually interact with the boundaries of the domain. At the domain walls, the interaction of the critical shock with the wall creates an oblique reflected shock, which interacts with the critical shock front [36]. The oblique reflected shock increases the strength of the critical shock, which decreases the apparent curvature of the shock front at the edges of the domain. As the domain of the room region in the computational model was not designed to completely replicate the room in which the experiment was conducted, it is anticipated that the curvature of the shock predicted in the simulation would differ from experimental conditions. However, as the region of interest tested by the sensing apparatus was small in comparison with the room region, it is hypothesized that any differences would only be apparent at the longitudinal measurement locations farthest from the shock tube exit.

Vortex ring

Following the shock front, the secondary flow phenomenon observed in the experimental results was identified as a vortex ring. A vortex ring is formed as the fast-moving volume of compressed air moves into stationary air. The energy of the shock front is locally reduced due to the interaction of the shocked and unshocked air, reducing the velocity of the shocked air. The slowed air then moves around the mass of compressed air, then rejoins the fast-moving air, forming a toroidal ring. The simulation showed the rotating ring forming at the exit of the

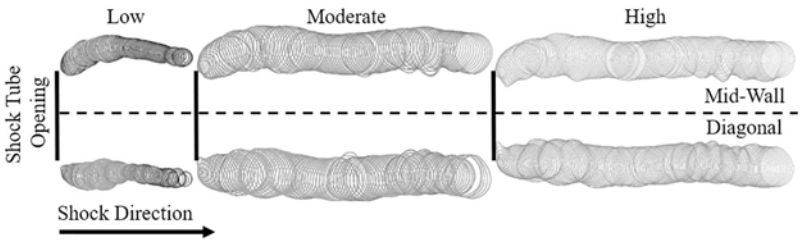


Fig 10. The location of the vortex ring with respect to time. Contour plots of the pressure for a cut through the middle of the shock tube wall (upper) and along the diagonal of the square (lower) display the vortex ring location with time following the expansion of the (left) low, (middle) moderate, and (right) high strength shocks.

https://doi.org/10.1371/journal.pone.0227125.g010

shock tube and following the shock front at a slower velocity. The velocity of the vortex ring was dependent on the shock strength, where the highest strength shock produced a vortex ring which propagates at 90.6 m/s; and with decreasing shock strength, the velocity decreased to 79.8 and 40.3 m/s for the moderate and low strength shocks, respectively. Observed vortex ring propagation velocity aligns well with the approximation where the vortex ring propagation velocity is approximately half of the piston velocity, with theoretical velocities of 83.3, 73.2, and 44.9 m/s for the high, moderate, and low strength shocks respectively [37]. The path of the vortex ring also varied with shock strength (Fig 10). Following the formation of the ring, the vortex ring follows the shock front and the diameter of the vortex ring core at the mid-wall increases to match the diameter of the vortex ring core at the corners. The ring over-expands and comes back to reach a more stable diameter. The diameter of the ring itself increases as it forms and reaches a relatively stable size. The lower severity shock exhibited a reduction in ring size as it propagates, indicating that the ring may have begun to dissipate.

At the time of arrival of the vortex ring, an increase in total pressure was observed experimentally and confirmed in the simulation results. A jet of air behind the shock front exists within the core of the vortex ring. This jet of air arrives with the vortex ring, and the air particles within the jet of air are stopped by an object in the path, resulting in an increase in total pressure. The structure of the vortex ring means that the pressure profile varied for each vertical measurement (Fig 11). Along the longitudinal axis, at vertical location H1, the center of the

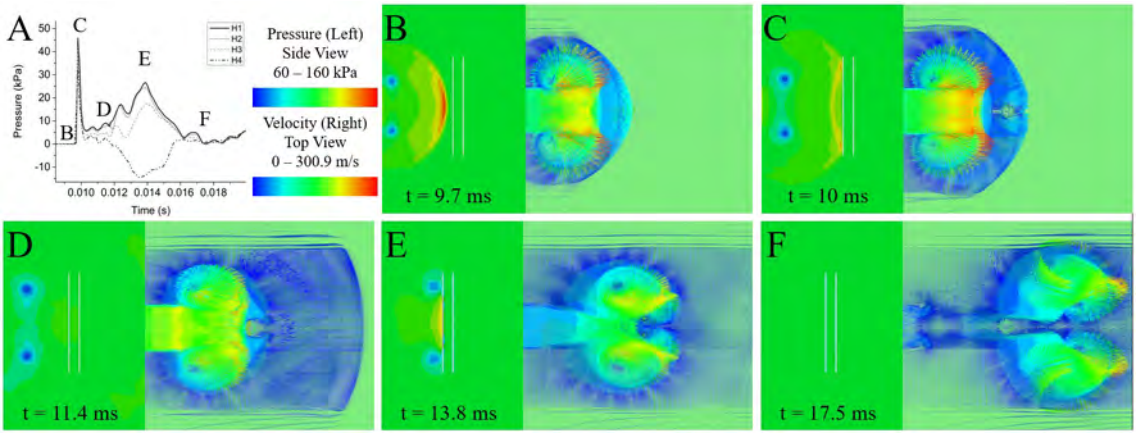


Fig 11. Pressure contours and velocity fields depicting how the vortex ring interacts with the cylindrical sensing apparatus. The interaction of the vortex ring at the O3 location under a moderate-intensity shock, visualized in (left) a side view of the pressure field, shown in MPa, and (right) a top-view of the velocity vectors, shown in m/s for (B) shock front arrival, (C) peak pressure, (D) vortex ring arrival, (E) peak vortex ring interaction, and (F) complete passage of the vortex ring.

https://doi.org/10.1371/journal.pone.0227125.g011

ring accelerated air, which caused the largest total pressure impulse. The impulse decreases with increasing vertical distance, as the sensing location approaches the center of the vortex ring. The vortex ring itself has an underpressure region within the vortex core, where the pressure is falling below atmospheric pressure [38]. The H4 sensor location is closest to the vortex core and characteristically drops in pressure as the vortex ring interacts with the testing apparatus.

Rarefaction wave

Another flow artifact was observed following the exit of the shock wave from the confines of the shock tube. A rarefaction wave radiated upstream back into the shock tube, causing as a decrease in blast overpressure. The pressure along the longitudinal axis of the shock tube was mapped with time to capture the nature of this flow phenomenon (Fig 12). After the time point in which the planar shock front exits the shock tube, a fan can be observed which radiates upstream, into the shock tube. The speed of this rarefaction wave and the affected area changes with shock strength, with the rarefaction wave in the low strength shock exhibiting the largest area of influence, with a notable depression observed as deep as sensor I4. The rapid expansion of the shock front at the shock tube exit causes a density gradient to form, which initiates the rarefaction wave. Previously, we have shown that a reflection generated from a reflector plate at an appropriate offset can largely nullify the impact of the rarefaction wave on the incident waveform within the shock tube [29]. A normal reflection of the shock on a perpendicular endplate causes a reflected compressive wave that greatly reduces the effect of the

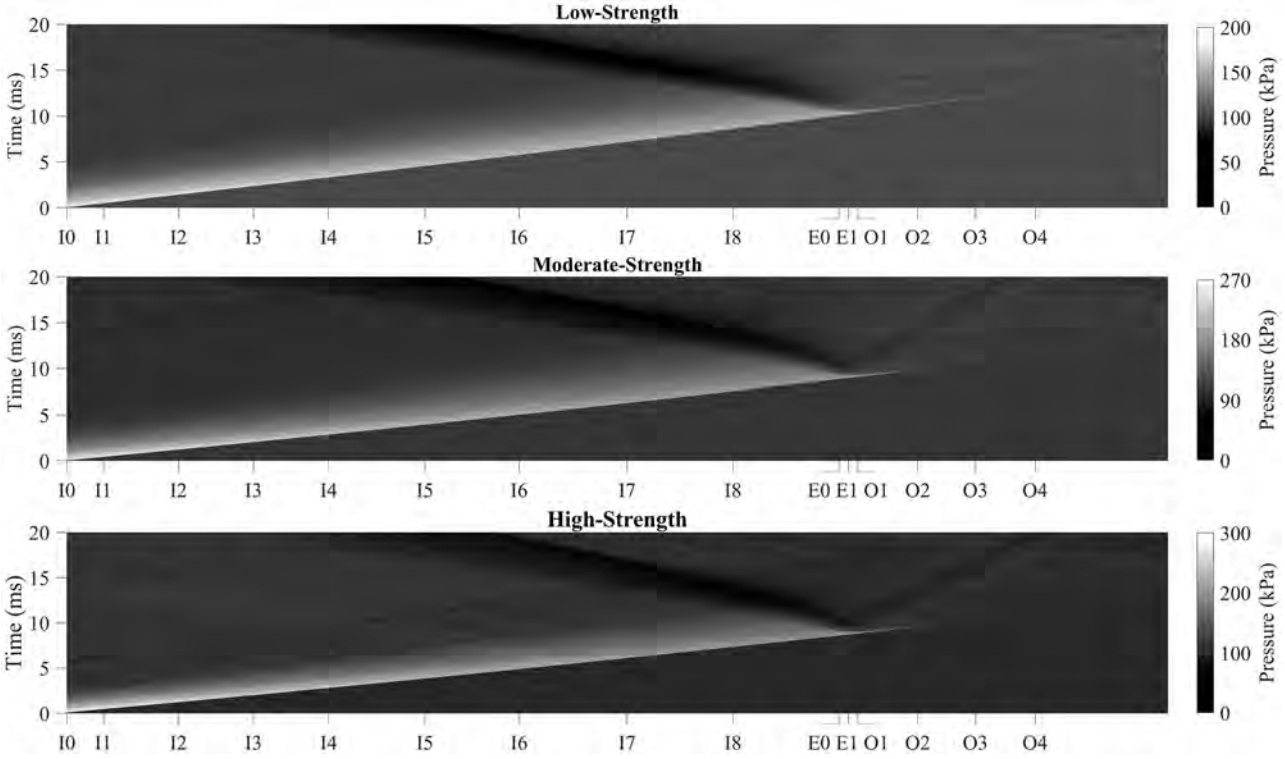


Fig 12. Pressure-time contour plots along the longitudinal axis. A surface map of the pressure for each node along the longitudinal axis plotted as longitudinal location vs. time, shows a rarefaction wave for the (top) low strength, (middle) moderate-strength, and (bottom) high-strength shock. The posteriorly traveling dark fan shows the region of low pressure, which is characteristic of the rarefaction wave.

https://doi.org/10.1371/journal.pone.0227125.g012

tensile rarefaction wave. However, without an endplate, the tensile wave travels unimpeded and can affect the nature of the pressure waveform.

Conclusions

The presented work highlights the spatial and temporal evolution of flow phenomena in the shock tube experimental setup relevant to the field of blast-induced traumatic brain injury. Corroborated with pressure measurements and numerical simulations, the nature of these flow phenomena are confirmed and discussed in the range of shock strengths and shock tube dimensions commonly used to generate field-relevant shock exposures to study traumatic brain injury in animal models. In summary, while the shock front is constrained within the shock tube, the shock exhibits strong similarities to a primary blast in the free field. The sudden expansion of the shock front into the free ambient air induces two flow phenomena which initiate changes to the flow system. The sudden expansion causes a vortex ring formation, which develops and moves sub-sonically along the longitudinal axis, following the shock front. The vortex ring and high dynamic pressures are observed as the vorticity forms around the accelerated air within its core. Additionally, a rarefaction wave develops which propagates upstream into the shock tube, which decreases the overpressure, reducing the impulse and duration of the waveform. The shock front expands non-uniformly into the ambient air. This expanded critical shock continues to dissipate energy through expansion and experiences a reduction in peak overpressure and duration. These observations were simulated using a numerical model, validated extensively against experimental pressure measurements. This work strives to better inform the biomedical field of study by identifying the nature and extent of these flow phenomena in the common testing regime.

The limitations of this work are primarily associated with the fidelity of the numerical modeling domain. The room region outside of the shock tube exit was unobstructed by any other objects. This created an idealized flow field which does not reflect realistic experimental conditions, which would introduce reflections which cause the experiment to deviate from numerical predictions. Additionally, only a limited room domain was considered. This was shown to have a potential influence on the evolution of the critical shock, altering how planar the shock front would appear. This simplification enabled for more efficient simulations, but potentially reduced the simulation fidelity of later time points. And finally, the influence of shock tube size and cross-sectional shape were only postulated in this work. This assumption is supported by the findings of other researchers but is not confirmed through a parametric study. Despite these limitations, we are confident in the reported trends.

These observed phenomena are essential to consider in the planning of biomedical shock tube experiments. If the experimental goal is to capture a primary shock waveform, it is recommended that the experimentalist test in locations which are not affected by the passing of the vortex ring or which experience the expansion rarefaction wave. Failure to do so would result in an alteration of the ideal primary shock characteristics. Similarly, if the goal of the experiment is to examine the interaction of an object with a vortex ring, the experimentalist is encouraged to examine the production and evolution of the vortex ring at the shock strengths investigated. The propagation speed of the vortex ring is dependent on the shock strength, and the size of the vortex ring will be dependent on the size and shape of the shock tube. Within the vortex ring, an area with pseudo-blast winds is observed, but the diameter of the vortex ring, if formed, should be compared to the experimental area to ensure that the specimen is not inadvertently experiencing pressure reductions from the vortex ring. Within the shock tube, close to the shock tube opening, regions of decreased incident pressure impulses and durations can be isolated by targeting the area of influence of the rarefaction wave. Therefore,

it is recommended that experimentalists gather incident and total pressures at the experimental testing location to capture the nature of the desired flow field.

Supporting information

S1 Fig. Modeling of the room region of the shock tube. Various sizes of the room region the shock tube were modeled. The pressures at the experimental measurement locations O1-O4 were compared. Three room configurations were modeled, (A) the whole room region, (B) a partial section of the room, and (C) a room region only around the exit of the shock tube. The partial room model was selected to minimize computational errors and simulation time.
(TIF)

S2 Fig. Convergence study of the shock tube with a 130 kPa shock wave. (A) The pressure at the testing location within the shock tube was plotted against the number of simulated elements. (B) The internal energy in the shock tube with respect to the number of simulated elements. (C) Table comparing the percent change between mesh seed lengths. Convergence was observed by a mesh seed length of 8 mm.
(TIF)

S3 Fig. Convergence study of the Lagrangian sensing apparatus exposed to a 130 kPa shock wave. (A) The pressure at the midline of the sensing apparatus, corresponding with the longitudinal axis of the shock tube, was plotted against the number of Lagrangian elements. (B) The percent change between the pressure prediction for varying mesh seed lengths shows convergence at 6 mm.
(TIF)

S4 Fig. The average experimental measurements taken at sensor location I0. Grey bands indicate ± one standard deviation.
(TIF)

S5 Fig. A comparison between different methods of simulating the incident pressures. Simulations using the cylindrical sensing apparatus to simulate the incident pressure measurements exhibited a larger underpressure.
(TIF)

S6 Fig. Pressure metrics for the low strength and high strength shocks.
(TIF)

S1 Table. Literature survey of recent studies conducted with shock tubes.
(DOCX)

S2 Table. Significant differences in pressure readings. The significant differences between the peak overpressure, signal duration, and signal impulses between vertical measurements. Data were analyzed using a two-way ANOVA with Bonferroni's multiple comparisons test. Significance was set to be 0.05.
(DOCX)

Author Contributions

Conceptualization: Maciej Skotak, Namas Chandra.

Formal analysis: Sudeepto Kahali, Molly Townsend, Eren Alay, Maciej Skotak, Namas Chandra.

Funding acquisition: Namas Chandra.

Investigation: Sudeepto Kahali, Molly Townsend, Melissa Mendez Nguyen, Jeffrey Kim, Eren Alay, Maciej Skotak.

Methodology: Molly Townsend, Maciej Skotak, Namas Chandra.

Project administration: Namas Chandra.

Resources: Namas Chandra.

Supervision: Maciej Skotak, Namas Chandra.

Writing – original draft: Sudeepto Kahali, Molly Townsend, Maciej Skotak, Namas Chandra.

Writing – review & editing: Sudeepto Kahali, Molly Townsend, Maciej Skotak, Namas Chandra.

References

1. Southard EE. Shell-shock and other neuropsychiatric problems: WM Leonard; 1919.
2. Jones E, Fear NT, Wessely S. Shell shock and mild traumatic brain injury: a historical review. Am J Psychiatry. 2007; 164(11):1641–5. Epub 2007/11/03. https://doi.org/10.1176/appi.ajp.2007.07071180 PMID: 17974926.
3. Stuhmiller JH. Blast Injury: Translating Research Into Operational Medicine. Santee WR, Fried KE, editors: United States Dept. of Defense; 2008.
4. Clemedson C, Criborn C. A detonation chamber for physiological blast research. The Journal of aviation medicine. 1955; 26(5):373. PMID: 13263274
5. Henshall BD, Aeronautical Research C. On some aspects of the use of shock tubes in aerodynamic research. London: H.M. Stationery Off.; 1957.
6. Griffith W. Shock-tube studies of transonic flow over wedge profiles. Journal of the Aeronautical Sciences. 1952; 19(4):249–57.
7. Frohn A, De Boer P. Measurement of ionization relaxation times in shock tubes. The Physics of Fluids. 1969; 12(5):I-54–I-7.
8. Hertzberg A. A shock tube method of generating hypersonic flows. Journal of the Aeronautical Sciences. 1951; 18(12):803–4.
9. Masel BE, Bell RS, Brossart S, Grill RJ, Hayes RL, Levin HS, et al. Galveston Brain Injury Conference 2010: clinical and experimental aspects of blast injury. Journal of neurotrauma. 2012; 29(12):2143–71. https://doi.org/10.1089/neu.2011.2258 PMID: 22655746
10. Hoge CW, McGurk D, Thomas JL, Cox AL, Engel CC, Castro CA. Mild traumatic brain injury in US Soldiers returning from Iraq. New England Journal of Medicine. 2008; 358(5):453–63. https://doi.org/10.1056/NEJMoa072972 PMID: 18234750
11. Koroteeva EY, Znamenskaya I, Glazyrin F, Sysoev N. Numerical and experimental study of shock waves emanating from an open-ended rectangular tube. Shock Waves. 2016; 26(3):269–77.
12. Chandra N, Sundaramurthy A. Acute Pathophysiology of Blast Injury—From Biomechanics to Experiments and Computations. In: Kobeissy FH, editor. Brain Neurotrauma: Molecular, Neuropsychological, and Rehabilitation Aspects. Boca Raton, FL: Taylor & Francis Group; 2015. p. 199–255.
13. Chandra N, Sundaramurthy A, Gupta RK. Validation of Laboratory Animal and Surrogate Human Models in Primary Blast Injury Studies. Mil Med. 2017; 182(S1):105–13. Epub 2017/03/16. https://doi.org/10.7205/MILMED-D-16-00144 PMID: 28291460.
14. Arakeri J, Das D, Krothapalli A, Lourenco L. Vortex ring formation at the open end of a shock tube: A particle image velocimetry study. Physics of fluids. 2004; 16(4):1008–19.
15. Onodera O, Jiang Z, Takayama K. Holographic Interferometric Observation of Shock Waves Discharged from an Open-Eng of a Square Cross-Sectional Shock Tube. JSME International Journal Series B Fluids and Thermal Engineering. 1998; 41(2):408–15.
16. Elder F Jr, De Haas N. Experimental study of the formation of a vortex ring at the open end of a cylindrical shock tube. Journal of Applied Physics. 1952; 23(10):1065–9.
17. Murugan T, De S, Dora C, Das D, Kumar PP. A study of the counter rotating vortex rings interacting with the primary vortex ring in shock tube generated flows. Fluid Dynamics Research. 2013; 45 (2):025506.

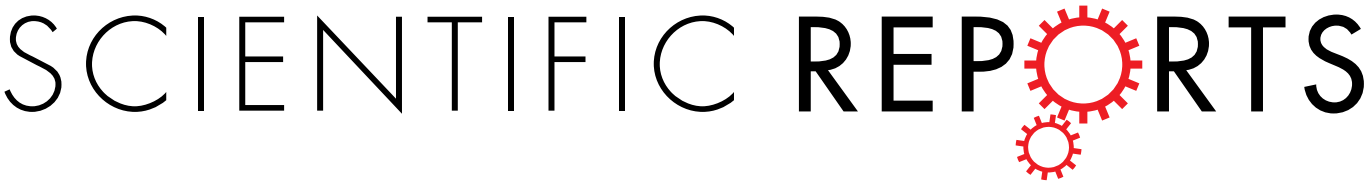
18. Murugan T, De S, Dora C, Das D. Numerical simulation and PIV study of compressible vortex ring evolution. Shock waves. 2012; 22(1):69–83.
19. Abe A, Takayama K. Numerical simulation and density measurement of a shock wave discharged from the open end of a shock tube. JSME international journal Ser 2, Fluids engineering, heat transfer, power, combustion, thermophysical properties. 1990; 33(2):216–23.
20. Mariani R, Kontis K. Experimental studies on coaxial vortex loops. Physics of Fluids. 2010; 22(12):126102.
21. Condon JA, Lottero RE, Loucks RB. Construction and Testing of the ARL 1.68-m Diameter Shock Tube Exit Jet Spreader for Non-Ideal Blast Simulation. ARMY RESEARCH LAB ABERDEEN PROVING GROUND MD, 1997.
22. Murugan T, De S, Sreevatsa A, Dutta S. Numerical simulation of a compressible vortex–wall interaction. Shock Waves. 2016; 26(3):311–26.
23. Murugan T, Dora CL, De S, Das D. A comparative three-dimensional study of impulsive flow emanating from a shock tube for shock Mach number 1.6. Journal of Visualization. 2018; 21(6):921–34.
24. Zare-Behtash H, Kontis K, Gongora-Orozco N. Experimental investigations of compressible vortex loops. Physics of Fluids. 2008; 20(12):126105.
25. Maeno K, Kaneta T, Morioka T, Honma H. Pseudo-schlieren CT measurement of three-dimensional flow phenomena on shock waves and vortices discharged from open ends. Shock Waves. 2005; 14(4):239–49.
26. Abdul-Muneer PM, Schuetz H, Wang F, Skotak M, Jones J, Gorantla S, et al. Induction of oxidative and nitrosative damage leads to cerebrovascular inflammation in an animal model of mild traumatic brain injury induced by primary blast. Free Radic Biol Med. 2013; 60:282–91. https://doi.org/10.1016/j.freeradbiomed.2013.02.029 PMID: 23466554.
27. Needham CE, Ritzel D, Rule GT, Wiri S, Young L. Blast Testing Issues and TBI: Experimental Models That Lead to Wrong Conclusions. Front Neurol. 2015; 6:72. Epub 2015/04/24. https://doi.org/10.3389/fneur.2015.00072 PMID: 25904891.
28. Sundaramurthy A, Alai A, Ganpule S, Holmberg A, Plougonven E, Chandra N. Blast-induced biomechanical loading of the rat: an experimental and anatomically accurate computational blast injury model. J Neurotrauma. 2012; 29(13):2352–64. Epub 2012/05/25. https://doi.org/10.1089/neu.2012.2413 PMID: 22620716.
29. Kuriakose M, Skotak M, Misistia A, Kahali S, Sundaramurthy A, Chandra N. Tailoring the Blast Exposure Conditions in the Shock Tube for Generating Pure, Primary Shock Waves: The End Plate Facilitates Elimination of Secondary Loading of the Specimen. PloS one. 2016; 11(9):e0161597. https://doi.org/10.1371/journal.pone.0161597 PMID: 27603017
30. Holmberg A. Development and Characterization of Shock Tubes for Laboratory Scale Blast Wave Simulation: University of Nebraska, Lincoln; 2010.
31. Coulter GA. Blast wave loading of a two-dimensional circular cylinder. ARMY BALLISTIC RESEARCH LAB ABERDEEN PROVING GROUND MD, 1982.
32. Skotak M, Alay E, Chandra N. On the accurate determination of shock wave time-pressure profile in the experimental models of blast induced neurotrauma. Frontiers in Neurology. 2018; 9:52. https://doi.org/10.3389/fneur.2018.00052 PMID: 29467718
33. Abate G, Shyy W. Dynamic structure of confined shocks undergoing sudden expansion. Progress in Aerospace Sciences. 2002; 38:23–42. https://doi.org/10.1016/S0376-0421(01)00016-1.
34. Chisnell RF. The motion of a shock wave in a channel, with applications to cylindrical and spherical shock waves. Journal of Fluid Mechanics. 1957; 2(3):286–98. https://doi.org/10.1017/S0022112057000130
35. Skews BW. The perturbed region behind a diffracting shock wave. Journal of Fluid Mechanics. 1967; 29(4):705–19.
36. Kinney GF, Graham KJ. Explosive Shocks in Air. 2nd ed: Springer Science; 1985.
37. Mohseni K. A formulation for calculating the translational velocity of a vortex ring or pair. Bioinspiration & biomimetics. 2006; 1(4):S57.
38. Jiang Z, Onodera O, Takayama K. Evolution of shock waves and the primary vortex loop discharged from a square cross-sectional tube. Shock Waves. 1999; 9(1):1–10. https://doi.org/10.1007/s001930050133

Appendix A –Publication Cover #7
2019

Authors: M. Kuriakose, D. Younger, A. R. Ravula, E. Alay, K.V. Rama Rao, N. Chandra

Title: *"Synergistic role of oxidative stress and blood-brain barrier permeability as injury mechanisms in the acute pathophysiology of blast-induced neurotrauma"*

Journal Publication: Nature- Scientific Reports, 9 (1), 7717**,** (2019), [19-7]



OPEN

Synergistic Role of Oxidative Stress and Blood-Brain Barrier Permeability as Injury Mechanisms in the Acute Pathophysiology of Blast-induced Neurotrauma

Received: 13 December 2018
Accepted: 7 May 2019
Published online: 22 May 2019

Matthew Kuriakose, Daniel Younger, Arun Reddy Ravula, Eren Alay, Kakulavarapu V. Rama Rao & Namas Chandra

Blast-induced traumatic brain injury (bTBI) has been recognized as the common mode of neurotrauma amongst military and civilian personnel due to an increased insurgent activity domestically and abroad. Previous studies from our laboratory have identified enhanced blood-brain barrier (BBB) permeability as a significant, sub-acute (four hours post-blast) pathological change in bTBI. We also found that NADPH oxidase (NOX)-mediated oxidative stress occurs at the same time post-blast when the BBB permeability changes. We therefore hypothesized that oxidative stress is a major causative factor in the BBB breakdown in the sub-acute stages. This work therefore examined the role of NOX1 and its downstream effects on BBB permeability in the frontal cortex (a region previously shown to be the most vulnerable) immediately and four hours post-blast exposure. Rats were injured by primary blast waves in a compressed gas-driven shock tube at 180 kPa and the BBB integrity was assessed by extravasation of Evans blue and changes in tight junction proteins (TJPs) as well as translocation of macromolecules from blood to brain and vice versa. NOX1 abundance was also assessed in neurovascular endothelial cells. Blast injury resulted in increased extravasation and reduced levels of TJPs in tissues consistent with our previous observations. NOX1 levels were significantly increased in endothelial cells followed by increased superoxide production within 4 hours of blast. Blast injury also increased the levels/activation of matrix metalloproteinase 3 and 9. To test the role of oxidative stress, rats were administered apocynin, which is known to inhibit the assembly of NOX subunits and arrests its function. We found apocynin completely inhibited dye extravasation as well as restored TJP levels to that of controls and reduced matrix metalloproteinase activation in the sub-acute stages following blast. Together these data strongly suggest that NOX-mediated oxidative stress contributes to enhanced BBB permeability in bTBI through a pathway involving increased matrix metalloproteinase activation.

Blast-induced traumatic brain injuries (bTBIs) are the most prevalent form of neurotrauma amongst soldiers and some in civilian populations due to asymmetric warfare with increased acts of terrorism domestically and abroad[1–6]. In spite of the increase in blast-induced neurotrauma (BINT) studies, there are still significant gaps in the understanding of how the acute shockwave induced biomechanical injury plays a role in the subsequent secondary biochemical injuries in the chronic stages. A recent survey reported that more than 30 phase III clinical trials aimed at targeting TBI have failed and, to this effect, our group has attempted to elucidate the temporal and spatial neuropathology of bTBI, in relation to blast-overpressure, as it pertains to two commonly identified pathological factors: oxidative stress increase and blood-brain barrier (BBB) breakdown[7–10].

Center for Injury Biomechanics, Materials and Medicine (CIBM3), Department of Biomedical Engineering, New Jersey Institute of Technology, Newark, NJ, 07102-1982, USA. Matthew Kuriakose and Daniel Younger contributed equally. Correspondence and requests for materials should be addressed to K.V.R.R. (email: kakulava@njit.edu) or N.C. (email: namas.chandra@njit.edu)

Oxidative stress has been implicated in multiple modes of TBI[11,12] and is mainly induced by reactive oxidative species (ROS). These include, but are not limited to, superoxide ($O2\cdot-$), hydroxyl radical ($HO\cdot$), and hydrogen peroxide (H_2O_2)[13,14]. While a basal level of ROS is to be expected to occur during normal reactions in redox-reactions during and the electron transport chain operation, an excess amount, as seen after injury, can be harmful. NADPH oxidase (NOX) is a multi-subunit enzyme that catalyzes the formation of superoxide radicals from available molecular oxygen. As previously reported by our group and other investigators[15–17], NOX is upregulated in multiple brain regions following blast injury and neurons maximally contribute to the highest increase in hippocampus compared to other neural cells. It is also worth noting that a single blast substantially increases superoxide levels in multiple brain regions from the pre-frontal cortex to hippocampus to cerebellum, all along the direction of shock wave propagation[17].

We also recently identified that direct blast biomechanical loading causes disruption of brain vascular integrity (BBB) in multiple brain regions within minutes of loading and that this BBB disruption further increased in four hours following blast before returning to normal at 24 hours post-injury[18]. The BBB is a selectively-permeable membrane separating the brain from the circulatory system, consisting of tight junction complexes, which attach adjacent endothelial cells together, as well as a host of modulating neural cells including pericytes and astrocytes, which wrap around the endothelium. In a recent work by our group, increased permeability of the BBB was most significantly seen four hours post-blast across the cerebral hemisphere, with highest permeability seen in the frontal cortex[18]. Damage to the BBB was established through extravasation of tracers Evans blue and sodium fluorescein, the dislodging of tight junction proteins, and leakage of blood-borne cells into the brain parenchyma and brain parenchymal molecules into the blood[18]. Increased permeability of the BBB has been observed in several other animal models of TBI including closed cortical injuries[19–21], weight drop models[22,23], as well as blast models[24–29].

Oxidative stress is a well-known factor for BBB disruption in blunt TBI as well as other neurological disorders including Alzheimer's and Parkinson's diseases[30–32]. However, no studies have been performed on the interaction between oxidative stress and BBB permeability changes in blast TBI. Since our recent studies indicate blast injury results in disruption of BBB and activation of factors conducive to oxidative stress[17,18], we sought to examine the interaction of these two well-known pathogenic factors in BINT. We hypothesize that while BBB is acutely disrupted immediately following blast injury through biomechanical means, and enhanced BBB disruption in later stages (zero to four hours) is due, at least in part, to the activation of NADPH oxidase (NOX) and associated increase in oxidative stress. This study therefore employed apocynin, which is known to block the assembly of NOX subunits and prevent activation of NOX, and reduce superoxide production to ascertain if NOX plays a role in the manifestation of BBB breakdown. Apocynin was used to examine the role of NOX on BBB disruption and not as a therapeutic agent though such a treatment possibility exists; however, that is not the purpose of the present study.

Materials and Methods

Animal preparation. Adult (10-week old), male Sprague-Dawley rats (Charles River Laboratories) weighing between 350 ± 50 g were used in accordance with protocols approved by Rutgers University Institutional Animal Care and Use Committee (IACUC). Animals were housed at 22 °C with free access to food and water in a 12 hour light-dark cycle. Animals were divided among sham, blast, and treatment groups, all to be sacrificed 15 min or four hours post-blast (or, in the case of sham animals, with only noise exposure). All methods used throughout the study were performed in accordance with protocols, guidelines, and regulations approved by Rutgers University IACUC.

Exposure to blast and apocynin pre-treatment. Rats were exposed to a single shock wave at the New Jersey Institute of Technology (Center for Injury Biomechanics, Materials, and Medicine) in the shock tube described in previous publications[16,33–35]. A total of 54 rats were used in the study for different experimental methods with at least 4–5 animals in each experimental group (power value of 0.8, $\alpha = 0.05$) based on a priori power analysis. Prior to blast exposure, all animals (controls, blast, blast + apocynin) were anesthetized with 5% isoflurane, released in a chamber containing 95% air and 5% CO_2, until rats were unresponsive to noxious stimulation. Apocynin (5 mg/kg, Sigma-Aldrich) was administered intraperitoneally 30 min prior to blast exposure. Sham animals were kept near the shock tube to expose them to noise but not any shock wave. A separate group of animals with sham + apocynin treatment was not included in the present study, since several investigators have reported apocynin (5 mg/kg wt) administration to control/sham animals did not exert any toxicity nor affected physiological and behavioral parameters assessed in parallel to animals subjected to traumatic brain injury[36], splanchnic artery occlusion[37], liver injury[38] and experimental epilepsy[39]. Following blast injury, animals were closely monitored for any signs of apnea, loss of motor coordination and neurological severity score (NSS) was evaluated five minutes post exposure. None of the animals included in this study displayed NSS scores that differed from sham animals. Animals were exposed to a single blast of 180 kPa peak overpressure. Prior to transcardial perfusion, animals were anesthetized with a mixture of ketamine and xylazine (1:10 ratio), perfused either 15 min or four hours post-blast. For immunofluorescence and extravasation studies, animals were first perfused with PBS followed by 4% paraformaldehyde, whereas for ELISA studies, animals were perfused with only PBS and brain tissue was collected for preparation of homogenates. Prior to initiation of perfusion, CSF was extracted from the cisterna magna using a 25 gauge butterfly needle from scalp vein set (Exelint International, CA) and was freely allowed to collect into catheter. Blood (about 4 ml) was collected by cardiac puncture (left ventricle) and allowed to settle in vacutainer tubes (BD Bioscience) containing 3.2% sodium citrate for 10 minutes. Plasma was separated from blood by centrifuging at 2000 g. Extravasation of Evans blue was assessed by method recently published by us[18]. All the blast exposures were continuously monitored with high-speed video recording (5000 fps) as described previously[18] as a quality control measure to ensure that potential secondary/tertiary injuries are absent.

Immunofluorescence and microscopy. In order to evaluate the increase in NOX1 expression in vascular endothelial cells following blast injury, double immunofluorescence studies were conducted for NOX1 and RECA-1 (a marker of endothelial cells) in the frontal cortex. Briefly, four hours post-injury, both sham and injured animals were transcardially perfused with PBS and brains were fixed with 4% paraformaldehyde (PFA). Tissue section and staining procedure was done in similar manner described in our previous publication[17]. Fixed tissues were incubated overnight at 4 °C with respective primary antibodies to NOX1 (Rabbit polyclonal, Sigma-Aldrich, 1:400) and RECA-1 (mouse monoclonal, Abcam, 1:50). Double immunofluorescence was performed using Alexa Fluor 488 for NOX1 and Alexa Fluor 594 for RECA-1. Quantification of the fluorescence intensities was performed following the method recently published by us[17,18]. Briefly, slides containing mounted coronal sections of frontal cortex were imaged at 20x magnification using a Leica Aperio Versa 200 digital pathology scanner. Control sections were used as reference for adjusting the exposure times and gray scale balance for optimal image quality; once set, these parameters were fixed and used for image acquisition of the remainder of both control and experimental groups. To remove variability that might arise, all sections to be compared were scanned on the same day using the same established scanning protocol. For the immunostained sections, three channels were collected for each coronal section. Blue: 405 nm (DAPI), red: 594 nm (NOX1), and green: 488 nm (RECA-1). For the extravasation studies, two channels were collected. Red: 594 nm (Evans blue) and green: 488 nm (NaFl). Values were expressed as average fluorescence intensity/unit stained area. For the EB extravasation and dihydroethidium (DHE) study we expressed results as percentage change from control due to an absence of a negative control that can be used to remove autofluorescence from the analysis. A maximum intensity threshold was also set to remove any oversaturation from excess fluorescent dye. The algorithm outputs the area of positive staining for each brain region, the average intensity of each channel, and intensity profile of each antigen.

Superoxide production. Superoxide ($O_2^{\cdot -}$) levels in different brain regions were measured using DHE following the method of Kim *et al.*[39], and was previously described[17]. Briefly, animals were injected with 5 mg/kg DHE (Molecular probes, MA, dissolved in DMSO) intraperitoneally 30 minutes prior to blast and 4 hours after exposure; animals were transcardially perfused first with PBS followed by 4% PFA ($n = 6$, per group). Brains were extracted and 50 µm sections were cut using Leica VT 1000S vibratome and mounted. DHE immunofluorescence in each region was visualized and quantified using similar protocol as described above.

ELISA. As a means to determine the abundance of tight junction proteins and matrix metalloproteinases in the brain tissue, GFAP in the blood plasma, and albumin in the cerebrospinal fluid, ELISAs were performed in the lysates obtained from cerebral hemispheres. Following perfusion with PBS, brains were excised from the skull and cerebrum was homogenized in CellLytic-M (Sigma-Aldrich) using sonicator (Fisher Scientific, IL). Samples were then centrifuged at 14,000 g at 4 °C. The protein concentration in the samples was estimated by bicinchoninic acid (BCA) method (Thermo Scientific, Rockford, IL). Subsequently, samples were diluted in PBS and loaded onto specific ELISA plates for MMP3, MMP9, occludin, and claudin-5 and GFAP (LSBio, Seattle, WA). Plates were read in microplate reader (Spectra Max i3, Molecular Devices) at wavelength of 450 nm. Steps of ELISA were conducted in accordance with manufacturer instructions and samples plotted against a standard curve made up of eight samples using SoftMax Pro 6.5 software.

***Ex-Vivo* Imaging and Analysis.** Slides containing EB extravasated tissue sections were digitized (10x magnification) using Leica Aperio Versa 200 digital pathology grade slide scanner. Fluroescent intensities were quantified after excitation at 594 nm, 125 ms exposure, using AreaQuant, software specifically designed for this imaging application (Leica Biosystems) using similar protocol described in the previous section.

Statistical analysis. Data are presented as mean ± standard error of the mean. Statistical significance was determined using one-way analysis of variance (ANOVA) to compare mean fluorescence intensities between control, blast, and blast + treatment groups with a post-hoc analysis using Tukey pairwise test to determine differences between individual groups. Normalcy and population variance homogeneity were assessed with Shapiro-Wilk and Levene's tests respectively. Differences between means were assessed and probability levels of $p < 0.05$ were considered statistically significant. Minitab 17 Statistical Software was used for all analyses and Origin 2017 was used for generation of bar plots. Bar plots presented in semi-log scale are done so as to capture the intensities when the differences between groups are several orders of magnitude. Fluorescent images were taken using Aperio Versa software and analysis and export done via ImageScope software (LEICA Corp.).

Results

NOX1 is upregulated in neurovascular endothelial cells four hours following moderate blast injury. Previous studies in our laboratory identified increased levels of NOX1 and NOX2 in neurons, astrocytes, and microglia following mild blast injury (180 kPa) across the cerebral hemisphere and cerebellum[17]. In the present study, we examined the levels of NOX1 in the vascular endothelial cells in the frontal cortex. The double immunofluorescence for NOX1 and RECA-1 (endothelial cell marker) showed a significant increase in amount of co-localization following blast (Fig. 1). Fifteen minutes post-exposure, there was no change in the fluorescent intensity from controls (Fig. 1B), whereas there was a robust increase (ten-fold) in NOX1 concentration in vascular endothelial cells (Tukey test, $p = 0.023$) 4 h post-injury. Noteworthy that such increase in NOX1 at 4 h post injury correlated well with our previous observation of highest increase in BBB permeability following blast injury[18].

Apocynin significantly reduces superoxide production following blast injury. Several groups have demonstrated that activation of NOX results in increased superoxide production[40,41]. After demonstrating the increase of NOX1 concentration in neurovasculature in the frontal cortex, we sought to determine if

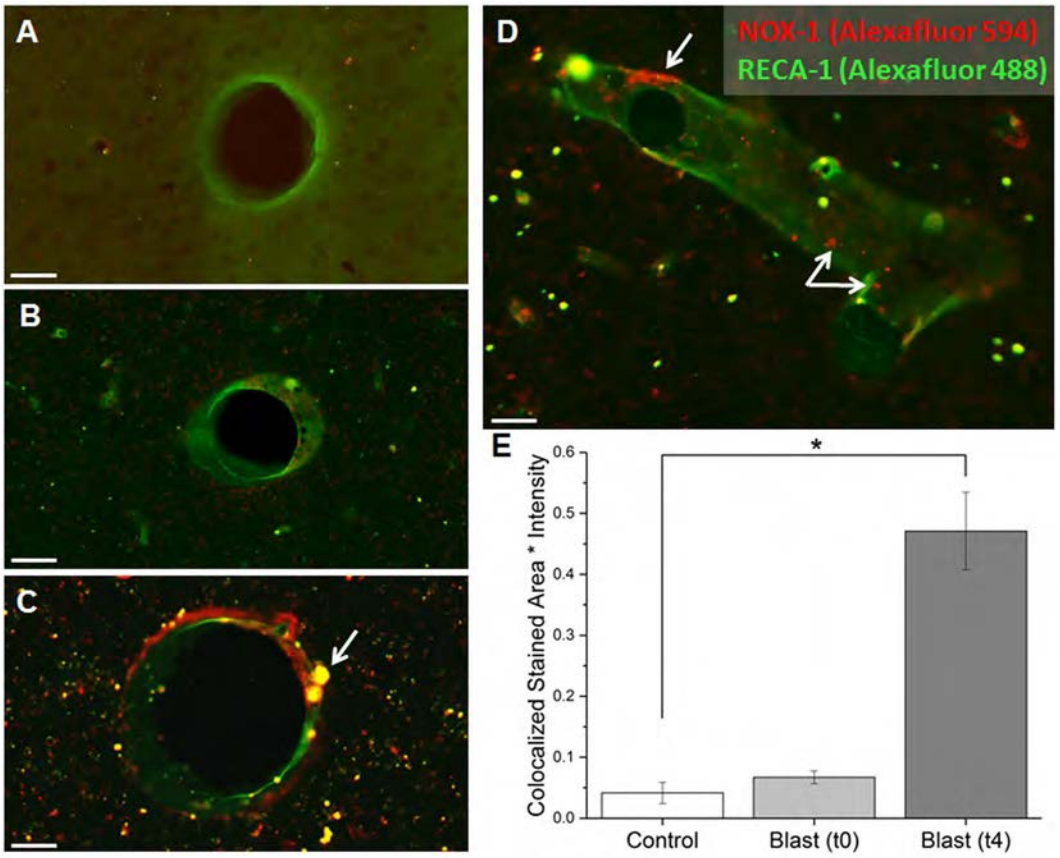


Figure 1. Co-localization of NOX-1 (red) and RECA-1 (green) on vascular endothelial cells in the frontal cortex. (**A**) Controls show negligible NOX-1 on vascular endothelial cells. (**B**) Blast injury after 15 min shows a slight increase in colocalization. (**C**) Four hours following blast, there is a significant upregulation of NOX-1 on marked endothelial cells, with the yellow indicating an overlap of NOX-1 and RECA-1. (**D**) Image showing an alternative view of the vessel in order to show highlight that NOX-1 is upregulated across the length of the vessel lumen, as indicated by the arrows. (**E**) Quantitation of the co-localization between control (n = 5), 15 minutes post-blast n = 5), and 4 hours post-blast groups (n = 5). Scale bars = 30 μm. *Indicates a difference in intensity compared to control with a statistical significance of $p < 0.05$.

this increase leads to an increase of superoxide production. *In-vivo* levels of superoxide were measured using DHE and we observed a clear increase in superoxide produced in the frontal cortex, which not only correlated well with our earlier observation[17] but is also consistent with the upregulation of NOX1 in the present study (Fig. 2A,B). Differences between control and blast groups (post-ANOVA Tukey test, $p = 0.004$) and blast and treatment groups (Fig. 2A–C) (Tukey test, $p = 0.001$) were found to be statistically significant, as seen in Fig. 2D.

Apocynin significantly attenuates the reduction of tight junction proteins following blast injury. In order to determine the degree of BBB breakdown following blast injury, ELISA was conducted for tight junction proteins occludin and claudin-5 for control, blast, and blast + apocynin groups (Fig. 3). Occludin decreased by 20.3% four hours post-blast compared to controls (ANOVA followed by Tukey test, $p = 0.002$), but barely changed in animals treated with apocynin (Tukey test, $p = 0.946$). The difference between the blast group and the treatment group was also significant (Tukey test, $p = 0.001$). Claudin-5 also displayed a similar trend of decrease in animals four hours post-blast compared to controls (Tukey test, $p = 0.001$). But similar to occludin, apocynin treatment significantly reversed the reduction of clausin-5 (Fig. 3) as well.

Apocynin significantly reverses blood-brain barrier permeability changes 4 hours following blast injury. The extent of extravasation was evaluated in the frontal cortex at both fifteen minutes and four hours post-blast injury (Fig. 4). Our group previously displayed that extravasation of Evans blue was significant at both time points at moderate blast injury[18] and our current results also support our earlier observations. Blast injury caused a significant extravasation in frontal cortex as early as 15 min post injury. Interestingly, apocynin treatment did not attenuate the extravasation at this time point. At four hours post injury, there was a robust extravasation (1300 fold) of EB in the brain parenchyma compared to the control in the frontal cortex (ANOVA followed by Tukey test, $p < 0.01$) and such extravasation was completely attenuated by treatment with apocynin ($p < 0.01$).

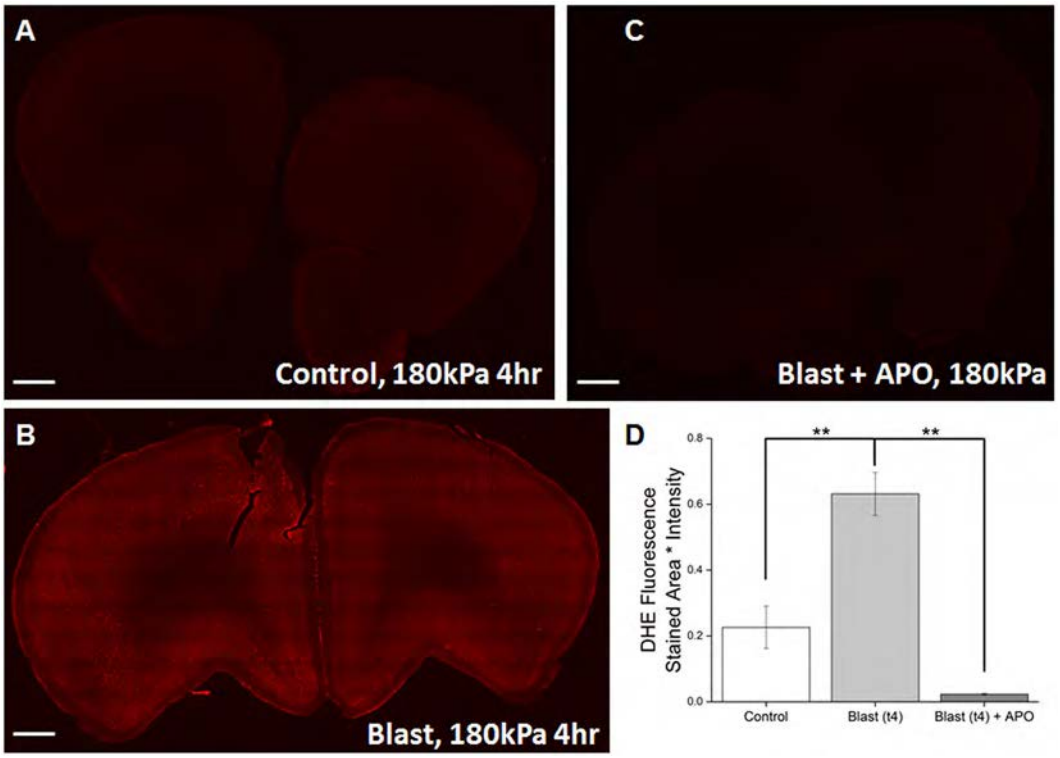


Figure 2. DHE fluorescence in frontal cortex indicating superoxide production. (**A**) Low level of flurescence intensity in control tissue, basal level of superoxide. (**B**) Levels of superoxide robustly increase four hours following blast exposure, (**C**,**D**). Supreoxide is brought back down to basal levels with pretreatment of apocynin Quantitation of DHE fluorescence intensity for the three aforementioned groups. Scale bar = 1 mm. **Indicates a difference between control ((n = 4) and blast groups (n = 4) as well as blast + apocynin group (n = 4) with a statistical significance of $p < 0.01$.

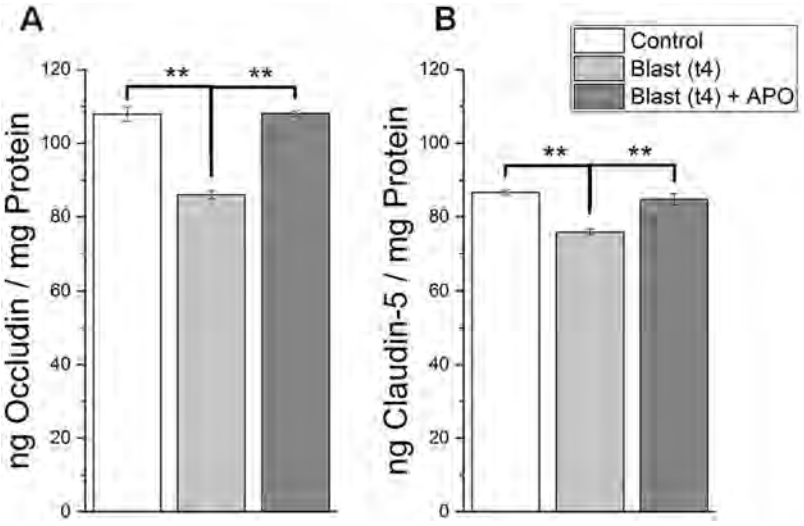


Figure 3. Levels of tight junction proteins, occludin and claudin-5 in control and blast groups as determined by ELISA. (**A**) Shows levels of occludin determined four hours after exposure and compared against controls. (**B**) Shows levels of clasudin-5 in control (n = 5), blast (n = 5), and apocynin treatment groups (n = 5). *Indicates a difference in intensity with a statistical significance of $p < 0.05$, ** Indicates $p < 0.01$.

Moderate blast induces translocation of glial fibrillary acidic protein into the blood stream. Concentration of GFAP in the blood plasma was determined by ELISA (Fig. 5). Statistically significant increase in GFAP concentration was seen compared to controls in both blast and apocynin treatment groups 15 minutes after

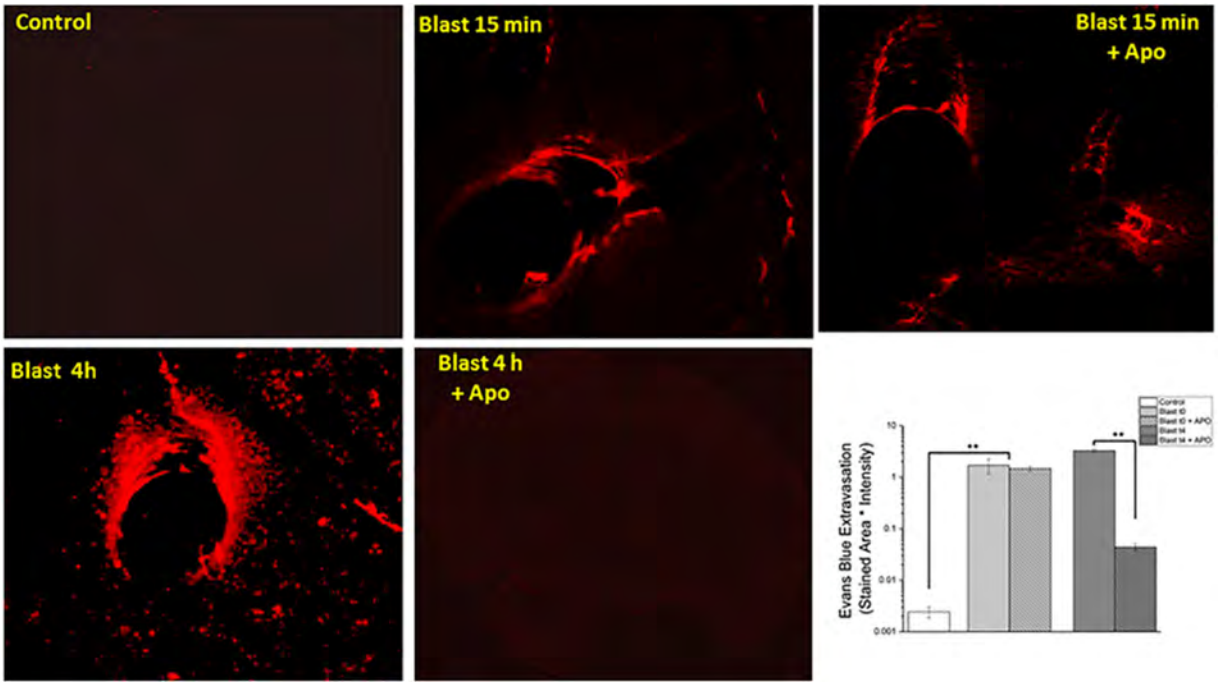


Figure 4. Fluorescence images of Evans blue extravasation. Images at 20x magnification in the frontal cortex in control (n = 4), animals exposed to blast (180 kPa BOP) (n = 4) and apocynin treated groups (n = 4). (**A**) Cortical section of a control animal, with almost no observable extravasation of leakage. Note that blast caused robust extravasation as early as 15 min post-injury and such extravasation was much more pronounced 4 h after the blast injury. A pretreatment with apocynin did not attenuate EB extravasation in animals immediately (15 min) following blast, whereas apocynin completely inhibited the extravasation 4 h post injury, strongly suggesting that acute BBB permeability is a result of direct mechanical loading by stress wave causing vascular rupture. Quantitation of extravasation is shown using a semilog plot in order magnitude differences. Scale bar = 30 μm ** Indicates a difference in intensity with a statistical significance of $p < 0.01$.

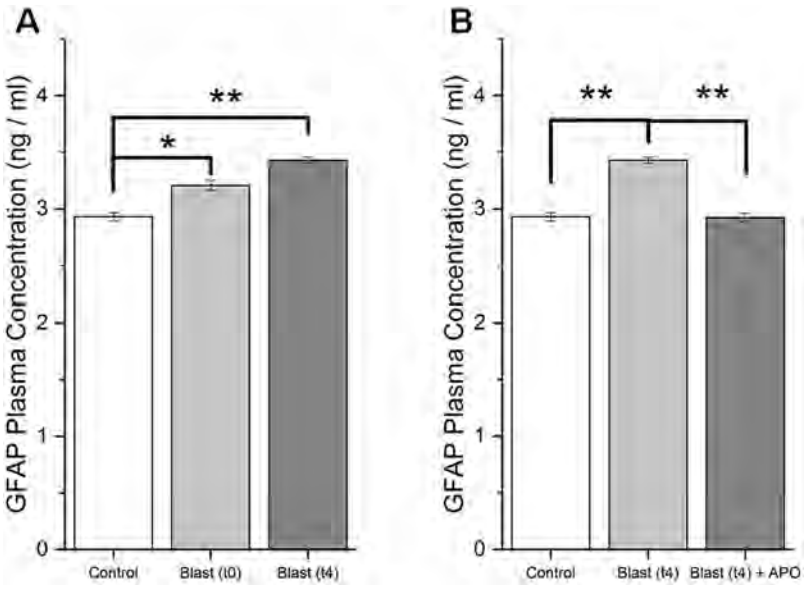


Figure 5. GFAP concentration in blood plasma as determined by ELISA. (**A**) Levels of GFAP in Control (n = 5), 15 minutes post-blast (n = 5) and 4 hours post-blast (n = 5). (**B**) GFAP levels in animals 4 hours following blast with and without apocynin pretreatment (n = 5). * Indicates a difference in intensity with a statistical significance of $p < 0.05$, ** Indicates $p < 0.01$.

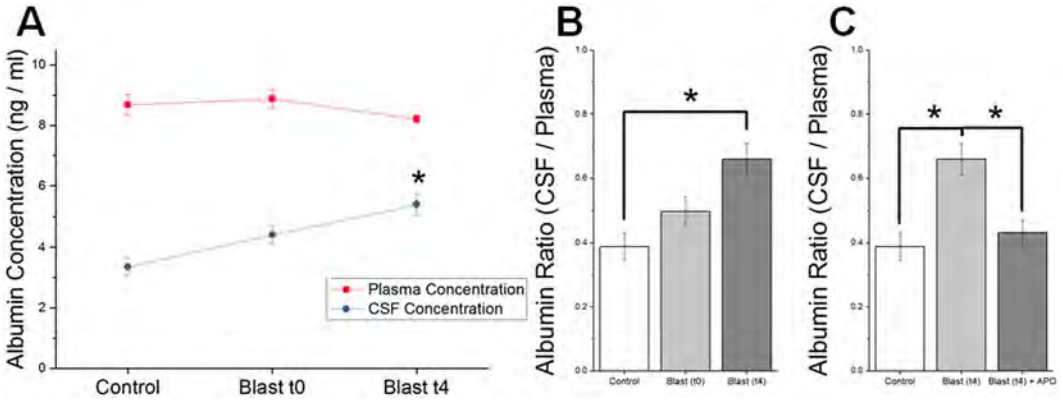


Figure 6. Effect of apocynin on blood-CSF albumin ratio in animals exposed to blast injury. (**A**) Levels of albumin concentration in CSF and blood plasma as determined by ELISA. * Indicates a difference in intensity compared with control with a statistical significance of $p < 0.05$. (**B,C**) Ratio of albumin concentration in CSF and blood plasma in control ($n = 5$), 15 min ($n = 5$) and 4 hours ($n = 5$) following blast compared with and without apocynin pretreatment ($n = 5$). * Indicates a difference in intensity with a statistical significance of $p < 0.05$.

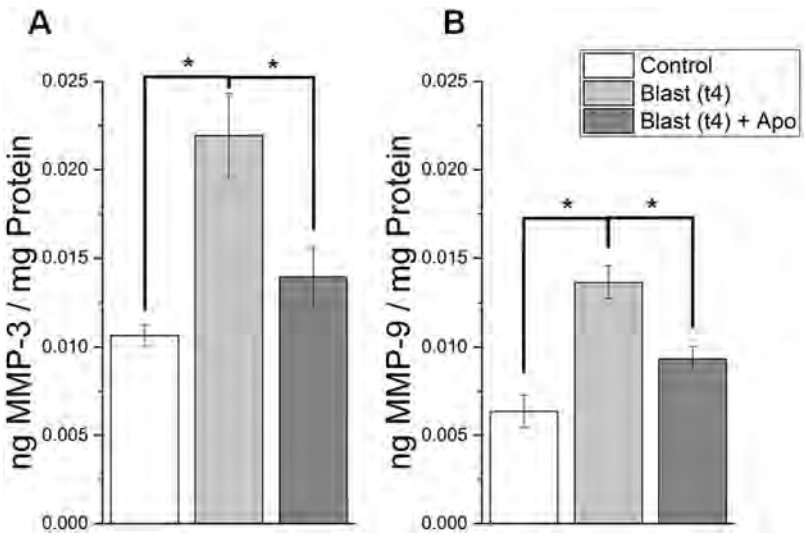


Figure 7. Effect of apocynin on protein levels of matrix metalloproteinases 3 (**A**) and 9 (**B**) in control ($n = 5$), blast ($n = 5$), and apocynin treatment groups ($n = 5$). * Indicates a difference in intensity with a statistical significance of $p < 0.05$.

injury (post-ANOVA Tukey test, $p = 0.016$ and $p = 0.002$, respectively), whereas apocynin did not alter its levels compared to blast group. At four hours post-blast, there is a further increase in GFAP concentration in blood plasma (Tukey test, $p = 0.002$), and treatment with apocynin showed a complete restoration of GFAP to that of control levels (Tukey test, $p > 0.05$). Intergroup comparison reveals a statistically significant difference between blast and treatment groups four hours after injury (Tukey test, $p = 0.001$).

CSF-Plasma ratio of albumin increases following moderate blast injury. In order to determine the ratio of albumin in the CSF and blood plasma, ELISA was conducted on both samples (Fig. 6). While an increase in the CSF-Plasma albumin ratio was observed acutely (fifteen minutes post-blast) for both blast and treatment groups, statistical significance was not achieved in either ($p > 0.05$). It should be noted that CSF-plasma ratio is used as a gold standard in clinical settings to determine BBB breakdown[42]. Four hours following blast, a statistically significant increase over control was observed in the injured group (post-ANOVA Tukey test, $p = 0.044$). Comparison between blast and treatment group at this point also revealed statistically significant difference (Tukey test, $p = 0.048$).

Apocynin mitigates the increase of matrix metalloproteinase 3 and 9 following blast injury. In order to examine the role of matrix metalloproteinases in the breakdown of the BBB, we conducted an ELISA for MMPs 3 & 9 for control, blast, and blast + apocynin groups (Fig. 7). MMP3 increased by 105% (ANOVA followed by Tukey test, $p = 0.020$) compared to controls in the injured group, while the difference between the

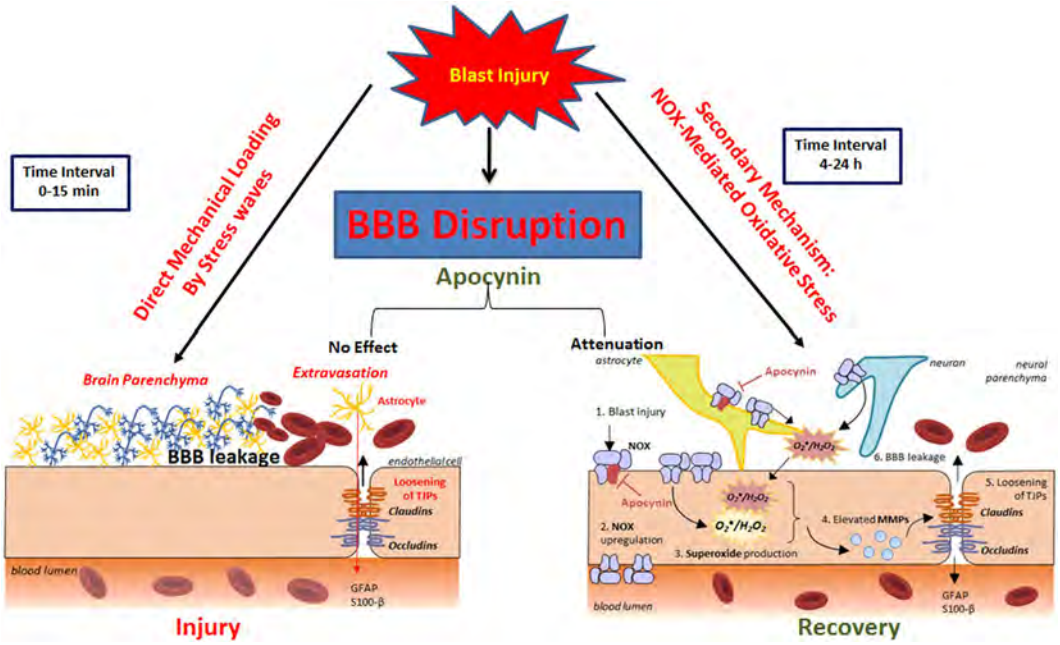


Figure 8. Schematic illustrating the primary and secondary events that contribute to BBB permeability changes following blast TBI. The left panel represents the primary damage caused by direct mechanical loading by stress wave rupturing the vasculature immediately (t0–t15 min) following blast without any biochemical events. The right panel represents secondary biochemical mechanisms such as oxidative stress that are activated by blast, exacerbate the primary mechanical injury to vasculature. Oxidative stress derived by the upregulation of NOX on neurovascular endothelial cells (and other neural cells) cause increased superoxide production both within and outside the endothelial cells. This superoxide elevates MMP production, which breaks down the tight junction complexes connecting adjacent endothelial cells, causing increased permeability of the BBB. Use of apocynin prevents the translocation of the NOX p47 phox subunit, thereby preventing the increase in superoxide production in the later stages of BBB permeability but not immediately after blast.

blast + apocynin and control groups was not statistically significant (Tukey test, $p > 0.05$). Similarly, MMP9 increased by 115% (Tukey test, $p = 0.007$) compared to the controls in the injured group, but the difference between blast + apocynin and control groups was not statistically significant (Tukey test, $p > 0.05$). However, it is important to note that there is still an observed increase in both MMP3 and MMP9 in the blast + apocynin groups, which suggests that NOX activation and subsequent superoxide production *per se* are responsible for MMP activation.

Discussion

This work aims to investigate the role of NOX-mediated oxidative stress as a mechanism for increased BBB permeability in blast-induced traumatic brain injury, immediately following blast and further increase between blast and 4 hours post-blast. Using apocynin, which inhibits the assembly of various NOX subunits rendering the enzyme inactive, we found that apocynin significantly attenuated the extravasation, preventing the reduction in tight junction proteins as well as reduced the levels of MMPs, between the time points of blast and 4 hours post-exposure. These data together strongly suggest that NOX-mediated oxidative stress significantly contributes to BBB permeability.

It should however be noted that in the current study, we employed apocynin as a proof of concept to examine whether oxidative stress contributes to BBB disruption after blast exposure, rather than a therapeutic paradigm. Additionally, we sought to examine whether apocynin has any impact on BBB permeability changes that we earlier observed immediately (15 min) following blast exposure. Accordingly, apocynin was administered 30 min prior to blast exposure. Noteworthy that apocynin did not show any beneficial effects during the acute phase (15 min) of the injury (biomechanical phase) suggesting that oxidative stress and associated effects on BBB permeability are predominantly secondary biochemical factors. As shown in Fig. 8, while the initial disruption of BBB in the acute phase could possibly be attributed to direct mechanical loading on vasculature caused by shock-wave, effects seen past the initial stage ought to arise from biochemical effects. As discussed in our earlier work, BBB breakdown can occur both as a direct consequence of mechanical stress wave interaction with vasculature in the immediate stages and continue to increase at 4 h post injury. What we needed to demonstrate is that while apocynin has the ability to reduce oxidative stress induced BBB permeability (secondary) but it could not mitigate the mechanical breakdown. This critical factor would not have been ascertained if the apocynin is administered post-blast.

The pharmacokinetics and the bioavailability of apocynin have been well established. Apocynin appears to be a stable compound once administered into the system with a bioavailability of >8%; half-life of the compound has

been determined using LC-MS to be 48 h in the blood circulation[43,44]. A dose of 5 mg/kg employed in the current study also has been used by several investigators to examine the role of NOX-mediated responses in various experimental conditions including stroke[37,45], and blunt model of TBI[46–51]. A complete restoration of blast-induced BBB permeability at 4-hours' time point by apocynin strengthens our hypothesis that though initial BBB increase is minimal, sustained BBB disruption is primarily contributed by oxidative stress. However, few studies have reported anti-inflammatory properties of apocynin. Thus, Anter *et al*., [52] reported that topical application of apocynin showed anti-inflammatory properties as indicated by reduction in paw swelling in rats. Likewise, another study showed that apocynin significantly reduced the levels of TNF-alpha in animals subjected lateral fluid percussion model of TBI[53,54]. Additionally, diapocynin (a dimer of apocynin) significantly reduced microglial activation in MPTP model of Parkinson disease[55]. Further, apocynin derivative dihydrocoumarin also exerted anti-inflammatory properties *in vitro* in erythrocytes subjected to oxidative injury[56]. Similarly, apocynin has shown anti-inflammatory effects in mouse model of stroke[57] by reducing the NLRP3 inflammasome. Taken together, these reports also attribute anti-inflammatory actions of apocynin. Noteworthy that we identified robust activation of microglia as early as 4 h after moderate blast injury (180 kPa) (unpublished observation) and that such activation was more pronounced near the site of vascular rupture (increased blood brain barrier permeability) we observed earlier[18] as well as in the current study. Based on these reports, it is also likely that protective effect of apocynin in the present study may in part mediated by suppressing the neuroinflammation following blast injury.

In the present study, we observed a robust (10-fold) increase in NOX1 expression four hours following blast injury in endothelial cells in the frontal cortex as demonstrated by double immunofluorescence staining of NOX1 with RECA-1, an endothelial cell marker. Our recent observations along with other investigations also report increased activation of NOX1 between four hours and a few days in animal models of TBI[15,17,46,54,58].

In order to confirm that increased NOX1 expression activates downstream pathways, we examined the superoxide production by prior administration of dihydroethidium (DHE). There was a robust increase in superoxide production in animals subjected to blast injury, which parallels the increased NOX1 expression on vascular endothelial cells. While precise cellular origin of superoxide in the present study is not identified, it is highly likely that the superoxide produced by neural cells including neurons, astrocytes and microglia as a result of increased activation of NOX[17] may exert a paracrine effect on vascular endothelial cells and cause BBB disruption. Alternatively, vascular endothelial cells *per se* could produce superoxide since our current study display a robust increase in NOX1 levels following blast in these cells, and such superoxide production within the endothelial cells would have caused BBB disruption in an autocrine mechanism. We further established that the superoxide production regardless of its cellular origin, is indeed mediated by NOX1 expression as apocynin inhibits assembly of NOX subunits and renders NOX functionally inactive, completely reducing the production of superoxide consistent with our previous work[17].

It is interesting to note that our present study observed a close correlation between increased NOX1 expression, its associated increase in superoxide production, and the heightened disruption of the BBB 4 hours after blast injury[18]. The BBB permeability changes were represented not only by the extravasation of EB but also by the reduced levels of tight junction proteins as well as cross translocation of substances between brain and blood and *vice versa*. A significant reduction in both occludin and claudin-5, four hours after blast injury is consistent with extravasation of tracers since loss of tight junction protein integrity is well known to allow leakage of tracers and other blood borne macromolecules into brain parenchyma. Accordingly, increased presence of astrocytic protein, GFAP, in plasma as well as increased CSF-blood ratio of albumin observed in the present study confirm the reciprocal translocation of brain and blood-borne macromolecules as a result of BBB disruption. Noteworthy that a pretreatment with apocynin significantly attenuated the extravasation of tracers, prevented the loss of TJPs and brought back the CSF-blood albumin ratio to that of controls, as well as attenuated increased presence of GFAP in plasma. Together these data again strongly suggest that NOX-mediated oxidative stress contributes to heightened BBB disruption four hours following blast injury.

Several groups have attempted to establish a connection between oxidative stress and BBB breakdown by implicating matrix metalloproteinases[15,59–63]. MMPs are endopeptidases that degrade the extracellular matrix (ECM) in various cell types. While the activity of MMPs are tightly controlled in normal, "uninjured" conditions by endogenous MMP inhibitors, uncontrolled activation has been observed due to oxidative stress[15,64–67]. This in-turn degrades the brain endothelium and substantially increases the permeability of the BBB. The role of MMPs in BBB degradation has been well-investigated[15,59–63]. The present study showed that the levels of both MMP3 and MMP9 significantly increased over controls four hours after blast exposure. Rats pretreated with apocynin displayed significant reduction in the levels of MMPs as compared to animals subjected to blast injury again indicates that NOX-mediated oxidative stress contributes to increase in MMPs, likely leading to degradation of tight junction proteins ultimately causing BBB breakdown.

While it is strongly suggested that oxidative stress is a secondary event that contributes to heightened BBB disruption in the later stages after blast injury, we further extended studies to address whether BBB disruption immediately after blast injury is caused by a direct mechanical loading or in part mediated by any presence of oxidative stress. Accordingly, the ability of apocynin to reduce BBB breakdown only at 4 h post injury but not in the acute phase (prior to 4 h post-injury) in conjunction with our observation of robust increase in NOX1 four hours after blast strongly suggest that oxidative stress appears to be a secondary event occurring following blast injury. Further, our study also strongly suggests that the disruption of BBB immediately after blast is attributable to a direct mechanical loading created by shockwave. Figure 8 illustrates how primary mechanical damage and secondary events such as oxidative stress caused BBB disruption following blast TBI.

It is notable that although we did not observe any changes in the neurological severity scores (NSS) following blast, our recent studies display that either single blast injury at moderate BOP (180 kPa) or repeated (5 successive times) low-level blast (70 kPa) resulted in significant neurobehavioral deficits as identified by anxiety/depression like symptoms, loss of short-term memory as well as sleep disturbances (unpublished observations). Together these observations strongly suggest that (1). Blast induces long-term neurobehavioral deficits and (2). There will

be a higher propensity that repeated blast exposures at lower BOP will cumulatively impact on the neurobehavioral changes, in both conditions without any overt NNS NSS change.

In summary, our studies demonstrate that moderate blast injury causes disruption of BBB by loss of TJPs and results in leakage of macromolecules across brain-to-blood as well as increase in NOX expression on vascular endothelial cells and associated increased production of superoxide 4 h after blast injury. BBB breakdown occurs immediately due to direct stress-cell interactions, and further increase in BBB between injury and 4 hours can be attributed to oxidative stress. These events corroborate with the heightened activation of MMP-3 and MMP-9. Pretreatment with NOX inhibitor apocynin, BBB permeability is significantly reduced and the increase in MMPs levels were prevented. This study therefore indicates a strong relationship between NOX-mediated oxidative stress and blood brain barrier breakdown, which may lead to further investigation delineating relationships between other injury mechanisms, a prerequisite for better therapeutic interventions.

References

1. Ling, G. S. *et al*. Traumatic brain injury in modern war. *Current Opinion in Anesthesiology* **24**, 124–130 (2013).
2. Mathews, Z. R. & Koyfman, A. Blast injuries. *The Journal of Emergency Medicine* **49**, 573–587 (2015).
3. Moore, B. Blast injuries-a prehospital perspective. *Australasian Journal of Paramedicine* **4** (2015).
4. Bochicchio, G. V. *et al*. Blast injury in a civilian trauma setting is associated with a delay in diagnosis of traumatic brain injury. *The American Journal of Surgery* **74**, 267–270 (2008).
5. DuBose, J. J. *et al*. Isolated severe traumatic brain injuries sustained during combat operations: demographics, mortality outcomes, and lessons to be learned from contrasts to civilian counterparts. *Journal of Trauma* **70**, 11–16; discussion 16–18, https://doi.org/10.1097/TA.0b013e318207c563 (2011).
6. Reid, M. W. & Velez, C. S. Discriminating military and civilian traumatic brain injuries. *Molecular and Cellular Neuorscience* **66**, 123–128, https://doi.org/10.1016/j.mcn.2015.03.014 (2015).
7. Loane, D. J. & Faden, A. I. Neuroprotection for traumatic brain injury: translational challenges and emerging therapeutic strategies. *Trends in Pharmacological Sciences* **31**, 596–604, https://doi.org/10.1016/j.tips.2010.09.005 (2010).
8. Maas, A. I., Roozenbeek, B. & Manley, G. T. Clinical trials in traumatic brain injury: past experience and current developments. *Neurotherapeutics* **7**, 115–126 (2010).
9. Narayan, R. K. *et al*. Clinical trials in head injury. *Journal of Neurotrauma* **19**, 503–557 (2002).
10. Schouten, J. W. Neuroprotection in traumatic brain injury: a complex struggle against the biology of nature. *Current Opinion in Critical Care* **13**, 134–142 (2007).
11. Bayir, H., Kochanek, P. M. & Kagan, V. E. Oxidative stress in immature brain after traumatic brain injury. *Developmental Neuroscience* **28**, 420–431, https://doi.org/10.1159/000094168 (2006).
12. Cornelius, C. *et al*. Traumatic brain injury: oxidative stress and neuroprotection. *Antioxidants & Redox Signaling* **19**, 836–853, https://doi.org/10.1089/ars.2012.4981 (2013).
13. Koppula, S., Kumar, H., Kim, I. S. & Choi, D. K. Reactive oxygen species and inhibitors of inflammatory enzymes, NADPH oxidase, and iNOS in experimental models of Parkinson's disease. *Mediators of Inflammation* **2012**, 823902, https://doi.org/10.1155/2012/823902 (2012).
14. Lewen, A. & Hillered, L. Involvement of reactive oxygen species in membrane phospholipid breakdown and energy perturbation after traumatic brain injury in the rat. *Journal of Neurotrauma* **15**, 521–530 (1998).
15. Abdul-Muneer, P. M., Chandra, N. & Haorah, J. Interactions of oxidative stress and neurovascular inflammation in the pathogenesis of traumatic brain injury. *Molecular Neurobiology* **51**, 966–979, https://doi.org/10.1007/s12035-014-8752-3 (2015).
16. Mishra, V. *et al*. Primary blast causes mild, moderate, severe and lethal TBI with increasing blast overpressures: Experimental rat injury model. *Scientific Reports* **6**, 26992, https://doi.org/10.1038/srep26992 (2016).
17. Rama Rao, K. V. *et al*. A single primary blast-induced traumatic brain injury in rodent model causes cell-type dependent increase in NADPH oxidase isoforms in vulnerable brain regions. *Journal of Neurotrauma* (2018).
18. Kuriakose, M., Kakulavarapu, V., Younger, D. & Chandra, N. Temporal and spatial effects of blast overpressure on blood-brain barrier permeability in traumatic brain injury. *Scientific Reports* **8** (2018).
19. Baldwin, S. A., Fugaccia, I., Brown, D. R., Brown, L. V. & Scheff, S. W. Blood-brain barrier breach following cortical contusion in the rat. *Journal of Neurosurgery* **85**, 476–481 (1996).
20. Başkaya, M. K., Rao, A. M., Doğan, A., Donaldson, D. & Dempsey, R. J. The biphasic opening of the blood–brain barrier in the cortex and hippocampus after traumatic brain injury in rats. *Neuroscience Letters* **226**, 33–36 (1997).
21. Hicks, R. R., Baldwin, S. A. & Scheff, S. W. Serum extravasation and cytoskeletal alterations following traumatic brain injury in rats. *Molecular and Chemical Neuropathology* **32**, 1–16 (1997).
22. Higashida, T. *et al*. The role of hypoxia-inducible factor-1α, aquaporin-4, and matrix metalloproteinase-9 in blood-brain barrier disruption and brain edema after traumatic brain injury: laboratory investigation. *Journal of Neurosurgery* **114**, 92–101 (2011).
23. Shapira, Y., Setton, D., Artru, A. A. & Shohami, E. Blood-brain barrier permeability, cerebral edema, and neurologic function after closed head injury in rats. *Anesthesia & Analgesia* **77**, 141–148 (1993).
24. Elder, G. A. *et al*. Vascular and inflammatory factors in the pathophysiology of blast-induced brain injury. *Frontiers in Neurology* **6**, 48, https://doi.org/10.3389/fneur.2015.00048 (2015).
25. Hue, C. D. *et al*. Dexamethasone potentiates *in vitro* blood-brain barrier recovery after primary blast injury by glucocorticoid receptor-mediated upregulation of ZO-1 tight junction protein. *Journal of Cerebral Blood Flow & Metabolism* **35**, 1191–1198 (2015).
26. Kawoos, U., Gu, M., Lankasky, J., McCarron, R. M. & Chavko, M. Effects of exposure to blast overpressure on intracranial pressure and blood-brain barrier permeability in a rat model. *PloS One* **11**, e0167510 (2016).
27. Readnower, R. D. *et al*. Increase in blood-brain barrier permeability, oxidative stress, and activated microglia in a rat model of blast-induced traumatic brain injury. *Journal of Neuroscience Research* **88**, 3530–3539, https://doi.org/10.1002/jnr.22510 (2010).
28. Shetty, A. K., Mishra, V., Kodali, M. & Hattiangady, B. Blood brain barrier dysfunction and delayed neurological deficits in mild traumatic brain injury induced by blast shock waves. *Frontiers in Cellular Neuroscience* **8** (2014).
29. Yeoh, S., Bell, E. D. & Monson, K. L. Distribution of blood-brain barrier disruption in primary blast injury. *Annals of Biomedical Engineering* **41**, 2206–2214, https://doi.org/10.1007/s10439-013-0805-7 (2013).
30. Abdul Muneer, P. M., Alikunju, S., Szlachetka, A. M. & Haorah, J. The mechanisms of cerebral vascular dysfunction and neuroinflammation by MMP-mediated degradation of VEGFR-2 in alcohol ingestion. *Arterioscler Thromb Vasc Biol* **32**, 1167–1177, https://doi.org/10.1161/ATVBAHA.112.247668 (2012).
31. Jenner, P. Oxidative damage in neurodegenerative disease. *The Lancet* **344**, 796–798 (1994).
32. Uttara, B., Singh, A. V., Zamboni, P. & Mahajan, R. Oxidative stress and neurodegenerative diseases: a review of upstream and downstream antioxidant therapeutic options. *Current Neuropharmacology* **7**, 65–74 (2009).
33. Chandra, N., Holmberg, A. & Feng, R. Controlling the shape of the shock wave profile in a blast facility. *US Provisional patent application* **61542354** (2011).

34. Chandra, N., Sundaramurthy, A. & Gupta, R. K. Validation of Laboratory Animal and Surrogate Human Models in Primary Blast Injury Studies. *Military Medicine* **182**, 105–113, https://doi.org/10.7205/milmed-d-16-00144 (2017).
35. Kuriakose, M. *et al*. Tailoring the blast exposure conditions in the shock tube for generating pure, primary shock waves: The end plate facilitates elimination of secondary loading of the specimen. *PloS One* **11**, e0161597 (2016).
36. Ferreira, A. P. *et al*. The effect of NADPH-oxidase inhibitor apocynin on cognitive impairment induced by moderate lateral fluid percussion injury: role of inflammatory and oxidative brain damage. *Neurochem Int* **63**, 583–593, https://doi.org/10.1016/j.neuint.2013.09.012 (2013).
37. Paterniti, I. *et al*. Protective effects of apocynin, an inhibitor of NADPH oxidase activity, in splanchnic artery occlusion and reperfusion. *J Leukoc Biol* **88**, 993–1003, https://doi.org/10.1189/jlb.0610322 (2010).
38. Mitazaki, S. *et al*. Apocynin reduced doxycycline-induced acute liver injury in ovariectomized mice. *Toxicol Rep* **3**, 357–363, https://doi.org/10.1016/j.toxrep.2016.02.003 (2016).
39. Kim, J. H. *et al*. Post-treatment of an NADPH oxidase inhibitor prevents seizure-induced neuronal death. *Brain Research* **1499**, 163–172, https://doi.org/10.1016/j.brainres.2013.01.007 (2013).
40. Fernandez, V., Barrientos, X., Kipreos, K., Valenzuela, A. & Videla, L. A. Superoxide radical generation, NADPH oxidase activity, and cytochrome P-450 content of rat liver microsomal fractions in an experimental hyperthyroid state: relation to lipid peroxidation. *Endocrinology* **117**, 496–501, https://doi.org/10.1210/endo-117-2-496 (1985).
41. Infanger, D. W., Sharma, R. V. & Davisson, R. L. NADPH oxidases of the brain: distribution, regulation, and function. *Antioxidants & Redox Signaling* **8**, 1583–1596, https://doi.org/10.1089/ars.2006.8.1583 (2006).
42. Parrado-Fernandez, C. *et al*. Evidence for sex difference in the CSF/plasma albumin ratio in ~20 000 patients and 335 healthy volunteers. *J Cell Mol Med* **22**, 5151–5154, https://doi.org/10.1111/jcmm.13767 (2018).
43. Chandasana, H. *et al*. Pharmacokinetic, bioavailability, metabolism and plasma protein binding evaluation of NADPH-oxidase inhibitor apocynin using LC-MS/MS. *J Chromatogr B Analyt Technol Biomed Life Sci* **985**, 180–188, https://doi.org/10.1016/j.jchromb.2015.01.025 (2015).
44. Wang, Q. *et al*. Bioavailability of apocynin through its conversion to glycoconjugate but not to diapocynin. *Phytomedicine* **15**, 496–503, https://doi.org/10.1016/j.phymed.2007.09.019 (2008).
45. Tang, X. N., Cairns, B., Cairns, N. & Yenari, M. A. Apocynin improves outcome in experimental stroke with a narrow dose range. *Neuroscience* **154**, 556–562, https://doi.org/10.1016/j.neuroscience.2008.03.090 (2008).
46. Choi, B. Y. *et al*. Prevention of traumatic brain injury-induced neuronal death by inhibition of NADPH oxidase activation. *Brain Research* **1481**, 49–58, https://doi.org/10.1016/j.brainres.2012.08.032 (2012).
47. Loane, D. J., Stoica, B. A., Byrnes, K. R., Jeong, W. & Faden, A. I. Activation of mGluR5 and inhibition of NADPH oxidase improves functional recovery after traumatic brain injury. *Journal of neurotrauma* **30**, 403–412 (2013).
48. Lu, X.-Y., Wang, H.-D., Xu, J.-G., Ding, K. & Li, T. NADPH oxidase inhibition improves neurological outcome in experimental traumatic brain injury. *Neurochemistry international* **69**, 14–19 (2014).
49. Zhang, Q.-G. *et al*. Critical role of NADPH oxidase in neuronal oxidative damage and microglia activation following traumatic brain injury. *PloS one* **7**, e34504 (2012).
50. Kahles, T. *et al*. NADPH oxidase plays a central role in blood-brain barrier damage in experimental stroke. *Stroke* **38**, 3000–3006, https://doi.org/10.1161/STROKEAHA.107.489765 (2007).
51. Rochfort, K. D., Collins, L. E., Murphy, R. P. & Cummins, P. M. Downregulation of blood-brain barrier phenotype by proinflammatory cytokines involves NADPH oxidase-dependent ROS generation: consequences for interendothelial adherens and tight junctions. *PLoS One* **9**, e101815, https://doi.org/10.1371/journal.pone.0101815 (2014).
52. Anter, H. M., Abu, H. II, Awadin, W. & Meshali, M. M. Novel anti-inflammatory film as a delivery system for the external medication with bioactive phytochemical "Apocynin". *Drug Des Devel Ther* **12**, 2981–3001, https://doi.org/10.2147/DDDT.S176850 (2018).
53. Ghosh, A. *et al*. Anti-inflammatory and neuroprotective effects of an orally active apocynin derivative in pre-clinical models of Parkinson's disease. *J Neuroinflammation* **9**, 241, https://doi.org/10.1186/1742-2094-9-241 (2012).
54. Ferreira, A. P. *et al*. The effect of NADPH-oxidase inhibitor apocynin on cognitive impairment induced by moderate lateral fluid percussion injury: role of inflammatory and oxidative brain damage. *Neurochemistry International* **63**, 583–593, https://doi.org/10.1016/j.neuint.2013.09.012 (2013).
55. Kim, S. Y. *et al*. Anti-inflammatory effects of apocynin, an inhibitor of NADPH oxidase, in airway inflammation. *Immunol Cell Biol* **90**, 441–448, https://doi.org/10.1038/icb.2011.60 (2012).
56. Paracatu, L. C. *et al*. Synthesis, Antioxidant and Anti-inflammatory Properties of an Apocynin- Derived Dihydrocoumarin. *Med Chem* **13**, 93–100, https://doi.org/10.2174/1573406412666160610093216 (2016).
57. Qin, Y. Y. *et al*. Combined NADPH and the NOX inhibitor apocynin provides greater anti-inflammatory and neuroprotective effects in a mouse model of stroke. *Free Radic Biol Med* **104**, 333–345, https://doi.org/10.1016/j.freeradbiomed.2017.01.034 (2017).
58. Song, S. X. *et al*. Attenuation of brain edema and spatial learning deficits by the inhibition of NADPH oxidase activity using apocynin following diffuse traumatic brain injury in rats. *Molecular Medicine Reports* **7**, 327–331, https://doi.org/10.3892/mmr.2012.1147 (2013).
59. Grossetete, M., Phelps, J., Arko, L., Yonas, H. & Rosenberg, G. A. Elevation of matrix metalloproteinases 3 and 9 in cerebrospinal fluid and blood in patients with severe traumatic brain injury. *Neurosurgery* **65**, 702–708 (2009).
60. Hanumegowda, U. M. *et al*. Basement membrane and matrix metalloproteinases in monocrotaline-induced liver injury. *Toxicological Sciences* **76**, 237–246 (2003).
61. Jia, F., Pan, Y.-h, Mao, Q., Liang, Y.-m & Jiang, J.-Y. Matrix metalloproteinase-9 expression and protein levels after fluid percussion injury in rats: the effect of injury severity and brain temperature. *Journal of Neurotrauma* **27**, 1059–1068 (2010).
62. Reijerkerk, A. *et al*. Diapedesis of monocytes is associated with MMP-mediated occludin disappearance in brain endothelial cells. *The FASEB journal* **20**, 2550–2552 (2006).
63. Rosell, A. *et al*. Increased brain expression of matrix metalloproteinase-9 after ischemic and hemorrhagic human stroke. *Stroke* **37**, 1399–1406 (2006).
64. Galli, A. *et al*. Oxidative stress stimulates proliferation and invasiveness of hepatic stellate cells via a MMP2-mediated mechanism. *Hepatology* **41**, 1074–1084 (2005).
65. Gasche, Y. *et al*. Early appearance of activated matrix metalloproteinase-9 after focal cerebral ischemia in mice: a possible role in blood—brain barrier dysfunction. *Journal of Cerebral Blood Flow & Metabolism* **19**, 1020–1028 (1999).
66. Kim, G. W. *et al*. Neurodegeneration in striatum induced by the mitochondrial toxin 3-nitropropionic acid: role of matrix metalloproteinase-9 in early blood-brain barrier disruption? *Journal of Neuroscience* **23**, 8733–8742 (2003).
67. Machado, L. S. *et al*. Delayed minocycline inhibits ischemia-activated matrix metalloproteinases 2 and 9 after experimental stroke. *BMC Neuroscience* **7**, 56 (2006).

Acknowledgements

This work was supported by U.S Army Medical Research and Materiel Command project *Primary Blast Injury Criteria for Animal/Human TBI Models using Field Validated Shock Tube*, grant number: 14059001 (PI: Dr. Namas Chandra). Authors gratefully acknowledge Jose Rodrigues, Stephanie Iring, Madison Taylor, and Smit Shah and Madhuvika Murugan for their contributions to this work.

Author Contributions

M.K., K.V.R. and N.C. wrote the main manuscript text, M.K. and K.V.R. A.R. and D.Y. conducted experiments described in this work and E.A. performed blast exposures to animals. M.M. assisted in the preparation of schematic diagram. All authors reviewed the manuscript.

Additional Information

Competing Interests: The authors declare no competing interests.

Publisher's note: Springer Nature remains neutral with regard to jurisdictional claims in published maps and institutional affiliations.

Open Access This article is licensed under a Creative Commons Attribution 4.0 International License, which permits use, sharing, adaptation, distribution and reproduction in any medium or format, as long as you give appropriate credit to the original author(s) and the source, provide a link to the Creative Commons license, and indicate if changes were made. The images or other third party material in this article are included in the article's Creative Commons license, unless indicated otherwise in a credit line to the material. If material is not included in the article's Creative Commons license and your intended use is not permitted by statutory regulation or exceeds the permitted use, you will need to obtain permission directly from the copyright holder. To view a copy of this license, visit http://creativecommons.org/licenses/by/4.0/.

© The Author(s) 2019

Appendix A –Publication Cover 8
2019

Authors: X. Ma, A. Aravind, BJ Pfister, N. Chandra and J. Haorah

Title: *"Animal models of traumatic brain injury and assessment of injury severity"*

Journal Publication: Molecular Neurobiology, https://doi.org/10.1007/s12035-018-1454-5, 1-14, (2019), [19-8]

Molecular Neurobiology
https://doi.org/10.1007/s12035-018-1454-5

Animal Models of Traumatic Brain Injury and Assessment of Injury Severity

Xiaotang Ma[1] · Aswati Aravind[1] · Bryan J. Pfister[1] · Namas Chandra[1] · James Haorah[1]

Received: 4 October 2018 / Accepted: 7 December 2018
© Springer Science+Business Media, LLC, part of Springer Nature 2019

Abstract

Traumatic brain injury (TBI) contributes a major cause of death, disability, and mental health disorders. Most TBI patients suffer long-term post-traumatic stress disorder, cognitive dysfunction, and disability. The underlying molecular and cellular mechanisms of such neuropathology progression in TBI remain elusive. In part, it is due to non-standardized classification of mild, moderate, and severe injury in various animal models of TBI. Thus, a better diagnosis and treatment requires a better understanding of the injury mechanisms in a well-defined severity of mild, moderate, and severe injury in different models that may potentially reflect the various types of human brain injuries. The purpose of this review article is to highlight the classification of mild, moderate, and severe injury in various animal models of TBI with special focus on mixed injury that represents a translational concussive head injury. We will classify animal models of TBI broadly into focal injury, diffuse injury, and mixed injury. Focal injury, a localized injury, is represented by animal models of controlled cortical impact, penetrating ballistic-like brain injury, and Feeney or Shohami weight drop injury. A global diffuse injury is best represented by shock tube model of primary blast injury, and Marmarou or Maryland weight drop model. A mixed injury consists of focal and diffuse injury which reproduces the concussive clinical syndrome, and it is best studied in animal model of lateral fluid percussion injury.

Keywords Traumatic brain injury · Animal models · Injury severity · Mixed injury · Focal injury · Diffuse injury

Introduction

Traumatic brain injury (TBI) is caused by an external mechanical force such as concussive head injury, penetration of objects, sudden acceleration-deceleration of motor vehicle accidents, and propagation of supersonic blast waves [1]. There are about 1.7 million people who suffer TBI each year in the USA, which accounts for more than 3 million people living with a life-long disability [2]. The number of TBI incidence is still rising with 2.8 million TBI-related emergency hospital visits and deaths in 2013 in the USA, consisting of about 54% children and 79% seniors that resulted from falls [3]. The incidence of motor vehicle accidents, athletic sports head injury, and blast-wave diffuse injury is also a major cause of TBI [4]. Many of these brain injuries when left untreated properly lead to development of cognitive/behavioral impairment [5, 6], PTSD [7–9], chronic encephalopathy [10–12], epileptic seizure [13, 14], and neurodegenerative Alzheimer's disease [15–17]. The prevention of TBI-related neurodegenerative disorders has not been satisfactorily successful despite the number of clinical trials and treatment [18, 19], which was partly attributed to clinical irrelevance of the animal models [20]. Yet, we have to consider the fact that TBI in itself involves complex mechanisms of brain injuries in human, which poses challenges for accurate replication of human TBI in animal models. Thus, there is not a single animal model that can accurately mimic human brain injury [21]. However, animal models of TBI offer the best alternative to examine the biomechanical, cellular, and molecular mechanisms of TBI-associated neuropathological progression and the time-dependent effects.

The assessment of injury severity post-TBI has played a critical role for an effective evaluation of therapeutic treatments. In clinical settings, the Glasgow Coma Scale (GCS) [22, 23] or improved/extended GCS (GCSE) [23] is used for the severity of TBI diagnosis and prognosis. The GCS is based on a 15-point neurological scale according to eye, verbal, and motor movements. The clinical guidelines incorporating duration of loss of

✉ James Haorah
james.haorah@njit.edu

[1] Laboratory of Neurovascular Inflammation and Neurodegeneration, Department of Biomedical Engineering, Center for Injury Bio Mechanics, Materials and Medicine, New Jersey Institute of Technology, Newark, NJ 07102, USA

Published online: 02 January 2019

unconsciousness and structural imaging with GSC classify human TBI into mild, moderate, and severe level. However, there is no established guideline or standard to assess injury severity in experimental TBI, which makes it challenging for animal model findings to a clinical translation. Such differential parameters for a consensus standardization of injury severity in various TBI models include the mechanical parameters like the peak pressure and duration [24]; neurological changes like apnea, righting reflex time, and pinna reflex [25]; physiological changes like weight loss and intracranial pressure increment [26]; histological changes like infarct volume and neuronal loss [27]; and behavioral changes like the neurological severity score (NSS) and motor function tests [28]. Even though there is no consensus on grading standard injury severity, this review article provides the up-to-date knowledge on severity of injury criteria for each model based on focal, diffuse, and mixed injury. We also discuss on the use of mortality rate and brain infarct volume as possible standard criteria for defining mild, moderate, and severe injury.

Table 1 shows the animal models of TBI, the types of injury, the clinical relevance, and the strengths or the weaknesses of each TBI model within the category of focal, diffuse, and mixed mechanisms of injury. The principal mechanisms of focal brain injury known as the localized tissue damage resulted from a blow to the head, car accidents, or violent assaults, while diffuse injury is caused by acceleration or deceleration impact including the unrestricted head movement in motor vehicle accidents or blast-wave propagation [29]. The mixed injury model represents the types of head injury resulted from falls or athletic sports injury. In this review article, the rat model of fluid percussion injury (FPI) typifies the mixed injury, the open-skull controlled cortical impact (CCI) model mimics the focal injury, and shock-wave model represents the mechanisms of diffuse injury. Irrespective of focal, diffuse, or mixed type of injury, the nature of TBI involves the damage mechanisms of primary and secondary injury. Primary injury is directly caused by mechanical pulse/force that includes surface contusion, blood vessel damage, laceration, hemorrhage, and perhaps axonal shearing [26]. The secondary injury is a consequential event of the primary injury that involves the cascade of biochemical activation including molecular, cellular, and metabolic events that lead to neuroinflammation, neurodegeneration, and atrophy [11]. The biochemical mechanisms of injury in these various animal models include oxidative stress, inflammation [30], apoptosis [31], necrosis [32], diffuse axonal injury [33], neurodegeneration, and cognitive deficits [34] at the impact sites and remote sites.

Diffuse Injury Model—Shock Tube Model

In this review, we describe the mechanisms of diffuse injury represented by a rodent model of shock-wave primary blast injury. Primary blast injury has attracted much

Table 1 Animal models of traumatic brain injury discussed in this review

Model	Injury	Clinical relevance	Strength	Weakness
Fluid percussion	Mixed	Direct brain deformation. Cerebral concussion, focal contusion. Example: Sports-related TBI: boxing, football	Well characterized; severity of injury can be easily adjusted; highly reproducible across laboratories	Requires craniotomy; no immediate post-injury neuroscoring; high mortality rate due to apnea
Midline lateral	Mixed			
Controlled cortical impact	Mainly focal	Direct brain deformation. Cerebral contusion with subarachnoid hemorrhage. Example: Sports-related TBI: boxing, football	Severity of injury can be controlled; highly reproducible among laboratories	Lack of brain stem deformation, resulting in minimal mortality; no immediate post-injury neuroscoring
Open skull				
Closed skull				
Weight drop	Mainly focal	Hemorrhage and diffuse axonal injury. Example: falling down, motor vehicle accidents	Mechanism is similar to human TBI, severity of injury can be adjusted; well-characterized neuroscoring post-injury; inexpensive, easy and convenient	High mortality rate due to apnea and skull fractures, possibility of rebound injury, chance of inaccuracy
Feeney				
Shohami	Mainly focal			
Marmarou	Mainly diffuse			
Blast wave model	Diffuse	Blast-wave-induced TBI (battlefield)	Similar to soldiers in battlefield	Standardization is needed
Shock/blast tube				

attention in recent time because of the serious injury happening in the battlefield [35]. Primary blast-wave injury is a pure form of diffuse injury in which the damage is caused by non-penetrating supersonic blast-wave loading impulse. Shock tube blast wave is generated in the laboratory conditions by using compressed air or by field detonation of explosives. The commonly used animal species in these various blast-wave models include rodents [36], swine [37–39], and primates [40]. The shock tube model is more reproducible than field explosion due to precise control [39, 41]. Thus, laboratory design of shock tube models uses the linear propagation of primary blast-wave energy inside the cylindrical tube, unlike the exponential decay of blast wave that is commonly observed in free-field explosions [37, 42, 43]. The shock tube is made by a cylindrical metal tube consisting of a gas compressor chamber and a blast-wave energy propagation tube with a catch tang metal diaphragm at the end of the tube [41]. Figure 1 shows the laboratory design of shock tube model for exposing the animals in the middle location, at Center for Injury Bio Mechanics, Materials and Medicine, New Jersey Institute of Technology.

In shock tube models, anesthetized animals are restrained in a specimen holder inside, at the exit or outside the propagation tube. The animals are fixed with a Kevlar thoracic protective vest to protect the thorax and part of the abdomen. The pressure wave is generated by releasing the compressed air from the compressor chamber along the closed cylindrical metal tube. The mechanical parameters of the shock wave include the peak pressure, duration, and the shape of the pulse. The mechanism of blast TBI as a closed skull injury is related to the movement of the brain inside the skull caused by rapid rotation of the head [44]. Tissue distortion and shearing produced by inertial forces is believed to cause diffuse axonal injury, diffuse brain swelling, and ischemic brain injury [33, 36, 42, 45, 46].

Locations and Orientation of Test Animal in Shock Tube

The location of specimen inside, near the exit or outside the shock tube, produces different severity of injury and mortality due to varying mechanical loading [47]. Dynamic loads on animals at different location along the shock-wave tube are associated with static and time-dependent overpressure pulses. When the animal is placed inside the tube, it is insulted by a load from the pure blast wave comparable to the shock wave generated in open-field conditions. On the other hand, the animal at the exit point undergoes a decay of the initial shock front due to expansion of pressure wave, which is caused by expansion wave from the exit of the shock tube eliminating the exponentially decaying blast wave [47]. This phenomenon causes significant reduction of the positive blast impulse and converts most of the blast energy from supersonic blast wave to subsonic jet wind. This was demonstrated in a blast TBI model by placing the rat 50 mm outside of the shock tube, in which the bulk of the blast impulse was found to be subsonic jet wind. However, the injury was caused by the combination of subsonic jet wind and blast wave, compared with the animal inside the tube [48]. Recent studies using human and animal surrogates at different locations in shock-wave tube model concluded that there are significant deviations when surrogate specimens are placed inside, near exit, or outside the shock tube [49]. The orientation of specimen in prone or supine position inside the shock tube was also found to produce different severity of injury and mortality [47]. The placing of animals in prone or supine position is tailored to mimic differential positions of soldiers in the battlefield. The most common position of animal model in shock tube is placed in prone position with head oriented towards the direction of blast-wave propagation [50, 51].

Assessment of Mild, Moderate, and Severe Injury in Blast TBI

Clinical assessment method such as the Glasgow Coma Scale is not possible to define the severity of brain injuries in animal models because the severity of TBI in human is assessed in verbal response to the state of consciousness immediately at post-injury. It is also challenging to assess animals at such state of consciousness without considering the effects of anesthesia at post-injury. The NSS is commonly used in animal model to assess the severity of injury. This may not be the appropriate factors to define mild, moderate, and severe types of TBI in pure primary blast injury, since the determination of NSS was derived from Shohami model



Fig. 1 Shock-wave tube model. An overview of the 9-in. square cross-section shock tube instrument with pressure sensors designed by Dr. Namas Chandra's group

of focal injury [52, 53]. However, the NSS index score of lower than 20 at 1 h post-injury could be a useful indicator for survival rate, assuming that the neurological severity score within zero to few minutes post-injury is 24 total points. As per NSS, the animal has loss of movement, walking straight, righting reflex, eye reflexes, limb reflexes, beam walking and balancing, and seeking behavior, and there is presence of hemiplegia at this maximum point of 24. These clinical functions will improve during recovery period, which means NSS points will decrease from the total point of 24, and if the NSS points of certain animals remain above 20 at 1 h post-injury, those animals will be non-survival. It is stated that the change in NSS from 1.0 to 24 h post-injury reflects the recovery improvement, which is used for assessment of potential neuroprotective agents but not necessarily defining the classification of mild, moderate, and severe types of TBI.

Cernak et al. (2011) investigated the pathophysiological consequences and functional deficits of graded blast TBI by a developed multi-chamber shock-wave tube model. They tested both supine and prone position of mice in the shock tube, and generated mild, moderate, and severe injury at 103 KPa, 124 KPa, and 190 KPa, respectively. Mortality rate according to mild, moderate, and severe level is 5%, 37%, and 53% at supine position and 0%, 11%, and 33% in prone position. Prone position leads to less injury severity in mortality rate and pathology scoring system compared with supine position [54]. We made an attempt to standardize the scale of mild, moderate, and severe injury in animal model of TBI using the shock tube primary blast [51]. The injury scale determination was based on the percent of rat survival in response to blast overpressure (BOP) dose-dependent from 60 to 450 kPa within 2–8 ms wave propagation. The mortality rate and severity of brain injury increases with increments in BOP and impulse dose-dependently. Moreover, blood-brain barrier (BBB) damage is most commonly observed in BOP-induced traumatic brain injury; thus, the severity of brain injury can also be assessed by the extent of the BBB oxidative damage [51, 55]. A sigmoidal survival over BOP dose-response curve determined the mortality rate. Using this survival-BOP dose-response curve, the upper threshold of mild TBI (145 kPa), moderate TBI (146–220 kPa), and severe TBI (221–290 kPa) were determined based on the logistic regression [55]. As per the logistic regression model, the predicted mortality rates were < 5%, 35%, and 70% respectively for upper mild TBI threshold, moderate, and severe TBI. Although behavior or cognitive function assessment is absent, classification of TBI into mild, moderate, and severe injury on the basis of mortality rate is reliable in animal model because such changes in mortality rate are further validated by neuropathological markers and mechanical injury parameters.

Focal Injury Model: Controlled Cortical Impact Injury Model

The direct cause of focal brain injury such as ballistic injury, contusion, or boxing injury is best reflected in laboratory experimental condition by animal model of CCI as shown in Fig. 2. The model was first developed in ferret [56] and then expanded to rats [57], mice [58], swine [59], and monkeys [60] as experimental subjects. Figure 2 shows the classical rodent model of controlled cortical impact. The brain impacted through a surgically exposed dura by rapidly accelerated rod in which computer-guided software controls the depth of the impact. The size and geometry of the rod can be varied for different species, and the rod is under the control of a pneumatic piston or electromagnetic actuator [57]. The rod hits directly on the exposed brain tissue, which causes blood vessel breakage (blood-brain barrier damage), cortical tissue loss, acute hematoma, and brain cellular injury. Thus, CCI model induces significant cortical contusion, deep brain injury, and neurodegeneration around the impact site mostly at ipsilateral cortex [61]. In recent years, CCI model is expanded to closed skull injury for investigating mild and repetitive TBI [61, 62]. With this improved device, the model appears to take advantage of generating controlled tissue deformation, controlled time, velocity, and depth of impact without causing the risks of rebound injury, which otherwise is commonly observed in gravity-driven weight drop injury (WDI) model. This improved CCI model is believed to offer better understanding of the underlying cellular, biochemical, and molecular mechanisms of brain injury than other models since it has a well-controlled mechanical parameters and depth of brain tissue damage [63].



Fig. 2 Controlled cortical impact device fabricated by Amscien Instruments. This model uses pressed air or an electromagnetic-driven piston to penetrate the brain at a known velocity and distance

Assessment of Mild, Moderate, and Severe Injury in CCI Model

The CCI model of TBI has produced a wide range of neurohistopathology and behavioral outcomes as a result of mild, moderate, and severe TBI. There is no gold-standard definition of mild, moderate, and severe injury in CCI model. The depth of the tissue injury and the velocity of the rod that impacts the head injury determine the type of mild, moderate, and severe injury in open-skull CCI model. The depth of injury and velocity of the rod differ from one lab to the other for generating mild, moderate, and severe injury depending on the calibration of the CCI device. For example, Yu et al. induced brain injury in rat at the depth of 0.5 mm, 1.0 mm, or 2.0 mm with a velocity of 6.0 m/s to generate mild, moderate, and severe TBI respectively [2, 64], while Washington et al. generated brain injury in mice at the depth of 1.5 mm, 2.0 mm, and 2.5 mm with a velocity of 5.25 m/s for mild, moderate, and severe TBI [65]. Interestingly, there is a similar pattern of brain damage from these independent findings as observed in the visualization of metabolically active brain tissue from dead tissue. In this regard, there was about 10%, 25%, and 40% tissue damage in rat and about 5%, 15%, and 30% tissue damage in mice that corresponded to mild, moderate, and severe respectively [65]. However, the mechanical parameters differ across different laboratories, for example, in a recent study, Wang et al. induced mild, moderate, and severe CCI by depth of 0.2 mm, 1.0 mm, and 1.2 mm at a velocity of 3.5 m/s [66]. These different definitions of injury severity make it challenging to clarify specific sequelae and treatment development according to severity levels. Recently, Siebold et al. conducted a PubMed search on articles that used CCI mice models in the past 5 years. After thorough evaluation and analysis, they proposed guiding principles by recommending the use of depth < 1.0 mm and velocity < 4.0 m/s for mild TBI; the use of depth 1.0–1.5 mm and velocity 4.0–5.0 m/s for moderate TBI; and the use of depth > 2.0 mm at velocity 5.0–6.0 m/s for severe level [67].

Weight Drop Injury Model

Focal Injury WDI model has been used in rodents for several decades to promote understanding of pathophysiology of TBI [68]. As shown in Fig. 3, it utilizes the gravitational forces of a free-falling weight to generate a focal [69] or diffuse brain injury [70]. Initially, Feeney's WDI model was developed to deliver the impact to the intact dura through a craniotomy that leads to cortical contusion [71, 72], hemorrhage lesions [73], BBB damage [74, 75], infiltration of immune cells, and activation of glial cells according to the severity of injury [76, 77]. Later on, the closed head WDI rodent model of Shapira et al. (1988) and Chen et al. (1996) introduced the fixing of head on a hard platform to avoid impact of acceleration diffuse injury in rat and mouse [69, 78]. Then modified models of shorter fall heights were developed to generate concussion, cell death, short-term edema, and long-term cognitive deficits [73]. In general, such weight drop injury models in mild WDI are related to a diffuse injury pattern while the more severe injury generates a focal contusion [79].

Diffuse Injury The Shohami, Feeney, or Shapira weight drop models of focal injury are different from Marmarou WDI model of diffuse TBI. Marmarou model is resulted from "whole head" accelerated motion that represents human diffuse TBI from falls or car accidents [80]. The whole head acceleration and rotational acceleration models are capable of producing hemorrhage, cell loss, diffuse axonal injury, and astrogliosis from mild to severe range [81]. This injury model was designed to mimic motor vehicles accidental injury caused by rotational acceleration following linear acceleration injury [33]. The accuracy of brain tissue deformation and injury severity is highly variable in these models because of the involvement of rebound impact and variation of impact velocity by the falling impactor. Marmarou WDI model of diffuse TBI was further modified as Maryland model to cause frontal acceleration impact [82] or lateral impact on a helmet-protected head to mimic concussive head injury in football players [83]. Weight drop models of Shohami's, Feeney's, or

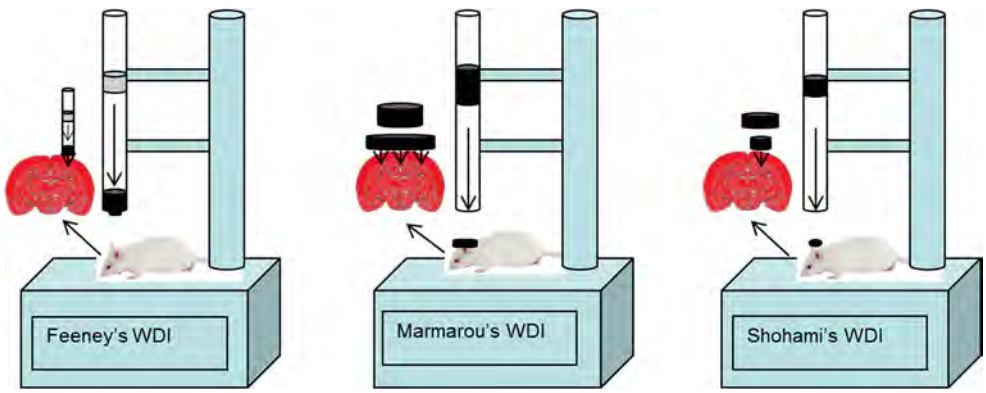


Fig. 3 Weight drop injury models. In the Feeney's weight drop model, the weight is delivered directly onto the exposed dura through craniotomy. In the Marmarou's weight drop model, a metal disk is placed over the skull to protect bone fractures and mimic diffuse TBI. In the Shohami's model, the weight is dropped on one side of the unprotected skull, to duplicate focal injury

Shapira's are also utilized in repeated mild concussive TBI studies, as mixed type of injury models [69, 71, 78].

Assessment of Injury Severity of Weight Drop Injury

Unlike the classification of other animal models as mild, moderate, and severe levels from pathological and functional changes, WDI severity level is less investigated in the past. In WDI, injury severity is related to the gravity force, which is associated by the different mass of the weight and the height it falls. NSS is used to evaluate the neurological impairment for the assessment of injury severity in WDI models. Khalin et al. (2016) used a modified mouse closed head Shohami model, to investigate cognitive deficient assessments [84]. They induced severe weight drop injury using 250 g falling weight from 2 cm height, while 200 g weight falling from 2 cm height generated mild closed head injury in mice, depending on the cognitive deficiency. By using Marmarou's impact acceleration model, Hsieh et al. (2017) claim that the WDI model can generate graded brain injury as well as neurobehavioral deficits [85]. Mild, moderate, and severe WDI was generated by using a 450 g weight falling from 1.0, 1.5, and 2.0 m height, and the mortality rates were 0%, 12.5%, and 50%, respectively. They observed progressive degrees of injury severity in the neurological score and balance function, which is associated with graded mechanical impact levels. Overall, WDI models provide a simple way to mimic clinical conditions ranging from focal to diffuse injuries, and it is inexpensive and capable to reproduce graded DAI. However, the risk of rebound impact and variation of impact velocity by the falling impactor may lead to failure of accurately describe the brain deformation, and the injury severity is relatively high variable.

Mixed Injury Model: Lateral Fluid Percussion Injury Model

Lateral fluid percussion injury (LFPI) is one of the best characterized and mostly used animal models of TBI. The injury in FPI is induced by a pendulum striking the piston at the end of a tube filled with fluid, shown in Fig. 4. The fluid pressure impulse then hits the exposed dura directly through the Luer-Lock that has been implanted surgically known as craniotomy [86]. Briefly, a Luer-Lock is implanted into a 3.0-mm diameter of an opened skull circular window, which is connected to FPI device fluid impulse outlet and fluid pressure detector. In this way, the fluid pressure delivered on the exposed dura is accurately measured by the detector at the time of injury. The location of the craniotomy is the site of Luer-Lock implantation and the site of impact, and it defines the types of injury in FPI models. Thus, when craniotomy is performed at the center of the sagittal suture, it is known as Midline FPI [87]. In Lateral FPI, craniotomy is performed at 3.5 mm lateral to midline [88], and for parasagittal FPI, the Luer-Lock is implanted less than 3.5 mm lateral to midline [89, 90]. Brain tissue deformation, displacement, and severity of the injury in these types of FPI are resulted from fluid pressure pulse [88]. The pathophysiological changes in FPI are correlated with the pressure transients, in which upper mild, moderate, or severe type of pressure impulse causes focal and diffuse injury, while the lower threshold of mild pressure impulse produces diffuse injury [68].

The application of FPI model is used for replicating the human TBI without skull fracture that generates edema,

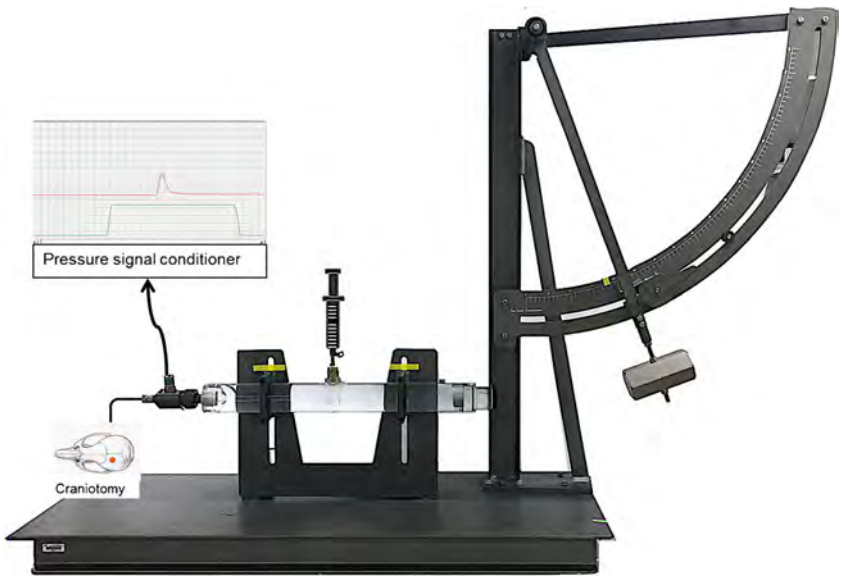


Fig. 4 Fluid percussion injury device with pressure signal conditioner. The fluid pulse impacts at the exposed dura by craniotomy

hemorrhage, and gray matter damage [86]. The primary type of injury in fluid pressure impulse includes contusion, shearing/stretching of tissue, subdural hematoma, and hemorrhage as seen in concussive sports injury [91]. Such primary injury is followed by secondary mechanisms of molecular, biochemical, and cellular changes arising from focal and diffuse injury. The vascular disruption like hemorrhage and onsite necrotic cell death are likely an outcome of primary injury, while activation of inflammatory glial cells and neuronal cell death could be resulted predominantly from secondary mechanisms of injury. The LFPI model has the advantage of comparing the extent of damage in ipsilateral (injured side) and contralateral (non-injured side) of the brain hemisphere. LFPI produces focal cortical contusion and diffuse subcortical neuronal injury in the ipsilateral side of the brain [92], which is also believed to be minimally expanded in contralateral hemisphere. A post-injury cavity line is generated around glial cells at the impact site, which appears to result from continuous chronic cell death [93]. This progressive neurodegeneration that begins from seconds to year post-injury at the ipsilateral side of brain region appears to occur predominantly at the cortex, hippocampus, thalamus, striatum, and amygdala [94].

Such differential regional neuronal loss in LFPI appears to produce neurobehavioral impairments that are observed in TBI patients, such as reflex suppression, vestibulomotor function, and cognitive function [73, 95]. The impairments are believed to continue for years after severe LFPI [96]. Reliability and reproducibility of FPI-induced neurodegeneration, neurological impairments, and mortality rate are dependent on the location of craniotomy. This is because a small shift from the midline FPI (MFPI) can cause significant changes in brain infarct volume and neurological outcomes. The mortality of MFPI is higher than other models, which is due to brainstem-compromised apnea [26]. The LFPI is the improved model of FPI that has reliability and reproducibility to human head injury in terms of neurohistopathology, behavioral outcomes, and physiological function like blood pressure or electroencephalogram. In addition, unraveling of the cellular, molecular mechanisms of injury and subsequent development of experimental therapy is best studied in LFPI model. The evolution of recent computer-controlled LFPI device that can monitor the fluid percussion waveforms with adjustable rise times, peak pressures, and durations is an advanced reliable improvement to the model [97].

Assessment of Mild, Moderate, and Severe Injury in FPI Model

Perhaps the definition of mild, moderate, and severe injury is the best established in animal model of FPI. The strength of the injury classification lies in the combination of mortality rate, the pressure exposure range, the righting reflexes, and reliably reproducibility of the injury model. For example, Alder et al. (2011) performed mild to moderate injury in mice model of LFPI on the basis of mortality rate, pressure range, and righting reflexes [91]. Injury pressures are delivered in the range of 0.9–2.1 atmospheric (atm) pressure that produces mild injury with 0–5% mortality rate and a righting reflex time of 2–4 min or moderate injury with a mortality rate of 10–20% and a righting reflex time of 6–10 min.

Kabadi et al. (2010) described that mild, moderate, and severe injury occurs at 1.8–2.2 atm (26–32 psi), 2.4–2.8 atm (35–41 psi), and pressures greater than 2.8 atm (41 psi), respectively in standard lateral FPI model (Amscien Instruments) [98]. They also established these classifications in developed rat model of microprocessor-controlled, pneumatically driven instrument, micro-FP device. With micro-FPI, pressures of 2.2–2.4 atm (32–35 psi), 2.6–2.8 atm (38–41 psi), and > 3.0 atm (44 psi) correspond to mild, moderate, and severe magnitudes of injury, respectively. They observed that mortality rates were 0% at 2.4 atm, 12% at 2.6 atm, 20% at 2.8 atm, 33% at 3.0 atm, and > 65% above 3.2 atm. The cognitive performance, lesion volume, and neuronal loss were significantly different between mild and moderate level. Similarly, Prins et al. (1996) classified the types of injuries in rat model of FPI through a comparative study on mortality rate, morphology, intracranial pressure, and mean arterial blood pressure [99]. They investigated mild pressure range from 1.35 to 1.45 atm (20–21 psi), moderate injury pressure range from 2.65 to 2.75 atm (39–40 psi), and severe injury pressure range from 3.65 to 3.75 atm (54–55 psi). The mortality rate corresponding to mild, moderate, and severe injury pressure range was respectively 27%, 36%, and 100% for postnatal 17 days, and 0%, 20%, and 55% mortality for adult rats [99]. They reported that the duration of apnea for adult rat was 10.4 s, 20.3 s, and 24.9 s and duration of unconsciousness was 97.8 s, 183.0 s, and 291.2 s for mild, moderate, and severe, respectively. The increment of intracranial pressure and mean arterial blood pressure appeared to contribute the mortality rate in the corresponding mild, moderate, and severe injuries. Moreover, weight loss post-injury is also correlated with injury severity. Mild, moderate, and severe injury was found to result in 0–10%, 15–20%, and 25–30% weight loss, respectively [25]. Here, we summarized the injury severity range from all these FPI studies where a mild TBI is defined at the pressure range of 0.9–1.5 atm (13–22 psi) [30, 100, 101], moderate TBI range is at 1.6–2.5 atm (23–37 psi) [102–104], and severe injury is defined above 2.5 atm (37 psi) [105–107], as given in Table 2.

The suppression time of reflexes such as pinna, cornea, and righting has been established as a standard indicator of neurological evaluation in animal model immediately after FPI. The pinna reflex is defined as a head shake or twitching of ear

Table 2 Parameters to assess injury severity levels for each type of animal models

Injury model	Injury severity	Parameters to assess injury severity				References
		Pressure range (atm)	Mortality rate	Righting reflex time (min)	Apnea (s)	
Fluid percussion injury (lateral FPI)	Mild	0.9–1.5	0–5%	2–4	~10.4	[91, 99–107]
	Moderate	1.6–2.5	10–25%	6–10	~20.3	
	Severe	> 2.5	> 33%	> 10	~24.9	
Weight drop injury (Marmarou model)	Injury severity	Weight (g)	Height (m)	Mortality rate		[85]
	Mild	450	1.0	0%		
	Moderate		1.5	12.5%		
	Severe		2.0	50%		
Controlled cortical injury (open skull)	Injury severity	Depth (mm)	Velocity (m/s)	Infarct volume		[65–67]
	Mild	< 1.0	< 4.0	5–10%		
	Moderate	1.0–1.5	4.0–5.0	15–25%		
	Severe	> 2.0	5.0–6.0	30–40%		
Blast TBI shock-wave tube	Injury severity	Blast overpressure (kPa)		Mortality rate		[51]
	Mild	80–145		< 5%		
	Moderate	146–220		35%		
	Severe	221–290		70%		

when touching the inside of the pinna with a cotton-tip applicator. The corneal relax is when there is a blink response after touching the cornea gently with a saline-moistened wisp of cotton. The righting reflexed is examined by recording the time for the animal to roll over on their feet when they are placed on their back, for three times [108]. The non-invasive righting reflex appears to correlate with injury severity; thus, it is used commonly as an indicator of injury severity [95, 109]. Apart from righting, apnea, and pinna reflexes, the types of injury severity are also assessed by physiological functions such as arterial blood gases, vital signs, intracranial pressure, and electrophysiology.

It is true that there is no common standard for classification of mild, moderate, and severe injury in animal models, like the Glasgow Coma Scale in human TBI patients. The classification of mild, moderate, and severe injury in animal models differs from model devices, and from one laboratory to another. In FPI, some groups do not record the apnea duration since immediate ventilation support is given post-injury to alleviate apnea-induced effects. The use of different anesthesia methods may also influence the outcomes of injury, including apnea and righting reflex. In CCI model, the velocity of punch varies across laboratories, leading to different depth of injury. In addition to the depth of injury, brain infarct volume is used as a standard to assess mild, moderate, and severe TBI in CCI models. Although challenging, a reliable classification of mild, moderate, and severe TBI needs the combined knowledge of injury mechanics, mortality rate, neurological reflexes, physiological function, and histological outcomes.

Neurobehavioral Assessment in TBI

The neurobehavioral deficits that are commonly assessed in fluid percussion-induced traumatic brain injury include the functional outcomes of motor, cognition, and depression or anxiety-like behaviors. Motor tests measure the motor co-ordination, grip, and balance of the animal, while cognitive tests examine the working memory and learning in rats with the help of visual cues. Tests that measure anxiety and depression often study the explorative behavior of animals and correlate anxiety to decreased exploration in a new environment. Such behavioral deficiencies originating from fluid percussive TBI are mostly observed at the early time points of post-injury with gradual improvement over time depending on the severity of the FPI [110, 111], although the outcome measures after few weeks post-injury may not match sham animals at the same time-point [112]. A similar pattern of improvement in cognitive deficits over time has also been observed in cases of human TBI, which was implicated to compensatory strategies of the neurons or new learning [113]. The post-injury motor deficits in rats have been assessed by beam balance, beam walking test, ladder rung walk test [114], inclined plane test, rotating pole test, rope grip, and rota-rod test [115–118]. The rotating rod of constant or accelerating speed in rota-rod tests of the vestibular motor co-ordination appears to be the most sensitive measure in midline FPI model [119]. The rota-rod test is believed to be capable of detecting deficits in mild midline TBI-inflicted animals unlike the beam balance or the beam walk test.

The post-injury cognitive deficiencies in rats are commonly evaluated by using the Morris water maze test, radial arm

maze, and novel object recognition tests [120–122]. Both the lateral and midline FPI models are known to affect the hippocampus leading to deficits in learning and memory, which can last for days or weeks post-injury [25]. In a study comparing LFPI to weight drop impact-acceleration model with 10 min of secondary hypoxia, it was identified that the lateral FPI produced more cognitive impairments. The cognitive deficits remained higher in the LFPI model even when injury severity, measured by the righting reflex, was matched in the two models [123]. These findings suggest that cognitive deficits differ between an opened head injury and closed head injury model in spite of maintaining the same physiological condition. Although the controlled cortical impact (CCI) produces significantly more sensory deficits than LFPI, there was no significant difference found in the motor co-ordination and cognitive deficits between these two TBI models [124]. The sensory deficit was assessed by the bilateral tactile adhesive removal task. In FPI models, the location of craniotomy plays a key role in determining the extent of cognitive deficits. A small shift of 1–2 mm craniotomy location from the midline FPI can significantly affect the cognitive outcome, as such midline FPI is known to produce more severe cognitive impairments than the LFPI [89, 125].

A short-term exhibition of behavioral changes is anxiety-like symptom in rats at post-injury in LFPI model. It has been shown that there is a significant increase in plus maze time spent in the open arms at 24 h post-injury even at mild 1–1.5 atm pressure compared with sham control animals. This effect seems to decline gradually with time that the effect diminishes at 4 weeks post-injury [100]. Such short-term observation of plus maze elevation was true for moderate LFPI at 2.2 atm pressure; however, a depression-like behavior was exhibited by rats during novelty suppressed feeding, forced swim, and social interaction tests [126]. These findings indicate that anxiety-like behavior changes occur only in first few days at post-TBI. Thus, blunt injury like LFPI is increasingly associated with motor deficits, cognitive deficits, and depression/anxiety behavior that can last for a few days to weeks post-injury. Cognitive deficits in rodent blunt TBI model have been consistently reported by the Morris water maze test, while vestibular and motor co-ordination deficits have been demonstrated using beam balance, beam walk, and rota-rod tests post FPI [90, 111, 127]; these tests are the most investigated and well-established in behavioral studies of animal models. The severity of injury, the location of injury, and the types of open/closed head injury can affect the behavioral and cognitive function.

Future Scope

Although, animal models of head injury have been developed more than half a century ago, it is still an evolving field of research. It is so because of the complexity of head injury itself and development of innovative technology devices for better understanding of the injury mechanisms. With such progress in head injury targeted devices, the scientific community is able to define the different types of injury mechanisms in focal, diffuse, or mixed injury that represent certain traumatic brain injury in human. One of the advancements made in such animal models is fluid percussive methods, which reproduces concussive clinical syndrome in human. The orientation of lateral fluid percussion injury has emerged as the most reliable, reproducible, and utilized models in experimental TBI. Bruce Lyeth (2016) comprehensively described the advantages of LFPI in his article "Historical Review of the Fluid-Percussion on TBI Model" [128]. The advantages of LFPI model include the comparison of injury vulnerability between contralateral (non-injured side) and ipsilateral (injured side) of brain hemisphere, and being able to distinguish focal injury and diffuse injury in the ipsilateral. Craniotomy involved in LFPI diminishes the rupture of sagittal sinus, blood loss, and reduction of venous blood outflow that was commonly observed in midline FPI model. The LFPI model appears to produce consistent cortical and hippocampal neuronal degeneration that recapitulate concussive TBI in human. The improvement of LFPI also includes the reduction of direct compression on the brain stem and respiratory center, which allows application of higher fluid percussive pressure with lower mortality rate than midline FPI.

It is obvious now that LFPI and CCI models have contributed much better understanding of the cellular and molecular mechanisms of TBI and its subsequent neurocognitive outcomes. The mechanistic nature of opened skull CCI model is purely a focal injury. In FPI, the upper threshold of mild to severe type of pressure impulse produces mostly focal and less of diffuse injury, but the lower threshold of mild pressure impulse causes diffuse injury. Here, we propose the sequence of injury event and the mechanisms of injury for a moderate LFPI pressure pulse exposure in experiment TBI, as shown in Fig. 5. Tissue deformation at the site of impact includes rupturing the subarachnoid and pial vessels that leads to intracranial hemorrhage of the ventricle area on the impact side. The subsequent event of hemorrhage is likely to produce subarachnoid coagulation preventing effective CSF clearance and thrombotic vessel occlusion. Such events of hemorrhage and coagulative thrombosis resulting from primary focal contusive injury are likely to cause necrotic cell death that is different from the secondary mechanisms of injury/cell death as depicted in the two arms of schematic pathways. The critical role of coagulation in trauma patients after TBI has become a reality that majority of TBI patients are treated with novel oral anticoagulants therapy [129]. The objective of anticoagulants therapy trauma patients is to prevent the intracranial hemorrhage after TBI. The same study reported that severity of intracranial hemorrhage, neurosurgical intervention, and

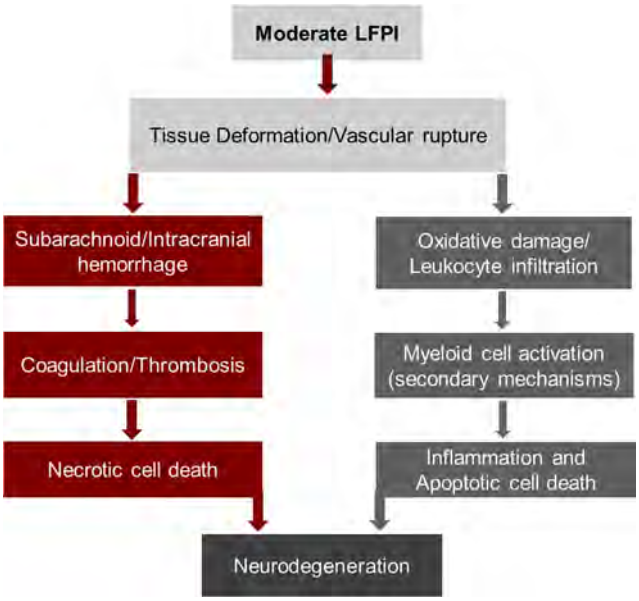


Fig. 5 Schematic drawing showing underlying mechanism of moderate lateral fluid percussion injury

mortality rate gets worsened in trauma patients who are on anticoagulants prior to brain injury. It makes sense because the presence of anticoagulants before or immediately after TBI will prevent the coagulative immune reaction with a possible outcome of bleeding to death, as we have observed in experimental TBI.

The consequence of primary injury leads to the propagation of secondary mechanisms of injury. It involves the alterations of molecular, biochemical, and cellular components that are mostly regulated by a sequence of signaling pathways. For example, there is immediate induction of oxidative stress and infiltration of immune cells at the deformed and vascular rupture area. Myeloid cells like microglia are spontaneously activated in response to ongoing necrotic cell death (right arm) and changes in brain microenvironment (left arm) as depicted in the pathways (Fig. 5). These cascades of inflammatory processes like the oxidative stress, neuroimflammation, and apoptotic cell death comprise the secondary mechanisms of brain injury and neurodegeneration. In LFPI model, such post-TBI neurodegenerative process appears to occur at certain specific brain region of the ipsilateral side. Whether such secondary mechanisms of neurodegenerative process can be classified as diffuse axonal injury resulting from rapid acceleration and deceleration of brain volume during TBI is debatable. Unfortunately, this knowledge gap in TBI arising from diffuse injury models still remains unclear, unlike in CCI/FPI models. A better understanding of the injury mechanisms proposed in the two arms of the pathways is expected to contribute successful regenerative therapy for millions of trauma patients. Such effective neuroprotective therapy is much needed for alarming incidence of 69 million individuals worldwide who sustain TBI each year as per recent epidemiological reports [4].

Conclusion

In order to strategize a proper diagnosis and an effective therapeutic application, we need to define convergent standard criteria for mild, moderate, and severe TBI in these various animal models of TBI. Such preclinical criteria in complex focal, diffuse, and mixed types of brain injury should be *in sync* with clinical outcomes. To this end, first, mortality rate in response to dose-dependent pressure force can be used as common criteria. Here, we postulate mortality rate of 0–5%, 6–25%, and greater than 25% to be classified as mild, moderate, and severe TBI respectively. Such mortality rate can be further correlated to the extent of brain infarct volume and histological validation in all animal models of TBI. Second, the types of injury mechanisms need to be defined in various TBI models for formulating a logical therapeutic application. In that, delineating the distinction between primary and secondary types of injury as described in the "Future Scope" section will be useful for effective therapeutic treatment of TBI. It may be reasonable to state that deficits of cognitive and motor functions are the outcomes of these primary and secondary injuries during the neuropathological progression of TBI. However, such functional outcomes may also be used as reliable pointer for injury severity.

Authors' Contributions XM carried out the studies of literature research and performed the acquisition of data and writing in manuscript preparation. AA wrote the part of "behavioral assessment" and helped XM in manuscript preparation. BJF and NC proofread the manuscript and gave important comments from their area of expertise. JH supervised the development of work, gave critical revisions, and edited the manuscript. All authors read and approved the final manuscript.

Funding Information This work was supported by grant 1R21AA022734-01A1 (to JH).

Compliance with Ethical Standards

Conflict of Interest The authors declare that they have no competing interests.

Publisher's Note Springer Nature remains neutral with regard to jurisdictional claims in published maps and institutional affiliations.

References

1. Thurman DJ, Alverson C, Dunn KA, Guerrero J, Sniezek JE (1999) Traumatic brain injury in the United States: a public health perspective. J Head Trauma Rehabil 14(6):602–615
2. Faul M, Coronado V (2015) Epidemiology of traumatic brain injury. Handb Clin Neurol 127:3–13. https://doi.org/10.1016/b978-0-444-52892-6.00001-5
3. Taylor CA, Bell JM, Breiding MJ, Xu L (2017) Traumatic brain injury-related emergency department visits, hospitalizations, and deaths - United States, 2007 and 2013. Morb Mortal Wkly Rep

Surveill Summ 66(9):1–16. https://doi.org/10.15585/mmwr.ss6609a1
4. Dewan MC, Rattani A, Gupta S, Baticulon RE, Hung YC, Punchak M, Agrawal A, Adeleye AO, Shrime MG, Rubiano AM, Rosenfeld JV, Park KB (2018) Estimating the global incidence of traumatic brain injury. J Neurosurg 1–18. https://doi.org/10.3171/2017.10.Jns17352
5. Arciniegas DB, Held K, Wagner P (2002) Cognitive impairment following traumatic brain injury. Curr Treat Options Neurol 4(1):43–57
6. Barman A, Chatterjee A, Bhide R (2016) Cognitive impairment and rehabilitation strategies after traumatic brain injury. Indian J Psychol Med 38(3):172–181. https://doi.org/10.4103/0253-7176.183086
7. Chen Y, Huang W (2011) Non-impact, blast-induced mild TBI and PTSD: concepts and caveats. Brain Inj 25(7–8):641–650. https://doi.org/10.3109/02699052.2011.580313
8. Bryant R (2011) Post-traumatic stress disorder vs traumatic brain injury. Dialogues Clin Neurosci 13(3):251–262
9. Prasad KN, Bondy SC (2015) Common biochemical defects linkage between post-traumatic stress disorders, mild traumatic brain injury (TBI) and penetrating TBI. Brain Res 1599:103–114. https://doi.org/10.1016/j.brainres.2014.12.038
10. Johnson VE, Stewart W, Smith DH (2012) Widespread tau and amyloid-beta pathology many years after a single traumatic brain injury in humans. Brain Pathol (Zurich, Switzerland) 22(2):142–149. https://doi.org/10.1111/j.1750-3639.2011.00513.x
11. Hay J, Johnson VE, Smith DH, Stewart W (2016) Chronic traumatic encephalopathy: the neuropathological legacy of traumatic brain injury. Annu Rev Pathol 11:21–45. https://doi.org/10.1146/annurev-pathol-012615-044116
12. Stern RA, Riley DO, Daneshvar DH, Nowinski CJ, Cantu RC, McKee AC (2011) Long-term consequences of repetitive brain trauma: chronic traumatic encephalopathy. PM & R 3(10 Suppl 2):S460–S467. https://doi.org/10.1016/j.pmrj.2011.08.008
13. DeGrauw X, Thurman D, Xu L, Kancherla V, DeGrauw T (2018) Epidemiology of traumatic brain injury-associated epilepsy and early use of anti-epilepsy drugs: an analysis of insurance claims data, 2004-2014. Epilepsy Res 146:41–49. https://doi.org/10.1016/j.eplepsyres.2018.07.012
14. Semple BD, Zamani A, Rayner G, Shultz SR, Jones NC (2018) Affective, neurocognitive and psychosocial disorders associated with traumatic brain injury and post-traumatic epilepsy. Neurobiol Dis. https://doi.org/10.1016/j.nbd.2018.07.018
15. Fleminger S, Oliver DL, Lovestone S, Rabe-Hesketh S, Giora A (2003) Head injury as a risk factor for Alzheimer's disease: the evidence 10 years on; a partial replication. J Neurol Neurosurg Psychiatry 74(7):857–862
16. Salib E, Hillier V (1997) Head injury and the risk of Alzheimer's disease: a case control study. Int J Geriatr Psychiatry 12(3):363–368
17. Guo Z, Cupples LA, Kurz A, Auerbach SH, Volicer L, Chui H, Green RC, Sadovnick AD et al (2000) Head injury and the risk of AD in the MIRAGE study. Neurology 54(6):1316–1323
18. Narayan RK, Michel ME, Ansell B, Baethmann A, Biegon A, Bracken MB, Bullock MR, Choi SC et al (2002) Clinical trials in head injury. J Neurotrauma 19(5):503–557. https://doi.org/10.1089/089771502753754037
19. Menon DK (2009) Unique challenges in clinical trials in traumatic brain injury. Crit Care Med 37(1 Suppl):S129–S135. https://doi.org/10.1097/CCM.0b013e3181921225
20. Marklund N, Hillered L (2011) Animal modelling of traumatic brain injury in preclinical drug development: where do we go from here? Br J Pharmacol 164(4):1207–1229. https://doi.org/10.1111/j.1476-5381.2010.01163.x
21. Briones TL (2015) Chapter 3 animal models of traumatic brain injury: is there an optimal model that parallels human brain injury? Annu Rev Nurs Res 33:31–73. https://doi.org/10.1891/0739-6686.33.31
22. Maas AI, Lingsma HF (2008) New approaches to increase statistical power in TBI trials: insights from the IMPACT study. Acta Neurochir Suppl 101:119–124
23. Lu J, Marmarou A, Lapane K, Turf E, Wilson L (2010) A method for reducing misclassification in the extended Glasgow Outcome Score. J Neurotrauma 27(5):843–852. https://doi.org/10.1089/neu.2010.1293
24. Xiong Y, Mahmood A, Chopp M (2013) Animal models of traumatic brain injury. Nat Rev Neurosci 14(2):128–142. https://doi.org/10.1038/nrn3407
25. Eakin K, Rowe RK, Lifshitz J (2015) Modeling fluid percussion injury: relevance to human traumatic brain injury. In: Kobeissy FH (ed) Brain neurotrauma: molecular, neuropsychological, and rehabilitation aspects. Frontiers in Neuroengineering, Boca Raton (FL)
26. Cernak I (2005) Animal models of head trauma. NeuroRx 2(3):410–422. https://doi.org/10.1602/neurorx.2.3.410
27. Johnson VE, Meaney DF, Cullen DK, Smith DH (2015) Animal models of traumatic brain injury. Handb Clin Neurol 127:115–128. https://doi.org/10.1016/b978-0-444-52892-6.00008-8
28. Osier ND, Carlson SW, DeSana A, Dixon CE (2015) Chronic histopathological and behavioral outcomes of experimental traumatic brain injury in adult male animals. J Neurotrauma 32(23):1861–1882. https://doi.org/10.1089/neu.2014.3680
29. Gennarelli TA (1994) Animate models of human head injury. J Neurotrauma 11(4):357–368. https://doi.org/10.1089/neu.1994.11.357
30. Bhowmick S, D'Mello V, Abdul-Muneer PM (2018) Synergistic inhibition of ERK1/2 and JNK, not p38, phosphorylation ameliorates neuronal damages after traumatic brain injury. Mol Neurobiol. https://doi.org/10.1007/s12035-018-1132-7
31. Patel RK, Prasad N, Kuwar R, Haldar D, Abdul-Muneer PM (2017) Transforming growth factor-beta 1 signaling regulates neuroinflammation and apoptosis in mild traumatic brain injury. Brain Behav Immun 64:244–258. https://doi.org/10.1016/j.bbi.2017.04.012
32. Gaetz M (2004) The neurophysiology of brain injury. Clin Neurophysiol 115(1):4–18
33. Wang HC, Duan ZX, Wu FF, Xie L, Zhang H, Ma YB (2010) A new rat model for diffuse axonal injury using a combination of linear acceleration and angular acceleration. J Neurotrauma 27(4):707–719. https://doi.org/10.1089/neu.2009.1071
34. Bramlett HM, Dietrich WD (2007) Progressive damage after brain and spinal cord injury: pathomechanisms and treatment strategies. Prog Brain Res 161:125–141. https://doi.org/10.1016/s0079-6123(06)61009-1
35. DeWitt DS, Prough DS (2009) Blast-induced brain injury and posttraumatic hypotension and hypoxemia. J Neurotrauma 26(6):877–887. https://doi.org/10.1089/neu.2007.0439
36. Kaur C, Singh J, Lim MK, Ng BL, Yap EP, Ling EA (1995) The response of neurons and microglia to blast injury in the rat brain. Neuropathol Appl Neurobiol 21(5):369–377
37. Bauman RA, Ling G, Tong L, Januszkiewicz A, Agoston D, Delanerolle N, Kim Y, Ritzel D et al (2009) An introductory characterization of a combat-casualty-care relevant swine model of closed head injury resulting from exposure to explosive blast. J Neurotrauma 26(6):841–860. https://doi.org/10.1089/neu.2009-089810.1089/neu.2008.0898
38. de Lanerolle NC, Bandak F, Kang D, Li AY, Du F, Swauger P, Parks S, Ling G et al (2011) Characteristics of an explosive blast-induced brain injury in an experimental model. J Neuropathol Exp Neurol 70(11):1046–1057. https://doi.org/10.1097/NEN.0b013e318235bef2

39. Zhu F, Skelton P, Chou CC, Mao H, Yang KH, King AI (2013) Biomechanical responses of a pig head under blast loading: a computational simulation. Int J Numer Methods Biomed Eng 29(3):392–407. https://doi.org/10.1002/cnm.2518
40. Lu J, Ng KC, Ling G, Wu J, Poon DJ, Kan EM, Tan MH, Wu YJ et al (2012) Effect of blast exposure on the brain structure and cognition in Macaca fascicularis. J Neurotrauma 29(7):1434–1454. https://doi.org/10.1089/neu.2010.1591
41. Reneer DV, Hisel RD, Hoffman JM, Kryscio RJ, Lusk BT, Geddes JW (2011) A multi-mode shock tube for investigation of blast-induced traumatic brain injury. J Neurotrauma 28(1):95–104. https://doi.org/10.1089/neu.2010.1513
42. Axelsson H, Hjelmqvist H, Medin A, Persson JK, Suneson A (2000) Physiological changes in pigs exposed to a blast wave from a detonating high-explosive charge. Mil Med 165(2):119–126
43. Savic J, Tatic V, Ignjatovic D, Mrda V, Erdeljan D, Cernak I, Vujnov S, Simovic M et al (1991) Pathophysiologic reactions in sheep to blast waves from detonation of aerosol explosives. Vojnosanit Pregl 48(6):499–506
44. Elder GA, Cristian A (2009) Blast-related mild traumatic brain injury: mechanisms of injury and impact on clinical care. Mt. Sinai J Med 76(2):111–118. https://doi.org/10.1002/msj.20098
45. Garman RH, Jenkins LW, Switzer RC 3rd, Bauman RA, Tong LC, Swauger PV, Parks SA, Ritzel DV et al (2011) Blast exposure in rats with body shielding is characterized primarily by diffuse axonal injury. J Neurotrauma 28(6):947–959. https://doi.org/10.1089/neu.2010.1540
46. Ryu J, Horkayne-Szakaly I, Xu L, Pletnikova O, Leri F, Eberhart C, Troncoso JC, Koliatsos VE (2014) The problem of axonal injury in the brains of veterans with histories of blast exposure. Acta Neuropathol Commun 2:153. https://doi.org/10.1186/s40478-014-0153-3
47. Sundaramurthy A, Alai A, Ganpule S, Holmberg A, Plougonven E, Chandra N (2012) Blast-induced biomechanical loading of the rat: an experimental and anatomically accurate computational blast injury model. J Neurotrauma 29(13):2352–2364. https://doi.org/10.1089/neu.2012.2413
48. Svetlov SI, Prima V, Kirk DR, Gutierrez H, Curley KC, Hayes RL, Wang KK (2010) Morphologic and biochemical characterization of brain injury in a model of controlled blast overpressure exposure. J Trauma 69(4):795–804. https://doi.org/10.1097/TA.0b013e3181bbd885
49. Alay E, Skotak M, Misistia A, Chandra N (2018) Dynamic loads on human and animal surrogates at different test locations in compressed-gas-driven shock tubes. Shock Waves 28(1):51–62. https://doi.org/10.1007/s00193-017-0762-4
50. Dal Cengio Leonardi A, Keane NJ, Bir CA, Ryan AG, Xu L, Vandevord PJ (2012) Head orientation affects the intracranial pressure response resulting from shock wave loading in the rat. J Biomech 45(15):2595–2602. https://doi.org/10.1016/j.jbiomech.2012.08.024
51. Mishra V, Skotak M, Schuetz H, Heller A, Haorah J, Chandra N (2016) Primary blast causes mild, moderate, severe and lethal TBI with increasing blast overpressures: experimental rat injury model. Sci Rep 6:26992. https://doi.org/10.1038/srep26992
52. Flierl MA, Stahel PF, Beauchamp KM, Morgan SJ, Smith WR, Shohami E (2009) Mouse closed head injury model induced by a weight-drop device. Nat Protoc 4(9):1328–1337. https://doi.org/10.1038/nprot.2009.148
53. Beit-Yannai E, Zhang R, Trembovler V, Samuni A, Shohami E (1996) Cerebroprotective effect of stable nitroxide radicals in closed head injury in the rat. Brain Res 717(1–2):22–28
54. Cernak I, Merkle AC, Koliatsos VE, Bilik JM, Luong QT, Mahota TM, Xu L, Slack N et al (2011) The pathobiology of blast injuries and blast-induced neurotrauma as identified using a new experimental model of injury in mice. Neurobiol Dis 41(2):538–551. https://doi.org/10.1016/j.nbd.2010.10.025
55. Abdul-Muneer PM, Schuetz H, Wang F, Skotak M, Jones J, Gorantla S, Zimmerman MC, Chandra N et al (2013) Induction of oxidative and nitrosative damage leads to cerebrovascular inflammation in an animal model of mild traumatic brain injury induced by primary blast. Free Radic Biol Med 60:282–291. https://doi.org/10.1016/j.freeradbiomed.2013.02.029
56. Lighthall JW (1988) Controlled cortical impact: a new experimental brain injury model. J Neurotrauma 5(1):1–15. https://doi.org/10.1089/neu.1988.5.1
57. Dixon CE, Clifton GL, Lighthall JW, Yaghmai AA, Hayes RL (1991) A controlled cortical impact model of traumatic brain injury in the rat. J Neurosci Methods 39(3):253–262
58. Smith DH, Soares HD, Pierce JS, Perlman KG, Saatman KE, Meaney DF, Dixon CE, McIntosh TK (1995) A model of parasagittal controlled cortical impact in the mouse: cognitive and histopathologic effects. J Neurotrauma 12(2):169–178. https://doi.org/10.1089/neu.1995.12.169
59. Manley GT, Rosenthal G, Lam M, Morabito D, Yan D, Derugin N, Bollen A, Knudson MM et al (2006) Controlled cortical impact in swine: pathophysiology and biomechanics. J Neurotrauma 23(2):128–139. https://doi.org/10.1089/neu.2006.23.128
60. King C, Robinson T, Dixon CE, Rao GR, Larnard D, Nemoto CE (2010) Brain temperature profiles during epidural cooling with the ChillerPad in a monkey model of traumatic brain injury. J Neurotrauma 27(10):1895–1903. https://doi.org/10.1089/neu.2009.1178
61. Chen Y, Mao H, Yang KH, Abel T, Meaney DF (2014) A modified controlled cortical impact technique to model mild traumatic brain injury mechanics in mice. Front Neurol 5:100. https://doi.org/10.3389/fneur.2014.00100
62. Smith SL, Hall ED (1996) Mild pre- and posttraumatic hypothermia attenuates blood-brain barrier damage following controlled cortical impact injury in the rat. J Neurotrauma 13(1):1–9. https://doi.org/10.1089/neu.1996.13.1
63. Osier ND, Dixon CE (2016) The controlled cortical impact model: applications, considerations for researchers, and future directions. Front Neurol 7:134. https://doi.org/10.3389/fneur.2016.00134
64. Yu S, Kaneko Y, Bae E, Stahl CE, Wang Y, van Loveren H, Sanberg PR, Borlongan CV (2009) Severity of controlled cortical impact traumatic brain injury in rats and mice dictates degree of behavioral deficits. Brain Res 1287:157–163. https://doi.org/10.1016/j.brainres.2009.06.067
65. Washington PM, Forcelli PA, Wilkins T, Zapple DN, Parsadanian M, Burns MP (2012) The effect of injury severity on behavior: a phenotypic study of cognitive and emotional deficits after mild, moderate, and severe controlled cortical impact injury in mice. J Neurotrauma 29(13):2283–2296. https://doi.org/10.1089/neu.2012.2456
66. Wang X, Gao X, Michalski S, Zhao S, Chen J (2016) Traumatic brain injury severity affects neurogenesis in adult mouse hippocampus. J Neurotrauma 33(8):721–733. https://doi.org/10.1089/neu.2015.4097
67. Siebold L, Obenaus A, Goyal R (2018) Criteria to define mild, moderate, and severe traumatic brain injury in the mouse controlled cortical impact model. Exp Neurol 310:48–57. https://doi.org/10.1016/j.expneurol.2018.07.004
68. O'Connor WT, Smyth A, Gilchrist MD (2011) Animal models of traumatic brain injury: a critical evaluation. Pharmacol Ther 130(2):106–113. https://doi.org/10.1016/j.pharmthera.2011.01.001
69. Shapira Y, Shohami E, Sidi A, Soffer D, Freeman S, Cotev S (1988) Experimental closed head injury in rats: mechanical, pathophysiologic, and neurologic properties. Crit Care Med 16(3):258–265

70. Foda MA, Marmarou A (1994) A new model of diffuse brain injury in rats. Part II: morphological characterization. J Neurosurg 80(2):301–313. https://doi.org/10.3171/jns.1994.80.2.0301
71. Feeney DM, Boyeson MG, Linn RT, Murray HM, Dail WG (1981) Responses to cortical injury: I. Methodology and local effects of contusions in the rat. Brain Res 211(1):67–77
72. Dail WG, Feeney DM, Murray HM, Linn RT, Boyeson MG (1981) Responses to cortical injury: II. Widespread depression of the activity of an enzyme in cortex remote from a focal injury. Brain Res 211(1):79–89
73. Morales DM, Marklund N, Lebold D, Thompson HJ, Pitkanen A, Maxwell WL, Longhi L, Laurer H et al (2005) Experimental models of traumatic brain injury: do we really need to build a better mousetrap? Neuroscience 136(4):971–989. https://doi.org/10.1016/j.neuroscience.2005.08.030
74. Mikawa S, Kinouchi H, Kamii H, Gobbel GT, Chen SF, Carlson E, Epstein CJ, Chan PH (1996) Attenuation of acute and chronic damage following traumatic brain injury in copper, zinc-superoxide dismutase transgenic mice. J Neurosurg 85(5):885–891. https://doi.org/10.3171/jns.1996.85.5.0885
75. Bellander BM, von Holst H, Fredman P, Svensson M (1996) Activation of the complement cascade and increase of clusterin in the brain following a cortical contusion in the adult rat. J Neurosurg 85(3):468–475. https://doi.org/10.3171/jns.1996.85.3.0468
76. Uhl MW, Biagas KV, Grundl PD, Barmada MA, Schiding JK, Nemoto EM, Kochanek PM (1994) Effects of neutropenia on edema, histology, and cerebral blood flow after traumatic brain injury in rats. J Neurotrauma 11(3):303–315. https://doi.org/10.1089/neu.1994.11.303
77. Holmin S, Schalling M, Hojeberg B, Nordqvist AC, Skeftruna AK, Mathiesen T (1997) Delayed cytokine expression in rat brain following experimental contusion. J Neurosurg 86(3):493–504. https://doi.org/10.3171/jns.1997.86.3.0493
78. Chen Y, Constantini S, Trembovler V, Weinstock M, Shohami E (1996) An experimental model of closed head injury in mice: pathophysiology, histopathology, and cognitive deficits. J Neurotrauma 13(10):557–568. https://doi.org/10.1089/neu.1996.13.557
79. Kalish BT, Whalen MJ (2016) Weight drop models in traumatic brain injury. Methods Mol Biol (Clifton, NJ) 1462:193–209. https://doi.org/10.1007/978-1-4939-3816-2_12
80. Marmarou A, Foda MA, van den Brink W, Campbell J, Kita H, Demetriadou K (1994) A new model of diffuse brain injury in rats. Part I: pathophysiology and biomechanics. J Neurosurg 80(2):291–300. https://doi.org/10.3171/jns.1994.80.2.0291
81. Albert-Weissenberger C, Varrallyay C, Raslan F, Kleinschnitz C, Siren AL (2012) An experimental protocol for mimicking pathomechanisms of traumatic brain injury in mice. Exp Transl Stroke Med 4:1. https://doi.org/10.1186/2040-7378-4-1
82. Kilbourne M, Kuehn R, Tosun C, Caridi J, Keledjian K, Bochicchio G, Scalea T, Gerzanich V et al (2009) Novel model of frontal impact closed head injury in the rat. J Neurotrauma 26(12):2233–2243. https://doi.org/10.1089/neu.2009.0968
83. Viano DC, Hamberger A, Bolouri H, Saljo A (2009) Concussion in professional football: animal model of brain injury–part 15. Neurosurgery 64(6):1162–1173; discussion 1173. https://doi.org/10.1227/01.neu.0000345863.99099.c7
84. Khalin I, Jamari NL, Razak NB, Hasain ZB, Nor MA, Zainudin MH, Omar AB, Alyautdin R (2016) A mouse model of weight-drop closed head injury: emphasis on cognitive and neurological deficiency. Neural Regen Res 11(4):630–635. https://doi.org/10.4103/1673-5374.180749
85. Hsieh TH, Kang JW, Lai JH, Huang YZ, Rotenberg A, Chen KY, Wang JY, Chan SY et al (2017) Relationship of mechanical impact magnitude to neurologic dysfunction severity in a rat traumatic brain injury model. PLoS One 12(5):e0178186. https://doi.org/10.1371/journal.pone.0178186
86. Thompson HJ, Lifshitz J, Marklund N, Grady MS, Graham DI, Hovda DA, McIntosh TK (2005) Lateral fluid percussion brain injury: a 15-year review and evaluation. J Neurotrauma 22(1):42–75. https://doi.org/10.1089/neu.2005.22.42
87. Ziebell JM, Rowe RK, Harrison JL, Eakin KC, Colburn T, Willyerd FA, Lifshitz J (2016) Experimental diffuse brain injury results in regional alteration of gross vascular morphology independent of neuropathology. Brain Inj 30(2):217–224. https://doi.org/10.3109/02699052.2015.1090012
88. McIntosh TK, Vink R, Noble L, Yamakami I, Fernyak S, Soares H, Faden AL (1989) Traumatic brain injury in the rat: characterization of a lateral fluid-percussion model. Neuroscience 28(1):233–244
89. Floyd CL, Golden KM, Black RT, Hamm RJ, Lyeth BG (2002) Craniectomy position affects Morris water maze performance and hippocampal cell loss after parasagittal fluid percussion. J Neurotrauma 19(3):303–316. https://doi.org/10.1089/089771502753594873
90. Sanders MJ, Dietrich WD, Green EJ (1999) Cognitive function following traumatic brain injury: effects of injury severity and recovery period in a parasagittal fluid-percussive injury model. J Neurotrauma 16(10):915–925. https://doi.org/10.1089/neu.1999.16.915
91. Alder J, Fujioka W, Lifshitz J, Crockett DP, Thakker-Varia S (2011) Lateral fluid percussion: model of traumatic brain injury in mice. J Vis Exp 54. https://doi.org/10.3791/3063
92. Hicks R, Soares H, Smith D, McIntosh T (1996) Temporal and spatial characterization of neuronal injury following lateral fluid-percussion brain injury in the rat. Acta Neuropathol 91(3):236–246
93. Bramlett HM, Dietrich WD (2002) Quantitative structural changes in white and gray matter 1 year following traumatic brain injury in rats. Acta Neuropathol 103(6):607–614. https://doi.org/10.1007/s00401-001-0510-8
94. Liu YR, Cardamone L, Hogan RE, Gregoire MC, Williams JP, Hicks RJ, Binns D, Koe A et al (2010) Progressive metabolic and structural cerebral perturbations after traumatic brain injury: an in vivo imaging study in the rat. J Nucl Med 51(11):1788–1795. https://doi.org/10.2967/jnumed.110.078626
95. Hamm RJ (2001) Neurobehavioral assessment of outcome following traumatic brain injury in rats: an evaluation of selected measures. J Neurotrauma 18(11):1207–1216. https://doi.org/10.1089/089771501317095241
96. Pierce JE, Smith DH, Trojanowski JQ, McIntosh TK (1998) Enduring cognitive, neurobehavioral and histopathological changes persist for up to one year following severe experimental brain injury in rats. Neuroscience 87(2):359–369
97. Wahab RA, Neuberger EJ, Lyeth BG, Santhakumar V, Pfister BJ (2015) Fluid percussion injury device for the precise control of injury parameters. J Neurosci Methods 248:16–26. https://doi.org/10.1016/j.jneumeth.2015.03.010
98. Kabadi SV, Hilton GD, Stoica BA, Zapple DN, Faden AI (2010) Fluid-percussion-induced traumatic brain injury model in rats. Nat Protoc 5(9):1552–1563. https://doi.org/10.1038/nprot.2010.112
99. Prins ML, Lee SM, Cheng CL, Becker DP, Hovda DA (1996) Fluid percussion brain injury in the developing and adult rat: a comparative study of mortality, morphology, intracranial pressure and mean arterial blood pressure. Brain Res Dev Brain Res 95(2):272–282
100. Shultz SR, MacFabe DF, Foley KA, Taylor R, Cain DP (2011) A single mild fluid percussion injury induces short-term behavioral and neuropathological changes in the Long-Evans rat: support for

an animal model of concussion. Behav Brain Res 224(2):326–335. https://doi.org/10.1016/j.bbr.2011.06.012
101. Griesbach GS, Hovda DA, Gomez-Pinilla F (2009) Exercise-induced improvement in cognitive performance after traumatic brain injury in rats is dependent on BDNF activation. Brain Res 1288:105–115. https://doi.org/10.1016/j.brainres.2009.06.045
102. Chitturi J, Li Y, Santhakumar V, Kannurpatti SS (2018) Early behavioral and metabolomic change after mild to moderate traumatic brain injury in the developing brain. Neurochem Int 120:75–86. https://doi.org/10.1016/j.neuint.2018.08.003
103. Li Y, Korgaonkar AA, Swietek B, Wang J, Elgammal FS, Elkabes S, Santhakumar V (2015) Toll-like receptor 4 enhancement of non-NMDA synaptic currents increases dentate excitability after brain injury. Neurobiol Dis 74:240–253. https://doi.org/10.1016/j.nbd.2014.11.021
104. Kinoshita K, Chatzipanteli i K, Vitarbo E, Truettner JS, Alonso OF, Dietrich WD (2002) Interleukin-1beta messenger ribonucleic acid and protein levels after fluid-percussion brain injury in rats: importance of injury severity and brain temperature. Neurosurgery 51(1):195–203 discussion 203
105. Vitarbo EA, Chatzipanteli K, Kinoshita K, Truettner JS, Alonso OF, Dietrich WD (2004) Tumor necrosis factor alpha expression and protein levels after fluid percussion injury in rats: the effect of injury severity and brain temperature. Neurosurgery 55(2):416–424 discussion 424-415
106. D'Ambrosio R, Fairbanks JP, Fender JS, Born DE, Doyle DL, Miller JW (2004) Post-traumatic epilepsy following fluid percussion injury in the rat. Brain J Neurol 127(Pt 2):304–314. https://doi.org/10.1093/brain/awh038
107. Sanders MJ, Sick TJ, Perez-Pinzon MA, Dietrich WD, Green EJ (2000) Chronic failure in the maintenance of long-term potentiation following fluid percussion injury in the rat. Brain Res 861(1):69–76
108. Schmidt RH, Grady MS (1993) Regional patterns of blood-brain barrier breakdown following central and lateral fluid percussion injury in rodents. J Neurotrauma 10(4):415–430. https://doi.org/10.1089/neu.1993.10.415
109. Morehead M, Bartus RT, Dean RL, Miotke JA, Murphy S, Sall J, Goldman H (1994) Histopathologic consequences of moderate concussion in an animal model: correlations with duration of unconsciousness. J Neurotrauma 11(6):657–667. https://doi.org/10.1089/neu.1994.11.657
110. Schmidt RH, Scholten KJ, Maughan PH (1999) Time course for recovery of water maze performance and central cholinergic innervation after fluid percussion injury. J Neurotrauma 16(12):1139–1147. https://doi.org/10.1089/neu.1999.16.1139
111. Fujimoto ST, Longhi L, Saatman KE, Conte V, Stocchetti N, McIntosh TK (2004) Motor and cognitive function evaluation following experimental traumatic brain injury. Neurosci Biobehav Rev 28(4):365–378. https://doi.org/10.1016/j.neubiorev.2004.06.002
112. Bramlett HM, Green EJ, Dietrich WD (1997) Hippocampally dependent and independent chronic spatial navigational deficits following parasagittal fluid percussion brain injury in the rat. Brain Res 762(1–2):195–202
113. Rabinowitz AR, Levin HS (2014) Cognitive sequelae of traumatic brain injury. Psychiatr Clin North Am 37(1):1–11. https://doi.org/10.1016/j.psc.2013.11.004
114. Metz GA, Whishaw IQ (2009) The ladder rung walking task: a scoring system and its practical application. J Vis Exp (28): e1204. https://doi.org/10.3791/1204
115. Hicks RR, Boggs A, Leider D, Kraemer P, Brown R, Scheff SW, Seroogy KB (1998) Effects of exercise following lateral fluid percussion brain injury in rats. Restor Neurol Neurosci 12(1):41–47
116. Clough RW, Neese SL, Sherill LK, Tan AA, Duke A, Roosevelt RW, Browning RA, Smith DC (2007) Cortical edema in moderate fluid percussion brain injury is attenuated by vagus nerve stimulation. Neuroscience 147(2):286–293. https://doi.org/10.1016/j.neuroscience.2007.04.043
117. Alessandri B, Rice AC, Levasseur J, DeFord M, Hamm RJ, Bullock MR (2002) Cyclosporin A improves brain tissue oxygen consumption and learning/memory performance after lateral fluid percussion injury in rats. J Neurotrauma 19(7):829–841. https://doi.org/10.1089/08977150260190429
118. Gold EM, Su D, Lopez-Velazquez L, Haus DL, Perez H, Lacuesta GA, Anderson AJ, Cummings BJ (2013) Functional assessment of long-term deficits in rodent models of traumatic brain injury. Regen Med 8(4):483–516. https://doi.org/10.2217/rme.13.41
119. Hamm RJ, Pike BR, O'Dell DM, Lyeth BG, Jenkins LW (1994) The rotarod test: an evaluation of its effectiveness in assessing motor deficits following traumatic brain injury. J Neurotrauma 11(2):187–196. https://doi.org/10.1089/neu.1994.11.187
120. Smith DH, Okiyama K, Thomas MJ, Claussen B, McIntosh TK (1991) Evaluation of memory dysfunction following experimental brain injury using the Morris water maze. J Neurotrauma 8(4):259–269. https://doi.org/10.1089/neu.1991.8.259
121. Lyeth BG, Jenkins LW, Hamm RJ, Dixon CE, Phillips LL, Clifton GL, Young HF, Hayes RL (1990) Prolonged memory impairment in the absence of hippocampal cell death following traumatic brain injury in the rat. Brain Res 526(2):249–258
122. Harrison JL, Rowe RK, Ellis TW, Yee NS, O'Hara BF, Adelson PD, Lifshitz J (2015) Resolvins AT-D1 and E1 differentially impact functional outcome, post-traumatic sleep, and microglial activation following diffuse brain injury in the mouse. Brain Behav Immun 47:131–140. https://doi.org/10.1016/j.bbi.2015.01.001
123. Hallam TM, Floyd CL, Folkerts MM, Lee LL, Gong QZ, Lyeth BG, Muizelaar JP, Berman RF (2004) Comparison of behavioral deficits and acute neuronal degeneration in rat lateral fluid percussion and weight-drop brain injury models. J Neurotrauma 21(5):521–539. https://doi.org/10.1089/089771504774129865
124. Peterson TC, Maass WR, Anderson JR, Anderson GD, Hoane MR (2015) A behavioral and histological comparison of fluid percussion injury and controlled cortical impact injury to the rat sensorimotor cortex. Behav Brain Res 294:254–263. https://doi.org/10.1016/j.bbr.2015.08.007
125. Vink R, Mullins PG, Temple MD, Bao W, Faden AI (2001) Small shifts in craniotomy position in the lateral fluid percussion injury model are associated with differential lesion development. J Neurotrauma 18(8):839–847. https://doi.org/10.1089/089771501316919201
126. Kuo JR, Cheng YH, Chen YS, Chio CC, Gean PW (2013) Involvement of extracellular signal regulated kinases in traumatic brain injury-induced depression in rodents. J Neurotrauma 30(14):1223–1231. https://doi.org/10.1089/neu.2012.2689
127. Deng-Bryant Y, Leung LY, Caudle K, Tortella F, Shear D (2016) Cognitive evaluation using Morris water maze in neurotrauma. Methods Mol Biol(Clifton, NJ) 1462:539–551. https://doi.org/10.1007/978-1-4939-3816-2_29
128. Lyeth BG (2016) Historical review of the fluid-percussion TBI model. Front Neurol 7:217. https://doi.org/10.3389/fneur.2016.00217
129. Zeeshan M, Jehan F, O'Keeffe T, Khan M, Zakaria ER, Hamidi M, Gries L, Kulvatunyou N et al (2018) The novel oral anticoagulants (NOACs) have worse outcomes compared to warfarin in patients with intracranial hemorrhage after TBI. J Trauma Acute Care Surg 85:915–920. https://doi.org/10.1097/ta.0000000000001995

Appendix A –Publication Cover 9
2019

Authors: M. T. Townsend, E. Alay, M. Skotak, N. Chandra

Title: "*Effect of tissue material properties in blast loading: coupled experimentation and finite element simulation*"

Journal Publication: Annals of Biomedical Engineering, ABME-D-18-0051, 1-14**,** (2019), [19-9]

Annals of Biomedical Engineering (© 2018)
https://doi.org/10.1007/s10439-018-02178-w

BMES BIOMEDICAL ENGINEERING SOCIETY

State-of-the-Art Modeling and Simulation of the Brain's Response to Mechanical Loads

Effect of Tissue Material Properties in Blast Loading: Coupled Experimentation and Finite Element Simulation

MOLLY T. TOWNSEND, EREN ALAY, MACIEJ SKOTAK, and NAMAS CHANDRA

Biomedical Engineering Department, New Jersey Institute of Technology, Newark, NJ, USA

(*Received 20 June 2018; accepted 28 November 2018*)

Associate Editor Raj K. Prabhu oversaw the review of this article.

Abstract—Computational models of blast-induced traumatic brain injury (bTBI) require a robust definition of the material models of the brain. The mechanical constitutive models of these tissues are difficult to characterize, leading to a wide range of values reported in literature. Therefore, the sensitivity of the intracranial pressure (ICP) and maximum principal strain to variations in the material model of the brain was investigated through a combined computational and experimental approach. A finite element model of a rat was created to simulate a shock wave exposure, guided by the experimental measurements of rats subjected to shock loading conditions corresponding to that of mild traumatic brain injury in a field-validated shock tube. In the numerical model, the properties of the brain were parametrically varied. A comparison of the ICP measured at two locations revealed that experimental and simulated ICP were higher in the cerebellum ($p < 0.0001$), highlighting the significance of pressure sensor locations within the cranium. The ICP and strain were correlated with the long-term bulk ($p < 0.0001$) and shear moduli ($p < 0.0001$), with an 80 MPa effective bulk modulus value matching best with experimental measurements. In bTBI, the solution is sensitive to the brain material model, necessitating robust validation methods.

Keywords—Shock wave, Intracranial pressure, Brain properties.

INTRODUCTION

Traumatic brain injuries (TBIs) resulting from exposures to blast waves have been recognized as the signature injuries in recent military conflicts due to high frequency usages of improvised explosive devices (IEDs), resulting in over 312,000 mild TBIs in American service members between 2000 and 2018.[10] Explosive blasts create a shock pressure wave which can injure the brain with no visible trauma, creating a diffuse injury that can often go undiagnosed. The mechanism of TBI from this pressure wave is still debated. Proposed injury mechanisms include direct cranial transmission,[8] skull flexure,[27] thoracic pressure surge,[3] acceleration,[25] and cavitation.[41] As practical limitations preclude investigating the nature and progression of this injury in humans, rodent blast-induced TBI (bTBI) models are often used to simulate human bTBI. However, the small temporal and spatial scales in which measurements must be made in the rodent model make experimental evaluation of biomechanical loading and resulting injury mechanisms technically challenging. Computational modeling holds great promise in complementing experimentation to better understand the biomechanical loading and injury pathways.

Several computational models of blast TBI have been developed. These finite element (FE) models were primarily focused on the simulation of helmeted[19,30,32,34,35,42] and unprotected[4,26,28,39,43] human subjects in free field explosions. Some human-subject FE models were partially validated by matching surface pressures measured with human head and neck surrogates, but practical hurdles prevent validation with intracranial pressure (ICP) measurements or strain fields. Some research groups sought to leverage computational modeling to understand inter-species scaling,[22,44] but to the authors' knowledge, no scaling studies have utilized FE models validated by experimental data. The wide use of the rodent model of bTBI to study injury mechanisms has enabled researchers to compare simulation-predicted ICP with experimentally-gathered

Address correspondence to Namas Chandra, Biomedical Engineering Department, New Jersey Institute of Technology, Newark, NJ, USA. Electronic mail: namas.chandra@njit.edu

© 2018 Biomedical Engineering Society

Published online: 06 December 2018

pressures.[25,37,45] However, validation using ICP is incomplete validation of the FE model prediction, which requires an understanding of the response of the brain to both pressure and shear waves. As strain validation measurements within the intact cranium are not capable of resolving displacements on the time scale of bTBI, computational models rely heavily upon obtaining accurate constitutive material models of the brain.

The brain exhibits an anisotropic[7] response that is conventionally considered a linear viscoelastic[2] or hyper-viscoelastic[7,9] material, varying in response by region[14] and strain rate.[31] However, variability in the experimental methodology, including post-mortem time,[40] specimen species,[16,29] specimen age,[11] and sample preparation[12] has led to reported values that vary by several orders of magnitude.[7]

FE models of the brain, thus far, have utilized material properties and constitutive models that offer numerical stability and convergence, approximate incompressibility, assume homogeneity, and validate against experimental measurements of ICP in blunt impacts.[17] However, material data corresponding to very high rate loading experienced under shock waves are not available. The short time scale and high strain rate of bTBI indicate that low strain rate validation data sets and incomplete validation will affect the quality of the simulation results. Therefore, this work seeks to understand the influence of the constitutive model and material parameters of the brain on a simulation of the brain's response to a shock wave loading. This will be conducted through parametric variation of the constitutive model of the brain, guided by experimental data of a rodent shock wave exposure. A high-fidelity FE model of a rodent exposed to a shock wave investigated how sensitive the ICP and maximum principal strain of brain tissue are to different brain constitutive models and material parameter values.

MATERIALS AND METHODS

Material Constitutive Models

The constitutive response of the brain can be divided into two independent parts: a time-independent (elastic) and time-dependent (viscoelastic and/or mixed media) response. The time-independent constitutive response is conventionally represented by linear elastic or hyperelastic models, which are considered to be comparable at small strains in the linear regime.[2,9] In this work, two time-independent models were considered—a linear elastic[36,37,45] and an Ogden hyperelastic.[11] The linear elastic is the simplest of the constitutive models, in which the stress–strain relationship is linear, given as

$$\boldsymbol{\sigma_{ij}} = 2G\left(\boldsymbol{\varepsilon_{ij}} + \frac{v}{1-2v}\boldsymbol{\varepsilon_{kk}}\delta_{ij}\right). \tag{1}$$

The Cauchy stress tensor, $\boldsymbol{\sigma_{ij}}$, is related to the strain tensor, $\boldsymbol{\varepsilon_{ij}}$, through the shear modulus, G, and the Poisson's ratio, υ. Although linear elasticity is most widely used in rat FE modeling, there exists some evidence in bovine tissue that the linear regime of brain tissue is limited to small strains, below 0.1% strain.[2] This has led to the rising popularity of the Ogden hyperelastic constitutive material model being used to describe the time-independent response of brain tissue. As with all hyperelastic constitutive models, the Ogden model describes the material behavior using the strain energy density, $\boldsymbol{W}$, given in its first order form as

$$\boldsymbol{W}(\lambda_1,\lambda_2,\lambda_3) = \frac{2G_0}{\alpha^2}\left(\bar{\lambda}_1{}^{\alpha} + \bar{\lambda}_2{}^{\alpha} + \bar{\lambda}_3{}^{\alpha} - 3\right) + 2K_0(J-1), \tag{2}$$

where λ_1, λ_2, and λ_3 are the principal stretches and α is a material constant. An overbar denotes that the principal stress was multiplied by $J^{-1/3}$, where the Jacobian is the determinant of the deformation matrix, $J = \det(\boldsymbol{F_{ij}})$. G_0 and K_0 are the instantaneous shear and bulk moduli. The Cauchy stress is derived from the strain energy density by

$$\boldsymbol{\sigma_{ij}} = \frac{1}{J}\frac{\delta \boldsymbol{W}}{\delta \boldsymbol{F_{kj}}}\boldsymbol{F_{ik}} \tag{3}$$

The time-dependent constitutive model defines the response of the brain to shear. The most common constitutive model used to describe the viscoelastic response of the rat brain is the Prony series, where the shear stress is derived from the tissue stiffness from relaxation experiments. The Prony series defines the time-dependent shear modulus, $G(t)$, in terms of the long-term and instantaneous shear moduli, G_∞ and G_0 respectively, as

$$G(t) = G_\infty + \sum_{k=1}^{N_G} G_k e^{-t/\tau_k} \tag{4}$$

and

$$G(t) = G_0 - \sum_{k=1}^{N_G} G_k(1 - e^{-t/\tau_k}), \tag{5}$$

where N_G, τ_k, and G_k are curve-fit material constants associated with the order, relaxation time, and shear modulus.

In the linear, isotropic viscoelastic model the Cauchy stress is calculated in terms of the deviatoric, ***eij***, and volumetric, ***φij***, strain tensors by the hereditary integral

$$\boldsymbol{\sigma_{ij}}(t) = \int_0^t 2G(t-s)\dot{\boldsymbol{e}}_{\boldsymbol{ij}}(s)ds + K_\infty \boldsymbol{\varphi_{ij}}(t)\delta_{ij}. \quad (6)$$

The Ogden hyper-viscoelastic model is implemented through finite-strain viscoelasticity, defined in terms of the instantaneous Kirchhoff stress, $\boldsymbol{\tau_{ij_0}}$, as a combination of the deviatoric, $\boldsymbol{\tau_{ij_0}}^{\boldsymbol{D}}$, and volumetric, $\boldsymbol{\tau_{ij_0}}^{\boldsymbol{V}}$, parts of the instantaneous Kirchhoff stress as

$$\boldsymbol{\tau_{ij_0}}(t) = \boldsymbol{\tau_{ij_0}}^{\boldsymbol{D}}(\bar{\boldsymbol{F}}(t)) + \boldsymbol{\tau_{ij_0}}^{\boldsymbol{V}}(J(t)). \quad (7)$$

The time-dependent deviatoric component of the Kirchhoff stress can then be derived using the push-forward operator by

$$\boldsymbol{\tau_{ij}}^{\boldsymbol{D}}(t) = \boldsymbol{\tau_{ij_0}}^{\boldsymbol{D}} - \mathrm{SYMM}\left[\sum_{k=1}^{N_D} \frac{G_k}{G_0\tau_k}\int_0^t \boldsymbol{F}_{\boldsymbol{ij}_t}^{-1}(t-s)\boldsymbol{\tau_{ij_0}}^{\boldsymbol{D}}(t-s)\boldsymbol{F}_{\boldsymbol{ij}_t}(t-s)e^{-s/\tau_k}ds\right], \quad (8)$$

where $\boldsymbol{F}_{\boldsymbol{ij}_t}(t-s)$ is the deformation gradient at time instant $(t-s)$ relative to the state at time t, given by $\boldsymbol{F}_{\boldsymbol{ij}_t}(t-s) = \boldsymbol{F_{ij}}(t-s)\boldsymbol{F_{ij}}(t)$. We assume that the volumetric component of the constitutive model is defined by the relationship derived from the integration of Eq. (2), the volumetric component of the Cauchy stress will result directly using the relationship in Eq. (3). The volumetric Cauchy stress is converted to the volumetric Kirchhoff stress by

$$\boldsymbol{\sigma_{ij}}^{\boldsymbol{V}}(t) = -\frac{1}{3}\frac{\boldsymbol{\tau_{ij}}^{\boldsymbol{V}}(t)}{J(t)}\delta_{ij}. \quad (9)$$

The deviatoric Kirchhoff stress can then be converted to the deviatoric Cauchy stress *via* the following relationship:

$$\boldsymbol{\sigma_{ij}}^{\boldsymbol{D}}(t) = \frac{\boldsymbol{\tau_{ij}}^{\boldsymbol{D}}(t)}{J(t)}. \quad (10)$$

Constitutive Model Parameters

Constitutive models and model parameters for the brain material were parametrically varied to elucidate the influence of brain material properties on the ICP and maximum principal strains. The ICP was chosen as a field output of interest, as it is a commonly measured parameter during *in vivo* blast loading. However, pressures are strongly coupled with the volumetric component of the constitutive model, potentially occluding the sensitivity of the solution to the deviatoric model. Therefore, the maximum principal strain was also investigated as field output of interest, as it is likely to highlight the strain history of the brain and its response to shear waves.

All material models and model parameter ranges investigated were taken from literature-derived material testing of rat tissue. A baseline model was parametrically varied. The material property values for the baseline model were assumed to be those most commonly used in literature, a linear viscoelastic one-term Prony model. This baseline model had a long-term bulk modulus of 2.19 GPa, a Poisson's ratio of 0.4999, an instantaneous shear modulus of 1.48 MPa, a Prony series shear modulus of 1.05 MPa, and a relaxation time constant of 0.02 s. The sensitivity of the simulation was examined through three comparisons, designed to enable full characterization of the brain material under blast loading. The long-term bulk modulus (2.19 MPa to 21.9 GPa), time-independent model (linear elastic and Ogden hyperelastic), and time-dependent model (one-term Prony series and three-term Prony series) of the brain material were parametrically varied from the baseline model. The investigation into the sensitivity of the long-term bulk modulus on the field variable outputs was determined by parametrically varying the long-term bulk modulus, while maintaining the Poisson's ratio, the dimensionless Prony series shear modulus (given by the Prony series shear modulus normalized with respect to the instantaneous shear modulus), and the relaxation time. The time-independent model was investigated using two Ogden hyperelastic models[11] and two linear elastic models with comparable orders of magnitude the long-term bulk modulus, with a constant viscoelastic model. Finally, sensitivity of the solution to the time-dependent model was investigated using four three-term Prony series viscoelastic models derived from literature while maintaining the elastic model[13] (Fig. 1). The material properties for the brain in all test cases and comparison groups are described in Table 1.

The soft tissue, brain, and dura were approximated as linear elastic materials. Air was described using the ideal gas equation of state at ambient pressure and temperature. Material properties common to all test cases are described in Table 2.

Shock Tube Exposures to Experimental Rat Model

An adult 10-week-old Sprague–Dawley rat (Charles River Laboratory) was used in this study. The animal was housed in a 12 h light–dark cycle at 22°C, with free access to food and water. All procedures were approved by the Rutgers University Institutional Animal Care and Use Committee. The animal was sacrificed using carbon dioxide and, immediately after sacrifice, two holes were drilled into the occipital bone. Two pressure sensors (Millar SPR-407, ADInstru-

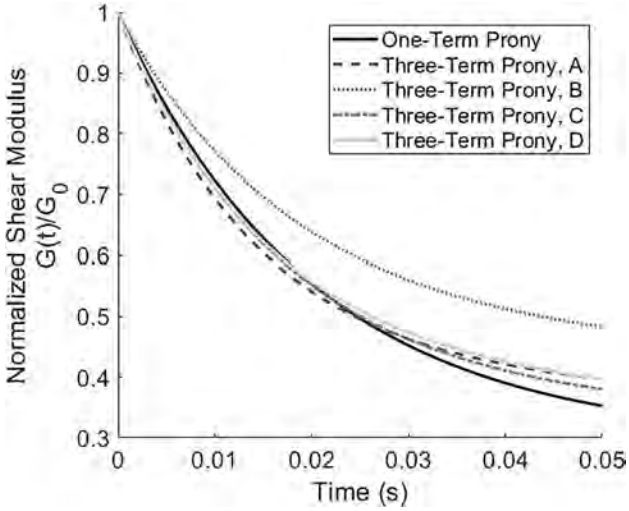


FIGURE 1. Shear modulus values normalized with respect to the instantaneous shear modulus decaying with time.

ments; Colorado Springs, CO) were implanted into the left and right hemispheres of the brain through 19-gage stainless-steel cannulas at depths of 11.5 and 8.5 mm, respectively. Contact was assured between the pressure sensor and the brain by backfilling the cannulas with

TABLE 2. The constitutive models and material properties used in all simulations.

	Elastic modulus, E (MPa)	Poisson's ratio, ν
Linear elastic		
Skull[1,21]	9500	0.3
Soft tissue[15]	16.7	0.42
Dura[1]	20.0	0.45
	Gas constant, R	**Specific heat, c_p**
Ideal gas equation of state		
Air	287 J kg^{-1} K^{-1}	1010 J kg^{-1} K^{-1}

TABLE 1. The brain constitutive material models tested in this study.

Long-term bulk modulus, K_∞	Inst. shear modulus, G_0 or μ_0	Ogden material constant, α	Prony series shear modulus, G_i	Relaxation time constant, τ_i (s)
Sensitivity to long term bulk modulus				
Linear viscoelastic, one-term Prony[18,33]				
21.9 GPa	14.8 MPa	–	10.5 MPa	0.02
2.19 GPa	1.48 MPa	–	1.05 MPa	0.02
219 MPa	148 kPa	–	105 kPa	0.02
80.8 MPa	54.8 kPa	–	38.6 kPa	0.02
21.9 MPa	14.8 kPa	–	10.5 kPa	0.02
2.54 MPa	1.72 kPa	–	1.21 kPa	0.02
2.19 MPa	1.48 kPa	–	1.05 kPa	0.02
Sensitivity to time-independent model				
Linear viscoelastic, one-term Prony[18,33]				
219 MPa	148 kPa	–	105 kPa	0.02
80.8 MPa	54.8 kPa	–	38.6 kPa	0.02
Ogden hyper-viscoelastic, one-term Prony[11]				
187 MPa	126 kPa	20.6	918 kPa	0.02
94 MPa	63.7 kPa	20.6	325 kPa	0.02
Sensitivity to time-dependent model				
Linear viscoelastic, one-term Prony[18,33]				
2.19 GPa	1.48 MPa	–	1.05 MPa	0.02
Linear viscoelastic, three-term Prony[13]				
2.19 GPa	1.48 MPa	–	G_1 = 3.14 kPa	τ_1 = 0.0137
			G_2 = 1.06 kPa	τ_2 = 0.195
			G_3 = 749 Pa	τ_3 = 5.06
2.19 GPa	1.48 MPa	–	G_1 = 744 Pa	τ_1 = 0.293
			G_2 = 1.94 kPa	τ_2 = 0.0177
			G_3 = 572 Pa	τ_3 = 6.34
2.19 GPa	1.48 MPa	–	G_1 = 1.84 kPa	τ_1 = 0.0161
			G_2 = 578 Pa	τ_2 = 0.211
			G_3 = 459 Pa	τ_3 = 4.83
2.19 GPa	1.48 MPa	–	G_1 = 936 Pa	τ_1 = 0.015
			G_2 = 346 Pa	τ_2 = 0.176
			G_3 = 267 Pa	τ_3 = 4.54

agarose gel. The locations of the pressure sensors were confirmed through a 11.6-μm resolution microcomputed tomography scan (μCT) (Skyscan 1172, Brucker; Kontich, Belgium). A three-dimensional reconstruction of the μCT was used to identify the locations of the cannula tips with respect to the dimensions of the cranial cavity (Fig. 2). The cannula locations from the experiment were then scaled to the cranial cavity of the FE model to identify the locations of interest in the simulation.

The 229 × 229 mm^2 shock tube at the Center for Injury Biomechanics, Materials, and Medicine at the New Jersey Institute of Technology was used for the experimental exposures. The test apparatus, explained in more detail elsewhere,[5,24] has been shown to emulate a primary blast similar to those seen in free-field explosions in a reliable and controlled manner.[6] The specimen was placed at the test location, 2.80 m from the breech or 3.05 m from the shock tube exit. The animal was strapped tightly in the prone position using a thin cotton cloth (Fig. 2b). The specimen was exposed to a repeat of four Helium-driven shock waves of 130 kPa overpressure. Incident pressure measurements were taken along the length of the shock tube using 134A24 series sensors (PCB Piezotronics, Depew, NY) to verify the exposure conditions (shock wave intensity and velocity). All data were recorded at 1.0 MHz sampling frequency, with the acquisition time of 100 ms per experiment.

High-speed videos were recorded for every experiment using Photron FASTCAM Mini UX100 camera operating at framerate of 5000 fps, and Photron FASTCAM Viewer 3.3.5 software. This was done as a quality assurance method to ensure that proper head strapping eliminated unwanted head motion during the blast.

Finite Element Model

The experimental setup was modeled as a coupled Eulerian–Lagrangian system, which has been used previously to model shock propagation.[19] The system consisted of a Eulerian representation of a section of the shock tube that interacted with a Lagrangian rat head. The rat head, based on a magnetic resonance imaging scan of a 10-week-old Sprague–Dawley rat, was segmented into the skin/soft tissue, skull, dura, and brain (Simpleware, Synopsys, Exeter, UK). The rat used in model generation and the experimental test subject were matched for age, sex, and weight. A comparison of the skulls highlighted a good morphological match between the two specimens (mean surface deviation of 0.056 mm, RMSE of 0.43 mm). A quadratic tetrahedral mesh converged at 196,000 elements with an average elemental minimum edge length of 0.62 mm, where a 30% reduction in characteristic element length did not result in a 5% change in the peak pressure within the brain at the regions of interest (Fig. 3c).

A 1 m section of the shock tube was modeled using a linear hexahedral Eulerian mesh at a converged characteristic element length of 8 mm. Convergence testing identified that this mesh density reproduced contact surface pressures at the Eulerian–Lagrangian interface with $< 2\%$ difference when element number was doubled. This resulted in a domain of 218,000

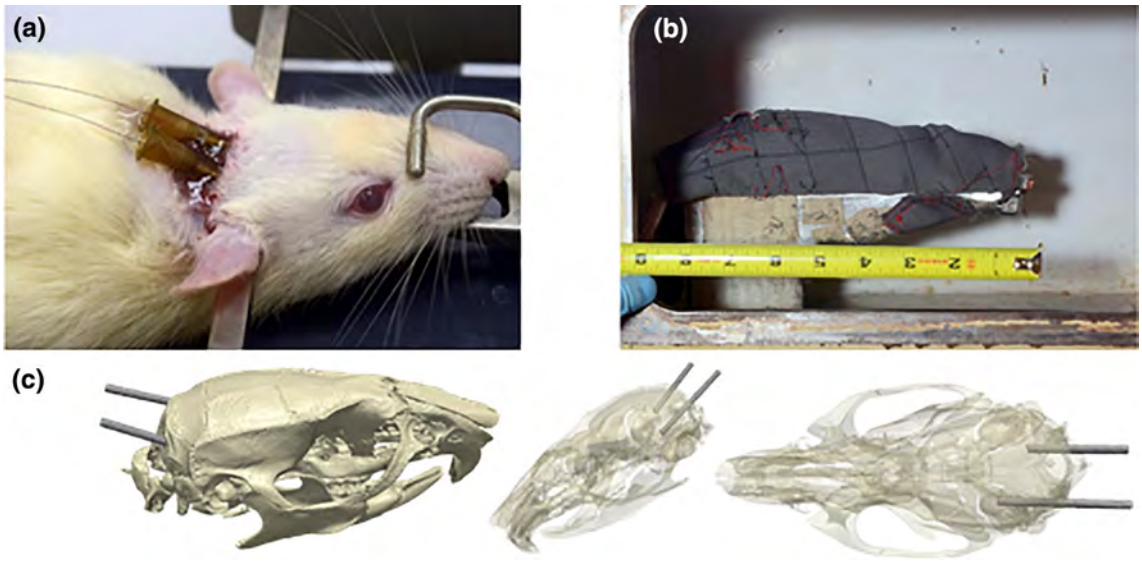


FIGURE 2. (a) The specimen with cannulas inserted into the left and right hemispheres. (b) The specimen secured in the cotton wrap within the shock tube in the prone position. (c) Three-dimensional reconstruction of the μCT of the rat skull, showing the positions of the cannulas within the cranial cavity in the experimental study (μCT image not shown).

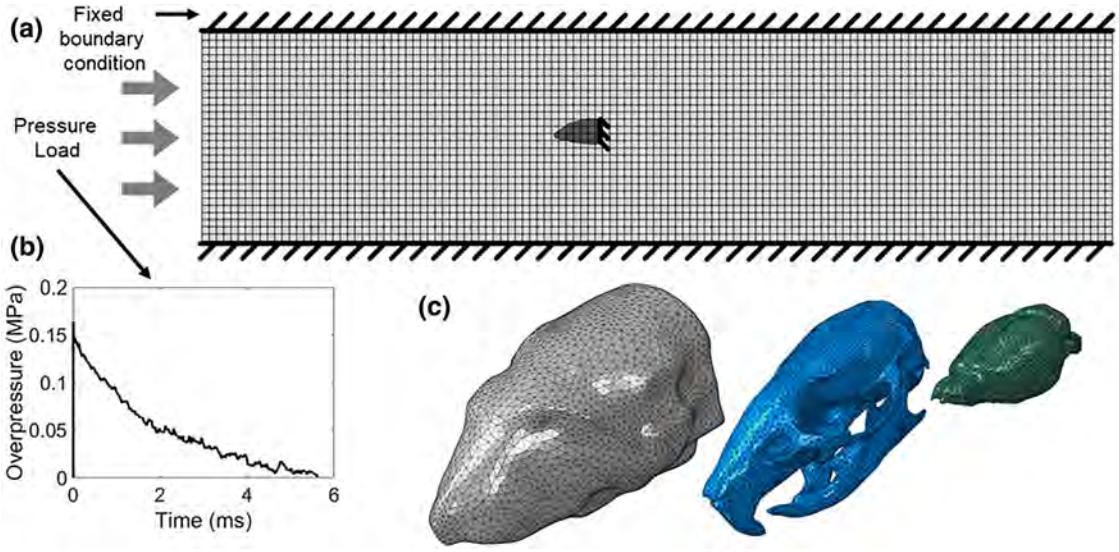


FIGURE 3. The (a) Eulerian and Lagrangian finite element model of the shock tube system, (b) the pressure loading curve, and (c) the Lagrangian finite element model of the rat head with the soft tissue (left), cranium, and brain (right) isolated. The rat head is positioned within the Eulerian shock tube domain at the test section.

elements (Fig. 3a). The length of the shock tube section was set to 1 m to minimize computational run time and to not influence the solution with artifacts from the end of the domain.

The edges of the shock tube model that coincided with the walls of the shock tube were fixed in all translational degrees of freedom. A non-reflecting boundary condition was placed on exit of the shock tube section. A loading pressure wave was placed on the shock tube section opening. The loading pressure wave (Fig. 3b) was generated by averaging the four incident pressure measurements taken by a sensor at that location. The simulation time was set to 2.5 ms, a simulation duration which has previously been reported in literature for the simulation of blast loading on a rat head.[45] Validation of the shock tube model was confirmed through a comparison of the experimental incident pressure measurement and the simulated incident pressure, which demonstrated an excellent match (Fig. S1).

The Lagrangian rat head was placed at the test section within the Eulerian shock tube section and the posterior surface was fixed against all translational and rotational degrees of freedom. This assumption reflected the rigid mounting of the experimental test specimen. To investigate the potential influence of the boundary conditions assumption on the solution, the solution was compared to a model with a more complex boundary condition, where the neck surface was tied to a point mass representing the body weight of the rat. The results showed a difference between the peak ICP of approximately 5%. Due to the large number of simulations proposed in this work, the more constrained boundary conditions were used. A higher fidelity approximation of the boundary conditions will be used in future models to aid future validation efforts.

The Eulerian domain interacted with the Lagrangian domain using a general contact algorithm on all surfaces, excluding the posterior surface of the rat head model, as hard contact with complete separation after contact. The contact algorithm minimized co-localization of the Lagrangian and Eulerian domains. The simulations were performed using Abaqus/Explicit 6.14-1 (Simulia, Dassault Systemes; Johnston, Rhode Island) with two Intel Xeon CPUs (2.1 GHz) with 128 GB RAM on 20 cores. All data were recorded at a sampling rate of 80 kHz for the duration of the 2.5 ms simulation. Solutions averaged 850 $\pm$ 423 CPU hours (42.5 h on 20 processors).

Data Analysis

Data analysis was performed using Origin 2017 (OriginLab; Northhampton, Massachusetts) and MATLAB R2018a (Mathworks; Natick, Massachusetts). Quantification was performed for the peak overpressure for the experimental incident shock wave, and both intracranial pressure profiles. Data are presented as average and standard deviation. The multiple comparison t test with Bonferroni correction was performed to identify the differences between characteristic parameters of recorded pressure profiles. The strength of the relationship between material models and the computed output field variables was found using the Pearson correlation coefficient. The multiple

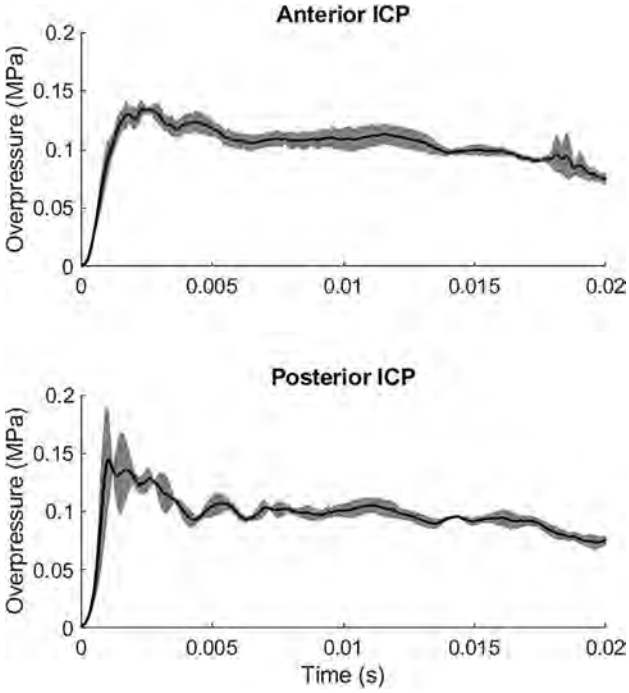


FIGURE 4. The average ICP profiles for the anterior (above) and posterior (below) experimental measurement locations with the standard deviations included in greyscale ($n = 4$ repeated 130 kPa exposures).

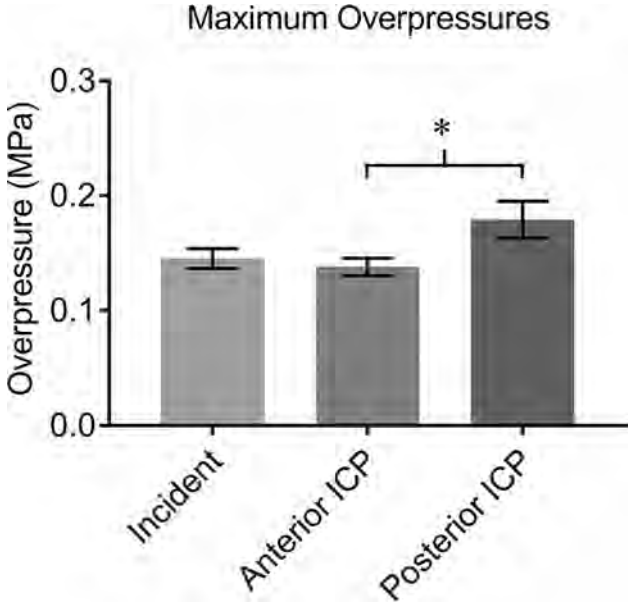


FIGURE 5. The maximum experimentally-measured pressures for the incident pressure wave, measured from a sensor on the shock tube wall, and the anterior and posterior ICPs, measured intracranially ($n = 4$ repeated 130 kPa exposures) *$p < 0.015$.

comparison t test was used to identify the differences between the predicted values in the anterior and posterior locations. In all cases, $p < 0.015$ was used as a threshold of statistical significance.

RESULTS

Experimental Pressure Measurements

Average ICP profiles in the anterior and posterior locations, initialized with respect to arrival time, are included in Fig. 4. The maximum ICP values in the posterior were significantly higher than those in the anterior brain ($p = 0.013$) and there was no significant difference in the ICP measurements in the anterior and posterior brain with respect to the incident pressure wave (Fig. 5).

Computational Simulation Transmission Pathway

The computational simulation coinciding with the baseline material properties ($K_\infty = 2.19$ GPa, linear, one-term Prony viscoelastic model) was qualitatively evaluated to visualize the temporal and spatial development of ICP and maximum principal strain within the mid-sagittal brain (Fig. 6). The incident pressure wave began interaction with the head at $t = 0.8000$ ms. The compressive pressure wave enters the brain at $t = 0.8375$ ms in the anterior, superior brain and travels posteriorly. A small secondary pressure wave is transmitted along the superior surface of the brain ($t = 0.8625$–0.9625 ms) where a compressive pressure wave (330 kPa) is followed by a small tensile wave (-60 kPa). This secondary pressure wave coincides with a superior–inferior wave that is transmitted through the cranium. Peak compressive pressures are observed at the posterior, inferior brain, where the brain interfaces with the foramen magnum of the skull, from $t = 0.9875$–1.1875 ms, reaching a peak value of 490 kPa at $t = 1.0500$ ms, These peak compressive pressures are followed by an increase in the maximum principal strain. From $t = 1.0625$–1.1375 ms, tensile pressures develop in the anterior brain, reaching a peak value of -120 kPa at $t = 1.1125$ ms. Shortly after the final timepoint shown in Fig. 6, the ICP is dominated by motion of the skull. The skull motion is apparent in concentric waves of the maximum principal strain (Fig. 6b).

Sensitivity of Solution to Long-Term Bulk Modulus

Pearson's correlation analysis revealed a strong positive correlation between the maximum ICP and the logarithm of the long-term bulk modulus in the anterior ($r = 0.9477$, $N = 7$, $p = 0.0012$) and posterior brain ($r = 0.9181$, $N = 7$, $p = 0.0035$) (Fig. 7a). The best match to experimental ICP values was seen with a long-term bulk modulus of approximately 80 MPa,

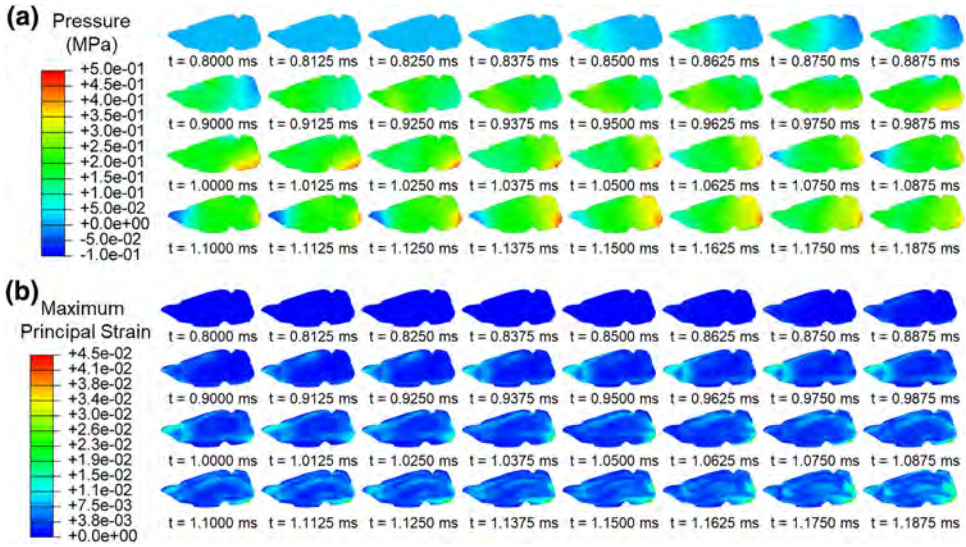


FIGURE 6. The time-evolution of the (a) ICP, given in MPa, and (b) the maximum principal strain in the midsagittal plane of the rat brain over the course of 0.4 ms at a time interval of 12.5 μs.

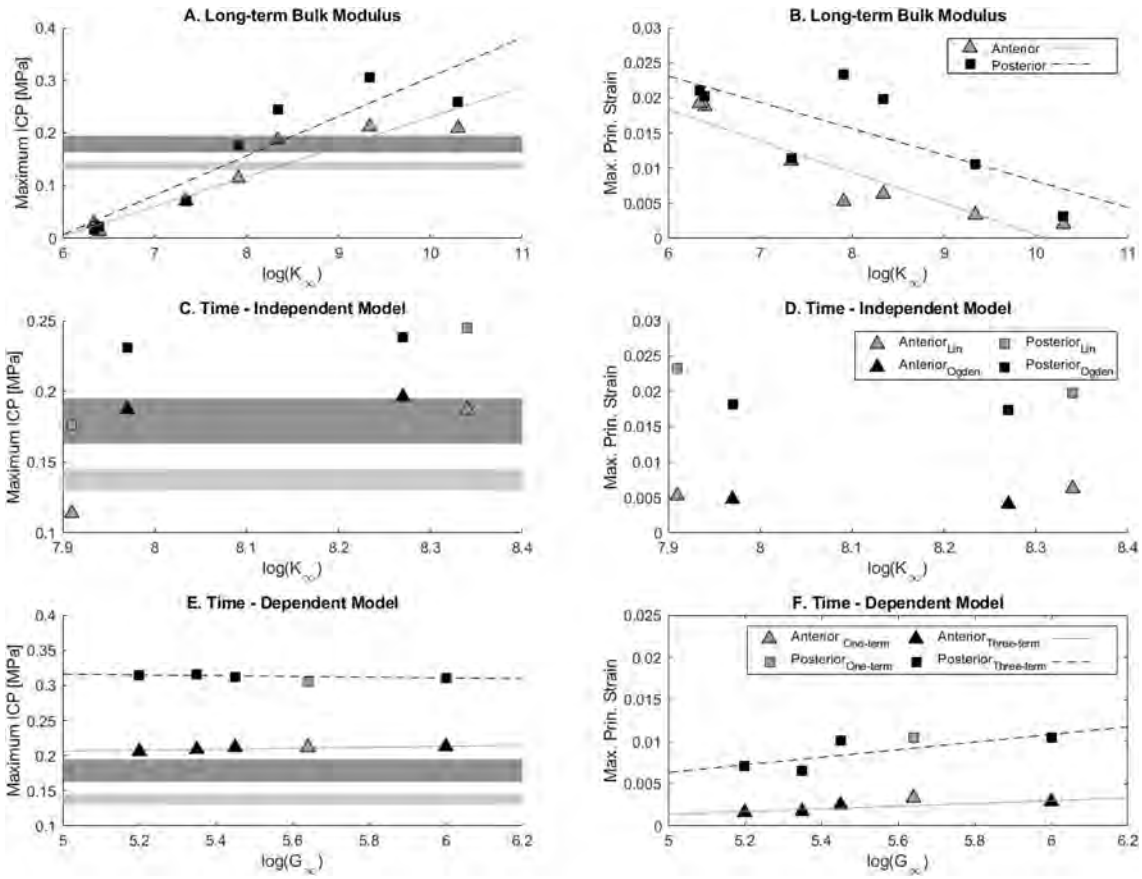


FIGURE 7. Assessment of the sensitivity of the ICP (left) and the maximum principal strain (right) to variability of the (a/b) long-term bulk modulus, (c/d) time-independent model, and (e/f) time-dependent model. Model variability is described as the order of magnitude of the long-term bulk or shear moduli. (a, c, e) Include a band noting the range of values falling within one standard deviation of the mean experimental values for the anterior (lighter) and posterior (darker) ICPs.

with the anterior and posterior ICP measurements falling 17.4% and 1.9% below the experimental values. Likewise, Pearson's correlation analysis revealed a strong negative correlation between the logarithm of the long-term bulk modulus and the maximum principal strain in the anterior ($r = -0.9838$, $N = 7$, $p < 0.0001$) and the posterior brain ($r = -0.9838$, $N = 7$, $p < 0.0001$) (Fig. 7b). The posterior maximum principal strain was higher in every time-independent model ($p = 0.0022$). The pressure–time profiles comparing the simulated and experimentally-measured ICP profiles highlighted the influence of the skull motion on the ICP profile (Figs. 8a and 8b). Large amplitude, low frequency oscillations are seen in the simulated ICP profiles that are not apparent in the experimental measurements. The nature of these oscillations appears to change with the long-term bulk modulus, but a signal analysis did not produce conclusive results.

Sensitivity of Solution to Time-Independent Model

The effect of the constitutive time-independent model was identified by comparing simulation results between a linear elastic model and two Ogden hyper-elastic models with the same long-term bulk moduli and viscoelastic model. The difference between the anterior and posterior ICP measurements was lower in the Ogden hyper-viscoelastic models (Fig. 7c), with the posterior ICP being 18.4 ± 0.99% larger in the Odgen models, in comparison to 29.5 ± 8.17% in the linear models (Table 3). The Ogden hyper-viscoelastic models exhibited lower maximum principal strains than the linear viscoelastic models with similar bulk moduli (Fig. 7d, Table 3). Pressure–time profiles comparing the ICP waveforms between time-independent models display a larger amplitude and lower frequency oscillation in the dissipating ICP profile (Figs. 8c and 8d).

Sensitivity of Solution to Time-Dependent Model

The time-dependent model was varied using five representations of the Prony series with the same long-term bulk modulus ($K_\infty = 2.19$ GPa). There exhibited little difference in maximum ICP predictions between time-dependent models, with a maximum percent difference between the three-term series model and the one-term series model of 3.3% (Fig. 7e, Table 3). The three-term Prony series models did tend to exhibit a lower maximum principal strain in the anterior measurement, while the difference was less pronounced in the posterior measurement (Fig. 7f, Table 3). Field variable outputs were compared with the log of the long-term shear modulus, as the long-term bulk mod-

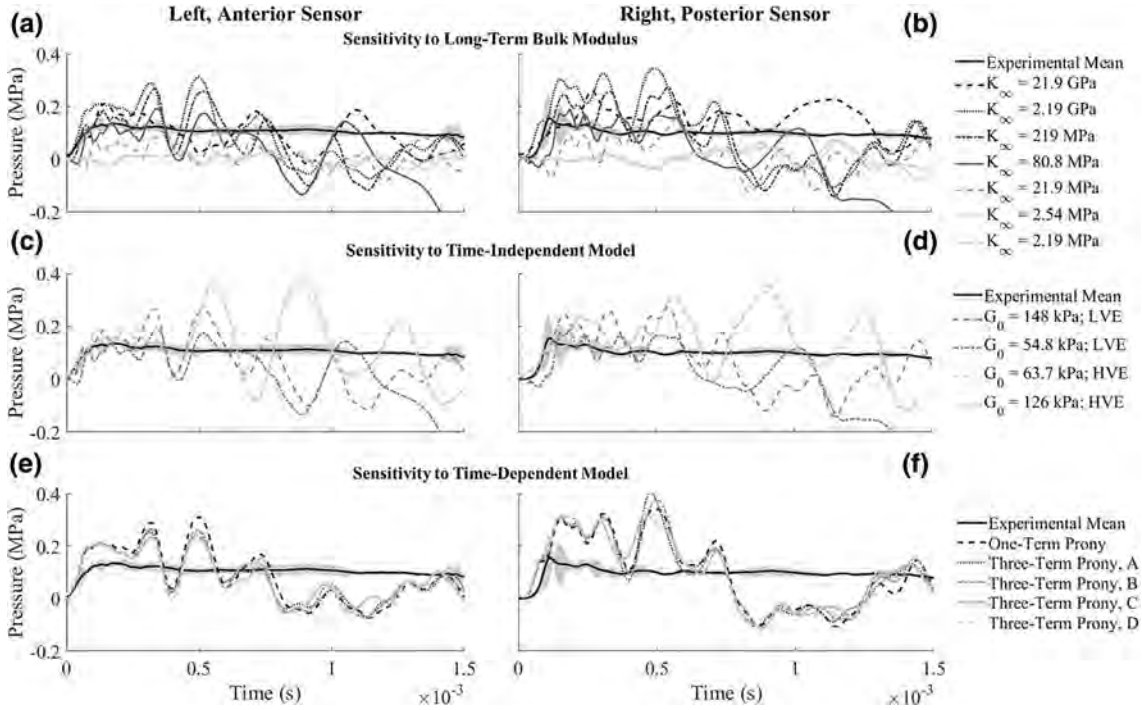


FIGURE 8. The pressure–time profiles for the experimentally-measured ICP profiles (mean ± one SD) and the simulated ICP profiles in the left, anterior (left) and right, posterior (right) sensors. All ICP profiles have been normalized with respect to arrival time. The sensitivity of the solution to the long-term bulk modulus (a, b), the time-independent model (c, d), and the time-dependent model (e, f) show oscillatory behavior approximately 0.4 ms after the shock wave reaches the brain tissue, observed to be the effect of skull deformation. LVE, linear viscoelastic; HVE, Ogden hyper-viscoelastic.

TABLE 3. Peak compressive ICP values, peak tensile ICP values, and maximum principal strains for all simulations.

	Peak compressive ICP (kPa)		Peak tensile ICP (kPa)		Maximum principal strain	
Simulation	Left, anterior	Right, posterior	Left, anterior	Right, posterior	Left, anterior	Right, posterior
Sensitivity to long term bulk modulus						
K_∞ = 21.9 GPa	209	260	− 20.6	N/A	2.02e−3	3.13e−3
K_∞ = 2.19 GPa	212	305	− 55.9	− 102	3.33e−3	1.05e−2
K_∞ = 219 MPa	187	245	− 101	− 119	6.31e−3	1.98e−2
K_∞ = 80.8 MPa	114	176	− 135	− 45.9	5.28e−3	2.33e−2
K_∞ = 21.9 MPa	71.4	70.4	− 54.4	− 126	1.10e−2	1.14e−2
K_∞ = 2.54 MPa	13.1	21.7	− 38.4	− 50.2	1.92e−2	2.11e−2
K_∞ = 2.19 MPa	11.8	16.2	− 42.5	− 38.1	1.88e−2	2.03e−2
Sensitivity to time-independent model						
G_0 = 148 kPa, LVE	187	245	− 101	− 119	6.31e−3	1.98e−2
G_0 = 54.8 kPa, LVE	114	176	− 135	− 45.9	5.28e−3	2.33e−2
G_0 = 126 kPa, HVE	196	238	− 69.9	− 8.70	4.10e−3	1.74e−2
G_0 = 63.7 kPa, HVE	187	231	− 82.7	− 9.29	4.79e−3	1.82e−2
Sensitivity to time-dependent model						
One-term Prony	212	305	− 55.9	− 102	3.33e−3	1.05e−2
Three-term Prony, A	212	312	− 38.7	− 106	2.52e−3	1.02e−2
Three-term Prony, B	213	311	− 51.0	− 116	2.90e−3	1.05e−2
Three-term Prony, C	206	315	− 55.2	− 111	1.62e−3	7.10e−3
Three-term Prony, D	209	316	− 73.6	− 112	1.73e−3	6.60e−3

N/A the simulation did not experience tensile pressures at the measurement location.
LVE, linear viscoelastic; HVE, Ogden hyper-viscolastic.

ulus was maintained between test cases. Pearson correlation analysis did not reveal statistically significant relationships for the anterior or posterior maximum ICP ($r = 0.8365$, $N = 5$, $p = 0.0774$; $r = -0.5532$, $N = 5$, $p = 0.3334$) or maximum principal strains ($r = 0.7741$, $N = 5$, $p = 0.1245$; $r = -0.7592$, $N = 5$, $p = 0.1366$). A comparison of the ICP-time profiles at the left, anterior and right, posterior sensors further confirm this conclusion. Visually, slight differences are observed in the dissipation of the ICP, but the pattern of dissipation are maintained, with the amplitudes of the oscillatory peaks varying slightly between the five models (Figs. 8e and 8f). As previously, when comparing the shape of the ICP profiles between the experimental and simulated pressures, the simulation is largely dominated by oscillations reflecting movements of the skull.

DISCUSSION

This work offers a detailed examination of the material properties and constitutive models which are best suited for the simulation of blast loading on the rat brain.

This was performed by investigating the sensitivity of a rat FE model exposed to a 130 kPa overpressure shock wave to the material properties and constitutive models generally used in the numerical simulation of the brain. Simulation results were compared to ICP readings taken experimentally as a point of validation. Simulated ICP and maximum principal strains were compared between variations in the long-term bulk modulus and the time-independent and time-dependent constitutive models.

Experimental ICP measurements indicate that the maximum ICP in the posterior brain is significantly higher than at the anterior brain. This experimental observation was confirmed in the computational simulations. This indicates that transmission of the pressure wave does not translate into an even pressure distribution throughout the entire brain tissue. The posterior brain is theorized to be loaded by a reflected wave through the cranium. The high bulk and shear moduli of the bone in the cranium allow for faster transmission of the pressure wave, loading the posterior brain with a reflected wave, leading to a higher ICP observed in the cerebellum.[37,38] This finding highlights the importance of reporting pressure sensor location within the cranium *via* histology or radiology.

This work concludes that the ICP and the maximum principal strain are correlated to the long-term bulk modulus. Previous FE models of the head have been investigated for their sensitivity to bulk modulus values,[17] but their primary focus have been on blunt TBI. However, the difference in loading time scales between blunt and blast TBI make direct application of their findings a questionable assumption. Our results indicate that, in the early time scale of bTBI, the ICP is sensitive to the long-term bulk modulus and that the

solution was largely insensitive to the viscoelastic model used. This is expected as large differences between the bulk and shear moduli affect the speed of wave propagation for the pressure and shear wave within the cranium. The bulk modulus is largely responsible for determining the speed at which a pressure wave will propagate, demonstrated by Eq. (11). For a linear viscoelastic material, at the long-term bulk moduli investigated in this work (2.19 MPa–21.9 GPa), the maximum pressure wave speed, v_p, is 84.5–8,450 m/s.

$$v_p = \sqrt{\frac{K_0 + \frac{4}{3}G_0}{\rho}}. \tag{11}$$

As the rat brain is approximately 0.03 m in length, the pressure wave and resulting intracranial reflections will occur on the order of 0.35 ms–3.5 μs. However, the maximum shear wave speed, v_s given by Eq. (12), is 70.7 times slower than the pressure wave speed, indicating that the effect of shear wave development will take upwards of 24.7 ms to be transmitted through the skull.

$$v_s = \sqrt{\frac{G_0}{\rho}}. \tag{12}$$

This is beyond the time scale of interest selected in this study and is confirmed in the lack of sensitivity observed in the solution to changing time-dependent models.

An effective long-term bulk modulus on the order of 80 MPa was found to best match the experimental ICP readings. This value is lower than the most commonly used literature value of 2.19 GPa, determined from post-mortem human and non-human primate subjects in hydrodynamic compression tests.[36] Values on the order of GPa have been corroborated through FE model investigations of the human head in response to an impact[33] or a rotational acceleration,[17] validated against cadaveric and live human subject data. The lower effective long-term bulk modulus identified from experimental observations indicates that further investigation into the long-term bulk modulus value is required. The observed difference between the long-term bulk modulus used largely in literature and the value identified in this work is likely a result of the FE modeling assumptions. Evidence suggests that material properties used to model the skull can alter the ICP, with a stiffer skull exhibiting a higher ICP.[38] Likewise, other material properties, such as those for the skin and the CSF, are likely to contribute to the biomechanical response of brain tissue to a blast. As parametrically investigating the material properties of all structures was beyond the scope of this work, the influence of the skull stiffness, skin and soft tissue model, and CSF material properties and modeling technique on ICP measurements can only be theorized. Biological tissues are, by nature, viscoelastic and exhibit strain rate dependence, with a proportional relationship between stiffness and strain rate. In the high strain rate loading of bTBI, tissue material models exhibiting a stiffer response are likely necessary to increase the apparent long-term bulk modulus to a range that is more in line with literature values. Additionally, multiple approaches to modeling the CSF and the subarachnoid have been proposed, varying from an elastic approximation,[37] modeling the shear resistance offered by the CSF/subarachnoid space as a boundary condition,[20] or modeling the CSF as a fluid.[4] It is recommended that systematic investigations of all material models within the headform be conducted to further facilitate model development and validation efforts.

A lack of sensitivity of the ICP and the maximum principal strain to the time-dependent constitutive material models was observed. This observation can be attributed to the short loading period experienced in bTBI. In the time scale investigated, the relaxation constants did not allow for large variability in the shear models, as seen by the small range of long-term shear moduli. Additionally, it is theorized that the large difference between the long-term bulk modulus and the long-term shear modulus limits the size of its effect. In this work, all viscoelastic models investigated were derived from low strain rate testing of rodent brain tissue. This resulted in a cluster of models that all behaved very similarly. Therefore, it is recommended that future computational modeling of bTBI focus precisely on the instantaneous and long-term shear moduli rather than the Prony viscoelastic model, expanding beyond the range of literature examined values.

The applicability of computational modeling is constrained by the modeling assumptions made. As this work was focused on understanding the sensitivity of the brain material properties on field outputs, and not in the generation of a fully validated bio-fidelic model, assumptions were made to be able to conduct a large number of simulations without compromising the quality of the results. First, it was assumed that the rat body would have a negligible effect on the ICP. The inclusion of a body may potentially influence the aerodynamics of the shock wave, but this effect would not influence the field variables chosen in this work, the early time-scale peak compressive pressures and strains within the brain. Second, the experimental measurements were taken with stainless-steel cannulas and these cannulas were excluded from the simulation. This exclusion was based upon the assumption that the

experimental pressure readings are not heavily influenced by the presence of the stainless-steel cannulas. The experimental ICP measurements in both sensors maintain a characteristic Friedlander profile, similar in nature to an incident pressure waveform, indicating that reflections from the cannulas are not significantly affecting the waveform. As this work reports the transmission pathway of an unimpeded shock wave, it is not anticipated that this simplification will significantly affect the reported relationships and conclusions. Finally, it was assumed that a 2.5 ms simulation duration, sampled at a rate of 80 kHz, would resolve the sensitivity of the solution with enough accuracy. This simulation length and sampling rate falls within the range of other finite element models of blast loading on rat brains.[45] However, our experimental results indicate that the duration of an ICP pulse is, on average, 7.6 ms. The simulated time of 2.5 ms, of which 1.7 ms of ICP signal is captured, is insufficient to calculate the duration or impulse. Additionally, the sampling rate was not high enough to resolve the signal rise times, experimentally measured to be as low as 4 μs. Therefore, in future work it is recommended that simulated time includes the entire ICP profile and that the sampling rate during the loading period is high enough to capture the rise time. This would permit more detailed analysis, enabling an investigation of how material properties effect the dissipation of the ICP profile.

A major limitation of all computational modeling of bTBI, including this work, is that it indicates that the maximum principal strain is sensitive to the chosen constitutive material models, yet there is no experimental validation of these results. The lack of experimental validation criteria precludes the identification of the ideal brain material model. Researchers have attempted to quantify the strain *in vivo* during a sub-injurious event by tagging radiological images.[23] While this method offers a novel and innovative method of validating FE models of rotational and blunt injuries, the 18 ms temporal resolution precludes its applicability to the investigation of blast TBI. Therefore, caution should be exercised when validating an FE model against pressure readings alone. A discussion of the sensitivity of solution results to variable brain constitutive models is necessary for complete understanding of the results. It is also identified that there is a distinct need in the scientific literature for accurate high strain rate deformation measurements within the brain.

This work offers, exclusively, insight into the effect of brain material parameters and constitutive models on computational modeling of rat bTBI. By parametrically varying the constitutive material models, it was concluded that the long-term bulk modulus is the most sensitive brain material property in shock wave propagation-dominated bTBI problems. The maximum ICP increases and the maximum principal strain decreases proportionally with the order of magnitude of the long-term bulk modulus. No significant effect was observed between time-independent models or between time-dependent models. The posterior brain exhibited higher ICP and higher strains than the anterior brain. This indicates that the pressure transmission is influenced by the presence of reflected waves from the cranium. An effective long-term bulk modulus value of 80 MPa was determined to best match experimental measurements. This work highlights that material properties and constitutive models derived for low strain rate applications are not directly applicable to high strain rate loading events, necessitating sensitivity analyses to fully characterize FE models of bTBI.

ELECTRONIC SUPPLEMENTARY MATERIAL

The online version of this article (https://doi.org/10.1007/s10439-018-02178-w) contains supplementary material, which is available to authorized users.

ACKNOWLEDGMENTS

This work was supported by Grant No. 14059001 (W81XWH-15-1-0303) under the U.S. Army Medical Research and Materiel Command. Authors acknowledge the assistance of Dr. Saikat Pal with proof reading, Debrina Roy in model development, and Dr. Raj Gupta in theoretical discussions.

CONFLICT OF INTEREST

The authors have no conflicts to disclose.

REFERENCES

[1]Baumgartner, D., M. Lamy, R. Willinger, P. Choquet, C. Goetz, A. Constantinesco, and J. Davidsson. Finite element analysis of traumatic brain injuries mechanisms in the rat. In: IRCOBI Conference, 2009, pp. 97–108.

[2]Bilston, L. E., Z. Liu, and N. Phan-Thien. Linear viscoelastic properties of bovine brain tissue in shear. *Biorheology* 34(6):377–385, 1997. https://doi.org/10.1016/S0006-355X(98)00022-5.

[3]Cernak, I., Z. Wang, J. Jiang, X. Bian, and J. Savic. Ultrastructural and functional characteristics of blast injury-induced neurotrauma. *J. Trauma* 50:695–706, 2001.

[4]Chafi, M. S., G. Karami, and M. Ziejewski. Biomechanical assessment of brain dynamic responses due to blast pres-

sure waves. *Ann. Biomed. Eng.* 38(2):490–504, 2010. https://doi.org/10.1007/s10439-009-9813-z.

[5]Chandra, N., S. Ganpule, N. N. Kleinschmit, R. Feng, A. D. Holmberg, A. Sundaramurthy, V. Selvan, and A. Alai. Evolution of blast wave profiles in simulated air blasts: experiment and computational modeling. *Shock Waves* 22(5):403–415, 2012. https://doi.org/10.1007/s00193-012-0399-2.

[6]Chandra, N., A. Sundaramurthy, and R. K. Gupta. Validation of laboratory animal and surrogate human models in primary blast injury studies. *Mil. Med.* 182:105–113, 2017. https://doi.org/10.7205/MILMED-D-16-00144.

[7]Chatelin, S., C. Deck, and R. Willinger. An anisotropic viscous hyperelastic constitutive law for brain material finite-element modeling. *J. Biorheol.* 27:26–37, 2013. https://doi.org/10.1007/s12573-012-0055-6.

[8]Clemedson, C. J. Shock wave transmission to the central nervous system. *Acta Physiol. Scand.* 37(2–3):204–214, 1956. https://doi.org/10.1111/j.1748-1716.1956.tb01356.x.

[9]de Rooij, R., and E. Kuhl. Constitutive modeling of brain tissue: current perspectives. *Appl. Mech. Rev.* 68(1):010801–010801-16, 2016. https://doi.org/10.1115/1.4032436.

[10]Defense and Veterans Brain Injury Center. DoD Numbers for Traumatic Brain Injury. Silver Spring: Defense and Veterans Brain Injury Center, pp. 1–5, 2013.

[11]Elkin, B. S., A. I. Ilankovan, and B. Morrison. Age-dependent regional mechanical properties of the rat hippocampus and cortex. *J. Biomech. Eng.* 132(1):011010, 2009. https://doi.org/10.1115/1.4000164.

[12]Fallenstein, G., V. Hulce, and J. Melvin. Dynamic mechanical properties of human brain tissue. *J. Biomech.* 2(3):217–226, 1969. https://doi.org/10.1016/0021-9290(69)90079-7.

[13]Finan, J. D., B. S. Elkin, E. M. Pearson, I. L. Kalbian, and B. Morrison. Viscoelastic properties of the rat brain in the sagittal plane: effects of anatomical structure and age. *Ann. Biomed. Eng.* 40(1):70–78, 2012. https://doi.org/10.1007/s10439-011-0394-2.

[14]Finan, J. D., S. N. Sundaresh, B. S. Elkin, G. M. McKhann, and B. Morrison. Regional mechanical properties of human brain tissue for computational models of traumatic brain injury. *Acta Biomater.* 55:333–339, 2017. https://doi.org/10.1016/j.actbio.2017.03.037.

[15]Gadd, C. W., A. M. Nahum, D. C. Schneider, and R. G. Madeira. Tolerance and properties of superficial soft tissues in situ. *SAE Techn. Pap.* 1970. https://doi.org/10.4271/700910.

[16]Galford, J. E., and J. H. McElhaney. A viscoelastic study of scalp, brain, and dura. *J. Biomech.* 3(2):211–221, 1970. https://doi.org/10.1016/0021-9290(70)90007-2.

[17]Ganpule, S., N. P. Daphalapurkar, M. P. Cetingul, and K. T. Ramesh. Effect of bulk modulus on deformation of the brain under rotational accelerations. *Shock Waves* 28(1):127–139, 2018. https://doi.org/10.1007/s00193-017-0791-z.

[18]Gefen, A., N. Gefen, Q. Zhu, R. Raghupathi, and S. S. Margulies. Age-dependent changes in material properties of the brain and braincase of the rat. *J. Neurotrauma* 20(11):1163–1177, 2003. https://doi.org/10.1089/089771503770802853.

[19]Grujicic, M., W. C. Bell, B. Pandurangan, and P. S. Glomski. Fluid/structure interaction computational investigation of blast-wave mitigation efficacy of the advanced combat helmet. *J. Mater. Eng. Perform.* 20(6):877–893, 2011. https://doi.org/10.1007/s11665-010-9724-z.

[20]Gupta, R. K., X. G. Tan, M. R. Somayaji, and A. J. Przekwas. Multiscale modelling of blast-induced TBI mechanobiology—from body to neuron to molecule. *Def. Life Sci. J.* 2(1):3–13, 2017. https://doi.org/10.14429/dlsj.2.10369.

[21]Hua, Y., P. Akula, M. Kelso, and L. Gu. Characterization of closed head impact injury in rat. *Biomed Res. Int.* 2015. https://doi.org/10.1155/2015/272976.

[22]Jean, A., M. K. Nyein, J. Q. Zheng, D. F. Moore, J. D. Joannopoulos, and R. Radovitzky. An animal-to-human scaling law for blast-induced traumatic brain injury risk assessment. *Proc. Natl. Acad. Sci.* 111(43):15310–15315, 2014. https://doi.org/10.1073/pnas.1415743111.

[23]Knutsen, A. K., E. Magrath, J. E. McEntee, F. Xing, J. L. Prince, P. V. Bayly, J. A. Butman, and D. L. Pham. Improved measurement of brain deformation during mild head acceleration using a novel tagged MRI sequence. *J. Biomech.* 47(14):3475–3481, 2014. https://doi.org/10.1016/j.jbiomech.2014.09.010.

[24]Kuriakose, M., M. Skotak, A. Misistia, S. Kahali, A. Sundaramurthy, and N. Chandra. Tailoring the blast exposure conditions in the shock tube for generating pure, primary shock waves: the end plate facilitates elimination of secondary loading of the specimen. *PLoS ONE* 11(9):e0161597, 2016. https://doi.org/10.1371/journal.pone.0161597.

[25]Mao, H., G. Unnikrishnan, V. Rakesh, and J. Reifman. Untangling the effect of head acceleration on brain responses to blast waves. *J. Biomech. Eng.* 137(12):124502, 2015. https://doi.org/10.1115/1.4031765.

[26]Moore, D. F., A. Jérusalem, M. Nyein, L. Noels, M. S. Jaffee, and R. A. Radovitzky. Computational biology—modeling of primary blast effects on the central nervous system. *Neuroimage* 47:T10–T20, 2009. https://doi.org/10.1016/j.neuroimage.2009.02.019.

[27]Moss, W. C., M. J. King, and E. G. Blackman. Skull flexure from blast waves: a mechanism for brain injury with implications for helmet design. *Phys. Rev. Lett.* 103(10):4–7, 2009. https://doi.org/10.1103/PhysRevLett.103.108702.

[28]Nyein, M. K., A. M. Jason, L. Yu, C. M. Pita, J. D. Joannopoulos, D. F. Moore, and R. A. Radovitzky. In silico investigation of intracranial blast mitigation with relevance to military traumatic brain injury. *Proc. Natl. Acad. Sci.* 107(48):20703–20708, 2010. https://doi.org/10.1073/pnas.1014786107.

[29]Prange, M. T., D. F. Meaney, and S. S. Margulies. Defining brain mechanical properties: effects of region, direction, and species. *Stapp Car Crash J.* 44:205–213, 2000.

[30]Przekwas, A., V. C. Chancey, X. G. Tan, Z. J. Chen, P. Wilkerson, A. Zhou, V. Harrand, C. Imielinska, and D. Reeves. Development of physics-based model and experimental validation of helmet performance in blast wave TBI. In: ASME 2009 Summer Bioengineering Conference (2009). https://doi.org/10.1115/sbc2009-206839.

[31]Qian, L., H. Zhao, Y. Guo, Y. Li, M. Zhou, L. Yang, Z. Wang, and Y. Sun. Influence of strain rate on indentation response of porcine brain. *J. Mech. Behav. Biomed. Mater.* 82:210–217, 2018. https://doi.org/10.1016/j.jmbbm.2018.03.031.

[32]Rodríguez-Millán, M., L. B. Tan, K. M. Tse, H. P. Lee, and M. H. Miguélez. Effect of full helmet systems on human head responses under blast loading. *Mater. Des.* 117:58–71, 2017. https://doi.org/10.1016/j.matdes.2016.12.081.

[33]Ruan, J. S., T. Khalil, and A. I. King. Human head dynamic response to side impact by finite element modeling. *J. Biomech. Eng.* 113(3):276–283, 1991. https://doi.org/10.1115/1.2894885.

[34]Sarvghad-Moghaddam, H., A. Rezaei, M. Ziejewski, and G. Karami. CFD modeling of the underwash effect of military helmets as a possible mechanism for blast-induced traumatic brain injury. *Comput. Methods Biomech. Biomed. Eng.* 20:16–26, 2016. https://doi.org/10.1080/10255842.2016.1193597.

[35]Singh, D., and D. S. Cronin. Efficacy of visor and helmet for blast protection assessed using a computational head model. *Shock Waves* 27:905–918, 2017. https://doi.org/10.1007/s00193-017-0732-x.

[36]Stalnaker, R. L. Mechanical Properties of the Head. Morgantown: West Virginia University, pp. 1–131, 1969.

[37]Sundaramurthy, A., A. Alai, S. Ganpule, A. Holmberg, E. Plougonven, and N. Chandra. Blast-induced biomechanical loading of the rat: an experimental and anatomically accurate computational blast injury model. *J. Neurotrauma* 29(13):2352–2364, 2012. https://doi.org/10.1089/neu.2012.2413.

[38]Tan, X. G., A. J. Przekwas, and R. K. Gupta. Computational modeling of blast wave interaction with a human body and assessment of traumatic brain injury. *Shock Waves* 27:889–904, 2017. https://doi.org/10.1007/s00193-017-0740-x.

[39]Taylor, P. A., and C. C. Ford. Simulation of blast-induced early-time intracranial wave physics leading to traumatic brain injury. *J. Biomech. Eng.* 131:061007, 2009. https://doi.org/10.1115/1.3118765.

[40]Vappou, J., E. Breton, P. Choquet, R. Willinger, and A. Constantinesco. Assessment of in vivo and post-mortem mechanical behavior of brain tissue using magnetic resonance elastography. *J. Biomech.* 41(14):2954–2959, 2008. https://doi.org/10.1016/j.jbiomech.2008.07.034.

[41]Ward, J. W., L. H. Montgomery, and S. L. Clark. A mechanism of concussion: a theory. *Science* 107:349–353, 1948. https://doi.org/10.1126/science.107.2779.349.

[42]Zhang, L., R. Makwana, and S. Sharma. Brain response to primary blast wave using validated finite element models of human head and advanced combat helmet. *Front. Neurol.* 4:1–12, 2013. https://doi.org/10.3389/fneur.2013.00088.

[43]Zhang, J., N. Yoganandan, F. A. Pintar, T. A. Gennarelli, and B. S. Shender. A finite element study of blast traumatic brain injury. *Biomed. Sci. Instrum.* 45:119–124, 2009.

[44]Zhu, F., A. Kalra, T. Saif, Z. Yang, K. H. Yang, and A. I. King. Parametric analysis of the biomechanical response of head subjected to the primary blast loading—a data mining approach. *Comput. Methods Biomech. Biomed. Engin.* 19(10):1053–1059, 2015. https://doi.org/10.1080/10255842.2015.1091887.

[45]Zhu, F., H. Mao, A. Dal Cengio Leonardi, C. Wagner, C. Chou, X. Jin, C. Bir, P. Vandevord, K. H. Yang, and A. I. King. Development of an FE model of the rat head subjected to air shock loading. *Stapp Car Crash J.* 54:211–225, 2010.

Appendix A –Publication Cover 10
2019

Authors: D. Younger, M. Murugan, K.V. Rama Rao, L.J. Wu, N. Chandra

Title: "*Microglia Receptors in Animal Models of Traumatic Brain Injury*"

Journal Publication: Molecular Neurobiology, MOLN-D-18-00916R1, 1-27**,** (2019), [19-10]

Molecular Neurobiology
https://doi.org/10.1007/s12035-018-1428-7

Microglia Receptors in Animal Models of Traumatic Brain Injury

Daniel Younger[1] · Madhuvika Murugan[1] · Kakulavarapu V. Rama Rao[1] · Long-Jun Wu[2] · Namas Chandra[1]

Received: 30 July 2018 / Accepted: 13 November 2018
© Springer Science+Business Media, LLC, part of Springer Nature 2018

Abstract

Microglia have been implicated as a key mediator of chronic inflammation following traumatic brain injury (TBI). The animal models of TBI vary significantly based on the type of brain injury (focal versus diffuse). This has made it extremely difficult to assess the role of microglia and the window of microglia activation. Hence, the focus of this review is to summarize the time course of microglia activation in various animal models of TBI. The review explores the repertoire of secondary injury mechanisms such as aberrant neurotransmitter release, oxidative stress, blood-brain barrier disruption, and production of pro-inflammatory cytokines that follow microglia activation. Since receptors act as sensors for activation, we highlight certain microglia receptors that have been implicated in TBI pathology, including fractalkine receptor (CX3CR1), purinergic receptor (P2Y12R), Toll-like receptor (TLR4), scavenger receptors, tumor necrosis factor receptor (TNF-1R), interleukin receptor (IL-1R), complement receptors, and peroxisome proliferator-activated receptor (PPAR). In addition to describing their downstream signaling pathways in TBI, we describe the functional consequences of their activation and the implication in behavioral outcomes. Taken together, this review will provide a holistic view of the role of microglia and its receptors in TBI based on animal studies.

Keywords Microglia · Brain injury · Receptors

Introduction

Traumatic brain injury (TBI) is one of the leading causes of mortality and morbidity around the world. In 2013, in the USA alone, there were about 2.8 million emergency room visits, among which there were 282,000 hospitalizations, and 56,000 deaths related to TBI. The three leading causes of TBI related hospitalizations include falls (47%), impact by striking objects (15%), and automobile accidents (14%) [1]. TBI accounts for approximately 30.5% of all injury-related deaths in the US. Over the past decade, there has been a sharp increase in incidents of TBI resulting from combat-related injuries as well as insurgent activities on civilian population [2]. In 2010, the direct medical costs of TBI were 76.5 billion dollars [3]. Although there has been a lot of effort focusing on treatment modalities for TBI, there has not been much success in developing a therapeutic strategy to treat TBI-associated deficits. Accordingly, over 30 stage III clinical trials failed to show significant improvement in TBI patients [4]. This is probably due to lack of clear understanding of the secondary mechanisms in the evolution of injury pathology and due to highly heterogeneous nature of TBI phenotype [4]. This has led scientists and researchers to look for novel methods to delay and prevent TBI-induced pathology.

Microglia are the immune cells in the brain and have been implicated in pathogenesis following TBI. In this review, we highlight the response of microglia to injury, specifically, the involvement in secondary injury mechanisms such as neurotransmitter release, oxidative stress, and blood-brain barrier (BBB) breakdown after TBI. We then describe some of the receptors that are known to be critical in microglia activation and response following TBI.

Microglia Response to Brain Injury

Microglia constantly survey the central nervous system (CNS) microenvironment for any changes in homeostasis using their

Daniel Younger and Madhuvika Murugan contributed equally to this work.

Electronic supplementary material The online version of this article (https://doi.org/10.1007/s12035-018-1428-7) contains supplementary material, which is available to authorized users.

✉ Namas Chandra
namas.chandra@njit.edu

[1] Department of Bioengineering, New Jersey Institute of Technology, 111 Lock Street, Room105 CHEN bldg, Newark, NJ 07102, USA

[2] Department of Neurology, Mayo Clinic, Rochester, MN 55905, USA

Published online: 16 December 2018

highly motile processes. In their resting state, microglia possess a rod-shaped soma with processes extending out symmetrically in all directions [5]. Processes are motile with an average extension and retraction rate of 1.47 μm per minute and ranging from 0.4 and 3.8 μm per minute, respectively. Upon microglia activation a series of characteristic morphological changes occur. Usually, the motility change of their processes from undirected to targeted movement towards the injury site [5]. The processes begin to retract and the soma enlarges and become spherical in shape [6]. Finally, microglia begin to migrate to the site of injury at a rate of 1–2 μm per hour [5].

The classification of microglia activation has long been debated. The classical method of macrophage classification was borrowed and applied to microglia and categorizes activated states as either M1 (proinflammatory) state or M2 (anti-inflammatory) state [7, 8]. The M1state is initiated by events such as TBI, wherein, the microglia synthesize and release excess superoxide, nitric oxide, proinflammatory cytokines, and chemokines. Although the secretion of these compounds by microglia is primarily for host defense, often an exaggerated response follows an insult resulting in by-stander injury of the surrounding tissue [9]. When in M2 state, microglia produce anti-inflammatory cytokines (IL-4, IL-10, IL-13, IL-18) which promotes matrix remodeling, angiogenesis, tissue repair, and regeneration among other functions [10].

The application of the nomenclature of macrophages to microglia from the study of peripheral macrophages is often considered to be irrelevant in classifying microglia [11]. First, the M1/M2 definition was derived from exposing isolated cells to purified stimuli in vitro. These conditions are rarely found in vivo. Second, the cardinal regulators of macrophages bias are never found in vivo in isolation. Third, M1 and M2 states fail to emerge as an isolated pure phenomena in vivo. Fourth and possibly most important, macrophage polarization was developed using monocyte or bone-marrow-derived macrophages, that invade infected, traumatized or neoplastic tissues. By contrast, microglia are resident tissue macrophages, originating from extra-embryonic yolk sac [12], distinct from the circulating hematopoietic system [13] and highly adapted to their environment [14].

A recent study showed that activated microglia could exist in both states simultaneously where individual cells produce danger-associated molecular patterns (DAMPS) or pathogen-associated molecular patterns (PAMPS) [15]. This implies that activated microglia phenotypes fall along a spectrum as opposed to two binary states [16]. Depending on the stimulus present in the local microenvironment, microglia will be polarized to either the M1 or M2-like states. Particularly in TBI, the repertoire of microglia/macrophage activation is very diverse depending upon the type of mechanical impact, severity, and location of impact (discussed in paragraph below). Hence, it is suggested that a new classification be created based on but not limited to transcriptomic and proteomic profiles, regional heterogeneity, sexual dimorphism, function in healthy nervous system, and pattern of response to changes caused by trauma, infection, systemic inflammation, tumor, ischemia, and neurodegeneration [11].

There are currently 4 major animal models used to simulate the heterogeneous pathology of human TBI. These include weight drop injury (WD), controlled cortical impact injury, (CCI), fluid percussion injury (FPI), and blast / diffuse brain injury [17]. The WD model mimics closed head injuries frequently associated with falls, dropping of heavy objects in construction sites which lead to cerebral contusions found in TBI. It is performed by dropping a weight from a predetermined height onto the skull or exposed dura. In a modified version of WD model, also known as the closed head injury model, a metal plate is placed above the skull to distribute weight over a larger area and prevent skull fracture. WD model in mice showed signs of diffuse neuronal loss, neuroinflammation, markers of apoptosis, and short- and long-term cognitive impairments [18]. Similar to the WD model, CCI injury uses a solid impactor to damage exposed dura. To increase the reproducibility of the injury a pneumatic or electrochemical device is used. This mechanism also reduces rebound injury produced by gravity-driven devices [19]. By adjusting location, shape of impactor, velocity, and the depth of brain deformation, different types of injuries can be produced. CCI injuries typically manifest as cortical tissue loss, axonal injury, BBB dysfunction, and/ or subdural hematoma [20–23].

In FPI injury model, a craniotomy is performed to expose a portion of the dura. The injury is inflicted by directing a fluid pulse, produced by a pendulum striking a piston of fluid reservoir, against the exposed dural surface [19]. The injury model is characterized by a locally diffuse injury producing vascular and axonal damage and produces an amalgamation of cortical contusion and diffuse subcortical neuronal injury [17]. Studies have varied the location of injury site, but most commonly, the injury is performed lateral to the sagittal suture (LFPI) or medially (CFPI) [19]. The blast/ diffuse injury attempts to replicate the shockwaves from explosive devices to cause a diffuse brain injury. To recreate the Friedlander waveform produced in explosion from live explosives, gas driven shock tubes are used. Blast/ diffuse injury is characterized by diffuse cerebral brain edema, extreme hyperemia, a delayed vasospasm, and diffuse axonal injury [2, 24].

Microglia activation follows a different temporal pattern depending upon the type and severity of brain injury (Fig. 1). CCI and FPI are the most studied among different injury mechanisms, and therefore, microglia activity state has been thoroughly investigated. Markers such arginase (Arg-1) [61], CD206 [25, 62], and YM-1 [26, 62] are used to identify M2 activated microglia versus CD16 [62], CD 86 [25, 62], which are markers for M1 activated microglia. In TBI models, such as blast and weight drop, only the time profile of microglia activation has been studied. For instance, following CCI

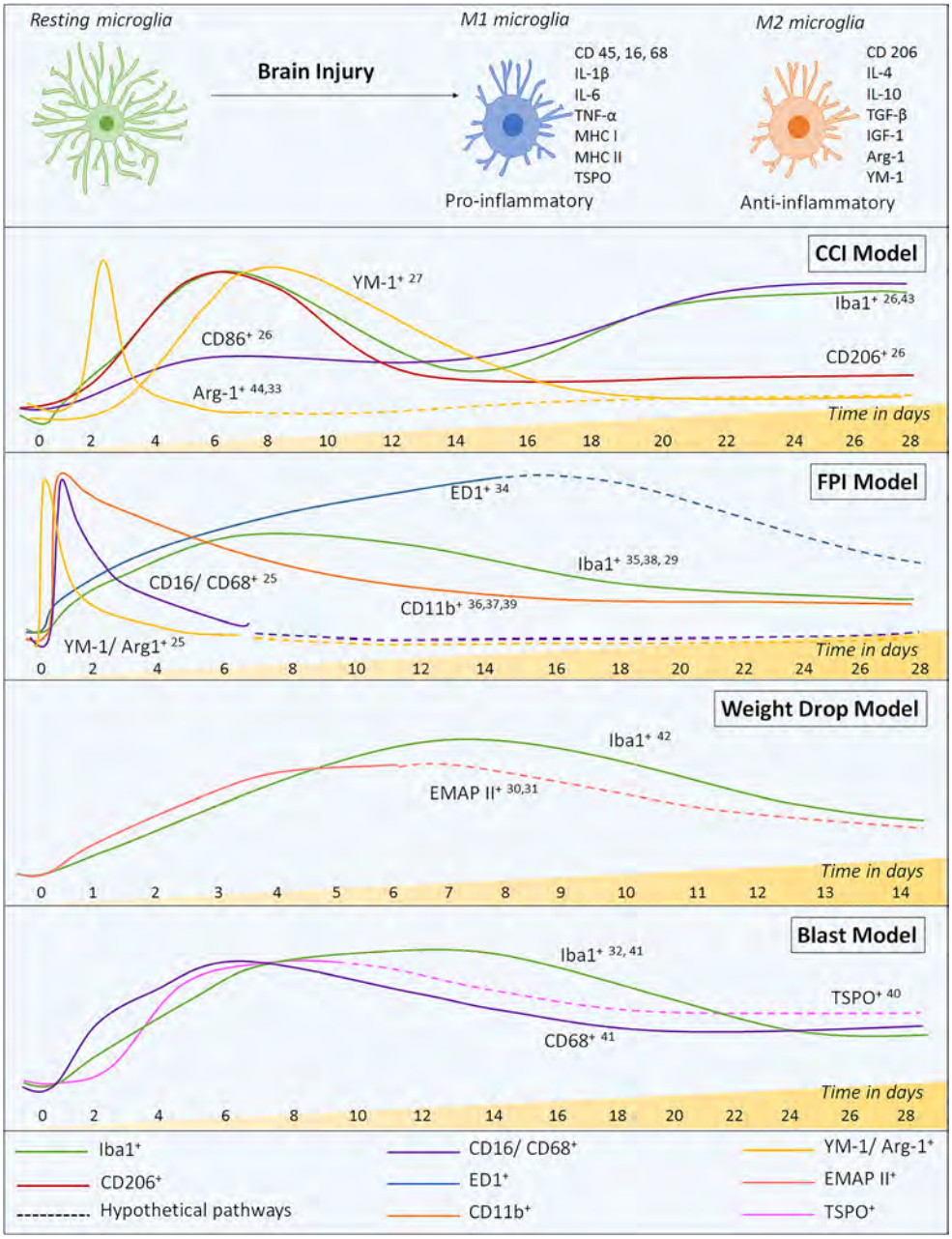


Fig. 1 Microglia activation markers and time-course in various animal models of traumatic brain injury. The top panel depicts the two forms of microglia activation states: M1 and M2 and the markers used to identify each state. The lower panels illustrate how the expression levels of the microglia activation markers (Iba1, ED1, CD11b, CD16, CD68, YM-1, Arg-1. EMAP II and TSPO) change with $t = 0$ representing time of injury in various animal injury models. Note that the y-axis denoting expression levels is arbitrary and is used to show the upregulated/peak expression of the particular protein. Solid lines indicate proven studies, while dotted lines represent hypothetical expression. The numbers in superscript refers to the cited literature. In addition to portraying the stages of microglia activation, this illustration reveals that there is no absolute standard for defining microglia activation. Further, the evidence for long-term chronic activation of microglia following brain injury is lacking [25–60]

injury, M2-like microglia increase in the first week following injury. The number of M2 microglia peak at 5 days post injury but decreases rapidly in number immediately afterwards [25, 63]. M1 microglia begin to increase in the cortex, striatum and corpus callosum at 1 week [63], peaking at 4 weeks following injury [25]. M2 type microglia predominate in the acute phase of injury while the M1 phase of microglia remain during the chronic phase after focal injury produced by CCI. Similar to focal injury, diffuse injury produced by FPI induced transient activation of M2 type of microglia that resolved within 7 days after injury, whereas, M1 type microglia remained in their activated amoeboid morphology for up to 30 days following injury [63].

It is interesting to note that microglia activation patterns differ not only temporally but also spatially following brain injury. The spatial variability in microglia response to injury may depend upon regional differences in mechanical loading and/ or the intrinsic property of the tissue. Despite the limited studies on mechanical signaling in microglia, a recent study showed cultured microglia cells were susceptible to mechanical changes [64]. In line with this, another study showed that mechanical loading was capable of modulating microglia proliferation, activation, and chemotaxis [65]. The response of microglia to injury may also depend on the intrinsic property of the tissue such as microglia/ blood vessel distribution and neuronal vulnerability within the region. There is a lower occurrence of

microglia in gray matter areas compared to the white matter. Regionally, the lowest of occurrence is the cerebellum (0.3%), frontal (4.7%), parietal (3.6%) and occipital (2.9%) lobes of the cerebrum with highest expression levels in the white matter track of the medulla oblongata (16.9%) [66]. A recent study showed that microglia activation paralleled the pattern of neuronal loss in a mouse model of CCI injury [67] which is in line with another study that observed prominent occurrence of activated microglia in regions of neuronal loss including the ipsilateral cortex, hippocampus, and thalamus after injury [68]. In a blast model of brain injury, microglia activation was found to be closely associated around the blood vessels suggesting that the difference in the distribution of microglia and blood vessels may underlie some of the regional vulnerabilities to injury [6].

Delineating the Functions of Microglia and Macrophages in Brain Injury

TBI causes a dramatic increase in microglia/macrophages in the area of injury. This increased number is contributed in part by local proliferation of resident microglia and infiltration of bloodborne-macrophages [69–71]. Blood-borne macrophages and microglia have distinct roles in TBI pathology and progression, however are difficult to distinguish since they share many common characteristics. Recent identification of microglia-specific markers, advent of transgenic animal models and techniques such as flow cytometry has made the distinction feasible [72, 73]. Using flow cytometry, Hsieh et al. distinguished macrophages ($CD45^{high}$, $CD11b^{+}$, $Ly6G^{-}$) from microglia ($CD45^{low}$, $CD11b^{+}$, $Ly6G^{-}$) and found that the populations contributed distinctly to inflammation after CCI injury [74]. Another study used $CX3CR1^{GFP/+}CCR2^{RFP/+}$, in which CX3CR1-positive resident microglia were labeled with GFP and CCR2-positive infiltrating monocytes are labeled with RFP. Specifically targeting CCR2 macrophages with CCX872, a novel Phase I CCR2 selective antagonist, significantly reduced TBI-induced macrophage accumulation and inflammation [75]. Similarly, mice lacking CCR2 ($CCR2^{-/-}$) with reduced macrophage infiltration after TBI, demonstrated improved functional recovery and neuronal survival [76]. These investigations on delineating the functional role of microglia and macrophages are limited and have only been performed in a few TBI models. Hence, further examination on dissecting the temporal and spatial contribution of resident microglia and infiltrating monocytes to the neuro-inflammatory profiles following TBI is much warranted.

Microglia-Mediated Secondary Mechanisms in Brain Injury

Depending on the type of TBI, the secondary injury may involve a wide array of mechanisms including oxidative stress, production of pro-inflammatory cytokines, BBB disruption, cell death, mitochondrial dysfunction and neurotransmitter release [77, 78]. Studies conducted thus far, have reported the involvement of microglia receptor activation in not only altering microglia morphology and motility, but also in neurotransmitter release, modulating neuron-glia synaptic transmission, secretion of cytokines, generation of reactive oxygen species and production of nitric oxide. Here, we summarize the microglia-mediated secondary mechanisms following brain injury.

Aberrant Neurotransmitter Release

Activated microglia contribute to neuronal excitotoxicity by releasing neurotransmitters in response to several external stimuli. The known neurotransmitters released by microglia include glutamate and ATP. Glutamate release by microglia can be triggered by activation through multiple receptor systems. For instance, microglia release of glutamate may be induced by secreted amyloid precursor protein (APP) [79] or amyloid β [80]. Similarly, TNF-α can induce the release of glutamate by upregulating glutaminase. Microglia are capable of releasing sufficient amount of glutamate to contribute to neural degeneration [81]. Such excess release of glutamate has been reported following ischemic brain injury [82]. However, there has been no study investigating the microglia release of glutamate in TBI models. The excess glutamate may activate pre and post-synaptic glutamate receptors in neurons leading to excitotoxicity. Alternatively, they can activate microglia glutamate receptors including AMPA receptor [83–85], metabotropic glutamate receptors [86–89] and NMDAR [90–92], resulting in a cascade of secondary events.

Adenosine triphosphate (ATP) is the other commonly released neurotransmitter by microglia. ATP release from microglia cells can be induced by bacterial endotoxin lipopolysaccharide (LPS) [93, 94]. Lysophosphatidic acid (LPA) induces the release of ATP via activation of the LPA_3 receptor [95]. High intracellular calcium levels have been shown to induce ATP release in microglia [96]. Extracellular ATP was shown to enhance radiation-induced brain injury through microglial activation and paracrine signaling via P2X7 receptor [97]. ATP release following brain injury triggers a microglia response via purinergic signaling [98]. The purinergic receptors in microglia are abundant and are implicated in important functions such as cytokine production (P2X receptors), motility (P2Y12 receptor) and in phagocytosis (P2Y6 receptors) [99–101]. The expression and function of these receptors in neuronal/glial cells in neuropathologies have been reviewed previously [102] and their role in TBI and is worthy of investigation.

Oxidative Stress

Under normal physiological conditions, there is a delicate balance between reactive oxygen/nitrogen species (ROS/RNS) and their removal via antioxidants. Following TBI, the balance can be disrupted leading to an excess buildup of ROS [103, 104]. Accumulation of ROS/RNS is known to mediate cellular damage via lipid peroxidation, protein modification, and/or DNA strand breaks [105]. Activated microglia produce superoxide by the enzymatic activity of NADPH oxidase (NOX), a multi-subunit enzyme that catalyzes the production of superoxide from oxygen [106]. Microglia, like all phagocytic cells, express NOX2 [107]. NOX 2 generates superoxide molecules which help in the neutralization of foreign pathogens [108]. It was shown that NOX2 mediated ROS production was strongly upregulated in M1 but not M2 polarized microglia in CCI injury. Inhibiting NOX2, by using selective peptide inhibitor gp91ds-tat or NOX2 knockout mice, reduced markers for M1 activated microglia, limited tissue loss, and improved motor recovery. Inhibition of NOX2 also promoted M2-like activation in microglia [109]. In FPI injury, inhibition of NOX with apocyanin had no effect on neuromotor function but reduced the release the proinflammatory cytokines IL-1β, and TNF-α at 3 and 24 h after injury [110]. Recently, it was shown that NOX2 expression was increased at 24 h after moderate blast injury (180 kPa) and this directly correlated with elevated ROS production [111]. Activation of cytokine receptors such as IL-2R [112, 113], IL-15R [114], TNFR1 [115], INF-γR and thrombin receptor [116] in microglia have also been implicated in ROS production. ROS production by microglia may also be mediated by Notch-1 receptor [117, 118], dopamine receptor D_1, D_2 [45, 119], and Angiotensin II receptor [120].

BBB Disruption

The CNS vasculature differs from the rest of the vasculature in that it has intricate connections and innervations with neural cells particularly astrocytes (astrocyte end feet), pericytes and microglia to form the functional BBB, a specialized structure that selectively separates the brain parenchyma from the peripheral blood. Studies on the interaction between microglia and BBB in both physiological and pathological conditions are limited and have recently gained more attention [121, 122]. The perivascular microglia communicate with the endothelial cells and survey the influx of blood-borne components into the CNS. Hence, any disruption of the BBB as reported following brain injury, can prime, and attract microglia [6].

Microglia activation dependent alterations to BBB after TBI is thought to be predominantly mediated by neuroinflammation and oxidative stress [123–125]. Therefore, most TBI studies that investigate both microglia activation and BBB disruption focus on shifting microglia from their proinflammatory M1state to their anti-inflammatory M2 state. For instance, following CCI injury binding of 2 arachidonylglycerol (2-AG) (agonist) to the cannabinoid receptor in microglia shifted microglia at 3 and 7 days from M1 to M2 activated phenotypes. This shift in activation was coupled with the reduction of BBB permeability at the same time point [126]. Reduction in the release of pro-inflammatory cytokines and reduction of inducible ROS production prevented further degradation of BBB [126]. Pretreatment with apocynin (NOX inhibitor) prevented BBB disruption following WD injury [127], as well as in blast injury model [128]. Microglia as the major source of NOX mediated ROS production are implicated as the cause for the increase in permeability of the BBB following injury [127]. In a mouse model of mild blast injury, microglia activation was restricted to regions close to the blood vessel microdomains, as evidenced by rapid microglial process retraction and increased amoeboid morphology [6]. Taken together, these TBI studies confirm that there is a close association between microglia activation and BBB disruption and vice-versa following injury.

Release of Cytokines

Neuroinflammation is one of the key mediators of secondary injuries following brain injury. The acute response includes secretion of pro-inflammatory cytokines within minutes following injury. The activation of resident microglial cells, alongside the infiltration of peripheral macrophages, is key mediator of neuroinflammatory responses after TBI. Several studies have attempted to discriminate the differential roles of resident microglia and infiltrated monocytes after brain/ spinal cord injury [69, 129, 130]. In this review, we highlight the contribution of microglia to the release of pro-inflammatory cytokines, however, the role of infiltrating monocytes/ macrophages in secreting cytokines and overall TBI pathology cannot be overlooked.

Upon the detection of foreign macromolecules such as DAMPS/PAMPS, microglia can release a wide range of cytokines and chemokines. These molecules guide the expression of adhesion molecules, signal peripheral immune cells to infiltrate the injury site, and further release pro-inflammatory mediators and growth factors that regulate neuronal death or regeneration [131]. Many studies have investigated cytokines and chemokines expression following TBI. These studies have focused on levels of cytokines found in homogenized tissue section or CSF. These studies attribute the increased expression of cytokine to the activity of activated microglia. This assertion may be correct, but microglia's contribution to the inflammatory environment is unlikely to be exclusive [132].

Following CCI injury, levels of IL-1β and IL-18 increased in brain homogenates surrounding the contusion site. Levels of IL-1β peaked at 6 h post injury and decreased to control level by 7 days. IL-18 levels gradually increased over the 7 d observation period. Microglia-specific release was confirmed by colocalization of NLRP-3 inflammasome and its associated components (ASC and caspase1) in microglia cells but not with astrocytes or neurons [133]. Chio et al. found that administration of Etanercept, a TNF-α receptor antagonist, attenuated the release of TNF-α following FPI leading to reduced motor and neurological deficits as compared to the control and saline-treated groups. At 72 h after injury, TNF-α secreted by microglia increased in ischemic cortex, white matter, hippocampus, and hypothalamus. Double immunostaining confirmed that neuronal and astrocytic TNF-α levels were not significantly different between control, saline- and etanercept-treated groups leading to the conclusion that microglia was the prominent source of TNF-α production following diffuse TBI [134].

Bachstetter et al. showed that p38α (MAPK14) protein kinase plays a role in the production of TNF-α and IL-1β by cultured microglia cells [44]. Using midline FPI model they investigated whether myeloid-specific deletion of p38α influenced microglia cytokine production following injury. Unexpectedly they found that during the acute phase (0–12 h), release of IL-1β, IL-6, and TNFα was greater in the p38α knockout (KO) compared to the wild-type injured animal. This increase could not be accounted for by the increase in infiltrating immune cells (macrophages and neutrophils) or by astrogliosis, as cell numbers were decreased in the KO animals relative to the WT. In the chronic phase (7 days), levels of IL-1 were significantly reduced in the p38α KO animals as compared to the WT injured animals. These findings suggest that microglia may not contribute significantly to inflammation in the acute phase but is responsible for the pro-inflammatory environment found in the chronic phase of injury [27].

Microglia release proinflammatory cytokines such as IL-1β upon ligand binding to the NMDAR [90], angiotensin II receptor [120], and IFN-γR [131]. Release of TNF-α has been reported upon activation of AMPA receptor [83, 84], NMDAR [90], kainate receptor [85, 91], metabotropic glutamate receptor [87, 89, 135, 136] α_{1a}, α_{2a}, β_1 adrenergic receptor [137], IFN-γR [131], TLR2 [138], TLR3 [139], TLR9 [140], CD-14 [141] and thrombin receptors [141]. Release of IL-6 upon GABAR [142] α_{1a}, α_{2a}, $\beta_1$adrenergic receptor [137], TNFR1 [143], IFN-γ [131], IL-1R1 [144], TLR2 [138], TLR3 [139], TLR5 [140], TLR9 [140], CD-14 [141], Thrombin receptor [116] activation. Release of IL-12 was noted upon activation of GABAR [142], IFNγR [145], TLR3 [139], TLR9 [140], CD-14 [141], and thrombin receptors [116].

Microglia are also capable of releasing chemokines such as release of CCL2 upon IFN-γR [145] TLR2 [138] activation. Release of CCL3 upon IL-13R [146, 147] CD-14 activation. Release of CCL5 upon IL-3R [146, 147] activation. Release of CXCL-10 upon TLR3 [139] and TLR4 [139] activation. Release of CXCL2 upon CD-14 [141] activation. Once released, these factors affect adjacent cells such as astrocytes and/or neurons in a paracrine manner since these cells possess receptors for these factors. Additionally, these factors could also affect microglia in an autocrine manner. In both scenarios, the net effect exerted by these factors includes lipid peroxidation, immune cell recruitment, BBB disruption, and the development of cerebral edema [148–150].

Microglial Receptors in Brain Injury

The microglia express a repertoire of receptors which act as sensors for specific ligands in the neuronal parenchyma. A comprehensive list of receptors expressed in microglia, the known receptor agonists/ antagonists, their physiological function and the functional relevance of receptor activation is provided in Supplementary Table 1. Although many receptors have been indicated to be part of microglia sensor system (Supplementary Table 1) only a fraction of them are activated during TBI (Table 1). In the following section, we summarize some of the microglia receptors most investigated in TBI, their downstream signaling pathway (Fig. 2), the functional consequences of their activation and the implication in behavioral outcomes.

Chemokine Receptor (CX3CR1)

Microglia in the CNS are characterized by the prominent expression of the chemokine receptor 1 (CX3CR1). The sole ligand for the receptor is fractalkine (CX3CL1) which is produced by neurons. CX3CL1 is known to induce microglia activation and release of proinflammatory factors [177]. Following brain injury, affected neurons release CX3CL1 allowing for microglia activation [178]. The schematic in Fig. 2 summarizes the known intracellular signaling pathways associated with CX3CR1 receptor activation in microglia. It has been shown that CX3CL1 induces chemotaxis of microglia cells via chemokine macrophage inflammatory protein-1α (MIP-1α) to the site of neuronal damage [179]. CX3CL1 is also known to induce microglia activation through intracellular phosphorylation of microglial p38 mitogen-activated protein kinase (MAPK) [180, 181]. Further, treatment of cultured microglia with CX3CL1 promoted cell survival and inhibited Fas ligand-induced cell death via the Akt signaling pathway [182].

In a mouse model of CCI, they found that CX3CR1 KO mice had reduced cellular damage in the cortex and fewer

Table 1 Microglia receptors in various TBI models

Injury Model	Receptor	Animal model	Microglia marker	Time points	Effect of Receptor antagonist/blocker in TBI conditions
CCI	Insulin-like growth factor 1 receptor (IGF1R)/ SOC2 [151]	Mouse C57Bl/6, SOCS2 transgenic (Tg) over-expression	CD11b (general), CD206(M2), and CD16/32 (M1)	3 days, 7 days, 33 days, 35 days	Injury induces higher number of M1 than M2 microglia • Erythropoitin treatment (IP injection) 7 days daily ○ EPO treatment had no effect on behavior • SOCS2Tg animals showed ○ Improved motor function by 7 days ○ Showed smaller lession at 7 days but not at 35 days post injury ○ No effect on cortical neurogenesis after TBI ○ Increased number of newly proliferated microglia (7 day) not at 35 day ○ Increase in M2-like and but no increase in M1 microglia in perilesional area at 7 day ○ Area covered by CD11b + cells not different between genotypes
	IL-1βR/ IL-1β [152]	Mouse C57BL / 6	Mac2	1 day, 3 days, 7 days, (immuno) 2 days, 5 days, 12–15 days	Microglia activation began at day 1 and peaked at day 7. Activated microglia appeared in the vicinity of the cortical contusion and ipsilateral hippocampus. • IgG2a/k IL-1β neutralizing antibody administered vio osmotic pump for 2 weeks. IL-1β neutrilization - ○ Reduced number of activated microglia at day 3 and 7 ○ Reduced number of cortical neutorphils and infiltrating activated T-cells ○ Reduced lession volume and hemispheric tissue loss ○ No effect on motor function loss but treatment reduced memory decline
	IL-4R/Il-4 [46]	Mouse C57Bl/6 (3 month and 24 month)	Iba-1 (general), M1 markers (IL-1β, TNFα) M2a marker (Arg-, Ym,CD68, iNOS, Mrc, Fizz-1, CCL2, and CCL3) M2c markers (IL-4Rα, TGFβ, SOC3)	24 h, 7 days	• Significant increase in IL-4Rα in both young and adult mice with a greater increase in young animals • IL-4Rα activation shown by STAT6 expression upregulated in both young and adult mice with greater levels in young mice. • Age produced imbalance of M1 and M2 patterns with significant increase in M1 and M2a genes and lower expression of M2c • Increase in activated microglia in the hippocampus of aged TBI mice compared to young mice
	Sigma-1 Receptor [153]	Mouse C57Bl/6 (10–-12 weeks)	Iba-1	days 1, 3, 7, 14, 21, and 28	• PRE-084 selective sigma 1 agonist treatment given 15 min after TBI ○ Decreased lesion volume and brain water content (day 3 and 28) ○ Improved neurological recovery (mNSS) on day 21 and 28 but no effect on days 1–14 ○ Decrease in neurodegeneration by 57% ○ Attenuated Iba intensity at 3 days ○ Decreased Nitrosative and oxidative stress at 3 h after TBI
	Cannabinoid-2 Receptor [154]	Mouse C57Bl/6 (8 weeks)	Iba-1 Iba-1	48 h	• CB2R agonist 0–1966 vip IP injection at 1 and 24 h after injury ○ Improved Llocomotor performance and exploratory behavior ○ Decreased Edema (water content) and substance P immunoreactivity ○ Decreased number of Iba positive cells ○ Fewer Iba positive cells showed activated morphology

Table 1 (continued)

Injury Model	Receptor	Animal model	Microglia marker	Time points	Effect of Receptor antagonist/blocker in TBI conditions
	CX3CR1 [132, 155, 156]	Mouse C57Bl/6 (3 month) Mouse C57Bl/6 Mouse C57Bl/6	Cd11b (general) M2 (Ym1, CD206, TGFβ) M1 (Marco, CD 68) Cd11b (general) M1: Cd68 M2: Ym1	2 days, 1 week, 2 weeks, 4 weeks, 8 weeks, 18 weeks, 1 year and 1.5 years 24 h, 7 days, 15 days, 30 days 1 day, 2 days, 4 days. 7 days, and 5 weeks	• At 7 days total number of microglia increased over control but returned to control levels at 4 months • Levels of activated microglia remained increased in both the ipsilateral and contralateral cortex • Levels of CX_3CR1 increased 2 days after injury and persisted for 1.5 years following injury • Heterozygous $CX_3CR1^{\pm}$ mice ○ Only females had less degeneration of brain tissue ○ No change in microglia number but fewer infiltration macrophages and lymphocytes • CX_3CR1 ($CX_3CR1^{-/-}$) knockout animals ○ Reduced motor deficit, cell death, and neuronal loss at acute phase (24 h-15 days). ○ Greater cognitive disfunction, and increasecd neuronal death at chronic phase (30 days). ○ CX3CR1 deficiency correlates with increased microglial proliferation ○ M2 marker increase at 7 days only in knockout animals but not detected at 15 and 30 day ○ Significant reduction in iNOS and IL-1. ○ M1 phenotype (Marco, and CD68) was dominant at the chronic phase
	Adenosine A1 Receptor [157]	Mouse C57Bl/6 A1AR KO mice	Iba	24 h, 7 days	• A1AR KO transgenic mice showed ○ Significant increased in Iba-1 staining compared to WT in six of the eight brain regions examined including ipsilateral CA3, cortex, and thalamus, and contra-lateral CA1, cortex and thalamus ○ No change in cortical volume between knockout and WT
	TLR4 [47, 158]	Mouse C3H/OuJ, C3H/HeJ non functional TLR4 Mouse C57BL/10ScNJ (TLR4 knockout) And control	Iba M1: iNOS, TNF-α M2: Arg-1 VEGF, IL-10	1 day, 3 days, 4 days, 5 days, 7 days	• TLR4 expression restricted to microglia within the peri-contusional cortex • VGX-1027 TLR4 antagonist administered via tail vein 15 min before or up to 8 h after TBI ○ Injury increase TLR4 gene and protein expression in ipsilateral cortex between 6 and 24 h ○ C3H/HeJ mice and VGX treated mice at 4 h had similar effect on edema volume ○ Reduced IL-6 expression • TLR4 knockout mice showed ○ Improved recovery of learning and memory ○ Decreased brain edema volume ○ Attenuated expression of M1 markers at 3 and 7 days and increase in M2 marker at same time point ○ Number of microglia increased peaking at 3d and increased levels compared to control at 7 days
	mGluR5 [159, 160]	Mouse C57Bl/6 (3 months) Mouse C57Bl/6 (3 months)	Iba CD11b M2: Arginase-1 Ym-1)	1 day, 3 days, 7 days, 14 days, 21 days, and 28 days	• At 3 h and 24 h post injury mice received an ip injection of VU0360172 a possive allosteric modulator of mGluR5 or MTEP (a slective mGluR5 antagonist) + VU0360172 ○ VU0360172 improved motor recovery at day 28

Table 1 (continued)

Injury Model	Receptor	Animal model	Microglia marker	Time points	Effect of Receptor antagonist/blocker in TBI conditions
			M1: iNOS, CD68 ED-1	1 day, 7 days, 14 days, 15 days, 16 days, 17 days, 21 days	○ VU0360172 had no effect on spatial lerning ○ VU0360172 reduced cortical tissue loss and reduced hippocampal regeneration ○ VU0360172 polarized microglia to the M2 phenotype ○ VU0360172 reduced the upregulation of NOX-2 induced by mGluR5 activation • 30 min post-injury, mice received a single intracerebroventricular (ICV) injection of CHPG or CHPG and MPEP ○ CHPG treated animals had improved sensorimotor proformance on dat 14 and 21 ○ CHPG + MPEP performed similar to vehicle-treated animals ○ CHPG animals improved spatial learning on day 15, 16, and 17 ○ CHPG reduced lession volume ○ Level of ED1 were decreased in CHPG groups indicating lower microglia activation ○ Inhibition of NADPH odidase does not enhance neuroprotective effect of CHPG
	TNFR [161]	Mouse C57Bl/6WT/ p55(−/−) and p75(−/−)	CD11b M2: Ym-1	48 h, 4 weeks	• p55(−/−) and p75(−/−) trangenic mice ○ P55 (−/−) mice showed the greatest deficit followed by p75 (−/−) and finally WT. Observed at both 48 h and 4w ○ P55 (−/−) mice showed significantly reduced injured area compared to WT and p75 (−/−) ○ At 24 h P55 (−/−) mice showed a reduced number of damaged cells ○ 3 zones characterized by different morphology of microglia, Border of contusion (ameboid), Transition zone (ramified and ameboid), and periferal zone (ramified) ○ Zone 1 and 2 had significant reduction in microlgia activation in P55 conpared to WT and P75 ○ Ym1 increased immunoreactivity in p55 (−/−) compared with p75 (− /−) mice
	Peripheral benzodiazepine receptor [48, 162]	Rat Sprague–Dawley Adult rat	ED-1 DC68	6 h, 1 day, 3 days, 14 days 7 days	• PTBR antagonist [3H]PK11195 to visualize recepter density • [3H]PK11195 specific binding was uniformly distributed in rat brain with the highest density in striatal cortex (83.4 fmol/mg tissue) and the lowest density in the caudate-putamen (49.4 fmol/mg tissue) ○ Increase in ED1 by 40–79% at day 3 and increase by 106–185% at 14 days post injury. ○ Binding positively correlated with the degree of microglial activation, and to a lesser degree with reactive astrocytosis ○ Binding is higher in regions with neuronal loss
	NLRP3 [133]	Mouse C57BL/6 (age 10–12 weeks)	Iba-1	6 h, 1 day, 3 days, 7 days	• Protein expression of NLRP-3, ASC, and Caspase-1 localized to microglia • Hyperbaric oxygen treatment ○ Attenuated motor deficits ○ Alleviated cerebral edema ○ Decreased levels of IL-1β and IL-18 ○ Inhibited mRNA and protein expression of NLRP-3, ASC, and Caspase-1
	PPAR [49, 163, 164]	Rat Sprague–Dawley Rat Sprague–Dawley Mouse C57BL/6	Iba-1 CD11b GSI B_4	Day 1–5 motor function Day 14–18 spatial learning Day 21 biochemistry	• Rosiglitazone PPAR-γ agonist treatment (6 mg/kg at 5 min, 6 h and 24 h post injury) ○ Improved motor function (d 1–5) ○ No effect on spatial learning

Table 1 (continued)

Injury Model	Receptor	Animal model	Microglia marker	Time points	Effect of Receptor antagonist/blocker in TBI conditions
				25 h, Day 10–14 spatial learning, day 16 biochemical analysis	○ No effect on contusion volume ○ Increased cell survival in CA3 region of hippocampus (d21) ○ Microglia activation decreased in CA1 and cortex and trend in CA3 and thalamus rosiglitazone treatment
				1 day, 2 days, 7 days	○ Attenuates TNFα gene expression (24 h) ○ no mRNA reduction in the matrix metallopeptidase gene, MMP9 the cytokine-inducible enzyme, iNOS, or in COX2, a gene whose expression is increased after inflammation • Pioglitazone (PPAR-γ agonist), or Pioglitazone and the antagonist T0070907 treatment at 10 mg/kg beginning 15 min after the injury and subsequently every 24 h for 5 days ○ Significant increase in mitochondrial function was observed ○ Reduction in lession size by 55% ○ Few microglia cells and fewer activated microglia basses on morphology in treated group ○ Administering the antagonist removed the therapuetic effect of Pioglitazone treatment • Rosiglitazone treatment or Rosiglitazone + GW9662 (PPAR-γ antagonist) (of 6 mg/kg was given 5 min, 6 h and 24 h after TBI ○ Induced 2.1 fold increase in PPAR-γ mRNA expression with Rosiglitazone treatment increasing 4.4 fold from sham(1 day) ○ Decreased cortical contusion volume (day 7) ○ Decreased Tunnel positive cells mainly neurons(day 2) ○ Decreased GSI-B_4+ cells (activated microglia ○ mRNA levels of the pro-inflammatory genes IL6, MCP1 and ICAM1 were significantly lower in the rosiglitazone-treated group (1 day) ○ Increased expression of HSP and antioxidant genes (1 day) ○ Administering the antagonist removed the therapuetic effect of Rosiglitazone treatment
FPI	TSPO [28]	Rat Sprague-Dawley	Iba-1 Classical activation: TNFα, and CD45 Acquired deactivation: TGF-βI, TGF-βRII, Alternative activation: ARG1	7 days, 21 days	• Measured receptor density using [3H]PK-11195 • Rats given anti-inflammatory dug ibuprofen (20 mg/kg) ip daily for 7 days • Transient S1BF and sustained VPM microglial activation after diffuse brain injury shown by morphological changes and enhanced iba staining • Increased TSPO binding density especially in the S1BF and VPM at 7 days • Classical activation and acquired deactivation gene expression was increased transiently at 7 days postinjury with no change in alternative activation observed
	TLR4 [165]	Mouse C57Bl/6	Iba-1	1 day, 3 days, 7 days	• VEGI treatment mice were injected i.p. on three consecutive days of 2 h, day1 and day2 ○ Reduced contical contusion volume ○ Reduced blood-brain barrier permeability (day 7) ○ Decrease in Iba positive cells in the contusion margin

Table 1 (continued)

Injury Model	Receptor	Animal model	Microglia marker	Time points	Effect of Receptor antagonist/blocker in TBI conditions
					○ Expression of TLR4 reduced by 19.73% and 61.09% compared to saline treated injured animnals(day 1 and 3) ○ Decrease in NF-κB which requires TLR4 activation ○ Reduced the IL-1β, TNF-α and iNOS expression (day 1 and 3)
	CX3CR1 [69]	Mouse C57Bl/6 Cx3cr1 defecient	Iba	3 days	CX3CR1 deficiency had no effect ○ Cavity volume ○ Monocytic reaction ○ Microglia activation
	IL-1R [166]	Mouse	Mac-2	1 day, 2 days, 9 days, day 14–21	IL-1β-neutralizing antibody resulted in ○ Normalized behavior profile in the MCSF test (day 2 and 9) ○ Increased memory in MWM (day 14–21) but no effect on learning (MWM) ○ Treatment had no effect on microglia number or ventricle size
	PPAR [167]	Rat Winstar	Iba	24 h, 48 h	• i.p. administered by 1 mg/kg Pioglitazone or vehicle 10 min after the TBI induction ○ Reduced lipid peroxidation and protein oxidative products in the cortex ○ TBI-induced COX-2 overexpression was not significantly affected by treatment ○ No significant effect of the treatments on the cortical IL-lβ, IL-6. And TNFα ○ Reduced both percentage of iba possitive cells as well as decreased the number of activated microglia based on morphology ○ Reduced cortical edema formation
Weight drop	NMDAR [168, 169]	Mouse C57Bl/6	F4/80	1 day, 2 days, 3 days, 4 days, 5 days, 6 days, 7 days	• Minocycline injected i.p. 45 mg/kg at 30 min post injury and every subsequent 12 h until sacrificed ○ Transient improvement in neurological recovery following injury ○ Improved motor performance at day 1 post injury ○ Reduces periconusional lesion volume on day 1 but no effect on day4 ○ NO significant effect on apoptotic cells ○ Decrease of 43% in the density of activated microglia in the treated group ○ Reduced cortical IL-1β level
	EPO receptor [170]	Rat Sprague-Dawley	CD68	1 h, 2 h, 1 day, 7 days, 14 days	• Marmarou model followed by 30 min of hypoxic (Hx, 12% O2) or normoxic ventilation, and were administered recombinant human EPO-α (5000 IU/kg) or saline at 1 and 24 h post-injury ○ Significantly improved sensorimotor and cognitive recovery when administered to TAI rats with Hypoxia ○ Reduced axonal damage in white matter ○ Maintained neuronal density ○ Reduced IL-1β to sham levels (2 h) ○ increase in receptor density, expresses on both neurons and microglia but only a subset of microglia cells expressed the receptor
	TLR2 [29]	Rat Sprague-Dawley	EMAPII	24 h, 48 h, 96 h	• Few TLR2+ cells expressed day 1 • accumulation of TLR2+ cells became significant on day 2 and increased at day 4 • Nearly all TLR2+ cells in the lesion area were double labeled with EMAPII (activated microglia)

Table 1 (continued)

Injury Model	Receptor	Animal model	Microglia marker	Time points	Effect of Receptor antagonist/blocker in TBI conditions
					• TLR2+ cells in the subcortical white matter expressed GFAP(astrocyte)
	TLR4 [29, 171]	Rat Sprague-Dawley Rat Sprague-Dawley	EMAPII	24 h, 48 h, 96 h 0 h, 6 h, 12 h, 18 h, 24 h, 48 h. 72 h, 7 days, 10 days, 14 days, 21 days	Study 1: • Significant accumulation of TLR4+ cells at day 1 • Increasing continuously until day 4 in both the lesion area and ipsilateral subcortical white matter. TLR4 protein expression in vehicle TBI group increased significatly at 12, 18, 24, 48, and 72 h peaking at 24 h. • TLR4+ cells in the lesion area colocalized with EMAPII, while TLR4+ cells in the subcortical white matter colocalized with GFAP positive astrocytes. • MYD88 levels found same pattern as TLR4 showing activation of the receptor Study 2: • TLR4 proteins were localized to microglia and neurons but not astrocytes. Only morphologically active microglia expresssed TLR4. • PACAP38 peptide Intracerebroventricular treatment was injected before TBI or 24 h after LPS injection • Pretreatment with PACAP38 caused a significant reduction in neurological and motor deficits day 1–21 ○ Decreased edema volume ○ Inhibited TLR4 expression in injured cortex and hipocampus ○ Decreased number of TLR4 expressing microglia but microglia still exhinited reactive morphology ○ Suppressed expression of proteins in the MyD88/NF-jB pathway in the injured cortex and hippocampus
	metabotropic glutamate receptor 5[172, 173]	Rat Sprague-Dawley (250-300 g) Rat Sprague-Dawley (250-300 g)	ED-1 ED-1	24 h 0.5 h, 1 h, 6 h, 12 h 24 h, 3 days	• mGluR5 protein levels rise was significant at 24 h and remained upregulated until 3 days • mGLuR5 mRNA levels upregulated at 0.5 h and peaked at 1 h then decreased below control levels at 24 h • mGluR5 colocalized with NeuN(neurons), GFAP(astrocyte) and ED-1(microglia) • CHPG (mGluR5 agonist) single intracerebroventricular injection ○ Treatment reduced cerebral edema (24 h) ○ Attenuated neuronal degeneration ○ Decreased number of activated microglia ○ Decreased protein levels and mRNA levels of IL-1b, IL-6 and TNF-a ○ Reduced number of degenerating neurons
	P2X4R [30]	Rat Lewis (8–9 weeks)	EMAP-II	24 h, 48 h, 96 h, or 144 h	• P2X4R expression in neurons and perivascular cells did not change with TBI • Morphology and distribution of P2X4R+ cells similar to EMAP-II+ cells • P2x4R+ cells significant increase at day 1 and increasing to maximal levels at day 4 and 6 • intraperitoneal (i.p.) injections of dexamethasone (1 mg/kg, in 1 ml saline, every 2 days ○ Increase in EMAP-II cells at 1 day and 2 days peaking at day 4 and 6 ○ Attenuated increase only on day 1 and 2 not on day 4 or 6 ○ Decreased P2X4R cells day 1 and 2 but no affect on day 4 and 6
		Mouse C57/BL6	CD11b	3 h, 6 h, 24 h, 48 h, 72 h	• TNF/FAS KO mice influenced cognitive deficits independent of cell death

Table 1 (continued)

Injury Model	Receptor	Animal model	Microglia marker	Time points	Effect of Receptor antagonist/blocker in TBI conditions
	TNFR1 and Fas receptor [174]	WT, TNFa knockout (TNFa KO), and TNFa/Fas double-KO			• IBA injured cortex, hippocampus, corpus callosum, periventricular white matter, and choroid plexus at 48 and 72 h after injury • Tumor necrosis factor-a mRNA, Fas mRNA, and TNFa protein were increased in the brain at 3 to 6 h after injury
Blast	CB2 [175, 176]	Mouse C57BL/6 Mouse C57BL/6	CD68 Iba-1, MHC-II	3 days, 2 months, 3 months 3 days, 1 week, 2 weeks, 8 weeks	• Were injected intraperitoneally daily with 6 mg/kg SMM-189 (CB2 agonist) or vehicle for 14 days beginning 2 h after blast exposure ○ SMM-189 biases the CB2 receptor conformation to an inactive state leading to Phosphorylation of CREB ○ Phosphorylation of CREB, promotes transcription Of M2 genes and represses transcription of M1genes ○ Blast alone less than 95% of microglia had no evidence of pCREB (3 days) ○ In treated most if not all microglia exhibited pCREB ○ cortical and striatal neuron loss is reduced by treatment by 50% ○ Reduced motor deficit • injected mice with 6 mg/kg SMM-189 i.p. or vehicle daily for 14 days beginning 2 h after 50-psi blast ○ In vitro SMM-189 decrease microglia expression of IFN-γ, IL-6, IL-10, TNF-α, IL-8, MCP-1, MIP-1β, TARC, MDC, and eotaxin-3 ○ Microglia activation using IBA found by third day in the right dorsal lateral geniculate nucleus and the upper layers of the right superior colliculus ○ Microglia activation evident by third day more prominent by at 1 week, and no longer prominent by 2–8 weeks ○ Microglia activation oberved in brain region with axonal pathology ○ nearly all activated microglia appear to have prominent nuclear labeling for pCREB after daily SMM-189 ○ prevented motor deficits observed in vehicle-treated blast animals ○ reduced deficits invisual acuity ○ treatment reduced depressive symptoms
	Complement type three receptors (CR3), [31]	Rat winstar	ED-1 MHC-II	1 day, 4 days, 7 days, 14 days, 21 days and 28 days	• Expression of CR3 (OX42) increased as early as day 1 in both white and gray matter • Cells appeared hypertrophied and bearing short stout processes. • Immunoreactivity of microglia began to decrease at 21 days and returned to control levels by 28 days

sensorimotor deficits at 4 days post injury. In contrast, at 5 weeks, the CX3CR1 KO mice showed greater sensory motor deficits than that of control mice [156]. These results suggest that microglia-mediated fractalkine receptor signaling is associated with early toxicity but subsequent protection against TBI-induced pathology [156]. Drawing from this study, microglia seem to exacerbate injury outcome at the acute phase, however, it plays a more neuroprotective role at the chronic phase after injury. This was supported by another report that demonstrated a time-dependent role for CX3CL1/CX3CR1 signaling after TBI [132]. They showed that microglia exhibited M2 phenotypic markers (Ym1, CD206, and TGFβ) in the acute phase and predominantly exhibited M1 phenotypic markers CD68 in the chronic phase, owing to the differential outcomes to CX3CR1 deletion after TBI [132]. Moreover, CX3CR1 signaling has been implicated in the infiltration of peripheral immune cells and the resultant neurodegeneration [155]. Taken together, CX3CL1/CX3CR1 signaling modulates microglia activation, and depending upon the type and time of injury, either protects or exacerbates the injury response following TBI.

Purinergic Receptor (P2Y12R)

Microglia respond to extracellular changes in ATP concentration via numerous purinergic receptors. Microglia express both P2Y receptors coupled to G-proteins, as well as, P2X receptors coupled to ligand gated cation channels [183]. In this review, we focus on purinergic receptor P2Y12R, a microglia-specific receptor [184] that mediates microglial chemotaxis towards site of injury [185]. Activation of P2Y12R results in the opening of K+ channel and increased cAMP levels that is implicated in microglia surveillance and chemotaxis towards injury site [186, 187] (Fig. 2). A recent study identified a two-pore domain channel, namely, THIK-1 as the potassium channel involved in microglia ramification and surveillance [186]. However, THIK-1 did not account for site-directed chemotaxis of microglia processes suggesting that another K+ channel may be coupled with P2Y12R and warrants further investigation [186, 187].

In addition to promoting microglia dynamic properties, ATP strongly activates microglia P2Y12R and stimulates the production of cytokines (IL-4, IL-6, IL13, and TNF-α) and chemokines (CCL3) by elevating the intracellular calcium levels [188, 189]. P2Y12R expression in activated microglia is controversial. A number of studies report increased expression of P2Y12R in activated microglia [190–192]. However, there are equally compelling studies that claim that P2Y12R is expressed exclusively in non-activated microglia [50] or alternatively activated microglia [188]. This discrepancy can be explained by the direct correlation between P2Y12R expression and ramified state of microglia [193]. Hence, although these studies claim microglia activation, the expression levels of P2Y12R is a good indication of level and direction of transformation that occurs to the microglia morphological and dynamic state (hyperramified with chemotactic processes versus hyporamified microglia with amoeboid soma).

Microglia P2Y12R is well known for its role as facilitator of process extension and migration following focal injury [193, 194]. In a pig model of diffuse central FPI, microglia processes converged on axonal swellings and exacerbated diffuse axonal injury [195]. Microglia process convergence towards swollen axons and dendrites are mediated by P2Y12R [196, 197]. Recently, P2Y12R-dependant microglial closure of injured blood-brain barrier was shown [98]. Given the cellular specificity of P2Y12R in microglia, it would be the ideal target for targeting microglia activation after TBI.

Toll-like Receptor 4 (TLR4)

Toll-like receptors (TLRs) are first-line molecules for initiating immune responses. Microglia being the only innate immune cells in the CNS, they highly express TLRs, particularly TLR4. Some of the known ligands of TLR4 include lipopolysaccharide (LPS) [198], fibrinogen, heat shock proteins (HSP), high mobility group box protein 1 (HMGB-1) and monosodium urate [199]. TLR signaling initiates acute inflammatory response by promoting the release of proinflammatory cytokines. Ligand binding to TLR4 activates either a MyD88-dependent NF-κB activation or MyD88-independent activation of interferon regulatory factor–3 (IRF-3) activation and the subsequent expression of IFNβ [200] (Fig. 2). In MyD88 deficient mice, Esen and Kielian found that the microglia was only partially inhibited, implying that both MyD88 dependent and independent pathways are functional in microglia [198].

The expression of TLR4 has been shown to be upregulated in various animal models of TBI [171]. Administration of pituitary adenylate cyclase-activating polypeptide (PACAP30), a known TLR4 antagonist, reduced the cognitive and motor decline, neural apoptosis and reduced brain edema in a WD model of TBI [171]. The effects of PACAP30 were strongly associated with microglia-mediated release of IL-1β, and TNF-α, implicating TLR4 in microglia activation and inflammation [171]. Release of excess ~~(~~HMGB1~~)~~, a ligand for TLR4 was reported in TBI patients, as well as in CCI animal model [158]. Genetic or pharmacological (VGX-1027) inhibition of TLR4 attenuated the microglial neuroinflammatory response (IL-6) and limited post-traumatic edema [158]. In line with this, another study demonstrated that deletion of TLR4 (TLR4 KO) resulted in lower M1 phenotypic genes and higher expression of M2 phenotypic markers in microglia [47]. Consequently, the TLR4 KO mice exhibited decreased infarct volumes and improved

outcomes in behavioral tests after TBI [47]. Taken together, TLR4 deficiency contributes to regulating microglia to switch to the M2 phenotype, which ameliorates neurological impairment after TBI.

Scavenger Receptors

Scavenger receptors are a group of evolutionally conserved proteins expressed on the surface of microglia/macrophages and are implicated in initiating phagocytosis, cell adhesion and uptake of ligands [201, 202]. The scavenger receptors known to be expressed in microglia include scavenger receptor-A (SR-A), SR-BI, CD36, and RAGE [201]. Although little is known about the role and function of microglia scavenger receptors in TBI, in this section, we discuss CD36 and RAGE which have been reasonably investigated in animal models of brain injury.

CD36 Receptor

The CD36 receptor, abundantly expressed on microglia/macrophages [203], is used as a marker for microglia activation (M2 state) in TBI [32, 75].

CD36 receptors are activated by the ligand thrombospondin-1 (TSP-1) [204]. Sometimes, the presence of a co-receptor such as TLRs is required for activation, in which case, ligands such as DAMP and oxLDL can also activate CD36 receptors [205, 206]. The activation of CD36 activates different intracellular signaling pathways depending on the ligand, co-receptor, and cell type (Fig. 2). In microglia, CD36 with CD47 activates specific Src family kinases (Lyn, Fyn or Syk) [207], and phosphorylates Vav [208] leading to NADPH oxidase-mediated generation of ROS and promoting phagocytosis [208, 209]. Whereas, co-assembly of CD36 with TLR4/6 is implicated in an inflammatory response through the activation of NLRP3 inflammasome [210].

Although much is known about microglia CD36 in phagocytosis and inflammation, much of this information comes from studies on ischemic injury or AD. The investigation of CD36 in TBI is important because M2-like microglia/macrophages, enriched with CD36, may present a stronger phagocytic ability to remove dead neurons than the M1-like phenotype [211]. Hence, promoting the expression of CD36 may be an ideal therapeutic intervention for attenuating tissue damage and improved recovery following TBI.

RAGE Receptor

The receptor for advanced glycation end products (RAGE) is a multiligand receptor that propagates inflammatory response in various CNS disorders. RAGE expression has been found in microglia, in addition to neurons, astrocytes and endothelial cells in the normal brain [212]. The expression of RAGE and one of its ligands high-mobility group box 1 (HMGB1) was found to be increased in rat and human brains after TBI [213]. They showed that RAGE expression increased mainly in the cytoplasm of phagocytic microglia in the regions surrounding the contused area following TBI [213]. In addition to RAGE, HMGB1 also activates TLR receptors [199]. The intracellular signaling pathway of RAGE involves the key adaptor proteins, MyD88 and TIRAP, which it shares in common with TLR4 signaling [214] (Fig. 2). Activation of these cascades is implicated in the production and release of proinflammatory cytokines, TNFα, IL-1, IL-6, and IL-8, and several chemokines [215, 216].

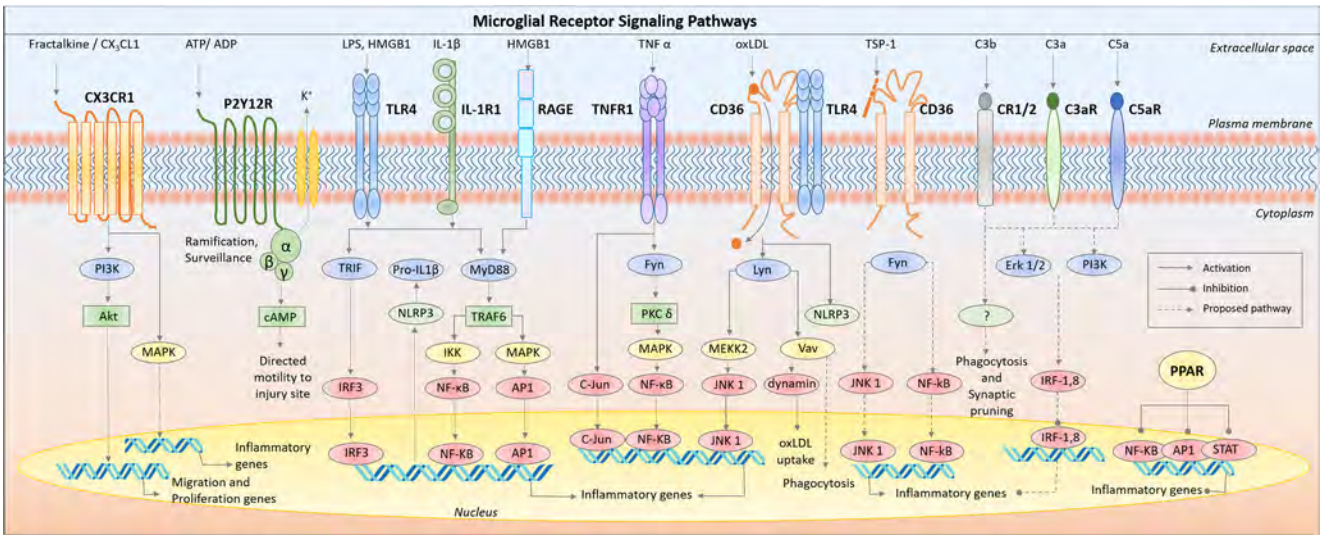


Fig. 2 A schematic depicting various molecular signaling pathway of microglial receptors including CX3CR1, P2Y12R, TLR4, IL1R1, RAGE, TNFR1, CD36, CR1/2, C3aR, C5aR and PPAR

To investigate the role of HMGB1 and RAGE in TBI, Weber et al. used mice deficient in RAGE (RAGE $^{-/-}$) in a CCI model of brain injury [217]. They showed that systemic hypoxia, acute lung injury and pulmonary neutrophilia were attenuated in RAGE −/− mice, suggesting that HMGB1-RAGE axis plays a role in TBI-induced lung dysfunction. In a hemorrhage-induced brain injury model, the expression of HMGB1 and all of its receptors (RAGE and TLR2/4) was upregulated. However, treatment with the RAGE antagonist (FPS-ZM1) significantly reduced the infiltration of inflammatory cells and the expression of IL-1β and MMP-9 after injury. Moreover, the mRNA level of RAGE was also decreased by treatment with anti-HMGB1 mAb after hemorrhagic injury [218]. These studies suggest that RAGE, expressed in microglia or other cells, may be the predominant receptor for HMGB1 in the pathogenesis of inflammation in brain injury.

It is important to note that scavenger receptors have been proposed as targets for therapy in a variety of CNS disorders, including Alzheimer's disease (AD). Hence, understanding the role of scavenger receptors in brain injury may have a major impact on the development of novel therapeutic interventions for the treatment of TBI.

Interleukin-1 Receptor1 (IL-1R1)

Microglia are the prominent source of cytokine interleukin-1 (IL-1) production, yet little is known about the expression of the receptor IL-1R1 in them. Highest expression of IL-1R1 is found on endothelial cells with low expression in microglia and astrocytes [219]. The ligands of the IL-1R1 include IL-1α and IL-1β. The activation of IL-1R1 is transduced through both the NF-kB and the mitogen-activated protein kinase (MAPK) pathways [220]. Upon ligand binding IL-1R accessory protein (IL-1RAP) is recruited. Similar to TLR4 signaling, the formation of the IL11R1 and IL-1RAP heterodimer initiated signal transduction by allowing for recruitment of MyD88 and IL-1R associated kinase 4 (IRAK4), TNFR-associated factor 6 (TRAF6) [220] (Fig. 2).

It has been shown that proliferating microglia express high amounts of IL-1R1 [221]. IL-1β exacerbated, whereas IL-1R agonist attenuated neuronal injury and microglial activation after excitotoxic damage in organotypic hippocampal slice cultures [222]. In a CCI model, neutralization of IL-1β prevented the activation of IL-1R and reduced the activation of microglia at 3 and 7 days post injury [152]. Subsequently, a reduction in lesion volume attenuated cognitive deficits and decreased hemispheric tissue loss [152]. In mice lacking IL-1R1, fewer amoeboid microglia/macrophages appeared adjacent to the injured brain tissue and those microglia present at early post-injury intervals retained their resting morphology in a penetrating brain injury model [223]. This was followed by a significant reduction in inflammatory response such as Cox-2, IL-1, and IL-6 release [223]. These results implicate IL-1R1 in microglial activation after TBI. Since microglia are not the sole expressers of IL-1R1, the recently developed IL1R1$^{loxP/loxP}$ transgenic mouseline [224] can be used to study the microglia-specific role of IL-1R1 in TBI pathology.

NLRP3 inflammasome is a major mediator of IL-1β production via activation of caspase-1. Studies have reported the activation of NLRP3 inflammasome in blunt models of TBI, whereas very few studies were performed in blast TBI [225, 226]. Our interest focus on the NLRP3 inflammasome is due to its known expression in microglia cells [227–229] and that microglial activation is well known in various forms of TBI. NLRP3 the most studied inflammasome is typically found in innate immune cells and is found to be activated by a wide range of stimuli such as viral, bacterial, and fungal components [230, 231], endogenous danger signals such as extracellular ATP [232–234], amyloid-β [227], uric acid crystals [227, 234, 235], and environmental micro particles such as silica crystals [236]. Originally thought to be expressed exclusively in microglia NLRP3 is now found to be expressed in neurons. The time course for expression following TBI differs among the two cell types. Whereas, early (acute) expression is found in neurons and later (subacute) expression to be found in microglia [237]. Weight drop model measured colocalization at 3 days post injury. Liu et found that the mRNA levels of NLRP3 increased at 6 h, 3 days, and 7 days post injury but were at control levels at 24 h after injury. In line with mRNA levels, protein levels increased at all time points except the 6 h time point. NLRP3 was coexpressed in neurons, astrocytes and microglia at the 3 day time point. IL-1β peaked at 6 h and decreased to sham levels by day 7 [238].

Quian et al. found that IL-1beta levels peaked at 6 h and decreased steadily to control levels by day 7 in a mouse model of CCI. IL-18 levels were at control concentration at 6 h but increased at all time points peaking at 7 days. mRNA levels for NLRP3, ASC, and caspase-1 levels increased at 6 h and maximal at 7 days. Although both astrocytes and microglia were activated following injury only microglia were accompanied by strong NLRP3 expression [133].

Tumor Necrosis Factor Receptor (TNFR1)

Microglia express both tumor necrosis factor-α (TNFα), as well as its receptors, TNFR1 (p55) and TNFR2 (p75) [239]. The two native receptors have differential intracellular signaling pathways. In this section, we focus on TNFR1, which contains a death domain. Activation of TNFR1 normally leads to cellular apoptosis; however, under specific conditions,

receptor activation can also lead to the activation of NFκB and contribute to cell survival. These divergent outcomes have been linked to receptor localization with receptor internalization leading to cell death and membrane localization supporting cell survival [240]. Upon ligand binding with TNFR1, the signal is transduced via transcription factors such as NF-κB and c-Jun which in turn are involved in immune, stress and inflammatory responses [241] (Fig. 2).

The expression levels of TNF- α and its associated receptors have been correlated with trauma severity in patients admitted with TBI [242]. Genetic deletion of TNFR1 (TNFR1 KO) showed attenuation of motor deficits at 4-weeks following CCI [161]. In contrast, absence of TNFR2 (TNFR2 KO) resulted in worsening of motor deficits as compared to the control [161]. The study showed that TNF-α-TNFR1 signaling was proinflammatory in nature whereas, TNF-α-TNFR2 signaling was anti-inflammatory in nature [161]. Surprisingly, an independent study observed no differences in motor or cognitive outcome in either TNFR1, TNFR2 KO, or TNFR1/TNFR2/Fas mice, versus wild-type mice following CCI [243]. These conflicting data may be attributable to differences in the severity of the CCI models used, as well as anesthetic agent, differences in background strain genetics in TNFR KO mice, and other model-specific factors in the studies [244].

As mentioned earlier, the downstream signaling of TNFR1 may be neuroprotective or neurotoxic depending upon the sub-cellular localization of the receptor. In the normal rat cortex, a portion of TNFR1 is located in lipid raft microdomains, where it is associated with the adaptor proteins TRADD (TNF receptor-associated death domain), TNF receptor-associated factor-2 (TRAF-2), the Ser/Thr kinase RIP (receptor-interacting protein), TRAF1, and cIAP-1 (cellular inhibitor of apoptosis protein-1), forming a survival signaling complex. Moderate TBI resulted in rapid recruitment of TNFR1, but not TNFR2 or Fas, to lipid rafts and induced alterations in the composition of signaling intermediates. Activation of TNFR1 after TBI induced the expression of caspase-8, thus initiating apoptosis and transient activation of NF-κB [245]. In CCI model, studies have identified co-expression of TNFR1 and TNFR2 in both microglia and endothelial cells, thereby implicating TNFR signaling in the pathogenesis of TBI [246, 247]. In brain injury models such as FPI and CCI, elevated TNF-α levels are found in the injured brain and inhibition of TNF- α and its receptors has been beneficial to postinjury cell death and functional outcome [163, 248]. However, in WD/concussive brain injury model, inhibition of TNF- α and Fas receptor resulted in cognitive decline independent of neuronal loss [174]. Hence, a better understanding of TNF-α -TNF1R signaling in the various injury models is needed to develop therapies targeting TNF1R for treatment of TBI.

Compliment Receptor

The complement receptors, part of the innate immune system, are expressed by astrocytes and microglia in the brain. The complement receptors expressed by microglia include CR1, CR2 C3aR, and C5aR [249–252]. The CR1 and CR2 are activated by C3b ligand, whereas, C3aR and C5sR are activated by C3a and C5a, respectively. The intracellular signaling following complement receptor activation involves ERK1/2 and PI3K that in turn suppresses transcription factors such as IRF-1 and IFR-8, reducing the expression of IL-12, IL23 and Il-27 [253, 254] (Fig. 2). A detailed review on complement systems and their role in various CNS disorders such as TBI have been described previously [255–257].

In the normal brain, the endogenous levels of complement ligands such as C3 and C5a are low. However, TBI is often accompanied by breakdown of the BBB which introduces a massive influx of complement components to the low endogenous levels, as well as, infiltration of adaptive immune cells capable of producing complement components [258]. In addition, TBI can also elevate the endogenous levels of C3, as noted in rat models of TBI and in head-injured patients [259–261].

The role of complement receptors in TBI was first shown by Kaczorowski et al., using soluble complement receptor 1 (sCR1) [262]. They showed that rats treated with sCR1 resulted in reduced brain neutrophil infiltration compared to vehicle-treated rats, suggesting that complement plays a pivotal role in the neuroinflammatory response induced by TBI [262]. This was further confirmed in mice lacking C3 ($C3^{-/-}$), in which there was reduced leukocyte infiltration, microglial activation, and edema following intracerebral hemorrhage-induced brain injury [263]. Similarly, in a CCI model of TBI, $C3^{-/-}$ mice showed reduced leukocyte infiltration compared to the wild-type mice; however, there was no difference in lesion size or behavioral deficits [264]. In a closed head injury model, mice lacking CR1/CR2 receptors demonstrated decreased astrocytosis, reduced microglial activation, and attenuated immunoglobulin M deposition in injured brains compared to wild-type mice [265].

Studies have also investigated the role of C5aR and its ligand C5a in TBI-induced secondary injury. To this end, mice lacking C5 ($C5^{-/-}$) or administration of C5aR antagonist resulted in reduced secondary damage in a cryoinjury model of TBI [266]. In an intracerebral hemorrhage-induced brain injury model, application of hexapeptide-derived macrocycle AcF (OPdChaWR), a C5aR antagonist, improved the spatial memory as well as general neurological outcomes [267]. This improvement correlated with a reduction in infiltrated leukocytes and edema formation [267]. In addition, a combination of C5aR and a C3aR antagonist compounded the observed neuroprotective effect [267]. Taken together, these studies suggest that targeting the complement system (receptors and/or their

ligands) may represent a promising future approach for therapeutic immunomodulation after TBI.

Peroxisome Proliferator-Activated Receptor (PPAR)

The peroxisome proliferator-activated receptors (PPAR) are a member of nuclear membrane receptor family and have been shown to be important for inflammatory signaling in microglia [149]. There are three isoforms of the receptor PPARα, PPAR δ/β, and PPARγ [268]. Of the three isoforms, only PPARα and PPARγ are implicated in inflammation. The numerous agonists and antagonists of PPARs are listed in Supplementary Table 1. Upon activation, the PPARs regulate inflammation via trans-reexpression of multiple inflammatory signaling systems such as nuclear factor-kappa B (NFκB), activator protein-1 (AP-1), signal transducer and activator of transcription (STAT) [269]. Although the endogenous ligand may not achieve critical concentration to activate the receptor a lot of research has gone into its role in TBI treatment.

Following CCI, mRNA levels of PPARγ have been reported to be elevated surrounding the injury site [49]. Agonists for both PPARα and PPARγ have been studied due to their ability to affect multiple signaling pathways and reduce TBI-induced neuropathology. Fenofibrate, a PPARα agonist, has been shown to reduce oxidative stress and inflammation after TBI [270, 271]. Similarly, Pioglitazone and Rosiglitazone, both PPARγ agonists, have been shown to reduce oxidative stress [49], inflammation [272–274], mitochondrial dysfunction [164, 275] and cell death [163, 272, 276] following CNS injury. Using rosiglitazone, a known PPAR-γ agonist, Liu et al. observed a decrease in expression of TNF-α, decreased microglia activation, increased neuronal survival and improved performance in motor function tasks at 24 h after CCI [163]. Pioglitazone also reduced lesion volume by 55% and prevented microglial activation in the tissue surrounding lesion after TBI [164]. In FPI injury model, a single dose of Pioglitazone administration reduced oxidative damage, decreased microglia activation, decreased neural degeneration, and reduced edema formation [167]. However, Pioglitazone administration was not found to have an influence on reactive astrogliosis [167]. It is important to note that PPAR expression in the brain in not exclusive to microglia [277]. Hence, whether the effect of the PPAR agonist/antagonists is due to the direct/ indirect action on microglia PPAR remains unclear. However, the pharmacological studies consistently show the involvement of PPAR signaling in microglial activation after TBI, making it a worthy therapeutic target.

Conclusion

In the various models of TBI, microglia activation varies based on the type and severity of injury. Microglia receptors act as sensors for identifying these subtle changes in the neuronal parenchyma and lead to various modes of microglia activation. Hence, the expression pattern of microglia receptors can be used as a signature to identify the injury severity/ mechanism following TBI. In the light of the above, it is evident that microglia receptor activation plays an important role in post-injury pathology and may be a sensitive diagnostic tool. Moreover, pharmacologically targeting microglia-specific receptors will prevent alterations in neuronal physiology, and thereby reduce unwanted side-effects. Hence, microglia receptors may be a potent therapeutic target for the treatment of brain injury. An ideal therapeutic strategy would be to potentiate the protective properties of microglia and attenuate its neurotoxic behavior by activating and inhibiting the appropriate anti-inflammatory and pro-inflammatory receptors, respectively.

Funding Information This work was supported by funding from the US Army Medical Research and Material Command (W81XWH-15-1-0303), New Jersey Commission for Brain Injury Research (CBIR17PIL020), and Rutgers Brain Health Institute (BHI-RUN-NJIT-2016).

Compliance with Ethical Standards

Conflict of Interest The authors declare that they have no competing interests.

Abbreviations Akt, protein kinase B; AP-1, activator protein-1; APP, amyloid precursor protein; Arg-1, arginase-1; ATP, adenosine triphosphate; BBB, blood-brain barrier; CCI, controlled cortical impact/injury; cFPI, central FPI; cIAP-1, cellular inhibitor of apoptosis protein-1; CNS, central nervous system; CR, complement receptor; CX3CR1, chemokine receptor 1; CXCL1, fractalkine; DAMPS, danger associated molecular patterns; EC, endothelial cells; FPI, fluid percussion injury; GOAD, Gila open access database; HAPI, highly aggressively proliferating immortalized; HMGB1, high mobility group box protein 1; HSP, heat shock protein; IL-1R1, interleukin 1 receptor; IL-1β, interleukin 1β; IRAK4, IL-1R associated kinase 4; IRF-3, interferon regulatory factor–3; KO, knockout; LFPI, lateral FPI; LPA, lysophosphatidic acid; LPS, lipopolysaccharide; MAPK, mitogen-activated protein kinase; MIP-1α, macrophage inflammatory protein-1α; mRNA, messenger RNA; NADPH, nicotinamide adenine dinucleotide phosphate; NFκB, nuclear factor-kappa B; NOX, NADPH oxidase; PACAP30, adenylate cyclase-activating polypeptide; PAMPS, pathogens associated molecular patterns; PCR, polymerase chain reaction; PPAR, peroxisome proliferator-activated receptors; RAGE, receptor for advanced glycation end products; RIP, receptor-interacting protein; RNA, ribonucleic acid; RNA-seq, RNA sequencing; RNS, reactive nitrogen species; ROS, reactive oxygen species; STAT, signal transducer and activator of transcription; TBI, traumatic brain injury; TLR4, Toll-like receptor 4; TNF α, tumor necrosis factor α; TNF-R1, TNFα receptor 1; TRADD, TNF receptor-associated death domain; TRAF-2, TNF receptor-associated factor-2; TSPO, translocator protein; WD, weight drop

Publisher's Note Springer Nature remains neutral with regard to jurisdictional claims in published maps and institutional affiliations.

References

1. Taylor CA et al (2017) Traumatic brain injury-related emergency department visits, hospitalizations, and deaths—United States, 2007 and 2013. MMWR Surveill Summ 66(9):1–18
2. Cernak I, Noble-Haeusslein LJ (2010) Traumatic brain injury: an overview of pathobiology with emphasis on military populations. J Cereb Blood Flow Metab 30(2):255–266
3. Faul MX, Likang, Wald M, Coronado V (2010) Traumatic brain injury in the United States: emergency department visits, hospitalizations and deaths 2002–2006, C.f.D.C.a. Prevention, Editor. National Center for Injury Prevention and Control, Atlanta
4. Maas AIR, Roozenbeek B, Manley GT (2010) Clinical trials in traumatic brain injury: Past experience and current developments. Neurotherapeutics 7(1):115–126
5. Nimmerjahn A, Kirchhoff F, Helmchen F (2005) Resting microglial cells are highly dynamic surveillants of brain parenchyma in vivo. Science 308(5726):1314–1318
6. Huber BR et al (2016) Blast exposure causes dynamic microglial/macrophage responses and microdomains if brain microvessel dysfunction. Neuroscience 319:206–220
7. Loane DJ, Kumar A (2016) Microglia in the TBI brain: the good, the bad, and the dysregulated. Exp Neurol 275:316–327
8. Boche D, Perry VH, Nicoll JA (2013) Review: activation patterns of microglia and their identification in the human brain. Neuropathol Appl Neurobiol 39(1):3–18
9. Ding AH, Nathan CF, Stuehr DJ (1988) Release of reactive nitrogen intermediates and reactive oxygen intermediates from mouse peritoneal-macrophages—comparison of activating cytokines and evidence for independent production. J Immunol 141(7):2407–2412
10. Sica A et al (2006) Tumour-associated macrophages are a distinct M2 polarised population promoting tumour progression: potential targets of anti-cancer therapy. Eur J Cancer 42(6):717–727
11. Ransohoff RM (2016) A polarizing question: do M1 and M2 microglia exist? Nat Neurosci 19(8):987–991
12. Ginhoux F et al (2010) Fate mapping analysis reveals that adult microglia derive from primitive macrophages. Science 330(6005):841–845
13. Schulz C et al (2012) A lineage of myeloid cells independent of Myb and hematopoietic stem cells. Science 336(6077):86–90
14. Link VM, Gosselin D, Glass CK (2015) Mechanisms underlying the selection and function of macrophage-specific enhancers. Cold Spring Harb Symp Quant Biol 80:213–221
15. Butovsky O et al (2014) Identification of a unique TGF-beta dependent molecular and functional signature in microglia. Nat Neurosci 17(1):131–143
16. Cherry JD, Olschowka JA, O'Banion MK (2014) Neuroinflammation and M2 microglia: the good, the bad, and the inflamed. J Neuroinflammation 11:15
17. Chiu CC et al (2016) Neuroinflammation in animal models of traumatic brain injury. J Neurosci Methods 272:38–49
18. Deselms H et al (2016) Novel pharmaceutical treatments for minimal traumatic brain injury and evaluation of animal models and methodologies supporting their development. J Neurosci Methods 272:69–76
19. Xiong Y, Mahmood A, Chopp M (2013) Animal models of traumatic brain injury. Nat Rev Neurosci 14(2):128–142
20. Dixon CE et al (1991) A controlled cortical impact model of traumatic brain injury in the rat. J Neurosci Methods 39(3):253–262
21. Lighthall JW (1988) Controlled cortical impact: a new experimental brain injury model. J Neurotrauma 5(1):1–15
22. Smith DH et al (1995) A model of parasagittal controlled cortical impact in the mouse—cognitive and histopathologic effects. J Neurotrauma 12(2):169–178
23. Lighthall JW, Goshgarian HG, Pinderski CR (1990) Characterization of axonal injury produced by controlled cortical impact. J Neurotrauma 7(2):65–76
24. Garman RH et al (2011) Blast exposure in rats with body shielding is characterized primarily by diffuse axonal injury. J Neurotrauma 28(6):947–959
25. Jin XM et al (2012) Temporal changes in cell marker expression and cellular infiltration in a controlled cortical impact model in adult male C57BL/6 mice. PLoS One 7(7):13
26. Loane DJ et al (2014) Progressive neurodegeneration after experimental brain trauma: association with chronic microglial activation. J Neuropathol Exp Neurol 73(1):14–29
27. Bachstetter AD et al (2013) The p38 alpha MAPK regulates microglial responsiveness to diffuse traumatic brain injury. J Neurosci 33(14):6143–6153
28. Cao T et al (2012) Morphological and genetic activation of microglia after diffuse traumatic brain injury in the rat. Neuroscience 225:65–75
29. Zhang ZR et al (2012) Immunolocalization of Toll-like receptors 2 and 4 as well as their endogenous ligand, heat shock protein 70, in rat traumatic brain injury. Neuroimmunomodulation 19(1):10–19
30. Zhang ZY et al (2007) Dexamethasone attenuates early expression of three molecules associated with microglia/macrophages activation following rat traumatic brain injury. Acta Neuropathol 113(6):675–682
31. Kaur C et al (1995) The response of neurons and microglia to blast injury in the rat-brain. Neuropathol Appl Neurobiol 21(5):369–377
32. Morganti JM, Riparip LK, Rosi S (2016) Call off the dog(ma): M1/M2 polarization is concurrent following traumatic brain injury. PLoS One 11(1):13
33. Urrea C et al (2007) Widespread cellular proliferation and focal neurogenesis after traumatic brain injury in the rat. Restor Neurol Neurosci 25(1):65–76
34. Ziebell JM et al (2012) Rod microglia: Elongation, alignment, and coupling to form trains across the somatosensory cortex after experimental diffuse brain injury. J Neuroinflammation 9:11
35. Huang EYK et al (2014) Remote effects on the striatal dopamine system after fluid percussion injury. Behav Brain Res 267:156–172
36. Carbonnel WS, Grady MS (1999) Regional and temporal characterization of neuronal, glial, and axonal response after traumatic brain injury in the mouse. Acta Neuropathol 98(4):396–406
37. Morrison H et al (2017) Quantitative microglia analyses reveal diverse morphologic responses in the rat cortex after diffuse brain injury. Sci Rep 7:12
38. Kelley BJ, Lifshitz J, Povlishock JT (2007) Neuroinflammatory responses after experimental diffuse traumatic brain injury. J Neuropathol Exp Neurol 66(11):989–1001
39. Readnower RD et al (2010) Increase in blood-brain barrier permeability, oxidative stress, and activated microglia in a rat model of blast-induced traumatic brain injury. J Neurosci Res 88(16):3530–3539
40. Xu LY et al (2016) Neuroinflammation in primary blast neurotrauma: time course and prevention by torso shielding. Exp Neurol 277:268–274
41. Israel I et al (2016) Combined F-18 DPA-714 micro-positron emission tomography and autoradiography imaging of microglia activation after closed head injury in mice. J Neuroinflammation 13:13

42. Kabadi SV et al (2015) S100B inhibition reduces behavioral and pathologic changes in experimental traumatic brain injury. J Cereb Blood Flow Metab 35(12):2010–2020
43. Kumar A et al (2016) Microglial/macrophage polarization dynamics following traumatic brain injury. J Neurotrauma 33(19):1732
44. Bachstetter AD et al (2011) Microglial p38α MAPK is a key regulator of proinflammatory cytokine up-regulation induced by toll-like receptor (TLR) ligands or beta-amyloid (Aβ). J Neuroinflammation 8(1):79
45. Mastroeni D et al (2009) Microglial responses to dopamine in a cell culture model of Parkinson's disease. Neurobiol Aging 30(11):1805–1817
46. Kumar A et al (2013) Traumatic brain injury in aged animals increases lesion size and chronically alters microglial/macrophage classical and alternative activation states. Neurobiol Aging 34(5):1397–1411
47. Yao XL et al (2017) TLR4 signal ablation attenuated neurological deficits by regulating microglial M1/M2 phenotype after traumatic brain injury in mice. J Neuroimmunol 310:38–45
48. Rao VLR et al (2000) Traumatic brain injury leads to increased expression of peripheral-type benzodiazepine receptors, neuronal death, and activation of astrocytes and microglia in rat thalamus. Exp Neurol 161(1):102–114
49. Yi JH et al (2008) PPAR gamma agonist rosiglitazone is neuroprotective after traumatic brain injury via anti-inflammatory and anti-oxidative mechanisms. Brain Res 1244:164–172
50. Sipe GO et al (2016) Microglial P2Y12 is necessary for synaptic plasticity in mouse visual cortex. Nat Commun 7:15
51. Balcaitis S et al (2003) Expression of proteinase-activated receptors in mouse microglial cells. Neuroreport 14(18):2373–2377
52. Mitrasinovic OM, Murphy GM (2002) Accelerated phagocytosis of amyloid-beta by mouse and human microglia overexpressing the macrophage colony-stimulating factor receptor. J Biol Chem 277(33):29889–29896
53. Mitrasinovic OM, Murphy GM (2003) Microglial overexpression of the M-CSF receptor augments phagocytosis of opsonized A beta. Neurobiol Aging 24(6):807–815
54. Mitrasinovic OM et al (2003) Macrophage colony stimulating factor promotes phagocytosis by murine microglia. Neurosci Lett 344(3):185–188
55. Wang XJ et al (2007) CD200-CD200R regulation of microglia activation in the pathogenesis of Parkinson's disease. J NeuroImmune Pharmacol 2(3):259–264
56. Moller T et al (2001) Expression and function of lysophosphatidic acid receptors in cultured rodent microglial cells. J Biol Chem 276(28):25946–25952
57. Tiffany HL et al (2001) Amyloid-beta induces chemotaxis and oxidant stress by acting at formylpeptide receptor 2, a G protein-coupled receptor expressed in phagocytes and brain. J Biol Chem 276(26):23645–23652
58. Cui YH et al (2002) Bacterial lipopolysaccharide selectively upregulates the function of the chemotactic peptide receptor formyl peptide receptor 2 in murine microglial cells. J Immunol 168(1): 434–442
59. Hall AA et al (2009) Sigma receptors suppress multiple aspects of microglial activation. Glia 57(7):744–754
60. Gekker G et al (2006) Cocaine-induced HIV-1 expression in microglia involves sigma-1 receptors and transfonning growth factor-beta 1. Int Immunopharmacol 6(6):1029–1033
61. Truettner JS, Bramlett HM, Dietrich WD (2017) Posttraumatic therapeutic hypothermia alters microglial and macrophage polarization toward a beneficial phenotype. J Cereb Blood Flow Metab 37(8):2952–2962
62. Wen L et al (2018) Polarization of microglia to the M2 phenotype in a PPAR-gamma dependent manner attenuates axonal injury induced by traumatic brain injury in mice. J Neurotrauma
63. Wang GH et al (2013) Microglia/macrophage polarization dynamics in white matter after traumatic brain injury. J Cereb Blood Flow Metab 33(12):1864–1874
64. Bollmann L et al (2015) Microglia mechanics: Immune activation alters traction forces and durotaxis. Front Cell Neurosci 9:16
65. Navone SE et al (2018) Mechanical loading of intervertebral disc modulates microglia proliferation, activation, and chemotaxis. Osteoarthr Cartil 26(7):978–987
66. Mittelbronn M et al (2001) Local distribution of microglia in the normal adult human central nervous system differs by up to one order of magnitude. Acta Neuropathol 101(3):249–255
67. Igarashi T, Huang TT, Noble LJ (2001) Regional vulnerability after traumatic brain injury: Gender differences in mice that overexpress human copper, zinc superoxide dismutase. Exp Neurol 172(2):332–341
68. Tong W et al (2002) Traumatic brain injury in the immature mouse brain: characterization of regional vulnerability. Exp Neurol 176(1):105–116
69. Gyoneva S et al (2015) Ccr2 deletion dissociates cavity size and tau pathology after mild traumatic brain injury. J Neuroinflammation 12:12
70. Kelso ML, Gendelman HE (2014) Bridge between neuroimmunity and traumatic brain injury. Curr Pharm Des 20(26):4284–4298
71. Abe N et al (2018) Comparison of the detrimental features of microglia and infiltrated macrophages in traumatic brain injury: a study using a hypnotic bromovalerylurea. Glia
72. Sedgwick JD et al (1991) Isolation and direct characterization of resident microglial cells from the normal and inflamed central nervous system. Proc Natl Acad Sci U S A 88(16):7438–7442
73. Ransohoff RM (2011) Microglia and monocytes: 'tis plain the twain meet in the brain. Nat Neurosci 14(9):1098–1100
74. Hsieh CL et al (2013) Traumatic brain injury induces macrophage subsets in the brain. Eur J Immunol 43(8):2010–2022
75. Morganti JM et al (2015) CCR2 antagonism alters brain macrophage polarization and ameliorates cognitive dysfunction induced by traumatic brain injury. J Neurosci 35(2):748–760
76. Hsieh CL et al (2014) CCR2 deficiency impairs macrophage infiltration and improves cognitive function after traumatic brain injury. J Neurotrauma 31(20):1677–1688
77. Prins M et al (2013) The pathophysiology of traumatic brain injury at a glance. Dis Model Mech 6(6):1307–1315
78. Werner C, Engelhard K (2007) Pathophysiology of traumatic brain injury. Br J Anaesth 99(1):4–9
79. Barger SW, Harmon AD (1997) Microglial activation by Alzheimer amyloid precursor protein and modulation by apolipoprotein E. Nature 388(6645):878–881
80. Noda M, Nakanishi H, Akaike N (1999) Glutamate release from microglia via glutamate transporter is enhanced by amyloid-beta peptide. Neuroscience 92(4):1465–1474
81. Barger SW, Basile AS (2001) Activation of microglia by secreted amyloid precursor protein evokes release of glutamate by cystine exchange and attenuates synaptic function. J Neurochem 76(3): 846–854
82. Faden AI et al (1989) The role of excitatory amino-acids and Nmda receptors in traumatic brain injury. Science 244(4906): 798–800
83. Christensen RN et al (2006) Kainate induces rapid redistribution of the actin cytoskeleton in ameboid microglia. J Neurosci Res 84(1):170–181
84. Hagino Y et al (2004) Heterogeneity and potentiation of AMPA type of glutamate receptors in rat cultured microglia. Glia 47(1): 68–77
85. Noda M et al (2000) AMPA-kainate subtypes of glutamate receptor in rat cerebral microglia. J Neurosci 20(1):251–258

86. Biber K et al (1999) Expression and signaling of group I metabotropic glutamate receptors in astrocytes and microglia. J Neurochem 72(4):1671–1680
87. Taylor DL et al (2002) Activation of group II metabotropic glutamate receptors underlies microglial reactivity and neurotoxicity following stimulation with chromogranin A, a peptide upregulated in Alzheimer's disease. J Neurochem 82(5):1179–1191
88. Taylor DL, Diemel LT, Pocock JM (2003) Activation of microglial group III metabotropic glutamate receptors protects neurons against microglial neurotoxicity. J Neurosci 23(6):2150–2160
89. Taylor DL et al (2005) Stimulation of microglial metabotropic glutamate receptor mGlu2 triggers tumor necrosis factor alpha-induced neurotoxicity in concert with microglial-derived fas ligand. J Neurosci 25(11):2952–2964
90. Murugan M et al (2011) Expression of N-methyl D-aspartate receptor subunits in amoeboid microglia mediates production of nitric oxide via NF-kappa B signaling pathway and oligodendrocyte cell death in hypoxic postnatal rats. Glia 59(4):521–539
91. Liu GJ et al (2006) Purine release from spinal cord microglia after elevation of calcium by glutamate. Mol Pharmacol 70(3):851–859
92. Gottlieb M, Matute C (1997) Expression of ionotropic glutamate receptor subunits in glial cells of the hippocampal CA1 area following transient forebrain ischemia. J Cereb Blood Flow Metab 17(3):290–300
93. Ferrari D et al (1997) ATP-mediated cytotoxicity in microglial cells. Neuropharmacology 36(9):1295–1301
94. Ferrari D et al (1997) Purinergic modulation of interleukin-1 beta release from microglial cells stimulated with bacterial endotoxin. J Exp Med 185(3):579–582
95. Fujita R, Ma Y, Ueda H (2008) Lysophosphatidic acid-induced membrane ruffling and brain-derived neurotrophic factor gene expression are mediated by ATP release in primary microglia. J Neurochem 107(1):152–160
96. Ballerini P et al (2005) P2Y(1) and cysteinyl leukotriene receptors mediate purine and cysteinyl leukotriene co-release in primary cultures of rat microglia. Int J Immunopathol Pharmacol 18(2): 255–268
97. Xu PF et al (2015) Extracellular ATP enhances radiation-induced brain injury through microglial activation and paracrine signaling via P2X7 receptor. Brain Behav Immunity 50:87–100
98. Lou NH et al (2016) Purinergic receptor P2RY12-dependent microglial closure of the injured blood-brain barrier. Proc Natl Acad Sci U S A 113(4):1074–1079
99. Koizumi S et al (2007) UDP acting at P2Y(6) receptors is a mediator of microglial phagocytosis. Nature 446(7139):1091–1095
100. Koizumi S et al (2013) Purinergic receptors in microglia: functional modal shifts of microglia mediated by P2 and P1 receptors. Glia 61(1):47–54
101. Hidetoshi TS, Makoto T, Inoue K (2012) P2Y receptors in microglia and neuroinflammation. Wiley Interdisciplinary Reviews: Membrane Transport and Signaling 1(4):493–501
102. del Puerto A, Wandosell F, Garrido JJ (2013) Neuronal and glial purinergic receptors functions in neuron development and brain disease. Front Cell Neurosci 7:15
103. Ozdemir D et al (2005) Effect of melatonin on brain oxidative damage induced by traumatic brain injury in immature rats. Physiol Res 54(6):631–637
104. Solaroglu I et al (2005) Increased xanthine oxidase activity after traumatic brain injury in rats. J Clin Neurosci 12(3):273–275
105. Lewen A, Matz P, Chan PH (2000) Free radical pathways in CNS injury. J Neurotrauma 17(10):871–890
106. Bedard K, Krause KH (2007) The NOX family of ROS-generating NADPH oxidases: Physiology and pathophysiology. Physiol Rev 87(1):245–313
107. Sankarapandi S et al (1998) Measurement and characterization of superoxide generation in microglial cells: Evidence for an NADPH oxidase-dependent pathway. Arch Biochem Biophys 353(2):312–321
108. Nauseef WM (2007) How human neutrophils kill and degrade microbes: an integrated view. Immunol Rev 219:88–102
109. Kumar A et al (2016) NOX2 drives M1-like microglial/macrophage activation and neurodegeneration following experimental traumatic brain injury. Brain behavior and Immunity 58: 291–309
110. Ferreira APO et al (2013) The effect of NADPH-oxidase inhibitor apocynin on cognitive impairment induced by moderate lateral fluid percussion injury: role of inflammatory and oxidative brain damage. Neurochem Int 63(6):583–593
111. Rao KVR et al A single primary blast-induced traumatic brain injury in a rodent model causes cell-type dependent increase in nicotinamide adenine dinucleotide phosphate oxidase isoforms in vulnerable brain regions. J Neurotrauma:14
112. Petitto JN et al (2003) IL-2 gene knockout affects T lymphocyte trafficking and the microglial response to regenerating facial motor neurons. J Neuroimmunol 134(1–2):95–103
113. Sakai N, Kaufman S, Milstien S (1995) Parallel induction of nitric-oxide and tetrahydrobiopterin synthesis by cytokines in rat glial-cells. J Neurochem 65(2):895–902
114. Hanisch UK et al (1997) Mouse brain microglia express interleukin-15 and its multimeric receptor complex functionally coupled to janus kinase activity. J Biol Chem 272(46):28853–28860
115. Bruce AJ et al (1996) Altered neuronal and microglial responses to excitotoxic and ischemic brain injury in mice lacking TNF receptors. Nat Med 2(7):788–794
116. Moller T, Hanisch UK, Ransom BR (2000) Thrombin-induced activation of cultured rodent microglia. J Neurochem 75(4): 1539–1547
117. Cao Q et al (2008) Expression of Notch-1 receptor and its ligands Jagged-1 and Delta-1 in amoeboid microglia in postnatal rat brain and murine BV-2 cells. Glia 56(11):1224–1237
118. Grandbarbe L et al (2007) Notch signaling modulates the activation of microglial cells. Glia 55(15):1519–1530
119. Farber K, Pannasch U, Kettenmann H (2005) Dopamine and noradrenaline control distinct functions in rodent microglial cells. Mol Cell Neurosci 29(1):128–138
120. Miyoshi M et al (2008) Angiotensin type 1 receptor antagonist inhibits lipopolysaccharide-induced stimulation of rat microglial cells by suppressing nuclear factor kappa B and activator protein-1 activation. Eur J Neurosci 27(2):343–351
121. Zhao X et al (2018) Microglial interactions with the neurovascular system in physiology and pathology. Dev Neurobioy
122. Stankovic ND et al (2016) Microglia-blood vessel interactions: a double-edged sword in brain pathologies. Acta Neuropathol 131(3):347–363
123. Thal SC, Neuhaus W (2014) The blood-brain barrier as a target in traumatic brain injury treatment. Arch Med Res 45(8):698–710
124. Chodobski A, Zink BJ, Szmydynger-Chodobska J (2011) Blood–brain barrier pathophysiology in traumatic brain injury. Transl Stroke Res 2(4):492–516
125. Shlosberg D et al (2010) Blood-brain barrier breakdown as a therapeutic target in traumatic brain injury. Nat Rev Neurol 6(7):393–403
126. Tchantchou F, Zhang YM (2013) Selective inhibition of alpha/beta-hydrolase domain 6 attenuates neurodegeneration, alleviates blood brain barrier breakdown, and improves functional recovery in a mouse model of traumatic brain injury. J Neurotrauma 30(7): 565–579
127. Choi BY et al (2012) Prevention of traumatic brain injury-induced neuronal death by inhibition of NADPH oxidase activation. Brain Res 1481:49–58

128. Kuriakose M et al (2018) Synergistic roles of oxidative stress and blood-brain barrier permeability as injury mechanisms in the acute pathophysiology of blast-induced neurotrauma. J Neurotrauma under review
129. Trahanas DM et al (2015) Differential activation of infiltrating monocyte-derived cells after mild and severe traumatic brain injury. Shock 43(3):255–260
130. Shechter R et al (2009) Infiltrating blood-derived macrophages are vital cells playing an anti-inflammatory role in recovery from spinal cord injury in mice. PLoS Med 6(7):17
131. Hanisch UK (2002) Microglia as a source and target of cytokines. Glia 40(2):140–155
132. Febinger HY et al (2015) Time-dependent effects of CX3CR1 in a mouse model of mild traumatic brain injury. J Neuroinflammation 12:16
133. Qian HH, Li QH, Shi WD (2017) Hyperbaric oxygen alleviates the activation of NLRP-3-inflammasomes in traumatic brain injury. Mol Med Rep 16(4):3922–3928
134. Chio CC et al (2013) Etanercept attenuates traumatic brain injury in rats by reducing early microglial expression of tumor necrosis factor-alpha. BMC Neurosci 14:12
135. Pinteaux-Jones F et al (2008) Myelin-induced microglial neurotoxicity can be controlled by microglial metabotropic glutamate receptors. J Neurochem 106(1):442–454
136. McMullan SM et al (2012) Metabotropic glutamate receptors inhibit microglial glutamate release. Asn Neuro 4(5):323–330
137. Mori K et al (2002) Effects of norepinephrine on rat cultured microglial cells that express alpha 1, alpha 2, beta 1 and beta 2 adrenergic receptors. Neuropharmacology 43(6):1026–1034
138. Farez MF et al (2009) Toll-like receptor 2 and poly(ADP-ribose) polymerase 1 promote central nervous system neuroinflammation in progressive EAE. Nat Immunol 10(9):958–U44
139. Jack CS et al (2005) TLR signaling tailors innate immune responses in human microglia and astrocytes. J Immunol 175(7): 4320–4330
140. Suuronen T et al (2006) Characterization of the pro-inflammatory signaling induced by protein acetylation in microglia. Neurochem Int 49(6):610–618
141. Kielian T, Mayes P, Kielian M (2002) Characterization of microglial responses to Staphylococcus aureus: effects on cytokine, costimulatory molecule, and Toll-like receptor expression. J Neuroimmunol 130(1–2):86–99
142. Charles KJ et al (2003) GABA(B) receptor subunit expression in glia. Mol Cell Neurosci 24(1):214–223
143. Harry GJ et al (2008) Tumor necrosis factor p55 and p75 receptors are involved in chemical-induced apoptosis of dentate granule neurons. J Neurochem 106(1):281–298
144. Kettenmann H et al (2011) Physiology of microglia. Physiol Rev 91(2):461–553
145. Hausler KG et al (2002) Interferon-gamma differentially modulates the release of cytokines and chemokines in lipopolysaccharide- and pneumococcal cell wall-stimulated mouse microglia and macrophages. Eur J Neurosci 16(11): 2113–2122
146. Lee YB, Nagai A, Kim SU (2002) Cytokines, chemokines, and cytokine receptors in human microglia. J Neurosci Res 69(1): 94–103
147. van Rossum D et al (2008) Myelin-phagocytosing macrophages in isolated sciatic and optic nerves reveal a unique reactive phenotype. Glia 56(3):271–283
148. McIntosh TK et al (1996) Neuropathological sequelae of traumatic brain injury: Relationship to neurochemical and biomechanical mechanisms. Lab Investig 74(2):315–342
149. Kumar A, Loane DJ (2012) Neuroinflammation after traumatic brain injury: Opportunities for therapeutic intervention. Brain Behav Immunity 26(8):1191–1201
150. Loane DJ, Faden AI (2010) Neuroprotection for traumatic brain injury: translational challenges and emerging therapeutic strategies. Trends Pharmacol Sci 31(12):596–604
151. Basrai HS et al (2016) Suppressor of cytokine signaling-2 (SOCS2) regulates the microglial response and improves functional outcome after traumatic brain injury in mice. PLoS One 11(4):24
152. Clausen F et al (2009) Neutralization of interleukin-1 beta modifies the inflammatory response and improves histological and cognitive outcome following traumatic brain injury in mice. Eur J Neurosci 30(3):385–396
153. Dong H et al (2016) Sigma-1 receptor modulates neuroinflammation after traumatic brain injury. Cell Mol Neurobiol 36(5): 639–645
154. Elliott MB et al (2011) Acute effects of a selective cannabinoid-2 receptor agonist on neuroinflammation in a model of traumatic brain injury. J Neurotrauma 28(6):973–981
155. Erturk A et al (2016) Interfering with the chronic immune response rescues chronic degeneration after traumatic brain injury. J Neurosci 36(38):9962–9975
156. Zanier ER et al (2016) Fractalkine receptor deficiency is associated with early protection but late worsening of outcome following brain trauma in mice. J Neurotrauma 33(11):1060–1072
157. Haselkorn ML et al (2010) Adenosine a(1) receptor activation as a brake on the microglial response after experimental traumatic brain injury in mice. J Neurotrauma 27(5):901–910
158. Laird MD et al (2014) High mobility group box protein-1 promotes cerebral edema after traumatic brain injury via activation of toll-like receptor 4. Glia 62(1):26–38
159. Loane D et al (2014) Novel mGluR5 positive allosteric modulator improves functional recovery, attenuates neurodegeneration, and alters microglial polarization after experimental traumatic brain injury. Neurotherapeutics 11(4):857–869
160. Loane DJ et al (2013) Activation of mGluR5 and inhibition of NADPH oxidase improves functional recovery after traumatic brain injury. J Neurotrauma 30(5):403–412
161. Longhi L et al (2013) Tumor necrosis factor in traumatic brain injury: effects of genetic deletion of p55 or p75 receptor. J Cereb Blood Flow Metab 33(8):1182–1189
162. Venneti S et al (2007) The high affinity peripheral benzodiazepine receptor ligand DAA1106 binds specifically to microglia in a rat model of traumatic brain injury: Implications for PET imaging. Exp Neurol 207(1):118–127
163. Liu H et al (2016) Rosiglitazone attenuates inflammation and CA3 neuronal loss following traumatic brain injury in rats. Biochem Biophys Res Commun 472(4):648–655
164. Sauerbeck A et al (2011) Pioglitazone attenuates mitochondrial dysfunction, cognitive impairment, cortical tissue loss, and inflammation following traumatic brain injury. Exp Neurol 227(1): 128–135
165. Gao WW et al (2015) VEGI attenuates the inflammatory injury and disruption of blood-brain barrier partly by suppressing the TLR4/NF-kappa B signaling pathway in experimental traumatic brain injury. Brain Res 1622:230–239
166. Ekmark-Lewen S et al (2016) Diffuse traumatic axonal injury in mice induces complex behavioural alterations that are normalized by neutralization of interleukin-1. Eur J Neurosci 43(8): 1016–1033
167. Pilipovic K et al (2015) A single dose of PPAR gamma agonist pioglitazone reduces cortical oxidative damage and microglial reaction following lateral fluid percussion brain injury in rats. Prog Neuro-Psychopharmacol Biol Psychiatry 59:8–20
168. Bye N et al (2007) Transient neuroprotection by minocycline following traumatic brain injury is associated with attenuated microglial activation but no changes in cell apoptosis or neutrophil infiltration. Exp Neurol 204(1):220–233

169. Chang CZ et al (2015) Magnesium lithospermate B implicates 3 '-5 '-cyclic adenosine monophosphate/protein kinase a pathway and N-methyl-D-aspartate receptors in an experimental traumatic brain injury. World Neurosurgery 84(4):954–963
170. Hellewell SC et al (2013) Erythropoietin improves motor and cognitive deficit, axonal pathology, and neuroinflammation in a combined model of diffuse traumatic brain injury and hypoxia, in association with upregulation of the erythropoietin receptor. J Neuroinflammation 10:21
171. Mao SS et al (2012) Exogenous administration of PACAP alleviates traumatic brain injury in rats through a mechanism involving the TLR4/MyD88/NF-kappa B pathway. J Neurotrauma 29(10): 1941–1959
172. Wang JW et al (2013) Activation of metabotropic glutamate receptor 5 reduces the secondary brain injury after traumatic brain injury in rats. Biochem Biophys Res Commun 430(3):1016–1021
173. Wang JW et al (2012) Expression and cell distribution of metabotropic glutamate receptor 5 in the rat cortex following traumatic brain injury. Brain Res 1464:73–81
174. Khuman J et al (2011) Tumor necrosis factor alpha and Fas receptor contribute to cognitive deficits independent of cell death after concussive traumatic brain injury in mice. J Cereb Blood Flow Metab 31(2):778–789
175. Bu W et al (2016) Mild traumatic brain injury produces neuron loss that can be rescued by modulating microglial activation using a CB2 receptor inverse agonist. Front Neurosci 10:17
176. Reiner A et al (2015) Motor, visual and emotional deficits in mice after closed-head mild traumatic brain injury are alleviated by the novel CB2 inverse agonist SMM-189. Int J Mol Sci 16(1): 758–787
177. Cardona AE et al (2006) Control of microglial neurotoxicity by the fractalkine receptor. Nat Neurosci 9(7):917–924
178. Tarozzo G et al (2002) Expression of fractalkine and its receptor, CX(3)CR1, in response to ischaemia-reperfusion brain injury in the rat. Eur J Neurosci 15(10):1663–1668
179. Harrison JK et al (1998) Role for neuronally derived fractalkine in mediating interactions between neurons and CX3CR1-expressing microglia. Proc Natl Acad Sci U S A 95(18):10896–10901
180. Clark AK et al (2007) Inhibition of spinal microglial cathepsin S for the reversal of neuropathic pain. Proc Natl Acad Sci U S A 104(25):10655–10660
181. Zhuang ZY et al (2007) Role of the CX3CR1/p38 MAPK pathway in spinal microglia for the development of neuropathic pain following nerve injury-induced cleavage of fractalkine. Brain behavior and Immunity 21(5):642–651
182. Boehme SA et al (2000) The chemokine fractalkine inhibits Fas-mediated cell death of brain microglia. J Immunol 165(1):397–403
183. Abbracchio MP, Burnstock G (1994) Purinoceptors—are there families of P2X and P2Y Purinoceptors. Pharmacol Ther 64(3): 445–475
184. Sasaki Y et al (2003) Selective expression of Gi/o-coupled ATP receptor P2Y(12) in microglia in rat brain. Glia 44(3):242–250
185. Honda S et al (2001) Extracellular ATP or ADP induce chemotaxis of cultured microglia through G(i/o)-coupled P2Y receptors. J Neurosci 21(6):1975–1982
186. Madry C et al (2018) Microglial ramification, surveillance, and Interleukin-1 beta release are regulated by the two-pore domain K+ channel THIK-1. Neuron 97(2):299
187. Swiatkowski P et al (2016) Activation of microglial P2Y12 receptor is required for outward potassium currents in response to neuronal injury. Neuroscience 318:22–33
188. Moore CS et al (2015) P2Y12 expression and function in alternatively activated human microglia. Neurology-Neuroimmunology & Neuroinflammation 2(2):10
189. Tozaki-Saitoh H et al (2017) P2Y12 receptors in primary microglia activate nuclear factor of activated T-cell signaling to induce C-C chemokine 3 expression. J Neurochem 141(1):100–110
190. Kobayashi K et al (2008) P2Y(12) receptor upregulation in activated microglia is a gateway of p38 signaling and neuropathic pain. J Neurosci 28(11):2892–2902
191. Gu N et al (2016) Microglial P2Y12 receptors regulate microglial activation and surveillance during neuropathic pain. Brain Behav Immunity 55:82–92
192. Avignone E et al (2008) Status epilepticus induces a particular microglial activation state characterized by enhanced purinergic signaling. J Neurosci 28(37):9133–9144
193. Haynes SE et al (2006) The P2Y(12) receptor regulates microglial activation by extracellular nucleotides. Nat Neurosci 9(12):1512–1519
194. Sieger D et al (2012) Long-range Ca2+ waves transmit brain-damage signals to microglia. Dev Cell 22(6):1138–1148
195. Lafrenaye AD et al (2015) Microglia processes associate with diffusely injured axons following mild traumatic brain injury in the micro pig. J Neuroinflammation 12:15
196. Eyo UB et al (2015) Modulation of microglial process convergence toward neuronal dendrites by extracellular calcium. J Neurosci 35(6):2417–2422
197. Kato G et al (2016) Microglial contact prevents excess depolarization and rescues neurons from excitotoxicity. Eneuro 3(3):9
198. Esen N, Kielian T (2006) Central role for MyD88 in the responses of microglia to pathogen-associated molecular patterns. J Immunol 176(11):6802–6811
199. Zhang Z, Schluesener HJ (2006) Mammalian toll-like receptors: from endogenous ligands to tissue regeneration. Cell Mol Life Sci 63(24):2901–2907
200. Ock J et al (2007) Regulation of toll-like receptor 4 expression and its signaling by hypoxia in cultured microglia. J Neurosci Res 85(9):1989–1995
201. El Khoury J et al (1998) Microglia, scavenger receptors, and the pathogenesis of Alzheimer's disease. Neurobiol Aging 19(1 Suppl):S81–S84
202. Wilkinson K, El Khoury J (2012) Microglial scavenger receptors and their roles in the pathogenesis of Alzheimer's disease. Int J Alzheimers Dis 2012:489456
203. El Khoury JB et al (2003) CD36 mediates the innate host response to β-amyloid. J Exp Med 197(12):1657–1666
204. Yehualaeshet T et al (1999) Activation of rat alveolar macrophage-derived latent transforming growth factor beta-1 by plasmin requires interaction with thrombospondin-1 and its cell surface receptor, CD36. Am J Pathol 155(3):841–851
205. Means TK et al (2009) Evolutionarily conserved recognition and innate immunity to fungal pathogens by the scavenger receptors SCARF1 and CD36. J Exp Med 206(3):637–653
206. Stewart CR et al (2010) CD36 ligands promote sterile inflammation through assembly of a Toll-like receptor 4 and 6 heterodimer. Nat Immunol 11(2):155–161
207. Moore KJ et al (2002) A CD36-initiated signaling cascade mediates inflammatory effects of beta-amyloid. J Biol Chem 277(49): 47373–47379
208. Wilkinson B et al (2006) Fibrillar beta-amyloid-stimulated intracellular signaling cascades require Vav for induction of respiratory burst and phagocytosis in monocytes and microglia. J Biol Chem 281(30):20842–20850
209. Cho S et al (2005) The class B scavenger receptor CD36 mediates free radical production and tissue injury in cerebral ischemia. J Neurosci 25(10):2504–2512
210. Sheedy FJ et al (2013) CD36 coordinates NLRP3 inflammasome activation by facilitating the intracellular nucleation from soluble to particulate ligands in sterile inflammation. Nat Immunol 14(8): 812–820

201. Woo MS et al (2016) Cell surface CD36 protein in monocyte/macrophage contributes to phagocytosis during the resolution phase of ischemic stroke in mice. J Biol Chem 291(45):23654–23661
212. Lue LF et al (2001) Involvement of microglial receptor for advanced glycation endproducts (RAGE) in Alzheimer's disease: identification of a cellular activation mechanism. Exp Neurol 171(1):29–45
213. Gao TL et al (2012) Expression of HMGB1 and RAGE in rat and human brains after traumatic brain injury. J Trauma Acute Care Surg 72(3):643–649
214. Weber DJ et al (2015) The HMGB1-RAGE inflammatory pathway: implications for brain injury-induced pulmonary dysfunction. Antioxid Redox Signal 23(17):1316–1328
215. Wang WY et al (2015) Role of pro-inflammatory cytokines released from microglia in Alzheimer's disease. Ann Transl Med 3(10):136
216. Fang F et al (2010) RAGE-dependent signaling in microglia contributes to neuroinflammation, Abeta accumulation, and impaired learning/memory in a mouse model of Alzheimer's disease. FASEB J 24(4):1043–1055
217. Weber DJ et al (2014) The HMGB1-RAGE axis mediates traumatic brain injury–induced pulmonary dysfunction in lung transplantation. Sci Transl Med 6(252):252ra124–252ra124
218. Wang H et al (2017) HMGB1/advanced glycation end products (RAGE) does not aggravate inflammation but promote endogenous neural stem cells differentiation in spinal cord injury. Sci Rep 7(1):10332
219. Zhang Y et al (2014) An RNA-sequencing transcriptome and splicing database of glia, neurons, and vascular cells of the cerebral cortex. J Neurosci 34(36):11929–11947
220. Sims JE, Smith DE (2010) The IL-1 family: regulators of immunity. Nat Rev Immunol 10(2):89–102
221. Bruttger J et al (2015) Genetic cell ablation reveals clusters of local self-renewing microglia in the mammalian central nervous system. Immunity 43(1):92–106
222. Stavridis S et al (2005) Characterisation of transverse slice culture preparations of postnatal rat spinal cord: preservation of defined neuronal populations. Histochem Cell Biol 123(4–5):377–392
223. Basu A et al (2002) The type 1 Interleukin-1 receptor is essential for the efficient activation of microglia and the induction of multiple proinflammatory mediators in response to brain injury. J Neurosci 22(14):6071
224. Robson MJ et al (2016) Generation and characterization of mice expressing a conditional allele of the Interleukin-1 receptor type 1. PLoS One 11(3):17
225. Ma J et al (2016) Propofol inhibits NLRP3 Inflammasome and attenuates blast-induced traumatic brain injury in rats. Inflammation 39(6):2094–2103
226. Fan KH et al (2017) Mangiferin attenuates blast-induced traumatic brain injury via inhibiting NLRP3 inflammasome. Chem Biol Interact 271:15–23
227. Halle A et al (2008) The NALP3 inflammasome is involved in the innate immune response to amyloid-beta. Nat Immunol 9(8):857–865
228. Hanamsagar R, Torres V, Kielian T (2011) Inflammasome activation and IL-1 beta/IL-18 processing are influenced by distinct pathways in microglia. J Neurochem 119(4):736–748
229. Shi FS et al (2013) Inhibition of phagocytosis and lysosomal acidification suppresses neurotoxic prion peptide-induced NALP3 inflammasome activation in BV2 microglia. J Neuroimmunol 260(1–2):121–125
230. Duncan JA et al (2009) Neisseria gonorrhoeae activates the proteinase Cathepsin B to mediate the signaling activities of the NLRP3 and ASC-containing Inflammasome. J Immunol 182(10):6460–6469
231. Ichinohe T et al (2009) Inflammasome recognition of influenza virus is essential for adaptive immune responses. J Exp Med 206(1):79–87
232. Cruz CM et al (2007) ATP activates a reactive oxygen species-dependent oxidative stress response and secretion of proinflammatory cytokines in macrophages. J Biol Chem 282(5):2871–2879
233. Hoegen T et al (2011) The NLRP3 inflammasome contributes to brain injury in pneumococcal meningitis and is activated through ATP-dependent lysosomal Cathepsin B release. J Immunol 187(10):5440–5451
234. Mariathasan S et al (2006) Cryopyrin activates the inflammasome in response to toxins and ATP. Nature 440(7081):228–232
235. Martinon F et al (2006) Gout-associated uric acid crystals activate the NALP3 inflammasome. Nature 440(7081):237–241
236. Hornung V et al (2008) Silica crystals and aluminum salts activate the NALP3 inflammasome through phagosomal destabilization. Nat Immunol 9(8):847–856
237. Lee SW et al (2018) Microglial inflammasome activation in penetrating ballistic-like brain injury. J Neurotrauma:13
238. Liu HD et al (2013) Expression of the NLRP3 inflammasome in cerebral cortex after traumatic brain injury in a rat model. Neurochem Res 38(10):2072–2083
239. Kuno R et al (2005) Autocrine activation of microglia by tumor necrosis factor-alpha. J Neuroimmunol 162(1–2):89–96
240. Kraft AD, McPherson CA, Harry GJ (2009) Heterogeneity of microglia and TNF signaling as determinants for neuronal death or survival. Neurotoxicology 30(5):785–793
241. Chen GQ, Goeddel DV (2002) TNF-R1 signaling: A beautiful pathway. Science 296(5573):1634–1635
242. Liu C, Tang JW (2014) Expression levels of tumor necrosis factor-alpha and the corresponding receptors are correlated with trauma severity. Oncol Lett 8(6):2747–2751
243. Yang JS et al (2010) Genetic analysis of the role of tumor necrosis factor receptors in functional outcome after traumatic brain injury in mice. J Neurotrauma 27(6):1037–1046
244. Longhi L et al (2008) Effect of traumatic brain injury on cognitive function in mice lacking p55 and p75 tumor necrosis factor receptors. In: Manley G, Hemphill C, Stiver S (eds) Intracranial pressure and brain monitoring Xiii: mechanisms and treatment. Springer-Verlag, Wien, p. 409
245. Lotocki G et al (2004) Tumor necrosis factor receptor 1 and its signaling intermediates are recruited to lipid rafts in the traumatized brain. J Neurosci 24(49):11010–11016
246. Yager PH et al (2008) Mannose binding lectin gene deficiency increases susceptibility to traumatic brain injury in mice. J Cereb Blood Flow Metab 28(5):1030–1039
247. Hailer NP (2008) Immunosuppression after traumatic or ischemic CNS damage: It is neuroprotective and illuminates the role of microglial cells. Prog Neurobiol 84(3):211–233
248. Bermpohl D et al (2007) TNF alpha and Fas mediate tissue damage and functional outcome after traumatic brain injury in mice. J Cereb Blood Flow Metab 27(11):1806–1818
249. Gasque P et al (1998) The receptor for complement anaphylatoxin C3a is expressed by myeloid cells and nonmyeloid cells in inflamed human central nervous system: analysis in multiple sclerosis and bacterial meningitis. J Immunol 160(7):3543–3554
250. Stahel PF et al (2000) Intracerebral complement C5a receptor (CD88) expression is regulated by TNF and lymphotoxin-alpha following closed head injury in mice. J Neuroimmunol 109(2):164–172
251. Osaka H et al (1999) Expression of C5a receptor in mouse brain: role in signal transduction and neurodegeneration. Neuroscience 88(4):1073–1082
252. Fumagalli S et al (2015) The ischemic environment drives microglia and macrophage function. Front Neurol 6:19

253. Hajishengallis G et al (2007) Complement receptor 3 blockade promotes IL-12-mediated clearance of Porphyromonas gingivalis and negates its virulence in vivo. J Immunol 179(4):2359–2367
254. Kohl J (2006) The role of complement in danger sensing and transmission. Immunol Res 34(2):157–176
255. Hammad A, Westacott L, Zaben M (2018) The role of the complement system in traumatic brain injury: a review. J Neuroinflammation 15:24
256. Veerhuis R, Nielsen HM, Tenner AJ (2011) Complement in the brain. Mol Immunol 48(14):1592–1603
257. Crehan H, Hardy J, Pocock J (2012) Microglia, Alzheimer's disease, and complement. Int J Alzheimers Dis 2012:983640
258. Brennan FH et al (2012) Complement activation in the injured central nervous system: another dual-edged sword? J Neuroinflammation 9:137
259. Keeling KL et al (2000) Local neutrophil influx following lateral fluid-percussion brain injury in rats is associated with accumulation of complement activation fragments of the third component (C3) of the complement system. J Neuroimmunol 105(1):20–30
260. Bellander BM et al (2011) Secondary insults following traumatic brain injury enhance complement activation in the human brain and release of the tissue damage marker S100B. Acta Neurochir 153(1):90–100
261. Kossmann T et al (1997) Elevated levels of the complement components C3 and factor B in ventricular cerebrospinal fluid of patients with traumatic brain injury. J Neuroimmunol 73(1–2):63–69
262. Kaczorowski SL et al (1995) Effect of soluble complement receptor-1 on neutrophil accumulation after traumatic brain injury in rats. J Cereb Blood Flow Metab 15(5):860–864
263. Yang S et al (2006) The role of complement C3 in intracerebral hemorrhage-induced brain injury. J Cereb Blood Flow Metab 26(12):1490–1495
264. Rancan M et al (2003) Central nervous system-targeted complement inhibition mediates neuroprotection after closed head injury in transgenic mice. J Cereb Blood Flow Metab 23(9):1070–1074
265. Neher MD et al (2014) Deficiency of complement receptors CR2/CR1 in Cr2(−)/(−) mice reduces the extent of secondary brain damage after closed head injury. J Neuroinflammation 11:95
266. Leinhase I et al (2006) Pharmacological complement inhibition at the C3 convertase level promotes neuronal survival, neuroprotective intracerebral gene expression, and neurological outcome after traumatic brain injury. Exp Neurol 199(2):454–464
267. Garrett MC et al (2009) Synergistic neuroprotective effects of C3a and C5a receptor blockade following intracerebral hemorrhage. Brain Res 1298:171–177
268. Michalik L, Wahli W (1999) Peroxisome proliferator-activated receptors: three isotypes for a multitude of functions. Curr Opin Biotechnol 10(6):564–570
269. Delerive P, Fruchart JC, Staels B (2001) Peroxisome proliferator-activated receptors in inflammation control. J Endocrinol 169(3):453–459
270. Besson VC et al (2005) Fenofibrate, a peroxisome proliferator-activated receptor alpha agonist, exerts neuroprotective effects in traumatic brain injury. Neurosci Lett 388(1):7–12
271. Chen XR et al (2007) Neurological recovery-promoting, anti-inflammatory, and anti-oxidative effects afforded by fenofibrate, a PPAR alpha agonist, in traumatic brain injury. J Neurotrauma 24(7):1119–1131
272. Park SW et al (2007) Thiazolidinedione class of peroxisome proliferator-activated receptor gamma agonists prevents neuronal damage, motor dysfunction, myelin loss, neuropathic pain, and inflammation after spinal cord injury in adult rats. J Pharmacol Exp Ther 320(3):1002–1012
273. Hyong A et al (2008) Rosiglitazone, a PPAR gamma agonist, attenuates inflammation after surgical brain injury in rodents. Brain Res 1215:218–224
274. Kapadia R, Yi JH, Vemuganti R (2008) Mechanisms of anti-inflammatory and neuroprotective actions of PPAR-gamma agonists. Front Biosci Landmark 13:1813–1826
275. Hunter RL et al (2007) Inflammation induces mitochondrial dysfunction and dopaminergic neurodegeneration in the nigrostriatal system. J Neurochem 100(5):1375–1386
276. McTigue DM et al (2007) The PPAR gamma agonist pioglitazone improves anatomical and locomotor recovery after rodent spinal cord injury. Exp Neurol 205(2):396–406
277. Warden A et al (2016) Localization of PPAR isotypes in the adult mouse and human brain. Sci Rep 6:15
278. Kust BM et al (1999) Regulation of K+ channel mRNA expression by stimulation of adenosine A(2a)-receptors in cultured rat microglia. Glia 25(2):120–130
279. Fiebich BL et al (1996) Cyclooxygenase-2 expression in rat microglia is induced by adenosine A(2a)-receptors. Glia 18(2):152–160
280. Heese K et al (1997) Nerve growth factor (NGF) expression in rat microglia is induced by adenosine A(2a)-receptors. Neurosci Lett 231(2):83–86
281. Hammarberg C, Schulte G, Fredholm BB (2003) Evidence for functional adenosine A(3) receptors in microglia cells. J Neurochem 86(4):1051–1054
282. Xiang ZH, Burnstock G (2005) Expression of P2X receptors on rat microglial cells during early development. Glia 52(2):119–126
283. Horvath RJ, Deleo JA (2009) Morphine enhances microglial migration through modulation of P2X(4) receptor signaling. J Neurosci 29(4):998–1005
284. Cavaliere F, Dinkel K, Reymann K (2005) Microglia response and P2 receptor participation in oxygen/glucose deprivation-induced cortical damage. Neuroscience 136(3):615–623
285. Visentin S, Nuccio CD, Bellenchi GC (2006) Different patterns of Ca^{+} signals are induced by low compared to high concentrations of P2Y agonists in microglia. Purinergic Signalling 2(4):605–617
286. Light AR et al (2006) Purinergic receptors activating rapid intracellular Ca2+ increases in microglia. Neuron Glia Biol 2:125–138
287. Liu GJ et al (2009) Glutamate induces directed chemotaxis of microglia. Eur J Neurosci 29(6):1108–1118
288. Drouin-Ouellet J et al (2011) Neuroinflammation is associated with changes in glial mGluR5 expression and the development of neonatal excitotoxic lesions. Glia 59(2):188–199
289. Geurts JJG et al (2003) Altered expression patterns of group I and II metabotropic glutamate receptors in multiple sclerosis. Brain 126:1755–1766
290. Byrnes KR et al (2009) Metabotropic glutamate receptor 5 activation inhibits microglial associated inflammation and neurotoxicity. Glia 57(5):550–560
291. Loane DJ et al (2009) Activation of metabotropic glutamate receptor 5 modulates microglial reactivity and neurotoxicity by inhibiting NADPH oxidase. J Biol Chem 284(23):15629–15639
292. Kuhn SA et al (2004) Microglia express GABA(B) receptors to modulate interleukin release. Mol Cell Neurosci 25(2):312–322
293. De Simone R et al (2005) Activation of alpha 7 nicotinic acetylcholine receptor by nicotine selectively up-regulates cyclooxygenase-2 and prostaglandin E-2 in rat microglial cultures. J Neuroinflamm 2:10
294. Shytle RD et al (2004) Cholinergic modulation of microglial activation by alpha 7 nicotinic receptors. J Neurochem 89(2):337–343
295. Suzuki T et al (2006) Microglial alpha 7 nicotinic acetylcholine receptors drive a phospholipase C/IP3 pathway and modulate the cell activation toward a neuroprotective role. J Neurosci Res 83(8):1461–1470
296. Rock RB et al (2008) Potentiation of HIV-1 expression in microglial cells by nicotine: Involvement of transforming growth factor-beta 1. J NeuroImmune Pharmacol 3(3):143–149

297. Liu J et al (2009) Nicotinic acetylcholine receptor subunits in rhesus monkey retina. Invest Ophthalmol Vis Sci 50(3):1408–1415
298. Fujita H et al (1998) Adrenergic agonists suppress the proliferation of microglia through beta 2-adrenergic receptor. Neurosci Lett 242(1):37–40
299. Mori M et al (1996) Predominant expression of platelet-activating factor receptor in the rat brain microglia. J Neurosci 16(11):3590–3600
300. Sattayaprasert P et al (2005) Platelet-activating factor enhancement of calcium influx and interleukin-6 expression, but not production, in human microglia. J Neuroinflamm 2:8
301. Wang X et al (1999) Platelet-activating factor induced Ca2+ signaling in human microglia. Brain Res 842(1):159–165
302. Noda M et al (2004) Kinin receptors in cultured rat microglia. Neurochem Int 45(2–3):437–442
303. Noda M et al (2007) Neuroprotective role of bradykinin because of the attenuation of pro-inflammatory cytokine release from activated microglia. J Neurochem 101(2):397–410
304. Ifuku M et al (2007) Bradykinin-induced microglial migration mediated by B-1-bradykinin receptors depends on Ca2+ influx via reverse-mode activity of the Na+/Ca2+ exchanger. J Neurosci 27(48):13065–13073
305. Noda M et al (2003) Expression and function of bradykinin receptors in microglia. Life Sci 72(14):1573–1581
306. Bader MF et al (1994) Bacterial-endotoxin induces Ca2+ I transients and changes the Organization of Actin in microglia. Glia 11(4):336–344
307. McLarnon JG et al (1999) Endothelin-induced changes in intracellular calcium in human microglia. Neurosci Lett 263(1):9–12
309. Moller T et al (1997) Endothelin-induced calcium signaling in cultured mouse microglial cells is mediated through ETB receptors. Neuroreport 8(9–10):2127–2131
309. Yamashita K et al (1994) Microglia with an endothelin et(B) receptor aggregate in rat Hippocampus Ca1 subfields following transient forebrain ischemia. J Neurochem 63(3):1042–1051
310. Cabral GA, Marciano-Cabral F (2005) Cannabinoid receptors in microglia of the central nervous system: immune functional relevance. J Leukoc Biol 78(6):1192–1197
311. Facchinetti F et al (2003) Cannabinoids ablate release of TNF alpha in rat microglial cells stimulated with lypopolysaccharide. Glia 41(2):161–168
312. Ramirez BG et al (2005) Prevention of Alzheimer's disease pathology by cannabinoids: neuroprotection mediated by blockade of microglial activation. J Neurosci 25(8):1904–1913
313. Maresz K et al (2005) Modulation of the cannabinoid CB2 receptor in microglial cells in response to inflammatory stimuli. J Neurochem 95(2):437–445
314. Feindt J, Schmidt A, Mentlein R (1998) Receptors and effects of the inhibitory neuropeptide somatostatin in microglial cells. Mol Brain Res 60(2):228–233
315. Tanaka J et al (1997) Glucocorticoid- and mineralocorticoid receptors in microglial cells: the two receptors mediate differential effects of corticosteroids. Glia 20(1):23–37
316. Chao CC et al (1996) Kappa opioid receptors in human microglia downregulate human immunodeficiency virus 1 expression. Proc Natl Acad Sci U S A 93(15):8051–8056
317. Dobrenis K, Makman MH, Stefano GB (1995) Occurrence of the opiate alkaloid-selective mu(3) receptor in mammalian microglia, astrocytes and Kupffer cells. Brain Res 686(2):239–248
318. Lai JP et al (2000) Detection of substance P and its receptor in human fetal microglia. Neuroscience 101(4):1137–1144
319. Rasley A et al (2002) Expression of functional NK-1 receptors in murine microglia. Glia 37(3):258–267
320. Delgado M, Ganea D (2003) Vasoactive intestinal peptide prevents activated microglia-induced neurodegeneration under inflammatory conditions: potential therapeutic role in brain trauma. FASEB J 17(11):1922
321. Delgado M, Jonakait GM, Ganea D (2002) Vasoactive intestinal peptide and pituitary adenylate cyclase-activating polypeptide inhibit chemokine production in activated microglia. Glia 39(2):148–161
322. Gonzalez-Rey E, Delgado M (2008) Vasoactive intestinal peptide inhibits cycloxygenase-2 expression in activated macrophages, microglia, and dendritic cells. Brain Behav Immunity 22(1):35–41
323. Mizoguchi Y et al (2009) Brain-derived neurotrophic factor induces sustained elevation of intracellular Ca2+ in rodent microglia. J Immunol 183(12):7778–7786
324. Cowell RM et al (2006) Microglial expression of chemokine receptor CCR5 during rat forebrain development and after perinatal hypoxia-ischemia. J Neuroimmunol 173(1–2):155–165
325. Boddeke E et al (1999) Cultured rat microglia express functional beta-chemokine receptors. J Neuroimmunol 98(2):176–184
326. Bordey A, Spencer DD (2003) Chemokine modulation of high-conductance Ca2+−sensitive K+ currents in microglia from human hippocampi. Eur J Neurosci 18(10):2893–2898
327. Rappert A et al (2002) Secondary lymphoid tissue chemokine (CCL21) activates CXCR3 to trigger a Cl- current and chemotaxis in murine microglial. J Immunol 168(7):3221–3226
328. Boddeke E et al (1999) Functional expression of the fractalkine (CX3C) receptor and its regulation by lipopolysaccharide in rat microglia. Eur J Pharmacol 374(2):309–313
329. Lacy M et al (1995) Expression of the receptors for the C5a anaphylatoxin, Interleukin-8 and Fmlp by human astrocytes and microglia. J Neuroimmunol 61(1):71–78
330. Butovsky O et al (2007) Microglia can be induced by IFN-gamma or IL-4 to express neural or dendritic-like markers. Mol Cell Neurosci 35(3):490–500
331. Hanisch UK et al (2001) The protein tyrosine kinase inhibits AG126 prevents the massive microglial cytokine induction by pneumococcal cell walls. Eur J Immunol 31(7):2104–2115
332. Syed MM, Phulwani NK, Kielian T (2007) Tumor necrosis factor-alpha (TNF-alpha) regulates Toll-like receptor 2 (TLR2) expression in microglia. J Neurochem 103(4):1461–1471
333. Michelucci A et al (2009) Characterization of the microglial phenotype under specific pro-inflammatory and anti-inflammatory conditions: effects of oligomeric and fibrillar amyloid-beta. J Neuroimmunol 210(1–2):3–12
334. Stohwasser R et al (2000) Biochemical analysis of proteasomes from mouse microglia: induction of immunoproteasomes by interferon-gamma and lipopolysaccharide. Glia 29(4):355–365
335. Butovsky O et al (2005) Activation of microglia by aggregated beta-amyloid or lipopolysaccharide impairs MHC-II expression and renders them cytotoxic whereas IFN-gamma and IL-4 render them protective. Mol Cell Neurosci 29(3):381–393
336. Prinz M et al (2008) Distinct and nonredundant in vivo functions of IFNAR on myeloid cells limit autoimmunity in the central nervous system. Immunity 28(5):675–686
337. McNamee EN et al (2010) Noradrenaline induces IL-1ra and IL-1 type II receptor expression in primary glial cells and protects against IL-1 beta-induced neurotoxicity. Eur J Pharmacol 626(2–3):219–228
338. Pinteaux E et al (2002) Expression of interleukin-1 receptors and their role in interleukin-1 actions in murine microglial cells. J Neurochem 83(4):754–763
339. Andre R et al (2005) Regulation of expression of the novel IL-1 receptor family members in the mouse brain. J Neurochem 95(2):324–330
340. Cunningham ET, Desouza EB (1993) Interleukin-1 receptors in the brain and endocrine tissues. Immunol Today 14(4):171–176

341. Sawada M, Suzumura A, Marunouchi T (1995) Induction of functional Interleukin-2 receptor in mouse microglia. J Neurochem 64(5):1973–1979
342. Shimizu E et al (2008) IL-4-induced selective clearance of oligomeric beta-amyloid peptide(1-42) by rat primary type 2 microglia. J Immunol 181(9):6503–6513
343. Gonzalez P et al (2009) Interleukin-10 and Interleukin-10 receptor-I are upregulated in glial cells after an Excitotoxic injury to the postnatal rat brain. J Neuropathol Exp Neurol 68(4):391–403
344. Huang Z, Ha GK, Petitto JM (2007) IL-15 and IL-15R alpha gene deletion: Effects on T lymphocyte trafficking and the microglial and neuronal responses to facial nerve axotomy. Neurosci Lett 417(2):160–164
345. Prinz M, Hanisch UK (1999) Murine microglial cells produce and respond to interleukin-18. J Neurochem 72(5):2215–2218
346. Bernardino ALF et al (2008) Toll-like receptors: Insights into their possible role in the pathogenesis of Lyme neuroborreliosis. Infect Immun 76(10):4385–4395
347. Bsibsi M et al (2002) Broad expression of Toll-like receptors in the human central nervous system. J Neuropathol Exp Neurol 61(11): 1013–1021
348. Olson JK, Miller SD (2004) Microglia initiate central nervous system innate and adaptive immune responses through multiple TLRs. J Immunol 173(6):3916–3924
349. Zuiderwijk-Sick EA et al (2007) Differentiation of primary adult microglia alters their response to TLR8-mediated activation but not their capacity as APC. Glia 55(15):1589–1600
350. Babcock AA et al (2006) Toll-like receptor 2 signaling in response to brain injury: an innate bridge to neuroinflammation. J Neurosci 26(49):12826–12837
351. Chen KQ et al (2006) Activation of toll-like receptor 2 on microglia promotes cell uptake of Alzheimer disease-associated amyloid beta peptide. J Biol Chem 281(6):3651–3659
352. Ebert S et al (2005) Dose-dependent activation of microglial cells by Toll-like receptor agonists alone and in combination. J Neuroimmunol 159(1–2):87–96
353. Lehnardt S et al (2006) A mechanism for neurodegeneration induced by group B streptococci through activation of the TLR2/ MyD88 pathway in microglia. J Immunol 177(1):583–592
354. Town T et al (2006) Microglia recognize double-stranded RNA via TLR3. J Immunol 176(6):3804–3812
355. Qin LY et al (2005) Interactive role of the toll-like receptor 4 and reactive oxygen species in LPS-induced microglia activation. Glia 52(1):78–84
356. Lehnardt S et al (2002) The toll-like receptor TLR4 is necessary for lipopolysaccharide-induced oligodendrocyte injury in the CNS. J Neurosci 22(7):2478–2486
357. Butchi NB, Du M, Peterson KE (2010) Interactions between TLR7 and TLR9 agonists and receptors regulate innate immune responses by astrocytes and microglia. Glia 58(6):650–664
358. Cervantes JL et al (2012) TLR8: the forgotten relative revindicated. Cell Mol Immunol 9(6):434–438
359. Dalpke AH et al (2002) Immunostimulatory CpG-DNA activates murine microglia. J Immunol 168(10):4854–4863
360. Prinz M et al (1999) Microglial activation by components of Gram-positive and -negative bacteria: distinct and common routes to the induction of ion channels and cytokines. J Neuropathol Exp Neurol 58(10):1078–1089
361. Bate C, Boshuizen R, Williams A (2005) Microglial cells kill prion-damaged neurons in vitro by a CD14-dependent process. J Neuroimmunol 170(1–2):62–70
362. Beschorner R et al (2002) CD14 expression by activated parenchymal microglia/macrophages and infiltrating monocytes following human traumatic brain injury. Acta Neuropathol 103(6):541–549
363. Chattopadhyay N et al (1999) The extracellular calcium-sensing receptor is expressed in rat microglia and modulates an outward K+ channel. J Neurochem 72(5):1915–1922
364. Moller T et al (1997) Mechanisms of C5a and C3a complement fragment-induced Ca2+ (i) signaling in mouse microglia. J Neurosci 17(2):615–624
365. Nolte C et al (1996) Complement 5a controls motility of murine microglial cells in vitro via activation of an inhibitory G-protein and the rearrangement of the actin cytoskeleton. Neuroscience 73(4):1091–1107
366. Ilschner S, Nolte C, Kettenmann H (1996) Complement factor C5a and epidermal growth factor trigger the activation of outward potassium currents in cultured murine microglia. Neuroscience 73(4):1109–1120
367. Wright GJ et al (2003) Characterization of the CD200 receptor family in mice and humans and their interactions with CD200. J Immunol 171(6):3034–3046

Appendix A –Publication Cover 11
2019

Authors: M. Skotak, MT Townsend, KV Rama Rao, N. Chandra

Title: *"A comprehensive review of experimental rodent models of repeated blast TBI"*

Journal Publication: Frontiers in Neurology, 10:1015, DOI: 10.3389/fneur.2019.01015, (2019), [19-11]

frontiers in Neurology

REVIEW
published: 27 September 2019
doi: 10.3389/fneur.2019.01015

A Comprehensive Review of Experimental Rodent Models of Repeated Blast TBI

Maciej Skotak, Molly T. Townsend, Kakulavarapu V. Ramarao and Namas Chandra**

Department of Biomedical Engineering, Center for Injury Biomechanics, Materials, and Medicine, New Jersey Institute of Technology, Newark, NJ, United States

We reviewed the relevant literature delineating advances in the development of the experimental models of repeated blast TBI (rbTBI). It appears this subject is a relatively unexplored area considering the first work published in 2007 and the bulk of peer-reviewed papers was published post-2011. There are merely 34 papers published to date utilizing rodent rbTBI models. We performed an analysis and extracted basic parameters to capture the characteristics of the exposure conditions (the blast intensity, inter-exposure interval and the number of exposures), the age and weight of the animal models most commonly used in the studies, and their endpoints. Our analysis revealed three strains of rodents are predominantly used: Sprague Dawley and Long Evans rats and wild type (C57BL/6J) mice, and young adult animals 8 to 12-week-old are a preferred choice. Typical exposure conditions are the following: (1) peak overpressure in the 27–145 kPa (4–21 psi) range, (2) number of exposures: 2 (13.9%), 3 (63.9%), 5 (16.7%), or 12 (5.6%) with a single exposure used for a baseline comparison in 41.24% of the studies. Two inter-exposure interval durations were used: (1) short (1–30 min.) and (2) extended (24 h) between consecutive shock wave exposures. The experiments included characterization of repeated blast exposure effects on auditory, ocular and neurological function, with a focus on brain etiology in most of the published work. We present an overview of major histopathological findings, which are supplemented by studies implementing MRI (DTI) and behavioral changes after rbTBI in the acute (1–7 days post-injury), subacute (7–14 days), and chronic (>14 days) phases post-injury.

Keywords: low-level blast, repeated blast exposure, peak overpressure, inter-exposure interval, Sprague-Dawley rat, Long-Evans rat, C57BL/6J mouse

OPEN ACCESS

Edited by:
Jia Lu,
DSO National Laboratories, Singapore

Reviewed by:
Denes V. Agoston,
Karolinska Institute (KI), Sweden
Hibah Omar Awwad,
University of Oklahoma Health Sciences Center, United States

****Correspondence:***
Maciej Skotak
maciej.skotak@njit.edu
Namas Chandra
namas.chandra@njit.edu

Specialty section:
This article was submitted to Neurotrauma, a section of the journal Frontiers in Neurology

Received: *20 March 2019*
Accepted: *06 September 2019*
Published: *27 September 2019*

Citation:
Skotak M, Townsend MT, Ramarao KV and Chandra N (2019) A Comprehensive Review of Experimental Rodent Models of Repeated Blast TBI. Front. Neurol. 10:1015. doi: 10.3389/fneur.2019.01015

INTRODUCTION

The research on combat injuries is traditionally invigorated during and in the aftermath of military conflicts which increases the likelihood to sustain combat-related trauma among warfighters. The complexity and severity of these injuries vary and have been covered extensively by numerous retrospective studies published over the years (1–3). The review of Rustemeyer et al. (2) identified combat injury patterns which characterize combat operations using 10 studies selected from the period 1982 to 2005. They found differences in the causality: fragmentation injuries were predominant during the 90s compared to the Vietnam War, where shooting injuries were the most common. The trunk injuries were reduced in conflicts from 1991 onwards with the advances in military personal protective equipment (PPE) including combat body armor (CBA). They also

concluded the mortality of wounded soldiers in all conflicts was consistently between 10 and 14%, and these numbers were even lower for the Afghanistan and Iraq operational theaters (4, 5). The review of Tong et al. concluded that the side effect of the deployment of CBA was an increase in combat-related head, face, and neck (HFN) injuries among service personnel wearing CBA in Iraq and Afghanistan (6). Modern ceramic plate CBA has decreased the incidence of fatal-penetrating injuries to the torso but offers no protection to the limbs and face which remain exposed to gunshot wounds and fragments from improvised explosive devices (IEDs). Three major contributing factors were identified: the increased survivability of soldiers because of CBA, fragmentation injuries from explosive devices, and the lack of protection to the face and limbs. The higher incidence of injuries caused by fragmentation to the HFN region was attributed to the more common use of IEDs and other explosive devices. The military helmet offers protection against ballistic projectiles and fragmentation, but studies from our laboratory and by the others (7–9) suggest that Advanced Combat Helmet (ACH) and derivatives offer limited to no protection against the blast waves. It is one of the leading root causes behind the epidemics of the blast-related mild TBI in veterans (10, 11). Of all soldiers returning from Iraq and Afghanistan with blast-induced mild TBI, 43.9% of them have been shown to have PTSD (11) and considerable effort has been devoted toward discriminating the symptoms of blast mTBI and PTSD. It was concluded that battlefield PTSD is most likely to be a psychological consequence of physical trauma and it is solely caused by exposure to an over-pressure wave that is generated by the blast (12).

Despite extensive human studies, until relatively recently the most mystifying among the combat injuries was undoubtedly Blast-Induced Neurotrauma (BINT). The efforts using animal models helped formulate the body of knowledge and shed light on the effects of the blast wave on the central nervous system (CNS). In the early days of animal model research on BINT was focused on demonstration whether a shock wave alone can cause measurable physical injury to the brain structures, and subsequently can lead to long term pathological and behavioral changes. A few excellent reviews have been published on the subject, and the informed reviewer is directed to these works for a detailed summary of the findings (13–15). These animal studies used an educated guess approach with respect to the exposure conditions, considering there is no publicly available data on the exposure conditions in theater. Even in case studies where there was no doubt the subject was exposed to multiple blast waves terms like "large blast" were used to describe the intensity of the blast waves (16). Similarly, the early attempts at neurological effects in training with heavy weapons or breaching lack characterization of exposure conditions (17, 18). Only in recent years, the deployment of the B3 blast gauges held the promise to acquire the exposure parameters (19, 20), which can be used as injury predictors, if correlated with the observed neurological abnormalities. The service life of the blast gauge in the combat zone was relatively short (2011–2016) and ended with a decision to abandon the program (21). There is growing concern about the neurological effects of exposure to low-level blast (LLB) experienced by military and law enforcement members during the training (22). One of the advantages of the training setting compared to the active combat zone is ordered sequence of events, predetermined beforehand, which facilitates precise monitoring of the individual and cumulative overpressure dosages. These dosages can be then correlated with blood biomarker levels, and results of neurocognitive tests applied timely. The characteristics of the overpressure dosage (the most critical set include peak overpressure, impulse, and inter-exposure interval, Δt) can be easily obtained from the blast gauges worn by trainees. One successful attempt to extract these vital data is presented in the paper by our group working in collaboration with the Walter Reed Army Institute of Research (WRAIR) team lead by Dr. Kamimori (23). The significance of the availability of this kind of data is paramount: for the first time, it creates an opportunity to develop animal models based on quantified human data. In our view, this is a unique opportunity in the TBI research area where human exposure data are usually not available.

This review focuses on the scrutiny of existing models of repeated blast TBI with an emphasis on rodent models using shock tubes. We performed the analysis to identify existing exposure paradigms, strains of animal models (age, body mass) used, the focus areas of the studies and we summarize the most important findings. The guidelines for the future development of animal models of LLB are also included.

REPEATED BLAST TBI RODENT MODELS: AN OVERVIEW OF THE EXPERIMENTAL VARIABLES

This review is focused on the presentation of advances made in the development of experimental animal models of repeated blast TBI. The literature review indicates it is a relatively new and unexplored research area, considering the number of papers (36) published in the last 12 years (**Figure 1**). Three strains of rodents are the most frequently used for this purpose: C57BL/CJ mouse (12 papers) and Sprague-Dawley (12 articles) and Long-Evans rats (10 publications), with two papers which used Wistar rats (24, 25). We extracted basic exposure parameters used in these studies: peak overpressure, number of exposures, and the interval between consecutive exposures, to gain an insight on existing practices and evaluate their relevance for the future development of the animal models of low-level blast exposure.

Two animal related basic parameters typically reported are body mass and the age at injury. Surprisingly the age of rodents used in the studies was reported only in 55.6% of the papers (20 out of 36), the body mass was reported in 88.9% of the articles (32 out of 36), while both parameters were reported in 50% of the time. The age of the mice was usually 8 to 10 weeks (11 out of 12 papers), and only in one instance, they were older (12–16 weeks, reported in all 12 articles) (26). The age of Long-Evans rats was 10–12 weeks (4 out of 10 articles), and Sprague-Dawley rats 8–10 weeks (3 out of 12 articles).

The typical body mass of the mice was in the 21–26 grams range (reported in 10 out of 12 papers). Not surprisingly, the reported body mass variation was much higher among the rats

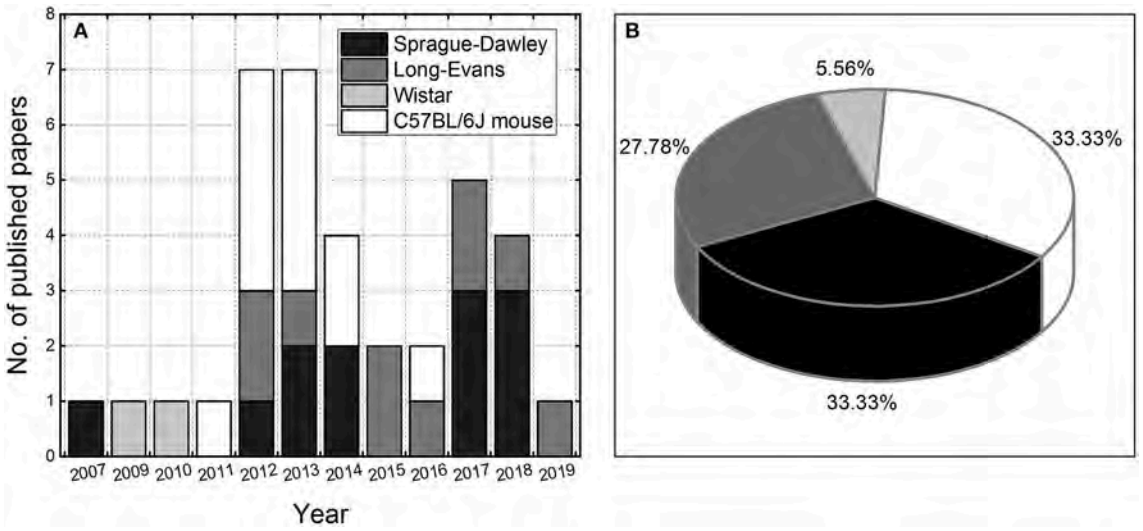


FIGURE 1 | The number of peer-reviewed papers published per year on repeated blast TBI using rodent models **(A)**. The pie chart illustrating the utilization of rodent models in rbTBI studies included in the analysis **(B)**.

(min.-max.): 250–400 g (Long-Evans, reported in all 10 published papers) and 200–400 g (Sprague-Dawley, reported in 10 out of 12 papers). It would appear that these two strain have different growth rates with a clear body mass difference at 8 weeks onwards [see Figure 1 in Turner and Burne (27)], and for LE rats the housing conditions (standard vs. enriched environment) might also play a role. At 16 weeks the body mass disparity almost reached the threshold of statistical significance [$t_{(10.85)}$, $p = 0.052$] between standard and enriched environment housed animals (27). A comparison of the growth rates of a Sprague-Dawley rats form two different sources, Charles River Labs (CRL) and Harlan Laboratories (HAR) lead to conclusions that animals from CRL were gaining weight at a more rapid rates compared to HAR rats starting at 10 weeks of age (28). However, when the second cohort of animals from both sources was subjected to a similar study the overall findings from the first cohort were confirmed, but there was obvious difference in growth rates (body mass) between cohorts from the initial time point (6–7 weeks). The analysis of weekly food intake per 100 g body weight revealed some disparities at 17 and 19 weeks, but overall there were no differences. Body composition, organ weights, tibial lengths and blood parameters were measured. CRL rats showed higher body fat mass (49.6%), liver weights (22.2%), lower testicular weights (30.8%), and lower cholesterol levels (25.4%) than HAR rats. This study demonstrated that the outbred SD rats obtained from two different sources showed significant differences in growth rates which were manifested differences in body composition most likely caused by differences in genetic makeup. Authors also cautioned that "the difference in body composition among various sources will be a potential confounding factor in model creation and its effects on therapeutic intervention, thus making the model and therapy less reliable (28)."

We performed the analysis of the experimental variables reported in available rbTBI literature using as inclusion criteria only studies conducted in shock tubes and where repeated exposure was performed on rodent models. These criteria yielded 36 peer-reviewed papers. There are three main parameters evaluated: peak overpressure, number of exposures, and inter-exposure interval, which was also supplemented by analysis of experimental endpoints (**Figure 2**). Majority of studies used relatively high blast overpressures (BOPs): in 80% of reported data blast intensities higher than 69 kPa (10 psi) were used (**Figure 1A**). Three blast exposures were the most popular injury paradigm (66% of the cases, **Figure 2B**) and as well as the Δt of 24 h between consecutive injuries (42% of the data, **Figure 2C**). The focus of most of the studies were acute pathological changes with the endpoint of 24 h the most frequently used (38%, **Figure 2D**). The analysis of the distribution of the endpoints with a 7-day bin size indicates there is a balance between "acute" (<7 days), "subacute" (7–14 days) and "chronic" characterization (inset in **Figure 2D**). These results indicate that animal models developed to replicate occupational low-level blast conditions a fine-tuning of experimental variables is necessary. Notably, peak overpressures of <70 kPa (10 psi) should be employed, the number of exposures increased, which should be accompanied by a shortening of the inter-exposure intervals.

Long-Evans Rats

Studies on effects of repeated blast exposure which employed Long Evans rats almost exclusively used Δt of 24 h, relatively low BOPs, generally below 75 kPa, and the number of repetitions which between 3, 5, and 12 (**Table 1**). Majority of the studies focused on chronic effects including comprehensive characterization of behavioral changes, with less emphasis on the acute characterization.

Low-Level Blast Exposure Studies

Ahlers et al. developed a multiple blast exposure rodent model which was designed to mimic conceptually training environment of the breachers and military/law-enforcement populations

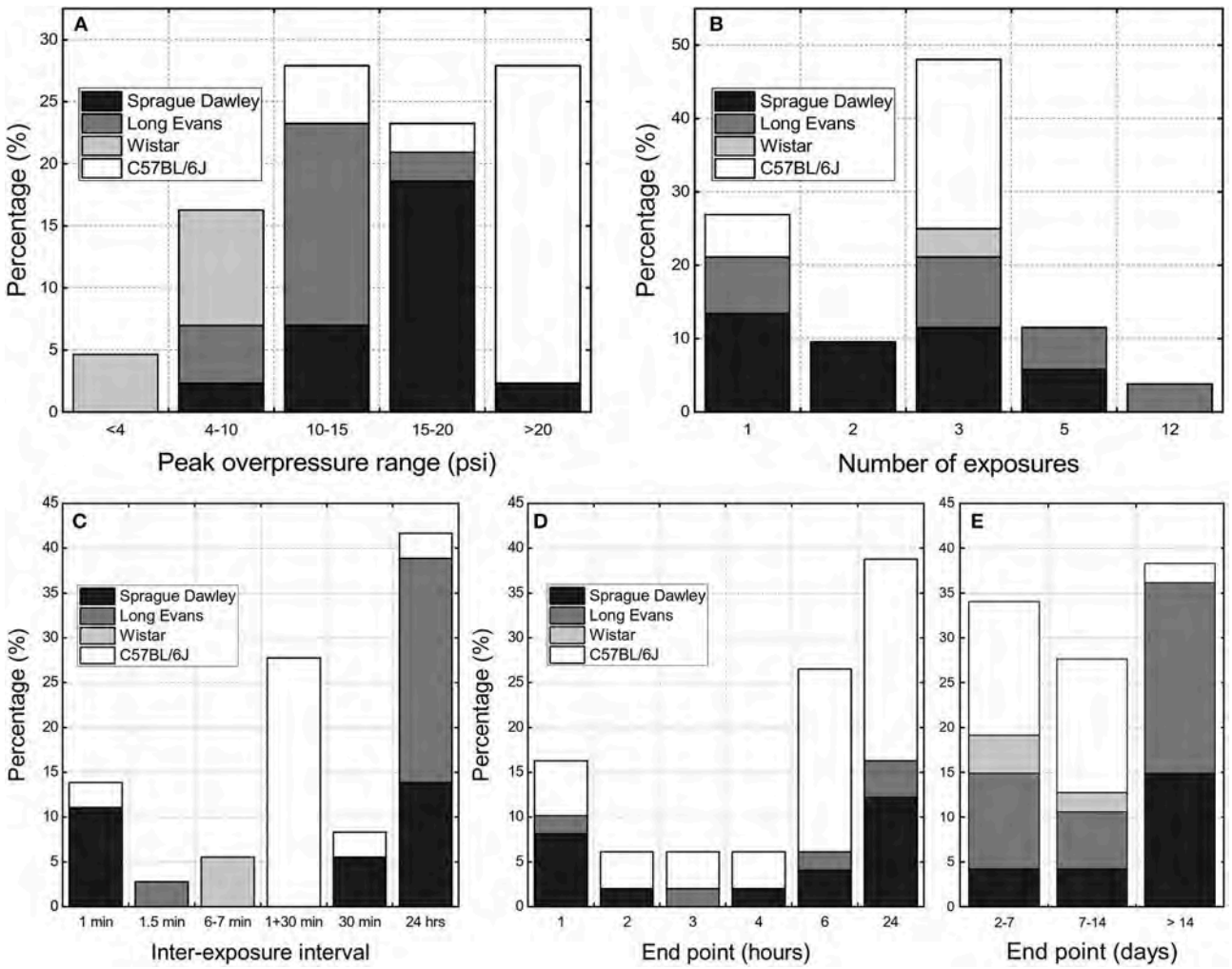


FIGURE 2 | The overview of the experimental design parameters used in the repeated bTBI studies with rodent models expressed as percentage of published peer-reviewed papers: **(A)** peak overpressure ranges, **(B)** number of exposures, **(C)** inter-exposure interval. The terminal endpoints used in the studies: **(D)** within 24 h post-injury, **(E)** classified as "acute" (<7 days), "sub-acute" (7 to 14 days), and "chronic" (>14 days).

exposed to multiple IEDs or breaching blast events (38). In their studies they used three BOPs: 36.6, 74.5, and 116.7 kPa (equivalent to 5.3, 10.8, and 16.9 psi) and animals were exposed 1 or 12 times with 24 h between exposures in frontal or side orientations and followed for up to 1 week. The other two shock wave characteristics, the duration, and impulse were also reported: 4.1, 4.8, and 6.8 ms, and 75.2, 175.8, and 335.5 Pa·s, respectively. To the best of our knowledge, it is one of the two published studies to date (32, 38), which used such high (12) number of exposures. Behavioral tests used were: balance beam task, passive avoidance task, evaluation of retrograde and anterograde amnesia [via passive avoidance (PA)] and Morris water maze, supplemented by immunohistochemistry analysis of amyloid precursor protein (APP). There were only transient effects of blast exposure: impairment of gross motor function in rats exposed to 116.7 kPa with recovery after 2 h and no changes after that. This effect was more severe in the side orientation, compared to animals which faced the blast wave. Exposure to BOP produced significant anterograde impairment only in the 116.7 kPa (side) and the 74.5 kPa (frontal) groups. Authors reported no accumulation of APP in white matter at any time point post-injury in the cerebrum, brainstem, and cerebellum, and there was no evidence of altered APP immunostaining within cell bodies or perivascular regions. The follow up study (32), focused on the effects associated with low-level blast exposure retained the exposure conditions from the original experimental design (BOP: 36 kPa, 12 exposures with 24 h in between) and focused on characterization of endothelial glycocalyx (a carbohydrate-rich layer that lines the luminal side of the vascular endothelium) and related behavioral tests. The multiple exposures to LLB resulted in a mild performance decrement in the MWM task, which suggests learning and memory deficits. Authors reported that: "administration of hyaluronidase, an enzyme that binds to and degrades hyaluronan

TABLE 1 | The summary of experimental variables (exposure conditions: BOP, number of exposures and inter-exposure interval, analyzed brain region, tissue or organs, behavioral testing and end points) in studies using Long Evans rats.

BOP, kPa	Number of exposures	Inter-exposure interval	Brain region (other tissue or organ)[a]	Behavior	End points[b]			References
					Acute, hours	Sub-acute, days	Chronic, days	
75	3	24 h	C, H, WB				42, 98, 224, 280	(29)
75	3	24 h	H	+			175	(30)
69	1, 5	24 h	TG, Plasma	+	120		9	(31)
36	12	24 h	AM, C, CC, H, S	+	48			(32)
69	1, 5	24 h	Eye, Plasma		24, 96			(33)
75	3	24 h	C				217	(34)
76	1, 5	24 h	Eye		96			(35)
96	3	1.5 min	AC, C, CN, H, IC, MGN			7	21	(36)
75	3	24 h	AM, C, H	+	73	7	42, 112, 175	(37)
36, 75, 116	12	24 h	BSt, C, CRB, Lungs	+	6, 24			(38)

[a] *AC, auditory cortex; AM, amygdala; BSt, brain stem; C, cortex; CBL, cerebellum; CC, corpus callosum; CN, cochlear nucleus; CRB, cerebrum; H, hippocampus; IC, inferior colliculus; MB, midbrain; Me, medulla; MGN, medial geniculare nucleus; OT, optic tract; S, striatum; TG, trigeminal ganglion; Th, thalamus; WB, whole brain.*

[b] *End points defined as: (1) acute: <7 days, (2) sub-acute: 7–14 days, (3) chronic: >14 days.*

(a major structural component of the glycocalyx) before blast exposure reduced the observed behavioral deficits and induced thickening of the glycocalyx layer." The connection between the suggested BBB impairment and observed behavioral changes was not explored.

The Animal Model of PTSD Associated With Repeated Blast Exposure

The association of post-traumatic stress disorder (PTSD) traits in association with mild blast TBI was a subject of work of Elders and colleagues (37). Rats were exposed three times to a shock wave with 74.5 kPa (10.8 psi) BOP spanning 24 h, and then subjected to a battery of behavioral tests including locomotor activity and open field, light/dark emergence, elevated zero, Morris water, and eight-arm radial mazes, prepulse inhibition/acoustic startle, contextual and cued fear conditioning, and predator scent exposure. In this study, blast exposure induced a variety of PTSD-related behavioral traits that were present many months, including anxiety, enhanced contextual fear conditioning, and an altered response in a predator scent assay. Elevation of the stathmin-1 in the amygdala was also reported, which is implicated in the generation of fear responses. Authors concluded that due to the application of general anesthesia, blast-related mTBI in the absence of any psychological stressor, induced chronic PTSD-related traits. The follow-up work focused on remediation of the anxiety and reverse PTSD-related behaviors and characterization of chronic neurovascular disruption in Long-Evans rats using the same injury paradigm (3 × 74.5 kPa within 3 days) (29, 30). The administration of BCI-838, a group II metabotropic glutamate receptor (mGluR2/3) antagonist prodrug (its active metabolite BCI-632 has pro-neurogenic, procognitive, and antidepressant activities in animal models) reversed PTSD related behavioral impairment and improved anxiety and fear-related behaviors and long-term recognition memory. Authors reported that the treatment with BCI-838 also increased neurogenesis in the dentate gyrus (DG) of blast-exposed rats (30). The perivascular disruption was reported in animals 6 weeks post-exposure, including decreased levels GFAP, α-internexin, and several neuronal filament proteins via 2D SDS PAGE and MALDI-TOF spectrometry. These results demonstrate that multiple blast exposure at relatively low levels has the potential to disrupt gliovascular and neurovascular interactions, which was confirmed via electron microscopy (swelling and degeneration of astrocytic end-feet in the brain cortical vasculature).

The effect of antioxidant [N-acetylcysteine (NAC) and 2,4-disulfonyl α-phenyl t-butyl nitrone (HPN-07)] treatment on biomarker expression was evaluated in the brains of Long-Evans rats exposed to three successive 96.5 kPa (14 psi) BOP exposures (the time interval between exposures was 1.5 min) (36). The set of examined biomarkers included: (1) 4-hydroxy-2-nonenal (4-HNE) an oxidative stress marker, (2) c-fos: an immediate early gene, (3) glial fibrillary acidic protein (GFAP), and (4) two markers of axonal injury: APP and 68 kDa neurofilament (NF-68). The blast exposure induced acute (24 h post blast) upregulation of 4-HNE, APP and c-fos, which gradually decreased by day 7, while GFAP and NF-68 levels continued to increase for up to 21 days. The antioxidant treatment was generally an effective strategy to reduce the levels of tested biomarkers. Additionally, authors reported lack of neuronal cell death and no evidence of apoptosis via caspase-3 staining, and that the antioxidant treatment reduced blast-induced ABR (auditory brainstem response), DPOAE (distortion product otoacoustic emission) level shifts, and hair cell loss.

The Effect of Repeated Blast on DNA Methylation

The chronic (8 months) changes in DNA methylation were evaluated in the frontal cortex of rats exposed three times to 74.5 kPa BOP within 24 h of each other (34). Brain lysates were used to separate cells into neurons and glia, and the

DNA methylation profiles in these cells were then studied using ERRBS (Expanded Reduced Representation Bisulfite Sequencing) method. It turned out neurons, and glia have distinct methylation profiles characterized by an increase in global methylation in neuronal vs. glial cells ($p < 10^{-7}$). The differential (blast vs. control animals) DNA methylation perturbations were noted in blast-exposed animals within 458 and 379 genes in neurons and glia, respectively. The gene ontology (GO) and pathway analysis revealed that methylated neuronal genes showed enrichment in cell death and survival, nervous system development and function. The ERRBS gene expression analysis was validated using a set of 30 differentially methylated neuronal and glial genes selected based on GO analysis, e.g., a 1.2-fold change in gene expression of the serotonin N-acetyltransferase gene (Aanat) in blast animals was noted ($p < 0.05$). This level of change is relatively modest, and the authors noted it is presently unclear how it might affect the brain function. Interestingly, this work is the first genomic study on changes in DNA methylation induced by multiple blast overpressure exposure.

Ocular Trauma After Repeated Blast Exposure

The ocular trauma associated with repeated blast was also evaluated (33, 35). Rats were exposed to a single (1x) or repeated (5x) blast with 70 kPa (10 psi) average BOP with the $\Delta t = 24$ h. Activated caspase-3 was detected in ocular tissues, and it scaled with the number of exposures. GFAP and CD68 were identified in the retinas from all animals subjected to BOP, but not quantified. Single and repeated blast exposure resulted in increased expression of TRPV1 (Transient Receptor Potential Vanilloid 1), CGRP (calcitonin gene-related peptide), SP (substance P), and ET-1 (endothelin-1), but except for TRPV1, no quantification was performed on the IHC samples, and no verification with additional methods. Neutrophil infiltration was significant only in multiple exposed animals. A study utilizing the same set of exposure conditions and biomarkers supplemented with ET-A and Ca^{2+} imaging, found increased levels of TRPV1 and ET-1 in trigeminal ganglion (31).

Sprague-Dawley Rats

Study Design

The majority (58% of studies, **Table 2**) used exposures in the BOP range falling between 130 and 140 kPa (40–42, 45, 46, 48, 49), while the remaining 42% of studies included a blast exposure below 100 kPa (39, 42, 44, 47, 50).

The number of exposures ranged from 1 to 5 (**Table 2**), and a single exposure was used as a reference in 50% of studies. The most common exposure numbers were two and three exposures (42%, in both cases, respectively). The remaining three studies had an injured group with five total exposures. Elsayed and Gorbunov's (50) paper was the only investigation which varied the number of multiple exposures, including injury test groups with one, two, and three exposures.

The inter-injury interval also varied among the studies examined. Four studies exposed their animals successively, where the animal was kept under anesthesia for the duration of testing, and there were <3 min between each exposure (41, 42, 45, 50). It constituted the most severe blast exposures investigated and were argued to be analogous to same-day exposures in humans. Four studies allowed for 30 min between exposures (39, 40, 43, 44) and five studies examined the effect of daily exposures (44, 46–49). These allowed for the animal to come out of anesthesia between subsequent blasts. Kawoos et al. (44) examined the effect of two different inter-exposure intervals, comparing the injury response between three 110 kPa exposures with 30 min and 24 h between exposures.

One study sought to compare results from exposure in the WRAIR shock tube with a blast-driven shock tube design (400 mm diameter, 1.5 m long), generating an overpressure using an explosion of Swedish Army plastic explosives (39). It resulted in a vastly different incident shock wave, with the blast-driven shock tube generating an 800 kPa overpressure, 0.25 ms duration, incident wave. It is a substantially higher overpressure and lower duration than those waveforms generated by the WRAIR shock tube (110 ± 26.3 kPa overpressure, 8.47 ± 1.50 ms duration).

Physiological Measurements and Monitoring

Physiological health is vital to assess the effect of shock exposure on specimen health. Longitudinal monitoring of physiological measurements was conducted to evaluate the long-term changes that occur following a single and multiple shock exposures. It was found that there were no significant differences observed in pulse distension or breath rate for single or multiple exposure animals when examined longitudinally for 42 days (one vs. five daily 138 kPa exposures). Transient significant differences were observed in arterial oxygenation levels and heart rate between injured groups and sham animals, while no significance was observed for the number of exposures (48).

Elevated levels of intracranial pressure (ICP) could signify changes which, unchecked, could contribute to adverse outcomes, e.g., increased mortality, following TBI (44). ICP reportedly exhibits a transient or sustained increase after single and multiple shock exposures, showing dependence on blast overpressure, number of exposures, and Δt (44). A single low-level shock (72 kPa) produced a transient response, with ICP returning to baseline within 3 h, while multiple exposures (three exposures every 30 min) produced a sustained increased ICP which lasted up to 5 days after injury. Higher BOPs (72 vs. 110 kPa) produced a biphasic response, with an immediate increase in ICP after exposure and a gradual increase to the maximum ICP, occurring 1–2 days after exposure. When comparing the biphasic responses of the ICP after single and multiple shocks (1 vs. 3), multiple shocks induced a more rapid increase in ICP, with the peak occurring more quickly. Increasing the Δt (30 min vs. 24 h) lowered the peak ICP and eliminated the biphasic response, with ICP remaining elevated (44). Results indicate that ICP elevation shows dependency on the number, intensity, and time between exposures. It supports a hypothesis that rbTBI outcomes will differ from a single exposure and that the time between exposures and the number of exposures exacerbates is important when considering outcomes.

Pathological Changes

The assessment of gross pathology and morphological changes of the tissues can be used to assess the injury. Only one study

TABLE 2 | The summary of experimental variables (exposure conditions: BOP, number of exposures and inter-exposure interval, analyzed brain region, behavioral testing and end points) in studies using Sprague Dawley rats.

BOP, kPa	Number of exposures	Inter-exposure interval	Brain region (other tissue or organ)[a]	Behavior	End points[a]			References
					Acute, hours	Sub-acute, days	Chronic, days	
89, 552	1, 2	30 min	BSt		24			(39)
106, 134, 123	3	30 min	CRB	+		7	90	(40)
131	2	1 min	C		24		28	(41)
83, 131	2	1 min	BSt, CBL, OT	+	1, 6, 24	7		(42)
110	3	30 min	C, H		24			(43)
69, 110	1, 3	30 min, 24 h	CRB		24	5		(44)
126	2, 3	1 min	CRB		72			(45)
138	1, 5	24 h	CBL, H, Th				42	(46)
75	3	24 h	–	+			56	(47)
138	1, 5	24 h	Plasma				42	(48)
138	1, 5	24 h	AM, C, H, Plasma		1, 2		16, 22	(49)
62	1, 2, 3	1 min	Lungs		1, 6, 24			(50)

[a] *See* ***Table 1*** *annotations for details.*

noted the presence of gross pathological changes, i.e., contusions in the cortical surface 3 days following two subsequent 130 kPa exposures (45). Elsayed and Gorbunov performed extensive pathological investigations, yet only presented the histological examination of the lung tissues. Brain tissue was reported to be less sensitive to shock exposures when compared with lung tissue, but no quantification was presented (50).

Some groups used histopathological examinations to stain for signs of cellular damage. The hematoxylin-eosin staining 1 day after three 110 kPa exposures with 30 min between exposures. The cortex showed signs of cytoplasmic vacuolization, nucleus shrinkage, and perivascular vacuolization (43). The hippocampus showed eosinophilia of the cytoplasm in CA1, CA2, and CA3, but not in the dentate gyrus (43). Silver staining was used by several groups to grade neurodegeneration and to examine patterns of morphological changes. Three days after two consecutive 130 kPa exposures, silver staining revealed mild to moderate neuronal degeneration in the multiple exposures experimental group in the cortex (45). Additionally, patterns of diffuse axonal injury (DAI) were observed following single and multiple exposures in the cerebellar white matter, optic tracts, and the cerebral peduncles, with double-exposed groups, exhibited a stronger response (45). With the same exposure conditions, Wang et al. reported that axonal damage in the cerebellar white matter persists in both injury groups for 7 days and the double-exposed group continues to show the highest levels of axonal injury (42). Kawa et al. used Fluoro-Jade and beta-amyloid precursor protein staining to label degenerated neurons in the hippocampus 1 day after one and two exposures spaced by 30 min in two shock conditions, one high BOP-low impulse exposure condition in the KI shock tube (800 kPa, 0.25 ms duration) and one low BOP-high impulse exposure condition in the WRAIR shock tube (89 kPa, 8.5 ms duration). No positively stained neurons were identified, implying that neither exposure condition induced neurodegeneration. DNA fragmentation and presumed apoptosis were examined in the hippocampus 2 h and 22 days after single and multiple shock exposures using terminal deocynucleotidyl transferase dUTP nick end labeling (TUNEL). Notably, no difference was observed between single and multiple exposures (five daily 138 kPa exposures) and the significant changes were only seen in the granular cell layer of the ventral hippocampus of the multiple exposed group at the chronic time point, at 22 days post-injury.

Several studies used MRI diffusion tensor imaging (DTI) to quantify changes to the white matter tracts following single and multiple shock exposures. Different quantitative measures, including fractional anisotropy (FA), radial diffusivity (RD), axial diffusivity (AD), and apparent diffusion coeÿ cients (ADC), were compared between experimental groups via pair comparisons at the voxel, white matter tract, or regions of interest (ROI) levels. Comparion of a single exposure to five daily mild shock exposures, a significant difference in AD and RD at the thalamus and cerebellum was observed at 2 h after injury (46). The decreased FA and increased RD in the cerebellum was also seen 72 h after two consecutive exposures when compared to a single exposure and an uninjured sham (45). At 7 days post-injury, widespread changes in AD, RD, and AFD, occurred in the thalamus, cerebellum, corpus callosum, and axial hindbrain, while no significant changes in FA were found (40).

Examination of chronic timepoints results in less cohesive observations. At 42 days, no significant changes are reported when comparing one and five daily 137 kPa exposures (46). However, at 90 days three exposures (107, 133, and 123 kPa) delivered every 30 min resulted in widespread changes in FA, AD, RD, and ADC using both voxel-wise and ROI comparisons (40). These seemingly contradictory results could highlight the importance of the inter-exposure interval in the development of chronic pathologies. Daily exposures did not develop a chronic response. The lack of significant evidence of cumulative effects

was seen in two other studies which used daily exposures, where no differences were observed between the single exposure and the multiple exposure models (44, 48). It could highlight that daily exposures allow ample time to recover between exposures (49).

Biochemical Changes

Neuronal loss following rbTBI was implicated through immunohistochemical evaluation of neuronal nuclei (NeuN) showed a significant decrease in the immunoreactivity of neurons in the cortex and hippocampus 1 day after three 30 min 110 kPa exposures (43). Further neuronal damage was evaluated by examining plasma concentrations of neurofilament-H (NF-H) and neuron-specific enolase (NSE) following five daily 138 kPa exposures. NF-H plasma concentrations were elevated compared to sham 2 h after exposure and both NF-H and NSE concentrations were elevated 22 days post-injury, but no differences were observed between single and multiple exposure experimental groups (49). Under the same exposure conditions, NF-H, and myelin basic protein (MBP) plasma concentrations are elevated in injury groups, with the rbTBI group exhibiting a higher MBP concentration when compared to the single exposure group (48). Additionally, increased immunofluorescence of doublecortin (DCX) in the hippocampus 22 days after injury indicates a late onset of *de novo* neurogenesis (49). In the same study the protein levels in tissue homogenates that indicate neuron functionality were also investigated. Tau protein concentration increased following a single 138 kPa exposure in the hippocampus 22 days post-injury when no change was seen 2 h after injury or following five daily 138 kPa exposures (49). The rbTBI group exhibited a higher concentration of n-cadherin (NCad) in tissue homogenates of the prefrontal cortex 22 days post-injury (49).

Reactive astrogliosis following injury was probed by evaluating protein levels of glial fibrillary acidic protein (GFAP) within the brain tissue or plasma. An increase in GFAP immunoreactivity 2 h after one 138 kPa exposure in the hippocampus was noted (49). At 22 days, the rbTBI group, with five daily 138 kPa exposures, showed more immunoreactivity than the single exposure group (49). Plasma concentrations of GFAP were elevated for both the single and multiple exposed groups, but no difference was seen between the two injury conditions (49). Ahmed et al. reported an upregulation of plasma GFAP 42 days post-injury for a single and five daily 138 kPa exposures, with the rbTBI exhibiting higher plasma concentrations when compared to the single exposure (48).

A proposed injury mechanism following TBI is the development of neuroinflammation mediated by blood-brain barrier damage (51, 52). Kamnaksh et al. and Ahmed et al. examined concentrations of von Willebrand factor (vWF), a protein involved in mediating inflammation, following one or five daily 138 kPa exposures. No changes were seen in concentrations of vWF in tissue homogenates of the amygdala, hippocampus, and prefrontal cortex 2 h and 22 days post-injury in either the single or multiple exposed groups (49). However, by 42 days, significant increases in the plasma concentrations of vWF, matrix metalloproteinase 8 (MMP8), formyl peptide receptor 1 (FPR1), and p38 mitogen-activated protein kinase (p38) were observed for both injury groups (48). No changes were seen in the levels of toll-like receptor 9 (TLR9), and the plasma concentrations of chemokine (C-C motif) receptor 5 (CCR5) were elevated in the single exposure group alone (48). Chemokine (C-C motif) ligand 2 (CCL2) concentrations in CSF, plasma, and tissue homogenates highlighted that CCL2 is elevated after two consecutive 130 kPa exposures (6, 24 h, and 7 days post-injury) (42). Additionally, total RNA extracted from the cerebellum showed increased CCL2 gene expression and CCL2 mRNA as well (42).

Oxidative stress has also been identified as a secondary injury mechanism following rbTBI. Gu et al. examined 3-nitrotyrosine (3-NT), a marker of oxidative/nitrosative damage, following three 30 min 110 kPa exposures. 3-NT immunoreactivity was increased in the cortex 1 day after injury, but no difference was observed in the hippocampus. When compared to sham, tissue homogenates of the cortex at 1 and 28 days post-injury, also showed a higher total ROS level following two consecutive 130 kPa exposures (41). Untargeted metabolomics at 28 days post-injury highlighted that methionine and ascorbic acid metabolism were significantly altered after the blast. Methionine metabolism disruption was seen via changes in cysteine, methionine sulfoxide, and glutathione (41). Likewise, ascorbic acid metabolism showed a persistent oxidative stress for up to 28 days post-injury, with decreased levels of ascorbic acid and increased levels of dehydroascorbic acid and its metabolic derivatives (41). Proteomics analysis of plasma 42 days after one and five daily 138 kPa exposures highlighted increased concentrations of 4-hydoxynonenal, hypoxia-inducible factor 1α, and ceruloplasmin. For all three proteins, concentrations were higher in the rbTBI experimental group.

Several groups investigated markers of vascular health following single and multiple exposures. Immunoreactivity of endothelin-1 receptor A (ETRA) and aquaporin-4 (AQP-4) were notably higher in the cortex and hippocampus 1 day following three 30 min 110 kPa exposures with respect to sham (43). Changes to plasma concentration VEGF were observed following one or five daily 138 kPa exposures. VEGF concentrations were elevated for both single and multiple exposure groups 2 h post-injury (49), in single exposures 22 days post-injury (49), and in both single and multiple exposure groups 42 days post-injury (48). The lack of significance seen at 22 days post-injury can be attributed to inadequate experimental group size ($n = 7$), as VEGF plasma concentration in the multiple exposure group at 22 days was elevated when compared to a single injury, and the multiple exposed sham group. Kamnaksh et al. (49) also reported that fetal liver kinase 1 (FLK-1) levels were unchanged and comparable to sham values in the amygdala, hippocampus, and prefrontal cortex at 2 h and 22 days after one and five daily 138 kPa exposures (49).

The *in situ* hybridization was used to probe the mRNA levels for galanin, tyrosine hydroxylase (TH), and tryptophan hydroxylase (TPH2) in the brainstem (39). The purpose of this analysis was to compare injury modalities resulting from exposures with a $\Delta t = 30$ min in two rbTBI models conditions, one high BOP-low impulse exposure condition in the KI shock tube (800 kPa, 0.25 ms duration) and one low BOP-high impulse

exposure condition in the WRAIR shock tube (89 kPa, 8.5 ms duration). Transcript levels showed dependence on exposure type and animal handling (39). Increases in TH and galanin were significant in the KI experimental model, but significance was not observed in the WRAIR model and, importantly, no effect was observed when comparing single and multiple exposures (39).

The existing results highlight that consistent exposure conditions across various exposure models facilitate the direct comparison of experimental findings. However, there exists a perpetuation of animal group sizes and exposure conditions which do not show significant differences between single and multiple exposure groups. A third of the studies with SD rats do not include an experimental group with a single exposure, and another 33% cite that no cumulative effect was observed, with results trending toward significance. In general, the disparity between selected endpoints and inter-exposure intervals were not ideal for yielding significant results and can be regarded as aggravating factors preventing direct comparison between adopted injury models. Additionally, there were no investigations of the effect of BOP or Δt on the biochemical, histological, or immunohistochemical changes following rbTBI.

Behavioral Alteration

Behavioral assessments were conducted in 25% of studies which involve Sprague-Dawley rats. The goal of behavioral assessments is to connect exposure conditions to neurobehavioral changes which may mirror symptomology seen in humans. Studies in SD rats examined behaviors associated with PTSD, spatial learning, spatial memory, anxiety, depression, and motor coordination.

To evaluate the connection between rbTBI and PTSD-like symptoms, Genovese et al. investigated the conditioned fear response following three daily 74.5 kPa exposures. Fear conditioning was cultivated via an inescapable electric shock (IES), coupled with an audio-visual stimulus. Longitudinal testing for 2 months following repeated shock exposures revealed, counter-intuitively, that coupling a rbTBI exposure with an IES reduced the conditioned fear when compared to a sham animals (47). It was concluded that this result can be attributed to a reduction in inhibitory function after rbTBI (47).

Spatial learning and memory were evaluated using the Barnes maze, in which a specimen is placed on a circular platform. An escape box is located under one of twenty holes evenly spaced around the circumference of the platform. Visual cues around the room and pre-training the animal facilitates learning the location of the escape box. The latency to find the escape box over the course of 5 testing days following single and multiple exposures ($\Delta t = 24$ h, BOP = 138 kPa exposures). In the acute phase, no significant differences were seen between experimental groups (49). A trend was observed at later time points (17–21 days post-injury), where multiple exposed animals ($n = 7$) tended to have a longer latency time than the multiple sham group ($n = 6$), however the specimen number was not high enough to see significance (49).

Anxiety- and depression-like behaviors were evaluated using the open field test, where a specimen is placed in a large plexiglass arena and the horizontal activity, vertical activity, and time spent in the center of the field are tracked over the course of the testing session. Changes in the vertical activity of a specimen indicate alterations in exploratory behavior and act as an index of depression-related behaviors (49). Directly after injury (24 h), multiple exposed animals (five daily 138 kPa exposures) had lower vertical activity than single exposed, sham, and naïve test groups (49). No differences were seen at day 16, indicating a transient response. A single exposed animals, did not show any significant changes in vertical activity. Anxiety-like behaviors, as defined by decreased time spent in the center of the field, were seen in multiple injured and multiple sham animals 1 day after the injury, indicating that anxiety in rbTBI animals may be linked to multiple bouts of anesthesia. Further work is required to determine if the injury itself induces anxiety-like behaviors. This highlights the necessity of the inclusion of multiple sham testing groups in experimental design.

Impairments in general locomotion have been evaluated in two reports. Transient response was seen, with multiple exposed animals (five daily 138 kPa exposures) showed signs of locomotor impairment directly after exposure, but no difference was seen at day 16 (49). Similarly, two exposures increased motor impairment in a rodent model, as defined by the rotarod test. The rotarod is a test which quantifies changes in motor coordination and balance through a forced motor activity which can be longitudinally compared to baseline performance. Briefly, a specimen is placed on a rotating drum and the latency to fall is recorded. Following a single shock exposure, motor impairment and coordination were not altered (42). However, significantly higher motor impairment was observed when animals were exposed to two consecutive shocks, with significant differences between single and double exposed injury experimental groups (42). These studies indicate that a single exposure is not enough to affect the motor coordination, but cumulative exposures may impair locomotion.

Treatments

Two treatments have been attempted to mitigate the effects of multiple shock exposures in the SD animal model, and both were focused on the ICP. Mechanical compression of the internal jugular vein (IJV) was performed prior to shock exposure to determine if an increase in ICP and/or an increase in brain volume could attenuate TBI following repeated exposures. The hippocampal NeuN and AQP-4 levels showed that IJV compression was partially effective in prevention of neuronal loss, edema formation, and vascular dysfunction. Although treated groups did not return to baseline values, results indicate that increased ICP and/or increased brain volume could have a neuroprotective effect (43). Kawoos et al. tested the effect of intraperitoneal injections of *N*-acetylcysteine amide (NACA) on the ICP in the acute and sub-acute period after injury. This antioxidant was found to effectively reduce blast-induced ICP elevation after single and multiple exposures (44).

Studies Using C57BL/6J Mouse Model

In addition to two different strains of rats discussed earlier, a few studies have employed an inbred C57BL/6J mouse strain to investigate various physiological, pathological and

neurobehavioral alterations following rbTBI (**Table 3**). Notably, except for one study (26), all the studies were performed in the shock tube located in Walter Reed Army Institute of Research (WRAIR). This model used 3 exposures separated by 1 and 30 min, and relatively high BOPs in the 142–144 kPa range. Majority of the studies focused on the characterization of acute effects, typically with several endpoints in the initial 24 h post-injury (**Table 3**).

Biochemical Markers

Wang et al. (63) exposed 8–10 weeks old C57BL/6J male mice weighing 22–26 g. After an initial titration of BOPs at 96, 142, and 172 kPa, a BOP of 142 kPa was selected as primary BOP intensity. Assessment of mortality rates in the animals revealed that at 96 kPa (13.9 psi), there was no mortality observed whereas a single exposure at 142 kPa resulted in 8% mortality, which further increased to 28% after 3 repeated exposures at the same BOP. These observations clearly indicate that there was a cumulative impact of shockwave load. Similarly, neurological scores (righting reflex) worsened in repeated compared to single exposure groups. A significantly higher loss of body weights was also observed in animals exposed to multiple BOPs. Neuropathological observations revealed a significant increase in brain water content (edema) within 4 h in animals exposed to multiple blasts, however by 24 and 48 after injury, the water content restored to that of normal. Multiple blast injury also displayed increased oxidative stress as indicated by a progressive crease in ROS production between 4 and 48 h in brain homogenates and such increased ROS correlated with the increased neurodegeneration as indicated by significantly increasing the number of FluoroJade-positive neurons. These neuropathological alterations also disturbed motor performance. It is noteworthy that a single blast exposure itself significantly decreased the latency to fall in a rotarod device. However, such defects were reversed in animals exposed to a single blast after 5 days, whereas multiple exposure group continued to display motor deficits. In another study by the same group (53), much lower BOP (92 kPa) was employed. A progressive DNA damage was found with an incremental increase in fragmentation of DNA in cerebral cortex and cerebellum and a concomitant rise in cell-free DNA levels in plasma indicating cerebral and systemic cellular DNA damage. Additionally, a profound increase in mitochondrial damage was also reported as estimated by decreased mitochondrial membrane potential loss and increased release of cytochrome C into the cytosol in animals exposed to multiple blasts. It indicates that shockwaves not only disrupt the cellular architecture but also damage sub-cellular structures. Additional studies by lead by Peethambaran (56), showed a significant reduction in ATP levels in the cerebral cortex of animals exposed to both single or rbTBI at 145 kPa 24 h post-injury. An examination of possible reasons for reduced brain ATP by proteomic analysis further revealed a reduction in pyruvate dehydrogenase (PDH) and mitochondrial glutamate-oxaloacetate transaminase (mGOT) which indicate defective glycolysis and mitochondrial tricarboxylic acid (TCA) cycle enzyme pathways contributing to reduced ATP levels following repeated blast exposure.

Few follow up studies have also been performed using mice model of repeated and single blast exposure to identify biomarkers of injury. Accordingly, studies by Peethambaran et al. (61) subjected mice to single exposure at 70, 103, and 145 kPa, as well as rbTBI at 145 kPa repeated 3 times. A significant increase in plasma levels of aspartate aminotransferase (AST), alanine aminotransferase (ALT) creatine kinase (CK) and lactate dehydrogenase enzymes (LDH) were observed. All the enzyme levels were significantly altered in mice exposed to single BOP, and there was a progressive increase in the levels of these enzymes as a function of the BOP, observed as early as 1 h post injury. Multiple exposures at 145 kPa significantly increased the plasma levels of these enzymes as early as 1 h after the blast and continued to show increased levels until 24 h. Interestingly, mice covered with body armor did not show any changes in the plasma levels of these enzymes indicating that increased plasma levels of these enzymes were due to damage to systemic organs and that body armor offered an effective protection. Considering all enzymes studied are markers of liver damage, a follow up histopathological studies demonstrated moderate coagulative necrosis, pyknosis, and karyolysis. Additional studies performed by the same investigators (57) report increase plasma levels of serotonin and myeloperoxidase which indicate that repeated blast exposure also causes hematological changes including platelet aggregation and polymorphonuclear changes. These studies have also identified simultaneous changes in brain histopathology in cerebral cortex showing a prominent cerebral vasoconstriction.

Increased plasma levels of glial fibrillary acidic protein (GFAP) and Tau proteins were identified in a model of rbTBI where 145 kPa BOP was used (58). The degradation of cytoskeletal marker α-spectrin was also observed indicating disruption of cellular integrity in the brain (54).

Hearing Impairment

Mice models have also been used to identify hearing impairments following repeated blast exposure considering hearing loss and development of tinnitus are most prevalent in service members (64, 65). Accordingly, proteomic studies were performed using inner ear and cochlea, as well as brain tissue homogenates of mice exposed to 145 kPa BOP for 3 times, to identify changes in hearing-related proteins. The increased protein levels of calretinin, a calcium binding protein, and parvalbumin, a marker of neurons in both cochlea, and cerebellum were demonstrated. The calretinin and parvalbumin alterations are associated with hearing impairment (66, 67) and changes in these proteins following repeated exposure strongly suggest that rbTBI can cause hearing impairment. An additional study by the same group also observed differential expression of auditory-related genes such as otoancorin, otoferlin and protocatherin-α in the hippocampus of mice exposed to rbTBI at 145 kPa (21 psi) with $\Delta t = 3$ (60).

Neurotransmitters

Alterations in specific neurotransmitter's enzymatic systems following repeated blast exposure were also reported. Acetylcholine is a neurotransmitter and neuromodulator involved in neuromuscular coordination. Acetylcholine esterase

TABLE 3 | The summary of experimental variables (exposure conditions: BOP, number of exposures and inter-exposure interval, analyzed brain region, behavioral testing and end points) in studies using C57BL/6J mice.

BOP, kPa	Number of exposures	Inter-exposure interval	Brain region (other tissue or organ)[a]	Behavior	End points[a]			References
					Acute, hours	Sub-acute, days	Chronic, days	
131	1, 3	24 h	CBL	+	1, 4, 14, 30		120	(26)
92	3	1 + 30[b]	C, CBL	+	2, 6, 24	7		(53)
142	3	1 + 30	C, CBL		6, 24, 72	7	14	(54)
142	3	1 + 30	C, CBL, H, MB		3, 6, 24, 72	7	14	(55)
145	1, 3	1 + 30	C		1, 6, 24			(56)
142	3	1 + 30	C, Plasma		2, 24, 72			(57)
145	3	1 + 30	CBL, Plasma		6, 24			(58)
145 (69, 103)	3	1 + 30	Plasma Liver, Muscle		1, 6, 24			(59)
142	3	1 + 30	C, CBL, H, MB		6, 24			(60)
142	3	1 + 30	CBL, Inner ear		6, 24			(61)
142	3	1 + 30	C, CBL, H, MB, Me		3, 6, 24, 72	7	14	(62)
142 (96, 172)	3	1 + 30	C, CBL	+	2, 4, 6, 24, 48, 72, 120			(63)

[a] *See **Table 1** annotations for details.*

[b] *1 + 30: animals were exposed three times with inter exposure interval of 1 min. between exposures 1 and 2, and inter-exposure interval of 30 min. between exposures 2 and 3.*

(AChE) is a central part of cholinergic neurotransmission as this enzyme catalyzes the hydrolysis of acetylcholine (68). Few studies reported a differential alteration in the activity of AChE as a function of time and such changes were found to be region-specific in the brains of mice exposed to 145 kPa BOP repeated 3 times. The increase in AChE in frontal cortex 6 h post injury was noted, whereas its levels significantly decreased in hind cortex and hippocampus at 6, 24 h, and 3 days post injury. Cerebellum showed a biphasic response: initial decrease at 6 h followed by increase at 3 days post-injury. Analysis of blood levels of AChE showed a decrease at 6 and 24 h, and 3 days post-injury indicating a differential response of this enzyme to rbTBI. Such organ- and tissue-specific temporal variations in may in part be due to differences in the density of cholinergic neurons in different brain regions so that the ACh metabolism may be modulated accordingly.

Correlation With Human Brain Pathology

A comprehensive study performed by research group at the University of Washington (26), adopted different mouse injury model than other reports included in this review (**Table 3**). In this model mice were exposed 131 kPa BOP repeated 3 times with 24 h delay between consecutive exposures. They performed a variety of pathological and behavioral studies with a focus only on the cerebellum. Both single and repeated blast exposures at 131 kPa caused disruption of blood-brain barrier (BBB) as indicated by extravasation of fluorescent dextran (10 kDa) into the ventral region of cerebellar parenchyma. Analysis of cerebellar Purkinje cell number showed a moderate loss of cells in animals exposed to a single blast, whereas multiple exposures synergistically increased the Purkinje cell loss. A robust number of activated microglial cells was observed in the vicinity of vascular rupture in the cerebellum as indicated by increased expression of Iba1. Further, microglia in the vicinity of vascular rupture appear more activated than their distant counterparts as indicated by more pronounced colocalization of Iba1 with CD68 (a marker of activated microglia) immunofluorescence. Both BBB disruption and microglial activation in cerebellum were concomitant with motor deficits, synaptic (loss of PSD95) and axonal pathology and reactive gliosis.

CONCLUSIONS

Three strains of rodents are currently employed to investigate mechanisms of repeated exposure to blast overpressure using shock tubes: C57BL/6J mice, Sprague-Dawley, and Long-Evans rats. The character of exposure conditions, i.e., the blast intensity levels, and inter-exposure intervals, employed in these studies suggests that they were developed to replicate etiology of mild blast TBI of improvised explosive devices (IEDs) and high-explosive detonations rather than exposure to low-level blast encountered by military and law enforcement populations in training.

Our analysis indicated existing trends in the experimental animal models developed to replicate injury conditions associated with repeated blast exposure. There seem to exist a disparity in exposure conditions between laboratories using different animal models: studies which employed Long Evans rats used Δt of 24 h and relatively low intensity BOPs (<76 kPa), while in studies employing C57BL/6J mice a relatively short Δt's (1 and 30 min) and high BOPs (∼145 kPa) were used. Studies using Long Evans rats focused predominantly on the evaluation of chronic effects, while research performed on mice was focused on acute effects. Studies performed with Sprague Dawley rats are characterized by the largest diversity in exposure conditions

and end point selection. However, in none of the existing studies to date a systematic evaluation of the inter-exposure interval was performed. Moreover, a viable experimental animal model replicating appropriate occupational low-level blast injury conditions must rely on available human data. Notably, peak overpressures of <70 kPa (10 psi) should be employed, and the number of exposures increased, which should be accompanied by a shortening of the inter-exposure intervals.

The discrepancies in the existing rodent models make diÿ cult to draw general conclusions regarding existing mechanisms common for divergent injury paradigms. However, despite the scarcity of the research in this area, a number of acute and chronic mechanisms was successfully identified. There exists strong evidence that exposure to repeated blast causes transient ocular injury and hearing loss. The repeated exposure causes changes in DNA methylation, BBB impairment accompanied by microglial activation and prolonged inflammatory response. These changes translate to behavioral effects, most notably a well-demonstrated brain pathology with PTSD.

AUTHOR CONTRIBUTIONS

MS and MT performed the analysis and literature search. MS, MT, KR, and NC wrote the manuscript.

FUNDING

This work was supported by the U.S. Army Medical Research and Materiel Command award no. 14059001 (W81XWH-15-1-0303).

REFERENCES

1. Islinger RB, Kuklo TR, Mchale KA. A review of orthopedic injuries in three recent U.S. military conflicts. *Mil Med*. (2000) 165:463–5. doi: 10.1093/milmed/165.6.463
2. Rustemeyer J, Kranz V, Bremerich A. Injuries in combat from 1982-2005 with particular reference to those to the head and neck: a review. *Br J Oral Maxillofac Surg*. (2007) 45:556–60. doi: 10.1016/j.bjoms.2007.01.003
3. Ivey KM, White CE, Wallum TE, Aden JK, Cannon JW, Chung KK, et al. Thoracic injuries in US combat casualties: a 10-year review of Operation Enduring Freedom and Iraqi Freedom. *J Trauma Acute Care Surg*. (2012) 73:S514–9.
4. Gawande A. Casualties of war–military care for the wounded from Iraq and Afghanistan. *N Engl J Med*. (2004) 351:2471–5. doi: 10.1056/NEJMp048317
5. Bosco MA, Murphy JL, Clark ME. Chronic pain and traumatic brain injury in OEF/OIF service members and Veterans. *Headache*. (2013) 53:1518–22. doi: 10.1111/head.12172
6. Tong D, Beirne R. Combat body armor and injuries to the head, face, and neck region: a systematic review. *Mil Med*. (2013) 178:421–6. doi: 10.7205/MILMED-D-12-00522
7. Grujicic M, Bell WC, Pandurangan B, He T. Blast-wave impact-mitigation capability of polyurea when used as helmet suspension-pad material. *Mater Design*. (2010) 31:4050–65. doi: 10.1016/j.matdes.2010.05.002
8. Ganpule S, Gu L, Alai A, Chandra N. Role of helmet in the mechanics of shock wave propagation under blast loading conditions. *Comput Methods Biomech Biomed Eng*. (2012) 15:1233–44. doi: 10.1080/10255842.2011.597353
9. Kulkarni SG, Gao XL, Horner SE, Zheng JQ, David NV. Ballistic helmets – Their design, materials, and performance against traumatic brain injury. *Compos Struct*. (2013) 101:313–31. doi: 10.1016/j.compstruct.2013.02.014
10. Taber KH, Warden DL, Hurley RA. Blast-related traumatic brain injury: what is known? *J Neuropsychiatry Clin Neurosci*. (2006) 18:141–5. doi: 10.1176/jnp.2006.18.2.141
11. Hoge CW, Mcgurk D, Thomas JL, Cox AL, Engel CC, Castro CA. Mild traumatic brain injury in U.S. Soldiers returning from Iraq. *N Engl J Med*. (2008) 358:453–63. doi: 10.1056/NEJMoa072972
12. Chen Y, Huang W. Non-impact, blast-induced mild TBI and PTSD: concepts and caveats. *Brain Inj*. (2011) 25:641–50. doi: 10.3109/02699052.2011.580313
13. Elder GA, Mitsis EM, Ahlers ST, Cristian A. Blast-induced mild traumatic brain injury. *Psychiatr Clin North Am*. (2010) 33:757–81. doi: 10.1016/j.psc.2010.08.001
14. Risling M, Davidsson J. Experimental animal models for studies on the mechanisms of blast-induced neurotrauma. *Front Neurol*. (2012) 3:30. doi: 10.3389/fneur.2012.00030
15. Agoston DV. Modeling the long-term consequences of repeated blast-induced mild traumatic brain injuries. *J Neurotrauma*. (2017) 34:S44–52. doi: 10.1089/neu.2017.5317
16. Warden DL, French LM, Shupenko L, Fargus J, Riedy G, Erickson ME, et al. Case report of a soldier with primary blast brain injury. *Neuroimage*. (2009) 47(suppl. 2):T152–3. doi: 10.1016/j.neuroimage.2009.01.060
17. Zetterberg H, Jonsson M, Rasulzada A, Popa C, Styrud E, Hietala MA, et al. No neurochemical evidence for brain injury caused by heading in soccer. *Br J Sports Med*. (2007) 41:574–7. doi: 10.1136/bjsm.2007.037143
18. Tate CM, Wang KK, Eonta S, Zhang Y, Carr W, Tortella FC, et al. Serum brain biomarker level, neurocognitive performance, and self-reported symptom changes in soldiers repeatedly exposed to low-level blast: a breacher pilot study. *J Neurotrauma*. (2013) 30:1620–30. doi: 10.1089/neu.2012.2683
19. Duckworth J, Ling G, Rodgers J. Blast gauge: quantifying exposure during an improvised explosive device attack. *Neurocrit Care*. (2012) 17:S84.
20. Bennett S, Fintelman G, Patchell M, Webb A, Wynen B, Costello J, et al. Project cerebro: an evaluation of blast gauges in the Australian Defence Force. *J Mil Veteran Health*. (2015) 23:27. Available online at: https://jmvh.org/article/project-cerebro-an-evaluation-of-blast-gauges-in-the-australian-defence-force/
21. Hamilton J. *Pentagon Shelves Blast Gauges Meant To Detect Battlefield Brain Injuries* (2016). Available online at: https://www.npr.org/sections/health-shots/2016/12/20/506146595/pentagon-shelves-blast-gauges-meant-to-detect-battlefield-brain-injuries (accessed August 28, 2019).
22. Engel CC, Hoch E, Simmons M. The neurological effects of repeated exposure to military occupational blast: implications for prevention and health. In: *The Seventh Department of Defense State-of-the-Science Meeting*. Arlington, VA: RAND Corporation (2018).
23. Skotak M, Lavalle C, Misistia A, Egnoto MJ, Chandra N, Kamimori G. Occupational blast wave exposure during multiday 0.50 caliber rifle course. *Front Neurol*. (2019) 10:797. doi: 10.3389/fneur.2019.00797
24. Saljo A, Svensson B, Mayorga M, Hamberger A, Bolouri H. Low-level blasts raise intracranial pressure and impair cognitive function in rats. *J Neurotrauma*. (2009) 26:1345–52. doi: 10.1089/neu.2008.0856
25. Saljo A, Bolouri H, Mayorga M, Svensson B, Hamberger A. Low-level blast raises intracranial pressure and impairs cognitive function in rats: prophylaxis with processed cereal feed. *J Neurotrauma*. (2010) 27:383–9. doi: 10.1089/neu.2009.1053
26. Meabon JS, Huber BR, Cross DJ, Richards TL, Minoshima S, Pagulayan KF, et al. Repetitive blast exposure in mice and combat veterans causes persistent cerebellar dysfunction. *Sci Transl Med*. (2016) 8:L321ra326. doi: 10.1126/scitranslmed.aaa9585
27. Turner KM, Burne TH. Comprehensive behavioural analysis of Long Evans and Sprague-Dawley rats reveals differential effects of housing conditions on tests relevant to neuropsychiatric disorders. *PLoS ONE*. (2014) 9:e93411. doi: 10.1371/journal.pone.0093411
28. Brower M, Grace M, Kotz CM, Koya V. Comparative analysis of growth characteristics of Sprague Dawley rats obtained from different sources. *Lab Anim Res*. (2015) 31:166–73. doi: 10.5625/lar.2015.31.4.166

29. Gama Sosa MA, De Gasperi R, Perez Garcia GS, Perez GM, Searcy C, Vargas D, et al. Low-level blast exposure disrupts gliovascular and neurovascular connections and induces a chronic vascular pathology in rat brain. *Acta Neuropathol Commun*. (2019) 7:6. doi: 10.1186/s40478-018-0647-5
30. Perez-Garcia G, De Gasperi R, Gama Sosa MA, Perez GM, Otero-Pagan A, Tschiffely A, et al. PTSD-related behavioral rraits in a rat model of blast-induced mTBI are reversed by the mGluR2/3 receptor antagonist BCI-838. *eNeuro*. (2018) 5:ENEURO.0357-17.2018. doi: 10.1523/ENEURO.0357-17.2018
31. Por ED, Sandoval ML, Thomas-Benson C, Burke TA, Doyle Brackley A, Jeske NA, et al. Repeat low-level blast exposure increases transient receptor potential vanilloid 1 (TRPV1) and endothelin-1 (ET-1) expression in the trigeminal ganglion. *PLoS ONE*. (2017) 12:e0182102. doi: 10.1371/journal.pone.0182102
32. Hall AA, Mendoza MI, Zhou H, Shaughness M, Maudlin-Jeronimo E, Mccarron RM, et al. Repeated low intensity blast exposure is associated with damaged endothelial glycocalyx and downstream behavioral deficits. *Front Behav Neurosci*. (2017) 11:104. doi: 10.3389/fnbeh.2017.00104
33. Por ED, Choi JH, Lund BJ. Low-level blast exposure increases transient receptor potential vanilloid 1 (TRPV1) expression in the rat cornea. *Curr Eye Res*. (2016) 41:1294–301. doi: 10.3109/02713683.2015.1122812
34. Haghighi F, Ge Y, Chen S, Xin Y, Umali MU, De Gasperi R, et al. Neuronal DNA methylation profiling of blast-related traumatic brain injury. *J Neurotrauma*. (2015) 32:1200–9. doi: 10.1089/neu.2014.3640
35. Choi JH, Greene WA, Johnson AJ, Chavko M, Cleland JM, Mccarron RM, et al. Pathophysiology of blast-induced ocular trauma in rats after repeated exposure to low-level blast overpressure. *Clin Exp Ophthalmol*. (2015) 43:239–46. doi: 10.1111/ceo.12407
36. Du X, Ewert DL, Cheng W, West MB, Lu J, Li W, et al. Effects of antioxidant treatment on blast-induced brain injury. *PLoS ONE*. (2013) 8:e80138. doi: 10.1371/journal.pone.0080138
37. Elder GA, Dorr NP, De Gasperi R, Gama Sosa MA, Shaughness MC, Maudlin-Jeronimo E, et al. Blast exposure induces post-traumatic stress disorder-related traits in a rat model of mild traumatic brain injury. *J Neurotrauma*. (2012) 29:2564–75. doi: 10.1089/neu.2012.2510
38. Ahlers ST, Vasserman-Stokes E, Shaughness MC, Hall AA, Shear DA, Chavko M, et al. Assessment of the effects of acute and repeated exposure to blast overpressure in rodents: toward a greater understanding of blast and the potential ramifications for injury in humans exposed to blast. *Front Neurol*. (2012) 3:32. doi: 10.3389/fneur.2012.00032
39. Kawa L, Kamnaksh A, Long JB, Arborelius UP, Hokfelt T, Agoston DV, et al. A Comparative study of two blast-induced traumatic brain injury models: changes in monoamine and galanin systems following single and repeated exposure. *Front Neurol*. (2018) 9:479. doi: 10.3389/fneur.2018.00479
40. Badea A, Kamnaksh A, Anderson RJ, Calabrese E, Long JB, Agoston DV. Repeated mild blast exposure in young adult rats results in dynamic and persistent microstructural changes in the brain. *Neuroimage Clin*. (2018) 18:60–73. doi: 10.1016/j.nicl.2018.01.007
41. Arun P, Rittase WB, Wilder DM, Wang Y, Gist ID, Long JB. Defective methionine metabolism in the brain after repeated blast exposures might contribute to increased oxidative stress. *Neurochem Int*. (2018) 112:234–8. doi: 10.1016/j.neuint.2017.07.014
42. Wang Y, Wei Y, Oguntayo S, Wilder D, Tong L, Su Y, et al. Cerebrospinal fluid chemokine (C-C Motif) ligand 2 is an early-response biomarker for blast-overpressure-wave-induced neurotrauma in rats. *J Neurotrauma*. (2017) 34:952–62. doi: 10.1089/neu.2016.4465
43. Gu M, Kawoos U, Mccarron R, Chavko M. Protection against blast-induced traumatic brain injury by increase in brain volume. *Biomed Res Int*. (2017) 2017:2075463. doi: 10.1155/2017/2075463
44. Kawoos U, Mccarron RM, Chavko M. Protective effect of N-acetylcysteine amide on blast-induced increase in intracranial pressure in rats. *Front Neurol*. (2017) 8:219. doi: 10.3389/fneur.2017.00219
45. Calabrese E, Du F, Garman RH, Johnson GA, Riccio C, Tong LC, et al. Diffusion tensor imaging reveals white matter injury in a rat model of repetitive blast-induced traumatic brain injury. *J Neurotrauma*. (2014) 31:938–50. doi: 10.1089/neu.2013.3144
46. Kamnaksh A, Budde MD, Kovesdi E, Long JB, Frank JA, Agoston DV. Diffusion tensor imaging reveals acute subcortical changes after mild blast-induced traumatic brain injury. *Sci Rep*. (2014) 4:4809. doi: 10.1038/srep04809
47. Genovese RF, Simmons LP, Ahlers ST, Maudlin-Jeronimo E, Dave JR, Boutte AM. Effects of mild TBI from repeated blast overpressure on the expression and extinction of conditioned fear in rats. *Neuroscience*. (2013) 254:120–9. doi: 10.1016/j.neuroscience.2013.09.021
48. Ahmed FA, Kamnaksh A, Kovesdi E, Long JB, Agoston DV. Long-term consequences of single and multiple mild blast exposure on select physiological parameters and blood-based biomarkers. *Electrophoresis*. (2013) 34:2229–33. doi: 10.1002/elps.201300077
49. Kamnaksh A, Kwon SK, Kovesdi E, Ahmed F, Barry ES, Grunberg NE, et al. Neurobehavioral, cellular, and molecular consequences of single and multiple mild blast exposure. *Electrophoresis*. (2012) 33:3680–92. doi: 10.1002/elps.201200319
50. Elsayed NM, Gorbunov NV. Pulmonary biochemical and histological alterations after repeated low-level blast overpressure exposures. *Toxicol Sci*. (2007) 95:289–96. doi: 10.1093/toxsci/kfl138
51. Readnower RD, Chavko M, Adeeb S, Conroy MD, Pauly JR, Mccarron RM, et al. Increase in blood–brain barrier permeability, oxidative stress, and activated microglia in a rat model of blast-induced traumatic brain injury. *J Neurosci Res*. (2010) 88:3530–9. doi: 10.1002/jnr.22510
52. Elder GA, Gama Sosa MA, De Gasperi R, Stone JR, Dickstein DL, Haghighi F, et al. Vascular and inflammatory factors in the pathophysiology of blast-induced brain injury. *Front Neurol*. (2015) 6:48. doi: 10.3389/fneur.2015.00048
53. Wang Y, Arun P, Wei Y, Oguntayo S, Gharavi R, Valiyaveettil M, et al. Repeated blast exposures cause brain DNA fragmentation in mice. *J Neurotrauma*. (2014) 31:498–504. doi: 10.1089/neu.2013.3074
54. Valiyaveettil M, Alamneh YA, Wang Y, Arun P, Oguntayo S, Wei Y, et al. Cytoskeletal protein alpha-II spectrin degradation in the brain of repeated blast exposed mice. *Brain Res*. (2014) 1549:32–41. doi: 10.1016/j.brainres.2013.12.031
55. Valiyaveettil M, Alamneh YA, Miller SA, Hammamieh R, Arun P, Wang Y, et al. Modulation of cholinergic pathways and inflammatory mediators in blast-induced traumatic brain injury. *Chem Biol Interact*. (2013) 203:371–5. doi: 10.1016/j.cbi.2012.10.022
56. Arun P, Abu-Taleb R, Oguntayo S, Wang Y, Valiyaveettil M, Long JB, et al. Acute mitochondrial dysfunction after blast exposure: potential role of mitochondrial glutamate oxaloacetate transaminase. *J Neurotrauma*. (2013) 30:1645–51. doi: 10.1089/neu.2012.2834
57. Valiyaveettil M, Alamneh Y, Wang Y, Arun P, Oguntayo S, Wei Y, et al. Contribution of systemic factors in the pathophysiology of repeated blast-induced neurotrauma. *Neurosci Lett*. (2013) 539:1–6. doi: 10.1016/j.neulet.2013.01.028
58. Arun P, Abu-Taleb R, Oguntayo S, Tanaka M, Wang Y, Valiyaveettil M, et al. Distinct patterns of expression of traumatic brain injury biomarkers after blast exposure: role of compromised cell membrane integrity. *Neurosci Lett*. (2013) 552:87–91. doi: 10.1016/j.neulet.2013.07.047
59. Arun P, Oguntayo S, Alamneh Y, Honnold C, Wang Y, Valiyaveettil M, et al. Rapid release of tissue enzymes into blood after blast exposure: potential use as biological dosimeters. *PLoS ONE*. (2012) 7:e33798. doi: 10.1371/journal.pone.0033798
60. Valiyaveettil M, Alamneh Y, Miller SA, Hammamieh R, Wang Y, Arun P, et al. Preliminary studies on differential expression of auditory functional genes in the brain after repeated blast exposures. *J Rehabil Res Dev*. (2012) 49:1153–62. doi: 10.1682/JRRD.2011.09.0182
61. Peethambaran A, Valiyaveettil M, Biggemann L, Alamneh Y, Wei Y, Oguntayo S, et al. Modulation of hearing related proteins in the brain and inner ear following repeated blast exposures. *Interv Med Appl Sci*. (2012) 4:125–31. doi: 10.1556/IMAS.4.2012.3.2
62. Valiyaveettil M, Alamneh Y, Oguntayo S, Wei Y, Wang Y, Arun P, et al. Regional specific alterations in brain acetylcholinesterase activity after repeated blast exposures in mice. *Neurosci Lett*. (2012) 506:141–5. doi: 10.1016/j.neulet.2011.10.067

63. Wang Y, Wei Y, Oguntayo S, Wilkins W, Arun P, Valiyaveettil M, et al. Tightly coupled repetitive blast-induced traumatic brain injury: development and characterization in mice. *J Neurotrauma*. (2011) 28:2171–83. doi: 10.1089/neu.2011.1990
64. Lew HL, Gray M, Poole JH. Temporal stability of auditory event-related potentials in healthy individuals and patients with traumatic brain injury. *J Clin Neurophysiol*. (2007) 24:392–7. doi: 10.1097/WNP.0b013e31814a56e3
65. Lew HL, Jerger JF, Guillory SB, Henry JA. Auditory dysfunction in traumatic brain injury. *J Rehabil Res Dev*. (2007) 44:921–8. doi: 10.1682/JRRD.2007.09.0140
66. Idrizbegovic E, Bogdanovic N, Canlon B. Modulating calbindin and parvalbumin immunoreactivity in the cochlear nucleus by moderate noise exposure in mice. A quantitative study on the dorsal and posteroventral cochlear nucleus *Brain Res*. (1998) 800:86–96. doi: 10.1016/S0006-8993(98)00504-6
67. Alvarado JC, Fuentes-Santamaria V, Henkel CK. Rapid modifications in calretinin immunostaining in the deep layers of the superiorcolliculus after unilateral cochlear ablation. *Hear Res*. (2009) 247:78–86. doi: 10.1016/j.heares.2008.10.005
68. Scremin OU, Li MG, Roch M, Booth R, Jenden DJ. Acetylcholine and choline dynamics provide early and late markers of traumatic brain injury. *Brain Res*. (2006) 1124:155–66. doi: 10.1016/j.brainres.2006.09.062

Conflict of Interest: The authors declare that the research was conducted in the absence of any commercial or financial relationships that could be construed as a potential conflict of interest.

Copyright © 2019 Skotak, Townsend, Ramarao and Chandra. This is an open-access article distributed under the terms of the Creative Commons Attribution License (CC BY). The use, distribution or reproduction in other forums is permitted, provided the original author(s) and the copyright owner(s) are credited and that the original publication in this journal is cited, in accordance with accepted academic practice. No use, distribution or reproduction is permitted which does not comply with these terms.

Appendix A –Publication Cover 12
2019

Authors: B. Swietek, M. Skotak, N. Chandra, B. Pfister

Title: "*Characterization of a controlled shock wave delivered by a pneumatic table-top gas driven shock tube*"

Journal Publication: Review of Scientific Instruments, 90 (7), 075116 (2019), [19-12]

Review of Scientific Instruments

Characterization of a controlled shock wave delivered by a pneumatic table-top gas driven shock tube

Cite as: Rev. Sci. Instrum. **90**, 075116 (2019); https://doi.org/10.1063/1.5099633
Submitted: 11 April 2019 . Accepted: 25 June 2019 . Published Online: 25 July 2019

Bogumila Swietek, Maciej Skotak, Namas Chandra, and Bryan J. Pfister

View Online Export Citation CrossMark

ARTICLES YOU MAY BE INTERESTED IN

A high-precision eight-AFM probe rotary exchange module
Review of Scientific Instruments **90**, 076110 (2019); https://doi.org/10.1063/1.5094063

A torsional thrust balance with asymmetrical configuration for microthruster performance evaluation
Review of Scientific Instruments **90**, 076111 (2019); https://doi.org/10.1063/1.5063852

Analytical electrolyzer enabling operando characterization of flow plates
Review of Scientific Instruments **90**, 074103 (2019); https://doi.org/10.1063/1.5053600



© 2019 Author(s).

Review of Scientific Instruments ARTICLE scitation.org/journal/rsi

Characterization of a controlled shock wave delivered by a pneumatic table-top gas driven shock tube

Cite as: Rev. Sci. Instrum. 90, 075116 (2019); doi: 10.1063/1.5099633
Submitted: 11 April 2019 • Accepted: 25 June 2019 •
Published Online: 25 July 2019

View Online Export Citation CrossMark

Bogumila Swietek,[1,2] Maciej Skotak,[1] Namas Chandra,[1] and Bryan J. Pfister[1,a)]

AFFILIATIONS

[1] Department of Biomedical Engineering, New Jersey Institute of Technology, University Heights, Fenster Hall, Newark, New Jersey 07103, USA

[2] Department of Pharmacology, Physiology and Neuroscience, Rutgers, The State University of New Jersey, Newark, New Jersey 07103, USA

[a)] **Author to whom correspondence should be addressed:** pfister@njit.edu. **Telephone:** 973-596-3401. **Fax:** +1 973-596-5222

ABSTRACT

Blast simulators facilitate the creation of shock waves and measurement of pressure morphology in a controlled laboratory setting and are currently a vital model for replicating blast-induced neurotrauma. Due to the maintenance and operation cost of conventional blast simulators, we developed a pneumatic, table-top, gas-driven shock tube to test an alternative method of shock wave generation using a membraneless driver section. Its unique operational mechanism based on air gun technology does not rely on a plastic membrane rupture for the generation of pressure pulses, allowing the simulator to be quickly reset and thus decreasing the experimental turnaround time. The focus of this study is to demonstrate that this proof-of-concept device can generate shock waves with diverse characteristics based on the selection of driver gas, driver pressurization, and driven section material. Pressure waves were generated using compressed nitrogen or helium at 15 psig and 80 psig and were analyzed based on their velocity and profile shape characteristics. At 15 psig, independent of the type of driver gas, driver pressurization, and driven section material, pressure pulses travelled at sonic velocities. At 80 psig, generation of shock waves was observed in all conditions. The choice of the driver gas affected the velocities of the resulting pressure waves and the shape of pressure waveforms, particularly the peak overpressure and rise time values. Our results demonstrate that depending on the selection of driver gas and magnitude of driver pressurization, the shock wave signatures can be controlled and altered using a piston-based driver section.

Published under license by AIP Publishing. https://doi.org/10.1063/1.5099633

I. INTRODUCTION

Laboratory replication of high-yield or large-scale explosions has been possible through the use of shock tubes that can closely mimic pressure profiles generated in free-field blasts using chemical explosives.[1] Away from the center of the explosion, the blast wave in a free-field environment has been mathematically described and modeled as the Friedlander waveform (Fig. 1).[2–4] The shock front of a blast wave is created by the expanding gaseous chemical products that compress the preceding air particles, leading to an instantaneous rise in pressure (the overpressure). The high-pressure region continues to expand, generating a shock wave that propagates at supersonic velocities (>343 m/s). The shock front is followed by violent movement of the gas particles along the direction of the shock wave propagation, the blast wind. As the shock wave propagates away from the source of explosion, an overexpansion can occur with sudden movement of the air toward the epicenter, causing the pressure to drop below atmospheric pressure (the underpressure or negative phase; Fig. 1).

While the net movement of particles is zero in an acoustic wave, the shock wave is characterized by an air particle velocity greater than zero. The strength of the shock scales with the particle velocity. Energy in the shock wave attenuates as it travels further from the epicenter, the peak overpressure reduces, and eventually the shock wave velocity is reduced to the acoustic velocity, and particle motion vanishes. Thus, shock waves are characterized by a wave velocity

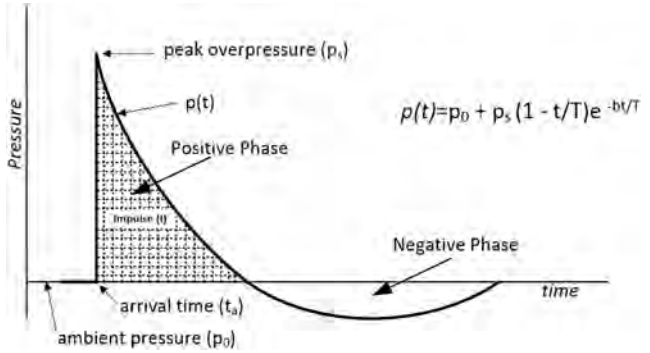


FIG. 1. The idealized pressure-time curve waveform is a mathematical representation of a shock wave as it propagates away from the epicenter of a free-field explosion. The Friedlander equation is used to describe the overpressure at specific location as a function of time, $p(t)$, where p_0 is ambient pressure, p_s is the peak overpressure, T is the duration of the positive phase and b is a decay rate constant that is dependent on the overpressure decrease after reaching its maximum value, p_s.

greater than the acoustic velocity of the medium at specific environmental conditions (e.g., pressure, temperature, and humidity) and by the particle velocities greater than zero. Since particle velocity determines the dynamic portion of the total pressure, this can also be construed as the condition at which total pressure equals static (side-on) pressure. Once established as shock waves, they typically are described by the positive pressure phase characteristics including rise time, peak overpressure (pressure above atmosphere), positive phase duration, and positive impulse. These parameters and wave velocities have been examined to describe the formation of the shock wave using the Friedlander equation and have allowed for the prediction and verification of experimental data by theoretical methods for different loading conditions.[2–4]

The study of free-field explosions has resulted in the development of blast scaling laws which have been used in the assessment of structural damage based on varying the parameters of blast loading. These laws, however, have considered only limited set of blast conditions and structural properties due to the high cost and complexity of such experiments. The development of laboratory shock wave generators has allowed for the replication of large-scale blasts in a controlled laboratory setting with relative ease. Shock tubes have been widely used to study the various aspects of shock wave physics and material response.[1,5–7]

The typical shock tube is a two-chamber system composed of a high (driver) and low (driven) pressure section separated by a membrane (e.g., Mylar, aluminum) that ruptures when driver gas pressure exceeds the threshold of mechanical stability of the membrane.[8–11] Upon rupture of the membrane, the compressed driver gas enters the driven section, which results in a rapid compression of the ambient air. The shock magnitude and impulse are dictated by the membrane thickness (burst pressure), the rate of energy release, driver gas (helium or nitrogen), driver volume, and ambient conditions (e.g., temperature, ambient gas type, pressure, and humidity).

Utilization of these simple principles of operation led to the widespread adaptation of shock tubes in various research areas over the past six decades.[12–16] A search using "shock tube" keyword performed within the *Review of Scientific Instruments* journal domain covering years 1930–2018 returned 750 results in the "Equipment and apparatus" topic (January 2019). In the recent years, shock tubes have played a pivotal role in the reinvigorated field of characterization of blast-induced neurotrauma (BINT) mechanisms, and some of the most advanced blast simulators generate pressure-time curves similar to those seen in the free-field environment.[1,7,11,17,18] However, the need to use membranes can be considered a serious drawback: (1) depending on the scale of the device, the operational costs can be substantial; (2) the ejecta of membrane fragmentation products can impact the specimen and adversely affect the experimental outcome; and (3) the variability of the membrane properties result in the variation in shock wave intensity. These disadvantages were recognized for some time, but technical challenges in the membrane-free (or membrane-less) driver section design limit their application and widespread use in the laboratory research.[19–23] Undoubtedly, there are definite advantages in using a classical gas-driven shock tube with membrane separation; however, there is still a niche for the design of an inexpensive, easy-to-operate, table-top model that can produce shock waves with highly reproducible characteristics.

We implemented these design considerations during the development of a table-top, pressure-driven shock tube, with a triggering mechanism based on air gun technology. The proof-of-concept device presented herein does not require laborious membrane replacement between tests and thus would allow experiments with relatively short interexposure time intervals such that 2 blasts can be performed within a minute. Moreover, the pressurization level of the driver section can be arbitrarily changed and adjusted with precision limited only by the pressurization system and speed of the mechanical release system. The main goal of this work is to demonstrate that this shock tube design can generate shock waves with well-defined characteristics based on manipulation of two key components, the driver pressurization and the type of driver gas.

II. MATERIALS AND METHODS

A. The shock tube

A table-top, compressed gas-driven shock tube was designed and constructed (Fig. 2) to test if our membrane-less driven section design could produce controllable shock wave characteristics. The shock tube consists of two sections made of cost-effective and readily available materials: a 13-in.-long driver section with a 3-in.-diameter opening that outlets into a 72-in.-long tube (driven section) of either 3 in. outer diameter (OD) made of polyvinyl chloride (PVC) or 2.5 in. OD made of steel. The driver section is a pneumatic actuated piston valve consisting of two chambers: the reservoir and trigger. Nestled between 4 steel rods that protrude throughout the reservoir chamber, a dumbbell-shaped stainless steel piston with round disks on opposite ends (see inset in Fig. 2) creates a seal between the driver and trigger chambers and uses similar operating principles to a spool valve. The smaller disk on the $Rotor_2$ (OD: 3 in.), together with the larger disk on the $Rotor_3$ (OD: 4.5 in.), interlocks and creates the seal on the back of the driver section. The $Rotor_1$ has a larger OD than the smaller disk on the $Rotor_2$ (3.75 in. vs 3 in., respectively)

Published under license by AIP Publishing

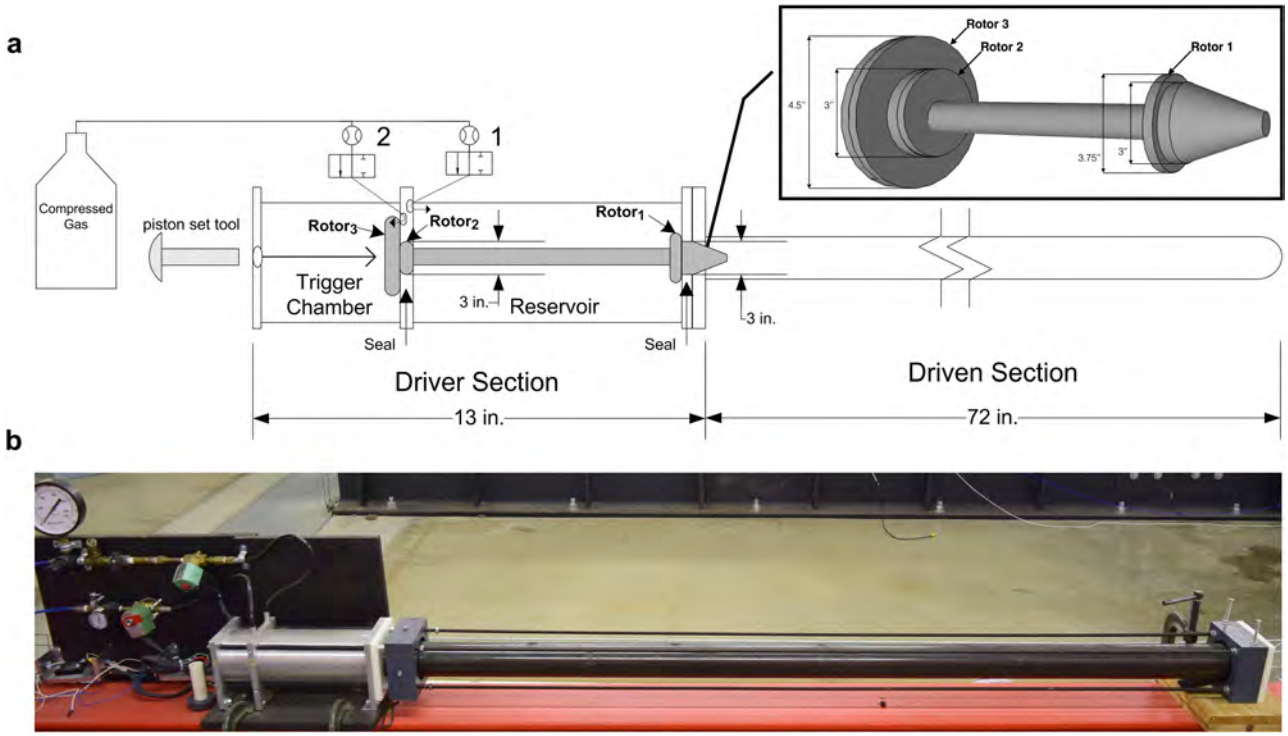


FIG. 2. (a) Schematic representation of the shock tube assembly. A piston set tool drives the piston, pictured in the inset of (a), forward, where it interlocks and creates a seal between the reservoir and trigger chamber. The piston disengages and retracts when compressed gas is introduced into the trigger chamber, causing an imbalance due to the differences in solid, centric, flat-faced gaskets [OD ($Rotor_3$) > OD ($Rotor_1$)]. (b) Photo of the shock tube device.

and hence larger area. When the reservoir is pressurized, the larger diameter of $Rotor_1$ creates the imbalance in force, which results in a self-sealing the chamber as it is filled with the driver gas. Pressurization of the trigger chamber acts on the larger disk of $Rotor_3$ causing the piston to destabilize and rapidly move toward the back, resulting in driver gas being rapidly released into the driven section that is open at the end.

The driver chamber is filled from a gas cylinder equipped with two-stage pressure regulators. The cylinder regulator is set at 200 psig and fed to a secondary regulator (range of 1–100 psig) for fine pressure control. The trigger chamber is fed through a separate secondary regulator and is set to a higher pressure (Fig. 2). The gas flow to the reservoir and trigger chambers is controlled by two solenoid valves. The solenoid valves are normally closed and only open when a trigger signal is sent from the PC. The driver gas of choice is the first inlet into the reservoir via solenoid valve 1, and upon reaching the specified pressure set by regulator 1, the compressed gas set forth by regulator 2 is then introduced into the trigger chamber via solenoid valve 2. A sudden rush of gas to a concentrated area on the back-end gasket creates a force imbalance, and the interlocked aluminum piston is rapidly disengaged from the reservoir. The valves close and the piston is loaded back into the firing position by a piston set tool that drives the piston forward to interlock position and restore the seal between the reservoir and trigger chamber. The whole process takes less than 30 s if the desired pressure levels are preset beforehand and remain unchanged during the experiment.

B. Data acquisition and analysis

The acquisition of pressure traces was realized using 5 PCB sensors model 134A24 (PCB Piezotronics, Depew, NY) that was flush mounted along the inside wall of the driven section spaced 12 in. apart. The signal was transmitted to a signal conditioner 483C (PCB Piezotronics, Depew, NY) for amplification and then routed to a desktop PC via National Instruments PXI-6133 S Series 6 111 multifunction DAQ modules and PXIe-1082 PCI Express (Austin, TX). Data were acquired by a custom LabView program (National Instruments, Austin, TX) at 250 kHz. All signal analyses were performed using NI Diadem version 2015 (National Instruments, Austin, TX). GraphPad Prism version 7 (La Jolla, California, USA) was used for statistical analysis. The data were graphed using Origin version 9.4 (OriginLab, Northampton, MA) or GraphPad Prism version 7.

C. Experimental design

The goal of this study is to demonstrate that this shock tube with membrane-less driver design can produce controlled and consistent shock waves with pressure-time histories of similar signatures as those of conventional Mylar membrane-driven shock tubes.

Published under license by AIP Publishing

While the membrane thickness is reported as the key experimental parameter in producing shock fronts of desired intensities, the type of driver gas, burst pressure, shock tube geometry (driver-to-driven cross-section ratio) have also influenced the pressure pulse profile.[24] To establish the threshold and location for shock wave generation, the driver gas and reservoir pressure were varied and corresponding pressure traces were recorded at five locations along the driven section.

The time domain data were plotted, and the following shock wave characteristics were quantified: peak overpressure, positive phase duration, positive phase impulse, rise time, and shock wave velocity. Peak overpressure was defined as the first highest peak of the waveform after the arrival time (t_o). Positive phase duration was calculated by the time difference between the initial rise in pressure above ambient air to the point where the pressure decays below atmospheric pressure. Positive phase impulse, I, was calculated for the positive phase duration by integrating overpressure profile in the time domain. Rise time was determined by the time difference for a pressure trace to rise from 10% to 90% of its peak overpressure (Fig. 3). Shock wave velocity was calculated using arrival time (t) for the shock wave traveling in the driven section, and the distance, d, between the two adjacent sensors typically were considered, i.e., s1 and s2, s2 and s3, and so on (Fig. 3).

D. Statistical analysis

Six experimental trials, n = 6, were performed for each experimental setup. All data are presented as mean ± standard deviation. Measurements were analyzed for normality using the Kruskal-Wallis normality test, followed by a two-tailed t-test with a post-hoc Tukey test to make comparisons between and within experimental groups, and $p < 0.05$ was considered as a threshold for statistical significance.

III. RESULTS

The formation of pressure-time histories with a similar characteristic profile as that of the Friedlander waveform was observed for both helium- and nitrogen-generated pressure pulses at 5 feet away from the driver (pressure sensor location s5) in both PVC and steel driven sections but was pressure dependent (Fig. 4). In the PVC driven section, pressurization of 80 psig [Figs. 4(a) and 4(b)] as opposed to 15 psig [Figs. 4(c) and 4(d)] resulted in Friedlander waveforms at the s5 location. Similarly, in the steel driven section, pressurization of 80 psig [Figs. 4(e) and 4(f)] in contrast to 15 psig [Figs. 4(g) and 4(h)] produced pressure waveforms that were observed to resemble the ideal Friedlander waveforms.

Peak overpressure magnitude was preceded by a low magnitude pressure waveform observed at s1–s5 locations but disappeared at the s5 pressure sensor location only with 80 psig helium pressurization. The presence of this wavelet was suspected to be caused by unequal opening of the valve and biphasic release of the driver gas [Figs. 4(a)–4(f)] and was more prominent in the PVC tube. Furthermore, waveforms produced with the PVC driven section were noisy primarily due to the vibration of the PVC plastic, whereas the use of the steel driven section that possesses higher structural stiffness eliminated these vibrational effects. Despite stark pressure profile differences between driven section material and pressurization, velocity was calculated to further investigate if the produced waveforms could be considered shock waves (Fig. 5).

In the PVC tube, unlike nitrogen, helium-generated shock waves exceeded the velocity of sound (343.6 m/s in the air at atmospheric pressure and the temperature of 21 °C) throughout the driven section as measured by sensors s1–s5 in both PVC and steel driven sections [Fig. 5(a)]. At the s5 location, helium-generated shock waves had higher velocities upon higher pressurization, while

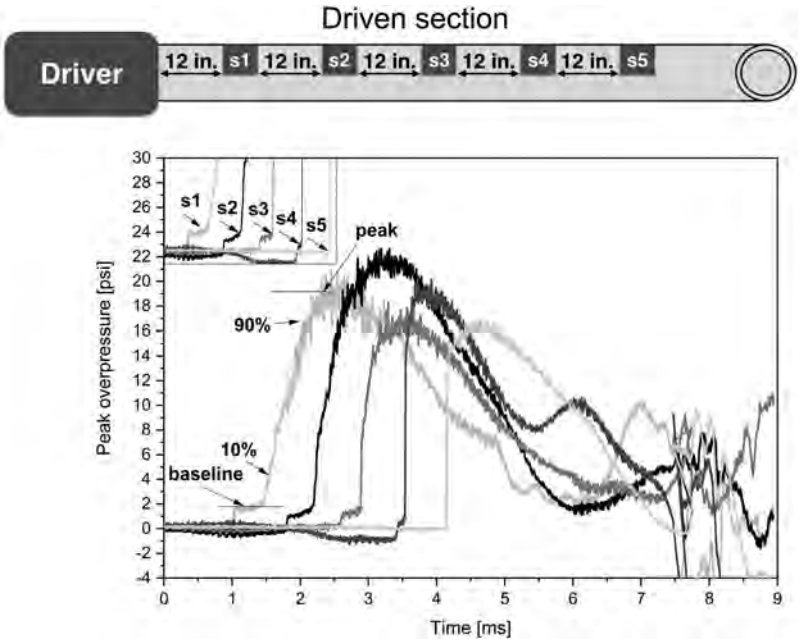


FIG. 3. Calculation of the rise time and velocity of pressure waveforms generated by the driver gases.

Published under license by AIP Publishing

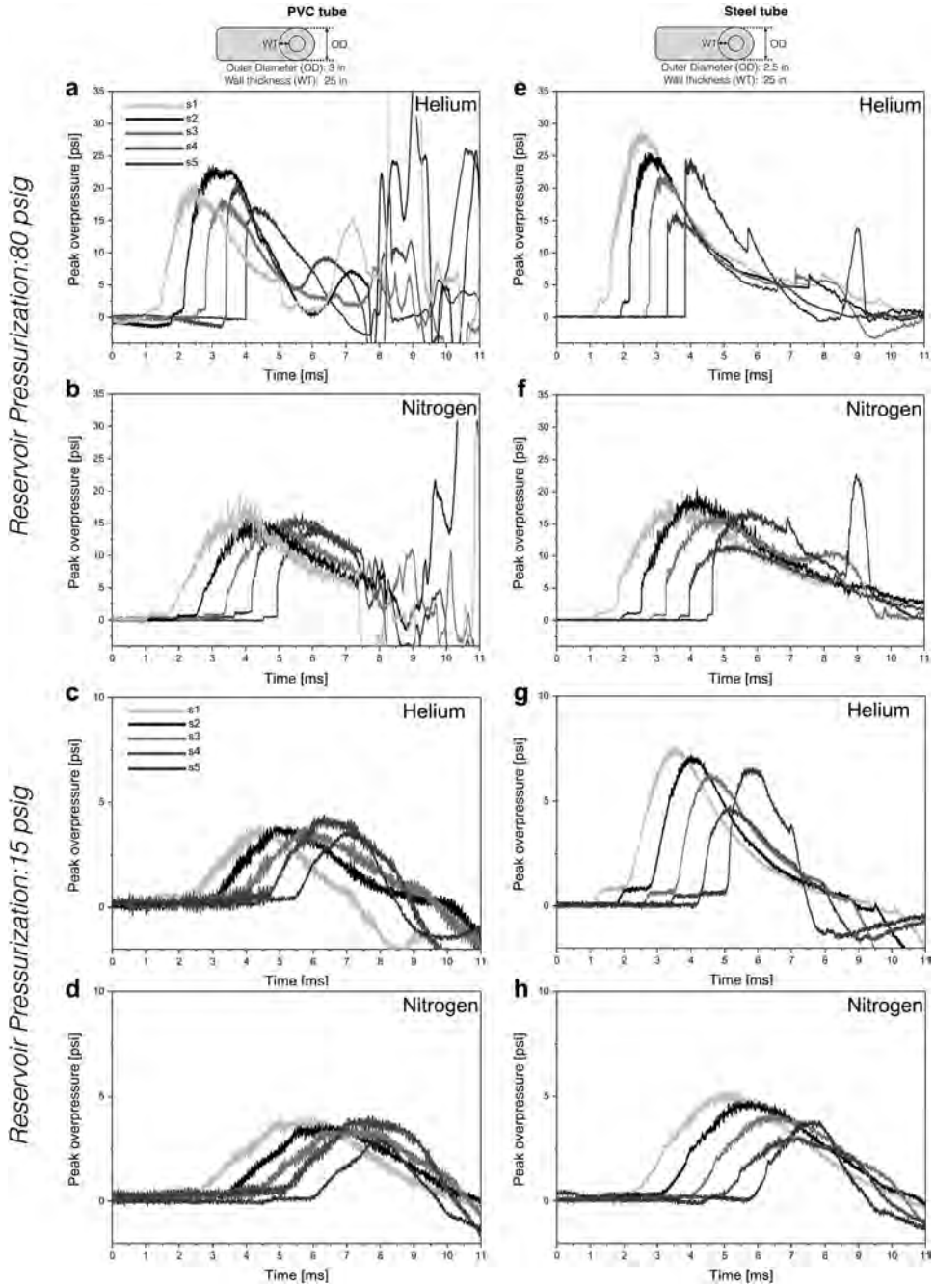


FIG. 4. Representative pressure waveforms generated by helium and nitrogen at 5 locations along the length of the shock tube. Helium- and nitrogen-generated pressure waveforms at 80 psig and 15 psig in the PVC [(a)–(d)] and steel [(e)–(h)] driven sections. In the inset of (a), the sequential number following the pressure gauge *s* indicates the sensor location in the shock tube, with 1, 2, 3, 4, and 5 feet, respectively, being the distance from the driver.

nitrogen pressure waveforms did not have statistically significant differences in their velocities [Fig. 5(b)]. In the steel tube, both gases produced pressure waveforms that exceed the criterion for the classification of a shock wave [Fig. 5(c)]. At the s5 location, statistically significant differences were observed between velocities of shock waves between pressurization of 15 psig and 80 psig with nitrogen and helium [Fig. 5(d)]. Overall, at the s5 location, helium pressurization of 15 and 80 psig was significantly different in both PVC and steel driven sections, while nitrogen pressurization of 15 psig and 80 psig in either driven section materials was not statistically significant. This indicated that nitrogen produced waveforms that traveled at velocities at similar speeds despite an increase in pressurization from 15 to 80 psig [Figs. 5(b) and 5(d)]. The characteristic pressure profile parameters for 15 psig and 80 psig and driver gas (helium or nitrogen) were analyzed, and the results are presented in Fig. 6.

Published under license by AIP Publishing

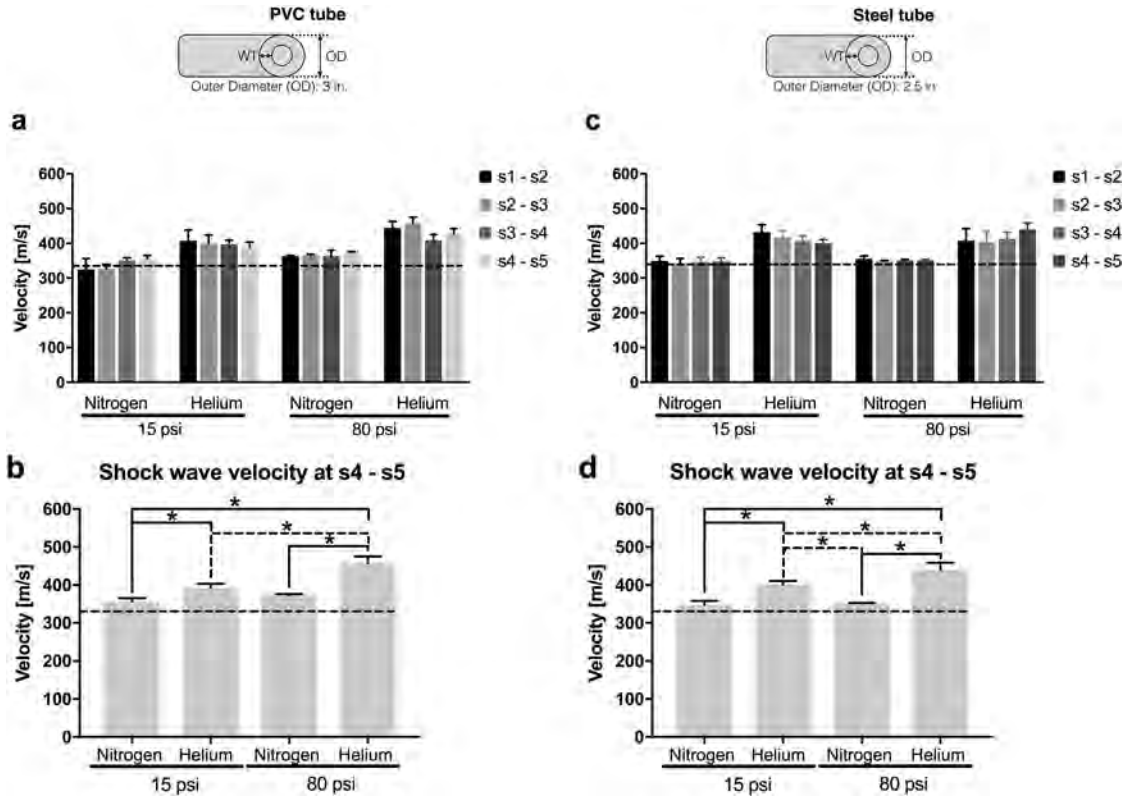


FIG. 5. Velocity quantification for pressure traces using low (15 psig) and high (80 psig) pressurization at various locations [(a) and (c)] and the s5 location [(b) and (d)] in the shock tube. The horizontal dash line indicates the velocity of sound (343.6 m/s). Groups where the statistical significant differences ($p < 0.05$) were detected are marked with an asterisk.

In general, higher driver pressure resulted in the pressure waves with higher intensities [Figs. 6(a) and 6(e)]. The rise time values reached the value of nearly 1000 μs for most combinations of driver gas (helium or nitrogen), driver pressure (15 or 80 psig), and the type of driven section (PVC or steel). Only when helium at 80 psig was used as a driver gas, the rise time values were below 100 μs and 10 μs for PVC and steel tubes, respectively [Figs. 6(b) and 6(f)]. The duration of the pressure waves was less than 4 ms for the PVC tube and steel tube when the driver gas pressure was 15 psig. At higher level of driver pressurization, 80 psig, the duration was 6.2 ms and 4.0 ms for nitrogen and helium, respectively [Figs. 6(c) and 6(g)]. The impulse values were in the 40–50 kPa·ms range for the low pressurization (15 psig) independent of the driver gas and the type of expansion tube used [Figs. 6(d) and 6(h)]. On the other hand, there seemed to be a strong dependence of the impulse on the geometry of the expansion tube at higher pressurization (80 psig): the steel expansion tube, which had a smaller diameter compared with the PVC (2.5 in. vs 3 in.), resulted in impulse values of 300 and 400 kPa·ms [for nitrogen and helium, respectively; Fig. 6(h)]. Experiments performed in analogous conditions using PVC expansion tube resulted in impulse values of approx. 200 kPa·ms [Fig. 6(d)].

IV. DISCUSSION

The selection of driver gas and input pressure played a critical role in obtaining pressure traces similar to the Friedlander waveform.[3] Helium used as a driver gas at "burst" pressure of 80 psig resulted in the generation of pressure trace with shock wave characteristics at the sensor location s5 (5 ft away from the driver) and had a similar magnitude and duration as those seen in the literature.[5,8–11] The differences in the rise time for the evolving waveform as it traveled down the PVC tube are illustrated in Figs. 4(c) and 4(d) (low driver pressure, 15 psig) and Figs. 4(a) and 4(b) (high driver pressure, 80 psig). Only the waveforms produced by helium at sensor locations s4 and s5 [Fig. 4(e)] are characterized by "almost instantaneous" (5–6 μs) rise time to peak overpressure.

The speed of sound is inversely proportional to the molecular weight of the carrying gas. A gas with a lower molecular weight is easier to accelerate and hence will be a more efficient "compressing agent" to produce shock waves with greater intensity and velocity.[4] Accordingly, helium-generated shock waves were overall more well defined with sharp rise to peak overpressure and had a smoother decay to partial vacuum conditions as opposed to nitrogen pressure trace profiles. Independent of the selection of the driver gas, we

Published under license by AIP Publishing

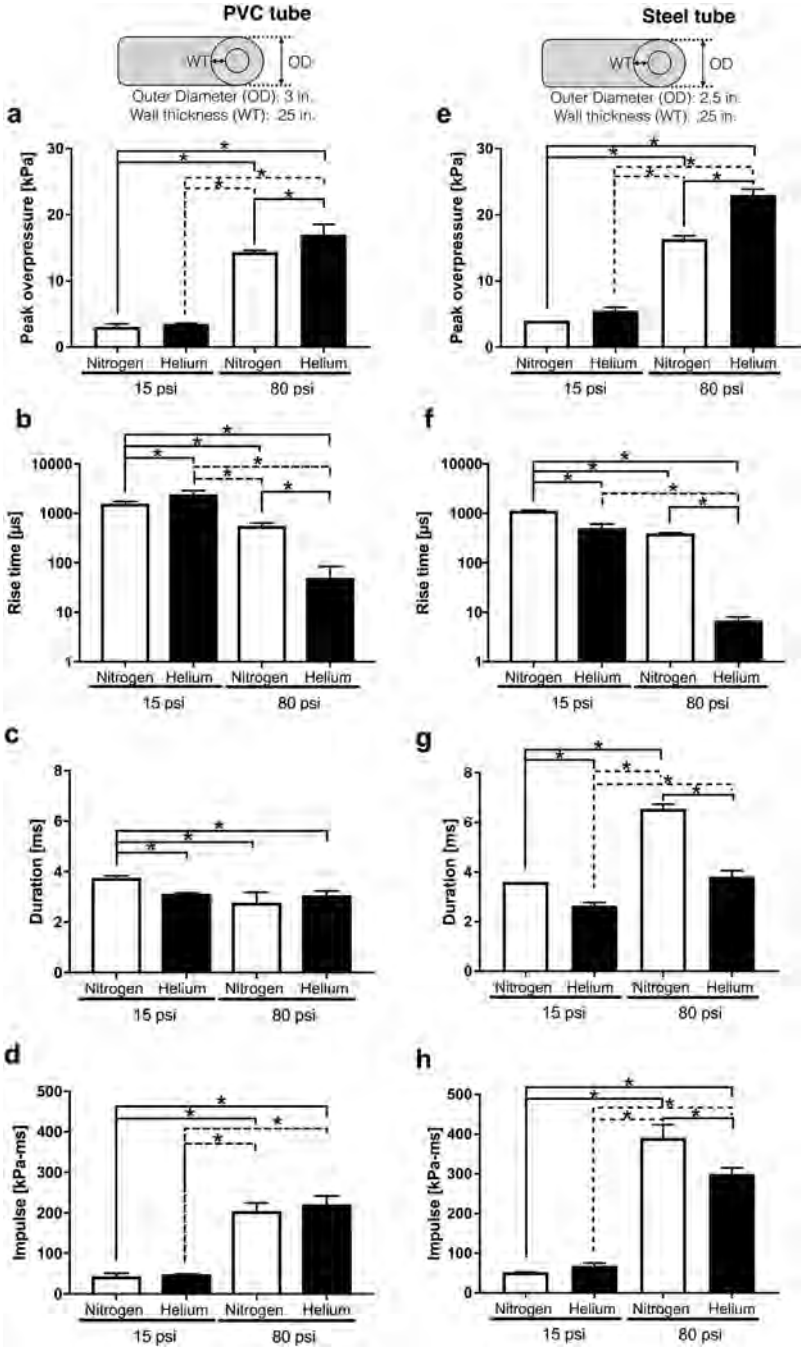


FIG. 6. The peak overpressure, rise time, positive phase duration, and positive phase impulse of helium- and nitrogen-generated pressure recordings at low (15 psig) and high (80 psig) pressurization at 5 feet away from the driver (s5) inside the PVC [(a)–(d)] and steel [(e)–(h)] driven sections. Significance threshold is set to * $p < 0.05$.

measured additional high frequency noise following the main waveform, which is likely caused by the vibration of the PVC driven section of the shock tube. This is consistent with structural vibrations typically observed in shock tubes[25] and plastic specimen exposed to shock waves.[26] These issues were successfully resolved by the utilization of the steel driven section and proper securement of the sensor plates to prevent their motion.[25]

Decreasing the driver pressure to 15 psig resulted in the generation of pressure waveforms that were starkly different in the formation and shock wave characteristics from waveforms produced at the higher burst pressure. The most striking differences were observed in the positive phase duration and rise time, suggesting that the increased driver pressure causes a sharper increase (shorter rise time) without alteration of the peak overpressure. These results

Published under license by AIP Publishing

demonstrate that manipulation of burst pressure and gas selection alters the overpressure profile and the pressure waveform characteristics and can be used to study the effects associated with the loading rates. Consequently, unlike blast scaling of free-field explosion that entails standoff distance and explosive charge as parameters in predicting self-similar blast waves traces, scaling of confined blasts involves many variables, making modeling of these confined blasts difficult.[1,14]

V. CONCLUSIONS

This proof-of-concept, table-top shock tube has a simplified design to generate shock waves in a membrane-less configuration. The advantages of using this kind of shock tube are the following: (1) compact size, which facilitates its application in confined space, even in laboratories with limited bench space; (2) easy to set and repeatable driver pressure settings; (3) simplified operation and maintenance, there is no need for membrane replacement or debris from membrane rupture; and (4) the ability to fine tune the driver pressure (and volume) to generate shock waves with precisely controlled characteristics. Considering the compact size, the production of wide range of pressure waveforms with variable loading rates and intensities, and the shock wave reproducibility, it can be used for a variety of applications including blast research for civil engineering structures and biological modeling of blast traumatic brain injury.

ACKNOWLEDGMENTS

This study was supported by the New Jersey Commission of Brain Injury Research (Grant No. BIR11PJT003). This study would have not been possible if not due to Dr. William Spillers and Dr. Robert D. Stoll, Department of Civil Engineering and Engineering Mechanics, Columbia University, NY. The authors would like to express great appreciation to Dr. Patrick L. Walter at Department of Engineering, Texas Christian University, Fort Worth, Texas, for sharing his extensive knowledge on shock tube design and pressure sensor measurements, and to Eren Alan for his technical help. We acknowledge also the help received from Karlin Yeh, who contributed to LabView program development.

The authors declare that they have no conflict of interest.

REFERENCES

[1] N. Chandra, S. Ganpule, N. Kleinschmit, R. Feng, A. Holmberg, A. Sundaramurthy, V. Selvan, and A. Alai, Shock Waves **22**, 403–415 (2012).
[2] W. E. Baker, *Explosions in Air* (University of Texas Press, 1973).
[3] G. F. Kinney and K. J. Graham Berlin, *Explosions in Air* (Springer-Verlag, New York, 1985), Vol. 282, p. 1.
[4] J. N. Bradley, *Shock Waves in Chemistry and Physics* (Methuen, London, 1962).
[5] T. Ngo, P. Mendis, A. Gupta, and J. Ramsay, Electron. J. Struct. Eng. **7**, 76–91 (2007).
[6] Z. Jiang, O. Onodera, and K. Takayama, Shock Waves **9**, 1–10 (1999).
[7] N. N. Kleinschmit, "A shock tube technique for blast wave simulation and studies of flow structure interactions in shock tube blast experiments," Engineering Mechanics Dissertations & Thesis (University of Nebraska-Lincoln, 2011), Vol. 22, see http://digitalcommons.unl.edu/engmechdiss/22.
[8] A. Boyer, DTIC Document, 1965.
[9] R. S. Birch, S. N. Gerges, and E. F. Vergara, Appl. Acoust. **64**, 269–286 (2003).
[10] R. Tranter, K. Brezinsky, and D. Fulle, Rev. Sci. Instrum. **72**, 3046–3054 (2001).
[11] A. Sundaramurthy, A. Alai, S. Ganpule, A. Holmberg, E. Plougonven, and N. Chandra, J. Neurotrauma **29**, 2352–2364 (2012).
[12] M. Dryer, D. L. Merritt, and P. M. Aronson, J. Geophys. Res. **72**, 2955–2962, https://doi.org/10.1029/jz072i011p02955 (1967).
[13] W. J. Hooker and R. C. Millikan, J. Chem. Phys. **38**, 214–220 (1963).
[14] J. Kiefer, L. Mizerka, M. Patel, and H. Wei, J. Phys. Chem. **89**, 2013–2019 (1985).
[15] C. Park and J. P. Appleton, Combust. Flame **20**, 369–379 (1973).
[16] R. Emrich and C. Curtis, J. Appl. Phys. **24**, 360–363 (1953).
[17] M. Kuriakose, M. Skotak, A. Misistia, S. Kahali, A. Sundaramurthy, and N. Chandra, PLoS One **11**, e0161597 (2016).
[18] J. M. Varas, M. Philippens, S. Meijer, A. Van Den Berg, P. Sibma, J. Van Bree, and D. De Vries, *Traumatic Injuries in the Nervous System* (Frontiers in Neurology, 2011).
[19] M. Downey, T. Cloete, and A. Yates, Shock Waves **21**, 315–319 (2011).
[20] K. Heufer, H. Olivier, S. Drumm, and H. Murrenhoff, in *Proceedings of 28th International Symposium on Shock Waves* (Springer, 2012).
[21] R. Mejia-Alvarez, B. Wilson, M. Leftwich, A. Martinez, and K. Prestridge, Shock Waves **25**, 635–650 (2015).
[22] Y. Takano and T. Akamatsu, J. Phys. E: Sci. Instrum. **17**, 644 (1984).
[23] R. S. Tranter and B. R. Giri, Rev. Sci. Instrum. **79**, 094103 (2008).
[24] D. V. Reneer, R. D. Hisel, J. M. Hoffman, R. J. Kryscio, B. T. Lusk, and J. W. Geddes J. Neurotrauma **28**, 95–104 (2011).
[25] M. Skotak, E. Alay, and N. Chandra, Front. Neurol. **9**, 52 (2018).
[26] V. Selvan, S. Ganpule, N. Kleinschmit, and N. Chandra, J. Biomech. Eng. **135**, 061002 (2013).

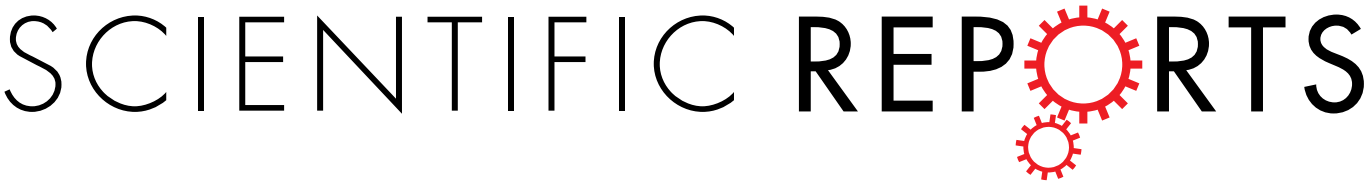
Published under license by AIP Publishing

Appendix A –Publication Cover 13
2018

Authors: G. Ordek, A. S. Asan, E Centinkaya, M. Skotak, K.V. Rama Rao, N. Chandra, M. Sahin

Title: "*Electrophysiological correlates of blast-wave induced cerebellar injury*"

Journal Publication: Nature- Scientific Reports, 8 (1), 13633**,** (2018), [18-13]



OPEN

Electrophysiological Correlates of Blast-Wave Induced Cerebellar Injury

Received: 7 July 2017
Accepted: 24 August 2018
Published online: 11 September 2018

Gokhan Ordek[1], Ahmet S. Asan[1], Esma Cetinkaya[1], Maciej Skotak[1,2], Venkata R. Kakulavarapu[1,2], Namas Chandra[1,2] & Mesut Sahin[1]

Understanding the mechanisms underlying traumatic neural injury and the sequelae of events in the acute phase is important for deciding on the best window of therapeutic intervention. We hypothesized that evoked potentials (EP) recorded from the cerebellar cortex can detect mild levels of neural trauma and provide a qualitative assessment tool for progression of cerebellar injury in time. The cerebellar local field potentials evoked by a mechanical tap on the hand and collected with chronically implanted micro-ECoG arrays on the rat cerebellar cortex demonstrated substantial changes both in amplitude and timing as a result of blast-wave induced injury. The results revealed that the largest EP changes occurred within the first day of injury, and partial recoveries were observed from day-1 to day-3, followed by a period of gradual improvements (day-7 to day-14). The mossy fiber (MF) and climbing fiber (CF) mediated components of the EPs were affected differentially. The behavioral tests (ladder rung walking) and immunohistological analysis (calbindin and caspase-3) did not reveal any detectable changes at these blast pressures that are typically considered as mild (100–130 kPa). The results demonstrate the sensitivity of the electrophysiological method and its use as a tool to monitor the progression of cerebellar injuries in longitudinal animal studies.

The devastating consequences of severe head injuries are well known to the public. It is also known that undetected mild TBI can be a high risk factor for subsequent injuries and repeated mTBI, whether identified or not, leads to much more serious injuries[1]. Time of intervention is a critical parameter to achieve the best results in the treatment of TBI patients. This requires the knowledge of the time course of injury and its severity. To this end, animal models have been developed to generate better controllable results such as injury severity, type, and location, as well as the age, gender and genetic composition of the subjects, for investigations of immunohistochemical and biomechanical aspects of TBI. Although animal models continue to provide valuable insights into the mechanisms of brain injury, the need to terminate the animals for histological evaluation introduces a significant source of variability by preventing data collection at multiple time points in the same animals during injury progression. Thus, post-mortem techniques rely on statistics to account for inter-animal variations. Cascaded sequelae of the initial and delayed phases of neural injury make it further difficult to determine the temporal course of the injury. Secondary (or delayed) injury mechanisms can last minutes to months including cascaded metabolic, cellular and molecular events that lead to brain cell and tissue damage[2–4]. On the other hand, the electrophysiological technique can provide a powerful tool for multi-point measurements or continuous monitoring of the biomarkers correlated with injury while cascaded changes are taking place in live animals. We developed a novel approach to monitoring various phases of injury using multi-electrode arrays (MEAs) implanted on the cerebellar surface (micro-ECoG technique) to detect any subtle changes in the cortical network excitability. Implanting the rats with MEAs before the blast exposure provided a baseline within the same subject for comparison.

Traditionally, the cerebellum has been considered as a brain center for sensorimotor integration and motor coordination. In recent years the cerebellum has been implicated in cognitive functions and emotions[5,6]. Despite numerous studies, there is still no consensus either on the nature of the information provided by the cerebellar outputs to other brain centers, or how the disruption of these outputs leads to the observed functional deficits

[1]Department of Biomedical Engineering, New Jersey Institute of Technology, Newark, 07102-1982, NJ, USA. [2]Center for Injury Biomechanics, Materials, and Medicine (CIBM3), New Jersey Institute of Technology, Newark, 07103-3540, NJ, USA. Correspondence and requests for materials should be addressed to N.C. (email: namas.chandra@njit.edu) or M.Sahin (email: sahin@njit.edu)

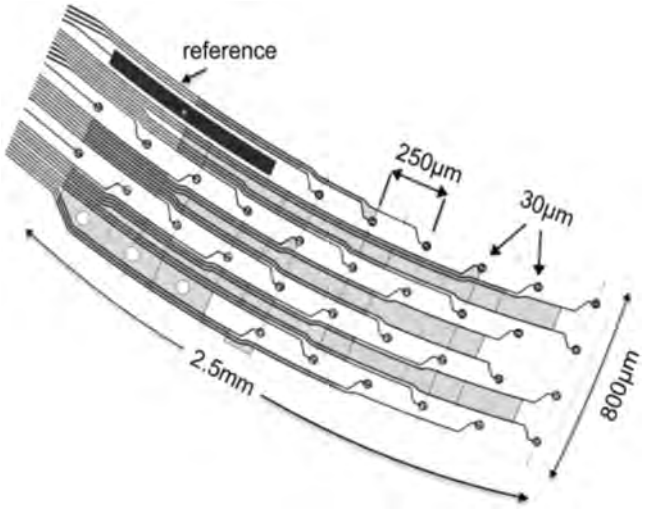


Figure 1. Custom-design multi-electrode array contained 32 Pt contacts (30 μm diam.) that were arranged in 4 rows and 10 columns that cover most of the right PML. The first four contacts are missing in the design on the first row, where the reference contact is, and also on the fourth row.

after head trauma. The neurologic disabilities that result from a direct insult to the cerebellum include ataxias, tremors, loss of balance and motor skills, and cognitive deficits[7–10].

To date, the cerebellum has been understudied in the field of TBI research because of the notion that majority of cerebellar deficits occur only by direct impacts on the cerebellum, which rarely occurs in accidents. However, a recent report showed functional and structural cerebellar deficits as a result of blast induced repeated mTBI where the entire brain was affected[11]. Another report suggested a lower threshold for cerebellar injuries in veterans exposed to repetitive blasts[12]. Although diffuse axonal injury (DAI) is the main focus of mTBI research, recent evidence also indicated vulnerability of the synaptic mechanisms to blast injuries[13–16]. Other findings in cerebellar injuries included Purkinje cell (PC) deterioration[17–19], synaptic disruptions[11,20] and behavioral deficits[8,17,18].

Scientific evidence is building up to suggest that mild head injuries, including concussions, can leave permanent damage in the brain especially if they reoccur before the person completely recovers from the first injury[21]. These mild injuries are difficult to study in experimental animals because the damage may not cause the brain cells to show any anatomical changes or complete degenerations, but rather slowing down of their communication with other cells. Furthermore, mild injuries cannot be detected using behavioral measures since the impairments may be too subtle to affect the motor function or cognition or need a prohibitively large sample size to be detected. Here, we propose a highly sensitive electrophysiological method as a tool to monitor the state of on-going cerebellar injury with repeated or continuous recordings of evoked potentials in anesthetized animals.

Results

We first studied the effects of blast injury on the cerebellar local field potentials evoked by dorsal hand and whisker mechanical stimulation using a custom-design multi-electrode array (Fig. 1). Changes in the EP waveforms were shown on the post-injury days compared to the control day for a sample rat (Fig. 2). In general, the cerebellar EPs demonstrated characteristic waveforms that are reproducible. The amplitudes of evoked potentials (EPAs) were in the 120 ± 10 μV-160 ± 20 μV range for the largest deflections (latency of 8–10 ms) as a response to whisker stimulation in the pre-injury period. The largest deflection amplitude drastically dropped down to 10 ± 5 μV immediately after the blast injury (<10 min). The EPs evoked by hand stimulation persisted around the same amplitudes immediately after injury (paired t-test, $n = 4$ trials, $p > 0.5$) but decreased substantially on the next day (day-1). The EPs for both hand and whisker stimulations were very small and barely above the baseline noise on day-1 (red traces, $5–8 \pm 2–4$ μV). On day-3 of injury, both signals showed larger and multiple volleys compared to day-1, which suggested a partial recovery from injury (green trace, $60–80 \pm 8–13$ μV).

The changes in EPAs were quantified by calculating the area under the curve (AUC) as a measure, which reflects both the amplitude and duration information of a deflection in the EPs. An illustrative example from a control (pre-injury) animal was shown for a single channel of the MEA (Fig. 3A) and in multiple animals for hand and whisker stimulations (Fig. 3B, $N = 7$ rats). The raw AUC values were normalized by the maximum AUC that was observed in the pre-injury period within each animal individually and then averaged across all animals. The AUC values decreased significantly after the blast exposure during the 7 days after injury ($N = 7$ rats). Most drastic changes occurred within one hour after injury for the whisker EPs and on the next day for the hand EPs (a decline by ~56% in whisker AUCs at 1 h, $p < 0.001$ and by 43% in hand AUCs on day-1, $p < 0.01$; Dunnett's test). On day-3, AUCs increased slightly compared to day-1 measurements (Whisker ~13%, $p < 0.44$; Hand ~%24, $p < 0.16$) similar to the trend in EP amplitude measures in Fig. 2, which suggested a partial recovery. On day-7, the average AUCs were still lower than the control values by ~44% ($p = 0.003$, Dunnett's test) and ~32% ($p = 0.07$, Dunnett's test) for whisker and hand stimulation respectively. However, the AUC measures that were obtained from day-3 ($73.1 \pm 10\%$) and day-7 ($58.3 \pm 17.1\%$) for the hand EPs were not significantly different from pre-injury values ($90.3 \pm 4.3\%$).

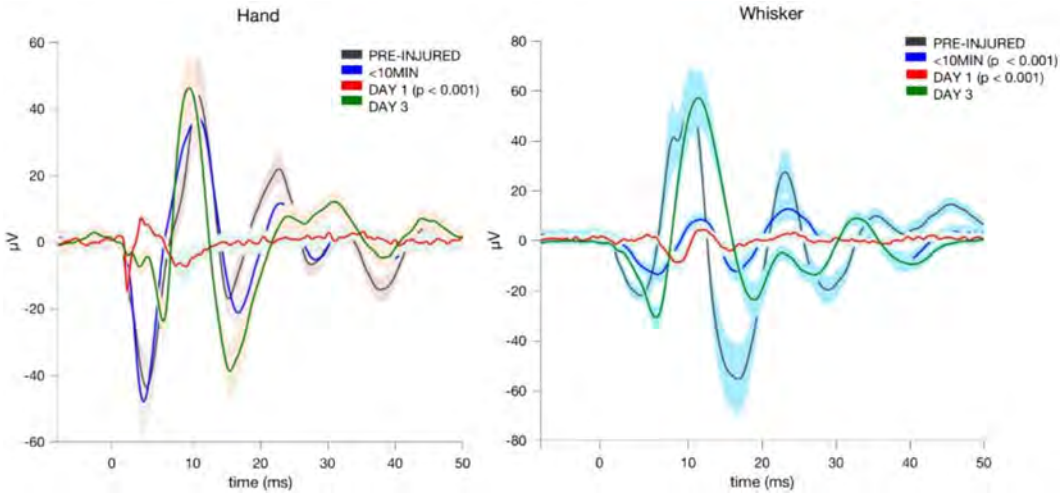


Figure 2. Sample evoked potential (EP) waveforms for hand and whisker stimulations before and after injury in a rat. Stimulus-trigger averaged (STA) signals were filtered at 10–500 Hz, and then averaged across channels. Multiple recordings (4–5 STAs) were averaged for each time point (i.e. each trace) and plotted as mean (solid) ± s.d (shades) from the time of stimulus arrival (t = 0 ms). While pronounced changes in EPs to whisker stimulations occurred immediately after injury (<10 min, T = 9 recordings, $p < 0.001$), hand EPs indicated significant changes only on the next day (T = 10, $p < 0.001$).

Next, the EPs were segregated into MF and CF mediated potentials as identified by their characteristic latencies from the time of stimulus (Fig. 4A), i.e. 2–10 ms for MF (red) and 12–20 ms for CF (blue). Because hand EPs were more reproducible than that of whiskers, we used only the hand evoked signals in the rest of the analysis. For precise measurements of arrival times, the EPs were spike-trigger averaged across multiple trials in each day for individual channels of the recording array separately. Consequently, each dot in the x-y plots of Fig. 4B represents a single contact out of 31 contacts of the array for the specified day of recording (color coded) in one of the animals. The histograms on the top and the right side of each plot show distributions of the MF and CF arrival times (latencies) across the array contacts in all animals as group data. The results suggest that there was a transient lengthening of MF onset latencies from the control values of 5.5–6.5 ms to 6–8 ms within the first hour of injury, which was followed by a decrease to the 4–6 ms range on day-1. On the following days, there was a progressive increase in MF delays with mean values of 6.05 ms, 6.6 ms, and 7.05 ms on days 3, 7, and 14 respectively. The variance of the MF latencies across the channels was much wider on the post-injury days compared to the pre-injury values. Conversely, the CF peak delays started increasing immediately after injury (1 h) from a range of 15–16 ms and reached to 16–20 ms with a mean of ~19 ms, and stayed higher for the rest of the study period without a specific pattern in the trend. Most notably, significant changes were observed both in MF and CF arrival times within the first hour, although they moved in different directions specifically on day-1. Overall, these results suggest that the injury induces differential effects on the MF and CF arrival times.

As a measure of excitability in the cerebellar network, we used z-scores of the normalized amplitudes (nEPAs) of the MF- and CF-EPs (Fig. 5). In each animal, the majority of supra-threshold CF responses occurred before the injury (Fig. 5A; control, 90% or 19/21 trials in the pooled data). Conversely, none of the MF responses reached the excitability threshold on the day before the injury (Fig. 5A; $Z_{score} > 2.05$, no blue markers <10 ms, a gray area excluded). After the injury, the ratio of supra-threshold CF components declined to 66% (63/95 trials for all time points) from 90% (pre-injury), showing the sharpest decline within the hour (Fig. 5A; red markers). While all of the supra-threshold MF-nEPAs were registered in the post-injury period for all animals (Most heightened at ~1 hour; red markers, $Z_{score} = 2.25 \pm 0.11$), CF-nEPAs were much stronger in the pre-injury period in comparison (blue markers in $t \geq 10$ ms area, $Z_{score} = 2.56 \pm 0.13$).

All supra-threshold responses (shown in Fig. 5A) were averaged for each day across animals and replotted (Fig. 5B). The z_{score} threshold was lowered to 1.55 for this particular analysis in order to include at least one data point per day. In each animal, the data set was normalized to the largest amplitude that was recorded during pre- or post-injury periods, following z-score qualification. Significant changes were detected in nEPAs of both MF and CF responses from pre- to post-injury (MF; $F_{(6,522)} = 7.12$, CF; $F_{(6,593)} = 14.51$) recordings. Within the first hour, CF-nEPAs were diminished almost completely down from 0.89 ± 0.09 in pre-injury. After day-1 of injury, the magnitudes of CF-nEPAs were still nearly 3-fold smaller (0.27 ± 0.2) than the pre-injury values and did not differ significantly on day-14 from day-7 ($p = 0.22$, one tailed t-test). Contrarily, MF-nEPAs increased to 0.22 ± 0.12 ($p < 0.01$; single data point from the pre-injury period in each rat) in the first hour and sustained higher magnitudes than the controls during the two weeks of the post-injury period (nEPAs = 0.14 ± 0.08 on day-14). These results suggest that the MF and CF amplitudes were also affected differentially by the injury, and analogous to the trend in their arrival times. Note that the overall effect of injury on the EP amplitudes was a net decrease by the AUC measures before separating the MF and CF components (Fig. 3).

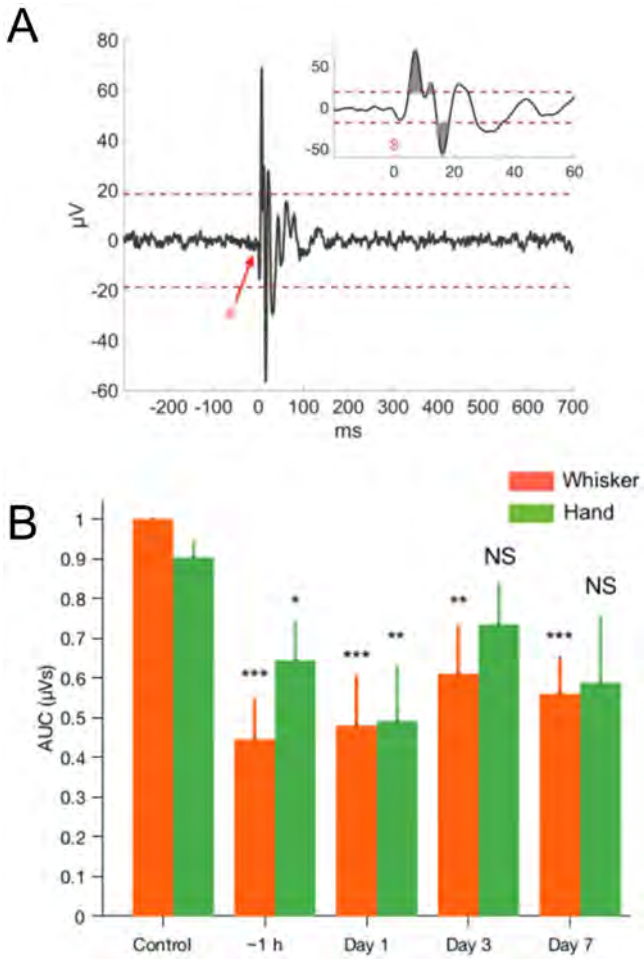


Figure 3. EP quantification by the area under the curve (AUC) method. (**A**) An example of AUC calculation is shown on a stimulus-trigger averaged signal that had a sufficient amplitude to be included in the analysis (threshold ± 20 μV). (**B**) Mean EP changes during the 7 days following blast injury (N = 7 rats). AUCs showed significant drops for both whisker ($F(4, 30) = 5.69$, $p = 0.0016$; rmANOVA) and hand evoked potentials ($F(4, 30) = 2$, $p = 0.011$; rmANOVA). Bars indicate ± s.d. Significance vs. control (pre-injury) is indicated by the asterisks according to Dunnett's test. ***$P < 0.001$, **$P < 0.01$, *$P < 0.05$. NS: not significant.

Ladder Walking. The functional impact of injury was assessed using the skilled locomotion test on the horizontal ladder rung (HLR) in a group of rats that were exposed to the same blast-pressures as the rats with array electrode implants (Fig. 6A, N = 3 rats). The walking performances improved during one-week of pre-injury training period as indicated by the lower number of foot slips (1.33 ± 0.28, $p = 0.001$; Tukey test, day-1 vs. day-4) and the body falls (1.44 ± 0.37, $p = 0.009$, Tukey test, day-1 vs. day-6). Interestingly, HLR scores did not present any significant differences after the blast injury ($F_{(2,32)} = 0.909$, $p = 0.512$; from day 4 to day 12). In fact, they showed nearly the same number of misses and falls on day-1 (Tukey test, $p > 0.99$; Day 7 vs Day 8) and day-2 (Tukey test, $p > 0.95$; Day 7 vs. Day 9) of the post-injury period. Results indicated no behavioral deficits in the limb functions during the learned HLR walking due to blast-exposure.

Rotarod tests. As another method to assess motor coordination in animals exposed to blast injury, rotarod testing was done in animals 24 h, 3 days and 7 days post-injury. Similar to ladder walking performance test, at any time point after the injury, latency times between control and injured animals did not display any statistically significant differences (Fig. 6B). These results are consistent with the ladder performance tests, and further confirms that electrophysiological measures are more sensitive tools to identify progressive cerebellar injuries following mild blast injury.

Assessment of Neuronal Loss. In order to identify any potential neuronal loss contributing to electrophysiological disturbances at 24 h and 7 day post-injury, immunohistochemical analysis of calbindin D28K, an intracellular Ca^{2+} binding protein and a marker of Purkinje cells, as well as cleaved caspase-3, a marker of apoptosis was performed. Results indicate immunoreactivity (intensity) of calbindin D28K or a number of calbindin D-28K positive cells did not change in the paramedian lobule of cerebella in rats exposed to 130 kPa over pressure compared to controls (Fig. 7). Likewise, a number of caspase-3 positive cells did not change following injury. Calbindin D-28K and caspase-3 immunostaining were also performed 7 days post-injury and similar to 24 h data,

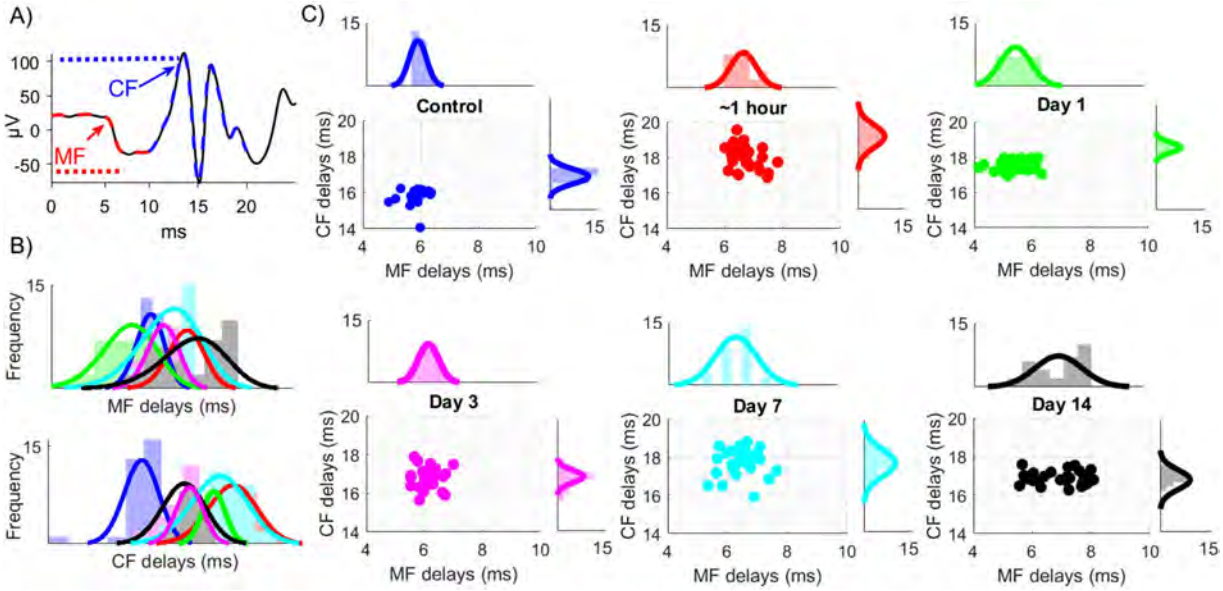


Figure 4. Arrival times of MF and CF mediated local field potentials evoked by mechanical hand stimulation before and after injury. (**A**) Identification of the MF onset and the CF peak, based on arrival times (arrows). Stimulus is at 0 ms. (**B**) MF and CF delays for each array contact were averaged across multiple trials (2–3 trials per day) separately in each day and animal (3 rats indicated by different symbols) and plotted against each other as an x-y chart to show the variation across 31-channels of the recording array. Histograms show day-by-day (color coded) changes in the mean and distribution of the delays. All statistical significances were performed with paired comparisons between pre-injury (control) vs. each day of post-injury. N = 3, Mann-Whitney; *P < 0.01, **P < 0.001, ***P < 0.0001. (**C**) All histograms from different days are merged into a single plot to demonstrate the trends in MF and CF delays day-by-day.

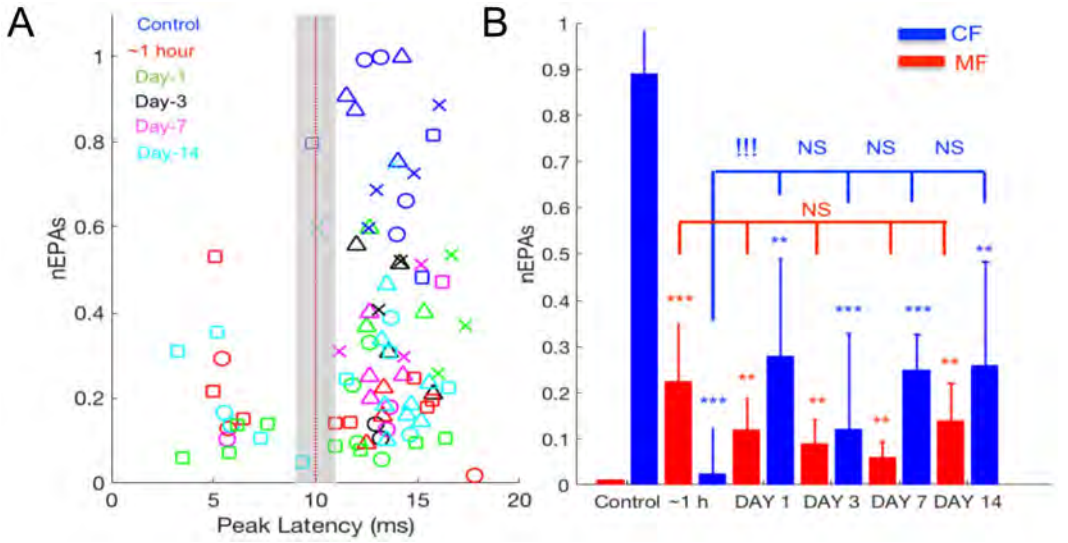


Figure 5. Excitability changes after injury in EP components by hand stimulation. (**A**) Amplitude distribution of MF (latency < 10 ms) and CF (latency > 10 ms) components. EPAs were normalized (nEPA) to a maximum recorded amplitude on any day throughout the pre-/post injury period in each rat, and then a z-score value was applied as a threshold (Zscore > 2.05, 15 MFs and 71 CFs). The data were gathered from 4 rats as indicated by different marker shapes. While CF-EPAs indicated the strongest responses in the pre-injury (control) recordings in all animals (blue markers, T = 14/19 trials; Zscore > 2.05), MF-EPAs showed supra-threshold responses only in the post-injury period (T = 15/89 Trials, Zscore > 2.05), except day-3. (**B**) Same data with a lower threshold (Zscore > 1.55) were averaged and shown as mean ± s.d for MF (red) and CF (blue), respectively. Statistical analysis indicated significant increases in MF-nEPAs, and significant decreases in CF-nEPAs in the post-injury period (ANOVA followed by Dunnett's test; control vs. post-injury time points, n = 5 days, n = 32 MF-nEPAs, n = 105 CF-nEPAs; ***P < 0.001, **P < 0.01, *P < 0.05). Individual days were compared using pairwise t-test (CF ~1 h vs. day-1; $^{!!!}$P = 0.0013, NS: Not significant).

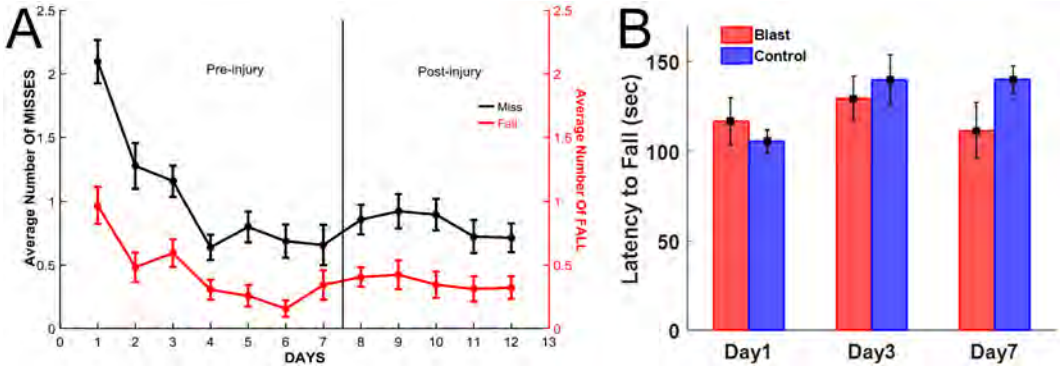


Figure 6. (**A**) Walking performances during repeated horizontal ladder crossings. Number of slips (misses) and falls in any of the four feet were scored in three rats. Rats demonstrated improved walking skills during the training period of one week with lowered number of falls and misses prior to injury (Days 1–7). Animals showed no statistically significant changes in motor performance scores with nearly the same miss and fall scores on day-1 (Day 8) and day-2 (Day 9) of injury. (**B**) Effect of mild blast injury on rotarod performance. Values were recorded from control and blast-injured animals on day 1, day 3 and day post-injury. Results are the mean ± SEM of the time animals remained on the rotarod before falling. There was no significant difference between control and injured animal groups at any time point ($p > 0.05$).

no significant changes were observed between controls and 7-day post-injury animals. Additionally, to evaluate whether purkinje cells were undergoing apoptosis, we performed double immunostaining of calbindin-D28K and caspase-3. We did not observe any colocalization of caspase-3 positive staining in purkinje cells. These results indicate that Purkinje cell loss does not contribute to the observed disturbances in electrophysiological functions in this study.

Discussion

Electrophysiological Correlates of TBI. Electrophysiological detection of TBI related neurological abnormalities has been investigated in humans[22,23] and animal models[24,25]. While researchers and clinicians mostly focused on the cerebral regions such as the neocortex[24,25] and hippocampus[26–28], reports on the cerebellum also presented strong evidence for the use of electrophysiology in TBI detection[20,29–31]. A wide spectrum of electrophysiological classifiers has been investigated. Nevertheless, amplitude and frequency analyses remain as the most sensitive parameters to identify abnormalities in the altered electrophysiology of the injured cerebellum. Amplitude variations in the electrical activity has previously been correlated to the cell loss in the cerebellum[20], while the frequency[32] and coherence spectra[33] of the cerebellar oscillations have also been shown to change due to the injury.

Recently, we introduced the use of evoked potentials for detection of cerebellar injury in focal fluid percussion model with chronic implantation of multi-electrode arrays in rodents[30]. Our published data demonstrated the sensitivity of the electrophysiological assessment method in detection of cerebellar injuries earlier than the onset of molecular degeneration in fluid percussion injured (FPI) rats. Despite the differences in the injury mechanism between FPI-induced (both focal and locally diffuse) and blast-exposed (whole-brain diffuse) TBI models, cerebellar recordings showed a number of akin findings that support the sensitivity of the electrophysiological method. As a result of EPA amplitude variations between the animals, the recovery on day-3 (and day-7) was not statistically strong in the group data (Fig. 3) to unambiguously confirm the distinct recovery shown in the sample animal of Fig. 2. The amplitude analysis in conjunction with the time of arrivals (Fig. 5) suggests that the recovery is not complete within our observation window after injury. In contrast, we did not observe any signs of recovery in our previous FPI work within one week, which may be explained by different injury mechanisms.

Our definition of the MF time window was relaxed to account for additional propagation delays from periphery and we essentially used the first volley after the stimulus for the analysis. Here, we strictly defined the MF component with latencies less than 10 ms and extended our previous findings by separating the EP components into MF and CF mediated components. The former showed an increased and the latter showed a decreased excitability after the injury. Increased excitability in mossy fiber responses after FPI induction has been reported before. In Ai and Baker[20,29], FPI applied over the posterior fossa immediately behind the lambda line in the center resulted in presynaptic hyperexcitability within mossy fiber granule cell synapses at 3 days post-injury along with by hyperexcitability of the parallel fiber-Purkinje cell synapses at 3–7 days post-injury. The major discrepancy between our and Ai and Baker's results is that they did not observe any significant changes in neither of these synaptic strengths at 1 day after injury, a finding that was clearly suggested by our data with both FPI[30] and blast injury mechanisms. A potential explanation was offered by our observation that the whisker EPs declined within the first hour post-injury as opposed to the hand EPs showing major changes on the next day. This suggests that different cerebellar networks may have varying time windows to respond to the injury depending on whether they are affected directly or indirectly.

The pre-implantation of an MEA may be a risk factor that the presence of the MEA on the cerebellar cortex during exposure to the blast wave may augment the impact and exacerbate the resulting injury. This concern was invalidated to a large extent by the fact that the whisker and hand evoked potentials were affected differentially

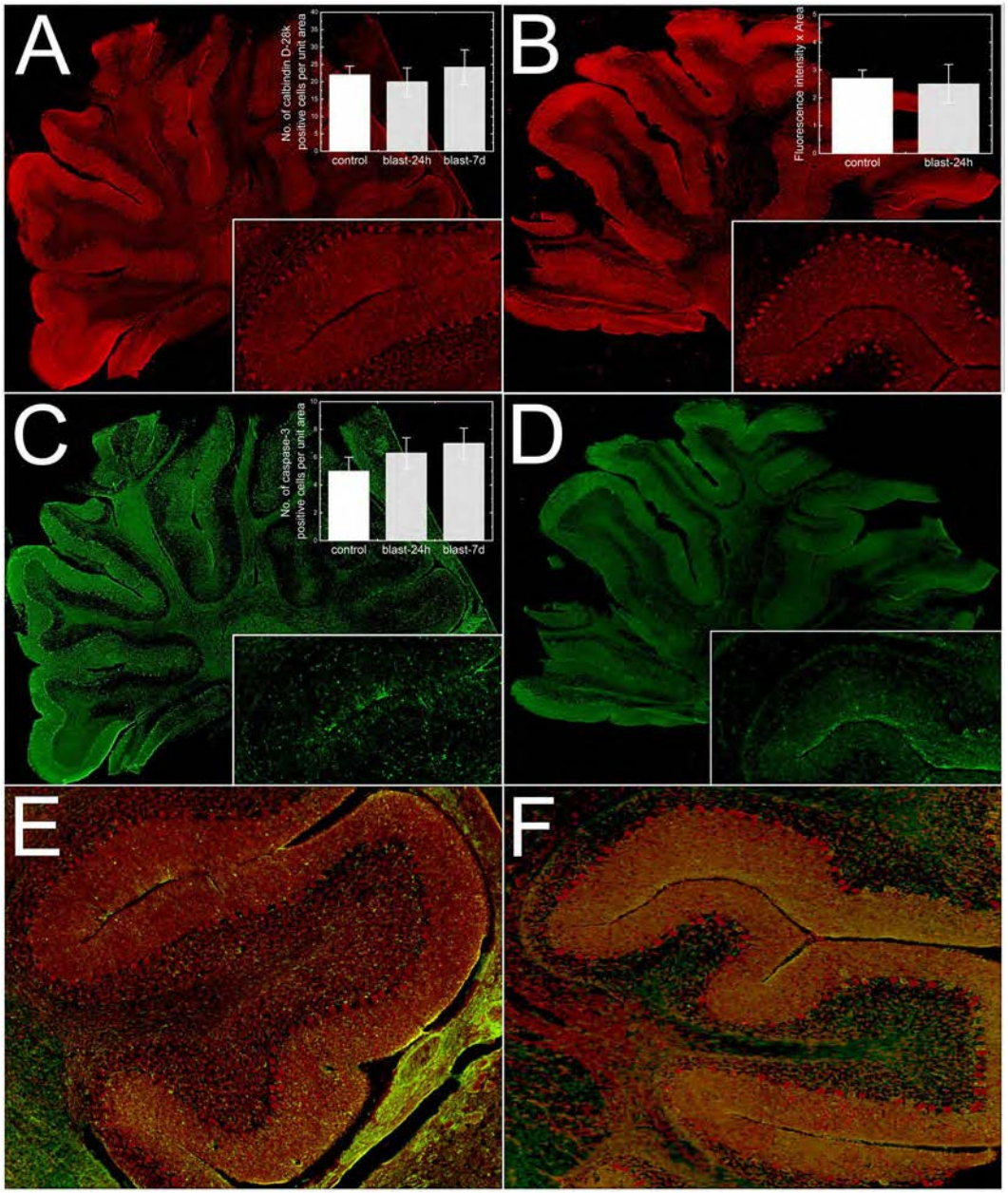


Figure 7. Immunofluorescence images of calbindin-D28K (**A**,**B**) and cleaved caspase-3 (**C**,**D**) in control, 24 hours and 7 days after blast injury. Sagittal sections with enlarged fragments from the paramedian lobules (insets) captured at 40x magnification and quantification results are presented. Paramedial lobules double stained for calbindin-D28K (red) and caspase-3 (green) showing no colocalization of caspase-3 in Purkinje cells (**E**,**F**). Bar plots present quantification of: 1) a cell count for: calbindin-28k (**A**), and capsase-3 (**C**) positive cells, and 2) calbindin-28k fluorescence signal (**B**). No appreciable changes in the levels of calbindin-D28K or cleaved caspase-3 were observed between control and the injured cerebella ($p > 0.05$).

and that the hand evoked signals did not differ significantly in recordings immediately after the injury. The deterioration of the signal amplitudes may still be occurring due to tissue encapsulation around the electrode until the chronic tissue response is complete in about two to three months[34–36]. The stability of the signals in a group of uninjured control animals with implantation times up to 21 days suggested that the signals do not deteriorate significantly within this time window[30]. The subdural implantation of the MEA can also provide a sub millimeter level spatial resolution for localization of injury if needed, as demonstrated by EP amplitude distributions from whisker and hand stimulation in uninjured animals[37].

Hand vs. Whisker Stimulation. Unlike the hand stimulation, the EPAs by whisker stimulation were significantly lower at each measurement point as seen in the pooled data from all animals (Fig. 3). This may be due to several factors. Cerebellar cortex contains multimodal functional topography[38–41] that is defined by discrete

clusters of neurons, which may receive multi-variant projections during stimulation of different body parts[38]. For instance afferent information from whisker activation is transmitted through a more direct and shorter pathway that involves trigeminal nuclei and inferior olive via middle cerebellar peduncle before reaching granule cells and PCs in the cerebellar cortex[42]; while inputs from the hand are mediated by spino-olivary pathways ascending via inferior cerebellar peduncle to activate the same type of neurons in the cerebellum[43–45]. Biomechanical factors during blast injury might induce differential effects on the hand and whisker networks of the cerebellum that are defined by different ascending pathways. This is supported by studies indicating a higher sensitivity of the vestibular nucleus to shock-wave induced blast injuries in humans and rats[46–48], although we cannot confirm a similar effect since we did not include behavioral tests to verify balance and coordination deficits in our experimental animals. Nevertheless, it is possible that an adjacent structure to the vestibular fibers, the trigeminal tract, may also have a higher sensitivity to the blast-waves.

Additionally, we observed large differences in EPAs, particularly in those from the hand, between the animals that were exposed to blast pressures with lower (100 psi) and higher (130 psi) pressure peaks (data not shown). While the whisker EPAs showed rapid drops within hours of injury, only at higher pressures the hand EPAs presented discernible deteriorations. While the differences in the measured peak pressures explain the variations in our pooled data, this observation also suggests the sensitivity of the cerebellar EPs to graded levels of injury severity. In our blast experiments the animals were held in prone position with shock waves traveling from rostral to caudal direction and reaching the cerebellum last. In FPI experiments, the injury is usually induced just above the cerebellum. Though the blast loading is biomechanically distinct from FPI, the subtle electrophysiological changes were measurable in both injury types.

MF vs. CF Mediated Components. Cerebellar evoked potentials were previously investigated with penetrating as well as surface electrodes and characteristic waves (amplitude, onset time, duration, etc.) were linked to cerebellar morphology[37,49–52]. The sole output of the cerebellar cortex, the Purkinje cells (PCs), receive inputs through two major pathways. First, the mossy fibers (MF) that project on PCs via granule cell (GC)-parallel fiber (Pf) pathway and generate an early (2–6 ms; onset latency, P1-N1, N2) excitatory post synaptic potentials (EPSPs) in the evoked potential waveform. Second, the climbing fibers (CF) that originate from the inferior olive (IO) and make strong excitatory connections with the PCs and give rise to local field deflections with 8–20 ms latencies in response to a sensory stimulus[52,53].

The evoked potentials, identified by their anatomical origins within the cerebellar cortex, were shown to detect changes of excitability[54,55]. We separated the cerebellar EPs into mossy and climbing fiber components with respect to their arrival times (Figs 4 and 5). While the CF components presented delayed arrival times (up to ~4 ms) for all days of post-injury, the MF responses had a changing trend. We noted that the MF onsets were initially increased (~1 h), then decreased (day 1) and finally increased again from day-3 to day-14 of the injury period. Finally, the increasing standard deviation of the CF delays between the recording channels indicated a wider spatial distribution of arrival times across the cerebellar cortex.

Differential effects in the timing of the MF and CF signals prompted a similar analysis to be performed on the amplitudes. Typically, the MF deflections exhibited smaller amplitudes with negative polarity, which is plausible considering the weakness of PF-PC synapses. The effect of the CF pathway on PC dendrites is much stronger with hundreds of synapses[56], and thus the CF component is recorded with larger amplitudes and positive polarity. Figure 5 suggests an increase in the MF mediated volleys and a decrease in the CF mediated components during the post-injury period, particularly at early stages, from 1 hour to a day. The higher z-score threshold yielded many more MF component detections after the injury suggests hyperexcitability. Increased excitability of pre-synaptic inputs at the mossy fibers-granule cell terminals was reported before[20]. Although our findings suggested a similar trend, we argue that the time window for MF hyperexcitability may be occurring in the earlier acute stage (hours to a day) rather than in the delayed phase (day-3 to day-7) of injury.

Behavioral Tests. We hypothesized that electrophysiological approach could be sensitive enough to investigate mild injuries that would be too subtle to detect with conventional methods. To confirm this hypothesis, we first evaluated the behavioral scores during a skilled walking task on a horizontal ladder rung. The cerebellum plays a major role in motor learning tasks when the predictive timing and coordination is essential[57,58]. Animal models suggest that cerebellar injury can lead to Purkinje cell losses and behavioral deficits in moderate to severe head injuries[17,59]. We implemented a horizontal ladder rung test to evaluate skilled walking parameters such as foot slips, step cycle, limb coordination to complement foot fault scorings in pre- and post-injury periods. Although multiple parameters were analyzed (not shown), we observed only clear improvements in the reduction of foot slips and partial (or complete) falls in the learning period prior to injury induction. After blast exposure, animals showed no differences in their walking performance on the ladder. In our previous study, FPI at 15–30 psi induced detectable changes in step duration, suggesting that the HLR task is a proper behavioral paradigm to demonstrate cerebellar injuries[60]. The absence of walking alterations in the HLR task among blast injury cohort suggests that the cerebellum is affected only mildly. These results show that the electrophysiological method can detect changes in the cerebellar circuits even in the absence of behavioral deficits.

Immunohistochemistry. Neuronal loss, particularly the Purkinje cell loss has been reported in different forms of TBI with different injury severities[18]. Earlier, employing fluid percussion model of TBI, we also observed that mild injury (~15 psi) caused a significant Purkinje cell loss (decreased calbindin D28K immunoreactivity and increased Fluoro-Jade C staining) in parasagittal sections of cerebellar cortex 7 days post-injury[30]. Our previous observation is in contrast with our present study showing no Purkinje cell loss following blast injury at 24 h or 7 days post-injury, although the peak over pressure appear to be similar (15 psi = 103 kPa). It is possible that the injury outcomes may be dictated by the mode of injury (e.g., blast vs. blunt injury). Accordingly, direct tissue

injury at the epicenter in the blunt TBI could trigger a cascade of events (neuroinflammation, local blood brain barrier breakdown) that may be different from blast injury. Additionally, a single blast at moderate levels may not be sufficient to trigger neurodegeneration whereas a single blunt impact and associated direct tissue damage could render Purkinje neurons more vulnerable. In fact, employing a repetitive blast model in mice (3 blasts at 19 psi over 24 h interval) chronic Purkinje cell loss and persistent synaptic disturbances occurred[12], which supports our tenet. Nevertheless, electrophysiological disturbances observed in the present study appear to be not due to neuronal loss.

Methods

Implant Surgery. Custom-design flexible multi-electrode arrays (E32_250_25_30_PML, NeuroNexus, MI) were implanted using sterile surgical techniques in 10 Long Evans rats (male, 250–275 g) one week prior to blast exposure. Data from 7 rats that were collected at matching time points in the post-injury period are presented here. All procedures were approved and performed in accordance to the guidelines of the Institutional Animal Care and Use Committee, Rutgers University, Newark, NJ. Anesthesia was induced using isoflurane (4% in 100% O_2) and maintained with lower doses of the same (1.5–2.5%). Dexamethasone sodium phosphate was administered (2 mg/kg, IM) before surgery to reduce cerebellar edema. A craniotomy of ~2 mm^2 was made over the right cerebellum (corner at 1.7 mm lateral from midline and 2.5 mm caudal from the posterior edge of the skull) in order to implant the flexible MEA subdurally on the paramedian lobule (PML). The platinum contacts (30 µm diam.) of the MEA had a pitch of 200 µm and 250 µm in AP and ML directions respectively in 4 × 10 configuration (Fig. 1). The MEA substrate was a thin polymer (polyimide, thickness 12 µm) and fabricated in a slightly curved shape to fit between the blood vessels without occluding them and cover most of the PML. Contact impedances varied between 800 kΩ–1.2 MΩ in saline prior to implantation and stabilized around 1–1.5 MΩ after the first week of surgery. A large reference electrode was incorporated into the MEA at one corner to suppress common-mode signals originating from subcortical locations within the cerebellum. The leftmost edge of the array was juxtaposed to the paravermal vein on the right PML. Trace amounts of octyl cyanoacrylate tissue adhesive (Nexaband, WPI, Inc., FL) was applied on the edges of the MEA to fix it on the pia surface before covering it with autologous connective tissue for sealing the dural opening. The micro connector at the end of the MEA ribbon cable was fixed to the skull using octyl cyanoacrylate first as an adhesive layer over the skull followed by dental acrylic.

Blast-Wave Injury. Seven to ten days were allowed for the animals to recover from the surgery and the evoked potentials to stabilize before the injury. Then, the rats were exposed to a single blast wave in a 6 m long shock tube with 9-inch square cross-section located in the Center of Injury Biomechanics, Materials and Medicine, NJIT[61]. The shock tube generates blast overpressure vs. time pulses that have been validated against live-fire explosions so that the experimental conditions reported here are both field-validated and realistic[62]. Rats were anesthetized with a cocktail of ketamine and xylazine (100 mg/10 mg/kg, IP) before mounting them inside the test chamber located 2.80 m from the point where the shock-wave was generated at one end of the tube and 3.05 m from its exit. The incident blast pressures, as measured near the test subject, varied between 110 and 130 kPa, had a duration of 5.7 ± 0.3 ms, and corresponding impulse values, i.e. the area under the overpressure curve, of 234 ± 27 Pa·s. As in previously reported experiments[63,64], animals were exposed to the blast in a horizontal head-on position while strapped to an aerodynamic aluminum holder with a thin cotton cloth wrapped around the body. By this experimental setting the gross head motion was eliminated almost entirely as confirmed by high-speed video recording. The high-speed videos were recorded on Photron FASTCAM Mini UX100 camera equipped with Tokina 100 mm f/2.8 macro lens and operating at a frame rate of 5000 fps. Typically, 8000 frames of video footage were recorded in a single experiment and subsequently saved via Photron FASTCAM Viewer 3.3.5 software. The incident overpressure was recorded at the location of the specimen in the test chamber using a LabView program running on a customized data acquisition system based on National Instruments PXI-6133 S-Series DAQ Module. The pressure waveform was recorded using PCB Piezotronics sensors model 134A24 (Depew, NY) at 1.0 MHz sampling frequency for a duration of 100 ms.

Electrophysiological Signals. This study utilized the sensory evoked potentials as a measure of electrophysiological intactness of the cerebellar cortex in a rat model. Sensory evoked potentials were elicited by a mechanical stimulation device, a 1 mm diameter cylindrical wood stick attached to the center of an audio speaker and activated by a short-pulse through a computer with milli-second accuracy. The control pulse was passed through a high-voltage solenoid driver circuit (SDM840, Magnetic Sensor Systems, CA) to achieve a fast and large displacement (3–4 mm) of the speaker coil. A train of mechanical stimuli (20 stimuli at 1 pps) were delivered to ipsilateral whiskers (not necessary the same one in each session) and the back of the hand to evoke local field potentials in the PML cortex of the cerebellum also under ketamine/xylazine anesthesia (30 mg/kg and 2 mg/kg, IP). The neural recordings were performed in a large Faraday cage through a 34-channel headstage amplifier (Gain 800, 0.8 Hz–3 kHz, Triangular Biosystems, NC). Signals were sampled at 16 kHz and filtered at 10 Hz-500 Hz in Matlab (Mathworks). Stimulus-triggered averaging (STA) was employed to suppress the background noise. Further details of electrophysiological methods were previously described elsewhere[30,37].

Characterization of EPs. Evoked potentials were characterized by amplitude (EPA) and latencies following the time of stimulus arrival, marked as 0 ms in Fig. 2A. Two different methods were followed for EPA quantification. First, we calculated the area under the curve (AUC) of any potential deflections that is above five times the standard deviation of the baseline activity in the post-stimulus time window, i.e. 0–50 ms (shaded areas of top right panel in Fig. 3A). Any signal component arriving 50 ms after the stimulus was discarded since these may be

the responses to the stimuli relayed through the brain centers outside the cerebellar network, such as those from the cerebral cortex[65,66].

In the second method, evoked volleys were first identified as either mossy fiber (MF) or climbing fiber (CF) mediated potentials based on the timing of their peaks (before or after 10 ms, left Figs 4–5). Then, it was determined whether the MF and CF volleys were significantly greater ($Z_{score} > 2.05$) than the baseline fluctuation. Those peak values that exceeded three times the background standard deviation was taken. If there was more than one volley for each type, only the largest deflection was included in the analysis. All quantitative measures used the EPAs normalized (nEPA) by the maximum EPA ever recorded before or after injury in that given animal.

Behavioral Testing. Three additional rats of the same size, strain, and gender as in the MEA implants were used for the behavioral testing. Walking on horizontal ladder rung (HLR) was chosen as the behavioral paradigm in order to investigate the impact of blast injury on the motor function. The HLR method is sensitive to the injury of the cerebellum[67]. The custom-designed ladder was assembled by 90 × 19 cm Plexiglas side walls that were separated by metal rungs of 3 mm diameter. The spacing between the rungs was set to 1 cm (regular) for habituation and 1–3 cm (irregular) in the training sessions. The ladder was elevated to 30 cm from the ground and two video cameras (220 × 330 pixels, 100 fps, Allied Vision) were installed to image the entire terrain while being able to see the hands and the feet without obstruction. Both ends of the ladder had a chamber where the animal could receive a food reward. During the first week, animals became accustomed to the environment and slowly learned to cross the ladder. Each rat had two ~10 min sessions per day for 7 days, at which point all animals learned to cross the ladder without hesitation. After this pre-training, the ladder rung pattern was changed by removing some of the rungs randomly and their walking was scored by counting the steps in which they missed the rung momentarily but corrected quickly (miss) or lost their balance before placing the hand correctly (fall). The same random rung pattern was used for all rats. Then, the animals were injured using a single blast wave at ~130 kPa, as in the other group of rats for electrophysiological recordings. Behavioral data collection sessions consisted of 10 crossings on each day of pre- and post-injury periods. The video recordings were analyzed frame-by-frame using VirtualDub software. The number of missed steps and falls were counted for each crossing and used for statistical analysis in IBM SPSS Statistics software.

Rotarod tests. We also performed rotarod performance test as an additional measure to investigate the effect of blast injury on motor function. A set of 12 rats were subjected to pretraining for 3 days twice daily (with 30 min resting period) to acclimate to the testing procedures before exposing the animals to blast injury. During the testing phase, rotarod was set in the accelerated mode with increasing number of revolutions from 4–40 rpm reaching within 90 s (2.5 s intervals for 1 rpm increment). The average time each rat spent on the rotarod during the 3-day pertaining was calculated and the values were statistically validated using nonparametric test to meet non-gaussian distribution to eliminate bias in the distribution of animals (with approximately equal latency times in control and experimental groups) before exposing the animals to blast injury. Rats were then exposed to blast injury and rotarod testing was performed at 24 hours, 3- and 7-days post-injury and results were expressed as mean ± SEM of latency time.

Immunohistochemistry. Three rats Long Evans rats (male, 250–275 g) were subjected to a single blast injury with 130 kPa peak overpressure and animals were euthanized 24 hours post-TBI for the immunological analysis. Three sham control rats of the same size, strain and gender received anesthesia and noise exposure but without blast exposure, i.e. anesthetized animals were placed next to the shock tube on the outside and then a single shot was fired. Following blast injury, animals were monitored closely for any signs of trauma-related distress such as apnea.

Immunofluorescence and microscopy. Twenty-four-hour and 7 days post-injury, both sham and TBI animals (4 animals in each group for 24 h study and 6 animals in each group for 7-day study) were transcardially perfused with PBS followed by 4% paraformaldehyde. Cerebella were dissected and post-fixed in 4% paraformaldehyde (PFA) for additional 48 h and cryoprotected by immersing in 30% sucrose. Fixed cerebellum was vertically cut into two halves and left half of the cerebellum from control or blast animals was embedded in OCT (Optimal Cutting Temperature) in sagittal orientation and quickly frozen in isopentane cooled to liquid nitrogen temperature. 15 μm thick slices were collected 3 mm from the surface of the embedded frozen cerebellum blocks, using Leica CM3050 cryostat and mounted on glass slides. At least 3 sections from each animal cut serially were mounted on each slide. Sections were washed with 10 mM phosphate buffered saline (PBS), fixed in ice-cold methanol (100%) solution for 10 min at −20 °C. The tissue sections were blocked with 10% donkey serum at room temperature for 1 hour in PBS containing 0.03% Triton X-100. Fixed tissues were incubated with anti-calbindin D-28K (rabbit polyclonal, Calbiochem, 1:300) or anti-cleaved caspase-3 (rabbit polyclonal, Millipore Inc, 1:100) overnight at 4 °C, followed by incubation (1 h) with Alexa Fluor 594 secondary antibody. We also performed a double immunostaining of calbindin D-28K (mouse monoclonal, Calbiochem, 1:400) and caspase-3 (Rabbit polyclonal, Millipore 1:100). The tissue was counterstained with DAPI (Invitrogen, Carlsbad, CA) to visualize cellular nuclei and facilitate quantification (cell count).

Image acquisition and analysis. Slides were digitized (40x magnification) using a Leica Aperio Versa 200 fluorescent microscope. For fluorescence intensity quantification, exposure times and grey scale balance were adjusted manually for each channel prior to scanning. Fluorescence intensity of calbindin D-28K cerebellar sections (2–3 in each slide) derived from 3 individual animals/group was quantitated using a FLAreaQuantV1 algorithm (Leica Biosystems) and expressed as average fluorescence intensity per unit area. Briefly, in each image, a minimum intensity threshold value was set that will exclude any background fluorescence caused by nonspecific binding of the fluorescent secondary antibody. This was followed by setting a maximum intensity threshold as

to remove any oversaturation due to excess fluorescent dye. The area quantification algorithm then determines if the intensity value of each pixel within the specified region falls between the minimum and maximum intensity thresholds. The algorithm outputs the area of positive stain for each brain region, the average intensity of each channel, and expression profile of the protein. For visualization of calbindin D-28K and caspase-3 positive cells, ImageJ software (NIH) was used. Briefly, color images were converted to gray scale and different regions of interest (ROIs, 10–15 random areas of approximately 4 mm^2 diameter) were drawn in the paramedian lobe, and the images were thresholded to separate background from particles of interest, in this instance, number of calbindin D-28K and caspase-3 positive particles which different ROIs with varying area were counted, averaged and represented as total number of cells/unit area.

Conclusions

The acute phases of injury were monitored *in vivo* using local field potentials recorded with chronically implanted micro-electrode arrays. The results demonstrate the sensitivity of the electrophysiological measures for detection of cerebellar injuries at levels of blast pressure that are not detectable by behavioral (ladder walking) or immunohistological assays. The two main findings are: First, the largest modulations of the EP amplitudes were seen within the first 24 hours after injury, which was followed by a slower pace of recovery period. Second, blast-wave injury produced differential effects both on the amplitudes and arrival times of the MF and CF mediated components. Taken together, we can conclude that micro EcoG method can identify subtle neurological changes triggered by mTBI conditions.

References

1. Slemmer, J. E., Matser, E. J., De Zeeuw, C. I. & Weber, J. T. Repeated mild injury causes cumulative damage to hippocampal cells. *Brain* **125**, 2699–2709 (2002).
2. Bramlett, H. M. & Dietrich, W. D. Progressive damage after brain and spinal cord injury: pathomechanisms and treatment strategies. *Prog. Brain Res.* **161**, 125–141 (2007).
3. Marklund, N., Bakshi, A., Castelbuono, D. J., Conte, V. & McIntosh, T. K. Evaluation of pharmacological treatment strategies in traumatic brain injury. *Curr. Pharm. Des.* **12**, 1645–1680 (2006).
4. Thompson, H. J. *et al*. Lateral fluid percussion brain injury: a 15-year review and evaluation. *J. Neurotrauma* **22**, 42–75 (2005).
5. Adamaszek, M. *et al*. Consensus Paper: Cerebellum and Emotion. *Cerebellum (London, England)* (2016).
6. Schmahmann, J. D. & Sherman, J. C. The cerebellar cognitive affective syndrome. *Brain: A Journal of Neurology* **121**(Pt 4), 561–579 (1998).
7. Basford, J. R. *et al*. An assessment of gait and balance deficits after traumatic brain injury. *Arch Phys Med Rehabil* **84**, 343–349 (2003).
8. Braga, L. W., Souza, L. N., Najjar, Y. J. & Dellatolas, G. Magnetic resonance imaging (MRI) findings and neuropsychological sequelae in children after severe traumatic brain injury: the role of cerebellar lesion. *Journal of Child Neurology* **22**, 1084–1089 (2007).
9. Kuhtz-Buschbeck, J. P. *et al*. Sensorimotor recovery in children after traumatic brain injury: analyses of gait, gross motor, and fine motor skills. *Developmental Medicine and Child Neurology* **45**, 821–828 (2003).
10. Louis, E. D. *et al*. Delayed-onset cerebellar syndrome. *Archives of Neurology* **53**, 450–454 (1996).
11. Mautes, A. E., Fukuda, K. & Noble, L. J. Cellular response in the cerebellum after midline traumatic brain injury in the rat. *Neuroscience Letters* **214**, 95–98 (1996).
12. Meabon, J. S. *et al*. Repetitive blast exposure in mice and combat veterans causes persistent cerebellar dysfunction. *Science Translational Medicine* **8**, 321ra326 (2016).
13. Miller, D. R., Hayes, J. P., Lafleche, G., Salat, D. H. & Verfaellie, M. White matter abnormalities are associated with overall cognitive status in blast-related mTBI. *Brain Imaging Behav* (2016).
14. Przekwas, A., Somayaji, M. R. & Gupta, R. K. Synaptic Mechanisms of Blast-Induced Brain Injury. *Front. Neurol*., 2 (2016).
15. Taber, K. H. *et al*. White matter compromise in veterans exposed to primary blast forces. *J Head Trauma Rehabil* **30**, E15–25 (2015).
16. Taber, K. H., Warden, D. L. & Hurley, R. A. Blast-Related TraumaticBrain Injury: What Is Known? *JNP* **18**, 141–145 (2006).
17. Hallam, T. M. *et al*. Comparison of behavioral deficits and acute neuronal degeneration in rat lateral fluid percussion and weight-drop brain injury models. *J. Neurotrauma* **21**, 521–539 (2004).
18. Park, E., McKnight, S., Ai, J. & Baker, A. J. Purkinje cell vulnerability to mild and severe forebrain head trauma. *Journal of Neuropathology and Experimental Neurology* **65**, 226–234 (2006).
19. Sato, M., Chang, E., Igarashi, T. & Noble, L. J. Neuronal injury and loss after traumatic brain injury: time course and regional variability. *Brain Res.* **917**, 45–54 (2001).
20. Ai, J. & Baker, A. Presynaptic hyperexcitability at cerebellar synapses in traumatic injury rat. *Neurosci Lett* **332**, 155–158 (2002).
21. DeKosky, S. T., Ikonomovic, M. D. & Gandy, S. Traumatic Brain Injury — Football, Warfare, and Long-Term Effects. *New England Journal of Medicine* **363**, 1293–1296 (2010).
22. Kershman, J., Elvidge, A. & Jasper, H. H. Electroencephalographic studies of injury to the head. *Archives of Neurology & Psychiatry* **328**, 44 (1940).
23. Williams, D. The Electro-encephalogram in acute head injuries. *Journal of Neurology and Psychiatry* **4**, 107–130 (1941).
24. D'Ambrosio, R. *et al*. Progression from frontal-parietal to mesial-temporal epilepsy after fluid percussion injury in the rat. *Brain* **128**, 174–188 (2005).
25. Sanders, M. J., Dietrich, W. D. & Green, E. J. Behavioral, electrophysiological, and histopathological consequences of mild fluid-percussion injury in the rat. *Brain Res* **904**, 141–144 (2001).
26. Witgen, B. M. *et al*. Regional hippocampal alteration associated with cognitive deficit following experimental brain injury: a systems, network and cellular evaluation. *Neuroscience* **133**, 1–15 (2005).
27. Reeves, T. M., Zhu, J., Povlishock, J. T. & Phillips, L. L. The effect of combined fluid percussion and entorhinal cortical lesions on long-term potentiation. *Neuroscience* **77**, 431–444 (1997).
28. Miyazaki, S. *et al*. Enduring suppression of hippocampal long-term potentiation following traumatic brain injury in rat. *Brain Res* **585**, 335–339 (1992).
29. Ai, J. & Baker, A. Presynaptic excitability as a potential target for the treatment of the traumatic cerebellum. *Pharmacology* **71**, 192–198 (2004).
30. Ordek, G., Proddutur, A., Santhakumar, V., Pfister, B. J. & Sahin, M. Electrophysiological monitoring of injury progression in the rat cerebellar cortex. *Frontiers in Systems Neuroscience* **8**, 197 (2014).
31. Watase, K. *et al*. Motor discoordination and increased susceptibility to cerebellar injury in GLAST mutant mice. *Eur J Neurosci* **10**, 976–988 (1998).
32. Culic, M. *et al*. Spectral analysis of cerebellar activity after acute brain injury in anesthetized rats. *Acta neurobiologiae experimentalis* **65**, 11–17 (2005).

33. Thatcher, R. W., Walker, R. A., Gerson, I. & Geisler, F. H. EEG discriminant analyses of mild head trauma. *Electroencephalography and clinical neurophysiology* **73**, 94–106 (1989).
34. Sankar, V. *et al*. Electrode impedance analysis of chronic tungsten microwire neural implants: understanding abiotic vs. biotic contributions. *Frontiers in neuroengineering* **7**, 13 (2014).
35. Liu, X. *et al*. Stability of the interface between neural tissue and chronically implanted intracortical microelectrodes. *IEEE transactions on rehabilitation engineering: a publication of the IEEE Engineering in Medicine and Biology Society* **7**, 315–326 (1999).
36. Polikov, V. S., Tresco, P. A. & Reichert, W. M. Response of brain tissue to chronically implanted neural electrodes. *Journal of neuroscience methods* **148**, 1–18 (2005).
37. Ordek, G., Groth, J. D. & Sahin, M. Differential effects of ketamine/xylazine anesthesia on the cerebral and cerebellar cortical activities in the rat. *Journal of Neurophysiology* **109**, 1435–1443 (2013).
38. Apps, R. & Garwicz, M. Anatomical and physiological foundations of cerebellar information processing. *Nature Reviews Neuroscience* **6**, 297–311 (2005).
39. Dietrichs, E. The cerebellar corticonuclear and nucleocortical projections in the cat as studied with anterograde and retrograde transport of horseradish peroxidase: IV. The paraflocculus. *Experimental Brain Research* **44** (1981).
40. Ji, Z. & Hawkes, R. Topography of purkinje cell compartments and mossy fiber terminal fields in lobules ii and iii of the rat cerebellar cortex: Spinocerebellar and cuneocerebellar projections. *Neuroscience* **61**, 935–954 (1994).
41. Shambes, G. M., Gibson, J. M. & Welker, W. Fractured Somatotopy in Granule Cell Tactile Areas of Rat Cerebellar Hemispheres Revealed by Micromapping; pp. 116–140. *Brain, Behavior and Evolution* **15**, 116–140 (2008).
42. Mehler, W. R. & Nauta, W. J. Connections of the basal ganglia and of the cerebellum. *Confin Neurol* **36**, 205–222 (1974).
43. Oscarsson, O. Functional Organization of Spinocerebellar Paths, In *Somatosensory System*, Vol. 2. (ed. Iggo, A.) 339–380 (Springer Berlin Heidelberg, Berlin, Heidelberg; 1973).
44. Jörntell, H., Ekerot, C., Garwicz, M. & Luo, X. L. Functional organization of climbing fibre projection to the cerebellar anterior lobe of the rat. *The Journal of Physiology* **522**(Pt 2), 297–309 (2000).
45. Zucca, R., Rasmussen, A. & Bengtsson, F. Climbing Fiber Regulation of Spontaneous Purkinje Cell Activity and Cerebellum-Dependent Blink Responses. *eNeuro* **3** (2016).
46. Awwad, H. O. *et al*. Blast Overpressure Waves Induce Transient Anxiety and Regional Changes in Cerebral Glucose Metabolism and Delayed Hyperarousal in Rats. *Frontiers in Neurology* **6** (2015).
47. Myers, P., Wilmington, D., Gallun, F., Henry, J. & Fausti, S. Hearing Impairment and Traumatic Brain Injury among Soldiers: Special Considerations for the Audiologist. *Seminars in Hearing* **30**, 005–027 (2009).
48. Scherer, M. R. & Schubert, M. C. Traumatic Brain Injury and Vestibular Pathology as a Comorbidity After Blast Exposure. *Physical Therapy* **89**, 980–992 (2009).
49. Eccles, J. C., Hubbard, J. I. & Oscarsson, O. Intracellular recording from cells of the ventral spinocerebellar tract. *The Journal of Physiology* **158**, 486–516 (1961).
50. Eccles, J., Llinas, R. & Sasaki, K. Excitation of cerebellar purkinje cells by the climbing fibres. *Nature* **203**, 245–246 (1964).
51. Armstrong, D. M., Harvey, R. J. & Schild, R. F. Climbing fibre pathways from the forelimbs to the paramedian lobule of the cerebellum. *Brain Research* **25**, 199–202 (1971).
52. Armstrong, D. M. & Drew, T. Responses in the posterior lobe of the rat cerebellum to electrical stimulation of cutaneous afferents to the snout. *The Journal of Physiology* **309**, 357–374 (1980).
53. Bengtsson, F. & Jörntell, H. Ketamine and xylazine depress sensory-evoked parallel fiber and climbing fiber responses. *Journal of Neurophysiology* **98**, 1697–1705 (2007).
54. Ding, M.-C., Wang, Q., Lo, E. H. & Stanley, G. B. Cortical excitation and inhibition following focal traumatic brain injury. *J. Neurosci.* **31**, 14085–14094 (2011).
55. Alwis, D. S., Yan, E. B., Morganti-Kossmann, M.-C. & Rajan, R. Sensory cortex underpinnings of traumatic brain injury deficits. *PloS One* **7**, e52169 (2012).
56. Palay, S. L. & Chan-Palay, V. The Purkinje Cell, in *Cerebellar Cortex* 11–62 (Springer Berlin Heidelberg, Berlin, Heidelberg; 1974).
57. Manto, M. *et al*. Consensus Paper: Roles of the Cerebellum in Motor Control—The Diversity of Ideas on Cerebellar Involvement in Movement. *The Cerebellum* **11**, 457–487 (2012).
58. Mauk, M. D., Medina, J. F., Nores, W. L. & Ohyama, T. Cerebellar function: coordination, learning or timing? *Curr. Biol.* **10**, R522–525 (2000).
59. Joyal, C. C. *et al*. Effects of midline and lateral cerebellar lesions on motor coordination and spatial orientation. *Brain Research* **739**, 1–11 (1996).
60. Binion, D. J., Keller, S. B., Ordek, G. & Sahin, M. In Annual Meeting of Biomedical Engineering Society (San Antonio, TX; 2014).
61. Kuriakose, M. *et al*. Tailoring the Blast Exposure Conditions in the Shock Tube for Generating Pure, Primary Shock Waves: The End Plate Facilitates Elimination of Secondary Loading of the Specimen. *PLoS One* **11**, e0161597 (2016).
62. Chandra, N., Sundaramurthy, A. & Gupta, R. K. Validation of Laboratory Animal and Surrogate Human Models in Primary Blast Injury Studies. *Military medicine* **182**, 105–113 (2017).
63. Mishra, V. *et al*. Primary blast causes mild, moderate, severe and lethal TBI with increasing blast overpressures: Experimental rat injury model. *Scientific reports* **6**, 26992 (2016).
64. Skotak, M. *et al*. Rat injury model under controlled field-relevant primary blast conditions: acute response to a wide range of peak overpressures. *Journal of neurotrauma* **30**, 1147–1160 (2013).
65. Watson, T. C. Electrophysiological mapping of novel prefrontal - cerebellar pathways. *Frontiers in Integrative Neuroscience* **3** (2009).
66. Watson, T. C., Becker, N., Apps, R. & Jones, M. W. Back to front: cerebellar connections and interactions with the prefrontal cortex. *Frontiers in Systems Neuroscience* **8** (2014).
67. Van Der Giessen, R. S. *et al*. Role of olivary electrical coupling in cerebellar motor learning. *Neuron* **58**, 599–612 (2008).

Acknowledgements

This study was supported by: 1) New Jersey Commission for Brain Injury Research (grant # CBIR15IRG022, recipient: Me.S.), and 2) U.S. Army Medical Research and Materiel Command (grant # 14059001, recipient: N.C.). The funding agencies had no role in the design and execution of the study, data collection, analysis and interpretation of the data, preparation, review or approval of the manuscript, and decision for publication. We are grateful for the help obtained during blast exposure experiments and imaging from Eren Alay and Daniel Younger, respectively.

Author Contributions

Ma.S. and G.O. carried out blast exposure experiments, G.O. and A.S.A. performed electrophysiological and behavioral tests, E.C., A.S.A. and V.R.K. performed histological evaluation, N.C. and Me.S. designed the study and critically evaluated the data, G.O., A.S.A., Me.S., Ma.S., V.R.K. and N.C. wrote the manuscript, Me.S. supervised the execution the experiments. All authors read and approved the final version of manuscript.

Additional Information

Competing Interests: The authors declare no competing interests.

Publisher's note: Springer Nature remains neutral with regard to jurisdictional claims in published maps and institutional affiliations.

Open Access This article is licensed under a Creative Commons Attribution 4.0 International License, which permits use, sharing, adaptation, distribution and reproduction in any medium or format, as long as you give appropriate credit to the original author(s) and the source, provide a link to the Creative Commons license, and indicate if changes were made. The images or other third party material in this article are included in the article's Creative Commons license, unless indicated otherwise in a credit line to the material. If material is not included in the article's Creative Commons license and your intended use is not permitted by statutory regulation or exceeds the permitted use, you will need to obtain permission directly from the copyright holder. To view a copy of this license, visit http://creativecommons.org/licenses/by/4.0/.

© The Author(s) 2018

Appendix A –Publication Cover 14
2018

Authors: M. Skotak, E. Alay, JQ. Zheng, V. Halls, N. Chandra

Title: *"Effective testing of personal protective equipment in blast loading conditions in shock tube: comparison of three different testing locations"*

Journal Publication: PloS one, 13 (6), e018968**,** (2018), [18-14]

PLOS ONE

RESEARCH ARTICLE

Effective testing of personal protective equipment in blast loading conditions in shock tube: Comparison of three different testing locations

Maciej Skotak[1³] *, Eren Alay[1³], James Q. Zheng[2], Virginia Halls[2], Namas Chandra[1] *

1 Department of Biomedical Engineering, New Jersey Institute of Technology, Newark, NJ, United States of America, **2** Program Executive OfficeÐ Soldier, United States Army, Fort Belvoir, VA, United States of America

[3] MS and EA are joint primary authors on this work.
* maciej.skotak@njit.edu (MS); namas.chandra@njit.edu (NC)

Check for updates

OPEN ACCESS

Citation: Skotak M, Alay E, Zheng JQ, Halls V, Chandra N (2018) Effective testing of personal protective equipment in blast loading conditions in shock tube: Comparison of three different testing locations. PLoS ONE 13(6): e0198968. https://doi.org/10.1371/journal.pone.0198968

Editor: Yih-Kuen Jan, University of Illinois at Urbana-Champaign, UNITED STATES

Received: February 4, 2018

Accepted: May 28, 2018

Published: June 12, 2018

Copyright: This is an open access article, free of all copyright, and may be freely reproduced, distributed, transmitted, modified, built upon, or otherwise used by anyone for any lawful purpose. The work is made available under the Creative Commons CC0 public domain dedication.

Data Availability Statement: All relevant data are within the paper and its Supporting Information files.

Funding: This research was supported by Program Executive Office—Soldier, award no. W91CRB-16-C-0025 to MS and NC.

Competing interests: The authors have declared that no competing interests exist.

Abstract

We exposed a headform instrumented with 10 pressure sensors mounted flush with the surface to a shock wave with three nominal intensities: 70, 140 and 210 kPa. The headform was mounted on a Hybrid III neck, in a rigid configuration to eliminate motion and associated pressure variations. We evaluated the effect of the test location by placing the headform inside, at the end and outside of the shock tube. The shock wave intensity gradually decreases the further it travels in the shock tube and the end effect degrades shock wave characteristics, which makes comparison of the results obtained at three locations a difficult task. To resolve these issues, we developed a simple strategy of data reduction: the respective pressure parameters recorded by headform sensors were divided by their equivalents associated with the incident shock wave. As a result, we obtained a comprehensive set of non-dimensional parameters. These non-dimensional parameters (or amplification factors) allow for direct comparison of pressure waveform characteristic parameters generated by a range of incident shock waves differing in intensity and for the headform located in different locations. Using this approach, we found a correlation function which allows prediction of the peak pressure on the headform that depends only on the peak pressure of the incident shock wave (for specific sensor location on the headform), and itis independent on the headform location. We also found a similar relationship for the rise time. However, for the duration and impulse, comparable correlation functions do not exist. These findings using a headform with simplified geometry are baseline values and address a need for the development of standardized parameters for the evaluation of personal protective equipment (PPE) under shock wave loading.

Introduction

The survival rate among injured warfighters in recent Operation Enduring Freedom and Operation Iraqi Freedom exceeds 90% [1±3]. It is a dramatic improvement among casualty survival compared to previous military conflicts, and it is attributed to advancements in the following areas: 1) battlefield hemorrhage control, 2) far forward trauma surgical and resuscitation techniques, 3) rapid evacuation to higher medical capability facilities and 4) advances in body armor [1, 3]. Among these factors, the impact of the helmet design is not well-established and received relatively little importance as a factor directly implicated in blast mitigation, in spite high prevalence of mild Traumatic Brain Injury among military personnel in the 2000± 2017 period (82.3% as of Aug. 2017) [4]. Traditionally, the perception of the helmet is that it is personal protective equipment (PPE) against the ballistic impact of high-energy projectiles and shrapnel, and thus the blast protection was not considered as top priority until recently [5±8].

The evolution of military ballistic helmets to meet ever increasing demands of the battlefield lead to the development of advanced composite materials which outperform their steel-based counterparts used in the WWI to Vietnam War era [5]. The advent of these contemporary modern designs was possible with the invention of high-performance fiber-reinforced polymer-matrix composites, which allow weight reduction without adverse impact or even improvement of the ballistic performance [5, 9]. Typical mechanical properties of these high-performance polymers are the following: 1) failure strength (2.7±5.6 GPa), 2) axial modulus (60±340 GPa), 3) failure strain (0.011±0.045), and 4) relatively low densities (970±1710 kg/m^3) [10]. The mass-based specific energy absorption capacity is important selection criterion, which favors high molecular weight polyethylene (50±65 kJ/kg) based designs over aramid (25±35 kJ/kg) composites [10, 11]. The ballistic performance of armor materials can be further augmented by preparation of highly ordered structures made of high-performance fibers. Work in this area is relying heavily on the use of numerical [10, 12, 13] and phenomenological models [11, 14].

Evaluation of military helmets under blast loading conditions is still relatively unexplored and developing field. There are no existing field data on the effectiveness of helmets used in the theatre just because of the implementation of the pressure sensors to measure the pressure inside of the helmet is both impractical and technically challenging. Only until recently the surface pressure measurements in active military personnel via deployment of the Blast Gauge™ was realized [15]. Hence, the evaluation of the performance of helmets rests exclusively in the domain of laboratory research. In this context, numerical simulations have dominated the research area thanks to the availability of high-resolution CT and MRI scans, which allow reconstruction of high fidelity 3D computer models with segmentation of specific anatomical details of the human head [16±18].

Typically two related areas of interest are investigated using numerical models: 1) the effects of stress waves propagation in the brain originating from blast wave transmission through the unprotected head [18±20], and 2) the protective properties of helmets [6±8, 21±26] or other PPE designed to mitigate blast effects in the craniofacial area [23]. Numerical simulations are supplemented by experimental data, most often either surface pressure measured on the helmet/head [6, 7, 20], or intracranial pressure [19, 26], to validate the model. Experimental work, which used surrogate anthropometric models, also requires validation via application of surface and intracranial pressure measurements in post-mortem human specimens (PMHSs) [24, 27, 28]. These studies are relatively rare, difficult to execute and impractical for the evaluation of PPE under blast loading conditions. The alternative is to use human head surrogates, which replicate the geometry but are made of non-biological materials [7, 19, 20, 29, 30].

The methodologies for helmet testing in the blunt and ballistic impact are well established, but there are no such tests methodologies available for helmets under blast loading. Shock tubes offer the best mode of testing new and existing helmet designs as means of effective blast protection. However, there are no existing standards for blast testing of helmets, and this work aims to examine the effect of test location on the efficacy of helmet testing. We performed experimental surface pressure mapping on the headform exposed to three blast overpressures at three different locations: inside, end and outside. The goal is to evaluate whether there exists the correlation between four characteristics (peak overpressure, rise time, duration and impulse) of the pressure pulse measured at 10 discrete locations on the headform, and at three test locations. Ultimately, we are seeking the answer to the question whether the comparison between different test setups is possible, or alternative solutions for PPE blast evaluation are necessary. This work is an initial step towards standardization of the PPE testing.

Materials and methods

The shock tube

The square cross section (0.71 x 0.71 m) shock tube was used in all experiments. This device is located at the Shock Wave Testing facility at the Center for Injury Biomechanics, Materials and Medicine (CIBM^3) at the New Jersey Institute of Technology campus. There are four principal components of this shock tube (Fig 1): 1) adjustable volume breech, 2) transition section, 3) the test section including bullet-proof glass observation station for high-speed video monitoring, and 4) the catch tank designed to contain exhaust gases and dissipate the noise (not shown). The catch tank was not used in the exposures where headform was mounted in the outside test location. We used compressed helium (ultra-high purity, 99.99%, Airgas, Oakland, NJ) as driver gas for all experiments. Helium was allowed to flow into the breech separated from the main body of the shock tube with a stack of Mylar membranes (Grafix, Cleveland, OH) until mechanical failure. We used circular Mylar membranes with the standard thickness of 10 mil (1 mil = 0.001 inch) arranged together to the total thickness of 40, 80 and 150 mil, to generate shock waves with three discrete peak overpressures (approximately 70, 140 and 210 kPa) in the test section (T5 sensor, Fig 1). All tests were performed at room temperature.

Pressure measurement, headform preparation, and instrumentation

The overpressure of incident (side-on, static) blast waves was measured using a series of seven high frequency pressure sensors model 134A24 (PCB Piezotronics, Inc., Depew, NY), which were distributed along the shock tube (Fig 1). Incident static pressure on the outside was measured using pencil probe ICP® 137B24B (PCB Piezotronics Inc., Depew, NY). The FOCUS headform [31], was instrumented with 10 PCB Piezotronics (Depew, NY) model 102B06 pressure sensors: five medial sensors, denoted as H1 to H5, are located along midline anterior-posterior in 45Êintervals, and five circumferential sensors mounted in the following order: two on the right parietal side (H6 and H7, in 60Êdegrees intervals), two in both eye sockets (H8 and H9) and one on the left parietal side of the headform (H10, 90Êinterval, Fig 2). These sensors were mounted flush to the surface using tapped holes. The six-axis accelerometer DTS 6DX PRO (Diversified Technical Systems, Seal Beach, CA) was mounted in the center of gravity. A LabView program running on a data acquisition system based on National Instruments PXI-6133 S Series multifunction DAQ modules and PXIe-1082 PCI Express chassis was used to capture the signal. All data were recorded at 1.0 MHz sampling frequency and the typical acquisition time was 50 milliseconds. The signal of pressure sensors was fed through 8-channel signal conditioners PCB 483C05 (PCB Piezotronics Inc., Depew, NY) and did not require additional filtration. The signal from accelerometers was filtered with 9.5 kHz low pass filter.

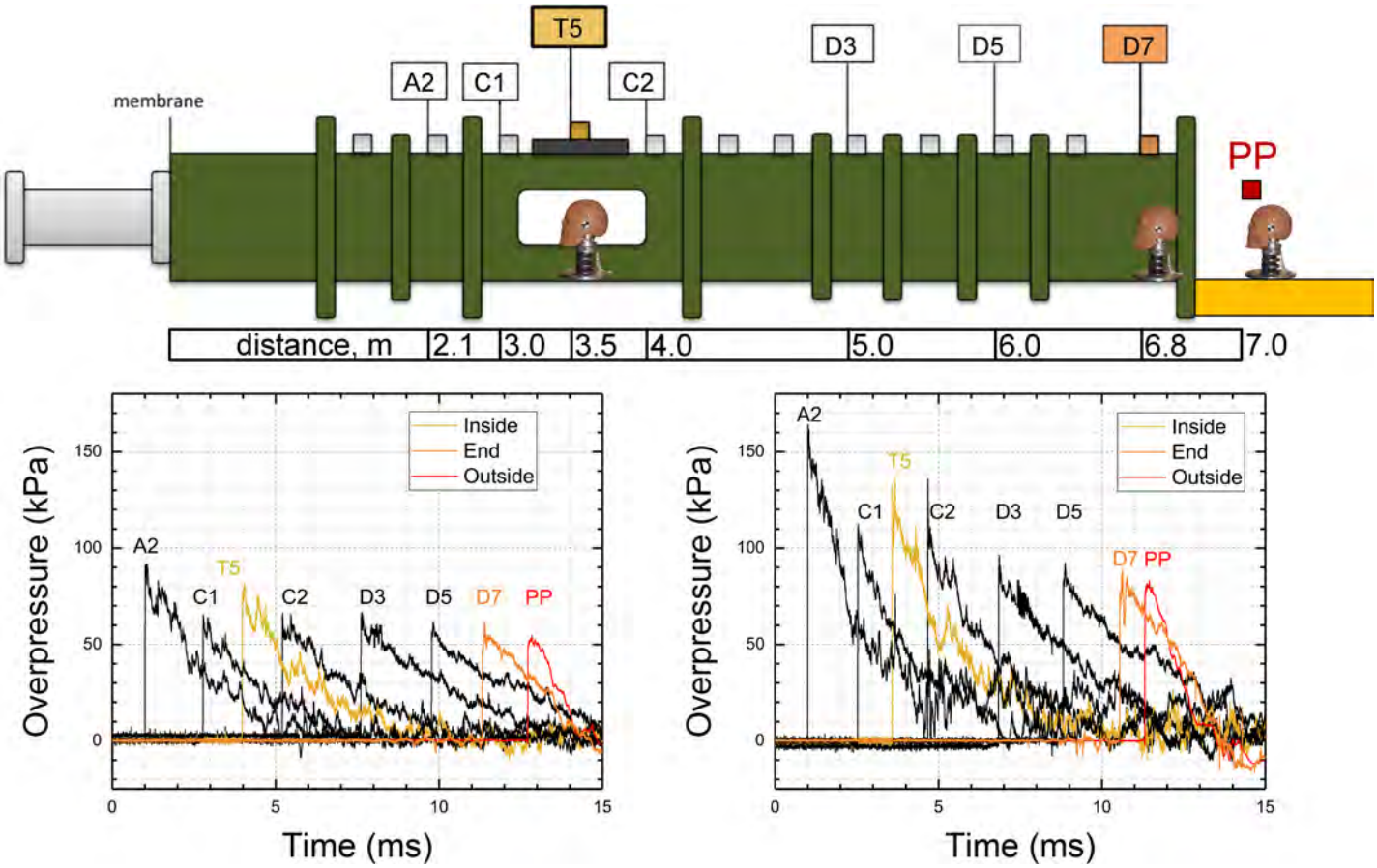


Fig 1. Schematic representation of the 28-inch shock tube illustrating sensor notation and their distribution. The distance between sensors and the membrane mounting port is indicated. The headform was mounted in three different locations: 1) T5 (denoted as [a]Inside[o]), 2) D7 (denoted as [a]End[o]) and 3) PP (denoted as [a]Outside[o]). Bottom panel presents the evolution of the shock wave profile as a function of sensor location for two nominal BOPs of approximately 70 kPa (T5, left) and 140 kPa (T5, right). The arrival times were adjusted for the clarity of presentation. Profiles for T5, D7 and PP locations are highlighted in color.

https://doi.org/10.1371/journal.pone.0198968.g001

The headform was mounted on the Hybrid III neck (Humanetics, Plymouth, MI)[32], in a rigid configuration to eliminate the motion of the headform during shock wave impact. The FOCUS headform-Hybrid III neck the assembly was attached to the adapter plate and bolted to the bottom of the shock tube in the test section in three different locations (Fig 1).

Experimental design

The study was designed as two-factor experimental design, 3 x 3. Two experimental variables investigated in this study are 1) the headform location (three levels: inside, end and outside, Fig 1) and 2) shock wave intensity (three levels: 70, 140 and 210 kPa). The incident blast overpressure was controlled by adjusting the thickness of Mylar membranes sandwiched between the breech and expansion section. The thickness was adjusted by stacking individual membranes with thickness of 10 mil (0.01 inches, or 0.254 mm). All tests were repeated four times (n = 4) per nominal shock wave intensity and headform location.

Data reduction and statistical analysis

All waveforms were imported, processed and quantified in Origin 2017 software (OriginLab Corp., Northampton, MA). Data from experiments performed at different experimental

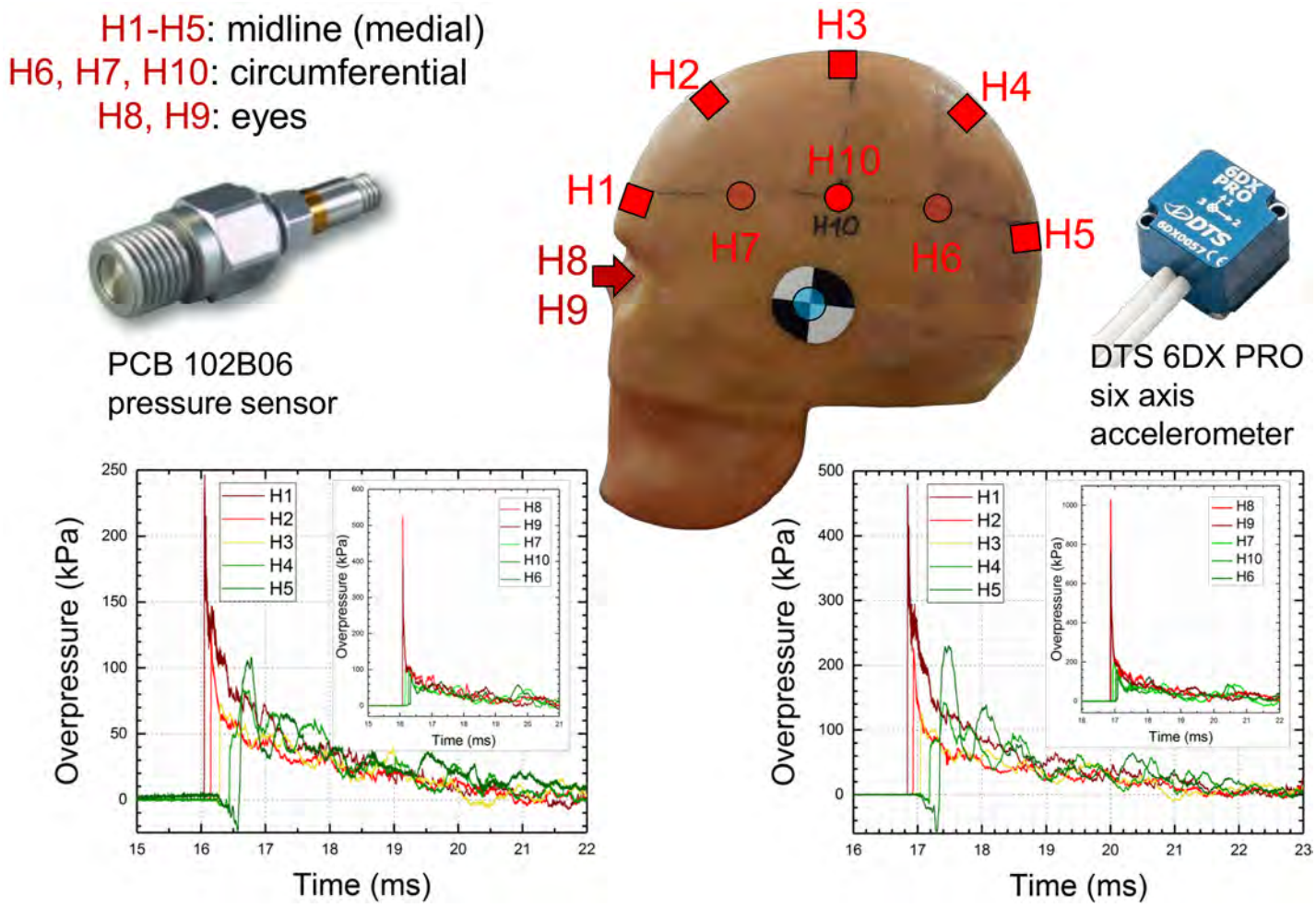


Fig 2. The schematic representation of the headform pressure sensor distribution. The PCB 102B06 sensors were used exclusively: the five medial sensors H1-H5 are mounted at 45 degrees intervals along the midline, while additional sensors are mounted on the circumference: H6, H7 on the right side, H8 and H9 in the eye cavities and H10 on the right side. The DTS 6DX PRO six-axis accelerometer is mounted inside of the headform in the center of gravity. Representative pressure profiles recorded by surface pressure sensors at nominal BOPs of 70 kPa (left, bottom) and 140 kPa (right, bottom) are presented.

https://doi.org/10.1371/journal.pone.0198968.g002

conditions (shock wave intensity and headform location) were pooled together in 3 subsets according to blast intensity (membrane thickness).

The normalization and data reduction procedure were performed as follows. The tabulated values of the four characteristics were divided by their equivalents of the incident shock wave e.g., BOP_{H1} /BOP_{T5} will yield normalized BOP value for the inside of the shock tube (T5 location). Similarly, the normalization was performed for the remaining three parameters: rise time, duration and impulse (Eq 1):

$$x_{non} = \frac{x_p}{x_i} \tag{1}$$

where: x_pÐpeak overpressure, rise time, duration or impulse of the resulting pressure waveform on the headform, x_iÐpeak overpressure, rise time, duration or impulse of the incident shock wave.

Multiple comparison, two-tailed t-test was performed with Bonferroni correction and $p < 0.003$ was considered statistically significant. All data are presented as mean and standard deviation.

Results

Incident shock wave characterization

In the initial phase of this project we had adjusted the breech volume necessary to generate three shockwave intensities approximately 70, 140 and 210 kPa peak overpressure in the test section (T5 sensor, Fig 1). The duration was adjusted to be in the range of 5±7 milliseconds (Fig 1). We tracked the evolution of the shock wave profile using a set of 8 sensors: seven of these sensors were mounted on the shock tube wall (A2 to D7, Fig 1) and a single additional one was a pencil probe and mounted on a platform just 0.14 m (approx. 5.5 inches) outside of the shock tube mouth (denoted as PP in Fig 1).

The velocity of the incident shock wave was measured using arrival times with the A2 sensor as a reference. In these experiments, headform was not present in the test section. For all three nominal shock wave intensities, the shock wave velocities along the shock tube decrease proportionally with the distance from the membrane mounting port and the velocity decay follows linear function (Fig 3). The quality of the linear function fit is excellent in all three cases

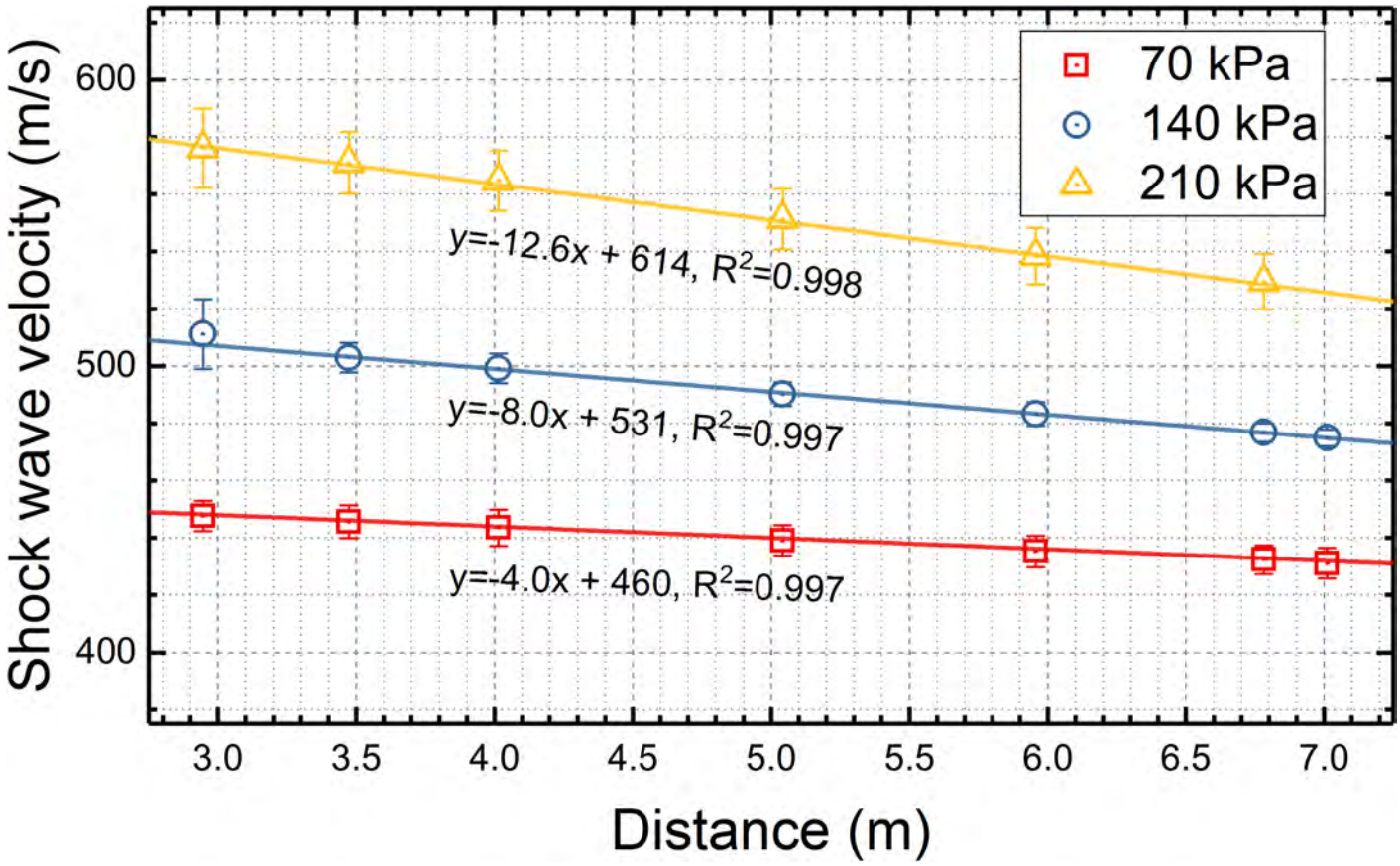


Fig 3. The incident shock wave velocities. The shock wave velocities were calculated at different sensor locations at three discrete BOPs, 70, 140 and 210 kPa, used in this study. Shock wave velocities were averaged for twelve individual measurements, and average values were fitted using the linear function. For a diagram of sensor distribution and dimensions refer to Fig 1.

https://doi.org/10.1371/journal.pone.0198968.g003

based on the R^2 values, which are above 0.99. Velocity at the outside location for 210 kPa nominal shock wave intensity was not measured.

We quantified the four characteristic parameters of the shock wave: peak overpressure, rise time, impulse and duration (Fig 4) to gain insight into their spatiotemporal evolution and to establish a baseline for comparison with pressures reported by sensors mounted on the headform (Fig 2). The peak overpressure decreases in a non-linear fashion in all three shockwave intensities used (Fig 4A). The rise time values are in the 4 to 6 microseconds range for sensors located further away from the exit (from A2 to D3, 2 meters upstream from the exit) independently on the shock wave intensity, but there is a noticeable trend of decreasing rise time with shock wave intensity at any specific location (Fig 4C). At the D5 location (1 meter upstream from the exit) the rise time is significantly increased and this trend continues in D7 and PP locations with where the rise time values are exceeding 7 microseconds (6.8 for 210 kPa BOP).

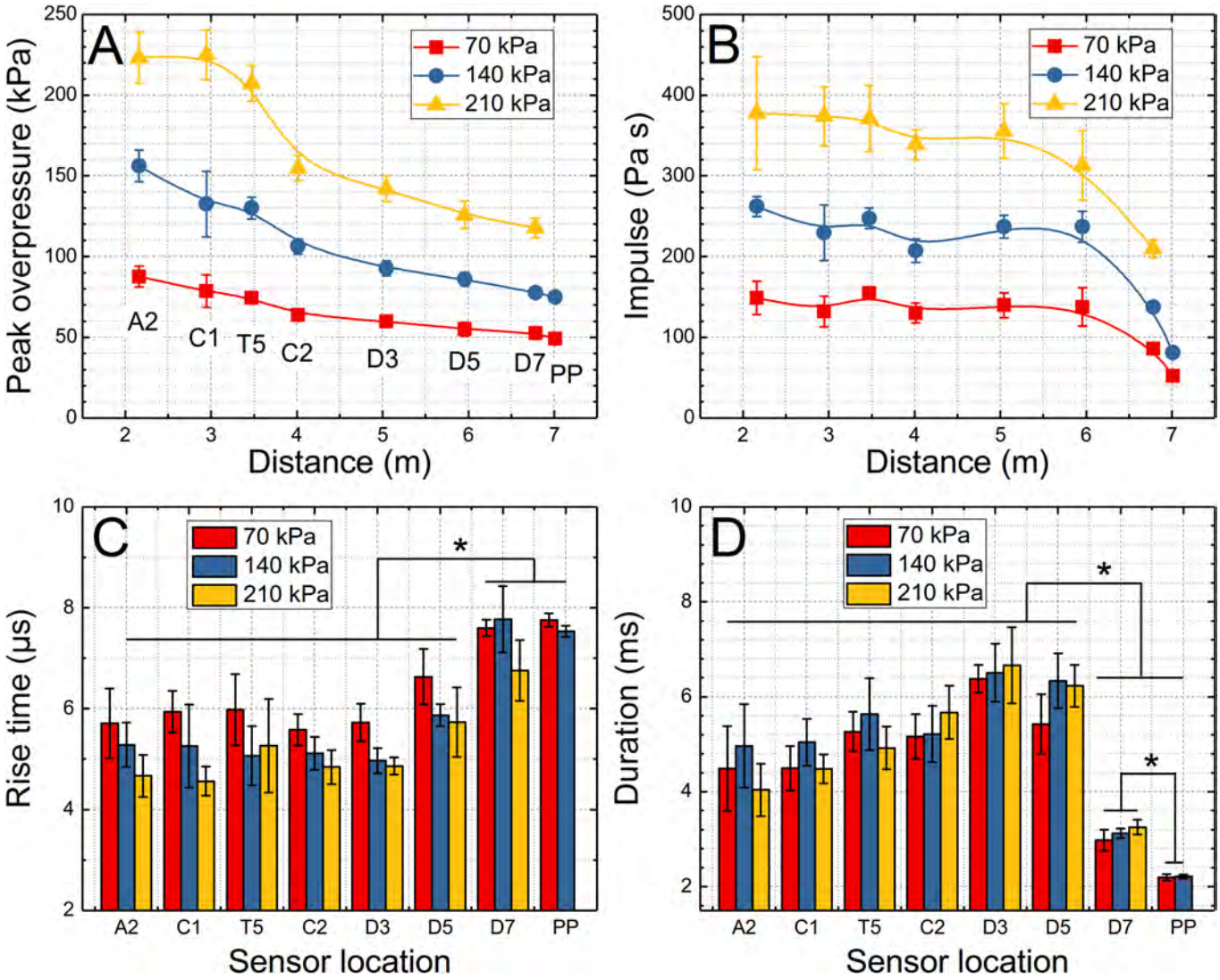


Fig 4. Quantification of four characteristics of the incident shock wave. The peak overpressure (A), impulse (B), rise time (C) and duration (D) for three nominal BOPs used in the experimental design are presented. The evolution of the peak overpressure and impulse values is expressed as a function of sensor distance from the membrane mounting port. The bar plots were used to illustrate the evolution of the rise time and duration as a function of sensor location and BOP. Asterisk indicates the statistical significance exists between respective groups shown in both plots.

https://doi.org/10.1371/journal.pone.0198968.g004

The impulse values remain relatively stable for up to 6 meters from the membrane location (which corresponds to D5 sensor location). At the end (D7) and outside (PP) of the shock tube, the impulse values are severely reduced, which is associated with a reduction of the shock wave duration (Fig 4D). The duration values are initially relatively short, i.e., in the 4±5 ms range for the A2 sensor and gradually increase to reach a maximum value at the D3 location (6.2±6.3 ms range). Then somewhat reduced values can be noticed at the D5 location, which is followed by a severe decrease to 2.8±3 ms (D7) and 2.1 ms on the outside.

Surface pressure on the headform

Representative pressure profiles recorded by the surface sensors mounted on the headform are presented in Fig 2. The sensors located on the front face of the headform (H1, H2) and in the eye sockets (H8, H9) report the highest pressures, irrespectively of the nominal shock wave intensity. Interestingly, the H5 sensor located on the back of the headform records significantly elevated pressures compared to the nominal shock wave intensity. In Fig 5 the results of the surface pressure measurements at various locations on the headform are summarized. We quantified four characteristic parameters of the shock wave: 1) peak overpressure (Fig 5A), 2) rise time (Fig 5B), 3) impulse (Fig 5C), and 4) the duration (Fig 5D). The results in the bar plots are categorized according to the sensor location: 1) eyes (H8 and H9), 2) midline (H1 to H5) and 3) circumference (H6, H7, and H10). Incident shock wave characteristics for all three test locations (inside, end and outside) are also presented. The peak overpressure values vary in the 260 to 540 kPa for eye socket mounted sensors (H8, H9). In general, the headform peak overpressure scales with the peak overpressure of the incident shock wave. For a specific sensor mounted on the headform, the peak overpressure decreases in the order of headform location: inside, end and outside. The rise time for incident shock waves is in the range of 6±8 μs independently on the test location (Fig 5B). The rise time values increase gradually for the midline group: the rise time of the H1 sensor is in the 1±3 μs range, followed by H2 (5±6 μs), H3 (7±8 μs), reaching maximum at H4 (approx. 110 μs) and decreasing somewhat at H5 location (70±90 μs). The eye sensors have the rise times in the range between 8 to 10 μs, while sensors on the circumference report rise times of 6±9 microseconds. The impulse values are the highest for the entire set of pressure sensor locations when the headform was placed in the inside of the shock tube (120±190 Pa·s). In the end and outside locations the impulse values are in the range of 80±160 Pa·s and 40±90 Pa·s, respectively. A similar trend is observed for the duration of the shock wave: inside (3.6±5.4 ms), end (3.0±4.8 ms) and outside (1.3±2.8 ms). Similar trends are true also at higher nominal shock wave intensities (140 kPa and 210 kPa, S2 and S3 Figs, respectively).

Normalized shock wave characteristics

The normalized characteristic parameters for two nominal shockwave intensities and three test locations in the shock tube are presented in Fig 6. The normalization procedure for all four characteristic parameters of the shock wave was described in experimental section.

It is evident from Fig 6 that this transformation allows comparison of results obtained at different locations and wide-range of shock wave intensities. The peak overpressure and rise time (Fig 6A and 6B) show a high level of uniformity, with the exception of eye socket sensors (H8 and H9), which have elevated values in the range of 5.0 to 7.0. The normalized peak overpressure for the H1 sensor is around 3.0, and in the 1.0 to 1.6 range for the remaining sensors, with the exception of H2 and H5 where values from 1.8 to 2.4 are apparent.

The most extensive distribution of values is noticeable for the rise time, which spans from 0.2 (H1) to 35 (H4), but for the majority of sensor locations, these numbers are around 1.0

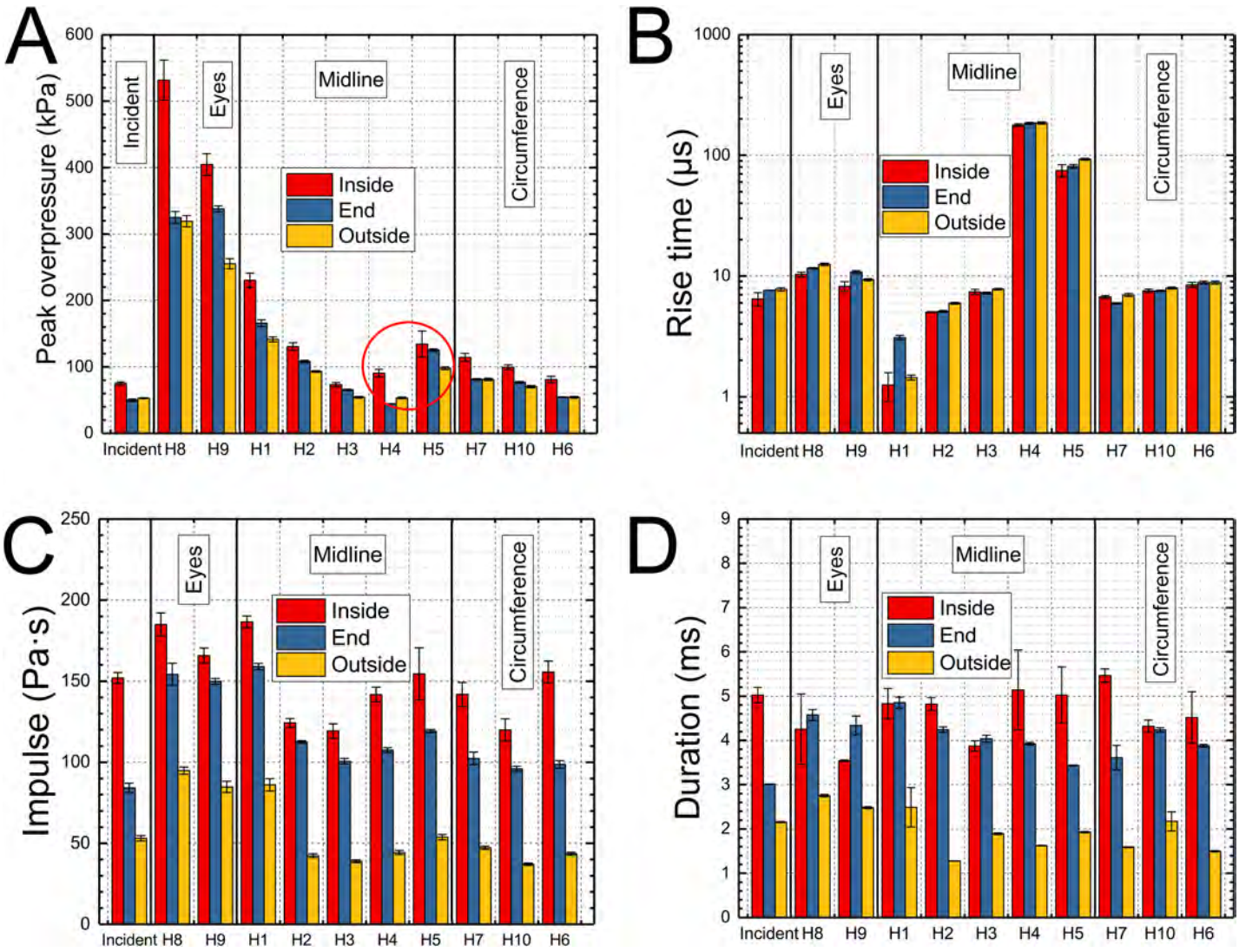


Fig 5. The quantification of four pressure wave characteristics for the headform exposed to at a nominal incident shock wave intensity of 70 kPa. The quantification of peak overpressure (A), rise time (B), impulse (C) and duration (D) recorded for a nominal BOP of 70 kPa. The average values (n = 4) in bar plots were grouped into the four following categories concerning sensor location: incident, eyes (H8 and H9), midline (H1 to H5) and circumference (H6, H7, and H10). For the quantification of the data recorded at 140 and 210 kPa BOPs refer to Supporting information, S2±S5 Figs in the supporting information.

https://doi.org/10.1371/journal.pone.0198968.g005

(Fig 6B). The normalized impulse values for front face sensors (H1, H8, and H9) have values in the range of 1.1±1.4 (Inside), 1.8±2.1 (End) and 1.6±2.0 (Outside). The remaining sensors have the values in the range 0.6 to 1.0 (Inside and End) and 1.1 to 1.5 (End). The normalized duration values for the inside location are within 0.7±1.0 range with the exception of H7 sensor (0.4). For the end location the normalized duration values exceed 1.0, and are in the range from 1.2 to 1.7. Normalized duration values for the outside depends highly on the sensor position on the headform and have the largest variation, i.e., from 0.6 to 1.5. The normalized parameters are called amplification-attenuation factors in Fig 7.

The relationships between the peak overpressure and the rise time as a function of respective surface sensors of the distance along the X-axis on the headform (the nose tip is a reference) is presented in Fig 7. We used fourth order polynomial fit to model these data points, and eye sensor data were excluded from the fit with good results ($R^2 = 0.84$). Similarly, the

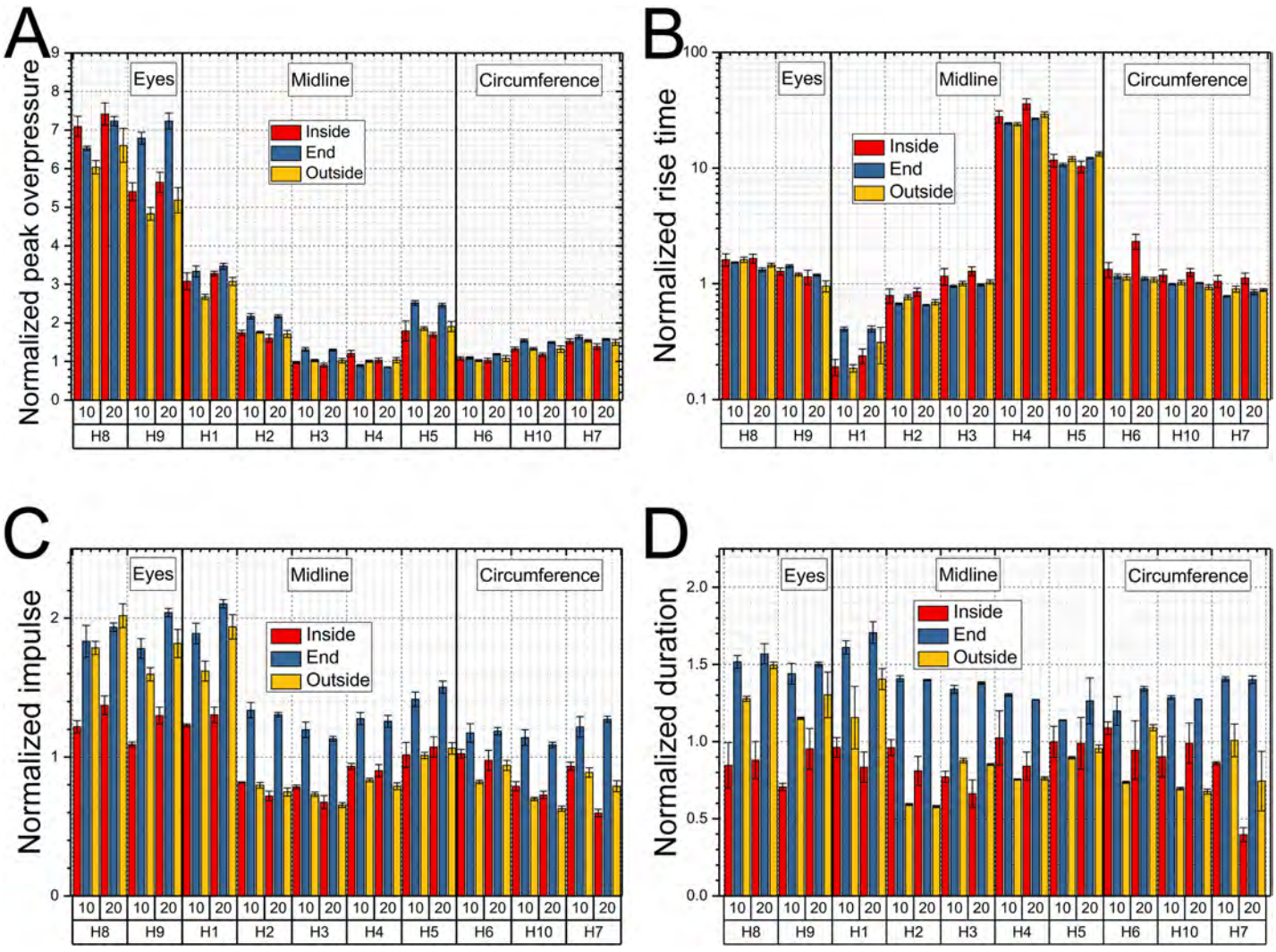


Fig 6. The normalization of the four characteristics of the pressure waveform recorded by headform surface sensors. The bar plots of the normalized peak overpressure (A), rise time (B), impulse (C) and duration (D) for surface pressure profiles recorded at various locations on the headform as a function of shock wave intensity (70 and 140 kPa) and headform location (inside, end and outside). The values for 210 kPa BOP are not included for clarity. The values in bar plots were grouped into the four following categories with respect to sensor location: incident, eyes (H8 and H9), midline (H1 to H5) and circumference (H6, H7 and H10).

https://doi.org/10.1371/journal.pone.0198968.g006

fourth order polynomial fit was used for the rise time and in this case data from both eyes and H4 sensors were excluded from the fit to obtain high fit fidelity ($R^2 = 0.99$). However, the polynomial fit of the other two parameters, impulse, and duration, give unsatisfactory results ($R^2 = 0.42$ and 0.09, for impulse and duration, respectively see S4 and S5 Figs).

Acceleration

The representative linear acceleration profiles are presented in Fig 8A±8C (only X and Z axis profiles are presented for brevity). The quantification of the peak acceleration as a function of shock wave intensity and test location is presented in Fig 8D and 8E. The general trend for peak acceleration measured along both axes is that it increases with nominal shock wave intensity for the inside location ($p < 0.05$). The same is true for the end and outside locations independently on the axis of acceleration, where the nominal intensity of 70 kPa results in the lowest acceleration and these results are statistically significant ($p < 0.05$).

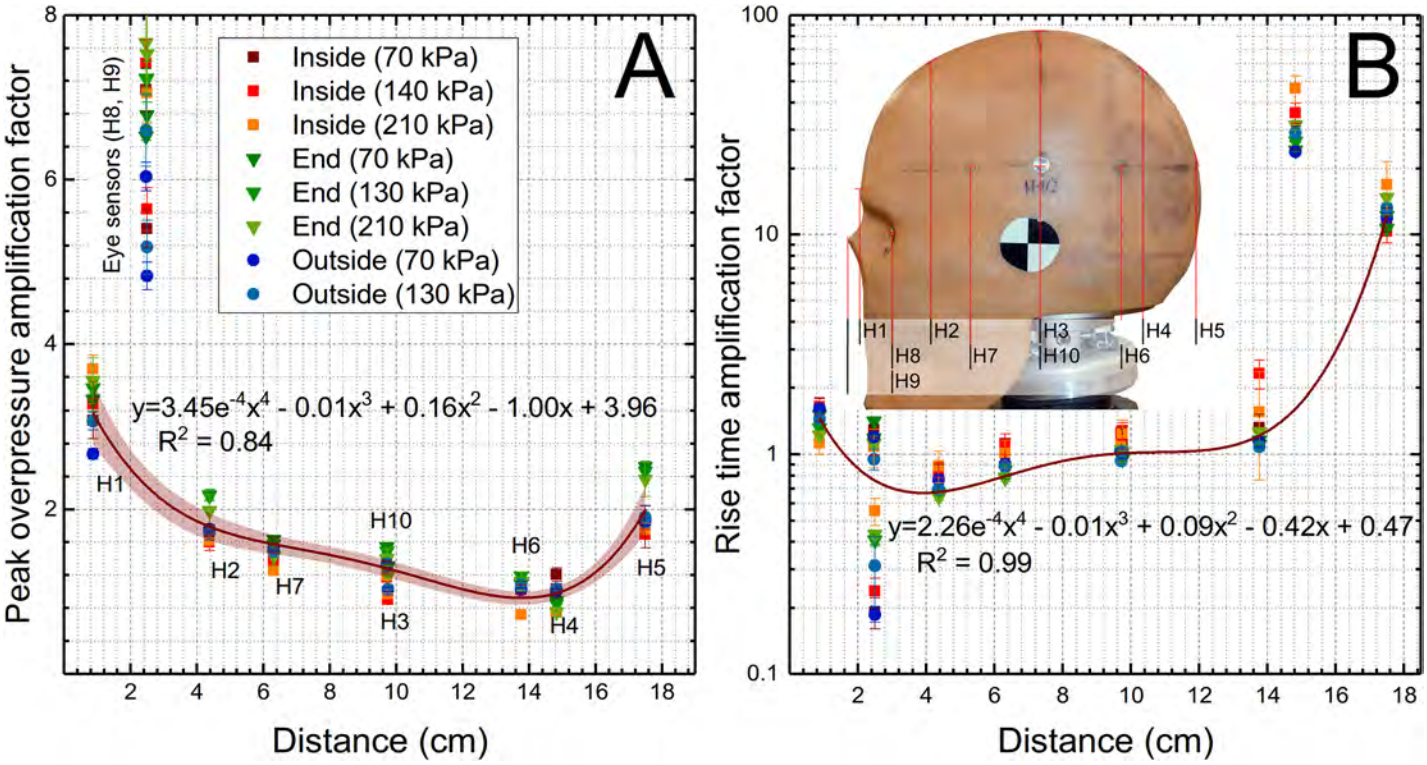


Fig 7. The amplification factors for the peak overpressure and rise time at three nominal shock wave intensities. The plots demonstrating peak overpressure (A) and rise time amplification factors as a function of sensor location along the abscissa of the direction of the shock wave propagation. Normalized values for pressure sensors calculated for measurements performed at 70, 140 and 210 kPa BOPs are presented. Inset: the schematic illustrating the origin and sensor distances used in fits where fourth-degree polynomial functions were used. The H8 and H9 data were excluded from fitting procedure in both cases, while for the rise time the data for H4 sensor were also eliminated.

https://doi.org/10.1371/journal.pone.0198968.g007

The point of peak acceleration is marked with an arrow in Fig 8A±8C. For the inside and end location, the elapsed time to peak acceleration (ETPA) is nearly the same, i.e., in the 0.7± 0.8 range, while for the outside the maximum acceleration is reached after 1.8±2.0 milliseconds (acceleration measured along X-axis, S6A Fig). For the Z-axis acceleration the ETPA is gradually increasing in the order depending on the test location: inside < end < outside (S6B Fig). The ETPA doesn't seem dependent on the nominal intensity of the shock wave.

We evaluated whether the maximum acceleration is a function of shock wave intensity, i.e., peak overpressure and impulse, and the results are presented in Fig 9. It would appear the experimental data follow exponential growth function expressed by the following equation:

$$y = ab^x \quad (2)$$

The values of the goodness of fit parameter, R^2, indicate this function fits the data with higher fidelity where peak overpressure is used as the abscissa, as compared to impulse (R^2 = 0.80 and 0.69, respectively, Fig 9). For the acceleration measured along the Z-axis, the values of these parameters increase to 0.87 and 0.91 (S7 Fig) for peak overpressure and impulse.

Discussion

The motivation of this work is to standardize test parameters for evaluating personal protective equipment (PPE) performance in blast loading conditions. Considering there is no shock tube

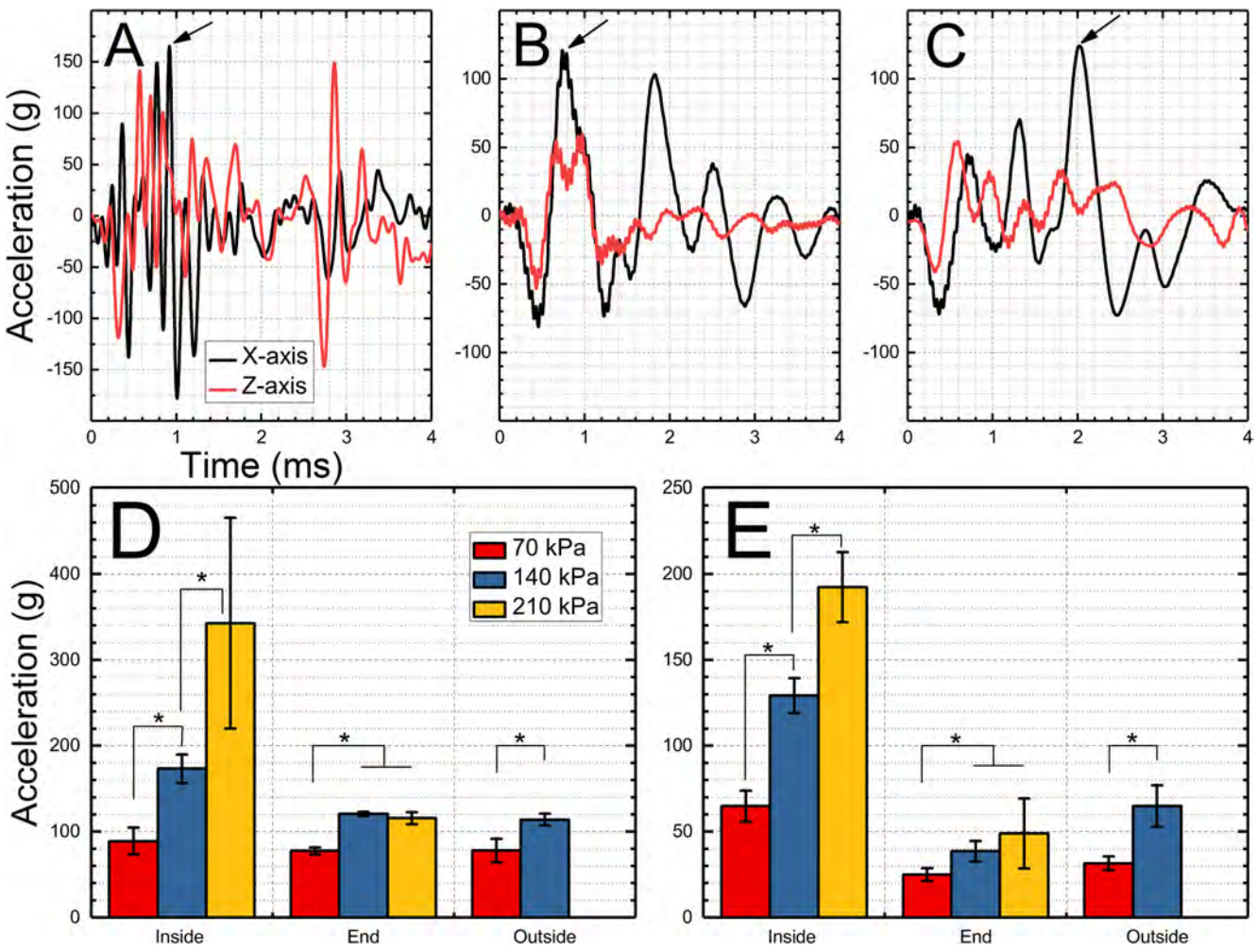


Fig 8. Comparison of the linear acceleration of the headform tested in three different locations. Linear acceleration (X and Z axis) signals for the headform exposed to a 140 kPa nominal intensity shock wave at different locations: A) inside, B) end, and C) outside of the shock tube. The arrival time of the H1 sensor was used as a reference. Quantification of the peak acceleration for the acceleration along the X-axis (D) and Z-axis (E) for three nominal shock wave intensities and three test locations. Asterisk indicates groups with statistical significance threshold $p < 0.05$.

https://doi.org/10.1371/journal.pone.0198968.g008

testing standards a number of approaches are used for this purpose. In the early days, the experimental were frequently performed on the outside or at the end of the shock tube [6, 7, 19, 33]. This approach while not without some merit is a convenience-driven rather than rational design to replicate true field conditions [34, 35], with a possibility of the significant contribution of dynamic loading [36]. The testing of the specimen with the dimensions of the human head requires a broad cross-section shock tube to be employed, which otherwise would result in the pressure artifacts associated with the blockage [36]. However, a literature survey of military PPE evaluation methodologies indicates most of the work in this area relies heavily on numerical simulations evaluating the protective effect of helmets [6, 8, 21, 23, 25, 28, 37] including helmet performance under ballistic impact [10±12]. Numerical simulations are an invaluable tool for to examine mechanistic aspects of blast induced neurotrauma [18], effects of existing and new padding materials [8] and helmet designs [21, 28] on the pressure attenuation and transmission pathways [23, 25], among others. However, their primary limitation from the perspective of quality control of PPE is lack of necessary fidelity when

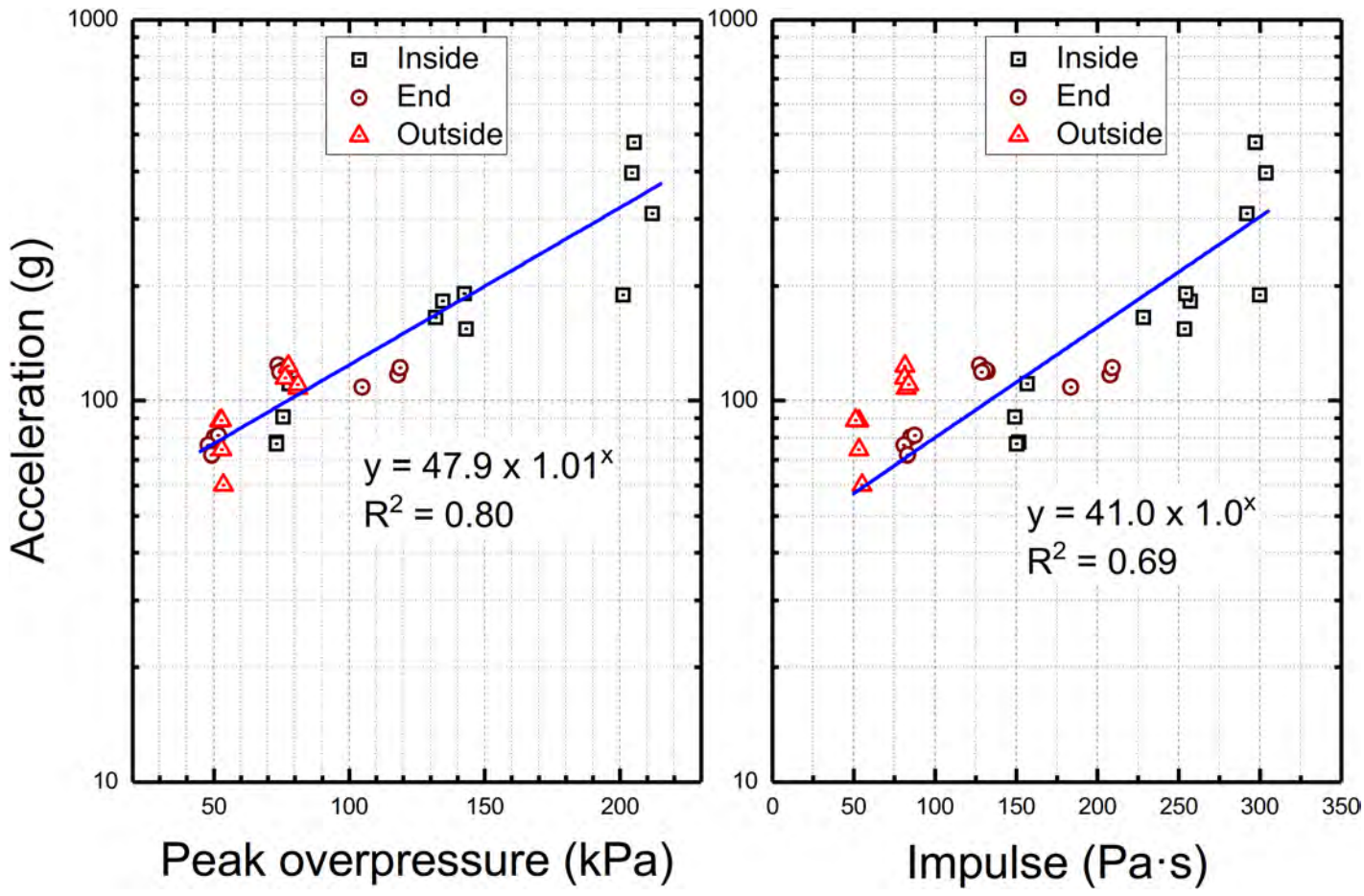


Fig 9. The effect of peak overpressure and impulse on the peak acceleration. The semi-log plots of the peak acceleration as a function of the peak overpressure (left) and impulse (right) measured at the respective test locations. The experimental data points for the Z-axis were fitted using exponential growth function $y = a \cdot b^x$.

https://doi.org/10.1371/journal.pone.0198968.g009

confronted with basic materials imperfections and variability of their properties [38]. It's been also demonstrated that simple tasks like fitting the helmet model with pads to the anthropometric head phantom might pose a substantial challenge during model preparation step [7]. For day-to-day operations in the research facility, it is just impractical and time-consuming, while simultaneously lacking in information about material properties (especially true for proprietary foam designs used in padding materials) and defects leading to the variability of the experimental results. With that in mind, we employed in the initial step of this project a comprehensive characterization of the headform in the shock tube.

The evaluation of the relationship between different test locations was performed using the headform mounted in three different places: inside, at the end and on the outside of the shock tube (Figs 1 and 2). These three test locations are typically used in the laboratory shock wave testing [7, 22, 38±41], but flow fields generated in these places vary significantly [34, 42]. Growing body of evidence suggests outside location is not representative of the field conditions associated with high explosive blast waves [36].

We first evaluated the evolution of the shock wave traveling in the test section and quantified four characteristic parameters: peak overpressure, rise time, duration and impulse (Fig 4). The peak overpressure for all 3 nominal shock wave intensities decreases monotonically, accompanied by declining shock wave velocity (Figs 3A and 4). It is typically observed in the

shock tubes with similar length when a sufficient number of pressure sensors is employed to track the progression of the shock wave [34, 42]. Similarly, the duration of the incident shock wave increases, which is accompanied by a concomitant increase in the rise time However, the shock wave duration is reduced severely by the rarefaction at the exit of the shock tube, while the rise time of the shock front continues to increase even for the outside location. Considering the impulse values are correlated primarily with the duration it is evident that the sharp decrease in impulse values is observed at the end and on the outside.

The experiments with the headform were executed in the next step, which was followed by quantification of the four characteristics of each pressure waveform reported by ten surface mount sensors (Fig 2). The highest peak overpressures are observed for the eye socket sensors and forehead mounted sensor (Figs 2, 5 and 6), which was also reported by others using numerical models [7, 37, 41]. The pressure profiles of all surface sensors closely resembles the incident shock wave profile: there is obvious peak pressure increase for the front face sensors (H1, H8, and H9), but there is also a short underpressure occurring before the shock front for two midline sensors mounted on the back of the headform (H4 and H5) indicating the flow separation region (not reported in earlier studies using this headform [6, 20]). The rise times display relative invariance concerning the headform location, and the larges difference is for the H1 sensor: 1.2 ms (inside), 3 ms (end) and 1.5 ms (outside). However, it is apparent the duration and impulse values are strongly dependent on the test location (Fig 5C and 5D). The same general observations are valid for tests performed at 140 and 210 kPa (S2 and S3 Figs).

It is thus apparent a further data reduction is necessary to compare data collected at three different intensities and three different headform locations. The most intuitive approach is to take the characteristic parameters of the incident shock wave waveform (input) recorded at a specific area, i.e., T5 for inside, D7 for the end and PP for outside position, and compare them with waveforms recorded by pressure sensors on the headform (output). The resulting dimensionless parameters are a measure of the disturbance caused by the introduction of headform into the flow field of the shock wave traveling in the shock tube. The values other than 1 indicate divergence from the incident waveform characteristics at the specific test location, and in the particular position on the headform, compared to the incident shock wave. These can be attributed to geometric factors, changes in shock wave characteristics and presence of additional high velocity flows. We demonstrated the shock wave properties are gradually evolving while traveling in the shock tube (Fig 3), and it is reasonable to expect the similar distribution of non-dimensional parameters as a function of their physical location on the headform.

These non-dimensional parameters become the only defining parameter of the system and depend only on the characteristics of the incident pressure waveform. The non-dimensional parameters (amplification factors) allow for direct comparison of pressure waveform characteristic parameters generated by a range of incident shock waves differing in intensity. With this concept in mind, we performed further data reduction for peak overpressures, rise time, impulse and durations in all datasets (Fig 6). The amplification factors for peak overpressures have relatively narrow distribution and follow clear trend independently on the test location. The first sensor H1 has the highest values in the range of 2.4 to 3.6, which gradually decrease along the headform reaching minimum values of about 1 for the H4 and H6 sensors on the back of the headform, and reaching a value of 2 for the H5 sensor at the very end of the headform. This increase is purely due to combined effect of the shock wave wrapping around the headform and its two streams converging at the back. It is accompanied by increased duration of the rise time for the H5 sensor by a factor of 10 compared to the incident shock wave, which is markedly higher compared to all other sensors, where the rise time amplification factor never exceeds the value of 2. Amplification factors for sensors mounted in the eye sockets are very high (in the range of 5±8), and they do not follow the same trend as the other sensors. The

concave geometry of eye sockets is responsible for the compressed air entrapment and stagnation during shock wave exposure, which results in extreme pressures [7], compared to other locations on the headform. It would appear that both normalized peak overpressures and rise time follow the well-defined trend as a function of the sensor location on the headform (Fig 7). However, the same is not true for the duration and impulse (S4 and S5 Figs), which exhibit robustly test location dependence.

We have also quantified the linear acceleration along the X- and Z-axis (Fig 8). In both instances, the peak acceleration correlates strongly with incident peak overpressure (Fig 9) and follows exponential function (Eq 2). However, the elapsed time to peak acceleration (S6 Fig) is dependent on the test location. The acceleration persists only for short durations of time (~5 ms), and the headform deflection was usually less than 4 degrees, based on the analysis of high-speed video footage. These peak acceleration values are below 5% head injury threshold [43]. Moreover, relatively large acceleration values were observed in spite of the rigid configuration of the Hybrid III neck used in this study, which is caused by the rubber parts, which constitute this neck. We wanted to eliminate the possibility that material properties of the rubber might change during the experiments, which was a definite possibility considering exposure to 210 kPa uncontrollably deflects the headform. The deflection of the headform is fast enough to affect the pressure distribution on the headform, which was obvious during the preliminary phase of our studies (data not shown).

Conclusions

We performed a mapping of the pressure distribution using 10 pressure sensors on the headform exposed to a shock wave with three intensities (70, 140 and 210 kPa) and in three different test locations: inside, end, outside. We demonstrated that peak overpressure on the headform can be predicted with reasonable accuracy based only on the peak overpressure of the incident shock wave and is independent of the headform location. Similarly, the rise time can be calculated based solely on the rise time of the incident shock wave. The analysis of the duration and impulse amplification factors indicates these two parameters do not follow simple relationships and their values strongly depend on the test location. Notably, the end location divergence compared to other data is noticeable and consistent across all three shock wave intensities used in this study. A simplified headform model used in this study is suitable for mapping accurately the surface pressure field, which is a critical step to establish a baseline values for evaluation of PPE efficiency. The extension of this work, which is currently in progress, will include evaluation of blast mitigation of currently existing designs of combat helmets, and the development of corresponding numerical models.

Supporting information

S1 Fig. Details of the headform instrumentation with PCB 102B06 pressure sensors.
(PNG)

S2 Fig. Quantification results of the peak overpressure for 10 pressure sensors mounted on the headform and exposed to shock wave with nominal BOP of 140 kPa (approx. 20 psi). Tests were performed at three locations: inside, end and outside of the shock tube.
(PNG)

S3 Fig. Quantification results of the peak overpressure, rise time, impulse and duration for 10 pressure sensors mounted on the headform and exposed to shock wave with nominal BOP of 210 kPa (approx. 30 psi). Tests were performed at two locations: inside and the end

of the shock tube.
(PNG)

S4 Fig. The impulse amplification factor as a function of sensor location along abscissa of the direction of the shock wave propagation (see Fig 7 for details). Normalized values for pressure sensors calculated for measurements performed at 70, 140 and 210 kPa BOPs are presented. All data points are included in the fit.
(PNG)

S5 Fig. The duration amplification factor as a function of sensor location along abscissa of the direction of the shock wave propagation (see Fig 7 for details). Normalized values for pressure sensors calculated for measurements performed at 70, 140 and 210 kPa BOPs are presented. All data points are included in the fit.
(PNG)

S6 Fig. Elapsed time to peak acceleration along the X-axis (A) and Z-axis (B) as a function of nominal shock wave intensity and test location (inside, end and outside).
(PNG)

S7 Fig. The semi-log plots of the peak acceleration as a function of the peak overpressure (left) and impulse (right) measured at the respective test locations. The experimental data points for the Z-axis were fitted using exponential growth function $y = a \cdot b^x$.
(PNG)

Acknowledgments

This work was supported by PEO Soldier award no. W91CRB-16-C-0025 (PEO Soldier). Help received during shock tube experiments from lab members is gratefully acknowledged.

Author Contributions

Conceptualization: Maciej Skotak, James Q. Zheng, Virginia Halls, Namas Chandra.

Data curation: Maciej Skotak, Eren Alay.

Formal analysis: Maciej Skotak, Eren Alay.

Funding acquisition: Namas Chandra.

Investigation: Maciej Skotak, Eren Alay.

Methodology: Eren Alay, James Q. Zheng, Virginia Halls, Namas Chandra.

Project administration: Maciej Skotak.

Supervision: Maciej Skotak, Namas Chandra.

Writing ± original draft: Maciej Skotak.

Writing ± review & editing: Maciej Skotak, James Q. Zheng, Virginia Halls, Namas Chandra.

References

1. Gawande A. Casualties of warÐmili tary care for the wounded from Iraq and Afghanistan. N Engl J Med. 2004; 351(24):2471±5. Epub 2004/12/14. https://doi.org/10.1056/NEJMp048317 PMID: 15590948.
2. Bosco MA, Murphy JL, Clark ME. Chronic pain and traumatic brain injury in OEF/OIF service members and Veterans. Headache. 2013; 53(9):1518±22. Epub 2013/07/16. https://doi.org/10.1111/head.12172 PMID: 23848062.

3. Buckenmaier CC, 3rd, Brandon-Edwards H, Borden D Jr., Wright J. Treating pain on the battlefield: a warrior's perspective. Curr Pain Headache Rep. 2010; 14(1):1±7. Epub 2010/04/29. https://doi.org/10.1007/s11916-009-0090-1 PMID: 20425208.
4. DoD Worldwide Numbers for TBI Aug. 2017 [updated 06-04-2017]. Available from: http://dvbic.dcoe.mil/dod-worldwide-numbers-tbi.
5. Kulkarni SG, Gao XL, Horner SE, Zheng JQ, David NV. Ballistic helmets±Their design, materials, and performance against traumatic brain injury. Composite Structures. 2013; 101(Supplement C):313±31. https://doi.org/10.1016/j.compstruct.2013.02.014.
6. Ganpule S, Gu L, Alai A, Chandra N. Role of helmet in the mechanics of shock wave propagation under blast loading conditions. Computer Methods in Biomechanics and Biomedical Engineering. 2012; 15 (11):1233±44. https://doi.org/10.1080/10255842.2011.597353 PMID: 21806412
7. Przekwas A, Tan XG, Harrand V, Reeves D, Chen ZJ, K. S, et al. Integrated Experimental and Computational Framework for the Development and Validation of Blast Wave Brain Biomechanics and Helmet Protection. Proc HFM-207 NATO Symposium on a Survey of Blast Injury Across the Full Landscape of Military Science; Oct. 3±5, 2011; Halifax NS, Canada2011. p. 34±1±43±20.
8. Grujicic M, Bell WC, Pandurangan B, He T. Blast-wave impact-mitigation capability of polyurea when used as helmet suspension-pad material. Materials & Design. 2010; 31(9):4050±65. https://doi.org/10.1016/j.matdes.2010.05.002.
9. Walsh SM, Scott RR, Spagnuolo DM. The Development of a Hybrid Thermoplastic Ballistic Material with Application to Helmets. Army Research Laboratory, Adelphi, MD: 2005 Contract No.: ARL-TR-3700.
10. Grujicic M, Glomski PS, He T, Arakere G, Bell WC, Cheeseman BA. Material Modeling and Ballistic-Resistance Analysis of Armor-Grade Composites Reinforced with High-Performance Fibers. Journal of Materials Engineering and Performance. 2009; 18(9):1169±82. https://doi.org/10.1007/s11665-009-9370-5
11. Karthikeyan K, Russell B, Fleck N, Wadley H, Deshpande V. The effect of shear strength on the ballistic response of laminated composite plates. European Journal of Mechanics-A/Solids. 2013; 42:35±53.
12. Grujicic M, Glomski P, Pandurangan B, Bell W, Yen C, Cheeseman B. Multi-length scale computational derivation of Kevlar® yarn-level material model. Journal of materials science. 2011; 46(14):4787±802.
13. Palta E, Fang H, Weggel DC. Finite element analysis of the Advanced Combat Helmet under various ballistic impacts. International Journal of Impact Engineering. 2018; 112(Supplement C):125±43. https://doi.org/10.1016/j.ijimpeng.2017.10.010.
14. Jacobs MJN, Van Dingenen JLJ. Ballistic protection mechanisms in personal armour. Journal of Materials Science. 2001; 36(13):3137±42. https://doi.org/10.1023/a:1017922000090
15. Ostertag MH, Kenyon M, Borkholder DA, Lee G, da Silva U, Kamimori G, editors. The Blast Gauge™ System as a Research Tool to Quantify Blast Overpressure in Complex Environments. ASME 2013 International Mechanical Engineering Congress and Exposition; 2013: American Society of Mechanical Engineers.
16. Makris N, Angelone L, Tulloch S, Sorg S, Kaiser J, Kennedy D, et al. MRI-based anatomical model of the human head for specific absorption rate mapping. Medical & biological engineering & computing. 2008; 46(12):1239±51. doi: 10.1007/s11517-008-0414-z. PMC2828153. PMID: 18985401
17. Chen Y, Ostoja-Starzewski M. MRI-based finite element modeling of head trauma: spherically focusing shear waves. Acta Mechanica. 2010; 213(1):155±67. https://doi.org/10.1007/s00707-009-0274-0
18. Moore DF, Jérusalem A, Nyein M, Noels L, Jaffee MS, Radovitzky RA. Computational biologyÐm odeling of primary blast effects on the central nervous system. Neuroimage. 2009; 47:T10±T20. https://doi.org/10.1016/j.neuroimage.2009.02.019 PMID: 19248833
19. Roberts J, Harrigan T, Ward E, Taylor T, Annett M, Merkle A. Human head±neck computational model for assessing blast injury. Journal of biomechanics. 2012; 45(16):2899±906. https://doi.org/10.1016/j.jbiomech.2012.07.027 PMID: 23010219
20. Ganpule S, Alai A, Plougonven E, Chandra N. Mechanics of blast loading on the head models in the study of traumatic brain injury using experimental and computational approaches. Biomechanics and modeling in mechanobiology. 2013; 12(3):511±31. https://doi.org/10.1007/s10237-012-0421-8 PMID: 22832705
21. Grujicic M, Bell WC, Pandurangan B, Glomski PS. Fluid/Structure Interaction Computational Investigation of Blast-Wave Mitigation Efficacy of the Advanced Combat Helmet. Journal of Materials Engineering and Performance. 2010; 20(6):877±93. https://doi.org/10.1007/s11665-010-9724-z
22. Merkle AC, Wing ID, Roberts JC. Human Surrogate Head Response to Dynamic Overpressure Loading in Protected and Unprotected Conditions. In: Herold KE, Vossoughi J, Bentley WE, editors. 26th

Southern Biomedical Engineering Conference SBEC 2010, April 30ÐMay 2, 2010, College Park, Maryland, USA. Berlin, Heidelberg: Springer Berlin Heidelberg; 2010. p. 22±5.

23. Nyein MK, Jason AM, Yu L, Pita CM, Joannopoulos JD, Moore DF, et al. In silico investigation of intracranial blast mitigation with relevance to military traumatic brain injury. Proceedings of the National Academy of Sciences. 2010; 107(48):20703±8.

24. Ott K, Voo L, Merkle A, Iwaskiw A, Wickwire A, Wester B, et al., editors. Experimental Determination of Pressure Wave Transmission to the Brain During Head-Neck Blast Tests. Proceedings of the ASME 2013 Summer Bioengineering Conference 2013 June 26±29, 2013; Sunriver, Oregon, USA. Volume 1A: Abdominal Aortic Aneurysms; Active and Reactive Soft Matter; Atherosclerosis; BioFluid Mechanics; Education; Biotransport Phenomena; Bone, Joint and Spine Mechanics; Brain Injury; Cardiac Mechanics; Cardiovascular Devices, Fluids and Imaging; Cartilage and Disc Mechanics; Cell and Tissue Engineering; Cerebral Aneurysms; Computational Biofluid Dynamics; Device Design, Human Dynamics, and Rehabilitation; Drug Delivery and Disease Treatment; Engineered Cellular Environments.

25. Zhang L, Makwana R, Sharma S. Brain response to primary blast wave using validated finite element models of human head and advanced combat helmet. Frontiers in neurology. 2013; 4.

26. Grujicic M, Ramaswami S, Snipes J, Dudt P. Potential improvement in helmet blast-protection via the use of a polyurea external coating: Combined experimental/computational analyses. Proceedings of the Institution of Mechanical Engineers, Part L: Journal of Materials: Design and Applications. 0 (0):1464420716644472. 10.1177/1464420716644472.

27. Ouellet S, Bir C, Bouamoul A. Direct comparison of the primary blast response of a physical head model with post-mortem human subjects. Defence Research and Development Canada-Valcartier Research Center Quebec, QC Canada, 2014.

28. Ganpule S, Salzar R, Perry B, Chandra N. Role of helmets in blast mitigation: insights from experiments on PMHS surrogate. International Journal of Experimental and Computational Biomechanics. 2016; 4 (1):13±31. https://doi.org/10.1504/ijecb.2016.081745

29. Zhu F, Wagner C, Dal Cengio Leonardi A, Jin X, VandeVord P, Chou C, et al. Using a gel/plastic surrogate to study the biomechanical response of the head under air shock loading: a combined experimental and numerical investigation. Biomechanics and Modeling in Mechanobiology. 2012; 11(3):341±53. https://doi.org/10.1007/s10237-011-0314-2 PMID: 21590345

30. Banton R, Piehler T, Zander N, Benjamin R, Duckworth J. Comparison of Numerical Simulations with Experiments of Blast-Induced Pressure Wave Impact on a Surrogate Head Model. In: Kimberley J, Lamberson L, Mates S, editors. Dynamic Behavior of Materials, Volume 1: Proceedings of the 2017 Annual Conference on Experimental and Applied Mechanics. Cham: Springer International Publishing; 2018. p. 181±7.

31. Crowley JS, Brozoski FT, Duma SM, Kennedy EA. Development of the facial and ocular countermeasures safety (FOCUS) headform. Aviation, space, and environmental medicine. 2009; 80(9):831-. PMID: 19750883

32. Foster JK, Kortge JO, Wolanin MJ. Hybrid III-A Biomechanically-Based Crash Test Dummy. SAE International; 1977.

33. Thielen P, Mehoke T, Gleason J, Iwaskiw A, Paulson J, Merkle A, et al. Exploration of the molecular basis of blast injury in a biofidelic model of traumatic brain injury. Shock Waves. 2017. https://doi.org/10.1007/s00193-017-0769-x

34. Alay E, Skotak M, Misistia A, Chandra N. Dynamic loads on human and animal surrogates at different test locations in compressed-gas-driven shock tubes. Shock Waves. 2017. https://doi.org/10.1007/s00193-017-0762-4

35. Chandra N, Sundaramurthy A, Gupta RK. Validation of Laboratory Animal and Surrogate Human Models in Primary Blast Injury Studies. Military Medicine. 2017; 182:105±13. https://doi.org/10.7205/MILMED-D-16-00144 PMID: 28291460.

36. Needham CE, Ritzel D, Rule GT, Wiri S, Young L. Blast Testing Issues and TBI: Experimental Models That Lead to Wrong Conclusions. Frontiers in Neurology. 2015; 6(72). https://doi.org/10.3389/fneur.2015.00072 PMID: 25904891

37. Tan LB, Chew FS, Tse KM, Chye Tan VB, Lee HP. Impact of complex blast waves on the human head: a computational study. International Journal for Numerical Methods in Biomedical Engineering. 2014; 30(12):1476±505. https://doi.org/10.1002/cnm.2668 PMID: 25132676

38. Tan X, Przekwas AJ, Long JB, editors. Validations of Virtual Animal Model for Investigation of Shock/Blast Wave TBI. ASME 2013 International Mechanical Engineering Congress and Exposition; 2013: American Society of Mechanical Engineers.

39. Shridharani JK, Wood GW, Panzer MB, Capehart BP, Nyein MK, Radovitzky RA, et al. Porcine head response to blast. Frontiers in neurology. 2012; 3.

40. Iwaskiw AS, Ott KA, Armiger RS, Wickwire AC, Alphonse VD, Voo LM, et al. The measurement of intracranial pressure and brain displacement due to short-duration dynamic overpressure loading. Shock Waves. 2017. https://doi.org/10.1007/s00193-017-0759-z

41. Tan XG, Przekwas AJ, Gupta RK. Computational modeling of blast wave interaction with a human body and assessment of traumatic brain injury. Shock Waves. 2017. https://doi.org/10.1007/s00193-017-0740-x

42. Kuriakose M, Skotak M, Misistia A, Kahali S, Sundaramurthy A, Chandra N. Tailoring the Blast Exposure Conditions in the Shock Tube for Generating Pure, Primary Shock Waves: The End Plate Facilitates Elimination of Secondary Loading of the Specimen. PLoS One. 2016; 11(9):e0161597. https://doi.org/10.1371/journal.pone.0161597 PMID: 27603017; PubMed Central PMCID: PMCPMC5014318.

43. Marjoux D, Baumgartner D, Deck C, Willinger R. Head injury prediction capability of the HIC, HIP, SIMon and ULP criteria. Accid Anal Prev. 2008; 40(3):1135±48. Epub 2008/05/08. https://doi.org/10.1016/j.aap.2007.12.006 PMID: 18460382.

Appendix A –Publication Cover 15
2018

Authors: M. Skotak, E. Alay, N. Chandra

Title: "*On the accurate determination of shock wave time-pressure profile in the experimental models of blast induced neurotrauma*"

Journal Publication: Frontiers in Neurology, 9, 52, (2018), [18-15]

frontiers in Neurology

ORIGINAL RESEARCH
published: 06 February 2018
doi: 10.3389/fneur.2018.00052

On the Accurate Determination of Shock Wave Time-Pressure Profile in the Experimental Models of Blast-Induced Neurotrauma

*Maciej Skotak, Eren Alay and Namas Chandra**

Department of Biomedical Engineering, New Jersey Institute of Technology, Newark, NJ, United States

Measurement issues leading to the acquisition of artifact-free shock wave pressure-time profiles are discussed. We address the importance of in-house sensor calibration and data acquisition sampling rate. Sensor calibration takes into account possible differences between calibration methodology in a manufacturing facility, and those used in the specific laboratory. We found in-house calibration factors of brand new sensors differ by less than 10% from their manufacturer supplied data. Larger differences were noticeable for sensors that have been used for hundreds of experiments and were as high as 30% for sensors close to the end of their useful lifetime. These observations were despite the fact that typical overpressures in our experiments do not exceed 50 psi for sensors that are rated at 1,000 psi maximum pressure. We demonstrate that sampling rate of 1,000 kHz is necessary to capture the correct rise time values, but there were no statistically significant differences between peak overpressure and impulse values for low-intensity shock waves (Mach number <2) at lower rates. We discuss two sources of experimental errors originating from mechanical vibration and electromagnetic interference on the quality of a waveform recorded using state-of-the-art high-frequency pressure sensors. The implementation of preventive measures, pressure acquisition artifacts, and data interpretation with examples, are provided in this paper that will help the community at large to avoid these mistakes. In order to facilitate inter-laboratory data comparison, common reporting standards should be developed by the blast TBI research community. We noticed the majority of published literature on the subject limits reporting to peak overpressure; with much less attention directed toward other important parameters, i.e., duration, impulse, and dynamic pressure. These parameters should be included as a mandatory requirement in publications so the results can be properly compared with others.

Keywords: shock wave, shock tube, peak overpressure, impulse, sampling frequency, electrostatic charges, baseline drift

OPEN ACCESS

Edited by:
Kevin K. W. Wang,
University of Florida, United States

Reviewed by:
Karin A. Rafaels,
Army Research Laboratory, United States
Eugene Golanov,
Houston Methodist Hospital, United States

***Correspondence:**
Namas Chandra
namas.chandra@njit.edu

Specialty section:
This article was submitted to Neurotrauma, a section of the journal Frontiers in Neurology

Received: *03 June 2017*
Accepted: *19 January 2018*
Published: *06 February 2018*

Citation:
Skotak M, Alay E and Chandra N (2018) On the Accurate Determination of Shock Wave Time-Pressure Profile in the Experimental Models of Blast-Induced Neurotrauma. Front. Neurol. 9:52. doi: 10.3389/fneur.2018.00052

INTRODUCTION

The blast-induced traumatic brain injury (bTBI) is a signature "invisible wound" among active military personnel partaking in war theaters in Iraq and Afghanistan (1–3). Specifically, the mild TBI (mTBI) remains an important public health problem: 2000–2016 period, the Department of Defense reported more than 360,000 cases of combat- and non-combat-related head injuries of which 82.4%

were mTBI (4, 5). A recent analysis of literature related to studies performed on veterans returning from deployment indicates the "at least half of the TBIs related to the wars in Iraq and Afghanistan appears to be blast related" (6). Human studies provide an array of health outcomes associated with mTBI, ranging from anxiety, depression, post-traumatic stress disorder, and post-concussive symptoms (7), but it is difficult to correlate precisely these symptoms with exposure to blast without knowledge about levels and frequency of exposure. This situation was partially ameliorated by the deployment of Blast Gauge™ system (8), which aids in the retrieval of this crucial information about overpressure "dosage" (a waveform exceeding the predefined threshold is recorded with 100 kHz sampling frequency) and in turn, allows reconstruction of specific incidents involving blasts (9). A large amount of collected data, issues with data interpretation and lack of associated medical history has inhibited the development of correlations between exposure levels with outcomes (10).

Animal models are, thus used to gain an insight into etiology of brain trauma and to study underlying molecular mechanism. The success of these studies in bTBI research area relies on a number of factors, and the two chief ones are: (1) appropriate exposure condition, equivalent to those experienced in the field and (2) proper animal restraint to eliminate injuries other than those classified as primary bTBI (exposure to shock wave only) (11, 12). In the laboratory setting, the shock tubes are used to re-create bTBI etiology in animal models (13–15). The importance of animal location on the characteristics of the loading conditions has been recently demonstrated (16): in general, animals mounted for testing inside of the shock tube are exposed to shock wave resulting in primary blast TBI (17). Animal models tested inside experience a higher level of loading caused by static pressure, simply because higher peak overpressures and durations can be achieved inside when compared with the outside. This difference is demonstrated in reported durations in the published literature where unlike inside the shock tube, overpressure durations longer than 2 ms have not been reported outside of the shock tube (18–22). Furthermore, acceleration of the rodent head, and body caused by dynamic pressure (jet effect) of expanding shock wave (classified as tertiary blast injury) are characterized by increased level of injury compared with primary blast TBI (23).

The distinction between primary and other types of TBI is important to allow comparison of results between laboratories. However, this comparison will not be complete if shock wave-associated parameters are not measured and disclosed in the reports. We have screened a pool of 100 papers selected from existing literature on animal and *in vitro* models of bTBI covering the last 20 years of research to identify reporting standards regarding shock wave parameters. This survey gives an overview and revealed the following trends: in a majority of the published work (97%), peak overpressure is reported as the most important parameter (see Table S1 in Supplementary Material for details). Interestingly, little attention is devoted to other characteristics of the shock wave waveform: the duration (51%), impulse (18%), the sampling frequency (46%), and finally the rise time, which is essentially neglected (2%). Only in very few papers, all four of these parameters were provided (20, 24–27), including or not sampling rates used in these studies.

In this paper, we discuss issues related to overpressure measurements: the importance of pressure transducer calibration, the effect of sampling frequency on the quantification of shock waveform characteristics, and preventive measures to avoid signal corruption. Electromagnetic interference and mechanical vibration are two aggravating factors that lead to an acquisition of incorrect waveforms with exaggerated peak overpressure values and baseline drifts, which might lead to erroneous duration and impulse values. We present preventive measures, which are illustrated with examples of experimental data.

MATERIALS AND METHODS

The Shock Tubes

Both large (28-inch square cross section) and small (9-inch square cross section) scale shock tubes at the New Jersey Institute of Technology have modular design and the following characteristics (**Figure 1**): (1) adjustable volume breech, (2) variable length transition section, (3) the 6 m long test section, equipped with bullet-proof glass windows for high-speed video observation of the specimen during the shock wave exposure, and (4) the reflector end-plate. In all experiments described in this contribution, the compressed helium was filled into the fixed volume breech, which is separated from the main body of the shock tube by Mylar membranes [for a detailed description of the principles of operation an informed reader is referred to Ref. (28, 29)].

Overpressure Measurement

A series of pressure sensors distributed along the length of the shock tube was used to measure pressure-time profiles of incident shock wave (**Figure 1B**) (28). The incident pressure was measured using high-frequency Tourmaline pressure transducers model 134A24 (1,000 psi maximum pressure, resonant frequency ≥1,500 kHz, 0.2 μs rise time, PCB Piezotronics, Depew, NY, USA). These sensors use 402 charge amplifiers, which are connected in series with pressure transducers *via* 3-inch-long low-noise cable with 10–32 coaxial jacks. In headform exposure experiments, we used high-frequency ICP® model 102B06 pressure transducers (500 psi maximum pressure, resonant frequency ≥500 kHz, and ≤1.0 μs rise time, PCB Piezotronics, Depew, NY, USA). All data were recorded at 1.0 MHz sampling frequency, and the typical acquisition time ranged from 50 to 200 ms. The 134A series sensors have 1/2–20 thread and require mounting holes of larger diameter; we used 5/8–18 tapped threaded holes, which are blinded with appropriate screws when not in use. Sensors are mounted in 0.25-inch thick steel brackets with rubber feet to prevent the transfer of the vibrations from the shock tube wall. Brackets with sensors are clamped to the shock tube wall, which prevents their displacement by pressure during shock wave experiments (**Figure 1A**, inset). There are 11 pressure sensor mounting openings in the shock tube designated as An, Bn, Cn, or Dn, depending on which module of the shock tube these sensors are located, where the number $n = 1, 2, 3,\ldots$ indicates the consecutive sensor count for that specific module (**Figure 1B**). There are an additional nine ports in the test section located in the

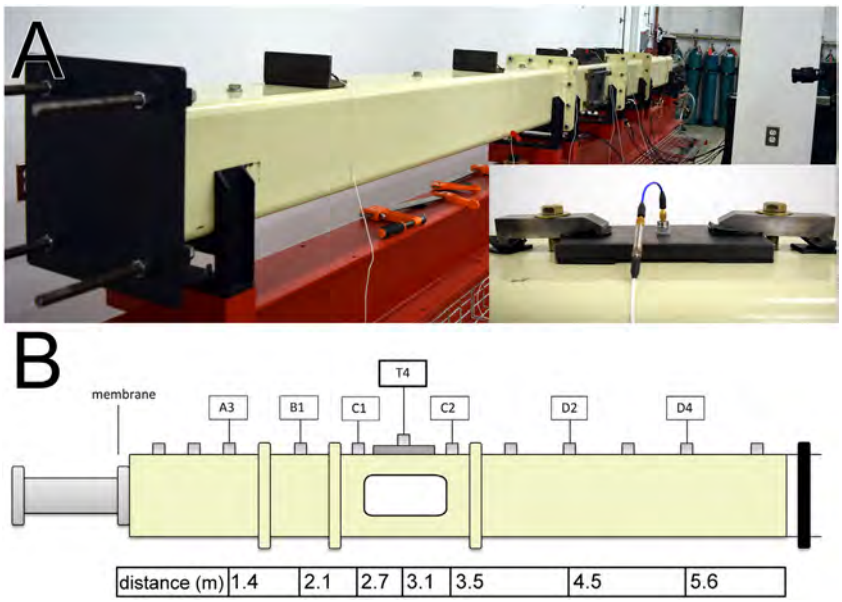


FIGURE 1 | The 9-inches square cross section shock tube: the rear view with the reflector plate and sensor brackets distributed along the shock tube **(A)**. The inset depicts PCB 134A24 sensor (connected *via* 3 in long low-noise cable to a series 402 charge amplifier) in the modified sensor mounting system with rubberized brackets and steel clamps preventing vertical movement of the sensor caused by the pressure of the passing shock wave. Schematic representation of the shock tube with sensor labeling and sensor distances from the membrane mounting port in the breech **(B)**. Only ports used in experiments described therein are indicated in the diagram.

C module of the shock tube and denoted as *Tn* (for $n = 1$–9). Typically, only six to seven sensors are used at the same time to capture a representative snapshot of the evolution of the shock wave profile.

Pressure Sensor Calibration

Pressure sensor calibration methodology developed in our lab relies on the measurement of the shock wave velocity which is related to the overpressure using Rankine–Hugoniot relationship:

$$\Delta P = \frac{\left(M^2 - 1\right) 2\gamma_i P_{at}}{\gamma_i}, \quad (1)$$

where ΔP—overpressure, M—Mach number, γ_i—specific heat ratio (1.4 for nitrogen, 1.66 for helium), P_{at}—atmospheric pressure.

Typically, an array of seven sensors is mounted in a straight-line along the shock tube axis spanning the distance of 10 inches (first to last, **Figure 2A**). Sensors are mounted using tapped holes in a single steel plate and mounted in the test section and the plate is secured in place using clamps, to prevent vertical displacement. This is an important precaution for accurate measurement of the sensor output (in volts) which is used to calculate calibration constant. The shock wave velocity is calculated based on the arrival time between sensors and typically a combination of 21 measurements is used. The average velocity is used to calculate corresponding experimental overpressure, ΔP from Eq. 1. The voltage output from the sensor divided by ΔP gives calibration factor.

Electrostatic Interference

The baseline drift caused by electrostatic charges was recorded using six pressure sensors (PCB 134A24) distributed along the 9-inch cross section shock tube. Silicone grease (Dow Corning, four Electrical Insulating Grease, McMaster-Carr, cat. no. 1204K12) was purchased and applied to the sensing surface of the sensors to eliminate the baseline drift.

The electrostatic charges leaking into the data acquisition system were observed in experiments with the headform instrumented with 10 PCB 102B06 sensors. These sensors are mounted flush with the surface of the headform and signal cabling is extending from the interior of the headform through the metallic plate (base), the neck and then is lead on the outside of the shock tube. We have routinely observed signal corruption in the event of compromised electrical insulation of the coaxial signal cable caused by shock wave impact and loosening of connector nut. This was also investigated using a dummy sensor setup. Briefly, a 1/4-inch stainless steel tubing was insulated with electrical insulation tape and inserted in the bolt. The entire assembly was mounted in the A3 port in the shock tube (Figure S1 in Supplementary Material), and connected to the data acquisition system.

The Effect of Sampling Frequency

The effect of sampling frequency on characteristic parameters of the shock wave was evaluated using three sampling frequencies: 10, 100, and 1,000 kHz (**Figure 3**). A single sampling frequency was set in the DAQ and all experiments were performed using a single shock wave with a nominal intensity of 130 kPa in the test section (T4 sensor, **Figure 1B**). All tests were repeated four

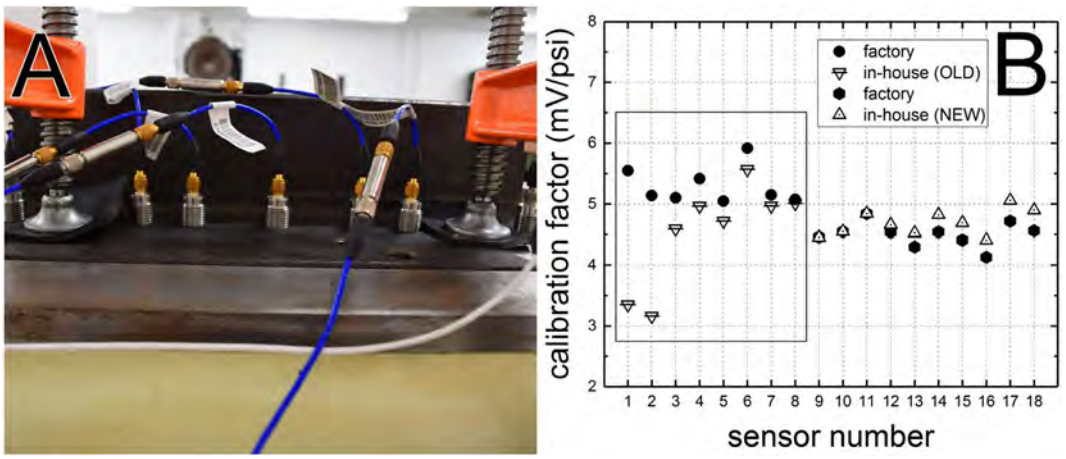


FIGURE 2 | An array of seven pressure transducers (PCB 134A24) mounted on a plate in the test section and ready for calibration shots **(A)**. The plate is protected against vertical displacement using two clamps with rubber padding. Comparison of the factory calibration factors and those obtained using experiments performed in-house **(B)**. Data for sensors with long experimental life are outlined with a black rectangle (sensor nos. 1–8). Discrepancies in calibration factor values of below 5% were noted for brand new sensors (sensor nos. 9–18). Pressure transducers are connected *via* 3 in long low-noise cable to the charge amplifier *via* 10–32 jacks, and then *via* long low-noise cable to the data acquisition system.

times and the signal was recorded by six pressure sensors located along the shock tube. A total of 72 waveforms was analyzed ($3 \times 4 \times 6 = 72$), which included quantification of peak overpressure, rise time, duration, and impulse.

Sensor Misalignment

The effect of sensor misalignment with respect to the shock tube wall on the pressure profile was tested using sensor located in a T4 position in two configurations: (1) sensor was protruding by 0.25 inch into the shock tube and (2) sensor was receded from the flush position by 0.25 inch. A single shock wave with 130 kPa nominal peak overpressure was generated and compared with an adjacent sensor (denoted as T1, located five inches downstream of the T4 sensor). All measurements were repeated four times and peak overpressure was quantified.

Statistical Analysis

Data from experiments performed at different experimental conditions were pooled together and checked for normality using Ryan–Joiner test (similar to Shapiro–Wilk) in Minitab 17.0 (Minitab Inc., State College, PA, USA). Then a multiple comparison two-tailed *t*-test (statistical significance threshold was set at $p < 0.05$) was performed with Bonferroni correction on data for evaluation of the effect of sampling frequency and sensor misalignment. All data are presented as a mean and SD.

RESULTS AND DISCUSSION

Sensor Calibration

The accurate measurements of shock waves rely solely on the characteristics of the sensing element in the pressure transducer, appropriate calibration, and sampling frequency [details of pressure profile evolution in the shock tube are discussed extensively in Ref. (28)]. Tourmaline is among the most popular materials employed as a sensing element in pressure transducers. Its piezoelectric properties were recognized more than 80 years ago with some of the earliest publications on the subject issued in the early 1930s (30), while its crystallographic structure was determined in the early 1950s of the twentieth century (31). This coincided with the extensive development work on pressure transducers (32). Typically, two pressure calibration methods can be employed in the manufacturing facility (33): (1) using Aronson pressure generator (34) and (2) in the shock tube. However, to check the characteristic frequency of the sensor and its rise time in response to shock loading, only a shock tube can be used since loading rates of Aronson's apparatus are insufficient for this purpose.

Typically, sensor calibration performed in the factory establishes maximum pressure and linear dependency between the applied pressure and voltage output from the sensor. Standard parts and equipment used for this purpose are hardly ever replicated in the laboratory, particularly if long signal cables are used. The differences between factory calibration setup and instrumentation used in the laboratory have to be checked to account for possible discrepancies in sensor response caused by impedance and triboelectric effects associated with cabling of different length. The methodology used in our lab relies on the measurement of the shock wave velocity which is related to pressure using Rankine–Hugoniot relationship. **Figure 2B** presents the discrepancies between factory calibration factors, and those obtained using the procedure developed in-house. For brand new sensors (number 9–18), the discrepancies are less than 7%; however, we must stress our method of calibration covers 0–60 psi range, which lies within practical interest for studying of blast TBI. Older sensors (3 years old, after hundreds of exposures), possibly due to wear and tear and some differences in manufacturing showed somewhat larger differences (sensitivity loss up to −10%) in calibration factors with two on the extreme

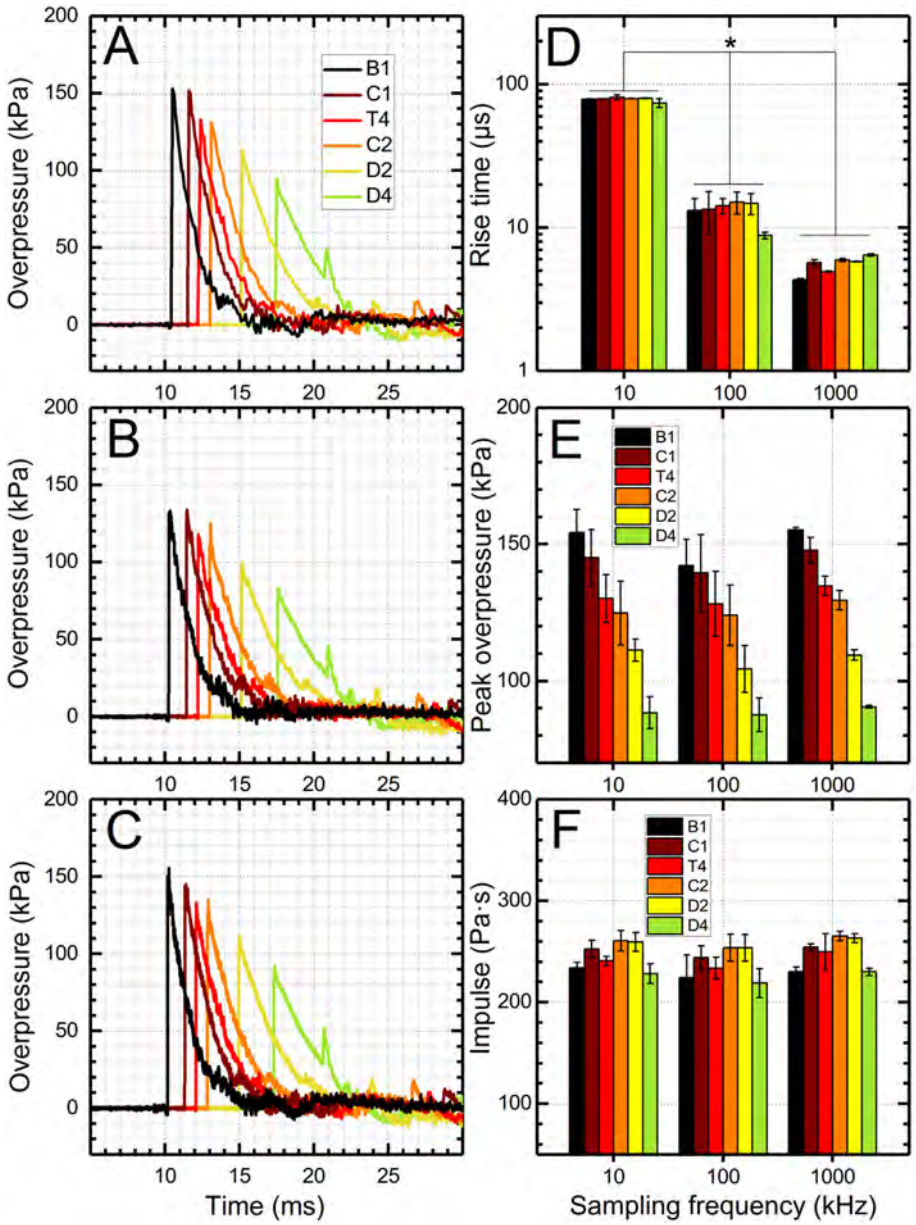


FIGURE 3 | The effect of sampling frequency on the quality of shock wave pressure profiles. Representative pressure profiles recorded using a sampling frequency of 10 kHz **(A)**, 100 kHz **(B)**, and 1,000 kHz **(C)**. Rise time values calculated from respective data sets depend strongly on the sampling frequency **(D)**, while peak overpressure and impulse values are independent of the sampling frequency **(E,F)**, for sampling frequencies used in this study. Statistical significance between respective groups is marked with asterisk ($p < 0.05$).

end where the discrepancy was almost −40% (for sensors 1 and 2 in **Figure 2B**). We have not observed any consistent trends in the calibration factor differences, and it would appear it is a case-by-case occurrence. This observation, combined with a random occurrence of larger deviations in calibration factor values, necessitates this type of sensor evaluation, and justifies the additional time spent on these tests. For new sensors, the calibration is thus recommended before routine use, while experimentally observed loss of sensitivity and history of particular sensor should dictate the need for additional calibration.

Sampling Rate

The sampling rate is an important experimental variable to capture the shape of the pressure profile. Since there are no universal measurement and reporting standards on shock wave parameters and data acquisition settings in the blast-induced neurotrauma (BINT) research field, a broad variety of sampling rates are typically reported, ranging from 10 kHz to 10 MHz (20, 24, 25, 28, 35–41). However, in a majority of publications, this parameter is omitted from reporting whatsoever, either because it was reported earlier in the original report on the characterization

of the blast generating device, or simply because it is treated as a trivial test parameter. Not only is the sampling frequency important for capturing the shape of the pressure profile, it is also an important factor in optimizing the output file size, along with the number of recorded channels and acquisition time. Moreover, it is unknown what sampling frequencies are adequate to accurately capture the shock wave profile traveling at supersonic speeds. To address these questions and establish adequate thresholds, we have performed a series of experiments where three sampling frequencies were used: 10, 100, and 1,000 kHz (**Figure 3**). We used a single shock wave with a nominal intensity of 130 kPa in the test section (T4 sensor, **Figure 1B**). At first glance, there are no significant differences between the three sampling frequencies (**Figures 3A–C**), but differences have become obvious after quantification of three basic shock wave characteristics: rise time, peak overpressure, and impulse. The most significant changes are with respect to the rise time (**Figure 3D**): only at 1,000 kHz sampling rate it is captured accurately. Note, that time resolution at this frequency is 1 μs which is adequate to capture rise times on the order of 4–5 μs which are typical for moderate intensity shock waves (Mach number below 2) based on our experience to date (28). Interestingly, sampling frequency as low as 10 kHz still allows accurate capture of peak overpressure and impulse values. This is simply because in this case, the shock wave with 5-ms duration traveling at 400 m/s velocity is a 2-m long (head to tail) mass of compressed air traveling in the 6 m long shock tube. With this sampling frequency, 10 data points per millisecond will be captured resulting in 50 data points for the 5 ms duration, which appears adequate to capture pressure-time outline without significant errors. However, when shorter duration shock waves are of interest, i.e., below 1 ms, which is characteristic of shock waves generated outside the shock tube, the sampling frequency needs to be increased to more than 1 MHz (20, 41).

Electrostatic Interference

We have performed more than 7,000 tests during the longevity of the shock wave testing laboratories at the University of Nebraska-Lincoln and then at New Jersey Institute of Technology. The shock tube walls have been painted to protect against rusting, but the downside is the paint also diminished dissipation of static electricity generated by the propagating shock wave. The PCB 134A24 tourmaline sensors mounted on the walls of both shock tubes for measurements of incident pressure suffer from a severe baseline drift which occurs as early as 1 ms after the shock front passage (**Figure 4**). The pressure reading reaches unrealistic values depending on the location of the sensor: nearly 5,400 kPa for the A3 sensor, and below −100 kPa for the D2 and D4 sensors; the unrealistic negative overpressure of less than 100 kPa are observed at 360 ms for sensors A3-T4. The maximum positive pressure for the A3 sensor is higher than burst pressure recorded for this test (5,200 kPa) and values of negative overpressure below −100 kPa are physically impossible to attain (vacuum pressure of outer space is below 10^{-7} kPa). These values demonstrate some other phenomenon is affecting pressure sensor readings. Considering extreme temperature variations on the order of hundreds of degrees are necessary to cause baseline drift in this class of pressure sensors, it leaves only electromagnetic radiation

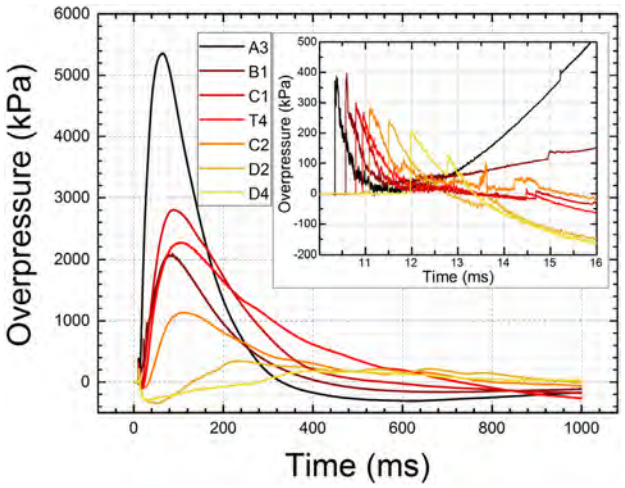


FIGURE 4 | The baseline drift recorded by seven PCB 134A24 pressure sensors distributed along the shock tube (see **Figure 1** for details). The data were recorded at 1 MHz frequency for 1 s (1 million data points per channel) for a shock wave with a nominal intensity of 250 kPa (a T4 sensor located in the test section). The burst pressure was 5,309 kPa (770 psi) for this test while erroneous peak pressure is 5,360 kPa for sensor A3 located at 1.43 m distance from the breech. The inset illustrates the shock wave profiles and baseline drift within 7 ms time frame. Note unrealistic negative pressure levels of −150 kPa reported by sensors D2 and D4.

as the source of observed anomalous readings and baseline drifts. These baseline drifts while apparently not interfering with measurements of the shock front characteristics (rise time and peak overpressure) adversely affect the estimation of the shock wave duration and hence lead to the erroneous calculation of the impulse values. We have performed additional verification that the static electricity is associated with shock wave passage using a dummy sensor (Figure S1 in Supplementary Material). The voltage variations were observed and coincided with a shock wave initiation.

The PCB Tourmaline Pressure Bars series 134A24 high-pressure, fast rise time sensors, with ranges up to 20,000 psi, are best suited for applications which require high-frequency measurements of the incident or reflected shock wave pressures like those found in studies of plasma physics and hypersonics. These sensors are factory protected against baseline drifts caused by high temperatures which exist near the epicenter of explosions or other high-pressure phenomena where heat is generated (42, 43), by a layer of a thermal insulator like vinyl tape. This method of sensor protection has proven ineffective against the level of static electricity generated in our shock tubes. We decided to resort to another compound with similar electrical insulation properties, commercially available silicone grease. Application of a thin 2–3 mm layer on the sensing surface of the sensors prevents baseline drifts and other adverse effects associated with static electricity as illustrated by overpressure profiles presented in **Figure 5**. It is obvious the baseline drift is virtually eliminated with this method. Periodic inspection and reapplication of the grease is necessary in order to record high quality, repeatable shock wave pressure profiles.

The second type of manifestation of the static electricity has become obvious during the testing of the effect of the shock wave loading conditions at different locations in the shock tube using the headform instrumented with PCB 102B06 (**Figure 6B**, inset). The sensor is connected to the low-noise data cable *via* 10-32 plug (PCB 002C10 low-noise cable) and then to the signal conditioner using a BNC connector *via* expansion terminal. Repeated exposure to the shock wave with 70–210 kPa intensity caused vibration of the headform which resulted in loosening of a connector between the pressure sensor and data cable. This in turn caused loss of electrical insulation of the data line running in the middle of the cable and results in a static electricity surge, i.e., a large number of high-intensity spikes randomly embedded in the pressure signal (**Figure 6**). Fast Fourier Transform analysis performed on this signal revealed three high-frequency bands: 50, 70, and 130 kHz. Due to relatively small amount of the signal contamination, in this case, it was possible to salvage the pressure data by running low-pass filter. However, in extreme cases, the loosening of 10–32 jacks resulted in unrecoverable levels of static electricity flooding the data channel (**Figure 6B**). The only remedy for this type of artifact is to secure the 10–32 plug with an electrical insulation tape to prevent the disconnection and a breach in electrical insulation.

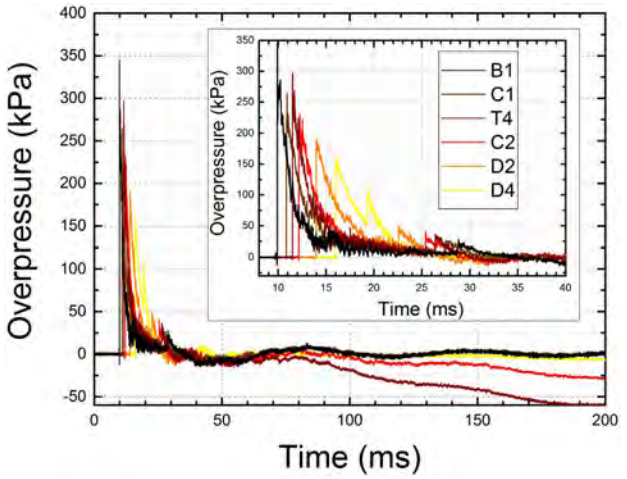


FIGURE 5 | Baseline drift was eliminated with an aid of silicone insulator grease applied on the tip of the sensors. The baseline shows no signs of drifts toward positive or negative range over 200 ms of signal. Some baseline drift is observed for sensors T4 and C2, most likely due to gradual deterioration of silicone insulator layer caused by repeated exposure. The inset shows enlarged shock wave profiles recorded by six sensors for the nominal intensity of 250 kPa (T4 sensor).

The Effect of Vibration on Pressure Signal Quality

The peak overpressure is the only parameter consistently reported among shock wave characteristics (peak overpressure, rise time, duration, impulse, and sampling frequency). Sensor mounting and mechanical vibrations have the tremendous effect on the signal quality of the shock front and peak overpressure is an extremely sensitive parameter prone to misinterpretation. We observed sensors mounted on the top wall of the shock tube are being pushed upwards by the pressure of the passing shock

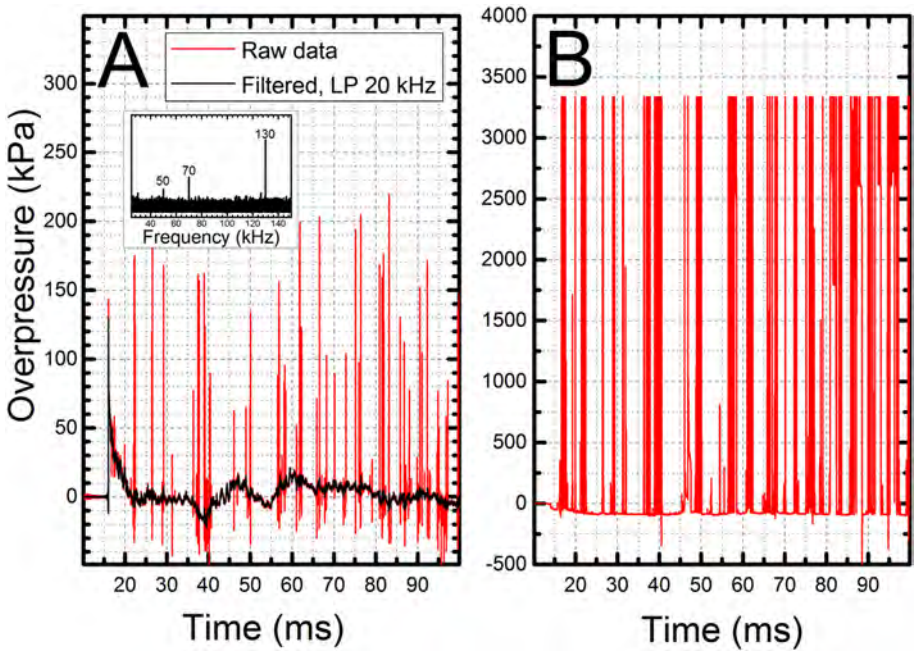


FIGURE 6 | Electrostatic interference caused by breach of signal line insulation: **(A)** high-frequency components (inset) can be removed even from relatively contaminated data set using low pass (or equivalent) filter and **(B)** in extreme cases electrostatic interference reaches such levels the experimental data cannot be salvaged. This type of interference can be dangerous also for signal conditioners and DAQ modules due to sudden surges of DC currents *via* signal cables.

wave: this is obvious on the high-speed videos (not shown) and the results in the corrupted initial part of the shock wave signal as seen in **Figure 7**. The upward motion of the sensor and its return to the resting position lasts only approximately 200 μs for the shock wave with 280 kPa peak overpressure (**Figure 7B**). The resulting signal is corrupted by the sensor translation within the opening of the mounting port. We have noticed this particular artifact present on numerous occasions in our data, and decided to install clamps on both sides of the pressure brackets to prevent the displacement of the bracket-pressure sensor assembly (**Figure 1A**, inset). However, to explore the origin of the exaggerated peak overpressure values in the controlled and systematic way, we decided to mount one of our sensors receded by 0.25 inch, and compare results with two other configurations where the sensor is mounted flush (default configuration for all experiments) and protruding by 0.25 inch (**Figure 8**). In both cases of non-flush sensor mounting, there is an excessive pressure buildup which lasts less than 100 μs (**Figures 8A,B**). Quantification of peak overpressure for $n = 4$ repeated trials indicates that the receded configuration results in a higher overestimation of peak overpressure (**Figure 8C**), and observed changes are statistically significant ($p < 0.05$). However, non-optimal sensor location cannot explain vibrations in the signal (**Figure 7**), which is likely associated with the impact of the sensor by the shock wave, and unrestricted displacement path while free-floating in the air. It would appear sensor vibration upon the initial shock wave impact leads to gross overestimation of the peak overpressure, while not affecting other characteristics. Literature survey related to reporting and existing standards of pressure measurements revealed some research groups were aware of the consequences of the improper sensor mounting. For example, Kochanek and co-workers mentioned in their recent work that "surface flush gauges were used for the shock measurements because it is known that a gauge protruding or recessed by less than 1 mm will affect measurements" (17). Examples of waveforms with a sharp spike at the beginning of the shock wave are scattered through the literature. Chavko and colleagues report that when they measured the pressure with a miniature fiber-optic sensor made by Fiso, they detected "a lower pressure spike than the spike measured with the PCB probe." It would appear both sensors were not mounted perfectly flush, which was not recognized at the time and the difference in spike intensity was explained by mere differences in sampling rate, which was 40 kHz for Fiso sensor and 500 kHz for PCB sensors or by their specific characteristics (44). Similarly, the presence of high-intensity spikes in the reflected pressure measured at the end of the closed shock tube was interpreted as a peak reflected overpressure (45, 46), most likely incorrectly based on our experimental data (**Figure 8**).

However, while consequences of non-flush mounting are recognized, far less attention is dedicated to proper signal analysis and preventive measures when high-frequency artifacts are present in the signal. For example, a quick glimpse on the overpressure profiles published by Svetlov and co-workers reveals that in their experiments, this artifact leads to twofold overestimation of the peak overpressure [see **Figure 2** in Ref. (47)], i.e., it was erroneously reported as 358 kPa, while, in fact, it was merely 180 kPa. Only in some instances where the sharp spike is present in the data correct peak pressure was reported, i.e., as the highest pressure resulting from the exponential decay part of the waveform (48).

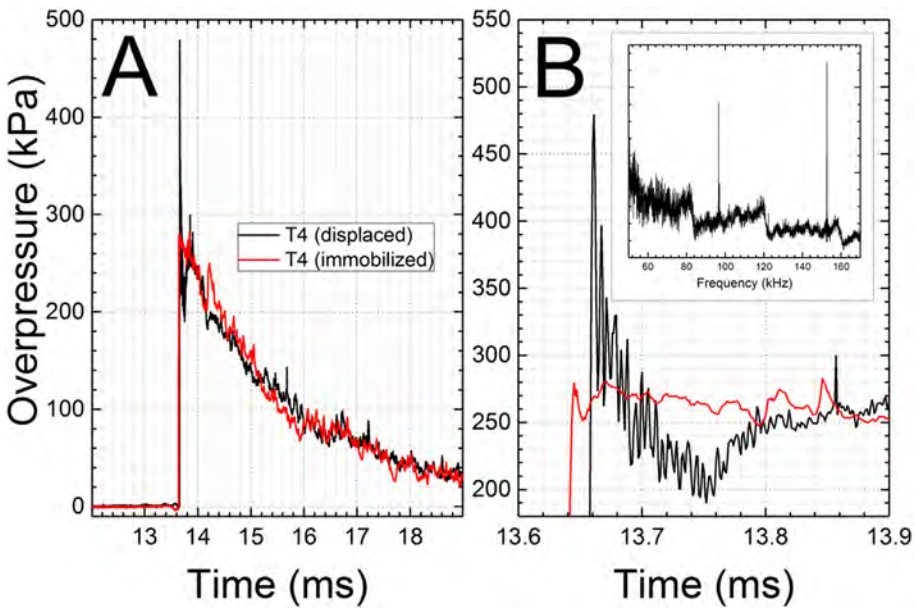


FIGURE 7 | High-frequency signal observed in experiments where the sensor and the mounting bracket were pushed upwards by the passing shock wave. Comparison of the recorded overpressure with the artifact associated with the sensor [T4 (displaced)] and the signal with eliminated artifact **(A)**. Two brackets were used to prevent the displacement of the sensor resulting in clean waveform [T4 (immobilized)]. The magnified part of the pressure history reveals the presence of high-frequency noise and excessive peak pressure level **(B)**. Inset: FFT results of the pressure signal with artifact reveal characteristic frequencies: 96 and 152 kHz.

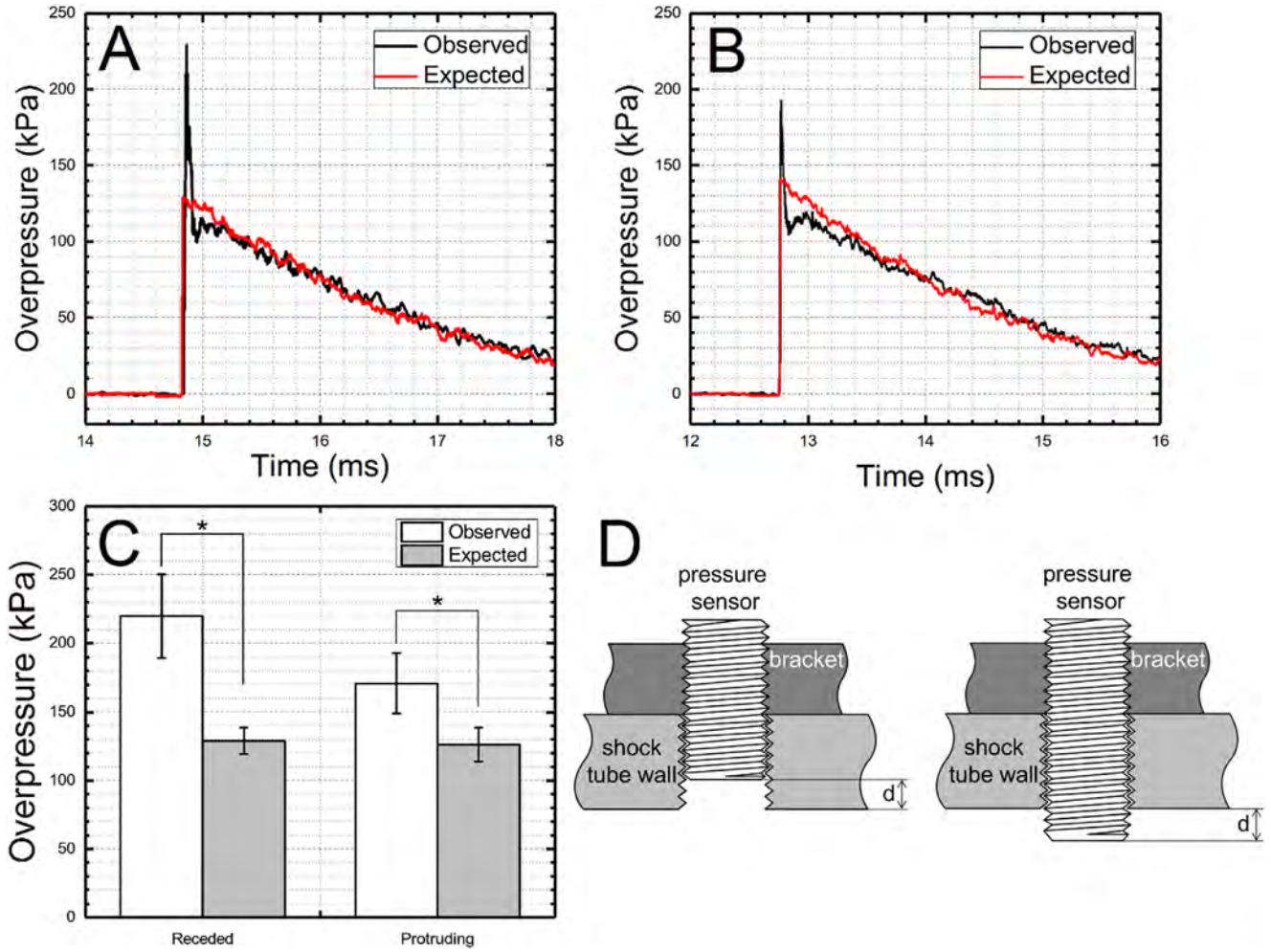


FIGURE 8 | The effect of sensor misalignment with the shock tube wall on the resulting pressure profile. The exaggerated peak overpressure values are observed when the sensor is: receding **(A)** or protruding **(B)** from the shock tube wall. Quantification results ($n = 4$) for both tested scenarios demonstrate peak overpressure values are higher for receded sensor configuration than when the sensor was protruding **(C)**. These differences are statistically significant ($p < 0.05$). Nominal shock wave intensity of 130 kPa measured in the test section (T4 location) was used for these tests. Schematic representation of two sensor configurations resulting in peak overpressure artifacts is presented **(D)**. The distance between shock tube wall and sensing surface was the same in both cases ($d = 0.25$ in). Statistically significant differences are indicated with an asterisk ($p < 0.05$).

CONCLUSION

We have discussed two important experimental variables, mechanical vibration and electromagnetic interference on the quality of a waveform recorded using state-of-the-art high-frequency pressure sensors. The importance proper implementation of preventive strategies, understanding of pressure measurement artifacts, and data interpretation with examples provided in this paper will help the community at large avoid these mistakes. In order to facilitate interlaboratory data comparison on the BINT research area, common reporting standards should be developed. We noticed the majority of published literature on the subject limits reporting to peak overpressure, with much less attention directed toward other important parameters, i.e., duration and especially impulse, which should be included as mandatory in future contributions. We have demonstrated sampling frequency as low as 10 kHz can be used to capture correctly the shape of the shock wave with a few milliseconds duration. However, shock waves with shorter durations might require higher sampling rates, and a sampling rate of 1,000 kHz is typically necessary to capture the rise time, which might be an important parameter depending upon the design of the study. We have also demonstrated sensor calibration is a significant quality measure, particularly for sensors with an extended lifetime. While there were only slight differences between factory and in-house generated calibration factors, we must stress the importance of this step to obtain correct pressure values. It is extremely important in the recording of peak overpressure values, which seem to be very prone to errors.

AUTHOR CONTRIBUTIONS

MS and EA performed experiments and data analysis, MS and NC wrote the manuscript.

FUNDING

This work was supported by grant no. 14059001 entitled "Primary Blast Injury Criteria for Animal/Human TBI Models using Field Validated Shock Tubes" received from the U.S. Army Medical Research and Materiel Command. The headform testing was funded by award no. W91CRB-16-C-0025 (PEO Soldier).

SUPPLEMENTARY MATERIAL

The Supplementary Material for this article can be found online at http://www.frontiersin.org/articles/10.3389/fneur.2018.00052/full#supplementary-material.

REFERENCES

1. Moore DF, Jaffee MS. Military traumatic brain injury and blast. *Neuro Rehabil* (2010) 26(3):179–81. doi:10.3233/NRE-2010-0553
2. Hoge CW, McGurk D, Thomas JL, Cox AL, Engel CC, Castro CA. Mild traumatic brain injury in U.S. soldiers returning from Iraq. *N Engl J Med* (2008) 358(5):453–63. doi:10.1056/NEJMoa072972
3. Elder GA, Cristian A. Blast-related mild traumatic brain injury: mechanisms of injury and impact on clinical care. *Mt Sinai J Med* (2009) 76(2):111–8. doi:10.1002/msj.20098
4. DePalma RG, Cross GM, Beck L, Chandler D. Epidemiology of mTBI (mild traumatic brain injury) due to blast: history, DOD/VA data bases: challenges and opportunities. *Proc NATO RTO-MP-HFM-207 Symposium on a Survey of Blast Injury across the Full Landscape of Military Science*. Washington, DC (2011).
5. *DoD Worldwide Numbers for TBI*. (2017). Available from: http://dvbic.dcoe.mil/dod-worldwide-numbers-tbi
6. Greer N, Sayer N, Koeller E, Velasquez T, Wilt TJ. Outcomes associated with blast versus nonblast-related traumatic brain injury in US military service members and veterans: a systematic review. *J Head Trauma Rehabil* (2017). doi:10.1097/HTR.0000000000000304
7. Vanderploeg RD, Belanger HG, Horner RD, Spehar AM, Powell-Cope G, Luther SL, et al. Health outcomes associated with military deployment: mild traumatic brain injury, blast, trauma, and combat associations in the Florida National Guard. *Arch Phys Med Rehabil* (2012) 93(11):1887–95. doi:10.1016/j.apmr.2012.05.024
8. Ostertag MH, Kenyon M, Borkholder DA, Lee G, da Silva U, Kamimori G. The blast gauge™ system as a research tool to quantify blast overpressure in complex environments. *ASME 2013 International Mechanical Engineering Congress and Exposition*. San Diego, California: American Society of Mechanical Engineers (2013). p. A17–13.
9. Wiri S, Needham C. Reconstruction of improvised explosive device blast loading to personnel in the open. *Shock Waves* (2016) 26(3):279–86. doi:10.1007/s00193-016-0644-1
10. Bennett S, Fintelman G, Patchell M, Webb A, Wynen B, Costello J, et al. Project cerebro: an evaluation of blast gauges in the Australian Defence Force. *J Mil Vet Health* (2015) 23(3):27–30.
11. Phillips Y, Richmond DR. Primary blast injury and basic research: a brief history. In: Zatchuck R, Jenkins D, Bellamy R, Quick C, editors. *Textbook of Military Medicine Part I Warfare, Weapons, and the Casualty. Vol. 5, Conventional Warfare. Ballistic, Blast, and Burn Injuries*. Washington, DC: TMM Publications (1991). p. 221–240.
12. DePalma RG, Burris DG, Champion HR, Hodgson MJ. Blast injuries. *N Engl J Med* (2005) 352(13):1335–42. doi:10.1056/NEJMra042083
13. Cernak I. The importance of systemic response in the pathobiology of blast-induced neurotrauma. *Front Neurol* (2010) 1:151. doi:10.3389/fneur.2010.00151
14. Cernak I, Savic J, Ignjatovic D, Jevtic M. Blast injury from explosive munitions. *J Trauma Acute Care Surg* (1999) 47(1):96–103. doi:10.1097/00005373-199907000-00021
15. Richmond DR, Gaylord CS, Damon EG, Taborelli R. DASA-AEC-Lovelace foundation blast-simulation facility. *Defense Nuclear Agency (Formerly Defense Atomic Support Agency)*. Washington, DC: Department of Defense (1966). Technical Progress Report No. DASA-1853.
16. Sundaramurthy A, Alai A, Ganpule S, Holmberg A, Plougonven E, Chandra N. Blast-induced biomechanical loading of the rat: an experimental and anatomically accurate computational blast injury model. *J Neurotrauma* (2012) 29(13):2352–64. doi:10.1089/neu.2012.2413
17. Garman RH, Jenkins LW, Switzer RC III, Bauman RA, Tong LC, Swauger PV, et al. Blast exposure in rats with body shielding is characterized primarily by diffuse axonal injury. *J Neurotrauma* (2011) 28(6):947–59. doi:10.1089/neu.2010.1540
18. Irwin RJ, Lerner MR, Bealer JF, Mantor PC, Brackett DJ, Tuggle DW. Shock after blast wave injury is caused by a vagally mediated reflex. *J Trauma* (1999) 47(1):105–10. doi:10.1097/00005373-199907000-00023
19. Awwad HO, Gonzalez LP, Tompkins P, Lerner M, Brackett DJ, Awasthi V, et al. Blast overpressure waves induce transient anxiety and regional changes in cerebral glucose metabolism and delayed hyperarousal in rats. *Front Neurol* (2015) 6:132. doi:10.3389/fneur.2015.00132
20. Miller AP, Shah AS, Aperi BV, Budde MD, Pintar FA, Tarima S, et al. Effects of blast overpressure on neurons and glial cells in rat organotypic hippocampal slice cultures. *Front Neurol* (2015) 6:20. doi:10.3389/fneur.2015.00020
21. Effgen GB, Hue CD, Vogel E III, Panzer MB, Meaney DF, Bass CR, et al. A multiscale approach to blast neurotrauma modeling: part II: methodology for inducing blast injury to in vitro models. *Front Neurol* (2012) 3:23. doi:10.3389/fneur.2012.00023
22. Alay E, Skotak M, Misistia A, Chandra N. Dynamic loads on human and animal surrogates at different test locations in compressed-gas-driven shock tubes. *Shock Waves* (2017):1–12. doi:10.1007/s00193-017-0762-4
23. Gullotti DM, Beamer M, Panzer MB, Chen YC, Patel TP, Yu A, et al. Significant head accelerations can influence immediate neurological impairments in a murine model of blast-induced traumatic brain injury. *J Biomech Eng* (2014) 136(9):091004. doi:10.1115/1.4027873
24. Cernak I, Merkle AC, Koliatsos VE, Bilik JM, Luong QT, Mahota TM, et al. The pathobiology of blast injuries and blast-induced neurotrauma as identified using a new experimental model of injury in mice. *Neurobiol Dis* (2011) 41(2):538–51. doi:10.1016/j.nbd.2010.10.025
25. Saljo A, Arrhen F, Bolouri H, Mayorga M, Hamberger A. Neuropathology and pressure in the pig brain resulting from low-impulse noise exposure. *J Neurotrauma* (2008) 25(12):1397–406. doi:10.1089/neu.2008.0602
26. Lu J, Ng KC, Ling G, Wu J, Poon DJF, Kan EM, et al. Effect of blast exposure on the brain structure and cognition in *Macaca fascicularis*. *J Neurotrauma* (2012) 29(7):1434–54. doi:10.1089/neu.2010.1591
27. Huber BR, Meabon JS, Martin TJ, Mourad PD, Bennett R, Kraemer BC, et al. Blast exposure causes early and persistent aberrant phospho- and cleaved-tau expression in a murine model of mild blast-induced traumatic brain injury. *J Alzheimers Dis* (2013) 37(2):309–23. doi:10.3233/jad-130182
28. Kuriakose M, Skotak M, Misistia A, Kahali S, Sundaramurthy A, Chandra N. Tailoring the blast exposure conditions in the shock tube for generating pure, primary shock waves: the end plate facilitates elimination of secondary loading of the specimen. *PLoS One* (2016) 11(9):e0161597. doi:10.1371/journal.pone.0161597
29. Holmberg AD. *Development and Characterization of Shock Tubes for Laboratory Scale Blast Wave Simulation*. University of Nebraska-Lincoln (2010).
30. Fox GW, Underwood M. On the piezoelectric properties of tourmaline. *J Appl Phys* (1933) 4(1):10–3. doi:10.1063/1.1745137
31. Wooster W. Physical properties and atomic arrangements in crystals. *Rep Prog Phys* (1953) 16(1):62. doi:10.1088/0034-4885/16/1/302
32. Walter PL. Air-blast and the science of dynamic pressure measurements. *Sound Vib* (2004) 38(12):10–7.

33. Lally J, Cummiskey D. Dynamic pressure calibration. *Sensors* (2003) 20(4):15–21.
34. Aronson P, Waser R. *Pressure-Pulse Generator for the Calibration of Pressure Gages*. White Oak, MD: DTIC Document (1963).
35. Ahlers ST, Vasserman-Stokes E, Shaughness MC, Hall AA, Shear DA, Chavko M, et al. Assessment of the effects of acute and repeated exposure to blast overpressure in rodents: toward a greater understanding of blast and the potential ramifications for injury in humans exposed to blast. *Front Neurol* (2012) 3:32. doi:10.3389/fneur.2012.00032
36. Cho HJ, Sajja V, Vandevord PJ, Lee YW. Blast induces oxidative stress, inflammation, neuronal loss and subsequent short-term memory impairment in rats. *Neuroscience* (2013) 253:9–20. doi:10.1016/j.neuroscience.2013.08.037
37. Rubovitch V, Ten-Bosch M, Zohar O, Harrison CR, Tempel-Brami C, Stein E, et al. A mouse model of blast-induced mild traumatic brain injury. *Exp Neurol* (2011) 232(2):280–9. doi:10.1016/j.expneurol.2011.09.018
38. Skotak M, Wang F, Alai A, Holmberg A, Harris S, Switzer RC, et al. Rat injury model under controlled field-relevant primary blast conditions: acute response to a wide range of peak overpressures. *J Neurotrauma* (2013) 30(13): 1147–60. doi:10.1089/neu.2012.2652
39. Svetlov SI, Prima V, Glushakova O, Svetlov A, Kirk DR, Gutierrez H, et al. Neuro-glial and systemic mechanisms of pathological responses in rat models of primary blast overpressure compared to "composite" blast. *Front Neurol* (2012) 3:15. doi:10.3389/fneur.2012.00015
40. Tompkins P, Tesiram Y, Lerner M, Gonzalez LP, Lightfoot S, Rabb CH, et al. Brain injury: neuro-inflammation, cognitive deficit, and magnetic resonance imaging in a model of blast induced traumatic brain injury. *J Neurotrauma* (2013) 30(22):1888–97. doi:10.1089/neu.2012.2674
41. Yeoh S, Bell ED, Monson KL. Distribution of blood-brain barrier disruption in primary blast injury. *Ann Biomed Eng* (2013) 41(10):2206–14. doi:10.1007/s10439-013-0805-7
42. De Vries J, Petersen E. Autoignition of methane-based fuel blends under gas turbine conditions. *Proc Combust Inst* (2007) 31(2):3163–71. doi:10.1016/j.proci.2006.07.206
43. Mathieu O, Kopp M, Petersen E. Shock-tube study of the ignition of multi-component syngas mixtures with and without ammonia impurities. *Proc Combust Inst* (2013) 34(2):3211–8. doi:10.1016/j.proci.2012.05.008
44. Chavko M, Watanabe T, Adeeb S, Lankasky J, Ahlers ST, McCarron RM. Relationship between orientation to a blast and pressure wave propagation inside the rat brain. *J Neurosci Methods* (2011) 195(1):61–6. doi:10.1016/j.jneumeth.2010.11.019
45. Courtney E, Courtney A, Courtney M. Shock tube design for high intensity blast waves for laboratory testing of armor and combat materiel. *Defence Technol* (2014) 10(2):245–50. doi:10.1016/j.dt.2014.04.003
46. Courtney AC, Andrusiv LP, Courtney MW. Oxy-acetylene driven laboratory scale shock tubes for studying blast wave effects. *Rev Sci Instrum* (2012) 83(4):045111. doi:10.1063/1.3702803
47. Svetlov SI, Prima V, Kirk DR, Gutierrez H, Curley KC, Hayes RL, et al. Morphologic and biochemical characterization of brain injury in a model of controlled blast overpressure exposure. *J Trauma* (2010) 69(4):795–804. doi:10.1097/TA.0b013e3181bbd885
48. Reneer DV, Hisel RD, Hoffman JM, Kryscio RJ, Lusk BT, Geddes JW. A multi-mode shock tube for investigation of blast-induced traumatic brain injury. *J Neurotrauma* (2011) 28(1):95–104. doi:10.1089/neu.2010.1513

Conflict of Interest Statement: The authors declare that the research was conducted in the absence of any commercial or financial relationships that could be construed as a potential conflict of interest.

Copyright © 2018 Skotak, Alay and Chandra. This is an open-access article distributed under the terms of the Creative Commons Attribution License (CC BY). The use, distribution or reproduction in other forums is permitted, provided the original author(s) and the copyright owner are credited and that the original publication in this journal is cited, in accordance with accepted academic practice. No use, distribution or reproduction is permitted which does not comply with these terms.

Appendix A –Publication Cover 16
2018

Authors: A. Sundaramurthy, M. Skotak, E. Alay, G. Unnikrishnan, H. Mao, X. Duan, S. T. Williams, T. H. Harding, N. Chandra, and J. Reifman

Title: "*Assessment of the effectiveness of combat eyewear protection against blast overpressure*"

Journal Publication: Journal of Biomechanical Engineering, 140, 071003-1-12, (2018), [18-16]

A. Sundaramurthy
Department of Defense,
Biotechnology High Performance Computing
Software Applications Institute,
Telemedicine and Advanced Technology
Research Center,
U.S. Army Medical Research and Materiel
Command,
504 Scott Street,
Fort Detrick, MD 21702
e-mail: asundaramurthy@bhsai.org

M. Skotak
Department of Biomedical Engineering,
Center for Injury Biomechanics, Materials
and Medicine,
New Jersey Institute of Technology,
University Heights,
Newark, NJ 07102
e-mail: maciej.skotak@njit.edu

E. Alay
Department of Biomedical Engineering,
Center for Injury Biomechanics, Materials
and Medicine,
New Jersey Institute of Technology,
University Heights,
Newark, NJ 07102
e-mail: ea79@njit.edu

G. Unnikrishnan
Department of Defense,
Biotechnology High Performance Computing
Software Applications Institute,
Telemedicine and Advanced Technology
Research Center,
U.S. Army Medical Research and Materiel
Command,
504 Scott Street,
Fort Detrick, MD 21702
e-mail: gunnikrishnan@bhsai.org

H. Mao
Department of Defense,
Biotechnology High Performance Computing
Software Applications Institute,
Telemedicine and Advanced Technology
Research Center,
U.S. Army Medical Research and Materiel
Command,
504 Scott Street,
Fort Detrick, MD 21702
e-mail: hmao@bhsai.org

X. Duan
Department of Defense,
Biotechnology High Performance Computing
Software Applications Institute,
Telemedicine and Advanced Technology
Research Center,
U.S. Army Medical Research and Materiel
Command,
504 Scott Street,
Fort Detrick, MD 21702
e-mail: xduan@bhsai.org

Assessment of the Effectiveness of Combat Eyewear Protection Against Blast Overpressure

It is unclear whether combat eyewear used by U. S. Service members is protective against blast overpressures (BOPs) caused by explosive devices. Here, we investigated the mechanisms by which BOP bypasses eyewear and increases eye surface pressure. We performed experiments and developed three-dimensional (3D) finite element (FE) models of a head form (HF) equipped with an advanced combat helmet (ACH) and with no eyewear, spectacles, or goggles in a shock tube at three BOPs and five head orientations relative to the blast wave. Overall, we observed good agreement between experimental and computational results, with average discrepancies in impulse and peak-pressure values of less than 15% over 90 comparisons. In the absence of eyewear and depending on the head orientation, we identified three mechanisms that contributed to pressure loading on the eyes. Eyewear was most effective at 0 deg orientation, with pressure attenuation ranging from 50 (spectacles) to 80% (goggles) of the peak pressures observed in the no-eyewear configuration. Spectacles and goggles were considerably less effective when we rotated the HF in the counter-clockwise direction around the superior-inferior axis of the head. Surprisingly, at certain orientations, spectacles yielded higher maximum pressures (80%) and goggles yielded larger impulses (150%) than those observed without eyewear. The findings from this study will aid in the design of eyewear that provides better protection against BOP. [DOI: 10.1115/1.4039823]

[1]Corresponding author.
Manuscript received August 7, 2017; final manuscript received March 19, 2018; published online April 19, 2018. Assoc. Editor: Barclay Morrison.

 Copyright © 2018 by ASME

Downloaded From: https://biomechanical.asmedigitalcollection.asme.org/ on 05/14/2018 Terms of Use: http://www.asme.org/about-asme/terms-of-use

S. T. Williams
Visual Protection and Performance Division,
U.S. Army Aeromedical Research Laboratory,
Bldg. 6901, Farrel Road,
Fort Rucker, AL 36362
e-mail: steven.t.williams26.ctr@mail.mil

T. H. Harding
Visual Protection and Performance Division,
U.S. Army Aeromedical Research Laboratory,
Bldg. 6901, Farrel Road,
Fort Rucker, AL 36362
e-mail: thomas.h.harding.civ@mail.mil

N. Chandra
Department of Biomedical Engineering,
Center for Injury Biomechanics, Materials and Medicine,
New Jersey Institute of Technology,
University Heights,
Newark, NJ 07102
e-mail: namas.chandra@njit.edu

J. Reifman[1]
Department of Defense,
Biotechnology High Performance Computing Software Applications Institute,
Telemedicine and Advanced Technology Research Center,
U.S. Army Medical Research and Materiel Command,
504 Scott Street,
Fort Detrick, MD 21702
e-mail: jaques.reifman.civ@mail.mil

Introduction

Exposure to explosive devices has been associated with 80% of eye injuries observed in United States (U.S.) Service members deployed to the recent conflicts in Iraq and Afghanistan [1]. This includes members who wore eye protection (24%; 34% of whom wore spectacles, 22% goggles, and the rest wore non-U.S. Department of Defense issued eyewear), members who did not (34%), and those whose use of eyewear protection is not known [1]. The shock wave, and the subsequent blast wind, resulting from such high-energy explosive devices can lead to different types of eye injuries. These include those potentially caused by the direct interaction of the blast wave itself with the eyes (i.e., primary blast injury) as well as injuries caused by the contact of objects with the eyes, including both blunt force trauma and penetrating trauma (e.g., from impinging shrapnel) [2]. Therefore, since 2005, Service members have been required to use protective eyewear, such as spectacles and goggles, during training and deployment [3]. Puzzlingly, while this requirement reduced the number of penetrating eye injuries, proving to be effective against shrapnel, no such relationship was observed for nonpenetrating injuries, i.e., closed-eye injuries [4].

One possible explanation is that military-issued eyewear is not effective against blast waves. However, to date, there is no consensus on whether a blast wave alone can cause eye injury [5]. This is because in a battlefield environment, Warfighters can be simultaneously exposed to a blast wave, blunt force trauma, and shrapnel, making it nearly impossible to isolate a primary blast injury from the other types of eye injuries. In contrast, studies using different rodent animal models have shown that exposure to a blast wave alone can cause eye injury. For example, incident pressures above 120 kPa can cause corneal edema and photoreceptor cell loss in mice [6], a decrease in retinal ganglion cell response in mice [7], and damage to cells of the optic nerves in rats [8]. These results suggest that a blast wave can potentially cause eye injury in humans as well. Indeed, recent finite element (FE) studies have investigated the potential causes of primary-blast-induced eye injury, suggesting different mechanisms of injury without providing, difficult-to-obtain, supporting experimental evidence [9,10].

Bailoor and colleagues investigated the effectiveness of eyewear in reducing the blast-induced pressure, the so-called blast overpressure (BOP), on the eyes [11]. They performed three-dimensional (3D) FE simulations using models of a human head equipped with spectacles and goggles, and used the mass of trinitrotoluene and stand-off distance as input conditions in their model to simulate the incident BOP. They reported that both spectacles and goggles offer protection, with goggles providing greater protection than spectacles at BOPs of 53 and 216 kPa. However, they used a mechanically rigid model for representing the goggles, which may eliminate loading on the eyes due to deflection of the goggles, and did not incorporate the soft padding of the goggles in the model, creating a gap between the goggles and the face, which can lead to incorrect predictions of the pressure on the eyes. Moreover, this study only investigated eyewear effectiveness with the head model directly facing the blast wave, and only reported experimental results for the maximum pressure on the eyes, with no comprehensive comparison between experimental data and simulations. In addition, none of these studies revealed potential

Downloaded From: https://biomechanical.asmedigitalcollection.asme.org/ on 05/14/2018 Terms of Use: http://www.asme.org/about-asme/terms-of-use

correlations between blast wave parameters (e.g., peak overpressure, impulse, or positive time duration) and eye injury.

The objective of this work was to assess the effectiveness of combat eyewear against BOP by performing experiments and 3D FE simulations. In particular, using the FE model, we sought to characterize the mechanisms by which BOP bypasses eyewear and loads the surface of the eyes at different head orientations relative to the oncoming blast wave. In total, we investigated 45 conditions, including a head form (HF) with no eyewear, spectacles, or goggles, five different head orientations relative to the oncoming blast wave, and three BOPs.

Materials and Methods

Shock Tube Experiments. We used a compressed-gas shock tube located at the New Jersey Institute of Technology. The shock tube had a cylindrical driver section (197 mm in inner diameter) that transitioned to a square-driven section with a cross-sectional length of 711 mm, which housed the test section (Fig. 1(*a*)). The driver and driven sections were 438- and 6871-mm long, respectively, and were separated by several frangible Mylar membranes. We pumped helium into the driver section until the membranes ruptured and generated a Friedlander-type blast wave [12]. We measured the static pressure-time profile of the blast wave at a point 2,946 mm from the membranes using a pressure sensor (model 134A24; PCB Piezotronics, Depew, NY) with its sensing surface parallel to the flow of the blast wave. For data acquisition, we used a custom LabVIEW code running on a National Instruments PXI-6133 S Series multifunction data acquisition modules and PXIe-1082 PCI Express chassis. We recorded the data at a sampling frequency of 1.0 MHz.

We developed a human head form using a polyurethane resin (BC 8007-2; Prospector, Overland Park, KS). The head height (the distance between the tragion and the top of the head) conformed to that of the 50th percentile male based on the U.S. Army anthropometric survey [13]. The head form had two hollow shafts, one at the left cornea and the other at the right cornea, which were equipped with a pressure sensor (model 113B26; PCB Piezotronics, Depew, NY) to measure the surface pressure on each eye. We fastened the head form rigidly in the driven section at a distance of 3,310 mm from the membranes. We used a large advanced combat helmet (ACH) for head protection, and separately tested the Revision Sawfly spectacles (Revision Military, Essex Junction, VT) and the Arena Flakjak goggles (Arena Tactical, Orange, CA) (Fig. 1(*a*)). We chose Revision Sawfly spectacles and Arena Flakjak goggles because, when we conducted this study, they were included in the authorized protective eyewear list. We placed the eyewear on the head form and marked reference points on the head form. Then, before each test in the shock tube, we adjusted the eyewear to align with these reference points.

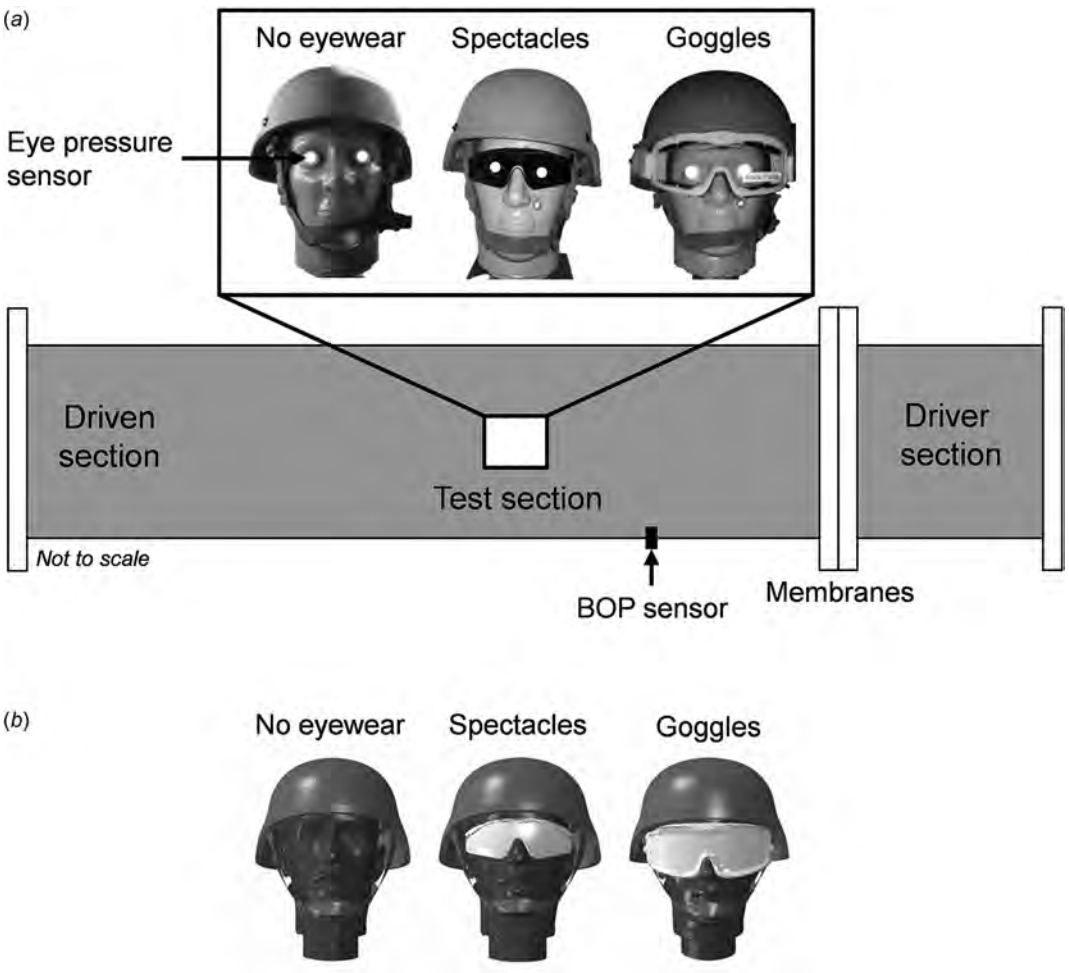


Fig. 1 (*a*) Schematic representation of a 711-mm square cross-sectional shock tube, indicating the driver section, driven section, and test section. We used a BOP sensor to measure the pressure of the oncoming blast wave in the driven section. We equipped the HF used in the experiment with two pressure sensors, one on each eye, outfitted the HF with an ACH, and assessed two eyewear protective equipment, the revision Sawfly spectacles and the Arena Flakjak goggles. (*b*) FE model of the head equipped with ACH for no eyewear, spectacles, and goggles.

Downloaded From: https://biomechanical.asmedigitalcollection.asme.org/ on 05/14/2018 Terms of Use: http://www.asme.org/about-asme/terms-of-use

Table 1 Material properties for spectacles and goggles

Eyewear	Component	Material	Density (kgm^{-3})	Young's modulus (MPa)	Poisson's ratio	References
Spectacles	Lens and frame	Polycarbonate	1220	2400	0.37	[15]
Goggles	Frame	Neoprene	1300	5	0.45	[15]
	Lens	Polycarbonate	1220	2400	0.37	[15]
	Foam	Soft foam	136	1	0.21	[14,16,17]

Finite Element Model. Similar to the previous studies that have modeled shock tubes, our FE model represented a portion of the driven section of the experimental shock tube [14]. The modeled portion was 1300-mm long and had a square cross-sectional length of 711 mm. We meshed the geometry with eight-noded hexahedral Eulerian elements using a biased meshing technique in ABAQUS (Dassault Systèmes, Vélizy-Villacoublay, France). With this technique, we assigned finer elements near the eyes of the head form and coarser elements elsewhere in the shock tube FE model. Finally, we assigned an ideal gas material property with an adiabatic constant of 1.4, a density of 1.2 kg·m^{-3}, and a temperature of 300 K for the atmospheric air within the shock tube FE model.

To represent the head form, ACH, spectacles, and goggles in our 3D FE model, we digitized them with a Creaform HandyScan 300 scanner (Creaform, Costa Mesa, CA) to create surface mesh models. Then, we imported these models into HyperMesh 12.0 (Altair, Inc., Troy, MI) (Fig. 1(*b*)). Next, we converted the head form and ACH surface meshes to discretely rigid shell elements (not deformable), and converted the surface mesh of the spectacles and goggles to a ten-node quadratic tetrahedral mesh (deformable). Finally, we assigned homogenous, isotropic elastic material properties to both spectacles and goggles (Table 1) [14–17].

We applied the BOPs measured in front of the head (Fig. 1(*a*)) during the experiments as an inlet boundary condition to the shock tube FE model. For the remaining surfaces of the model, we constrained the displacement in the direction perpendicular to each surface. The spectacles and goggles used in the model were not constrained; however, we constrained the head form and ACH along all degrees-of-freedom. Finally, as described by Ganpule and colleagues, we used the coupled Eulerian–Lagrangian method in ABAQUS to simulate blast-wave propagation [14].

Test Conditions and Mesh Convergence. We outfitted the head form with the ACH without eyewear, and performed shock-wave exposure experiments and computer simulations at BOPs of 70, 140, and 210 kPa, with the head facing the oncoming blast wave (0 deg orientation). Next, we rotated the head counterclockwise by 45, 90, 135, and 180 deg to study the effect of head orientation on eye surface pressure (Fig. 2(*a*)). Then, we separately equipped the head with spectacles or goggles and repeated the studies for the same BOPs and head orientations. Overall, we performed 45 simulations and 135 experiments (3 per condition), measuring the pressure on the left and right eyes (REs). Finally, to assess the accuracy of the simulations, we compared the pressure-time profiles, their integrated values (i.e., the impulse), and the maximum pressure between the experiments and simulations.

We performed mesh convergence studies for the shock tube elements using a 70 kPa BOP loading for each eyewear condition and determined 1.5 mm as an adequate edge length for the elements. With the biased meshing technique, we assigned 1.5-mm edge-length elements near the eyes and coarser elements elsewhere, which helped us reduce the total number of elements used for meshing the shock tube FE model from 194.7 to 4.1 million without affecting the accuracy of the results.

Results

Incident Blast Overpressures. Figure 2(*b*) shows the experimentally measured pressure-time profiles of incident blast waves for 70, 140, and 210 kPa. Each pressure-time profile had a Friedlander-type waveform, with a nearly instantaneous rise to the peak overpressure followed by an exponential-like decay.

Validation of Finite Element Models. To validate our FE model, we compared the experimentally obtained and simulated values of peak pressure on the surface of the eyes (Fig. 3 and Table 2). We observed good overall agreement between the simulations (bars) and the experiments (markers), with a mean error of 15% [standard deviation (SD) = 12%] over 90 comparisons on both eyes. We observed no systematic reason for such differences. Furthermore, we analyzed Pearson's correlation between the simulated and experimental values of maximum pressure, which yielded R^2 values of 0.98 and 0.95 for the left and right eyes, respectively. By comparing the experimental and simulated pressure-time profiles for all BOPs and orientations, we observed that our model also captured the essential features of the

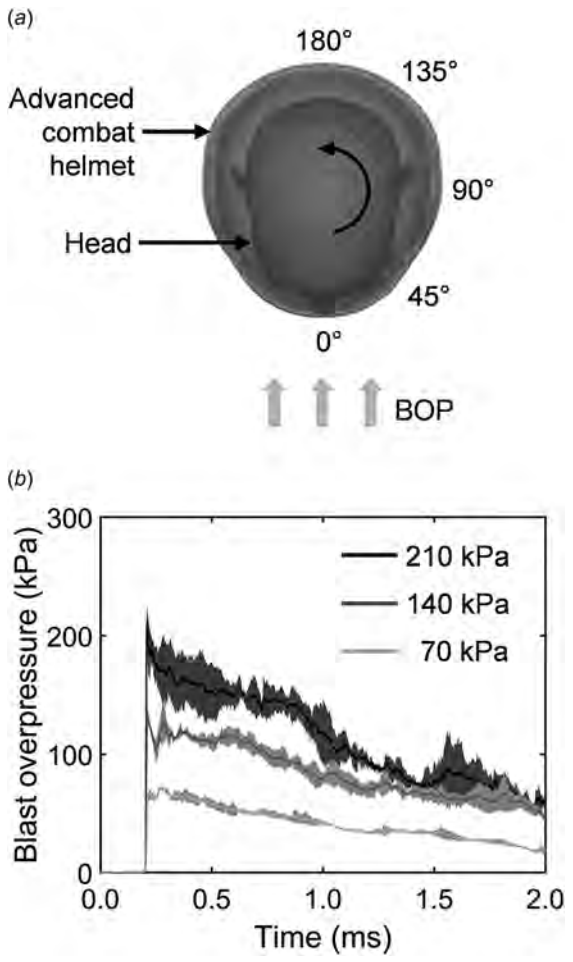


Fig. 2 (*a*) We investigated the effects of orientation by performing experiments and simulations at five orientations 0 (head on), 45, 90, 135, and 180 deg with and without eyewear and (*b*) experimentally measured pressure-time profiles ($N = 3$) for incident BOPs of 70, 140, and 210 kPa (line and shaded region; mean ± one standard deviation)

Downloaded From: https://biomechanical.asmedigitalcollection.asme.org/ on 05/14/2018 Terms of Use: http://www.asme.org/about-asme/terms-of-use

experimental profiles. Figures 4 and 5 compare the experimental and simulated profiles for the left eye (LE) and the right eye, respectively, at a BOP of 210 kPa. The figures show that the simulated profiles captured key features of the experiment, such as the multiple peaks observed on the right eye for 90 and 135 deg orientations. In addition, we compared the impulse (the area under the pressure-time profile) between experiments and simulations. This also yielded good overall agreement with a mean error of 13% (SD = 9%) over 90 comparisons on both eyes (Table 3). We also analyzed Pearson's correlation between the simulated and experimental values of impulse, which yielded R^2 values of 0.94 and 0.91 for the left and right eyes, respectively.

No-Eyewear Condition

Maximum Eye Surface Pressure. We investigated the interactions between the blast wave and eyes by varying the BOP and the angle of blast exposure (where 0 deg indicated the condition when the head directly faced the oncoming blast wave), and then measuring the maximum eye surface pressures. From our simulations, without eyewear at 0 deg, for both eyes, a BOP of 70 kPa led to a maximum pressure of 216.33 kPa, while a BOP of 140 kPa resulted in a maximum pressure of 465.95 kPa. Hence, the maximum pressure increased by approximately threefold relative to the incident BOP (Fig. 3 and Table 2). Interestingly, a BOP of 210 kPa resulted in an average maximum eye surface pressure for both eyes of 1114.95 kPa, a fivefold increase relative to the incident BOP.

Pressure-Time Profiles. For no eyewear at 0 deg and 210 kPa, the experimental and simulated pressures on the eyes rose to their peak values, and then decayed exponentially on both eyes (Figs. 4 and 5, top left). Interestingly, the pressure on the left eye, at 90 and 135 deg orientations, after an initial rise, decayed exponentially after an initial rise and then began to increase again at ~0.5 ms (Fig. 4). On the right eye, we observed two distinct peaks in the pressure-time profiles at 90 and 135 deg (Fig. 5). At 180 deg orientation, the pressure-time profiles for both eyes showed delayed peaks, which were considerably higher than those at 90 and 135 deg, followed by an exponential decay.

Impulse. For no eyewear at each BOP, both experiments and simulations showed that the impulse on the left eye decreased monotonically when we rotated the head in the counter-clockwise direction from 0 to 90 deg (Table 3). However, it increased when we rotated the head from 90 to 180 deg. Interestingly, at 135 deg and all BOPs, the impulse on the left eye was higher than that on the right eye.

Effect of Spectacles

Maximum Eye Surface Pressure. From simulations, with the spectacles at a BOP of 70 kPa and 0 deg orientation, we observed that the maximum pressure decreased by an average of ~50% on both eyes (Fig. 3, top). Furthermore, for BOPs of 140 and 210 kPa, the percentage reduction in eye surface pressures increased to ~60 and ~75%, respectively (Fig. 3, middle and bottom). Interestingly, beyond 45 deg for all BOP intensities, spectacles offered little benefit, and in some cases, resulted in higher pressures than those for no eyewear (e.g., 70 kPa at 90 deg, 140 kPa at 180 deg, and 210 kPa at 90 deg).

Pressure-Time Profiles. From both experiments and simulations, with the spectacles for a BOP of 210 kPa at 90 and 135 deg orientations, similar to the no-eyewear condition, the pressure on the left eye decayed exponentially followed by a pressure rise at ~1.0 and 0.5 ms, respectively (Fig. 4).

Effect of Goggles

Maximum Eye Surface Pressure. From both experiments and simulations, with the goggles at 0 deg, the maximum pressure decreased by an average of ~80% on both eyes for all BOPs (Fig. 3). Likewise, at 45 and 90 deg, we observed a decrease in left and right eye surface pressures relative to the no-eyewear condition. Interestingly, at 135 deg orientation, the maximum pressure on the left eye was higher with the goggles than it was in the no-eyewear condition at all three BOPs.

Pressure-Time Profiles. From both experiments and simulations, the use of goggles resulted in a markedly longer rise time to maximum pressure than the no-eyewear and spectacles conditions for all orientations and BOPs (Figs. 4 and 5).

Impulse. From our simulations, with the goggles at 90 deg orientation and 70 kPa BOP, we observed a ~25% increase in the impulse on the left eye, when compared to the no-eyewear condition (Table 3). Similarly, at BOPs of 140 and 210 kPa, the impulse on the left eye increased by ~65 and ~180%, respectively. We observed a similar trend in the impulse from our experimental results.

Discussion

We investigated the effectiveness of combat eyewear against primary blast exposure and determined the mechanisms by which blast waves load the surface of the eyes with and without eyewear protection. Specifically, we characterized the effectiveness of the eyewear using physical and simulated models of a head form with and without eyewear to experimentally measure and computationally determine the temporal evolution of pressure on the eyes, their integrated values (i.e., the impulse), and the maximum eye surface pressures caused by oncoming blast waves of 70, 140, and 210 kPa at five orientations (from 0 to 180 deg at 45 deg increments). We chose these pressures because the previous animal model studies have shown that blast waves can cause eye injury when the BOP exceeds 120 kPa [6–8]. Overall, we observed good agreement between experimental and computational results, with average impulse and peak-pressure discrepancies of less than 15% over 90 comparisons. To determine the mechanisms of blast loading to the surface of the eyes, we evaluated the development of pressure patterns in our FE simulations.

Our simulations suggest that in the absence of eyewear, three mechanisms contribute to pressure loading on the eyes: (1) direct interaction of the BOP with the eyes, (2) reflection of the BOP from facial features, such as the nose, cheeks, and forehead, and (3) a pressure surge (PS) around the head due to the combination of diffracted pressures (Fig. 3). At 0 deg orientation, the maximum pressure on both eyes was approximately threefold higher than the applied BOPs of 70 and 140 kPa. Our simulations suggest that this increase is due to a combination of two of these mechanisms. First, when the BOP directly interacted with the eye surface normally, the incident pressure was transformed into reflected pressure. This reflected pressure has been estimated to be between 2 and 8 times the incident BOP [18]. Second, our simulations demonstrated that the reflected pressures from the nose, forehead, and cheek funneled toward the eyes, which then combined with and amplified the pressure on the eyes (in front of the cornea). Similarly, using a FE model of a human head, Bhardwaj et al. also predicted that reflections from facial features influence the pressure loading on the eyes [9]. Although the mechanisms of loading did not change with an increase in the BOP, we observed a fivefold increase in the maximum eye surface pressures at 210 kPa. This increase was due to the nonlinear increase in the reflected pressure when we increased the BOP [18].

In contrast to the pressure-time profile at the 0 deg orientation, the profiles for the right eye at orientations of 90 and 135 deg with no eyewear had two peaks followed by an exponential decay (Fig. 5, left column). The first peak was due to the direct interaction of the BOP with the eye. Subsequently, the pressure reflected off the nose reloaded the eye to form the second peak. In this case, only two mechanisms—the direct interaction of the BOP with the eye and the reflection of the pressure wave from the nose—

Downloaded From: https://biomechanical.asmedigitalcollection.asme.org/ on 05/14/2018 Terms of Use: http://www.asme.org/about-asme/terms-of-use

contributed to the total pressure load on the right eye. Figure 6(*a*) shows the simulated temporal pressure evolution on the right eye at the 90 deg orientation. The direct interaction occurred at 0.27 ms, whereas the reloading by the pressure reflected off the nose occurred at 0.36 ms.

For the left eye, at 90 and 135 deg with no eyewear, the pressure first declined after reaching an initial peak, and then increased again, albeit at different rates and to different levels relative to the first peak (Fig. 4, left column). Our simulations showed that this secondary increase was due to the pressure surge originating from a combination of diffracted pressures around the head, which moved toward and reloaded the left eye. Figure 6(*b*) illustrates this process at 135 deg, where the surge formed around the head at 0.58 ms and the subsequent loading on the left eye occurred at 0.75 ms. Because for this orientation the left eye was closer to the surge than the right eye and because at this time the pressure from the direct interaction was still unloading the eyes, unexpectedly, the left eye experienced higher pressures and larger impulses than the right eye for all BOPs.

Finally, at 180 deg with no eyewear, our simulations showed that the blast waves diffracted by the helmet engulfed the head and directly loaded the eyes. Subsequently, the pressure reflected off the nose reloaded both eyes and, at the same time, the waves diffracted from both sides of the head combined in front of the head and generated a pressure surge that loaded the eyes. Therefore, at this orientation, all three mechanisms contributed to the pressure loading on the eyes.

With spectacles at 0 deg, the maximum eye surface pressures decreased by ~50% relative to the no-eyewear condition at a BOP of 70 kPa (Fig. 3, top row). Our simulations suggest that this reduction occurred because the spectacles prevented the blast wave from directly loading the eyes. However, the pressure reflected off the cheek entered through the gap between the spectacles and the face, and then loaded the eyes indirectly.

Table 2 Peak eye surface pressure from experiments ($N = 3$) and simulations on the left and REs at BOPs of 70, 140, and 210 kPa for three eyewear conditions and five head orientations relative to the incident BOP

			Peak eye surface pressure (kPa)			
			Left eye		Right eye	
Blast overpressure (kPa)	Eyewear type	Counter-clockwise orientation (Deg)	Experiment ($N = 3$) [Mean (SD*)]	Simulation	Experiment ($N = 3$) [Mean (SD*)]	Simulation
70	No eyewear	0	218.05 (6.05)	218.11	194.64 (4.44)	214.55
		45	126.93 (5.78)	141.60	192.14 (16.29)	195.30
		90	52.82 (1.12)	57.03	102.93 (0.95)	99.87
		135	62.51 (2.94)	58.11	53.29 (1.00)	64.65
		180	70.68 (2.52)	55.11	63.51 (2.39)	55.99
	Spectacles	0	140.37 (11.00)	99.93	134.73 (21.98)	114.22
		45	124.60 (15.52)	126.06	144.38 (15.34)	139.81
		90	66.47 (5.27)	65.92	114.55 (3.49)	106.35
		135	59.48 (1.84)	52.84	86.93 (0.69)	89.85
		180	70.77 (4.17)	72.68	66.55 (1.61)	72.23
	Goggles	0	41.44 (1.77)	42.07	40.70 (5.97)	39.28
		45	41.69 (0.80)	40.30	38.55 (0.87)	30.18
		90	40.81 (0.60)	36.03	35.29 (1.48)	34.37
		135	67.27 (2.83)	60.68	47.76 (0.83)	37.40
		180	64.97 (2.61)	47.07	48.05 (2.63)	56.64
140	No eyewear	0	532.82 (53.56)	459.35	537.59 (38.66)	472.55
		45	297.79 (2.84)	259.09	492.25 (8.31)	386.31
		90	121.39 (4.72)	140.92	179.12 (10.25)	239.17
		135	94.90 (0.51)	95.12	77.47 (5.36)	110.47
		180	138.46 (8.78)	116.94	134.70 (6.46)	109.24
	Spectacles	0	241.72 (24.59)	175.40	234.26 (10.42)	215.18
		45	207.02 (17.06)	242.46	323.57 (34.38)	361.80
		90	127.10 (11.52)	141.46	261.54 (30.99)	240.35
		135	116.86 (10.72)	96.12	159.28 (4.88)	109.61
		180	132.33 (7.12)	157.93	126.53 (9.37)	127.20
	Goggles	0	108.72 (14.39)	87.33	96.73 (16.04)	82.66
		45	96.64 (17.07)	72.33	95.14 (12.97)	62.86
		90	78.91 (9.88)	74.66	82.79 (3.37)	68.07
		135	124.39 (5.47)	104.95	81.98 (3.43)	74.58
		180	101.68 (6.14)	92.69	96.01 (4.54)	111.35
210	No eyewear	0	1064.53 (121.88)	1064.90	1049.69 (122.09)	1165.03
		45	403.90 (61.48)	384.97	780.31 (132.14)	678.68
		90	136.12 (18.20)	117.31	179.57 (29.74)	207.62
		135	103.89 (1.65)	92.44	99.20 (6.96)	114.90
		180	201.57 (15.71)	210.13	172.28 (16.79)	178.41
	Spectacles	0	322.77 (35.88)	239.20	342.77 (62.52)	252.26
		45	283.36 (12.86)	254.16	525.09 (117.85)	391.64
		90	186.78 (16.07)	173.11	412.55 (116.96)	307.41
		135	139.85 (14.95)	92.34	176.39 (9.46)	211.89
		180	182.83 (6.65)	195.76	166.38 (5.72)	144.06
	Goggles	0	171.06 (21.95)	187.45	175.63 (15.33)	184.56
		45	127.85 (7.77)	112.93	149.74 (3.44)	146.97
		90	84.07 (2.07)	99.11	120.64 (8.38)	102.36
		135	148.72 (6.60)	108.76	102.54 (6.26)	78.17
		180	122.42 (5.56)	108.89	142.90 (10.17)	123.76

Downloaded From: https://biomechanical.asmedigitalcollection.asme.org/ on 05/14/2018 Terms of Use: http://www.asme.org/about-asme/terms-of-use

Subsequently, the pressure rebounded off the brow ridges and started to travel back-and-forth in the pocket between the face and the inner wall of the spectacles, which further increased the eye surface pressure. These findings are consistent with those reported by Bailoor et al., who used a FE model of a human head equipped with spectacles [11]. Interestingly, with the use of spectacles, an increase in the BOP resulted in an increase in the percentage reduction in the eye surface pressures. This is because the spectacles prevented the formation of reflected pressure, which increased nonlinearly with an increase in the BOP for the no-eyewear condition.

For the right eye, at 90 and 135 deg, the gap between the face and the spectacles was directly exposed to the blast wave. Under this condition, our simulations showed that the pressure wave entered through the gap and loaded the right eye. Then, the wave reflected off the nose reloaded the eye, generating a second peak (Fig. 5, middle column). Next, owing to the back-and-forth interaction, the pressure further increased within the pocket. This surge in pressure was responsible for the third peak observed in the simulated pressure-time profile. In contrast to the no-eyewear condition, which showed only two peaks (Fig. 5, left column), the spectacles caused this rise in pressure by preventing the pressure reflected off the nose to expand and dissipate. As a consequence, the use of spectacles was not beneficial at these orientations. For the left eye, at 90 and 135 deg, as seen in the no-eyewear condition, the pressure first decayed after reaching an initial peak, and then increased again (Fig. 4, middle column). This increase was due to the pressure surge from the diffracted pressures that entered through the gap between the spectacles and the face and reloaded the eye. Although the eye surface pressure was higher with spectacles compared to the no-eyewear condition at the 90 deg orientation, it is important to note that the peak pressures reached were still lower than those at the 0 and 45 deg orientations.

At 180 deg, the BOP entered through the gap between the spectacles and the face on the side of the spectacles (near the temples) and loaded both eyes. Subsequently, the pressure loading on the eyes increased in intensity within the pocket formed by the inner wall of the spectacles with the nose and the face.

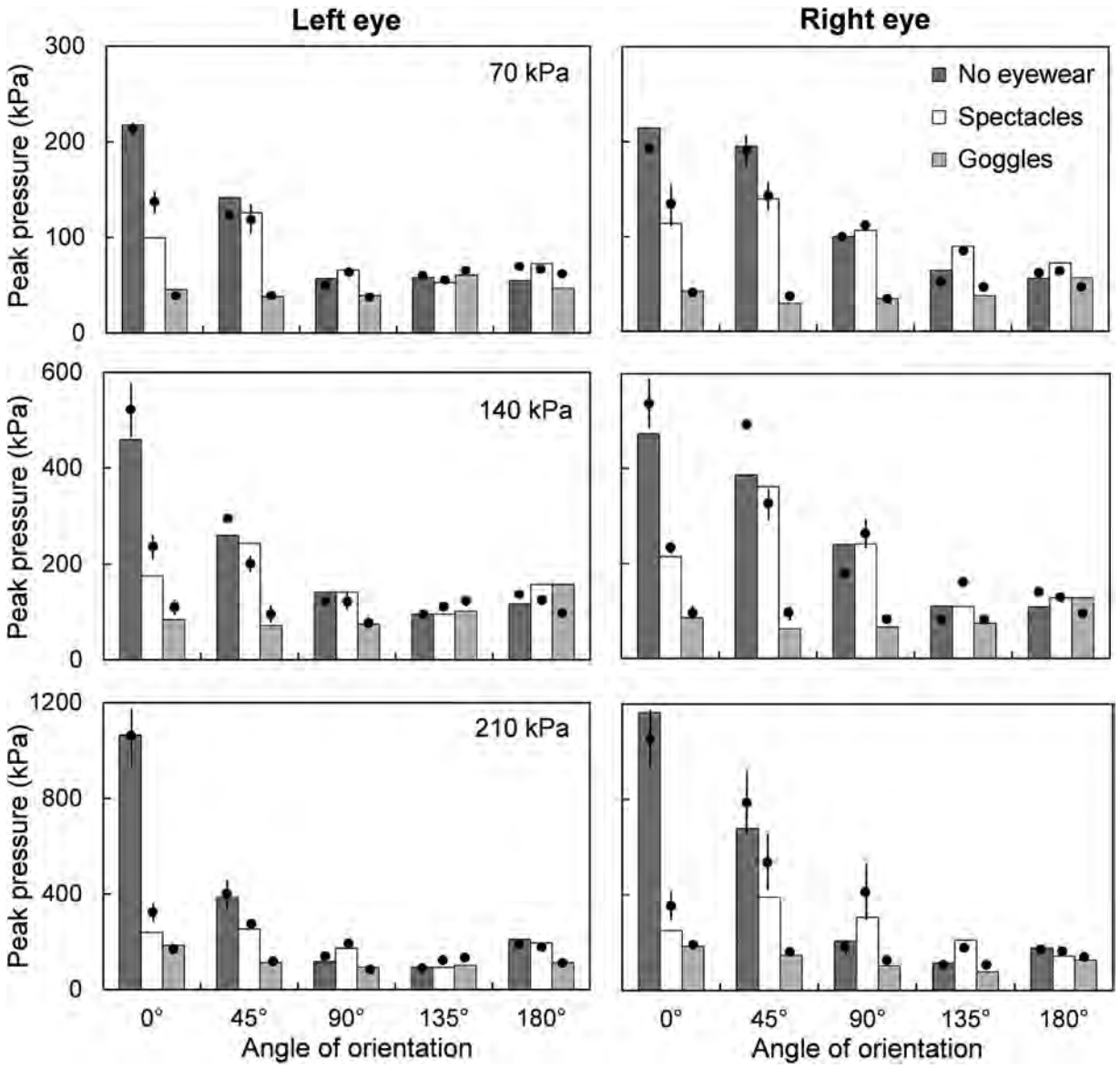


Fig. 3 Maximum average pressure from experiments (markers and vertical lines; mean ± one standard deviation) ($N = 3$) and simulations (bars) on the left and right eyes at BOPs of 70, 140, and 210 kPa for three eyewear conditions and five head orientations relative to the incident BOP

Downloaded From: https://biomechanical.asmedigitalcollection.asme.org/ on 05/14/2018 Terms of Use: http://www.asme.org/about-asme/terms-of-use

Simultaneously, the waves diffracted by the helmet combined in front of the head and formed a pressure surge, which the spectacles prevented from directly interacting with the eyes. However, it entered through the gap between the spectacles and the face, and loaded the eyes.

With goggles at 0 deg, the maximum eye surface pressure decreased by ~80% relative to the no eyewear condition for all BOPs (Fig. 3). Our simulations showed that when the BOP impinged upon the goggles, the lens deflected inward and initiated a pressure wave within the goggles, which caused the primary loading on the eyes. Subsequently, the pressure wave underwent back-and-forth reflections in the pocket between the inner walls of the goggles and the face, which slowly increased the pressure on the eyes (Figs. 4 and 5, right column). Because the goggles fitted the face snugly, the pressure within the goggles dissipated more slowly than when using spectacles or in the no-eyewear condition. Consequently, the pressure on the eyes was sustained for a longer duration for all BOPs.

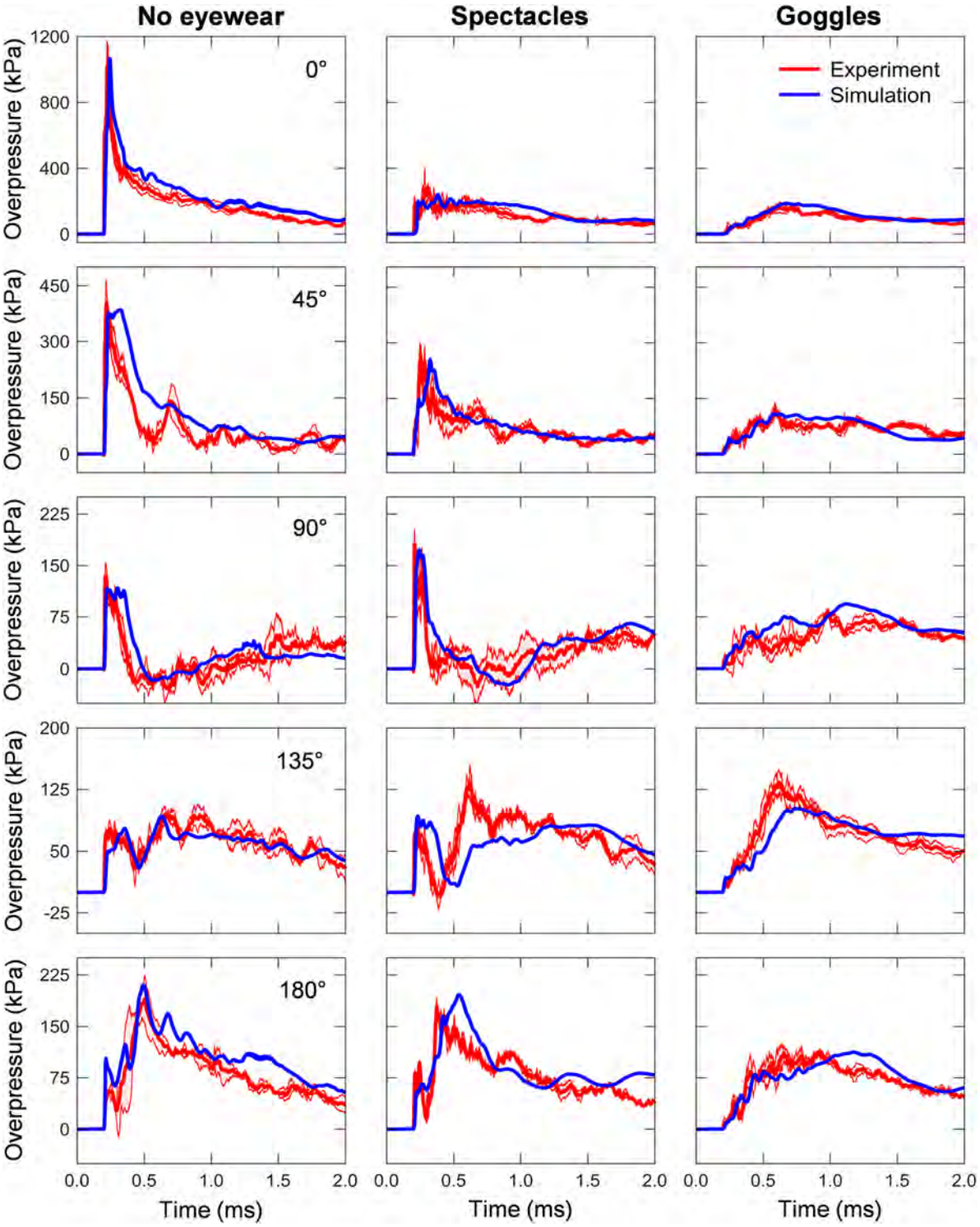


Fig. 4 Left eye surface pressure-time profile comparisons between experiments (red line (grey in B/W) and shaded region; mean ± standard deviation) ($N = 3$) and simulations (blue line (black in B/W)) at 210 kPa BOP for three eyewear conditions and five head orientations relative to the incident BOP

Downloaded From: https://biomechanical.asmedigitalcollection.asme.org/ on 05/14/2018 Terms of Use: http://www.asme.org/about-asme/terms-of-use

The maximum eye surface pressure with goggles was less than the no-eyewear condition for both eyes in almost all conditions (BOPs and orientations), with the exception of the left eye at 135 deg. At this orientation, the initial loading on the left eye occurred when the BOP impinged on the goggles. Then, the pressure surge from the combination of diffracted pressures also loaded the left side of the goggles, resulting in a higher left eye surface pressure relative to the no-eyewear condition for all BOPs (Figs. 3 and 4). At 180 deg, the goggles prevented the direct interaction of the combination of diffracted pressures with the eyes. Consequently, the pressures were lower relative to the no-eyewear condition for all BOPs.

Perhaps the most surprising finding of our work was that, in stark contrast to the maximum eye surface pressure, at a head orientation of 90 deg, the impulse on the left eye was substantially higher with goggles than without eyewear for all BOPs (Table 3), whereas the opposite was true for the maximum pressure (Fig. 3, left column). Our simulations showed that when the pressure

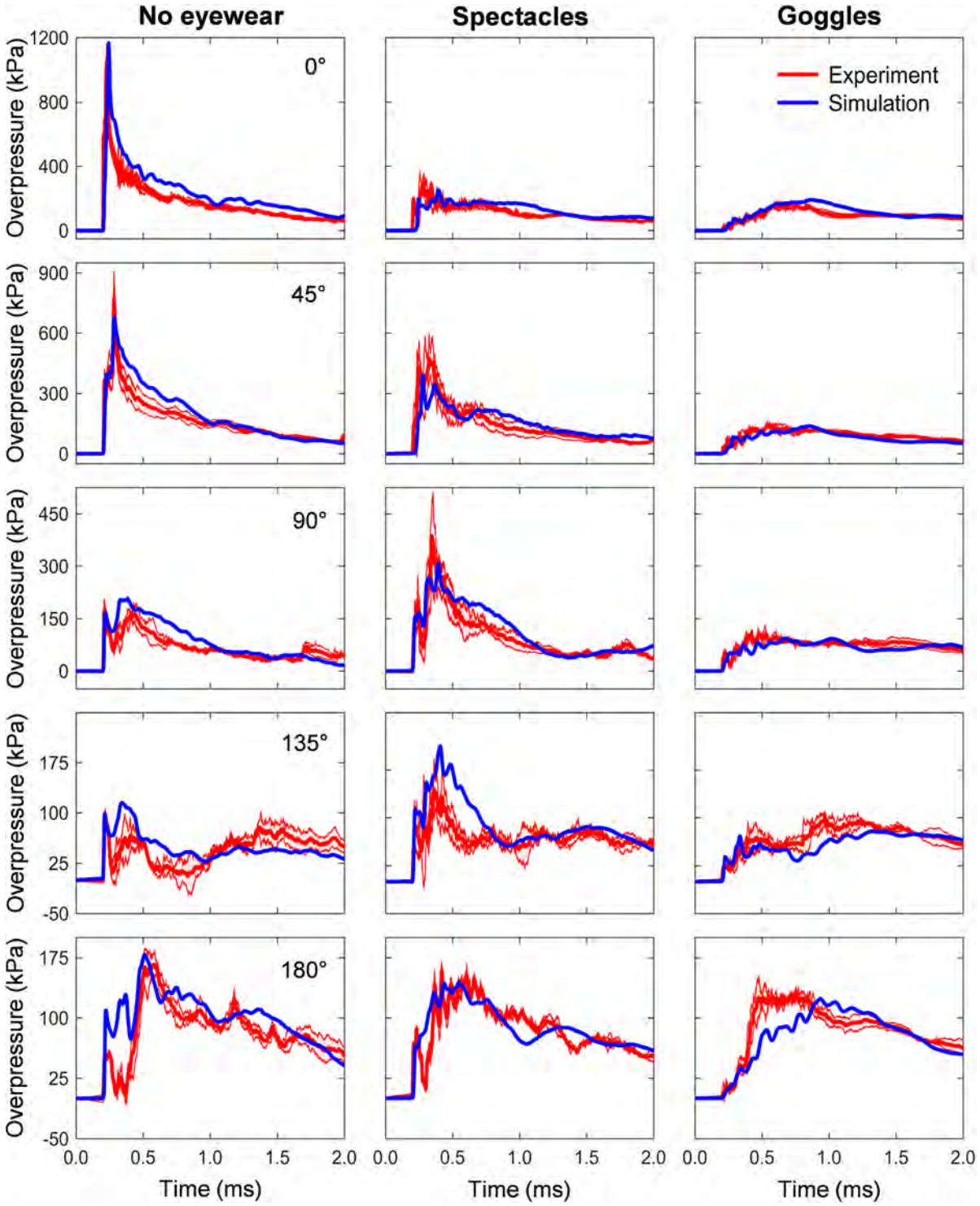


Fig. 5 Right eye surface pressure-time profile comparisons between experiments (red line (grey in B/W) and shaded region; mean ± standard deviation) ($N = 3$) and simulations (blue line (black in B/W)) at 210 kPa BOP for three eyewear conditions and five head orientations relative to the incident BOP

Downloaded From: https://biomechanical.asmedigitalcollection.asme.org/ on 05/14/2018 Terms of Use: http://www.asme.org/about-asme/terms-of-use

loading on the left eye from the direct interaction of the BOP with the goggles started to decay, the pressure loading from the combination of the diffracted pressures loaded and sustained the pressure on the eye (Fig. 4, right column, middle panel). Consequently, the pressure on the eye was prolonged, which resulted in a higher impulse than the no-eyewear condition despite the lower maximum pressure. Although these results suggest that goggles may not protect the eyes from BOP beyond the 90 deg orientation, they still perform better than spectacles in reducing surface pressure on the eyes and are protective against secondary blast injuries, which are the major cause of eye injuries in the field [2,4].

One limitation of our study was that we used an ideal Friedlander waveform, whereas in real-world conditions the loading pressure is more complex, because it is influenced by surrounding structures. Nevertheless, the use of such a waveform has become a standard practice when studying the effects of primary blast exposure mimicking an open-field environment. Second, in our FE model, we assumed the ACH, the head form, and the face, including the eyes, to be rigid materials. Although this might have resulted in slight overestimation of the eye surface pressures, we expect the findings discussed herein to remain valid despite such simplifications. Third, although our study design covered 45 distinct conditions, the realities of time and cost prevented us from studying certain configurations, such as head-form rotations upward and downward from the horizontal plane. Such a shortcoming notwithstanding, the benefit of a validated FE model is that it could reliably predict other configurations beyond those experimentally explored. Fourth, we mounted the head form rigidly to the shock tube, preventing its movement. This assumption does not realistically emulate loading conditions in the field because, in reality, relative motion between the body and the head can occur. To investigate the validity of this assumption, we performed an additional FE simulation where we changed the boundary condition and allowed the head form to move freely. When compared to the rigidly fixed head-form results, we observed no differences in the reflected pressure and surge effects, leading us to conclude that these responses occur within a few milliseconds

Table 3 Impulse from experiments ($N = 3$) and simulations on the left and REs at BOPs of 70, 140, and 210 kPa for three eyewear conditions and five head orientations relative to the incident BOP

			Left eye impulse (kPa·ms)		Right eye impulse (kPa·ms)	
Blast overpressure (kPa)	Eyewear type	Counter-clockwise orientation (Deg)	Experiment ($N = 3$) [Mean (SD*)]	Simulation	Experiment ($N = 3$) [Mean (SD*)]	Simulation
70	No eyewear	0	88.91 (1.96)	95.42	83.75 (1.55)	94.22
		45	60.83 (8.83)	68.48	80.02 (6.34)	94.36
		90	43.13 (1.34)	42.15	54.32 (0.54)	67.81
		135	69.23 (0.88)	58.19	38.06 (0.69)	56.16
		180	71.61 (1.93)	66.74	68.57 (0.79)	67.85
	Spectacles	0	79.80 (6.01)	103.64	69.11 (3.71)	97.86
		45	51.91 (0.20)	79.07	74.33 (2.08)	113.70
		90	50.38 (1.74)	53.24	63.63 (1.16)	82.67
		135	66.76 (2.55)	72.18	56.52 (7.29)	75.56
		180	75.55 (2.39)	68.91	70.92 (6.11)	68.17
	Goggles	0	63.34 (2.08)	57.91	52.55 (9.25)	57.79
		45	53.88 (2.40)	54.90	54.39 (1.81)	51.91
		90	57.25 (1.89)	53.92	52.80 (0.80)	47.58
		135	70.53 (1.59)	71.42	59.06 (0.98)	47.29
		180	69.63 (1.12)	69.72	66.11 (2.34)	71.86
140	No eyewear	0	202.91 (14.94)	225.69	197.29 (13.58)	229.70
		45	117.37 (3.90)	123.36	202.30 (4.32)	196.65
		90	51.10 (6.01)	66.82	124.50 (6.31)	186.12
		135	114.40 (0.73)	104.40	85.93 (12.20	91.38
		180	122.23 (5.01)	141.28	125.08 (7.77)	134.96
	Spectacles	0	129.46 (16.35)	176.15	134.75 (14.80)	141.55
		45	98.96 (5.32)	121.54	163.24 (7.97)	255.72
		90	62.29 (7.67)	56.46	133.73 (6.16)	138.22
		135	117.66 (2.39)	121.74	104.84 (5.78)	140.43
		180	125.79 (4.60)	149.21	122.53 (5.23)	143.40
	Goggles	0	119.77 (10.07)	123.01	119.90 (7.85)	122.26
		45	105.57 (8.78)	100.66	112.77 (7.55)	101.35
		90	91.39 (4.04)	111.60	102.11 (0.76)	114.85
		135	118.09 (5.08)	123.40	96.68 (10.07)	104.34
		180	107.30 (3.33)	124.48	103.55 (4.72)	133.64
210	No eyewear	0	359.71 (40.36)	456.04	339.35 (33.04)	453.97
		45	133.03 (6.13)	198.43	320.72 (36.60)	366.26
		90	39.44 (8.20)	45.88	132.03 (8.37)	112.28
		135	118.58 (10.17)	124.27	94.34 (13.86)	102.51
		180	156.70 (7.35)	202.20	164.89 (15.25)	192.52
	Spectacles	0	219.47 (20.50)	259.15	215.88 (12.25)	217.74
		45	138.90 (8.84)	157.16	272.55 (54.13)	293.15
		90	55.64 (18.16)	74.89	189.42 (31.85)	217.01
		135	128.31 (5.54)	123.33	139.07 (6.90)	169.42
		180	147.73 (4.97)	181.30	169.76 (3.79)	169.43
	Goggles	0	186.13 (14.98)	179.53	191.16 (12.55)	188.43
		45	135.37 (9.65)	141.83	180.07 (3.52)	170.13
		90	98.90 (2.73)	129.36	149.10 (8.49)	145.06
		135	150.21 (11.67)	135.61	137.98 (11.73)	117.38
		180	142.26 (3.14)	148.95	172.08 (4.21)	157.88

Downloaded From: https://biomechanical.asmedigitalcollection.asme.org/ on 05/14/2018 Terms of Use: http://www.asme.org/about-asme/terms-of-use

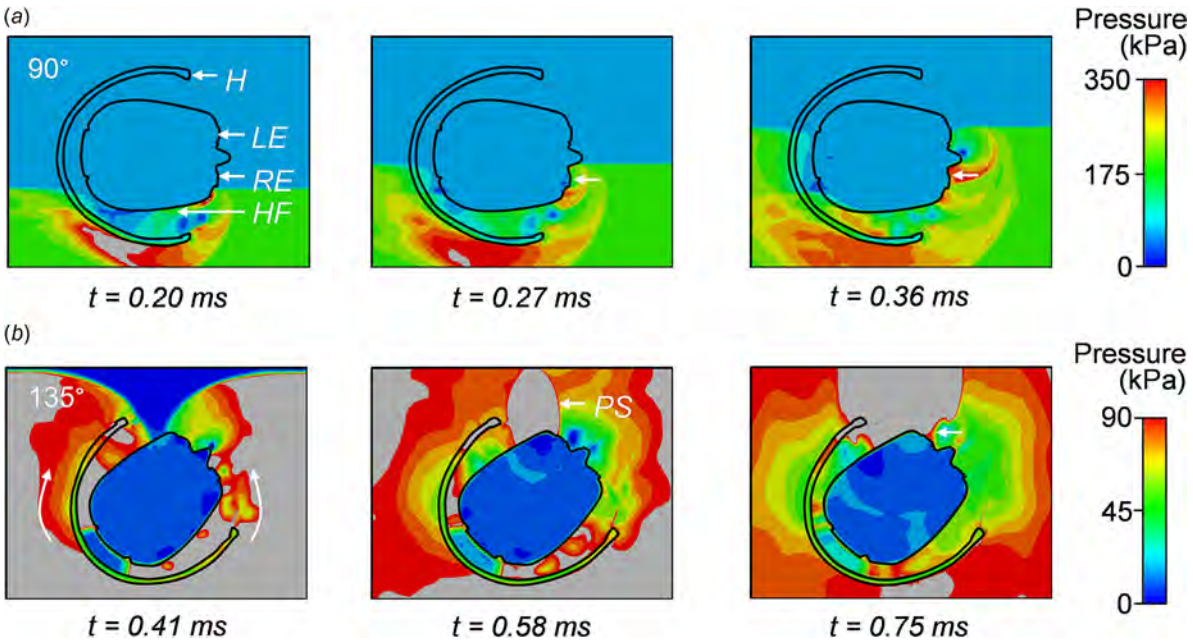


Fig. 6 Evolution of BOP on the LE and RE at the cross section of the HF and helmet (*H*) models seen from the top. (*a*) At 90 deg, we observed a BOP approaching the head at $t = 0.20$ ms, directly interacting (white arrow) with the RE at $t = 0.27$ ms, and reflecting off the nose and reloading the eye (white arrow) at $t = 0.36$ ms. (*b*) At 135 deg, we observed diffracted pressures engulfing the helmet and HF (white arrow) at $t = 0.41$ ms, followed by the formation of a PS from the combination of the diffracted pressures at $t = 0.58$ ms and the PS loading the LE (white arrow) at $t = 0.75$ ms.

after the blast wave interacts with the face during which the headform motion is negligible. Fifth, we modeled the eyewear using linear elastic material properties when most likely it is a viscoelastic material. Nevertheless, our comparison of the simulated peak eye surface pressures, pressure-time profiles, and impulse with 45 experiments suggests that this assumption has a small effect on the results. Finally, in the current form, our model cannot be used for predicting intraocular pressure or tissue strains. Therefore, we cannot make injury threshold predictions. Nonetheless, it revealed important insights on the mechanisms of BOP loading on the eyes at different orientations relative to the oncoming blast wave, with and without eyewear. Such knowledge is essential in developing a more detailed model, which may ultimately allow for such predictions in the future.

Conclusion

Our study revealed how a BOP with an ideal Friedlander waveform loads the eyes without and with eyewear (spectacles and goggles) on a rigid head form. We found that compared to Revision Sawfly spectacles, Arena Flakjak goggles offered better protection against such a BOP. However, the protective benefits depend on the shape and fit of the eyewear, as well as the size of the gap between the eyewear and the face. We also identified the mechanisms by which blast waves bypass these spectacles and goggles, and load the eyes at different head orientations relative to the oncoming blast waves. Finally, we quantitatively showed that, to different extents, both spectacles and goggles lose their effectiveness as the angle of the head orientation relative to the oncoming blast wave increases.

Acknowledgment

This research was supported by the U.S. Army Military Operational Medicine Research Program at the U.S. Army Medical Research and Materiel Command, Fort Detrick, MD. We thank the Air Force Research Laboratory, Dayton, OH, and the Army Research Laboratory, Adelphi, MD, for the use of high performance computing systems. The opinions and assertions contained herein are the private views of the authors and do not reflect the views of the U.S. Army or of the U.S. Department of Defense.

Funding Data

- Medical Research and Materiel Command (MOMRP-19780).

References

[1] Weichel, E. D., Colyer, M. H., Ludlow, S. E., Bower, K. S., and Eiseman, A. S., 2008, "Combat Ocular Trauma Visual Outcomes During Operations Iraqi and Enduring Freedom," Ophthalmology, **115**(12), pp. 2235–2245.
[2] Scott, R., 2011, "The Injured Eye," Philos. Trans. R. Soc. London B Biol. Sci., **366**(1562), pp. 251–260.
[3] Adams, G. L., 2004, "Combat Eye Protection, the FY 2005 Rapid Fielding Initiative (RFI), and the Approved Product List (APL)," U.S. Army Office of the Surgeon General and Assistant Chief, Medical Service Corps, Falls Church, VA.
[4] Cockerham, G. C., Rice, T. A., Hewes, E. H., Cockerham, K. P., Lemke, S., Wang, G., Lin, R. C., Glynn-Milley, C., and Zumhagen, L., 2011, "Closed-Eye Ocular Injuries in the Iraq and Afghanistan Wars," N. Engl. J. Med., **364**(22), pp. 2172–2173.
[5] Abbotts, R., Harrison, S. E., and Cooper, G. L., 2007, "Primary Blast Injuries to the Eye: A Review of the Evidence," J. R. Army Med. Corps, **153**(2), pp. 119–123.
[6] Hines-Beard, J., Marchetta, J., Gordon, S., Chaum, E., Geisert, E. E., and Rex, T. S., 2012, "A Mouse Model of Ocular Blast Injury That Induces Closed Globe Anterior and Posterior Pole Damage," Exp. Eye Res., **99**, pp. 63–70.
[7] Mohan, K., Kecova, H., Hernandez-Merino, E., Kardon, R. H., and Harper, M. M., 2013, "Retinal Ganglion Cell Damage in an Experimental Rodent Model of Blast-Mediated Traumatic Brain Injury," Invest. Ophthalmol. Vis. Sci., **54**(5), pp. 3440–3450.
[8] Wang, H. C., Choi, J. H., Greene, W. A., Plamper, M. L., Cortez, H. E., Chavko, M., Li, Y., Dalle Lucca, J. J., and Johnson, A. J., 2014, "Pathophysiology of Blast-Induced Ocular Trauma With Apoptosis in the Retina and Optic Nerve," Mil. Med., **179**(8S), pp. 34–40.
[9] Bhardwaj, R., Ziegler, K., Seo, J. H., Ramesh, K. T., and Nguyen, T. D., 2014, "A Computational Model of Blast Loading on the Human Eye," Biomech. Model. Mechanobiol., **13**(1), pp. 123–140.
[10] Rossi, T., Boccassini, B., Esposito, L., Clemente, C., Iossa, M., Placentino, L., and Bonora, N., 2012, "Primary Blast Injury to the Eye and Orbit: Finite Element Modeling," Invest. Ophthalmol. Vis. Sci., **53**(13), pp. 8057–8066.
[11] Bailoor, S., Bhardwaj, R., and Nguyen, T. D., 2015, "Effectiveness of Eye Armor During Blast Loading," Biomech. Model. Mechanobiol., **14**(6), pp. 1227–1237.

Downloaded From: https://biomechanical.asmedigitalcollection.asme.org/ on 05/14/2018 Terms of Use: http://www.asme.org/about-asme/terms-of-use

[12] Chandra, N., Ganpule, S., Kleinschmit, N. N., Feng, R., Holmberg, A. D., Sundaramurthy, A., Selvan, V., and Alai, A., 2012, "Evolution of Blast Wave Profiles in Simulated Air Blasts: Experiment and Computational Modeling," Shock Waves, **22**(5), pp. 403–415.
[13] Gordon, C. C., Blackwell, C. L., Bradtmiller, B., Parham, J. L., Barrientos, P., Paquette, S. P., Corner, B. D., Carson, J. M., Venezia, J. C., and Rockwell, B. M., 2014, "2012 Anthropometric Survey of U.S. Army Personnel: Methods and Summary Statistics," U.S. Army Natick Soldier Research, Development and Engineering Center, Natick, MA, DTIC Document No. ADA611869.
[14] Ganpule, S., Gu, L., Alai, A., and Chandra, N., 2012, "Role of Helmet in the Mechanics of Shock Wave Propagation Under Blast Loading Conditions," Comput. Methods Biomech. Biomed. Eng., **15**(11), pp. 1233–1244.
[15] Ellis, B., and Smith, R., 2008, *Polymers: A Property Database*, CRC Press, Boca Raton, FL.
[16] Lee, T., and Lakes, R. S., 1997, "Anisotropic Polyurethane Foam With Poisson's Ratio Greater Than 1," J. Mater. Sci., **32**(9), pp. 2397–2401.
[17] Shiina, Y., Hamamoto, Y., and Okumura, K., 2006, "Fracture of Soft Cellular Solids—Case of Non-Crosslinked Polyethylene Foam," Europhys. Lett., **76**(4), pp. 588–594.
[18] Needham, C. E., 2010, *Blast Waves*, Springer, Berlin.

Downloaded From: https://biomechanical.asmedigitalcollection.asme.org/ on 05/14/2018 Terms of Use: http://www.asme.org/about-asme/terms-of-use

Appendix A –Publication Cover 17
2018

Authors: K.V. Rama Rao, S. Iring, D. Younger, M. Kuriakose, M. Skotak, E. Alay, R. K. Gupta, N. Chandra

Title: "*A single primary blast-induced traumatic brain injury in rodent model causes cell-type dependent increase in NADPH oxidase isoforms in vulnerable brain regions*"

Journal Publication: Journal of Neurotrauma, 35,1-14, (2018), [18-17]

JOURNAL OF NEUROTRAUMA 35:1–14 (XXXX 00, 2018)
Mary Ann Liebert, Inc.
DOI: 10.1089/neu.2017.5358

Original Article

A Single Primary Blast-Induced Traumatic Brain Injury in a Rodent Model Causes Cell-Type Dependent Increase in Nicotinamide Adenine Dinucleotide Phosphate Oxidase Isoforms in Vulnerable Brain Regions

Kakulavarapu V. Rama Rao,[1] Stephanie Iring,[1] Daniel Younger,[1] Matthew Kuriakose,[1] Maciej Skotak,[1] Eren Alay,[1] Raj K. Gupta,[2] and Namas Chandra[1]

Abstract

Blast-induced traumatic brain injury (bTBI) is a leading cause of morbidity in soldiers on the battlefield and in training sites with long-term neurological and psychological pathologies. Previous studies from our laboratory demonstrated activation of oxidative stress pathways after blast injury, but their distribution among different brain regions and their impact on the pathogenesis of bTBI have not been explored. The present study examined the protein expression of two isoforms: nicotinamide adenine dinucleotide phosphate (NADPH) oxidase 1 and 2 (NOX1, NOX2), corresponding superoxide production, a downstream event of NOX activation, and the extent of lipid peroxidation adducts of 4-hydroxynonenal (4HNE) to a range of proteins. Brain injury was evaluated 4 h after the shock-wave exposure, and immunofluorescence signal quantification was performed in different brain regions. Expression of NOX isoforms displayed a differential increase in various brain regions: in hippocampus and thalamus, there was the highest increase of NOX1, whereas in the frontal cortex, there was the highest increase of NOX2 expression. Cell-specific analysis of changes in NOX expression with respect to corresponding controls revealed that blast resulted in a higher increase of NOX1 and NOX 2 levels in neurons compared with astrocytes and microglia. Blast exposure also resulted in increased superoxide levels in different brain regions, and such changes were reflected in 4HNE protein adduct formation. Collectively, this study demonstrates that primary blast TBI induces upregulation of NADPH oxidase isoforms in different regions of the brain parenchyma and that neurons appear to be at higher risk for oxidative damage compared with other neural cells.

Keywords: astrocytes; blast injury; 4-hydroxynonenal; microglia; neuron; NADPH oxidase; oxidative stress; traumatic brain injury

Introduction

Traumatic brain injury (TBI) resulting from different episodes of head trauma is one of the leading causes of morbidity and death in both military personnel and civilian populations. TBI causes approximately 1.5 million deaths and hospitalizations annually in the United States.[1–3] Blast-induced TBI (bTBI) is the most prevalent form of brain injury in soldiers in combat zones because of the widespread use of high explosives in the war zones, and an increasing number of cases has also been reported in civilian populations with the use of improvised explosive devices by insurgents.[4,5]

Among many pathological factors associated with either primary mechanical injury or secondary biochemical cascades, oxidative stress has been shown to play a major role in various models of TBI.[6,7] The main inducers of oxidative stress are reactive oxygen species (ROS), which include superoxide ($O2\bullet-$), hydroxyl radical ($HO\bullet$), and hydrogen peroxide (H_2O_2).[8,9] ROS are normally produced in several metabolic reactions, including redox-reactions (oxidation/reduction), oxidative phosphorylation, and in a normal

[1]Center for Injury Biomechanics, Materials and Medicine (CIBM[3]), Department of Biomedical Engineering, New Jersey Institute of Technology, Newark, New Jersey.
[2]Department of Defense Blast Injury Research Program Coordinating Office, United States Army Medical Research and Materiel Command, Fort Detrick, Maryland.

© Kakulavarapu V. Rama Rao et al., 2018. Published by Mary Ann Liebert, Inc. This Open Access article is distributed under the terms of the Creative Commons License (http://creativecommons.org/licenses/by/4.0), which permits unrestricted use, distribution, and reproduction in any medium, provided the original work is properly credited.

process of electron transport chain reactions. There are a number of enzymes that produce free radicals during their catalytic reactions, which include the nicotinamide adenine dinucleotide phosphate (NADPH) oxidase family, cytochrome P450 (CYP450), cyclooxygenase (COX), lipoxygenase (LOX), and xanthine oxidase.

The NADPH oxidase (NOX) is a multi-subunit enzyme that catalyzes the reduction of molecular oxygen and oxidation of NADPH to generate superoxide radicals ($O_2^{\bullet}-$). NOX is comprised of subunits that are both plasma membrane-bound (cytochrome b_{558}, composed of $p22^{phox}$ and $gp91^{phox}$) and cytoplasmic ($p40^{phox}$, $p47^{phox}$, and $p67^{phox}$), which spans across the lipid bilayers.[10,11] A number of NOX isoforms were identfied in the brain, which include NOX1, NOX2, and NOX4, and their cellular distribution is highly dependent on the cell type. Neurons express both NOX1 and NOX2, microglia are enriched with NOX2, while only small amounts of NOX isoforms were identified in astrocytes.[12]

Extensive experimental evidence suggests NOX plays a significant role in the pathophysiology of various forms of TBI. NOX has been shown to be upregulated in a brain in a controlled cortical impact model of trauma[13] and closed head injury models.[14–16] We have previously reported increased protein expression of NOX1 in a rodent model of a single blast injury at different blast overpressure exposures.[17,18] While these studies establish a primary role of NOX1 in the pathophysiology of various forms of TBI, no studies have been performed to determine the spatial and temporal resolution of NOX family of enzymes in the brain and their role in the pathophysiology of bTBI. It is hypothesized that in bTBI, a single blast overpressure exposure is capable of biomechanically loading the whole brain, which may trigger a cascade of biochemical events consistent with regional vulnerabilities.

The present study therefore examined the spatial resolution of two isoforms of NOX (NOX1 and NOX2) and their cellular distribution and changes in rats exposed to moderate blast TBI. Levels of superoxide and formation of protein adducts of 4-hydroxynonenal (4HNE) were also determined. Based on the evidence that blast overpressure waves travel through the whole brain, we hypothesize that blast-induced NOX-related oxidative stress will be diffuse across the brain. Moreover, we hypothesize that different neural cell types have differential susceptibility to the oxidative stress-inducing effect of the primary blast.

Methods

Animals

Adult 10-week-old male Sprague-Dawley (Charles River Laboratories) rats weighing 320–360 g were used in all the studies. The animals were housed with free access to food and water in a 12-h dark-light cycle at 22°C. All procedures followed the guidelines established in the *Guide for the Care and Use of Laboratory Animals* and were approved by Rutgers University Institutional Animal Care and Use Committee before experiments. Rats were divided into two groups (sham controls and animals exposed to a moderate blast of 180 kPa).

A total number of 24 rats was used in this study as follows: immunoblotting (three controls and three blast injured); immunofluorescence studies (four controls and four blast-injured); superoxide production studies (five controls and five blast-injured). For immunofluorescence studies, each brain tissue was processed to obtain several sections (>10) from frontal cortex, striatum, hippocampus, thalamus, and cerebellum. Each of those sections were used for identification of NOX1 and NOX2 isoforms in neurons, astrocytes, and microglia by double immunofluorescence analysis. Similarly, for superoxide production, several sections from different brain regions of animals (five control and five blast-injured) were used for regional analyses.

Blast injury

Rats were exposed to a single blast wave at the Center of Injury Biomechanics, Materials and Medicine (New Jersey Institute of Technology, Newark) in the 9-inch square cross section shock tube as described previously.[18,19] The primary shockwave generated in

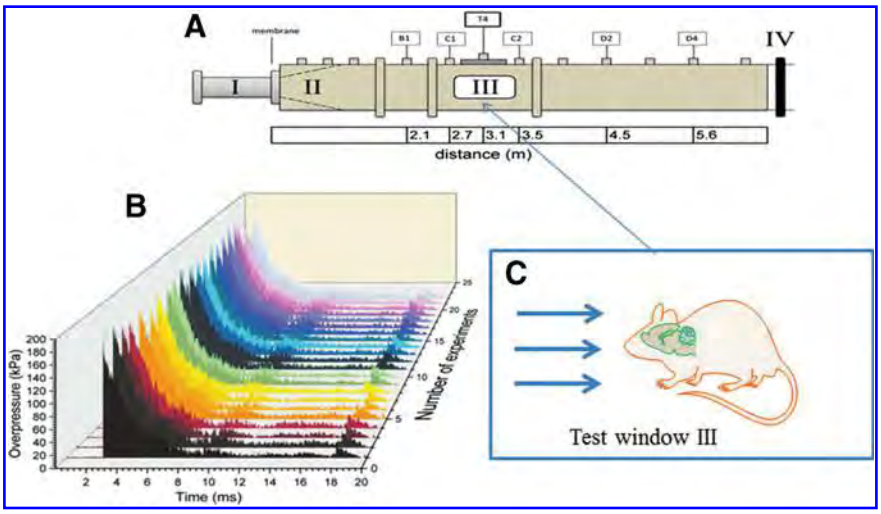


FIG. 1. Schematic depiction of the shock tube. (**A**) Schematic of 9×9 inch square, 30 feet long shock tube with section I-Breech with high pressure helium gas separated from section II by different thickness of mylar sheets that generate pure shockwave in section III where the specimens are located. Section IV is past the section and is a design requirement; the pressure-time cycle is identical to live fire tests with actual C-4 (or trinitrotoluene equivalent) explosives at specified standoff distance. (**B**) Composite of actual experimental profiles that generate 180 kPa with only about five kPa variation in peak pressure and less than a millisecond in duration. The front of the pressure rise indicates shock-wave conditions. (**C**) Schematic of rodent model in prone position facing the shock front. The shock travels in the rostral-caudal direction traversing the pre-frontal cortex, striatum, hippocampus, thalamus, visual cortex, and cerebellum within a period of a millisecond with minimal attenuation of pressure loading. Color image is available online at www.liebertpub.com.neu

this shock tube has been validated against the pressure-time profiles measured experimentally in the live-fire explosion experiments[10] and against theoretical pressure-time profiles associated with the detonation of C4 explosive (see Kuriakose and colleagues[20] for details).

All rats were anesthetized with a mixture of ketamine (100 mg/kg) and xylazine (10 mg/kg) at 10:1 ratio administered via intraperitoneal injection. Rats underwent a single exposure to 180 ± 5 kPa peak overpressure (duration: 6.5 ± 0.5 msec, impulse: 320 ± 20 kPa·msec) and euthanized 4 h post-TBI. All rats were mounted in the middle of the shock tube (2.8 meters from the breech, and 3 meters from the exit) in a prone position—i.e. were strapped securely to the aluminum plate using a cotton cloth wrapped around the body (see Mishra and associates,[18] Fig. 1B). The cloth provides no protection against the shockwave, but prevents any excessive head motion.[19] Sham control rats received anesthesia and noise exposure but without blast exposure—i.e., anesthetized animals were placed next to the shock tube, and then a single blast was fired.

As a quality control measure, we have also monitored a high-speed video recording to capture any substantial head and body motion during the blast so as to exclude the impact of tertiary bTBI. After blast injury, animals were monitored closely for any signs of trauma-related distress (e.g., apnea). For immunoblot analysis, rats were anesthetized and transcardially perfused with phosphate buffered saline (PBS, pH 7.0) whereas for immunofluorescence studies, rats were first perfused with PBS followed by 4% paraformaldehyde (PFA); brains were then isolated and cryoprotected in 30% sucrose.

Western blotting

Before evaluating spatial resolution of NOX1 and NOX2 protein changes in different brain regions by immunofluorescence, we first examined their levels in cerebral hemisphere and cerebellum by immunoblot. After perfusion with PBS, brains were excised from the cranial vaults, the whole left hemisphere and cerebellum were separately homogenized in ice-cold conditions using CellLytic-M (Sigma) using sonicator with probe amplitude set to 45%. Samples were then centrifuged at $14{,}000 \times g$ at 4°C. The protein concentration in the samples was estimated by bicinchoninic acid (BCA) method (Thermo Scientific, Rockford, IL).

Subsequently, 10–20 μg of protein per lane was loaded into 4–15% SDS-PAGE gradient gels (Bio Rad). Proteins separated according to their molecular size were then transferred onto polyvinylidene difluoride (PVDF) membranes using Turbo Protein Transfer instrument (Bio Rad Laboratories) according to manufacturer instructions. Membranes were blocked with 5% milk dissolved in Tris-Buffered saline containing 0.1% Tween-20 (TBS-T) and incubated overnight at 4°C with NOX 1 antibody (Sigma-Aldrich) or NOX2 antibody (Novus Biologicals) or 4HNE (Abcam, Cambridge, MA) at a dilution of 1:1000. Bands were visualized using Western Pico Chemiluminescence Substrate (Thermo Scientific) on Chemi Doc Imaging System (Bio Rad Laboratories). For densitometric quantitation of Western blots, images were digitized using a BioRad GS800 calibrated densitometer, and analyzed with BioRad Quantity One software.

Immunofluorescence and microscopy

To evaluate the spatial changes of NOX1 and NOX2 proteins in different brain regions, as well as to identify cell-specific changes in discrete brain regions, we performed double-immunofluorescence studies of two isoforms of NOX with NeuN, glial fibrillary acidic protein (GFAP) and Iba1, markers of neurons, astrocytes, and microglia, respectively, in frontal cortex, striatum, hippocampus, thalamus, and cerebellum. Briefly, 4 h post-injury, both sham and TBI animals were transcardially perfused with phosphate buffered saline (PBS) followed by 4% paraformaldehyde (PFA). After perfusion, the brains were removed from cranial vaults and incubated in 4% PFA for an additional 48 h and cryoprotected by immersing in 30% sucrose. Brains were then dissected into 2 mm thick sections using rat brain slicer (Kent Scientific Corp.) and embedded in OCT (Optimal Cutting Temperature) media and frozen quickly in isopentane cooled to liquid nitrogen temperature. Frozen sections were stored at −80°C until ready for sectioning.

Brain sections (20 μm thick) were prepared from the frozen tissue blocks, using Leica CM3050 cryostat, and immunofluorescence was performed. Briefly, tissue sections mounted on glass slides prepared from four individual animals in each group were washed with 10 mM PBS, fixed in ice-cold methanol (100%) solution for 10 min at −20°C. The tissue sections were blocked with 10% donkey serum at room temperature for 1 h in PBS containing 0.03% Triton X-100. Fixed tissues were incubated overnight at 4°C with respective primary antibodies to NOX1, NOX2, GFAP, NeuN, and Iba1. The details on the source, clonality, and the dilution of each antibody used are provided in Table 1.

Double immunofluorescence was performed using donkey-antirabbit Alexafluor 594 for NOX1 or NOX2 and donkey-antimouse Alexafluor 488 for GFAP, donkey-antirabbit Alexafluor 488 for NeuN, and donkey-antigoat Alexafluor 488 for Iba1. The specificity of each antibody staining was validated by excluding each primary antibody (negative controls) and visualized for any nonspecific fluorescence. The primary antibody specificity, however, was not validated independently by blocking the binding to tissue with the corresponding antigen. Slides containing different brain regions were digitized (20x magnification) using Leica Aperio Versa 200 fluorescent microscope and slide scanner. Fluorescence intensities in each region were quantitated using AreaQuant software (Leica Biosystems) and expressed as average fluorescence intensity/unit area.

Superoxide production

Superoxide ($O_2^{\cdot -}$) levels in different brain regions were measured using dihydroethidium (DHE) following the method of Kim and coworkers.[21] Briefly, control and blast-induced animals (five controls and five animals immediately after blast) were injected with 5 mg/kg DHE (Molecular Probes, MA), dissolved in dimethylsulfoxide (DMSO) intraperitoneally, and 4 h after blast, animals were

Table 1. Antibodies Used in the Current Study

Antibody	*Source*	*Catalog number*	*Host-species*	*Dilution*
NADPH oxidase 1	Sigma-Aldrich Inc.	SAB420097-200UL	Rabbit (polyclonal)	1:400
NADPH oxidase 2	Invitrogen Inc.	PA5-34600	Rabbit (Polyclonal)	1:250
Glial fibrillary acidic protein (GFAP)	ThermoFisher Scientific Inc.	MA5-12023	Mouse (Monoclonal)	1:400
NeuN	Abcam	AB104224	Mouse (Monoclonal)	1:400
Iba1	Invitrogen Inc.	PA5-18039	Goat (Polyclonal)	1:250

NADPH, nicotinamide adenine dinucleotide phosphate.

transcardially perfused first with PBS followed by 4% PFA, brains excised, and 50 μm thin sections of different brain regions were prepared using Leica VT 1000S vibratome and mounted. DHE immunofluorescence in each region was visualized by digitizing the images using Leica Aperio Versa 200 slide scanner. Fluorescent intensities in each region were quantitated using AreaQuant software (Leica Biosystems) and expressed as average fluorescence intensity/unit area.

Image acquisition and analysis

Slides with mounted coronal sections from the brain were imaged at 20x magnification using a Leica Aperio Versa 200 digital pathology scanner. Control sections were used as reference for adjusting the exposure times and gray scale balance for optimal image quality; once set, these parameters were fixed and used for image acquisition of the reminder of both control and experimental groups. Three channels were collected for each coronal section. Blue: 405 nm (DAPI), red: 594 nm (NOX1), and green: 488 nm (cell specific marker GFAP [astrocytes], Iba1 [microglia], and NeuN [neurons]). We then manually outlined the regions of interest in different brain structures, and the fluorescence intensities in each brain region were quantitated using FLAreaQuantV1 algorithm (Leica Biosystems) and expressed as average fluorescence intensity/unit stained area.

For each channel, we set a minimum intensity threshold value using control sections as reference that will exclude any background fluorescence caused by nonspecific binding of fluorescent secondary antibody, and the same threshold values were used to quantify both control and experimental groups. A maximum intensity threshold was also set to remove any oversaturation from excess fluorescent dye. The algorithm outputs the area of positive staining for each brain region, the average intensity of each channel, and intensity profile of each protein.

Statistical analysis

Data are presented as mean ± standard error of the mean (SEM). Between-group comparisons were made by one-way analysis of variance (ANOVA) with a *post hoc* test (Bonferroni) to determine individual group differences. Differences between means were assessed at the probability level of $p \leq 0.05$, 0.01, and 0.001. GraphPad Prism 6.0 software was used in all analyses and preparation of plots.

Results

Moderate blast over pressure increases the protein levels of NOX1 and NOX2

Previous studies in this laboratory identified increased oxidative and nitrosative stress factors in the cerebral cortex in rats exposed to mild bTBI.[17,18] This study evaluated further the effect of moderate blast (180 kPa peak overpressure) on the early evolution of the protein expression of NOX isoforms (NOX1 and NOX2). Immunoblot analysis of NOX1 and NOX2 in the whole cerebral hemisphere showed a significant increase (87% and 52%, respectively, $p < 0.05$) (Fig. 2). To assess the diffuse nature of primary blast (shockwave) in the posterior region of the brain, NOX1 and NOX2 protein levels were also determined in the cerebellum, and we found that similar to cerebral hemisphere, cerebellar levels of NOX1and NOX2 protein were significantly increased (60% and 40%, respectively, $p < 0.05$) (Fig. 2).

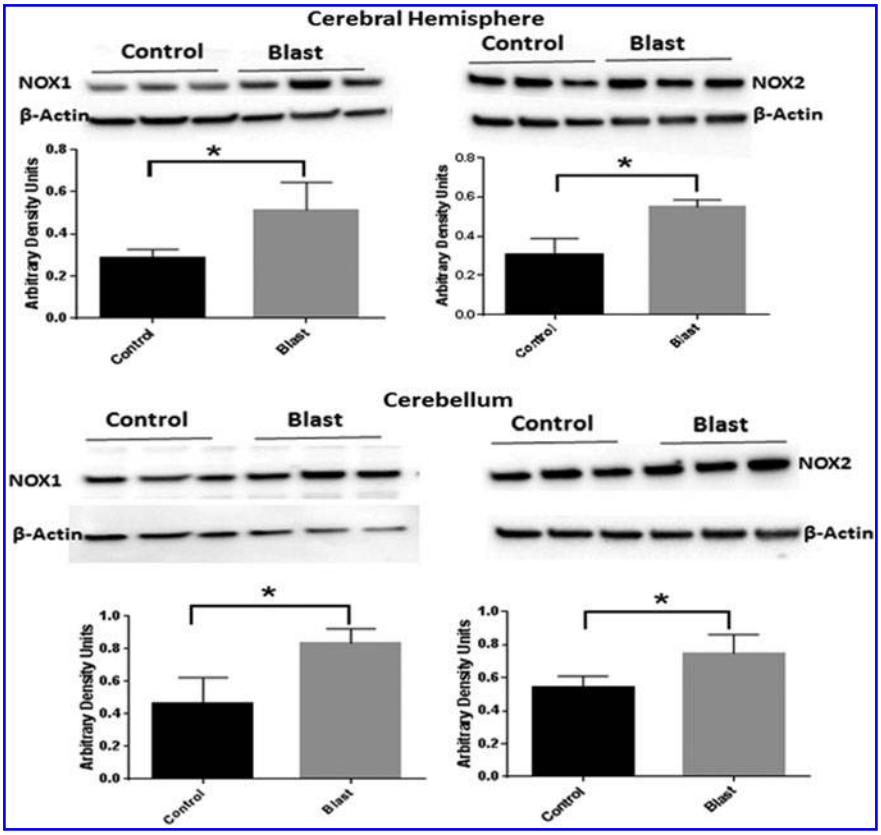


FIG. 2. Blast increases the expression of nicotinamide adenine dinucleotide phosphate oxidase (NOX) isoforms. Immunoblots of NOX1 and NOX2 isoforms in the cerebral hemisphere and cerebellum 4 h after blast at 180 kPa blast over pressure. There was a significant increase (80%) in NOX1 in both cerebral hemispheres and cerebellum, while NOX2 increased by 83% in cerebral hemispheres and 38% in cerebellum. $n = 3$, $^*p < 0.05$.

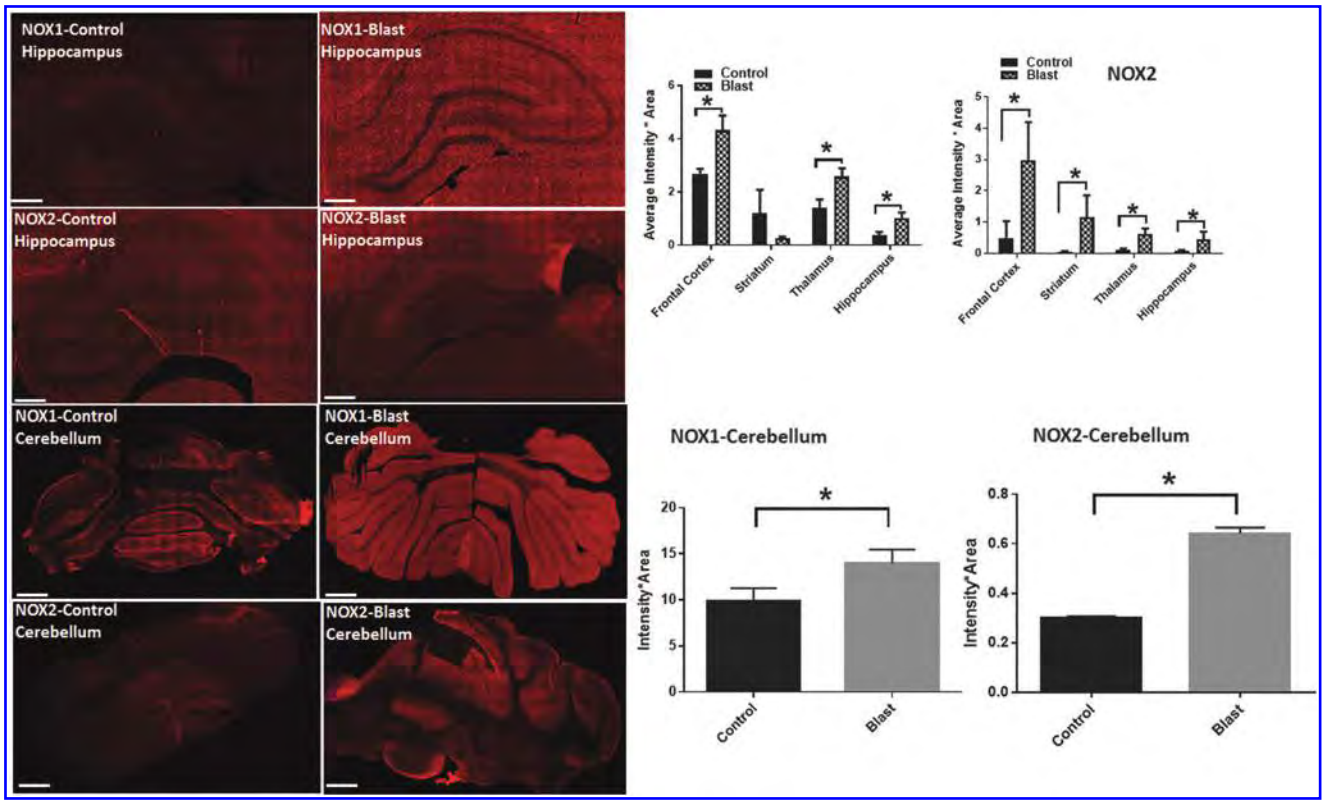


FIG. 3. Nicotinamide adenine dinucleotide phosphate oxidase (NOX) isoforms show a differential increase in different brain regions. Fluorescence intensities (red) of NOX1 and NOX2 in the hippocampus and cerebellum from control and blast-injury animals. Quantification of fluorescence intensities in different brain regions show a striking increase in NOX1 in the hippocampus of blast-injured animals compared with controls. Intensities of NOX2 display a higher increase in the frontal cortex compared with other regions. $n=4$. $^*p<0.01$–0.05. Fluorescent intensities NOX1 in the cerebellum display a striking increase (96%) compared with NOX2 (38%). Color image is available online at www.liebertpub.com.neu

Differential changes in NOX isoforms expression in different brain regions

We next examined regional variations in NOX1 and NOX2 protein levels in the following brain structures: frontal cortex, striatum, hippocampus, thalamus, and cerebellum. The rationale in examining these regions is as follows: (a) NOX1 and NOX 2 isoforms are ubiquitously expressed in all brain regions, (b) the effect of shockwave propagation over the entire brain is not known, and (c) to use NOX1 and NOX2 as markers to evaluate whether there exists any selective vulnerability of various brain structures, a phenomenon that has not been investigated previously.

Under primary blast loading conditions, the pathological changes were found throughout the brain as indicated by changes in the fluorescent intensities of NOX1 and NOX 2 in different brain regions. Interestingly. various regions displayed a differential response. Thus, NOX1 levels in the frontal cortex showed a 49% increase; hippocampus showed the highest degree of increase (107%) followed by thalamus displaying a 90% increase (Fig. 3). Total NOX1 levels did not change in the striatum and somatosensory barrel cortex (S1BF) (data not shown).

The regional variations in the levels of NOX2 are slightly different from that of NOX1. Total NOX2 levels were highest in the frontal cortex (>two-fold) followed by the striatum and hippocampus that showed the lowest increase (Fig. 3). NOX isoform expression was also increased in other discrete brain regions from rostral and caudal areas, among which theCA1 region of a hippocampus displayed the biggest increase (Table 2).

Different neural cell types display differential vulnerability to oxidative damage

To evaluate cellular vulnerability to oxidative damage resulting from primary blast, changes in NOX1 expression patterns in astrocytes, neurons, and microglia were determined by double immunofluorescence staining. In addition, simultaneous

Table 2. Protein Levels of Nicotinamide Adenine Dinucleotide Phosphate Oxidase Isoform Expression in Different Brain Regions (from Rostral to Caudal Areas) in Control and Animals Four Hours after Exposed to Moderate Blast (180 kPa)

Region	*NOX 1 (% over Control)*	*NOX2 (% over Control)*
Hippocampus CA1	411%	+142%
Hippocampus CA3	265%	+203%
Dentate gyrus	605%	+20%
Corpus callosum	–77%	–65%
Cingulate cortex	+0.4%	–12.8%
Amygdala	+89%	+51.8%
Hypothalamus	+69%	+33.13

NOX, nicotinamide adenne dincleotide phosphate.

Note that highest increase in NOX expression was found in the CA1 region of the hippocampus that correlates with the known vulnerability to oxidative damage.

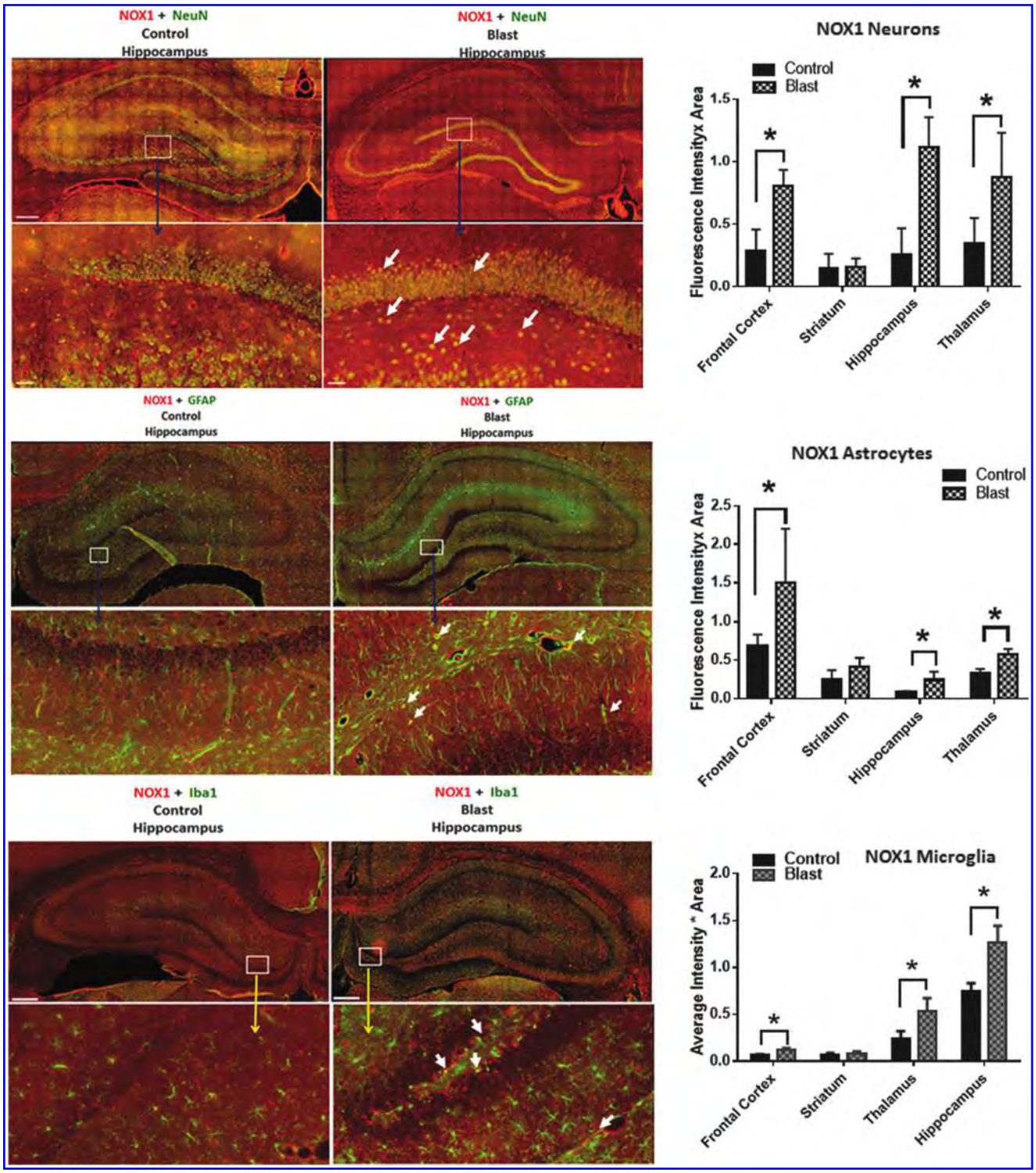


FIG. 4. Nicotinamide adenine dinucleotide phosphate oxidase (NOX)1 shows greater co-localization in neurons. Representative merged images showing the co-localization of NOX1 with NeuN, GFAP and Iba1 in the hippocampus indicating neuronal, astrocytic, and microglia localization, respectively, of NOX1 in control and blast-injured animals. Majority of increase in NOX1 with respect to corresponding controls is in neurons compared with astrocytes and microglia. Quantification of florescence intensities in different brain regions show a striking increase in NOX1 fluorescence in neurons in the hippocampus of blast-injured animals compared with controls. $n=4$, $*p<0.01$–0.05. Color image is available online at www.liebertpub.com.neu

quantification of NOX immunofluorescence using cell-specific markers will provide an insight into changes in its expression in different neural cells including astrocytes, neurons, and microglia.

Cell-specific analysis of increase in NOX1 and NOX2 levels after bTBI compared with their baseline expression (controls) indicate that neurons display a higher increase compared with astrocytes and microglia. In addition, NOX1 and NOX2 increases were more pronounced in neurons in the hippocampus and thalamus, respectively, compared with the frontal cortex. These conclusions were deduced based on the double immunofluorescence analysis showing co-localization of NOX1 with NeuN (a marker protein for neurons), with GFAP (a marker for astrocytes) and with Iba1 (a marker for microglia). (Fig. 4 and 5).

Primary blast also significantly affects posterior brain structures including the cerebellum

Primary blast caused diffused pathological changes not only in the perpendicular direction (deeper brain structures, hippocampus, thalamus) but also in the parallel direction to the wave propagation from the pre-frontal cortex to the cerebellum. The total tissue levels of NOX1 in the cerebellum not only increased, but this increase was highest in neurons (Fig. 6). Such higher expression of NOX1 in neurons compared with other neural cells also correlates with the known fact that the cerebellum contains the highest density of neurons compared with other brain regions.[22,23] Similar to NOX1, elevated levels of NOX2 expression were also found to be mainly co-localized with neurons (Fig. 7).

Primary blast increases superoxide levels in different brain regions

The activation of a variety of NOX isoforms is usually associated with the increased production of superoxide.[12,24] Because the present study showed increased protein levels of NOX isoforms, we then sought to examine whether increased NOX protein after blast has a functional significance. Accordingly, *in vivo* levels of superoxide in the frontal cortex, hippocampus, thalamus, and cerebellum were measured using DHE. Hippocampus displayed a robust level of the increase in superoxide (>10 fold, $p < 0.001$) followed by thalamus and frontal cortex. It is noteworthy that the extent of the rise in superoxide production in the hippocampus and thalamus (Fig. 8) correlated well with the increased degree of NOX expression. In addition, a pre-treatment of animals with apocynin, which is known to block the assembly of different NOX subunits, completely inhibited the increase in superoxide production indicating an essential role of NOX in brain superoxide production after moderate blast.

Primary blast results in oxidative damage and lipid peroxidation products in different brain structures

Several reports indicate the TBI resulting from different etiologies, including primary blast and blunt injuries, display oxidative stress during the evolution of its symptoms.[7,25–27] Accordingly,

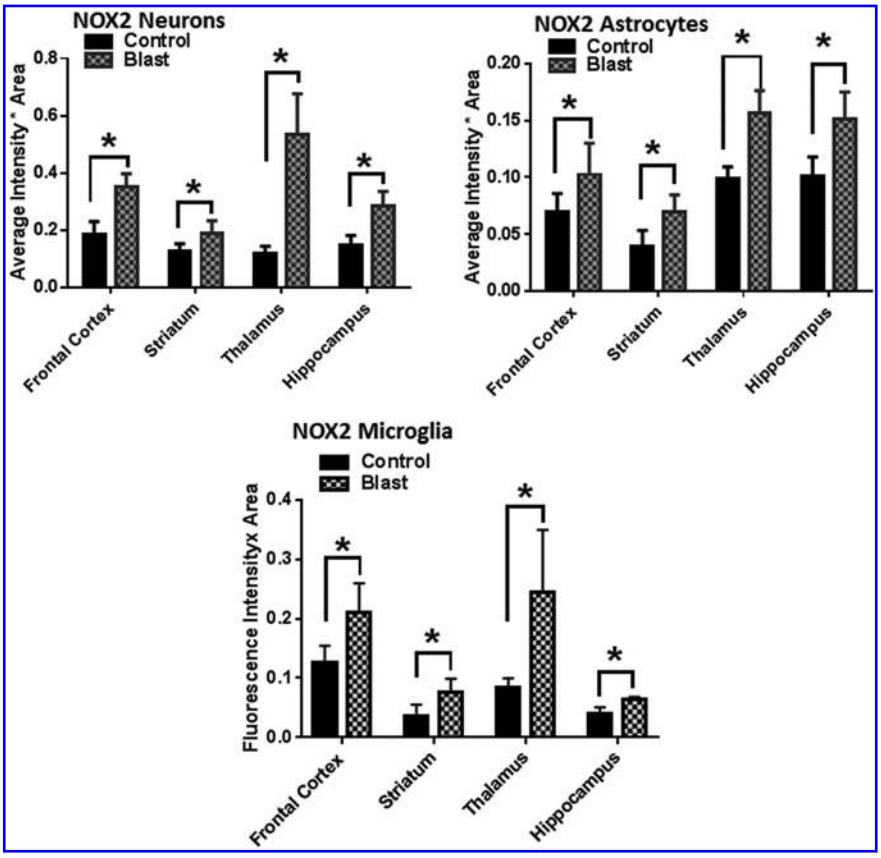


FIG. 5. Neurons show the highest increase in nicotinamide adenine dinucleotide phosphate oxidase (NOX)2 expression. Quantification of florescence intensities in different brain regions show a striking increase in NOX2 fluorescence in the hippocampus and thalamus of blast-injured animals compared with other brain regions. $n = 4$, $^*p < 0.01$–0.05.

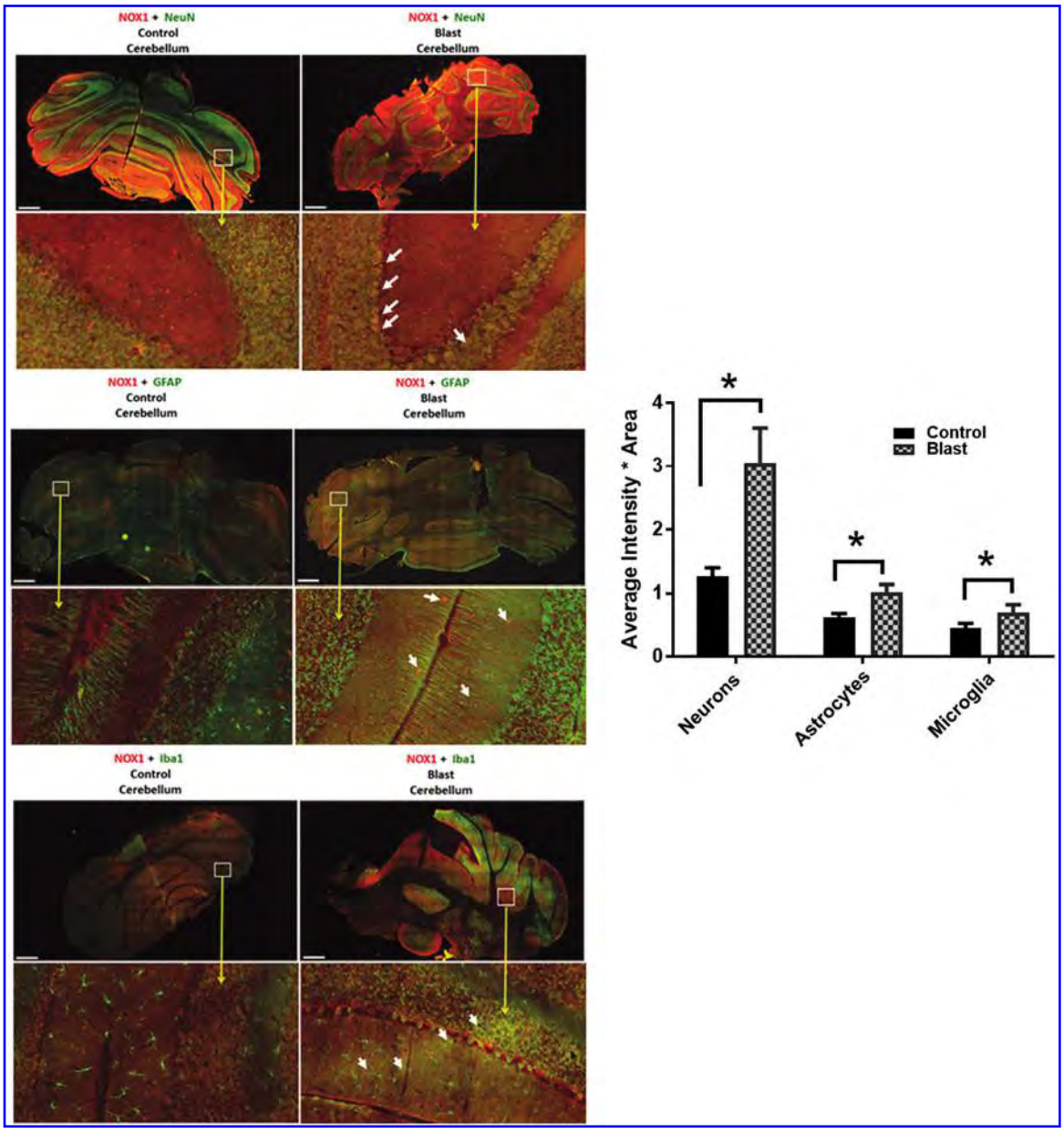


FIG. 6. Cerebellum displays an increased nicotinamide adenine dinucleotide phosphate oxidase (NOX)1 expression in neurons compared with astrocytes and microglia. Representative merged images showing the co-localization of NOX1 with NeuN, GFAP, and Iba1 in the cerebellum indicating neuronal, astrocytic, and microglia localization, respectively, of NOX1 in control and blast-injured animals. $n = 4$, $*p < 0.01$–0.05. Color image is available online at www.liebertpub.com.neu

several pathways are involved directly in the induction of oxidative stress including the activation of NOX[15,28–30] and alterations of antioxidant defense mechanisms (a reduction in superoxide dismutase, catalase, glutathione peroxidase).[9,31]

One of the major downstream effects of oxidative stress in many neurological disorders and TBI is the formation and accumulation of lipid peroxidation products.[32–35] Lipid peroxidation is a process under which oxidants such as free radicals attack various lipids containing carbon double bonds, and the resulting aldehyde products such as 4HNE generated by the lipid peroxidation directly modify amino acid structures in proteins and form adducts.[36]

Superoxide is one of the free radicals that can directly oxidize lipids to aldehydes that leads to the formation of protein adducts and activation of NOX produces excess levels of superoxide.[25,37,38] Because the present study clearly showed an increase in NOX proteins and increased levels of superoxide after bTBI, we sought to examine the levels of 4HNE adducts in discrete brain regions in rats subjected to moderate blast (180 kPa, 4 h). Immunoblot analysis of 4HNE products identified two major bands corresponding to molecular weights of 70 and 100 kDa, which showed a trend toward an increase in cerebral hemispheres, hippocampus, thalamus, and cerebellum; however, such changes were not significant (Fig. 9).

Discussion

This study demonstrates that protein levels of superoxide producing enzymes NOX1 and NOX2 were significantly increased to different levels in various brain regions in rats exposed to moderate

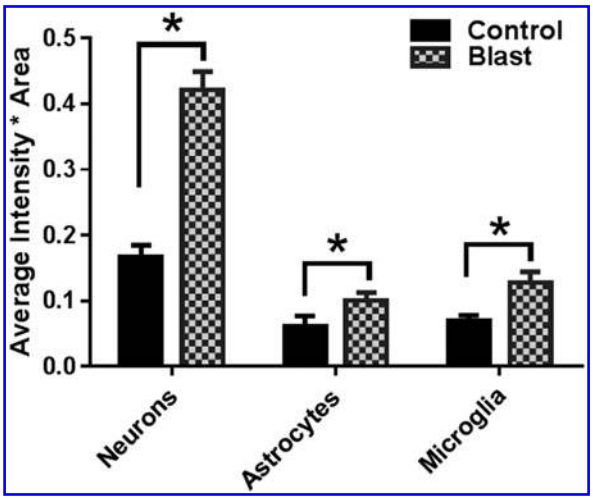


FIG. 7. Nicotinamide adenine dinucleotide phosphate oxidase-2 (NOX)2 displays a greater increase in neurons compared with astrocytes and microglia. Similar to NOX1, the majority of NOX2 is localized in neurons compared with astrocytes and microglia. n = 4, $*p < 0.01$–0.05.

primary blast overpressure. Increased NOX expression was accompanied by increased superoxide production and a strong tendency toward increased HNE adduct formation in two proteins. Together these observations strongly indicate that there is an increase in oxidative stress and oxidative damage occurring in the early phase after a single exposure to a shockwave. This work is motivated by two related questions: (1) does the blast TBI affect different brain regions equally assuming homogeneous spatial distribution of biomechanical loading, and (2) does the extent of the damage vary between different brain regions containing disparate ratios of neural cells (neurons, astrocytes, and microglia)? Hence, we focused on the role of two different forms of superoxide producing enzymes and their downstream oxidative damage markers to understand both the spatial and cellular effects.

The bTBI has an unique pattern of biomechanical phenotype in that the external forces are dictated by the size and shape of the interacting body—in this instance, skull and brain structures. Further, the magnitude of forces generated depends on the contact area and interaction time that in turn determine the overall biomechanical loads at the tissue level. This loading triggers secondary biochemical cascades depending on the local tissue content. The cascade of secondary events usually develops over a period of hours to days that ultimately lead to additional neuropathological sequela.[39–41] Among many causal factors implicated in the pathophysiology of bTBI, oxidative stress represents an important early pathological outcome resulting from either the activation of free radical producing enzymes or downregulation of antioxidant defense mechanisms.[7,26,27,42]

NOX is a superoxide producing enzyme and different isoforms of NOX, including NOX1, NOX2, and NOX4 have been identified in the brain.[12] Studies reported increased activation of different isoforms of NOX in various forms of TBI. Accordingly, in a mouse model of controlled cortical impact (CCI), increased NOX2 expression was observed at 24–48 h after injury[43] whereas Byrnes and associates[44] found a delayed increase in NOX2 activity one month post-injury. In a rat model of CCI, however, increased NOX activity was observed as early as 1 h post-injury.[44] Increased NOX expression was also found in different animal models of fluid percussion injury.[14.45.46] In addition, apocynin, an inhibitor of NOX activation, showed protective effects on various models of blunt TBI.[16,46] Together these studies highlight the critical role of NOX in the pathology of TBI.

While studies have established the importance of NOX in the pathophysiology of blunt TBI, there are limited studies of NOX in bTBI.[47–49] This could in part be because of the lack of a true understanding the role of biomechanical loading in blast injury from

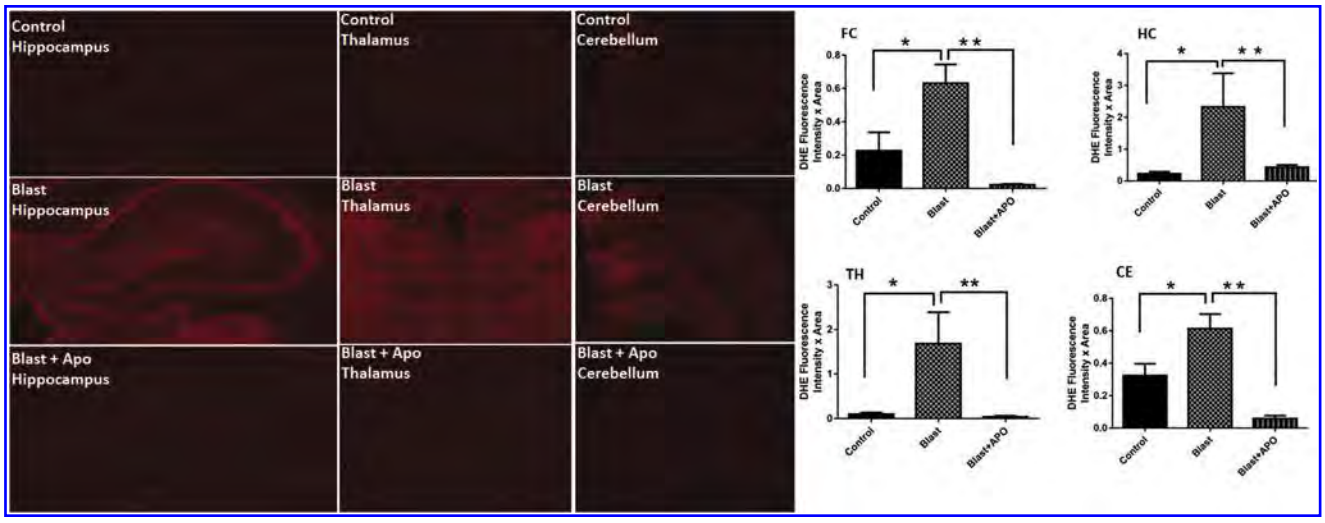


FIG. 8. Primary blast increases superoxide levels in different brain regions. Representative fluorescent intensities (red) of dihydroethidium (DHE, dye that recognizes superoxide production) in hippocampus, thalamus and cerebellum in control, Blast-injured and blast+ apocynin. Quantification of fluorescence intensities in different brain regions shows a striking increase in DHE fluorescence in the hippocampus of blast-injured animals compared with controls indicating high levels of superoxide production in the hippocampus. Note that a pre-treatment with apocynin (APO), an inhibitor of nicotinamide adenine dinucleotide phosphate oxidase (NOX) activation, completely blocks the DHE fluorescence increase indicating that the superoxide increase is mediated by activation of NOX. $n = 5$ $*p < 0.01$–0.05. Color image is available online at www.liebertpub.com.neu

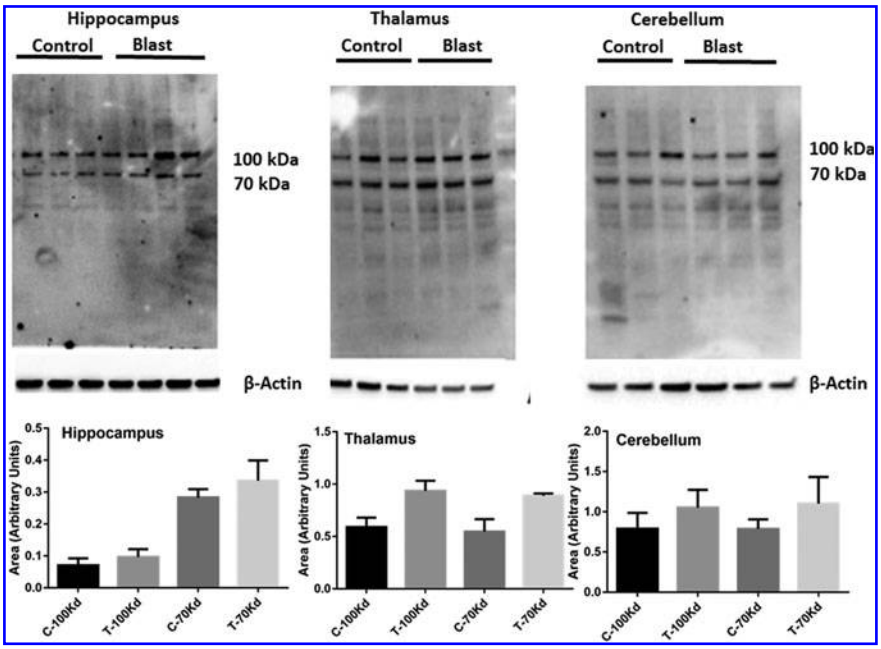


FIG. 9. Primary blast displays a strong tendency to increase 4HNE protein adducts. Immunoblot analysis of 4HNE in lysates from the hippocampus, thalamus, and cerebellum 4 h after blast at 180 kPa blast overpressure is shown. Two proteins of 100 and 70 kDa show a strong tendency to increase in the hippocampus and thalamus. $n = 3$.

limited availability of a field validated shock tube that simulates battlefield injuries. In the present study, we therefore characterized the spatial resolution of two isoforms of NOX (NOX1 and NOX2) in various brain regions and their localization in neurons, astrocytes, and microglia 4 h after blast injury in a field validated shock tube.[10,19,20]

A generalized increase in NOX protein levels by immunoblots in the present study is comparable to our previous reports indicating its upregulation in the homogenates of a cerebral cortex in rats exposed to different blast overpressures.[17,18] Further, using immunofluorescence analysis, the present study identified regional variations in the expression pattern of NOX 1 in that the highest increase is found in the hippocampus followed by the thalamus. Interestingly, the frontal cortex showed higher expression in NOX2 compared with that in the hippocampus and thalamus. Other fine brain structures, including motor cortex, amygdala, and hypothalamus, also showed a significant increase in both the isoforms of NOX with the exception that NOX2 levels were significantly lower in a motor cortex (Table 2).

Interestingly, in the present study, a single blast exposure also affected distal brain structures, including the cerebellum, suggesting that blast injury propagation is highly diffusive in nature. While it is interesting to observe differential vulnerability of various brain structures to blast injury, in blast, a high-velocity shockwave traverses across and through the entire body loading all the regions almost simultaneously within a matter for 5–10 milliseconds. Recent experimental evidence in animal models and human cadeveric heads has shown that the shockwaves are capable of passing through the skin and skull and load all the brain structures.[10]

In addition to regional variations observed in NOX levels, we also found a cellular heterogeneity in the expression of NOX isoforms. Thus, blast injury displayed a robust increase in the levels of both isoforms of NOX in neurons compared to astrocytes and microglia with respect to their baseline values (controls). Studies have shown that all neural cells express different isoforms of NOX, including NOX1, NOX2, and NOX4.[50] In addition, within the neurons, NOX1 is abundantly expressed in cerebellar granule cells,[51] while NOX2 has been shown to be expressed in both cerebellar granule cells as well as hippocampal neurons.[52] In addition to NOX1, the present study found a striking increase in NOX2 in neurons of the hippocampus, thalamus, and cerebellum compared with microglia.

Our results are in slight contrast to other reports wherein NOX2 is abundantly expressed in microglia.[44,53–55] While the reason for apparent abundance of NOX2 in neurons in our study is not known, studies report that NOX2 upregulation in hippocampal pyramidal neurons drives neuropathology associated with psychosocial stress in rats.[56,57] Further, studies also report that cellular injury to neurons after stroke resulted in an early upregulation of NOX2 in neurons (3–6 h after injury) whereas NOX2 was upregulated in microglia at later time points (72 h post-injury).[58,59] Such temporal difference in the expression pattern of NOX2 between neurons and microglia is reasonable because neurons may be far more vulnerable acutely in the evolution of the injury process whereas microglial activation could be a relatively late phenomenon.

Superoxide is a major free radical produced in the brain by a variety of reactions, including disturbances in mitochondrial oxidative phosphorylation, increased production of arachidonic acid as a consequence of activation of phosphilipase A2 (PLA2), activation of xanthine oxidase as well as by the activation of NOX.[60–63] Increased superoxide production has been shown in different models of TBI.[64–67] The present study observed a striking increase in superoxide production in the hippocampus, thalamus, and frontal cortex, areas where corresponding increases in NOX levels were found. Moreover, our studies showing a complete absence of $O_2^{\bullet}-$ in animals treated with apocynin (an inhibitor of NOX activation) before the exposure to blast injury reinforces the finding that the increase in $O_2^{\bullet}-$ is indeed mediated by NOX activation. Our results are also in agreement with previous studies showing protective effects of apocynin in attenuating oxidative damage in different models of TBI.[15,16,30,47,68,69]

While in the present study, the superoxide levels were found to be strikingly increased in different brain regions, the levels of 4HNE adducts showed a trend toward the increase in two proteins with average molecular weights of 70 and 100 kDa, but did not show statistically significant changes. The reason behind the lack of significant changes is not known. The 4HNE products, however, can be formed via peroxidation of unsaturated fatty acids not only by superoxide radical but also by a variety of other reactive oxygen species, including hydroxyl, peroxyl as well as a varety of cyclic compounds.[70] It is therefore likely that lipid peroxidation reaction and subsequent 4HNE formation may not have achieved a threshold as to show significant changes at 4 h after blast because reactive oxygen species other than superoxide (e.g., hydroxyl radicals among others) may not have been increased in the early phase of blast injury.

Despite an observed increase in factors conducive to oxidative damage in neurons, in the present study, we did not observe neurodegeneration nor apoptotic cell death as investigated by fluorescent staining for Fluorojade C and cleaved caspase-3 4 h after blast injury (data not shown). Perhaps a 4 h window of blast injury may be too early to detect neuronal death. It is also likely that moderate blast may not cause neuronal death because of the diffuse nature of the shockwave unlike blunt injuries where neuronal death was observed close to the epicenter in the acute phase of injury.[71]

The selective vulnerability of neurons to oxidative damage may be dictated not only by the propagation of primary shockwave, the so-called direct mechanical impact throughout the brain regions, but also in part influenced by the cellular density and cell types distribution in different brain regions. Recently, it has been shown that the cerebellum and hippocampus contain the highest density of neurons compared with a cerebral cortex although relative mass of the hippocampus and cerebellum is far lesser than cerebral cortex.[23,72] In the present study, our observation of the highest increase in NOX levels in neurons in the hippocampus and cerebellum after blast suggests that neuron rich regions may be at higher risk for oxidative damage than other brain regions. This is further supported by our observation of a striking increase in superoxide levels in the hippocampus after blast. Also, within the hippocampus, studies have shown that neurons in CA1 region are more vulnerable to superoxide than CA3 neurons.[73,74]

Moreover, it is interesting to note that NOX1 showed a greater increase in CA1 region compared with CA3 (Table 2). Such higher level of neuronal oxidative damage in discrete brain regions may also depend on a number of other factors, including vascular density and associated metabolic supply and consumption of glucose and oxygen, neuronal excitability, and synaptic transmission.[75] In support of this tenet, it has been shown that the density (and perhaps subsequent nutrient supply) of brain capillaries was far less in the CA1 region of the hippocampus compared with the CA3 region, which likely places the CA1 region at higher risk for ischemia and hypoxia.[76]

The precise mechanism by which bTBI increases NOX isoform expression is not known. A shock-wave passage throughout the brain during a transient period could initiate a mechanical disturbance to plasma membrane structures within the brain parenchyma. It is reasonable, considering the small size of the rat brain and relatively thin skull, to assume the shockwave loading of the brain is uniform within brain structures investigated in this work (frontal cortex, striatum, hipocampus, and thalamus and cerebelllum). The uniformity of the pressure field within the rat brain under blast loading conditions was demonstrated in a numerical model[77] and was validated via intracranial pressure measurements by our group (data not published). If this is true—i.e. the mechanical forces created by the shockwave are distributed uniformly, and considering the brain's highly anisotropic and heterogeneous organization—our data suggest the extent of the local damage would depend on the composition and microarchitecture of a specific brain region (Fig. 10).

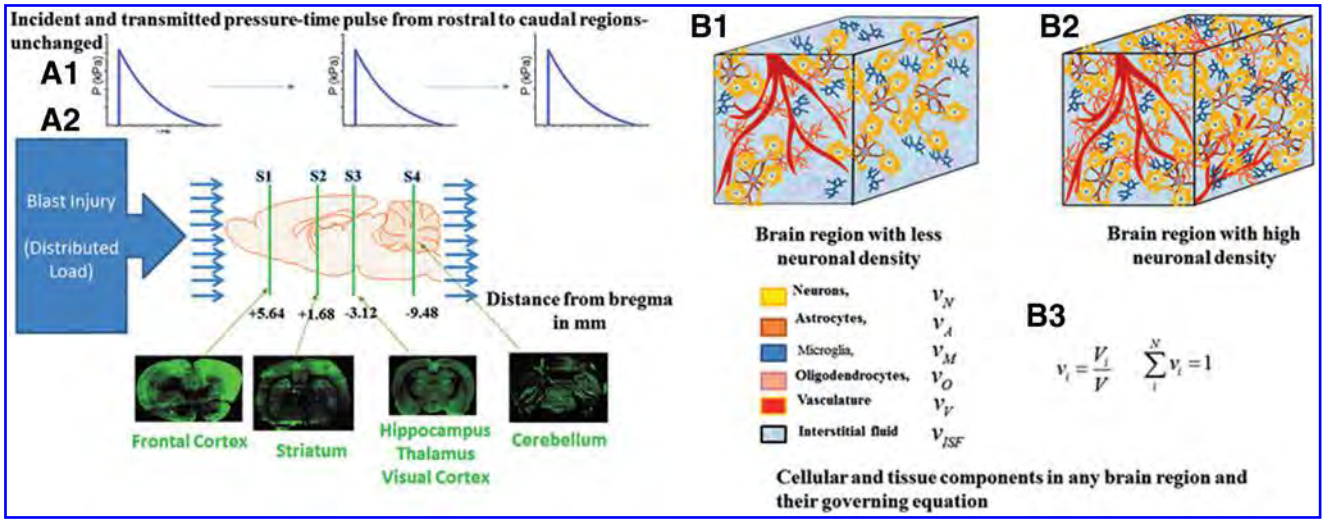


FIG. 10. Schematic of experimental blast injury model and effective loading and tissue-specific response. (**A**) The top panel shows the blast overpressure-time pulse applied to the rostral to caudal to rostral regions of the rodent brain travels with minimal change because of very short duration of less than a millisecond. The bottom panel shows different regions S1 to S4 analyzed in this study (**B**) A given brain volume comprises the six components (neurons, astrocytes, microglia, oligodendrocyte, vasculature, and interstitial/cerebrospinal fluid) that can vary from region to region. The mechanical properties of the representative volume given in B3 indicate that the effective mechanical stresses in the volume and hence the neural components will be determined by the differential volume fraction of that cell type. The different nicotinamide adenine dinucleotide phosphate oxidase expressions seen in this work are hypothesized to be driven by this differential cell volume fraction. Color image is available online at www.liebertpub.com.neu

Conclusion

Our studies demonstrate that moderate blast injury causes an increase in NOX isoforms in various brain regions to a differential degree. Increased NOX isoforms correlated with a concomitant rise in superoxide levels in corresponding regions that show a higher increase in NOX expression indicating oxidative damage. In addition, protein oxidation product 4HNE showed a strong tendency to increase in different brain regions. Further, higher increase in NOX isoforms in neurons compared with other brain cells strongly suggests neurons are by far the most vulnerable to oxidative damage in the early evolution of injury pathology.

Acknowledgments

This work was supported by grant no. 14059001, W81XWH-15-1-0303, entitled ''Primary Blast Injury Criteria for Animal/Human TBI Models using Field Validated Shock Tubes'' received from the U.S. Army Medical Research and Materiel Command. Authors greatly acknowledge the assistance of Arun Ravula, Debanjan Haldar, Jose Rodriguez, Yonatan Sheer, Madison Taylor, Smit Shah for tissue sectioning and experimental data analysis.

Author Disclosure Statement

No competing financial interests exist.

References

1. Bochicchio, G.V., Lumpkins, K., O'Connor, J., Simard, M., Schaub, S., Conway, A., Bochicchio, K., and Scalea, T.M. (2008). Blast injury in a civilian trauma setting is associated with a delay in diagnosis of traumatic brain injury. Am. Surg. 74, 267–270.
2. DuBose, J.J., Barmparas, G., Inaba, K., Stein, D.M., Scalea, T., Cancio, L.C., Cole, J., Eastridge, B., and Blackbourne, L. (2011). Isolated severe traumatic brain injuries sustained during combat operations: demographics, mortality outcomes, and lessons to be learned from contrasts to civilian counterparts. J. Trauma 70, 11–16.
3. Reid, M.W. and Velez, C.S. (2015). Discriminating military and civilian traumatic brain injuries. Mol. Cell. Neurosci. 66, 123–128.
4. Wallace, D. (2009). Improvised explosive devices and traumatic brain injury: the military experience in Iraq and Afghanistan. Australas. Psychiatry 17, 218–224.
5. Singleton, J.A., Gibb, I.E., Hunt, N.C., Bull, A.M., and Clasper, J.C. (2013). Identifying future 'unexpected' survivors: a retrospective cohort study of fatal injury patterns in victims of improvised explosive devices. BMJ Open 3.
6. Bayir, H., Kochanek, P.M., and Kagan, V.E. (2006). Oxidative stress in immature brain after traumatic brain injury. Dev. Neurosci. 28, 420–431.
7. Cornelius, C., Crupi, R., Calabrese, V., Graziano, A., Milone, P., Pennisi, G., Radak, Z., Calabrese, E.J., and Cuzzocrea, S. (2013). Traumatic brain injury: oxidative stress and neuroprotection. Antioxid. Redox. Signal 19, 836–853.
8. Koppula, S., Kumar, H., Kim, I.S., and Choi, D.K. (2012). Reactive oxygen species and inhibitors of inflammatory enzymes, NADPH oxidase, and iNOS in experimental models of Parkinson's disease. Mediators Inflamm. 2012, 823902.
9. Lewen, A. and Hillered, L. (1998). Involvement of reactive oxygen species in membrane phospholipid breakdown and energy perturbation after traumatic brain injury in the rat. J. Neurotrauma 15, 521–530.
10. Chandra, N., Sundaramurthy, A., and Gupta, R.K. (2017). Validation of laboratory animal and surrogate human models in primary blast injury studies. Mil. Med. 182, 105–113.
11. Carbone, F., Teixeira, P.C., Braunersreuther, V., Mach, F., Vuilleumier, N., and Montecucco, F. (2015). Pathophysiology and treatments of oxidative injury in ischemic stroke: focus on the phagocytic NADPH oxidase 2. Antioxid. Redox. Signal 23, 460–489.
12. Infanger, D.W., Sharma, R.V., and Davisson, R.L. (2006). NADPH oxidases of the brain: distribution, regulation, and function. Antioxid. Redox. Signal 8, 1583–1596.
13. Cooney, S.J., Bermudez-Sabogal, S.L., and Byrnes, K.R. (2013). Cellular and temporal expression of NADPH oxidase (NOX) isotypes after brain injury. J. Neuroinflammation 10, 155.
14. Ferreira, A.P., Rodrigues, F.S., Della-Pace, I.D., Mota, B.C., Oliveira, S.M., de Campos Velho Gewehr, C., Bobinski, F., de Oliveira, C.V., Brum, J.S., Oliveira, M.S., Furian, A.F., de Barros, C.S., dos Santos, A.R., Ferreira, J., Fighera, M.R., and Royes, L.F. (2014). HOE-140, an antagonist of B2 receptor, protects against memory deficits and brain damage induced by moderate lateral fluid percussion injury in mice. Psychopharmacology (Berl) 231, 1935–1948.
15. Choi, B.Y., Jang, B.G., Kim, J.H., Lee, B.E., Sohn, M., Song, H.K., and Suh, S.W. (2012). Prevention of traumatic brain injury-induced neuronal death by inhibition of NADPH oxidase activation. Brain Res. 1481, 49–58.
16. Song, S.X., Gao, J.L., Wang, K.J., Li, R., Tian, Y.X., Wei, J.Q., and Cui, J.Z. (2013). Attenuation of brain edema and spatial learning deficits by the inhibition of NADPH oxidase activity using apocynin following diffuse traumatic brain injury in rats. Mol. Med. Rep. 7, 327–331.
17. Abdul-Muneer, P.M., Schuetz, H., Wang, F., Skotak, M., Jones, J., Gorantla, S., Zimmerman, M.C., Chandra, N., and Haorah, J. (2013). Induction of oxidative and nitrosative damage leads to cerebrovascular inflammation in an animal model of mild traumatic brain injury induced by primary blast. Free Radic. Biol. Med. 60, 282–291.
18. Mishra, V., Skotak, M., Schuetz, H., Heller, A., Haorah, J., and Chandra, N. (2016). Primary blast causes mild, moderate, severe and lethal TBI with increasing blast overpressures: experimental rat injury model. Sci. Rep. 6, 26992.
19. Skotak, M., Wang, F., Alai, A., Holmberg, A., Harris, S., Switzer, R.C., and Chandra, N. (2013). Rat injury model under controlled field-relevant primary blast conditions: acute response to a wide range of peak overpressures. J. Neurotrauma 30, 1147–1160.
20. Kuriakose, M., Skotak, M., Misistia, A., Kahali, S., Sundaramurthy, A., and Chandra, N. (2016). Tailoring the blast exposure conditions in the shock tube for generating pure, primary shock waves: the end plate facilitates elimination of secondary loading of the specimen. PLoS One 11, e0161597.
21. Kim, J.H., Jang, B.G., Choi, B.Y., Kim, H.S., Sohn, M., Chung, T.N., Choi, H.C., Song, H.K., and Suh, S.W. (2013). Post-treatment of an NADPH oxidase inhibitor prevents seizure-induced neuronal death. Brain Res. 1499, 163–172.
22. Herculano-Houzel, S., Mota, B., and Lent, R. (2006). Cellular scaling rules for rodent brains. Proc. Natl. Acad. Sci. U. S. A. 103, 12138–12143.
23. Fu, Y., Rusznak, Z., Herculano-Houzel, S., Watson, C., and Paxinos, G. (2013). Cellular composition characterizing postnatal development and maturation of the mouse brain and spinal cord. Brain Struct. Funct. 218, 1337–1354.
24. Fernandez, V., Barrientos, X., Kipreos, K., Valenzuela, A., and Videla, L.A. (1985). Superoxide radical generation, NADPH oxidase activity, and cytochrome P-450 content of rat liver microsomal fractions in an experimental hyperthyroid state: relation to lipid peroxidation. Endocrinology 117, 496–501.
25. Cernak, I., Savic, V.J., Kotur, J., Prokic, V., Veljovic, M., and Grbovic, D. (2000). Characterization of plasma magnesium concentration and oxidative stress following graded traumatic brain injury in humans. J. Neurotrauma 17, 53–68.
26. Rodriguez-Rodriguez, A., Egea-Guerrero, J.J., Murillo-Cabezas, F., and Carrillo-Vico, A. (2014). Oxidative stress in traumatic brain injury. Curr. Med. Chem. 21, 1201–1211.
27. Abdul-Muneer, P.M., Chandra, N., and Haorah, J. (2015). Interactions of oxidative stress and neurovascular inflammation in the pathogenesis of traumatic brain injury. Mol. Neurobiol. 51, 966–979.
28. Angeloni, C., Prata, C., Dalla Sega, F.V., Piperno, R., and Hrelia, S. (2015). Traumatic brain injury and NADPH oxidase: a deep relationship. Oxid. Med. Cell. Longev. 2015, 370312.
29. Lu, X.Y., Wang, H.D., Xu, J.G., Ding, K., and Li, T. (2014). NADPH oxidase inhibition improves neurological outcome in experimental traumatic brain injury. Neurochem. Int. 69, 14–19.
30. Ma, M.W., Wang, J., Zhang, Q., Wang, R., Dhandapani, K.M., Vadlamudi, R.K., and Brann, D.W. (2017). NADPH oxidase in brain injury and neurodegenerative disorders. Mol. Neurodegener. 12, 7.
31. Muir, J.K., Tynan, M., Caldwell, R., and Ellis, E.F. (1995). Superoxide dismutase improves posttraumatic cortical blood flow in rats. J. Neurotrauma 12, 179–188.

32. Butterfield, D.A. and Reed, T.T. (2016). Lipid peroxidation and tyrosine nitration in traumatic brain injury: insights into secondary injury from redox proteomics. Proteomics Clin. Appl. 10, 112.
33. Cristofori, L., Tavazzi, B., Gambin, R., Vagnozzi, R., Vivenza, C., Amorini, A.M., Di Pierro, D., Fazzina, G., and Lazzarino, G. (2001). Early onset of lipid peroxidation after human traumatic brain injury: a fatal limitation for the free radical scavenger pharmacological therapy? J. Investig. Med. 49, 450–458.
34. Roof, R.L., Hoffman, S.W., and Stein, D.G. (1997). Progesterone protects against lipid peroxidation following traumatic brain injury in rats. Mol. Chem. Neuropatho.l 31, 1–11.
35. Wada, K., Alonso, O.F., Busto, R., Panetta, J., Clemens, J.A., Ginsberg, M.D., and Dietrich, W.D. (1999). Early treatment with a novel inhibitor of lipid peroxidation (LY341122) improves histopathological outcome after moderate fluid percussion brain injury in rats. Neurosurgery 45, 601–608.
36. Arlt, S., Beisiegel, U., and Kontush, A. (2002). Lipid peroxidation in neurodegeneration: new insights into Alzheimer's disease. Curr. Opin. Lipidol. 13, 289–294.
37. Banakou, E. and Dailianis, S. (2010). Involvement of Na+/H+ exchanger and respiratory burst enzymes NADPH oxidase and NO synthase, in Cd-induced lipid peroxidation and DNA damage in haemocytes of mussels. Comp. Biochem. Physiol. C. Toxicol. Pharmacol. 152, 346–352.
38. Stanger, O., Renner, W., Khoschsorur, G., Rigler, B., and Wascher, T.C. (2001). NADH/NADPH oxidase p22 phox C242T polymorphism and lipid peroxidation in coronary artery disease. Clin. Physiol. 21, 718–722.
39. Chandra, N. and Sundaramurthy, A. (2015). Acute pathophysiology of blast injury-from biomechanics to experiments and computations: implications on head and polytrauma. In: *Brain Neurotrauma: Molecular, Neuropsychological, and Rehabilitation Aspects*. Kobeissy, F.H. (ed): Boca Raton, FL.
40. Courtney, A. and Courtney, M. (2015). The complexity of biomechanics causing primary blast-induced traumatic brain injury: a review of potential mechanisms. Front. Neurol. 6, 221.
41. Bandak, F.A., Ling, G., Bandak, A., and De Lanerolle, N.C. (2015). Injury biomechanics, neuropathology, and simplified physics of explosive blast and impact mild traumatic brain injury. Handb. Clin. Neurol. 127, 89–104.
42. Chong, Z.Z., Li, F., and Maiese, K. (2005). Oxidative stress in the brain: novel cellular targets that govern survival during neurodegenerative disease. Prog. Neurobiol. 75, 207–246.
43. Dohi, K., Ohtaki, H., Nakamachi, T., Yofu, S., Satoh, K., Miyamoto, K., Song, D., Tsunawaki, S., Shioda, S., and Aruga, T. (2010). Gp91phox (NOX2) in classically activated microglia exacerbates traumatic brain injury. J. Neuroinflammation 7, 41.
44. Byrnes, K.R., Loane, D.J., Stoica, B.A., Zhang, J., and Faden, A.I. (2012). Delayed mGluR5 activation limits neuroinflammation and neurodegeneration after traumatic brain injury. J. Neuroinflammation 9, 43.
45. Luo, T., Wu, J., Kabadi, S.V., Sabirzhanov, B., Guanciale, K., Hanscom, M., Faden, J., Cardiff, K., Bengson, C.J., and Faden, A.I. (2013). Propofol limits microglial activation after experimental brain trauma through inhibition of nicotinamide adenine dinucleotide phosphate oxidase. Anesthesiology 119, 1370–1388.
46. Ferreira, A.P., Rodrigues, F.S., Della-Pace, I.D., Mota, B.C., Oliveira, S.M., Velho Gewehr Cde, C., Bobinski, F., de Oliveira, C.V., Brum, J.S., Oliveira, M.S., Furian, A.F., de Barros, C.S., Ferreira, J., Santos, A.R., Fighera, M.R., and Royes, L.F. (2013). The effect of NADPH-oxidase inhibitor apocynin on cognitive impairment induced by moderate lateral fluid percussion injury: role of inflammatory and oxidative brain damage. Neurochem. Int. 63, 583–593.
47. Cho, H.J., Sajja, V.S., Vandevord, P.J., and Lee, Y.W. (2013). Blast induces oxidative stress, inflammation, neuronal loss and subsequent short-term memory impairment in rats. Neuroscience 253, 9–20.
48. Readnower, R.D., Chavko, M., Adeeb, S., Conroy, M.D., Pauly, J.R., McCarron, R.M., and Sullivan, P.G. (2010). Increase in blood-brain barrier permeability, oxidative stress, and activated microglia in a rat model of blast-induced traumatic brain injury. J. Neurosci. Res. 88, 3530–3539.
49. Lucke-Wold, B.P., Naser, Z.J., Logsdon, A.F., Turner, R.C., Smith, K.E., Robson, M.J., Bailes, J.E., Lee, J.M., Rosen, C.L., and Huber, J.D. (2015). Amelioration of nicotinamide adenine dinucleotide phosphate-oxidase mediated stress reduces cell death after blast-induced traumatic brain injury. Transl. Res. 166, 509–528 e1.
50. Sorce, S. and Krause, K.H. (2009). NOX enzymes in the central nervous system: from signaling to disease. Antioxid. Redox. Signal. 11, 2481–2504.
51. Coyoy, A., Olguin-Albuerne, M., Martinez-Briseno, P., and Moran, J. (2013). Role of reactive oxygen species and NADPH-oxidase in the development of rat cerebellum. Neurochem. Int. 62, 998–1011.
52. Park, K.W. and Jin, B.K. (2008). Thrombin-induced oxidative stress contributes to the death of hippocampal neurons: role of neuronal NADPH oxidase. J. Neurosci. Res. 86, 1053–1063.
53. Surace, M.J. and Block, M.L. (2012). Targeting microglia-mediated neurotoxicity: the potential of NOX2 inhibitors. Cell. Mol. Life Sci. 69, 2409–2427.
54. Guilarte, T.R., Loth, M.K., and Guariglia, S.R. (2016). TSPO finds NOX2 in microglia for redox homeostasis. Trends Pharmacol. Sci. 37, 334–343.
55. Kumar, A., Barrett, J.P., Alvarez-Croda, D.M., Stoica, B.A., Faden, A.I., and Loane, D.J. (2016). NOX2 drives M1-like microglial/macrophage activation and neurodegeneration following experimental traumatic brain injury. Brain Behav. Immun. 58, 291–309.
56. Sorce, S., Schiavone, S., Tucci, P., Colaianna, M., Jaquet, V., Cuomo, V., Dubois-Dauphin, M., Trabace, L., and Krause, K.H. (2010). The NADPH oxidase NOX2 controls glutamate release: a novel mechanism involved in psychosis-like ketamine responses. J. Neurosci. 30, 11317–11325.
57. Schiavone, S., Jaquet, V., Sorce, S., Dubois-Dauphin, M., Hultqvist, M., Backdahl, L., Holmdahl, R., Colaianna, M., Cuomo, V., Trabace, L., and Krause, K.H. (2012). NADPH oxidase elevations in pyramidal neurons drive psychosocial stress-induced neuropathology. Transl. Psychiatry 2, e111.
58. Zhang, Q.G., Raz, L., Wang, R., Han, D., De Sevilla, L., Yang, F., Vadlamudi, R.K., and Brann, D.W. (2009). Estrogen attenuates ischemic oxidative damage via an estrogen receptor alpha-mediated inhibition of NADPH oxidase activation. J. Neurosci. 29, 13823–13836.
59. Yoshioka, H., Niizuma, K., Katsu, M., Okami, N., Sakata, H., Kim, G.S., Narasimhan, P., and Chan, P.H. (2011). NADPH oxidase mediates striatal neuronal injury after transient global cerebral ischemia. J. Cereb. Blood Flow Metab. 31, 868–880.
60. Siesjo, B.K., Agardh, C.D., and Bengtsson, F. (1989). Free radicals and brain damage. Cerebrovasc. Brain Metab. Rev. 1, 165–211.
61. Jesberger, J.A. and Richardson, J.S. (1991). Oxygen free radicals and brain dysfunction. Int. J. Neurosci. 57, 1–17.
62. Evans, P.H. (1993). Free radicals in brain metabolism and pathology. Br. Med. Bull. 49, 577–587.
63. O'Connell, K.M. and Littleton-Kearney, M.T. (2013). The role of free radicals in traumatic brain injury. Biol. Res. Nurs. 15, 253–263.
64. Brown, S.A. and Hall, E.D. (1992). Role of oxygen-derived free radicals in the pathogenesis of shock and trauma, with focus on central nervous system injuries. J. Am. Vet. Med. Assoc. 200, 1849–1859.
65. Mattson, M.P. (1996). Calcium and free radicals: mediators of neurotrophic factor and excitatory transmitter-regulated developmental plasticity and cell death. Perspect. Dev. Neurobiol. 3, 79–91.
66. Deng-Bryant, Y., Singh, I.N., Carrico, K.M., and Hall, E.D. (2008). Neuroprotective effects of tempol, a catalytic scavenger of peroxynitrite-derived free radicals, in a mouse traumatic brain injury model. J. Cereb. Blood Flow Metab. 28, 1114–1126.
67. Willmore, L.J. and Ueda, Y. (2009). Posttraumatic epilepsy: hemorrhage, free radicals and the molecular regulation of glutamate. Neurochem. Res. 34, 688–697.
68. Zhang, Q.G., Laird, M.D., Han, D., Nguyen, K., Scott, E., Dong, Y., Dhandapani, K.M., and Brann, D.W. (2012). Critical role of NADPH oxidase in neuronal oxidative damage and microglia activation following traumatic brain injury. PLoS One 7, e34504.
69. Loane, D.J. Stoica, B.A., Byrnes, K.R., Jeong, W., and Faden, A.I. (2013). Activation of mGluR5 and inhibition of NADPH oxidase improves functional recovery after traumatic brain injury. J. Neurotrauma 30, 403–412.
70. Schaur, R.J., Siems, W., Bresgen, N., and Eckl, P.M. (2015). 4-Hydroxy-nonenal-A bioactive lipid peroxidation product. Biomolecules 5, 2247–2337.
71. Raghupathi, R. (2004). Cell death mechanisms following traumatic brain injury. Brain Pathol. 14, 215–222.

72. Herculano-Houzel, S., Ribeiro, P., Campos, L., Valotta da Silva, A., Torres, L.B., Catania, K.C., and Kaas, J.H. (2011). Updated neuronal scaling rules for the brains of Glires (rodents/lagomorphs). Brain Behav. Evol. 78, 302–314.
73. Wang, X. and Michaelis, E.K. (2010). Selective neuronal vulnerability to oxidative stress in the brain. Front. Aging Neurosci. 2, 12.
74. Wang, X., Pal, R., Chen, X.W., Limpeanchob, N., Kumar, K.N., and Michaelis, E.K. (2005). High intrinsic oxidative stress may underlie selective vulnerability of the hippocampal CA1 region. Brain Res. Mol. Brain Res. 140, 120–126.
75. Friedman, J. (2011). Why is the nervous system vulnerable to oxidative stress? in: *Oxidative Stress and Free Radical Damage in Neurology*. Gadoth, N., Göbel, H.H. (eds). Humana Press: New York, pps. 19–27.
76. Cavaglia, M., Dombrowski, S.M., Drazba, J., Vasanji, A., Bokesch, P.M., and Janigro, D. (2001). Regional variation in brain capillary density and vascular response to ischemia. Brain Res. 910, 81–93.
77. Tan, X., Przekwas, A.J. and Long, J.B. (2013). Validations of virtual animal model for investigation of shock/blast wave TBI, in: *ASME 2013 International Mechanical Engineering Congress and Exposition*. American Society of Mechanical Engineers, pps. V03AT03A011–V003AT003A011.

Address crrespondence to:
Kakulavarapu V. Rama Rao, PhD
Namas Chandra, PhD, PE
Center for Injury Biomechanics, Materials and Medicine
Department of Biomedical Engineering
New Jersey Institute of Technology
111 Lock Street
Newark, NJ 07102

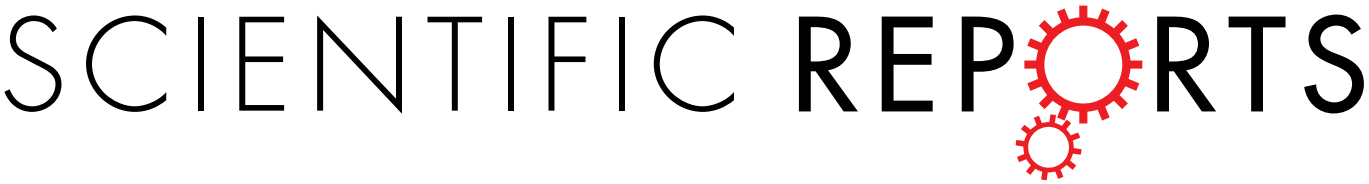
E-mail: kakulava@njit.edu;
kakulavarapuvenkata41@gmail.com;
namas.chandra@njit.edu

Appendix A –Publication Cover 18
2018

Authors: M. Kuriakose, K.V. Rama Rao, D. Younger, N. Chandra

Title: *"Temporal and Spatial Effects of Blast Overpressure on Blood-Brain Barrier Permeability in Traumatic Brain Injury"*

Journal Publication: Nature-Scientific Reports, 8(1), 8681, (2018), [18-18]



OPEN

Temporal and Spatial Effects of Blast Overpressure on Blood-Brain Barrier Permeability in Traumatic Brain Injury

Received: 16 November 2017
Accepted: 1 May 2018
Published online: 06 June 2018

Matthew Kuriakose, Kakulavarapu V. Rama Rao, Daniel Younger & Namas Chandra

Blast-induced traumatic brain injury (bTBI) is a "signature wound" in soldiers during training and in combat and has also become a major cause of morbidity in civilians due to increased insurgency. This work examines the role of blood-brain barrier (BBB) disruption as a result of both primary biomechanical and secondary biochemical injury mechanisms in bTBI. Extravasation of sodium fluorescein (NaF) and Evans blue (EB) tracers were used to demonstrate that compromise of the BBB occurs immediately following shock loading, increases in intensity up to 4 hours and returns back to normal in 24 hours. This BBB compromise occurs in multiple regions of the brain in the anterior-posterior direction of the shock wave, with maximum extravasation seen in the frontal cortex. Compromise of the BBB is confirmed by (a) extravasation of tracers into the brain, (b) quantification of tight-junction proteins (TJPs) in the brain and the blood, and (c) tracking specific blood-borne molecules into the brain and brain-specific proteins into the blood. Taken together, this work demonstrates that the BBB compromise occurs as a part of initial biomechanical loading and is a function of increasing blast overpressures.

Blast-induced traumatic brain injuries (bTBIs) are the signature wounds in military and civilian populations due to the increased use of improvised explosive devices and asymmetric warfare in military conflicts and acts of terrorism, domestically and overseas[1–3]. Despite the increase in studies related to bTBI in recent years, there is only a limited understanding of how blast waves interact with the brain and cause injury, which has precluded the establishment of comprehensive diagnostic criteria for bTBI and the potential of therapeutic strategies. A recent survey reported that more than 30 phase III clinical trials aimed at targeting TBI have failed[4–7]. Understanding how blast-induced neurotrauma displays a temporal and spatial evolution of neuropathology in various regions of the brain is critical for the identification of injury mechanisms and the development of preventative measures and treatments for bTBI patients. Among many mechanisms of injury, damage to the BBB has been identified as a potential candidate and has been the focus of several clinical and experimental investigations aimed to establish injury baselines and to determine the timelines for therapeutic interventions for neurotrauma[8,9].

The blood-brain barrier (BBB) is a highly, selectively-permeable membrane that separates the brain from the circulatory system. The BBB is dynamically modulated by cellular interactions between endothelial cells, the tight junctions that join them, pericytes, and astrocytes that support the endothelial capillaries[10–16]. Many neurological disorders including stroke[17–20], Alzheimer's disease[21,22], Parkinson's disease[14,23], HIV-1 encephalitis[16,24], epilepsy[25,26], and multiple sclerosis[27–29] display impaired BBB permeability. BBB disruption is also one of the most frequently investigated mechanisms of injury in blunt TBI and has been commonly used to evaluate the degree and extent of injury[30–34]. Several groups have reported abnormal opening of the BBB in closed cortical injuries[35–37], weight drop models[38,39], and blast models[34,40–45]. Reported results are derived from different probing methodologies, with different injury models, at different injury intensities, in different spatial regions of the brain. A limited number of studies has implicated increased BBB permeability in the pathology of blast-induced traumatic brain injury but, to the author's knowledge, no such investigation has resolved the temporal and spatial resolution of BBB changes in bTBI, especially as a function of increasing biomechanical blast loadings. While a number of groups have assessed the BBB permeability following blast[42,46–49], it is important to note that not all

Center for Injury Biomechanics, Materials and Medicine (CIBM3), Department of Biomedical Engineering, New Jersey Institute of Technology, Newark, NJ, 07102-1982, USA. Correspondence and requests for materials should be addressed to K.V.R.R. (email: kakulava@njit.edu) or N.C. (email: namas.chandra@njit.edu)

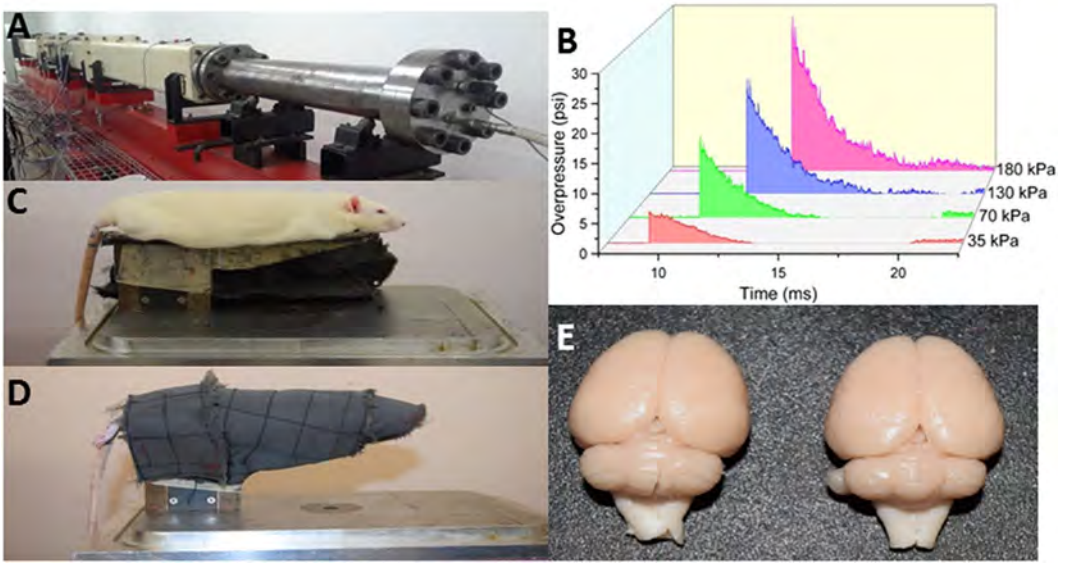


Figure 1. The shock tube housed in the blast laboratory in the Center for Injury Biomechanics, Materials, and Medicine at NJIT. (**A**) The 9-inch, square cross-section, 6 meters long shock tube instrumented with pressure sensors along the top of the shock tube. (**B**) Representative pressure-time profiles acquired from pressure sensors in the shock tube at the four overpressures used in this study. (**C**) Rat holder mounted in the test section of the shock tube, with rat placed in the prone position (top) and (**D**) tightly wrapped in a harness to minimize head and body motion during the blast (bottom). (**E**) Control (left) and injured (right) brains following perfusion-fixation. All blood in the neurovasculature has been washed away, as seen from the white appearance of brains, confirming that all tracers measured has leaked from the vessels into the brain parenchyma.

blast models impart the same type of injury on experimental animals and, for this reason, authors compared the results of this work only to models that feature pure, primary blast injury void of secondary and tertiary effects[50,51].

In this study, rats were exposed to a range of shock waves in a field-validated shock tube and permeability of the BBB was assayed by extravasation of Evans blue (which binds to albumin, a 66 kDa protein abundant in blood) and sodium fluorescein (a 376 Da molecule) in the frontal cortex, striatum, somatosensory barrel-field cortex, hippocampus, thalamus, and cerebellum. Rats were exposed to sub-mild (35 kPa), mild (70 kPa), mild-moderate (130 kPa), and moderate (180 kPa) blast overpressures; these classifications were based on a 24-hour survival dose-response of rodent models based on our previous results (see Fig. 2 of ref.[52]). Also, the Department of Defense (DOD) Instruction 6490.11 dated September 18, 2012 has established policies, responsibilities and procedures for mTBI occurring in the battlefield. When service members are involved in a potential concussive event, they are separated for medical observations and mandatory rest period. DOD defines potential concussive events as the presence of service members within 50 m of a blast or exposure to more than a single blast in a year[1]. Based on theoretical analysis, the peak blast overpressure of 180 kPa can occur at a distance of about 10 m for 100 kg TNT explosive. The same blast will produce 130 kPa BOP in about 12 m, 70 kPa in a distance of 16 m and 35 kPa in a distance of 23 m[53]. We had achieved these field blast loadings using operating characteristics like membrane thickness, transition length, driver gas, driver volume, and end plates[54]. Additionally, three different time-points post-injury (15 min, 4 hr, and 24 hr) were chosen in order to develop a temporal profile of BBB opening and to identify the extent of barrier breach.

Results

Primary blast induces breakdown of the blood-brain barrier. The blast injury model developed at NJIT, capable of reproducing field-relevant blast overpressures and previously characterized[52,55–57] was used throughout this study (Fig. 1A,B). All test animals were mounted in the custom-made rat holder and placed in the test section of the shock tube (Fig. 1C). Rats were immobilized with the head restrained in order to ensure no confounding head movements or possible acceleration/deceleration that can be artifacts of this study (Fig. 1C,D). Rats were exposed to a single blast exposure of varying overpressures (see above) and subjected to transcardial perfusion (with phosphate buffered saline)-fixation (with 4% paraformaldehyde) within 15 min from exposure of animals to blast loading, which was the earliest time point that was assessed for BBB extravasation. The extent of extravasation of both sodium fluorescein and Evans blue was evaluated in all selected regions of the brain (Figs 2 and 3). These quantitative results support the hypothesis that blast-induced BBB opening allows for extravasation of molecules of 69 kDa or smaller immediately following injury (biomechanical loading) and, given an increase in molecular mass, extravasation of tracers was less widespread.

The fluorescence detection method of extravasation was also validated with absorption spectrophotometry for Evans blue. Animals (n = 6) exposed to 180 kPa shock wave showed an average of 45.6% increase in the tissue

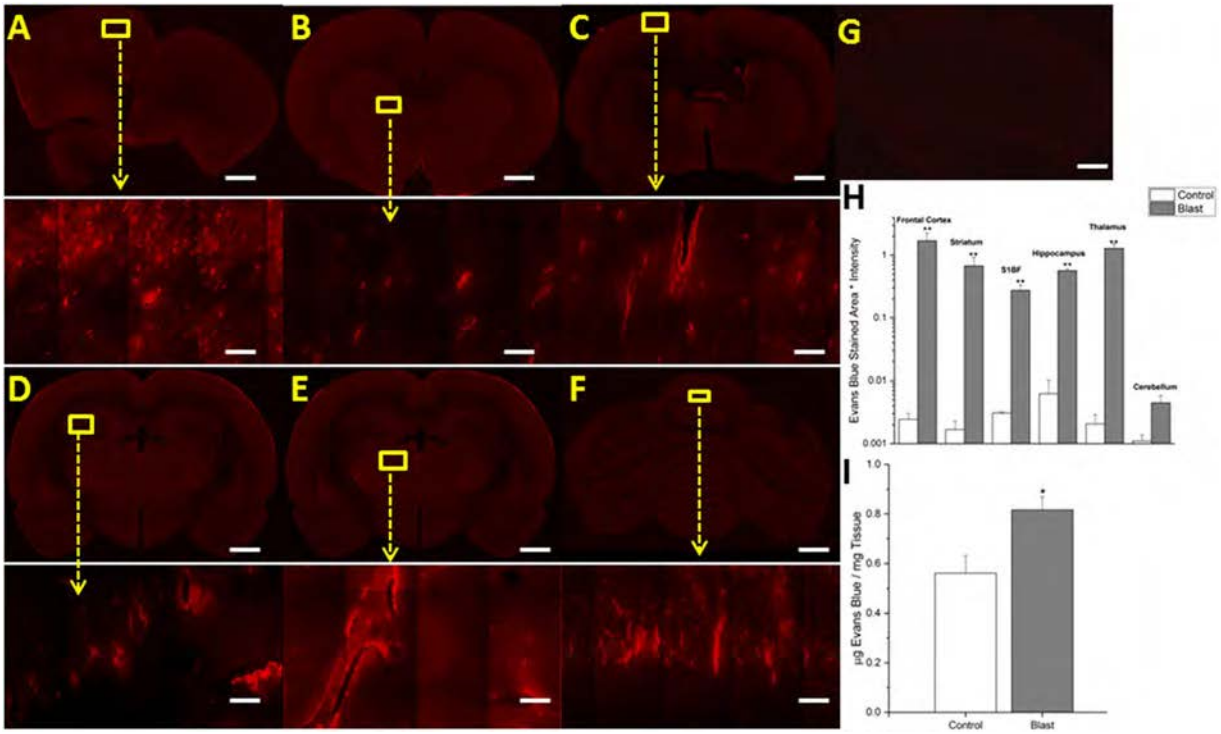


Figure 2. Fluorescent images of Evans blue extravasation. Images show 10x macro-shots as well as zoomed in 40x images in representative regions in the frontal cortex (**A**), striatum (**B**), somatosensory barrel-field cortex (**C**), hippocampus (**D**), thalamus (**E**) and cerebellum (**F**), 15 minutes following 180 kPa blast exposure. Control images were dramatically enhanced, yet still show limited visibility, due to the absence of extravasated dye. Frontal cortex was taken as a representative control image (**G**). Quantitation of extravasation is shown using a semilog plot in order to capture magnitudinal differences (**H**). Absorption spectrophotometry results of Evans blue in control and injured rats ($n = 5$) (**I**). *Indicates a difference in intensity compared with control with a statistical significance of $p < 0.05$, **Indicates $p < 0.01$. Scale bar = 1 mm in coronal sections and 50 μm in 40x images.

content of EB than control animals wherein the precise concentration of EB present in tissue was derived from a standard curve made of seven different EB dilutions (Fig. 2I).

Different brain regions express different degrees of BBB permeability following moderate blast injury. After exposing animals to moderate blast (180 kPa), differential damage was observed in six different regions immediately following trauma (~15 min). In almost every region studied, statistically significant differences ($p < 0.01$), as determined by ANOVA followed by Tukey test, in the levels of both extravasated dyes was observed, highlighting the diffuse nature of bTBI (Figs 2 and 3). The quantitative values of the fluorescence intensities of EB (as measured by intensity x stained area) between control and blast injury groups in different brain regions are as follows: frontal cortex (control 0.002432, blast 1.699085, 700-fold, $p = 0.006$), striatum (control 0.001674, blast 0.675456, 400-fold, $p = 0.001$), somatosensory-barrel field cortex (control 0.003094, blast 0.274115, 90-fold, $p = 0.009$), hippocampus (control 0.006258, blast 0.564796, 90-fold, $p = 0.001$), thalamus (control 0.002056, blast 1.282525, 600-fold, $p = 0.002$) and cerebellum (control 0.001102, blast 0.00448, 4-fold, $p > 0.05$); and for sodium fluorescein: frontal cortex (control 0.004555, blast 1.91963, 400-fold, $p = 0.008$), striatum (control 0.005134, blast 1.822249, 300-fold, $p = 0.008$), somatosensory barrel-field cortex (control 0.001584, blast 0.429447, 250-fold, $p = 0.009$), hippocampus (control 0.00794, blast 0.630788, 80-fold, $p = 0.009$), thalamus (control 0.003556, blast 1.767197, 500-fold, $p = 0.004$) and cerebellum (control 0.004479, blast 0.055629, 30-fold, $p > 0.05$). The most robust changes occurred in the frontal cortex, striatum, and thalamus for both tracers while minimal to no statistically significant extravasation was observed in the cerebellum, which aligns well with results from previous investigations[34,58]. In every other region analyzed, there is at least a tenfold difference in the amount of extravasated dyes compared to controls in the acute time period.

BBB permeability varies as a function of time following moderate blast injury. In order to determine the time-course for blood-brain barrier permeability following blast, groups of ($n = 4$–6 for each time point) rats were sacrificed at specified times post-injury (15 min, 4 hours, 24 hours). While the amount of extravasation was significant for both sodium fluorescein and Evans blue immediately after blast, there was an even greater increase in tracer penetration four hours following the blast exposure (Figs 4 and 5). Increases over controls were as follows for Evans blue at 4 hours, respectively (four hour blast values followed by fold-increase and 24 hour blast values followed by fold increase): frontal cortex (3.270751, 1300-fold, 0.005012, 2-fold), striatum (1.681731,

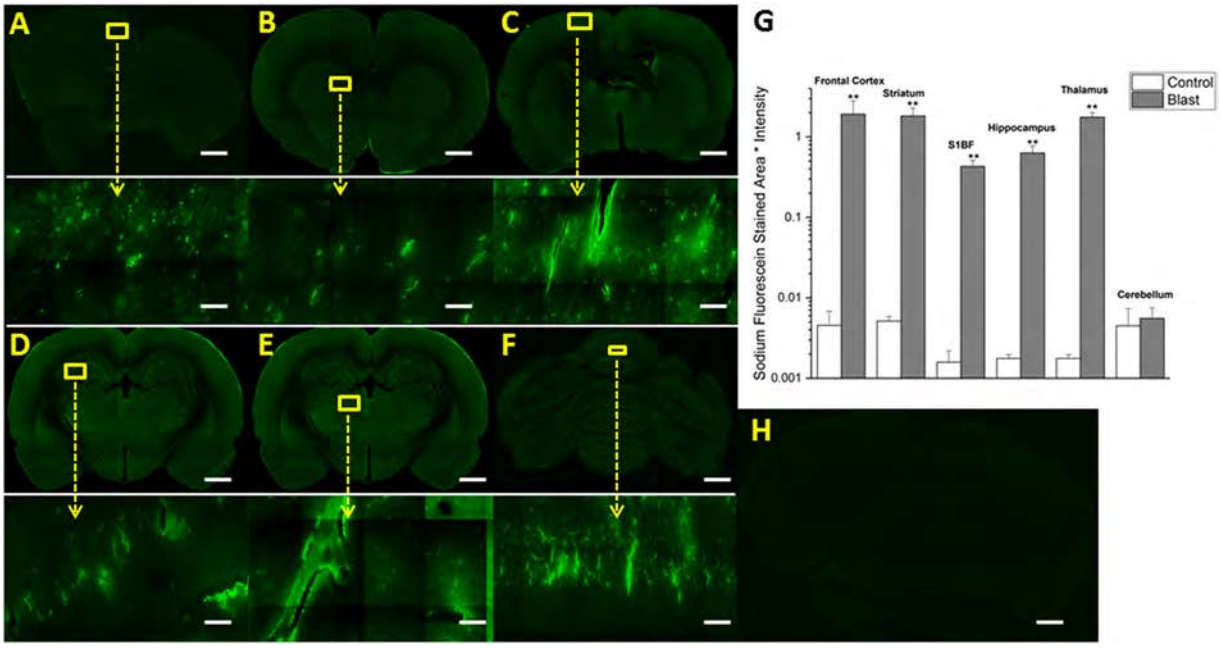


Figure 3. Fluorescent images of sodium fluorescein extravasation. Images show 10x macro-shots as well as zoomed in 40x images in representative regions in the frontal cortex (**A**), striatum (**B**), somatosensory barrel-field cortex (**C**), hippocampus (**D**), thalamus (**E**) and cerebellum (**F**) 15 minutes following 180 kPa blast exposure. Quantitation of extravasation is shown using a semilog plot in order to capture magnitudinal differences (**G**). Control images were dramatically enhanced, yet still show limited visibility, due to the absence of extravasated dye. Frontal cortex was taken as a representative image (**H**). **Indicates a difference in intensity compared with control with a statistical significance of $p < 0.01$. Scale bar = 1 mm in coronal sections and 50 μm in 40x images.

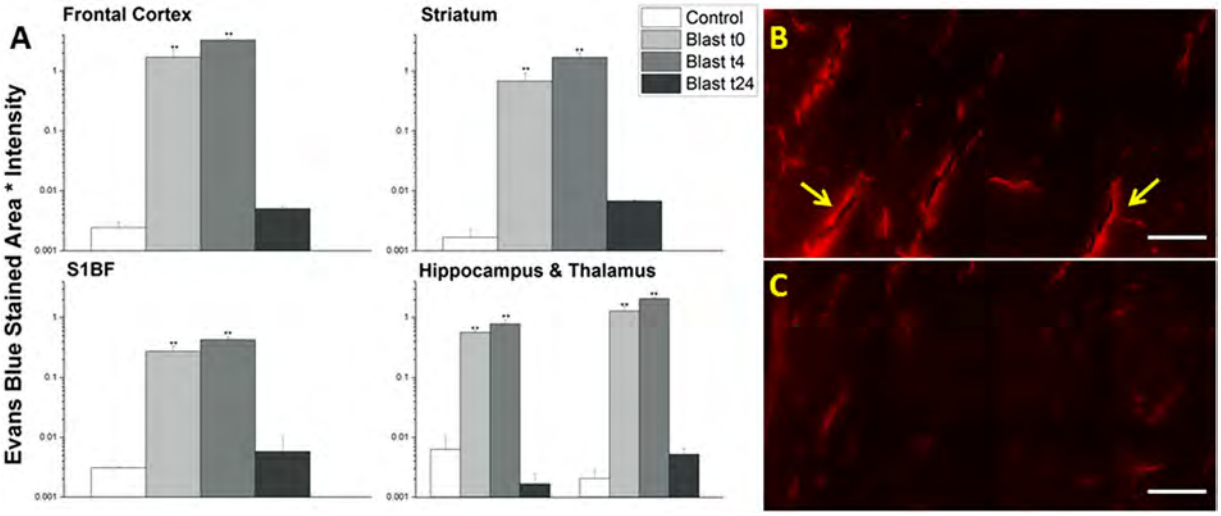


Figure 4. Quantitation of extravasation of Evans blue for 15 minutes (t0), 4 (t4), and 24 (t24) hours post-180 kPa blast exposure in frontal cortex, striatum, somatosensory barrel-field cortex, hippocampus, and thalamus using a semilog plot in order to capture magnitudinal differences (**A**). The frontal cortex was chosen for illustrative purposes and to qualitatively depict the difference between 4 (**B**) and 24 hrs (**C**). Arrows indicate areas of leakage from the vessels, which are more pronounced in 4 hours than any other time point studied in this investigation. **Indicates a difference in intensity compared with control with a statistical significance of $p < 0.01$. Scale bar = 100 μm.

1000-fold, 0.006758, 4-fold), somatosensory barrel-field cortex (0.427674, 150-fold, 0.005808, 1-fold), hippocampus (0.781473, 120-fold, 0.00166, <1-fold), and thalamus (2.080952, 1000-fold, 0.005169, 2-fold) and for sodium fluorescein: frontal cortex (3.365124, 700-fold, 0.014903, 3-fold), striatum (1.966033, 400-fold, 0.00229, <1-fold),

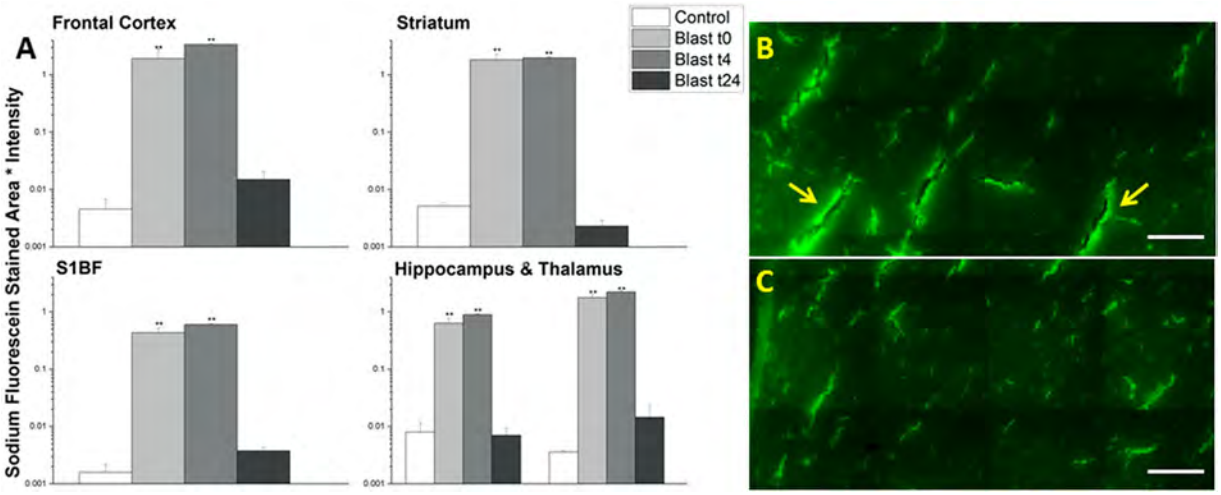


Figure 5. Quantitation of extravasation of sodium fluorescein for 15 minutes (t0), 4 (t4), and 24 (t24) hours post- 180 kPa blast exposure in frontal cortex, striatum, somatosensory barrel-field cortex, hippocampus, and thalamus using a semilog plot in order to capture magnitudinal differences (**A**). The frontal cortex was chosen for illustrative purposes and to qualitatively depict the difference between 4 (**B**) and 24 hrs (**C**). Arrows indicate areas of leakage from the vessels, which are more pronounced in 4 hours than any other time point studied in this investigation. **indicates a difference in intensity compared with control with a statistical significance of $p < 0.01$. Scale bar = 100 μm.

somatosensory barrel-field cortex (0.596185, 400-fold, 0.003732, 2-fold), hippocampus (0.885597, 100-fold, 0.006966, <1-fold), and thalamus (2.223883, 600-fold, 0.014472, 4-fold). Interestingly, 24 hours post-injury, the extravasation of EB and NaF returned back to that of control levels (Figs 4 and 5) suggesting possible resealing occurring at or before 24 hours.

As an alternate means to investigate BBB disruption as well as to examine possible mechanisms of BBB permeability change following blast, levels of tight junction proteins (TJPs) occludin and claudin-5 were determined in lysates from cerebral hemispheres by quantitative ELISAs. Statistically significant reductions in tight junction protein abundance were observed at this time point, which serves as further evidence of the compromised BBB (Fig. 6). Noteworthy that such reduction in TJPs in brain lysates is accompanied by a concomitant increase in their levels in serum samples obtained from the same animals that are used for evaluation of brain levels of tight junction proteins. These data not only strongly suggest that shockwave propagated from blast is able to dislodge TJPs from the cerebral vasculature but also that these proteins translocate to blood.

The extent of BBB permeability displays a tendency to increase as a function of blast overpressure. In order to determine the effects of blast overpressure on BBB permeability, groups of (n = 3) rats were exposed to mild shockwaves of 35, 70, and 130 kPa BOPs and sacrificed immediately after blast. While no measurable extravasation was induced at 35 kPa, there is clear evidence of leakage starting at 70 kPa (Figs 7 and 8) and extravasation quantitation for both tracers showed a tendency to increase with increasing overpressure. The fluorescence intensity increases over controls and were as follows for Evans blue at 35, 70 and 130 kPa, respectively as determined by post-ANOVA Tukey test: frontal cortex (0.014762, 6-fold, 0.826735, 340-fold, 0.898087, 370-fold), striatum (0.00983, 5-fold, 0.118309, 70-fold, 0.355441, 200-fold), somatosensory barrel-field cortex (0.0036, 1-fold, 0.101135, 30-fold, 0.215851, 70-fold), hippocampus (0.0.007685, 1-fold, 0.15515, 25-fold, 0.15437, 25-fold), and thalamus (0.003252, 2-fold, 0.380609, 180-fold, 0.773843, 380-fold) and for sodium fluorescein: frontal cortex (0.030414, 7-fold, 1.146571, 250-fold, 1.91895, 260-fold), striatum (0.012241, 2-fold, 0.201411, 40-fold, 0.545131, 100-fold), somatosensory barrel-field cortex (0.003914, 2-fold, 0.132123, 80-fold, 0.256239, 160-fold), hippocampus(0.013312, 1-fold, 0.172132, 20-fold, 0.205551, 25-fold), and thalamus (0.00404, 1-fold, 0.181371, 50-fold, 0.302787, 85-fold).

Primary blast induces translocation of astrocytic marker s100-β into blood stream and monocyte infiltration into brain. In order to more strongly display the presence of brain-specific proteins in circulation following blast injury, an ELISA was conducted for s100-β at 4 and 24 hours post-moderate blast (180 kPa) in serum samples (n = 3, Fig. 9). At four hours post-injury, concentration of s100-β rose from 399 pg/ml to 594 pg/ml, a statistically significant increase of 48.8% (post-ANOVA Tukey test, $p = 0.037$). However, after 24 hours, the protein levels in serum fall to 427 pg/ml, an increase of only 7% from control values (Tukey test, $p > 0.05$).

Similarly, as an alternative means to demonstrate the presence of blood-borne macromolecules/cells in the brain parenchyma, double immunofluorescence staining was performed for CCL2 (monocyte marker) and RECA-1 (endothelial cell marker) at 4 hours post-moderate blast in the frontal cortex (n = 3, Fig. 10). Results indicate that, qualitatively, the presence of monocytes around blood vessels increased following blast compared to controls.

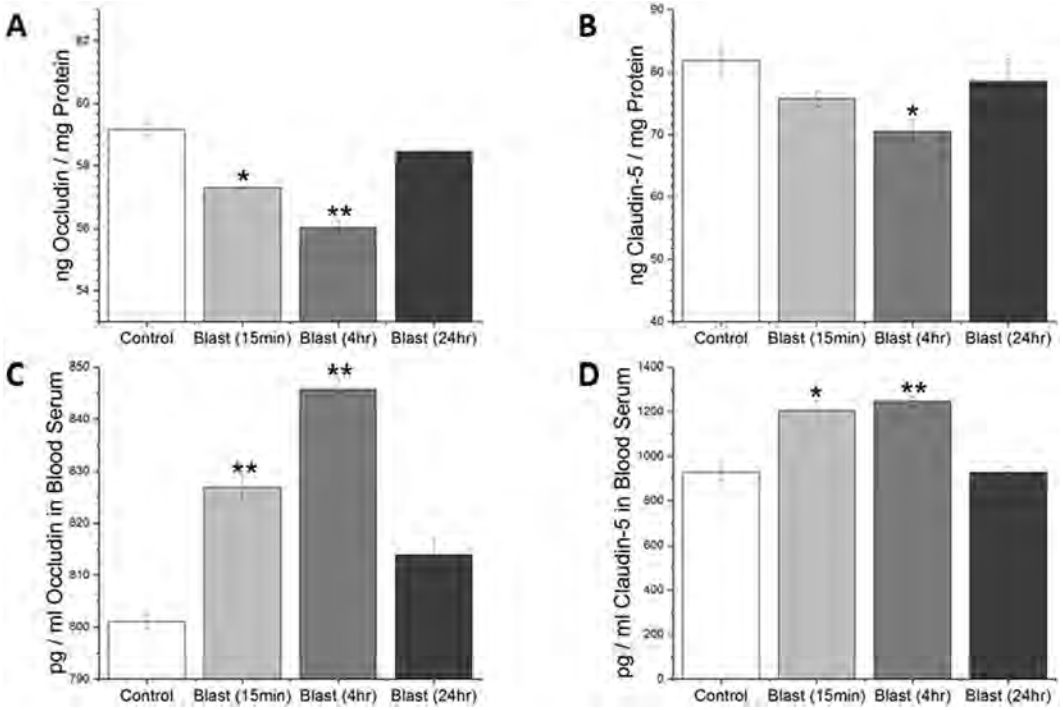


Figure 6. ELISA results for tight junction proteins occludin and claudin-5, respectively in brain (**A**,**B**) and blood serum (**C**,**D**). Assay conducted for blast (180 kPa BOP) samples fifteen minutes, four, and twenty four hours post-exposure and compared with controls. *Indicates a difference in intensity compared with control with a statistical significance of $p < 0.05$, **Indicates $p < 0.01$.

Discussion

This work focused on establishing spatial and temporal relationships of the BBB permeability as a function of overpressure in blast-induced traumatic brain injury. Through the use of two tracers (Evans blue and sodium fluorescein) injected intravenously in the lateral tail vein of the rat, the degree of the BBB disruption following injury was functionally assayed. At the sub-mild overpressure (35 kPa) very limited extravasation of dyes was observed. A breach in the BBB was first observed at a mild blast overpressure (70 kPa) which revealed a significant increase in barrier permeability almost immediately after blast (~15 min). In addition to extravasation of tracers (NaF and EB), absorption spectrophotometry was used to demonstrate the breakdown of the BBB by the presence of EB in brain parenchyma. The results of the absorption spectrophotometry offer interesting piece of corroboratory information; unlike gross blunt injuries, where there is a substantial amount of extravasated tracers recorded[59,60], in this mild-moderate blast injury, a difference of only about 250 picograms of EB was observed between injured and control groups (Fig. 2).

It is interesting to note that the extravasation of the tracers showed a significant increase as early as 15 min following the blast, strongly supporting the hypothesis that direct biomechanical loading of the primary blast was able to disrupt the BBB (Figs 2 and 3). We should note that there is no physical impact of external objects such as in CCI or weight drop models, nor a specific fluid pressure in subdural space as in fluid percussion model. However, while the degree of BBB disruption appears large when compared to controls (which was negligible), the physiological as well as neurological state of the animal were not altered based on visual observation of the animal's status including unaltered gait, righting and startle reflexes (data not shown). This strongly suggests that this injury can be classified as a subtle, tissue-level mechanical disruption of vasculature. Therefore, caution must be exercised when comparing these results with those from blunt injury models, where injury severity is greater and degree of extravasation is larger but the injury is highly local, mostly restricted to the site of external impact or fluid pressure[35,36,61]. As noted earlier, the degree of the BBB permeability increased further at 4 hours post-injury (Figs 4 and 5), which not only indicates the persistence of the BBB disruption but also indicates that, in addition to direct biomechanical loading (shock loads that lasts for a transient period of approximately 3 milliseconds), some secondary mechanisms may be activated post-injury and contribute to BBB disruption for hours after initial trauma.

While several secondary mechanisms have been implicated in the degradation of the BBB including oxidative stress[12,30,33,43], matrix metalloproteinase activity and neuroinflammation[12,33,38,62], pericyte detachment[15,63–65], astrocytic end-feet swelling and detachment[66–69], among others, precise involvement of one or more of these mechanisms contributing to BBB disruption in bTBI remains to be determined. Previous studies have cited maximum degree of damage to the BBB following mild-moderate TBI (although not blast) occurring between 4–6 hours of injury[8,35,39]. The lack of a detailed time course of BBB disruption in blast injury is a primary motivation for this work and a greater understanding of the temporal nature of the evolution of pathology and

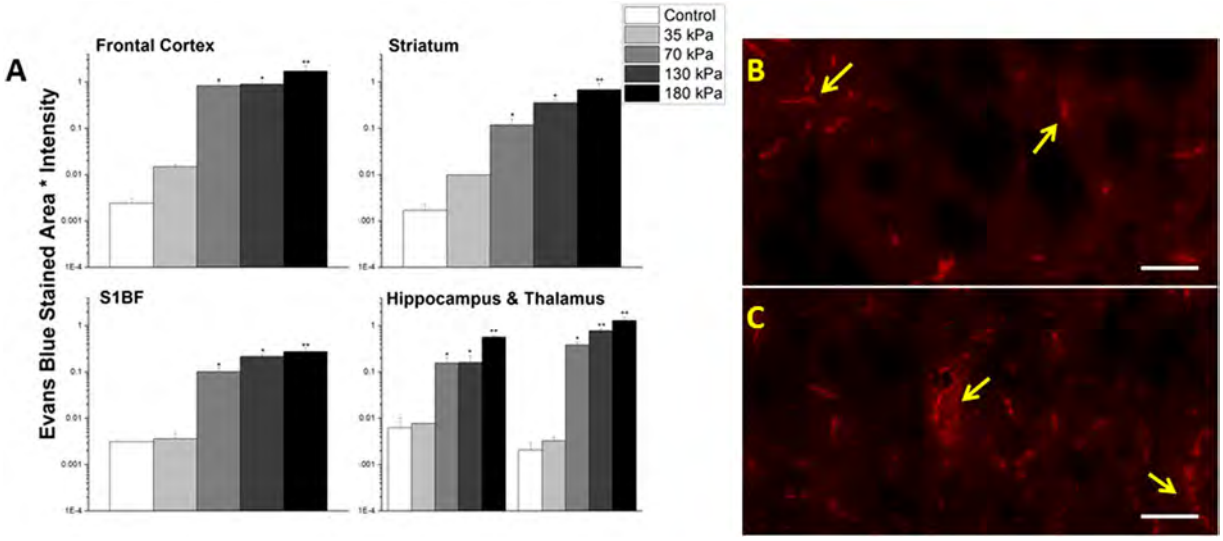


Figure 7. Quantitation of extravasation of Evans blue for 35, 70, 130, and 180 kPa blast overpressures, 15 minutes post-exposure in frontal cortex, striatum, somatosensory barrel-field cortex, hippocampus, and thalamus using a semilog plot in order to capture magnitudinal differences (**A**). The striatum was chosen for illustrative purposes and to qualitatively depict the difference between 70 (**B**) and 130 kPa (**C**). Leaks appear longer and more intense with increasing overpressure in the same brain regions. *Indicates a difference in intensity compared with control with a statistical significance of $p < 0.05$, **Indicates $p < 0.01$. Scale bar = 100 μm.

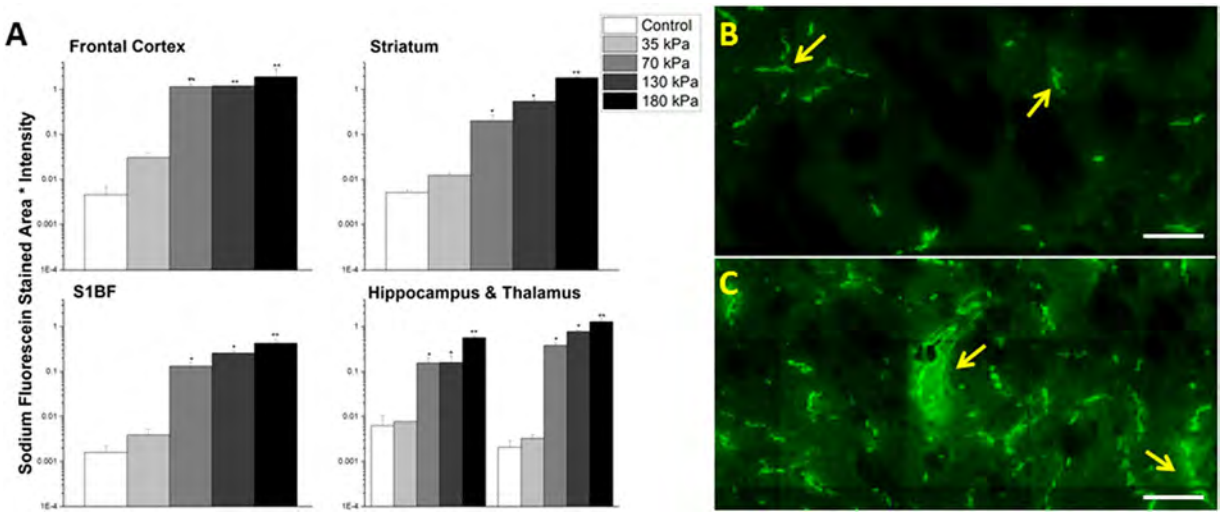


Figure 8. Quantitation of extravasation of sodium fluorescein for 35, 70, 130, and 180 kPa blast overpressures, 15 minutes post-exposure in frontal cortex, striatum, somatosensory barrel-field cortex, hippocampus, and thalamus using a semilog plot in order to capture magnitudinal differences (**A**). The striatum was chosen for illustrative purposes and to qualitatively depict the difference between 70 (**B**) and 130 kPa (**C**). Leaks appear longer and more intense with increasing overpressure in the same brain regions. *Indicates an intensity compared with control with a statistical significance of $p < 0.05$, **Indicates $p < 0.01$. Scale bar = 100 μm.

contributions of precise mechanisms during the time-course of BBB disruption in blast-induced neurotrauma will aid in diagnostic and therapeutic discoveries[70].

The integrity of the tight junctions was also assessed in the current study immediately following moderate blast, four, and twenty-four hours post injury. Tight junctions are water-tight seals that connect adjacent endothelial cells across the brain vasculature[11,13]. These complexes are comprised of several proteins that anchor the tight junction to the surface of endothelial cells and represent a strong mechanical junction that is the foundation of the BBB. Several groups have studied the integrity of the tight junctions as a means to assess the state of the BBB[30,44,56,71,72]. In the present study, the abundance of tight junction proteins (occludin and claudin-5) was evaluated quantitatively via ELISA (Fig. 6A,B). In the acute phase of injury (~15 mins), a reduction in tight junction protein abundance was observed in both occludin ($p = 0.012$) and claudin-5 ($p > 0.05$). Although the reduction

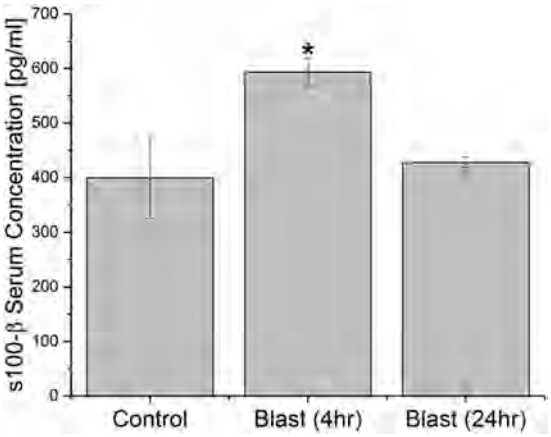


Figure 9. Concentration of s100-β in blood serum. Assay conducted for blast (180 kPa BOP) samples four and twenty four hours post-exposure and compared with controls. *Indicates a difference in intensity compared with control with a statistical significance of $p < 0.05$.

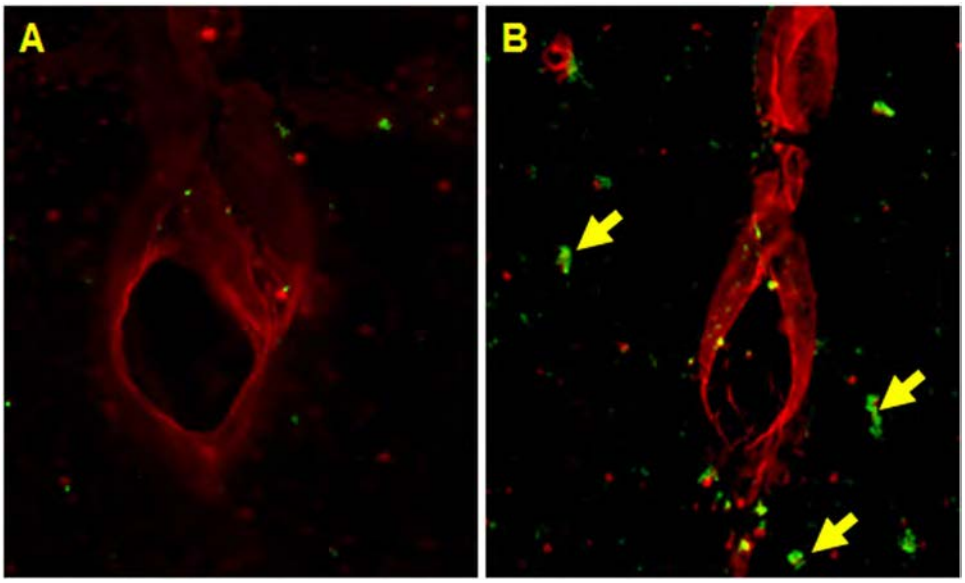


Figure 10. Double immunofluorescence of endothelial cell marker (RECA-1, red) and monocyte marker (CCL2, green) at four hours post-exposure in frontal cortex in animals from control (**A**) and moderate (180 kPa BOP) blast injury (**B**). Scale bar = 50 μm.

in claudin-5 was not statistically significant, it displays a strong tendency to decrease. These results strongly support our tenet that a direct mechanical loading may be able to break and dislodge tight junction complexes and cause subsequent reduction in integrity of the BBB, which may have manifested in the extravasation of the dyes. Further, at four hours post-blast, levels of occludin and claudin-5 were reduced ($p = 0.002$, $p = 0.035$, respectively) suggesting that, in addition to direct mechanical forces, secondary factors that are likely activated 4 hours post-injury also contribute to the reduction in TJPs. Such sustained decrease in these proteins may in part be responsible for greater compromise in BBB integrity 4 hours post-injury observed in the present study. While several factors have been implicated in the breakdown of tight junction proteins, oxidative stress and increased matrix metalloproteinase activity have been shown to contribute to the disruption of the BBB[12,30]. Moreover, restoration of the levels of occludin and claudin-5 observed in the present study within twenty-four hours post-blast corroborates the absence of extravasation seen at 24 hours post-blast.

While the reduction in the brain levels of tight junction proteins suggest a possibility of their dislodging by direct impact of the shockwaves, we sought to examine the accountability of these proteins in the blood stream, since it is likely that once dislodged, these proteins may be translocated into blood stream. Therefore, we estimated the levels of these proteins in serum samples by quantitative ELISA. Interestingly, we observed a close, inverse correlation on the levels of these proteins between brain homogenates and serum (Fig. 6C,D). Fifteen minutes post-injury, there was a significant increase in the amount of occludin ($p = 0.012$) and claudin-5

($p = 0.011$) detected in the blood serum compared to controls. The amount of detected tight junction proteins further increased four hours post-injury ($p < 0.001$, $p = 0.002$) for occludin and claudin-5, respectively. These results not only corroborate the ELISA results in the brain tissue, but also give strong support to the assertion that the tight junction proteins are being mechanically dislodged from the tight junction complexes and being taken up into circulation. Moreover, a complete recovery of these TJPs to the control levels in brain and blood 24 hours post-injury corroborates well with the absence of any extravasation of EB or NaF which together indicate the possibility of resealing of the BBB at this time point.

Several studies report that increased levels of astrocytic protein s100-β in the blood indicate the breakdown of the BBB[12,30,40,73–75]. The current study shows increased s100-β in serum from animals exposed to blast provides additional support to our extravasation studies and together represent the involvement of astrocytic defects in the compromise of BBB following blast injury.

To demonstrate infiltration of any blood-borne cells entering the brain parenchyma, an immunofluorescence stain was performed to identify the presence of monocytes in the vicinity of vascular endothelial cells using CCL2 and RECA-1, respectively ($n = 3$, Fig. 10). CCL2 is a monocyte chemoattractant protein which presents on blood monocytes and is integral in monocyte mobilization while RECA-1 is a common vascular endothelial marker[76–78]. The increased number of CCL2 staining in the frontal cortex near blood vessels indicates that monocytes are leaking from the blood into the brain parenchyma four hours post-injury. This qualitatively supports the extravasation results for Evans blue and sodium fluorescein.

In the current study, differential degree of BBB permeability was observed spatially across different brain regions. Such differential blood-brain barrier permeability may, in part, be due to variations in the vascular architecture (density, size, orientation) in different brain regions. Cavaglia's group characterized the variation in neurocapillary density in the adult rat hippocampus and cortical structures[79]. The hippocampal CA1 region revealed a significantly lower capillary density compared to CA3, but a much more extensive blood-brain barrier leakage. This may instinctively point to an inverse relationship between vascular density and BBB vulnerability; however Cavaglia's studies also showed that neocortical regions have a much higher vascular density compared to neighboring gray/white matter junctions. Since gray matter regions (frontal cortex, thalamus, etc.) have a higher vascular density than the white matter regions, the mechanical shock loading in the acute phase of injury in conjunction with the onset of secondary mechanisms during latter stages may damage the brain regions containing higher vascular densities more than others. Supporting this tenet, our results and many other studies reveal higher degree of BBB damage in the frontal cortex (Figs 2 and 5)[34,43,58,72]. In addition to vascular density (number of vessels, vessel length, etc.), it is also possible that vascular orientation and cellular architecture may also be, in tandem, responsible for the observed spatial variation of BBB permeability. From a purely biomechanical perspective, a combination of vascular architecture and, to some extent, perivascular attachment to astrocytes may dictate the response to the sudden physical motion of capillaries leading to the mechanical disruption of tight junctions.

While it is strongly assumed that the propagation of shock uniformly travels and loads the whole brain, absence of BBB damage in cerebellum is interesting. The lack of functional BBB damage in the cerebellar regions has been reported by several groups, but there is still uncertainty to its cause[34,58,80]. Several groups have shown vascular volume in the cerebellum to be higher than that in the cerebrum[81–83], but Holash et. al determined that this difference was due to the inclusion of pia vasculature[84]. Without pial vessels (which have a BBB quite different from the parenchymal vessels in terms of tight junction distribution and astrocytic ensheathment[85]), the vascular volume of the cerebellum and cerebrum are comparable. Most extravasation studies use intravascular tracers, which do not discriminate between pial and intraparenchymal vessels in the cerebellum. The authors speculate that the lack of extravasation in the cerebellum based on these methods is due to the presence of the pial vessels, but more work needs to be done to validate this hypothesis (ie. isolating parenchymal vessels).

Further, in the current study, based on the high magnification images (Figs 2, 3, 4, 5, 7 and 8) it is tempting to speculate that larger diameter blood vessels had greater leakage compared to smaller ones. Hypothetically, given a larger cross-sectional area, these vessels bear a greater brunt of the passing shock wave and hence are more damaged than their smaller counterparts. It is also possible that these larger vessels only appear to leak more because of a greater vascular volume: more vessel content, the more blood is able to leak out in the presence of a vascular rupture. In this case, vessels of all sizes would experience a similar mechanical load from the shock wave and show a similar pattern of leakage (with only differences in leakage volume, proportional to vessel size), which is consistent with the results of this study. When a shock/stress wave encounters vasculature, the biomechanical forces will be proportional to the projected area and the difference in acoustic impedance between the different materials that make up the local tissue construct. The resistance to deformation will be proportional to the structural integrity of the vasculature vis-à-vis the surrounding cellular architecture. As different subregions of the brain have different architectures and biomechanical characteristics, the forces, the deformation and hence the BBB leakage will be a function of the specific region under question even if the loading is identical.

After 24 hours following mild blast, a statistically significant decrease in extravasation was observed in all brain regions, which represents possible evidence of a BBB resealing in combination with the restoration of TJPs (Figs 4, 5, 6). A recent study also reported a reduction in BBB damage 24 hours after injury in mice exposed to moderate blast (100 kPa)[86]. This, however, may not preclude continued presence of phenotypic changes of the TBI in brain structures since vascular leakage of various blood born substances into the parenchyma may trigger secondary events such as microglial activation leading to neuroinflammation.

At all time-points, in all regions, the total amount of extravasated sodium fluorescein tracer was greater than Evans blue, an intuitive result given the difference in size between these two tracers. One needs to be careful in interpreting the results in terms of fold increase since the baseline data for the smaller molecule, sodium fluorescein, was higher than the larger Evans blue. In no region was there a collection of sodium fluorescein in the absence of Evans blue, meaning that in the current work, there was an insignificant number of breaches in the BBB which could accommodate the 376 Da sodium fluorescein but not the larger 69 kDa Evans blue.

The present study showing a strong tendency of higher extravasation in animals exposed to 130 kPa compared to 70 kPa in the acute phase of the injury suggests the BBB permeability changes are directly proportional to increasing BOP, at least in the acute phase of the injury. Interesting that 4 hours post-injury such magnitude of difference in the extravasation of EB and NaF as a function of BOP is absent. While the reason for this is not known, the authors speculate that differences in these injuries become more apparent after the acute phase of injury and such significant changes may be masked once secondary mechanisms begin to occur (4 hours), which may uniformly exacerbate injury conditions since, in the immediate phase of injury (~15 min), all leakage of the BBB is attributed to the mechanical insult of the shock wave. Therefore, the resulting biomechanical injury may not be grossly different between mild and moderate overpressures at time interval (4 h) where secondary mechanisms begin to occur. Indeed, such differential changes in BBB permeability have also been reported in other investigations[52,56], which may superimpose the mechanical injury with the influences of secondary biochemical mechanisms (e.g., oxidative stress, neuroinflammation).

Our efforts to establish a sub-mild injury model of bTBI led to the identification of 35 kPa as a BOP that does not show any tracer extravasation. However, the BBB permeability changes are significant with a minimal BOP of 70 kPa and increased further as a function of increasing BOPs (Figs 7 and 8). These results indicate that the mechanical loading sustained at 35 kPa is insufficient to cause the significant damage to the BBB that was seen at 70 kPa and higher overpressures. Therefore, 70 kPa BOP offers a basal injury threshold for the BBB permeability changes to occur under primary blast loading. These studies together demonstrate that BBB permeability is a sensitive phenotypic marker for mTBI in the acute phase of the injury wherein a direct mechanical disruption is able to cause vascular rupture. Accordingly, alterations in the integrity of BBB may be considered a prognostic event to scale the injury severity (i.e., sub-mild to mild vs moderate TBI) as well as the extent of pathological outcomes in blast TBI.

In summary, this work addresses a clear gap in knowledge in the understanding of the BBB permeability in the pathophysiology of blast-induced traumatic brain injury. The results and conclusions presented herein should provide the baseline for future studies attempting to connect the BBB permeability and the pathophysiological progression of bTBI. However, while the authors maintain that these results are reproducible in age-matched rats exposed under the same loading conditions, it is important that the described experimental model is replicated as closely as possible in order to reproduce these results. For example, non-primary injuries will likely be observed if animals are located outside or near the end of the shock tube or if animals are not properly fixed and thus may reveal an altered injury profile.

Materials and Methods

Animal Preparation. A total of 88 adult, 10-week old male Sprague Dawley rats (Charles River Laboratories) weighing between 300–350 g were used throughout this study, in accordance with protocols approved by Rutgers University Institutional Animal Care and Use Committee (IACUC). Animals were housed at 22 °C with free access to food and water in a 12 hour dark-light cycle. Animals were divided among sham and injured groups for four different blast overpressures and three different time-points post-injury. All methods used throughout the study were performed in accordance with protocols, guidelines, and regulations approved by Rutgers University IACUC.

Exposure to Blast and Tracer Injections. Rats were exposed to a single shock wave at the Center for Injury Biomechanics, Materials, and Medicine (New Jersey Institute of Technology) in the modular, field-validated shock tube described in previous publications[54–56,87]. Based on preliminary findings, we observed an obvious difference between sham and blast groups, where an $n = 4$ was sufficient to achieve a power value of 0.9 ($\alpha = 0.05$ and combined SD of 0.819) based on power analysis. An $n = 1–2$ was added in case of mortality or inadequate perfusion. As we continued the study, we maintained an $n = 5–6$ for all blast groups (for 70 and 130 kPa groups, only three animals were used, but statistical significance was achieved). Prior to blast exposure, animals were anesthetized with 5% isoflurane, released in a chamber containing 95% air and 5% CO_2, until unresponsive to noxious stimulation. At this point the rats were mounted and immobilized on a custom rat-holder in the test section of the shock tube. Sham animals were anesthetized and received noise exposure, but kept outside of the shock tube, away from the shock wave. Exposed animals were subjected to a single blast of 35, 70, 130, or 180 kPa peak overpressure and euthanized via transcardial perfusion-fixation at prescribed time-points (15 mins, 4 hrs, 24 hrs). Tracers were injected two hours prior to euthanasia (animals in the 15 min group received injections prior to blast exposure). Sodium fluorescein was administered via the lateral tail vein (376 Da, 20% dissolved in phosphate-buffered saline [PBS], 0.02 g/mL, 0.7 mL delivered) at the same time Evans blue was (69 kDa when bound to albumin, 2% solution dissolved in PBS, 0.002 g/ml, 0.7 mL delivered). Two hours were given as to give sufficient time for the tracers to circulate the body multiple times and perfuse even deeper neurovasculature across all experimental groups. Other groups have used both these dyes to assess BBB permeability up to four hours following tracer administration[34,88,89]. Half-life of EB in circulation was confirmed to be $>$ four hours, while the same is true for NaF half-life[90–92], instilling confidence that allowing two hours for circulation and extravasation for these tracers is adequate.

As a quality control measure, high-speed video was monitored and recorded with a Photron FASTCAM Mini UX100 operating at a framerate of 5000 fps to capture any substantial head/body movement during blast, in order to exclude the effects of secondary/tertiary injury from this study. Approximately two seconds of video footage were recorded per exposure and then saved via PFV (Photron FASTCAM Viewer) 3.3.5 software. Incident overpressure at the location of the animals in the test section of the shock tube was recorded at 1.0 MHz sampling frequency by a custom LabView program running on in-house built data acquisition system based on National Instruments PXI-6133 32 MS Memory S Series Multifunction DAQ Modules and PXIe-1082 PXI Express Chassis. PCB Piezotronics (Depew, NY) model 134A24 pressure sensors were used in all experiments.

Tissue Preparation, Absorption Spectrophotometry, and *Ex-Vivo* Imaging and Analysis. Rats were perfusion-fixed two hours following tracer administration. Prior to perfusion, blood serum was extracted from the heart (left ventricle, approximately 3 ml volume). Rats were transcardially perfused with phosphate buffered saline (PBS) and brains fixed with 4% paraformaldehyde (PFA). Brains were then liberated from cranial vaults, immersed in 4% PFA for an additional 48 hours and cryoprotected through immersion in 30% sucrose. Appearance of brains can be seen in Fig. 1E, wherein the brains were completely devoid of blood in the vasculature, indicating a complete saline perfusion. Brains were then dissected into 100 micron sections using Rat Brain vibratome (Kent Scientific Corp.) and mounted on glass slides. Regions of interest included the frontal cortex, striatum, somatosensory barrel-field cortex, hippocampus, thalamus, and cerebellum. Each animal offered 30 sections across five regions that were analyzed. Slides contained between two to three sections, resulting in over 200 slides scanned throughout this study. Slides containing different brain regions were digitized (10x magnification) using Leica Aperio Versa 200 digital pathology grade slide scanner. Fluorescent intensities were quantified after excitation at 488 nm (sodium fluorescein), 50 ms exposure, and 594 nm (Evans blue), 125 ms exposure, using AreaQuant software specifically designed for this imaging application (Leica Biosystems) and expressed as average fluorescence intensity/unit area. This imaging technique allows for visualization of micro-structural details and digital scanning affords the ability to image large brain regions with no loss of resolution. In order to quantify fluorescence intensities, regions of interest were manually outlined in different brain section. For each channel (green 488 nm and red 594 nm), a minimum intensity threshold value was selected to exclude any background fluorescence from our calculation. The AreaQuant algorithm then determines if the intensity value of each pixel enclosed in the outlined region exceeds the minimum intensity threshold and outputs the total area of positive stain for each brain regions, the average intensity in each channel, and the expression profile of the tracers.

As a means to validate the results of fluorescent image quantitation, absorption spectrophotometry was conducted on homogenized frontal cortices extracted from control and acutely injured rats ($n = 5$, 180 kPa). Rats were sacrificed via saline perfusion (no fixation) and brains were extracted, sectioned, and frozen in dry ice. Absorption was measured and standard curve generated from seven gradient dilutions of Evans Blue. Experimental samples were plotted against the curve ($R^2 = 0.998$) using SpectraMax i3 (Molecular Devices) microplate reader and SoftMax Pro 6.5 software. Output concentration was converted into micrograms per mg of brain tissue.

ELISA. As a means of alternative evidence for BBB disruption, tight junction protein changes were examined in the cerebral hemisphere by ELISA and immunoblot. Following perfusion with PBS, brains were excised from the skull and cerebrum was homogenized in CellLytic-M (Sigma) using sonicator with probe amplitude set to 45% on ice. Samples were then centrifuged at 14,000 g at 4 °C. The protein concentration in the samples was estimated by bicinochoninic acid (BCA) method (Thermo Scientific, Rockford, IL). Subsequently, samples were diluted in PBS and loaded onto ELISA plate (LSBio, Seattle, WA). Serum samples were also loaded onto same plate for tight junction protein quantification and separate serum ELISAs were run for s100-β. Plates were read in microplate reader (Spectra Max i3, Molecular Devices) at wavelength of 450 nm. All the Steps of ELISA procedure (washings, incubation time etc) were conducted in accordance with manufacturer instructions and samples plotted against a standard curve made up of eight samples ($R^2 = 0.995$, 0.999 for occludin and claudin-5 respectively) using SoftMax Pro 6.5 software.

Immunofluorescence. In order to further establish blood-to-brain leakage following blast injury, double-immunofluorescence studies for RECA-1 and CCL2 were performed in the frontal cortex, four hours post-injury ($n = 3$) as a means to detect infiltration of monocytes into the brain parenchyma. Following transcardial perfusion-fixation, tissue was cryoprotected in sucrose, and 20 μm thick sections were cut using Leica 1000 S vibratome. Sections were mounted on glass slides and washed with 10 mM PBS, fixed in ice-cold methanol (100%) solution for ten minutes at −20 °C. The tissue sections were blocked with 10% donkey serum at room temperature for 1 hour in PBS containing 0.03% Triton X-100. Fixed tissues were incubated overnight at 4 °C with respective primary antibodies to RECA-1 (Mouse monoclonal, Abcam, 1:50) and CCL2 (Rabbit polyclonal, Abcam, 1:50). Double immunofluorescence was performed using Alexafluor 594 for RECA-1 and Alexafluor 488 for CCL2. Slides containing different brain regions were digitized (20x magnification) using Leica Aperio Versa 200 fluorescent microscope and slide scanner.

Statistical Analysis. Data are presented as mean + standard error of the mean. Statistical significance was determined using one-way analysis of variance (ANOVA) to compare mean fluorescence intensities of different brain regions for sodium fluorescein and Evans blue with a Tukey pairwise test done to determine differences between individual time-point and overpressure groups. Statistical comparisons were also made for each blast overpressure and each time-point post injury. Normalcy and population variance homogeneity were assessed with Shapiro-Wilk and Levene's tests respectively. Differences between means were assessed and probability levels of $p < 0.05$ were considered statistically significant. Minitab 17 Statistical Software was used for all analyses and Origin 2017 was used for generation of bar plots. Bar plots presented are in semi-log scale in order to capture magnitudinal differences between groups. Fluorescent images were taken using Aperio Versa software and analysis and export done via ImageScope software (LEICA Corp.).

References

1. Ling, G. S. *et al*. Traumatic brain injury in modern war. *Sensing Technologies for Global Health, Military Medicine, and Environmental Monitoring III* **8723**, 87230K. International Society for Optics and Photonics. (2013).
2. Mathews, Z. R. & Koyfman, A. Blast injuries. *The Journal of emergency medicine* **49**, 573–587 (2015).
3. Moore, B. Blast injuries-a prehospital perspective. *Australasian Journal of Paramedicine* **4** (2015).

4. Loane, D. J. & Faden, A. I. Neuroprotection for traumatic brain injury: translational challenges and emerging therapeutic strategies. *Trends in Pharmacological Sciences* **31**, 596–604, https://doi.org/10.1016/j.tips.2010.09.005 (2010).
5. Maas, A. I., Roozenbeek, B. & Manley, G. T. Clinical trials in traumatic brain injury: past experience and current developments. *Neurotherapeutics* **7**, 115–126 (2010).
6. Narayan, R. K. *et al*. Clinical trials in head injury. *Journal of neurotrauma* **19**, 503–557 (2002).
7. Schouten, J. W. Neuroprotection in traumatic brain injury: a complex struggle against the biology of nature. *Current opinion in critical care* **13**, 134–142 (2007).
8. Chodobski, A., Zink, B. J. & Szmydynger-Chodobska, J. Blood–brain barrier pathophysiology in traumatic brain injury. *Translational stroke research* **2**, 492–516 (2011).
9. Hayes, R. L. & Dixon, C. E. In *Seminars in Neurology*. 25–31 (© by Thieme Medical Publishers, Inc.) (1994).
10. Abbott, N. J. Inflammatory mediators and modulation of blood-brain barrier permeability. *Cell. Mol. Neurobiol.* **20**, 131–147, https://doi.org/10.1023/a:1007074420772 (2000).
11. Abbott, N. J., Patabendige, A. A., Dolman, D. E., Yusof, S. R. & Begley, D. J. Structure and function of the blood-brain barrier. *Neurobiol Dis* **37**, 13–25, https://doi.org/10.1016/j.nbd.2009.07.030 (2010).
12. Abdul-Muneer, P. M., Chandra, N. & Haorah, J. Interactions of oxidative stress and neurovascular inflammation in the pathogenesis of traumatic brain injury. *Mol Neurobiol* **51**, 966–979, https://doi.org/10.1007/s12035-014-8752-3 (2015).
13. Ballabh, P., Braun, A. & Nedergaard, M. The blood–brain barrier: an overview: structure, regulation, and clinical implications. *Neurobiology of disease* **16**, 1–13 (2004).
14. Hawkins, B. T. & Davis, T. P. The blood-brain barrier/neurovascular unit in health and disease. *Pharmacological reviews* **57**, 173–185 (2005).
15. Obermeier, B., Daneman, R. & Ransohoff, R. M. Development, maintenance and disruption of the blood-brain barrier. *Nat Med* **19**, 1584–1596, https://doi.org/10.1038/nm.3407 (2013).
16. Zlokovic, B. V. The blood-brain barrier in health and chronic neurodegenerative disorders. *Neuron* **57**, 178–201 (2008).
17. Abbruscato, T. J., Lopez, S. P., Roder, K. & Paulson, J. R. Regulation of blood-brain barrier Na, K, 2Cl-cotransporter through phosphorylation during *in vitro* stroke conditions and nicotine exposure. *Journal of pharmacology and experimental therapeutics* **310**, 459–468 (2004).
18. Iłzecka, J. The structure and function of blood-brain barrier in ischaemic brain stroke process. *Annales Universitatis Mariae Curie-Sklodowska. Sectio D: Medicina* **51**, 123–127 (1996).
19. Khatri, R., McKinney, A. M., Swenson, B. & Janardhan, V. Blood–brain barrier, reperfusion injury, and hemorrhagic transformation in acute ischemic stroke. *Neurology* **79**, S52–S57 (2012).
20. Sandoval, K. E. & Witt, K. A. Blood-brain barrier tight junction permeability and ischemic stroke. *Neurobiol Dis* **32**, 200–219, https://doi.org/10.1016/j.nbd.2008.08.005 (2008).
21. Fiala, M. *et al*. Cyclooxygenase-2-positive macrophages infiltrate the Alzheimer's disease brain and damage the blood–brain barrier. *European journal of clinical investigation* **32**, 360–371 (2002).
22. Zlokovic, B. V. Neurovascular pathways to neurodegeneration in Alzheimer's disease and other disorders. *Nat Rev Neurosci* **12**, 723–738, https://doi.org/10.1038/nrn3114 (2011).
23. Desai, B. S., Monahan, A. J., Carvey, P. M. & Hendey, B. Blood–brain barrier pathology in Alzheimer's and Parkinson's disease: implications for drug therapy. *Cell transplantation* **16**, 285–299 (2007).
24. Persidsky, Y. *et al*. Rho-mediated regulation of tight junctions during monocyte migration across the blood-brain barrier in HIV-1 encephalitis (HIVE). *Blood* **107**, 4770–4780 (2006).
25. Oby, E. & Janigro, D. The blood–brain barrier and epilepsy. *Epilepsia* **47**, 1761–1774 (2006).
26. Remy, S. & Beck, H. Molecular and cellular mechanisms of pharmacoresistance in epilepsy. *Brain* **129**, 18–35 (2006).
27. Correale, J. & Villa, A. The blood–brain-barrier in multiple sclerosis: functional roles and therapeutic targeting. *Autoimmunity* **40**, 148–160 (2007).
28. de Vries, H. E. & Dijkstra, D. Mononuclear phagocytes at the blood-brain barrier in multiple sclerosis. *Blood-Spinal Cord and Brain Barriers in Health and Disease*, 409–417 (2004).
29. Opdenakker, G., Nelissen, I. & Van Damme, J. Functional roles and therapeutic targeting of gelatinase B and chemokines in multiple sclerosis. *The Lancet Neurology* **2**, 747–756 (2003).
30. Abdul-Muneer, P. M. *et al*. Induction of oxidative and nitrosative damage leads to cerebrovascular inflammation in an animal model of mild traumatic brain injury induced by primary blast. *Free Radic Biol Med* **60**, 282–291, https://doi.org/10.1016/j.freeradbiomed.2013.02.029 (2013).
31. Chen, Y. & Huang, W. Non-impact, blast-induced mild TBI and PTSD: concepts and caveats. *Brain injury* **25**, 641–650 (2011).
32. Haorah, J. *et al*. Ethanol-Induced Activation of Myosin Light Chain Kinase Leads to Dysfunction of Tight Junctions and Blood-Brain Barrier Compromise. *Alcoholism: Clinical and Experimental Research* **29**, 999–1009 (2005).
33. Haorah, J. *et al*. Oxidative stress activates protein tyrosine kinase and matrix metalloproteinases leading to blood–brain barrier dysfunction. *Journal of neurochemistry* **101**, 566–576 (2007).
34. Hue, C. D. *et al*. Time Course and Size of Blood-Brain Barrier Opening in a Mouse Model of Blast-Induced Traumatic Brain Injury. *J Neurotrauma*, https://doi.org/10.1089/neu.2015.4067 (2015).
35. Baldwin, S. A., Fugaccia, I., Brown, D. R., Brown, L. V. & Scheff, S. W. Blood-brain barrier breach following cortical contusion in the rat. *Journal of neurosurgery* **85**, 476–481 (1996).
36. Başkaya, M. K., Rao, A. M., Doğan, A., Donaldson, D. & Dempsey, R. J. The biphasic opening of the blood–brain barrier in the cortex and hippocampus after traumatic brain injury in rats. *Neuroscience letters* **226**, 33–36 (1997).
37. Hicks, R. R., Baldwin, S. A. & Scheff, S. W. Serum extravasation and cytoskeletal alterations following traumatic brain injury in rats. *Molecular and chemical neuropathology* **32**, 1–16 (1997).
38. Higashida, T. *et al*. The role of hypoxia-inducible factor-1α, aquaporin-4, and matrix metalloproteinase-9 in blood-brain barrier disruption and brain edema after traumatic brain injury: laboratory investigation. *Journal of neurosurgery* **114**, 92–101 (2011).
39. Shapira, Y., Setton, D., Artru, A. A. & Shohami, E. Blood-brain barrier permeability, cerebral edema, and neurologic function after closed head injury in rats. *Anesthesia & Analgesia* **77**, 141–148 (1993).
40. Elder, G. A. *et al*. Vascular and inflammatory factors in the pathophysiology of blast-induced brain injury. *Front Neurol* **6**, 48, https://doi.org/10.3389/fneur.2015.00048 (2015).
41. Hue, C. D. *et al*. Dexamethasone potentiates *in vitro* blood-brain barrier recovery after primary blast injury by glucocorticoid receptor-mediated upregulation of ZO-1 tight junction protein. *Journal of Cerebral Blood Flow & Metabolism* **35**, 1191–1198 (2015).
42. Kawoos, U., Gu, M., Lankasky, J., McCarron, R. M. & Chavko, M. Effects of Exposure to Blast Overpressure on Intracranial Pressure and Blood-Brain Barrier Permeability in a Rat Model. *PloS one* **11**, e0167510 (2016).
43. Readnower, R. D. *et al*. Increase in blood-brain barrier permeability, oxidative stress, and activated microglia in a rat model of blast-induced traumatic brain injury. *J Neurosci Res* **88**, 3530–3539, https://doi.org/10.1002/jnr.22510 (2010).
44. Shetty, A. K., Mishra, V., Kodali, M. & Hattiangady, B. Blood brain barrier dysfunction and delayed neurological deficits in mild traumatic brain injury induced by blast shock waves. *Frontiers in cellular neuroscience* **8** (2014).
45. Yeoh, S., Bell, E. D. & Monson, K. L. Distribution of blood-brain barrier disruption in primary blast injury. *Ann Biomed Eng* **41**, 2206–2214, https://doi.org/10.1007/s10439-013-0805-7 (2013).

46. Kabu, S. *et al*. Blast-associated shock waves result in increased brain vascular leakage and elevated ROS levels in a rat model of traumatic brain injury. *PloS one* **10**, e0127971 (2015).
47. Sosa, M. A. G. *et al*. Selective vulnerability of the cerebral vasculature to blast injury in a rat model of mild traumatic brain injury. *Acta neuropathologica communications* **2**, 67 (2014).
48. Sosa, M. A. G. *et al*. Blast overpressure induces shear-related injuries in the brain of rats exposed to a mild traumatic brain injury. *Acta neuropathologica communications* **1**, 51 (2013).
49. Stokum, J. A. *et al*. Glibenclamide pretreatment protects against chronic memory dysfunction and glial activation in rat cranial blast traumatic brain injury. *Behavioural brain research* **333**, 43–53 (2017).
50. Needham, C. E., Ritzel, D., Rule, G. T., Wiri, S. & Young, L. Blast testing issues and TBI: experimental models that lead to wrong conclusions. *Frontiers in neurology* **6**, 72 (2015).
51. Skotak, M., Alay, E. & Chandra, N. On the accurate determination of shock wave time-pressure profile in the experimental models of blast induced neurotrauma. *Frontiers in Neurology* **9**, 52 (2018).
52. Skotak, M. *et al*. Rat injury model under controlled field-relevant primary blast conditions: acute response to a wide range of peak overpressures. *J Neurotrauma* **30**, 1147–1160, https://doi.org/10.1089/neu.2012.2652 (2013).
53. Hyde, D. W. *ConWep: Conventional Weapon Effects (software)* (1991).
54. Chandra, N., Sundaramurthy, A. & Gupta, R. K. Validation of Laboratory Animal and Surrogate Human Models in Primary Blast Injury Studies. *Military medicine* **182**, 105–113, https://doi.org/10.7205/milmed-d-16-00144 (2017).
55. Kuriakose, M. *et al*. Tailoring the Blast Exposure Conditions in the Shock Tube for Generating Pure, Primary Shock Waves: The End Plate Facilitates Elimination of Secondary Loading of the Specimen. *PloS one* **11**, e0161597 (2016).
56. Mishra, V. *et al*. Primary blast causes mild, moderate, severe and lethal TBI with increasing blast overpressures: Experimental rat injury model. *Scientific reports* **6**, 26992 (2016).
57. Chandra, N. *et al*. Evolution of blast wave profiles in simulated air blasts: experiment and computational modeling. *Shock Waves* **22**, 403–415, https://doi.org/10.1007/s00193-012-0399-2 (2012).
58. Garman, R. H. *et al*. Blast exposure in rats with body shielding is characterized primarily by diffuse axonal injury. *Journal of neurotrauma* **28**, 947–959 (2011).
59. Li, W. *et al*. A quantitative MRI method for imaging blood-brain barrier leakage in experimental traumatic brain injury. *PloS one* **9**, e114173 (2014).
60. Su, E. J. *et al*. Imatinib treatment reduces brain injury in a murine model of traumatic brain injury. *Frontiers in cellular neuroscience* **9** (2015).
61. Tanno, H., Nockels, R. P., Pitts, L. H. & Noble, L. Breakdown of the blood–brain barrier after fluid percussive brain injury in the rat. *Part 1: distribution and time course of protein extravasation. Journal of neurotrauma* **9**, 21–32 (1992).
62. Candelario-Jalil, E., Yang, Y. & Rosenberg, G. Diverse roles of matrix metalloproteinases and tissue inhibitors of metalloproteinases in neuroinflammation and cerebral ischemia. *Neuroscience* **158**, 983–994 (2009).
63. Nishioku, T. *et al*. Detachment of brain pericytes from the basal lamina is involved in disruption of the blood–brain barrier caused by lipopolysaccharide-induced sepsis in mice. *Cell. Mol. Neurobiol.* **29**, 309–316 (2009).
64. Armulik, A., Abramsson, A. & Betsholtz, C. Endothelial/pericyte interactions. *Circ Res* **97**, 512–523, https://doi.org/10.1161/01.RES.0000182903.16652.d7 (2005).
65. Armulik, A. *et al*. Pericytes regulate the blood-brain barrier. *Nature* **468**, 557–561, https://doi.org/10.1038/nature09522 (2010).
66. Abbott, N. J. Astrocyte–endothelial interactions and blood–brain barrier permeability. *Journal of anatomy* **200**, 523–534 (2002).
67. Abbott, N. J., Rönnbäck, L. & Hansson, E. Astrocyte-endothelial interactions at the blood-brain barrier. *Nature reviews. Neuroscience* **7**, 41 (2006).
68. Benarroch, E. E. *Mayo Clinic Proceedings* **10**, 1326–1338. Elsevier (2005).
69. Polavarapu, R. *et al*. Tissue-type plasminogen activator–mediated shedding of astrocytic low-density lipoprotein receptor–related protein increases the permeability of the neurovascular unit. *Blood* **109**, 3270–3278 (2007).
70. Banks, W. A. From blood-brain barrier to blood-brain interface: new opportunities for CNS drug delivery. *Nature Reviews Drug Discovery* (2016).
71. Hue, C. D. *et al*. Blood-brain barrier dysfunction after primary blast injury *in vitro*. *Journal of neurotrauma* **30**, 1652–1663 (2013).
72. Lucke-Wold, B. P. *et al*. Bryostatin-1 Restores Blood Brain Barrier Integrity following Blast-Induced Traumatic Brain Injury. *Mol Neurobiol* **52**, 1119–1134, https://doi.org/10.1007/s12035-014-8902-7 (2015).
73. Blyth, B. J. *et al*. Validation of serum markers for blood-brain barrier disruption in traumatic brain injury. *Journal of neurotrauma* **26**, 1497–1507 (2009).
74. Burda, J. E., Bernstein, A. M. & Sofroniew, M. V. Astrocyte roles in traumatic brain injury. *Experimental neurology* **275**, 305–315 (2016).
75. Vajtr, D. *et al*. Correlation of Ultrastructural Changes of Endothelial Cells and Astrocytes Occurring during Blood Brain Barrier Damage after Traumatic Brain Injury with Biochemical Markers of Blood Brain Barrier Leakage and Inflammatory Response. *Physiological Research* **58**, 263–268 (2009).
76. Fernández-López, D. & Vexler, Z. S. In *The Blood Brain Barrier (BBB)* 91–116 (Springer, 2013).
77. Louboutin, J.-P., Chekmasova, A., Marusich, E., Agrawal, L. & Strayer, D. S. Role of CCR5 and its ligands in the control of vascular inflammation and leukocyte recruitment required for acute excitotoxic seizure induction and neural damage. *The FASEB Journal* **25**, 737–753 (2011).
78. Szmydynger-Chodobska, J., Fox, L. M., Lynch, K. M., Zink, B. J. & Chodobski, A. Vasopressin amplifies the production of proinflammatory mediators in traumatic brain injury. *Journal of neurotrauma* **27**, 1449–1461 (2010).
79. Cavaglia, M. *et al*. Regional variation in brain capillary density and vascular response to ischemia. *Brain research* **910**, 81–93 (2001).
80. Brown, R. C., Egleton, R. D. & Davis, T. P. Mannitol opening of the blood–brain barrier: regional variation in the permeability of sucrose, but not 86Rb+ or albumin. *Brain Research* **1014**, 221–227, https://doi.org/10.1016/j.brainres.2004.04.034 (2004).
81. Johanson, C. E. Permeability and vascularity of the developing brain: cerebellum vs cerebral cortex. *Brain research* **190**, 3–16 (1980).
82. LaManna, J. C. & Harik, S. I. Regional studies of blood—brain barrier transport of glucose and leucine in awake and anesthetized rats. *Journal of Cerebral Blood Flow & Metabolism* **6**, 717–723 (1986).
83. Pluta, R., Tomida, S., Ikeda, J., Nowak, T. S. Jr & Klatzo, I. Cerebral vascular volume after repeated ischemic insults in the gerbil: comparison with changes in CBF and brain edema. *Journal of Cerebral Blood Flow & Metabolism* **9**, 163–170 (1989).
84. Holash, J., Sugamori, K. & Stewart, P. The difference in vascular volume between cerebrum and cerebellum is in the pia mater. *Journal of Cerebral Blood Flow & Metabolism* **10**, 432–434 (1990).
85. Allt, G. & Lawrenson, J. G. Is the pial microvessel a good model for blood-brain barrier studies? *Brain Research Reviews* **24**, 67–76, https://doi.org/10.1016/S0165-0173 (1997).
86. Huber, B. R. *et al*. Blast exposure causes dynamic microglial/macrophage responses and microdomains if brain microvessel dysfunction. *Neuroscience* **319**, 206–220, https://doi.org/10.1016/j.neuroscience.2016.01.022 (2016).
87. Chandra, N., Holmberg, A. & Feng, R. Controlling the shape of the shock wave profile in a blast facility. *US Provisional patent application* **61542354** (2011).
88. Jiang, Z. *et al*. Role of hydrogen sulfide in early blood-brain barrier disruption following transient focal cerebral ischemia. *PloS one* **10**, e0117982 (2015).

89. Yen, L. F., Wei, V. C., Kuo, E. Y. & Lai, T. W. Distinct patterns of cerebral extravasation by Evans blue and sodium fluorescein in rats. *PloS one* **8**, e68595 (2013).
90. Kaya, M. & Ahishali, B. In *Permeability Barrier* 369–382 (Springer, 2011).
91. Sandel, W. R., Hubbard, R. W. & Schehl-Geiger, D. Indocyanine Green (ICG) and Evans Blue: Comparative Study of Plasma Volume Measurement. (Army Research Inst Of Environmental Medicine Natick Ma, 1982).
92. Wolman, M. *et al.* Evaluation of the dye-protein tracers in pathophysiology of the blood-brain barrier. *Acta neuropathologica* **54**, 55–61 (1981).

Acknowledgements

This work was supported by U.S Army Medical Research and Materiel Command project *Primary Blast Injury Criteria for Animal/Human TBI Models using Field Validated Shock Tube*, grant number: 14059001. Authors gratefully acknowledge Prof Raj Gupta, from Department of Defense Blast Injury Research Program Coordinating Office, United States Army Medical Research and Materiel Command, Fort Detrick, MD as well as our laboratory members Stephanie Iring, Madison Taylor, Eren Alay and Dr. Maciej Skotak for their contributions to this work.

Author Contributions

M.K., K.V.R. and N.C. wrote the main manuscript text, M.K. and K.V.R. conducted experiments described in this work and M.K. and D.Y. prepared the figures. All authors reviewed the manuscript.

Additional Information

Competing Interests: The authors declare no competing interests.

Publisher's note: Springer Nature remains neutral with regard to jurisdictional claims in published maps and institutional affiliations.

Open Access This article is licensed under a Creative Commons Attribution 4.0 International License, which permits use, sharing, adaptation, distribution and reproduction in any medium or format, as long as you give appropriate credit to the original author(s) and the source, provide a link to the Creative Commons license, and indicate if changes were made. The images or other third party material in this article are included in the article's Creative Commons license, unless indicated otherwise in a credit line to the material. If material is not included in the article's Creative Commons license and your intended use is not permitted by statutory regulation or exceeds the permitted use, you will need to obtain permission directly from the copyright holder. To view a copy of this license, visit http://creativecommons.org/licenses/by/4.0/.

© The Author(s) 2018

Appendix A –Publication Cover 19
2018

Authors: Daniel E Bonder, Carolyn E Keating, N. Chandra, D Kacy Cullen, B. Pfister

Title: "*Modeling Traumatic Brain Injury In-Vitro*"

Journal Publication: Preclinical and Clinical Methods in Brain Trauma Research, 37-69, (2018), [18-19]



Chapter 3

Modeling Traumatic Brain Injury In Vitro

Daniel E. Bonder, Carolyn E. Keating, Namas Chandra, D. Kacy Cullen, and Bryan J. Pfister

Abstract

Traumatic brain injury (TBI) is unique among neurological afflictions in that it is induced by a discrete physical event. To understand the relationship between mechanical loading and the evolution of structural and functional alterations of neural cells, TBI researchers have utilized in vitro models. These models were engineered to mimic loading conditions relevant for clinical TBI and to allow for the microscopic study of the cellular responses in real time. Collectively, this high degree of experimental control has resulted in robust platforms that enable the exploration of biological mechanisms involved in the progression of neural cellular injury. This chapter presents detailed background and methodology pertaining to two established in vitro models used in the field: (1) "stretch" injury to two-dimensional (2-D) cultures, and (2) simple shear deformation applied to three-dimensional (3-D) cell-containing matrices. The stretch injury paradigm uses a rapid pressure-pulse to stretch an elastic silicone membrane on which neural cells are cultured. The resulting deformation can be either biaxial or uniaxial, and is commonly applied to 2-D neuronal cultures with isolated axonal projections to model tensile loading in aligned axonal tracts, believed to be a proximal cause of diffuse axonal injury, the "hallmark" pathology of closed-head TBI. Rapid shear deformation to 3-D neural cellular constructs is applied using a linear actuator and is designed to replicate the complex loading conditions experienced by brain cells during inertial loading, with shear being the dominant mode of deformation in the nearly incompressible brain. This model has been utilized to study the acute and longer-term responses of 3-D neuronal cultures or 3-D neuronal-astrocytic cocultures to heterogeneous strain fields representative of loading patterns in vivo.

Key words Traumatic brain injury, Stretch injury, Axonal injury, Neuronal deformation, Astrocyte reactivity, Shearing injury, Plasma membrane permeability, In vitro model

1 Introduction

Traumatic brain injury (TBI) is unique among neurological afflictions in that it is induced by a discrete physical event, causing immediate effects on neural cells and vasculature while initiating a series of pathophysiological responses that may last over a protracted time frame.

The injury to neurons has been linked to the rapid deformation of brain tissue as a result of the damaging head motions [1, 2].

Amit K. Srivastava and Charles S. Cox, Jr. (eds.), *Pre-Clinical and Clinical Methods in Brain Trauma Research*, Neuromethods, vol. 139, https://doi.org/10.1007/978-1-4939-8564-7_3, © Springer Science+Business Media, LLC, part of Springer Nature 2018

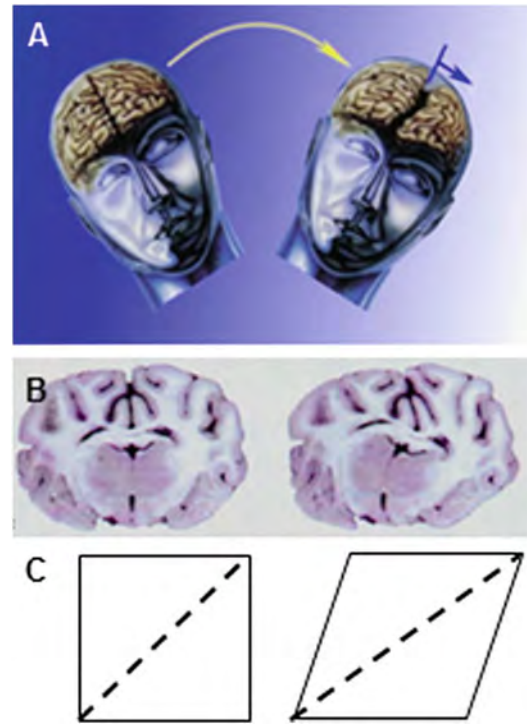


Fig. 1 Predicted Brain Tissue Deformation Patterns in TBI. (**a**) Illustrates how rotational motions can deform brain tissue. (**b**) Shows mock-up of a pig brain deforming in shear due to rotational motion (from [2]). (**c**) Illustrates the concept of shear deformation of a block of brain tissue, translating into a uniaxial stretch of neuronal fibers along the diagonal

Biomechanical studies have shown that rapid rotational motion of the head results in large intracranial shear deformation of the brain with respect to the comparatively rigid skull [3–5]. This macroscopic shear deformation can translate microscopically to rapid stretching of neurons and their axons, Fig. 1 [6, 7].

Understanding the relationship between mechanical loading and the evolution of structural and functional alterations of neural cells is essential, yet can be particularly challenging using animal models. Biomedical engineers have been instrumental in developing in vitro models to study TBI, which offer several advantages including (1) controlled biomechanical inputs designed to mimic loading conditions relevant for clinical TBI, (2) defined neural cellular populations to systematically build complexity, (3) ease of access for repeated measures, and (4) the potential to study cellular responses in real time. Collectively, this high degree of experimental control has resulted in robust platforms that enable the exploration of biological mechanisms involved in the progression of neural cellular injury. Over at least the past three decades, numerous in vitro injury models have been developed that apply mechanical

perturbations to cultured neural cells [6–13]. These models replicate many of the morphological and ultrastructural changes observed in vivo and have had significant impact in the field by identifying many important post-injury pathobiological processes [1, 12, 14–22].

Due to the biomechanical etiology of TBI, when utilizing reduced models for scientific investigation it is desirable to apply injury parameters that are scaled from the physical loading experienced by the human brain in TBI. The soft brain tissue reacts slower to the rotation of the head, often causing large intracerebral shear deformation with respect to the comparatively rigid skull. Macroscopic shear deformation of brain tissue translates microscopically to rapid longitudinal or uniaxial stretching along the diagonal of a representative cube, Fig. 1b. Axon fibers aligned along the diagonal will be stretched while perpendicular fibers will be compressed. It is believed that axons are mostly damaged by the stretching forces, whereas compression forces would simply release damaging forces and cause the axon to undulate. A uniaxial stretch to isolated axons would model tensile loading in aligned axonal tracts, believed to be a proximal cause of diffuse axonal injury, the "hallmark" pathology of closed-head TBI.

This chapter presents detailed background and methodology pertaining to two established in vitro models used in the field: (1) "stretch" injury to two-dimensional (2-D) cultures that may be biaxial [23–25] or uniaxial [6, 13, 26, 27], and (2) simple shear deformation applied to three-dimensional (3-D) cell-containing matrices [10, 17]. Most in vitro TBI models, similar to the systems described in this protocol, use a custom fabricated device, although there is at least one commercially available stretch system (Cell Injury Controller; Custom Design & Fabrication, Inc., Sandston, VA). While custom-built systems are not generally commercially available, the developing labs are often open to collaboration and assistance.

1.1 2-D In Vitro Stretch Injury Models

The 2-D stretch injury paradigm uses a rapid pressure-pulse to stretch an elastic silicone membrane on which neural cells are cultured. The deformation can be either biaxial or uniaxial, applied to either neuronal cultures including both soma and axons or to isolated axonal projections. Stretch injury models were first designed to apply a rapid pressure-pulse and cause *biaxial* deformation of the membrane, Fig. 2. To control the pressure pulse, high speed solenoid valves are used to inject compressed air into a chamber that contains the neuronal culture. Aspects of the pressure pulse can be controlled including: (1) peak pressure, which is proportional to the stretch of the axons, (2) pressure rise time, representing the rate of stretch (speed of injury), and (3) pressure pulse duration that defines the impulse of the stretch injury, Fig. 2F. Through calibration, the stretch of the membrane can be related to

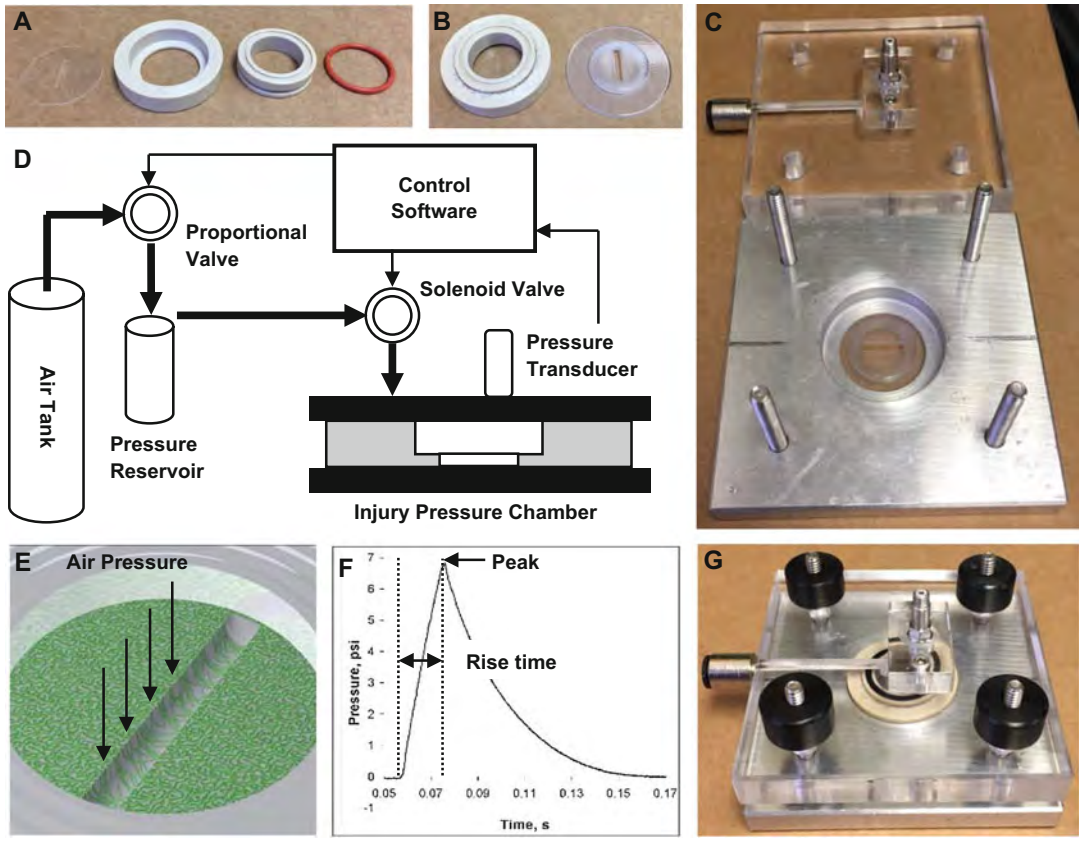


Fig. 2 The In Vitro Stretch Injury System. The stretch injury system uses a pressure-pulse to stretch-injure cultured axons on a deformable substrate. (**a**) Shows the components of the single well design (in order from left to right: Aclar® underside mask, bottom well piece, top well piece, well O-ring). (**b**) Shows the assembled well (left) and 3D-printed deformation mask (right). (**c**) Shows the top and bottom pieces of the injury chamber, while **g** shows the fully assembled injury chamber with culture well. Injuries are produced using an air pulse generating system, illustrated in **d**. Bold lines denote the flow of air through the system. (**e**) Illustrates the concept of uniaxial stretching of axons along a cell-free gap. Deformation is constrained by the deformation mask. (**f**) Shows a sample pressure pulse with relevant parameters, peak pressure amplitude and pressure rise time, labeled (see arrows)

the pressure pulse [6, 13]. The relevant strain fields that are generally considered can span a great amount; 10–70% strain with applied strain rates of 10–100 s^{-1} [6, 28, 29]. The amount of strain to induce injury will vary with the mode of deformation with biaxial requiring less deformation than uniaxial.

Since uniaxial (longitudinal) stretching of the axon is a mechanically relevant deformation in axonal injury, two models have been implemented to deliver a uniaxial stretch injury [7, 13]. Here we describe a protocol based on the method developed by Smith and Meaney where a cell-free gap is created across which cultured axons grow [6, 27]. Cells are restricted from adhering to a 1.5–2 mm line across the well by covering the region with a silicone divider.

Neurons are seeded on both sides of the divider and allowed to adhere to the substrate. Upon removal of the divider, developing axons grow across the gap over 9–11 days in vitro (DIV). This isolated axonal region is stretched by placing a complementary injury mask underneath the silicone substrate, only allowing the pressure pulse to deform this region, Fig. 2e.

1.2 3-D In Vitro Shear Deformation Injury Model

This model replicates two important parameters in TBI: (1) mechanical shear which is the dominant form of tissue deformation that occurs in the brain during trauma, Fig. 1 [5, 10] and (2) the 3-D cellular and extracellular matrix (ECM) environmental effects on injury. Cells in the brain exist in a complex environment in which they extend their processes and come in contact with both ECM and other cells in 3-D. This complex arrangement is an important consideration when examining the effects of physical forces on cells, especially in the study of mechanical trauma such as TBI. For instance, the translation of forces from bulk tissue (macro) to cellular (micro) deformation may occur differently in 2-D and 3-D configurations. The complexity of neural cell morphology, which increases in 3-D, affects the complexity of the strain field to which the cell is exposed [30], resulting in simultaneous combinations of compressive, shear, and tensile forces. As bulk deformation is translated through physical coupling, factors such as cell morphology, matrix mechanical properties, and cell-ECM or cell–cell interactions will have important effects on the transfer of strain to cells, and might underlie localized differences in susceptibility to stress.

Another factor affecting the transfer of bulk to cellular deformation is the bioactivity and physical properties of the ECM material. Viscoelasticity and porosity may affect how reliably bulk deformation is transferred to cells in a 3-D matrix, and these properties can be altered in vitro to approximate those of brain tissue. Cell-ECM and cell-cell contacts may also affect force translation. The number and spatial distribution of these interactions can affect the size and location of stresses that develop on and within cells, which may influence the probability of cellular structural failures. Additionally, these models have the advantage of being able to systematically control various cell culture parameters such as cell composition and matrix constituents that enable the elucidation of the roles of specific factors in bulk to cellular deformation and the associated responses.

Here we describe a protocol based on the method created by LaPlaca and Cargill, which uses 3-D neural cellular constructs (Fig. 3) subjected to controlled 3-D shear-strain based loading profiles [10, 30]. A custom-designed device uses a linear actuator to reproducibly deliver a specified strain field to neural cells within a 3-D bioactive ECM based scaffold. The device input approximates

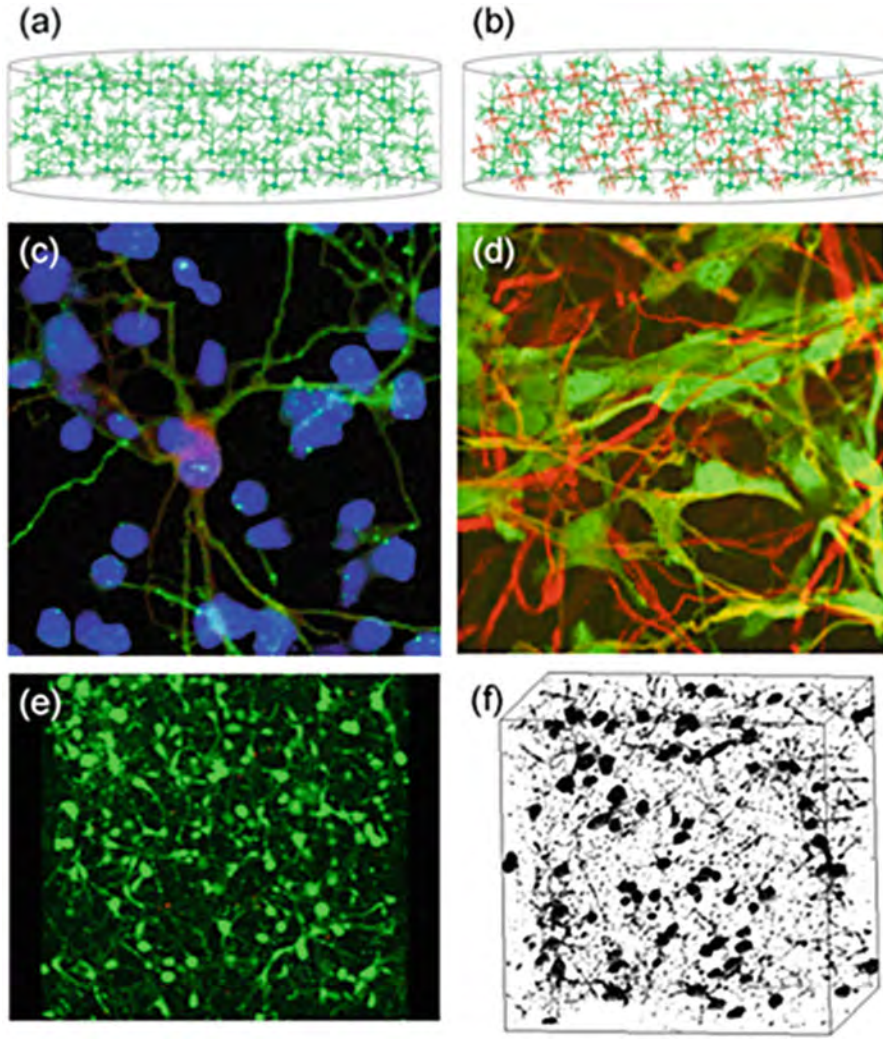


Fig. 3 Concept: Tissue Engineered 3-D Neural Cell Cultures for Neuromechanobiological Investigations In Vitro. Cellular constructs consist of (**a**) neurons or (**b**) neurons mixed with astrocytes, distributed throughout the full thickness of a 3-D matrix/scaffold ($>$500 μm). (**c**) Neurons in 3-D culture, shown to express neuronal-specific proteins MAP-2 (green) and tau-5 (red) with nuclear marker Hoechst 33258 (blue), assume complex morphologies with 3-D neurite extension. (**d**) These cultures are useful to study neuron–astrocyte interactions in 3-D. (**e**) Live neurons (green) demonstrating survival and network formation throughout the thickness of the 3-D cultures. (**f**) Volumetric rendering of live neurons in 3-D culture. Neurobiological studies of neural cells within 3-D matrices provide enhanced fidelity to in vivo while affording all advantages of traditional (planar) in vitro systems. Panels (**a**), (**b**), (**d**), and (**e**) reproduced with permission from Cullen et al., 2011, Begell House; panel (**c**) reproduced with permission from Irons et al., 2008, IOP Publishing; (and panel (**f**) reproduced from Cullen et al., 2006, Mary Ann Liebert, Inc.)

the 3-D strain fields predicted during closed-head diffuse injury in the human brain. This model has been utilized to study the acute and longer-term responses of 3-D neuronal cultures or 3-D neuronal-astrocytic cocultures to injury.

2 Materials: 2-D In Vitro Stretch Injury Model

- 7.8 mil (199 μm) or 2 mil (51 μm) aclar sheets (Electron Microscopy Sciences).
- Ultrapure water (Milli-Q).
- Sparkleen (Fisher, 04-320-4) or similar labware detergent.
- 70% ethanol (Ricca Chemical, 2546.70-2.5).
- Silicone sheets, 0.005″, 12″ × 12″ (Specialty Manufacturing Inc.).
- Poly-L-lysine (R&D Systems Cultrex, 34-382-0001).
- Leibowitz L-15 Medium (Gibco, 11-415-064).
- Hank's Balanced Salt Solution containing Ca^{2+} and Mg^{2+} (HBSS+, Gibco, 14-025-076).
- Hank's Balanced Salt Solution without Ca^{2+} and Mg^{2+} (HBSS−, Gibco, 14-175-095).
- Phosphate Buffered Saline (PBS, GIbco 10010031).
- Trypsin-EDTA (0.5%) (Gibco, 15-400-054).
- Fetal Bovine Serum (FBS, Gibco, 10-082-139).
- Neurobasal Medium (Gibco, 21-103-049).
- B27 Supplement (Gibco, 17-504-044).
- Penicillin/Streptomycin (P/S, Gibco, 15-140-163).
- GlutaMAX 100× (Gibco, 35-050-061).
- Trypan Blue Solution (0.4%) (Gibco, 15-250-061).
- Dash Number 018 high temperature silicone o-ring (McMaster Carr, 9396K65).
- Fluorescent Beads (Invitrogen, G0100).
- Compressed air tank (AirGas, UN1002).
- Surgical toolset (for instance: small scissors, curved forceps, two fine forceps, straight blade #11 scalpel, surgical spatula, fine angled forceps).

3 Methods: 2-D In Vitro Stretch Injury Model

3.1 Production of Injury Masks

The premise of the design is to unaxially stretch injure isolated tracks of axons (sparing the neuronal somata) to study the direct effect of mechanical stretch on the evolution of axonal pathology [6]. Our axonal injury system utilizes two types of injury masks, one of which is built into the injury well itself on the underside of the silicone membrane (referred to as the "underside mask") and another that is utilized during injuries to create uniaxial stretch

(the "injury mask") (Fig. 2). The underside mask is cut from sheets of 7.8 mil (~0.2 mm) Aclar® film using a Cricut Explore One stencil cutter. Details on mask thickness are described in greater detail below in the **Notes 1** and **2**.

Wells can be constructed lacking the underside mask. However this piece serves several important and helpful purposes. First, it constrains the stretch to be uniaxial rather than biaxial. Second, it clearly outlines the injury field, removing possible ambiguity about which cells or neurites were directly deformed. Third, it ensures that cellular elements outside of the injury field remain uninjured (*see* **Notes 1** and **2**).

The injury mask (Fig. 2b) can be 3-D printed. We have used both the Ultimaker 3 thermal deposition printer and Objet 30 Prime polyjet printer. There are not strict requirements concerning the type of print material, only that the mask be rigid enough to not bend significantly when pressure is applied to the injury chamber. A dual extrusion printer is needed, however, as the mask design requires a support material.

3.2 Nonsterile Preparation of Injury Wells for Device Calibration

3.2.1 Overview

The well design allows for rapid assembly by press-fitting two concentric polyetheretherketone (PEEK) rings together, held in place by an O-ring (Fig. 2a, b). The smaller of the PEEK rings contains a groove for the insertion of an O-ring. This O-ring served three purposes: (1) applied pre-stretch to the silicone membrane, (2) held the well together, and (3) acted as a gasket to prevent media leakage. A square of silicone membrane was placed flat over the larger ring, wrinkles in the membrane were straightened and the smaller ring was gently pressed into the larger. The circular geometry ensured that the membrane was pre-stretched equibiaxially and uniformly throughout the well. As previously mentioned, the well design is further modified by including an Aclar® underside mask (Fig. 2a) that sits underneath the silicone sheet and creates a seal with it.

For calibration purposes, the wells do not need to be assembled by the full sterilization procedure. The protocol below outlines a quicker way to prepare injury wells for nonsterile calibration experiments.

3.2.2 Protocol

1. Cut a silicone sheet into 3.5 cm × 3.5 cm^2 (or larger).
2. Place a Dash Number 018 high-temperature silicone O-ring on the small PEEK well piece.
3. Place an Aclar® underside mask within the large PEEK well piece.
4. Dip the large well piece with the Aclar® mask into a beaker of purified reverse osmosis (RO) water, holding the mask in place to prevent it from floating up. Lift up out of the beaker, keeping a pool of water within the well piece atop the mask.

5. Lay a precut square of silicone on top of the large PEEK well piece (*see* **Note 3**).
6. Center the small PEEK well piece on top of the silicone square, then press the well pieces together, ensuring that the silicone placement is more or less centered within the well. The well is now assembled.
7. If desired, trim the excess silicone using a razor.
8. Allow wells to air dry for a minimum of 1 h.

3.3 Calibration: Determining Static Pressure-to-Deformation Relationship

3.3.1 Overview

Each deformation geometry (equibiaxial, uniaxial and width of gap) will have a unique pressure to deformation relationship due to a changing membrane stiffness which is related to how the membrane is constrained. Polystyrene fluorescent beads (Invitrogen) were used to measure the uniaxial deformation of the silicone membrane. A picture of the adherent beads was taken in the undeformed state, that is, 0 psi (Fig. 4a). The chamber pressure was increased incrementally and pictures were taken of the membrane in its deformed state (Fig. 4b, c). All measurements were done using

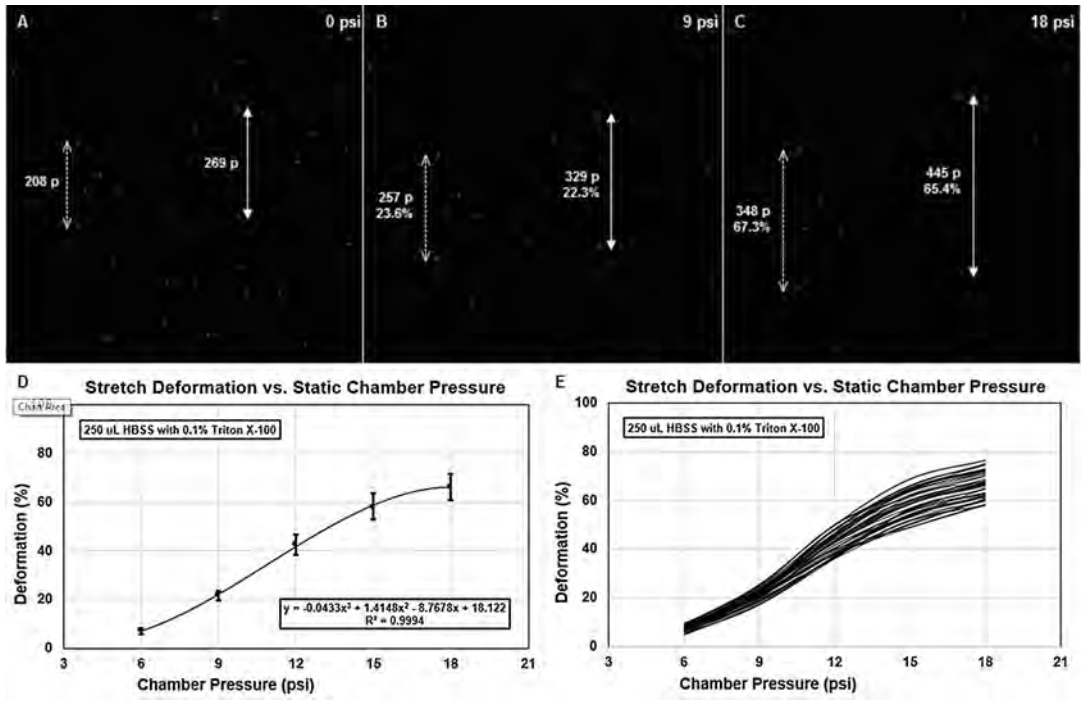


Fig. 4 Determining Relationship between Chamber Pressure and Stretch Deformation. Fluorescent beads are plated on injury wells. (**a**–**c**) Show representative images of the same field of fluorescent beads at 0 psi, 9 psi, and 18 psi. Arrows denote the distance, measured in image pixels, between two pairs of beads. (**d**) Shows the average percentage of stretch deformation across a range of chamber pressures. (**e**) Shows all measured data points that were used to calculate the average in **d**

deformation masks to create a uniaxial deformation. Strain was calculated using the equation:

$$\text{Strain} = \frac{l_f - l_0}{l_0} \times 100\%$$

Pairs of fluorescent beads were selected for measurement based on two factors: (1) pairs must be aligned within 5° of the stretch direction as to not affect linear measurement and (2) based on the ability to visualize the bead pair throughout the entire sequence of images. The distance between the selected pair of beads was measured in the undeformed state in terms of relative number of pixels (l_0) (Fig. 4d, e). This measurement was repeated for the same pair of beads for pictures of the membrane in its deformed state (l_f).

If desired, the system can also be used to induce biaxial stretch deformation on a cell culture (data not shown). Characterization of biaxial stretch is based on a similar principle using fluorescent beads, as described above. Specifically, three beads are chosen within an imaging field. Pictures of these three points are taken in the undeformed state (0 psi) and at chamber pressure increments in the deformed state [6, 13]. From the three points, two vectors can be defined, $dX^{(1)}$ and $dX^{(2)}$; these vectors represent the membrane stretch. Two vectors are used to define the membrane at each level of chamber pressure: $dx^{(1)}$ and $dx^{(2)}$. $\boldsymbol{F}$ is then defined to be the deformation gradient tensor such that:

$$dx^{(1)} = \boldsymbol{F} dX^{(1)}, \quad dx^{(2)} = \boldsymbol{F} dX^{(2)}$$

From this derivation, $\boldsymbol{F}$ is defined as:

$$\boldsymbol{F} = \left[dx^{(1)} \middle| dx^{(2)} \right] \left[dX^{(1)} \middle| dX^{(2)} \right]^{-1}$$

From this the Cauchy-Green deformation tensor is calculated:

$$\boldsymbol{C} = \boldsymbol{F}^{\mathrm{T}} \boldsymbol{F},$$

Finally, using the deformation, the Lagrangian finite strain tensor is derived:

$$\boldsymbol{E} = \frac{(\boldsymbol{C} - \boldsymbol{I})}{2}$$

The diagonal terms of tensor $\boldsymbol{E}$ provides strain information in the x, y directions, as well as information on shear stresses in the off diagonal terms. Thus the relationship between chamber pressure and biaxial stretch is established.

3.3.2 Protocol

1. Construct injury wells in nonsterile manner as described above.
2. Once fully dried, dilute fluorescent beads to 10^3 beads/mL from stock solution and plate on the injury wells.

3. Rock the wells side-to-side and back-to-front several times to ensure even distribution of the beads.
4. Incubate wells for a minimum of 15 min at room temperature, protected from light.
5. Aspirate fluorescent beads and gently rinse once with PBS, HBSS, or water.
6. Aspirate rinse and allow wells to dry for a minimum of 1 h, protected from light.
7. Once wells are dry, add 200 μL of HBSS with 0.1% Triton X-100 and secure a well inside the injury chamber (*see* **Note 4**).
8. Place injury chamber on an inverted microscope stage.
9. Connect the chamber to a tank containing compressed air with a regulator that allows for pressures up to around 20 psi to be applied to the chamber.
10. Using a 20× or 40× objective lens, focus on the center of the well's injury field (*see* **Note 5**).
11. Capture images of the same field of fluorescent beads at a range of pressure (e.g. 0, 6, 9, 12, 15, and 18 psi).
12. When all images have been captured, well can be rinsed once with PBS, HBSS, or water and allowed to dry.
13. Repeat procedure for desired number of injury wells.
14. For each well's series of images, choose pairs of beads that are aligned with the direction of uniaxial stretch and measure the distance (in pixels) between the beads in each pair, at each psi (Fig. 4a–c).
15. Calculate the percent change in distance for each bead pair relative to the initial 0 psi distance; this represents the percent stretch at each static pressure.
16. Plot the average deformation as a function of chamber pressure; determine the equation of the best fit trend line (Fig. 4d; *see* **Notes 6** and **7**).

3.4 Primary Cortical Neuronal Cell Culture Procedures

Preparation of the injury wells requires a full day, or the procedure can be split across 2 or more days.

3.4.1 Sterile Preparation of Injury Wells for Cell Culture

1. Soak the well pieces, Aclar® underside masks, and well O-rings in purified RO water with Sparkleen or similar laboratory detergent; scrub the well pieces with a toothbrush or glassware brush.
2. Rinse the well pieces, Aclar® underside masks, and O-rings thoroughly with RO water 3×.
3. Soak all well components in 70% ethanol and agitate by stirring or shaking; rinse 3× with RO water (*see* **Note 8**).
4. Sonicate all well components in RO water for 15 min, replacing the water after the sonication.

5. While sonicating, cut 3.5 cm × 3.5 cm^2 from a silicone sheet; soak the silicone squares in 70% ethanol (*see* **Note 9**).
6. Upon completion of sonication, assemble the wells; start by placing a Dash Number 018 high-temperature silicone O-ring on the small PEEK well piece.
7. Place an Aclar® underside mask within the large PEEK well piece.
8. Dip the large well piece with the Aclar® mask into a beaker of RO water, holding the mask in place to prevent it from floating up. Lift up out of the beaker, keeping a pool of water within the well piece atop the mask.
9. Lay a precut square of silicone on top of the large PEEK well piece.
10. Center the small PEEK well piece on top of the silicone square, then press the well pieces together, ensuring that the silicone placement is more or less centered within the well (*see* **Note 10**).
11. Trim the excess silicone using a razor.
12. Sonicate completed wells in fresh RO water for 15 min.
13. Transfer the wells to an autoclave-safe container, submerge the wells in RO water, and autoclave for 30 min.
14. Drain the water from the container and allow wells to air dry for at least 1 h in a sterilized biosafety cabinet for a minimum of 1 h (*see* **Note 11**).
15. Add 750 μL of poly-L-lysine solution to each injury well and incubate at 37 °C for at least 1 h.
16. Briefly rinse wells for 5 min with 1 mL of sterile culture-grade water and allow to air dry for at least 1 h; at this point the wells are ready for plating (*see* **Note 12**).
17. If a cell-free gap is desired for an axon-only region, cut 2 mm-wide silicone strips, rinse the strips in 70% ethanol followed by RO water, and autoclave dry for 1 h.
18. Allow the strips to dry, if necessary.
19. Lay the silicone strips across the center of the injury wells using forceps (*see* **Note 13**). The strips should stick well to the silicone well bottom.

3.4.2 Cortical Dissection and Cell Culture

Protocol

1. Prepare 50 mL of Cortical Media by combining 48.9 mL Neurobasal Media (4 °C), 1 mL B27 Supplement, and 100 μL GlutaMAX (0.4 mM).
2. Prepare 2 mL of Cortical Media + Penicillin/Streptomycin (Cortical Media + P/S) by removing 1.98 mL Cortical

Medium to a separate 15 mL tube and adding 20 μL penicillin/streptomycin (final concentration of 1%).

3. Prepare HBSS+/20% FBS/DNAse I solution by combining 1.9 mL HBSS containing calcium and magnesium, 0.5 mL FBS, and 0.1 mL DNAse I (100 units) in a 15 mL tube.
4. Obtain E17 or E18 rat embryos, maintain on ice, and remove embryos from placental sacs. Remove brains from the embryos. Remove meninges and isolate cortices from the rest of the brain, placing cortical fragments in 4 mL L-15 media kept on ice (*see* **Note 14**).
5. Once all cortices are removed, use the spear end of the surgical spatula to break apart the large cortical pieces using a mortar and pestle motion.
6. Allow cortical pieces to settle to bottom of tube and carefully remove the L-15 media.
7. Gently add 4 mL room temperature HBSS without calcium and magnesium to the tube. Allow the cortical pieces to settle to the bottom.
8. Remove the HBSS without calcium and magnesium and gently add 2.5 mL of 37 °C trypsin-EDTA solution (0.05%) diluted in HBSS without calcium and magnesium. Mix (do not vortex) and place at 37 °C for 20 min.
9. After 20 min add 2.5 mL of HBSS+/20% FBS/DNAse I at 37 °C to inactivate the trypsin-EDTA solution.
10. Triterate the cortical pieces using a glass pipette 20 times, then incubate the tube at 37 °C for 20 min (*see* **Note 15**).
11. Spin the tube at low speed (800 rpm) for 5 min.
12. Remove the supernatant, leaving the pellet undisturbed.
13. Resuspend the pellet in 2 mL of Cortical Media with penicillin/streptomycin by triterating 20 times using a glass pipette (*see* **Note 16**).
14. Dilute a portion of the final cell suspension 1:10 in Trypan Blue solution (100 μL cell suspension to 900 μL Trypan Blue). Count cell density with a hemocytometer.
15. Add 900 μL of 37 °C Cortical Media to each well.
16. Dilute a portion of the final cell suspension in a new tube such that each well will receive 100 μL of cell solution containing 175,000 cells per well (roughly 750 cells/mm^2; *see* **Notes 17** and **18**).
17. Slowly add 100 μL of cell dilution directly to the center of each well, and do not disturb the wells for 10 min.
18. Very gently mix the wells by rocking them from side to side, and front to back.

19. Place wells in 37 °C incubator.
20. If wells are to contain a cell-free gap, at least 2 h after plating, gently remove the cell-free gap silicone strip using autoclaved or ethanol-sterilized fine tip forceps.
21. Feed the wells every 2–3 days by replacing half the well volume (*see* **Notes 19** and **20**).

3.5 Basic Injury Device Operation

3.5.1 Hardware

The injury device delivers a precise air pressure pulse to the injury chamber, resulting in uniaxial stretch of the silicone membrane, and the axons or cells on the silicone, above the gap area of the deformation masks (Fig. 2e). In our stretch injury model, the control system needs to be able to control two important parameters, the pressure amplitude within the injury chamber and the duration of pressure release into the injury chamber. The control system must be able to precisely and consistently adjust these parameters to allow for stretch injuries across a diverse range of injury intensities and rates. Further, it is necessary to be able to measure these parameters in real time to know the exact attributes of injury being induced.

The degree of pressure increase in the injury chamber correlates to the magnitude of stretch injury inflicted upon the cells or axons within the injury zone. This is the basis for the static pressure-deformation characterization above; higher chamber pressures produce greater strain. Varying the chamber input pressure affects the rate at which the intra-chamber pressure rises. Modulating the chamber pressure could be controlled manually in a simplistic system using a pressure regulator setup, though the tradeoff would be greatly reduced precision especially with respect to the duration of the pressure pulse. We devised an automatic pressure control system using a Parker Hannifin VSO®-EP Miniature Electronic Pressure Control Unit. This component converts a tunable electrical control signal into a proportional pneumatic output with excellent precision and reproducibility. This unit regulates the pressure within a small reserve air tank, which acts as the reservoir of pressure to be released into the injury chamber (see. Fig. 2d).

The duration of the pressure pulse within the injury chamber correlates to the rise time and duration of the stretch injury. This parameter is dependent on the valve open time, that is, the length of time the pressure is allowed to be released into the chamber. The particular challenges for an in vitro stretch injury model hinge on achieving the fast rise times observed in traumatic brain injury, on the order of milliseconds. To achieve rapid pressure rise times, we utilize a solenoid valve, the Parker Hannifin Series 9 Miniature Calibrant Valve, which enables high speed, very low leak rate, and high flow control of air pressure into the injury chamber. The valve is situated in between the reserve air tank, which stores the pressure to be released into the chamber, and the chamber itself. Opening of

the valve releases the pressure pulse into the injury chamber. This valve should be three-way, so that the pressure pulse is vented out of the chamber upon valve closure.

The exact dynamics of the resulting injury are dependent on both the input pressure and valve open time. In general, higher input pressures result in greater degrees of strain and quicker injury rise times; longer valve open times result in longer pressure pulses and greater degrees of strain. These parameters are interdependent. For example, two pressure pulses with the same input pressure but different valve open times will produce two different injury profiles. The faster pulse (shorter valve open time) will also display a reduced pressure amplitude relative to the longer pulse. If a specific type of injury is desired, the device operator must first experimentally determine the necessary pulse parameters more or less by trial and error. Figure 5 shows representative pressure pulses across a range of strain amplitudes and strain rates, up to 60% strain and 90/s strain rate.

There are also other factors that can alter pulse dynamics from one device setup to the next. Namely these are the length and diameter of the tubing used to connect the reserve tank to the valve, and the valve to the injury chamber. For a single well system like the one described here, the air volume within the chamber is small. Therefore, changes to the tubing connecting the valve to the chamber can have a relatively large impact on the effective chamber air volume. A larger chamber volume requires greater input pressure to reach the same level of chamber pressure and therefore silicone stretch, and vice versa.

The tubing connecting the reserve tank to the valve can also play a role in modulating pressure pulse dynamics. Air flow from the reserve tank to the valve to the chamber is constrained by the smallest diameter orifice within the system. In our setup, this is the orifice within the solenoid valve itself, at 0.06″. If smaller diameter tubing or a smaller flow control orifice is placed directly behind the valve, then this will result in slower air flow velocity into the injury chamber. This serves to attenuate the pressure pulse amplitude.

Lastly, the system must be able to measure the pressure pulse delivered to the injury chamber in real time. An advantage of the silicone-based stretch injury model is that, since stretch deformation is related to chamber pressure, the deformation during a pressure pulse can be inferred from pressure amplitude measurements. The main requirement for measurement is a pressure transducer that is small enough to be mounted on the chamber and capable of measuring at high speeds. We have used both PCB transducers, such as the Model 113B28, and Measurement Specialties EPX miniature pressure sensor. Both sensor types are able to operate at kilohertz rates, readily capturing pressure changes taking place over several milliseconds.

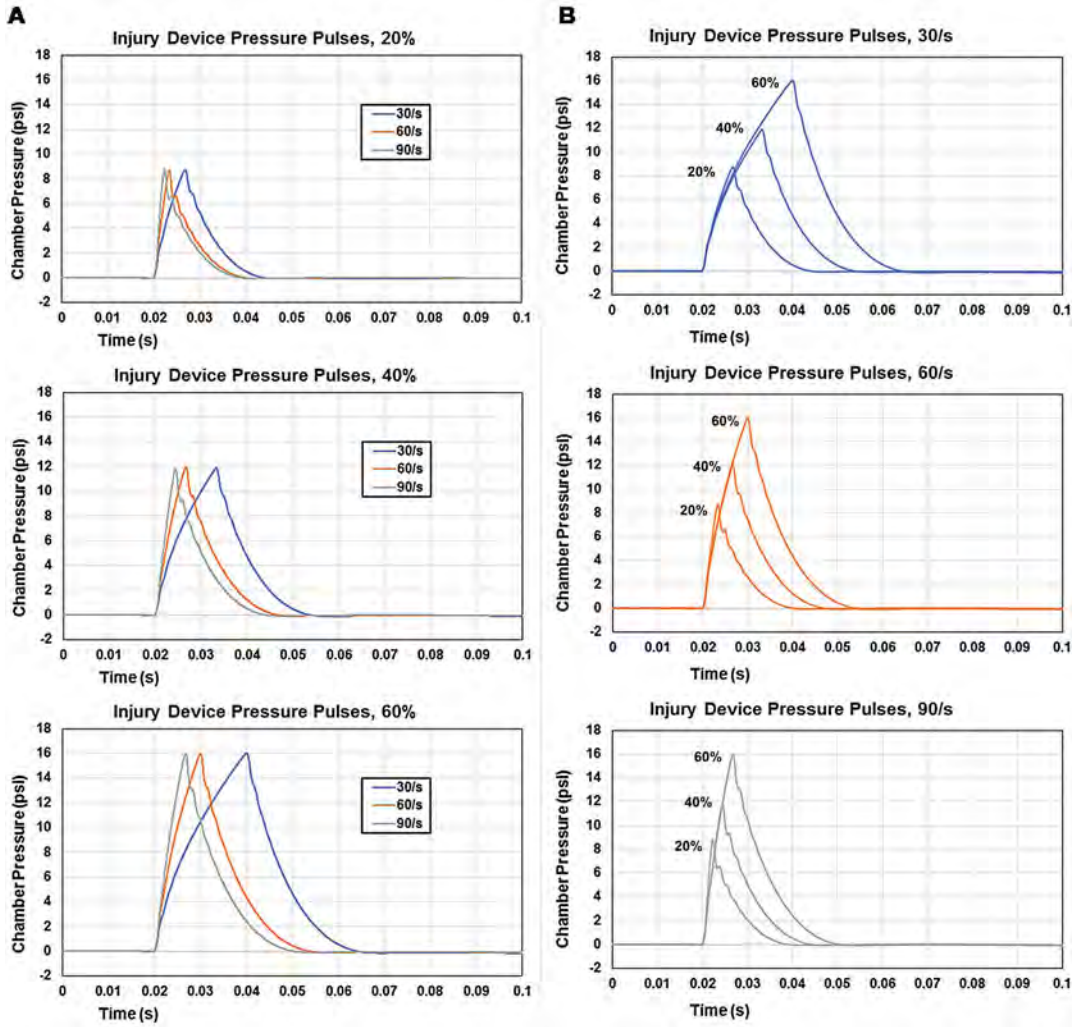


Fig. 5 Sample Pressure Pulses at 20%, 40%, and 60% Strain Amplitude, and 30/s, 60/s, and 90/s Strain Rates. Column **a** shows the individual pressure pulses arranged into separate plots by strain amplitude. Column **b** shows the same individual pressure pulses but arranged into separate plots based on strain rate

3.5.2 Software

A custom software program is required to operate the device components discussed above. As an example we will describe the LabView program we use to operate our injury device (Fig. 6). The pressure transducer, solenoid valve, and pressure control unit communicate with LabView via a multifunction DAQ device (we use a National Instruments USB-6211).

As described above, the two relevant parameters to control are the reserve tank pressure and valve open time. Our LabView program contains input boxes for modulating these two parameters (Fig. 6a). The voltage applied to the pressure control unit alters the pressure pumped into the reserve tank. In order for the software to accurately display the chamber pressure, an input needs to be

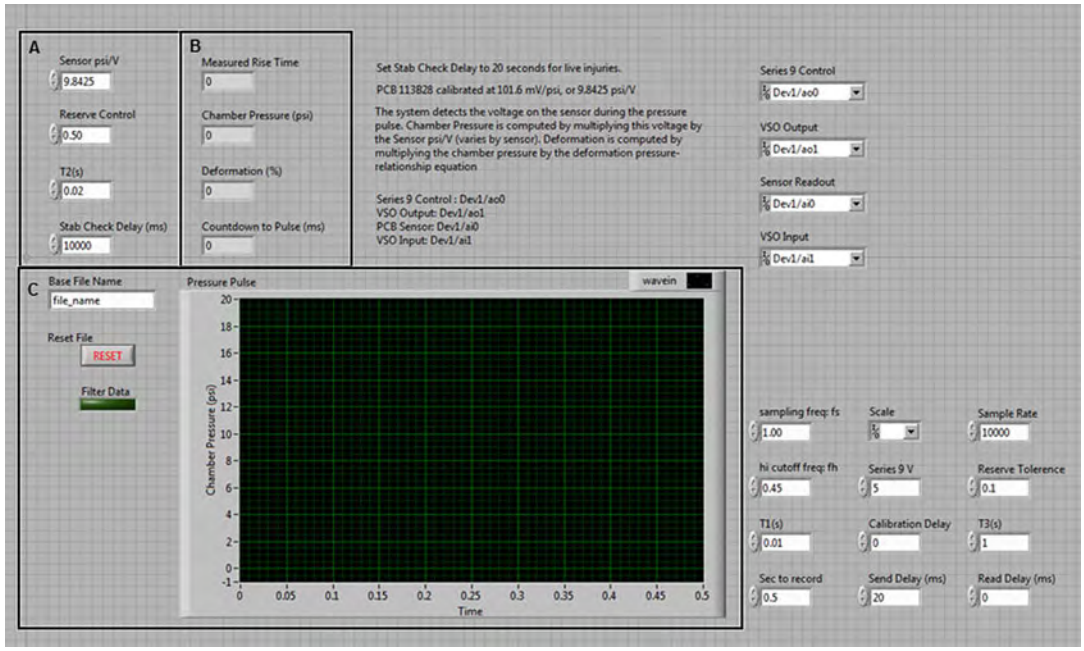


Fig. 6 Sample Custom LabView Program for Controlling Injury Device. (**a**) Shows the device parameters that can be modulated manually, in particular the input pressure (labeled as "Voltage Control") and valve open time (labeled as "T2(s)"). (**b**) Shows the automated outputs based on the pressure detected by the pressure transducer at the injury chamber. (**c**) Shows the graph produced from the sensor's measurements. This data is automatically saved

created to account for the pressure transducer calibration, commonly reported as mV/psi or similar units. It is helpful to see the pressure pulse graphed and logged automatically (Fig. 6c). LabView extracts the rise time based on the recorded data points.

Based on the chamber pressure-deformation relationship determined during the characterization steps, the program can also be designed to report the calculated silicone deformation based on the detected chamber pressure (Fig. 6b).

4 Notes: 2-D In Vitro Stretch Injury Model

1. NOTE 1: We noticed that, quite frequently, the silicone could stick to the injury mask surface. This posed the risk of additional strain during the removal of the culture well from the injury chamber. Additionally, microscopic imperfections in the mask surface, which results especially from thermal deposition prints, could permit unknown and unintended strains to occur in the "uninjured" regions of the culture well. The more rigid Aclar® (relative to the silicone sheet) prevents either of these from occurring, providing much more confidence that the injury is being restricted to the desired area.

2. NOTE 2: The choice of Aclar® film thickness for underside well mask depends on the specific experimental application. We designed this injury setup with certain types of experiments in mind, such that axons or cell bodies could be imaged simultaneously with the injury on an inverted microscope. Specifically, we needed to accommodate an objective lens with a 1 mm working distance; thus we were required to limit the combined thickness of both masks to less than 1 mm. Thinner Aclar® sheets could be used if required; it is only necessary that the masks create a rigid surface that remains largely undeformed when the chamber is pressurized.
3. NOTE 3: The silicone and Aclar® will form a seal when pressured together. Optimally, this seal will be free of any air pockets. Pressing the two together with water in the middle reduces the number and size of air pockets creating a more uniform seal.
4. NOTE 4: It is necessary to perform these calibrations under the same conditions as during an injury experiments. During injury experiments, fluid volume in the well should be minimized to allow for efficient gas exchange. In a well without any cells on the silicone substrate, adding a detergent to HBSS decreases the surface tension of the fluid thereby allowing a smaller volume to spread throughout the entire silicone surface.
5. NOTE 5: This can be achieved by increasing the chamber pressure and identifying the lowest point in the uniaxial curvature of the silicone.
6. NOTE 6: Depending on the pressure range chosen, the trend line may be roughly linear or a third degree (cubic) polynomial. This equation will be plugged into the software program that runs the injury device, as described below in the Injury Device Operation section.
7. NOTE 7: Biaxial calibration, for the most part, follows the same series of steps as far as data collection is concerned, with one major difference. Under biaxial conditions, the silicone will stretch easier, meaning it takes a lower chamber pressure to achieve the same percentage of stretch compared to uniaxial conditions. Consequently, other than the differing mathematical analysis described above, the only other protocol deviation is that the chamber pressure range over which the device is characterized will be narrower, usually only up to about 4 psi maximum. At higher pressures the silicone is likely to blow out.
8. NOTE 8: Ethanol seems to help completely remove any detergent residue on the pieces.
9. NOTE 9: If you notice smudges on the silicone squares, they can be removed by rubbing the sheets in between your fingers with ethanol. We have also noticed that nitrile gloves can sometimes have subtle residues on them which transfer onto

the silicone. Washing one's gloves with ethanol several times can also help eliminate residues and prevent them from transferring to the silicone sheet.

10. NOTE 10: The silicone and Aclar® will form a seal when pressured together. Optimally, this seal will be free of any air pockets. Pressing the two together with water in the middle reduces the number and size of air pockets creating a more uniform seal.
11. NOTE 11: In addition to autoclaving, well pieces can be surface treated using plasma cleaning. Plasma cleaning improves poly-L-lysine coating and cell attachment later on. For plasma cleaning, the autoclaved and dried wells should be placed inside a closed container. Oxygen plasma clean the container for 1 min. After this, the wells are ready for poly-L-lysine coating.
12. NOTE 12: If using wells that have been plasma cleaned, perform three minimum 30-min rinses with sterile culture-grade water. Culture-grade water can be purchased or prepared by autoclaving bottles of RO water.
13. NOTE 13: The two silicone surfaces will form a seal. At plating, cells will loosely adhere to the top of the silicone strips. Upon removal of the strips, a cell-free gap is left underneath allowing for the formation of an axon-only region. With proper plating density, axons will typically traverse the middle of the gap by 9–11 days in vitro. Silicone strips should not be plasma cleaned. If both the strips and wells are plasma cleaned, they will form a very strong seal upon coming into contact with one another.
14. NOTE 14: A typical E17 rat brain can provide at least 6–8 million cortical cells using this protocol, in our experience. E18 brains can provide up to around 10 million cortical cells. The difference is likely due to a combination of slightly increased size and also easier dissection (the meninges is substantially easier to remove) leading to lower cell loss during processing.
15. NOTE 15: DNAse I requires the presence of calcium ions to function. However, trypsin is usually diluted in a calcium-free solution and administered in conjunction with the calcium chelator EDTA, which aids in disrupting cell–cell interactions and dissociating the cells. For this reason, we do not mix the DNAse I with the trypsin-EDTA but instead do sequential treatments. First, cell–cell interactions are weakened with trypsin-EDTA, cells are then dissociated by triteration, and finally any free DNA that results from damaged cells is degraded by DNAse I following dissociation.
16. NOTE 16: Larger cell chunks and other cellular debris can be isolated from the cell suspension by several methods. The

suspension can be passed through a filter. Alternatively, larger pieces of debris can be allowed to sink to the bottom of the tube, the remainder of the fluid moved to a new tube, and the original tube disposed of. This can also be performed in between steps 10 and 11 prior to centrifugation.

17. NOTE 17: Example: Cell solution counted to be approximately 5000 cells/μL

    12 injury wells to plate at 175,000 cells/well.

    175,000 cells/well × 15 wells (*see* NOTE below) = 2,625,000 cells total needed.

    100 μL volume to add per well × 15 wells (*see* NOTE below) = 1500 μL.

18. NOTE 18: When diluting the cell plating suspension, it is advisable to add and account for more volume than is needed as the suspension has a tendency to bubble. In the above example, three extra wells worth of cells and media volume was included.

    2,625,000 cells/5000 cells/ μL = 525 μL

    Add 525 μL final cell suspension to 975 μL Cortical Media and add 100 μL of cell dilution to each well. Discard excess.

19. NOTE 19: To account for evaporation of the media, we assume 50 μL of media is lost each day. So, for example, if it has been 2 days since last feeding, 400 μL would be removed and 500 μL added back in order to maintain a 1 mL volume.
20. NOTE 20: If axons fail to grow across the cell free gap but the cells appear healthy, higher plating densities can be used. We have used plating densities up to 1500 cells/mm^2. If the density is too low, axons will not traverse the cell-free gap. Appropriate plating densities may differ across labs and setups.

5 Materials: 3-D In Vitro Injury Model

5.1 Materials for 3-D Constructs

- Surgical tools (large scissors, small scissors, one set of curved forceps, two sets of fine forceps, one set of fine angled forceps, two micro-scalpel blades, one surgical spatula).
- Hanks Balanced Salt Solution (HBSS, Gibco).
- Compressed CO_2 air tank.
- Guillotine.
- L-15 media (Gibco).
- B27 Supplement (Invitrogen).
- 0.25% tryspin + 1 mM ethylenediaminetetraacetic acid (EDTA, Invitrogen).

- DMEM/F12 media (Gibco).
- Fetal bovine serum (FBS, Atlanta Biologicals).
- DNase I (Roche).
- Magnesium sulfate ($MgSO_4$, Sigma).
- Matrigel (Corning).
- Trypan Blue.
- Neurobasal media (Gibco).
- G5 (100× concentrate, Gibco).
- Glutamax (100× concentrate, Gibco).
- Poly-L-lysine (PLL; Sigma).
- 70% ethanol.

5.2 Materials for Cell Shearing Device for In Vitro Injury

- Custom-designed Cell Shearing Device (Kinetic Software Atlanta) including:
  - Linear voice coil actuator (BEI Kimco; San Marcos, CA).
  - Custom-fabricated digital proportional-integral-derivative (PID) controller (25-kHz sampling rate, 16-bit sampling resolution).
  - Optical position sensor (OPS) (RGH-34, 400 nm resolution; Renishaw, New Mills, UK).
  - Custom-built polycarbonate cell chambers.
- Silicone adhesive.
- Plain glass microscope no. 1½ coverslip or slide (Fisherbrand, 25 × 75 × 1 mm).
- Sylgard 184 (Dow Corning; Midland, MI).
- Polycarbonate cylindrical cutouts (inner diameter roughly 15 mm).
- Scotch tape.
- Razor blade.
- 70% ethanol.

6 Methods: 3-D In Vitro Injury Model

6.1 Introduction to 3-D CSD

All strain fields in the brain are 3-D, yet most in vitro models of TBI use planar (2-D) cultures, which fail to replicate the complex 3-D strain fields of in vivo injury. To address this gap, LaPlaca and colleagues developed and validated the first in vitro model of TBI that employed custom-built 3-D neural cellular constructs subjected to controlled 3-D shear-strain based loading profiles [10]. The custom-designed device is referred to as the 3-D cell shearing

device (CSD), and is capable or reproducibly delivering a specified strain field to neural cells within a 3-D bioactive ECM based scaffold. The device input approximates the 3-D strain fields predicted during closed-head diffuse injury in the human brain. In addition to matching the tissue-level biomechanical inputs implicated in the etiology of clinical TBI, engineering neural constructs in vitro offers other advantages for investigating specific mechanisms of injury, including spatial and temporal control of cellular composition, matrix/scaffold properties, mechanical environment, and exogenous factors. Thus, a 3-D culture system more faithfully mimics the complex environment of the brain than 2-D cultures, and permits the application of strain fields to model forces seen in human injury. These 3-D constructs and 3-D CSD permit the investigation of complex responses that occur after traumatic loading and may provide a physiologically-relevant testbed to evaluate the efficacy of potential therapeutic agents.

6.2 Production of CSD Injury Chambers

1. Outline the bottom of the rectuangular polycarbonate well (cell reservoir) with silicon adhesive and attach precleaned, plain glass microscope coverslips or slides and let cure.
2. On the top plates, wrap approximately 30 cm of scotch tape around the cylindrical protrusions (*see* **Note 1**).
3. After the glass slide is sealed to the bottom of the reservoir (e.g., the next day), fill the chambers with PDMS (Sylgard 184 and curing agent mixed 10:1). Let the PDMS sit until the bubbles settle, and apply the top plate so that the two cylinders are centered in the reservoir. Allow this to cure for 24–48 h.
4. After the PDMS has cured sufficiently, slowly remove the top plate (*see* **Note 2**). Use a razor blade or a similar sharp object to cut away excess PDMS at the base of the chamber (on the glass), and remove the tape from the cylinders (*see* **Note 3**).
5. Test the cell chamber on the CSD to ensure that the top plate moves effectively. If it does not, additional tape may be added in order to further widen the holes.
6. To clean the chambers after use, soak in 70% ethanol for at least 4–6 h. Chambers are reusable after cleaning.

6.3 Primary Astrocyte and Neuron Cell Culture Procedures

6.3.1 Overview

We will describe the procedure for generating neuron-astrocyte 3-D cocultures in a bioactive ECM scaffold, though single cell types or other mixes of cells may be used. Embryonic day 17 (E17) Sprague-Dawley rats are used to harvest neurons, while postnatal day 1–2 (P1–2) Sprague-Dawley rat pups are used to harvest astrocytes. The astrocyte harvest should occur several weeks prior to generation of the 3-D constructs, so the astrocytes have a chance to be passaged 2–3 times before use in order to acquire a more mature phenotype.

6.3.2 Neuronal Harvest Protocol

All surgical tools should be sterilized by autoclave prior to dissection. The dissection is performed within a laminar flow hood.

1. Fill 4–6100 mm Petri-dishes with 15 mL each of sterile HBSS and place on ice.
2. Sacrifice the mother Sprague-Dawley rat with E17 pups via prolonged CO_2 and subsequent guillotine. Lay carcass ventral side up and rinse abdomen thoroughly with 70% ethanol. Cut beginning at the lower abdomen extending rostrally to expose the uterus. Remove the uterus and place in a sterile petri-dish with ice-cold sterile HBSS. Remove each fetus from the amniotic sacs and transfer to a new petri-dish containing ice-cold HBSS.
3. Decapitate each fetus and remove the brains by cutting and peeling back the top portion of the skull. Transfer the brains to a new petri-dish containing ice-cold HBSS.
4. To isolate the cortices, remove the hindbrain and perform a midsagittal cut. Remove the midbrain and place hemispheres with lateral surfaces facing down. Remove the olfactory bulbs and turn over the hemispheres such that the medial surfaces face down. Detach the meninges and again turn the hemispheres over such that lateral surfaces face down. Remove the cortical region from the remaining midbrain and cut the hippocampal region from the cortex (*see* **Note 4**).
5. Transfer the cortical regions to a 15 mL centrifuge tube of HBSS (4–6 cortices per tube) and place on ice (*see* **Note 5**).

6.3.3 Astrocyte Harvest Protocol

All surgical tools should be sterilized by autoclave prior to dissection. The dissection is performed within a laminar flow hood.

1. Sacrifice P1–P2 rat pups by placing each pup in the finger of a disposable glove and covering with ice for 5–10 min before dipping in ethanol and decapitating with scissors.
2. Remove the brain and proceed with the cortical isolation as described above for the neuronal harvest.
3. Mince cortices with micro-scalpel blades, then transfer the tissue to a 15 mL centrifuge tube with 900 μL 0.25% trypsin + 1 mM EDTA per brain and place in a 37 °C bath for 5–7 min.
4. After the tissue is clumped together, neutralize the trypsin with 1 mL DMEM/F12 media supplemented with 10% FBS, and also add 400 μL DNase solution (1.5 mg/mL DNase I, 2.5 mg/mL $MgSO_4$, in HBSS). Triturate with a fire-polished pipette until no clumps are visible.
5. Centrifuge at 3500 rpm for 3 min, then remove the supernatant and resuspend the pellet in plating media (DMEM/F12 + 10% FBS).

6. Plate one brain per T75 flask, with a final volume of 10 mL plating media, and place the flask in a tissue culture incubator (37 °C, 5% CO_2, 95% RH).
7. Completely change media about once a week.
8. Passage cells as when they become about 90% confluent. To do so, remove the media and add 5 mL 0.25% trypsin-EDTA. Return the flask to the incubator for 5–10 min, as astrocytes detach from the flask. Once lose, deactivate the trypsin with 1 mL DMEM/F12 + 10% FBS. Transfer the suspension to a 15 mL centrifuge tube and centrifuge at 3500 rpm for 3 min. Remove the supernatant and resuspend the pellet in plating media. Transfer the desired ratio of cells into a new T75 flask (i.e., 1:4, 1:10) with 10 mL plating media, and return flask (s) to incubator. For all steps, keep the tissue on ice when not in the centrifuge or 37 °C bath.

6.4 3-D Coculture Procedures

3-D cultures consist of neural cells embedded within a 3-D bioactive extracellular matrix-based scaffold. We will describe the procedure for generating neuron-astrocyte cocultures, though single cell types or other mixes of cells may be used.

6.4.1 Chamber Preparation

1. Make sure the injury chambers are clean (i.e., soaked in ethanol and rinsed with deionized water) and autoclaved.
2. Pretreat the chambers with 500 μL 0.5 mg/mL PLL and place in incubator (37 °C, 5% CO_2, 95% RH) for at least 4 h. Aspirate the PLL and let the excess evaporate by leaving the lid open under a laminar flow hood for ~2 min.
3. Precoat with 500 μL 0.5 mg/mL Matrigel and place the chambers in an incubator (37 °C, 5% CO_2, 95% RH) for at least 4 h.

6.4.2 Neuronal Dissociation

Tissue and reagents (except trypsin before and during tissue addition) should be kept on ice at all times.

1. Acquire cortices from E17 Sprague-Dawley rats as described above.
2. Mince the cortices with micro-scalpel blades, then transfer the tissue from 2 to 3 brains to a 15 mL centrifuge tube with 5 mL 0.25 tryspin + EDTA and place in a 37 °C bath.
3. After 5–7 min check the tissue for clumping and manually agitate. After the tissue is clumped together, carefully remove the trypsin and gently rinse with 1 mL cold DMEM/F12 + 10% FBS.
4. Remove the serum and gently rinse twice with cold HBSS.

5. After removing the rinse HBSS, add 1.8 mL HBSS + 400 μL DNase solution. Triturate with a fire-polished pipette until no clumps are visible.
6. Centrifuge at 3500 rpm for 3 min, then remove the supernatant and resuspend the pellet in 2 mL neuronal-astrocyte media (Neurobasal + B27 + glutamax + G5).
7. Count the cells in order to dilute them to the desired density. Ensure the cell solution is well-mixed (gently triturate 3–5 times) and remove a small sample to dilute and count (*see* **Notes 6** and 7). Dilute with neuron-astrocyte media to desired density (i.e., 5 million cells/mL).

6.4.3 Plating

1. Place Eppendorf tubes with frozen 500 μL 15 mg/mL Matrigel on ice to begin to thaw to a slush consistency.
2. Acquire astrocytes as if preparing for passaging (see 4.3.3, though do not transfer to a new flask after resuspending pellet), count cells, and dilute with neuron-astrocyte media to desired density (i.e., 5 million cells/mL).
3. Mix the neurons and astrocytes in the desired ratio (i.e., 1:1). From this mixture, take 500 μL of cells and use a cold pipet tip to gently (to avoid bubbles) yet thoroughly mix with the thawed Matrigel tube, bringing the final Matrigel concentration to 7.5 mg/mL (*see* **Note 8**).
4. Bring the injury chambers from the incubator and aspirate the Matrigel precoat from wells. Quickly add the Matrigel/gel suspension at the desired thickness for the construct (i.e., 200 μL) and immediately return the chamber to the incubator to gel.
5. After about 1 h, add 1 mL neuronal-astrocyte media to each well.
6. At 24 h post-plating, feed cells by removing half of the old media and replacing with fresh. Feed cells in this manner every 2–3 days.

Cultures should exhibit minimal clustering, meaning there should be few neurons demonstrating soma-soma contact (assessed visually). If astrocytes are included in the constructs, after several days constructs should look like they are contracting and may develop thicker outer rings as astrocytes remodel the ECM scaffold. Unless experiment-specific, cultures should be used at 14 DIV or later to permit neuronal maturation.

6.5 Injuring 3-D Cultures with Cell Shearing Device

6.5.1 Overview

The 3-D CSD consists of a (1) the device itself—a linear actuator coupled to a closed-loop control system (Fig. 7a), and (2) reusable cell chambers (Fig. 7b). The system was designed by LaPlaca, Cargill, and Cullen, with the final device(s) fabricated by Kinetic Software Atlanta. The cell chamber is comprised of the cell reservoir

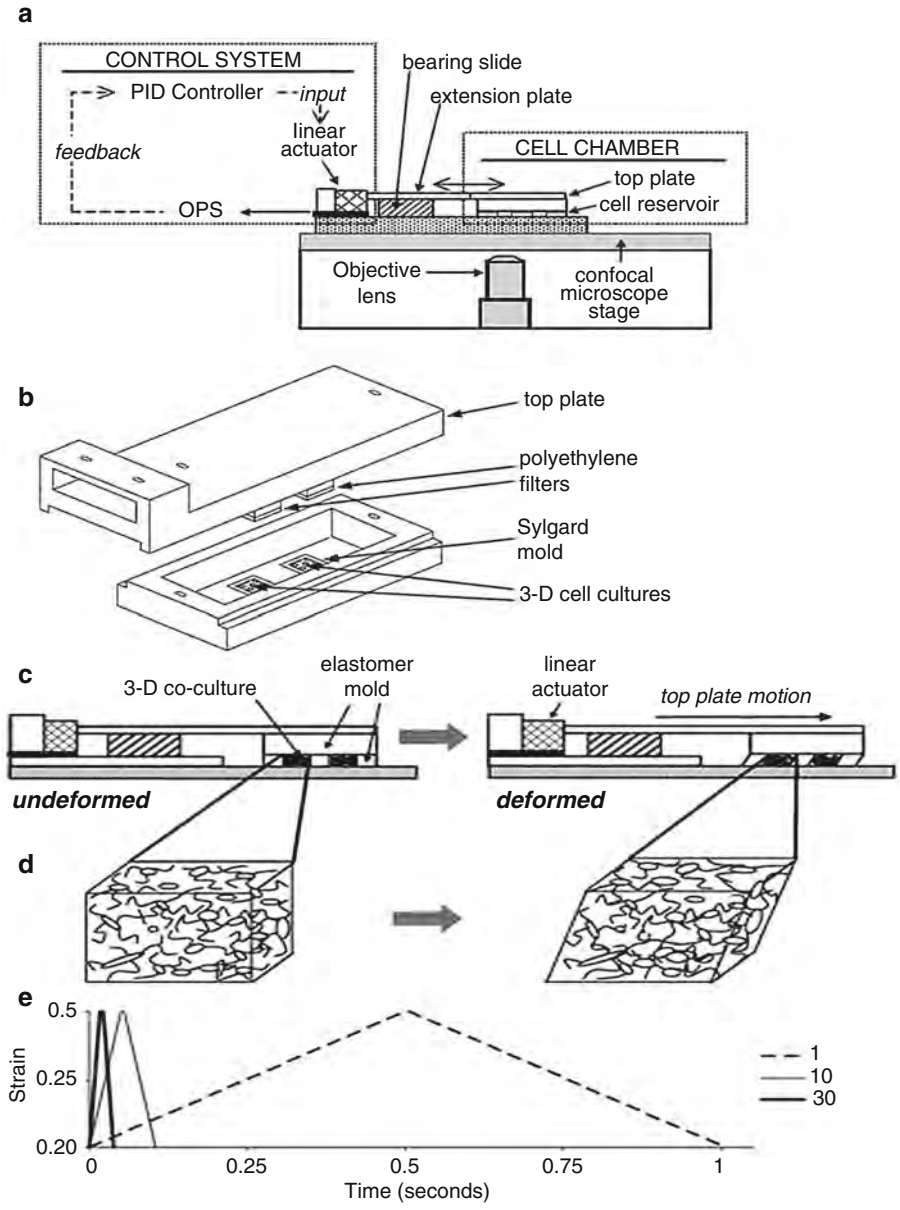


Fig. 7 3-D Cell Shearing Device (3-D CSD) Components. (**a**) A schematic representation of the 3-D CSD. The device can be mounted on a confocal microscope to obtain 3-D images before, during, and after mechanical deformation. A closed-loop control system consisting of a proportional-integral-derivative (PID) control with positional feedback from an optical position sensor (OPS) governs a linear actuator, inducing motion of the cell chamber top plate (not to scale). (**b**) The cell chamber consists of a top plate with polycarbonate protrusions to interface with the 3-D cell cultures. The top plate is mounted above the cell reservoirs and connected to the linear actuator to impart high rate deformation. (**c**) The 3-D CSD top plate motion is driven by a linear actuator. Neuronal–astrocytic cocultures in 3-D were plated throughout the thickness of a bioactive matrix and were laterally constrained by an elastomer mold. (**d**) Shear deformation of the elastomer mold and cell-embedded matrices was induced through horizontal displacement of the cell chamber top plate, which was coupled to the linear actuator. (**e**) Input to the system was a symmetrical trapezoidal input to a constant displacement

and the top plate. The cell reservoir is a rectangular polycarbonate well with a glass floor (no. 1 ½ coverslip or plain glass slide). Parallel shoulders were machined into the upper surface of the two long sides of the polycarbonate walls to provide proper alignment and constrain motion of the top plate to a single axis. The 3-D cultures (two per reservoir) are confined within an elastomer mold composed of Sylgard 184 and cast to the desired thickness. The cultures are contained by cylindrical cutouts (inner diameter of roughly 15 mm). Throughout experimentation, the mold adheres firmly to the bottom glass coverslip without any movement. The top plate is composed of a polycarbonate body. The cylindrical protrusions act as struts to transfer the transverse motion of the top plate to the cell cultures, which are situated, on the chamber base. The top plate is attached to the linear actuator by a polycarbonate extension plate that is mounted to a linear bearing system (Fig. 7).

This device generates a dynamic shear strain by the linear motion of the top plate with respect to the cell reservoir via a linear voice coil actuator coupled to a custom-fabricated digital proportional-integral-derivative (PID) controller with closed-loop motion control feedback from an optical position sensor (OPS). The linear actuator produces a rigid body translation of the top plate assembly. The input signal is the reference input to the PID controller and is compared internally to the actual displacement of the top plate provided by the OPS. The closed loop controller produces a self-correcting signal to minimize the error between the actual and desired position. PID control reduces steady-state error between the input signal and the motion of the top plate, eliminates possible oscillations in the response, and increases sensitivity of the system.

The device is controlled using a custom stimulation control program in LabVIEW. The device may be used on a bench top or mounted above a confocal microscope to image the deformation.

6.5.2 Application

Two parameters that control the severity of injury are the shear strain magnitude and the strain rate. Both can be controlled by a closed-loop actuator/controller system that develops shear strains of up to 0.5 (shear angle up to 45°) at rates from 1 to 50 s^{-1} in order to simulate the spatial and temporal strain patterns associated with inertial TBI. In our system we set several parameters to provide a trapezoidal input: the movement of the top-plate (in millimeters; corresponding to shear strain magnitude) and the desired rise-time (in milliseconds; corresponding to strain rate),

Fig. 7 (continued) (corresponding to 0.50 bulk shear strain) at strain rates of 1, 10 or 30 s^{-1} (corresponding to rise times of 500, 50, or 16.7 ms, respectively; hold time was held constant at 5 ms). Panels (**a**) and (**b**) reprinted with permission from LaPlaca et al., 2005, Elsevier; panels (**c–e**) reprinted with permission from Cullen et al., 2007, Elsevier

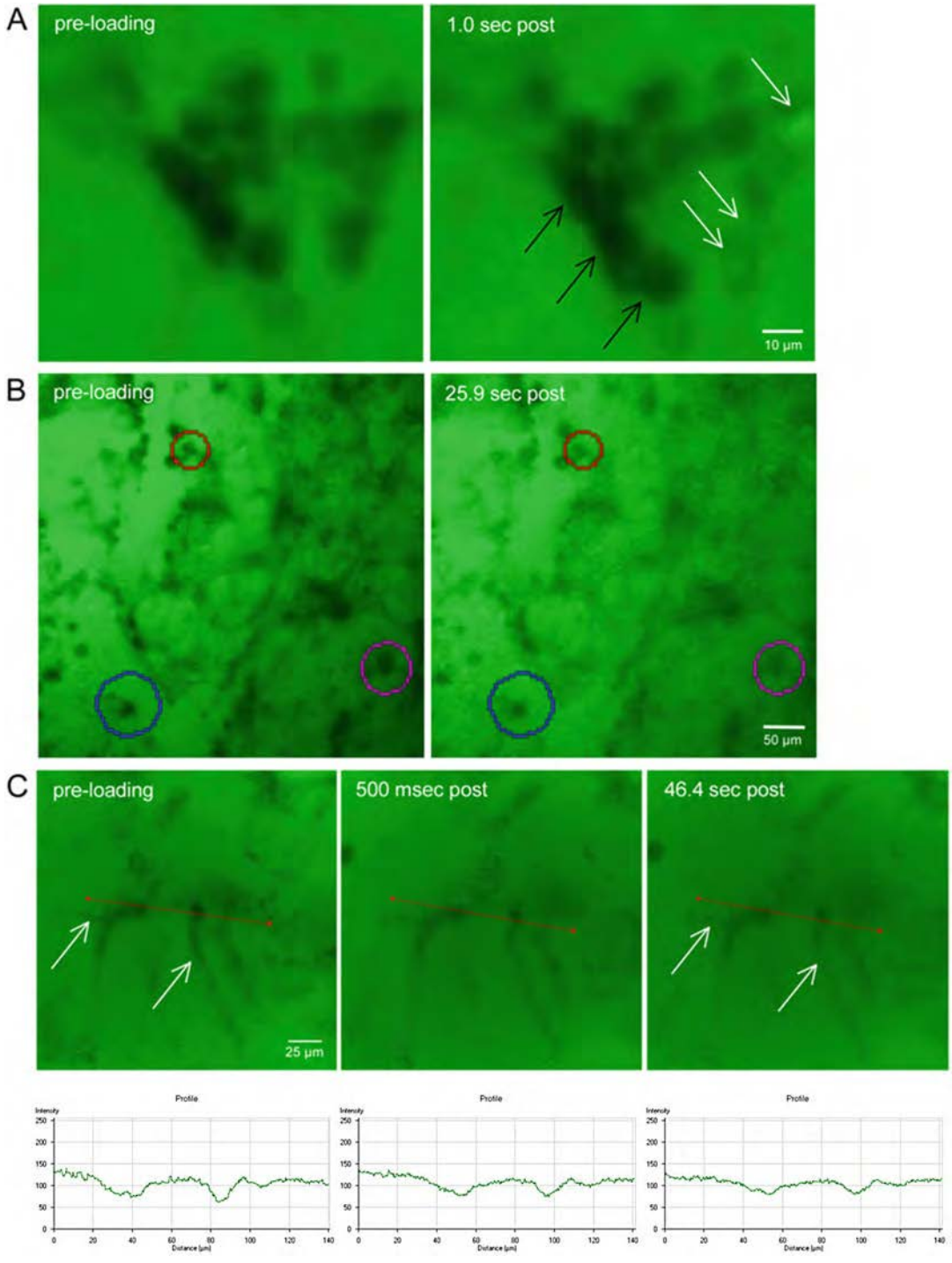


Fig. 8 Real-time Analyses of Calcein Uptake following Shear Deformation. The shear deformation device permits real-time imaging across the 3-D cultures before, during, and after loading. (**a**) Calcein diffused throughout the extracellular space prior to loading (resulting in relatively high fluorescence background during imaging). The 3-D cultures were dynamically deformed at 0.50 shear strain (10 or 30 s^{-1} strain rate).

hold-time, and ramp-down time. The firing of the linear actuator will deflect the top-plate horizontally while the chamber base is held stationary. Static control cultures experience all steps with the exception of device stimulation, thus controlling for the potential effects of media removal, top-plate application, and any temperature fluctuations.

A variety of outcome measures can be used to assess cellular responses after injury. One consequence of traumatic loading is transient micro- or nano-tears in the plasma membranes of cells. Cells that have become mechanoporated but then reseal can be labeled by adding small, nonpermeable molecules (such as calcein or Lucifer Yellow) to the media before an during injury. Because the CSD can be mounted on a confocal microscope, real-time imaging of the permeability event is possible (Fig. 8). Permeability can also be viewed post- injury (Fig. 9). We have shown that the faster the strain rate, the greater extent of membrane permeability, both in terms of the density of permeabilized cells and intensity of dye uptake. Cell death can also be assessed in these cultures. Using a standard viability/cytotoxicity assay (Live/Dead Viability/Cytotoxicity Kit, Molecular Probes), we have shown that at high strain rates, significant cell death and neural network disruption is evident (Fig. 10). The number of cells per construct is also amenable for standard biochemical assays. Moreover, the constructs may be fixed for immunocytochemistry across the full thickness, or the constructs may be embedded and sectioned using protocols similar to those applied for nervous system tissue.

7 Notes: 3-D In Vitro Injury Model

1. NOTE 1: This extra layer of tape makes the cylindrical holes wider than the dimensions of the protrusions (absent the tape), which facilitates the movement of the top plate during strain application.
2. NOTE 2: Be careful—do not remove PDMS mold as well.
3. NOTE 3: This step is not always necessary—if the tape is still in good condition it can be reused to make more chambers.
4. NOTE 4: Hippocampal regions may also be saved.

Fig. 8 (continued) Preloading, there were clear margins delineating neural somata and processes, indicating intact plasmalemma. However, immediately post-insult, there was a subset of cells that became calcein+ (white arrows in **a**), whereas some cells excluded calcein (black arrows in **a**). (**b**) In other cases, a widespread loss of definition was apparent in neurites as well as somata. Calcein uptake was tracked on a per-cell basis throughout loading (**c**). Within 500 ms post-insult, intracellular calcein intensity increased. This process continued throughout the first minute, resulting in processes gradually blending with the background (white arrows in **c**). (Figure reproduced from Cullen et al., 2011, Mary Ann Liebert, Inc.)

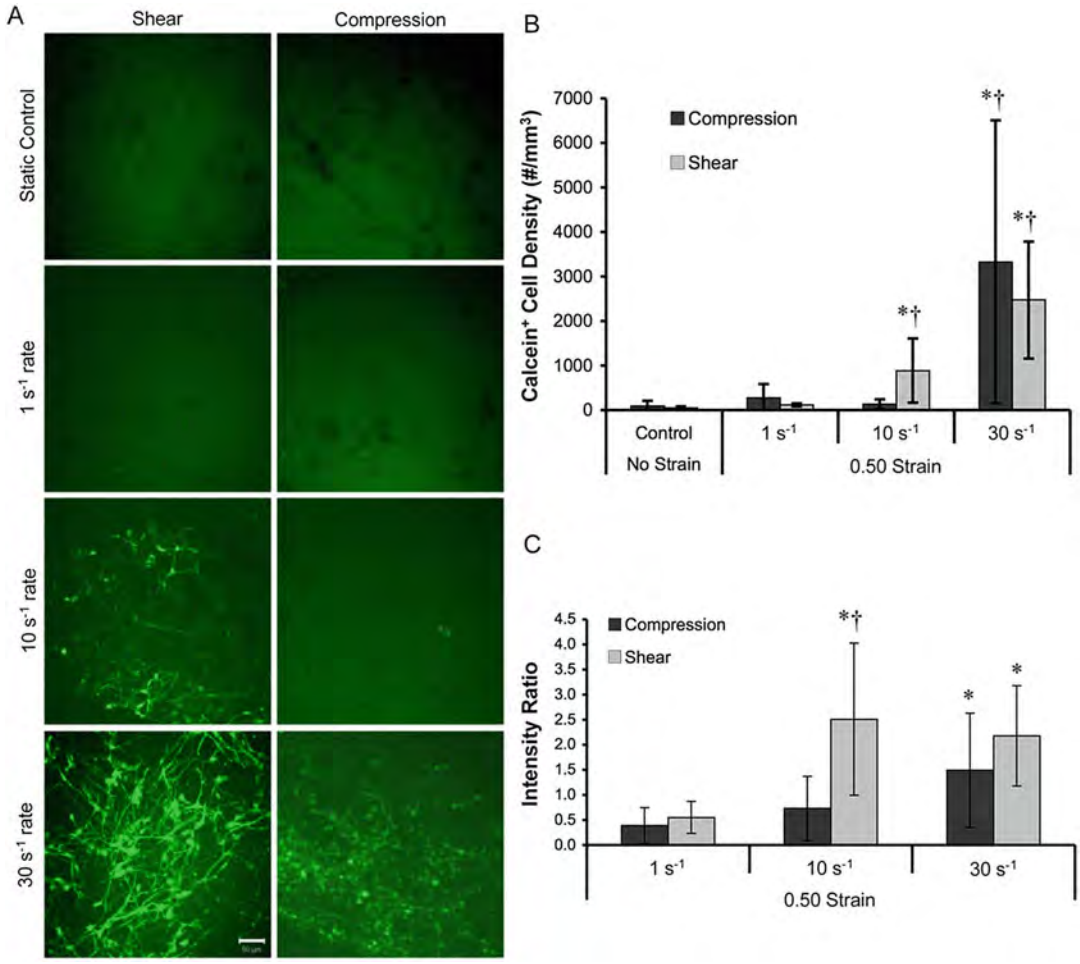


Fig. 9 Alterations in Acute Membrane Permeability in Shear versus Compression. (**a**) Representative confocal reconstructions of 3-D cultures following static control conditions or mechanical loading (0.50 strain at 1, 10, or 30 s^{-1} strain rate). (**b**) Calcein was added to the extracellular space prior to loading and enters permeable cells during or immediately following loading (reconstructions from 50-μm-thick z-stacks taken from cultures post-rinse; scale bar = 50 μm). Cell density of permeabilized (calcein+) cells. The 3-D cell density and percentage of calcein+ cells increased as a function of strain rate, and was highest at the maximum strain rate for both compressive and shear loading (*$p < 0.05$ versus static control; †$p < 0.05$ versus lower strain rates). (**c**) The degree of cell permeability following variable rate shear or compressive (0.50 strain) loading. There was a significant increase in the mean intensity of calcein+ cells versus quasi-static loading for both shear and compression at 30 s^{-1} and shear only at 10 s^{-1} (*$p < 0.05$). Also, at 10 s^{-1} loading, there was enhanced calcein uptake following shear versus compression (†$p < 0.05$). Note that the 3-D compression injury model is not described in this chapter, and the reader is encouraged to review the original publication, Cullen et al., 2011, for details. Data are mean ± standard deviation (Figure reproduced from Cullen et al., 2011, Mary Ann Liebert, Inc.)

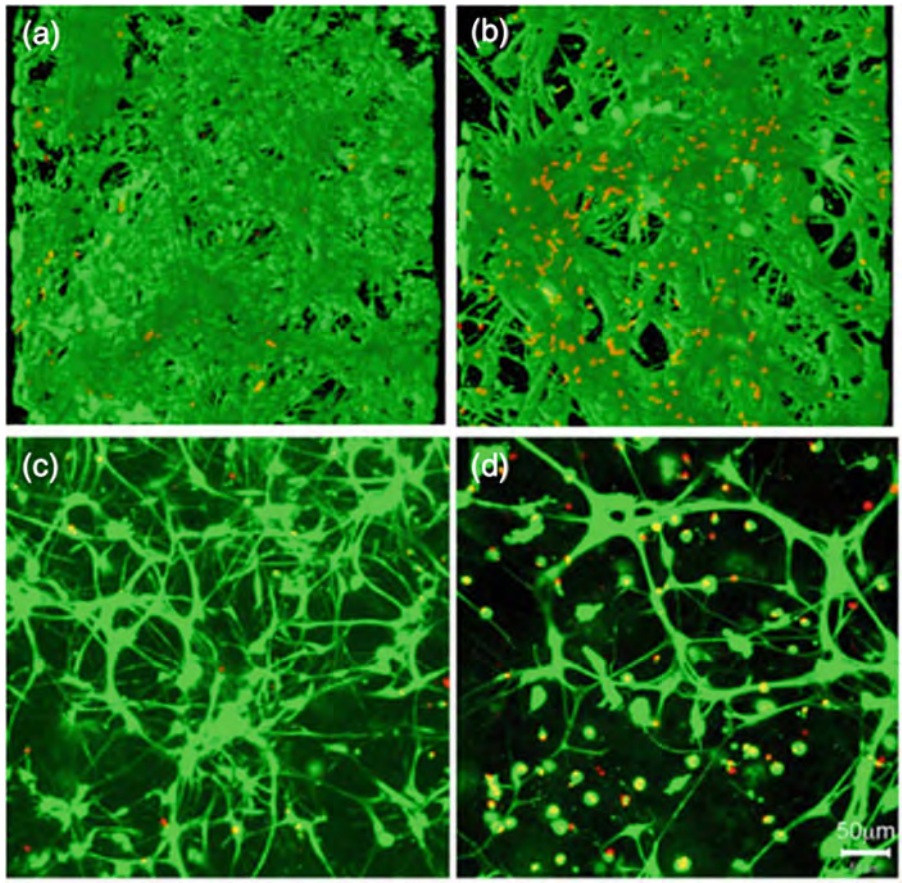


Fig. 10 3-D Neural Cocultures as an In Vitro Model of TBI. (**a**, **b**) Full thickness volumetric rendering and (**c**, **d**) optical slices showing live cells (green) and dead cells (red) in 3-D neuronal-astrocytic cocultures. High strain rate shear deformation (0.50 strain, 30 s^{-1}strain rate) causes significant cell death and neural network degradation at 48 h post-injury (**b**, **d**) compared to uninjured controls (**a**, **c**). Panels (**a**) and (**b**) reproduced with permission from Cullen et al., 2011, Begell House; panels (**c**) and (**d**) reprinted with permission from Cullen et al., 2007, Elsevier

5. NOTE 5: If not immediately proceeding with dissociation, cortices may be stored for 1–2 days. To store, rinse twice with cold HBSS (removing small debris). Add 2 mL L-15 supplemented with 2% B27. Wrap the tube in aluminum foil and place the tube on its side at 4 °C, ensuring that all cortices are submerged.
6. NOTE 6: Typically use a 1:40 dilution consisting of 10 μL cell solution + 190 μL HBSS and 200 μL trypan blue (let the diluted cell solution sit for 30 s prior to trypan blue addition). Ensure the diluted cell solution is well-mixed (gently triturate) and transfer 10 μL to each chamber of a hemocytometer. Count cells on hemocytometer to determine the total cell number and percent viability via trypan blue exclusion.

7. NOTE 7: Total cell yield should be 3–5 million cells/cortical hemisphere. Do not proceed if the yield is substantially less than this amount, or if neuronal viability is less than 90%.
8. NOTE 8: It is critical that the Matrigel remain cold throughout the plating procedure. If the Matrigel is too liquid at the time of plating, cells will sink to the bottom and not be distributed throughout the construct. Furthermore, warm temperatures cause the Matrigel to gel, so exposure to warmth must be avoided prior to placing Matrigel and cells into incubator. Handle the Matrigel with pipet tips that have been stored in a freezer.

References

1. Smith DH, Meaney DF (2000) Axonal damage in traumatic brain injury. Neuroscientist 6 (6):483–495
2. Cullen DK, Harris JP, Browne KD, Wolf JA, Duda JE, Meaney DF, Margulies SS, Smith DH (2016) A porcine model of traumatic brain injury via head rotational acceleration. Methods Mol Biol 1462:289–324. https://doi.org/10.1007/978-1-4939-3816-2_17
3. Margulies SS, Thibault LE, Gennarelli TA (1990) Physical model simulations of brain injury in the primate. J Biomech 23 (8):823–836
4. Meaney DF, Smith DH, Shreiber DI, Bain AC, Miller RT, Ross DT, Gennarelli TA (1995) Biomechanical analysis of experimental diffuse axonal injury. J Neurotrauma 12(4):689–694
5. Meaney DF, Thibault KL, Gennarelli TA, Thibault LE (1993) Experimental investigation of the relationship between head kinematics and intracranial tissue deformation. In: ASME Bioengineering Conference, Breckenridge, Colorado. ASME, pp 8–11
6. Magou GC, Guo Y, Choudhury M, Chen L, Hususan N, Masotti S, Pfister BJ (2011) Engineering a high throughput axon injury system. J Neurotrauma 28(11):2203–2218. https://doi.org/10.1089/neu.2010.1596
7. Smith DH, Wolf JA, Lusardi TA, Lee VM, Meaney DF (1999) High tolerance and delayed elastic response of cultured axons to dynamic stretch injury. J Neurosci 19 (11):4263–4269
8. Cargill RS 2nd, Thibault LE (1996) Acute alterations in [Ca2+]i in NG108-15 cells subjected to high strain rate deformation and chemical hypoxia: an in vitro model for neural trauma. J Neurotrauma 13(7):395–407
9. Ellis EF, McKinney JS, Willoughby KA, Liang S, Povlishock JT (1995) A new model for rapid stretch-induced injury of cells in culture: characterization of the model using astrocytes. J Neurotrauma 12(3):325–339
10. LaPlaca MC, Cullen DK, McLoughlin JJ, Cargill RS 2nd (2005) High rate shear strain of three-dimensional neural cell cultures: a new in vitro traumatic brain injury model. J Biomech 38(5):1093–1105
11. LaPlaca MC, Thibault LE (1997) An in vitro traumatic injury model to examine the response of neurons to a hydrodynamically-induced deformation. Ann Biomed Eng 25 (4):665–677
12. Morrison B 3rd, Elkin BS, Dolle JP, Yarmush ML (2011) In vitro models of traumatic brain injury. Annu Rev Biomed Eng 13:91–126. https://doi.org/10.1146/annurev-bioeng-071910-124706
13. Pfister BJ, Weihs TP, Betenbaugh M, Bao G (2003) An in vitro uniaxial stretch model for axonal injury. Ann Biomed Eng 31 (5):589–598
14. Cohen AS, Pfister BJ, Schwarzbach E, Sean Grady M, Goforth PB, Satin LS (2007) Injury-induced alterations in CNS electrophysiology. Prog Brain Res 161:143–169
15. LaPlaca MC, Simon CM, Prado GR, Cullen DK (2007) CNS injury biomechanics and experimental models. Prog Brain Res 161:13–26. https://doi.org/10.1016/S0079-6123(06)61002-9
16. Morrison B 3rd, Saatman KE, Meaney DF, McIntosh TK (1998) In vitro central nervous system models of mechanically induced trauma: a review. J Neurotrauma 15 (11):911–928
17. Cullen DK, Vernekar VN, LaPlaca MC (2011) Trauma-induced plasmalemma disruptions in three-dimensional neural cultures are dependent on strain modality and rate. J

Neurotrauma 28(11):2219–2233. https://doi.org/10.1089/neu.2011.1841

18. Iwata A, Stys PK, Wolf JA, Chen X-H, Taylor AG, Meaney DF, Smith DH (2004) Traumatic axonal injury induces proteolytic cleavage of the voltage-gated sodium channels modulated by tetrodotoxin and protease inhibitors. J Neurosci 24:4605–4613
19. Magou GC, Pfister BJ, Berlin JR (2015) Effect of acute stretch injury on action potential and network activity of rat neocortical neurons in culture. Brain Res 1624:525–535. https://doi.org/10.1016/j.brainres.2015.07.056
20. Pfister B, Oyler G, Betenbaugh M, Bao G (2004) The effects of BclXL and Bax overexpression on stretch-injury induced neural cell death. Mech Chem Biosyst 1(4):233–243
21. von Reyn CR, Mott RE, Siman R, Smith DH, Meaney DF (2012) Mechanisms of calpain mediated proteolysis of voltage gated sodium channel alpha-subunits following in vitro dynamic stretch injury. J Neurochem 121 (5):793–805. https://doi.org/10.1111/j.1471-4159.2012.07735.x
22. Abdul-Muneer PM, Conte AA, Haldar D, Long M, Patel RK, Santhakumar V, Overall CM, Pfister BJ (2017) Traumatic brain injury induced matrix metalloproteinase2 cleaves CXCL12alpha (stromal cell derived factor 1alpha) and causes neurodegeneration. Brain Behav Immun 59:190–199. https://doi.org/10.1016/j.bbi.2016.09.002
23. Kao CQ, Goforth PB, Ellis EF, Satin LS (2004) Potentiation of GABA(A) currents after mechanical injury of cortical neurons. J Neurotrauma 21(3):259–270
24. Rzigalinski BA, Weber JT, Willoughby KA, Ellis EF (1998) Intracellular free calcium dynamics in stretch-injured astrocytes. J Neurochem 70(6):2377–2385
25. Sherman SA, Phillips JK, Costa JT, Cho FS, Oungoulian SR, Finan JD (2016) Stretch injury of human induced pluripotent stem cell derived neurons in a 96 well format. Sci Rep 6:34097. https://doi.org/10.1038/srep34097
26. Lusardi TA, Rangan J, Sun D, Smith DH, Meaney DF (2004) A device to study the initiation and propagation of calcium transients in cultured neurons after mechanical stretch. Ann Biomed Eng 32(11):1546–1558
27. Wolf JA, Stys PK, Lusardi T, Meaney D, Smith DH (2001) Traumatic axonal injury induces calcium influx modulated by tetrodotoxin-sensitive sodium channels. J Neurosci 21 (6):1923–1930
28. Geddes DM, Cargill RS 2nd, LaPlaca MC (2003) Mechanical stretch to neurons results in a strain rate and magnitude-dependent increase in plasma membrane permeability. J Neurotrauma 20(10):1039–1049
29. Yuen TJ, Browne KD, Iwata A, Smith DH (2009) Sodium channelopathy induced by mild axonal trauma worsens outcome after a repeat injury. J Neurosci Res 87 (16):3620–3625. https://doi.org/10.1002/jnr.22161
30. Cullen DK, LaPlaca MC (2006) Neuronal response to high rate shear deformation depends on heterogeneity of the local strain field. J Neurotrauma 23(9):1304–1319. https://doi.org/10.1089/neu.2006.23.1304

Appendix A –Publication Cover 20
2017

Authors: E. Alay, M. Skotak, A. Misistia, N. Chandra

Title: "*Dynamic loads on human and animal surrogates at different test locations in compressed gas driven shock tubes*"

Journal Publication: Shock Waves, 28, 51-62, (2017), [17-20]

Shock Waves (2018) 28:51–62
https://doi.org/10.1007/s00193-017-0762-4

ORIGINAL ARTICLE

Dynamic loads on human and animal surrogates at different test locations in compressed-gas-driven shock tubes

E. Alay[1] · M. Skotak[1] · A. Misistia[1] · N. Chandra[1]

Received: 20 December 2016 / Revised: 30 August 2017 / Accepted: 1 September 2017 / Published online: 6 October 2017
© Springer-Verlag GmbH Germany 2017

Abstract Dynamic loads on specimens in live-fire conditions as well as at different locations within and outside compressed-gas-driven shock tubes are determined by both static and total blast overpressure–time pressure pulses. The biomechanical loading on the specimen is determined by surface pressures that combine the effects of static, dynamic, and reflected pressures and specimen geometry. Surface pressure is both space and time dependent; it varies as a function of size, shape, and external contour of the specimens. In this work, we used two sets of specimens: (1) anthropometric dummy head and (2) a surrogate rodent headform instrumented with pressure sensors and subjected them to blast waves in the interior and at the exit of the shock tube. We demonstrate in this work that while inside the shock tube the biomechanical loading as determined by various pressure measures closely aligns with live-fire data and shock wave theory, significant deviations are found when tests are performed outside.

Keywords Shock wave · Peak overpressure · Impulse · Shock tube · Static pressure · Total pressure · End effect · Surrogate head · Overpressure

Communicated by O. Petel and S. Ouellet.

EA and MS are joint primary authors.

✉ N. Chandra
namas.chandra@njit.edu

[1] Department of Biomedical Engineering, New Jersey Institute of Technology, Newark, NJ 07102-1982, USA

1 Introduction

Blast-induced neurotrauma (BINT) has been recognized as a major health problem, has affected approximately 1.64 million US service members deployed in Operations Enduring Freedom and Iraqi Freedom (OEF/OIF) in Afghanistan and Iraq [1], and remains a major concern in combat veterans [2] and active military personnel [3]. Blast-related injuries have been identified as the "invisible wounds of war": These account for nearly 70% as a cause of injuries among wounded service members and frequently result in mild traumatic brain injury (mTBI) [4]. In an idealized single isolated high-explosive blast scenario, we can define near-, mid-, and far-fields based on the strength of the explosive and stand-off distance between the object and the center of the explosion. In the study of BINT etiology, we are mostly concerned with the mid- to far-field blast effects, where the positive pressure pulse [sharply rising shock front followed by exponentially decaying blast overpressure (BOP)] determines the biomechanical loading [5]. In this range, the effect of fire, heat and toxic gases, and fragmentation is negligible, but the acceleration/deceleration may still be a contributing factor. The magnitude of BOP, duration, and impulse are readily computed in software such as ConWep [6], which then can be curve-fitted to empirical data [7]. The agreement between live-fire data and ConWep predictions is quite good. These pressure–time profiles are obtained as a function of the "TNT equivalence of explosives" and radial distances from the explosion epicenter. The implicit assumption in these BOP–time curves is that the shock-blast waves are planar in nature at the large distance from the epicenter relevant to BINT; here, the radius of expanding shock wave is large compared to the radius of the charge [8].

Explosive blasts cause significant damage to the civil structures they encounter; they also cause short- and long-

term injuries to biological matters in their pathway. A number of experimental approaches were devised to study the effect of the blast waves on civil structures and to identify the blast effects on biological specimens, including: live explosives field testing [9,10], explosive-driven shock tubes [11,12], combustion (detonation)-driven shock tubes [13,14], and compressed-gas-driven shock tubes [15]. Shock tubes have been used to simulate blast waves for more than a century to study a variety of high-temperature gas dynamics phenomena and deflagration–detonation in combustion [16]. In the late 1950s and 1960s a group from the Lovelace Foundation led by Bowen and Richmond conducted a series of blast experiments on small and large animals to study blast lung injuries [17]. This work was one of the very first systematic studies evaluating living organisms' response to shock wave impact, with the explicit goal of relating BOP to inflicted systemic injuries and mortality. The current problem of BINT is quite different from that of lung injuries in terms of fundamental mechanisms, short- and long-term health effects, and design criteria of systems for personal protection [18]. Thus, in the last two decades, shock tubes and live explosives field testing schemes have been designed to study BINT and personnel protection systems. A recent review article by Kobeissy and his colleagues shows that out of 49 studies, only 8 used field testing and that 92% of shock tubes (33 out of 36) used were compressed-gas-driven shock tubes (see Table 1 in Ref. [19]).

2 Shock-blast loading in explosions and in shock tubes

2.1 Scope of shock tube testing

Compressed-gas-driven shock tubes have been extensively used to simulate live-fire explosive conditions in the laboratory, mainly because of their simpler designs and ease of operations [19]. The primary purpose of these devices is to generate pressure–time loading profiles virtually identical with conditions experienced by warfighters in the theater, i.e., closely simulating a practical range of explosive strengths at realistic stand-off distances. Generally, these experiments serve two different purposes: (1) to examine the efficacy of protective systems (e.g., helmets, eye wear, ear protection) using surrogate heads and (2) to understand the injury severity and mechanisms using live animal models. Dynamic pressure forces induced by the shock waves are determined by not only the magnitude of the static BOP–time pulse, but also the size, shape, and orientation of the subjects with respect to the incident blast wave. Recently, Needham and coauthors critically examined the issue of right measurement methods and emphasized the need to use the right pressure measures in describing the loading conditions [20].

2.2 Physics of blast wave and dynamic loading parameters

The intensity of blast-induced biomechanical loading is usually described in terms of the Friedlander equation [21]. One form of this equation is as follows:

$$p(t) = p_0 \left(1 - \frac{t}{t_\mathrm{d}}\right) \mathrm{e}^{-\left(\frac{t}{\alpha}\right)}, \tag{1}$$

where p_0 represents the BOP, t_d is the positive time duration, and α is the time decay constant [22]. In general, p_0 is construed as static (side-on) pressure, which is the pressure measured by a gauge that excludes the effect of the velocity of air particles. Such measurements can be taken by having a pressure probe that moves with the same velocity of the particles. In a more practical sense, a flat surface parallel to the flow can be constructed that brings the particle motion to zero at the surface, and when the pressure is measured normal to this surface then that represents the static pressure. In the case of the shock tube, measurement on the side walls yields this value. However, care needs to be exercised so that the flat surface of the sensor is perfectly aligned with the wall, without any protrusion or cavity and further that the sensors are isolated from the vibration of the shock tube walls. Equation (1) describes the blast overpressure–time of the blast wave at a given location. In explosive waves, there will be changes in both the pressure and duration as the wave propagates away from the epicenter adapting ever expanding hemispherical (for ground explosion) or spherical shape (for explosions initiated with charge suspended above the surface).

If a surface is acted upon by a normal surface pressure $p_\mathrm{sur}(x)$ on a flat surface, then the force $\overline{F}$ on that surface is given by $\overline{F} = \int p_\mathrm{sur}(x)\mathrm{d}x$. Here the shock is assumed to flow normal to the surface, and the force is not static, but induced by the shock wave; then, we need to identify the right surface pressure measures to use in the integral. We can identify four different pressure types in the definition of $p_\mathrm{sur}(x)$ in shock wave propagation problems: (1) static (side-on) pressure (p_0), (2) total (or stagnation) pressure (p_tot, measured in the head-on sensor orientation), (3) p_dyn dynamic pressure (for more details the interested reader is referred to chapter 3 in [23]), and (4) reflection pressure, p_ref. If a blast wave interacts with a surface, the surface pressure p_sur will both vary along different points on the body and evolve with time and thus $p_\mathrm{sur} = p_\mathrm{sur}(x, t)$. The pressure variation at a given surface point is then a function of not only the magnitude and duration of incident static pressure, $p_0(t)$, given by (1), but also the size, rigidity, fixedness, and orientation of the target during the shock–structure interaction. Pressure on the surface can change depending on the location of the incident angle of the surface with respect to the direction of propaga-

tion of the shock wave and its strength (for more details, see chapter 10 in reference [22]).

In order to compute the load in a section of a surface, it is important to understand the relationship between all four types of pressure measures. For air blast, the shock front is an extremely thin layer (micrometers thick) across which many thermodynamic quantities such as density, pressure, temperature, enthalpy, and energy density change abruptly as a step function. Many of these quantities can be computed using Rankine–Hugoniot relationships and gas dynamics equations. The Appendix describes the various relationships between different pressure quantities across a shock front in a blast wave, based on a single input parameter the blast overpressure p_o.

2.3 Dynamic shock loading on structures

When a blast wave encounters a target, the force on the body is determined by the time-dependent pressure acting on the surface. When the shock front of the blast wave first impinges on a semi-infinite plane, then the instantaneous surface pressure increases to the level described by the reflected pressure (see the Appendix for details) p_{ref} and not any other three pressure measures discussed earlier. The magnitude of p_{ref} is significantly higher than any one of them and is sometimes expressed as the reflection ratio Λ (reflection over static pressure) with typical values between 2 and 8 of static blast overpressure value. Thus, the body might experience significantly higher load and hence higher force than described by the numerical value of the static pressure. However, for any unyielding target with finite size, the reflected pressure is rapidly dissipated. Moreover, when the reflection occurs at the edges of an object, release (tensile) waves are generated that travel along the surface reducing the surface pressure. Thus, the type of pressure and resulting forces are quite complex and depend on the strength and duration of the wave, size, geometry, and boundary conditions of the target.

In a free-field explosive detonation, the shock wave is created by almost instantaneous solid-to-gas conversion with accompanying exothermal combustion reaction and shrapnel projected outward. However, in a compressed-gas shock tube the mechanics of formation of the shock wave is quite different. Here, high-pressure driver gas compresses the air in the downstream tube causing generation of a shock front. Near the breech (i.e., close to the shock tube membranes) the shock wave is not fully formed (see Ref. [24] and references therein for details), develops as fully planar shock front at a further distance, and continues to be planar until it reaches the exit at which point a spherical release wave travels from the edges of the shock tube. Exit conditions in the shock tube are highly detrimental to shock wave characteristics, particularly duration and planarity of and hence faithful reproduction of field explosions [25,26]. However, even when the specimen is kept inside of the shock tube it can still be affected by rarefaction wave traveling inside when the end of the shock tube is not engineered properly [7,25]. The closer the specimen location to the end of the shock tube, the more pronounced the end effects will be on the loading. Capturing these differences requires an understanding of these phenomena, combined with careful planning and elaborate experimental setup. These kinds of measurements are very often not considered important or are relegated as outside of the scope of research in the BINT domain.

In this contribution we are concerned with quantification of loading in two locations commonly used in laboratory shock wave testing: (1) inside of the test section (marked as T4 in Fig. 1a) and (2) outside of the shock tube (marked as PP in Fig. 1a). To compare these two very different testing environments we have measured static and total pressures (Fig. 1b, c) at three discrete blast intensities with the empty shock tube. The static pressure inside of the shock tube was measured by the sensor mounted on the wall, while a pencil probe sensor mounted 4 in. outside and on the axis of symmetry of the shock tube was used to measure incident static pressure outside (Fig. 1a). The total pressure measurements were taken using modified pencil probe with a Kulite sensor mounted on the tip (Fig. 1b, c) and positioned at the same distance from the breech as static pressure sensors. The cross section of the total pressure sensor is small compared to the cross-sectional area of the shock tube, and hence, no reflections were observed in our experiments. Measurement of the incident static and total pressures inside of the shock tube was taken simultaneously, while for measurements outside two sets of measurements were necessary to avoid inconsistent results caused by the presence of additional sensors. First, we measured the static pressure, which was then followed by total pressure recording, while keeping the sensing element in exactly the same location.

3 Experimental methods

3.1 Shock wave generators

Two shock tubes (9 and 28 in. square cross section) used in this work are housed at the Shock Wave Testing facility at the New Jersey Institute of Technology. Both feature the same basic components (Fig. 1a): (1) breech with adjustable volume, (2) transition section with variable geometry, (3) square cross section test section, with laminate glass windows to facilitate high-speed video monitoring of the specimen during the shock wave exposure, and (4) optional reflector end-plate. The larger shock tube is also equipped with a catch tank used to attenuate the sound generated during experimentation. Both shock tubes have 6-m-long driven section and were described and characterized in detail previously [7,8,27–29]. In this study we used compressed helium as the

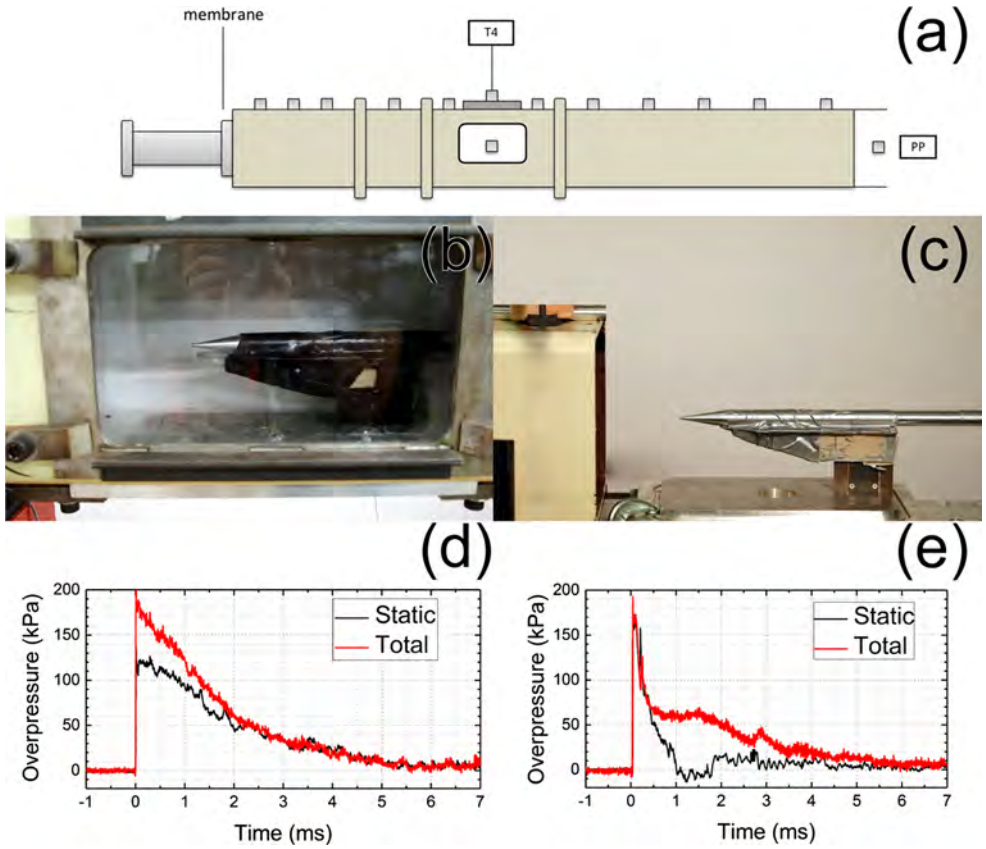


Fig. 1 Schematic representation of the shock tube indicating the location of sensors used to measure static and total pressures (**a**). For the inside location the T4 was used (2.8 m from breech), while testing outside was performed 0.1 m away from the mouth (PP location). Inside of the tube, the shock wave is fully developed and planar in T4, and thus incident static pressure is measured using wall mounted sensor, while total pressure is measured with modified pencil probe sensor in the middle with the tip aligned with T4 sensor (**b**). On the outside planarity of the shock wave is lost, and thus both total and static pressures were measured at the same point (**c**). Representative overpressure profiles for both locations are presented in (**d**) and (**e**)

driver gas and Mylar membranes in three thicknesses: 20, 40, and 60 mil (1 mil = 0.001 in.) were used to control the intensity of a single planar shock wave (with duration of 5–6 ms, Fig. 2). We investigated the effect of location on pressure profiles of generated shock waves and investigated its loading effect on a surrogate head models.

3.2 Incident static and total overpressure measurement

Measurement of the incident static overpressure shock wave was taken using a series of pressure sensors distributed along the shock tube (Fig. 1c in [7]). Pressure sensors are mounted using 0.5 in. thick holder brackets and attached on top of the shock tube in predetermined standard locations. Typically, BOP–time pulses are measured in six locations, but for brevity we are reporting only overpressures in the test section (T4 location). Fast-response piezoelectric sensors model 134A24 (PCB Piezotronics, Depew, NY) were used for measurements of static overpressures inside of the shock tube. The static pressure outside of the shock tube was measured 4 in. from the mouth of the shock tube (Fig. 1, PP location) using PCB 137B24B Free Field Blast ICP® pressure probe (PCB Piezotronics, Depew, NY).

The total overpressure measurement was taken using XCL-072-200A (Kulite Semiconductor Products, Inc., Leonia, NJ) sensor mounted in the specifically designed enclosure. The enclosure is 16 in. long, 0.9 in. OD stainless steel rod with a bore-through hole for signal and power leads and a pressure sensor mounted on the tip (Fig. 1b, c). The sensor is attached to the aerodynamic holder with minimized and streamlined cross section. This setup permits total pressure measurements undisturbed by reflections or other artifacts caused by obstruction of flow (Figs. 1, 2). All pressures were recorded at a sampling frequency of 1 MHz.

3.3 Surface overpressure measurements on the headform

Overpressure measurements on the surface of the modified Facial and Ocular Countermeasures Safety (FOCUS) head-

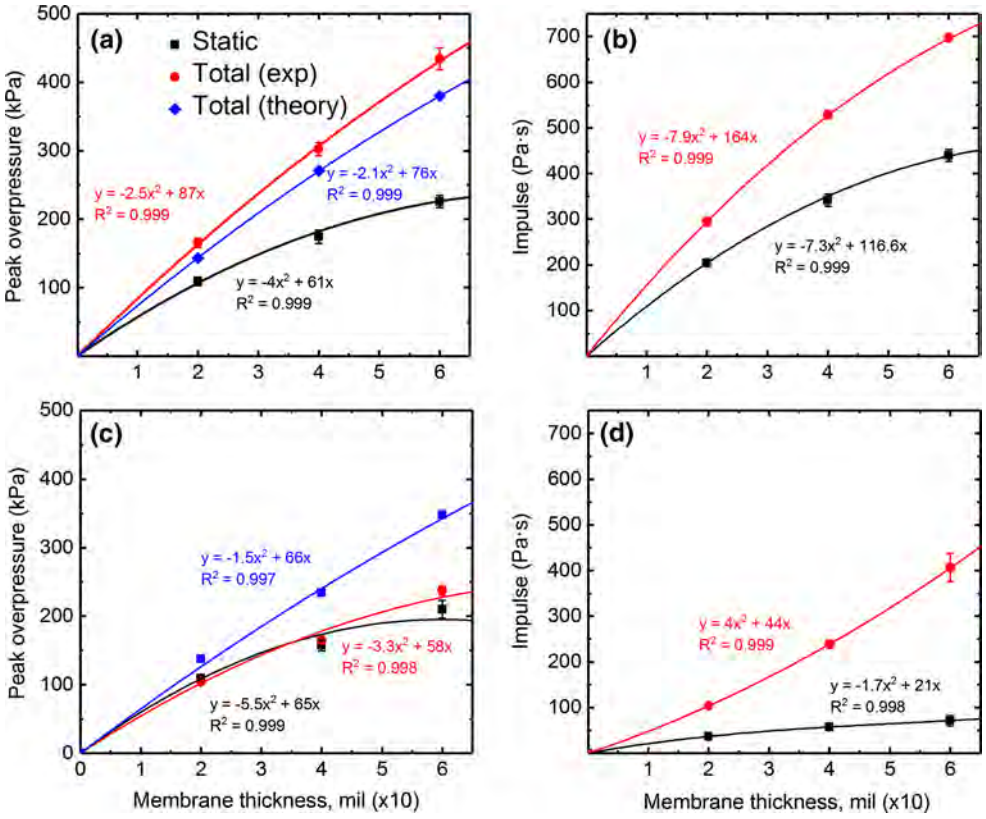


Fig. 2 The peak overpressure (**a**, **c**) and impulse (**b**, **d**) for static and total pressure (denoted as "exp") measured inside (**a**, **c**) and outside (**b**, **d**) were quantified for three different shock wave intensities generated using the following Mylar membrane thicknesses: 20, 40, and 60 mil (mil is 0.001 in.). The average values of 6 tests were then fitted with second-order polynomial function. Theoretical values for total pressure corresponding to experimental conditions and fitted functions are also presented for comparison (denoted as "theory")

form (Humanetics, Inc.) were performed using a series of five high-frequency ICP® pressure sensors model 102B06 (PCB Piezotronics, Depew, NY). The headform had skin and eyes removed for simplicity and to facilitate sensor installation in the hard shell made of plastic. The headform cross-sectional area in zero degrees orientation (facing the incoming shock wave) is 31.5 sq. in. (7×4.5 in.). Sensors were mounted along the midline of the headform from front to back at 45° intervals (Fig. 3). The headform was mounted in the test section (T4 location) of the 28 in. square cross section shock tube and 4 in. outside (PP location) using customized mounting plate and Hybrid III neck with an internal steel rope (which is a part of the device) tightened to increase neck stiffness and thus prevent headform motion. The assembly was exposed to a single blast wave with an intensity of 130 kPa peak overpressure (measured at T4, Fig. 4) in the 28 in. square cross section shock tube, and tests in each location were repeated four times.

3.4 Pressure measurements using surrogate rodent headform

The anatomically accurate surrogate rodent headform (SRH) was designed in Pro/Engineer Wildfire 5 (PTC, Boston, MA) CAD software and printed using polylactic acid (PLA) on the Ultimaker 2 Extended 3D printer (Ultimaker B.V., Netherlands). The high-density print mode was selected. The fixture of the rat was equipped with two Kulite pressure sensors of model number XCL-072 and XCL-152-17BARA (Kulite Semiconductor Products, Inc., Leonia, NJ). The XCL-152 was mounted at the nose to measure the stagnation pressure, and the XCL-072 was mounted at a 25° angle tangent to that of the muzzle stop. This model was used to measure the pressure experienced by an animal model exposed to a blast, and hence geometrical features of the snout and head were carefully replicated. The 3D-printed fixture was attached to a stainless steel rod with 0.9 in. OD, which was mounted

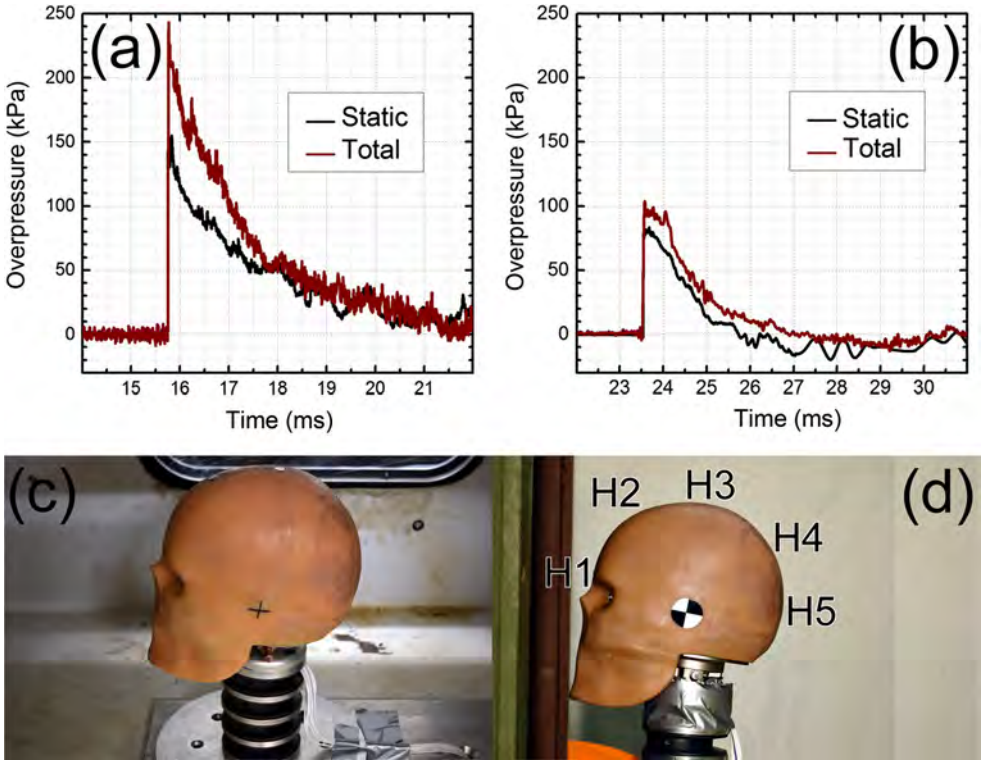


Fig. 3 Representative pressure profiles recorded in the test section inside (**a**) and outside (**b**) for the purpose of calibration of the shock tube before testing, without the headform. The FOCUS headform mounted on a Hybrid III neck and attached in the test section located inside (**c**) and outside (**d**) of the shock tube. Location of five pressure sensors (H1–H5) monitoring surface pressure on the headform during blast exposure is schematically presented (**d**)

on two steel posts with copper bands (Fig. 5). The support was designed with optimized aerodynamic parameters to minimize obstruction and reflections during experiments in the shock tube. The SRH has a cross-sectional area of approx. 1 sq. in. and was exposed to a single shock wave with 130 kPa nominal intensity in the 9 in. shock tube in two locations [inside (T4) and outside (PP)]. All tests were repeated four times.

3.5 Statistical analysis

All shock wave exposure experiments reported therein were repeated four times ($n = 4$), unless specified otherwise, and are expressed as an average value and standard deviation. The two-tailed t-test was used to discern differences between test groups, and statistical significance threshold was set at $p < 0.05$.

4 Results and discussion

Only in recent years, the importance of specimen location was recognized as an important factor in proper replication of field conditions in the study of BINT [25,29]. However, while there has been significant progress in this area, there still exists controversy regarding the applicability of the testing outside of the shock tube as a valid model for field conditions, considering a number of published research articles which use this injury paradigm [30,31]. This is particularly true for non-trivial aspects of the shock tube testing, which includes comprehensive specimen monitoring and evaluation of multiple parameters, including but not limited to (1) static and dynamic pressure, (2) acceleration of the specimen (restraint), and (3) pressure distribution on the specimen. Usually, this important step in discriminating whether appropriate injury conditions are comparable to open-field blast is limited to reporting static (incident) pressure [31]; however, it has been demonstrated that the conditions on the outside are far more complex and assumption of transferability between the open field and exit of the shock tube cannot be based on a single static pressure criterion [25]. In this paper, we further advance the understanding of the respective differences between testing conditions inside versus outside of the shock tube, by examining the static and dynamic components, as well as the distribution of pressure profiles on two surrogate head models. We developed a simple normalization methodology which aids in discerning the differences of experimental measurements between two testing locations,

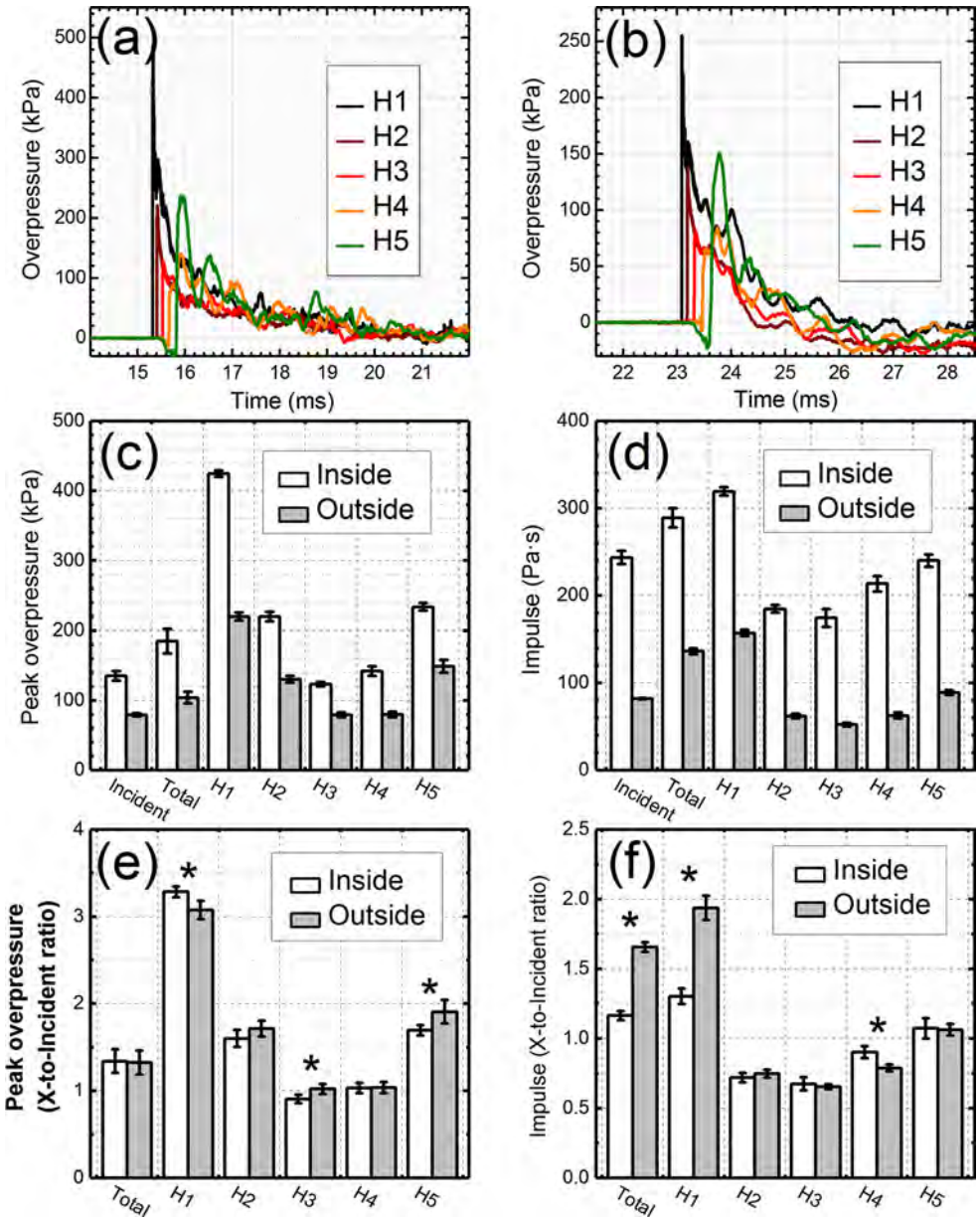


Fig. 4 Evolution of pressure profiles on the surface of the headform during blast exposure at 130 kPa incident static pressure in the test section (corresponds to 80 kPa incident static pressure on the outside), when headform was mounted inside (**a**) or outside (**b**) of the shock tube. Comparison of peak overpressure (**c**) and impulse (**d**) between these two respective locations as reported by static and total pressure sensors mounted on the headform (H1–H5). The experimental variables were normalized using incident peak overpressure and impulse to facilitate comparison between respective locations (**e**, **f**). Statistically significant differences are indicated with an asterisk ($p < 0.05$)

which do not rely on matching any particular characteristic parameters.

Total and static pressure profiles recorded inside versus outside of the shock tube reveal stark differences between these two locations (Fig. 1d, e). There are obvious differences in duration of the static pressure pulse, which is justifiable considering the environment of the shock wave travel: inside of the tube the shock wave is constrained to a 1D space, while on the outside is released into unrestricted 3D space. More importantly, in the area near the exit of the shock tube, the physics of the decompression of the shock wave is extremely complex, with the formation of highly anisotropic flows and compressible vortices, which were extensively documented in past decades [8,26,32–34]. The Complexity of the flow dynamics on the outside of the shock tube is so great that it is imperative to position the specimen in the same location with pinpoint precision in order to have the same loading conditions [8]. The degradation of "ideal" waveform is also

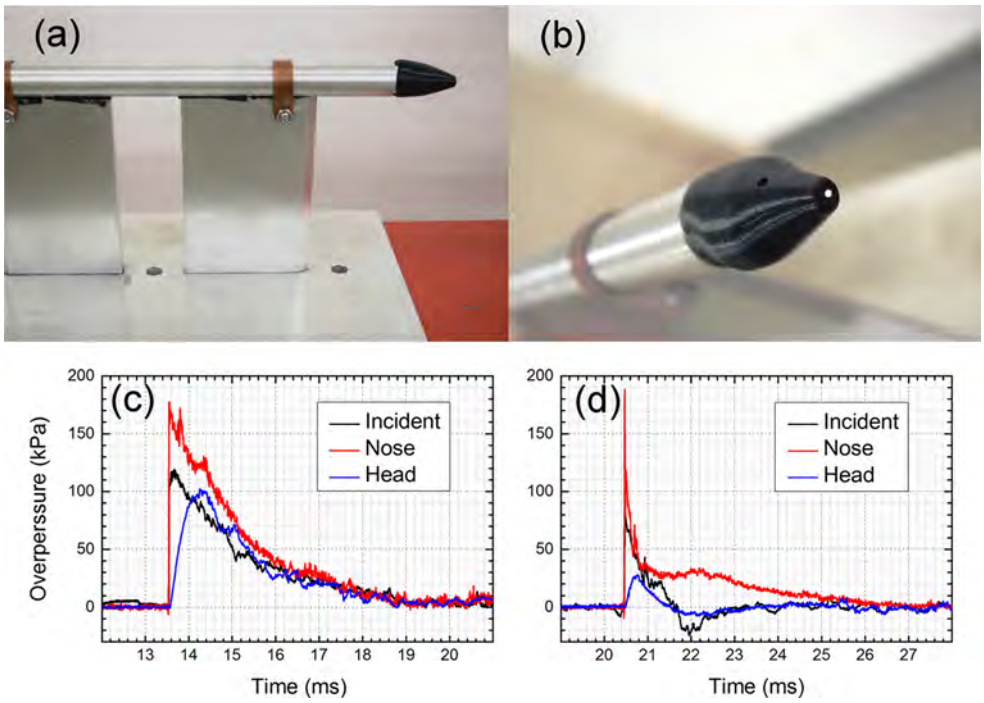


Fig. 5 Overview of composite surrogate rat head (**a**), and the detailed view of the complex shape of 3D-printed polymeric head housing two pressure sensors (the circular mounting port and white dot at the tip). The representative pressure profiles recorded using SRH, which was positioned inside (**c**) or outside (**d**) of the shock tube and exposed to blast wave with 120 kPa BOP. Profiles denoted as incident are static pressure

obvious in the total pressure traces, but in this case, the decay shape does not affect the durations which are comparable in both cases (5.5–6 ms, Fig. 1d, e). We fitted the respective peak overpressure and impulse values as a function of an operating parameter of the shock tube (Mylar membrane thickness) to gain insight into how testing location affects these two characteristics. Indeed, there are stark differences which are obvious (Fig. 2). The total pressure continues to increase as a function of static pressure, as the particle velocity increases in the inside of the tube. This is indicative of the ideal shock wave conditions, which is not the case for the measurements taken outside (Fig. 2a, c). On the other hand, the impulse inside and on the outside of the shock tube is a quadratic function, but the fitted parameter has a negative sign for inside (−1.15, Fig. 2b) and positive sign (0.57, Fig. 2d) for the outside of the shock tube. The total-to-static pressure ratio increases in the order of 1.44, 1.55, and 1.58 for both peak overpressure and impulse (inside) for 2, 4, and 6 membranes, respectively. However, on the outside it remains almost constant (0.96, 1.05, and 1.13) for peak overpressure and drastically increases (0.62, 1.28, and 4.50) for impulse values in the same range of membrane thickness. This indicates how nonlinear the loading changes on the outside and how progressively more dominant is the dynamic part of the loading with increasing blast intensity. The theoretical and experimental total pressure values for the inside location match well, and experimental values exceed the theory with a margin within experimental error. This is expected since the finite size of the sensor might contribute toward slight overestimation of experimental values. More importantly, for the outside location, this relationship is reversed and theoretical values appear to exceed the experiment by a large margin, which indicates strong deviation from ideal shock loading conditions.

Experiments with the FOCUS headform instrumented with five sensors along the mid-sagittal plane were used to further the understanding of the differences in the loading conditions between the two locations. Our experimental design included measurement of the total and static pressures, similar to that performed for the 9 in. square cross section (Fig. 3a, b). Pressure profiles indicate that while inside, they are very similar to those recorded in the smaller shock tube, the pressures for the outside location look different. This can be explained by off-axis placement of both sensors for 28 in. shock tube measurements, i.e., they were positioned 4 in. above the plane of the bottom wall, in the same location where the headform would be mounted (Fig. 3d). Representative pressure profiles recorded by five sensors mounted flush on the surface of the headform are presented in Fig. 4a, b. There are a number of similarities between them, which result from headform geometry: The general pattern of pressure intensity changes is the same in both cases. We observed, similarly to

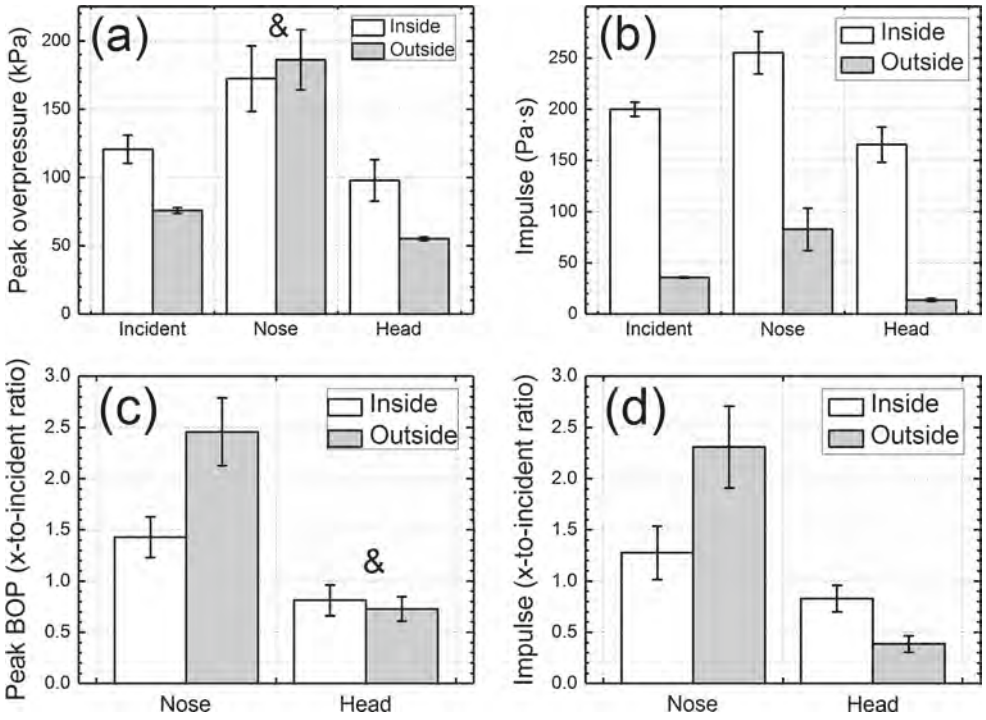


Fig. 6 Results of quantification of blast exposure experiments utilizing SRH: comparison of peak overpressure (**a**) and impulse (**b**) values recorded by incident (static pressure), nose and head sensors for inside and outside locations. Normalized peak overpressure (**c**) and impulse (**d**) in SRH experiments for both testing locations are presented. Ampersand (&) indicates test groups where no statistically significant differences are established ($p > 0.05$), while in other cases there is statistically significant difference

our earlier experiments with analogous headform [28], H1 sensor mounted on the forehead measures the reflected pressure p_{ref}, H3 sensor follows the free-field conditions of static and total pressure components while H4 sensor indicates lower pressure due to flow separation, and finally elevated pressure was reported by H5 sensor mounted on the back of the headform when the shock wave flow reunites [28]. Quantification of all performed experiments (Fig. 4c, d) revealed direct comparison of results from both locations is not trivial. Thus, we normalized the data using static peak overpressure and impulse values (Fig. 4e, f). Normalization is simply a division of respective peak overpressure and impulse values by peak overpressure and impulse of the incident shock wave (static overpressure) recorded in the specific test location. This arithmetic transformation allows direct comparison of the data generated at different blast intensities and test locations. It is clear that normalized data reveal virtually no changes in peak overpressure values among all locations on the headform used in this experiment and total pressure (Fig. 4e). Statistically significant differences were detected for H1, H3, and H5 sensors with overall difference in normalized peak overpressure of 6–12%. The impulse values for the total and H1 sensors are higher by 40–50% for the outside location. The impulse values reported by headform sensors follow a similar trend as peak overpressure: H1 is the highest and impulse decreases reaching a minimum at H3 and then increases gradually at H4 and H5 locations (Fig. 4f). Thus, it would appear that pressure on the surfaces facing the shock wave has exaggerated loading than if only static pressure were considered.

Additional verification experiments were performed using a surrogate rodent headform mounted on specifically designed adapter designed with optimized aerodynamic for shock tube testing (Fig. 5). The SRH has two sensors mounted flush with the surface only because of the limited space in spite of the miniature sensors used in this design: one nose pointing parallel to the flow and one on the head at 25° angle. We repeated the testing routine for the FOCUS headform and tested SRH inside and in the outside of the shock tube at 130 kPa nominal blast intensity (as reported by T4 sensor, Fig. 5a). The pressure profile recorded by the "head" sensor lost its shock characteristics based on substantially increased rise time, which reached 0.6 ms (inside) and 0.4 ms (outside) as compared to a $1-2\,\mu$s for static and total pressures (Fig. 5c, d). Quantification of pressure profiles revealed there are no universal observations which can be drawn from these data (Fig. 6a, b), similarly to tests performed with human surrogate headform. Normalization of the data using incident shock wave characteristics (peak overpressure and impulse) allowed extraction of relationships

present in this system. Similarly to FOCUS headform, the normalized peak overpressure recorded by "head" sensor in both testing locations is comparable, but the same is not true for "nose" sensor where outside signal value increased by more than 60%. The "nose" sensor is not simply a replacement of the total pressure sensor in spite of relatively similar geometry, and this strong disparity between the total pressure and "nose" sensors indicates how important the relationship between geometry of the test subject and the testing location is. It would appear that a smaller test specimen is more susceptible to overload than a larger one, which, if true, is a rather grim conclusion for rodent testing on the outside of the shock tube. Nonetheless, normalized impulse (Fig. 6d) reveals relationship between testing locations similar to normalized peak overpressure. Interestingly, the "head" sensor follows the trend observed in the case of H4 sensor on the headform, i.e., normalized peak overpressure is of similar magnitude for both testing locations, while normalized impulse is decreased when the specimen is mounted on the outside. It is imperative to note average nose-to-head peak overpressure ratio in experiments with SRH (1.43) performed at 130 kPa blast overpressure (BOP) is exactly in the same range as obtained in the past for expired rats exposed to a wide range of blast intensities, i.e., 1.38–1.48 at 130–290 kPa BOP [35]. The same observation is true for the impulse values for overpressure profiles recorded using a nose sensor on SRH versus expired rats: 1.27 (SRH) and 1.27 (rat).

5 Conclusions

The shock tube experimentation requires careful evaluation of the incident static and total pressures and informed decision regarding the specimen location. Measurements of static and total pressures in two locations, inside (2.8 m from breech) and outside (4 in. from the mouth of the shock tube) of the 9 in. square cross section shock tube, indicate that these locations are not equivalent; hence, the results obtained from experimentation in these specific locations should not be equated or even compared with each other. There is also growing evidence that the interior of the shock tube is preferred for correct replication of free-field blast conditions and offers better control in order to isolate effects of the primary blast. Using two surrogate headforms, we provide evidence regarding the differences between shock tube testing inside and outside. We used peak overpressure and impulse to gauge the differences, and experimental data were normalized using incident values extracted from experimental data recorded in respective locations. Experiments with surrogate human headform revealed that while normalized peak overpressures are comparable in both locations, the same is not true for impulse values, which were significantly higher for shock wave facing sensors when the headform was mounted on the outside. The surrogate rodent headform experiments revealed an even more complex issue scenario: The surface pressure and impulse on the nose of the surrogate were drastically higher when tested on the outside with respect to inside. We have also noted strong pressure gradients for the outside location, i.e., when the shock wave is unconstrained and is free to expand in three-dimensional space. All these observations based on carefully executed experiments suggest the inside of the shock tube as the preferred location for testing. This is particularly true for the use of small rodents as models in primary BINT research area.

Acknowledgements This work was supported by Grant No. 14059001 (total pressure measurements and quantification in 9 in. shock tube) entitled "Primary Blast Injury Criteria for Animal/Human TBI Models using Field Validated Shock Tubes" received from the US Army Medical Research and Materiel Command. The headform testing was performed using funds received from Award No. W91CRB-16-C-0025 (PEO Soldier) and is gratefully acknowledged.

Appendix

Calculation of static, dynamic, stagnation, and reflection pressures during blast

Pressures are measured both in live-fire and shock tubes using pressure gauges with time resolution sufficient to capture rise times of the order of a few microseconds, and hence the sensors and the data acquisition system should be rated with 1 MHz or higher sampling frequency. If blast overpressure p_0^{gauge} is measured as side-on pressure (either in the field or shock tube walls), then they are typically expressed in terms of either kPa or psi. This p_0^{gauge} should be converted to bars using $p_0 = p_0^{\text{gauge}}/101.32$ for kPa or $p_0 = p_0^{\text{gauge}}/14.7$ for psi; thus, p_0 is in bars. In the literature, the suffix x typically indicates ambient un-shocked conditions, while the y denotes values within the shocked gas. In this Appendix, we are mainly concerned with air blast with ambient condition denoted by $T_x = 15\,^{\circ}\text{C} = 288\,\text{K}$; pressure $= 1.01325$ bars; density $= 1.225\,\text{kg/m}^3$ and at sea level.

Some of the basic quantities can be found using the following equations.

$$\frac{p_y}{p_x} = \frac{p_0 + 1.0132}{1.0132} \tag{2}$$

$$M = \sqrt{\frac{1}{7}\left(1 + 6\frac{p_y}{p_x}\right)} \tag{3}$$

$$\frac{T_y}{T_x} = \frac{\left(5 + M^2\right)\left(7M^2 - 1\right)}{36M^2}. \tag{4}$$

Then the acoustic velocity in the shocked medium can be computed. Recall that velocity depends on the atomic vibration which depends on the temperature. If $a_x = 340\,\mathrm{m/s}$, then a_y the acoustic velocity in the shock can be computed using

$$\frac{a_y}{a_x} = \sqrt{\frac{T_y}{T_x}}. \tag{5}$$

The particle velocity in the shock tube which is the main cause of dynamic pressure can also be calculated. The particle velocity u_p just behind the shock front can be calculated using

$$u_\mathrm{p} = \frac{5\left(M^2-1\right)}{6M} a_x. \tag{6}$$

Stagnation pressure p_stag is the absolute pressure, when a moving flow stream with particle velocity is brought to rest isentropically. It is given by

$$p_\mathrm{stag} = \left[1 + \frac{\left(\frac{u_\mathrm{p}}{a_x}\right)^2}{5\left(\frac{T_y}{T_x}\right)}\right]\left(\frac{p_y}{p_x}\right). \tag{7}$$

For practical purposes p_stag can be assumed to be equivalent to p_tot the total pressure measured in gauge units using pencil probe. Equation (8) expresses p_stag in absolute units. In order to convert to gauge units for comparison purposes, we need to use $p_\mathrm{stag}^\mathrm{gauge} = p_\mathrm{stag} - 1.0132$. Thus, we can compute dynamic pressure as $p_\mathrm{dyn} = p_\mathrm{tot} - p_\mathrm{o} \approx p_\mathrm{stag} - p_\mathrm{o}$. While p_tot can be measured using pencil probe, this is not the pressure one will measure on a flat object normal to the shock flow. When the fast-moving particles are suddenly brought to rest instantaneously, it initiates a reflected shock that travels against the oncoming incident shock. The pressure acting on the target is given by the reflected pressure and not total pressure. This reflected pressure $p_\mathrm{ref} = p_\mathrm{r}$ can be computed using

$$p_\mathrm{r} = \left[\frac{\left(4M^2-1\right)\left(7M^2-1\right)}{3\left(M^2+5\right)}\right] p_x. \tag{8}$$

Reflection ratio

$$\Lambda = \frac{p_\mathrm{r} - p_x}{p_y - p_x} = \frac{\text{Reflection overpressure}}{\text{Blast overpressure}} = \frac{8M^2+4}{M^2+5}. \tag{9}$$

References

1. Jaycox, L., Tanielian, T.L., Rand Corporation. National Security Research, D., Health, R., California Community, F., Rand, C.: Invisible wounds of war: psychological and cognitive injuries, their consequences, and services to assist recovery (2008). https://www.rand.org/pubs/monographs/MG720.readonline.html. Accessed 18 Nov 2016
2. DePalma, R.G., Hoffman, S.W.: Combat Blast Related Traumatic Brain Injury (TBI): Decade of Recognition. Promise of Progress. Behavioural Brain Research, London (2016)
3. Mac Donald, C.L., Barber, J., Andre, J., Evans, N., Panks, C., Sun, S., Zalewski, K., Sanders, R.E., Temkin, N.: 5-Year imaging sequelae of concussive blast injury and relation to early clinical outcome. NeuroImage Clin. **14**, 371–378 (2017). doi:10.1016/j.nicl.2017.02.005
4. Heltemes, K.J., Holbrook, T.L., MacGregor, A.J., Galarneau, M.R.: Blast-related mild traumatic brain injury is associated with a decline in self-rated health amongst US military personnel. Inj. Int. J. Care Inj. **43**(12), 1990–1995 (2012). doi:10.1016/j.injury.2011.07.021
5. Ritzel, D., Parks, S., Roseveare, J., Rude, G., Sawyer, T.: Experimental blast simulation for injury studies. RTO-MP-HFM-207. Paper Presented at the RTO Human Factors and Medicine Panel (HFM) Symposium, pp. 3–5, Halifax, October 2011
6. Hyde, D.W.: ConWep: Conventional Weapon Effects (software) (1991)
7. Kuriakose, M., Skotak, M., Misistia, A., Kahali, S., Sundaramurthy, A., Chandra, N.: Tailoring the blast exposure conditions in the shock tube for generating pure, primary shock waves: The end plate facilitates elimination of secondary loading of the specimen. PLoS ONE **11**(9), e0161597 (2016). doi:10.1371/journal.pone.0161597
8. Chandra, N., Ganpule, S., Kleinschmit, N., Feng, R., Holmberg, A., Sundaramurthy, A., Selvan, V., Alai, A.: Evolution of blast wave profiles in simulated air blasts: experiment and computational modeling. Shock Waves **22**(5), 403–415 (2012). doi:10.1007/s00193-012-0399-2
9. Pun, P.B., Kan, E.M., Salim, A., Li, Z., Ng, K.C., Moochhala, S.M., Ling, E.A., Tan, M.H., Lu, J.: Low level primary blast injury in rodent brain. Front Neurol. **2**, 19 (2011). doi:10.3389/fneur.2011.00019
10. Lu, J., Ng, K.C., Ling, G., Wu, J., Poon, D.J., Kan, E.M., Tan, M.H., Wu, Y.J., Li, P., Moochhala, S., Yap, E., Lee, L.K., Teo, M., Yeh, I.B., Sergio, D.M., Chua, F., Kumar, S.D., Ling, E.A.: Effect of blast exposure on the brain structure and cognition in Macaca fascicularis. J. Neurotrauma **29**(7), 1434–1454 (2012). doi:10.1089/neu.2010.1591
11. Shreffler, R., Christian, R.: Boundary disturbances in high-explosive shock tubes. J. Appl. Phys. **25**(3), 324–331 (1954). doi:10.1063/1.1721633
12. Freiwald, D.: Approximate blast wave theory and experimental data for shock trajectories in linear explosive-driven shock tubes. J. Appl. Phys. **43**(5), 2224–2226 (1972). doi:10.1063/1.1661479
13. Coates, P., Gaydon, A.: A simple shock tube with detonating driver gas. Proc. R. Soc. Lond. A: Math. Phys. Eng. Sci. **1392**, 18–32 (1965). doi:10.1098/rspa.1965.0004
14. Olivier, H., Jiang, Z., Yu, H.R., Lu, F.K.: Detonation-driven shock tubes and tunnels. Prog. Astronaut. Aeronaut. **198**, 135–203 (2002). doi:10.2514/5.9781600866678.0135.0203
15. Vieille, P.: Sur les discontinuités produites par la détente brusque de gaz comprimes. C. R. Acad. Sci. A **129**, 1228–1230 (1899)
16. Fomin, N.A.: 110 Years of experiments on shock tubes. J. Eng. Phys. Thermophys. **83**(6), 1118–1135 (2010). doi:10.1007/s10891-010-0437-9
17. Richmond, D.R., Damon, E.G., Fletcher, E.R., Bowen, I.G., White, C.S.: The relationship between selected blast-wave parameters and the response of mammals exposed to air blast. Ann. N. Y. Acad. Sci. **152**(1), 103–121 (1968). doi:10.1111/j.1749-6632.1968.tb11970.x

18. Stuhmiller, J.H.: Blast Injury: Translating Research into Operational Medicine. United States Dept. of Defense (2008)
19. Kobeissy, F.H., Mondello, S., Tumer, N., Toklu, H.Z., Whidden, M.A., Kirichenko, N., Zhang, Z., Prima, V., Yassin, W., Namas, C., Anagli, J., Svetlov, S., Wang, K.K.W.: Assessing neuro-systemic and behavioral components in the pathophysiology of blast-related brain injury. Front. Neurol. **4**, 186 (2013). doi:10.3389/fneur.2013.00186
20. Needham, C.E., Ritzel, D., Rule, G.T., Wiri, S., Young, L.A.: Blast testing issues and TBI: Experimental models that lead to wrong conclusions. Front. Neurol. **6**, 72 (2015). doi:10.3389/fneur.2015.00072
21. Friedlander, R.G.: The diffraction of sound pulses: 1. Diffraction by a semi-infinite plane. Proc. R. Soc. Lond. A: Math. Phys. Eng. Sci. **186**(1006), 322–344 (1946). doi:10.1098/rspa.1946.0046
22. Kinney, G.F., Graham, K.J.: Explosive Shocks in Air, 2nd (edn.) Springer Science. Business Media, Heidelberg (1985). doi:10.1007/978-3-642-86682-1
23. Glasstone, S., Dolan, P.J.: The Effects of Nuclear Weapons. Prepared and published by the US Dept. of Defense and the US Dept. of Energy, Washington (1977). Accessed from http://nla.gov.au/nla.cat-vn2542355. Accessed 27 Sept 2017
24. Pakdaman, S., Garcia, M., Teh, E., Lincoln, D., Trivedi, M., Alves, M., Johansen, C.: Diaphragm opening effects on shock wave formation and acceleration in a rectangular cross section channel. Shock Waves **26**, 799–813 (2016). doi:10.1007/s00193-016-0628-1
25. Needham, C.E., Ritzel, D., Rule, G.T., Wiri, S., Young, L.: Blast testing issues and TBI: experimental models that lead to wrong conclusions. Front Neurol. **6**, 72 (2015). doi:10.3389/fneur.2015.00072
26. Elder Jr., F., De Haas, N.: Experimental study of the formation of a vortex ring at the open end of a cylindrical shock tube. J. Appl. Phys. **23**(10), 1065–1069 (1952). doi:10.1063/1.1701987
27. Ganpule, S., Alai, A., Plougonven, E., Chandra, N.: Mechanics of blast loading on the head models in the study of traumatic brain injury using experimental and computational approaches. Biomech. Model. Mechanobiol. **12**(3), 511–531 (2013). doi:10.1007/s10237-012-0421-8
28. Ganpule, S., Gu, L., Alai, A., Chandra, N.: Role of helmet in the mechanics of shock wave propagation under blast loading conditions. Comput. Methods Biomech. Biomed. Eng. **15**, 1233–1244 (2012). doi:10.1080/10255842.2011.597353
29. Sundaramurthy, A., Alai, A., Ganpule, S., Holmberg, A., Plougonven, E., Chandra, N.: Blast-induced biomechanical loading of the rat: An experimental and anatomically accurate computational blast injury model. J. Neurotrauma **29**(13), 2352–2364 (2012). doi:10.1089/neu.2012.2413
30. Gullotti, D.M., Beamer, M., Panzer, M.B., Chen, Y.C., Patel, T.P., Yu, A., Jaumard, N., Winkelstein, B., Bass, C.R., Morrison, B., Meaney, D.F.: Significant head accelerations can influence immediate neurological impairments in a murine model of blast-induced traumatic brain injury. J. Biomech. Eng. **136**(9), 091004 (2014). doi:10.1115/1.4027873
31. Shridharani, J.K., Wood, G.W., Panzer, M.B., Capehart, B.P., Nyein, M.K., Radovitzky, R.A., Bass, C.R.: Porcine head response to blast. Front Neurol. **3**, 70 (2012). doi:10.3389/fneur.2012.00070
32. Arakeri, J., Das, D., Krothapalli, A., Lourenco, L.: Vortex ring formation at the open end of a shock tube: A particle image velocimetry study. Phys. Fluids **16**(4), 1008–1019 (2004). doi:10.1063/1.1649339
33. Zare-Behtash, H., Kontis, K., Gongora-Orozco, N.: Experimental investigations of compressible vortex loops. Phys. Fluids **20**(12), 126105 (2008). doi:10.1063/1.3054151
34. Desmoulin, G.T., Dionne, J.P.: Blast-induced neurotrauma: Surrogate use, loading mechanisms, and cellular responses. J. Trauma **67**(5), 1113–1122 (2009). doi:10.1097/TA.0b013e3181bb8e84
35. Skotak, M., Wang, F., Alai, A., Holmberg, A., Harris, S., Switzer, R.C., Chandra, N.: Rat injury model under controlled field-relevant primary blast conditions: acute response to a wide range of peak overpressures. J. Neurotrauma **30**(13), 1147–1160 (2013). doi:10.1089/neu.2012.2652

Appendix A –Publication Cover 21
2017

Authors: N. Chandra, A. Sundaramurthy, R.K. Gupta,

Title: *"Validation of laboratory animal and surrogate human models in the primary blast injury studies"*

Journal Publication: Journal of Military Medicine, 182, 3/4:105, (2017), [17-21]

March/April 2017

SPECIAL ISSUE – Supplement to Military Medicine, Volume 182, Number 3/4

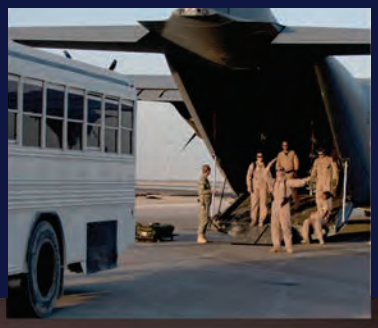
AMSUS
The Society of Federal Health Professionals

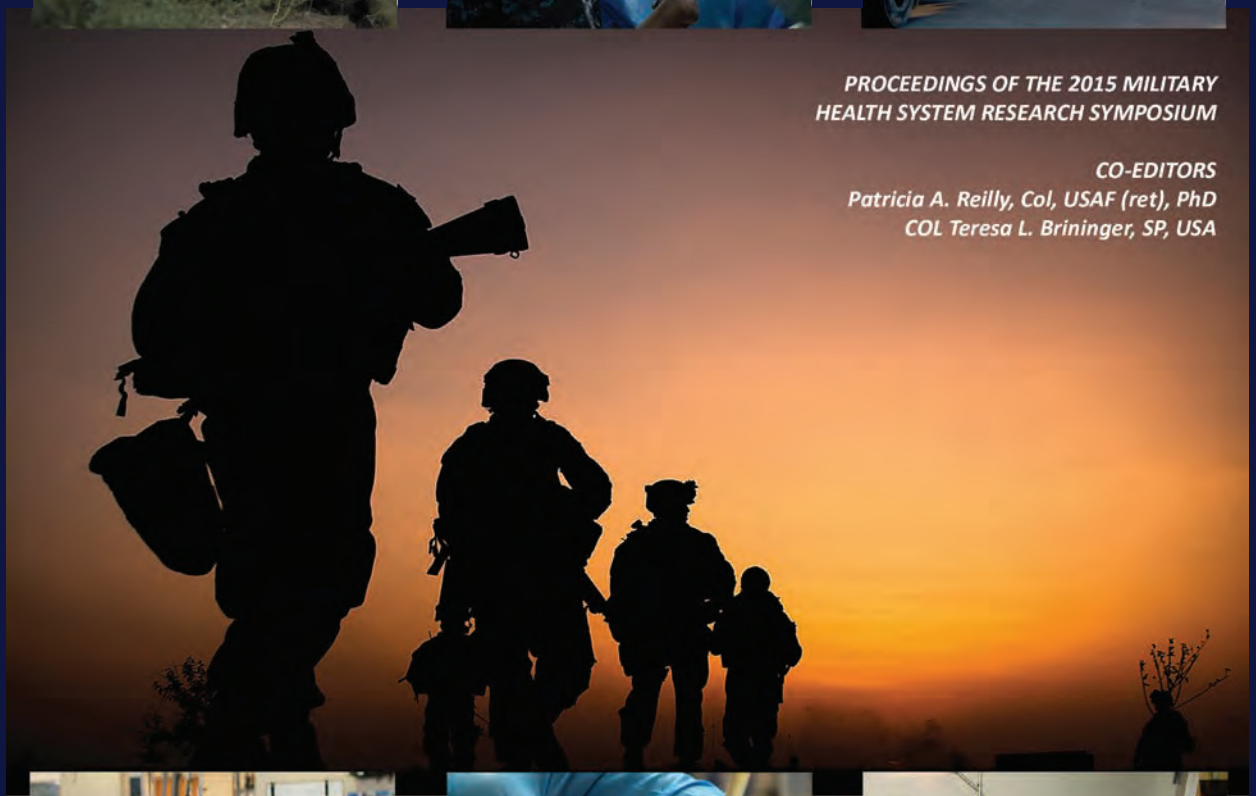
Military Medicine

International Journal of AMSUS



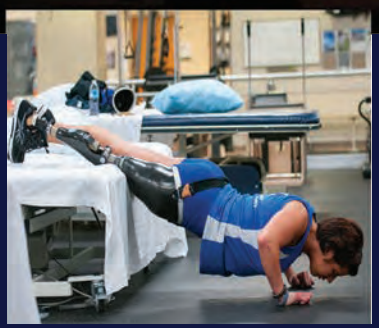






PROCEEDINGS OF THE 2015 MILITARY HEALTH SYSTEM RESEARCH SYMPOSIUM

CO-EDITORS
Patricia A. Reilly, Col, USAF (ret), PhD
COL Teresa L. Brininger, SP, USA







Validation of Laboratory Animal and Surrogate Human Models in Primary Blast Injury Studies

Namas Chandra, PhD, PE; Aravind Sundaramurthy, PhD*; Raj K. Gupta, PhD†*

ABSTRACT Blast-induced neurotrauma has affected more than 300,000 service members. It is important to understand the effect of single and repeated shock-blast wave exposures on the neuropsychological behavior of soldiers, to offer them better protection, diagnostics, and treatment. Preclinical animal models and helmet design studies on human surrogate models have relied on the use of compression gas–driven shock tubes. Traditional shock tubes are so simple that if not carefully designed and operated, the test results can easily introduce detrimental artifacts clouding the conclusions. In this work, we present live-fire test results of an instrumented human surrogate head–neck model and compare with the data obtained in a carefully designed shock tube. We present various features incorporated in the shock tube design that led to better fidelity between live-fire and laboratory shock-blast conditions. The effect of specimen placement, choice of driver gas, pressure and volume of driver, end-plate conditions, and measurement techniques all determine the successful replication of live-fire loading conditions. These parameters become more important when conducting animal testing as the totality of loading will dictate the injury severity and type which ultimately will determine the mechanisms of blast-induced neurotrauma and hence their prevention and treatment strategies.

INTRODUCTION

Blast-related mild traumatic brain injury has been identified as the signature injury of the recent conflicts in Iraq and Afghanistan; an estimated 320,000 or 19.5% of all U.S. service members deployed there have symptoms related to blast-induced neurotrauma (BINT) which accounts for over 92% of all battlefield injuries.[1] Although invisible to the naked eye, BINT is reported to cause debilitating changes in mood, thought, and behavior; medical symptoms associated include migraine, headaches, insomnia, blurred vision, dizziness, vertigo, tinnitus, nausea, and vomiting with exertion.[2] Other manifestation of BINT include memory and concentration problems, verbal and written language problems, emotional liability and depression, fatigue, light and noise intolerance, anxiety, and irritability.[1] It is postulated that all these medical outcomes can arise from a single exposure or multiple low-level exposures; simply feeling the blast wave is sufficient to cause injury.[3]

During an explosion, the high energy release rate compresses the surrounding air and the outer dome of air expands with an instantaneous jump in velocity (exceeding acoustic velocity of the air), density, and pressure, creating a shock front-blast wave pulse.[4] This shock front-blast wave pulse is strictly characterized by a sharp rising blast overpressure (BOP) with positive duration followed by underpressure (less than atmospheric pressure) with negative time duration.[4] In its simplest form, it is represented by a planar Friedlander-type pressure–time profile. A typical explosion can cause primary (pure shock), secondary (penetration by shrapnel), tertiary (inertial acceleration–deceleration), and quaternary (fire, toxic gases) when the subject is near the epicenter.[5] When the subject is at a greater standoff distance, then blast wave can cause either primary or/and tertiary injuries. However, since tertiary injuries are clearly visible, researchers mostly focus on the primary injury where the service member is subjected to blast wave without any gross motion.

Recently, an extensive research effort has been initiated toward the understanding of the mechanisms of primary blast injury from blast exposures. Current postulated mechanisms of BINT are direct transmission, skull flexure, thoracic surge, acceleration–deceleration, and cavitation. Experimental techniques using animal models and human surrogates and numerical simulations are being conducted to understand the origin of BINT. The outstanding questions are the following:

(1) How effective are the personal protective system (body armor, helmets, eye wear, and hearing protection) in combating BINT?
(2) Are the injury mechanisms in blast TBI same or different from that of blunt (tertiary) and ballistic (secondary) TBI?
(3) What are the acute (primary mechanical injury) and chronic (secondary neurobiochemical cascades) induced injury? How are these related to the cognitive, somatosensory, motor, and behavior outcomes observed in service members?
(4) What is the effect of repeated low-level blast exposures experienced in training and during combat? Is there a similarity between these repeated exposures and that observed as chronic traumatic encephalopathy in athletes?

*Department of Biomedical Engineering, Center for Injury Biomechanics, Materials and Medicine, New Jersey Institute of Technology, 111 Lock Street, Newark, NJ 07102-1982.

†DOD Blast Injury Research Program Coordinating Office, HQ, U.S. Army Medical Research and Material Command, 504 Scott Street, Fort Detrick, MD 21792-5012.

The views presented here are from the authors and do not represent the policy or position of the U.S. Army.

doi: 10.7205/MILMED-D-16-00144

To answer any or all of these questions, we can use actual clinical data and longitudinal medical outcome of service members; unfortunately, the history of exposure is not known and further, pure blast cases are far fewer. This leads us to conduct preclinical studies using animal models to examine biological outcomes, and human head–neck surrogates for helmet protection studies. Though actual exposure to live-fire conditions using known strengths of explosives is possible, it is neither economical nor practical. This leaves researchers to turn to laboratory tests; the use of compressed gas–driven shock tubes has emerged as the clear choice among various research groups.[6] Shock tubes have been used since the 1890s for a variety of other purposes (combustion, aerodynamics, detonation).[7] They comprise a compressed gas section (breech or driver) separated by membranes to a long driven section. When the gas pressure is increased, the membrane bursts (can be manually punctured as well) and the high-pressure gas compresses the atmospheric gas in the driven section, which generates a blast wave. A recent review article shows that there are numerous research groups investigating BINT using a variety of shock tubes with many variations in the design of the tube, animal location, holders and pressure–impulse–pulse generation, and measurements.[8] Since the method for imparting the load on the animal varies with different laboratories, the biomechanical loading experienced by the animal varies. Therefore, it is difficult to compare the results leave alone correlating with the live-fire conditions. The purpose of this article is to measure pressure–duration–impulse conditions of a human head–neck surrogate under live-fire conditions and examine under what experimental conditions those live-fire data can be replicated in the laboratories. Further, what are the key parameters in the design and operation of the shock tube that are needed to be monitored to assure the fidelity?

ConWep (Conventional Weapon Effects)[9] is a computer simulation program that was developed by U.S. Army Corps of Engineers which can accurately numerically simulate a variety of conventional weapons effect calculations including an assortment of air blast routines, fragment and projectile penetrations, breach, cratering, and ground shock. The program is capable of calculating the pressure–time–impulse profile experienced by a subject who is at a standoff distance, when a spherical charge of a given explosive (e.g., C4 or TNT) produces the shock blast when the charge is suspended in the air or on the ground or buried below the ground. Some of the commonly used improvised explosive devices and their strengths are shown in our previous work.[10] Figure 1 shows the schematic of an explosion in the range of 2 to 100 kg and BOP of 70 to 350 kPa. The figure shows that for a given explosive strength, BOP decreases and duration increases with increase in distance

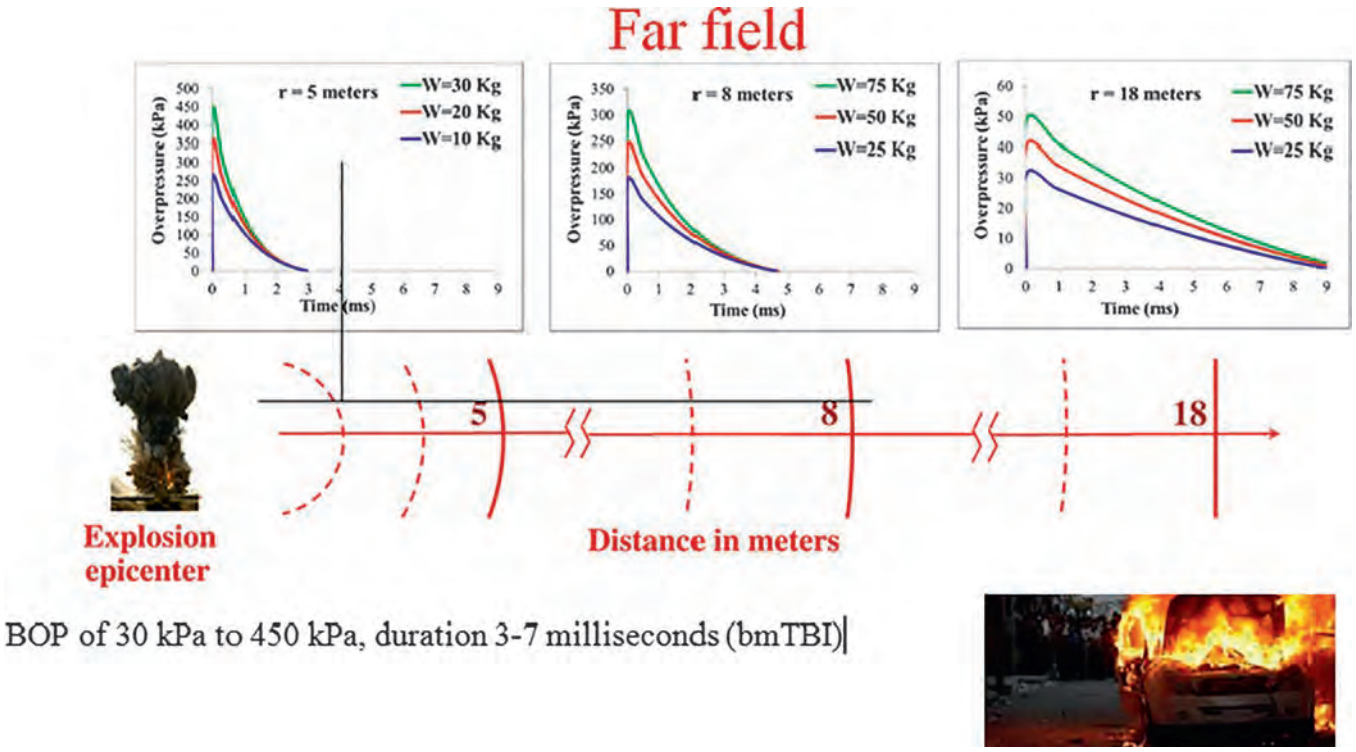


FIGURE 1. BOP–time variation as a function of charge strength and standoff distance. Beyond 5 m distance, the wave can be idealized as planar compared to a human head. For mild to moderate ranges based on 2 to 100 kg of C4 and 1 to 100 m distance, BOP of 30 to 450 kpa and duration of 3 to 7 milliseconds can be considered as the right range for laboratory replication. bmTBI, blast related mild traumatic brain injury.

from the explosion. Compared to the radius of hemisphere of 5 to 10 m, the human head occupies less than 1% of the circumference ensuring that the shock wave in the laboratory needs to be planar. Thus, the shock tube design should be able to generate a Friedlander-type blast wave with 70 to 350 kPa BOP and duration of 3 to 7 milliseconds and that wave shall remain planar. Further, there should be no other artifacts arising from wall reflections (e.g., specimen itself, instruments, end conditions-open or closed) which will drastically change the biomechanical loadings on the animal and hence the results.

In this study, the pressure-acceleration response of a head–neck human surrogate realistic explosion-resistant dummy (RED) head was evaluated in two different conditions; (1) in the field (live-fire) and (2) in the laboratory shock tube with the same set of 13 sensors, 11 pressure gauges, and 2 accelerometers. The RED head represents the anthropometry of 50th percentile male soldier in the tri-services. In the field, four pounds of C4 was used as the explosive to produce blast waves that interacted with the instrumented RED head facing the epicenter of the blast; the same surrogate was then tested inside the shock tube. In both cases, 11 different pressure measurements on the surface of the RED head and linear acceleration at the center of gravity (CG) of the surrogate were measured. Finally, the pressure and acceleration data obtained from field experiments were compared with pressure and acceleration data obtained from the shock tube experiments to determine the efficacy of the shock tube when simulating primary blast injury conditions in a laboratory.

METHOD

Field Experiments and RED Head Preparations

To produce air blast (i.e., without any ground reflection) four pounds of C4 explosive charge was placed at 2,438 mm from the ground, which produces an incident pressure of 25 psi which was measured 280 mm in front of the head (Fig. 2A). The goal was to expose the RED head to a simple Friedlander-type blast wave. The RED head was instrumented with 11 sensors (102B06) (PCB Piezotronics, Inc, Depew, New York) and two linear accelerometers (Endevco 7270A) (Meggitt Sensing Systems, Irvine, California) mounted to a tri-axial block fixed to the CG of the RED head, which measures the accelerations along the x and z directions (Fig. 3). Out of the 11 pressure sensors, five sensors were instrumented along the mid-sagittal plane along with the remaining six (three on each side) on the RED head (Fig. 3A). All the pressure sensors used in the experiments were calibrated using Rankine–Hugoniot equations of state ahead of time in separate tests. In the live-fire experiments, the RED head was positioned at a radial distance of 2,794 mm from the charge with its anterior side facing the epicenter of the blast (Fig. 2A). Accelerometers were mounted at the CG of the RED head. The head was then attached to Hybrid III neck and mounted on base. The checkered board behind the head form was also placed at 2,794 mm to observe the propagation of the shock front in the high-speed video. The field experiment was repeated 10 times.

Shock Tube Experiments

The shock tube shown in Figure 2B comprises of driver, transition, and driven sections as well as a catch tank. The driver section has a diameter of 203 mm and its length can be varied between 67 and 1,210 mm. Transition section is an adapter that connects the circular driver section to the square driven section and has a length of 1,829 mm. The driven section has a 711.2 mm×711.2 mm (28 in × 28 in) square cross-section and a length of 8,661 mm. Finally, catch tank absorbs the kinetic energy of the exiting jet from the shock tube and does not play any role in modifying the profile. The driver and driven sections are separated by frangible mylar membranes. When the high-pressure

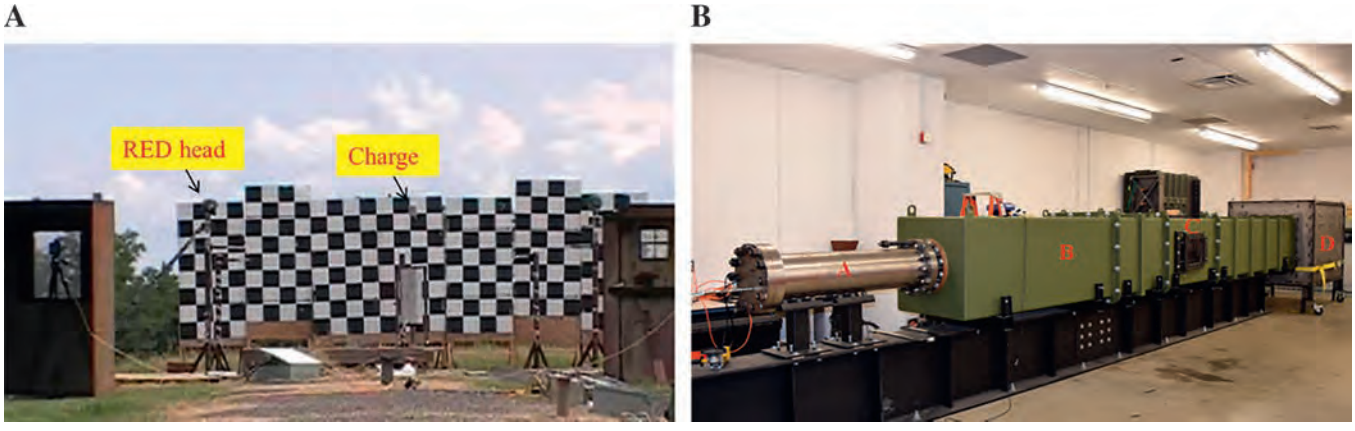


FIGURE 2. (A) Layout of the live-fire test. The charge and the specimen are kept elevated to avoid ground reflection effect: (B) A, 29 in × 29 in compressed gas–driven shock tube driver; B, driven with transition; C, test section; D, catch tank.

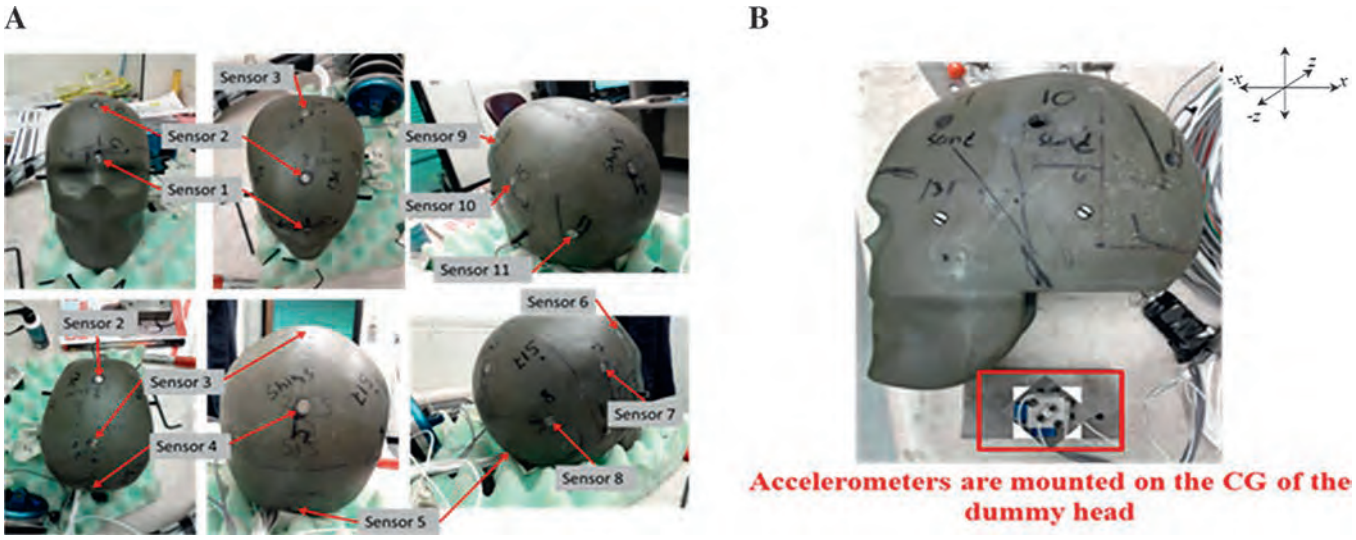


FIGURE 3. (A) Location of the pressure sensors and (B) location of the acceleration sensor with positive accelerations measured along x- and z-axis.

gas (helium or nitrogen) is pumped into the driver section, the membranes separating the driver and the driven section rupture resulting in the release of the high-pressure gas. This high-pressure gas expands into the driven section compressing the atmospheric air resulting in the formation of the blast wave. A detailed description of the design and operation of the shock tube can be seen in our previous work.[11]

The instrumented RED head was fixed inside the driven section at 2,096 mm downstream from the end of the driver section facing the blast wave. For this experiment, helium was used as the driver gas with a driver length of 143 mm. Fourteen mylar membranes with each having 0.254-mm thickness were used between driver and driven sections. This shock tube configuration resulted in an incident pressure of 28 psi, which was measured 137 mm in front of the head. These experiments were repeated 11 times.

RESULTS

RED Head Blast Wave Interaction in the Shock Tube and the Field Blast

The mechanics of the blast wave RED head interactions can be studied by monitoring the pressure on midsagittal plane of the head. Figure 4 shows the experimentally measured peak pressures on five locations along the midsagittal plane of the RED head for both shock tube and field tests. Peak overpressure corresponding to sensor 1 (between eyebrows) is 80 and 70 psi with pressure amplification from incident pressure of 2.85 and 2.8 for shock tube and field tests. The pressure starts to decrease from sensor 1 to sensor 4 with least pressure recorded in sensor 4 for both cases. At sensor 4 (just behind the crown of the head), the peak pressure is reduced to 17.5 and 20 psi for shock tube and field tests. However, at the location of sensor 5 (rear side of the head), the observed pressure is higher than sensor 4 for both shock tube and field experiments due to shock travel along the side compare to the top.

Comparison of Pressure Between Free Field and Shock Tube

Though peak pressures as shown in Figure 4 can be of interest, the actual profile of pressure-time is more illustrative of the flow field simulation. We observed significant correlation between the overall pressure time profiles on all the 11 sensors (Fig. 5A shows representative comparisons of sensors 1

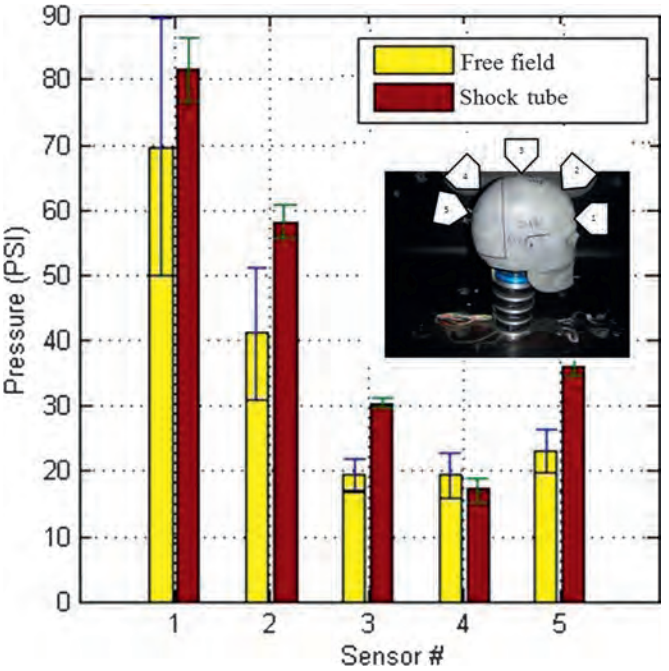


FIGURE 4. Comparisons of overpressure for bare head in free field and shock tube.

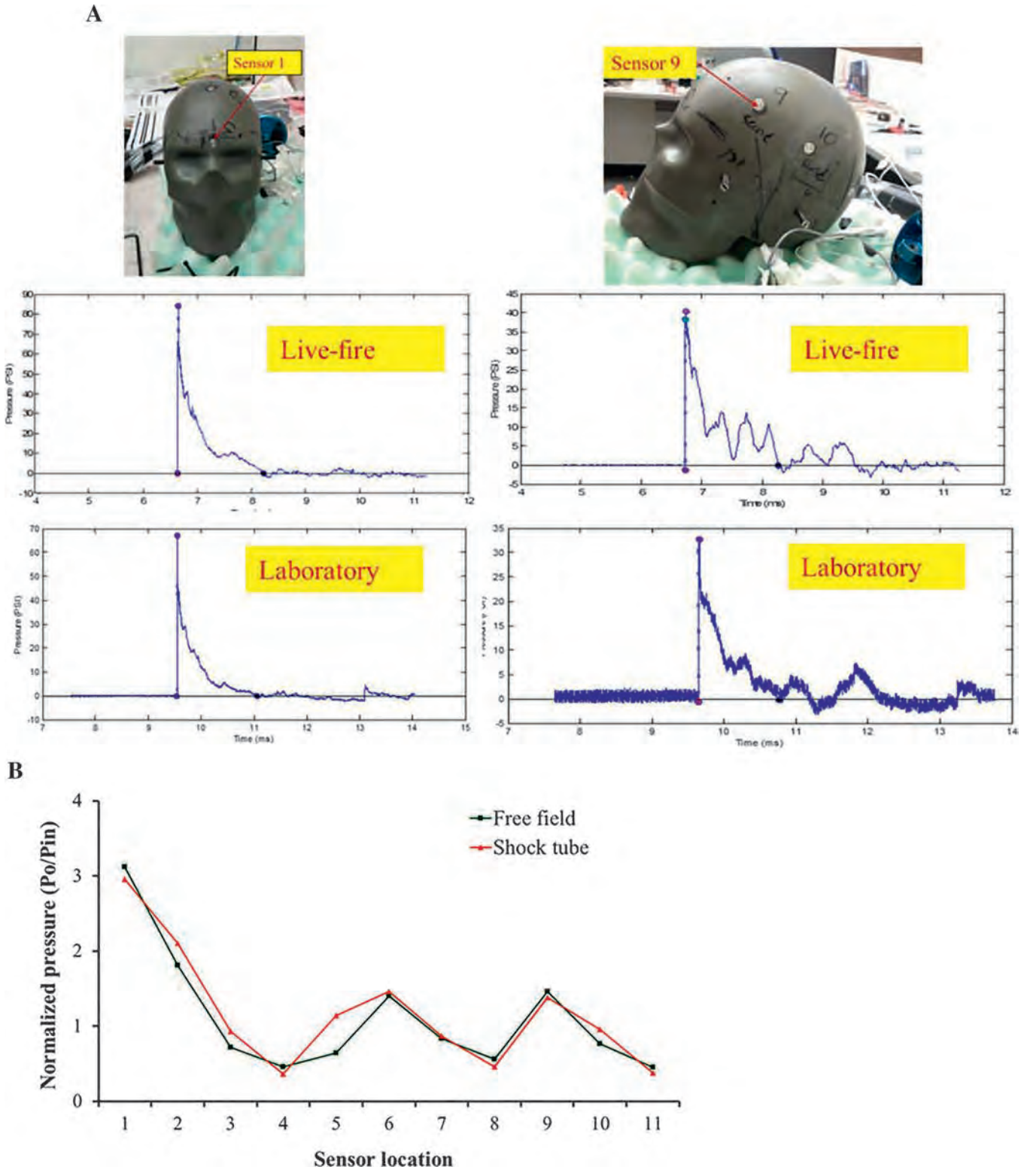


FIGURE 5. (A) Comparison of pressure profile between live-fire and shock tube experiments. First column shows live-fire and laboratory data on front sensor 1; second column shows data on the side of the dummy head for Sensor 9. See the variations in the profile of the pulse for the same shock-blast loading conditions. (B) Comparison of the normalized overpressure between live-fire and shock tube experimental data. The peak pressure (and the pulse) varies as the blast passes from the front to the back.

and 9). Since there is a difference in the exact magnitude of peak overpressure between field and shock tube experiments due to the difference in incident pressures, we normalized the peak overpressure (P_o) for all the 11 sensors from both field and shock tube experiments with their corresponding incident pressures (P_{in}) (Fig. 5B).

Comparison of Linear Acceleration Between Live Fire and Shock Tube

If we are concerned only with the primary shock loading, then the specimen can be fixed to the structure allowing no motion. If the RED head is allowed to rotate, then the linear and rotational acceleration will be dictated by the applied force as well as the stiffness of the Hybrid III neck as attached to the fixture. Figure 6 shows the comparison of the maximum positive and maximum negative acceleration along x and z directions between shock tube and field experiments. From the data, we observe a maximum positive acceleration of 150 and 145 g for shock tube and field experiments along x direction and 153 and 125 g for shock tube and field experiments along z direction. We observe a maximum negative acceleration of −205 and −110 g for shock tube and field experiments along x direction and −150 and −100 g for shock tube and field experiments along z direction. It is to be noted that although the maximum positive acceleration matches within experimental standard deviation, the maximum negative acceleration is higher in the laboratory compared to the field.

DISCUSSION

Mild to moderate primary blast TBI is believed to be caused by shock-blast wave pulse that interacts with the service members during improvised explosive device explosions. The pulse needs to be of Friedlander type with BOP ranging from 70 to 350 kPa and duration from 3 to 7 milliseconds with no other jet winds or reflection/expansion artifacts. The specimen (animal models or human surrogate) needs to be fixed and not allowed to toss around or ejected which are indicative of tertiary loading. These requirements arise from observations from live-fire experiments and should be replicated in the laboratories. In this work, we studied pressure at different points and acceleration at the CG of the instrumented head in both field experiment and shock tube.

Overall, there is a good match in BOP peak values for all the 11 sensors as shown in Figure 5B. Figure 5A shows the pressure–time–pulse at two sensor locations (sensors 1 and 9) with remarkable similarity. Sensor 1 is located on the forehead and faces the incident shock-blast pressure head on. The sensor data show that the Friedlander shape is maintained here with higher values of peak pressure due to reflection effects. Once the shock front interacts with the anterior part of the surrogate, it diffracts and envelopes the side and top of the head. During this traverse, the pressure starts to decrease between sensors 1 and 4. For the first 3 sensors, the decrease is because of the change in the incidence angle with sensor 1 being perpendicular to the flow of the blast wave resulting in the maximum pressure, whereas with sensors 2 and 3, the angle of incidence starts to change with sensor 3 being parallel to the flow of blast wave. Furthermore, a significant flow separation is observed (sensors 4 and 7); which results in the reduction of overpressure below the incident pressure. The blast wave traversing the head and the blast wave traversing the neck reunite at the back of the head. This reunion causes an increase in pressure on the backside of the head (sensor 5). These observations are similar to those reported by Ganpule et al.[12] There was a good agreement between the normalized pressure on all the sensor locations for both field and shock tube experiments (Fig. 5B). Therefore, it can be concluded that the physics of

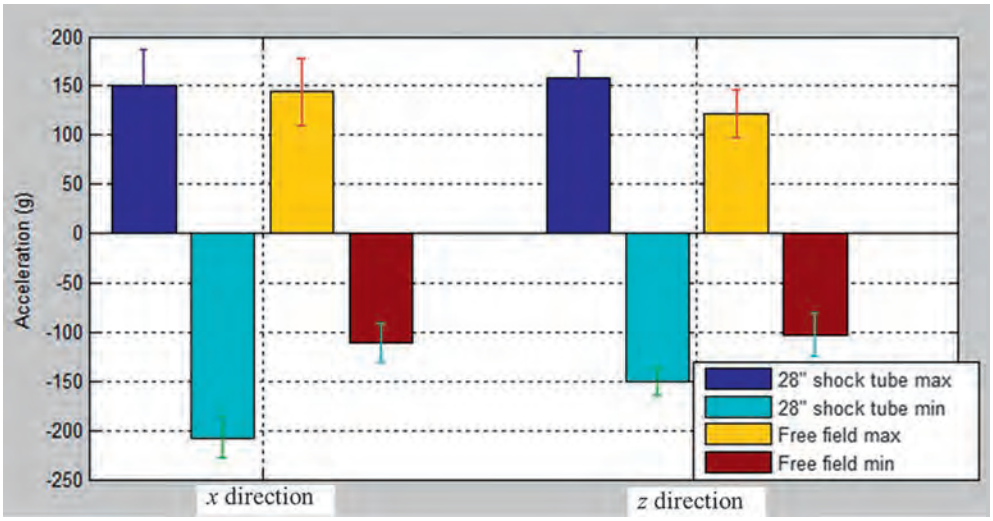


FIGURE 6. Comparisons of linear acceleration for bare head in free field and shock tube.

the blast-shock wave is captured in the shock tube as the blast wave traverses the dummy head.

We observed good agreement between the maximum positive accelerations recorded along both x and z directions; however, we observed a substantial difference in the maximum negative values of acceleration. The maximum positive acceleration is caused because of the loading of the oncoming blast wave. However, in the case of shock tube, there is more displacement of the head due to the buildup of air in front of the face (due to constraining from shock tube walls) and because the head is mounted on a H3 neck (neck acts like a spring), it springs back causing an increased negative acceleration. This may not have significant effect as the main loading occurs because of the direction of pressure transmission as well as the initial motion. In case of animal models, since the animals are constrained to simulate primary loading, tertiary blast injury will have less effect.

As the planar shock wave approaches a human head specimen, different types of shock-structure interaction takes place depending on the orientation of the surface with respect to the shock flow. For example, in sensor 1 mounted directly on the forehead, the shape of the shock pulse is maintained similar to that of Friedlander wave; however, the magnitude of peak pressure increases due to high reflection ratio. Conversely, we observe oscillations in the waveform recorded in sensor 9, we hypothesize that this is due to the combination of direct interaction of the undisturbed blast wave from the front as well as the diffracted wave from the facial features. The pulse shape changes completely and is captured in the laboratory as well. Figure 5B shows that the pressure profile varies from $\frac{P_0}{P_{in}}$ of around 3 in the front to about 0.8 at the rear sensor 11. Here, P_0 represents the peak overpressure measured by the sensor, whereas P_{in} is the

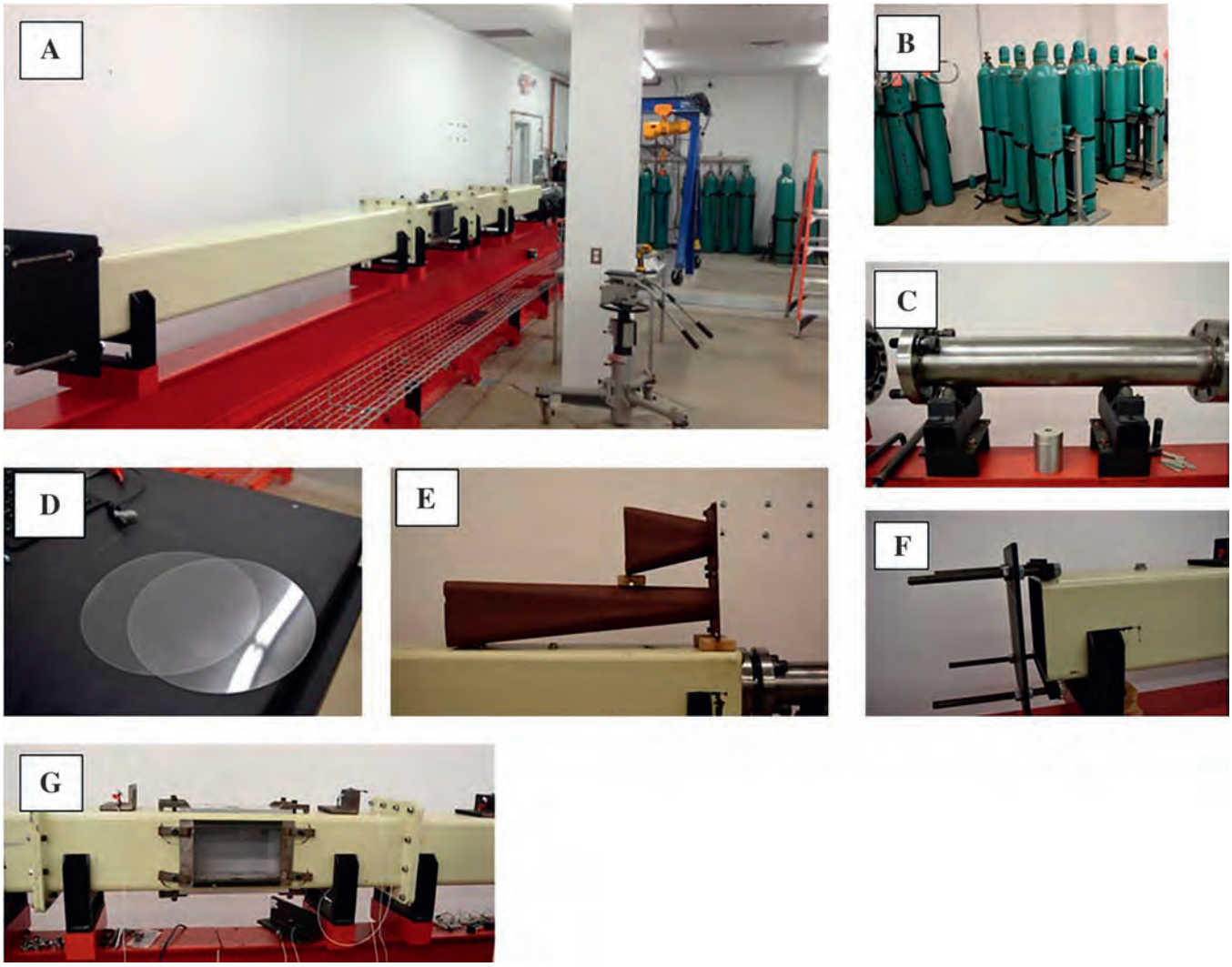


FIGURE 7. Unique design features of the shock tube that permits generation of planar shock wave without artifacts (A) 9 in × 9 in × 40 ft shock tube for animal model. (B) Options for different driver gas (helium, nitrogen, air), (C) variable breech length, (D) variable breech pressure, (E) variable transition length, (F) variable end conditions, (G) viewable test section that can be relocated.

incident pressure measured before the shock interacts with the RED head. As the laboratory data replicates accurately all the 11 sensors (Fig. 3), we can say with confidence that the laboratory shock tube conditions are identical to that of the live-fire conditions. The fact that the shape of the profile measured in the live-fire experiments matches the laboratory data ensures that the physics of the shock flow and its interaction with the structure are accurately captured in the laboratory. A number of experiments (not reported here) shows that such replication will not occur if the specimen is moved near the exit or kept outside. Similarly, if the size of the specimen (size of the RED head is 9 in length and 7 in width) is more than about 10% of the blast tube cross-sectional area, the secondary reflection from the specimen itself will alter the loading profile and hence the result. Furthermore, area of blockage also increases the dynamic pressure on the specimen. An analytical calculation presented by Needham and his colleagues showed that for cases with blast wavelength (defined approximately as the product of blast duration and speed of sound) longer than the characteristic length of the target species (diameter of the sphere), blockages of 10, 20, and 30% increased the dynamic pressure by 27, 64, and 113%.[13] However, according to Wortman and Lottero, in cases where blast wavelength is approximately same as the characteristic length of the target species, a 20% blockage is acceptable because of the rapid decay of dynamic pressure.[14] This is the very reason that we conduct small animal (rodent) experiment in the smaller (9 in × 9 in) shock tube while conducting human surrogate, swine, and postmortem human specimen (human cadavers) experiments in the larger tube. Numerical simulations of the shock-structure interactions on the RED head conducted by our group also validate this conclusion.[12]

Computational models on shock-head interaction has shown that if P_{in} is the incident BOP, then on the forehead of a front facing head the peak pressure is about 2 to 3 P_{in}, on the top and side (parallel to flow) the value is about P_{in}, and less than P_{in} in the rear. Similar ratios are also observed for impulse values (integral of shock pressure and duration).

There are a number of design and operation variables that are carefully controlled for the faithful replication of shock profile within the BOP duration range as shown in Figure 1. Though we do not claim that these features are the only way to achieve the fidelity, these will be very helpful in understanding the effect of certain features on the profile. In any case, any deviation from these basic principles will likely to cause minor to major variations in the shock profile and hence the experimental data. Some of these key features are shown in Figure 7. The picture depicts the smaller shock tube (9 in × 9 in × 20 ft) specifically meant for live rodent testing as the specimen will occupy less than 10% of the opening.

In our previous work, we have performed analysis on the different features of our shock tube and its influence on the blast wave it produces, results of which is not shown for the sake of brevity.[10] The ability to shape the pulse is determined by a number of factors, one of which is the choice of driver gas (Fig. 7B), helium, nitrogen, or compressed air. It should be recognized that the medium that loads the specimen is not these species but the atmospheric air that is present in the tube when the gas bursts. The bursting gas only acts as a fast-moving acoustic piston pushing the air and increasing air velocity to shock wave speed. Because of very low molar mass (0.004 kg/mol) and high acoustic speed (956 m/s), helium produces a much higher BOP compared to nitrogen (0.028 kg/mol and 352 m/s velocity). Thus in our studies, we used helium for achieving higher BOP and lower duration and nitrogen for lower BOP and higher duration.

The other variable that can be controlled is the driver (breech) length. Longer driver length results in longer positive pulse duration. When membranes separating the compressed gas and atmospheric air burst, two waves are generated: a compressive wave travel toward exit pressurizing the air and a tensile expansion wave travel in the opposite direction toward the closed end of the driver. When the latter reaches the closed end, the expansion wave is reflected and travels back into the driver section as a tensile wave (faster due to compressibility effects) and catches up with the first shock wave. Thus, this reflected tensile wave erodes the shock front producing the decreasing part of the Friedlander wave. Thus, if we delay this tensile wave by making the breech length longer, then we can produce longer duration in the shock pulse. The lengths are altered in practice through cylindrical inserts.

Burst pressure (P_B) is the pressure when the membranes burst (Fig. 7D) and directly dictates the magnitude of BOP. Higher P_B is obtained by stacking multiple membranes of varying thickness ranging from 0.001 to 0.01 in. Though the sheets are traditionally obtained from the same vendor using the same manufacturing process, still batch to batch variations are noticed. This has necessitated calibration of P_B vs. membrane thickness when starting a new lot. Other designs have used metallic membranes with fracture initiated manually through mechanical means to control P_B.

The end of the shock tube can be fully open, fully closed, or partially open as shown in Figure 7F. As the shock exits the tube, if the end is open, it will produce a release (tensile) wave that will now travel backward toward the driver and produce a sharp negative pressure (tensile) component. When the end is fully closed, the oncoming shock pulse gets fully reflected as an additional pressure pulse redoubling the BOP depending on the location of measurement. A partially open exit combines the effect of negative pressure due to opening with that of the positive pressure due to reflection. Depending on the desired pulse shape, we alter the exit opening.

The test section shown in Figure 7G can be moved anywhere along the driver length as the units are made in multiple sections with flanged joints and bolted assembly. The square section with shock-proof glass window permits the video capture of shock-structure interactions. With adequate lighting

provided from the front and top, we can capture up to 10,000 frames per second enough for capturing the motion of the specimen. It should be noted that while securing the specimen, the supporting structure should be aerodynamically smooth to avoid any reflection artifacts from the specimen or the structure.

Through these features, we have been able to not only recreate the Friedlander pressure–time–impulse profile similar to the field, but also vary the BOP-duration in the desirable range of 70 to 350 kPa and 3 to 7 milliseconds to simulate mild and moderate blast TBI conditions.

CONCLUSION

In this article, we have outlined the need to replicate the live-fire blast pressure-duration pulse in laboratory test conditions and delineated the BOP and duration ranges. We have shown that the pulse has to be planar and be of Friedlander type without any artifacts that can alter the test conditions. We have also described of the key parameters involved in replicating live-fire loading conditions in a shock tube. By careful planning and controlling the key parameters in shock tube studies, we believe that the preclinical test results for animal studies as well as personal protection design studies can be conducted with translatable results under field environments.

ACKNOWLEDGMENTS

NC acknowledges the financial support provided by the U.S. Army Research office with contract number W911NF-08-1-0483 and laboratory members for some of the laboratory shock field data.

REFERENCES

1. Tanielian TL, Jaycox LH (editors): Invisible Wounds of War: Psychological and Cognitive Injuries, Their Consequences, and Services to Assist Recovery, Vol. 1. Santa Monica, CA, Rand Corporation, 2008. Available at http://www.rand.org/pubs/monographs/MG720.html; accessed September 7, 2016.
2. Anderson RJ: Shell shock: an old injury with new weapons. Mol Interv 2008; 8(5): 204–18.
3. Warden D: Military TBI during the Iraq and Afghanistan wars. J Head Trauma Rehabil 2006; 21(5): 398–402.
4. Kinney GF, Graham KJ: Explosive shocks in air, Ed 2. New York, Springer Science & Business Media, 1985.
5. Wolf SJ, Bebarta VS, Bonnett CJ, Pons PT, Cantrill SV: Blast injuries. Lancet 2009; 374(9687): 405–15.
6. Kobeissy FH, Mondello S, Tumer N, et al: Assessing neuro-systemic and behavioral components in the pathophysiology of blast-related brain injury. Frontiers Neurol 2013; 4: 186.
7. Fomin NA: 110 years of experiments on shock tubes. J Eng Phys Thermophys 2010; 83(6): 1118–35.
8. Risling M, Davidsson J: Experimental animal models for studies on the mechanisms of blast-induced neurotrauma. Front Neurol 2012; 3: 30.
9. Hyde D: ConWep, conventional weapons effects program. U.S. Army Engineer Waterways Experiment Station, 1991. Available at https://pdc.army.mil/software/conwep; accessed April 13, 2016.
10. Sundaramurthy A, Chandra N: A parametric approach to shape field-relevant blast wave profiles in compressed-gas-driven shock tube. Front Neurol 2014; 5: 253.
11. Chandra N, Ganpule S, Kleinschmit N, et al: Evolution of blast wave profiles in simulated air blasts: experiment and computational modeling. Shock Waves 2012; 22(5): 403–15.
12. Ganpule S, Alai A, Plougonven E, Chandra N: Mechanics of blast loading on the head models in the study of traumatic brain injury using experimental and computational approaches. Biomech Model Mechanobiol 2013; 12(3): 511–31.
13. Needham CE, Ritzel D, Rule GT, Wiri S, Young L: Blast testing issues and TBI: experimental models that lead to wrong conclusions. Front Neurol 2015; 6: 72.
14. Wortman JD, Lottero RE: Comparison of HULL hydrocode computations of shock tube blockage effects on target loading for step shocks and rapidly-decaying shocks. DTIC Document, 1982. Available at http://www.dtic.mil/dtic/tr/fulltext/u2/a123274.pdf; accessed August 26, 2016.

Appendix A –Publication Cover 22
2016

Authors: M. Kuriakose, Skotak, M, Misistia, A, Kahali S, Sundaramurthy A, Chandra N

Title: *"Tailoring the Blast Exposure Conditions in the Shock Tube for Generating Pure, Primary Shock Waves: The End Plate Facilitates Elimination of Secondary Loading of the Specimen"*

Journal Publication: PLoS ONE 11(9): e0161597. doi:10.1371/journal.pone.0161597, (2016), [16-22]

PLOS ONE

RESEARCH ARTICLE

Tailoring the Blast Exposure Conditions in the Shock Tube for Generating Pure, Primary Shock Waves: The End Plate Facilitates Elimination of Secondary Loading of the Specimen

Matthew Kuriakose☯, Maciej Skotak☯, Anthony Misistia, Sudeepto Kahali, Aravind Sundaramurthy, Namas Chandra*

Center for Injury Biomechanics, Materials and Medicine (CIBM^3), Department of Biomedical Engineering, New Jersey Institute of Technology, Newark, NJ, 07102–1982, United States of America

☯ These authors contributed equally to this work.
* namas.chandra@njit.edu

CrossMark
click for updates

OPEN ACCESS

Citation: Kuriakose M, Skotak M, Misistia A, Kahali S, Sundaramurthy A, Chandra N (2016) Tailoring the Blast Exposure Conditions in the Shock Tube for Generating Pure, Primary Shock Waves: The End Plate Facilitates Elimination of Secondary Loading of the Specimen. PLoS ONE 11(9): e0161597. doi:10.1371/journal.pone.0161597

Editor: Firas H Kobeissy, University of Florida, UNITED STATES

Received: May 17, 2016

Accepted: August 8, 2016

Published: September 7, 2016

Copyright: © 2016 Kuriakose et al. This is an open access article distributed under the terms of the Creative Commons Attribution License, which permits unrestricted use, distribution, and reproduction in any medium, provided the original author and source are credited.

Data Availability Statement: Data are provided within the Supporting Information.

Funding: This work was supported by grant no. 14059001 entitled "Primary Blast Injury Criteria for Animal/Human TBI Models using Field Validated Shock Tubes" received from the U.S. Army Medical Research and Materiel Command.

Competing Interests: The authors have declared that no competing interests exist.

Abstract

The end plate mounted at the mouth of the shock tube is a versatile and effective implement to control and mitigate the end effects. We have performed a series of measurements of incident shock wave velocities and overpressures followed by quantification of impulse values (integral of pressure in time domain) for four different end plate configurations (0.625, 2, 4 inches, and an open end). Shock wave characteristics were monitored by high response rate pressure sensors allocated in six positions along the length of 6 meters long 229 mm square cross section shock tube. Tests were performed at three shock wave intensities, which was controlled by varying the Mylar membrane thickness (0.02, 0.04 and 0.06 inch). The end reflector plate installed at the exit of the shock tube allows precise control over the intensity of reflected waves penetrating into the shock tube. At the optimized distance of the tube to end plate gap the secondary waves were entirely eliminated from the test section, which was confirmed by pressure sensor at T4 location. This is pronounced finding for implementation of pure primary blast wave animal model. These data also suggest only deep in the shock tube experimental conditions allow exposure to a single shock wave free of artifacts. Our results provide detailed insight into spatiotemporal dynamics of shock waves with Friedlander waveform generated using helium as a driver gas and propagating in the air inside medium sized tube. Diffusion of driver gas (helium) inside the shock tube was responsible for velocity increase of reflected shock waves. Numerical simulations combined with experimental data suggest the shock wave attenuation mechanism is simply the expansion of the internal pressure. In the absence of any other postulated shock wave decay mechanisms, which were not implemented in the model the agreement between theory and experimental data is excellent.

Introduction

Exposure to shock waves is identified as the leading cause of Traumatic Brain Injury (TBI) in military personnel [1, 2]. The injuries associated with explosive detonation are classified into four different categories based on their etiology: 1) primary, caused by pure shock waves, 2) secondary, resulting from penetration of fragmentation (shrapnel) and other projectiles into the brain parenchyma, 3) tertiary, originating from impact with other objects, and 4) quaternary, caused by exposure to heat and toxic gases [3–5]. It appears mixed type of injuries are expected near the epicenter of a blast, while shock wave is far reaching, compared to the other TBI risk factors associated with explosive blast. Traveling over long-distances, the shock wave could thus be the sole source of injuries far from the explosion, making primary blast TBI (bTBI) particularly onerous [6]. Researchers have been attempting to replicate field-relevant shock waves in laboratory settings through the use of shock tubes in order to investigate the generation and propagation of shock waves and possible mechanisms of bTBI, also referred to as blast induced neurotrauma (BINT) [7, 8]. Increased focus on bTBI has resulted in intensified research efforts and a number of groups have opted to use compressed-gas driven shock tubes to study the etiology of blast injury [9–14]. All categories of blast injuries can occur in the field [15–17], and while it is challenging to isolate cases of pure primary blast injuries among military personnel, in order to study biological effects of shock waves in the laboratory, it is crucial that these generated experimental wave forms are free of any artifacts. To date, there is only a limited understanding of conditions affecting shock wave propagation inside of the shock tube, what crucial differences exist between testing inside versus outside of the shock tube, and how the end-effects affect the shock wave profile and propagation [18, 19].

Since their inception in 1899 [20], shock tubes have been widely used in a variety of research areas for studying phenomena which require extremely high temperatures and heating rates or occurring at extremely fast but controllable rates: high temperature chemical kinetics [21, 22], molecular spectroscopy [23], and to simulate interaction of plasma with Earth's magnetosphere [24], just to name a few prominent examples. However, in the biomedical field, shock tubes found application as research tools relatively recently, with just a few existing peer-reviewed reports published pre 2010 [25–28]. Typically shock tubes share major design features, which utilize three essential components: driver (breech), driven (which includes the test section) and the end-reflector. However, the subtle differences in the design and operation of the tube have significant impacts on the resulting pressure history measured inside of the tube: volume of the breech, breech-to-test section diameter ratio, circle-to-square transition and length of the driven section. It is generally accepted that the shock wave closely resembling the Friedlander waveform (Fig 1) should be used for any experiments aiming at replicating field blast conditions [29, 30]. This waveform consists of a sharp, almost instantaneous rise in pressure (shock front) followed by exponentially decaying pressure (blast wind) [31]. It is critical to accurately characterize the amount of loading sustained by subjects (it is of particular importance for studies which use animal models) and to tailor specific pressure profiles via optimization of shock tube configuration. To the best of our knowledge, systematic experimental characterization of conditions inside of the shock tube received only limited attention [32, 33], in spite of vast theoretical and empirical evidence regarding the fate of the shock wave traveling on the outside of the shock tube [34, 35].

In this work, the characteristics of the propagating shock wave (peak overpressure, duration, impulse and velocity) and secondary waves were followed by measuring the pressure-time profiles at six sensors distributed along the tube. We demonstrate conditions inside of the shock tube can be controlled and secondary waves eliminated by careful adjustment of the end plate reflector gap; thus the specimen is exposed only to a single shock wave with well-defined

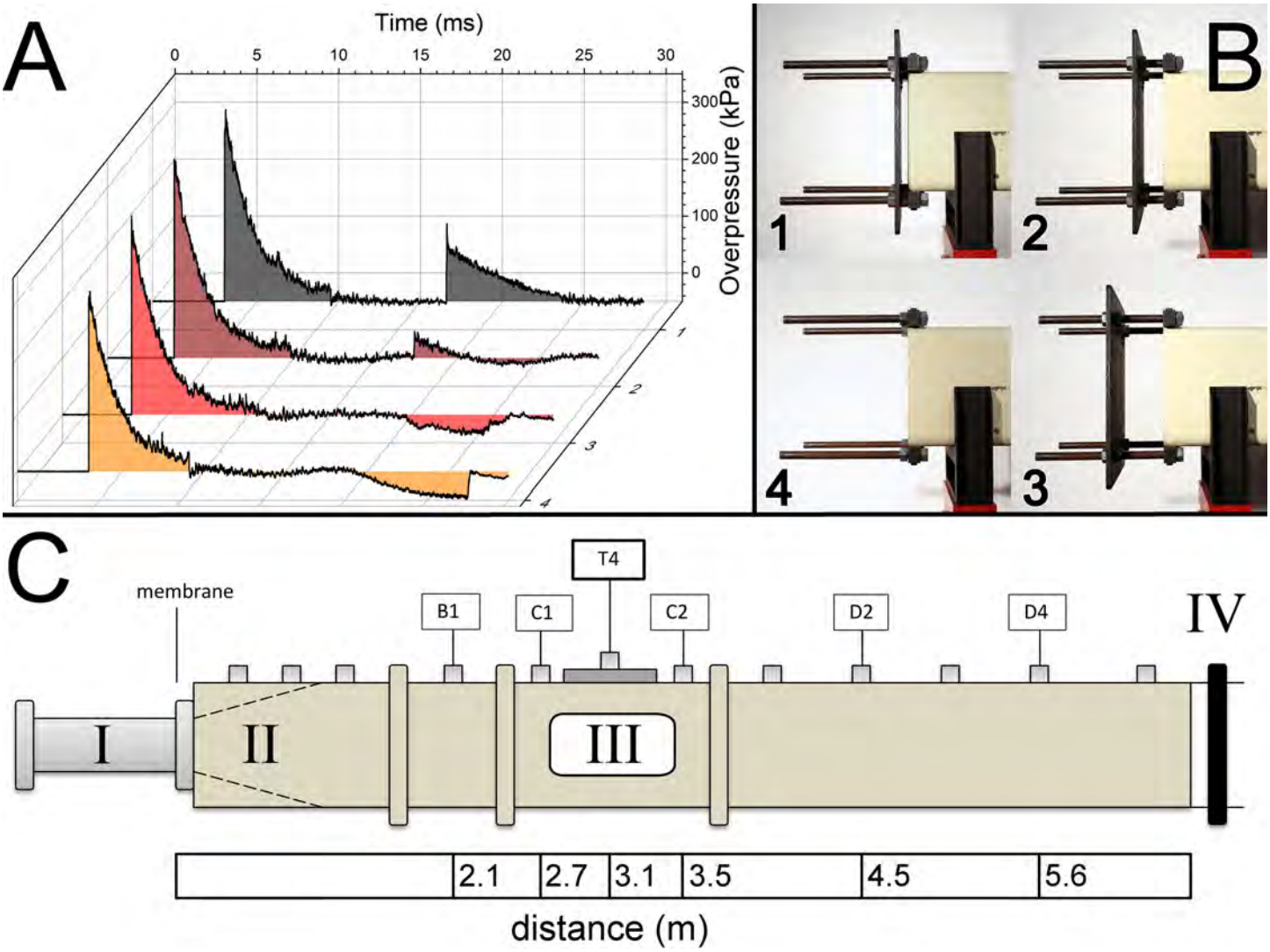


Fig 1. The representative incident shock wave profiles generated using helium as a driver gas and Mylar membrane (thickness of 1.016 mm), with accompanying secondary reflected shock and underpressure waves are presented (A). The profile of the secondary wave depends on the gap between the end plate reflector and the exit of the shock tube (B): 1. 0.625-inch, 2. 2-inch, 3. 4-inch, and 4. open end. C. Schematics of the 9-inch square cross section shock tube indicating the breech (I), transition (II), test section (III) and end plate (IV). Distribution of pressure sensor locations is also illustrated. Typically sensors B1, C1, T4, C2, D2 and D4 were used in our experiments to track the shock wave profile evolution along the entire length of the shock tube. The scale bar indicates the distance of specific sensor from the breech, i.e. Mylar membranes installation port.

doi:10.1371/journal.pone.0161597.g001

characteristics. This work has also wider implications for the testing using shock tubes: our data indicate the end of the shock tube is less desirable specimen location, since the incident shock wave exiting the shock tube is inseparable from secondary waves, and thus always exposed to mixed mode loading.

Materials and Methods

The shock tube

The shock tube housed at the Shock Wave Testing facility at the Center for Injury Biomechanics, Materials and Medicine (CIBM^3) at the New Jersey Institute of Technology has a 9" square cross section and a modular design with the following characteristics: 1) adjustable volume

breech, 2) variable length transition section, 3) the 6 meter long test section, equipped with bullet-proof glass windows for high speed video observation of the specimen during the shock wave exposure, and 4) the reflector end-plate (Fig 1). In this study, the compressed helium was filled into the fixed volume breech, separated from the main body of the shock tube with Mylar membranes of three thicknesses (*vide infra*). The pressure inside the breech was continuously monitored using a WIKA A-10 sensor (0–340 atm range) and the burst pressure was recorded for all the tests.

Overpressure measurement

We measured incident blast overpressure waves and secondary waves using a series of pressure sensors distributed along the shock tube (Fig 1C). A custom made LabView program running on in-house built data acquisition system based on National Instruments PXI-6133 S Series multifunction DAQ modules and PXIe-1082 PCI Express chassis was used for this purpose. Pressure sensors used in our experiments were PCB Piezotronics (Depew, NY) model 134A24. All data were recorded at 1.0 MHz sampling frequency and the typical acquisition time was 200 milliseconds.

Experimental design

This study was designed as two factor experimental design, 4 x 3. Two experimental variables investigated in this study are: 1) the distance between the reflector plate and the end of the shock tube (four levels) and 2) shock wave intensity (three levels). The distance between the reflector plate and the end of the shock tube was adjusted as shown in Fig 1B. Four different gap lengths were used: 1) 0.625", 2) 2" and 3) 4", and 4) open end. The incident blast overpressure was controlled by adjusting the thickness of Mylar membranes sandwiched between the breech and expansion section. The thickness was adjusted by stacking individual membranes with thickness of 0.01 inches (0.254 mm). In this study we used three membrane thicknesses (0.02, 0.04, and 0.06 inches, denoted as 2, 4 or 6 membranes, respectively). All tests were performed using single fixed breech volume of 6.5×10^{-3} m^3, and were repeated six times for each combination of experimental covariates. Additional tests were also performed with a fully closed shock tube (in triplicates for all three membrane thicknesses) to establish boundary conditions for reflected wave intensities and velocities.

Numerical simulations

The propagation of blast waves are modeled in the shock tube environment. The air inside the shock tube through which the blast wave propagates is modeled using Eulerian elements. The size of the Eulerian domain corresponds to the physical dimensions of the shock tube used in the experiments (cross-section: 229 x 229 mm). The heterogeneous meshing of the shock tube was adopted, with fine mesh near the end and coarse mesh elsewhere, in order to decrease total number of elements in the model without sacrificing accuracy.

Solution scheme. The finite element (FE) model is solved using the nonlinear transient dynamic procedure with the Euler-Lagrangian coupling method (Abaqus 6.10). In this procedure, the governing partial differential equations for the conservation of mass, momentum, and energy, along with the material constitutive equations and corresponding equations defining the initial and boundary conditions are solved simultaneously. The Eulerian framework allows the modeling of highly dynamic events (e.g., shock) which would otherwise induce heavy mesh distortion. An enhanced immersed boundary method was used to provide the coupling between the Eulerian and the Lagrangian domains.

Comparison with field blast waves

Comparison of experimental data (overpressure profile recorded by sensor at T4 location) with idealized field blast profiles were performed using ConWep 2.1.0.8. [36]. The blast wave profiles were simulated as hemispherical ground explosion which were generated by TNT charge with weight in the range 10–2000 kg in the standoff distance range of 2–25 m. Only these profiles falling within range of both BOP and impulse of experimental data were used.

Statistical analysis

Data from experiments preformed at different experimental conditions (end plate gap) were pooled together in 3 subsets according to blast intensity (membrane thickness). Data was checked for normality using Ryan-Joiner test (similar to Shapiro-Wilk) in Mintab 17.0. Then multiple comparison two-tailed t-test was performed with Bonferroni correction and $p < 0.003$ was considered statistically significant. Power analysis was performed with GPower 3.1.9.2 software. All data are presented as mean and standard deviation.

Results

Blast Overpressure and Burst Pressure

Peak blast overpressures (BOP) for different membrane thicknesses and back plate conditions are presented in Fig 2. BOP increased with membrane thickness and shows a direct correlation with the burst pressure (the maximum pressure measured in the breech at the time of membrane rupture). The variations between the measured BOP in experiments where the same membrane thicknesses were used are relatively small for all four back plate conditions, as evidenced by narrow standard deviation values (Fig 2A–2C). The blast overpressure is found to be a linear function of the burst pressure (S1 Fig). The variations of the maximum burst pressure can be attributed to sample-to-sample differences in Mylar membrane mechanical properties, typical for this class of commercially available materials [37]. The variation in burst pressure increases with Mylar membrane thickness (i.e. number of membranes), as evidenced by increasing standard deviation (S1 Fig).

The general observed trend is that the peak BOP decreases as the shock wave travels down the tube, and the end plate configuration has no effect on the peak BOP, with an exception of peak overpressures recorded at sensor locations C1 and T4, for which differences are not statistically significant ($p > 0.05$, Fig 2D).

Incident Shock Wave Velocities

The calculated values of the velocity of the shock front, traveling in the shock tube are presented in Fig 3. The shockwave velocities increase with the thickness of the Mylar membrane, but just as in the case of peak BOPs there appears to be virtually no difference between the shock velocities for varying back plate conditions. For all three Mylar membrane thicknesses used in these experiments the general observed trend is that the shock wave velocity decreases with the distance travelled in the shock tube: 540 to 500 m/s (deceleration: -16.4 m s^{-2}, Fig 3A), 630 to 570 m/s (-22.9 m s^{-2}, Fig 3B) and 680 to 620 m/s (-23.3 m s^{-2}, Fig 3C), for the membrane thickness of 0.02, 0.04 and 0.06 inches, respectively. It is also clear that the shock wave velocity variation is higher the closer the measurement location is to the breech. The pooled data for all measurements show narrow standard deviations for the velocities for all sensor locations after the test section sensor T4 (C2, D2 and D4). The velocities remain unchanged until shock wave reaches sensor D2 ($p < 0.005$, power: >0.95 with respect to velocities at T4 and C2) for all three tested membrane thicknesses (Fig 3D).

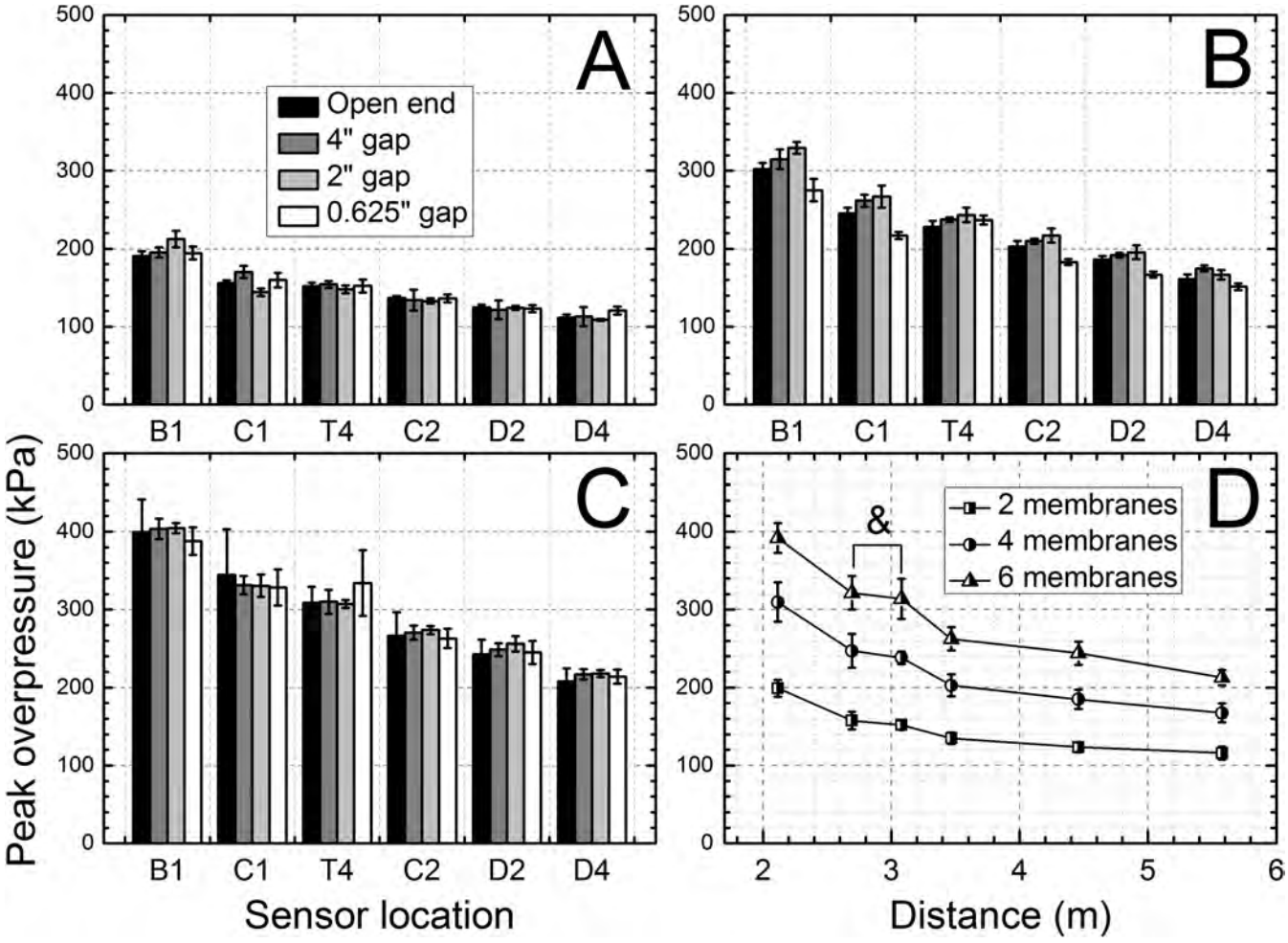


Fig 2. Peak overpressure inside of the shock tube as a function of sensor location and membrane thickness: A) 0.02", B) 0.04", and C) 0.06". Peak overpressure values averaged among experiments preformed using the same Mylar membrane thickness (D): differences of average BOPs for sensors C1 and T4 are not statistically significant (marked with ampersand **&**, $p > 0.05$) in respective test groups.

doi:10.1371/journal.pone.0161597.g002

Impulse

The integrals of the shock wave overpressures versus time (impulse) generated using three different membrane thicknesses are depicted in Fig 4. In general, the impulse values increase with increased number of Mylar membranes (burst pressure) used (Fig 4A–4C). Within the same group the impulse variation along the length of the shock tube is relatively small, except for the C1 and D4 sensors. The most important differences are observed for the sensor D4, where the impulse is significantly higher for 0.625" end gap, when are compared to other end plate configurations (Fig 4A–4C).

The results of analysis of all pooled data revealed (Fig 4D) that differences between impulse values recorded at the C1 and T4 locations are statistically significant ($p < 0.003$, power: >0.95) when compared to other sensor locations. Similarly to BOP measurements the standard deviations tend to increase with increasing burst pressure (number of Mylar membranes used).Our experimental overpressure profiles recorded in the test section (T4 sensor location) match field explosion BOPs and impulses retrieved simulated using TNT charge weight of 19.8, 34.2 and 66.0 kg at standoff distance of 7.0–7.6 m for 2, 4 and 6 membranes, respectively (S1 Table and S2 Fig).

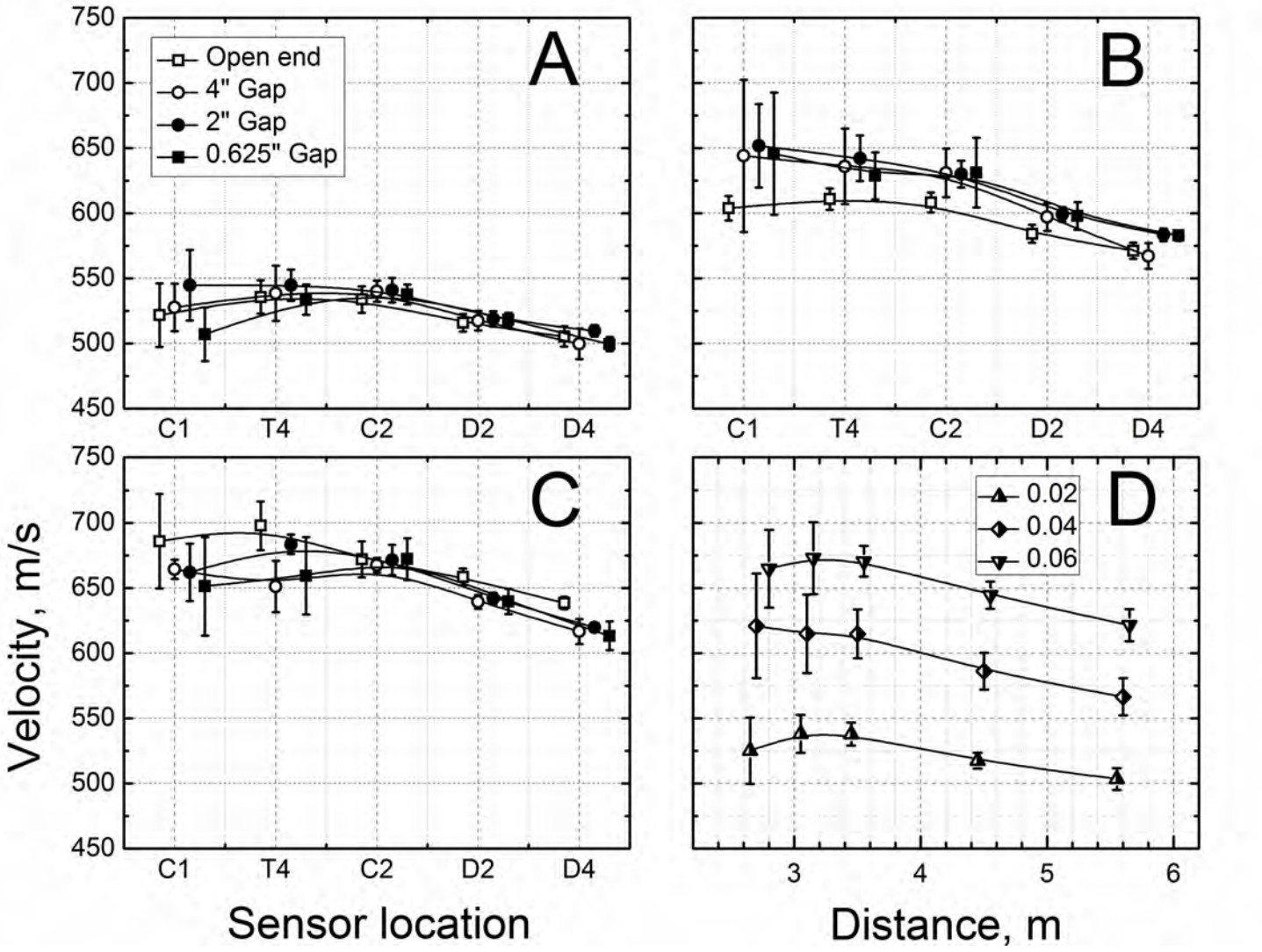


Fig 3. Calculated shock wave velocities at different sensor locations as a function of BOPs generated using Mylar membranes with thicknesses of: A) 0.02", B) 0.04", and C) 0.06". Shock wave velocities were averaged for all experiments preformed using the same Mylar membrane thickness (D). Individual data points were horizontally shifted for clarity of presentation. The B1 sensor was used as a reference for all calculations.

doi:10.1371/journal.pone.0161597.g003

Quantification of secondary positive and under-pressure waves

The significance of the reflection waves and under-pressure waves on the loading of the test subject (in the test section at the T4 sensor location) is illustrated in Fig 5. When the end is fully open, the under-pressure wave that was generated had a minimum peak within 35% to 45% of the intensity of the original shock wave in the test section (as measured at T4 location). This means that the test subject (i.e. animal model) is being loaded with the original shock wave, and then shortly thereafter also by under-pressure wave, coming from the opposite direction. Implementing a back plate 4 inches away from the mouth of the shock tube decreases the under-pressure ratio to about 20% in the test section. Bringing the plate two inches closer completely eliminates the observed under-pressure waves, but causes a secondary reflected shock wave to travel back into the shock tube. In this configuration, the test subject is exposed

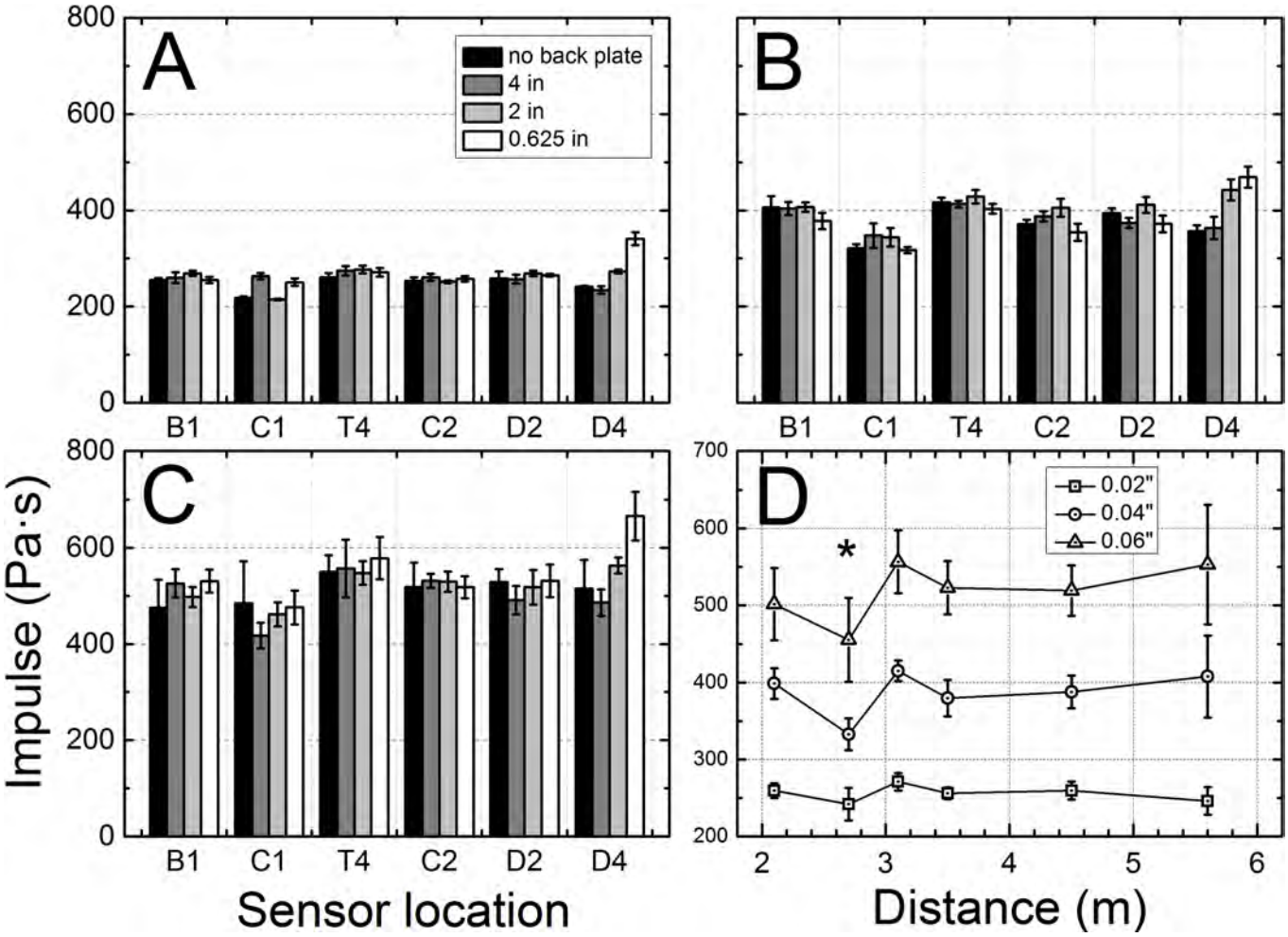


Fig 4. Positive phase impulse measured for the shock waves traveling inside of the shock tube as a function of sensor location and membrane thickness: A) 0.02", B) 0.04", and C) 0.06". The average impulse of shock waves recorded for three respective Mylar membrane thicknesses used as a function of sensor location along the shock tube (D). Asterisk indicates impulse value recorded by the C1 sensor, which shows statistically significant difference in respective data sets ($p < 0.003$, power: >0.95).

doi:10.1371/journal.pone.0161597.g004

to the original shock wave plus the additional reflection wave, with intensity of merely 10–15% of the original shock front, coming from the opposite direction. When the plate-to-shock tube gap is further decreased to 0.625 inches, the peak overpressure of incident to reflected shock wave ratio in the test section increases to 30–40% of the original shock front BOP. Velocities of reflected underpressure (open end and 4" gap) and overpressure waves (2" and 0.625" gap) are presented in Fig 6. The underpressure waves generated under all test configurations propagate inside of the shock tube with subsonic velocities (Fig 6A and 6B), while overpressure reflected waves retain supersonic but somewhat diminished velocities (Fig 6C and 6D).

Optimization of end plate gap

In this work we demonstrate control of the loading conditions inside of the shock tube can be easily achieved by the optimization of the end plate gap distance. The exposure of the specimen can be limited to a single shock wave without additional secondary over- or underpressure waves by optimization of the end plate gap distance. For this purpose we ran a series of tests

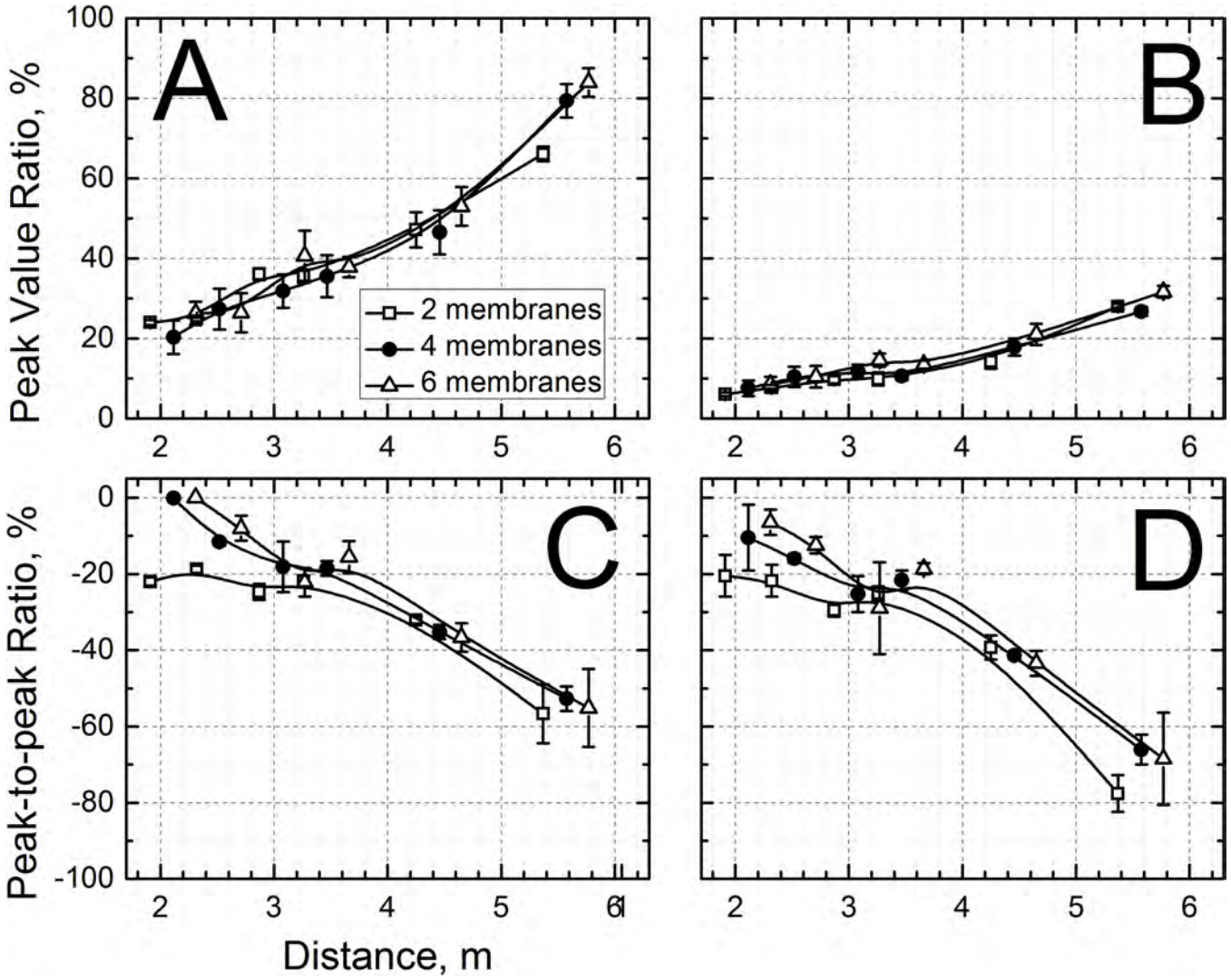


Fig 5. The ratios of peak overpressure between incident and reflected shock wave measured at different locations inside of the shock tube as a function of sensor distance from the breech and blast intensity: A) 0.625" gap, B) 2" gap between end of the shock tube and reflector plate. The ratios between incident peak overpressure and the lowest level (through) of measured reflected underpressure for blasts generated when the gap between the end of the shock tube and reflector plate was 4" (C) and with open end (D). The data points were horizontally shifted for clarity of presentation.

doi:10.1371/journal.pone.0161597.g005

generating shock waves with three different magnitudes. The shock tube end plate was set in the reflected shock wave regime (0.625" and 2" gap). Three linear functions were generated for both configurations (Fig 7A) and it turned out all these functions converge in a single point at 2.8 inches. The optimized end plate gap was then used to verify our predictions and as can be seen in Fig 7B–7D there are no secondary artifacts in the test section as measured by sensor located at T4.

Numerical simulations

We have also performed numerical simulations of the shock wave propagating in the tube (Fig 8). The data recorded by the T4 sensor was used as the input for all three membrane thicknesses used in our experimental design. A representative example of results is presented in

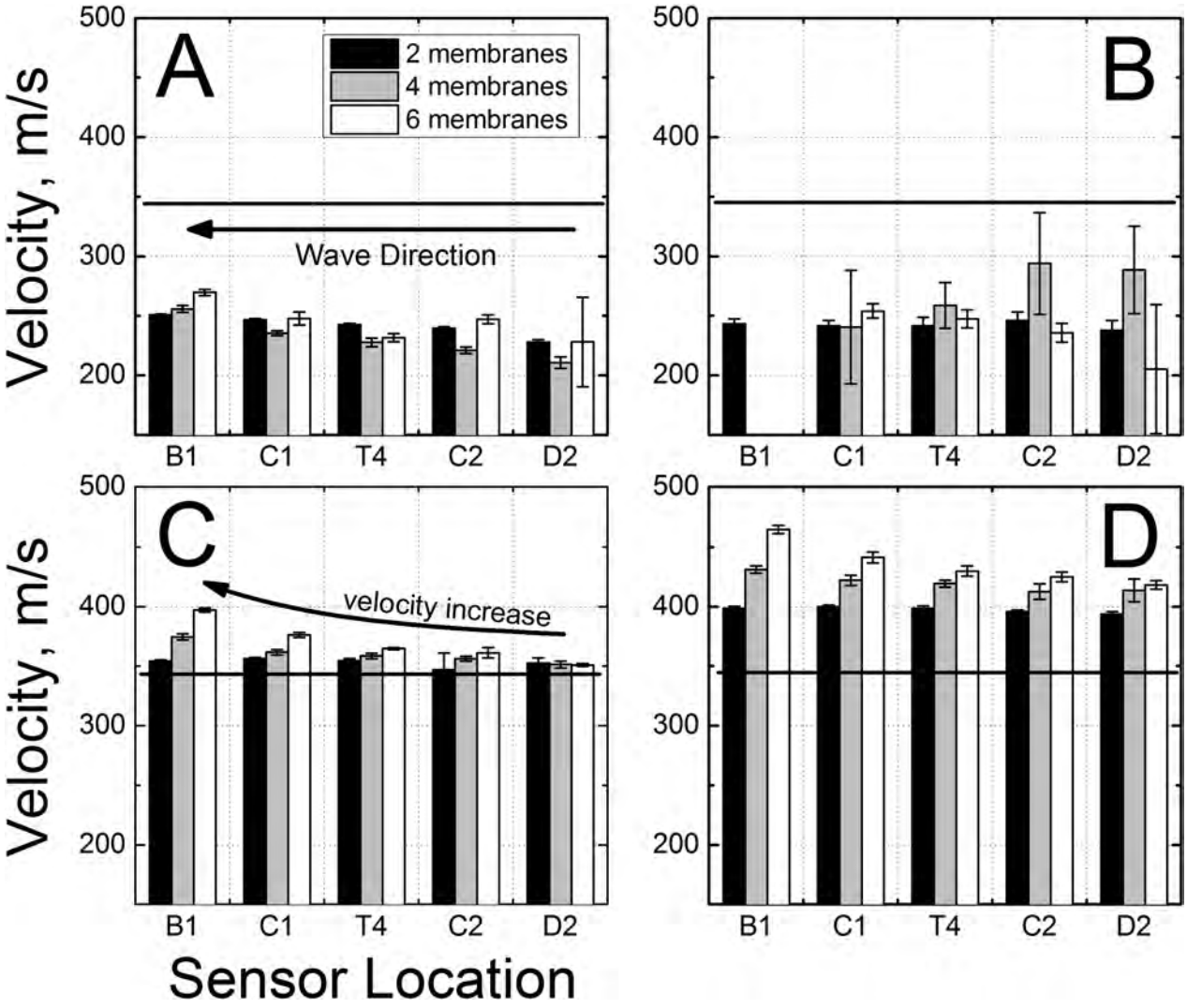


Fig 6. Velocities of reflected underpressure (A, B) and overpressure (C, D) waves generated with: A) open end, B) 4" gap, C) 2" gap and D) 0.625" gap. The straight arrow indicates the direction of the reflected waves' propagation. The red and green horizontal lines indicate sound speed in the air. The velocity of reflected waves increases with the distance from the end of the shock tube, which is caused by increased helium (driver gas) concentration closer to the breech. The D4 sensor was used as reference.

doi:10.1371/journal.pone.0161597.g006

Fig 8B for pressure history of a shock wave generated using Mylar membrane with thickness of 0.020" and 2 inch end plate gap (other results are presented in S3–S7 Figs). Overall the results between simulations and experiments agree well. It would appear all characteristic features (peak overpressure, duration, and velocity) are replicated with good accuracy and fidelity for incident as well as for secondary waves.

Experimental x-t diagram

In order to establish boundary conditions for the x-t diagram we performed measurements of shock wave traveling in the shock tube with closed end (S8 Fig). This configuration results in generation of the maximum reflected pressures in the shock tube, and we performed three replicates per each of three membrane thicknesses. The other extreme case is fully open end which

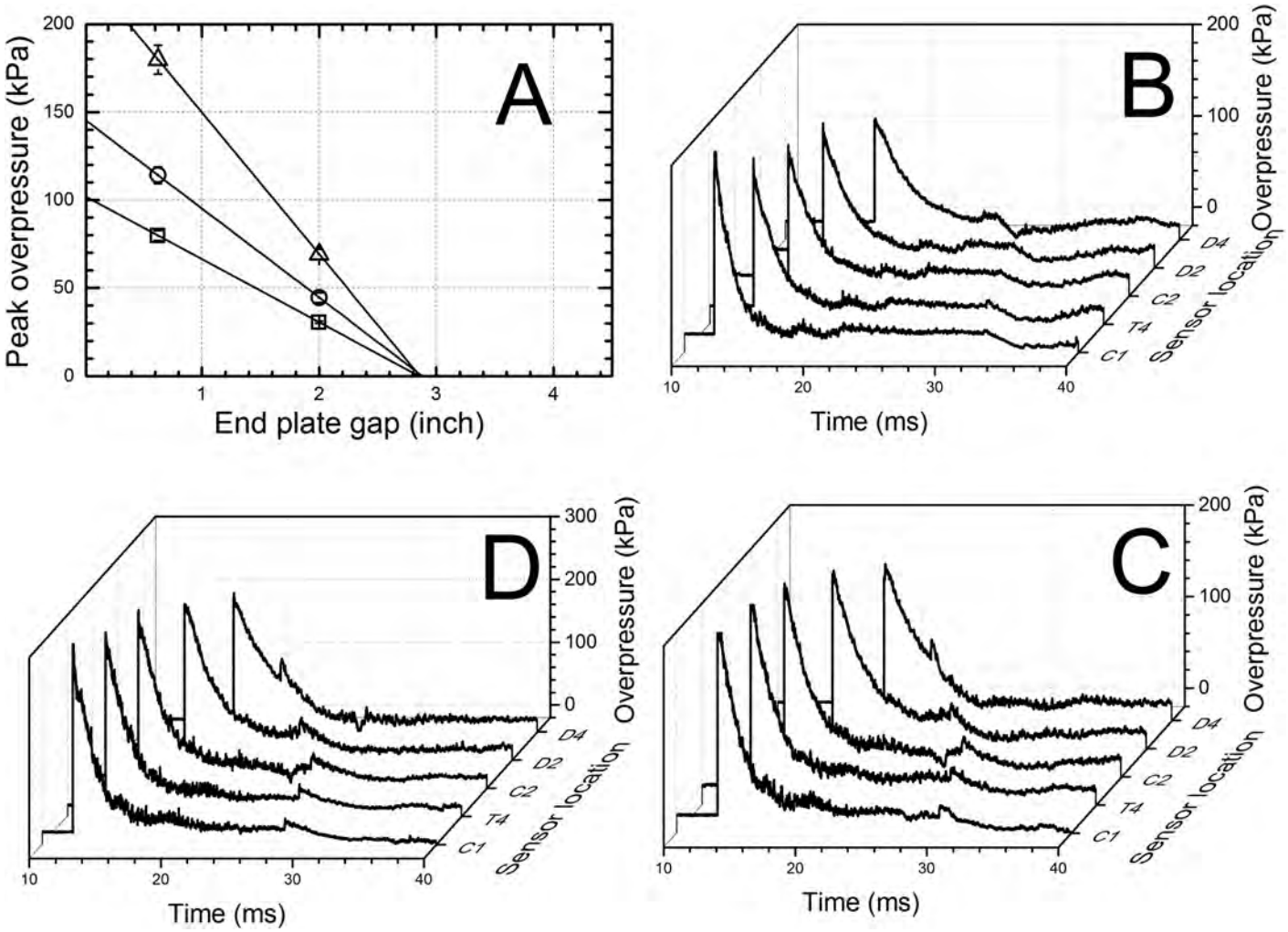


Fig 7. The optimization of the end plate to the shock tube gap distance. A. Reflected peak overpressure values measured at the D4 location for three different membrane thicknesses (0.02, 0.04 and 0.06 inch) and two different end plate gap sizes (0.625 and 2.0 inches) were used to identify the optimal gap size, i.e. the point on the plot where all linear functions converge (x_0 = 2.85 inch). Overpressure profiles recorded using optimized end plate position at three different blast intensities generated using: B. 0.02", C. 0.04" and D. 0.06".

doi:10.1371/journal.pone.0161597.g007

results in the underpressure secondary wave, and comparison between these two cases (fully closed reflected waves and the fully open underpressure waves) is presented in Fig 9.

Discussion

Compressed-gas driven shock tubes remain the most widely used and convenient method to generate controlled characteristics shock waves in laboratory setting [13, 38]. In spite of the popularity of this test device, the development of the blast wave along the length of the tube is not well understood, and clarification is required regarding the nature of loading conditions (presence of reflection and under-pressure waves) inside the shock tube. Our earlier work has clearly shown that in order to simulate primary blast conditions, the specimen have to be placed well inside the shock tube [19, 39]. However, compressive or expansive pressure waves can still affect the loading condition of the specimen. If these secondary waves are not properly extinguished they can be introduced after the original shock wave, and thus result in additional,

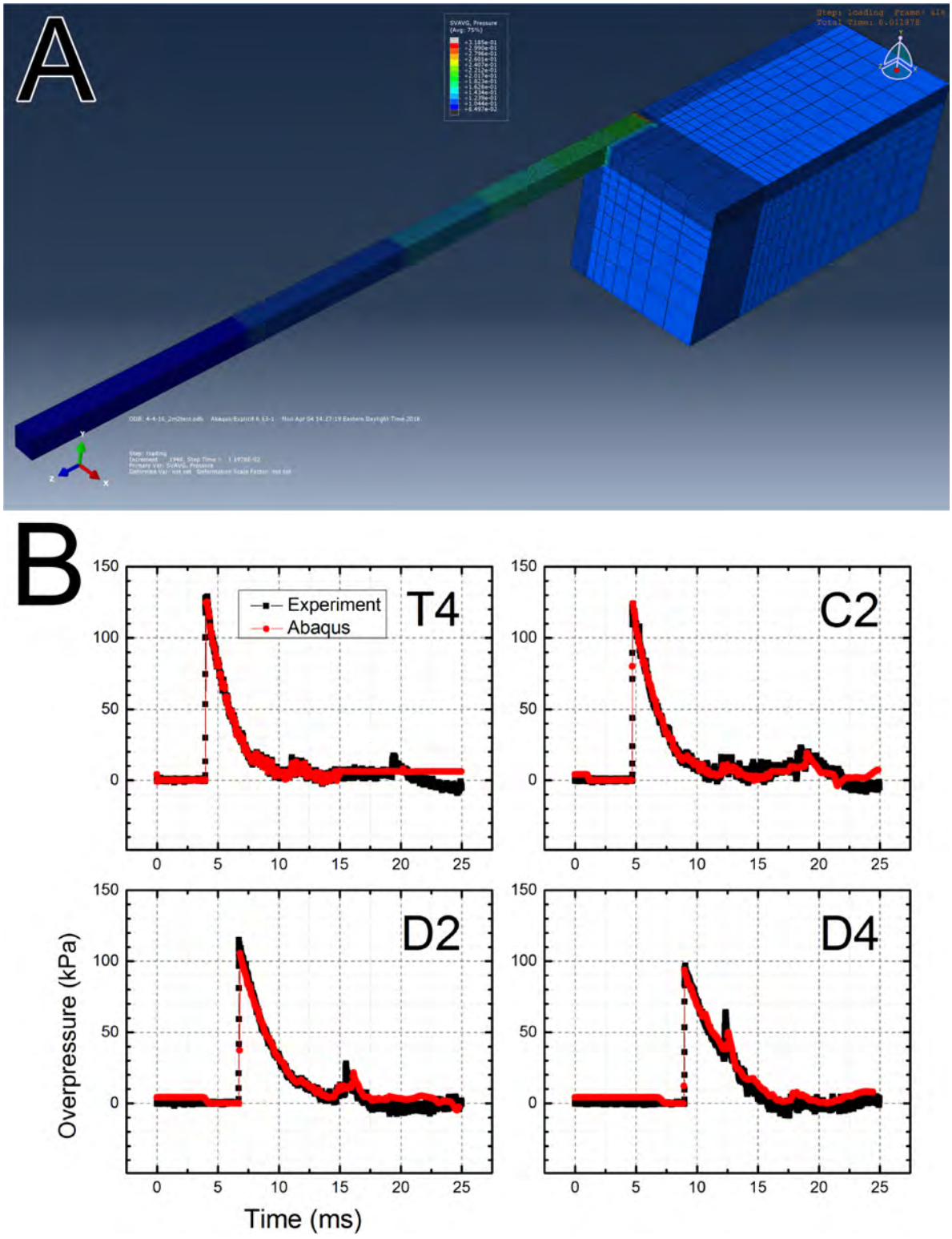


Fig 8. Numerical simulations: A) isometric view of the full scale model of the 9 inch square cross section shock tube, B) comparison of pressure traces recorded experimentally and obtained as results of numerical simulations with Abacus software for shock wave generated using 0.020" thick Mylar membrane and 2 inches end plate gap. Input feed for simulations was composed using initial 15 ms of the incident overpressure recorded by T4 sensor and 10 ms of baseline signal. This was done to eliminate secondary loading waveform from input data, which leads to erroneous calculations.

doi:10.1371/journal.pone.0161597.g008

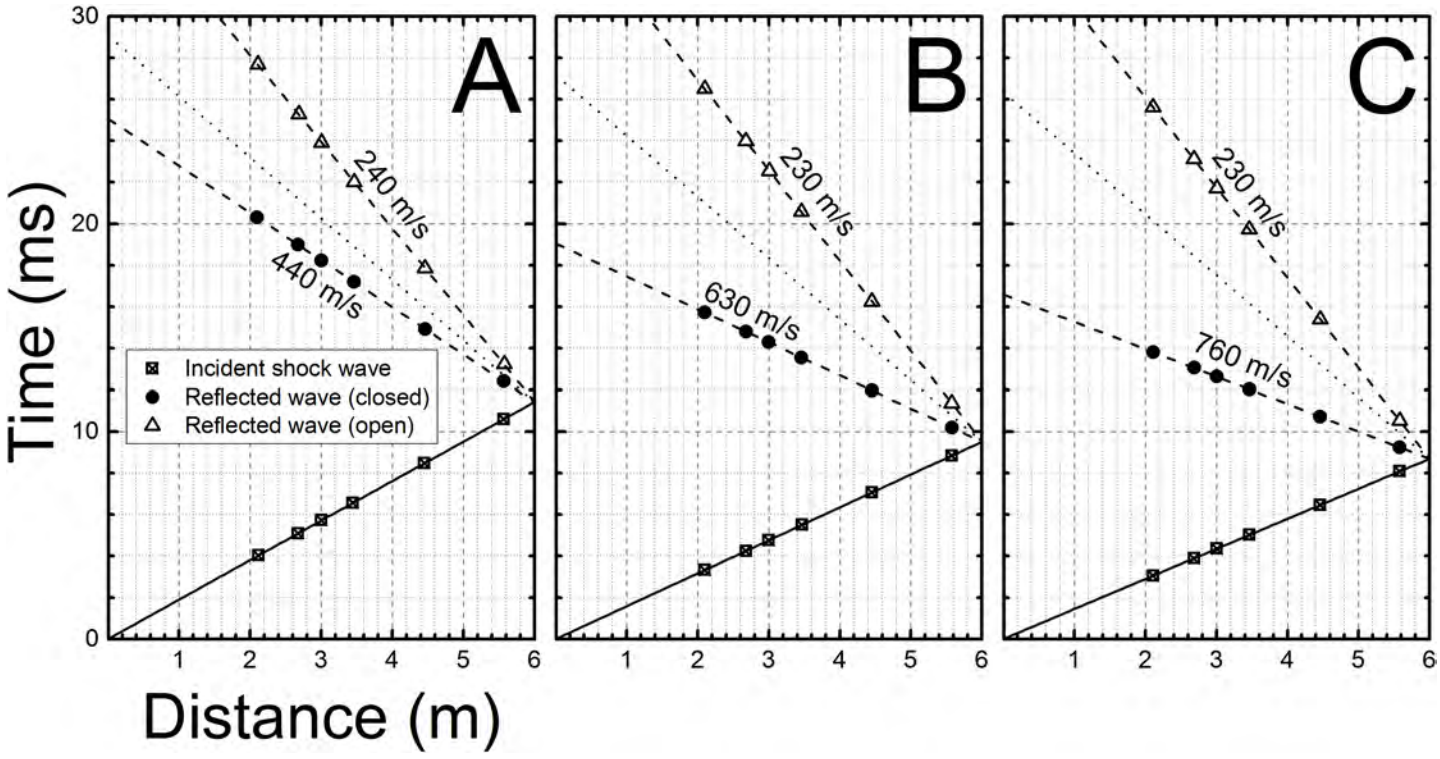


Fig 9. The distance-time (x-t) diagrams for incident and reflected waves based on experimental arrival times obtained at membrane thicknesses of: A) 0.02, B) 0.04, and C) 0.06 inches, respectively. The traces representing reflected waves are from experiments when the tube was fully closed and the underpressure waves observed when no endplate was present. Speed of sound for reflected wave domain is marked as dotted line.

doi:10.1371/journal.pone.0161597.g009

potentially unwanted biomechanical load sustained by the test subject. The mitigation of secondary loading is thus of paramount importance for studying the effects of shock waves, especially for delineation of elementary mechanisms of bTBI. In this paper, we investigate the use of an end-reflector plate to modify the reflection and under-pressure waves that reenter the shock tube and resulting loading conditions.

The incident pressure measured in the shock tube decreases as the shock wave propagates towards the exit (Fig 2), independent of the test configuration used. However, there are no statistically significant differences in BOPs measured by C1 and T4 sensors ($p > 0.05$, marked with ampersand). This indicates the dynamics of shock wave generation: the expanding driver gas impact is decreasing until it reaches minimum at C1, since the volume expansion exceeds B1 sensor position (calculated using ideal gas conditions), thus the BOP registered by C1 sensor remains virtually constant between C1 and T4 sensors, which is then followed by BOP decay further downstream (C2, D2 and D4 sensors, Fig 2D). The calculated average velocities of shock waves generated using three different membrane thicknesses, are in line with these observations (Fig 3), i.e. the decrease in BOP is accompanied by respective decrease in shock wave velocity. The impulse measurements reveal more detailed picture of the dynamics of the system (Fig 4). While the impulse is diminishing in the driver gas affected region (B1 to C1) the impulse of 'free' shock wave is increasing (C1 to T1) and thus fully developed shock wave is present at T4 location (Fig 4D). Further downstream the impulse is not changing its value, but considering the BOP is steadily decreasing with accompanying decreased velocity it indicates the dissipation of energy of the shock wave. There are currently a number of competing theories which explain the decay of shock waves. The decay of spherical and cylindrical shock

waves (3D and 2D waves encountered in the field conditions) is caused by purely geometrical factor as the intensity of the shock wave decreases with as an inverse of the square radius (distance) from the epicenter ($1/r^2$, for shock waves separated from the source) or following linear relationship (1/r), respectively [40]. However, these two are not applicable to unidimensional waves generated in the shock tube. The viscous effects near the shock tube walls (wall friction, growth of the boundary layer) were proposed as explanation of observed attenuation of the shock wave intensity in the tube [41, 42]. However, these effects are considered important for shock tubes with relatively small diameters ranging from 0.3 to 3.8 cm [41], while in our case the diameter is much larger (9 in, or 22.86 cm) and thus these effects are less likely to be responsible for observed attenuation. The dusty medium was proposed as responsible for decay of the shock waves propagating in the shock tube [32, 33]. In our case this effect is negligible, since no appreciable sized particles were purposely introduced into the environment and typically the number of dust particles in the air is insufficient to be solely responsible for the intensity decay. The hypothesis suggesting the rarefaction wave following the incident shock wave was also proposed as a mechanism of shock wave dissipation [39, 43], but in our experimental data this type of waves were never observed. However, in our model used for numerical simulations the agreement between experimental data and theory is excellent (Fig 8). This model doesn't include any of postulated mechanisms of shock wave attenuation discussed in this paragraph. Thus, it appears simple expansion of the pressure contained within the shock wave is solely responsible for observed attenuation.

The values of impulses at the D4 sensor location for both short gap (0.625" and 2", Fig 4) end plate configurations are obscured by presence of secondary shock waves, which overlap with a primary wave (Fig 8B, S4 and S6 Figs). This illustrates the loading experienced by the specimen in that location, i.e. the loading is never a single primary shock wave, but a sum of primary and secondary loading. The nature of secondary loading will depend on the end configuration and it will be: 1) additional reflected shock wave with intensity dependent on end plate gap, or 2) underpressure wave (for sufficiently large gap and open end). Independently on the nature of the secondary loading the conditions experienced by the specimen mounted in the location are the most complex than these encountered in any other location in the shock tube. The specimen receives almost double the loading of the original shock wave (for tests conducted with 0.625 and 2 inch gap) or mixed mode loading of incident over- and secondary under pressure waves (for 4 inches gap and open end configuration).

The gap size between the reflector plate and the end of the shock tube governs the type of generated secondary wave, i.e. when it is below critical distance reflected overpressure waves are generated, however when the gap size is larger than the critical size, the under-pressure waves are created (Figs 1A, 5 and 6). The nature of the generated waves dictates their propagation speed: the under-pressure waves generated during experimentation don't exceed the speed of sound (Mach number = 1.0, marked as horizontal lines in plots presented in Fig 6), which is in agreement with existing knowledge [44]. The reflected waves for the shortest end-plate gap travelled faster than the speed of sound, but were slower than the original shock front (Figs 3, 6 and 9). Moreover, we observed an increase in velocity with the time of propagation for all reflected positive pressure shock waves. This phenomenon is caused by increased concentration of the driver gas (helium) in the part of the shock tube closer to the breech (sound speed in helium is 1007 m/s, while it is 343 m/s in air at 20°C) shortly after the membrane burst. Also, it should be noted that these reflected over- and under-pressure waves travel in the opposite direction of the original shock wave.

The calculated velocities of the underpressure and reflected shock waves illustrate the impact of the driver gas has on the dynamics of the shock wave propagation. As the compressed helium ruptures the membrane, the original shock wave travels into the body of the

shock tube, and the driver gas is diffusing towards the test section. The reflected wave traveling towards the breech is propagating in the mixture of air and helium, and hence reflected shock wave velocity gradually increases. This effect is more pronounced for shots with six membranes (0.06" thickness), because higher helium pressure is necessary to cause membrane rupture (average burst pressure was 250, 490 and 730 psi, for membrane thickness of 0.02, 0.04 and 0.06 inch, respectively, S1 Fig). The velocity of reflection waves is decreased compared to the original shock front, because of energy loss after the reflection (and the portion of the blast that escapes through openings at the mouth of the tube).

The reflection and under-pressure ratios shown in Fig 6 demonstrate the effect of positioning an end-reflector plate at the end of the shock tube and potential additional loading that a test subject may sustain due to plate positioning or its absence. In order to minimize the loading caused by secondary waves reentering the shock tube, the end-reflector position has to be optimized to find the position where the action of over- or underpressure waves traveling back inside of the shock tube is minimized or completely eliminated. This can be achieved by running a series of calibration experiments at different incident shock wave intensities and end plate gap distances. However, this knowledge must be coupled with proper positioning of the specimen far away from the end of the shock tube to eliminate any possibility of end effects on the tests specimen.

Conclusions

In this work we have systematically evaluated means to eliminate unwanted secondary artifacts in order to obtain pure shock wave waveform in the test section inside of the shock tube (T4 location). It is of particular importance for the study of effects of shocks on biological systems, with particular emphasis on the brain. Application of reflector end plate positioned within optimized perimeter resulted in elimination of virtually all secondary positive and negative pressure waves. Our results indicate the end of the shock tube is less favorable location to test specimen due to complexity of loading conditions. Incident shock wave exiting shock tube results in formation of underpressure waves, while reflected pressure waves are created when the end is fully closed or the reflector plate is at relatively short distance from the muzzle. Numerical simulations were used to corroborate the findings and combined with analysis of experimental data these results indicate shock wave decompression as plausible decay mechanism. The tests done in this study should serve as a strong starting point for researchers attempting to ensure accurate loading of test subjects in a compressed-gas driven shock tubes.

Supporting Information

S1 Fig. Burst pressure as a function of Mylar membrane thickness (left panel) and linear fit of the experimental data (right panel).
(PNG)

S2 Fig. Comparison of blast overpressure profiles obtained experimentally in the 9-inch square cross section shock tube (T4 sensor) and simulated using ConWep and corresponding to explosion of: a) 19.8 kg TNT at standoff distance of 7.0 m, b) 34.2 kg of TNT at standoff distance of 7.0 m, and c) 66.0 kg of TNT at standoff distance of 7.6 m.
(PNG)

S3 Fig. The close up of the shock tube (end) and surrounding space used in the model for numerical simulations (top panel). Comparison of pressure traces recorded experimentally and obtained as results of numerical simulations with Abacus software for shock wave

generated using 0.020" thick Mylar membrane and 4 inches end plate gap. Input feed for simulations was composed using initial 15 ms of the incident overpressure recorded by T4 sensor and 10 ms of baseline signal. This was done to eliminate secondary loading waveform from input data, which leads to erroneous calculations. Underpressure wave penetrating inside of the shock tube is clearly visible at 12 ms (D4), 15 ms (C2), 18 ms (D2), and 20 ms (T4).
(PNG)

S4 Fig. Comparison of pressure traces recorded experimentally and obtained as results of numerical simulations with Abacus software for shock wave generated using 0.040" thick Mylar membrane and 2 inches end plate gap. Input feed for simulations was composed using initial 15 ms of the incident overpressure recorded by T4 sensor and 10 ms of baseline signal. This was done to eliminate secondary loading waveform from input data.
(PNG)

S5 Fig. Comparison of pressure traces recorded experimentally and obtained as results of numerical simulations with Abacus software for shock wave generated using 0.040" thick Mylar membrane and 4 inches end plate gap. Input feed for simulations was composed using initial 15 ms of the incident overpressure recorded by T4 sensor and 10 ms of baseline signal. This was done to eliminate secondary loading waveform from input data.
(PNG)

S6 Fig. Comparison of pressure traces recorded experimentally and obtained as results of numerical simulations with Abacus software for shock wave generated using 0.060" thick Mylar membrane and 2 inches end plate gap. Input feed for simulations was composed using initial 15 ms of the incident overpressure recorded by T4 sensor and 10 ms of baseline signal. This was done to eliminate secondary loading waveform from input data.
(PNG)

S7 Fig. Comparison of pressure traces recorded experimentally and obtained as results of numerical simulations with Abacus software for shock wave generated using 0.040" thick Mylar membrane and 4 inches end plate gap. Input feed for simulations was composed using initial 15 ms of the incident overpressure recorded by T4 sensor and 10 ms of baseline signal. This was done to eliminate secondary loading waveform from input data.
(PNG)

S8 Fig. Example pressure traces recorded along the shock tube (incident pressure) for closed end configuration shots at: A. 2, B. 4 and C. 6 membranes. Only incident shock wave and first reflected wave peak are presented for clarity.
(PNG)

S1 File. Tabulated numerical values of raw experimental data used in Figs 2 to 9.
(XLSX)

S1 Table. The comparison of the characteristic parameters of the shock waves generated in the 9-inch square cross section shock tube by sensor at T4 location and blast wave profiles generated using ConWep. Average values and standard deviations are reported.
(PDF)

Acknowledgments

Help received from Mr. Jonathan Salib during experiments using shock tube are gratefully acknowledged.

Author Contributions

Conceived and designed the experiments: MS NC.

Performed the experiments: AM MK MS.

Analyzed the data: MS MK AM.

Wrote the paper: MS MK NC.

Performed numerical simulations: SK AS.

References

1. Elder GA, Cristian A. Blast-related mild traumatic brain injury: mechanisms of injury and impact on clinical care. The Mount Sinai journal of medicine, New York. 2009; 76(2):111–8. doi: 10.1002/msj.20098 PMID: 19306373.
2. Elder GA, Stone JR, Ahlers ST. Effects of low-level blast exposure on the nervous system: is there really a controversy? Frontiers in neurology. 2014; 5:269. doi: 10.3389/fneur.2014.00269 PMID: 25566175; PubMed Central PMCID: PMC4271615.
3. DePalma RG, Burris DG, Champion HR, Hodgson MJ. Blast injuries. New England Journal of Medicine. 2005; 352(13):1335–42. PMID: 15800229
4. Hoge CW, McGurk D, Thomas JL, Cox AL, Engel CC, Castro CA. Mild traumatic brain injury in U.S. Soldiers returning from Iraq. The New England journal of medicine. 2008; 358(5):453–63. doi: 10.1056/NEJMoa072972 PMID: 18234750.
5. Vanderploeg RD, Belanger HG, Horner RD, Spehar AM, Powell-Cope G, Luther SL, et al. Health outcomes associated with military deployment: mild traumatic brain injury, blast, trauma, and combat associations in the Florida National Guard. Archives of physical medicine and rehabilitation. 2012; 93 (11):1887–95. doi: 10.1016/j.apmr.2012.05.024 PMID: 22705240.
6. Gould KE. High-Explosive Field Tests, Explosion Phenomena and Environmental Impacts. DTIC Document, 1981.
7. Cernak I. Blast Injuries and Blast-Induced Neurotrauma: Overview of Pathophysiology and Experimental Knowledge Models and Findings. In: Kobeissy FH, editor. Brain Neurotrauma: Molecular, Neuropsychological, and Rehabilitation Aspects. Frontiers in Neuroengineering. Boca Raton (FL)2015.
8. Knudsen SK, Oen EO. Blast-induced neurotrauma in whales. Neurosci Res. 2003; 46(3):377–86. PMID: 12804799.
9. Bolander R, Mathie B, Bir C, Ritzel D, VandeVord P. Skull flexure as a contributing factor in the mechanism of injury in the rat when exposed to a shock wave. Annals of biomedical engineering. 2011; 39 (10):2550–9. doi: 10.1007/s10439-011-0343-0 PMID: 21735320
10. Cernak I, Merkle AC, Koliatsos VE, Bilik JM, Luong QT, Mahota TM, et al. The pathobiology of blast injuries and blast-induced neurotrauma as identified using a new experimental model of injury in mice. Neurobiology of disease. 2011; 41(2):538–51. doi: 10.1016/j.nbd.2010.10.025 PMID: 21074615
11. Chavko M, Watanabe T, Adeeb S, Lankasky J, Ahlers ST, McCarron RM. Relationship between orientation to a blast and pressure wave propagation inside the rat brain. Journal of neuroscience methods. 2011; 195(1):61–6. doi: 10.1016/j.jneumeth.2010.11.019 PMID: 21129403
12. Rafaels KA. Blast brain injury risk2010.
13. Reneer DV, Hisel RD, Hoffman JM, Kryscio RJ, Lusk BT, Geddes JW. A multi-mode shock tube for investigation of blast-induced traumatic brain injury. Journal of Neurotrauma. 2011; 28(1):95–104. doi: 10.1089/neu.2010.1513 PMID: 21083431
14. Svetlov SI, Prima V, Kirk DR, Gutierrez H, Curley KC, Hayes RL, et al. Morphologic and biochemical characterization of brain injury in a model of controlled blast overpressure exposure. Journal of Trauma and Acute Care Surgery. 2010; 69(4):795–804.
15. Bell RS, Vo AH, Neal CJ, Tigno J, Roberts R, Mossop C, et al. Military traumatic brain and spinal column injury: a 5-year study of the impact blast and other military grade weaponry on the central nervous system. Journal of Trauma. 2009; 66(4 Suppl):S104–11. doi: 10.1097/TA.0b013e31819d88c8 PMID: 19359953.
16. Yattoo G, Tabish A. The profile of head injuries and traumatic brain injury deaths in Kashmir. Journal of Trauma Management & Outcomes. 2008; 2(1):5. doi: 10.1186/1752-2897-2-5 PMID: 18570674; PubMed Central PMCID: PMCPMC2464577.

17. Cernak I, Savic VJ, Kotur J, Prokic V, Veljovic M, Grbovic D. Characterization of plasma magnesium concentration and oxidative stress following graded traumatic brain injury in humans. Journal of Neurotrauma. 2000; 17(1):53–68. PMID: 10674758.

18. Needham CE, Ritzel D, Rule GT, Wiri S, Young L. Blast Testing Issues and TBI: Experimental Models That Lead to Wrong Conclusions. Frontiers of Neurology. 2015; 6:72. doi: 10.3389/fneur.2015.00072 PMID: 25904891; PubMed Central PMCID: PMCPMC4389725.

19. Sundaramurthy A, Alai A, Ganpule S, Holmberg A, Plougonven E, Chandra N. Blast-induced biomechanical loading of the rat: an experimental and anatomically accurate computational blast injury model. Journal of Neurotrauma. 2012; 29(13):2352–64. doi: 10.1089/neu.2012.2413 PMID: 22620716.

20. Vieille P. Sur les discontinuités produites par la détente brusque de gaz comprimes. Comptes Rendus de l'Académie des Sciences. 1899;A 129:1228–30.

21. Park C, Appleton JP. Shock-tube measurements of soot oxidation rates. Combustion and Flame. 1973; 20(3):369–79.

22. Kiefer J, Mizerka L, Patel M, Wei H. A shock tube investigation of major pathways in the high-temperature pyrolysis of benzene. The Journal of Physical Chemistry. 1985; 89(10):2013–9.

23. Hooker WJ, Millikan RC. Shock-Tube Study of Vibrational Relaxation in Carbon Monoxide for the Fundamental and First Overtone. The Journal of Chemical Physics. 1963; 38(1):214–20.

24. Dryer M, Merritt DL, Aronson PM. Interaction of a plasma cloud with the Earth's magnetosphere. Journal of Geophysical Research. 1967; 72(11):2955–62. doi: 10.1029/JZ072i011p02955

25. Cernak I, Wang Z, Jiang J, Bian X, Savic J. Ultrastructural and functional characteristics of blast injury-induced neurotrauma. Journal of Trauma. 2001; 50(4):695–706. PMID: 11303167.

26. Cernak I, Wang Z, Jiang J, Bian X, Savic J. Cognitive deficits following blast injury-induced neurotrauma: possible involvement of nitric oxide. Brain Injury. 2001; 15(7):593–612. doi: 10.1080/02699050010009559 PMID: 11429089.

27. Saljo A, Arrhen F, Bolouri H, Mayorga M, Hamberger A. Neuropathology and pressure in the pig brain resulting from low-impulse noise exposure. Journal of Neurotrauma. 2008; 25(12):1397–406. doi: 10.1089/neu.2008.0602 PMID: 19146459.

28. Saljo A, Svensson B, Mayorga M, Hamberger A, Bolouri H. Low-level blasts raise intracranial pressure and impair cognitive function in rats. Journal of Neurotrauma. 2009; 26(8):1345–52. doi: 10.1089/neu.2008-0856 PMID: 19317610.

29. Stuhmiller JH, Phillips Y, Richmond D. The physics and mechanisms of primary blast injury. Conventional Warfare: Ballistic, Blast, and Burn Injuries Washington DC: Office of the Surgeon General of the US Army. 1991:241–70.

30. Moore DF, Radovitzky RA, Shupenko L, Klinoff A, Jaffee MS, Rosen JM. Blast physics and central nervous system injury. Future Neurology. 2008; 3(3):243–50. doi: 10.2217/14796708.3.3.243

31. Cullis I. Blast waves and how they interact with structures. Journal of the Royal Army Medical Corps. 2001; 147(1):16–26. PMID: 11307674

32. Miura H. Decay of shock waves in a dusty-gas shock tube. Fluid Dynamics Research. 1990; 6(5–6):251.

33. Sommerfeld M. The unsteadiness of shock waves propagating through gas-particle mixtures. Experiments in Fluids. 1985; 3(4):197–206.

34. Newman AJ, Mollendorf JC. The Peak Overpressure Field Resulting From Shocks Emerging From Circular Shock Tubes. Journal of Fluids Engineering. 2010; 132(8):081204-. doi: 10.1115/1.4002183

35. Effgen GB, Hue CD, Vogel E 3rd, Panzer MB, Meaney DF, Bass CR, et al. A Multiscale Approach to Blast Neurotrauma Modeling: Part II: Methodology for Inducing Blast Injury to in vitro Models. Front Neurol. 2012; 3:23. doi: 10.3389/fneur.2012.00023 PMID: 22375134; PubMed Central PMCID: PMCPMC3285773.

36. Hyde DW. CONWEP 2.1.0.8. Vicksburg, MS: Conventional Weapons Effects Program. United States Army Corps of Engineers; 2004.

37. Becker H. Elastic modulus of Mylar sheet. Journal of Applied Polymer Science. 1965; 9(3):911–6. doi: 10.1002/app.1965.070090309

38. Glass II. A Theoretical and Experimental Study of Shock-Tube Flows. Journal of the Aeronautical Sciences. 1955; 22(2):73–100. doi: 10.2514/8.3282

39. Chandra N, Ganpule S, Kleinschmit N, Feng R, Holmberg A, Sundaramurthy A, et al. Evolution of blast wave profiles in simulated air blasts: experiment and computational modeling. Shock Waves. 2012; 22(5):403–15.

40. Needham CE. Blast Wave Propagation: Springer; 2010.

41. Emrich R, Curtis C. Attenuation in the shock tube. Journal of Applied Physics. 1953; 24(3):360–3.

42. Slepička F. Attenuation in Shock Tubes. Physics of Fluids (1958–1988). 1966; 9(9):1865–6.

43. Burnside R, Mackie A. A problem in shock wave decay. Journal of the Australian Mathematical Society. 1965; 5(02):258–72.

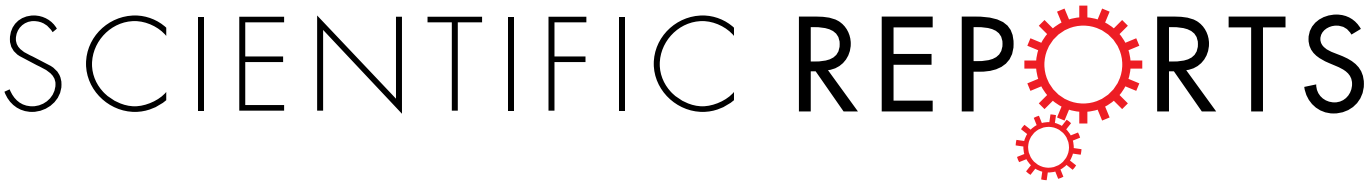
44. Zel'dovlch YB, Raizer YP. Physics of Shock Waves and High-Temperature Hydrodynamic Phenomena: Reprint of the Academic Press Inc., New York, 1966–1967 editions.; 1965.

Appendix A –Publication Cover 23
2016

Authors: V. Mishra, M. Skotak, H. Schuetz, A. Heller, J. Haorah, N. Chandra

Title: *"Primary blast causes mild, moderate, severe and lethal TBI with increasing blast overpressures: Experimental rat injury model"*

Journal Publication: Nature-Scientific Reports, **6**, 26992, (2016), [16-23]



OPEN

Primary blast causes mild, moderate, severe and lethal TBI with increasing blast overpressures: Experimental rat injury model

Received: 01 December 2015
Accepted: 27 April 2016
Published: 07 June 2016

Vikas Mishra[1,*], Maciej Skotak[1,*], Heather Schuetz[2], Abi Heller[2], James Haorah[1] & Namas Chandra[1]

Injury severity in blast induced Traumatic Brain Injury (bTBI) increases with blast overpressure (BOP) and impulse in dose-dependent manner. Pure primary blast waves were simulated in compressed gas shock-tubes in discrete increments. Present work demonstrates 24 hour survival of rats in 0–450 kPa (0–800 Pa·s impulse) range at 10 discrete levels (60, 100, 130, 160, 190, 230, 250, 290, 350 and 420 kPa) and determines the mortality rate as a non-linear function of BOP. Using logistic regression model, predicted mortality rate (PMR) function was calculated, and used to establish TBI severities. We determined a BOP of 145 kPa as upper mild TBI threshold (5% PMR). Also we determined 146–220 kPa and 221–290 kPa levels as moderate and severe TBI based on 35%, and 70% PMR, respectively, while BOP above 290 kPa is lethal. Since there are no standards for animal bTBI injury severity, these thresholds need further refinements using histopathology, immunohistochemistry and behavior. Further, we specifically investigated mild TBI range (0–145 kPa) using physiological (heart rate), pathological (lung injury), immuno-histochemical (oxidative/nitrosative and blood-brain barrier markers) as well as blood borne biomarkers. With these additional data, we conclude that mild bTBI occurs in rats when the BOP is in the range of 85–145 kPa.

Exposure to blasts is one of the leading causes of trauma experienced by military personnel as a result of widespread use of high explosives. Our unique animal models of primary blast waves generated in compressed gas shock tubes in discrete increments shows that 24-hour survival of animals depends on the magnitude of blast overpressure (BOP)[1,2]. Blast-induced traumatic brain injuries (bTBI) are classified as primary, secondary, tertiary, and quaternary[3–5], based on the type of biomechanical loading. An incident pressure of a shockwave on the body within the time duration of few-to-ten milliseconds causes primary blast injury, while secondary blast injuries are caused by impact of high-velocity fragmentation and debris. Tertiary blast injuries result when the body is violently accelerated and is forced to impact other objects. Quaternary blast injuries are caused by exposure to heat and toxic gases released resulting from explosive detonation[6]. The present study is focused on primary bTBI that was recognized as a separate neuropathological condition during the World War I and dubbed as 'shell shock'[7]. Soldiers afflicted with shell shock in the battle field sustained plethora of neurological deficits (or even death) without any visible injuries long after the shelling had ended[8].

The emergence of bTBI among active military personnel in recent Iraq and Afghanistan war gained considerable attention and remains an important public health problem[5,9,10]. In the past decade, the Department of Defense reported more than 200,000 head injuries due to combat-related incidents and in non-deployed environment[11]. The severity of brain injury is clinically classified as mild[12–14], moderate[15–18], severe[3,19–23], and vegetative state TBI[3] as per 15-point Glascow Coma Scale (GCS) in humans (including blast TBI cases[24–26]). Over 150,000 of these head injured military personnel were diagnosed with mild Traumatic Brain Injury (mTBI) and Post-Traumatic Stress Disorder (PTSD) exhibiting a wide range of neurological and psychological symptoms[4,5]. Blast mTBI is

[1]Center for Injury Biomechanics, Materials and Medicine (CIBM3), Department of Biomedical Engineering, New Jersey Institute of Technology, Newark, NJ 07102-1982, USA. [2]Department of Pharmacology and Experimental Neuroscience, University of Nebraska Medical Center, Omaha, 68198, NE,USA. *These authors contributed equally to this work. Correspondence and requests for materials should be addressed to J.H. (email: james.haorah@njit.edu) or N.C. (email: namas.chandra@njit.edu)

the most prevalent form of trauma among deployed military populations and it is labeled as the invisible signature wound among combat troops[27,28]. Currently, mTBI is clinically diagnosed using six categories of symptoms: 1) alteration and 2) loss of consciousness, 3) post-traumatic amnesia, 4) Glasgow Coma Scale (score of 13–15, 30 min. after the injury), 5) focal neurological signs and 6) brain imaging[29].

To study the origin of bTBI, live-fire testing, compressed-gas shock tubes, combustion shock tubes and small explosion shock tubes have been used with small animals (e.g. rats and mice) and large animals (e.g. swine). A number of shock-tube models of mice[30–32] and rats[1,33–38] have been developed to represent 'mild-moderate-severe' injury scale using a single[23,33,35–37,39–42] or a set of blast intensities[15,31,38,43,44]. Despite enormous gain of knowledge and advancement of bTBI research in animal model, there is lack of consensus and information about the rationale for selection of range of blast overpressure and impulse as accepted predictors of bTBI. These models are further confounded by variations in the test specimen locations such as inside[1,35] versus at the end/outside[33,38,45] of the shock tube, pressure data recording location, secondary loading as a consequence of inappropriate specimen-to-shock tube cross section ratio, lack of proper head restraint, and use of table-top devices[46,47]. Though each of these experiments show evidence of effect of blasts on biological materials, in order to study the effect of primary blast within the range of practical relevance (strengths of explosives and stand-off distances responsible for mTBI in military personnel), it is necessary to generate pure shock pulses with 0–450 kPa range and duration between 2 ms and 8 ms[1,35,48]. Thus, our objective in this study is to identify the thresholds of injury scale and in specific, to determine the mTBI range based on predicted mortality rate (PMR). The reason we have chosen to focus on mTBI is because more than 80% of bTBI cases belong to this category, while the general methodology will be applicable to all other ranges[46,47].

In the present studies, we exposed the animals to BOP ranging from 60 kPa to 450 kPa (equal to 8.7–65.3 psi) with duration of 2–8 milliseconds, as this corresponds to the shock-time pulse at a stand-off distance of 2–10 meters away from 1–100 kg of C4 explosion[49]. A sigmoidal survival-BOP dose-response curve was obtained which was then used to delineate the upper threshold of mild TBI based on the logistic regression model. We then carefully examined this range using other potential indicators of injury. This range was found to compromise the integrity of the blood-brain barrier (BBB). The rationale is based on our recent demonstration of BBB oxidative injury and other studies, that BBB damage is one of the major and most frequently investigated mechanisms of traumatic brain injury in blast TBI[50–52].

Results

Determination of predicted mortality rate (PMR). All the test animals were in a prone position with a head restrained (Fig. 1B), and thus no artifacts associated with uncontrolled head acceleration were present in this bTBI model, as demonstrated elsewhere[1]. The net movement of the specimen did not exceed 3 mm as determined by analysis of captured high speed video. We exposed 13 rats per discrete incident peak overpressure to develop a dose-response linear regression model for predicted mortality rate (PMR) as a function of BOP and corresponding impulse values (Fig. 2). We did not observe any mortality of animals exposed to blast intensity lower than 170 kPa (Fig. 2, left) or impulse 300 Pa·s (Fig. 2, right). However mortality rate gradually increased from 170 kPa to 300 kPa, and mortality rate was 100% above 300 kPa (or 500 Pa·s impulse). These accounted for an immediate loss (not delayed deaths, i.e. animals were removed from the shock tube in less than a minute after the shock wave exposure) of 45 rats as a consequence of shock wave exposure, consistent with our previous work[1].

The insets in Fig. 2 present receiver operating characteristic (ROC) curves for respective logistic regression fits with the following areas under ROC curves: 0.878 (left) and 0.882 (right), for BOP and impulse, respectively. Analysis from these models indicated good predictive power of mortality rate using peak overpressure and impulse as metrics to gauge injury risk under primary blast. The McFadden pseudo-R^2 values of 0.389 and 0.412 were obtained for fits using peak overpressure and impulse as independent variables, respectively. These values indicate a highly satisfactory quality of fit.

Primary blast impacts mild pulmonary injury. Animals tested in prone position have their abdomen partially protected from the blast wave by the aluminum holder (Fig. 1B) used in our experiments[1]. The observed levels of pulmonary injury expressed using Yelveton's scoring system[53] revealed a low level of injury (Fig. 3A,B). However, we observed an increasing trend of injury score with increasing peak overpressure and impulse. We observed only a few cases where pathological score exceeded 21 for the blast strength higher than 300 kPa BOP with high standard deviations (Fig. 3C). A score of 21 is considered as a cut-off threshold for mild pulmonary injury[53]. The pathological score at 50% PMR (at 260 kPa) was found to be less than 10, while the score was less than 4 in the 60–190 kPa range. Moreover, there are six animals which died as a result of blast exposure and had no lung injury (score of zero, Fig. 3C,D). These results suggested minimal pulmonary injuries and thus, we conclude lung injury is not a viable indicator of PMR.

Blast induced bradycardia. We evaluated the functional changes in the heart rate, blood oxygen saturation (spO_2) and perfusion index in the 60–250 kPa peak overpressure range over period of 30 minutes before and after blast exposure. We found that the onset of bradycardia occurred immediately after the blast exposure even at 60 kPa (Fig. 4, $p = 0.01$, power: 0.85 vs control). The values of the differential average heart rates (ΔHR) decreased gradually with increase in blast intensity: -29 ± 10 (60 kPa), -26 ± 20 (100 kPa), -43 ± 26 (130 kPa), -62 ± 21 (190 kPa), -62 ± 43 (230 kPa) and -62 ± 24 (250 kPa) bpm. These data were modeled using a simple dose-response function to quantify the characteristics of ΔHR as a function of two blast parameters, the peak overpressure and the impulse. This mathematical modeling generated asymptotic values of A_1 and A_2: -13.9 and -59.5 (for peak overpressure, Fig. 4A), and -12.7 and -67.1 (for impulse, Fig. 4B), respectively. The calculated inflection points ($\log(x_0)$) are 109.3 kPa and 186.9 Pa·s for both blast parameters (Fig. 4). The control group was not correlated with any of the blast exposure groups ($p < 0.05$).

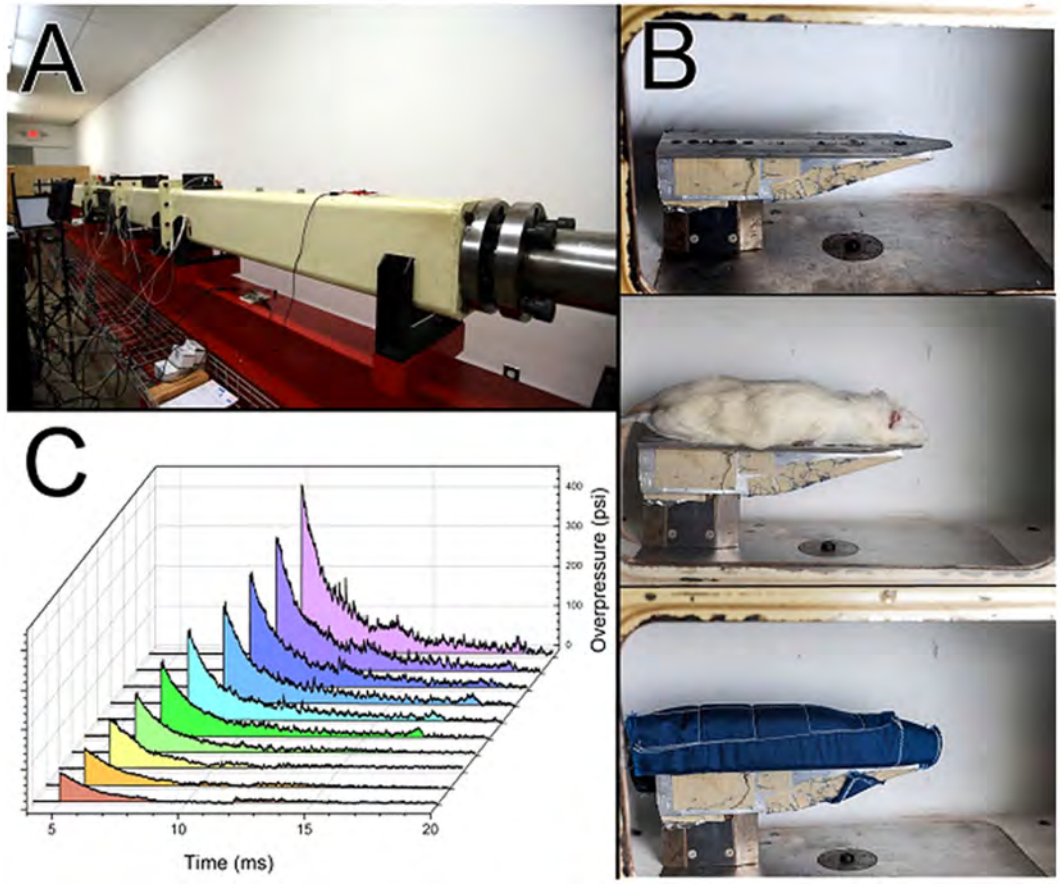


Figure 1. (**A**) An overview of the 9-inch square cross section, 6 meters long shock tube instrumented with pressure sensors. (**B**) Aerodynamic rat holder mounted in the test section (top), with rat placed on top (middle) and animal wrapped in a harness to minimize head and body motion during blast exposure (bottom). (**C**) Representative overpressure profiles (C) as measured in the test section at the location of the animal's head for 10 experimental groups used in our study.

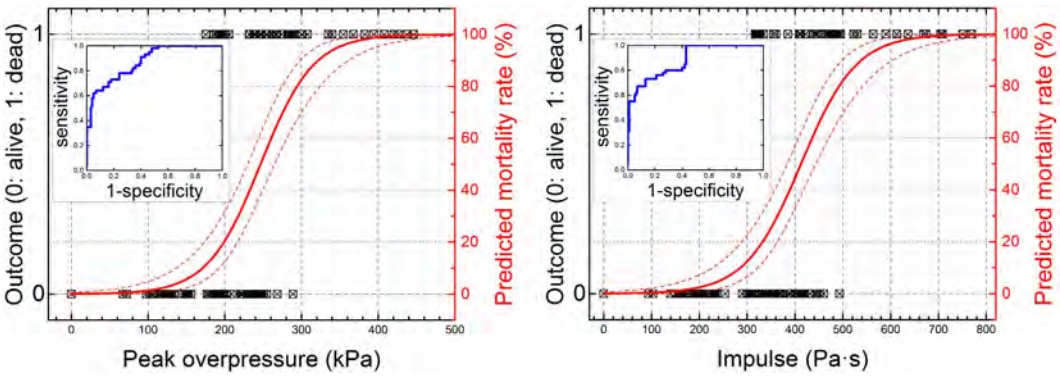


Figure 2. The logistic regression dose-response model for rats exposed to single blast with intensity in the range of 60–450 kPa peak overpressure (left) and corresponding impulse (90–780 Pa·s, right). The insets present receiver operating characteristic (ROC) curves for respective logistic regression fits with areas under ROC curves: 0.878 and 0.882. McFadden $R^2 = 0.389$ and 0.412, for fits using peak overpressure and impulse as independent variables, respectively. Dashed lines indicate confidence intervals of the model.

Induction of oxidative/nitrosative stress markers. Using our logistic regression risk injury model, we can define the upper level of mTBI at 145 kPa BOP as 5% PMR. We examined the oxidative/nitrosative injury and the BBB integrity in the range of 60 kPa to 130 kPa peak overpressure and determined lower threshold of mTBI at 80 kPa. These markers were evaluated 24 hours after the injury, at a time point which proved in our previous

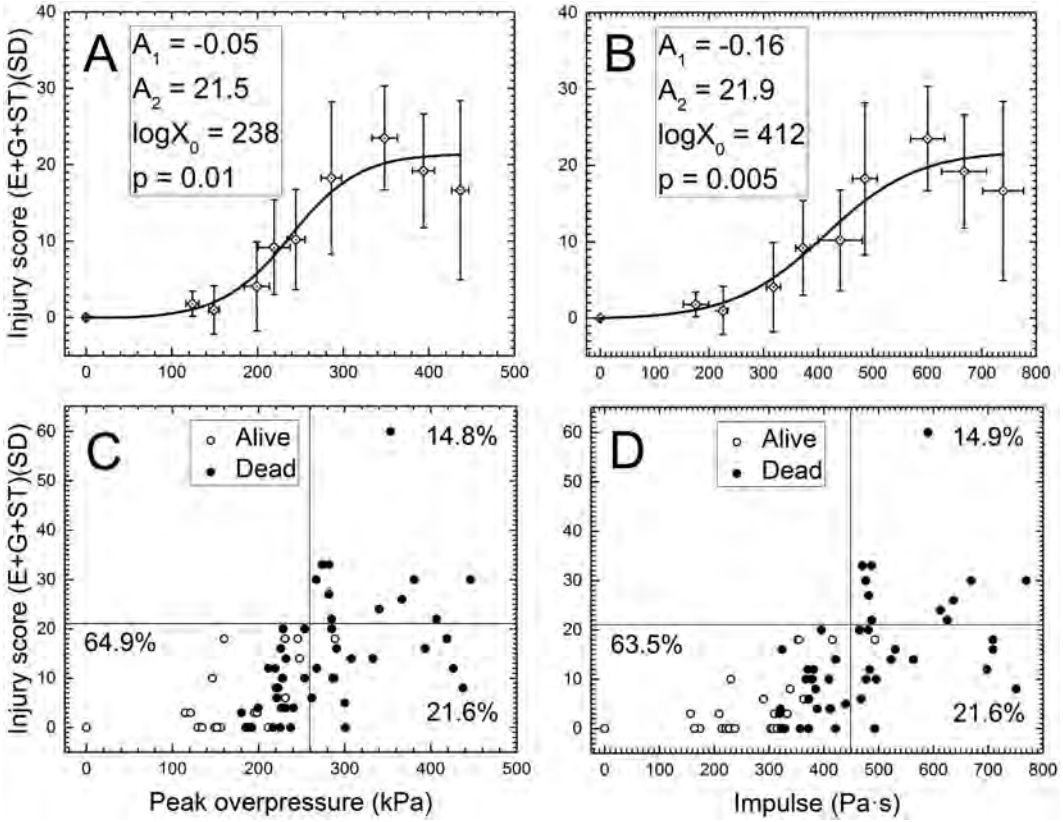


Figure 3. Lung injury scores for rats exposed to a single blast. The dose-response model was used to fit the IS as a function of peak overpressure (**A,C**) and impulse (**B,D**). The scattergrams (**C,D**) illustrate individual scores and their distribution among the cohort of 75 rats evaluated in this test. The value of 21 is the upper limit of the slight lung injury level as defined by Yelverton[53]. The vertical lines (peak overpressure of 260 kPa (**C**) or impulse of 450 Pa·s (**D**)) correspond to 50% predicted mortality rate according to the dose-response model in Fig. 2. There are six animals which died after the blast and had no apparent lung injuries (score of zero).

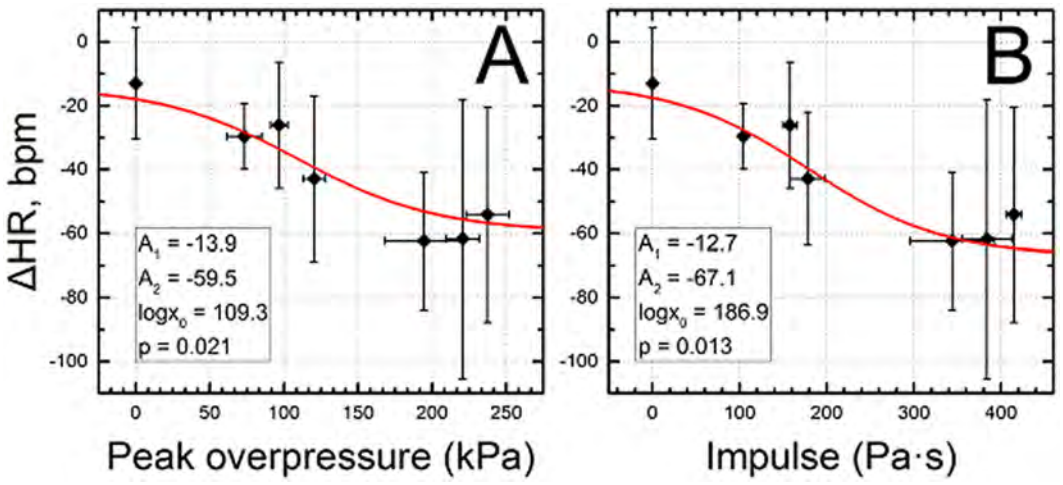


Figure 4. Blast induced bradycardia as a function of peak overpressure (**A**) and impulse (**B**). In both cases, the dose-response function (1) was used to model the pathological response and resulting parameters are listed in respective insets in both figures. All blast exposed groups have statistically significant heart rate decrease versus control ($p < 0.05$).

study to yield their maximum levels in analogous bTBI model[50]. We first evaluated the induction of free radical generating enzymes NADPH oxidase (NOX1) and inducible nitric oxide synthase (iNOS) in the brain capillary cross section tissues. We found that blast-wave exposure significantly up-regulated the induction of NOX1 with

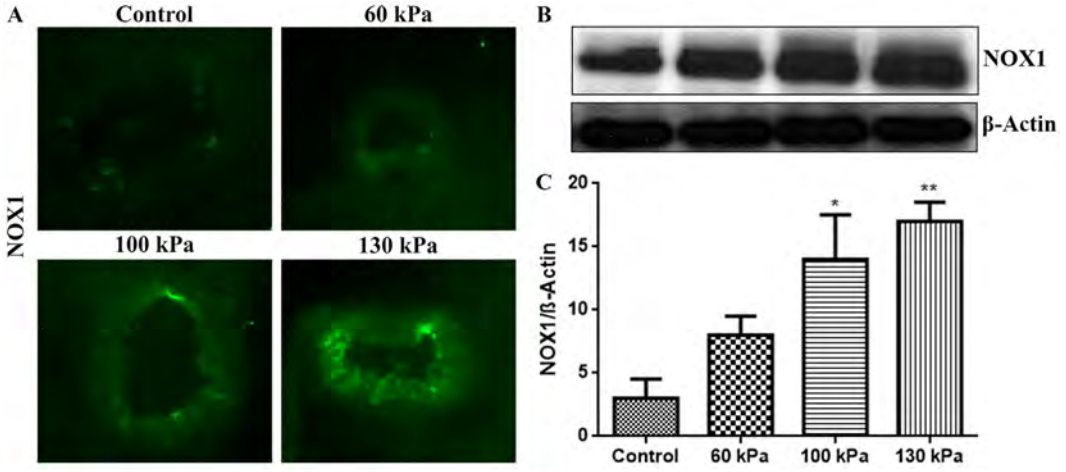


Figure 5. Mild TBI range of blast-wave exposure induces NADPH oxidase expression in rat brain microvessels. (**A**) A representative of immunofluorescent staining of NOX1 in intact microvessels of brain cross sections from rats subjected to a single exposure to 60, 100, or 130 kPa peak overpressure, and control. (**B**) Corresponding Western blot of NOX1 and housekeeping protein, β-actin. (**C**) Bar graphs show the quantitative results of the NOX1 immunoreactive fluorescence intensities. Values are mean ± SEM (n = 4) with p-value ≤0.01 compared with control.

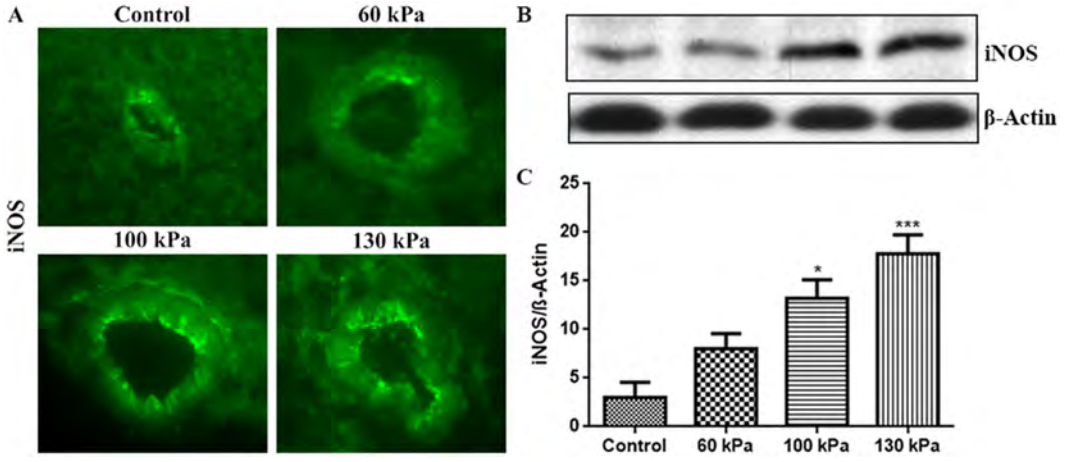


Figure 6. Mild TBI range of blast-wave exposure dose-dependently increased the levels of inducible nitric oxide synthase (iNOS) in rat brain microvessels. (**A**) A representative of immunofluorescent staining of iNOS in microvessel of whole brain tissue cross section in control and blast exposed animals. (**B**) Corresponding Western Blot of iNOS and housekeeping protein, β-actin. (**C**) Bar graphs show the quantitative results of the iNOS immunoreactive fluorescence intensities. Values are mean ± SEM, (n = 4), and asterisks indicate statistical significance (p-value <0.05) of blast intensity groups compared with control.

100 kPa (p = 0.02) and 130 kPa (p = 0.001) BOP (Fig. 5A–C). Similarly, iNOS expression was increased at 130 kPa BOP (p = 0.0005) and at 100 kPa BOP (p = 0.04) (Fig. 6A–C). Induction of NOX1 and iNOS produces superoxide and nitric oxide respectively, which will also react together to form peroxynitrite, a more reactive free radical. The oxidative/nitrosative damage is a post-oxidant production event. Proteins adducted with 4-hydroxynonenal (4HNE, oxidative stress marker) or 3-nitrotyrosine (3NT, nitrosative stress marker) are used for assessing the extent of injury in the tissue. In parallel with the induction of NOX1 and iNOS enzymes, we found that the level of oxidative damage signature 4HNE (Fig. 7A–C) is increased in mTBI range exposure with 100 kPa (p = 0.05) and 130 kPa (p = 0.0004). Similarly, 3NT (Fig. 8A–C) was found to be increased with the mTBI range exposure (100 kPa BOP, p = 0.04 and 130 kPa BOP, p = 0.002).

Disruption of the BBB integrity. The capillary oxidative/nitrosative damage might lead to BBB disruption, and thus we evaluated the alterations of tight junction (TJ) proteins claudin-5, occludin and zonula occluden 1 (ZO-1). TJ proteins are the primary functional barrier biomolecules of the BBB. A reduction in TJ protein levels or disruption of the architectural structure of any TJ protein is expected to impair BBB integrity, thereby enhances the chance of immune cell infiltration into the brain for initiation of neuroinflammation. Interestingly,

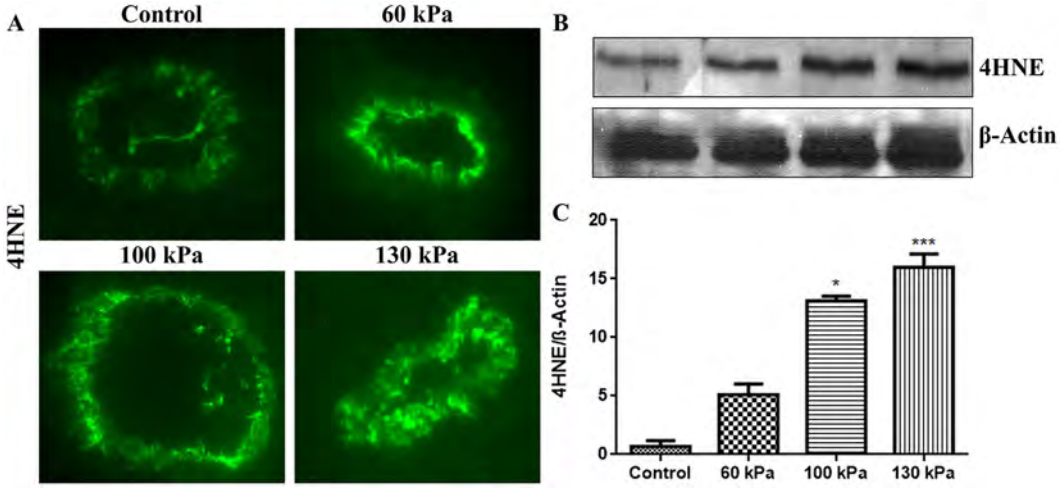


Figure 7. Formation of oxidative damage maker 4-hydroxynenonal (4HNE) in rat brain microvessels. (**A**) A representative of immunofluorescent staining of 4HNE in microvessel of whole brain tissue cross section in control and blast exposed animals. (**B**) Corresponding Western Blot of 4HNE and housekeeping protein, β-actin. (**C**) Bar graphs show quantification results of the 4HNE immunoreactive fluorescence intensities. Values are mean ± SEM, (n = 4), and asterisk indicates statistical significant (p-value <0.05) of each blast intensity compared with control.

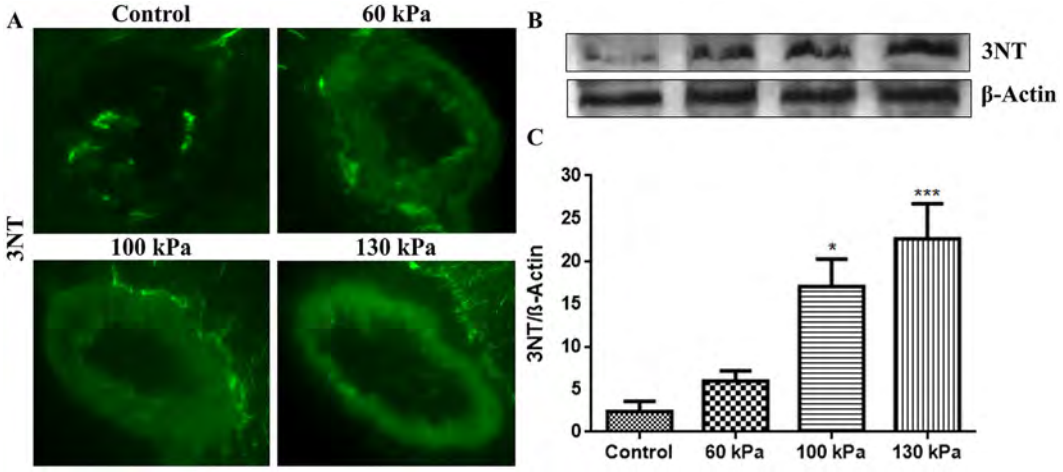


Figure 8. Formation of nitrosative damage maker 3-nitrotyrosine (3NT) in brain microvessels of low intensity blast range. (**A**) A representative of immunofluorescent staining of 3NT in microvessel of whole brain tissue cross section in control and blast exposed animals. (**B**) Corresponding Western Blot of 3NT and housekeeping protein, β-actin. (**C**) Bar graphs of quantification of the 3NT immunoreactive fluorescence. Values are mean ± SEM, (n = 4), and asterisk indicates statistical significant (p-value <0.05) of each blast intensity compared with control.

our results showed that mTBI range of blast-wave exposure decreased the levels of claudin-5 (130 kPa, $p = 0.001$) (Fig. 9a,d,e), occludin (130 kPa, $p = 0.002$) (Fig. 9b,f,g) and ZO-1 (100 kPa, $p = 0.03$; 130 kPa, $p = 0.0007$) (Fig. 9c,h,i) proteins in brain tissue sections. These data suggest possible leakiness of the BBB and it might result in neuronal inflammation around the perivascular region of the brain.

Assessment of BBB leakage. To assess this BBB leakiness and neuronal injury, we examined the leaking out of neuronal-specific enolase (NSE) into the blood samples of tissues exposed at BOP of 60, 100 and 130 kPa versus control animals. In agreement with a decrease in BBB integrity, we observed elevation of NSE levels in blood samples exposed to blast compared with controls (Fig. 10). The glycolytic enzyme enolase is a dimeric isoenzymes and also known as neuronspecific enolase (NSE-aa, ag and gg), as these isoenzymes were initially detected in neurons and neuronendocrine cells. However, in other pathological conditions such as small cell lung cancer and neuroblastoma, NSE exhibits a signatory value in disease detection and progression. In the absence of such pathological status or stimuli, as in our experimental setup, NSE detection in plasma samples establishes BBB leakage in primary bTBI.

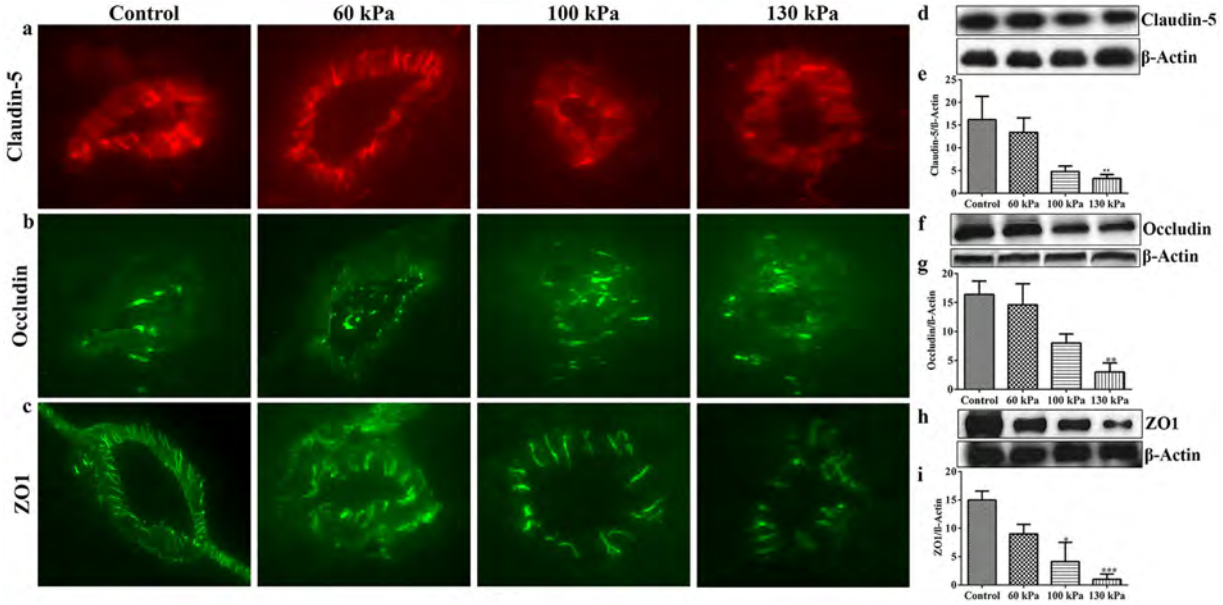


Figure 9. Oxidative/nitrosative damage of capillaries impaired BBB integrity by disrupting the tight junction proteins. (**a**) A representative of immunofluorescent staining of TJ protein Claudin-5 (**a**), Occludin (**b**), and zonula occluden 1 (ZO-1, **c**) in capillaries of whole brain cross-sections in control and blast exposed animals. (**b**) Corresponding Western blot and bar graphs showing the quantification of respective immunoreactive fluorescence intensity of Claudin-5 (**d**,**e**), Occludin (**f**,**g**), and zonula occluden 1 (**h**,**i**). Values are mean ± SEM, (n = 4), and asterisk indicates each blast intensity compared with control where level of statistical significance was achieved ($p < 0.05$).

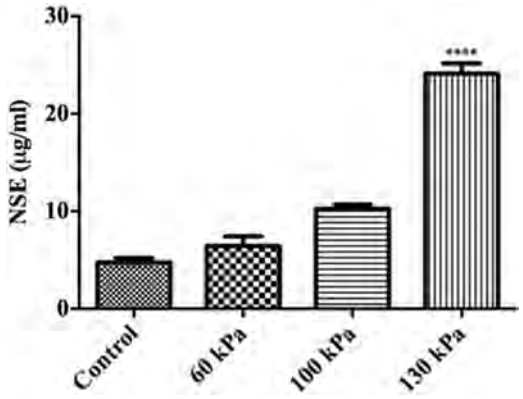


Figure 10. The neuronal damage marker leakage into serum is facilitated by BBB disruption. ELISA results show the levels of neuronal specific enolase (NSE) in rat blood serum collected from a single blast exposure at 60, 100 and 130 kPa. Blood samples were collected at the time of sacrifice after 24 hour post blast exposure. Values are mean ± SEM, n = 4. Statistical significance ($p < 0.01$) compared with control was observed at 130 kPa as the lowest blast intensity.

Discussion

The basic question not fully elucidated yet is the relationship between pure primary blast and bTBI and its quantification using injury predictors (BOP and impulse) and suitable set of injury markers. In this way the probabilistic TBI injury scale (mild, moderate and severe) in an animal model can be developed. In this work, we have presented the survival response of 10-week old male Sprague Dawley rats in supine position under carefully controlled pure primary shock-blast loading conditions from 0–450 kPa and durations in the range of 2 msec to 8 msec. These shock loading conditions correspond to live-fire conditions of 1 to 100 kg of C4 explosives at a stand-off distance of 2 m to 10 m distance, i.e. within practical, military relevant loading conditions[54]. The explosive strengths and the stand-off distance were selected based on the data available for IEDs and landmines (see Table 1 of ref. 48) and diagnostic criteria of military mTBI, where the inclusion threshold corresponds to overpressure of 4 psi responsible for tympanic membrane rupture[55]. However, these criteria for mTBI evaluation are not based on rigorous scientific evaluation, but conservative estimates based on pressure readings by blast gages used

by soldiers in the combat zone. The development of injury criteria and corresponding interspecies scaling laws should be based on the mechanisms of injury. For instance, if the injury is caused by acceleration-deceleration type biomechanical loading, then mass and momentum scaling are appropriate. In the angular rotation injury, the scaling factor for rats is of the order of 80–120[56,57], when compared to humans. In this case, rotational acceleration of approximately 600,000 rad/sec^2 will correspond to the established concussion human criterion of 6000 rad/sec^2. However, if predominant injury mechanism is direct transmission, then stress, strain and energy are more appropriate metrics and scaling laws based on mass are inappropriate. This approach was recently demonstrated by Radovizky and co-workers with an aid of advanced computational models to bTBI scaling law between mice, pigs and humans[58]. They used peak stresses transmitted to the brain tissue as the governing criterion and determined that humans are more vulnerable to blast by merely a factor of two, when compared to mouse. They further emphasized that ICP in the brain parenchyma is affected by the impedance of skin and skull, and is not correlated with mass of body or brain. In this work, we are mainly concerned with the primary blast that excludes any head motion and hence mass based criteria are not applicable. The blast conditions have been further validated by comparing shock pulse data around a human surrogate when exposed to live-fire and in the shock tube[59].

Our findings indicate (Fig. 2A,B), that animals exposed to BOP below a 170 kPa threshold (and corresponding 300 Pa·s impulse) have absolute survival, although presented with signs of altered biological state compared to sham, and above 300 kPa (500 Pa·s) threshold none survived. This data is captured in the form of a sigmoidal dose-response logistic regression curve with % survival response, a function of input injury predictor variables: peak overpressure and impulse (Fig. 2). In addition, we had earlier published histopathological and extensive immuno-histochemical findings that demonstrated BBB damage and neuronal degeneration around the BBB perivascular region in primary blast exposure of a single blast with peak overpressure of 130 kPa[1,50]. In this work we have carefully examined the brains of animals exposed to a single blast at 130 kPa and below, using biochemical changes which proved sensitive to acute brain pathology. Thus based on the survival and other complementary data, we are postulating that a range of mild (80 kPa–145 kPa), moderate (146 kPa–220 kPa), severe (221 kPa–290 kPa) and lethal (>290 kPa) be used for injury gradation. These peak overpressure ranges have the corresponding impulse values: mild (125–250 Pa·s), moderate (251–350 Pa·s), severe (351–450 Pa·s) and lethal (>451 Pa·s). We believe that BOP cannot be a single mechanical parameter defining injury, since a sharp pressure spike with a small duration will not produce the postulated injury severity. The positive phase pressure of BOP of a Friedlander type is given by equation[60]:

$$p(t) = p^*\left(1 - \frac{t}{t_d}\right)e^{-\frac{\alpha t}{t_d}} \tag{1}$$

where p^* is the BOP, t_d is the positive time duration, and α is the shape factor. I is the impulse which is the area under the pressure-time curve such that, $I = \int_0^{t_d} p(t)\,dt$ an often overlooked, but a key biomechanical loading parameter. For the same BOP, if the duration t_d is gradually increasing (e.g. 1 ms, 3 ms, 5 ms or 8 ms), the impulse values will follow the same trend (e.g. 40 Pa·s, 113 Pa·s, 183 Pa·s, and 293 Pa·s, respectively). Obviously higher impulse will have higher mechanical loading and hence more severe injuries, even though the BOP remains same at 140 kPa. This is analogous to the integral of acceleration and time, being used as a basis for head injury criterion in automotive accidents, or momentum (integral of force and time) in head injuries due to fall. Thus it is critical to identify both BOP and duration as two independent biomechanical parameters. Also, recent work has clearly shown that Bowen-type blast lung injury scaling laws for duration cannot be applied to blast brain injury[58,61].

The injury severity classifications (mild to severe) are mostly heuristic for animal models; however, they are very important measures for inter-laboratory cross-verification of results and data interpretation. Thus such classification is necessary to advance to the next level the research on bTBI field, and facilitate development of suitable strategies for prevention, diagnostic and treatment purposes. This strategy of defining a single biomechanical parameter as predictor of injury severity has worked very well for other type of animal injury models, e.g. lateral fluid percussion injury (LPI) and closed-cortical injury (CCI) models. For example, in LPI a peak inlet pressure of 50 to 120 kPa correspond to mild, 150 to 190 kPa to that of moderate and 200 to 220 kPa to severe[62–65]. Similarly in CCI model, a depth of penetration of 1.5 mm corresponds to mild, 2.0 mm to moderate and 2.5 mm to severe[66,67].

In this work, based on the logistic regression model (Fig. 2A,B), the upper and lower thresholds of mild TBI were found to be at 145 kPa and at 80 kPa, respectively. The upper threshold defined as 5% of PMR function is the cut-off threshold. Similar injury prediction model based on survival was developed for ferret, which was also used for scaling laws in blast injury risk curves for humans[68]. A total of 64 animals were exposed to blast with the peak overpressure in the range of 98 to 837 kPa. This model has a good predictive quality (area under ROC value of 0.77), but the McFadden R^2 value was only 0.16 for the fit, mostly because the data points at the upper extreme of blast intensities (above 900 kPa) were not collected. Further, in this model the test specimens were placed at end of the shock tube, while in our model test specimens were placed inside the shock tube. Typically shock wave profiles at end of the shock tube are characterized by shorter duration and much smaller impulse values than shock waves experienced by specimen located inside the shock tube for the same peak overpressure exposure[1,35,48]. Hence in this ferret model of blast, the animals may have been subjected to primary and tertiary loading (e.g. due to jet winds) different from that of our primary loading only condition. Hence a direct comparison between the results on ferrets outside the shock tube and our rat data inside the shock tube may not be possible. The researchers of Lovelace Foundation developed dose-response probit mortality models for a number of species for "long" (180–400 ms) and "short" (2.1–4.6 ms) duration blast waves[61]. Animals were exposed in the side-on position against the end plate in the shock tube ("long duration" group, LDG) or in prone position on a concrete pad to the high-explosive charge overhead ("short duration" group, SDG). These models developed for rats of unknown age and species have some similarity to our studies, in spite of the differences in positioning of

the animals. In particular, the overpressures for (5%, 10%, 50%, 90% and 95%) mortality rates were: 1) 165, 172, 213, 255 and 290 kPa (LDG), and 2) 193, 207, 241, 282 and 303 kPa (SDG), while in our model these are: 145, 170, 245, 320 and 340 kPa, respectively (Fig. 2A). Thus, low end of our observed mortality rates matches analogous region for the LDG, but not for SDG (approx. 50 kPa differences). However, 50% mortality overpressure matches between our model and SDG, but not for LDG (difference of 34 kPa). On the high-end of mortality curve (90% and 95%) we observe shift towards higher peak overpressures in our model compared to both, LDG and SDG by more than 40 kPa.

Riesling and co-workers[69] reported exposure to "pressure above 236 kPa results in lethal bleeding from the airways in more than 50% of the animals". However, there are clearly major differences between both models: while in their model rats were positioned perpendicularly to the direction of the blast and the side of the animal was exposed, in our model the animal is positioned head on and in parallel orientation with respect to incoming shock wave. We did not observe any bleeding from airways in our studies.

We observed that the thresholds for pulmonary injury and bradycardia were higher than that of brain injury[70,71]. The main reasons for diminished pulmonary injury could be attributed to the protective aluminum shielding in the prone position during blast exposure, characteristic for our model. The prone position with the protective aluminum may represent the protective body armor of soldiers, thus leading to the possibility that brain injury occurs at lower BOP than lung injury[72]. Soldiers are either in vertical or horizontal position while wearing body armors typically made of Kevlar-epoxy exterior with ceramic plates surrounded by rubber to contain the high velocity projectiles and shrapnel. In general, when an air shock encounters a structure, the proportion of energy reflected and transmitted will depend on the acoustic impedance mismatch between air and the structure. Impedance of a material is given by $Z = \rho c$ where c is the acoustic velocity in the medium and ρ the density. Transmission coefficient of energy is given by: $\frac{4Z_1Z_2}{(Z_1+Z_2)^2}$, where Z_1 and Z_2 are the impedance of air and medium[57]. Since impedances of aluminum and body armor material are very high, transmission is negligible. This observation was also independently verified in a number of experiments performed in our laboratory using different structural materials and measuring the pressure of the transmitted shock wave. Similarly, soldiers wearing body armors have reported no thoracic injuries, still reporting mild to moderate TBI[73]. In the present study, it is clear that, lung injury cannot be linked to the cause of death even at extreme BOP range: a number of animals exposed to BOP in the range of 180 to 300 kPa (300 to 500 Pa·s) died without apparent lung injuries (injury score of zero was recorded, see Fig. 3C,D). Bradycardia, mediated by vagal reflex, is one of the frequently reported hallmark physiological responses after the blast exposure[74–78], similar to our present findings. Although, we observed bradycardia even at the very low blast intensity (60 kPa), it was not statistically significant from one group to the other because the variability of results within the same discrete blast intensity were relatively big.

Finally, induction of oxidative/nitrosative damage of the BBB[30,33,50,79,80] and subsequent impairment of the BBB is now considered one of potential mechanisms of traumatic brain injury in blast-wave exposure[30,33,50–52,79–83]. Here, we use disruption of the BBB integrity to determine the lower threshold of the mTBI in bTBI rat model, while the upper threshold was based on PMR curve. Thus, based on our logistic regression model the upper threshold of mTBI was set at 145 kPa, while based on oxidative or nitrosative damage of the BBB, the lower threshold of mTBI was established at 85 kPa.

In this work, we have exposed rats to a wide range of intensities of primary blast waves (below 130 kPa), where we found observable changes in acute TBI biomarkers with 100% survival. When the animals are exposed to the blast with peak overpressure higher than 300 kPa (500 Pa·s), we observed only fatalities. The pooled survival data were used to calculate the PMR (response) as a function of BOP and impulse (input). While the results clearly delineate the different TBI injury severity levels in a wide range of BOP (0 to 450 kPa), it should be recognized, that these numbers should be used with caution. These data refer to the pure primary blast wave acting on a male, 10 week-old, 320–360 gram, Sprague-Dawley rats in prone position when the body is aligned with head facing the on-coming shock wave and the thoracic region protected by metallic plate (Fig. 1B). Any change of these conditions may alter the response and hence the upper and lower thresholds BOP for a given injury severity can be different.

Thus, caution needs to be exercised in using these biomechanical parameters as universal injury predictors for variety of blast experimental setups presently used in various laboratories. Currently, five possible biomechanical loading mechanisms are identified as potentially responsible for bTBI: direct shock wave transmission to the brain through the skin/skull[59]; skull deflection induced pressure wave in the brain[84]; acceleration/deceleration loading due to pressure forces[43]; cavitation due to reflection at the back side of the skull or underpressure[85]; and pressure surge to the brain caused by loading of the thorax[31]. The shock pressure loading in the brain (exhibited as intracranial pressure or biomechanical stretching/twisting) is governed by how the external shock wave is transmitted to the brain. That in turn is determined by the thickness of the skull, which varies with the age, weight, gender and strain of the rats. Hence any variation in this factor may affect the geometry and material properties and response to shockwave and hence the effective brain biomechanical loading. Any change in biomechanical loading of the brain tissue will alter the injury severity and shift the survival curve, either to the right or left. Similarly, while in prone position the thoracic region is protected, the testing in supine position may result in increased brain injury severity caused by pressure surge, and more pronounced lung injury. Both effects could affect the outcome, shifting the PMR function towards lower BOPs. In some laboratory settings, the rats are placed in cages, tied to the end of the rod, or inserted in a tube from the side. Such constraints will alter the loading and cause differential motion of parts not immobilized, resulting in additional injuries that may affect the response, which cannot be classified as primary blast injury. While we believe that our results are reproducible in age-matched rats in the same age group under similar loading conditions, care should be taken that the experimental conditions are causing primary bTBI and not mixed or other types of injuries. These, non-primary injuries, will likely be observed if animals are kept under non-ideal exposure conditions (e.g. near the exit of the shock

tube, independently whether it is inside or outside) and in smaller shock tubes (which will result in specimen overload caused by excessive reflected pressure buildup, when the animal body blocks the shockwave pathway).

Also, while we have used damage to neurovascular unit as possible markers to gauge the extent of TBI, application of other markers are equally viable. The wide variety of available imaging, electrophysiological, behavioral, cellular/molecular biomarkers can be used for this purpose and serve as response correlates. Such comprehensive approach will allow fine tuning of the threshold ranges for the various TBI injury severity levels.

Materials and Methods

Animals. Adult 10-weeks-old male Sprague-Dawley (Charles River Laboratories) rats weighing 320–360 g were used in all the studies. The animals were housed with free access to food and water in a 12-h dark-light cycle at 22 °C. All procedures followed the guidelines established in the Guide for the Care and Use of Laboratory Animals and were approved by the Rutgers-Newark Institutional Animal Care and Use Committee (IACUC). We used a total of 280 rats for three different experiments consisting of mortality rate in response to blast dose, evaluation of cardiac physiology, and evaluation of lung injury.

Mortality rate in response to primary blast. Rats were exposed to a single blast wave at the Center of Injury Biomechanics, Materials and Medicine (New Jersey Institute of Technology) in the modular, multi-size shock tube capable of reproducing complex shock wave signature (Fig. 1A,B)[2,86,87]. We have evaluated a 24-hour survival of the animals following exposure at 60, 100, 130, 160, 190, 230, 250, 290, 350 and 420 kPa peak overpressure range (Fig. 1C). We have used 13 rats for each discrete incident peak overpressure exposure ($13 \times 10 + 10$ control rats = 140 rats). These results were used to develop a logistic regression model of peak overpressure and impulse as a function of survival.

All rats were anesthetized with mixture of ketamine and xylazine (10:1 (100 mg/10 mg/kg), 0.1 mL/100 g) administered via intraperitoneal injection. Sham control rats received anesthesia and noise exposure but without blast exposure, i.e. anesthetized animals were placed next to the shock tube and then a single shot was fired. Specimen was mounted in the test section located inside of the shock tube, i.e. 2.80 m from the breech (3.05 m from the exit) for each discrete incident peak overpressure. The adjustment of Mylar membrane and keeping the breech length constant at 21.6875 inches (0.5508 m) controlled the incident pressure. We have used an aerodynamically optimized aluminum bed designed as a holder for shock wave exposure of small rodents. The riser attached to the holder helps to position the specimen in the center of the shock tube away from the walls. All rats were tested in a prone position and were strapped securely to the bed with a thin cotton cloth wrapped around the body (Fig. 1B). The strapping does not protect the animal from the intensity of the shock wave, but eliminates head motion that was verified in separate set of experiments. After experiments animals were returned to the holding room and were maintained on warming pads until recovery from anesthesia, to prevent any neuroprotection associated with hypothermia[88].

As a quality control measure, we have also monitored a high-speed video recording to capture any substantial head/body motion during the blast. The rationale is to exclude the impact of secondary/tertiary blast injuries. The high-speed camera video recording system with a Photron FASTCAM Mini UX100 operating at framerate of 5000 fps was used and typically 2 seconds of video footage per experiment were recorded. The recorded videos are then saved via PFV (Photron FASTCAM Viewer) 3.3.5 software. The incident overpressure at the location of the animals in the test section is recorded by a custom LabView program running on in-house built data acquisition system based on National Instruments PXI-6133 32 MS Memory S Series Multifunction DAQ Modules and PXIe-1082 PXI Express Chassis. Pressure sensors used in our experiments were PCB Piezotronics (Depew, NY) model 134A24. All data were recorded at 1.0 MHz sampling frequency. Typical acquisition times were 200 ms per experiment.

Evaluation of lung injury. Animals were anesthetized as described above and sham control rats were subjected to noise exposure. We used 10 rats per each discrete incident peak overpressure at 130, 160, 190, 230, 250, 290, 350, 390 and 420 kPa, and sham control using a total of 100 rats. Rats were sacrificed immediately after the blast exposure and the lungs were surgically removed from the thoracic cavity and the lungs were placed in 30–40 mL of freshly prepared 10% formalin solution. The severity of lung injury was performed using the Yelveton's Pathology Scoring System[53]. The severity of injury (IS) is defined by the equation:

$$IS = (E + G + ST)(SD) \tag{2}$$

where, E is the extent of injury to the lungs (range 0–7); G is the injury grade including the surface area of the lesions (range, 0–4). ST is severity type elements, which classify the type of the worst-case lesions (range, 0–5); and SD is the severity depth element, indicating the depth or the degree of disruption of the worst-case lesion (range, 1–4). The pathological scoring ranges from zero to 64, where, 64 being the worst pathology score.

Evaluation of cardiac physiology. For the evaluation of heart physiological function, we exposed 10 rats per discrete incident peak overpressure at 60, 100, 130, 190, 230, and 250 kPa, and sham controls following anesthetization as described. Here, we monitored the physiological vitals such as heart rate, blood oxygen saturation (spO_2) and perfusion index that were performed at 30 minutes before and after the blast injury. The multiple vital signs were measured using MouseSTAT system (Kent Scientific Corp., Torrington, CT). Animals under anesthesia were placed on a warm pad in a supine position to prevent hypothermia. The heart rate, blood oxygen saturation (spO_2) and perfusion index were recorded simultaneously using in-house developed LabView-based software using a pulse oximeter sensor attached to one of back paw of the rat. A rectal probe operating at a rate of 1.0 Hz was used to monitor the body temperature for 30 minutes before and after the blast exposure.

Reagents. Antibodies from: 1) rabbit selective to: anti-NOX1, anti-iNOS, anti-4HNE, anti-Claudin-5, anti-Aquaporin-4; 2) mouse and selective to anti-3NT; 3) sheep and selective to aquaporin-4 (AQP-4) were purchased from Abcam (Cambridge, MA). Mouse antibody against Occludin was purchased from Invtrogen (Carlsbad, CA, USA). Rabbit anti-zonula occluden-1 (ZO-1) was from US Biological (Massachusetts, MA) and mouse anti-β-actin was purchased from Millipore (Billerica, MA). All secondary Alexa Fluor conjugated antibodies were purchased from Invitrogen. The ELISA kit for Neuron-Specific Enolase (NSE) was acquired from Alpha Diagnostic (San Antonio, Texas, USA).

Immunofluorescence and microscopy. The desired post-BOP exposure and control, animals were sacrificed 24 hours after blast exposure, and freshly dissected brain tissue were embedded in OCT (Optimal Cutting Temperature) media. These preparations were stored frozen at −80 °C until ready for sectioning. Brain sections (8 μm thick) were prepared from the frozen tissue blocks, using Leica CM3050 cryostat. Tissue sections containing the external and internal capillaries were used for immunofluorescence staining. Briefly, tissue sections mounted on glass slides were washed with 10 mM phosphate buffered saline (PBS), fixed in ice-cold acetone-methanol (1:1 *v/v*) solution for 10 minutes at −20 °C. The tissue sections were blocked with 3% Bovine serum albumin (BSA) at room temperature for 1 hour in the presence of 0.4% Triton X-100. Fixed tissues were incubated overnight at 4 °C with respective primary antibodies (NOX1, iNOS, AQP-4, occludin, claudin-5 and ZO-1) containing 1% BSA and 0.3% Triton™ X-100. After washing with PBS, tissue slides were incubated with corresponding Alexa Fluor conjugated secondary antibodies for 1 hour and mounted with immunomount containing DAPI (Invitrogen). Fluorescence images were captured using fluorescent microscope Eclipse TE2000-U (Nikon, Melville, NY) with NIS elements software. Fluorescence was quantified by SigmaScan Pro program, Image Analysis version 5.0.0, 1987–1999 SPSS Inc. The fluorescence intensity quantification was carried out as the difference between the final fluorescence emitted by the tissue sections in the presence/absence of the blast exposure with reference to the background fluorescence of the tissue sections in triplicate.

Western blotting. Cortical brain tissues were lysed with CellLytic-M (Sigma) for 30 min at 4 °C, centrifuged at 14,000× g. The protein concentration in homogenate was estimated by bicinchoninic acid (BCA) method (Thermo Scientific, Rockford, IL). Subsequently, 20 μg of protein per lane was loaded into 4–15% SDS-PAGE gradient gels (Thermo Scientific). Proteins separated according to their molecular size were then transferred onto nitrocellulose membranes, blocked with SuperblockT20 (Thermo Scientific), and incubated overnight with respective primary antibody at 4 °C. Incubation with horse-radish peroxidase conjugated secondary antibodies for 1 hour, was followed by detection of immunoreactive bands by West Pico chemiluminescence substrate (Thermo Scientific). For densitometric quantitation of western blots, images were digitized using a BioRad GS800 calibrated densitometer, and analyzed with BioRad Quantity One software.

Enzyme-linked immunosorbent assay (ELISA). To determine the cerebral vascular BBB damage and neuronal damage by shock wave, we have analyzed blood serum samples from control and animals exposed to the blast with 60–130 kPa peak overpressure for the presence of human neuron-specific enolase (NSE/gamma enolase). The experiments were performed in triplicate with control positive peptide for NSE protein and non-immune rabbit IgG as negative control in accordance to the manufacturer's instructions (NSE/gamma enolase kit form Alpha Diagnostic, San Antonio, Texas, USA).

Data analysis. Statistical analysis on immunofluorescence and Western blot data was performed using one-way ANOVA, using SPSS version 22.0, and $p < 0.05$ were considered statistically significant. Boxplot analysis was performed to assess measurement outliers and Shapiro-Wilk and Levene's test were performed to assess normality of data distribution and homogeneity of variances, respectively.

The logistic regression models were developed and evaluated using Systat 13.0 software (Systat Software, Inc., San Jose, CA). Dose-response models for heart rate and pulmonary injury were fitted with Origin 9.0 software (OriginLab Corp., Northampton, MA) using dose-response function:

$$y = A_1 + (A_2 - A_1)/(1 + 10^{(\log x_0 - x)p}) \quad (3)$$

where A_1, A_2 are asymptotes, $\log x_0$ is an inflection point, and p is a slope value.

Power analysis was performed using freely available GPower software, version 3.1.9[89].

References

1. Skotak, M. *et al.* Rat injury model under controlled field-relevant primary blast conditions: acute response to a wide range of peak overpressures. *J. Neurotrauma* **30,** 1147–1160 (2013).
2. Sundaramurthy, A. *et al.* Blast-induced biomechanical loading of the rat: an experimental and anatomically accurate computational blast injury model. *J. Neurotrauma* **29,** 2352–2364 (2012).
3. Vasterling, J. J., Verfaellie, M. & Sullivan, K. D. Mild traumatic brain injury and posttraumatic stress disorder in returning veterans: perspectives from cognitive neuroscience. *Clin. Psychol. Rev.* **29,** 674–684 (2009).
4. Vanderploeg, R. D. *et al.* Health outcomes associated with military deployment: mild traumatic brain injury, blast, trauma, and combat associations in the Florida National Guard. *Arch. Phys. Med. Rehabil.* **93,** 1887–1895 (2012).
5. Hoge, C. W. *et al.* Mild traumatic brain injury in U.S. Soldiers returning from Iraq. *N. Engl. J. Med.* **358,** 453–463 (2008).
6. Zhang, J., Wang, Z., Leng, H. & Yang, Z. Studies on lung injuries caused by blast underpressure. *J. Trauma* **40,** S77–80 (1996).
7. Southard, E. E. Shell-shock and other neuropsychiatric problems presented in five hundred and eighty-nine case histories from the War literature, 1914–1918, In *The case history series* 905–982 (WM Leonard, Boston; 1919).
8. Jones, E., Fear, D., Phil, N. T. & Wessely, S. Shell shock and mild traumatic brain injury: a historical review. *Am. J. Psychiatry* **164,** 1641–1645 (2007).
9. Moore, D. F. & Jaffee, M. S. Military traumatic brain injury and blast. *NeuroRehabilitation* **26,** 179–181 (2010).

10. Elder, G. A. & Cristian, A. Blast-related mild traumatic brain injury: mechanisms of injury and impact on clinical care. *Mt. Sinai J. Med.* **76,** 111–118 (2009).
11. DePalma, R. G., Cross, G. M., Beck, L. B. & Chandler, D. W. Epidemiology of mTBI (mild traumatic brain injury) due to blast: history, DOD/VA data bases: challenges and opportunities, *At Proceedings of the NATO RTO-MP-HFM-207 Symposium on A Survey of Blast Injury across the Full Landscape of Military Science. Halifax, Canada,* https://www.cso.nato.int/pubs/rdp.asp?RDP=RTO-MP-HFM-207 (2011, October 3–5).
12. Alikunju, S., Abdul Muneer, P. M., Zhang, Y., Szlachetka, A. M. & Haorah, J. The inflammatory footprints of alcohol-induced oxidative damage in neurovascular components. *Brain. Behav. Immun.* **25** Suppl 1, S129–136 (2011).
13. Haorah, J. *et al.* Mechanism of alcohol-induced oxidative stress and neuronal injury. *Free Radic. Biol. Med.* **45,** 1542–1550 (2008).
14. Abdul Muneer, P. M., Alikunju, S., Szlachetka, A. M. & Haorah, J. The mechanisms of cerebral vascular dysfunction and neuroinflammation by MMP-mediated degradation of VEGFR-2 in alcohol ingestion. *Arterioscler. Thromb. Vasc. Biol.* **32,** 1167–1177 (2012).
15. Vandevord, P. J., Bolander, R., Sajja, V. S., Hay, K. & Bir, C. A. Mild neurotrauma indicates a range-specific pressure response to low level shock wave exposure. *Ann. Biomed. Eng.* **40,** 227–236 (2012).
16. Higashida, T. *et al.* The role of hypoxia-inducible factor-1alpha, aquaporin-4, and matrix metalloproteinase-9 in blood-brain barrier disruption and brain edema after traumatic brain injury. *J. Neurosurg.* **114,** 92–101 (2011).
17. Haorah, J., Floreani, N. A., Knipe, B. & Persidsky, Y. Stabilization of superoxide dismutase by acetyl-l-carnitine in human brain endothelium during alcohol exposure: novel protective approach. *Free Radic. Biol. Med.* **51,** 1601–1609 (2011).
18. Rump, T. J. *et al.* Acetyl-L-carnitine protects neuronal function from alcohol-induced oxidative damage in the brain. *Free Radic. Biol. Med.* **49,** 1494–1504 (2010).
19. Trudeau, D. L. *et al.* Findings of mild traumatic brain injury in combat veterans with PTSD and a history of blast concussion. *J. Neuropsychiatry Clin. Neurosci.* **10,** 308–313 (1998).
20. Santiago, P. N. *et al.* Screening for alcohol misuse and alcohol-related behaviors among combat veterans. *Psychiatr. Serv.* **61,** 575–581 (2010).
21. Wilk, J. E. *et al.* Relationship of combat experiences to alcohol misuse among US soldiers returning from the Iraq war. *Drug Alcohol Depen* **108,** 115–121 (2010).
22. Otis, J. D., McGlinchey, R., Vasterling, J. J. & Kerns, R. D. Complicating factors associated with mild traumatic brain injury: impact on pain and posttraumatic stress disorder treatment. *J Clin Psychol Med S* **18,** 145–154 (2011).
23. Kamnaksh, A. *et al.* Factors affecting blast traumatic brain injury. *J. Neurotrauma* **28,** 2145–2153 (2011).
24. Bell, R. S. *et al.* Military traumatic brain and spinal column injury: a 5-year study of the impact blast and other military grade weaponry on the central nervous system. *J. Trauma* **66,** S104–111 (2009).
25. Cernak, I. *et al.* Characterization of plasma magnesium concentration and oxidative stress following graded traumatic brain injury in humans. *J. Neurotrauma* **17,** 53–68 (2000).
26. Yattoo, G. & Tabish, A. The profile of head injuries and traumatic brain injury deaths in Kashmir. *J Trauma Manag Outcomes* **2,** 5 (2008).
27. Okie, S. Traumatic brain injury in the war zone. *N. Engl. J. Med.* **352,** 2043–2047 (2005).
28. Bhattacharjee, Y. Neuroscience. Shell shock revisited: solving the puzzle of blast trauma. *Science* **319,** 406–408 (2008).
29. Elder, G. A., Stone, J. R. & Ahlers, S. T. Effects of low-level blast exposure on the nervous system: is there really a controversy? *Front. Neurol.* **5,** 269 (2014).
30. Huber, B. R. *et al.* Blast exposure causes early and persistent aberrant phospho- and cleaved-tau expression in a murine model of mild blast-induced traumatic brain injury. *J. Alzheimers Dis.* **37,** 309–323 (2013).
31. Cernak, I. *et al.* The pathobiology of blast injuries and blast-induced neurotrauma as identified using a new experimental model of injury in mice. *Neurobiol. Dis.* **41,** 538–551 (2011).
32. Rubovitch, V. *et al.* A mouse model of blast-induced mild traumatic brain injury. *Exp. Neurol.* **232,** 280–289 (2011).
33. Readnower, R. D. *et al.* Increase in blood-brain barrier permeability, oxidative stress, and activated microglia in a rat model of blast-induced traumatic brain injury. *J. Neurosci. Res.* **88,** 3530–3539 (2010).
34. Saljo, A., Bao, F., Haglid, K. G. & Hansson, H. A. Blast exposure causes redistribution of phosphorylated neurofilament subunits in neurons of the adult rat brain. *J. Neurotrauma* **17,** 719–726 (2000).
35. Garman, R. H. *et al.* Blast exposure in rats with body shielding is characterized primarily by diffuse axonal injury. *J. Neurotrauma* **28,** 947–959 (2011).
36. Balakathiresan, N. *et al.* MicroRNA let-7i is a promising serum biomarker for blast-induced traumatic brain injury. *J. Neurotrauma* **29,** 1379–1387 (2012).
37. Leonardi, A. D., Bir, C. A., Ritzel, D. V. & VandeVord, P. J. Intracranial pressure increases during exposure to a shock wave. *J. Neurotrauma* **28,** 85–94 (2011).
38. Long, J. B. *et al.* Blast overpressure in rats: recreating a battlefield injury in the laboratory. *J. Neurotrauma* **26,** 827–840 (2009).
39. Kovesdi, E. *et al.* The effect of enriched environment on the outcome of traumatic brain injury; a behavioral, proteomics, and histological study. *Front. Neurosci.* **5,** 42 (2011).
40. Chavko, M., Koller, W. A., Prusaczyk, W. K. & McCarron, R. M. Measurement of blast wave by a miniature fiber optic pressure transducer in the rat brain. *J. Neurosci. Methods* **159,** 277–281 (2007).
41. Chavko, M. *et al.* Relationship between orientation to a blast and pressure wave propagation inside the rat brain. *J. Neurosci. Methods* **195,** 61–66 (2011).
42. Sajja, V. S. *et al.* Blast-induced neurotrauma leads to neurochemical changes and neuronal degeneration in the rat hippocampus. *NMR Biomed.* **25,** 1331–1339 (2012).
43. Bolander, R., Mathie, B., Bir, C., Ritzel, D. & VandeVord, P. Skull flexure as a contributing factor in the mechanism of injury in the rat when exposed to a shock wave. *Ann. Biomed. Eng.* **39,** 2550–2559 (2011).
44. Reneer, D. V. *et al.* A multi-mode shock tube for investigation of blast-induced traumatic brain injury. *J. Neurotrauma* **28,** 95–104 (2011).
45. Budde, M. D. *et al.* Primary blast traumatic brain injury in the rat: relating diffusion tensor imaging and behavior. *Front. Neurol.* **4,** 154 (2013).
46. Courtney, M. W. & Courtney, A. C. Note: A table-top blast driven shock tube. *Rev. Sci. Instrum.* **81,** 126103 (2010).
47. Kuehn, R. *et al.* Rodent model of direct cranial blast injury. *J. Neurotrauma* **28,** 2155–2169 (2011).
48. Sundaramurthy, A. & Chandra, N. A parametric approach to shape field-relevant blast wave profiles in compressed-gas-driven shock tube. *Front. Neurol.* **5,** 253 (2014).
49. Hyde, D.W. (Conventional Weapons Effects Program. United States Army Corps of Engineers, Vicksburg, MS; 2004).
50. Abdul-Muneer, P. M. *et al.* Induction of oxidative and nitrosative damage leads to cerebrovascular inflammation in an animal model of mild traumatic brain injury induced by primary blast. *Free Radic. Biol. Med.* **60,** 282–291 (2013).
51. Hue, C. D. *et al.* Blood-brain barrier dysfunction after primary blast injury *in vitro*. *J. Neurotrauma* **30,** 1652–1663 (2013).
52. Chen, Y. & Huang, W. Non-impact, blast-induced mild TBI and PTSD: concepts and caveats. *Brain Inj.* **25,** 641–650 (2011).
53. Yelveton, J. T. Pathology scoring system for blast injuries. *J. Trauma* **40,** S111–115 (1996).

54. Chandra, N. & Sundaramurthy, A. Acute Pathophysiology of Blast Injury: From Biomechanics to experiments and computations-implications on head and polytrauma, In *Brain Neurotrauma: Molecular, Neuropsychological, and Rehabilitation Aspects*. (ed. F. H. Kobeissy) Ch. 18, 199–258 (CRC Press, 2015).
55. Borkholder, D. A. & Duckworth, J. Biomedical Basis for Mild Traumatic Brain Injury (mTBI) Environmental Sensor Threshold Values *At International State-of-the-Science Meeting, McLean, VA* https://blastinjuryresearch.amedd.army.mil/docs/sos/SoS_Meeting_Proceedings_FINAL_12Feb15.pdf (2014, November 4–6).
56. Margulies, S. S. & Thibault, L. E. An analytical model of traumatic diffuse brain injury. *J. Biomech. Eng.* **111,** 241–249 (1989).
57. Panzer, M. B., Wood, G. W. & Bass, C. R. Scaling in neurotrauma: how do we apply animal experiments to people? *Exp. Neurol.* **261,** 120–126 (2014).
58. Jean, A. *et al.* An animal-to-human scaling law for blast-induced traumatic brain injury risk assessment. *Proc. Natl. Acad. Sci. USA* **111,** 15310–15315 (2014).
59. Selvan, V., Ganpule, S., Kleinschmit, N. & Chandra, N. Blast wave loading pathways in heterogeneous material systems–experimental and numerical approaches. *J. Biomech. Eng.* **135,** 061002 (2013).
60. Kinney, G. F. & Graham, K. J. *Explosive shocks in air*, Vol. 1, Edn. 2. (Springer-Verlag, Berlin and New York, 1985).
61. Richmond, D. R., Damon, E. G., Fletcher, E. R., Bowen, I. G. & White, C. S. The Relationship Between Selected Blast-Wave Parameters And The Response Of Mammals Exposed To Air Blast. *Ann. N. Y. Acad. Sci.* **152,** 103–121 (1968).
62. Smith, D. H., Okiyama, K., Thomas, M. J., Claussen, B. & McINTOSH, T. K. Evaluation of memory dysfunction following experimental brain injury using the Morris water maze. *J. Neurotrauma* **8,** 259–269 (1991).
63. Lowenstein, D. H., Thomas, M. J., Smith, D. H. & McIntosh, T. K. Selective vulnerability of dentate hilar neurons following traumatic brain injury: a potential mechanistic link between head trauma and disorders of the hippocampus. *J. Neurosci.* **12,** 4846–4853 (1992).
64. McIntosh, T. K. *et al.* Traumatic brain injury in the rat: characterization of a lateral fluid-percussion model. *Neuroscience* **28,** 233–244 (1989).
65. Thompson, H. J. *et al.* Lateral fluid percussion brain injury: a 15-year review and evaluation. *J. Neurotrauma* **22,** 42–75 (2005).
66. Washington, P. M. *et al.* The effect of injury severity on behavior: a phenotypic study of cognitive and emotional deficits after mild, moderate, and severe controlled cortical impact injury in mice. *J. Neurotrauma* **29,** 2283–2296 (2012).
67. Xiong, Y., Mahmood, A. & Chopp, M. Animal models of traumatic brain injury. *Nat. Rev. Neurosci.* **14,** 128–142 (2013).
68. Rafaels, K. A. *et al.* Brain injury risk from primary blast. *J Trauma Acute Care Surg* **73,** 895–901 (2012).
69. Risling, M. *et al.* Mechanisms of blast induced brain injuries, experimental studies in rats. *Neuroimage* **54,** S89–S97 (2011).
70. Chavko, M., Prusaczyk, W. K. & McCarron, R. M. Lung injury and recovery after exposure to blast overpressure. *J. Trauma* **61,** 933–942 (2006).
71. Stuhmiller, J. H. *et al.* A model of blast overpressure injury to the lung. *Journal of biomechanics* **29,** 227–234 (1996).
72. Chen, Y., Huang, W. & Constantini, S. Blast shock wave mitigation using the hydraulic energy redirection and release technology. *PLoS One* **7**, e39353 (2012).
73. Galarneau, M. R., Woodruff, S. I., Dye, J. L., Mohrle, C. R. & Wade, A. L.Traumatic brain injury during Operation Iraqi Freedom: findings from the United States Navy-Marine Corps Combat Trauma Registry. *J. Neurosurg.* **108,** 950–957 (2008).
74. Guy, R. J., Kirkman, E., Watkins, P. E. & Cooper, G. J. Physiologic responses to primary blast. *J Trauma* **45,** 983–987 (1998).
75. Irwin, R. J. *et al.* Shock after blast wave injury is caused by a vagally mediated reflex. *J Trauma* **47,** 105–110 (1999).
76. Knoferl, M. W. *et al.* Cardiopulmonary, histological, and inflammatory alterations after lung contusion in a novel mouse model of blunt chest trauma. *Shock* **19,** 519–525 (2003).
77. Ohnishi, M., Kirkman, E., Guy, R. J. & Watkins, P. E. Reflex nature of the cardiorespiratory response to primary thoracic blast injury in the anaesthetised rat. *Exp. Physiol.* **86,** 357–364 (2001).
78. Sawdon, M., Ohnishi, M., Watkins, P. E. & Kirkman, E. The effects of primary thoracic blast injury and morphine on the response to haemorrhage in the anaesthetised rat. *Exp Physiol* **87,** 683–689 (2002).
79. Cho, H. J., Sajja, V. S., Vandevord, P. J. & Lee, Y. W. Blast induces oxidative stress, inflammation, neuronal loss and subsequent short-term memory impairment in rats. *Neuroscience* **253,** 9–20 (2013).
80. Cernak, I., Wang, Z., Jiang, J., Bian, X. & Savic, J. Ultrastructural and functional characteristics of blast injury-induced neurotrauma. *J Trauma* **50,** 695–706 (2001).
81. Shetty, A. K., Mishra, V., Kodali, M. & Hattiangady, B. Blood brain barrier dysfunction and delayed neurological deficits in mild traumatic brain injury induced by blast shock waves. *Front. Cell. Neurosci.* **8,** 232 (2014).
82. Lucke-Wold, B. P. *et al.* Bryostatin-1 restores blood brain barrier integrity following blast-induced traumatic brain injury. *Mol. Neurobiol* **52,** 1119–1134 (2014).
83. Chodobski, A., Zink, B. J. & Szmydynger-Chodobska, J. Blood-brain barrier pathophysiology in traumatic brain injury. *Transl Stroke Res* **2,** 492–516 (2011).
84. Moss, W. C., King, M. J., & Blackman, E. G. Skull flexure from blast waves: a mechanism for brain injury with implications for helmet design. *Phys. Rev. Lett.* **103,** 108702 (2009).
85. Goeller, J., Wardlaw, A., Treichler, D., O'Bruba, J. & Weiss, G. Investigation of cavitation as a possible damage mechanism in blast-induced traumatic brain injury. *J. Neurotrauma* **29,** 1970–1981 (2012).
86. Chandra, N. *et al.* Evolution of blast wave profiles in simulated air blasts: experiment and computational modeling. *Shock Waves* **22,** 403–415 (2012).
87. Chandra, N., Holmberg, A. & Feng, R. Controlling the shape of the shock wave profile in a blast facility. U.S. Provisional patent application no. 61542354 (2011).
88. Clifton, G. L. *et al.* Marked protection by moderate hypothermia after experimental traumatic brain injury. *J Cereb Blood Flow Metab* **11,** 114–121 (2007).
89. Faul, F., Erdfelder, E., Lang, A. G. & Buchner, A. G*Power 3: a flexible statistical power analysis program for the social, behavioral, and biomedical sciences. *Behav. Res. Methods* **39,** 175–191 (2007).

Acknowledgements

This work was supported by NIH/NIAAA grants 1R21AA022734-01A1 to JH, and the U.S. Army Medical Research and Materiel Command grant Log No. 14059001 (W81XWH-15-1-0303) to NC. Authors declare no conflicts of interest.

Author Contributions

V.M., H.S. and A.H. carried out the experiments, data acquisition, and V.M. helped J.H. for statistical data analysis for Figure 5 through Figure 10 in Haorah's Lab. M.S. carried out the experiments, data acquisition, and statistical data analysis for Figure 1 through Figure 4 in NC's Lab. N.C. designed the project, supervised the experiments, and performed the data interpretation of the manuscript for Figure 1 through Figure 4. J.H. conceived the

scientific idea, designed the experiments, data interpretation, and manuscript write up for Figure 5 through Figure 10. All authors read and approved the final version of manuscript.

Additional Information

Competing financial interests: The authors declare no competing financial interests.

How to cite this article: Mishra, V. *et al.* Primary blast causes mild, moderate, severe and lethal TBI with increasing blast overpressures: Experimental rat injury model. *Sci. Rep.* **6**, 26992; doi: 10.1038/srep26992 (2016).

This work is licensed under a Creative Commons Attribution 4.0 International License. The images or other third party material in this article are included in the article's Creative Commons license, unless indicated otherwise in the credit line; if the material is not included under the Creative Commons license, users will need to obtain permission from the license holder to reproduce the material. To view a copy of this license, visit http://creativecommons.org/licenses/by/4.0/

Appendix A –Publication Cover 24
2016

Authors: S. Ganpule, R. Salzar, B. Perry and N. Chandra

Title: *"Role of helmets in blast mitigation: insights from experiments on PMHS surrogate"*

Journal Publication: International Journal of Experimental and Computational Biomechanics, (2016), [16-24]

Role of helmets in blast mitigation: insights from experiments on PMHS surrogate

Shailesh Ganpule*

Department of Mechanical and Materials Engineering,
University of Nebraska-Lincoln,
Lincoln, NE 68588, USA
Email: shailesh@huskers.unl.edu
Email: sgganpule@gmail.com

Robert Salzar and Brandon Perry

Center for Applied Biomechanics,
University of Virginia,
Charlottesville, Virginia, 22911, USA
Email: salzar@virginia.edu
Email: bperry@virginia.edu

Namas Chandra*

Center for Injury Biomechanics, Materials, and Medicine (CIBM3),
Department of Biomedical Engineering,
New Jersey Institute of Technology,
Newark, NJ, 07102-1982, USA
Email: namas.chandra@njit.edu
*Corresponding authors

Abstract: Blast induced traumatic brain injury (bTBI) has emerged as the most significant injury to war fighters in recent conflicts. Interaction of the blast wave with the head and helmet are not well understood. In this work, the effects of blast were investigated on the post-mortem human subject (PMHS) head using a compression driven shock tube. The results suggest that the evolution of intracranial pressure profiles is strongly governed by the wave propagation through skin-skull-brain parenchyma. It is also observed that the sinus cavities naturally attenuate the blast overpressure. Performance of two helmet configurations (padded and suspension) in mitigating the blast is also evaluated. The results suggest that the amount of mitigation offered by each helmet varies with the helmet configuration. For helmets with the suspension system, the blast wave is intensified beneath the helmet. Further, the degree of blast wave mitigation is affected by the morphology of the PMHS itself. Overall, these results suggest that the blast wave interacts with the head and the helmet in a complex manner and these interaction effects must be taken into account while designing strategies for protection of the head against the blast.

Keywords: blast; helmet; TBI.

Copyright © 2016 Inderscience Enterprises Ltd.

Reference to this paper should be made as follows: Ganpule, S., Salzar, R., Perry, B. and Chandra, N. (2016) 'Role of helmets in blast mitigation: insights from experiments on PMHS surrogate', *Int. J. Experimental and Computational Biomechanics*, Vol. 4, No. 1, pp.13–31.

Biographical notes: Shailesh Ganpule is currently a Post-Doctoral Fellow at the Hopkins Extreme Materials Institute of the Johns Hopkins University (JHU). His broad research interests pertain to computational and experimental mechanics with emphasis on applications of these topics in biology and biomedical engineering.

Robert Salzar is a Principal Scientist at the Center for Applied Biomechanics at the University of Virginia. He has over 25 years of experience in the field of engineering mechanics, with the last 15 years focusing on military injury biomechanics.

Brandon Perry is a Graduate Research Assistant at the University of Virginia's Center for Applied Biomechanics. His research interests are blast effects on mounted and unmounted warfighters, lower extremity and pelvic injury, and shockwave physics.

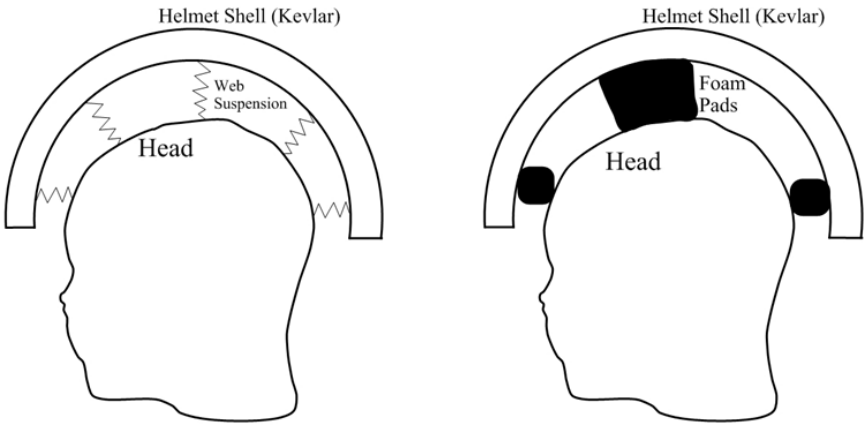
Namas Chandra is a Professor of Biomedical Engineering and the Director of Center for Injury Bio-mechanics, Materials, and Medicine at the New Jersey Institute of Technology. His research interests include computational mechanics of materials at various scales, superplasticity, interfaces, nano-bio materials, experimental mechanics, blast- and blunt-induced traumatic brain injury.

1 Introduction

Blast induced traumatic brain injury (bTBI) has been identified as the signature wound of recent conflicts in Iraq and Afghanistan (Tanielian and Jaycox, 2008). The Defense and Veterans Brain Injury Center (DVBIC) has reported 321,454 clinically confirmed TBI cases in US service members from 2000 to 2014 (http://dvbic.dcoe.mil/dod-worldwide-numbers-tbi). Most of these cases are due to the blast, although the separate classification of bTBI cases is not available. To address the growing concerns regarding bTBI, there has been a continual increase in the number of blast studies in recent years on animal models, head surrogates, and post-mortem human subjects (PMHSs) (Alley et al., 2011; Bolander et al., 2011; Cernak et al., 2001; Chavko et al., 2007; Cheng et al., 2010; Desmoulin and Dionne, 2009; Long et al., 2009; Pun et al., 2011; Rafaels et al., 2011; Rafaels, 2010; Risling et al., 2011; Saljo et al., 2008, 2010, 2011; Svetlov et al., 2009, 2010). In spite of these efforts, our current understanding of the pathophysiology of Btbi is far from complete (Meaney et al., 2014). How the blast wave interacts with the head and induces biomechanical loading to the brain is not fully understood. Several mechanisms of bTBI have emerged (Courtney and Courtney, 2011). These mechanisms are: direct transmission of a blast wave through cranium; skull deformation induced brain loading; cavitation at the tissue and neuronal levels; blood surge in the brain due to thoracic loading; and acceleration-deceleration of the head due to the loading. In addition, the efficacy of military helmets in mitigating the blast is not fully known as helmets have been conventionally designed for blunt and ballistic protections (Bhattacharjee, 2008;

Lew et al., 2005; Okie, 2005; Xydakis et al., 2007). Two types of helmet configurations are of particular interest: the suspension helmet configuration [Figure 1(a), and 1(b)] the padded helmet configuration [Figure 1(b)]. In the suspension helmet configuration, the helmet is separated from the head by a gap (subspace) typically containing a webbing suspension. A gap between the head and the helmet is deemed important for ballistic back-face deformation performance. In the padded helmet configuration, the head is typically coupled to the helmet through seven foam pads (front, back, crown, four side pads). Several studies have shown that, for the suspension helmet configuration, blast wave can focus under (beneath) the helmet and enhance the pressure in the head-helmet subspace (gap) and on the surface of the head (Ganpule et al., 2012; Moss et al., 2009; Mott et al., 2008). To the extent that pressure on the surface of the head is predictive of injury (assuming direct transmission through cranium is an important mechanism of bTBI), these data suggest that changes in the helmet configurations (i.e., suspension helmet configuration vs. padded helmet configuration), which result in different pressure distributions and magnitudes, may influence the location and severity of the injury. It is, however, not clear how pressure amplification seen on the surface of the head translates to the intracranial contents. Establishing this link is important considering the complex morphology of the skin-skull-brain parenchyma. In this work, this issue is addressed by studying the response of the PMHS head, both with and without the suspension and padded helmets, under blast loading conditions. Further, the focus of this work in on primary blast loading conditions that considers effects associated with the propagation of blast wave alone without considering other consequences of the blast(or explosion)such as interaction with shrapnel or fragments (secondary), impact with environmental structures (tertiary), and effect of toxic gases (quaternary).

Figure 1 Schematics of helmet configurations, (a) suspension helmet (b) padded helmet



Note: Representative midsagittal section is shown.

The paper is organised in the following manner. In the methods section, the details of the experiments that include the description of the PMHS surrogate, instrumentation, simulated blast loading conditions, data acquisition, and analysis are described. In the results section, the results of experiments on PMHS surrogate in terms of pressure-time histories of the incident, surface, and intracranial pressure profiles are presented. An

analysis of peak pressures with and without the helmet is also presented. In the next section on the discussion, results are discussed in the context of broader implications of this work in understanding the biomechanics of bTBI and the role of personal protective equipment in blast mitigation. The key findings of this work are also summarised in this section, along with the limitations.

2 Methods

2.1 Preparation of PMHS surrogate

Experiments were conducted on two PMHSs. PMHS specimens were obtained from the University of Virginia Center for Applied Biomechanics. The specimens were handled, prepared, and used in accordance with local and federal laws, and within the ethical guidelines and research protocols approved by the University of Virginia and University of Nebraska institutional review panel for PMHS use. Specimens were screened for any osseous disease and any pre-existing fractures, as confirmed by CT imaging. Table 1 lists the age, gender, and basic anthropometry of the PMHS specimens.

Table 1 Characteristics of the post-mortem human surrogate heads tested in this study

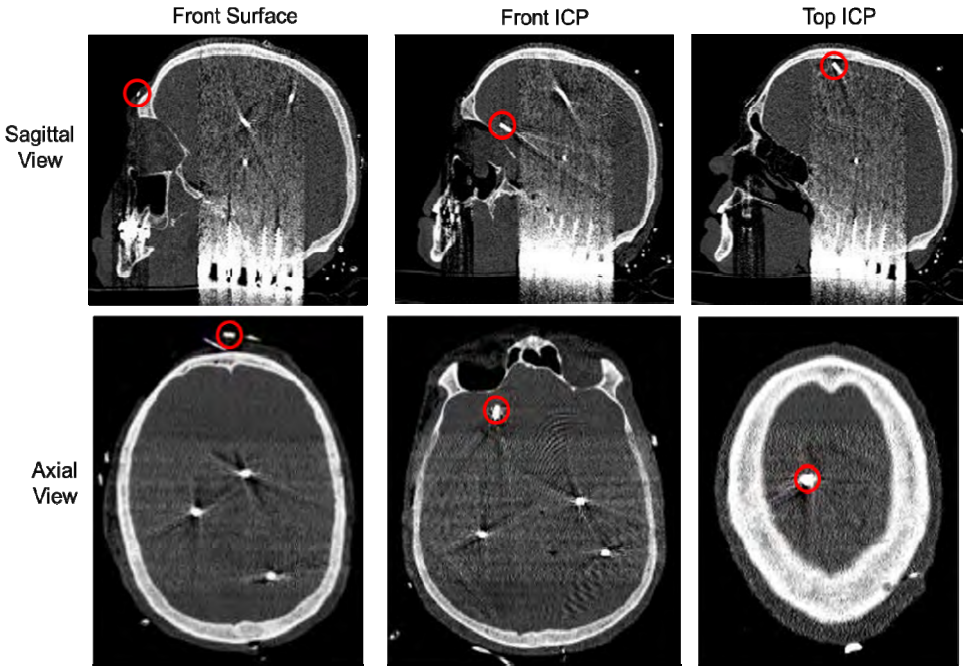
Sr. no.	*Surrogate ID*	*Sex*	*Age*	*Height (cm)*	*Weight (kg)*	*Cause of death*
1	476	M	75	173	79	Cardiovascular disease
2	513	M	65	175	73	Prostate cancer

PMHS specimens were fresh frozen and stored at the University of Virginia Center for Applied Biomechanics shipped to the University of Nebraska where they remained frozen until use. All heads were thawed at least 48 hours prior to the testing. Since PMHS brains autolyze quickly, the brains were significantly degraded at the time of preparation. To achieve a more homogenous state inside the skull, the brain and the stiff membranes (dura, falx, and tentorium) were removed from each PMHS intracranial space and backfilled with abrain simulant. However, it should be noted that anatomy and structure of skin-skull parenchyma were preserved in these experiments. To model the brain, the gel simulant with a density close to that of water (ρ = 1,000 kg/m^3) and with a nominal bulk (volumetric) modulus of ~2.2 GPa is sought. The Bulk modulus of the gel simulant under blast loading was verified through separate characterisation experiments on the gel simulant (details inthe supplementary material). Gelatin (Gelita USA Inc., Sioux, IA), a protein-derived polymer, was chosen. The gel was prepared by dissolving a gelatin powder (195 g/litre) in warm distilled water (at 40°C). The gel simulant was poured into the cranial cavity through the foramen magnum and allowed to cure at room temperature. Air bubbles were removed during curing by applying vacuum to the system. The foramen magnum was then sealed using a filler material (Bondo®). A Hybrid III neck (Humanetics, Huron, OH) was mated to the head using a fabricated-base plate that was mechanically fixed to the base of the skull by the use of screws.

2.2 Instrumentation

Each surrogate was instrumented to measure surface and intracranial pressures (ICPs). Surface pressure was measured using Kulite surface mount sensors (model LE-080, pressure range 0–1.72 MPa absolute) and ICPs were measured using Kulite probe sensor (model XCL-072, pressure range 0–3.45MPa absolute).In general, measurements were made at several locations. However, here, three locations that are relevant to this study are focused. These locations are: front surface pressure gauge, front ICP gauge, and top ICP gauge (Figure 2). The front surface pressure gauge was mounted on the forehead, ~20 millimetres above the glabella. The front ICP gauge was inserted in the gel simulant ~10 millimetres below the glabella. The top ICP gauge was inserted in the gel below the sagittal suture. CT images of the instrumented heads were taken to verify locations of the sensors inside the head (Figure 2). In addition to these sensors, the incident pressure of the incoming blast wave was also measured using PCB pressure sensor (model 134A24, pressure range 0–6.89 MPa absolute). An incident pressure gauge,mounted on the wall of the shock tube, was located at a distance of 200 mm (upstream) of the PMHS surrogate.

Figure 2 CT images of the instrumented PMHS surrogate head showing gauge (sensor) locations (see online version for colours)

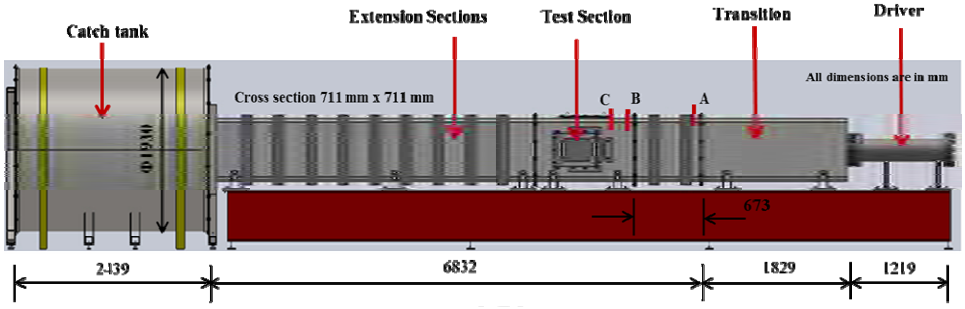


2.3 Blast wave exposure

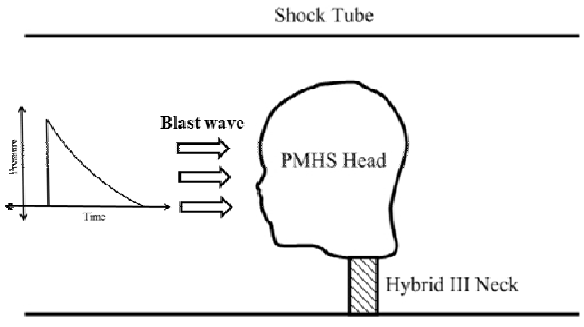
Experiments were carried out in the 711 mm × 711 mm cross section shock tube designed by and tested at the University of Nebraska-Lincoln's blast wave generation facility. The details of the shock tube design and operation are available in numerous earlier publications (Chandra et al., 2012; Ganpule et al., 2013; Sundaramurthy and Chandra,

2014) and avoided here for brevity. The head assembly was placed in the test section of the shock tube (Figure 3), and subjected to a primary blast wave of varying incident intensities (peak pressures of ~70 kPa, ~140 kPa, and ~200 kPa, respectively). This was achieved by varying the number of Mylar^{TM} membranes which resulted in different burst pressures. The surrogate head was oriented in an anterior-posterior (i.e., front-facing) direction to the blast. Each intensity was repeated three times for each surrogate head; totalling18 (3 × 3 × 2) shots (see Table 2 for test matrix). Experiments were also conducted with suspension and padded helmets fitted to the surrogate. For the suspension helmet configuration, there is a gap of ~13 mm (as per ballistic standard) between the head and the helmet (Reynosa, 1999); whereas for the padded helmet configuration, the helmet is coupled to the head through a seven-pad system. By design, the padded helmet is tightly fitted on the head so there are minimal gaps between the seven helmet pads and the head. Thus, the padded helmet is better integrated to the head as compared to suspension helmet. The padded helmet configuration was used with surrogate head 1 and the suspension helmet configuration was used with surrogate head 2. As with the no helmet tests, three repeated tests were performed at each of the three pressure intensities. Thus, there was a total of 36 shots performed, 18 without the helmet and 18 with the helmet (see Table 2 for test matrix).

Figure 3 Experimental setup, (a) schematic of the 711 mm × 711 mm shock tube (b) PMHS surrogate head along with hybrid 3 neck placed in the test section of the shock tube (see online version for colours)



(a)



(b)

Table 2 Test matrix

	Number of tests								
	No. helmet			*With padded helmet*			*With suspension helmet*		
Incident intensity (kPa) →	70	140	200	70	140	200	70	140	200
Surrogate head 1	3	3	3	3	3	3	-	-	-
Surrogate head 2	3	3	3	-	-	-	3	3	3
					Total				36

2.4 Data acquisition, processing, and analysis

Experimental data was collected at the sampling rate of 1MHz using two national instruments PXI-6133 data acquisition cards, each of which has eight analogue channels. The data acquisition cards were capable of 14 bit sampling at up to 2.5 MHz. Pressure sensors was connected to the data acquisition system through a 1 MHz differential amplifier. Experimental data was presented as the mean ± standard error of the mean (SEM). Pressures were reported in the form of gauge pressures or overpressures.

3 Results

3.1 Wave dynamics

Figure 4 shows sample pressure-time (*p*-*t*) profiles recorded by a selection of gauges for surrogate head 2; incident intensity ~140 kPa. While presenting sample *p*-*t* profiles, the arrival of the blast wave at the incident pressure gauge is treated as a reference time, i.e., $t = 0$. The arrival of the blast wave at other gauge locations is with respect to this reference time. The incident pressure gauge shows a sharp rise in pressure corresponding to a shock front followed by a nonlinear decay (shock tail). Secondary peaks seen in the incident pressure profile correspond to the reflections from the surrogate head and the walls of the shock tube. As the blast wave impacts the surrogate head, the pressure is amplified by ~2.75 times due to aerodynamic effects (Anderson, 2001; Kinney and Graham, 1985), which is evident from the surface pressure profile. The amplification factor (ratio of reflected to incident pressure) can vary from 2 to 8, based on the intensity of the incident wave and the shock wave speed (Kambouchev et al., 2007). In addition, the shape of the surface pressure profile is similar to the incident pressure profile. As the blast wave enters the intracranial contents through skin-skull parenchyma, wave action (dynamic events) play out in a very short time, as compared to the incident and surface pressure profiles. The peak pressure recorded by the front and top ICP gauges is lower than the peak pressure recorded by the surface gauge. In addition, the shape of the ICP profiles is different from the incident and surface pressure profiles. The response after 1 ms (milli second) is solely structural as intracranial waves equilibrate by that time (wave speed ~1,500 mm/ms). The wave propagation through skin-skull-brain parenchyma governs the *p*-*t* history. Numerous factors affect the blast wave propagation as it propagates through skin-skull-brain parenchyma. These factors are:

1 anatomy of the skin-skull-brain parenchyma, including material interfaces

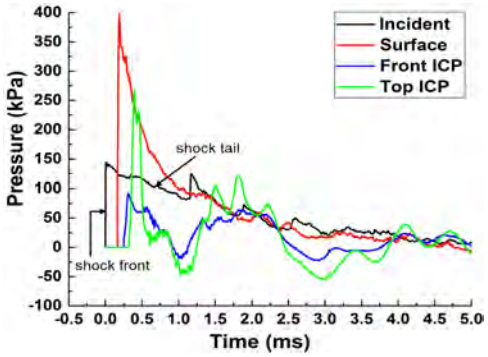
2 geometric features of the head e.g., curvature, thickness of various anatomical structures

3 ICP gauge location within the head

4 impedance mismatch between the skin, skull (including other anatomical structures such as sinus cavities, material interfaces), and brain.

These factors, in turn, govern the intracranial pressure time history. These aspects of the wave propagation from air shock to surface to skull parenchyma to intracranial contents are detailed in our earlier works (Ganpule, 2013; Ganpule et al., 2013). A brief description is provided here only for the sake of completeness. It is also interesting to note that the peak pressure recorded by the front ICP gauge is lower than the top ICP gauge. This may be because of the presence of sinus cavities in the vicinity of the 'front ICP' gauge. It should be noted that the observations made in this subsection regarding the wave dynamics are consistent across other incident intensities studied and for other PMHS surrogate.

Figure 4 Sample pressure-time (*p-t*) profiles recorded by various gauges for surrogate head 2; incident intensity ~140 kPa (see online version for colours)



Note: The profiles are based on the mean of three shots.

3.2 *Analysis of peak pressures with and without the helmet*

Figure 5 shows the recorded peak pressures at various gauge locations with and without the helmet for three incident intensities: ~70 kPa, ~140 kPa, and ~200 kPa. With the padded helmet [Figure 5 (a)], the recorded peak pressures are lower than the no helmet counterparts. The reduction in peak pressure for top ICP gauge is higher than that of the front ICP gauge, as the top ICP gauge is fully covered by the helmet. With the suspension helmet [Figure 5 (b)], recorded peak pressures for the surface gauge and front ICP gauge are lower than the no helmet counterparts. The top ICP gauge, however, shows an interesting pattern. For the top ICP gauge, the initial peak pressure is lower than the no helmet counterpart. At a later time, the peak pressures recorded by the top ICP gauge is either higher (for incident intensities of 70 kPa and 140 kPa) or equivalent (for the incident intensity of 200 kPa) than the no helmet counterparts. This is clearer after comparing *p-t* histories with and without the helmet. Figure 6(a) compares *p-t* histories

between no helmet and with the suspension helmet for top ICP gauge for the incident intensity of ~140 kPa. With the suspension helmet, the initial peak pressure, corresponding to the transmission of the shock front into intracranial contents is lower than the no helmet counterpart. However, at a later time (~1.4 ms), there is a secondary surge in the pressure. The peak pressure, corresponding to the secondary surge, is higher than the peak pressure seen in the no helmet scenario. This is due to the underwash effect of the helmet, which will be discussed in the discussion section. Amplification in pressure due to underwash effect was absent for the surface and front ICP gauges.

Figure 5 Comparison of peak pressures between no helmet with padded helmet and with suspension helmet scenarios for various incident intensities, (a) padded helmet (b) suspension helmet (see online version for colours)

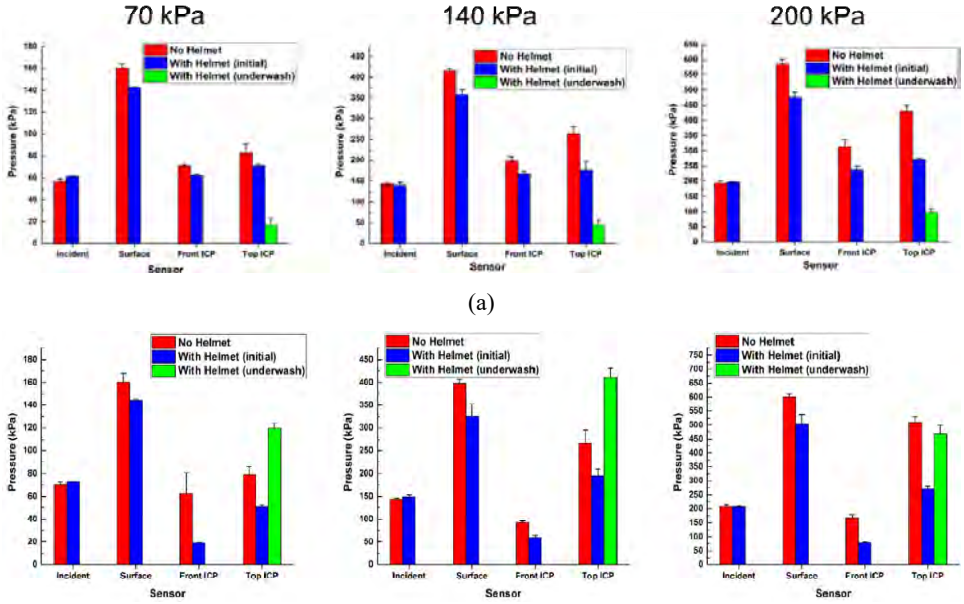
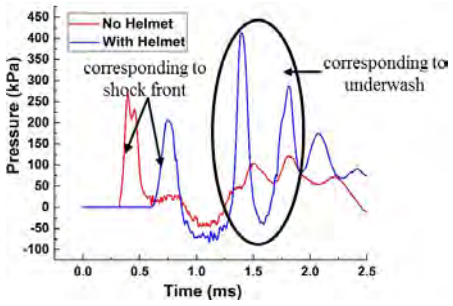


Figure 6 Comparison of *p-t* profile between no helmet and with suspension helmet scenarios for top ICP gauge for the incident intensity of ~140 kPa (see online version for colours)



Note: Underwash (focusing) effect beneath the suspension helmet is clearly translated to the intracranial contents as depicted in the ICP profile.

4 Discussion

The goal of this work was to study the response of PMHS surrogate with and without military helmets under primary blast loading conditions. PMHS surrogate is exposed to primary blast waves of varying incident intensities and studied the surrogates' response to this loading.

One of the interesting observations that was consistent across all experiments was the reduction of pressure that may be the result of the presence of the sinus cavities. The front ICP gauge always recorded lower peak pressure than the top ICP gauge. Peak pressure differences up to 50% were observed between the front ICP gauge and the top ICP gauge in the vicinity of front ICP gauge. The role of sinus cavities in attenuating the blast is further substantiated by analysing the head response in a rear blast scenario (see supplementary Figure S1). In a rear blast scenario, the peak pressures recorded by front and top ICP gauges were equivalent as sinus cavities were absent in the occipital region of the head. The details of a rear blast scenario are avoided here for brevity. Attenuation of the blast pressure due to sinus cavities was also observed in numerical simulations of the blast wave and head interactions. For example, Taylor et al. (2014) have reported lesser transmitted pressures in frontal (anterior-posterior) blast scenario as compared to rear (posterior to anterior) and lateral (right to left) blast scenarios from their computational simulations of a human head interacting with the blast wave. Authors attribute the attenuation in pressure in a frontal blast scenario to the presence of sinus cavities. In frontal blast scenarios, sinus cavities (that exist preliminary in the forehead/face structure), were directly exposed to the incoming blast wave, whereas in the rear and lateral blast scenarios the sinus cavities were not in the primary path of the incoming blast. Similar trends regarding the role of sinus cavities in blast wave attenuation were observed in a two-dimensional cylindrical head model of Akula et al. (2013).Our results support these numerical findings. Since sinus cavities are filled with the air, and air being of low impedance, the sinus cavities effectively attenuate incoming waves (Nakagawa et al., 2011) by degrading wave transmission. These results suggest that sinus cavities may provide intrinsic mitigation of blast wave. This aspect has direct implications for the design of helmets. Blast wave mitigation may be improved by incorporating tiny pockets of low impedance materials or voids in the design of the helmet liners and foam pads.

Protection against blast is an important aspect in reducing the incidences of bTBI. There is a continual interest in evaluating the role of a helmet under blast loading conditions (Baumer et al., 2013; Salimi Jazi et al., 2014; Sarvghad-Moghaddam et al., 2015; Zhang et al., 2013a, 2013b), which will eventually lead to better design and enhanced protection. In earlier works (Ganpule, 2013; Ganpule et al., 2012) the role of the helmet in the mechanics of the blast wave/head interactions was studied in terms of the pressure field experienced on the surface of a surrogate dummy head. The surrogate dummy headform used in these studies was based on the FOCUS headform, which was designed to replicate a 50th percentile male soldier across the three branches of the military (Army, Navy, and Air Force) (Kennedy, 2007). Surface pressures were measured at five different locations along the midsagittal plane [front, top (three locations) and back] on the surrogate dummy head [see supplementary material; Figure S2(a)]. From the recorded pressures, it was seen that the peak surface pressures were reduced with the padded helmet as compared to the no helmet counterparts. With the suspension helmet however, it was seen that the peak pressures were reduced only for locations near the

impact site (site of the initial contact with the blast wave). For locations away from the impact site, peak pressures were higher than their corresponding no helmet counterparts (see supplementary material; Figure S2(b), 2(c)]. Increase in surface pressures for locations away from the impact site were due to the focusing of the blast wave beneath the suspension helmet(See supplementary material; Figure S3) (Ganpule et al., 2012). The focusing occurs as a result of complex wave interaction of the blast wave with the head and the helmet. As the blast wave encounters the head-helmet assembly, it gets divided into two fronts. One front travels around the outer perimeter of the helmet, while the other front penetrates the gap between the head and the helmet (i.e., head-helmet subspace) and travels underneath the helmet towards the back of the head [Figure S3(a)]. The blast front travelling outside the helmet reaches the rear of the helmet before the blast front traverses through the gap [Figure S3(b)-i]; eventually, these two blast fronts focus at a region away from the initial impact site [Figure S3(b)-ii]. Subsequently, the high pressure air in the head-helmet subspace expands in all directions [Figure S3(b)-iii]. This focusing produces higher pressures in the head-helmet subspace in the regions a way from the impact site. The focusing phenomenon beneath the helmet was termed as an underwash effect, as initially reported by Mott et al. (2008) and Moss et al. (2009). Since then, the underwash effect has been reproduced both numerically (Ganpule et al., 2012; Sarvghad-Moghaddam et al., 2015; Zhang et al., 2013b) and experimentally (Baumer et al., 2013; Ganpule et al., 2012). However, how the underwash effect seen on the surface of the head affects the intracranial contents has not yet been established. This test series attempted to address this issue by conducting experiments on PMHS surrogate with and without the helmets.

As stated earlier peak pressures of the top ICP gauge with the suspension helmet were either higher (for incident intensities of 70 and 140 kPa) or equivalent (for the incident intensity of 200 kPa) than the no helmet counterparts [Figure 5(b)]. From the analysis of *p-t* profiles for the top ICP gauge, it was observed that these peak values corresponded to the distinct secondary surge in pressure [Figure 6(a)]. Such a secondary surge in the *p-t* profiles were absent for no helmet or padded helmet scenarios. The distinct secondary surge in intracranial pressure was correlated with the distinct secondary surge (due to underwash) observed in the surface pressure profiles with the suspension helmet [see supplementary material; Figure S2(c)]. This suggests that the underwash effect seen on the surface of the head translates to the intracranial contents. Further, these results also indicate that the suspension helmet configuration enables additional load transfer pathways to the intracranial contents through the head/helmet subspace. This is probably also true for any head-helmet configurations wherein gaps exist between the head and helmet, or when gaps are created between the head and helmet as a consequence of practical scenarios in the battlefield. This aspect should be taken into account while designing next generation helmets. To the best of our knowledge, this is the first experimental study that demonstrates how the underwash effect translates to the intracranial contents.

While discussing the underwash effect as a result of the suspension helmet, it is also important to discuss mitigation offered by current helmets. One goal of brain injury mitigation is the reduction of peak pressures, as injury criteria are often based on peak values (e.g., Courtney and Courtney, 2011). A more generic goal would be the reduction of cumulative strain energy in the entire brain. Calculating strain energies for the entire brain from these types of experiments is not possible as experimental measurements are

typically done at a limited number of discrete points. High-fidelity numerical simulations can provide additional insights in this regard.

The blast wave head interactions and efficacy of the helmets in mitigating the blast are typically studied by analysing:

a surface pressures (measured on the surface of the head)

b intracranial pressures (measured within the brain, the gel simulant in this work).

Further peak values are of particular interest for reasons articulated earlier. Detailed analysis of the interaction of blast wave with the head and the helmet is reported elsewhere (Ganpule et al. 2012, 2013; Ganpule, 2013). In brief, both suspension and padded helmets offer peak surface pressure reductions for regions near the impact site (Figure 5). In this work, the amount of pressure reduction on the surface of the head is similar between the suspension and padded helmets. This is mainly because the surface pressure gauge was not fully covered by the foam pads. Further in these experiments, the degree to which helmet pads were tightly coupled to the head is not known. Individual fitting of helmets to the head may have created small pre-existing gaps between the head and the helmet pads. Our computational work (Ganpule et al., 2012) indicate that head response is sensitive to small gaps (on the order of few millimetres) between the head and the helmet, and pressure amplification may also be possible in these gaps. In our earlier computational work (Ganpule et al., 2012), it is demonstrated that when the padded helmet is tightly fitted (ideal scenario) on the head without any gaps, then the padded helmet configuration significantly reduces surface pressures on the head as compared to the suspension helmet configuration. As we move away from the impact site, the wave dynamics become complex (e.g., see supplementary Figures S2 and S3). Wave dynamics and the resulting surface pressures are strongly governed by geometry induced flow separation for the no helmet case (Ganpule et al., 2013). For suspension and padded helmet cases, dynamics in the head/helmet subspace is critical in determining resulting pressures (Ganpule et al., 2012). Similar trends regarding the performance of the helmet are reported by Baumer et al. (2013) and Zhang et al. (2013b).

For regions inside the head (i.e., intracranial contents) the pressures are not only governed by the helmet configuration (e.g., suspension vs. padded) but also by the morphology (geometry and structure) of the PMHS surrogates, as demonstrated earlier. Thus, the recorded intracranial pressures are different between PMHS surrogates. From the data presented in this work, it is not possible to separate the effects of mitigation offered by the helmet and differences due to the morphological variations between PMHS surrogates. Similar variations, attributed to head morphology, are seen in other blast experiments using PMHS surrogates (Dal Cengio, 2011; Zhang et al., 2013a) and in rats (Dal Cengio et al., 2013). This also highlights the need for large amount of experimental effort to establish robust quantitative trends.

The work presented here has several limitations. Since only two PMHS surrogates were used in this study, it is not possible to establish the statistical significance of these results. Further, results with the helmet were based on a single surrogate for each helmet configuration. Thus, more studies are needed to corroborate these interesting findings. Also, since the heads were thawed and brains were removed from the PMHS surrogate, the observations should be treated only as a trend. Having listed these limitations, there is

enough in these results to further garner scientific inquiry in this important subject of blast induced brain injury and injury mitigation.

In summary, the response of PMHS surrogate heads under the primary blast loading conditions is studied. Post-mortem human heads were used; brain and meninges were removed from each head and intracranial contents were backfilled with a brain simulant prior to the experiments. The surrogate heads were subjected to varying incident blast intensities. Incident, surface, and intracranial pressures were measured at various locations on each surrogate head. Tests were also conducted with the addition of military helmets (suspension and padded configurations) on the surrogate heads. The analysis presented here is based on a total of 36 tests; which serve as a good dataset to establish the trends. Some of the key findings of this work are:

- The temporal variation of the ICP profiles is drastically different from the temporal variation of the incident and surface pressure profiles. The temporal variation of the ICP profiles is strongly governed by the wave propagation through skin-skull-brain parenchyma and the structural response of the entire head.

- The front ICP gauge, which is in the vicinity of the sinus cavities, records significantly lower pressure as compared to top ICP gauge. This indicates that sinus cavities may attenuate the blast overpressure.

- Analyses of the helmeted experiments on surrogate head show that peak ICP values are reduced with the padded helmet as compared to the no helmet counterparts.

- ICP measurements with the suspension helmet indicate that peak ICP values at the impact site are reduced with the suspension helmet as compared to the no helmet counterparts. Away from the impact site, blast wave focuses beneath the suspension helmet. The focusing of the blast wave under a suspension helmet accompanies a corresponding increase in ICP beneath the focused regions.

- Overall, these results suggest that blast mitigation, including the design of the helmet, involves a complex interplay of the blast wave with the structures of the head and helmet as well as their arrangement. Thus, the topic of protection of the head against the blast should be approached by taking into account all aforementioned effects.

Acknowledgements

This work was carried out when SG was a Ph.D. student and NC was a faculty member at the University of Nebraska-Lincoln. Authors gratefully acknowledge lab technician Aaron Alai and Aaron Holmberg for assistance in data acquisition. The authors acknowledge the financial support provided by the US Army Research Office for the project on Army-UNL Center for Trauma Mechanics, contract no. W911NF-08-1-0483 (project monitor: Larry Russel, PI: Namas Chandra).

References

Akula, P.K., Hua, Y. and Gu, L. (2013) 'Role of frontal sinus on primary blast-induced traumatic brain injury', *Journal of Medical Devices*, Vol. 7, No. 3, p.030925.

Alley, M.D., Schimizze, B.R. and Son, S.F. (2011) 'Experimental modeling of explosive blast-related traumatic brain injuries', *Neuro Image*, Vol. 54, Supplement 1, pp.S45–S54.

Anderson, J. (2001) *Fundamentals of Aerodynamics*, McGraw-Hill, New York.

Baumer, T.G., Rapo, M.A., Wong, J.M., Powell, B.J., Juhas, B.D., Chan, P.C. and Mackiewicz, J.F. (2013) 'Blast overpressure measured on a bare vs. helmeted rigid headform', *ASME 2013 International Mechanical Engineering Congress and Exposition, IMECE 2013*, American Society of Mechanical Engineers (ASME), ASME, San Diego, CA, USA, 15–21 November.

Bhattacharjee, Y. (2008) 'Neuroscience. Shell shock revisited: solving the puzzle of blast trauma', *Science*, Vol. 319, No. 5862, pp.406–408.

Bolander, R., Mathie, B., Bir, C., Ritzel, D. and Vandevord, P. (2011) 'Skull flexure as a contributing factor in the mechanism of injury in the rat when exposed to a shock wave', *Annals of Biomedical Engineering*, Vol. 39, No. 10, pp.1–10.

Cernak, I., Wang, Z., Jiang, J., Bian, X. and Savic, J. (2001) 'Cognitive deficits following blast injury-induced neurotrauma: possible involvement of nitric oxide', *Brain Injury*, Vol. 15, No. 7, pp.593–612.

Chandra, N., Ganpule, S., Kleinschmit, N.N., Feng, R., Holmberg, A.D., Sundaramurthy, A., Selvan, V. and Alai, A. (2012) 'Evolution of blast wave profiles in simulated air blasts: experiment and computational modeling', *Shock Waves*, Vol. 22, No. 5, pp.403–415.

Chavko, M., Koller, W.A., Prusaczyk, W.K. and Mccarron, R.M. (2007) 'Measurement of blast wave by a miniature fiber optic pressure transducer in the rat brain', *Journal of Neuroscience Methods*, Vol. 159, No. 2, pp.277–281.

Cheng, J., Gu, J., Ma, Y., Yang, T., Kuang, Y., Li, B. and Kang, J. (2010) 'Development of a rat model for studying blast-induced traumatic brain injury', *Journal of the Neurological Sciences*, Vol. 294, Nos. 1–2, pp.23–28.

Courtney, M.W. and Courtney, A.C. (2011) 'Working toward exposure thresholds for blast-induced traumatic brain injury: thoracic and acceleration mechanisms', *Neuroimage*, Vol. 54, Supplement 1, pp.S55–61.

Dal Cengio, L.A. (2011) *An Investigation of the Biomechanical Response from Shock Wave Loading to the Head*, PhD dissertation, Wayne State University.

Dal Cengio, L.A., Keane, N.J., Hay, K., Ryan, A.G., Ryan, A.G. Bir, C.A. and Vandevord, P.J. (2013) 'Methodology and evaluation of intracranial pressure response in rats exposed to complex shock waves', *Ann Biomed Eng.*, Vol. 41, No. 12, pp.2488–500.

Desmoulin, G.T. and Dionne, J.P. (2009) 'Blast-induced neurotrauma: surrogate use, loading mechanisms, and cellular responses', *The Journal of Trauma*, Vol. 67, No. 5, pp.1113–1122, 10.1097/TA.0b013e3181bb8e84.

Ganpule, S. (2013) *Mechanics of Blast Loading on Post-Mortem Human and Surrogate Heads in the Study of Traumatic Brain Injury (TBI) Using Experimental and Computational Approaches*, PhD dissertation, University of Nebraska, Lincoln.

Ganpule, S., Alai, A., Plougonven, E. and Chandra, N. (2013) 'Mechanics of blast loading on the head models in the study of traumatic brain injury using experimental and computational approaches', *Biomech Model Mechanobiol*, Vol. 12, No. 3, pp.511–31.

Ganpule, S., Gu, L., Alai, A. and Chandra, N. (2012) 'Role of helmet in the mechanics of shock wave propagation under blast loading conditions', *Computer Methods in Biomechanics and Biomedical Engineering*, Vol. 15, No. 11, pp.1233–1244.

Kambouchev, N., Noels, L. and Radovitzky, R. (2007) 'Numerical simulation of the fluid–structure interaction between air blast waves and free-standing plates', *Computers & Structures*, Vol. 85, Nos. 11–14, pp.923–931.

Kennedy, E.A. (2007) *The Development and Validation of a Biofidelic Synthetic Eye for the Facial and Ocular Countermeasure Safety (FOCUS) headform*, PhD Dissertation, Virginia Polytechnic Institute and State University, Blacksburg, Virginia.

Kinney, G.F. and Graham, K.J. (1985) *Explosive Shocks in Air*, Springer-Verlag, New York.

Lew, H.L., Poole, J.H., Alvarez, S. and Moore, W. (2005) 'Soldiers with occult traumatic brain injury', *American Journal of Physical Medicine & Rehabilitation*, Vol. 84, No. 6, pp.393–398, 10.1097/01.phm.0000163703.91647.a7.

Long, J.B., Bentley, T.L., Wessner, K.A., Cerone, C., Sweeney, S. and Bauman, R.A. (2009) 'Blast overpressure in rats: recreating a battlefield injury in the laboratory', *Journal of Neurotrauma*, Vol. 26, No. 6, pp.827–840.

Meaney, D.F., Morrison, B. and Dale Bass, C. (2014) 'The mechanics of traumatic brain injury: a review of what we know and what we need to know for reducing its societal burden', *Journal of Biomechanical Engineering*, Vol. 136, No. 2, pp.021008–021008.

Moss, W.C., King, M.J. and Blackman, E.G. (2009) 'Skull flexure from blast waves: a mechanism for brain injury with implications for helmet design', *Physical Review Letters*, Vol. 103, No. 10, p.108702.

Mott, D., Schwer, D., Young, T., Levine, J., Dionne, J-P., Makris, A. and Hubler, G. (2008) 'Blast-induced pressure fields beneath a military helmet', *20th International Symposium on Military Aspects of Blast and Shock*, Oslo, Norway, 1–5 September.

Nakagawa, A., Manley, G.T., Gean, A.D., Ohtani, K., Armonda, R., Tsukamoto, A., Yamamoto, H., Takayama, K. and Tominaga, T. (2011) 'Mechanisms of primary blast-induced traumatic brain injury: insights from shock-wave research', *Journal of Neurotrauma*, Vol. 28, No. 6, pp.1101–1119.

Okie, S. (2005) 'Traumatic brain injury in the war zone', *New England Journal of Medicine*, Vol. 352, No. 20, pp.2043–2047.

Pun, P.B., Kan, E.M., Salim, A., Li, Z., Ng, K.C., Moochhala, S.M., Ling, E.A., Tan, M.H. and Lu, J. (2011) 'Low level primary blast injury in rodent brain', *Frontiers in Neurology*, Vol. 2, Article 19.

Rafaels, K., Bass, C.R., Salzar, R.S., Panzer, M.B., Woods, W., Feldman, S., Cummings, T. and Capehart, B. (2011) 'Survival risk assessment for primary blast exposures to the head', *Journal of Neurotrauma*, Vol. 28, No. 11, pp.2319–2328.

Rafaels, K.A. (2010) *Blast Brain Injury Risk*, PhD dissertation, University of Virginia.

Reynosa, M.A. (1999) *The Personnel Armor System Ground Troops (PASGT) Helmet*, Schiffer Military History, Atglen, PA.

Risling, M., Plantman, S., Angeria, M., Rostami, E., Bellander, B.M., Kirkegaard, M., Arborelius, U. and Davidsson, J. (2011) 'Mechanisms of blast induced brain injuries, experimental studies in rats', *Neuroimage*, Vol. 54, Supplement 1, pp.S89–S97.

Salimi Jazi, M., Rezaei, A., Karami, G. and Azarmi, F. (2014) 'Biomechanical parameters of the brain under blast loads with and without helmets', *International Journal of Experimental and Computational Biomechanics*, Vol. 2, No. 3, pp.223–244.

Säljö, A., Arrhen, F., Bolouri, H., Mayorga, M. and Hamberger, A. (2008) 'Neuropathology and pressure in the pig brain resulting from low-impulse noise exposure', *Journal of Neurotrauma*, Vol. 25, No. 12, pp.1397–1406.

Säljö, A., Bolouri, H., Mayorga, M., Svensson, B. and Hamberger, A. (2010) 'Low-level blast raises intracranial pressure and impairs cognitive function in rats: prophylaxis with processed cereal feed', *Journal of Neurotrauma*, Vol. 27, No. 2, pp.383–389.

Säljö, A., Mayorga, M., Bolouri, H., Svensson, B. and Hamberger, A. (2011) 'Mechanisms and pathophysiology of the low-level blast brain injury in animal models', *NeuroImage*, Vol. 54, Supplement 1, pp.S83–S88.

Sarvghad-Moghaddam, H., Jazi, M.S., Rezaei, A., Karami, G. and Ziejewski, M. (2015) 'Examination of the protective roles of helmet/faceshield and directionality for human head under blast waves', *Computer Methods in Biomechanics and Biomedical Engineering*, Vol. 18, No. 16, pp.1846–1855.

Sundaramurthy, A. and Chandra, N. (2014) 'A parametric approach to shape field-relevant blast wave profiles in compressed-gas-driven shock tube', *Frontiers in Neurology*, Vol. 5, Article 253.

Svetlov, S.I., Larner, S.F., Kirk, D.R., Atkinson, J., Hayes, R.L. and Wang, K.K.W. (2009) 'Biomarkers of blast-induced neurotrauma: profiling molecular and cellular mechanisms of blast brain injury', *Journal of Neurotrauma*, Vol. 26, No. 6, pp.913–921.

Svetlov, S.I., Prima, V., Kirk, D.R., Gutierrez, H., Curley, K.C., Hayes, R.L. and Wang, K.K.W. (2010) 'Morphologic and biochemical characterization of brain injury in a model of controlled blast overpressure exposure', *The Journal of Trauma*, Vol. 69, No. 4, pp.795–804, 10.1097/TA.0b013e3181bbd885.

Tanielian, T. and Jaycox, L.H. (2008) *Invisible Wounds of War*, RAND Corp, Santa Monica, CA.

Taylor, P.A., Ludwigsen, J.S. and Ford, C.C. (2014) 'Investigation of blast-induced traumatic brain injury', *Brain Injury*, Vol. 28, No. 7, pp.879–895.

Xydakis, M.S., Bebarta, V.S., Harrison, C.D., Conner, J.C., Grant, G.A. and Robbins, A.S. (2007) 'Tympanic-membrane perforation as a marker of concussive brain injury in Iraq', *New England Journal of Medicine*, Vol. 357, No. 8, pp.830–831.

Zhang, L., Makwana, R. and Sharma, S. (2013a) 'Brain response to primary blast wave using validated finite element models of human head and advanced combat helmet', *Frontiers in Neurology*, Vol. 4, Article 88.

Zhang, T.G., Satapathy, S.S., Dagro, A.M. and Mckee, P.J. (2013b) 'Numerical study of head/helmet interaction due to blast loading', *ASME 2013 International Mechanical Engineering Congress and Exposition, IMECE 2013*, 15–21 November, American Society of Mechanical Engineers (ASME), ASME, San Diego, CA, USA.

Supplementary material: characterisation of the gel simulant

Preparation of the gel simulant

Preparation of the gel simulant was started with degasification by boiling of water (100°C) in a container. The water was cooled to 40°C and the appropriate amount of gelatin powder (195 g/litre in this case) was added to the water and the gel mixture was gently stirred to ensure that the powder was uniformly distributed. The gel simulant was filtered, using gauze, in a beaker. The gel simulant was then siphoned to the experimental apparatus and allowed to set at room temperature (21°C). The experimental apparatus consisted acrylic container of square cross section (cross sectional area 50 mm^2) and length of 50 mm. The pressure sensors were mounted on the front and back face of the acrylic container. The entire container was sealed once the mixture was set. The gel simulant was aged at room temperature for ~24 hours prior to the experiments. Since PMHS testing is desired at room temperature, the gel simulant was also characterised at the room temperature. The gel simulant had a density of ~1.05 g/cm^3.

Shock tube testing of a gelatin phantom

The gel simulant was subjected to shock loading in a manner described earlier. The wave speed was calculated from the wave traversal time between front and back sensors and distance between the sensors. Note that in the gel simulant, the wave propagates at the sound wave speed. The bulk modulus was calculated from the wave speed using a following equation.

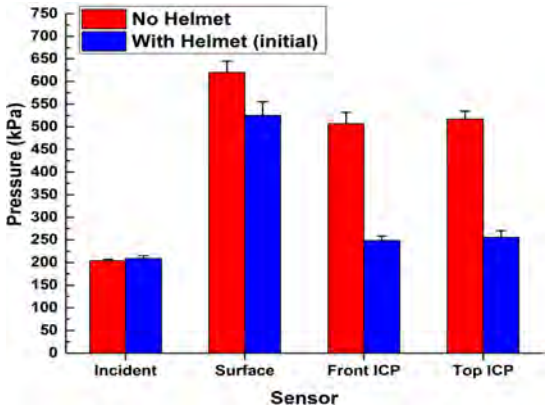
$$K = \rho C_L^2$$

where ρ is a density and C_L is a longitudinal wave speed. Experimental results are tabulated in Table S1.

Table S1 Characterisation of the gel simulant

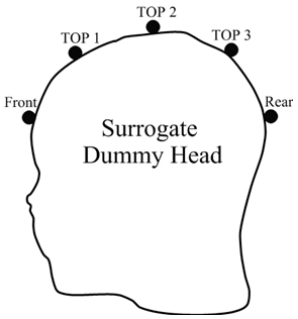
Test no.	*Wave traversal time between front and back sensor, Δt (μsec)*	*Longitudinal wave speed, C_L (m/sec)*	*Bulk modulus, K (GPa)*
1	19.90	1453.80	2.22
2	20.20	1432.21	2.15
3	19.70	1468.56	2.26
4	20.50	1411.25	2.09
5	20.00	1446.53	2.20
6	20.30	1425.15	2.13
			Mean: 2.18
			Standard error of mean: 0.026

Figure S1 Comparison of peak pressures between no helmet and with suspension helmet for a rear blast scenario (see online version for colours)

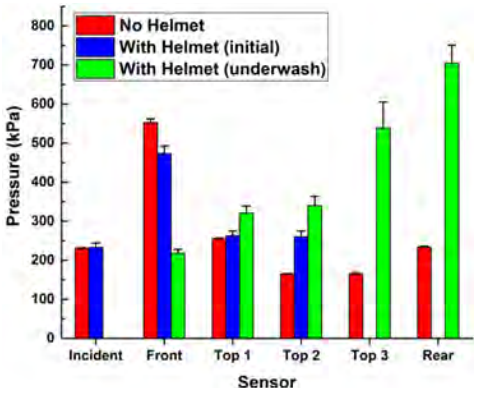


Note: The peak pressures recorded by front and top ICP gauges are equivalent for a rear blast scenario for no helmet and with suspension helmet cases.

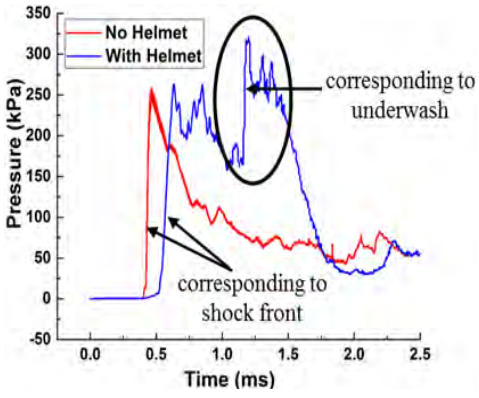
Figure S2 Measurements of surface pressures on a surrogate dummy head, (a) senor locations (b) comparison of peak surface pressures between no helmet and with suspension helmet scenarios (c) comparison of surface *p-t* profile between no helmet and with suspension helmet scenarios for the 'top 1' gauge location (see online version for colours)



(a)

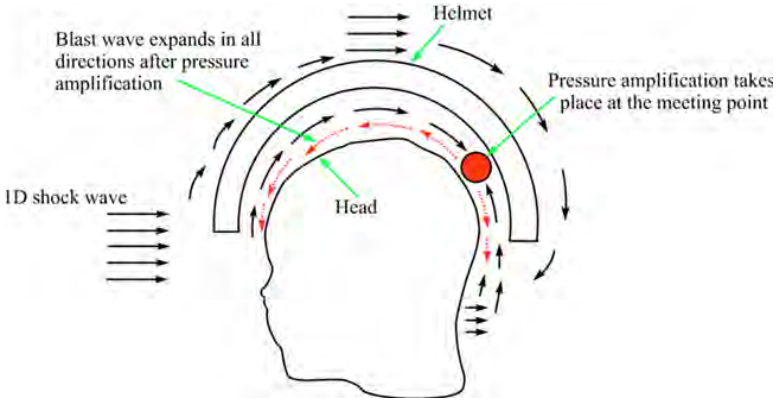


(b)

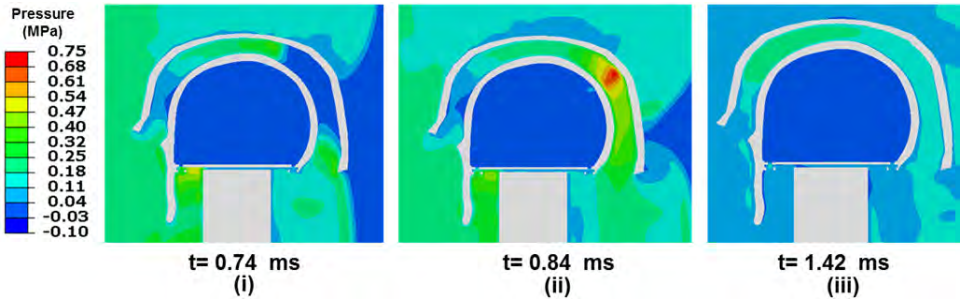


(c)

Figure S3 Underwash effect beneath the suspension helmet, (a) schematic explaining underwash effect of the helmet (b) flow field inside and outside of the head-helmet subspace (see online version for colours)



(a)



(b)

Appendix A –Publication Cover 25
2016

Authors: Y Qiu, Y Wang, Y Xu, N Chandra, J Haorah, B Hubbi, BJ Pfister, X Liu

Title: "*Quantitative optical coherence elastography based on fiber-optic probe for in situ measurement of tissue mechanical properties*"

Journal Publication: Biomedical optics express 7 (2), 688-700, (2016), [16-25]

Biomedical Optics EXPRESS

Quantitative optical coherence elastography based on fiber-optic probe for *in situ* measurement of tissue mechanical properties

Yi Qiu,[1] Yahui Wang,[1] Yiqing Xu,[2] Namas Chandra,[3] James Haorah,[3] Basil Hubbi,[4] Bryan J. Pfister,[3] and Xuan Liu[1,*]

[1]*Department of Electrical and Computer Engineering, New Jersey Institute of Technology, Newark, NJ, 07102, USA*
[2]*Department of Electrical and Electronic Engineering, Hong Kong University, Hong Kong, China*
[3]*Department of Biomedical Engineering, New Jersey Institute of Technology, Newark, NJ, 07102, USA*
[4]*Department of Radiology, New Jersey Medical School, Newark, NJ, 07103, USA*
[*]*xliu@njit.edu*

Abstract: We developed a miniature quantitative optical coherence elastography (qOCE) instrument with an integrated Fabry-Perot force sensor, for *in situ* elasticity measurement of biological tissue. The technique has great potential for biomechanics modeling and clinical diagnosis. We designed the fiber-optic qOCE probe that was used to exert a compressive force to deform tissue at the tip of the probe. Using the space-division multiplexed optical coherence tomography (OCT) signal detected by a spectral domain OCT engine, we were able to quantify the probe deformation that was proportional to the force applied, and to quantify the tissue deformation corresponding to the external stimulus. Simultaneous measurement of force and displacement allowed us to extract Young's modulus of biological tissue. We experimentally calibrated our qOCE instrument, and validated its effectiveness on tissue mimicking phantoms and biological tissues.

©2016 Optical Society of America

OCIS codes: (170.4500) Optical coherence tomography; (280.4788) Optical sensing and sensors; (280.3340) Laser Doppler velocimetry

References and links

1. J. G. Fujimoto, C. Pitris, S. A. Boppart, and M. E. Brezinski, "Optical Coherence Tomography: An Emerging Technology for Biomedical Imaging and Optical Biopsy," Neoplasia **2**(1-2), 9–25 (2000).
2. J. A. Izatt, M. D. Kulkarni, K. Kobayashi, M. V. Sivak, J. K. Barton, and A. J. Welch, "Optical coherence tomography for biodiagnostics," Opt. Photonics News **8**(5), 41 (1997).
3. J. Schmitt, "OCT elastography: imaging microscopic deformation and strain of tissue," Opt. Express **3**(6), 199–211 (1998).
4. R. K. Wang, Z. Ma, and S. J. Kirkpatrick, "Tissue Doppler optical coherence elastography for real time strain rate and strain mapping of soft tissue," Appl. Phys. Lett. **89**(14), 144103 (2006).
5. R. K. Wang, S. Kirkpatrick, and M. Hinds, "Phase-sensitive optical coherence elastography for mapping tissue microstrains in real time," Appl. Phys. Lett. **90**(16), 164105 (2007).
6. X. Liang and S. A. Boppart, "Biomechanical Properties of In Vivo Human Skin From Dynamic Optical Coherence Elastography," IEEE Trans. Biomed. Eng. **57**(4), 953–959 (2010).
7. C. Sun, B. Standish, and V. X. D. Yang, "Optical coherence elastography: current status and future applications," J. Biomed. Opt. **16**, 043001 (2011).
8. B. F. Kennedy, X. Liang, S. G. Adie, D. K. Gerstmann, B. C. Quirk, S. A. Boppart, and D. D. Sampson, "In vivo three-dimensional optical coherence elastography," Opt. Express **19**(7), 6623–6634 (2011).
9. T. M. Nguyen, S. Song, B. Arnal, Z. Huang, M. O'Donnell, and R. K. Wang, "Visualizing ultrasonically induced shear wave propagation using phase-sensitive optical coherence tomography for dynamic elastography," Opt. Lett. **39**(4), 838–841 (2014).
10. K. M. Kennedy, B. F. Kennedy, R. A. McLaughlin, and D. D. Sampson, "Needle optical coherence elastography for tissue boundary detection," Opt. Lett. **37**(12), 2310–2312 (2012).
11. A. L. McKnight, J. L. Kugel, P. J. Rossman, A. Manduca, L. C. Hartmann, and R. L. Ehman, "MR elastography of breast cancer: preliminary results," AJR Am. J. Roentgenol. **178**(6), 1411–1417 (2002).

#254870 Received 30 Nov 2015; revised 12 Jan 2016; accepted 16 Jan 2016; published 26 Jan 2016

12. A. Samani, J. Zubovits, and D. Plewes, “Elastic moduli of normal and pathological human breast tissues: an inversion-technique-based investigation of 169 samples,” Phys. Med. Biol. **52**(6), 1565–1576 (2007).
13. B. F. Kennedy, K. M. Kennedy, and D. D. Sampson, “A review of optical coherence elastography: fundamentals, techniques and prospects,” IEEE J. Sel. Top. Quantum Electron. **20**(2), 272–288 (2014).
14. B. F. Kennedy, T. R. Hillman, R. A. McLaughlin, B. C. Quirk, and D. D. Sampson, “In vivo dynamic optical coherence elastography using a ring actuator,” Opt. Express **17**(24), 21762–21772 (2009).
15. B. F. Kennedy, S. H. Koh, R. A. McLaughlin, K. M. Kennedy, P. R. T. Munro, and D. D. Sampson, “Strain estimation in phase-sensitive optical coherence elastography,” Biomed. Opt. Express **3**(8), 1865–1879 (2012).
16. K. M. Kennedy, C. Ford, B. F. Kennedy, M. B. Bush, and D. D. Sampson, “Analysis of mechanical contrast in optical coherence elastography,” J. Biomed. Opt. **18**(12), 121508 (2013).
17. C. Li, G. Guan, X. Cheng, Z. Huang, and R. K. Wang, “Quantitative elastography provided by surface acoustic waves measured by phase-sensitive optical coherence tomography,” Opt. Lett. **37**(4), 722–724 (2012).
18. K. D. Mohan and A. L. Oldenburg, “Elastography of soft materials and tissues by holographic imaging of surface acoustic waves,” Opt. Express **20**(17), 18887–18897 (2012).
19. V. Crecea, A. L. Oldenburg, X. Liang, T. S. Ralston, and S. A. Boppart, “Magnetomotive nanoparticle transducers for optical rheology of viscoelastic materials,” Opt. Express **17**(25), 23114–23122 (2009).
20. Y. Mao, S. Chang, S. Sherif, and C. Flueraru, “Graded-index fiber lens proposed for ultrasmall probes used in biomedical imaging,” Appl. Opt. **46**(23), 5887–5894 (2007).
21. R. A. McLaughlin, B. C. Quirk, A. Curatolo, R. W. Kirk, L. Scolaro, D. Lorenser, P. D. Robbins, B. A. Wood, C. M. Saunders, and D. D. Sampson, “Imaging of Breast Cancer With Optical Coherence Tomography Needle Probes: Feasibility and Initial Results,” IEEE J. Sel. Top. Quantum Electron. **18**(3), 1184–1191 (2012).
22. M. Zhao, Y. Huang, and J. U. Kang, “Sapphire ball lens-based fiber probe for common-path optical coherence tomography and its applications in corneal and retinal imaging,” Opt. Lett. **37**(23), 4835–4837 (2012).
23. D. Lorenser, X. Yang, and D. D. Sampson, “Ultrathin fiber probes with extended depth of focus for optical coherence tomography,” Opt. Lett. **37**(10), 1616–1618 (2012).
24. Y. Zhang, H. Shibru, K. L. Cooper, and A. Wang, “Miniature fiber-optic multicavity Fabry-Perot interferometric biosensor,” Opt. Lett. **30**(9), 1021–1023 (2005).
25. Z. Sun, M. Balicki, J. Kang, J. Handa, R. Taylor, and I. Iordachita, “Development and preliminary data of novel integrated optical microforce sensing tools for retinal microsurgery,” in IEEE International Conference on Robotics and Automation, 2009. ICRA '09 (IEEE, 2009), pp. 1897–1902.
26. X. Liu, I. I. Iordachita, X. He, R. H. Taylor, and J. U. Kang, “Miniature fiber-optic force sensor based on low-coherence Fabry-Pérot interferometry for vitreoretinal microsurgery,” Biomed. Opt. Express **3**(5), 1062–1076 (2012).
27. Y. Huang, X. Liu, and J. U. Kang, “Real-time 3D and 4D Fourier domain Doppler optical coherence tomography based on dual graphics processing units,” Biomed. Opt. Express **3**(9), 2162–2174 (2012).
28. Y. Wang, Y. Wang, A. Akansu, K. D. Belfield, B. Hubbi, and X. Liu, “Robust motion tracking based on adaptive speckle decorrelation analysis of OCT signal,” Biomed. Opt. Express **6**(11), 4302–4316 (2015).
29. G. Lamouche, B. F. Kennedy, K. M. Kennedy, C. E. Bisaillon, A. Curatolo, G. Campbell, V. Pazos, and D. D. Sampson, “Review of tissue simulating phantoms with controllable optical, mechanical and structural properties for use in optical coherence tomography,” Biomed. Opt. Express **3**(6), 1381–1398 (2012).
30. C. T. McKee, J. A. Last, P. Russell, and C. J. Murphy, “Indentation versus tensile measurements of Young’s modulus for soft biological tissues,” Tissue Eng. Part B Rev. **17**(3), 155–164 (2011).
31. D. D. Kalanovic, M. P. Ottensmeyer, J. Gross, G. Buess, and S. L. Dawson, “Independent testing of soft tissue viscoelasticity using indentation and rotary shear deformations,” Stud. Health Technol. Inform. **94**, 137–143 (2003).
32. K. M. Kennedy, L. Chin, R. A. McLaughlin, B. Latham, C. M. Saunders, D. D. Sampson, and B. F. Kennedy, “Quantitative micro-elastography: imaging of tissue elasticity using compression optical coherence elastography,” Sci. Rep. **5**, 15538 (2015).

1. Introduction

Optical coherence tomography (OCT) is a versatile, high-resolution imaging technique, with great potential in tissue characterization for various biomedical applications such as cancer diagnosis or surgical guidance [1, 2]. In addition to structural imaging, OCT can also be used to perform mechanical characterization of biological tissue with one of its functional extensions referred as optical coherence elastography (OCE) [3–10]. OCE can quantify mechanical response (deformation, resonant frequency, elastic wave propagation) of biological tissues under external or internal mechanical stimulation, and extract tissue properties related to its pathological and physiological status. For example, pathological tissue such as cancerous tissue is usually stiffer compared to normal tissue, in addition to structural abnormity [11, 12]. This tissue stiffening is exactly a clinician looks for when he/she manually palpitates the tissue for changes in mechanical properties. Compared to

#254870 Received 30 Nov 2015; revised 12 Jan 2016; accepted 16 Jan 2016; published 26 Jan 2016
(C) 2016 OSA

elastography techniques based on ultrasound or MRI, OCE has advantages in spatial resolution, mechanical sensitivity, and imaging speed.

Various OCE techniques have been developed to date including compression OCE, surface acoustic wave OCE (SAW OCE), and magnetomotive OCE (MM OCE) [13]. Compared to SAW OCE that has a spatial resolution in the order of millimeter and MM OCE that requires external contrast agent, compression OCE provides the highest spatial resolution for elastography and is based on intrinsic mechanical changes during compression [14–19]. On the other hand, recently developed fiber optic probes allowed endoscopic OCT imaging/sensing despite small penetration depth of OCT signal [20–23]. Needle OCE has been used to measure mechanical response from deep tissue [10]. Therefore, compression OCE based on a miniature fiber optic probe has a great potential for *in situ* characterization of mechanical properties of biological tissue. However, conventional compression OCE measures tissue displacement under quasi-static compression and does not quantify mechanical loading, unless the state of stress is established through an inverse elastic or viscoelastic solution to the boundary value problem. For quantitative characterization of tissue stiffness, current compressive OCE technique has limited significance because results obtained from different compression OCE measurement sessions are qualitative and cannot be correlated in longitudinal or comparison studies.

To obtain quantitative measurements of tissue elasticity, we proposed a novel quantitative optical coherence elastography (qOCE) technology that measures tissue elasticity using a miniature probe with integrated force sensing functionality [24–26]. The qOCE system developed in this study is significantly different from its predecessors, because it simultaneously measures the force/stress exerted on the tissue and the resultant tissue deformation/strain. In addition, the miniature probe can access deep tissues of interest at multiple locations required for clinical applications, for such variations lead to different biochemical pathways and hence different medical outcomes. In a word, qOCE has great potential in interstitial imaging/sensing for *in situ* tissue mechanical characterization.

In this study, we designed and fabricated the qOCE probe with an integrated Fabry-Perot (FP) cavity to quantify the force exerted at the probe tip. A spectral domain OCT engine at 1.3 μm was used to detect space-division multiplexed signal for simultaneous force and displacement (stress and strain) measurement. Signal processing was implemented in real-time using graphic processing units (GPU). We characterized the performance of our qOCE instrument, and validated its effectiveness on tissue mimicking phantoms as well as biological tissues.

The manuscript is organized as follows. We first illustrated the principle of qOCE technology and the system configuration. Then we showed the experiment results obtained with our qOCE setup, including calibration for deformation and force tracking, stress-strain curve acquisition, and measurements on three phantoms with different values of stiffness. Finally we presented qOCE measurement results obtained from biological tissue.

2. Principle of qOCE technology

2. 1 System configuration

The system schematic is shown in Fig. 1. Broadband output from a super luminescent diode (SLD) is routed by a fiber optic coupler (FC) to the qOCE probe and the reference arm. A miniature probe (qOCE probe) is used to induce compression in the sample. If the sample is mechanically homogeneous, the loading produces uniaxial compression. Otherwise, the state of stress is determined by the heterogeneity that can also be measured. To track probe deformation in response to the applied force, a common path OCT signal is detected. The common path OCT signal is derived from the interference from optical fields reflected from the tip of single mode fiber (E_{fp1}) and from the first surface of the GRIN (gradient index) lens (E_{fp2}). Another OCT signal derived from the interference between sample light (E_s) and

#254870 Received 30 Nov 2015; revised 12 Jan 2016; accepted 16 Jan 2016; published 26 Jan 2016
(C) 2016 OSA

reference light (E_r) through Michelson interferometry is used to track sample deformation in front of the probe tip.

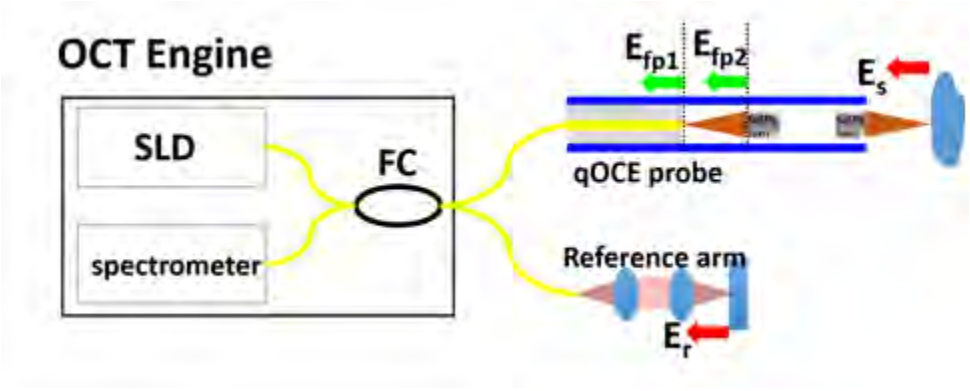


Fig. 1. Illustration of qOCE system (FC: fiber optic coupler; SLD: superluminescent diode; E_{fp1}, optical reflection from the tip of single mode fiber; E_{fp2}, optical reflection from the proximal end of the first GRIN lens; E_s, sample light; E_r, reference light.

As shown in Fig. 1, a lead-in single mode fiber (SMF) is attached to the proximal end of the qOCE probe shaft and a pair of GRIN lenses is attached to the distal end of the probe shaft. The cleaved SMF tip and the proximal surface of the first GRIN lens serve as two end surfaces of a low fineness Fabry Perot (FP) cavity. Incident light from the SLD is reflected by two end surfaces (E_{fp1} and E_{fp2}) of the FP cavity due to a discontinuity in refractive index (from glass to air and from air to glass). The common path interference between E_{fp1} and E_{fp2} generates an OCT signal (Ascan, $\boldsymbol{I}_p$) with a peak located at the depth L_{fp} that equals the FP cavity length. The phase of complex valued OCT signal at L_{fp} changes in proportion to the change in FP cavity length and thus the force exerted at the probe tip. Therefore, tracking Doppler phase shift of the common path OCT signal allows the quantification of probe deformation and force/stress exerted through the probe. On the other hand, the GRIN lens pair also functions as an objective lens to focus the light output from SMF for sample illumination. The backscattered light from the sample (E_s) is collected by the fiber optic probe and detected by the spectrometer for OCT imaging. E_s interferes with reference light (E_r) provided by the reference arm and generates depth profile of the sample. It is worth mentioning that we adjust the optical path length of reference arm, so that OCT signal from the sample ($\boldsymbol{I}_s$) starts beyond L_{fp}. Optical path length is matched by a single model fiber patch cord in reference arm and through coarse and fine adjustment of the position of the collimator in reference arm. This configuration allows spatial division multiplexing of the OCT signal for simultaneous probe deformation (ΔL_{probe}) tracking and tissue deformation (ΔL_{sample}) tracking. Notably, the compound lens (a pair of GRIN lenses) allows light beam to be tightly focused into sample and L_{fp} to be small. A shorter FP cavity length allows $\boldsymbol{I}_s$ to be located closer to the equal optical path plane with insignificant signal roll-off. Denote the optical path length (OPL) of light reflected by the distal surface of the second GRIN lens as L_{GRIN}. By choosing the OPL of the reference arm (L_{ref}) to be smaller than $L_{GRIN} + L_{fp}$, sample can be located beyond L_{fp} to eliminate overlap with signal from the FP cavity. If the material of the specimen (phantom or tissue) is linearly elastic, a static force yields a uniform displacement. If the material is viscoelastic, a dynamic sinusoidal force can be applied and the response measured. Since the mechanical property of the specimen is unknown, a simplified linear elastic model with a Young's modulus E is assumed in this study.

Using OCT signals obtained, we can quantify probe deformation ΔL_{probe} and derive the force exerted: $F = \alpha \Delta L_{probe}$ where α is a constant determined by the mechanical property of the probe and will be characterized through calibration experiments. We then quantify the

#254870 Received 30 Nov 2015; revised 12 Jan 2016; accepted 16 Jan 2016; published 26 Jan 2016
(C) 2016 OSA

stress applied to sample: $\sigma = F/A$ where A is the area of the GRIN lens. In addition, we can calculate tissue strain $\varepsilon = \Delta L_{sample}/L_0$. Here, L_0 is the initial specimen thickness before compression. Finally, the sample's Young's modulus (E) that is the linear slope of strain-stress curve can be obtained using Eq. (1) where tissue elasticity can be quantified by comparing the deformation of probe and sample.

$$E = \frac{\sigma}{\varepsilon} = \frac{\alpha L_0}{A}\left(\frac{\Delta L_{probe}}{\Delta L_{sample}}\right) \quad (1)$$

Notably, Eq. (1) is valid based on the following assumptions. First, the load is applied slowly. Therefore, force applied to tissue is equivalent to force measured by the integrated Fabry Perot force sensor. Second, the tissue specimen is elastic and viscoelasticity is not considered. Third, the materials are not compressible and therefore have a Poisson's ratio of 0.5.

In this study the elastic tissue specimen is sandwiched by two rigid compressors one of which is the qOCE probe tip. This configuration can provide the most simplified boundary condition and is equivalent to indentation measurement frequently used to characterize biomechanical properties of soft tissue. For example, indentation measurement on Young's moduli of breast tissues was performed through simultaneous quantification of mechanical loading and tissue deformation [12, 31]. Quantification of elasticity was also performed using OCT in a similar compression OCE setting [32].

2.2 Signal processing

For quantitative mechanical property measurement, we first perform DC subtraction and interpolation on spectral domain OCT data acquired by the CMOS camera to obtain *k* (wavenumber) space interferogram. Afterwards, Doppler analysis is performed to track probe and sample deformation. As shown in Fig. 2, slight different processing is applied to track probe deformation and sample deformation.

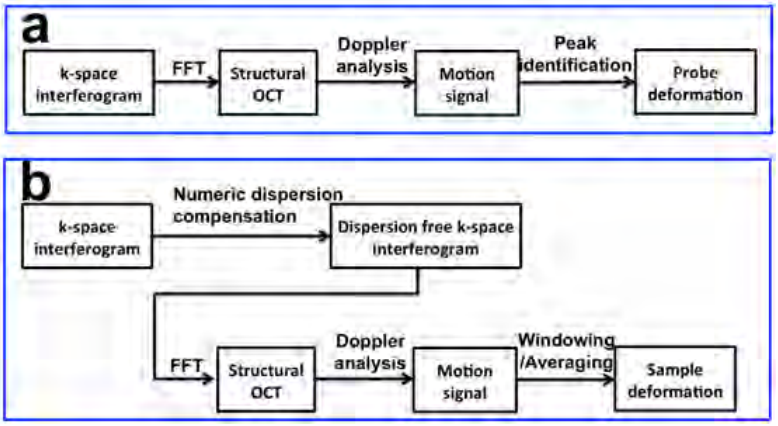


Fig. 2. (a) Signal processing for probe deformation tracking for the quantification of force/stress; (b) signal processing for tissue deformation tracking for the quantification of deformation/strain.

To track probe deformation (Fig. 2(a)), we simply apply fast Fourier transform (FFT) on k space interferogram to obtain a complex valued 1D OCT signal $I_p(z,t)$. Here *z* indicates axial coordinate and *t* indicates measurement time. We then identify the signal peak generated by the interference between optical waves from two end surfaces of the FP cavity: $I_p(L_{probe}, t)$. Doppler phase shift ($(\delta\phi_{probe}(t))$) between Ascans acquired at different time with interval δt_p

#254870 Received 30 Nov 2015; revised 12 Jan 2016; accepted 16 Jan 2016; published 26 Jan 2016
(C) 2016 OSA

(δt_p = 5 ms) is calculated according to Eq. (2) [27]. $\delta\phi_{\text{probe}}(t)$ is proportional to probe deformation and thus the force applied.

$$\delta\phi_{probe}(t) = \text{a tan}\left[I_p\left(L_{probe}, t+\delta t_p\right) I_p^*\left(L_{probe}, t\right)\right] \quad (2)$$

Sample deformation tracking is extracted from OCT signal from the sample ($I_s(z,t)$), also through Doppler analysis (Fig. 2(b)). Notably, signal processing to track sample deformation is slightly different from probe deformation tracking. First, as shown in Fig. 1, OCT signal from the sample derives from light interference between probe arm and reference arm; therefore suffers from signal degradation due to considerable amount of chromatic dispersion. To obtain high resolution, high signal to noise ratio OCT signal $I_s(z,t)$ from the sample, we measure the amount of dispersion mismatch in prior. The non-linear phase of the interferometric spectrum is extracted through Hilbert transformation on interferometric spectrum. Third order polynomial fitting is applied to approximate the non-linear phase: $\Phi(k) = p_3k^3 + p_2k^2 + p_1k + p_0$. The non-linear phase is then subtracted in the GPU based software before FFT for real-time dispersion compensation. Second, biological tissue is less rigid compared to the plastic probe shaft and deforms more. Therefore, we will use two Ascans acquired with smaller time interval (δt_s = 0.2 ms) for Doppler phase calculation (Eq. (3)). Otherwise, deformation obtained through Doppler analysis may suffer from phase wrapping artifact. Third, structural OCT signal from highly scattering sample is inevitably contaminated by speckle noise and so is Doppler OCT signal. To track sample deformation with higher accuracy, we will perform spatial average to obtain filtered phase shift ($\delta\phi_{sample,filtered}(t)$) for better accuracy (Eq. (4)). $\delta\phi_{sample,filtered}(t)$ is proportional to spatially resolved displacement of the sample that can be converted to local deformation and strain.

$$\delta\phi_{sample}(z,t) = \text{a tan}\left[I_s\left(z, t+\delta t_s\right) I_s^*\left(z,t\right)\right] \quad (3)$$

$$\delta\phi_{sample,\,filtered}(t) = \int_{L_0-\frac{\delta L}{2}}^{L_0+\frac{\delta L}{2}} \delta\phi_{sample}(z,t)\,dz \quad (4)$$

with $\delta\phi_{probe}(t)$ or $\delta\phi_{sample,filtered}(t)$ obtained, probe deformation (δL_{probe}) and sample deformation (δL_{sample}) can be calculated according to Eq. (5). For probe deformation tracking, the central wavelength of SLD output in air (λ_0 = 1.3μm) is used in Eq. (5). For sample deformation tracking, the wavelength is corrected by the refractive index ($\lambda = \lambda_0/n$).

$$\delta L_{probe,sample}(t) = \frac{\delta\phi_{probe,sample}(t)}{4\pi}\lambda \quad (5)$$

Notably, in compression OCE, mechanical loading is applied to tissue in a quasi-static process and it is essential to quantify deformation over the entire course of compression. Therefor, deformation of probe and sample are both integrated over the same time interval, as shown in Eq. (6). The time integration also improves signal to noise ration for elasticity measurement.

$$\Delta L_{probe,sample}(t) = \int_{t_{start}}^{t} \delta L_{probe,sample}(\tau)\,d\tau \quad (6)$$

with probe and sample deformation acquired using Eq. (5) and (6), we are able to quantify tissue elasticity using Eq. (1). In the real-time software, a variable is constantly updated to calculate the accumulated displacement: $\Delta L_{\text{probe,sample}} = \Delta L_{\text{probe,sample}} + dL_{\text{probe,sample}}$, where $dL_{\text{probe,sample}}$ is the incremental displacement. Signal processing for deformation tracking and elasticity sensing is implemented in real-time using graphic processing unit (GPU).

#254870 Received 30 Nov 2015; revised 12 Jan 2016; accepted 16 Jan 2016; published 26 Jan 2016
(C) 2016 OSA

3. Results

3.1 qOCE system and signal characteristics

The qOCE system is based on a 1.3 μm spectral domain OCT engine that tracks both probe and sample deformation. The SD OCT engine was described in detail in our previous publications [28]. Briefly, a superluminescent diode (SLD1325 Thorlabs, 100nm bandwidth, corresponding to a 7.4 μm axial resolution) is used as light source and interference signal is detected by a CMOS InGaAs camera (SUI1024LDH2, Goodrich).

According to the design described in **2.1**, we developed a qOCE probe as shown in comparison with a US quarter in Fig. 3. To fabricate the probe, we first inserted a single mode fiber into a 25-gauge stainless steel tube. The fiber and the tube were glued together with optical epoxy to achieve desired rigidity for elasticity measurement. With additional cascaded tubing, the fiber was integrated with a polyimide tube (Microlumen) with 1.8mm inner diameter. Optical epoxy was applied to the proximal end of the polyimide tube for fixation. A pair of GRIN lenses (Newport, LGI1300-1A, 0.23 pitch, 0.26 mm working distance) was attached to the distal end of the polyimide tube. The distance between the first GRIN lens and fiber tip was adjusted to collimate the light beam. The second GRIN lens was used to focus the light beam so that the waist of the output beam was located at a depth 0.26 mm away from the GRIN lens surface. Notably, the mechanically active segment for OCT sensing in this probe is the segment between the fixation points of the SMF and the first GRIN lens.

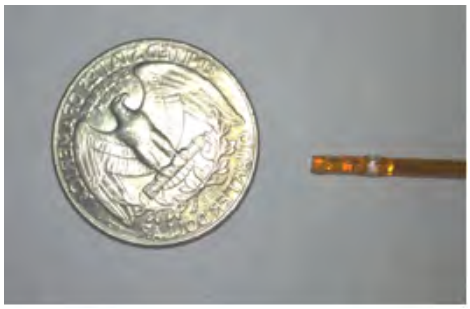


Fig. 3. Photo of qOCE probe in comparison with a US quarter.

Typical Ascan signals obtained from the qOCE probe are shown in Fig. 4. Figure 4(a) shows OCT signals obtained from the probe without (black) and with (blue) numeric dispersion compensation. The sample was a silicone phantom that used Titanium dioxide to provide light scattering. Both Ascans multiplex signals from the common path interferometer and the Michelson interferometer. For the Ascan obtained without dispersion compensation (black), a sharp signal peak (red arrow) is observed. This peak corresponds to common path OCT signal derived from the FP cavity (interference between optical fields E_{fp1} and E_{fp2} in Fig. 1). As E_{fp1} and E_{fp2} share the same optical path, the interferometric signal is free of dispersion mismatch and a sharp peak is obtained without dispersion compensation. On the other hand, this Ascan shows broadened signal at a larger imaging depth, as indicated by the dashed rectangle. Signal enclosed by the rectangle derives from the interference between the reference mirror (E_r) and the distal surfaces of the second GRIN lens (E_{GRIN}), as well as specimen (E_s) under imaging. Reference light and sample light in the Michelson interferometer travels in different medium (fiber and air). Therefore, considerable signal degradation is observed because of dispersion mismatch. In comparison, the blue curve in Fig. 4(a) obtained after dispersion compensation shows a sharp peak corresponding to the distal surface of the GRIN lens (indicated by the green arrow), a sharp peak corresponding to the sample surface (indicated by the orange arrow) and depth resolved sample profile. However, OCT signal due to interference between E_{fp1} and E_{fp2} diminishes in the blue curve because of additional non-linear phase induced to dispersion-free signal in the process of

#254870 Received 30 Nov 2015; revised 12 Jan 2016; accepted 16 Jan 2016; published 26 Jan 2016
(C) 2016 OSA

numerical dispersion compensation. Figure 4(a) clearly shows that OCT signal from the Fabry-Perot cavity for force/stress measurement is spatially demultiplexed with OCT signal from tissue for displacement/strain measurement. We multiplexed CP OCT signal obtained from the FP cavity without dispersion compensation, and Michelson OCT signal obtained from tissue with dispersion compensation and show the result in Fig. 4(b). By tracking phase shift between complex valued, spatial division multiplexed OCT signal as shown in Fig. 4(b), we were able to quantify probe and tissue deformation. Figure 4(c) shows segments of OCT signal obtained from the Michelson interferometer after dispersion compensation, with weakly scattering phantom as sample. Curves with different color were obtained when the sample was located at different depths. Signal peak derived from the GRIN lens surface (indicated by the green arrow) remains identical for different signals. Notably, focusing effect can be observed in Fig. 4(c) with focal plane approximately 0.26mm away from the GRIN lens surface.

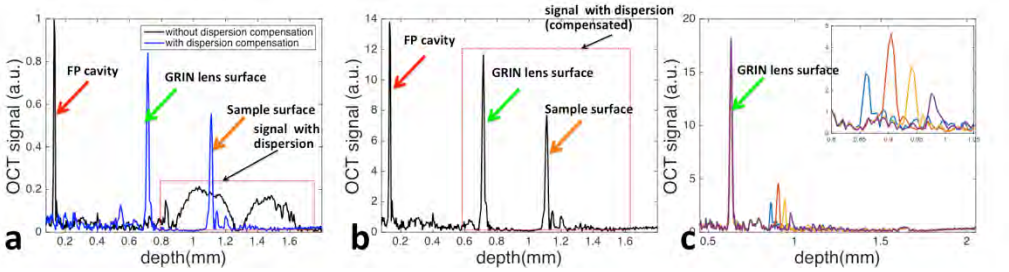


Fig. 4. (a) Typical Ascan obtained from the probe without (black) and with (blue) dispersion compensation; (b) multiplexed signal for simultaneous probe and tissue deformation tracking; (c) segments of OCT signal obtained from Michelson interferometry after dispersion compensation, with weakly scattered sample located at different depth.

To track probe and tissue deformation, we quantified temporal variation of Ascan in Doppler phase shift as shown in Fig. 5. Figure 5(a) (Visualization 1) shows a frame of sequentially acquired spectral interferograms. In Fig. 5(a), different coordinate in horizontal direction corresponds to different wavelength/wavenumber and different coordinate in vertical corresponds to different time. Fringes due to the interference between optical fields from the two end surfaces of the FP cavity are visible in Fig. 5(a). As the probe was used to compress tissue during the acquisition of Fig. 5(a), slight fringe shift over time can be observed due to probe shaft deformation. Fringe shift can be seen more clearly in Visualization 1. Using our real-time GPU software, we quantified the phase shift shown in Fig. 5(a) and Visualization 1 using Eq. (2) and converted the phase shift to probe deformation using Eq. (4) and (5). Figure 5(b) (Visualization 2) shows signal from tissue (screen capture of real-time display) when the qOCE probe was used to compress the phantom. Our software showed structural OCT signal (uppper), as well as Doppler OCT signal (ODT, lower) obtained by calculating inter Ascan signal phase shift. Sequentially acquired signals are displayed in Fig. 5(b) where different coordinate in horizontal direction corresponds to different time and different coordinate in vertical direction corresponds to different depth. Similarly, Fig. 5(c) (Visualization 3) is the screen capture of real-time display when releasing the compression exerted to the same phantom through the probe. Notably, in our software, the color of Doppler signal was used to identify the direction of the motion or phase shift. The negative phase shift was coded to be red and the positive phase shift was coded to be blue. Due to small time window (0.1s) for the acquisition of Ascans during quasi-static compression shown in Fig. 5(b) and 5(c), phantom deformation was small and could not be observed in structural OCT images (upper insets of Fig. 5(a) and 5(b)). However, the phase of OCT signal provides much higher sensitivity in deformation tracking. Deformation of

#254870 Received 30 Nov 2015; revised 12 Jan 2016; accepted 16 Jan 2016; published 26 Jan 2016
(C) 2016 OSA

phantom in different direction due to compression and removal of compression could be clearly observed in the lower panels of Fig. 5(b) and 5(c).

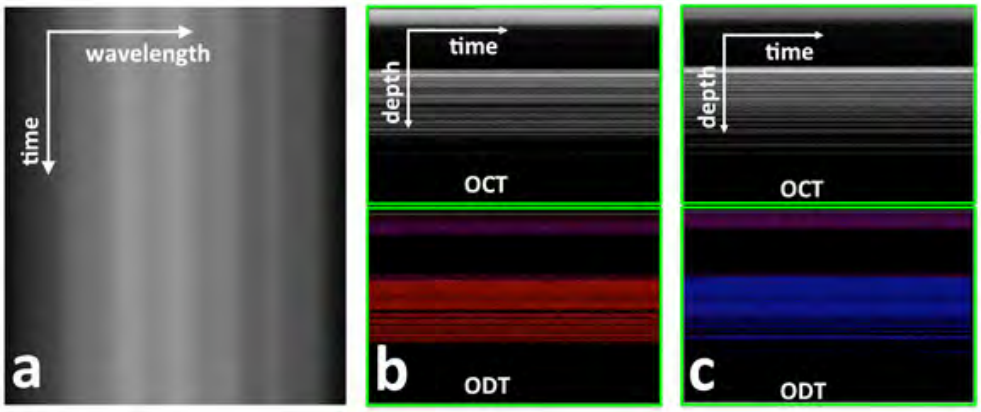


Fig. 5. (a) A frame of interferometric spectrum obtained when the probe was used to exert force (Visualization 1); (b) structural OCT image (upper) and Doppler OCT image (lower) obtained when the phantom was compressed by the qOCE probe (Visualization 2); (b) structural OCT image (upper) and Doppler OCT image (lower) obtained when the compression was released (Visualization 3).

3.2. qOCE probe calibration

Accurate characterization of elastic property of tissue depends on accurate measurement of externally applied force/stress and the tissue's response in the form of deformation/strain.

First, we calibrated the accuracy of deformation/displacement tracking experimentally. We attached the qOCE probe to a precise linear motor (Newport, ILS100CC DC). The probe was translated by the motor in axial direction and did not touch the rigid scattering sample. Therefore, the displacement between the probe and the sample was equivalent to the distance translated by the motor. Using OCT signal, we calculated displacement between qOCE probe and sample according to Eqs. (3)–(6), in our real-time GPU software. Displacement extracted through Doppler analysis of OCT signal was compared with the known motor displacement, as shown in Fig. 6. Clearly, displacement calculated using Doppler analysis has a linear dependency on actual displacement. We validated the following model $\boldsymbol{D}_{\text{physical}} = a\boldsymbol{D}_{\text{Doppler}} + b$ using linear regression, and our results indicated $a = 1.2$ and $b = 0.004$mm. R^2 statistic of the fitting is 0.9977, indicating a highly linear relationship between the calculated displacement and the actual displacement. The coefficient a accounts for the direction of light propagation traveling and the refractive index of the phantom.

#254870 Received 30 Nov 2015; revised 12 Jan 2016; accepted 16 Jan 2016; published 26 Jan 2016
(C) 2016 OSA

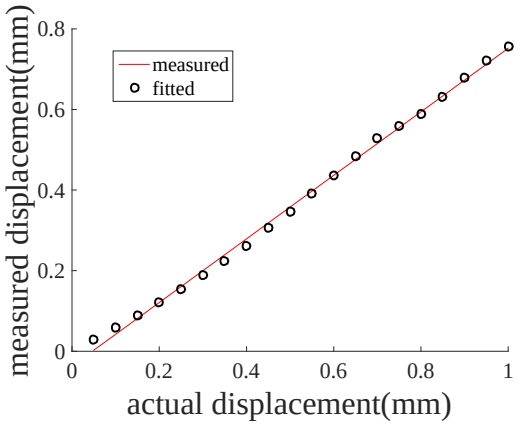


Fig. 6. Calibration results show displacement obtained from Doppler OCT signal is linearly related to actual displacement.

In addition, we calibrated the force/stress sensing capability of our qOCE system. We mounted the qOCE probe on a linear stage and translated the stage to exert force to the sensing tip of a digital force gauge (Shimpo, FG-3005) that provided high precision force measurement with 0.005 N resolution. We tracked the probe deformation using Doppler OCT signal obtained from the integrated FP cavity and compared the probe deformation with force exerted, as shown in Fig. 7. Clearly, the length of FP cavity varied linearly as the force. We validated the following model $\boldsymbol{D}_{\mathrm{FPC}} = \alpha \boldsymbol{F} + \beta$ using linear regression, and our results indicated α = 0.1795N/μm. R^2 statistic of the fitting is 0.9971, indicating a highly linear relationship between the force and the probe deformation.

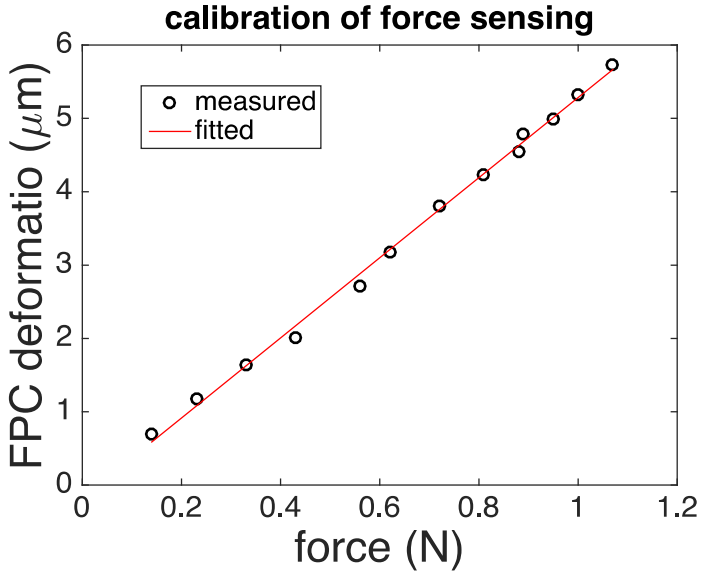


Fig. 7. Results of force calibration show FP cavity deforms proportionally to force exerted.

Figure 6 and Fig. 7 illustrate that the force and displacement can be quantified using OCT signal. Based on results obtained from the calibration experiments, we were able to convert phase shift extracted from OCT signal to tissue deformation and force. Stress was then calculated using the area of the GRIN lens (~2.54 mm^2) in contact with sample for compression.

#254870 Received 30 Nov 2015; revised 12 Jan 2016; accepted 16 Jan 2016; published 26 Jan 2016
(C) 2016 OSA

3.3. Elasticity measurement using qOCE

We developed phantoms to evaluate the qOCE technique. We choose silicone based phantom because the elastic modulus of silicone phantom can be varied in a range that well overlaps the elastic modulus of biological tissues and the optical property of silicone phantom in terms of refractive index is close to that of biological tissues. To obtain phantom with different stiffness, we combine polydimethylsiloxane (PDMS) fluid with curing agent at different volumetric ratios. In addition, we add titanium dioxide into silicone to provide light scattering [29].

To validate that our qOCE can simultaneously quantify stress and strain for elasticity measurement, we used the qOCE probe to compress an elastic phantom. Stress was obtained in real-time, using FP cavity deformation extracted from Doppler phase shift between OCT Ascans, calibrated force-deformation relationship, and known GRIN lens dimension. On the other hand, phantom strain was obtained in real-time, using OCT signal within a window (approximately 280 μm width) located in the vicinity of beam waist (approximately 260 μm from the surface of the second GRIN lens). Tissue deformation was obtained by averaging displacement signal obtained through Doppler analysis within the window and corrected by the refractive index of silicone phantom (n = 1.4). Strain was then calculated by dividing the deformation at each depth position and then averaged. We recorded stress and strain values during the compression of the probe, shown as the black curve in Fig. 8. In addition, we repeated the strain stress measurement, quantifying the force/stress with the commercial force gauge and quantifying the deformation/strain with the accurate linear translation stage. The results obtained are shown in Fig. 8 as the red curve that is highly consistent with qOCE measurement. Phantom elasticity was then obtained according to stress-strain curves shown in Fig. 8. The red curve results in an elasticity modulus that is 2.09 MPa and the black curve results in an elasticity modulus that is 2.02 MPa, indicating high accuracy qOCE measurement of tissue elasticity.

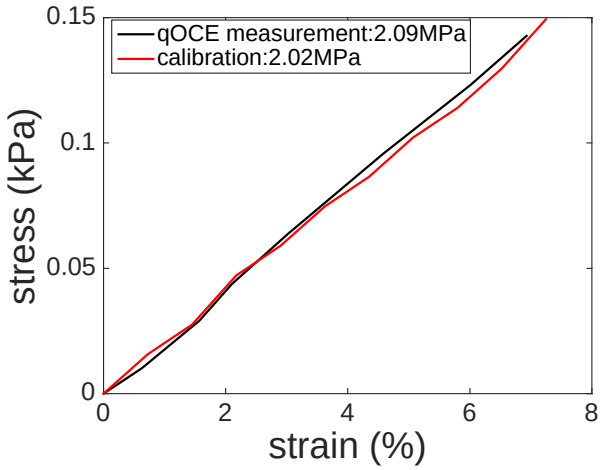


Fig. 8. Stress-strain curve obtained using qOCE measurement (black) and calibration of strain-stress curve (red).

To demonstrate that the qOCE technique developed in this study can be used to differentiate sample with different stiffness, we fabricated three PDMS phantoms to have different elastic moduli and performed qOCE measurement. Our real-time software tracked probe and sample deformation using OCT signal, and used Eq. (1) to calculated sample elasticity moduli. Results are shown in Table 1. In addition, we performed calibration experiments for elasticity measurement, shown as the second row of Table 1. In these

#254870 Received 30 Nov 2015; revised 12 Jan 2016; accepted 16 Jan 2016; published 26 Jan 2016
(C) 2016 OSA

calibration experiments, we measured force/stress using the force gauge and we obtained deformation/strain according to the reading of the linear stage. Table 1 indicates qOCE can provide reliable elasticity measurement.

Table 1. Elasticity measurement on phantom

Young's modulus	Phantom1	Phantom2	Phantom3
qOCE measurement (MPa)	0.72	0.99	2.51
Calibration (MPa)	0.69	0.94	2.45

We further validated qOCE technique on biological tissue, by measuring different tissues from chicken (*ex vivo*). We compared the elasticity of fat, muscle and heart of chicken. The Young's moduli obtained using qOCE are shown in Table 2. We can see the difference in stiffness between different tissues, suggesting our qOCE technique has the potential in distinguishing cancer tissue from normal tissue. However, it is challenging to correlate results shown in Table 2 with values of Young's moduli reported in literature. This is because reliable data on Young's moduli of soft tissue are very limited and available values tend to be inconsistent. A review study indicated that measured Young's moduli for any given tissue usually span several orders of magnitude [31]. For example, the Young's modulus of breast tissue has an average value of ~7kPa when measured by atomic force microscopy (AMF) but has an average value of ~480Mpa when measured by tensile stretching. Notably, Young's moduli obtained from qOCE measurement are generally larger than values obtained from AFM and smaller than values obtained through tensile stretching. This may be due to the tissue volume that qOCE characterizes is larger than the one in AFM measurement and smaller than the one in tensile stretching measurement.

Table 2. Elastic property measurement on chicken tissues

	Fat	Muscle	Heart
Young's modulus (Mpa)	0.21	0.63	7

Conclusion and discussion

To conclude, we demonstrated and validated to our knowledge the first time fiber-optic quantitative optical coherence elastography (qOCE) device, which simultaneously quantifies force exerted on the tissue and measures the resultant tissue deformation. The qOCE technique allows direct measurement of elastic properties and therefore has great potential in many applications, such as cancer diagnosis, brain injury study, tissue engineering and biomechanical modeling.

Currently, Young's modulus can be obtained from atomic force microscopy that studies tissue mechanics at the micro- through nanoscopic scale, or be obtained from tensile stretching or indentation measurement that studies tissue mechanics at the macroscopic scale [30]. However, these techniques rely on *ex vivo* tissue specimens that have different mechanical properties of tissue in living organism. Therefore, the proposed qOCE technique that allows *in situ* measurement of Young's modulus is highly significant for the study of tissue mechanics.

The axial resolution of qOCE was limited by the axial resolution (7.4μm) of OCT imaging. and the lateral resolution of qOCE was determined by optical confinement of light beam incident into sample. In principle, the qOCE technique developed in this study allowed spatially resolved characterization of mechanical property. However, the focus of this study was the quantification of elasticity modulus. Therefore, phantom with homogeneous mechanical property was tested using qOCE and spatial resolution for elastography was not the major concern.

The accuracy of qOCE measurement depends on the effectiveness of Doppler phase analysis in the quantification of force and sample deformation. The minimal displacement between Ascans that could be tracked using Doppler phase shift in the current OCT system

#254870 Received 30 Nov 2015; revised 12 Jan 2016; accepted 16 Jan 2016; published 26 Jan 2016
(C) 2016 OSA

was approximately 0.1nm, determined by random phase noise [26]. The maximum displacement between Ascans that could be tracked using Doppler phase shift in the current OCT system was approximately 325nm, limited by the range free of phase wrapping artifacts. In this study, we strategically chose the time interval between Ascans involved in Doppler phase calculation, to track phase shift during the process of quasi-static compression. The sensitivity of our device in force measurement could be higher than 0.25mN and the maximum force we applied through the qOCE probe was approximately 1N. The instrument is limited by the time derivative of force (dF/dt). Doppler analysis of OCT signal essentially quantifies the change of force (dF) within a small time interval (dt). Force is then obtained by integrating dF over time. The accuracy of force measurement is compromised, when dF is large and results in phase wrapping artifacts in Doppler OCT signal. Based on the stiffness of the probe shaft and the imaging speed of our OCT system, the system can theoretically quantify force with a 12,000 N/s derivative. It is possible to adaptively choose Ascans for Doppler phase analysis to improve the robustness in deformation tracking, in a way similar to adaptive speckle tracking method we developed before for lateral motion tracking [28].

We used a polyimide tube as qOCE probe shaft and assumed it deforms proportionally to force applied. The assumption was validated in experimental results shown in Fig. 7. Alternatively, we may use superelastic Nitinol that returns to its original shape when loading is released as the material for qOCE probe shaft.

We performed qOCE measurement to extract Young's modulus (Elasticity modulus) of sample. However, almost all of biological tissues are viscoelastic rather than elastic and therefore exhibit time-dependent strain under mechanical loading. Nevertheless, the elastic model for biological tissue is usually valid for small strain (<10%) under quasi-static mechanical loading. In fact, incremental sample deformation and probe deformation (δL_{sample} and δL_{probe}) were quantified over the entire process of compression of qOCE measurement, as shown (Eq. (5)). Although only two values, accumulated sample deformation and probe deformation (ΔL_{sample} and ΔL_{probe}) were involved in elasticity calculation, the qOCE technique developed in this study has the capability to track the temporal profile of deformation with mechanical stimulation to fully characterize viscoelasticity of biological tissue.

Acknowledgment

The research reported in this manuscript is supported by internal funding from New Jersey Institute of Technology.

#254870 Received 30 Nov 2015; revised 12 Jan 2016; accepted 16 Jan 2016; published 26 Jan 2016
(C) 2016 OSA

Appendix A –Publication Cover 26
2016

Authors: Y. Qiu, F.R. Zaki, N. Chandra, S. Chester and X. Liu

Title: "*Nonlinear characterization of elasticity using quantitative optical coherence elastography*"

Journal Publication: Biomedical Optics Express, 7 (11), 4702-4710 (2016), [16-26]

Research Article | Vol. 7, No. 11 | 1 Nov 2016 | BIOMEDICAL OPTICS EXPRESS 4702
Biomedical Optics EXPRESS

Nonlinear characterization of elasticity using quantitative optical coherence elastography

YI QIU,[1] FARZANA R. ZAKI,[1] NAMAS CHANDRA,[2] SHAWN A. CHESTER,[3] AND XUAN LIU[1,*]

[1]*Department of Electrical and Computer Engineering, New Jersey Institute of Technology, Newark, NJ 07102, USA*

[2]*Department of Biomedical Engineering, New Jersey Institute of Technology, Newark, NJ 07102, USA*
[3]*Department of Mechanical and Industrial Engineering, New Jersey Institute of Technology, Newark, NJ 07102, USA*
[*]*xliu@njit.edu*

Abstract: Optical coherence elastography (OCE) has been used to perform mechanical characterization on biological tissue at the microscopic scale. In this work, we used quantitative optical coherence elastography (qOCE), a novel technology we recently developed, to study the nonlinear elastic behavior of biological tissue. The qOCE system had a fiber-optic probe to exert a compressive force to deform tissue under the tip of the probe. Using the space-division multiplexed optical coherence tomography (OCT) signal detected by a spectral domain OCT engine, we were able to simultaneously quantify the probe deformation that was proportional to the force applied, and to quantify the tissue deformation. In other words, our qOCE system allowed us to establish the relationship between mechanical stimulus and tissue response to characterize the stiffness of biological tissue. Most biological tissues have nonlinear elastic behavior, and the apparent stress-strain relationship characterized by our qOCE system was nonlinear an extended range of strain, for a tissue-mimicking phantom as well as biological tissues. Our experimental results suggested that the quantification of force in OCE was critical for accurate characterization of tissue mechanical properties and the qOCE technique was capable of differentiating biological tissues based on the elasticity of tissue that is generally nonlinear.

©2016 Optical Society of America

OCIS codes: (170.4500) Optical coherence tomography; (280.4788) Optical sensing and sensors; (170.6935) Tissue characterization.

References and links

1. J. G. Fujimoto, C. Pitris, S. A. Boppart, and M. E. Brezinski, "Optical Coherence Tomography: An Emerging Technology for Biomedical Imaging and Optical Biopsy," Neoplasia **2**(1-2), 9–25 (2000).
2. J. A. Izatt, M. D. Kulkarni, K. Kobayashi, M. V. Sivak, J. K. Barton, and A. J. Welch, "Optical coherence tomography for biodiagnostics," Opt. Photonics News **8**(5), 41 (1997).
3. J. Schmitt, "OCT elastography: imaging microscopic deformation and strain of tissue," Opt. Express **3**(6), 199–211 (1998).
4. R. K. Wang, Z. Ma, and S. J. Kirkpatrick, "Tissue Doppler optical coherence elastography for real time strain rate and strain mapping of soft tissue," Appl. Phys. Lett. **89**(14), 144103 (2006).
5. R. K. Wang, S. Kirkpatrick, and M. Hinds, "Phase-sensitive optical coherence elastography for mapping tissue microstrains in real time," Appl. Phys. Lett. **90**(16), 164105 (2007).
6. X. Liang, S. G. Adie, R. John, and S. A. Boppart, "Dynamic spectral-domain optical coherence elastography for tissue characterization," Opt. Express **18**(13), 14183–14190 (2010).
7. C. Sun, B. Standish, and V. X. D. Yang, "Optical coherence elastography: current status and future applications," J. Biomed. Opt. **16**, 043001 (2011).
8. B. F. Kennedy, X. Liang, S. G. Adie, D. K. Gerstmann, B. C. Quirk, S. A. Boppart, and D. D. Sampson, "In vivo three-dimensional optical coherence elastography," Opt. Express **19**(7), 6623–6634 (2011).
9. K. M. Kennedy, B. F. Kennedy, R. A. McLaughlin, and D. D. Sampson, "Needle optical coherence elastography for tissue boundary detection," Opt. Lett. **37**(12), 2310–2312 (2012).
10. T. M. Nguyen, S. Song, B. Arnal, Z. Huang, M. O'Donnell, and R. K. Wang, "Visualizing ultrasonically induced shear wave propagation using phase-sensitive optical coherence tomography for dynamic elastography," Opt. Lett. **39**(4), 838–841 (2014).

#270300 http://dx.doi.org/10.1364/BOE.7.004702
Journal © 2016 Received 12 Jul 2016; revised 22 Oct 2016; accepted 22 Oct 2016; published 26 Oct 2016

Biomedical Optics EXPRESS

11. J. F. Greenleaf, M. Fatemi, and M. Insana, "Selected methods for imaging elastic properties of biological tissues," Annu. Rev. Biomed. Eng. **5**(1), 57–78 (2003).
12. T. A. Krouskop, T. M. Wheeler, F. Kallel, B. S. Garra, and T. Hall, "Elastic moduli of breast and prostate tissues under compression," Ultrason. Imaging **20**(4), 260–274 (1998).
13. A. Samani, J. Zubovits, and D. Plewes, "Elastic moduli of normal and pathological human breast tissues: an inversion-technique-based investigation of 169 samples," Phys. Med. Biol. **52**(6), 1565–1576 (2007).
14. K. Hoyt, B. Castaneda, M. Zhang, P. Nigwekar, P. A. di Sant'agnese, J. V. Joseph, J. Strang, D. J. Rubens, and K. J. Parker, "Tissue elasticity properties as biomarkers for prostate cancer," Cancer Biomark. **4**(4-5), 213–225 (2008).
15. K. Arda, N. Ciledag, E. Aktas, B. K. Aribas, and K. Köse, "Quantitative assessment of normal soft-tissue elasticity using shear-wave ultrasound elastography," AJR Am. J. Roentgenol. **197**(3), 532–536 (2011).
16. X. Liang, V. Crecea, and S. A. Boppart, "Dynamic Optical Coherence Elastography: a Review," J. Innov. Opt. Health Sci. **3**(4), 221–233 (2010).
17. K. M. Kennedy, L. Chin, R. A. McLaughlin, B. Latham, C. M. Saunders, D. D. Sampson, and B. F. Kennedy, "Quantitative micro-elastography: imaging of tissue elasticity using compression optical coherence elastography," Sci. Rep. **5**, 15538 (2015).
18. R. Karimi, T. Zhu, B. E. Bouma, and M. R. K. Mofrad, "Estimation of nonlinear mechanical properties of vascular tissues via elastography," Cardiovasc. Eng. **8**(4), 191–202 (2008).
19. Y. Qiu, Y. Wang, Y. Xu, N. Chandra, J. Haorah, B. Hubbi, B. J. Pfister, and X. Liu, "Quantitative optical coherence elastography based on fiber-optic probe for in situ measurement of tissue mechanical properties," Biomed. Opt. Express **7**(2), 688–700 (2016).
20. J. Y. Qiu, F. Zaki, Y. Wang, Y. Xu, N. Chandra, J. Haorah, B. Hubbi, B. Pfister, and X. Liu, "Depth resolved optical coherence elastography based on fiber-optic probe with integrated Fabry-Perot force sensor," in Conference on Lasers and Electro-Optics, OSA Technical Digest (online) (Optical Society of America, 2016), paper AW1O.3.
21. X. Liu, M. Kirby, and F. Zhao, "Motion analysis and removal in intensity variation based OCT angiography," Biomed. Opt. Express **5**(11), 3833–3847 (2014).
22. R. W. Ogden, *Non-Linear Elastic Deformations* (Courier Corporation, 1997).
23. A. F. Bower, *Applied Mechanics of Solids* (CRC press, 2009).
24. A. Delalleau, G. Josse, J.-M. Lagarde, H. Zahouani, and J.-M. Bergheau, "A nonlinear elastic behavior to identify the mechanical parameters of human skin in vivo," Skin Res. Technol. **14**(2), 152–164 (2008).
25. X. Liang and S. A. Boppart, "Biomechanical properties of in vivo human skin from dynamic optical coherence elastography," IEEE Trans. Biomed. Eng. **57**(4), 953–959 (2010).
26. S. Ganpule, A. Alai, E. Plougonven, and N. Chandra, "Mechanics of blast loading on the head models in the study of traumatic brain injury using experimental and computational approaches," Biomech. Model. Mechanobiol. **12**(3), 511–531 (2013).
27. V. Mishra, M. Skotak, H. Schuetz, A. Heller, J. Haorah, and N. Chandra, "Primary blast causes mild, moderate, severe and lethal TBI with increasing blast overpressures: Experimental rat injury model," Sci. Rep. **6**, 26992 (2016).
28. J. D. Finan, B. S. Elkin, E. M. Pearson, I. L. Kalbian, and B. Morrison 3rd, "Viscoelastic properties of the rat brain in the sagittal plane: effects of anatomical structure and age," Ann. Biomed. Eng. **40**(1), 70–78 (2012).
29. A. Karimi and M. Navidbakhsh, "An experimental study on the mechanical properties of rat brain tissue using different stress-strain definitions," J. Mater. Sci. Mater. Med. **25**(7), 1623–1630 (2014).
30. C. T. McKee, J. A. Last, P. Russell, and C. J. Murphy, "Indentation versus tensile measurements of Young's modulus for soft biological tissues," Tissue Eng. Part B Rev. **17**(3), 155–164 (2011).
31. S. A. Chester, C. V. Di Leo, and L. Anand, "A finite element implementation of a coupled diffusion-deformation theory for elastomeric gels," Int. J. Solids Struct. **52**, 1–18 (2015).
32. L. Dong, P. Wijesinghe, J. T. Dantuono, D. D. Sampson, P. R. T. Munro, B. F. Kennedy, and A. A. Oberai, "Quantitative Compression Optical Coherence Elastography as an Inverse Elasticity Problem," IEEE J. Sel. Top. Quantum Electron. **22**, 1–11 (2016).
33. A. Samani, J. Bishop, C. Luginbuhl, and D. B. Plewes, "Measuring the elastic modulus of ex vivo small tissue samples," Phys. Med. Biol. **48**(14), 2183–2198 (2003).
34. M. M. Doyley, "Model-based elastography: a survey of approaches to the inverse elasticity problem," Phys. Med. Biol. **57**(3), R35–R73 (2012).
35. A. A. Oberai, N. H. Gokhale, S. Goenezen, P. E. Barbone, T. J. Hall, A. M. Sommer, and J. Jiang, "Linear and nonlinear elasticity imaging of soft tissue in vivo: demonstration of feasibility," Phys. Med. Biol. **54**(5), 1191–1207 (2009).
36. D. R.Veronda and R. A. Westmann, "Mechanical characterization of skin—finite deformations," J. Biomechanics **3**, 122124 (1970).

1. Introduction

Optical coherence tomography (OCT) can be used to aid in the identification of diseased tissue such as cancerous tissue, for clinical diagnosis and surgical guidance [1, 2]. In addition to structural imaging, OCT has a functional extension referred as optical coherence

Biomedical Optics EXPRESS

elastography (OCE) that could be used to assess tissue stiffness [3–10]. OCE measures the mechanical response (deformation, resonant frequency, elastic wave propagation) of biological tissues under external or internal mechanical stimulation, and extracts mechanical properties of tissue related to its pathological and physiological status. Therefore, OCE has great potential in tissue characterization for various biomedical applications. It is generally accepted that the elasticity of tissue changes in pathological processes, as in the cases of breast or prostate cancer, and has the potential to be a discriminative biomarker for cancer diagnosis [11–14].

The most conventional way to describe the elasticity of a material is the Young's modulus measured at small strains. The Young's modulus can be directly measured using the stress-strain relationship through a compression process. Researchers also investigated indirect methods to quantify the Young's modulus of tissue. One of the indirect measurement technologies is dynamic elastography that generates dynamic excitation and propagating mechanical wave in tissue [15, 16]. In dynamic OCE, OCT imaging system is used to measure the propagation parameters of shear wave or surface wave for the estimation of Young's modulus. The mechanical excitation in dynamic OCT can be introduced by focused ultrasound or by photothermal effects, providing great opportunity for loading at depth. However, indirect measurement of tissue Young's modulus has limited spatial resolution and limited access to deep tissue. Conventional compression OCE that measures spatially resolved tissue displacement under compression has the potential to achieve high spatial resolution and can be implemented as an instrument with a small form factor. However, conventional compression OCE lacks the mechanism for force or stress quantification. This can limit its application in tissue characterization, because most of the biological tissues have different elastic behavior under large loads as compared to small loads. Strain stiffening is frequently observed in biological tissue at large loads, and the linear stress-strain relationship is limited to few tissues such as bone tissue in a very limited deformation regime. In other words, the displacement of tissue measured by OCE not only depends on the mechanical characteristics of the tissue, but also depends on the magnitude of loading [17]. Therefore, it is critical for OCE measurement to consider the nonlinear elasticity of tissue to achieve effective tissue differentiation, which has not been investigated extensively before [18].

In our previous work, we demonstrated a miniature quantitative OCE (qOCE) instrument which simultaneously measured the force exerted to tissue and the resultant tissue deformation [19]. We also demonstrated that our qOCE technique was able to provide depth resolved stiffness assessment in a muti-layer structure [20]. In this study, we explored the significance of force quantification in OCE for the characterization of nonlinear elasticity. We measured the apparent stress and the apparent strain of the tissue when the qOCE probe was used to slowly apply compressive load to the tissue, assuming the tissue is isotropic, homogeneous, elastic and incompressible within the volume interrogated by qOCE. Mechanical contrast between different biological tissues can be revealed using a calibrated qOCE instrument. Particularly, we used our qOCE technology to study the nonlinear elasticity of an elastic phantom and biological tissues, by characterization the apparent stress-strain relationship under different loading conditions.

2. qOCE system

The quantitative OCE (qOCE) system (Fig. 1(a)) utilizes a spectral domain OCT (SD OCT) engine operated at 1300nm. A detailed description of the system can be found in our previous publication [19, 21]. Briefly, the system has a 91 kHz Ascan rate and a ~7.5μm axial resolution. The phase noise of the SD OCT system has been measured to be 0.01 rad, corresponding to a 1nm sensitivity in displacement tracking. The output of the broadband light source illuminates the reference and sample arm of a fiber-optic Michelson interferometer through a fiber-optic coupler. When the system is used for mechanical characterization, we attach the fiber optic qOCE probe to the sample arm of the Michelson

Biomedical Optics EXPRESS

interferometer. When the system is used for 2D or 3D structural imaging, we interface the sample arm of the interferometer with a beam scanning system that consists of a collimator, a pair of galvanometers, and a scanning lens. Light returned from the interferometer is detected by a CMOS InGaAs camera (SUI1024LDH2, Goodrich). A frame grabber (PCIe-1433, National Instrument) streams the signal from the camera to the host computer (Dell Precision T7600) where the OCT signal is processed in real-time using graphic processing units (GPU).

A miniature fiber optic qOCE probe integrated with a Fabry-Perot (FP) interferometer is used to indent the tissue sample and collect optical signal for elasticity assessment [19]. The probe has a lead-in single mode fiber connected to its proximal end and a pair of GRIN lenses (1.8mm diameter) attached to its distal end. A low finesse Fabry-Perot (FP) cavity with two end surfaces (the cleaved SMF tip and the foremost surface of the first GRIN lens) are formed for force sensing. We used a polyimide tube with 1.8mm inner diameter as the probe shaft. Interference of the optical signals reflected from the end surfaces of the FP cavity produces a peak in the OCT A-scan ($\boldsymbol{I}_{\mathrm{FP}}$ in Fig. 1(b)). The force exerted through the probe causes deformation of the probe which in turn generates a detectable phase shift in the complex valued OCT signal. The sample is illuminated by the incident light from the broadband source through the probe. The backscattered light from the sample ($\mathbf{E}_{\mathrm{s}}$) generates a complex valued OCT signal ($\boldsymbol{I}_{\mathrm{tissue}}$). The displacement of the tissue can be quantified from the Doppler analysis of the complex valued OCT signal ($\arg(\boldsymbol{I}_{\mathrm{tissue}})$) in response to compression. Notability, $\boldsymbol{I}_{\mathrm{tissue}}$ is derived from the Michelson interferometer consisting of the reference arm and the sample arm, and $\boldsymbol{I}_{\mathrm{FP}}$ is derived from the common path interferometer (the FP cavity). Therefore, $\boldsymbol{I}_{\mathrm{tissue}}$ and $\boldsymbol{I}_{\mathrm{FP}}$ can be multiplexed in the same OCT Ascan without spatial overlapping by choosing appropriate optical path length for the reference arm, as shown in Fig. 1(b). In addition, the deformation of probe for force quantification has negligible impact on the measurement of tissue deformation, because the stiffness of the probe is orders of magnitude larger than that of soft tissue (GPa versus kPa). Therefore, the mechanical property of the tissue can be obtained by measuring the force and the depth resolved displacement simultaneously from the space-division-multiplexed OCT signal in our qOCE system. On the other hand, due to the large stiffness of the probe, the measurable sample stiffness has a lower limit. However, the small deformation of the stiff qOCE probe can still be quantified with high accuracy, if the Doppler phase is calculated using OCT signals acquired with larger time interval. In our future study, we will investigate a data-driven adaptive Doppler analysis method to achieve a larger dynamic range for stiffness assessment.

As illustrated in Fig. 1(b), we simultaneously measured the apparent stress and strain for the elastic characterization of biological tissue. These quantities are referred as apparent stress and strain in our description, because our measurement assumed a uniform spatial distribution of the stress and the strain within the tissue. The qOCE probe was used to perform slow indentation on the sample and OCT signals were acquired for mechanical characterization. We were able to quantify the probe-tissue interaction force (F) using Φ_{FP}, the accumulated phase shift at the signal peak for $\boldsymbol{I}_{\mathrm{FP}}$, because Φ_{FP} was proportional to probe shaft deformation and thus the force. Briefly, we calculated the Doppler phase shift $\phi_{\mathrm{FP}}(\tau)$ between A-scans and integrated the Doppler phase shift over time ($\Phi_{FP}(t) = \int_0^t \phi_{FP}(\tau) d\tau$). Full force transfer from the sample to the FP sensor was not expected. To quantify the force, we performed a calibration experiment to extract the constant (α) that correlated the probe tip force (F) with the phase shift (Φ_{FP}) due to FP cavity displacement: $F = \alpha\Phi_{\mathrm{FP}}$. The apparent stress was then obtained: $\sigma = F/A$. Here A indicates the area of the GRIN lens at the tip of the qOCE probe and $A = 2.5\mathrm{mm}^2$, calculated using the radius of the GRIN lens. On the other hand, we used $\boldsymbol{I}_{\mathrm{tissue}}$ to quantify tissue displacement and the apparent strain. We calculated tissue displacement (δl) using Doppler phase shift at depth d_0: $\delta l = \delta\phi_{\mathrm{tissue}}(d_0,\tau)\lambda_0/(4\pi)$ and integrated tissue displacement over time: $\Delta d = \int_0^t \delta l(d_0,\tau) d\tau$. This allowed us to calculate the apparent

Biomedical Optics EXPRESS

strain assuming uniform distribution of the displacement: $\varepsilon = \Delta d/(\Delta d + d_0)$. In this study, d_0 was chosen to be 0.63 mm where the tissue deformed substantially and the signal to noise ratio (SNR) of OCT signal was satisfactory. Notably, the apparent stress (σ) and the corresponding apparent strain (ε) were both obtained by integrating the Doppler phase from the beginning of indentation ($\tau = 0$) to the observation time point t ($\tau = t$). The fundamental data acquisition frequency for stress and strain signal was 10 kHz, determined by an external trigger source.

As described in our recent publication, we have calibrated our qOCE instrument and demonstrated force and displacement measurement with high linearity and accuracy [19]. We have developed high-speed software based on GPU to quantify stress and strain for our quantitative study of linear and nonlinear elasticity of tissue, as shown in Fig. 1(c) and Visualization 1.

To perform elastic characterization as shown in Fig. 1(c) and Visualization 1, we attached the qOCE probe to a high precision linear motor (Newport, ILS100CC DC) and translated the qOCE probe at small speed (~0.1 mm/s) in axial direction for indentation. This relatively slow motion was introduced to minimize any viscoelastic effects. The apparent stress-strain data were obtained during the indentation process for linear and nonlinear characterization of elastic properties of the material.

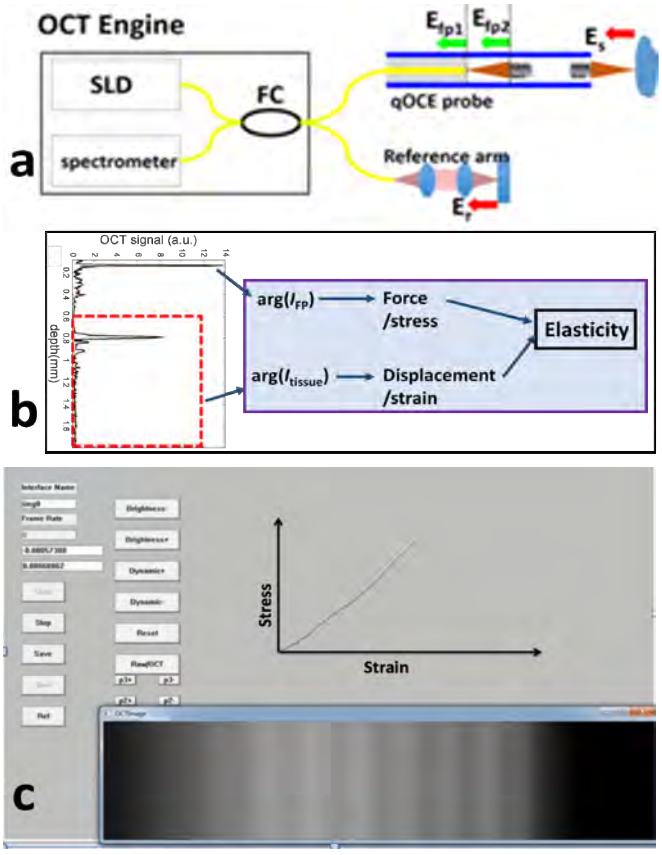


Fig. 1. (a) Illustration of qOCE system (FC: fiber optic coupler; SLD: superluminescent diode; $(\mathbf{E})_{fp1}$, optical reflection from the tip of single mode fiber; $(\mathbf{E})_{fp2}$, optical reflection from the proximal end of the first GRIN lens; $(\mathbf{E})_s$, sample light; $(\mathbf{E})_r$, reference light; (b) multiplexed signal for simultaneous probe and tissue deformation tracking; (c) software interface for real-time stress-strain characterization (Visualization 1).

Biomedical Optics EXPRESS

3. Results

To demonstrate qOCE's capability in linear and nonlinear mechanical characterization, we first performed qOCE measurement on an in-house fabricated elastic phantom. The phantom material was a room temperature platinum cure silicone rubber called RTV-22 purchased from Raw Material Suppliers. The solid material was prepared by mixing equal parts of base and catalyst, with titanium dioxide to provide scattering. The mixture was then thoroughly mixed, degassed for 15 minutes, and then cured on a 6-inch square glass plate overnight. From the cured sheet, specimens were cut using circular dies with a 0.5-inch diameter. Results obtained from qOCE characterization of the phantom are shown in Fig. 2. The apparent stress-strain relationship is linear when the apparent strain is small (Fig. 2(a)) and becomes nonlinear when the apparent strain increases (Fig. 2(b)). Using data obtained in linear regime of the apparent stress-strain curve (ε<0.1), we were able to evaluate the Young's modulus (E) of the material by fitting the linear model $\boldsymbol{\sigma} = E_{\text{linear}}\boldsymbol{\varepsilon}$, where $\boldsymbol{\sigma}$ indicates the apparent stress, $\boldsymbol{\varepsilon}$ indicates the apparent strain and E_{linear} indicates the Young's modulus for the linear material model. We performed regression analysis and obtained the value of E_{linear}: E_{linear} = 84.85kPa. The R^2 statistics of the regression was 0.9971. Using data obtained from a larger range of apparent strain as shown in Fig. 2(b), we extracted the Young's modulus of tissue by fitting a Neo-Hookean model: $\boldsymbol{\sigma} = E_{\text{nonlinear}}(\boldsymbol{\lambda}\text{-}1/\boldsymbol{\lambda}^2)/3$. Here λ indicates the magnitude of stretch and $\lambda = 1\text{-}\varepsilon$. The Neo-Hookean model is the simplest non-linear model possible. In the limit where the deformations are small, it reduces to linear elasticity [22, 23]. We performed regression to extract $E_{\text{nonlinear}}$, using the nonlinear material model. $E_{\text{nonlinear}}$ turned out to be 85.64kPa and was highly consistent with E_{linear}. The R^2 statistics of the regression was 0.9787. The fitting results are shown as the black curve in Fig. 2(b). For comparison, we also plot the linear stress-strain curve (blue curve) assuming a Young's modulus of E_{linear} in Fig. 2(b). Clearly, the experimental data became significantly different from the prediction made by the linear model for strain larger than 0.2.

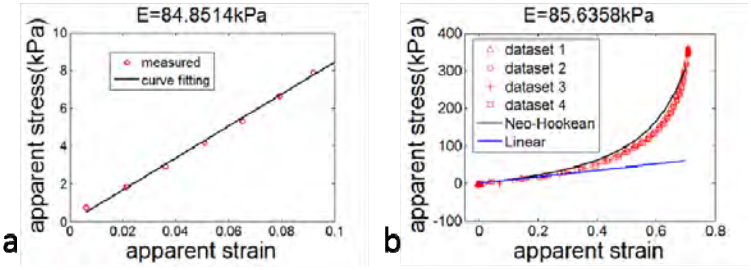


Fig. 2. (a) Linear stress-strain relationship at small strain; (b) nonlinear stress-strain relationship and curve fitting based on Neo-Hookean model.

To demonstrate that the qOCE technology could be used to study the nonlinear elasticity of biological tissue, we performed *in vivo* qOCE measurement of human skin tissue. Quasi-static indentation was applied to volar and dorsal skin of the forearm of a 32 years old healthy volunteer. To minimize the motion artifacts during the measurement, the arm was rested on a flat rigid surface. B-scan and *en face* images of volar skin are shown in Fig. 3(a) and 3(b), respectively. B-scan and *en face* images of dorsal skin are shown in Fig. 3(c) and 3(d), respectively. We selected a depth range of interest as indicated by the arrows in Fig. 3(a) and 3(c) assuming uniform distribution of tissue strain, for the analysis of dermis deformation and hence dermis stiffness. To calculate the apparent stress using the probe tip force, we assumed that equilibrium was achieved at arbitrary time during the indentation process. Experimentally acquired apparent stress-strain curves (black dashed curve: volar forearm skin; red dashed curve: dorsal forearm skin) are shown in Fig. 3(e). Clearly, both curves are nonlinear. The slope of the skin stress-strain curve increases with the magnitude of mechanical loading, because the dermis collagen fibers realign their orientations in response to the compression

Biomedical Optics EXPRESS

and the stiffness of the skin becomes larger [24]. As shown in Fig. 3(e), dorsal forearm skin has larger slope compared to volar skin over the entire range of loading, which is consistent with previous findings based on OCE [25]. Using data obtained at linear elasticity regime (apparent strain<0.1), we were able to derive the Young's moduli of dermis for volar (E_{volar} = 79.7 kPa) and dorsal skin (E_{dorsal} = 116.7 kPa). In other words, with the same qOCE system and measurement geometry, the apparent stress-strain curves obtained from different tissues were different. This validated the qOCE system's tissue differentiation capability. In comparison, structural OCT images in Fig. 3 do not show significant difference between volar and dorsal skins of the forearm, suggesting qOCE can potentially provide another dimension of information for tissue characterization. To further demonstrate that the elastic behaviour of skin tissue is nonlinear, we performed linear regression using the apparent stress-strain data obtained in the entire range of apparent strain. The resultant values of R-square statistics of the regression were 0.7616 and 0.8898, for the volar skin and the dorsal skin, respectively, suggesting a linear model could not provide satisfactory description of the apparent stress-strain relationship. In addition, we used the acquired apparent stress and apparent strain values to fit an existing nonlinear elastic model for skin tissue: $\sigma = 2\mu_0(\lambda^2 - \lambda^{-1})\{\exp[\gamma(\lambda^2 + 2\lambda^{-1} - 3)] - 1/(2\lambda)\}$, where σ indicates the stress and λ indicates the stretch [35, 36]. The model is known as Veronda-Westman Constitutive Law. It was originally developed for skin tissue and has been successfully used to fit experimental data. In the Veronda–Westman Constitutive Law, μ_0 is directly related to linear elasticity $E = 3\mu_0$ and γ determines the rate at which the apparent stress-strain curve departs from linear behaviour. The fitting results are shown as solid curves in Fig. 3(e). The resultant value of μ_0 was 14 kPa for volar skin and 38 kPa for dorsal skin, suggesting the nonlinear elastic behaviour characterized by qOCE could be used for tissue characterization, while the value of γ was approximately the same for both dorsal and volar skin: $\gamma \approx 5.3$. For dorsal skin, E extracted from linear regime of elasticity and μ_0 extracted from Veronda–Westman model approximately satisfy the following relationship: $E = 3\mu_0$. However, this relationship is not satisfied for volar skin, due to the limited data points within the linear elasticity regime to estimate the Young's modulus.

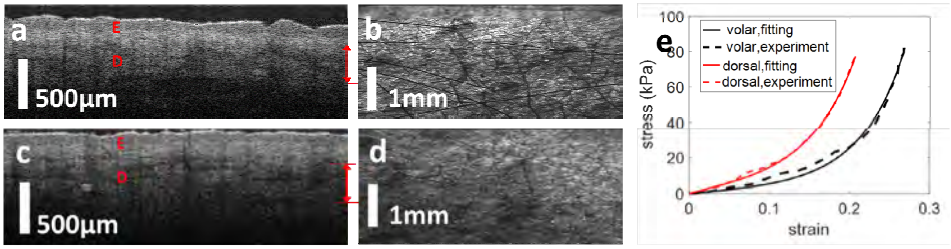


Fig. 3. Human skin at volar forearm: cross-sectional image (a) and (b) *en face* image; human skin at dorsal forearm: cross-sectional image (c) and (d) *en face* image; (e) stress-strain curve for volar (black) and dorsal (red) skin. In Fig. 3(a) and 3(c), E indicates epidermis and D indicates dermis.

We also performed a pilot study on *ex vivo* rat brain tissues using qOCE. 10-week-old Sprague Dawley rats (320-360 g in weight) from Charles River Labs were used. We harvested the brain from a rat that was sacrificed for other research purposes, and used a coronal brain slicer to cut the brain into slices with 3mm thickness. The miniature qOCE probe could perform localized mechanical characterization on hippocampus and other anatomical regions due to its small form factor (Fig. 4(a)). As shown in Fig. 4(a), the dimensions of hippocampus and cortex regions of the rat were comparable to the dimension of the qOCE probe and could be visually identified. Therefore, we performed visual inspection before the measurement started to make sure that the mechanical characterization was performed on anatomical structures of interest. We performed quasi-static indentation using the qOCE probe on the brain slice. Hippocampus (Fig. 4(b)) and cortex grey matter

Biomedical Optics EXPRESS

(Fig. 4(c)) were interrogated. In Fig. 4(b) and 4(c), the scale bars indicate 1mm. Hippocampus of the brain is thought to be the center for memory, emotion and spatial navigation and hippocampal damage in traumatic brain injury (TBI) is incredibly disabling. The mechanical contrast between hippocampus and other parts of the brain is directly related to the damage of hippocampus in TBI [26, 27]. Therefore, the mechanical properties of the hippocampus are of great interest. Before acquiring qOCE data, we translated the qOCE probe for 0.6mm to apply pre-compression. The apparent stress-strain curves obtained from the hippocampus (red) and the cortex (black) are shown in Fig. 4(d) as solid curves. Using data obtained at small apparent strain (strain<0.1) where the brain tissue had linear elasticity, we were able to determine Young's moduli for hippocampus (E_H) and cortex (E_C): E_H = 276 kPa and E_C = 74 kPa. This is consistent with results of previous studies that suggested the hippocampus tissue had larger stiffness compared to cortex [28]. The linear fittings of stress-strain relationships are shown as dashed curves in Fig. 4(d). The discrepancy between solid and dashed curves in Fig. 4(d) suggests the nonlinear stress-strain relationship for brain tissues. The loading could not be applied to the tissue when strain was larger than 0.2 due to material failure. This is consistent with published results [29]. We used the apparent stress-strain data corresponding to strain ranging from 0 to 0.2 to fit a linear model through regression and obtained the R^2 statistics to evaluate the quality of the fitting. The values of R^2 were 0.9472 and 0.8094 respectively for the hippocampus, and the grey matter, suggesting the elastic behaviour of hippocampus was approximately linear while the grey matter deviates from linear elastic behavior at a smaller strain.

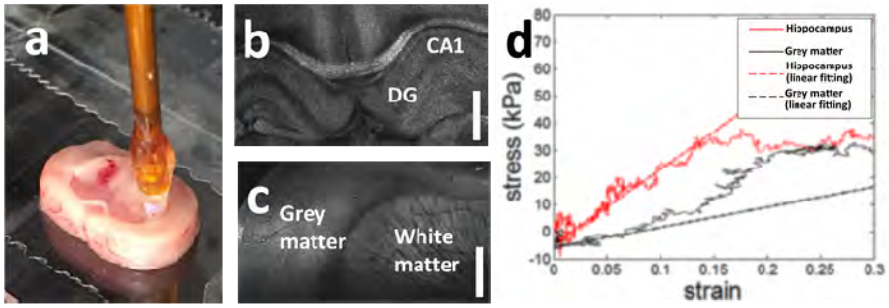


Fig. 4. (a) qOCE probe and brain slice; (b) *en face* OCT image of hippocampus obtained from the coronal plane (DG: dentate gyrus; CA1: Cornu Ammonis 1); (c) *en face* OCT image of cortex obtained from the coronal plane; (d) stress-strain curve for cortex grey matter (black) and hippocampus (red) of rat brain. Solid curves are experimental data and dashed curves are linear fitting of the stress-strain curve.

4. Discussion and conclusion

Unlike many engineered materials, biological tissues often exhibit nonlinear elastic behavior. Therefore, understanding the nonlinear elasticity is critical for elastography imaging and mechanical characterization of biological tissue. However, conventional OCE techniques lack the mechanism for force sensing. As a result, the nonlinearity of tissue elasticity has not been fully investigated and it remains challenging to establish the consistency in tissue stiffness obtained from different OCE measurements. In this study, we demonstrated the capability of qOCE in characterizing the nonlinear elasticity of biological tissue. We validated the effectiveness of our qOCE system by correlating its measurements with published values.

In our qOCE measurement, we used the qOCE probe to apply indentation on biological tissues and characterized the response of tissue in terms of depth resolved displacement and force. A significant advantage of depth resolved measurement of displacement enabled by the qOCE system is its potential in accurate strain measurement. In conventional apparatus for indentation test, the indenter displacement is measured. The measured displacement may be due to tissue deformation that generates stress, or due to the global motion of tissue that does

Biomedical Optics EXPRESS

not generate stress. This can be a source of inaccuracy when *in situ* measurement is conducted. In our qOCE system, we performed Doppler analysis on depth resolved OCT signal to extract depth resolved tissue displacement. As a result, the tissue deformation that generated the stress could be obtained by estimating the spatial derivative of the displacement, in other words, the strain. Moreover, qOCE technology will offer great opportunity for early detection of deep tumors that cannot be detected through manual palpation, because the miniature qOCE probe can be conveniently delivered to various tissue sites of interest for direct mechanical characterization. We will further optimize our instrument and miniaturize its dimension for such applications. The feasibility of such needle-based probes for mechanical characterization has been demonstrated before [9]. In summary, qOCE measurement of biological tissue, along with statistical analysis performed on qOCE data, will be able to reveal the difference in mechanical properties between different tissues.

Notably, the stress and strain fields within the sample under the compression of qOCE probe are generally nonuniform. However, we deliberately chose to estimate the strain using data obtained from a limited range of depth where the displacement varies as the axial depth in an approximately linear manner. In other words, in the limited depth range we considered, the axial strain and stress remain constant. As the strain and stress simply diminishes beyond the region effectively compressed by the qOCE probe, mechanical heterogeneity of tissue in a large scale would not affect the accuracy of qOCE characterization. Therefore, for accurate qOCE characterization, the elastic material (tissue) has to be incompressible, isotropic and homogeneous within the volume interrogated by qOCE, although the material does not have to be homogeneous beyond the region effectively compressed by the qOCE probe where the strain and stress simply diminish.

In the current study, the accuracy of the measurement is limited by the heterogeneous spatial distribution of actual stress and strain under indentation test, as well as the heterogeneous mechanical properties of tissue [30]. In principle, our qOCE technology can be used to study nonlinear elasticity with considerable spatial resolution [20]. However, accurate mechanical characterization of inhomogeneous sample is not trivial, even when the elastic behavior of the sample is linear. For a sample with microscopic mechanical heterogeneity, it is very challenging to determine the stress field within the sample based on the force measurement at the probe tip. In our future work, the Young's modulus of tissue will be extracted accurately using an inverse finite element approach where the impact of measurement geometry is considered [31–33]. In addition, a model-based approach will be developed to extract the spatial distribution of elasticity from inhomogeneous tissue, as demonstrated in ultrasound elastography [34]. The inter- and intra-sample and inter-measurement variability will be also investigated in our future study.

In this study, the elasticity of biological tissue is considered. However, most biological tissues have time dependent mechanical behavior and are essentially viscoelastic. To minimize the impact of viscoelasticity in our measurement, we translated the qOCE probe at a small speed such as 0.1 mm/s for tissue indentation and assumed the material achieved equilibrium at any time during the indentation process. qOCE measurement performed at different indentation speeds will allow more comprehensive mechanical characterization of biological tissues in both elasticity and viscoelasticity.

To conclude, we studied the nonlinear elastic property of tissue by the qOCE based system on a miniature probe with an integrated Fabry-Perot force sensor. We performed qOCE characterization on silicone rubber phantom, *in vivo* human skin tissues and *ex vivo* rat brain tissues. Our results have demonstrated the capability of our qOCE technology in characterizing nonlinear elasticity of biological tissue.

Acknowledgment

This study is supported by internal funding from New Jersey Institute of Technology.

Appendix A –Publication Cover 27
2015

Authors: PM Abdul-Muneer, BJ Pfister, J Haorah, N Chandra

Title: "*Role of matrix metalloproteinases in the pathogenesis of traumatic brain injury*"

Journal Publication: Molecular neurobiology, 1-18, (2015), [15-27]

Mol Neurobiol
DOI 10.1007/s12035-015-9520-8

Role of Matrix Metalloproteinases in the Pathogenesis of Traumatic Brain Injury

P. M. Abdul-Muneer[1] · **Bryan J. Pfister**[1] · **James Haorah**[1] · **Namas Chandra**[1]

Received: 19 September 2015 / Accepted: 28 October 2015
© Springer Science+Business Media New York 2015

Abstract Traumatic brain injury (TBI) is a major cause of mortality and morbidity worldwide. Studies revealed that the pathogenesis of TBI involves upregulation of MMPs. MMPs form a large family of closely related zinc-dependent endopeptidases, which are primarily responsible for the dynamic remodulation of the extracellular matrix (ECM). Thus, they are involved in several normal physiological processes like growth, development, and wound healing. During pathophysiological conditions, MMPs proteolytically degrade various components of ECM and tight junction (TJ) proteins of BBB and cause BBB disruption. Impairment of BBB causes leakiness of the blood from circulation to brain parenchyma that leads to microhemorrhage and edema. Further, MMPs dysregulate various normal physiological processes like angiogenesis and neurogenesis, and also they participate in the inflammatory and apoptotic cascades by inducing or regulating the specific mediators and their receptors. In this review, we explore the roles of MMPs in various physiological/pathophysiological processes associated with neurological complications, with special emphasis on TBI.

Keywords Traumatic brain injury · Matrix metalloproteinases · Extracellular matrix · Blood-brain barrier · Hemorrhage · Edema · Neuroinflammation · Neurodegeneration

✉ P. M. Abdul-Muneer
pmamuneer@gmail.com

[1] Department of Biomedical Engineering, New Jersey Institute of Technology, Newark, NJ 07102, USA

Introduction

Matrix metalloproteinases (MMPs) are zinc-dependent endopeptidases with multifactorial functions in the physiology and pathology of animal body. MMPs are collectively called matrixins as they participate mainly in the degradation of the extracellular matrix (ECM) [1]. MMPs are implicated to have a significant role in normal growth, development, wound healing, angiogenesis, neurogenesis, bone remodeling, ovulation, and implantation. However, during pathophysiological conditions, MMPs cause blood-brain barrier (BBB) disruption, hemorrhage, neuroinflammation, and cell death in various neurological diseases [2]. They are secreted by different cell types including astrocytes, endothelial cells, neurons, fibroblasts, osteoblasts, etc. A fair amount of MMPs are also produced by circulating leukocytes, including neutrophils, monocytes, and lymphocytes that invade the brain during inflammation. These enzymes are produced as zymogens (pro-MMPs), and they are further processed by proteolytic enzymes such as serine proteases, furin, and plasmin to convert into active forms [1]. MMPs are finely tuned enzymes, which are strategically regulated at the level of transcription, maturation from precursor pro MMPs, interaction with various ECM components, and inhibition by endogenous inhibitors [1, 3]. Hormones, growth factors, and certain cytokines regulate the activation of MMPs. Endogenous MMP inhibitors (MMPIs) and tissue inhibitors of MMPs (TIMPs) specifically control the activities of MMPs. Under normal physiological conditions, MMPs are expressed at the modest level. Overexpression/activation of MMPs results in an imbalance between the activities of MMPs and TIMPs, which is a major mechanism in the pathophysiology of various diseases such as arthritis, cancer, atherosclerosis, aneurysms, nephritis, tissue ulcers, fibrosis, and several

Published online: 05 November 2015

neurodegenerative diseases [4, 5]. Table 1 shows the classification and reported biological functions of MMPs with references.

Studies have suggested that MMPs are upregulated during traumatic brain injury (TBI). TBI causes upregulation of MMPs, particularly MMP-2, MMP-3, and MMP-9, and MMPs are involved in the pathophysiology of TBI including neuroinflammation and cell death. Secretion of MMP-2 and MMP-9 (gelatinases) is significantly increased in rat cortical neuronal culture, which has been induced by mechanical stretch injury [6]. TBI mediated motor deficits have been compared in traumatically injured MMP-9 knockout mice and wild mice in which a significant reduction in motor deficits was observed in knockout mice when compared with wild mice [7]. Likewise, several studies have suggested that TBI activates MMPs, which might play a critical role in the degradation of the extracellular matrix, disruption of the BBB, facilitation of leukocyte infiltration, hemorrhage, synaptic plasticity, angiogenesis, edema formation, neuroinflammation, and neurodegeneration. Table 2 shows the various reports on the roles of MMPs in different models of TBI.

TBI is characterized by physical brain injury associated with a broad spectrum of symptoms and disabilities. TBI causes approximately 1.7 million deaths and hospitalizations every year in the USA alone. Based on the injury severity, TBI is typically categorized into mild, moderate, and severe by using the Glasgow Coma Scale, a system used to assess coma and impaired consciousness [8]. Three components such as eye opening, verbal response, and motor responses are usually added together to produce a total score in the Glasgow Coma Scale. A Glasgow Coma Scale score of 13–15 is defined as mild, 9–12 as moderate, and 3–8 as severe [8]. Based on the mechanisms of brain tissue injury, TBI is classified as primary and secondary. Primary injury is the result of mechanical forces applied to the skull and brain and leads to skull fractures, brain contusions, axonal injuries, rupturing of blood vessels, and intracranial hemorrhages [9]. A series of molecular, neurochemical, cellular, and pathophysiological mechanisms contributes to secondary injury that leads to elevated intracranial pressure, BBB disruption, neuroinflammation, brain edema, cerebral hypoxia, ischemia, and delayed neurodegeneration [10–12]. Secondary brain injury may be reversible; therefore, the therapeutic intervention can be targeted.

Classifications of MMPs

To date, 24 different vertebrate MMPs have been identified, of which 23 are found in humans and are grouped into different classes. MMPs are broadly divided into two general classes: the secreted MMPs and the membrane-type MMPs [13]. They can be grouped into collagenases, gelatinases, stromelysins, and matrilysin according to their substrate specificity and domain structure (Table 1).

Collagenases

Collagenases are principal neutral proteinases capable of degrading interstitial collagens I, II, and III at a specific site [13]. Collagen is a fibrillar protein, the most abundant structural component of human connective tissue. The collagenases include collagenase-1 (MMP-1, interstitial collagenase), collagenase-2 (MMP-8, neutrophil collagenase), and collagenase-3 (MMP-13). MMP-18 (*Xenopus*) is also included in this group.

Gelatinases

The two best studied gelatinases, gelatinase A (MMP-2) and gelatinase B (MMP-9), belong to this group. MMP-2 and MMP-9 are found in the extracellular matrix, cerebrospinal fluid, and serum. These enzymes digest collagens and gelatins. MMP-2 digests type I, II, and III collagens. The activity of MMP-2 and MMP-9 can be easily detected by using gelatin-substrate zymography assay.

Stromelysins

This group of stromelysin includes stromelysin 1 (MMP-3) and stromelysin 2 (MMP-10). Both have similar substrate specificities, but MMP-3 has a proteolytic efficiency higher than that of MMP-10. Besides digesting ECM components, MMP-3 activates a number of pro-MMPs. For example, its action on pro-MMP-1 is critical to form active MMP-1.

Matrilysins

MMP-7 (Matrilysin 1) and MMP-26 (Matrilysin 2) are included in this group. The matrilysins do not contain hemopexin domain [14]. Matrilysin is preferentially expressed by cells of the glandular epithelium, so it is distinct from other known MMPs that are expressed in connective tissues [15]. Matrilysin 2 also digests ECM compounds.

Membrane-Type MMPs

Membrane-type MMPs (MT-MMPs) have common structural domains of the MMP family, but they have an additional domain that is anchored to the plasma membrane, making them important effectors of pericellular ECM degradation and proteolytic activities [16]. There are six MT-MMPs, in which four are type I transmembrane proteins (MMP-14,

Table 1 Biological activity of MMPs

MMP class	MMP	Enzyme	Biological activity	Reference
Gelatinases	MMP-2	Gelatinase A	Neurite outgrowth	[187]
			Mesenchymal cell differentiation with inflammatory phenotype	[188]
			Epithelial cell migration	[189]
			ECM and tight junction proteins degradation	[25, 29]
			Cleavage of SDF-1α	[157]
	MMP-9	Gelatinase B	Cleavage of several chemokines	[190]
			Angiogenesis and neovascularization	[191]
			Wound healing	[192]
			Development of aortic aneurysms	[193]
Collagenases	MMP-1	Collagenase-1 or interstitial collagenase	Keratinocyte migration and reepithelialization	[194]
			Platelet aggregation	[188]
			Involved in the process of HIV infection	[195]
	MMP-8	Neutrophil collagenase	Regulating lung inflammation	[196]
			Regulation of ovarian cancer,	[197]
	MMP-13	Collagenase-3	Osteoclast activation	[198]
			Release of bFGF	[199]
	MMP-18	Collagenase-4	Metamorphosis in *Xenopus*	[200]
Stromelysins	MMP-3	Stromelysin 1	Mammary epithelial cell apoptosis	[201]
			Mammary epithelial alveolar formation	[202]
			Disrupted cell aggregation and increased cell invasion	[203]
	MMP-10	Stromelysin 2	Skeletal development, wound healing, and vascular remodeling; its overexpression is implicated in lung tumorigenesis and tumor progression	[204]
	MMP-11	Stromelysin 3	Involved in aggressive basal cell carcinoma and in dermatofibroma	[205]
	MMP-27	Homology to stromelysin 2 (51.6 %)	Tissue homeostasis and tissue repair.	[141]
Matrilysins	MMP-7	Matrilysin 1 (Pump-1)	Adipocyte differentiation	[206]
			Disrupted cell aggregation and increased cell invasion	[203]
			Fas receptor-mediated apoptosis	[207]
	MMP-26	Matrilysin 2 (endometase)	Regulation of chondrosarcoma invasion	[208]
			Involved in colorectal cancer and endometrial carcinoma	[209]
Membrane type	MMP-14	MT1-MMP	Kidney tubulogenesis	[210]
			Epithelial cell migration	[211]
			Reduced cell adhesion and spreading	[212]
	MMP-15	MT2-MMP	Reduced cell adhesion and spreading	[212]
	MMP-16	MT3-MMP	Reduced cell adhesion and spreading	[212]
	MMP-17	MT4-MMP	Progression of breast cancer	[213]
	MMP-24	MT5-MMP	Neuronal plasticity	[214]
	MMP-25	MT6-MMP	Important role in colon cancer	[215]
Others	MMP-12	Macrophage metalloelastase	Generation of angiostatin-like fragment	[216]
	MMP-19	RASI-1	Participating in rheumatoid arthritis (RA)-associated joint tissue destruction	[217]
			Degradation of aggrecan, COMP in arthritic disease	[218]
			MMP-19 plays a role in cutaneous wound repair	[219]
	MMP-20	Enamelysin	Degradation of aggrecan, COMP in arthritic disease	[218]
	MMP-21	(In chromosome 1)	Upregulates TGF-β during epithelial cancer	[220]
	MMP-23	Femalysin	Role in potassium channel trafficking and are implicated in diseases including cancer and inflammatory disorders	[221]
	MMP-28	Epilysin	Induces TGF-β-mediated epithelial to mesenchymal transition in lung carcinoma cells	[222]
	MMPs		Generation of endostatin-like fragment	[223]

Table 1 (continued)

MMP class	MMP Enzyme	Biological activity	Reference
All MMPs (three or more MMPs having the same function)	MMPs	Activation of VEGF	[224]
	MMP-2, MMP-3, MMP-7	Increased bioavailability of TGF-β	[225]
	MMPs	Increased bioavailability of IGF1 and cell proliferation	[226]
	MMP-3, MMP-7, MMP-9, MMP-12	Generation of angiostatin-like fragment	[216, 227]
	MMP-1, MMP-3, MMP-9	Proinflammatory processing IL-1β from the precursor	[135]
	MMP-1, MMP-2, MMP-3	Cell migration	[228]
	MMP-1, MMP-2, MMP-3	Increased bioavailability of IGF1 and cell proliferation	[226]
	MMP-2, MMP-3, MMP-9	ECM and tight junction protein degradation	[25, 29]

MMP-15, MMP-16, and MMP-24) and two are glycosylphosphatidylinositol (GPI) anchored proteins (MMP-17 and MMP-25). Except MT4-MMP, all MT-MMPs are capable of activating pro-MMP-2. These enzymes can also digest ECM molecules and MT1-MMP is capable of degrading type I, II, and III collagens [17].

The actions of MMPs are strictly controlled by endogenous MMPIs and TIMPs. TIMPs are specific inhibitors of matrixins that participate in controlling the local activities of MMPs in tissues [18].

Role of MMPs in Brain Pathogenesis

MMPs are essential for the normal physiological functions as they are important in the dynamic remodulation of ECM. However, dysregulation of MMPs often leads to various pathophysiological complications such as BBB disruption, hemorrhage, neuroinflammation, and cell death [2]. High-level expression and activities of MMPs are reported in various neurological complications and diseases such as stroke, hemorrhage, Alzheimer's disease, and TBI [19–24]. During brain

Table 2 Role of MMPs in traumatic brain injury

MMP class	MMP	Enzyme	Biological activity	Reference
Gelatinases	MMP-2	Gelatinase A	Role of ERK MAPK pathway in inducing MMP-9 in CCI model	[6]
			Tight junction proteins degradation, BBB dysfunction in blast model of TBI	[32]
			Relationship between edema and MMP-2 in rodent surgical brain injury (SBI) model	[112]
	MMP-9	Gelatinase B	Apoptosis in infant brain, weight drop method in rat pups	[229]
			Role in edema and inflammation in weight drop model in mice	[230]
			Role in edema formation in human TBI after automobile accident	[231]
			Tight junction proteins degradation and BBB dysfunction in blast rat model	[32]
			BBB dysfunction in weight drop model in rats	[35]
			Involved in BBB dysfunction in cortical contusion in rats	[232]
			Relationship between edema and MMP-9 in rodent surgical brain injury (SBI) model	[112]
			Apoptosis in hippocampus in FPI injury, MMP-9 inhibitor attenuates	[233]
			Role of ERK MAPK pathway in inducing MMP-9 in CCI model	[234]
			Release of IL-1beta induced MMP-9 in in vitro mild stretch injury model	[235]
			Expression of MMP-9 and related to body temperature in FPI model in rats	[233]
			In association with the activation of IL-6 in humans	[138]
			Role in BBB permeability and fibrinogen deposit in cortical contusion injury	[236]
			Formation of edema is induced by VEGF and MMP-9 in humans	[231]
			The potential association between the extracellular matrix metalloproteinase inducer (EMMPRIN), or CD147 and MMP-9 expression in FPI model in rats	[237]
Collagenases	MMP-8	Neutrophil collagenase	Association of MMP-8 concentration and mortality in human brain microdialysate	[238]
Stromelysins	MMP-3	Stromelysin 1	Highly expressed during trauma-induced synaptogenesis in central FPI and combined central FPI and bilateral entorhinal cortical lesion (BEC) in rats	[86]
			Level of MMP-3 to determine age of brain contusion in rats	[239]
			Role in BBB dysfunction in blast TBI model in rats	[32]
Matrilysins	MMP-7	Matrilysin 1 (Pump-1)	Relationship between cerebral inflammation (cytokines) and MMP-7 in human TBI	[238]
Membrane type	MMP-24	MT5-MMP	Facilitate synapse reorganization in rat model of adaptive unilateral entorhinal cortical lesion (UEC) or maladaptive fluid percussion TBI + bilateral entorhinal cortical lesion (TBI + BEC)	[101]

injury or neurological diseases, MMPs are activated by various signaling mediators like reactive oxygen species (ROS), transforming growth factor-β (TGF-β), and inflammatory cytokines [25, 26]. MMPs in turn accelerate inflammation by activating inflammatory cytokines such IL-1β and TNF-α. MMP-mediated degradation of ECM proteins and tight junction (TJ) proteins of BBB leads to BBB disruption [27, 28]. MMPs play a key role in angiogenesis by stimulating the production of vascular endothelial growth factor (VEGF); however, augmented VEGF level in turn activates caspase-1 and causes apoptosis [29]. Further, caspase-1 matures pro-IL-1β to active IL-1β and leads to neuroinflammation. The neurodegenerative effect of MMPs comes mainly through its role in converting pro-caspases to active caspases and paves the way for cell apoptosis. In addition, MMPs induce cellular and vasogenic edema during brain injury. Figure 1 depicts the schematic presentation of the roles of MMPs in different cellular signaling cascades. The following review sessions will discuss the major roles of MMPs in neurovascular dysfunction, hemorrhage, angiogenesis, synaptic plasticity, edema formation, neuroinflammation, and neurodegeneration in various neurological complications with special emphasis on TBI. In the context of TBI, we discuss the roles of MMPs in the pathophysiology of neurotrauma by including human cases and animal models.

Blood-Brain Barrier Disruption

During normal physiological conditions, MMPs help to sustain the dynamic integrity of BBB through its role in the remodulation of ECM. However, during pathophysiological conditions, its upregulation impairs the neurovascular system. Abnormal MMP activation causes degradation of microvascular basement membrane proteins, resulting in the loss of brain endothelium stability and increases BBB permeability in animal models as well as in vitro studies [27, 28]. Several studies reported that oxidative stress is the major causative factor that activates MMPs [25]. Inflammatory cytokines and chemokines are also reported as MMP activators [30, 31]. Enhanced MMP activity degrades extracellular matrix proteins and tight junction proteins such as occludin, claudin-5, ZO-1-5, and it exacerbate BBB permeability [1, 29]. Recently, we have reported that blast-induced mild TBI (mTBI) enhances oxidative radicals, which activates MMPs, that degrade perivascular units and lead to BBB disruption [32]. In this study, we analyzed the different types of MMPs and their specific role in the degradation of the BBB in blast-induced mild TBI. We studied three types of MMPs such as MMP-2, MMP-3, and MMP-9 and their activation in single or repeated mild shock wave exposure in brain microvessels. The levels of MMP-3/-9 protein increased gradually for up to 24 h of blast injury, while upregulation of MMP-2 seems to be short durable because the level of MMP-2 gradually decreased after 6 h. It has been suggested that MMP-2, MMP-3, and MMP-9 are involved in the degradation of perivascular units and TJ proteins, which leads to BBB leakiness and inflammation of cerebral vascular unit [32]. Figure 2 shows the expression of MMP-2 in the frontal cortex of rat brain exposed to mild primary blast-induced TBI and lateral fluid percussion injury (FPI). Blast experiments were conducted by exposing rats to 123 kPa blast wave pressure and subjected to analysis for different markers of oxidative stress, MMP expression, neuroinflammation, and cell death [32]. Studies show that single mild shock wave exposure elevates MMP-2 expression after 24 h of blast (Fig. 2, top row). As an Alternative experimental model of TBI, FPI also shows elevated MMP-2 expression in

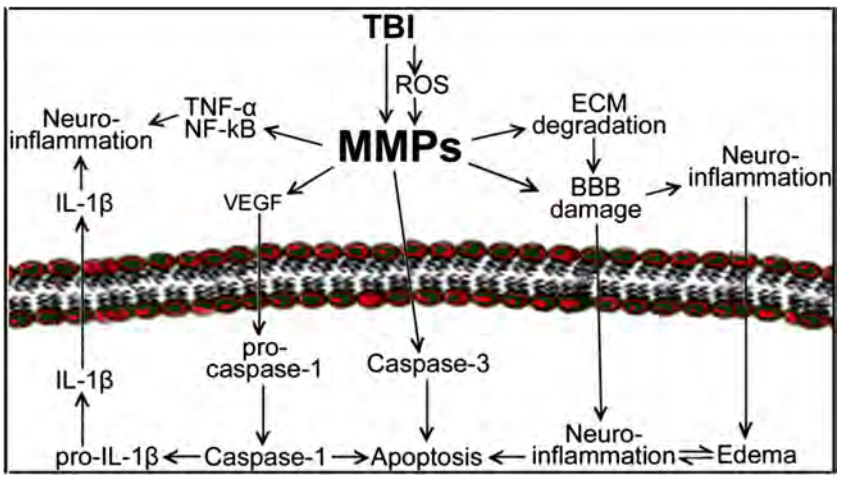


Fig. 1 Schematic representation of the role of MMPs in traumatic brain injury. Brain injury activates the expression of MMPs either directly or via other mediators like oxidative stress (reactive oxygen species, *ROS*). MMPs exacerbate the inflammatory cascades by activating inflammatory cytokines such as IL-1β and TNF-α. MMPs degrade ECM proteins and tight junction proteins of BBB lead to BBB disruption. In addition, MMPs involve in neurodegeneration by activating cell death inducing caspase enzymes and causing apoptosis. Similarly, MMPs induce cellular and vasogenic edema during brain injury

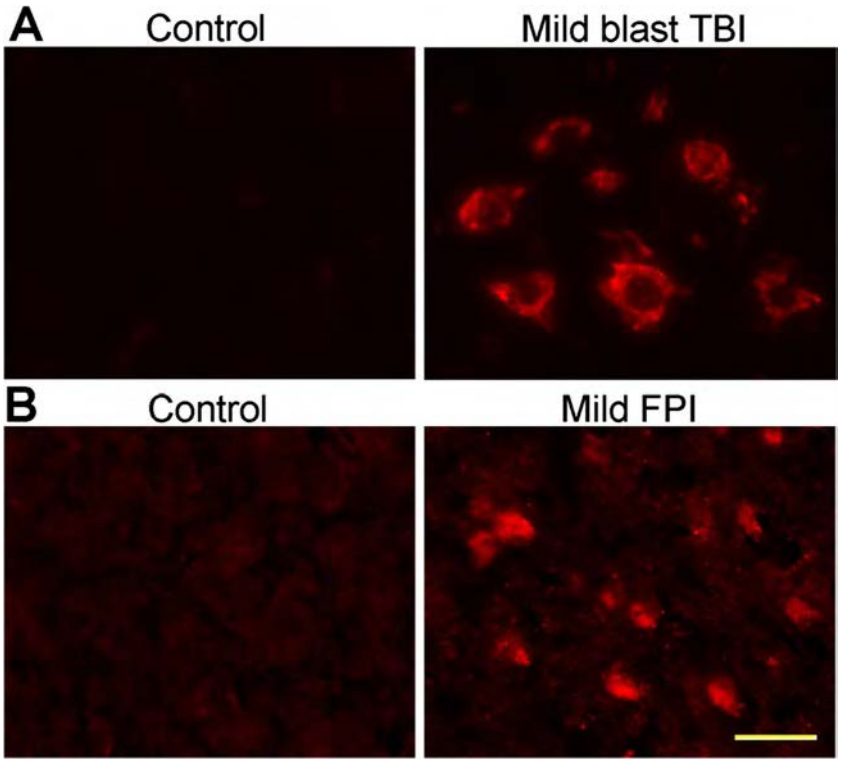


Fig. 2 Activation of MMP-2 in mild traumatic brain injury: Immunofluorescent staining of MMP2 in rat brain cortex of primary blast (123-kPa peak overpressure) induced mTBI [32] (**a**) and mild fluid percussion injury (15 psi) and compared with control (**b**). *Scale bar* (*yellow bar* in the last panel)=20 μm in all panels

the cortical brain tissue after 24 h of injury with 15 psi pressure (Fig. 2, bottom row).

There are several other reports on the involvement of MMPs in the degradation of various types of ECM proteins and TJ proteins of BBB in brain injury [27, 28]. TBI causes upregulation of MMPs, particularly MMP-2, MMP-3, and MMP-9, and leads to disruption of BBB, edema formation, and cell death [33, 34]. The role of MMP-9 in BBB disruption has been substantiated as the pharmacological inhibitor minocycline significantly attenuated TBI-mediated BBB impairment in rats [35].

Cerebral Hemorrhage

Often TBI encompasses hemorrhage in and around the contusion. The BBB becomes greatly disrupted during intracerebral hemorrhage; as a result, macrophages and leucocytes infiltrate the brain parenchyma and their presence has been proposed to constitute a primary mechanism of neuronal death [36]. Activated microglia also aggravates neuronal cell death after intracerebral hemorrhage [37, 38]. MMPs play a pivotal role for causing hemorrhage in brain injury and stroke. They enhance vascular permeability, which leads to BBB disruption and several neurological complications such as brain edema, neuroinflammation, and neurodegeneration [39, 40]. A high-level MMP expression is believed to contribute to tissue destruction in brain injury and neuronal damage [20–24]. MMPs cause hemorrhage by proteolytic degradation of the extracellular matrix and tight junction proteins of BBB, which leads to BBB dysfunction and leakage of blood into the brain side in mild TBI (reviewed in [41, 42]). Horstmann et al. reported that the level of MMP-2 and MMP-9 in serum of patients suffering from subarachnoid hemorrhage was very high compared to normal healthy individuals [19]. Recently, we experimentally demonstrated vascular leakage due to BBB disruption and increase in vascular permeability in mild blast TBI by infusing high and small molecular weight dyes such as Evans blue and sodium fluorescein through the carotid artery [32]. During hemorrhagic transformation, MMP-9 participates in BBB dysfunction and exacerbates brain injury after cerebral ischemia. There are several other reports in which MMPs cause hemorrhage due to BBB damage [43, 44].

Upregulation of MMPs has been reported in various other pathophysiological conditions such as hypertension. Several authors reported that the hypertension-inducing hormone, angiotensin II (Ang II), is one of main factors leading to hemorrhage [45–47]. In several other biochemical mechanisms, Ang II has been reported as a mediator of oxidative stress via activation/induction of free radical-generating enzymes such NOX and NOS [48–55]. Ang II stimulates the production of ROS in endothelial cells by upregulating NADPH oxidases [56, 57]. These free radicals especially ROS activates TGF-β1 in brain microvessels. Ang II induced oxidative stress and

TGF-β1 leads to the activation of MMPs [49]. The sustained activation of MMPs causes the degradation of TJ proteins such as occludin, claudin-5, and ZO-1, thereby impairing BBB and vascular wound healing process, that leads to chronic rupture of the capillaries leading to hemorrhagic stroke [58]. Degradation of basement membrane and TJ proteins of the BBB by MMPs enhances the BBB permeability and immune cell infiltration into the brain [59, 60], which is strongly associated with hemorrhagic and ischemic stroke [58, 61].

Angiogenesis

While reviewing the roles of MMPs in association with the pathophysiology of the brain, it is imperative to analyze its effect in angiogenesis. Angiogenesis is the physiological process in which new blood vessels emerge from existing endothelial-lined vessels [62]. Regarding the functional recovery after TBI, angiogenesis is a premier mechanism that includes mainly proliferation and migration of vascular endothelial cells. Being an invasive process, angiogenesis is always accompanied with degradation of basement membrane proteins [63, 64]. Here, the proteolytic activity of MMPs has greater roles to play. MMPs strategically degrade and remodulate various components of the extracellular matrix and pave the way for the emerging blood vessels [65]. MMP-3 and MMP-10 target proteoglycans, fibronectin, and laminin. MMP-8 and MMP-13 selectively target collagen I and II, respectively, whereas MMP-1 prefers collagen III. In addition, both MMP-2 and MMP-9 degrade denatured collagen (gelatin) [13]. By using both synthetic and endogenous MMP inhibitors, researchers inhibited angiogenic responses in vitro and in vivo [66–68]. In addition, the delayed or reduced angiogenic responses were reported in MMP-deficient mice during development [69, 70].

Apart from this, MMPs have a regulatory effect on the VEGF, one of the integral components of angiogenesis. But during pathophysiological conditions, MMPs impair angiogenesis through dysregulation of VEGF. VEGF is a ligand to the vascular endothelial growth factor receptor 1 or 2 (VEGFR-1 or VEGFR-2) and is a key regulator of angiogenic response and endothelium wound healing process [71]. When VEGF binds to VEGFR, the receptor dimerization and autophosphorylation occurs and promotes angiogenesis and repair damaged microvessels [72, 73]. Brain injury-associated upregulation of VEGF has been reported [74]. It has been reported that upregulation of VEGF or experimental administration of VEGF leads to induction of MMP-9 activity that causes BBB disruption [75]. In our previous study, we experimentally demonstrated that elevation of both MMP-3 and MMP-9 leads to upregulation of VEGF due to MMP-mediated proteolytic disruption of VEGFR-2 [29]. According to the study, sustained activation of MMPs leads to degradation of the VEGFR-2 protein, thereby making it difficult to repair injured capillaries. Exposure of hBECs to exogenous MMP-3 or MMP-9 leads to dimunition of VEGFR-2 protein, and the activation of MMP-3 or MMP-9 in brain microvessels was found to correlate with the downregulation of the VEGFR-2 protein [29]. Turk et al. reported the cleavage of VEGFR-2 by MMP-7 and MMP-9 at multiple positions (e.g., Leu-Ser/Met-Leu, Leu-Ser/Ile-Arg) [76]. In another study, it has been shown that the activation of plasma MMP cleaved the extracellular domain of VEGFR-2 on the endothelium [77]. As the receptor gets cleaved and becomes functionless, the level of ligand VEGF tends to increase. The upregulated VEGF is detrimental as it triggers caspases and aggravates apoptosis [77]. In our previous study, we demonstrated that elevated VEGF level could induce caspase-1 (interleukin converting enzyme) and cause apoptosis in alcohol-mediated vascular impairment in mice brain microvessels [29]. Treatment with the MMP inhibitor doxycycline attenuates VEGFR-2 cleavage as well as endothelial apoptosis [77]. In TBI, VEGFR-2 signaling blockage using the selective inhibitor SU5416 abrogates prosurvival response and induces high activation of caspase-3/7 leading to cell death [78]. However, in TBI, MMP-mediated regulation of VEGF and the associated biochemical cascades are elusive. Thus, it opens up a subject for future research. Angiogenic response is critical for the progression of wound healing in hemorrhage, stroke, and associated pathological conditions such as BBB impairment or inflammation. Therefore, a thorough understanding on the signaling events involved in angiogenesis and its molecular regulation has clinical implications.

Synaptic Plasticity

Impairment of cognitive function is one of the most devastating outcomes of TBI. Cognitive impairments often involve cell loss and vulnerability to different brain regions. Recovery of lost/impaired cognitive functions typically occurs via adaptive synaptic plasticity, which occurs in acute posttraumatic periods [79]. Though several factors contribute to the adaptive synaptic plasticity, MMPs have a significant role in posttraumatic synaptic reorganization through the dynamic modulation of ECM proteins ([80–84] and recently reviewed in [23, 85]). Here, we review the roles of MMPs in synaptic plasticity during the physiology and pathophysiology of the brain. MMPs play critical roles in neurite growth cone development, synaptic transmission, synaptic modification, and neuronal degeneration contributing to successful synaptic plasticity [3, 85–90]. In 2005, Mayer et al. reported MMP/substrate interaction during lesion-induced synaptogenesis [91]. MMPs influence axonal growth and synaptic modification with their regulatory effects on ECM [23, 85]. Redistribution of ECM proteins along deafferented dendrites leads to axon sprouting toward postsynaptic sites during cortical lesion synaptogenesis [92, 93]. Among the various MMPs, MMP-3 and MMP-9

are the most studied MMPs in synaptic plasticity. However, their effects in the adaptive synaptic plasticity during posttraumatic repair are not conclusively studied. MMP-3 targets ECM proteins, which are critical to neuronal growth and synaptic reorganization [84, 94–97]. Falo et al. reported significant elevation of MMP-3 in injury sites where active synaptogenesis is taking place [98]. High-level expression of MMP-2, MMP-3, and MMP-9 is observed in TBI models (our recent review [99]). An increase in MMP-3 activity has been reported as it persists toward the period of synapse regeneration [98]. MMP-9 is largely associated with modification of important synaptic receptors and altering the morphology of synapses [100]. In addition to these during synaptogenesis, the expression of MT5-MMP and ADAM-10 proteins elevates and supports a significant role in synaptic reorganization following TBI [101].

Upregulation of MMPs during various pathophysiological conditions of brain causes aberrant synoptic plasticity and spine dysmorphology [102, 103]. However, the signaling mechanisms involved in MMP-mediated synaptic dysfunction are largely unknown. Studies have suggested the roles of MMP-9 in mediating a typical synaptic plasticity in various neurological diseases like epilepsy and Alzheimer's disease [102, 104]. Michaluk et al. reported that beta-dystroglycan (beta-DG), a transmembrane protein, is a synaptic target for MMP-9 [105]. They demonstrated it in neuronal cultures; glutamate/bicuculline-mediated stimulation of neuronal cultures caused an increase in MMP-9 activity which coincides with the cleavage of beta-DG, and this cleavage could be attenuated by the overexpression of TIMP-1. Philips et al. reported evidence of the role of MMP in TBI neuroplasticity based on studies with targeted hippocampal deafferentation [103]. Thus, it appears that an appropriate level of MMP is very critical for the posttraumatic adaptive neuroplasticity; thorough understanding would help to develop strategies that can favor for adaptive neuroplasticity over maladaptive neuroplasticity.

Edema Formation

Cerebral edema is extra accumulation of fluid in intra- or extracellular spaces of the brain. It is one of the major factors that leads to high mortality and morbidity in TBI, and it accounts for up to half of the mortality in all victims of TBI [106]. Cerebral edema can be classified into two types: cellular and vasogenic [107]. Cellular edema is characterized by an increase in water content in intracellular compartments and will not be manifested as tissue swelling. Vasogenic edema allows intravascular proteins and fluid to penetrate into the parenchymal extracellular space and increases tissue water content and leads to swelling. This type of edema mainly results from the breakdown of BBB [108]. Usually, cellular edema appears after a few days of vasogenic edema, which develops in the first few hours after TBI. Cellular edema develops slowly and extends up to 2 weeks [109]. Usually in TBI, edema leads to swelling of brain tissue and elevates intracranial pressure (ICP) [110].

MMPs are one of the important mediators of edema formation in TBI. By using pharmacological inhibitors of MMPs such as minocycline or TIMP-1, the role of MMPs in edema formation has been demonstrated. The use of minocycline and TIMP-1 could abrogate TBI-mediated edema formation, BBB impairment, inflammatory responses, and cerebral ischemia [7, 43, 111]. In a surgical brain injury, edema is found around the surgical resection with simultaneous increases in MMP-9 and MMP-2 activity. In such injury, treatment with MMP inhibitor-1 decreased brain edema and attenuated the activation of MMP-9 and MMP-2 [112].

Several activators are involved in the formation of edema in TBI. Aquaporins (AQP) are one of the main activators that contribute to the development of cerebral edema [113]. Several investigators reported the role of AQPs in promoting edema formation after brain injury [114–116]. It is evident from the studies that inhibition of AQP4 using pharmacological inhibitors could mitigate the formation of edema in TBI [115, 117, 118]. AQPs are integral membrane proteins, which form pores in the membranes of mammalian cells; they selectively conduct water molecules in and out of the cells while preventing passage of ions and solutes [119, 120]. Among the known 13 AQPs, AQP1, AQP4, and AQP9 are highly expressed in the brain. AQP4 is mainly expressed in astrocytic end-feet [121]. In our previous blast-induced mild TBI study, we reported upregulation of AQP4 in the cerebral cortex of injured rats. This AQP4 co-expressed with the astrocytic marker GFAP in the perivascular area [32]. There are several reports in which MMPs induce or activate AQPs and lead to edema formation [35, 122]. The role of MMP-9 has been studied in the pathogenesis of brain edema and its associated neurological complications in ischemic and TBIs [21, 123, 124]. In 2000, Asashi et al. conducted a detailed study and reported that the brain extravasation significantly abrogated, and cognitive functions were protected when they conducted cerebral ischemia or trauma in MMP-9 knockout mice [125]. They also noticed similar protective effects when they treated the animals with the MMP inhibitor BB-94 [125]. These reports suggest that MMPs have a significant role in brain injury-mediated edema formation.

Neuroinflammation

Neuroinflammation is considered as a key secondary injury mechanism that sustains the damage long after TBI by exacerbating cerebral edema and intracranial pressure. Increasing amounts of evidence suggested that MMPs are instrumental in creating a proinflammatory microenvironment [126]. MMPs participate in the inflammatory cascade by inducing or

regulating various inflammatory mediators and their receptors [127, 128]. These inflammatory mediators and receptors include cytokines, interferons, growth factors, and other regulatory proteins [128]. Studies show that MMP regulates the activation of inflammatory cytokines such as IL-1β, TNF-α, and TGF-β.

The cytokine, IL-1β, is a common inflammatory cytokine, which is significantly elevated during neurological complications such as Alzheimer's disease, TBI, and stroke [129]. This is regarded as a major inflammatory biomarker. Activation of IL-1β involves proteolytic removal of the N-terminal part from its inactive precursor protein [130]. IL-1-converting enzyme (ICE), also called caspase-1, has been identified as the primary IL-1β activator [131]. There are several reports on the activation of IL-1β in caspase-1-independent pathways in vitro and in vivo [132, 133]. In 1996, Ito et al. first reported the MMP-mediated maturation of IL-1β [134]. Further studies suggested that MMPs like MMP-2, MMP-3, and MMP-9 are capable for the activation of IL-1β [135]. Converse to this finding when MMP-2-positive astrocytes were stimulated with IL-1β, they produced MMP-9 [136]. In another study, when IL-1β was injected to MMP-9 knockout mice, it showed reduced microglial activation [30] and attenuated BBB degradation [137]. Similarly, MMPs regulate the activation of other interleukins such as IL-6 and IL-18. Suehiro et al. reported that MMP-9 upregulated the level of IL-6 in systemic arterial and jugular venous blood from seven patients with TBI [138]. Thus, it appears that MMPs influence the inflammatory process by activating pro-IL or cleaving pro-IL to its active form.

TNF-α sheddase activity of MMPs provides another example on how MMPs influence inflammatory reaction by regulating cytokines. MMPs have the ability to release soluble TNF from its membrane-bound precursor. TNF-α is a pleiotropic proinflammatory cytokine produced by various cell types and is a central mediator of diverse cellular events. TNF-α is released from the cell surface by ADAM-17 (a disintegrin and metalloproteinase 17), which is also known as TNF-α-converting enzyme (TACE), the main TNF sheddase. It has been proven in ADAM-17 knockout mice, where it reduced the release of active TNF-α by 90 % [139]. Macrophage MMP-7 was found to be very important for TNF-α release [140]. In addition, several other MMPs such as MMP-1, MMP-2, MMP-3, MMP-9, MMP-12, MMP-14, and MMP-17 are reported as having role in releasing active TNF from the cell surface [141–143]. MMP-mediated activation of TNF-α has been reported in several signaling pathways associated with diseases and disorders. Xie et al. reported that MMP induced cerebral hemorrhage and involvement of TNF-α in subarachnoid hemorrhage patients [144]. Activated TNF-α in turn activates MMPs, and TNF-α-mediated activation of MMP-2 and MMP-9 is well documented. Lee et al. conducted a detailed study on the TNF-α-mediated activation of MMP-9 and reported that augmented MMP-9 gene expression was mediated through TNFR1/TRAF2/PKCalpha-dependent JNK1/2/c-Jun and c-Src/EGFR/PI3K/Akt signaling pathways in human A549 cells [145].

TGF-β is another cytokine with pleiotropic effect on which MMPs have regulatory roles. Several investigators reported the functional/regulatory interactions and interplay of MMPs with TGF-β. TGF-β has various physiological and pathological functions such as tissue wound healing, inflammation, cell proliferation, differentiation, migration, and ECM synthesis [146–148]. In addition, TGF-β has a significant role in regulating the immune system that controls both pro- and anti-inflammatory effects depending on the cell type [146–148]. In TBI, increased levels of TGF-β have been reported [149, 150]. In initial days of head-injured patients, high levels of TGF-β in CSF have been detected [150]. MMP-2 and MMP-9 can activate TGF-β through proteolytic degradation of the latent TGF-β complex. TGF-β is translated as a precursor protein of 75 kDa, containing a signaling peptide, latency-associated peptide (LAP), and the mature TGF-β. The precursor protein gets cleaved intracellularly by furin-type convertases, and upon secretion, the protein remains associated with ECM, still as latent TGF-β complex. ECM activation of TGF-β involves proteolytic cleavage by MMPs [151, 152]. Wang et al. demonstrated MMP-2-mediated activation of TGF-β1 in the arterial walls of aged rats. Recently, several studies have shown that TGF-β1 can upregulate MMP-9 expression and activity in different cell types [153, 154]; similarly, there are reports on the activation of MMP by TGF-β. Thus, MMPs play a key role in the regulation of TGF-β and thereby regulate inflammation, cell proliferation, and wound healing. Overall, MMPs modulate the process of neuroinflammation through their bidirectional interaction with cytokines.

Neurodegeneration

TBI almost always leads to progressive neurodegeneration depending on the severity. Proteases have a major role in cell death and it can trigger cell death by proteolytic damage [155]. MMPs upregulate apoptosis of several biologically active intra- and/or extracellular molecules [156]. The level of MMPs or activation of MMPs, tissue specificity, and the balance between MMPs and TIMPs are other important factors which influence apoptosis [156]. Studies established the role of MMPs in neuronal apoptosis [156]. Apoptosis is a type of programmed cell death, which is triggered mainly by caspase activity [155]. In response to injury stimuli, MMPs get activated and induce apoptotic caspase enzymes [156]. In our recent study, in blast-induced mild TBI, we illustrated MMP-mediated induction of caspase-3 and apoptosis [32]. Using the MMP inhibitor, TIMP-1, the role of MMPs in apoptosis has been demonstrated. In another study, we demonstrated MMP-3 and MMP-9 as the main contributors for the caspase-1-dependent cell death in human endothelial cells [29].

MMPs have role in cleaving pro-IL-1β to active IL-1β [135], the key component of the cytokine network involved in apoptosis. Another class of nonmatrix proteins cleaved by MMP is the cleavage of stromal cell-derived factor-α (SDF-α), a chemokine converted to a neurotoxic protein causing neurodegeneration after precise processing by active MMP-2 [157]. In 2005, Copin et al. reported the roles of MMPs in cerebral ischemia-induced apoptosis and studied the specific role of MMP-9 in cell death mechanism. They also analyzed the pro and cleaved forms of PARP (poly (ADP) ribose polymerase) and α-spectrin and investigated DNA fragmentation in rats treated with MMP inhibitor and in MMP-9 knockout mice [158]. MMPs can inactivate PARP in a time-dependent manner similar to caspase-3 and cause harmful effects by hampering DNA strand break repair [159].

MMPs act on *Proneurotrophins* (i.e., nerve growth factor and brain-derived neurotrophic factor) and cleave extracellularly. *Proneurotrophins* are known growth factors that regulate cell survival but also promote neuronal cell death [160]. In the cerebellum and retinal ganglion cells, MMP-9 is involved in apoptosis through precise degradation of ECM proteins [161]. In addition, MMPs stimulate apoptosis by interacting with cell surface receptors. For instance, MMP-9 activates neuronal cell death through the association with lipoprotein receptor-related protein [162] and MMP-1 interacts with α1β2-, αvβ3-, and α5β1-integrins and is involved in apoptosis [163]. MMP-12 may cleave other cell surface receptors including proteinase-activated receptors and involve in the apoptosis of endothelial and epithelial cells [164].

Regarding TBI, the most reported MMPs are MMP-2 (gelatinase A) and MMP-9 (gelatinase B). In our recent work, we demonstrated the roles of MMP-2, MMP-3, and MMP-9 in neuroinflammation and neurodegeneration after blast-induced mild TBI in rats [32]. The other MMPs such as MMP-1 [163], MMP-7 [165], and MMP-11 [166] are also involved in apoptosis in various cell death mechanisms. Thus, the protein levels and activities of various MMPs have a regulatory role in the transition between physiology and pathophysiology.

Endogenous and Exogenous MMP Inhibitors

MMP inhibitors include natural endogenous tissue inhibitors and exogenous synthetic pharmacological inhibitors. Two major endogenous inhibitors of MMPs are TIMPS and α2 macroglobulin. TIMPs are the most thoroughly studied class of endogenous MMP inhibitors. Four TIMPs (TIMP-1, TIMP-2, TIMP-3, and TIMP-4) have been identified in vertebrates [18]. These inhibitors bind MMPs in a 1:1 stoichiometry. This family of inhibitors has been extensively reviewed by several authors [167–169]. TIMPs inhibit all MMPs tested so far, except that TIMP-1 fails to inhibit MT1-MMP [168]. The human TIMP proteins contain 184 to 194 amino acids that form an N-domain and a C-subdomain that are stabilized by six disulfide bonds [169]. TIMPs are 40 % identical in structure and have similar characters to inhibit individual MMPs. The expression of TIMPs is tissue-specific and is regulated at the level of transcription. TIMP-1 is widely expressed in many mammalian tissues, especially in the reproductive organs. In the brain, expression of TIMP-1 is restricted to the hippocampus, olfactory bulb, and cerebellum [170]. TIMP-2 is the most common tissue inhibitor and is expressed in most of the organs and tissues. TIMP-3 is expressed in many tissues and especially in the basement membranes of the eye and kidney. TIMP-4 is relatively restricted in the heart, kidney, ovary, pancreas, colon, testes, brain, and adipose tissue [171].

Plenty of exogenous synthetic inhibitors of MMP (MMPIs) have been developed and most of them were formulated by incorporating zinc-binding globulin (ZBG). ZGBs inactivate MMPs by displacing zinc-bound water molecule [172]. Classically, MMPIs include hydroxamic acids (ZBG1), carboxylates (ZBG2), thiols, and phosphonic acids (phosphorus-based ZBGs). Most of the first-generation MMPIs are broad spectrum inhibitors with nontargeted effects. Attempts are ongoing regarding the development of active site-directed MMPIs with high specificity. Apart from these, there are natural MMP inhibitors derived from various resources such as herbs, plants, fruits, and other agriculture products. These natural MMP inhibitors include long chain fatty acids, epigallocatechin gallate (EGCG) and other polyphenols, flavonoids, and a variety of other natural compounds. A detailed account of the various classes of MMPs and their chemical structure and effects was reviewed by several authors [167, 173].

MMPs as Therapeutic Targets

Regulation of MMPs is generally considered as an ideal target for developing therapeutic strategies against various diseases and disorders including brain injuries because of their role in mediating pathophysiology. Experimental lines of evidence suggested that MMP inhibition can be an effective strategy to treat such diseases. MMP inhibitor-mediated attenuation of brain edema resulting from the BBB disruption during postsurgical brain injury by using MMP inhibitor has been reported by several investigators [112, 174]. Lines of evidence on the involvement of MMP-2 and MMP-9 on various neurovascular complications including TBI persuaded to target these MMPs to develop a successful therapeutic strategy. MMP-2 inhibition reversed sepsis-induced BBB permeability and reduced brain inflammation and oxidative damage in an animal model of sepsis [175]. Similarly, treatment with MMP-9 and MMP-2 inhibitors and dual MMP-2 and MMP-9 inhibitor could prevent BBB breakdown in Wistar rats subjected to pneumococcal meningitis [176]. A competitive, mechanism-based dual inhibitor of MMP-2 and MMP-9, SB-3CT,

successfully attenuated MMP-9 activity, reduced brain lesion volumes, and prevented neuronal loss and dendritic degeneration in an experimental mouse model of TBI [177]. A novel MMP inhibitor (Ro 28-2653) inhibits MT1-MMP (also known as MMP-14), MT3-MMP (also known as MMP-16), MMP-2, MMP-8, and MMP-9 and significantly reduced brain injury when administered in the first 2 days after focal cerebral ischemia [178]. The available animal data has shown that therapeutic MMP inhibition in acute brain injury and stroke has considerable potential [179]. Despite these promising results supporting MMP-based clinical trials, it is imperative to consider the apparent positive effects of MMP; both MMP-9 and MMP-2 are thought to be involved in repair and regeneration after nervous system injury [180]. Furthermore, the availability of a suitable noninvasive method of drug delivery through the BBB remains as a challenge for undertaking a successful MMP inhibitor-based clinical trial against brain injury and other disorders.

Although the use of pharmacological inhibitors against MMP seems a straightforward approach, there is only limited clinical success achieved so far. Regarding the clinical trials of MMP inhibitors, most of the attempts were carried out in the area of cancer therapy. Despite the fact that a number of preclinical data support the application of MMP inhibitors as anticancer drugs, all of these trials failed [179]. Failure of first-generation MMP inhibitors diminishes enthusiasm for MMP inhibitor-based drugs. Regardless of these disappointments, investigations on inhibiting MMP activity is still a rational therapeutic approach, particularly for inflammatory disorders in which MMPs often activate the signaling cascades leading to inflammation [181]. Several reasons are highlighted for the failure of clinical trials including poor knowledge of the complexity of MMP function, nonspecificity, and instability of inhibitors used. Broad spectrum MMP inhibitors like hydroxamate-based inhibitors are useful in a way because of their nontargeted undesirable effects. Investigating the precise isoform of MMP associated with specific pathological condition and spatiotemporal expression and functional diversity of the particular MMP involved is important in the design and development of highly specific inhibitors against the crucial MMP target.

Apart from the use of inhibitors, antibody-based biotherapy is also found to be promising as it can assure more selectivity and potency [182]. Devy et al. have identified a highly selective antibody-based MMP inhibitor (DX-2400) against MMP-14, which displays anti-invasive, antitumor, and antiangiogenic properties and blocks pro-MMP-2 processing and was suggested for breast cancer patients [183, 184]. The use of functional blocking antibodies often enables inhibition of specific functions of the MMP rather than their general proteolytic activity [179]. REGA-3G12 is a monoclonal antibody developed as a selective inhibitor against MMP-9 that specifically targets the catalytic domain, but the fibronectin or zinc-binding domains remain unaffected by it [182]. Similarly, the mouse 9E8 monoclonal antibody targets only the MMP-2 activating function of cellular MT1-MMP rather than the general proteolytic activity of this MMP [185].

Reestablishing the delicate normal balance between MMPs and their endogenous inhibitors to recoup the optimum MMP activity for normal physiological processes is another approach. Despite the disappointments from the clinical trials of first-generation MMP inhibitors, researchers are still hoping in the rise of MMP inhibition as a therapeutic approach by including more specific and precise inhibitory methods. Strategic upregulation of natural inhibitors, development of peptide inhibitors including functional blocking antibodies, optimization of available MMP inhibitors, and development of highly specific and stable pharmacological inhibitors with minimal adverse effects are the goals of future MMP-targeted therapeutic trials. Third-generation and highly specific MMP inhibitors designed to block only the target MMPs are currently being evaluated [186].

Conclusion and Perspectives

MMPs play significant roles in various physiological processes primarily through their effects on ECM remodeling. However, their elevated levels and activities are largely associated with several neurological complications that include neurovascular dysfunction, hemorrhage, neuroinflammation, neurodegeneration, and impairment in angiogenesis and neurogenesis. The current review focused mainly on the role of MMPs in accomplishing the specific pathophysiology of TBI. Among the different types of MMPs studied so far, gelatinases (MMP-2 and MMP-9) are highly referred by associating with various neurological complications including TBI. Our previous findings on the augmented levels and activities of MMP-2, MMP-3, and MMP-9 in blast-injured rats and the critical roles of MMPs in various neuronal signaling mechanisms reported by several other investigations persuade us to undertake a more comprehensive study in this topic. A detailed study will delineate the molecular aspects of MMP regulation in post-TBI including the potential epigenetic changes that can bring about rapid modulation in the MMP levels and activities. By exploring the signaling mechanism that could regulate MMPs in TBI, we are anticipating the possibility of developing it as a valid therapeutic strategy against mTBI. The conventional therapeutic approaches using endogenous and synthetic MMP inhibitors are usually unsuccessful mainly due to the lack of efficacy and specificity or due to untoward side effects. Thus, gene therapy-based interventions seem more promising as they have the potential to ensure specificity and efficacy with minimum risk factors. We can accomplish this in two ways: either through the downregulation of MMPs or by the overexpression of TIMPs after

deciphering the precise mechanisms of MMP regulation in mTBI. Since MMPs are indispensable in various normal physiological processes, regulatory strategies need to be adopted in a highly judicious manner.

Acknowledgments The authors gratefully acknowledge the financial support by the US Department of Army Materials and Medical Command under award number W81XWH-15-1-0303.

References

1. Nagase H, Woessner JF Jr (1999) Matrix metalloproteinases. J Biol Chem 274:21491–21494
2. Yong VW (2005) Metalloproteinases: mediators of pathology and regeneration in the CNS. Nat Rev Neurosci 6:931–944
3. Sternlicht MD, Werb Z (2001) How matrix metalloproteinases regulate cell behavior. Annu Rev Cell Dev Biol 17:463–516
4. Engel CK, Pirard B, Schimanski S, Kirsch R, Habermann J, Klingler O, Schlotte V, Weithmann KU et al (2005) Structural basis for the highly selective inhibition of MMP-13. Chem Biol 12:181–189
5. Visse R, Nagase H (2003) Matrix metalloproteinases and tissue inhibitors of metalloproteinases: structure, function, and biochemistry. Circ Res 92:827–839
6. Wang X, Mori T, Jung JC, Fini ME, Lo EH (2002) Secretion of matrix metalloproteinase-2 and -9 after mechanical trauma injury in rat cortical cultures and involvement of MAP kinase. J Neurotrauma 19:615–625
7. Wang X, Jung J, Asahi M, Chwang W, Russo L, Moskowitz MA, Dixon CE, Fini ME et al (2000) Effects of matrix metalloproteinase-9 gene knock-out on morphological and motor outcomes after traumatic brain injury. J Neurosci 20:7037–7042
8. Teasdale G, Jennett B (1974) Assessment of coma and impaired consciousness. A practical scale. Lancet 2:81–84
9. Maas AI, Stocchetti N, Bullock R (2008) Moderate and severe traumatic brain injury in adults. Lancet Neurol 7:728–741
10. Lotocki G, de Rivero Vaccari JP, Perez ER, Sanchez-Molano J, Furones-Alonso O, Bramlett HM et al (2009) Alterations in blood-brain barrier permeability to large and small molecules and leukocyte accumulation after traumatic brain injury: effects of post-traumatic hypothermia. J Neurotrauma 26:1123–1134
11. Pun PB, Lu J, Moochhala S (2009) Involvement of ROS in BBB dysfunction. Free Radic Res 43:348–364
12. Toklu HZ, Hakan T, Biber N, Solakoglu S, Ogunc AV, Sener G (2009) The protective effect of alpha lipoic acid against traumatic brain injury in rats. Free Radic Res 43:658–667
13. Nagase H, Visse R, Murphy G (2006) Structure and function of matrix metalloproteinases and TIMPs. Cardiovasc Res 69:562–573
14. Agnihotri R, Crawford HC, Haro H, Matrisian LM, Havrda MC, Liaw L (2001) Osteopontin, a novel substrate for matrix metalloproteinase-3 (stromelysin-1) and matrix metalloproteinase-7 (matrilysin). J Biol Chem 276:28261–28267
15. Wilson CL, Matrisian LM (1996) Matrilysin: an epithelial matrix metalloproteinase with potentially novel functions. Int J Biochem Cell Biol 28:123–136
16. Hernandez-Barrantes S, Bernardo M, Toth M, Fridman R (2002) Regulation of membrane type-matrix metalloproteinases. Semin Cancer Biol 12:131–138
17. Holmbeck K, Bianco P, Caterina J, Yamada S, Kromer M, Kuznetsov SA, Mankani M, Robey PG et al (1999) MT1-MMP-deficient mice develop dwarfism, osteopenia, arthritis, and connective tissue disease due to inadequate collagen turnover. Cell 99:81–92
18. Brew K, Dinakarpandian D, Nagase H (2000) Tissue inhibitors of metalloproteinases: evolution, structure and function. Biochim Biophys Acta 1477:267–283
19. Horstmann S, Su Y, Koziol J, Meyding-Lamade U, Nagel S, Wagner S (2006) MMP-2 and MMP-9 levels in peripheral blood after subarachnoid hemorrhage. J Neurol Sci 251:82–86
20. Wang X, Lo EH (2003) Triggers and mediators of hemorrhagic transformation in cerebral ischemia. Mol Neurobiol 28:229–244
21. Romanic AM, White RF, Arleth AJ, Ohlstein EH, Barone FC (1998) Matrix metalloproteinase expression increases after cerebral focal ischemia in rats: inhibition of matrix metalloproteinase-9 reduces infarct size. Stroke 29:1020–1030
22. Lo EH, Wang X, Cuzner ML (2002) Extracellular proteolysis in brain injury and inflammation: role for plasminogen activators and matrix metalloproteinases. J Neurosci Res 69:1–9
23. Yong VW, Power C, Forsyth P, Edwards DR (2001) Metalloproteinases in biology and pathology of the nervous system. Nat Rev Neurosci 2:502–511
24. Rosenberg GA (2002) Matrix metalloproteinases in neuroinflammation. Glia 39:279–291
25. Haorah J, Ramirez SH, Schall K, Smith D, Pandya R, Persidsky Y (2007) Oxidative stress activates protein tyrosine kinase and matrix metalloproteinases leading to blood-brain barrier dysfunction. J Neurochem 101:566–576
26. Hsieh HL, Wang HH, Wu WB, Chu PJ, Yang CM (2010) Transforming growth factor-beta1 induces matrix metalloproteinase-9 and cell migration in astrocytes: roles of ROS-dependent ERK- and JNK-NF-kappaB pathways. J Neuroinflammation 7:88
27. Yang Y, Estrada EY, Thompson JF, Liu W, Rosenberg GA (2007) Matrix metalloproteinase-mediated disruption of tight junction proteins in cerebral vessels is reversed by synthetic matrix metalloproteinase inhibitor in focal ischemia in rat. J Cereb Blood Flow Metab 27:697–709
28. Rosenberg GA, Cunningham LA, Wallace J, Alexander S, Estrada EY, Grossetete M et al (2001) Immunohistochemistry of matrix metalloproteinases in reperfusion injury to rat brain: activation of MMP-9 linked to stromelysin-1 and microglia in cell cultures. Brain Res 893:104–112
29. Abdul Muneer PM, Alikunju S, Szlachetka AM, Haorah J (2012) The mechanisms of cerebral vascular dysfunction and neuroinflammation by MMP-mediated degradation of VEGFR-2 in alcohol ingestion. Arterioscler Thromb Vasc Biol 32:1167–1177
30. Svedin P, Hagberg H, Savman K, Zhu C, Mallard C (2007) Matrix metalloproteinase-9 gene knock-out protects the immature brain after cerebral hypoxia-ischemia. J Neurosci 27:1511–1518
31. Van Lint P, Libert C (2007) Chemokine and cytokine processing by matrix metalloproteinases and its effect on leukocyte migration and inflammation. J Leukoc Biol 82:1375–1381
32. Abdul-Muneer PM, Schuetz H, Wang F, Skotak M, Jones J, Gorantla S, Zimmerman MC, Chandra N et al (2013) Induction of oxidative and nitrosative damage leads to cerebrovascular inflammation in an animal model of mild traumatic brain injury induced by primary blast. Free Radic Biol Med 60:282–291
33. Hayashi T, Kaneko Y, Yu S, Bae E, Stahl CE, Kawase T, van Loveren H, Sanberg PR et al (2009) Quantitative analyses of matrix metalloproteinase activity after traumatic brain injury in adult rats. Brain Res 1280:172–177
34. Tejima E, Guo S, Murata Y, Arai K, Lok J, van Leyen K, Rosell A, Wang X et al (2009) Neuroprotective effects of overexpressing tissue inhibitor of metalloproteinase TIMP-1. J Neurotrauma 26:1935–1941
35. Higashida T, Kreipke CW, Rafols JA, Peng C, Schafer S, Schafer P, Ding JY, Dornbos D 3rd et al (2011) The role of hypoxia-

inducible factor-1alpha, aquaporin-4, and matrix metalloproteinase-9 in blood-brain barrier disruption and brain edema after traumatic brain injury. J Neurosurg 114:92–101
36. Holmin S, Soderlund J, Biberfeld P, Mathiesen T (1998) Intracerebral inflammation after human brain contusion. Neurosurgery 42:291–298, discussion 298-299
37. Wang J, Rogove AD, Tsirka AE, Tsirka SE (2003) Protective role of tuftsin fragment 1-3 in an animal model of intracerebral hemorrhage. Ann Neurol 54:655–664
38. Wang J, Tsirka SE (2005) Tuftsin fragment 1-3 is beneficial when delivered after the induction of intracerebral hemorrhage. Stroke 36:613–618
39. Rosenberg GA, Navratil M (1997) Metalloproteinase inhibition blocks edema in intracerebral hemorrhage in the rat. Neurology 48:921–926
40. Gasche Y, Fujimura M, Morita-Fujimura Y, Copin JC, Kawase M, Massengale J, Chan PH (1999) Early appearance of activated matrix metalloproteinase-9 after focal cerebral ischemia in mice: a possible role in blood-brain barrier dysfunction. J Cereb Blood Flow Metab 19:1020–1028
41. Lakhan SE, Kirchgessner A, Tepper D, Leonard A (2013) Matrix metalloproteinases and blood-brain barrier disruption in acute ischemic stroke. Front Neurol 4:32
42. Shetty AK, Mishra V, Kodali M, Hattiangady B (2014) Blood brain barrier dysfunction and delayed neurological deficits in mild traumatic brain injury induced by blast shock waves. Front Cell Neurosci 8:232
43. Asahi M, Wang X, Mori T, Sumii T, Jung JC, Moskowitz MA, Fini ME, Lo EH (2001) Effects of matrix metalloproteinase-9 gene knock-out on the proteolysis of blood-brain barrier and white matter components after cerebral ischemia. J Neurosci 21:7724–7732
44. Barr TL, Latour LL, Lee KY, Schaewe TJ, Luby M, Chang GS, El-Zammar Z, Alam S et al (2010) Blood-brain barrier disruption in humans is independently associated with increased matrix metalloproteinase-9. Stroke 41:e123–128
45. Adamski MG, Golenia A, Turaj W, Baird AE, Moskala M, Dziedzic T, Szczudlik A, Slowik A et al (2014) The AGTR1 gene A1166C polymorphism as a risk factor and outcome predictor of primary intracerebral and aneurysmal subarachnoid hemorrhages. Neurol Neurochir Pol 48:242–247
46. Jusufovic M, Sandset EC, Bath PM, Berge E, Scandinavian Candesartan Acute Stroke Trial Study G (2014) Blood pressure-lowering treatment with candesartan in patients with acute hemorrhagic stroke. Stroke 45:3440–3442
47. Villapol S, Saavedra JM (2015) Neuroprotective effects of angiotensin receptor blockers. Am J Hypertens 28:289–299
48. El Bekay R, Alvarez M, Monteseirin J, Alba G, Chacon P, Vega A, Martin-Nieto J, Jimenez J et al (2003) Oxidative stress is a critical mediator of the angiotensin II signal in human neutrophils: involvement of mitogen-activated protein kinase, calcineurin, and the transcription factor NF-kappaB. Blood 102:662–671
49. Oudit GY, Kassiri Z, Patel MP, Chappell M, Butany J, Backx PH, Tsushima RG, Scholey JW et al (2007) Angiotensin II-mediated oxidative stress and inflammation mediate the age-dependent cardiomyopathy in ACE2 null mice. Cardiovasc Res 75:29–39
50. Landmesser U, Spiekermann S, Preuss C, Sorrentino S, Fischer D, Manes C, Mueller M, Drexler H (2007) Angiotensin II induces endothelial xanthine oxidase activation: role for endothelial dysfunction in patients with coronary disease. Arterioscler Thromb Vasc Biol 27:943–948
51. Wang HD, Xu S, Johns DG, Du Y, Quinn MT, Cayatte AJ, Cohen RA (2001) Role of NADPH oxidase in the vascular hypertrophic and oxidative stress response to angiotensin II in mice. Circ Res 88:947–953
52. Tan Y, Li X, Prabhu SD, Brittian KR, Chen Q, Yin X, McClain CJ, Zhou Z et al (2012) Angiotensin II plays a critical role in alcohol-induced cardiac nitrative damage, cell death, remodeling, and cardiomyopathy in a protein kinase C/nicotinamide adenine dinucleotide phosphate oxidase-dependent manner. J Am Coll Cardiol 59:1477–1486
53. Griendling KK, Minieri CA, Ollerenshaw JD, Alexander RW (1994) Angiotensin II stimulates NADH and NADPH oxidase activity in cultured vascular smooth muscle cells. Circ Res 74:1141–1148
54. Rajagopalan S, Kurz S, Munzel T, Tarpey M, Freeman BA, Griendling KK, Harrison DG (1996) Angiotensin II-mediated hypertension in the rat increases vascular superoxide production via membrane NADH/NADPH oxidase activation. Contribution to alterations of vasomotor tone. J Clin Invest 97:1916–1923
55. Mollnau H, Wendt M, Szocs K, Lassegue B, Schulz E, Oelze M, Li H, Bodenschatz M et al (2002) Effects of angiotensin II infusion on the expression and function of NAD(P)H oxidase and components of nitric oxide/cGMP signaling. Circ Res 90:E58–65
56. Rueckschloss U, Quinn MT, Holtz J, Morawietz H (2002) Dose-dependent regulation of NAD(P)H oxidase expression by angiotensin II in human endothelial cells: protective effect of angiotensin II type 1 receptor blockade in patients with coronary artery disease. Arterioscler Thromb Vasc Biol 22:1845–1851
57. Landmesser U, Cai H, Dikalov S, McCann L, Hwang J, Jo H, Holland SM, Harrison DG (2002) Role of p47(phox) in vascular oxidative stress and hypertension caused by angiotensin II. Hypertension 40:511–515
58. Rosell A, Ortega-Aznar A, Alvarez-Sabin J, Fernandez-Cadenas I, Ribo M, Molina CA, Lo EH, Montaner J (2006) Increased brain expression of matrix metalloproteinase-9 after ischemic and hemorrhagic human stroke. Stroke 37:1399–1406
59. Alikunju S, Abdul Muneer PM, Zhang Y, Szlachetka AM, Haorah J (2011) The inflammatory footprints of alcohol-induced oxidative damage in neurovascular components. Brain Behav Immun 25(Suppl 1):S129–136
60. Gursoy-Ozdemir Y, Can A, Dalkara T (2004) Reperfusion-induced oxidative/nitrative injury to neurovascular unit after focal cerebral ischemia. Stroke 35:1449–1453
61. Rosell A, Alvarez-Sabin J, Arenillas JF, Rovira A, Delgado P, Fernandez-Cadenas I, Penalba A, Molina CA et al (2005) A matrix metalloproteinase protein array reveals a strong relation between MMP-9 and MMP-13 with diffusion-weighted image lesion increase in human stroke. Stroke 36:1415–1420
62. Risau W, Flamme I (1995) Vasculogenesis. Annu Rev Cell Dev Biol 11:73–91
63. Egeblad M, Werb Z (2002) New functions for the matrix metalloproteinases in cancer progression. Nat Rev Cancer 2:161–174
64. van Hinsbergh VW, Engelse MA, Quax PH (2006) Pericellular proteases in angiogenesis and vasculogenesis. Arterioscler Thromb Vasc Biol 26:716–728
65. Menzel-Severing J (2012) Emerging techniques to treat corneal neovascularisation. Eye (Lond) 26:2–12
66. Hiraoka N, Allen E, Apel IJ, Gyetko MR, Weiss SJ (1998) Matrix metalloproteinases regulate neovascularization by acting as pericellular fibrinolysins. Cell 95:365–377
67. Benelli R, Adatia R, Ensoli B, Stetler-Stevenson WG, Santi L, Albini A (1994) Inhibition of AIDS-Kaposi's sarcoma cell induced endothelial cell invasion by TIMP-2 and a synthetic peptide from the metalloproteinase propeptide: implications for an anti-angiogenic therapy. Oncol Res 6:251–257
68. Murphy AN, Unsworth EJ, Stetler-Stevenson WG (1993) Tissue inhibitor of metalloproteinases-2 inhibits bFGF-induced human microvascular endothelial cell proliferation. J Cell Physiol 157:351–358

69. Vu TH, Shipley JM, Bergers G, Berger JE, Helms JA, Hanahan D, Shapiro SD, Senior RM et al (1998) MMP-9/gelatinase B is a key regulator of growth plate angiogenesis and apoptosis of hypertrophic chondrocytes. Cell 93:411–422
70. Itoh T, Tanioka M, Yoshida H, Yoshioka T, Nishimoto H, Itohara S (1998) Reduced angiogenesis and tumor progression in gelatinase A-deficient mice. Cancer Res 58:1048–1051
71. Carmeliet P (2005) Angiogenesis in life, disease and medicine. Nature 438:932–936
72. Millauer B, Wizigmann-Voos S, Schnurch H, Martinez R, Moller NP, Risau W, Ullrich A (1993) High affinity VEGF binding and developmental expression suggest Flk-1 as a major regulator of vasculogenesis and angiogenesis. Cell 72:835–846
73. Shalaby F, Rossant J, Yamaguchi TP, Gertsenstein M, Wu XF, Breitman ML, Schuh AC (1995) Failure of blood-island formation and vasculogenesis in Flk-1-deficient mice. Nature 376:62–66
74. Morgan R, Kreipke CW, Roberts G, Bagchi M, Rafols JA (2007) Neovascularization following traumatic brain injury: possible evidence for both angiogenesis and vasculogenesis. Neurol Res 29: 375–381
75. Valable S, Montaner J, Bellail A, Berezowski V, Brillault J, Cecchelli R, Divoux D, Mackenzie ET et al (2005) VEGF-induced BBB permeability is associated with an MMP-9 activity increase in cerebral ischemia: both effects decreased by Ang-1. J Cereb Blood Flow Metab 25:1491–1504
76. Turk BE, Huang LL, Piro ET, Cantley LC (2001) Determination of protease cleavage site motifs using mixture-based oriented peptide libraries. Nat Biotechnol 19:661–667
77. Tran ED, DeLano FA, Schmid-Schonbein GW (2010) Enhanced matrix metalloproteinase activity in the spontaneously hypertensive rat: VEGFR-2 cleavage, endothelial apoptosis, and capillary rarefaction. J Vasc Res 47:423–431
78. Lee C, Agoston DV (2009) Inhibition of VEGF receptor 2 increased cell death of dentate hilar neurons after traumatic brain injury. Exp Neurol 220:400–403
79. Levin HS, Mattis S, Ruff RM, Eisenberg HM, Marshall LF, Tabaddor K, High WM Jr, Frankowski RF (1987) Neurobehavioral outcome following minor head injury: a three-center study. J Neurosurg 66:234–243
80. Garcia de Yebenes E, Ho A, Damani T, Fillit H, Blum M (1999) Regulation of the heparan sulfate proteoglycan, perlecan, by injury and interleukin-1alpha. J Neurochem 73:812–820
81. Oh LY, Larsen PH, Krekoski CA, Edwards DR, Donovan F, Werb Z, Yong VW (1999) Matrix metalloproteinase-9/gelatinase B is required for process outgrowth by oligodendrocytes. J Neurosci 19:8464–8475
82. Phillips LL, Reeves TM (2001) Interactive pathology following traumatic brain injury modifies hippocampal plasticity. Restor Neurol Neurosci 19:213–235
83. Szklarczyk A, Lapinska J, Rylski M, McKay RD, Kaczmarek L (2002) Matrix metalloproteinase-9 undergoes expression and activation during dendritic remodeling in adult hippocampus. J Neurosci 22:920–930
84. Muir EM, Adcock KH, Morgenstern DA, Clayton R, von Stillfried N, Rhodes K, Ellis C, Fawcett JW et al (2002) Matrix metalloproteases and their inhibitors are produced by overlapping populations of activated astrocytes. Brain Res Mol Brain Res 100: 103–117
85. Dityatev A, Schachner M (2003) Extracellular matrix molecules and synaptic plasticity. Nat Rev Neurosci 4:456–468
86. Kim HJ, Fillmore HL, Reeves TM, Phillips LL (2005) Elevation of hippocampal MMP-3 expression and activity during trauma-induced synaptogenesis. Exp Neurol 192:60–72
87. Nelson RB, Linden DJ, Hyman C, Pfenninger KH, Routtenberg A (1989) The two major phosphoproteins in growth cones are probably identical to two protein kinase C substrates correlated with persistence of long-term potentiation. J Neurosci 9:381–389
88. Sheffield JB, Krasnopolsky V, Dehlinger E (1994) Inhibition of retinal growth cone activity by specific metalloproteinase inhibitors in vitro. Dev Dyn 200:79–88
89. Uhm JH, Dooley NP, Oh LY, Yong VW (1998) Oligodendrocytes utilize a matrix metalloproteinase, MMP-9, to extend processes along an astrocyte extracellular matrix. Glia 22:53–63
90. Vaillant C, Didier-Bazes M, Hutter A, Belin MF, Thomasset N (1999) Spatiotemporal expression patterns of metalloproteinases and their inhibitors in the postnatal developing rat cerebellum. J Neurosci 19:4994–5004
91. Mayer J, Hamel MG, Gottschall PE (2005) Evidence for proteolytic cleavage of brevican by the ADAMTSs in the dentate gyrus after excitotoxic lesion of the mouse entorhinal cortex. BMC Neurosci 6:52
92. Brodkey JA, Laywell ED, O'Brien TF, Faissner A, Stefansson K, Dorries HU, Schachner M, Steindler DA (1995) Focal brain injury and upregulation of a developmentally regulated extracellular matrix protein. J Neurosurg 82:106–112
93. Yuan W, Matthews RT, Sandy JD, Gottschall PE (2002) Association between protease-specific proteolytic cleavage of brevican and synaptic loss in the dentate gyrus of kainate-treated rats. Neuroscience 114:1091–1101
94. Bejarano PA, Noelken ME, Suzuki K, Hudson BG, Nagase H (1988) Degradation of basement membranes by human matrix metalloproteinase 3 (stromelysin). Biochem J 256:413–419
95. Imai K, Yokohama Y, Nakanishi I, Ohuchi E, Fujii Y, Nakai N, Okada Y (1995) Matrix metalloproteinase 7 (matrilysin) from human rectal carcinoma cells. Activation of the precursor, interaction with other matrix metalloproteinases and enzymic properties. J Biol Chem 270:6691–6697
96. Okada Y, Nagase H, Harris ED Jr (1987) Matrix metalloproteinases 1, 2, and 3 from rheumatoid synovial cells are sufficient to destroy joints. J Rheumatol 14 Spec No:41–42
97. VanSaun M, Werle MJ (2000) Matrix metalloproteinase-3 removes agrin from synaptic basal lamina. J Neurobiol 44:369
98. Falo MC, Reeves TM, Phillips LL (2008) Agrin expression during synaptogenesis induced by traumatic brain injury. J Neurotrauma 25:769–783
99. Abdul-Muneer PM, Chandra N, Haorah J (2015) Interactions of oxidative stress and neurovascular inflammation in the pathogenesis of traumatic brain injury. Mol Neurobiol 51:966–979
100. Stawarski M, Rutkowska-Wlodarczyk I, Zeug A, Bijata M, Madej H, Kaczmarek L, Wlodarczyk J (2014) Genetically encoded FRET-based biosensor for imaging MMP-9 activity. Biomaterials 35:1402–1410
101. Warren KM, Reeves TM, Phillips LL (2012) MT5-MMP, ADAM-10, and N-cadherin act in concert to facilitate synapse reorganization after traumatic brain injury. J Neurotrauma 29:1922–1940
102. Kamat PK, Swarnkar S, Rai S, Kumar V, Tyagi N (2014) Astrocyte mediated MMP-9 activation in the synapse dysfunction: an implication in Alzheimer disease. Ther Targets Neurol Dis 1
103. Phillips LL, Chan JL, Doperalski AE, Reeves TM (2014) Time dependent integration of matrix metalloproteinases and their targeted substrates directs axonal sprouting and synaptogenesis following central nervous system injury. Neural Regen Res 9: 362–376
104. Heuser K, Hoddevik EH, Tauboll E, Gjerstad L, Indahl U, Kaczmarek L, Berg PR, Lien S et al (2010) Temporal lobe epilepsy and matrix metalloproteinase 9: a tempting relation but negative genetic association. Seizure 19:335–338
105. Michaluk P, Kolodziej L, Mioduszewska B, Wilczynski GM, Dzwonek J, Jaworski J, Gorecki DC, Ottersen OP et al (2007)

Beta-dystroglycan as a target for MMP-9, in response to enhanced neuronal activity. J Biol Chem 282:16036–16041
106. Marmarou A (2003) Pathophysiology of traumatic brain edema: current concepts. Acta Neurochir Suppl 86:7–10
107. Klatzo I (1987) Pathophysiological aspects of brain edema. Acta Neuropathol 72:236–239
108. Donkin JJ, Vink R (2010) Mechanisms of cerebral edema in traumatic brain injury: therapeutic developments. Curr Opin Neurol 23:293–299
109. Barzo P, Marmarou A, Fatouros P, Hayasaki K, Corwin F (1997) Contribution of vasogenic and cellular edema to traumatic brain swelling measured by diffusion-weighted imaging. J Neurosurg 87:900–907
110. Unterberg AW, Stroop R, Thomale UW, Kiening KL, Pauser S, Vollmann W (1997) Characterisation of brain edema following "controlled cortical impact injury" in rats. Acta Neurochir Suppl 70:106–108
111. Candelario-Jalil E, Yang Y, Rosenberg GA (2009) Diverse roles of matrix metalloproteinases and tissue inhibitors of metalloproteinases in neuroinflammation and cerebral ischemia. Neuroscience 158:983–994
112. Jadhav V, Yamaguchi M, Obenaus A, Zhang JH (2008) Matrix metalloproteinase inhibition attenuates brain edema after surgical brain injury. Acta Neurochir Suppl 102:357–361
113. Papadopoulos MC, Verkman AS (2008) Potential utility of aquaporin modulators for therapy of brain disorders. Prog Brain Res 170:589–601
114. Qiu B, Li X, Sun X, Wang Y, Jing Z, Zhang X, Wang Y (2014) Overexpression of aquaporin1 aggravates hippocampal damage in mouse traumatic brain injury models. Mol Med Rep 9:916–922
115. Ding JY, Kreipke CW, Speirs SL, Schafer P, Schafer S, Rafols JA (2009) Hypoxia-inducible factor-1alpha signaling in aquaporin upregulation after traumatic brain injury. Neurosci Lett 453:68–72
116. Manley GT, Fujimura M, Ma T, Noshita N, Filiz F, Bollen AW, Chan P, Verkman AS (2000) Aquaporin-4 deletion in mice reduces brain edema after acute water intoxication and ischemic stroke. Nat Med 6:159–163
117. Fazzina G, Amorini AM, Marmarou CR, Fukui S, Okuno K, Dunbar JG, Glisson R, Marmarou A et al (2010) The protein kinase C activator phorbol myristate acetate decreases brain edema by aquaporin 4 downregulation after middle cerebral artery occlusion in the rat. J Neurotrauma 27:453–461
118. Taya K, Gulsen S, Okuno K, Prieto R, Marmarou CR, Marmarou A (2008) Modulation of AQP4 expression by the selective V1a receptor antagonist, SR49059, decreases trauma-induced brain edema. Acta Neurochir Suppl 102:425–429
119. Agre P, Kozono D (2003) Aquaporin water channels: molecular mechanisms for human diseases. FEBS Lett 555:72–78
120. Pasantes-Morales H, Cruz-Rangel S (2010) Brain volume regulation: osmolytes and aquaporin perspectives. Neuroscience 168: 871–884
121. Nicchia GP, Nico B, Camassa LM, Mola MG, Loh N, Dermietzel R, Spray DC, Svelto M et al (2004) The role of aquaporin-4 in the blood-brain barrier development and integrity: studies in animal and cell culture models. Neuroscience 129:935–945
122. Fukuda AM, Badaut J (2012) Aquaporin 4: a player in cerebral edema and neuroinflammation. J Neuroinflammation 9:279
123. Yong VW, Krekoski CA, Forsyth PA, Bell R, Edwards DR (1998) Matrix metalloproteinases and diseases of the CNS. Trends Neurosci 21:75–80
124. Hartung HP, Kieseier BC (2000) The role of matrix metalloproteinases in autoimmune damage to the central and peripheral nervous system. J Neuroimmunol 107:140–147
125. Asahi M, Asahi K, Jung JC, del Zoppo GJ, Fini ME, Lo EH (2000) Role for matrix metalloproteinase 9 after focal cerebral ischemia: effects of gene knockout and enzyme inhibition with BB-94. J Cereb Blood Flow Metab 20:1681–1689
126. Manicone AM, McGuire JK (2008) Matrix metalloproteinases as modulators of inflammation. Semin Cell Dev Biol 19:34–41
127. Hu J, Van den Steen PE, Sang QX, Opdenakker G (2007) Matrix metalloproteinase inhibitors as therapy for inflammatory and vascular diseases. Nat Rev Drug Discov 6:480–498
128. Konnecke H, Bechmann I (2013) The role of microglia and matrix metalloproteinases involvement in neuroinflammation and gliomas. Clin Dev Immunol 2013:914104
129. Allan SM, Tyrrell PJ, Rothwell NJ (2005) Interleukin-1 and neuronal injury. Nat Rev Immunol 5:629–640
130. Schmidt JA (1984) Purification and partial biochemical characterization of normal human interleukin 1. J Exp Med 160:772–787
131. Thornberry NA, Bull HG, Calaycay JR, Chapman KT, Howard AD, Kostura MJ, Miller DK, Molineaux SM et al (1992) A novel heterodimeric cysteine protease is required for interleukin-1 beta processing in monocytes. Nature 356:768–774
132. Nylander-Lundqvist E, Back O, Egelrud T (1996) IL-1 beta activation in human epidermis. J Immunol 157:1699–1704
133. Fantuzzi G, Ku G, Harding MW, Livingston DJ, Sipe JD, Kuida K, Flavell RA, Dinarello CA (1997) Response to local inflammation of IL-1 beta-converting enzyme-deficient mice. J Immunol 158:1818–1824
134. Ito A, Mukaiyama A, Itoh Y, Nagase H, Thogersen IB, Enghild JJ, Sasaguri Y, Mori Y (1996) Degradation of interleukin 1beta by matrix metalloproteinases. J Biol Chem 271:14657–14660
135. Schonbeck U, Mach F, Libby P (1998) Generation of biologically active IL-1 beta by matrix metalloproteinases: a novel caspase-1-independent pathway of IL-1 beta processing. J Immunol 161: 3340–3346
136. Gottschall PE, Yu X (1995) Cytokines regulate gelatinase A and B (matrix metalloproteinase 2 and 9) activity in cultured rat astrocytes. J Neurochem 64:1513–1520
137. Gidday JM, Gasche YG, Copin JC, Shah AR, Perez RS, Shapiro SD, Chan PH, Park TS (2005) Leukocyte-derived matrix metalloproteinase-9 mediates blood-brain barrier breakdown and is proinflammatory after transient focal cerebral ischemia. Am J Physiol Heart Circ Physiol 289:H558–568
138. Suehiro E, Fujisawa H, Akimura T, Ishihara H, Kajiwara K, Kato S, Fujii M, Yamashita S et al (2004) Increased matrix metalloproteinase-9 in blood in association with activation of interleukin-6 after traumatic brain injury: influence of hypothermic therapy. J Neurotrauma 21:1706–1711
139. Mohan MJ, Seaton T, Mitchell J, Howe A, Blackburn K, Burkhart W, Moyer M, Patel I et al (2002) The tumor necrosis factor-alpha converting enzyme (TACE): a unique metalloproteinase with highly defined substrate selectivity. Biochemistry 41:9462–9469
140. Haro H, Crawford HC, Fingleton B, Shinomiya K, Spengler DM, Matrisian LM (2000) Matrix metalloproteinase-7-dependent release of tumor necrosis factor-alpha in a model of herniated disc resorption. J Clin Invest 105:143–150
141. Lohi J, Wilson CL, Roby JD, Parks WC (2001) Epilysin, a novel human matrix metalloproteinase (MMP-28) expressed in testis and keratinocytes and in response to injury. J Biol Chem 276: 10134–10144
142. Gearing AJ, Beckett P, Christodoulou M, Churchill M, Clements J, Davidson AH, Drummond AH, Galloway WA et al (1994) Processing of tumour necrosis factor-alpha precursor by metalloproteinases. Nature 370:555–557
143. English WR, Puente XS, Freije JM, Knauper V, Amour A, Merryweather A, Lopez-Otin C, Murphy G (2000) Membrane type 4 matrix metalloproteinase (MMP17) has tumor necrosis factor-alpha convertase activity but does not activate pro-MMP2. J Biol Chem 275:14046–14055

144. Xie X, Wu X, Cui J, Li H, Yan X (2013) Increase ICAM-1 and LFA-1 expression by cerebrospinal fluid of subarachnoid hemorrhage patients: involvement of TNF-alpha. Brain Res 1512:89–96
145. Lee IT, Lin CC, Wu YC, Yang CM (2010) TNF-alpha induces matrix metalloproteinase-9 expression in A549 cells: role of TNFR1/TRAF2/PKCalpha-dependent signaling pathways. J Cell Physiol 224:454–464
146. Flanders KC, Ren RF, Lippa CF (1998) Transforming growth factor-betas in neurodegenerative disease. Prog Neurobiol 54: 71–85
147. Massague J (2000) How cells read TGF-beta signals. Nat Rev Mol Cell Biol 1:169–178
148. Bottner M, Krieglstein K, Unsicker K (2000) The transforming growth factor-betas: structure, signaling, and roles in nervous system development and functions. J Neurochem 75:2227–2240
149. Rimaniol AC, Lekieffre D, Serrano A, Masson A, Benavides J, Zavala F (1995) Biphasic transforming growth factor-beta production flanking the pro-inflammatory cytokine response in cerebral trauma. Neuroreport 7:133–136
150. Morganti-Kossmann MC, Rancan M, Stahel PF, Kossmann T (2002) Inflammatory response in acute traumatic brain injury: a double-edged sword. Curr Opin Crit Care 8:101–105
151. Yu Q, Stamenkovic I (2000) Cell surface-localized matrix metalloproteinase-9 proteolytically activates TGF-beta and promotes tumor invasion and angiogenesis. Genes Dev 14:163–176
152. Mu D, Cambier S, Fjellbirkeland L, Baron JL, Munger JS, Kawakatsu H, Sheppard D, Broaddus VC et al (2002) The integrin alpha(v)beta8 mediates epithelial homeostasis through MT1-MMP-dependent activation of TGF-beta1. J Cell Biol 157:493–507
153. Han YP, Tuan TL, Hughes M, Wu H, Garner WL (2001) Transforming growth factor-beta- and tumor necrosis factor-alpha-mediated induction and proteolytic activation of MMP-9 in human skin. J Biol Chem 276:22341–22350
154. Gordon GM, Ledee DR, Feuer WJ, Fini ME (2009) Cytokines and signaling pathways regulating matrix metalloproteinase-9 (MMP-9) expression in corneal epithelial cells. J Cell Physiol 221:402–411
155. Thompson CB (1995) Apoptosis in the pathogenesis and treatment of disease. Science 267:1456–1462
156. Mannello F, Luchetti F, Falcieri E, Papa S (2005) Multiple roles of matrix metalloproteinases during apoptosis. Apoptosis 10:19–24
157. Zhang K, McQuibban GA, Silva C, Butler GS, Johnston JB, Holden J, Clark-Lewis I, Overall CM et al (2003) HIV-induced metalloproteinase processing of the chemokine stromal cell derived factor-1 causes neurodegeneration. Nat Neurosci 6:1064–1071
158. Copin JC, Goodyear MC, Gidday JM, Shah AR, Gascon E, Dayer A, Morel DM, Gasche Y (2005) Role of matrix metalloproteinases in apoptosis after transient focal cerebral ischemia in rats and mice. Eur J Neurosci 22:1597–1608
159. Kwan JA, Schulze CJ, Wang W, Leon H, Sariahmetoglu M, Sung M, Sawicka J, Sims DE et al (2004) Matrix metalloproteinase-2 (MMP-2) is present in the nucleus of cardiac myocytes and is capable of cleaving poly (ADP-ribose) polymerase (PARP) in vitro. FASEB J 18:690–692
160. Lee R, Kermani P, Teng KK, Hempstead BL (2001) Regulation of cell survival by secreted proneurotrophins. Science 294:1945–1948
161. Chintala SK, Zhang X, Austin JS, Fini ME (2002) Deficiency in matrix metalloproteinase gelatinase B (MMP-9) protects against retinal ganglion cell death after optic nerve ligation. J Biol Chem 277:47461–47468
162. Wang X, Lee SR, Arai K, Lee SR, Tsuji K, Rebeck GW, Lo EH (2003) Lipoprotein receptor-mediated induction of matrix metalloproteinase by tissue plasminogen activator. Nat Med 9: 1313–1317
163. Meerovitch K, Bergeron F, Leblond L, Grouix B, Poirier C, Bubenik M, Chan L, Gourdeau H et al (2003) A novel RGD antagonist that targets both alphavbeta3 and alpha5beta1 induces apoptosis of angiogenic endothelial cells on type I collagen. Vascul Pharmacol 40:77–89
164. Lee SR, Lo EH (2004) Induction of caspase-mediated cell death by matrix metalloproteinases in cerebral endothelial cells after hypoxia-reoxygenation. J Cereb Blood Flow Metab 24:720–727
165. Strand S, Vollmer P, van den Abeelen L, Gottfried D, Alla V, Heid H, Kuball J, Theobald M et al (2004) Cleavage of CD95 by matrix metalloproteinase-7 induces apoptosis resistance in tumour cells. Oncogene 23:3732–3736
166. Boulay A, Masson R, Chenard MP, El Fahime M, Cassard L, Bellocq JP, Sautes-Fridman C, Basset P et al (2001) High cancer cell death in syngeneic tumors developed in host mice deficient for the stromelysin-3 matrix metalloproteinase. Cancer Res 61:2189–2193
167. Sang QX, Jin Y, Newcomer RG, Monroe SC, Fang X, Hurst DR, Lee S, Cao Q et al (2006) Matrix metalloproteinase inhibitors as prospective agents for the prevention and treatment of cardiovascular and neoplastic diseases. Curr Top Med Chem 6:289–316
168. Will H, Atkinson SJ, Butler GS, Smith B, Murphy G (1996) The soluble catalytic domain of membrane type 1 matrix metalloproteinase cleaves the propeptide of progelatinase A and initiates autoproteolytic activation. Regulation by TIMP-2 and TIMP-3. J Biol Chem 271:17119–17123
169. Murphy G (2011) Tissue inhibitors of metalloproteinases. Genome Biol 12:233
170. Rivera S, Khrestchatisky M, Kaczmarek L, Rosenberg GA, Jaworski DM (2010) Metzincin proteases and their inhibitors: foes or friends in nervous system physiology? J Neurosci 30:15337–15357
171. Greene J, Wang M, Liu YE, Raymond LA, Rosen C, Shi YE (1996) Molecular cloning and characterization of human tissue inhibitor of metalloproteinase 4. J Biol Chem 271:30375–30380
172. Rao BG (2005) Recent developments in the design of specific matrix metalloproteinase inhibitors aided by structural and computational studies. Curr Pharm Des 11:295–322
173. Benjamin MM, Khalil RA (2012) Matrix metalloproteinase inhibitors as investigative tools in the pathogenesis and management of vascular disease. EXS 103:209–279
174. Yamaguchi M, Jadhav V, Obenaus A, Colohan A, Zhang JH (2007) Matrix metalloproteinase inhibition attenuates brain edema in an in vivo model of surgically-induced brain injury. Neurosurgery 61:1067–1075, discussion 1075-1066
175. Dal-Pizzol F, Rojas HA, dos Santos EM, Vuolo F, Constantino L, Feier G, Pasquali M, Comim CM et al (2013) Matrix metalloproteinase-2 and metalloproteinase-9 activities are associated with blood-brain barrier dysfunction in an animal model of severe sepsis. Mol Neurobiol 48:62–70
176. Barichello T, Generoso JS, Michelon CM, Simoes LR, Elias SG, Vuolo F, Comim CM, Dal-Pizzol F et al (2014) Inhibition of matrix metalloproteinases-2 and -9 prevents cognitive impairment induced by pneumococcal meningitis in Wistar rats. Exp Biol Med (Maywood) 239:225–231
177. Hadass O, Tomlinson BN, Gooyit M, Chen S, Purdy JJ, Walker JM, Zhang C, Giritharan AB et al (2013) Selective inhibition of matrix metalloproteinase-9 attenuates secondary damage resulting from severe traumatic brain injury. PLoS One 8:e76904
178. Nagel S, Heinemann PV, Heiland S, Koziol J, Gardner H, Wagner S (2011) Selective MMP-inhibition with Ro 28-2653 in acute experimental stroke—a magnetic resonance imaging efficacy study. Brain Res 1368:264–270

179. Vandenbroucke RE, Libert C (2014) Is there new hope for therapeutic matrix metalloproteinase inhibition? Nat Rev Drug Discov 13:904–927
180. Verslegers M, Lemmens K, Van Hove I, Moons L (2013) Matrix metalloproteinase-2 and -9 as promising benefactors in development, plasticity and repair of the nervous system. Prog Neurobiol 105:60–78
181. Khokha R, Murthy A, Weiss A (2013) Metalloproteinases and their natural inhibitors in inflammation and immunity. Nat Rev Immunol 13:649–665
182. Martens E, Leyssen A, Van Aelst I, Fiten P, Piccard H, Hu J, Descamps FJ, Van den Steen PE et al (2007) A monoclonal antibody inhibits gelatinase B/MMP-9 by selective binding to part of the catalytic domain and not to the fibronectin or zinc binding domains. Biochim Biophys Acta 1770:178–186
183. Devy L, Huang L, Naa L, Yanamandra N, Pieters H, Frans N, Chang E, Tao Q et al (2009) Selective inhibition of matrix metalloproteinase-14 blocks tumor growth, invasion, and angiogenesis. Cancer Res 69:1517–1526
184. Devy L, Dransfield DT (2011) New strategies for the next generation of matrix-metalloproteinase inhibitors: selectively targeting membrane-anchored MMPs with therapeutic antibodies. Biochem Res Int 2011:191670
185. Shiryaev SA, Remacle AG, Golubkov VS, Ingvarsen S, Porse A, Behrendt N, Cieplak P, Strongin AY (2013) A monoclonal antibody interferes with TIMP-2 binding and incapacitates the MMP-2-activating function of multifunctional, pro-tumorigenic MMP-14/MT1-MMP. Oncogenesis 2:e80
186. Devel L, Czarny B, Beau F, Georgiadis D, Stura E, Dive V (2010) Third generation of matrix metalloprotease inhibitors: gain in selectivity by targeting the depth of the S1′ cavity. Biochimie 92: 1501–1508
187. Krekoski CA, Neubauer D, Graham JB, Muir D (2002) Metalloproteinase-dependent predegeneration in vitro enhances axonal regeneration within acellular peripheral nerve grafts. J Neurosci 22:10408–10415
188. Sawicki G, Salas E, Murat J, Miszta-Lane H, Radomski MW (1997) Release of gelatinase A during platelet activation mediates aggregation. Nature 386:616–619
189. Giannelli G, Falk-Marzillier J, Schiraldi O, Stetler-Stevenson WG, Quaranta V (1997) Induction of cell migration by matrix metalloprotease-2 cleavage of laminin-5. Science 277:225–228
190. Song J, Wu C, Zhang X, Sorokin LM (2013) In vivo processing of CXCL5 (LIX) by matrix metalloproteinase (MMP)-2 and MMP-9 promotes early neutrophil recruitment in IL-1beta-induced peritonitis. J Immunol 190:401–410
191. Rundhaug JE (2005) Matrix metalloproteinases and angiogenesis. J Cell Mol Med 9:267–285
192. Kyriakides TR, Wulsin D, Skokos EA, Fleckman P, Pirrone A, Shipley JM, Senior RM, Bornstein P (2009) Mice that lack matrix metalloproteinase-9 display delayed wound healing associated with delayed reepithelialization and disordered collagen fibrillogenesis. Matrix Biol 28:65–73
193. Ikonomidis JS, Barbour JR, Amani Z, Stroud RE, Herron AR, McClister DM Jr, Camens SE, Lindsey ML et al (2005) Effects of deletion of the matrix metalloproteinase 9 gene on development of murine thoracic aortic aneurysms. Circulation 112:I242–248
194. Pilcher BK, Dumin JA, Sudbeck BD, Krane SM, Welgus HG, Parks WC (1997) The activity of collagenase-1 is required for keratinocyte migration on a type I collagen matrix. J Cell Biol 137:1445–1457
195. Ragin AB, Wu Y, Ochs R, Scheidegger R, Cohen BA, McArthur JC, Epstein LG, Conant K (2009) Serum matrix metalloproteinase levels correlate with brain injury in human immunodeficiency virus infection. J Neurovirol 15:275–281
196. Owen CA, Hu Z, Lopez-Otin C, Shapiro SD (2004) Membrane-bound matrix metalloproteinase-8 on activated polymorphonuclear cells is a potent, tissue inhibitor of metalloproteinase-resistant collagenase and serpinase. J Immunol 172:7791–7803
197. Stadlmann S, Pollheimer J, Moser PL, Raggi A, Amberger A, Margreiter R, Offner FA, Mikuz G et al (2003) Cytokine-regulated expression of collagenase-2 (MMP-8) is involved in the progression of ovarian cancer. Eur J Cancer 39:2499–2505
198. Holliday LS, Welgus HG, Fliszar CJ, Veith GM, Jeffrey JJ, Gluck SL (1997) Initiation of osteoclast bone resorption by interstitial collagenase. J Biol Chem 272:22053–22058
199. Whitelock JM, Murdoch AD, Iozzo RV, Underwood PA (1996) The degradation of human endothelial cell-derived perlecan and release of bound basic fibroblast growth factor by stromelysin, collagenase, plasmin, and heparanases. J Biol Chem 271:10079–10086
200. Stolow MA, Bauzon DD, Li J, Sedgwick T, Liang VC, Sang QA, Shi YB (1996) Identification and characterization of a novel collagenase in Xenopus laevis: possible roles during frog development. Mol Biol Cell 7:1471–1483
201. Boudreau N, Sympson CJ, Werb Z, Bissell MJ (1995) Suppression of ICE and apoptosis in mammary epithelial cells by extracellular matrix. Science 267:891–893
202. Sympson CJ, Talhouk RS, Alexander CM, Chin JR, Clift SM, Bissell MJ, Werb Z (1994) Targeted expression of stromelysin-1 in mammary gland provides evidence for a role of proteinases in branching morphogenesis and the requirement for an intact basement membrane for tissue-specific gene expression. J Cell Biol 125:681–693
203. Noe V, Fingleton B, Jacobs K, Crawford HC, Vermeulen S, Steelant W, Bruyneel E, Matrisian LM et al (2001) Release of an invasion promoter E-cadherin fragment by matrilysin and stromelysin-1. J Cell Sci 114:111–118
204. Gill JH, Kirwan IG, Seargent JM, Martin SW, Tijani S, Anikin VA, Mearns AJ, Bibby MC et al (2004) MMP-10 is overexpressed, proteolytically active, and a potential target for therapeutic intervention in human lung carcinomas. Neoplasia 6: 777–785
205. Unden AB, Sandstedt B, Bruce K, Hedblad M, Stahle-Backdahl M (1996) Stromelysin-3 mRNA associated with myofibroblasts is overexpressed in aggressive basal cell carcinoma and in dermatofibroma but not in dermatofibrosarcoma. J Invest Dermatol 107:147–153
206. Fukai F, Ohtaki M, Fujii N, Yajima H, Ishii T, Nishizawa Y, Miyazaki K, Katayama T (1995) Release of biological activities from quiescent fibronectin by a conformational change and limited proteolysis by matrix metalloproteinases. Biochemistry 34: 11453–11459
207. Powell WC, Fingleton B, Wilson CL, Boothby M, Matrisian LM (1999) The metalloproteinase matrilysin proteolytically generates active soluble Fas ligand and potentiates epithelial cell apoptosis. Curr Biol 9:1441–1447
208. Xu X, Ma J, Li C, Zhao W, Xu Y (2015) Regulation of chondrosarcoma invasion by MMP26. Tumour Biol 36:365–369
209. Hu Q, Yan C, Xu C, Yan H, Qing L, Pu Y, He Z, Li X (2014) Matrilysin-2 expression in colorectal cancer is associated with overall survival of patients. Tumour Biol 35:3569–3574
210. Kadono Y, Okada Y, Namiki M, Seiki M, Sato H (1998) Transformation of epithelial Madin-Darby canine kidney cells with p60(v-src) induces expression of membrane-type 1 matrix metalloproteinase and invasiveness. Cancer Res 58:2240–2244
211. Koshikawa N, Giannelli G, Cirulli V, Miyazaki K, Quaranta V (2000) Role of cell surface metalloprotease MT1-MMP in epithelial cell migration over laminin-5. J Cell Biol 148:615–624
212. Belkin AM, Akimov SS, Zaritskaya LS, Ratnikov BI, Deryugina EI, Strongin AY (2001) Matrix-dependent proteolysis of surface

transglutaminase by membrane-type metalloproteinase regulates cancer cell adhesion and locomotion. J Biol Chem 276:18415–18422
213. Chabottaux V, Sounni NE, Pennington CJ, English WR, van den Brule F, Blacher S, Gilles C, Munaut C et al (2006) Membrane-type 4 matrix metalloproteinase promotes breast cancer growth and metastases. Cancer Res 66:5165–5172
214. Komori K, Nonaka T, Okada A, Kinoh H, Hayashita-Kinoh H, Yoshida N, Yana I, Seiki M (2004) Absence of mechanical allodynia and Abeta-fiber sprouting after sciatic nerve injury in mice lacking membrane-type 5 matrix metalloproteinase. FEBS Lett 557:125–128
215. Sun Q, Weber CR, Sohail A, Bernardo MM, Toth M, Zhao H, Turner JR, Fridman R (2007) MMP25 (MT6-MMP) is highly expressed in human colon cancer, promotes tumor growth, and exhibits unique biochemical properties. J Biol Chem 282:21998–22010
216. Lijnen HR, Ugwu F, Bini A, Collen D (1998) Generation of an angiostatin-like fragment from plasminogen by stromelysin-1 (MMP-3). Biochemistry 37:4699–4702
217. Sedlacek R, Mauch S, Kolb B, Schatzlein C, Eibel H, Peter HH, Schmitt J, Krawinkel U (1998) Matrix metalloproteinase MMP-19 (RASI-1) is expressed on the surface of activated peripheral blood mononuclear cells and is detected as an autoantigen in rheumatoid arthritis. Immunobiology 198:408–423
218. Stracke JO, Fosang AJ, Last K, Mercuri FA, Pendas AM, Llano E, Perris R, Di Cesare PE et al (2000) Matrix metalloproteinases 19 and 20 cleave aggrecan and cartilage oligomeric matrix protein (COMP). FEBS Lett 478:52–56
219. Hieta N, Impola U, Lopez-Otin C, Saarialho-Kere U, Kahari VM (2003) Matrix metalloproteinase-19 expression in dermal wounds and by fibroblasts in culture. J Invest Dermatol 121:997–1004
220. Ahokas K, Skoog T, Suomela S, Jeskanen L, Impola U, Isaka K, Saarialho-Kere U (2005) Matrilysin-2 (matrix metalloproteinase-26) is upregulated in keratinocytes during wound repair and early skin carcinogenesis. J Invest Dermatol 124:849–856
221. Galea CA, Nguyen HM, George Chandy K, Smith BJ, Norton RS (2014) Domain structure and function of matrix metalloprotease 23 (MMP23): role in potassium channel trafficking. Cell Mol Life Sci 71:1191–1210
222. Illman SA, Lehti K, Keski-Oja J, Lohi J (2006) Epilysin (MMP-28) induces TGF-beta mediated epithelial to mesenchymal transition in lung carcinoma cells. J Cell Sci 119:3856–3865
223. Lin HC, Chang JH, Jain S, Gabison EE, Kure T, Kato T, Fukai N, Azar DT (2001) Matrilysin cleavage of corneal collagen type XVIII NC1 domain and generation of a 28-kDa fragment. Invest Ophthalmol Vis Sci 42:2517–2524
224. Hashimoto G, Inoki I, Fujii Y, Aoki T, Ikeda E, Okada Y (2002) Matrix metalloproteinases cleave connective tissue growth factor and reactivate angiogenic activity of vascular endothelial growth factor 165. J Biol Chem 277:36288–36295
225. Imai K, Hiramatsu A, Fukushima D, Pierschbacher MD, Okada Y (1997) Degradation of decorin by matrix metalloproteinases: identification of the cleavage sites, kinetic analyses and transforming growth factor-beta1 release. Biochem J 322(Pt 3):809–814
226. Fowlkes JL, Enghild JJ, Suzuki K, Nagase H (1994) Matrix metalloproteinases degrade insulin-like growth factor-binding protein-3 in dermal fibroblast cultures. J Biol Chem 269:25742–25746
227. Patterson BC, Sang QA (1997) Angiostatin-converting enzyme activities of human matrilysin (MMP-7) and gelatinase B/type IV collagenase (MMP-9). J Biol Chem 272:28823–28825
228. Kajita M, Itoh Y, Chiba T, Mori H, Okada A, Kinoh H, Seiki M (2001) Membrane-type 1 matrix metalloproteinase cleaves CD44 and promotes cell migration. J Cell Biol 153:893–904
229. Sifringer M, Stefovska V, Zentner I, Hansen B, Stepulak A, Knaute C, Marzahn J, Ikonomidou C (2007) The role of matrix metalloproteinases in infant traumatic brain injury. Neurobiol Dis 25:526–535
230. Homsi S, Federico F, Croci N, Palmier B, Plotkine M, Marchand-Leroux C, Jafarian-Tehrani M (2009) Minocycline effects on cerebral edema: relations with inflammatory and oxidative stress markers following traumatic brain injury in mice. Brain Res 1291:122–132
231. Hirose T, Matsumoto N, Tasaki O, Nakamura H, Akagaki F, Shimazu T (2013) Delayed progression of edema formation around a hematoma expressing high levels of VEGF and mmp-9 in a patient with traumatic brain injury: case report. Neurol Med Chir (Tokyo) 53:609–612
232. Shigemori Y, Katayama Y, Mori T, Maeda T, Kawamata T (2006) Matrix metalloproteinase-9 is associated with blood-brain barrier opening and brain edema formation after cortical contusion in rats. Acta Neurochir Suppl 96:130–133
233. Jia F, Pan YH, Mao Q, Liang YM, Jiang JY (2010) Matrix metalloproteinase-9 expression and protein levels after fluid percussion injury in rats: the effect of injury severity and brain temperature. J Neurotrauma 27:1059–1068
234. Mori T, Wang X, Aoki T, Lo EH (2002) Downregulation of matrix metalloproteinase-9 and attenuation of edema via inhibition of ERK mitogen activated protein kinase in traumatic brain injury. J Neurotrauma 19:1411–1419
235. Ralay Ranaivo H, Zunich SM, Choi N, Hodge JN, Wainwright MS (2011) Mild stretch-induced injury increases susceptibility to interleukin-1beta-induced release of matrix metalloproteinase-9 from astrocytes. J Neurotrauma 28:1757–1766
236. Muradashvili N, Benton RL, Saatman KE, Tyagi SC, Lominadze D (2015) Ablation of matrix metalloproteinase-9 gene decreases cerebrovascular permeability and fibrinogen deposition post traumatic brain injury in mice. Metab Brain Dis 30:411–426
237. Wei M, Li H, Shang Y, Zhou Z, Zhang J (2014) Increased CD147 (EMMPRIN) expression in the rat brain following traumatic brain injury. Brain Res 1585:150–158
238. Roberts DJ, Jenne CN, Leger C, Kramer AH, Gallagher CN, Todd S, Parney IF, Doig CJ et al (2013) Association between the cerebral inflammatory and matrix metalloproteinase responses after severe traumatic brain injury in humans. J Neurotrauma 30:1727–1736
239. Li RB, Guo XC, Liang HX, Wang FY, Zhu BL (2009) Study on changes of MMP-3 expression after brain contusion in rats. Leg Med (Tokyo) 11 Suppl 1:S176–179

Appendix A –Publication Cover 28
2015

Authors: A. Sundaramurthy and Namas Chandra

Title: "*A parametric approach to shape field relevant blast wave profiles in compressed gas-driven shock tube*"

Journal Publication: Frontiers in Neurology, 1-17, (2015), [15-28]

frontiers in
NEUROLOGY

ORIGINAL RESEARCH ARTICLE
published: 02 December 2014
doi: 10.3389/fneur.2014.00253

A parametric approach to shape field-relevant blast wave profiles in compressed-gas-driven shock tube

Aravind Sundaramurthy and Namas Chandra*

Center for Injury Bio-Mechanics, Materials and Medicine, New Jersey Institute of Technology, Newark, NJ, USA

Edited by:
Liying Zhang, Wayne State University, USA

Reviewed by:
Luke R. Johnson, Uniformed Services University of the Health Sciences, USA
Vassilis E. Koliatsos, Johns Hopkins University School of Medicine, USA

***Correspondence:**
Namas Chandra, Center for Injury Bio-Mechanics, Materials and Medicine, New Jersey Institute of Technology, Newark, NJ 07102, USA
e-mail: namas.chandra@njit.edu

Detonation of a high-explosive produces shock-blast wave, shrapnel, and gaseous products. While direct exposure to blast is a concern near the epicenter, shock-blast can affect subjects, even at farther distances. When a pure shock-blast wave encounters the subject, in the absence of shrapnels, fall, or gaseous products the loading is termed as *primary blast loading* and is the subject of this paper. The wave profile is characterized by blast overpressure, positive time duration, and impulse and called herein as shock-blast wave parameters (SWPs). These parameters in turn are uniquely determined by the strength of high explosive and the distance of the human subjects from the epicenter. The shape and magnitude of the profile determine the severity of injury to the subjects. As shown in some of our recent works (1–3), the profile not only determines the survival of the subjects (e.g., animals) but also the acute and chronic biomechanical injuries along with the following biochemical sequelae. It is extremely important to carefully design and operate the shock tube to produce field-relevant SWPs. Furthermore, it is vital to identify and eliminate the artifacts that are inadvertently introduced in the shock-blast profile that may affect the results. In this work, we examine the relationship between shock tube adjustable parameters (SAPs) and SWPs that can be used to control the blast profile; the results can be easily applied to many of the laboratory shock tubes. Further, replication of shock profile (magnitude and shape) can be related to field explosions and can be a standard in comparing results across different laboratories. Forty experiments are carried out by judiciously varying SAPs such as membrane thickness, breech length (66.68–1209.68 mm), measurement location, and type of driver gas (nitrogen, helium). The effects SAPs have on the resulting shock-blast profiles are shown. Also, the shock-blast profiles of a TNT explosion from ConWep software is compared with the profiles obtained from the shock tube. To conclude, our experimental results demonstrate that a compressed-gas shock tube when designed and operated carefully can replicate the blast time profiles of field explosions accurately. Such a faithful replication is an essential first step when studying the effects of blast induced neurotrauma using animal models.

Keywords: primary blast injury, explosion modeling, shock tube, blast induced neurotrauma, shock tube adjustable parameters, shock wave parameters

INTRODUCTION

In the study of blast induced neurotrauma (BINT) using animal models, many research groups use compressed-gas-driven shock tubes to simulate primary blast injury conditions (4–9). Since the injury to animals critically depends on the nature of the shock-blast wave (from here on simply known as blast waves), it is important to standardize the blast wave across the various shock tubes. Though the generation of shock wave by itself is straightforward, controlling the shape and magnitude of the pressure-time pulse is not trivial, and is subject of the present paper.

In general, detonation of a high explosive on or near surface produces blast wave, noise, shrapnel, and toxic gaseous products. Blast (the air shock wave due to explosion) is a major concern due to its ability to cause damage at relatively long distances from the point of explosion (10, 11). Numerous cases of soldier injuries in operation Iraqi freedom (OIF) and operation enduring freedom (OEF) were directly attributed to the blasts, resulting from improvised explosive devices (IEDs) used by the insurgents. Among these injuries, the most common was the traumatic brain injury, which is the signature injury of these conflicts (12–15). In a study conducted by RAND Corporation, it was estimated that 320,000 service members or 20% of the deployed force (total deployed 1.6 million) potentially suffer from TBI (includes primary, secondary, tertiary, and quaternary injuries); however, out of this population, approximately 60% have never been assessed by a healthcare provider specifically for TBI and suffer from mild TBI (16). It should be noted that the blunt impacts (included in tertiary injury) can be ascribed to the blast events (e.g., mounted soldiers inside the vehicle subjected to IEDs); however, all the blunt impacts may or may not be related to blast events. The mild TBI is classified as loss of consciousness for <30 min or amnesia lasting <24 h, and is not detectable during

early stages post-injury using any of the current neuroimaging techniques.

Recently, an extensive research effort has been initiated toward the understanding of the mechanism of primary blast injury. Initial findings from the experimental models and the computer simulations suggest that most of these injuries may have been due to the direct impingement of the blast wave on the skull (3, 6, 8, 17–21). Other mechanisms including thoracic pressure surge, skull deflection, and cavitation are also being explored as the loading mechanisms. Although, the free-field blast testing closely replicates real-world blast conditions, there are some significant drawbacks: (i) free-field experiments are expensive and unsafe; (ii) time consuming; (iii) repeatability is difficult to achieve, as it is difficult to control the environment of the field blast with byproducts that include fireball interactions and penetration from high-rate shrapnel (15). This can also introduce unnecessary confounds to the experiments where the objective is to understand the mechanisms of primary blast injury and its subsequent biomechanical and bio-chemical sequelae. A recent review article by Kobeissy and his colleagues shows that out of 49 studies, only 8 used field testing and 92% of shock tubes (33 out of 36) used were compressed-gas-driven shock tubes (**Table 1**) (22).

Accurately, simulating blast wave in laboratory condition using a compressed-gas shock tube requires the ability to control shock-blast wave parameters (SWPs) independently to mimic a field explosion. For a simplified hemispherical explosion as shown in **Figure 1A**, depending on the length of the fireball radius, the blast is divided into three regimes, near field, mid field, and far field (25). Objects that are exposed to incident pressure of 1000 kPa or higher are typically within/near the fireball and considered as a near field condition. It is said within the near field condition the following is expected: (a) interaction with detonation products/shrapnel; (b) complex evolution of the waveforms; and (c) high gradients in the flow of temperature and density. In reality, flow conditions in the near field for IEDs are lot more complex due to the irregular charge shape, casing/shrapnel (where some of the kinetic energy of the blast is used for accelerating the shrapnel

Table 1 | Explosive capacity of the currently used IEDs and mines in the field.

Threat	Explosive capacity (TNT equivalent in kg)	Reference
Pipe bomb	2.28	(23)
Suicide bomber	9	
Briefcase bomb	22.70	
AP fragmentation device	0.55	(24)
AV blast landmine	6–10	

Explosive capacities of these IEDs are given in terms of TNT equivalents in kilograms.

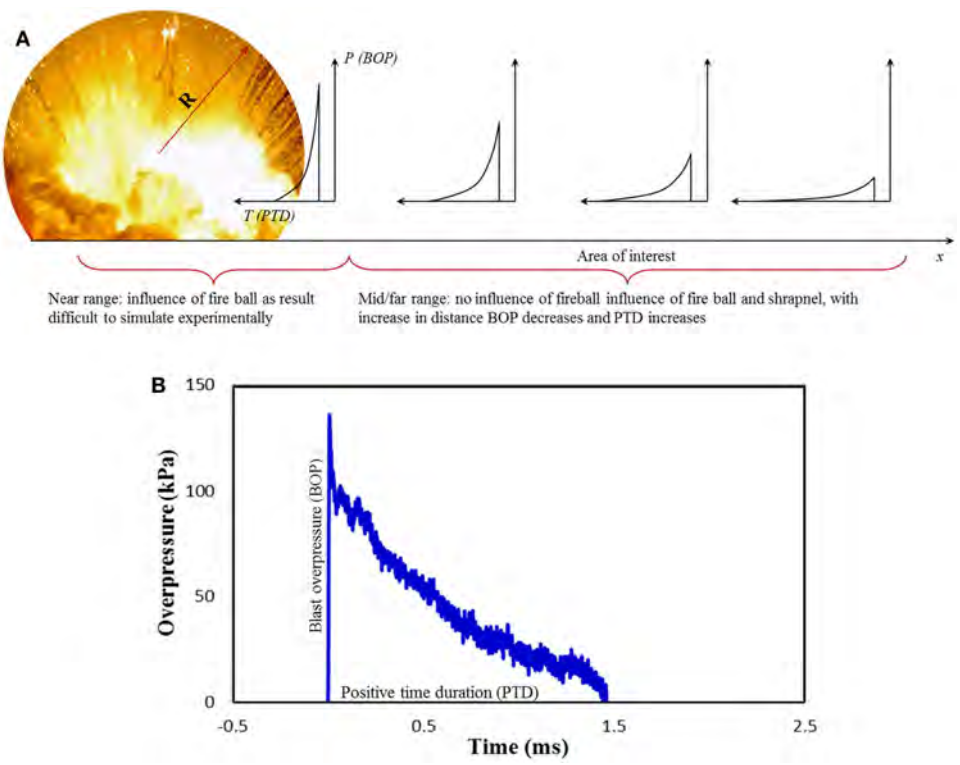


FIGURE 1 | (A) shows evolution of shock-blast profile as the distance from the epicenter increases. Radius from epicenter with BOP higher than 1000 kPa is considered far range, which is very close to the fireball (R) and outside this radius it is mid and far field range, **(B)** Shock-blast wave profile generated from the explosion of 1.814 kg of C_4 at a distance of 2.8 m.

from the casing), and buried/grounded. It is extremely difficult to device a methodology to simulate the near field condition due to its sheer unstable nature. These extreme conditions cause very severe injuries and immediate death. Following the near field is the mid field and far field, which is referred as the zone beyond fireball. Pressure profiles in the mid and far field have a similar shape with amplitude decaying monotonically and duration increasing with increasing distance (**Figure 1A**). Eventually, the wave loses its strength (i.e., Mach number <1) and decays into a sound wave (26). **Figure 1B** shows typical pressure-time profile recorded from a field explosion of 1.814 kg (4 lb) of C_4 at a distance of 2.8 m from the epicenter of the blast measured using a PCB press type pencil gage (model: 137A22). From the figure, it can be seen that there is a sudden rise in the pressure, which represents the shock front (i.e., blast overpressure) followed by an exponential decay. This sudden rise followed by an exponential decay comprises the positive phase of the blast wave, which can be described using a modified Friedlander equation.

$$p(t) = p_o \left(1 - \frac{t}{t_d}\right) e^{\left(\frac{-t}{\alpha}\right)}$$

where p_o represents the blast overpressure, t_d represents the positive time duration (PTD), and α represents the time decay constant (26). Although, this exponential decay reaches sub-atmospheric pressures generating a negative phase, Friedlander model does not take that into account (27). Obtaining a Friedlander type profile (sharp rise-exponential decay) does not guarantee realistic shock profile as the parameters (e.g., duration and impulse) may not match any combination of explosive strength and stand-off distance. In addition, in actual field explosions the shape of the curve may be complex, determined by the shape, size, and type of explosives; sub-surface burial depth; temperature, altitude, wind, and humidity of the environment; and presence/absence of enclosures and obstructions. However, a blast wave of Friedlander type can still be used as the basic building block to model the complex input condition, as followed by most researchers.

In this work, we are examining the role of different geometric, constructional, and operational features (such as breech length, type of gas, membrane thickness, and measurement location) of compressed-gas-driven shock tubes has on the SWPs (such as blast overpressure and PTD). We also characterize the flat top or plateau wave and determine the influence driver gas and breech length have on the blast profiles. Finally, we compare the blast wave profile from the shock tube with the field explosion profiles generated in ConWep (Conventional Weapons effects). With this, we hope to standardize the method for generating blast pulses so that the bio-chemical, biomechanical, and medical results obtained across various groups can be compared and correlated among themselves and with the field data.

MATERIALS AND METHODS

Experiments were carried out in the shock tube designed by our group and tested at the University of Nebraska-Lincoln's blast wave generation facility (**Figure 2**) (1) (a similar system has been developed in Center for injury biomechanics, materials, and medicine at NJIT). The four main components of any compressed-gas-driven shock tube are driver, transition, driven sections, and catch tank. The driver section (breech) contains pressurized gas (e.g., nitrogen, helium), which is separated from the transition by several frangible Mylar® membranes, while the driven section (including the expansion section) contains air at atmospheric pressure and room temperature. Transition section acts as an adapter, which is used to change the cross-section of the tube from a circular (breech) to a square (expansion section); the square section is a design element to observe events in the test section with high-speed video imaging. The driven section has a 711.2 mm × 711.2 mm (28″ × 28″), cross-section, and the length of 8661 mm. Finally, catch tank absorbs the kinetic energy of the exiting jet from the shock tube and does not play any role in modifying the profile. Upon membrane rupture, a blast wave is generated, which expands through the transition and develops into planar blast waveform in the driven section. Driven section also encompasses the test section. Finally, the blast wave exits the shock tube and enters the catch tank, which reduces the noise intensity. The cross-sectional dimension of this shock tube is designed such that subjects within the test section experiences a planar blast wave without significant sidewall reflections. The planarity of the blast wave is verified by pressure measurements across the test section of the shock tube (28).

Figure 3 shows the experimental variables and the sensor locations. The length of the breech is varied with discrete increments designated as L_1 (66.68 mm), L_2 (396.88 mm), L_3 (803.28 mm),

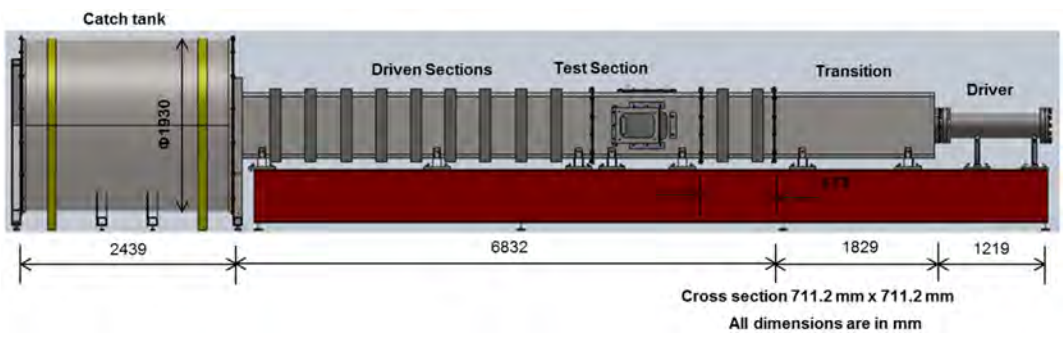


FIGURE 2 | 711 mm × 711 mm Shock tube system. (Note: compressed gas is pumped into driver section in the right and the shock propagates from right to left in the figure.)

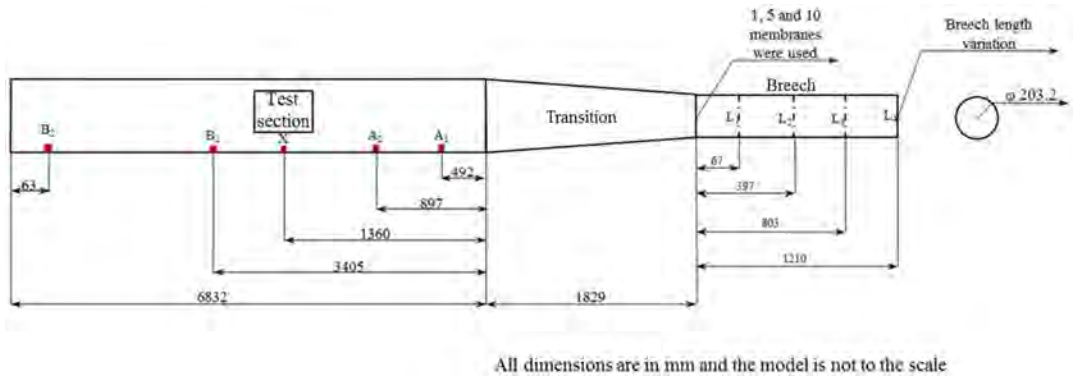


FIGURE 3 | Experimental variables and sensor location; here, A1, A2, X, B1, and B2 are the side-on pressure sensors. Here, L_1, L_2, L_3, and L_4 are the breech lengths used in the experiment, A_1, A_2, X, B_1, and B_2 are the incident pressure sensor locations and 1, 5, and 10 are the number of membranes used.

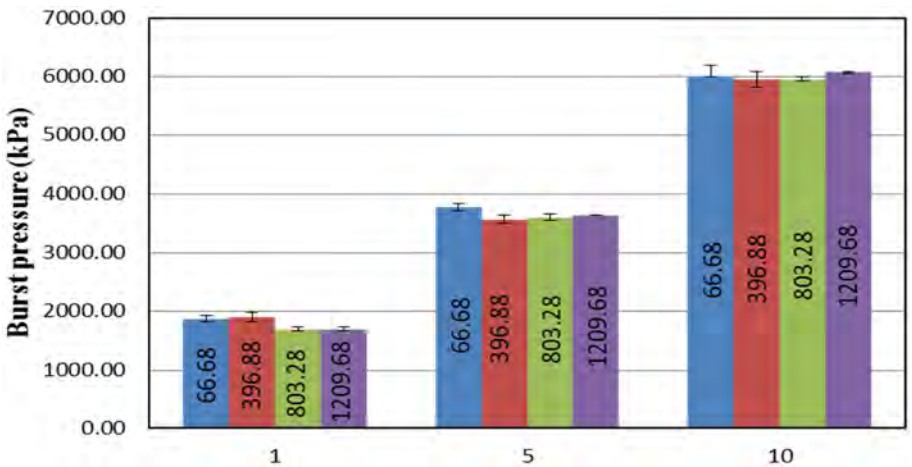


FIGURE 4 | Relationship between the number of membranes used and burst pressure produced with respect to different breech lengths. From this figure, it can be seen that there is no significant difference in the burst pressure with respect to the variations in the breech length. However, the burst pressure tends to increase with an increase in the number of membranes used.

and L_4 (1209.68 mm). The membrane thickness is varied by varying the number of membranes between 1, 5, and 10 (each membrane is 0.254 mm thick). In this work, both nitrogen and helium were used as the driver gas, and the driven gas was air at ambient laboratory conditions (temperature range of $23 \pm 2°$ C). The evolution of the blast wave along the length of the shock tube was measured using PCB pressure gages (model 134A24) mounted on the wall of the shock tube at locations A1, A2, X, B1, and B2 (**Figure 3**). Burst pressure in driver just before the rupture of the membranes was also recorded.

RESULTS

BURST PRESSURE

Burst pressure is the pressure in the driver section (breech) at the time of the membrane rupture. This highly compressed gas when allowed to expand rapidly compresses the atmospheric air in the transition and driven sections generating a shock front. Burst pressure for different membrane thicknesses and breech lengths are shown in **Figure 4**. The burst pressure increases with an increase in the membrane thickness. There is no discernible difference in the burst pressure with respect to increase in breech length for any of the three membrane thicknesses studied. It should be noted that any variation in the burst pressure for identical conditions (e.g., number of membranes, breech volume, and type of gas) will be due to the variations in filling rate of gas in the breech; since Mylar® membrane is viscoelastic in nature the rate of deformation depends on the rate of pressurization of the driver section. In our experience, there is a pronounced rate dependency effect for smaller breech lengths (results not shown for the sake of brevity), compared to larger ones.

SHOCK TUBE ADJUSTABLE PARAMETERS AND THEIR INFLUENCE ON THE BLAST WAVE PARAMETERS IN TEST SECTION

By changing the shock tube adjustable parameters (SAPs) such as membrane thickness (burst pressure) and breech length, we can alter the SWPs such as Mach number, blast overpressure, and

PTD in the test section. Mach number of the shock front refers to the ratio of the velocity of the shock in the given medium to the velocity of sound in the same medium. From **Figure 5**, it can be seen that the Mach number of the shock front depends on the burst pressure and has a positive linear relationship with burst pressure, i.e., shock front velocity increases with an increase in the burst pressure. When breech length is L_1 (small) Mach number increases at a lower rate (slope of the line) compared to that of the other breech lengths (L_2, L_3, and L_4). How and why the behavior for shorter breech length is different from that of the others will be discussed later.

Blast overpressure is the gage pressure measured in the air, which is the difference between absolute gas pressure and atmospheric pressure. Similar to Mach number, there is a linear relationship between blast overpressure and burst pressure (**Figure 6**). With increase in the burst pressure the blast overpressure for L_2, L_3, and L_4 increases with a higher rate (higher slope) compared to that of L_1. These results are intriguing and are explained in the discussion section.

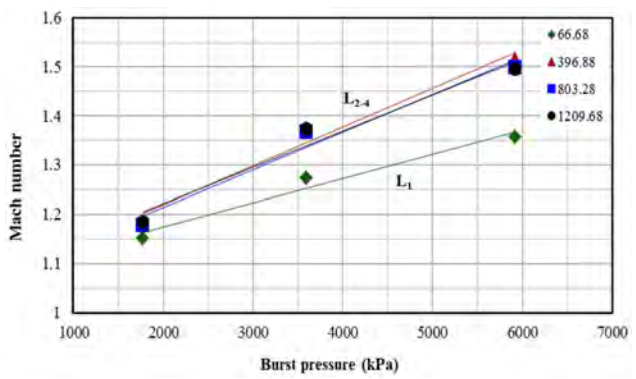


FIGURE 5 | Relationship between shock front Mach number and burst pressure for different breech lengths, there is linear relationship between Mach number and burst pressure (i.e., increase in membrane thickness).

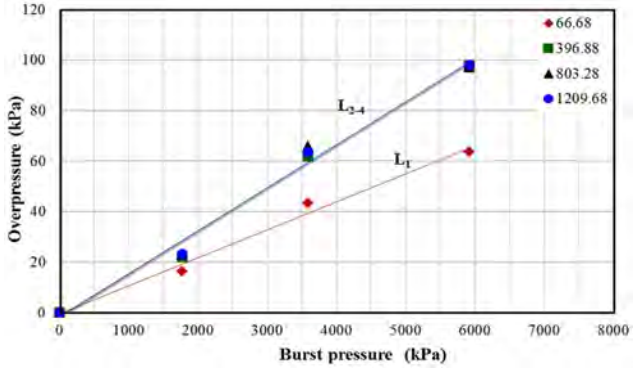


FIGURE 6 | Relationship between shock tube parameter burst pressure with overpressure measured in the test section for different breech lengths.

Positive time duration is the period when the blast overpressure reduces to 0, i.e., when it reaches the local atmospheric pressure. From **Figure 7**, it can be seen that for a given membrane thickness, PTD increases with an increase in the breech length. There is an increase in PTD between membrane thicknesses 1 and 5 for breech lengths L_1, L_2, and L_3; however, such an apparent difference is not observed between membrane thicknesses 5 and 10. Finally, for breech length L_4 there is no apparent difference in PTD for different membrane thicknesses.

EVOLUTION OF THE BLAST WAVE ALONG THE EXPANSION SECTION

Figures 8A–C show the evolution of the blast overpressure along the length of the expansion section. From **Figure 8A**, it can be seen that, for one membrane there is no discernible change in blast overpressure for breech lengths L_2, L_3, and L_4. For all cases with breech length L_1, there is a continuous decay in the blast overpressure downstream of the shock tube. For all the other breech lengths, unique points of blast overpressure decays are identified along the expansion section, which is illustrated in the following section.

For L_1, L_2, L_3, and L_4, we observe the following: (i) for any membrane thicknesses, an obvious difference in blast overpressure is observed between L_1 and other breech lengths (**Figures 8A–C**) (ii) beyond 3000 mm from the breech, for 5 and 10 membranes and breech length L_2, blast overpressure starts to decay (**Figures 8B,C**), and (iii) beyond 5000 mm from the breech, for 10 membranes and breech lengths L_3, the blast overpressure starts to decay (**Figure 8C**). Finally, for L_4 there is no unique decay point, which implies a flat top wave occurs throughout the expansion section.

Figures 8D–F show the evolution of the PTD along the length of the shock tube driven section. For any given breech length and membrane thickness, the PTD remains reasonably constant along the length, however, decreases drastically toward the exit of the shock tube. Positive impulse is the area under the blast wave profile.

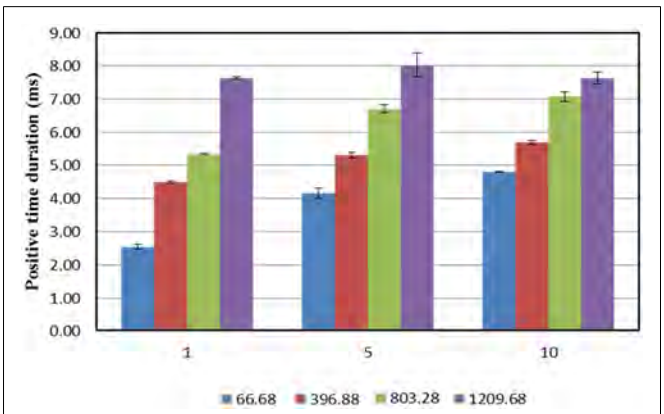


FIGURE 7 | Relationship between positive time duration (PTD) and membrane thickness used for different breech lengths. It can be seen that there PTD increases with increase in the breech length for any given membrane configuration; furthermore, for a lower breech lengths, the PTD tends to increase with increase in the number of membranes used, however, this change reduces with increase in breech length. For the maximum breech length, there is no significant change in the PTD.

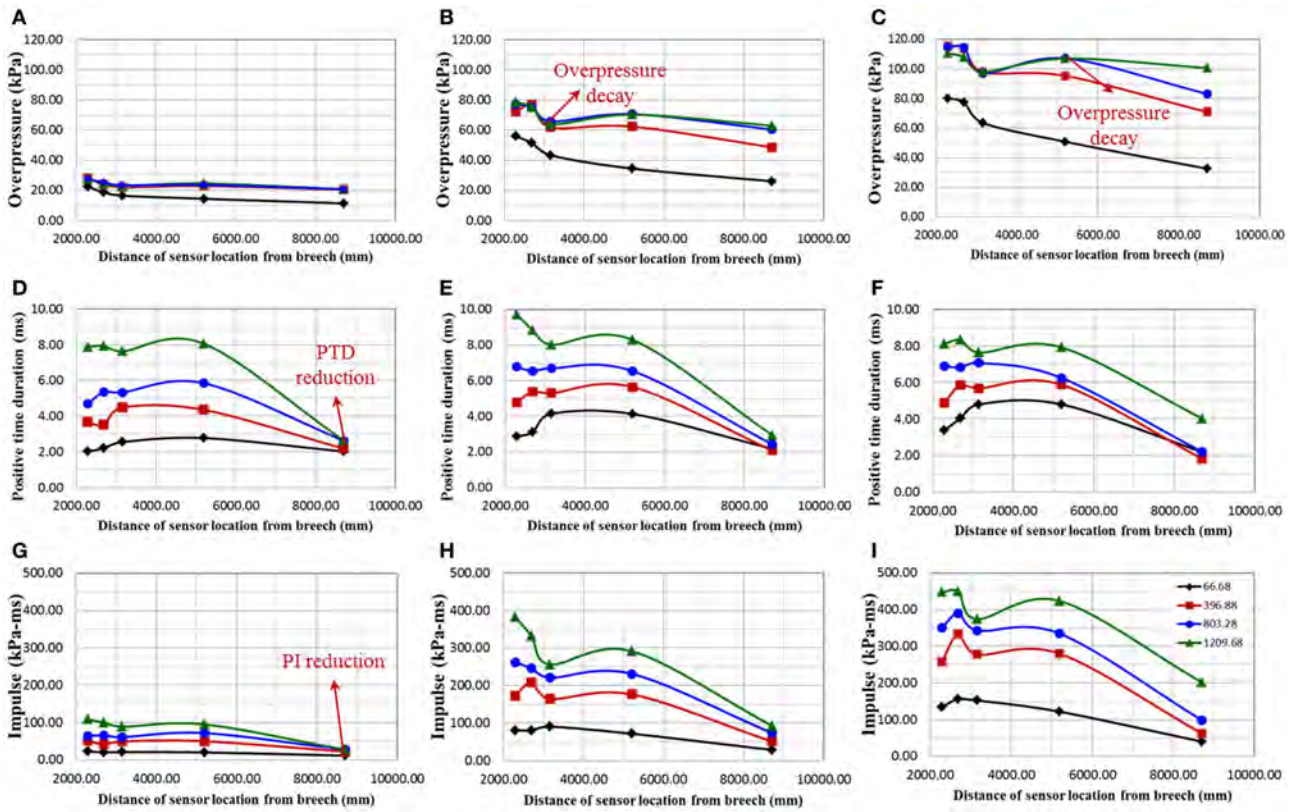


FIGURE 8 | Describes the variation of shock-blast profile parameters along the length of the shock tube expansion section; all these experiments were performed for breech lengths 66.68 (black), 396.88 (red), 803.28 (blue), and 1209.68 (green) mm. **(A–C)** show the variation of overpressure along the length of the expansion section for burst pressures corresponding to 1, 5, and 10 membranes, respectively; **(D–F)** show the positive time duration along the expansion section for burst pressures corresponding to 1, 5, and 10 membranes, respectively; **(G–I)** show the positive impulse along the expansion section for burst pressures corresponding to 1, 5, and 10 membranes, respectively.

Figures 8G–I show the evolution of the positive impulse along the length of the shock tube expansions section. Positive impulse is a function of both blast overpressure and PTD; hence, it increases with an increase in both membrane thickness and breech length. Owing to its relationship with the PTD, the impulse drastically reduces near the exit of the shock tube.

FLATTOP OR PLATEAU WAVE

A flattop or plateau wave is often observed in a gas-driven shock tube (9). In this case, the blast wave profile once reaching the peak blast overpressure maintains its peak value for a certain period of time before decay starts. Longer breech lengths in combination with the use of nitrogen as a driver gas can generate such a waveform. **Figure 9** shows the comparison between the blast wave profile with nitrogen and helium as driver gas measured at test section (sensor location X). In both cases, 10 membranes with a breech length of 1209.68 mm were used. It can be seen that only in the case of nitrogen as driver gas flat top wave is observed; in the case of helium, a pure Friedlander wave is obtained.

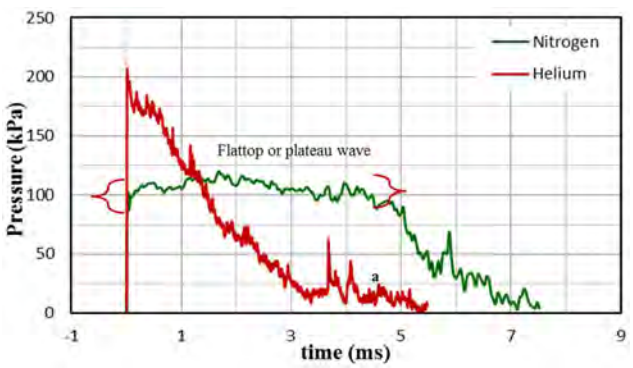


FIGURE 9 | Comparison of the shock-blast profile for helium and nitrogen with 10 membranes and breech length of 1209.68 mm; clearly the wave profile corresponding to helium gas is a Friedlander wave and wave profile corresponding to nitrogen is a flat top wave.

COMPARISON BETWEEN FIELD AND LABORATORY PROFILES

The primary objective of this work was to establish the shock tube parameters that can be used for generating specific blast profiles replicating field conditions. To validate this hypothesis, we compared the blast profiles of TNT explosive for different strength and range generated from ConWep with those generated from our

shock tube device. **Figures 10A–D** show one to one comparison of the incident pressure data from shock tube test section and TNT profiles of different strength and range.

DISCUSSION

Experiments using animal, cadaver, or test dummies remain the foremost means to investigate injury biomechanics as well as validate numerical models, for investigative, protective, diagnostics, and therapeutic purposes. It is well recognized that input biomechanical loading experienced by the subject determines both the injury and mortality (5, 29). Hence, in the study of mild and moderate TBI, it is important to reproduce the field conditions as accurately as possible without artifacts, for offering a range of engineering solutions (such as development of better helmets) and medical strategies (such as development of better therapies and pharmaceutical regimen). In this work, we identify the essential parameters of a blast wave and describe the methodology to control them by optimizing the parameters of the laboratory gas-driven shock tube. We also identify some of the common artifacts that render the wave profile invalid in a compressed-gas-driven shock tube and discuss techniques that can be used to eliminate them.

We observed that the burst pressure does not vary significantly with respect to increase in the breech length. The rupture of the membrane is based on the contained pressure and is not affected by the volume of the gas. Thus, burst pressure that occurs at a minimum breech length L_1 also initiates rupture at L_2, L_3, or L_4. Therefore, total thickness of the membrane determines the burst pressure (**Figure 4**). This result corroborates with the findings from the study conducted by Payman and Shepherd, where they used copper as their membrane. They determined that for the same thickness, the burst pressure does not vary more than ±3%. Similarly, they also determined that membrane thickness has a linear relationship with burst pressure (30).

Controlling blast overpressure and PTD is essential when replicating field blasts. By manipulating breech length, burst pressure (membrane thickness), type of gas, and test section location (by varying the test section within expansion section), it was shown that it is indeed possible to obtain specified profiles. It can be seen that within test section with an increase in burst pressure, both the blast overpressure and the Mach number (strength of shock wave) increases. This implies that both these variables can be increased by increasing the membrane thickness. Similarly, PTD increases with increase in breech length for any given burst pressure. However, at lower breech lengths both blast overpressure and PTD are affected by expansion waves (also known as rarefaction waves) released from the rear end of the breech, which is explained in the next section.

From the $x - t$ wave propagation diagram (**Figure 11**), it can be seen that the driver gas expansion initiates a family of infinite expansion waves or fan toward the closed end (rear end). Once the expansion head reaches the closed end, they are reflected and travel toward the transition. This reflected wave catches the shock front and since these waves are tensile in nature; since the shock front is compressive in nature, they start to cancel each other. With each successive expansion wave exiting the breech, the density of

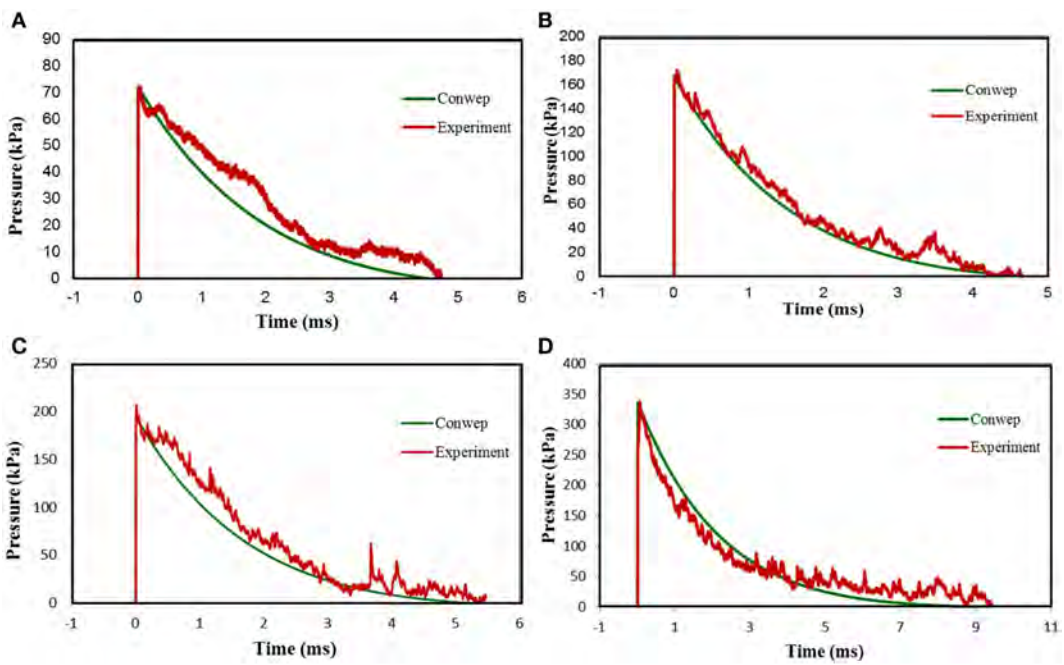


FIGURE 10 | Comparison of the shock-blast profiles from shock tube device and ConWep simulation software. **(A)** Comparison between shock-blast profile from a 10 membrane, 66.68 mm breech length shot with nitrogen as driver gas and 2.56 kg of TNT at 5.18 m, **(B)** comparison between shock-blast profile from a 8 membrane, 752.48 mm breech length shot with helium as driver gas and 7.68 kg of TNT at 5 m, **(C)** comparison between shock-blast profile from a 10 membrane, 1209.68 mm breech length shot with helium as driver gas and 14.08 kg of TNT at 5.7 m, **(D)** comparison between shock-blast profile from 15 membrane, 1209.68 mm breech length shot with helium as driver gas and 96 kg of TNT at 8.5 m.

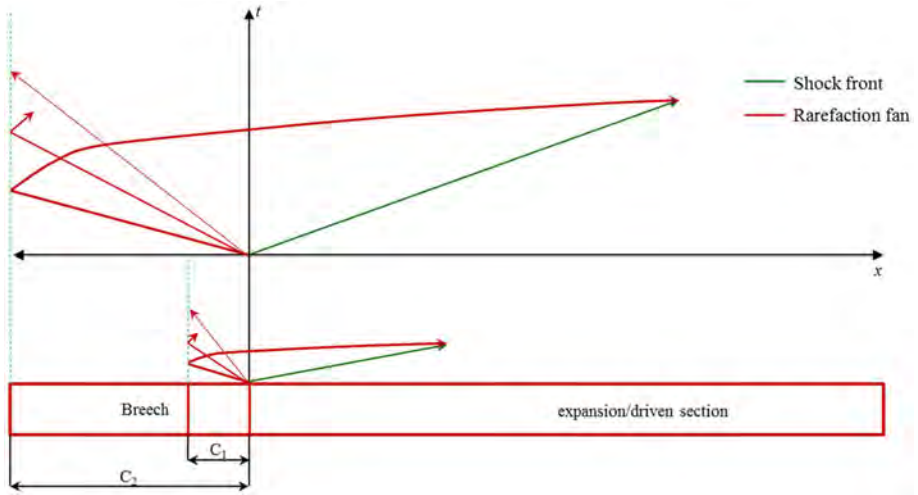


FIGURE 11 | *x* – *t* Diagram for compressed-gas shock tube. Here, a comparison was made between two driver lengths C_1 and C_2. Clearly, it can be seen that the expansion or rarefaction wave for C_1 reaches earlier than C_2.

the gases reduces, resulting in slowing the successive expansion wave of the fan. This fan of waves arriving one after the other leads to the non-linear decay and ultimately shaping the shock-blast wave (27). Once the waveform attains the shape shown in the **Figure 1B** expansion waves start to erode the blast overpressure and PTD. This was observed in the behavior of waves corresponding to breech length L_1 in the experiment, which is different from the other breech lengths. This is because for L_1, the expansion waves almost instantaneously catch up with the shock front. For other lengths, expansion waves catches shock front further down the shock tube (downstream). Therefore, when it arrives at the test section it has already gone through some blast overpressure and PTD reduction. Once the breech length is increased, the time taken by the expansion wave to reach the shock front increases. Consequently, for breech lengths L_2, L_3, and L_4 there is no change in the blast overpressure and PTD at the test section, which implies it is a flattop wave that will become a Friedlander type wave downstream (a pictorial representation is shown in **Figure 11** by comparing breech lengths C_1 and C_2). Similar to breech length, driver gas also plays a major role in the evolution and interaction of the expansion wave. The expansion wave while traveling toward the closed end of the driver section travels with the ambient sound speed in that medium. Therefore, for a given breech length and membrane thickness, having helium (helium has a higher sound speed compared to nitrogen for any temperature) as a driver gas increases the expansion wave velocity, resulting in Friedlander type wave even at an earlier point than nitrogen gas. Consequently, by varying the length of the breech in conjunction with using the appropriate driver gas, we would be able to optimize PTD and blast overpressure.

There is an inherent relationship between SAPs; optimization of one variable might have a negative effect on the other variables, resulting in the formation of a non-optimal blast wave. This problem arises depending on (i) type of driver gas and (ii) test section location. Although nitrogen due to its low-acoustic velocity has a tendency to produce longer PTD, using a longer breech length results in a flattop wave. Conversely, helium produces a lower PTD compared to nitrogen but has a sharp decay to the atmospheric pressure (**Figure 9**). Similar findings are reported in literature, where they compared the wave profiles generated from air (which has acoustic velocity close to nitrogen) and nitrogen with helium. They found that using air and nitrogen as a driver gas produces a flattop wave (9, 15). One technique used for avoiding a flattop wave when using long-breech length is to place the test section downstream of the expansion section, so that the expansion waves would eventually catch up and produces a Friedlander type wave; nevertheless, this method has its own limitation, as explained in the following section.

The evolution of the blast overpressure, PTD, positive impulse at five locations along the length of the expansion section was measured. In a typical free-field blast, the blast overpressure decreases rapidly with respect to increase in distance from the blast epicenter (31). However, blast overpressure in a shock tube does not show a drastic reduction due to its constant cross section. There is a considerable difference between the blast overpressures for L_1 and all the other breech lengths. As discussed earlier, this difference arises from the interaction of expansion waves that comes from rear end of the breech. This suggests that the expansion waves from the breech for breech length L_1 reaches earlier than all other breech length. With increase in the breech length and burst pressure, distinct points at which the blast starts to decay are identified as shown in **Figures 8B,C**, which implies that downstream to this point blast wave has a Friedlander form. Consequently, for longer breech lengths that tend to produce a flattop wave upstream (e.g., test section), the wave will assume a Friedlander type wave at some point downstream. However, when moving closer to the exit the rarefaction waves from the exit starts to interact with blast wave creating artifacts, which results in inaccurate blast simulation (27). As a result, PTD reduces drastically near the exit of the shock tube due to the interaction between shock front and exit

expansion waves. This has two consequences: first, the positive impulse (energy of blast wave) reduces drastically (**Figures 8G–I**). Second, since the total energy at the exit is conserved, all the blast energy is converted from supersonic blast wave to subsonic jet wind, which produces erroneous results (32). The effects of jet wind and specimen placement location along the expansion section for blast simulation using shock tube are illustrated in these references (2, 33).

The discussion above indicated that SAPs could be adjusted to generate a specific blast profile at a specific location (for the placement of animal model). In addition, the cross-sectional area of the specimen (animal) and specimen holder should be small compared to the entire cross-section of the tube. In all our experiments, we have found (through computer simulation and experiments) that if the specimen and holder occupy <25% of the tube area, then the reflection from the side walls do not interfere with the profile (1, 2). Further, it is always beneficial to measure the sidewall pressure just in front of the specimen and possibly one behind to get accurate loading information. A gage too far away upstream or downstream from the specimen may not yield a reliable loading data. If possible, one can actually measure the profile using surface pressure gages glued directly on the animal and this is the best choice. However, the effect of, surface orientation of the gage with respect to shock direction should also be considered.

Table 1 shows the IEDs, mine threats currently employed in the field, and their explosive capacity in TNT strength (23, 24). Using ConWep, we can determine the pressure profiles for TNT explosives within the range of strengths described in **Table 1**. We compared the shock tube generated wave profile with the incident wave obtained for TNT explosive in ConWep simulation software (**Figure 10**). Clearly, there is good match in the results (see **Table 1**) that indicates the wave profile generated from our shock tube can be directly related to relevant field conditions.

It may be instructive to examine how the results presented here can be applied to a variety of shock tubes currently being used in various laboratories to study blast injury animal models. What is shown in this work is to how to generate a planar shock wave that replicates mild and moderate TBI conditions when only blast (i.e., primary blast) is considered. Since blasts can be very easily produced by the sudden release of high-pressure gas, one should be careful that at the test location, the blast might not be planar. Since the planarity is achieved only after sufficient length from the membrane and away from the open end, locating specimens close to the end will result in primary plus tertiary loads (from blast wind) along with effects from the exit rarefaction wave. Thus, injury resulting from specimens kept near the open end of the tube will lead to mixed mode compared to pure primary type of loading.

CONCLUSION

Compressed-gas-driven shock tubes are used by different research groups to study BINT using animal models. In order to provide field-relevant blast waves and to compare the results among different groups, it is important to know the actual shock pulse impinging on the test objects. Since the pressure-time pulse vary significantly for different explosive strength and stand-off distance it is important to tailor the blast wave parameters for a wide range in controlled and repeatable manner. This study presents how the SAPs influence SWPs. Further, the need for optimization of SAPs to avoid a flattop wave or expansion waves from the exit, are also explained. Finally, a comparison is made between wave profiles generated from a shock tube and ConWep to show that our shock tube can replicate the pressure profiles within a range of practical interest. Key findings of this work are as follows:

- Burst pressure depends only on the membrane thickness and not on the breech length (for practical ranges tested); hence, the blast overpressure increases with increase in membrane thickness. At lower breech lengths blast overpressure is affected due to the shock front interaction with expansion waves from the breech.
- Positive time duration increases with increase in the breech length; however, higher breech lengths in conjunction with use of nitrogen gas produces a plateau or a flattop wave. This problem can be solved by either using helium as driver gas or in some cases by shifting the test section downstream of expansion section (a longer shock tube may be required for avoiding exit end effects).
- When the test section is moved closer to the exit of the shock tube, the rarefaction wave from the exit creates unacceptable artifacts in the wave profile.
- From the comparison of the profiles from ConWep TNT profiles and shock tube profiles it can be concluded that compressed-gas shock tube can be used to accurately simulate primary blast injury for BINT studies.

ACKNOWLEDGMENTS

We kindly acknowledge the financial support provided by the US Army Research Office. We are also grateful for Brandon Perry and Veera Selvan for their contribution to some of the experimental work.

REFERENCES

1. Chandra N, Holmberg A, Feng R. *Controlling the Shape of the Shock Wave Profile in a Blast Facility*. U.S. Provisional patent application no. 61542354 (2011).
2. Sundaramurthy A, Alai A, Ganpule S, Holmberg A, Plougonven E, Chandra N. Blast-induced biomechanical loading of the rat: an experimental and anatomically accurate computational blast injury model. *J Neurotrauma* (2012) **29**:2352–64. doi:10.1089/neu.2012.2413
3. Skotak M, Wang F, Alai A, Holmberg A, Harris S, Switzer I, et al. Rat injury model under controlled field-relevant primary blast conditions: acute response to a wide range of peak overpressures. *J Neurotrauma* (2013) **30**(13):1147–60. doi:10.1089/neu.2012.2652
4. Rafaels K. *Blast Brain Injury Risk. [Doctoral dissertation Ph.D.]*. Charlottesville, VA: University of Virginia (2010).
5. Svetlov SI, Prima V, Kirk DR, Gutierrez H, Curley KC, Hayes RL, et al. Morphologic and biochemical characterization of brain injury in a model of controlled blast overpressure exposure. *J Trauma* (2010) **69**:795–804. doi:10.1097/TA.0b013e3181bbd885
6. Bolander R, Mathie B, Bir C, Ritzel D, Vandevord P. Skull flexure as a contributing factor in the mechanism of injury in the rat when exposed to a shock wave. *Ann Biomed Eng* (2011) **39**(10):2550–9. doi:10.1007/s10439-011-0343-0
7. Cernak I, Merkle AC, Koliatsos VE, Bilik JM, Luong QT, Mahota TM, et al. The pathobiology of blast injuries and blast-induced neurotrauma as identified using a new experimental model of injury in mice. *Neurobiol Dis* (2011) **41**:538–51. doi:10.1016/j.nbd.2010.10.025
8. Chavko M, Watanabe T, Adeeb S, Lankasky J, Ahlers ST, Mccarron RM. Relationship between orientation to a blast and pressure wave propagation inside

the rat brain. *J Neurosci Methods* (2011) **195**:61–6. doi:10.1016/j.jneumeth.2010.11.019
9. Reneer DV, Hisel RD, Hoffman JM, Kryscio RJ, Lusk BT, Geddes JW. A multi-mode shock tube for investigation of blast-induced traumatic brain injury. *J Neurotrauma* (2011) **28**:95–104. doi:10.1089/neu.2010.1513
10. Gould KE, Tempo K. *High-Explosive Field Tests, Explosion Phenomena and Environmental Impacts*. Santa Barbara CA: Defense Technical Information Center (DTIC) (1981).
11. Elder GA, Cristian A. Blast-related mild traumatic brain injury: mechanisms of injury and impact on clinical care. *Mt Sinai J Med* (2009) **76**:111–8. doi:10.1002/msj.20098
12. Ruff RL, Ruff SS, Wang X-F. Headaches among operation Iraqi freedom/operation enduring freedom veterans with mild traumatic brain injury associated with exposures to explosions. *J Rehabil Res Dev* (2008) **45**:941–52. doi:10.1682/JRRD.2008.02.0028
13. Fischer H. *US Military Casualty Statistics: Operation New Dawn, Operation Iraqi Freedom, and Operation Enduring Freedom*. Washington DC: Congressional Research Service (2010).
14. Ropper A. Brain injuries from blasts. *N Engl J Med* (2011) **364**:2156–7. doi:10.1056/NEJMe1102187
15. Bass CR, Panzer MB, Rafaels KA, Wood G, Shridharani J, Capehart B. Brain injuries from blast. *Ann Biomed Eng* (2012) **40**(1):185–202. doi:10.1007/s10439-011-0424-0
16. Tanielian T, and Jaycox LH. *Invisible Wounds of War*. Santa Monica, CA: RAND Corporation (2008).
17. Zhu F, Mao H, Dal Cengio Leonardi A, Wagner C, Chou C, Jin X, et al. Development of an FE model of the rat head subjected to air shock loading. *Stapp Car Crash J* (2010) **54**:211–25.
18. Risling M, Plantman S, Angeria M, Rostami E, Bellander BM, Kirkegaard M, et al. Mechanisms of blast induced brain injuries, experimental studies in rats. *Neuroimage* (2011) **54**(Suppl 1):S89–97. doi:10.1016/j.neuroimage.2010.05.031
19. Säljö A, Mayorga M, Bolouri H, Svensson B, Hamberger A. Mechanisms and pathophysiology of the low-level blast brain injury in animal models. *Neuroimage* (2011) **54**:S83–8. doi:10.1016/j.neuroimage.2010.05.050
20. Ganpule S, Alai A, Plougonven E, Chandra N. Mechanics of blast loading on the head models in the study of traumatic brain injury using experimental and computational approaches. *Biomech Model Mechanobiol* (2012) **12**(3):511–31. doi:10.1007/s10237-012-0421-8
21. Kuppuswamy VS. *The Mechanics of Intracranial Loading During Blast and Blunt Impacts – Experimental and Numerical Studies*. Masters Thesis. Lincoln: University of Nebraska Lincoln (2013).
22. Kobeissy FH, Mondello S, Tumer N, Toklu HZ, Whidden MA, Kirichenko N, et al. Assessing neuro-systemic & behavioral components in the pathophysiology of blast-related brain injury. *Front Neurol* (2013) **4**:186. doi:10.3389/fneur.2013.00186
23. HSD. *Homeland Security Bomb Threat Chart*. Available from: https://www.llis.dhs.gov/sites/default/files/DHS-BombThreatChart-6-5-09.pdf
24. Aep-55 NATO. *Procedures for Evaluating the Protection Level of Logistic and Light Armoured Vehicle Occupants for Grenade and Blast Mine Threats Level, NATO/PFP Unclassified*. 1 ed. (Vol. 2). NATO (2006).
25. Ritzel D, Matthews K. An adjustable explosion-source model for CFD blast calculations. *Proc. of 21st International Symposium on Shock Waves*. Great Keppel Island, QLD (1997). p. 97–102.
26. Kinney GF, Graham KJ. *Explosive Shocks in Air*. New York, NY: Springer-Verlag (1985).
27. Ritzel D, Parks S, Roseveare J, Rude G, Sawyer T. Experimental blast simulation for injury studies. *Proc. HFM-207 NATO Symposium on a Survey of Blast Injury Across the Full Landscape of Military Science*. Symposium held in Halifax: NATO (2011).
28. Kleinschmit NN. *A Shock Tube Technique for Blast Wave Simulation and Studies of Flow Structure Interactions in Shock Tube Blast Experiments*. Masters Thesis. Lincoln: University of Nebraska Lincoln (2011).
29. Long JB, Bentley TL, Wessner KA, Cerone C, Sweeney S, Bauman RA. Blast overpressure in rats: recreating a battlefield injury in the laboratory. *J Neurotrauma* (2009) **26**:827–40. doi:10.1089/neu.2008.0748
30. Payman W, Shepherd WCF. Explosion waves and shock waves. VI. The disturbance produced by bursting diaphragms with compressed air. *Proc R Soc Lond A Math Phys Sci* (1946) **186**:293–321. doi:10.1098/rspa.1946.0045
31. Mott D, Schwer D, Young T, Levine J, Dionne J-P, Makris A, et al. Blast-induced pressure fields beneath a military helmet for non-lethal threats. In: *APS Division of Fluid Dynamics Meeting Abstracts*, Vol. 53. San Antonio, TX: APA physis (2008)
32. Prima V, Serebruany VL, Svetlov A, Hayes RL, Svetlov SI. Impact of moderate blast exposures on thrombin biomarkers assessed by calibrated automated thrombography in rats. *J Neurotrauma* (2013) **30**:1881–7. doi:10.1089/neu.2012.2758
33. Chandra N, Ganpule S, Kleinschmit N, Feng R, Holmberg A, Sundaramurthy A, et al. Evolution of blast wave profiles in simulated air blasts: experiment and computational modeling. *Shock Waves* (2012) **22**:403–15. doi:10.1007/s00193-012-0399-2

Conflict of Interest Statement: The authors declare that the research was conducted in the absence of any commercial or financial relationships that could be construed as a potential conflict of interest.

Received: 05 August 2014; accepted: 16 November 2014; published online: 02 December 2014.
*Citation: Sundaramurthy A and Chandra N (2014) A parametric approach to shape field-relevant blast wave profiles in compressed-gas-driven shock tube. Front. Neurol. **5**:253. doi: 10.3389/fneur.2014.00253*
This article was submitted to Neurotrauma, a section of the journal Frontiers in Neurology.
Copyright © 2014 Sundaramurthy and Chandra. This is an open-access article distributed under the terms of the Creative Commons Attribution License (CC BY). The use, distribution or reproduction in other forums is permitted, provided the original author(s) or licensor are credited and that the original publication in this journal is cited, in accordance with accepted academic practice. No use, distribution or reproduction is permitted which does not comply with these terms.

Appendix B – Book Chapter
2015

Authors: N. Chandra, A. Sundaramurthy, R.K. Gupta,

Title: *"Acute Pathophysiology of Blast Injury-From Biomechanics to Experiments and Computations: Implications on Head and Polytrauma"*

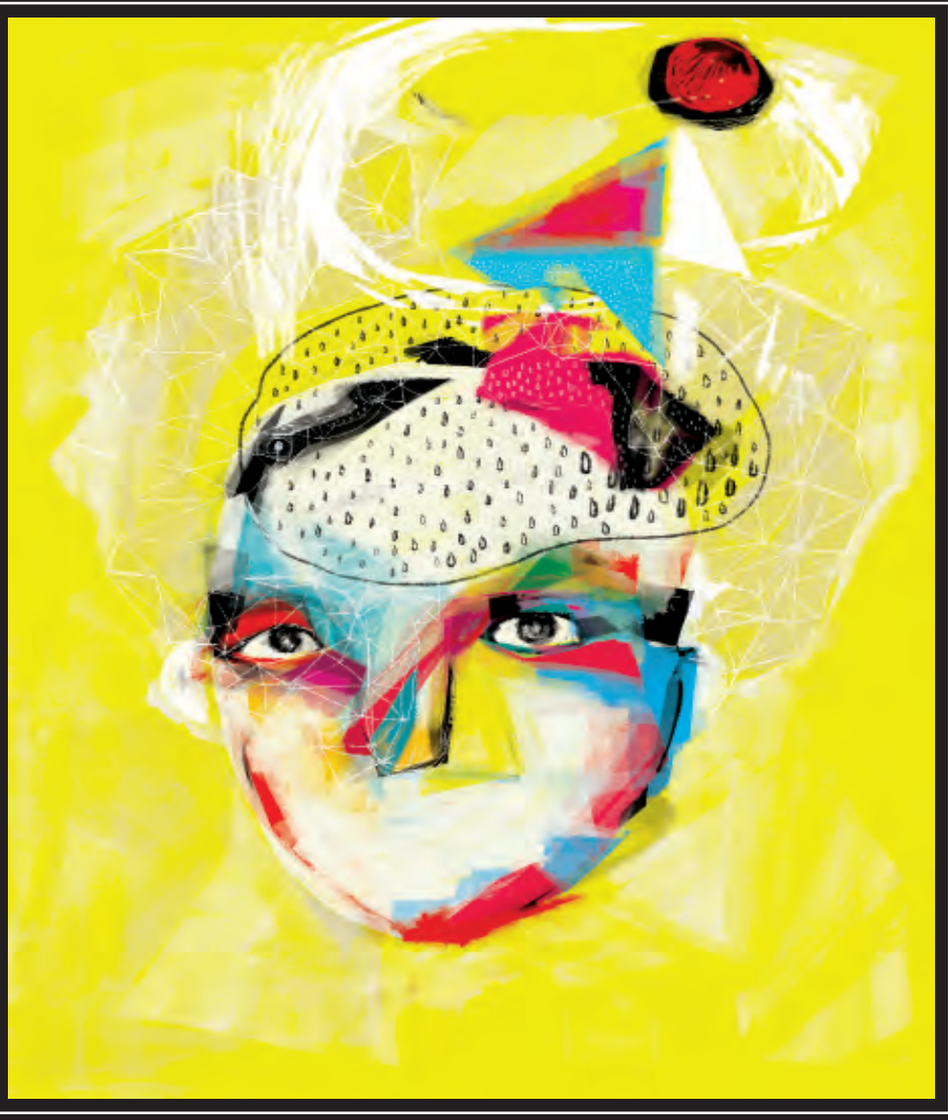
Journal Publication: Chapter 18, 196-253**, Brain Neurotrauma: Molecular, Neuropsychological and Rehabilitation Aspects, Ed. Firas H. Kobeissy,** (2015) [15-B1].

Kobeissy

CRC Press
Taylor & Francis Group

BRAIN NEUROTRAUMA

MOLECULAR, NEUROPSYCHOLOGICAL and REHABILITATION ASPECTS



Edited by Firas H. Kobeissy

BRAIN NEUROTRAUMA

FRONTIERS IN NEUROENGINEERING

18 Acute Pathophysiology of Blast Injury
From Biomechanics to Experiments and Computations: Implications on Head and Polytrauma

Namas Chandra and Aravind Sundaramurthy

CONTENTS

18.1 Introduction 196
18.1.1 Definitions of TBI and Blast-Induced TBI 197
18.1.2 Classification of TBI: Ballistics, Blunt, and Blast 198
18.1.2.1 Ballistics 198
18.1.2.2 Blunt 198
18.1.2.3 Blast 198
18.1.3 Mild/Moderate Blast TBI 199
18.1.4 Current State of the Research 199
18.1.5 Organization of the Chapter 200
18.1.6 Replicating Primary Blast in the Laboratory 201
18.1.7 Characteristics of Field Explosion 201
18.1.8 Laboratory Reproduction of Shock-Blast Wave 202
18.1.9 Types of Shock Tubes 203
18.1.9.1 Detonation Shock Tube 203
18.1.9.2 Combustion Shock Tube 203
18.1.9.3 Compressed Gas Shock Tube 203
18.1.9.4 General Features of Compressed Gas Shock Tube Construction 204
18.1.10 Test Section Location 205
18.1.10.1 Contact Surface 205
18.1.10.2 Planarity 206
18.1.10.3 Exit Rarefaction 206
18.1.11 Effects of Placing Specimen Outside the Shock Tube 206
18.1.11.1 Evolution of Shock-Blast Wave Outside the Shock Tube 207
18.1.11.2 Comparison of Mechanical Response Between Outside Versus Inside 207
18.1.12 Tailoring the Shock-Blast Wave Profile 211
18.1.12.1 Burst Pressure 212
18.1.12.2 SAPs and Their Influence on the SWPs in the Test Section 213
18.1.12.3 Evolution of the Shock-Blast Wave Along the Expansion Section 214
18.1.12.4 Flattop or Plateau Wave 215
18.1.12.5 Comparison Between Field and Laboratory Profiles 216
18.2 PMHS Blast Testing 216
18.2.1 Experiments 216
18.2.1.1 PMHS Testing in the 28-inch Shock Tube 216
18.2.1.2 Blast Wave Exposure 218
18.3 Animal Model Blast Testing 223
18.3.1 Experiment 223
18.3.1.1 Biomechanical Loading Evaluation in Cadaver Rats 225
18.3.1.2 Live Animal Testing 225

18.3.2 Results and Discussion 226
18.3.2.1 Biomechanical Loading Evaluation and ICP Analysis 226
18.3.2.2 Physiological Parameters 228
18.3.2.3 Shock Wave–Induced Acute Lung Injury 229
18.3.2.4 BBB Damage and IgG Uptake by Neurons 230
18.4 Computer Models 230
18.4.1 Development of Human Head Model 231
18.4.2 Development of Animal Head Model 232
18.4.3 General Theory of Material Models and Material Parameters Used in the Head Models 232
18.4.3.1 Material Models for Human Head Model 233
18.4.3.2 Material Models for Rat Head Model 233
18.4.4 Computational Framework for Blast Simulations 233
18.4.4.1 Numerical Approach for Shock Tube 233
18.4.4.2 Loading, Interface, and Boundary Conditions 234
18.4.5 Solution Scheme 235
18.4.6 Model Validations 235
18.4.6.1 Validation of the MRI-Based Human Head Model Against Blast Experiments 235
18.4.6.2 Validation of the MRI-Based Rat Head Model Against Blast Experiments 237
18.5 Mechanics of Blast Wave–Human Head Interactions With Helmets 238
18.5.1 Flow Field on the Surface of the Head with the Helmet 238
18.5.2 Comparison of Experiments and Numerical Simulations for Helmeted Cases 238
18.5.3 Underwash Effect of the Helmet 240
18.5.3.1 Effect of Curvature, Head–Helmet Gap Size, and Incident Peak Pressure Intensity 240
18.5.4 Effect of Orientation on Blast Wave–Head Interactions With and Without Head Protection 242
18.5.4.1 No Helmet Case 242
18.5.4.2 Suspension Helmet Case 243
18.5.4.3 Padded Helmet Case 243
18.5.5 Total Impulse Around the Head for Various Head–Helmet Configurations 243
18.5.6 Results from Numerical Simulations 243
18.5.7 Discussion on Orientation-Dependent Blast Wave–Head Interactions 244
18.5.8 Role of Helmet in Mechanics of the Blast Wave–Head Interactions: Effect on ICP Response 247
18.6 Conclusion 249
Acknowledgements 251
References 251

18.1 INTRODUCTION

Traumatic brain injury (TBI) has been a major public health concern in the United States for decades; from 1995 to 2001 with an average of 1.4 million Americans a year sustaining TBI, leading to 50,000 deaths, 235,000 hospitalizations, and 1.1 million emergency department visits (Langlois et al., 2004). Of these, an estimated of 80,000–90,000 experienced the onset of long-term disability (Langlois et al., 2004; Thurman et al., 1999). These TBIs were largely caused by falls, motor vehicle crashes, sports collisions, and firearm assaults (Langlois et al., 2004). However, in this chapter, we are concerned with a new type of brain injury arising from explosions commonly referred to as blast-induced neurotrauma (BINT). We will focus on the origin, mechanics, mechanisms of BINT, and the current state-of-the-art in terms of protection, diagnostics, prognostics, and therapeutics of the injury. We will outline the research approaches currently under way in terms of: experiments in laboratory on animals, surrogate heads, cadaveric heads; computer models of head–brain system; and finally an analysis on the protective capabilities of the current helmets against blast loading.

BINT has been recognized as a major problem among U.S. service members since Operation Enduring Freedom (OEF) began in Afghanistan in October 2001 and Operation Iraqi Freedom (OIF) began in Iraq in May 2003. Blasts have been considered a threat to soldiers and civilians since the early 1970s, when researchers mainly considered lung damage and designed better protective body armors. Ironically, these body armors have saved many during explosions, making them more vulnerable to brain injuries. A recent RAND report estimates that 320,000 service members or 20% of the deployed force (total deployed 1.6 million) potentially suffer from TBI (Tanielian, 2008). However, of this population, approximately 60% have never been assessed by a health care provider specifically for TBI. Department of Defense (DOD) based on data from 2004 to 2006 at selected military installations has estimated that 10%–20% of (the total deployed) OEF/OIF service members potentially sustain mild TBI (mTBI; Reneer et al., 2011). Other studies also report the occurrence of TBI in

OEF/OIF veterans. For example, a recent study has found that 22.8% of soldiers in an Army Brigade Combat Team returning from Iraq had clinically confirmed TBI (Terrio et al., 2009). A survey of OEF/OIF veterans, who had left combat theaters by September 2004, found that about 12% of the 2,235 respondents reported a history consistent with mTBI (Zhu et al., 2010). Among those who have been medically evacuated from theater, the proportions who have suffered TBI are predictably higher. For example, Between January 2003 and February 2007, 29% of the patients evacuated from the combat theater to Walter Reed Army Medical Center in Washington, DC, had evidence of TBI (Defense and Veterans Brain Injury Center, 2007). Of 50 OEF/OIF veterans treated at the Tampa Veterans Affairs Polytrauma Rehabilitation Center, 80% had incurred combat related TBI, with 70% of the injuries caused by improvised explosive devices (IEDs) (Clark et al., 2007).

For active-duty military personnel in war zones, blasts are the primary cause of TBI (Tanielian, 2008). Recent statistics from the conflict in Iraq show that several thousands of active duty U.S. soldiers have sustained TBI; 69% of these as a result of blasts (Warden, 2006). Analysis of data collected (collection period: March 2004–September 2004) from 115 patients from the Navy–Marine Corps that were identified with TBI, have found that IEDs were the most common mechanism of injury, responsible for 52% TBI cases overall. The analysis also showed that intracranial injuries particularly concussions were the most common diagnosed, especially among patients with nonbattle injuries (94%). Although multiple TBI-related diagnoses were common, 51% of the patient group had only an intracranial injury with no accompanying head fracture or open wound of the head. It was also found that of 115 patients analyzed, about 63% of patients were wearing helmet at the time of injury (Clark et al., 2007). In addition to the data reported previously, the DOD, in cooperation with the Armed Forces Health Surveillance Center and Defense and Veterans Brain Injury Center, has consolidated the data of clinically confirmed TBI cases among service members and categorized them based on the severity of injury as shown in Figure 18.1 (AEP-55, 2006). mTBI contributes to more than 80% of the total reported brain injuries (Fig. 18.1) because exposure to repeated low-level blasts is a common feature of the war zone personnel/civilian populations. Indeed, blast-induced mTBI has been identified as the signature injury of OEF and OIF (Jones et al., 2007; Tanielian, 2008; Terrio et al., 2009; Warden, 2006). It should also be noted that number of TBI cases reported by the DOD (AEP-55, 2006) is 10 times smaller than that estimated by the RAND (Tanielian, 2008) study. This discrepancy is attributed to methodology used for estimating the numbers. RAND estimates are often based on the subjective response to nonspecific screening questions asked to several hundred individuals; that resulting percentage was then generalized to the entire deployed population. On the contrary, DOD estimates are completed based on clinically confirmed TBI cases.

18.1.1 Definitions of TBI and Blast-Induced TBI

TBI is a silent epidemic with serious consequences that changes the lives of the victims and their families irrevocably (Thurman et al., 1995). The Centers for Disease Control and Prevention defines TBI as a head injury that is associated with decreased levels of consciousness, amnesia, other neurological or neurophysiological abnormalities, skull fracture, diagnosed intracranial lesions, or death. TBIs can be classified as mild, moderate, or severe.

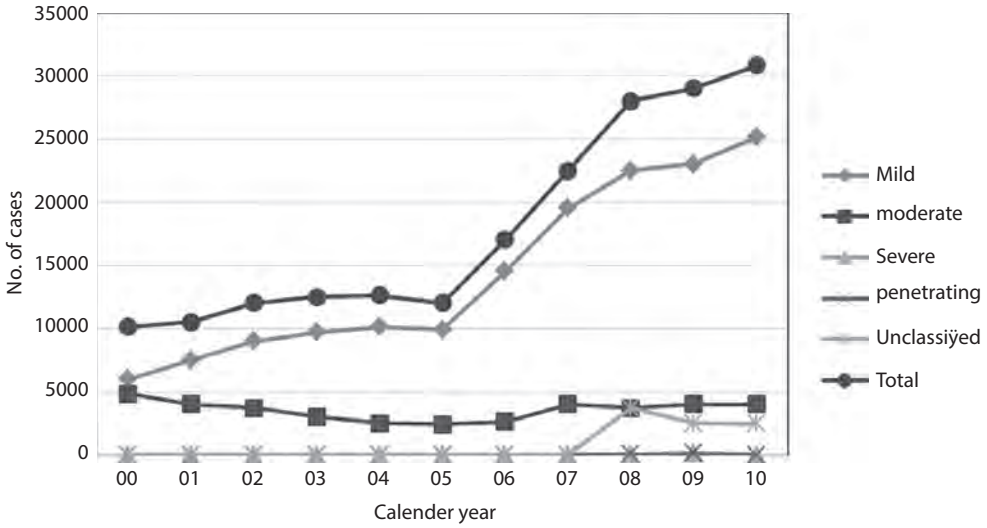


FIGURE 18.1 Blast-induced TBI in U.S. service members between 2000 and 2010 (source: Armed Forces Health Surveillance Center, Department of Defens. Accessed January 2012.). These numbers are based on clinically confirmed TBI cases. mTBI contributes to more than 80% of the total reported brain injuries.

The American Congress of Rehabilitation Medicine has defined blast-induced mTBI as a head injury resulting in at least one of: loss of consciousness (Lockhart) for 30 minutes or less; posttraumatic amnesia (PTA) for less than 24 hours; any alteration in the mental state immediately after the accident; or focal neurological deficit(s) that may or may not be transient. The emergency room physicians upon presentation of the patient routinely use the Glasgow Coma Scale to assess the state of TBI. The 15-point Glasgow Coma Scale defines the severity of injury as mild (13–15), moderate (9–12), severe (3–8), or vegetative state (<3) based on eye, verbal, and motor responses (Teasdale and Jennett, 1974). A new classification specific to blast-related TBI (bTBI) has been also proposed recently, in which a blast-induced mTBI is characterized by loss of consciousness (Lockhart) for less than 1 hour and PTA for less than 24 hours after exposure to an explosive blast. Moderate bTBI is characterized by loss of consciousness (Lockhart) for 1–24 hours and PTA for 1–7 days, and severe bTBI is characterized by loss of consciousness for more than 24 hours and PTA for more than 7 days (Ling et al., 2009). Mild to moderate cases of bTBI do not involve skull fracture; further, they are not detectable through current neuroimaging techniques. The Centers for Disease Control and Prevention has reported that up to 75% of TBIs that occur each year are mild, and a World Health Organization task force reported that 70%–90% of all treated TBI were mild (Kraus et al., 2007). mTBI is typically not associated with abnormalities in brain imaging (Okie, 2005), and most patients with mTBI recover fully in 4–12 weeks (Alexander, 1995; Kennedy et al., 2007). However, mTBI patients with more severe injuries, such as those who experienced loss of consciousness lasting more than 10 minutes or PTA lasting more than 4–6 hours, may require months to years to recuperate (Alexander, 1995). In addition, some mTBI patients develop postconcussive syndrome, experiencing persistent cognitive, behavioral, and/or somatic symptoms (Alexander, 1995; Heitger et al., 2009; Zhu et al., 2010). Studies have shown that 15%–35% of patients with mTBI experience onset of long-term disability (Alexander, 1995; Heitger et al., 2009; Thurman et al., 1999).

18.1.2 Classification of TBI: Ballistics, Blunt, and Blast

Head and brain injuries are categorized based on the origin of mechanical forces as blast, blunt, or ballistic injuries.

18.1.2.1 Ballistics

In a ballistic impact, the penetrating object pierces the skull and enters the brain parenchyma. Depending on the kinetic energy at the time of contact, a penetrating object may be ejected from the opposite side along with biological tissues or lodged inside the brain. All along the path of propagation of the penetrant, the tissue is dismembered and physical separation occurs, which affects both the neuronal tissues as well as the vasculature. Though ballistic injuries have been significantly prevented with composite armored helmets in the battlefield, this remains a major issue in the civilian population because of increased gun violence.

18.1.2.2 Blunt

In blunt impacts, the head of the victim collides with a stationary or moving object. During the process of collision, the head encounters a directional force in a local region. Furthermore, the head and the brain translate or rotate depending on the magnitude and direction of the impacting force. The energy transfer to the head is governed by the laws of conservation of energy; the peak force, contact area, and the duration of the impact are governed by the principles of conservation of momentum; and the actual state of strain/stress is governed by equilibrium of forces. The severity of injury is a function of the mass and velocity of the impactor, and form, shape, size, and material of the impactor as well as the protective state of the head (helmet type, padding system, impact location, and unprotected). Common types of blunt injuries include epidural/subdural hematoma, subarachnoid hematoma, and contusion and severe hemorrhage, with concomitant increase in intracranial pressure (ICP) (Bolander et al., 2011).

18.1.2.3 Blast

A field blast is extremely complex and the facets of the injuries include components of both blunt and ballistic impact. In general, blast injuries are classified into four main categories: (1) primary (direct effects of overpressure), (2) secondary (effects of projectiles/shrapnel), (3) tertiary (effects from fall from blast winds), and (4) quaternary (burns, asphyxia, and exposure to toxic inhalants). Usually, depending on the strength of explosive, casing, standoff distance, and scenario (urban, theater, indoor/outdoor), victims suffer a combination of these injuries. An illustration of these injuries is shown in Figure 18.2.

18.1.2.3.1 Primary Blast Injury

Once a bomb explodes, it results in a sudden rise in the atmospheric pressure, which represents the shock front followed by an exponential decay resulting from the expansion wave depleting the overpressure. This sudden rise followed by an exponential decay comprises the positive phase of the blast wave and is responsible for primary blast injury. Although the sharp rise constitutes the shock wave, the rest of the pressure pulse is referred to as blast wind. Furthermore, depending on surrounding (urban, indoor/outdoor) structure or an enclosure (such as interior of a bunker or a vehicle), the subjects are also exposed to a complex blast waves caused by multiple reflections from the walls, floor, and ceiling and their interactions.

18.1.2.3.2 Secondary Blast Injury

IEDs have metal casings and are usually filled with metal fragments. During the explosion, these metal fragments become highly accelerated projectiles that penetrate the body. The pathology associated with secondary blast injuries are similar to that of the ballistic injury discussed previously.

18.1.2.3.3 Tertiary Blast Injury

Tertiary injury includes those with nonpenetrating projectile impacts as well as from injuries from a fall. Explosion within a building may result in its collapse, causing impact and

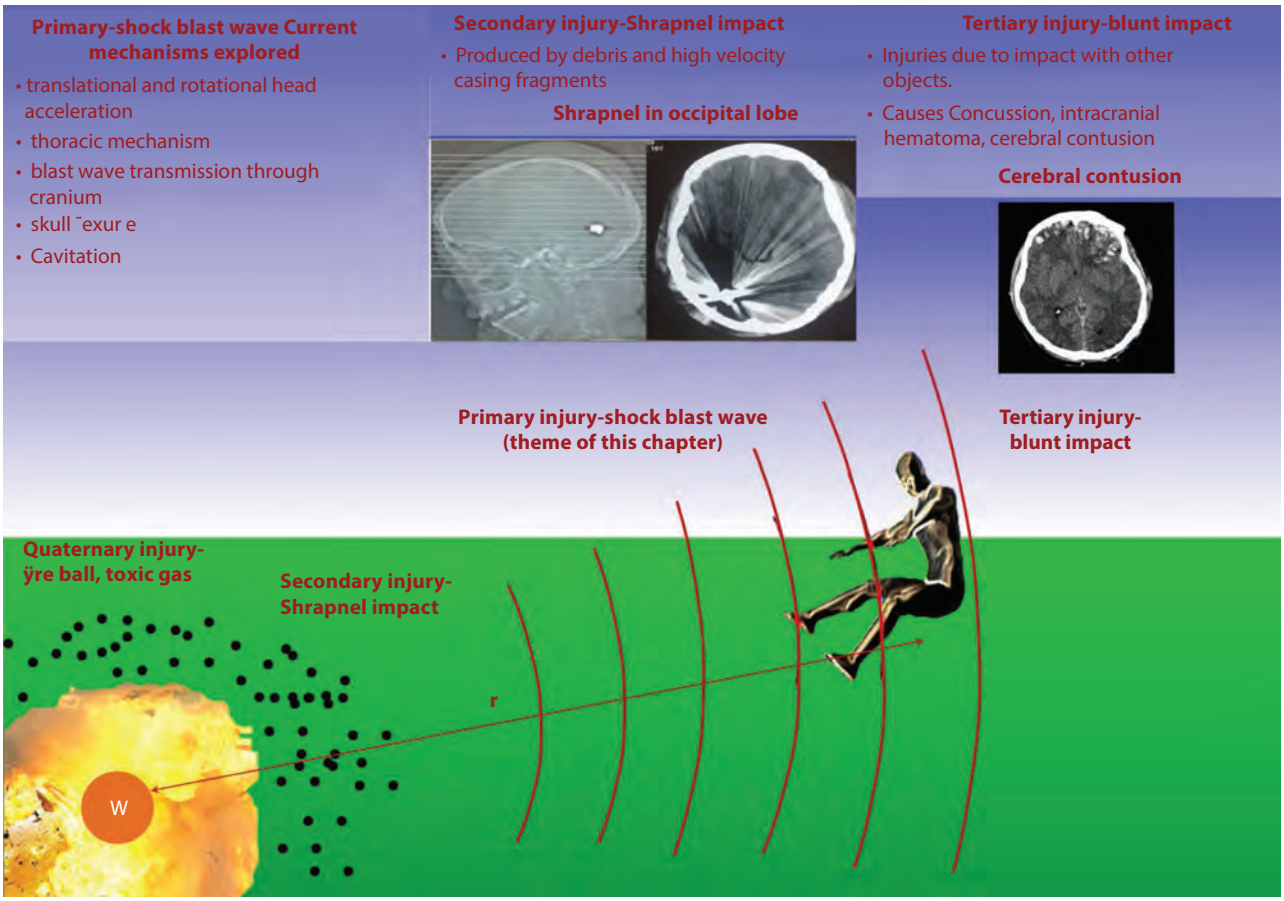


FIGURE 18.2 bTBI classification. In this figure, w is the charge weight and r is the standoff distance.

crushing of the body, whereas in an outdoor blast, depending on the proximity of the blast epicenter the whole body might be thrown, resulting in impact with hard surface. When seated inside a vehicle under explosive attacks or in a rollover or head-on collisions, the victims are thrown violently inside, leading to an impact-type injury. The pathology of this injury is similar to the blunt impact discussed previously.

18.1.2.3.4 Quaternary Blast Injuries Blast Injury

Quaternary blast injuries refer to explosion-related injuries that were not included in the primary, secondary, or tertiary injuries (DePalma et al., 2005). Quaternary injuries include burns (chemical or thermal), toxic inhalation, and exposure to radiation.

18.1.3 Mild/Moderate Blast TBI

When subjects are closer to the epicenter of the blast, they will endure injuries with the degree of severity, which in most cases will result in fatalities. However, at a sufficiently longer distance from the source (i.e., in the far field range) only primary or pure blast effects are dominant (Reynolds, 1998). It is conjectured that mild to moderate TBI seen in the theater is due to primary blast effects alone because injuries were nonfatal, with neither head fracture nor open wounds (Dewey, 1971; Kleinschmit, 2011; Skotak et al., 2013; Warden, 2006). In 2005, the U.S. military reported 10,953 IED attacks, at an average of 30 per day. As mentioned previously, these explosions were less fatal with much higher survivability rate than in previous wars, hence mostly resulting in mild or moderate TBI. Hence, in this chapter, we are only concerned with the primary blast injury wherein the victim is exposed to a pure shock-blast wave that eventually results in a mild or moderate TBI.

18.1.4 Current State of the Research

Creating conditions of blast loading and understanding the physics of the blast are fundamental elements in the study of acute and chronic ailments of primary blast injury. Field-testing and shock tubes are the main methods used for creating a primary blast injury. Among them, shock tubes are more commonly and frequently used in primary blast injury research. Table 1 from a review article by Kobeissy and his colleagues shows the recent major studies on primary blast injury (Kobeissy et al., 2013). Among this list, only eight cases of 49 used field explosive testing as a method of generating primary blast. In 36 other cases, shock tubes were used. Shock tubes are also classified into three types: (1) compressed gas shock tube, (2) detonation shock tube, and (3) combustion shock tube. Among them, compressed gas shock tubes are predominately used as the source for primary blast (in 33 cases).

Understanding the processes of primary blast inflicting loads (i.e., the mechanism of by which the injury occurs is a prerequisite to the design of proper animal model testing and interpretation of results) (Benzinger et al., 2009). Over the past few years, several mechanisms of mechanical insult have been suggested. These mechanisms are: (1) thoracic mechanism in which blast waves enter the brain through the thorax and increase brain pressure via vasculature (Cernak et al., 1997, 2001; Courtney and Courtney, 2009), (2) translational and rotational head acceleration (Courtney and Courtney, 2009), (3) blast wave transmission through cranium (Moore et al., 2009; Nyein et al., 2010; Taylor and Ford, 2009), (4) skull flexure (Bolander et al., 2011; Moss et al., 2009), and (5) cavitation (Panzer et al., 2012; Payman and Shepherd, 1946). Most of these mechanisms are proposed using numerical models alone and experimental evidence is needed to corroborate these proposed mechanisms. Postmortem human specimen (PMHS) heads, which is closest to humans in terms of anthropometry, can be used to study and validate these mechanisms. However, one main drawback with PMHS is that it is not possible to mimic material and biological aspects of a living brain.

Animal models are essential for studying the biomechanical, cellular, and molecular aspects of human TBI that cannot be addressed using surrogate models. Furthermore, a validated animal model is required for development and characterization of novel therapeutic interventions. Currently, the majority of this work is done using small mammals; very few studies use large mammals (Kobeissy et al., 2013). Animal models are used to investigate the physiological, neuropathological, and neurobehavioral consequences as well as identify biomarkers that are related to brain injury. However, one main issue with the current research in animal models is the inconsistency in specimen location, when doing experiments with a shock tube. This leads to two problems: (1) erroneous loading conditions (in some cases) and (2) comparison of the results between different laboratories is virtually impossible. Therefore, developing a standard experimental model that can be validated across laboratories is essential for the interpretation of the mechanisms of blast injury, the identification of biomarkers, and, eventually, the development of strategies for mitigating blast-induced brain injury (Xiong et al., 2013).

Given the difficulties to understand TBI associated with conducting experiments on PMHS or human volunteers and translating animal models results to human, computational modeling has always been an easier choice. As a result, there are a large number of models reported in the literature over past decades (refer to Table 2.2 in Ganpule, 2013). Computational modeling is currently used for studying the shock-blast interaction with the head (analysis of reflected pressure fields), flow field analysis for determining the flow separations, and pressure field distribution in the brain and loading mechanisms (skull flexure, direct pressure transmission) as well as the effect of helmets. One main drawback in computational modeling is the lack of consistent and accurate material models. Consequently, it is vital to validate the model against an accepted experimental standard to ensure the validity of the predictions in the model.

It is estimated that since 2005, 77% of soldiers who sustained any type of TBI were wearing their helmets at the time of injury (Wojcik et al., 2010). Although the role of helmets in bTBI is critical, there are very few investigations that have studied helmets in blast mitigation (Brown et al., 1993; Grujicic et al., 2011; Nyein et al., 2010; Sogbesan, 2011). These studies concluded that a padded helmet provides only some degree of protection to the head during blast loading. Reductions of pressure were noticed in coup regions, whereas in other areas (e.g., brainstem) the values of ICP, shear stress, and strain remained unchanged compared with no helmet case. A comprehensive study using both experiments and numerical models is essential to elucidate the role of helmets in blast mitigation and to gauge the capabilities of the different helmets currently used by the military personnel in the theater.

18.1.5 Organization of the Chapter

In this section, we examine the physics of explosion and the characteristics of shock-blast wave as a function of explosive strength and stand-off distance. Because experiments on biological medium require a large number of samples with variations in key parameters, conducting experiments with actual blasts is not an option in terms of time, cost, or safety. Properly designed laboratory-scale shock tubes can replicate field conditions. Unfortunately, many of the current experiments conducted by different experimental groups around the world have not paid attention to this detail; hence, their results should be viewed with caution. If pure primary blast conditions are not achieved during the test conditions, then the specimens are subjected to a combination of blast as well as the loads associated with tertiary injury. Compressed gas-driven shock tubes are very commonly used to replicate field conditions. In this section, we outline the basic components of the shock tube and how each of them interacts to produce the desired profile of shock wave. The location of test specimen within the length of the tube plays a major role.

In the PMHS Blast Testing section, we examine the basic question of how blast wave interacts with the human head and causes mechanical loading on the brain. Both the physics of the problem and preliminary experiments clearly showed that the brain loading would depend on the geometry (shape and size) of the head as well as the tissue properties of the head, in addition to the intensity of shock wave itself. To represent humans as accurately as possible, cadaveric heads (PMHS) back-filled with ballistic gels were subjected to field-relevant blast conditions. Deformation was measured both on the surface of the head and measuring ICP variations. These measurements were repeated when the intensity of the external shock was increased. The results showed that there is an increase in pressure excursion in the brain with an increase in the shock wave intensity.

In the Animal Model Blast Testing section, we examine the role of animal models in answering the fundamental question of whether the primary blast causes measurable changes at the cellular and tissue as well as behavioral patterns. We discuss the observed physiological changes occurring immediately after exposures in terms of heartbeat, pulse, blood

oxygen levels, and weight loss over time. We established a dose-response curve between external blast overpressure from 60 kPa to 450 kPa and mortality rates. The response shows a typical sigmoidal curve. Significant pathophysiological changes like plasma membrane integrity loss, blood-brain barrier damage, and elevated levels of reactive oxygen species are observed. The damage in the deeper brain regions distinguishes bTBI from the coup, contra coup type damage noticed in blunt impacts. Small, but not statistically significant changes are observed in the behavior.

Computer models play a key role in not only understanding individual test results but results across a range of species and loading conditions. This is the subject of the Computer Models section. Here we present basic mathematical formulations involved, geometric modeling techniques used to convert images to numerical models and material model parameter issues. In the Mechanics of Blast Wave Human Head Interactions with Helmets section, we address the key issue of protection. Though we do not fully understand the blast injury biomechanics, the adequacy or otherwise of current head protection devices still need to be studied. The role of geometry, material, and external loadings on the design of current helmets are discussed in this chapter.

18.1.6 Replicating Primary Blast in the Laboratory

To study mild/moderate BINT, it is vital to replicate field blast conditions associated with the injury. First, we explore the physics of explosion briefly and establish the shock wave parameters (SWPs) that can be measured and controlled. Further, some of the current techniques used for simulating the mild/moderate blast conditions are also outlined. Attention is paid to the compressed gas driven shock tube because most of the researchers tend to use this method. The dos and don'ts of the design, construction, and operation of the tubes are also elucidated.

18.1.7 Characteristics of Field Explosion

Explosives are often used by insurgents as improvised weapons. They are usually present in the form of homemade chemical explosives embedded with a variety of shrapnel and typically called IEDs. They are buried under the ground and detonated from a distance or left on the side of the road to injure a vehicle, occupants of the vehicle, pedestrians, or a gathering. The strength of the explosives is measured by kilogram of TNT-equivalent. When a chemical explosive detonates, enormous energy is released in a very short time. This energy expands very quickly and compresses the surrounding air. For a simplified spherical explosive suspended in air, the expansion is spherical in nature; the compression propagates in the form of a fast traveling wave. When the velocity of wave front exceeds the sonic velocity of air (corresponding to the temperature, altitude, and humidity) then the wave front is termed a shock wave. The shock wave is a very thin layer and the pressure increases from atmospheric to the peak overpressure within a few atomic distances and in a very short time, along the order of micro seconds. Therefore, the shock wave is front part of the blast wave and can be called as shock-blast wave. Though the term shock and blasts are used interchangeably, the shock is the very small portion of the entire blast wave profile.

Explosives can come from different sources (e.g., chemicals, high-pressure gas tanks, nuclear); their strength is expressed as a single unit in terms of TNT-equivalent. One gram of TNT produces a blast energy of 4610 J of energy; 1 ton of TNT produces about 4.61 million kJ. Explosive strength of a given chemical expresses the effectiveness of a given chemical in producing a blast wave comparable to that of the same weight of TNT. For example, pentaerythritol tetranitrate is 1.5 times more powerful than TNT, whereas C4 (composition B of 60% RDX/40% TNT) is 1.34 times more potent than TNT. When an explosive detonates, the matter of the explosive is converted to the heat of explosion (appearing as heat and fireball) and the energy of expanding gas (leading to blast waves). If the explosive mixture contains metallic products (e.g., nails, metallic sheaths), then part of the expansion energy appears as kinetic energy of the fragments acting as projectiles.

The destructive power of the blast wave increases as a function of its velocity of propagation. If a is the velocity of sound in the undisturbed air medium and u is the velocity of the blast wave, then $\frac{u}{a} \equiv M$ is defined as the Mach number. For example, the speed of sound at room temperature and pressure at sea level is approximately 343 m/sec (768 mph), a shock wave with a $M = 2$ travels at 686 m/second (1536 mph). The 1-m-long blast wave passes any given point in less than 2 msec, which is such a short time scale the exposed body is unable to react because of its inertial mass.

In the case of an idealized mid-air explosion, the gas products and the fireball expand in a spherical manner and compress the surrounding air. This expanding air continues to increase in velocity at the outer edge and at certain point, the velocity of the envelope just equals the velocity of sound (i.e., $M = 1$). When this happens, a shock front is formed. The shock front is extremely small, on the order of a few molecular diameters in width. Across this front, there is a sudden change of pressure from atmospheric of the undisturbed medium to a high pressure. There is a sudden change in pressure, velocity, and density across this narrow thickness. Behind the shock front, there is the blast wind in which the particles move at very high velocities. This shock front-blast wind continues to expand outward. However, because the expanding gas occupies an increasing volume (spherical radius r), the shock velocity slowly reduces and eventually becomes the same as the sonic velocity of the medium, at which point shock wave dies leaving behind a low velocity blast wind.

The strength of the shock wave is measured in terms of overpressure, termed as blast overpressure (BOP). BOP can be expressed as:

$$\text{BOP} = \frac{7\left(M^2 - 1\right)}{6} \text{bars}$$

Or, equivalently, the shock wave velocity can be found from BOP as

$$M = \sqrt{1 + \frac{6}{7}\mathrm{BOP}}$$

Thus we can see that there is a relationship between shock wave velocity and the blast overpressure. The shock wave velocity decreases as the spherical radius increases. At some distance (stand-off distance), this shock degenerates to a sound wave.

18.1.8 Laboratory Reproduction of Shock-Blast Wave

In this section, we consider the characteristics of a spherically expanding blast wave formed by the detonation of an explosive (e.g., an uncased C4 of charge weight W). The effects of fireball, ground reflections, and other artifacts are not considered because in the far field range of interest these effects are absent (Reynolds, 1998). The impulsive expansion of explosive product initiates first a shock wave propagating spherically outward in the surrounding air and then a family of infinite rarefaction waves propagating in the shock-compressed air. Across the shock front, pressure, density, particle velocity, and temperature rise significantly and rapidly in less than a microsecond. As the radial propagation distance r increases, the surface area of the spherical shock front increases as r^2 and consequently its intensity decreases as $1/r^2$.

The propagation of the shock front is supersonic with respect to the ambient air ahead (upstream) but subsonic with respect to the shocked air behind (downstream); the rarefaction waves remain supersonic with respect to the compressed air ahead (upstream) until the air compression is fully released. The sequential arrivals of rarefaction waves at a given r cause decrease of shock compression. Hence, in the intermediate to far range of r, more and more rarefaction waves catch up the shock front, giving rise to erosion of the shock front intensity, evolving nonlinear decay in overpressure p, and even a period of under pressure (negative overpressure) afterward. The shock front diminishes eventually at large r. Therefore, the p–t profiles of the blast waves of interest have a shock front with a peak overpressure p^* followed by a nonlinear decay during positive overpressure duration of t^* and then a period of underpressure. This is confirmed through open field-testing conducted by the authors at the Trauma Mechanics Research Facility at the University of Nebraska-Lincoln in conjunction with the U.S. Army. The laboratory and facility has since moved along with the authors to New Jersey Institute of Technology and is a part of the Center for Injury Bio-mechanics, Materials and Medicine. The test results is further corroborated with conventional weapons effects (ConWep; Ganpule et al., 2012; Sogbesan, 2011)(Figure 18.3).

Such p–t curves can be mathematically described by the so-called Friedlander waveform (Kinney and Graham, 1985) given by the following equation.

$$p(t) = p^*\left(1 - t/t^*\right)\exp\left(-bt/t^*\right) \tag{18.1}$$

where b is the decay constant.

Friedlander waveform is characteristic for open field blast. A typical Friedlander waveform profile is shown in Figure 18.4. The integration of $p(t)$ over t^* gives the positive impulse per unit area I^*. P^* (overpressure) and t^* (positive time duration) are the two independent parameters along with decay constant used for describing the essential characteristics of positive portions of the blast waves of interest. The ranges of P^* and t^* that are of interest for bTBI are postulated to

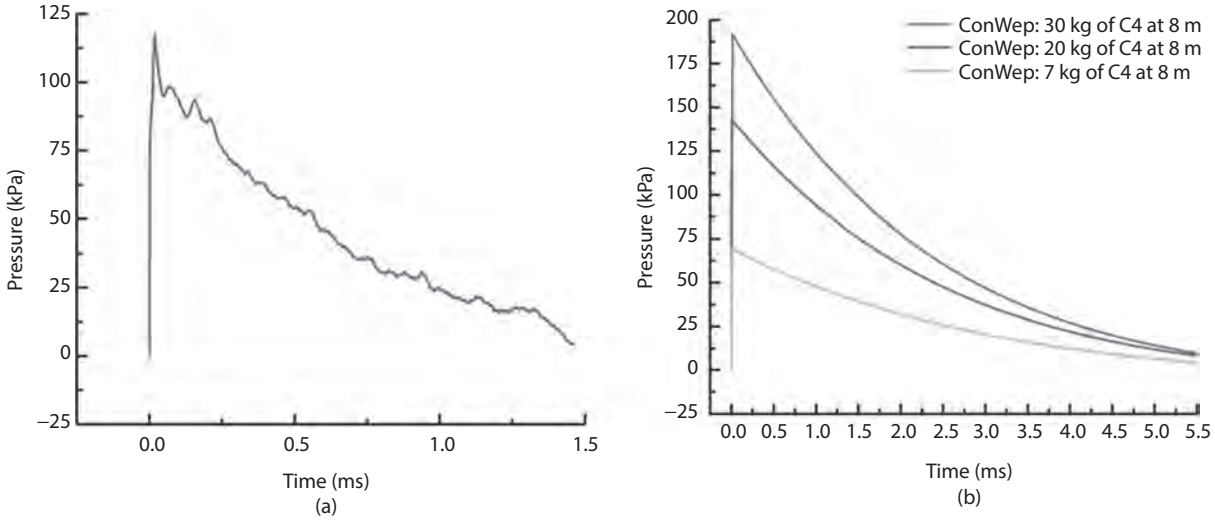


FIGURE 18.3 Pressure time profiles in a free field explosion: (a) IP profiles measured using a pencil gauge by a free field explosion of 1.81 kg of C4 at a distance of 2.8 m. The testing was conducted by Trauma Mechanics Research Facility at the University of Nebraska-Lincoln in conjunction with the U.S. Army. (b) Pressure profiles obtained using Conventional Weapons Effects calculations using ConWep.

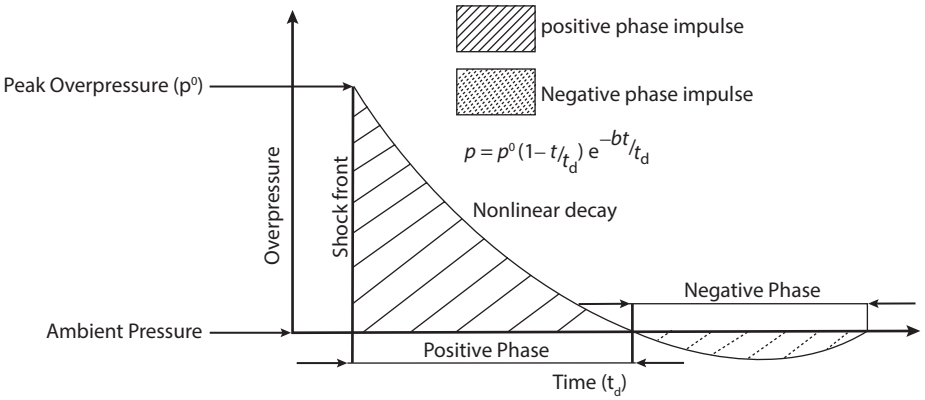


FIGURE 18.4 Mathematical representation of planar Friedlander waveform. Equation in the figure represents instantaneous overpressure $p+$ at given time t, where p^* is the peak overpressure, t^* is positive phase duration, I^* is positive phase impulse, and b is the decay constant. (From Sundaramurthy, A. et al. 2012. *Journal of Neurotrauma*. 29:2352, 2012.)

be 50–1,000 kPa and 1–8 ms respectively (Panzer et al., 2012); however, precise ranges are not available from the field data. Measurements conducted in our laboratory indicate that the upper range can be reduced to 400 kPa and the duration restricted to 7 ms. It should be noted that during an actual explosion, the p–t curve could be more complex because of reflections from ground, surrounding building structures (in an urban setting), and explosives that are cased and/or contain shrapnel. Furthermore, there are charge-to-charge variations possible from packing density, shape of the charge (spherical, cylindrical), the purity of explosives (pure or mixed with shrapnel), the type and material of the cover, and the type and location of the trigger. As far as the target is concerned, not only the distance but also the direction of the wave and environmental parameters (temperature, wind, dust, humidity) determine the loading as well as the shape, size, and material property of the target and its conditions (e.g., if human whether subjects is wearing a helmet). To conduct a fundamental scientific study of bTBI, it is critical to isolate these as extraneous effects and generate the blast waves with the Friedlander type wave profile.

Another important feature of the open-field blast waves in the intermediate to far range is that the sizes of wave front are much larger than that of a human body. The interactions of such a blast wave with a human body are influenced strongly by the confinement of an effectively edgeless (no flattop or plateau) wave front. This characteristic represents a planar wave and must be recreated in the laboratory testing to realistically simulate field blast loading.

A spherical wave in the near field while expanding becomes more planar at far field ranges. Therefore, a blast wave in the intermediate to far range can be well approximated with a planar Friedlander wave, within the ranges of p^*, t^*, and I^* shown in Figure 18.4.

18.1.9 Types of Shock Tubes

Although the free-field blast testing closely replicates real-world blast conditions, there are some significant drawbacks: (1) free-field experiments are expensive, (2) time consuming, and (3) repeatability is difficult to achieve. Furthermore, the by-products of HE testing include potential fireball interactions and penetration from high-speed shrapnel (Bass et al., 2012). This can introduce unnecessary confounds to the experiments in which the objective is to understand the effect of primary blast injury and its subsequent biomechanical and biochemical sequela.

18.1.9.1 Detonation Shock Tube

The idea of a detonation shock tube was first introduced by Clemedson in 1955 to study injuries from blast in animal models (Clemedson and Criborn, 1955). In this case, a tube with one end open and the other end closed is used. A chemical explosive is placed in the closed end of the shock tube and detonated to produce a shock blast wave (Risling et al., 2011; Säljö et al., 2000).

18.1.9.2 Combustion Shock Tube

In a combustion shock tube, a mixture of oxygen and acetylene is filled in the driver section and sealed using a polymer membrane. This mixture is then ignited using an electric match from a safe location. The fuel undergoes combustion and produces carbon dioxide, water vapor, and heat energy. Expanding gases that come from the driver compresses the air in the driven section and initiates a shock-blast wave (Courtney et al., 2012).

18.1.9.3 Compressed Gas Shock Tube

This is the most popular type of shock-blast generation device, which essentially uses a similar technique as a combustion and detonation type shock tube except here, the sudden release of compressed gas is used for generating the shock-blast wave. A detailed description of the theory and work of a shock tube will be discussed in the following sections. Currently, this technique has been adopted by many researchers who investigate bTBI because of its apparent simplicity, repeatability, and experimental control (Bolander et al., 2011; Leonardi et al., 2011; Long et al., 2009; Sundaramurthy et al., 2012; Zhu et al., 2010).

18.1.9.3.1 Theory of Compressed Gas Shock Tubes

Although individual shock tubes for blast wave simulation may have different features, the essential wave physics can be understood by analyzing the wave propagation in a generic shock tube configuration as shown in Figure 18.5. A typical (compressed gas-driven) shock tube consists of a driver section of pressurized gas and a driven section of air at atmospheric pressure with the two sections separated by a set of membranes. When the membranes burst, the driver gas expands rapidly and compresses the atmospheric air (i.e., driven gas) in front of a shocked state, which propagates forward as an air shock wave. Meanwhile, the driver gas expansion initiates a family of infinite rarefaction waves (expansion fan). These rarefaction waves first travel toward the closed end, are reflected at the closed end, and then travel toward the open end. Their sequential arrivals at a given location of driven section produce a nonlinear decay (see wave profiles a-c of Figure 18.5). The wave profile evolves with propagation distance to that of a Friedlander wave (curve c of Figure 18.5) when the fastest rarefaction wave (which is faster than the shock front) catches the shock front at $x = x^*$, where the shock front intensity is eroded the least by the rarefaction waves. Hence, at $x = x^*$, peak overpressure P^* has the maximum value with a Friedlander wave profile. The time for the nonlinear decay to reach $p = 0$ gives overpressure duration t^*, which has the minimum value at $x = x^*$. Before the initial catchup, $x < x^*$ (curves a and b of Figure 18.5), the blast wave assumes a flattop shape because rarefaction wave reflected from the closed end has not reached shock front yet. The flattop duration is given by the difference in the arrival times of the shock front and the fastest rarefaction wave. In the range $x^* < x < 0$ where $x = 0$ represents the shock tube exit, more and more rarefaction waves catch up the shock front causing decreasing P^* and increasing t^* with increasing x. The pressure-time (p-t) profile near (outside) the exit is shown by curve d of Figure 18.5; notice that the waveform is changed significantly (low P^*, low t^*, followed by jet wind).

18.1.9.4 General Features of Compressed Gas Shock Tube Construction

The design for a shock tube is shown in Figure 18.6. The four main components of the shock tube are the driver section or breech, transition, driven section or straight section, and the catch (or expansion) tank. The straight section includes the test section. The driver contains pressurized gas, which is separated from the transition by several frangible membranes. Upon membrane rupture, a shock wave expands through the transition and develops in the straight section. Subjects are placed in the test section, which is strategically placed to produce a desired shock wave profile. Finally, the shock wave exits the shock tube and enters the catch tank, which reduces the noise intensity. Each of the components is described below.

18.1.9.4.1 Driver Section

The driver section contains the compressed gas (e.g., air, helium, nitrogen) used in the generation of the shock-blast wave. It is a cylindrical tube with one end permanently sealed, whereas the other is sealed with frangible membranes such as Mylar. In some designs, thin sheets of metals (aluminum or steel) have been used. It is critical to strictly control the repeatability of burst characteristics by controlling the material and manufacturing processes of the membranes. Driver gas is filled into the driver section, pressurized, and allowed to burst depending on the membrane material and its thickness. Once the pressure reaches the burst pressure, the membranes rupture releasing the high-pressured gas into the transition.

18.1.9.4.2 Transition

Transition is a design element used to change the cross-section of the tube from a circular cylinder (driver section) to a square (driven sections). The transition was designed with a gradual expansion to minimize flow separation and turbulence associated (reflections from the sidewalls) with abrupt changes in a cross-sectional area. If the sections of the driver and the driven remain the same, there is no need for the transition. However, to produce an effective shock front the driven is usually larger and longer than the driver.

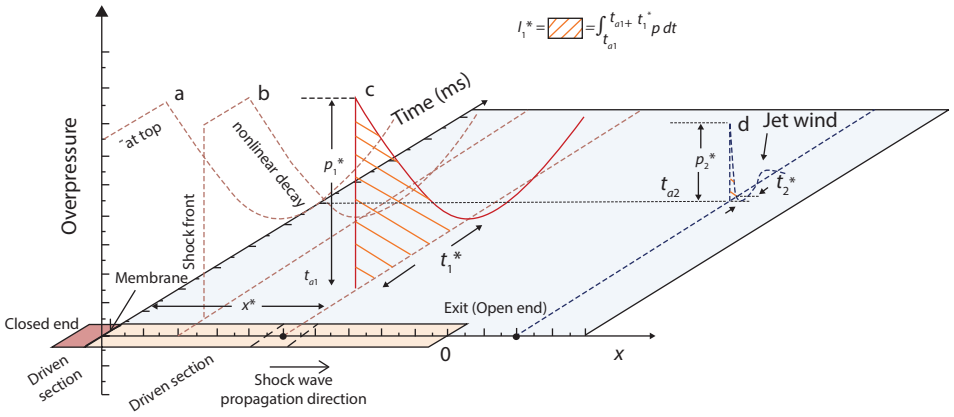


FIGURE 18.5 Evolution of shock wave in a generic shock tube. Source: Chandra et al. 2012.

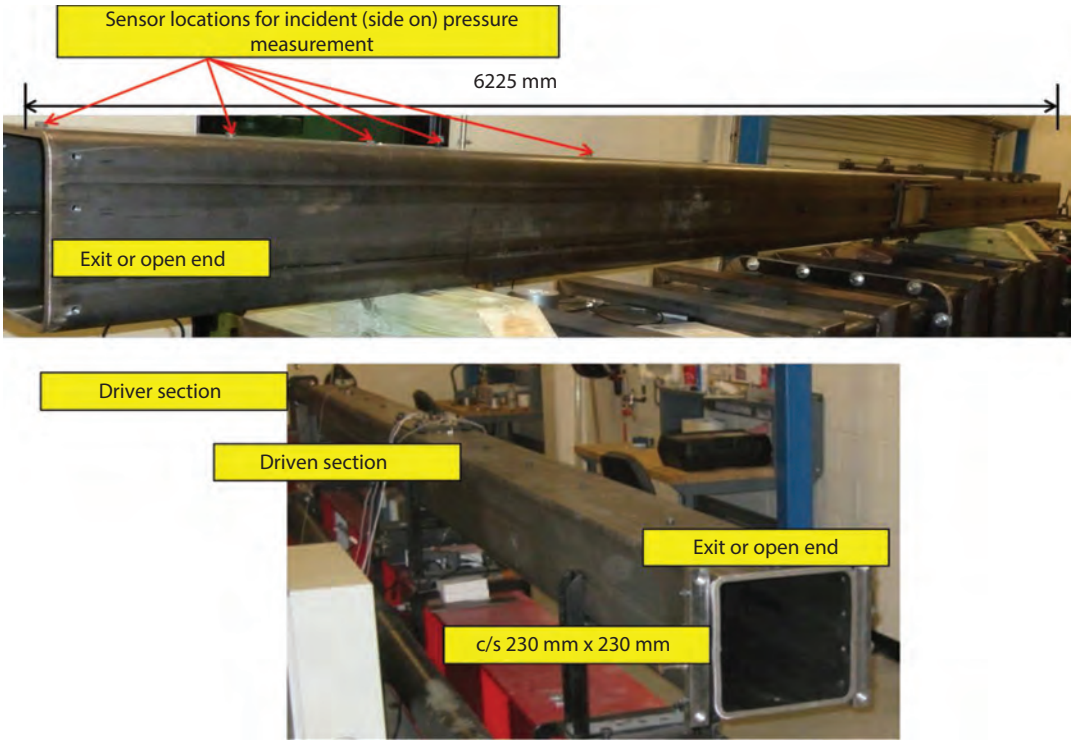


FIGURE 18.6 Photographs of 230 × 230-mm square shock tube used in this work. (From Chandra, N. et al., *Shock Waves*. 22:403–415, 2012; Sundaramurthy, A. et al. 2012. *Journal of Neurotrauma*. 29:2352, 2012.)

18.1.9.4.3 Driven Section

The driven section or the expansion section is the square section where the fully formed shock-blast wave is generated. In our design, we used a square driver section, which has since been followed by other research groups. The use of square cross-section as opposed to other geometric other sections serves two purposes: (1) uniform expansion from the breech, which is vital to have a planar wave, and (2) to observe and record events in the test section with high-speed camera (where having a circular section may cause image distortion)(Sundaramurthy et al., 2012). The test section is located within this part; while locating the test section, it is vital to note that the test section should be neither close to the breech nor to the exit. The reasons for which will be discussed in details in the coming sections.

18.1.9.4.4 Catch Tank

Depending on the strength of the shock-blast wave produced by the shock tube, the catch tank may or may not be included in a particular design. Its main purpose is to contain and release the large volume of expanded gas generated from a shot, minimizing blast loading of laboratory structures and reducing noise level. Further, the expansion waves from the open end will change the shape of the pressure pulse at the test section. The use of a suddenly changing cross-sectional area was studied and found to successfully mitigate energy (Jiang et al., 1999). The inside of the catch tank is lined with sound absorbing material for reducing the noise.

18.1.10 Test Section Location

Modular design of the shock tube allows the flexibility of altering the distance of the test section from the breech. In the following section, we will discuss the important criteria that have to be considered for test section location and their effect on the shock-blast wave profile. Important criteria include: (1) contact surface, (2) planarity, and (3) exit rarefaction.

18.1.10.1 Contact Surface

Upon rapid expansion of the driver gas, the temperature and pressure drop causing a density increase in the driver gas. The location of contact between the driver and driven gas is defined as the contact surface. The shock overpressure across a contact surface does not change, but the density difference causes a discontinuity in kinetic energy. This density difference can cause significant changes in reflected pressure across the contact surface. The contact surface can also be avoided by determining the fully expanded volume of the driver gas, and placing the sample beyond that location. The final volume of the expanded gas can be calculated using the isentropic expansion of an ideal gas, given by the following equation (Cengel et al., 2011).

$$\frac{P_2}{P_1} = \left(\frac{V_1}{V_2}\right)^k$$

Where P_2 is the burst pressure, P_1 is the atmospheric pressure (14.5 psi), V_1 is the driver volume, V_2 is the final volume

of the gas after complete expansion, and k (1.4 for nitrogen) is the adiabatic index. By knowing the breech volume, type of driver gas, and burst pressure, we can determine the final volume of the completely expanded driver gas. With this, we can theoretically approximate the minimum distance that is required to avoid any interference from the contact surface. However, this methodology does not consider effects from the mixing of driver and driven gases. Usually, the investigator has to be vigilant when analyzing the first 7–10 ms of *p-t* profile of the reflected pressure recorded in the test section to determine sudden changes in the reflected pressure. In such a case, either the test section should be moved downstream or the breech volume has to be reduced.

18.1.10.2 Planarity

In the mild/moderate range depending on the explosive strength and the distance from the epicenter, the shock front is planar. When simulating this type of blast in a laboratory shock tube, this feature is essential to replicate. Experiments can be done in the test section to determine the planarity by placing a bar with a linear array of sensors in the shock tube. The shock front planarity is determined by measuring the arrival time at various locations on the bar, and any deviation of arrival time will show the shock front curvature. With this idea, an experiment was conducted to determine the planarity of the shock front produced in our shock tube.

Along the bar, an array of eight sensors was placed with one sensor in the center and six at 4, 8, and 12 inches from the center in either direction. Assuming the bar is not mounted perfectly perpendicular to the shock tube, averaging of sensors equidistant from the center ensures that nonplanarity measurements caused by a skewed bar are corrected. The sensors at 8 and 12 inches were averaged in the same manner. A final sensor was located 13 inches from the center and was adjusted based on the calculated angle of the sensor bar (Figure 18.7a) (Kleinschmit, 2011).

After the sensor bar was mounted, shock waves were generated using a 11.75-inch nitrogen driver and 10 membranes. This produces shock waves with peak overpressures between 105 and 160 kPa, depending on the burst pressure and distance from the breech. The sensor bar was mounted 48, 98, and 136 inches from the transition exit. The planarity results shown in Figure 18.7b demonstrate nonplanarity with a shock front leading at the edges by approximately 0.15 inches at a location 48 inches from the transition exit.

The curvature corresponds to an approximate diameter of 47 feet, which can be considered planar. The results became increasingly planar to the location 136 inches from the transition exit. The general trends show increasing planarity with increase in the distances from the transition.

18.1.10.3 Exit Rarefaction

Figure 18.8 shows the untailored shock blast wave produced by a shock tube (Ritzel et al., 2011). The secondary decay and the following upstream recompression are the artifacts created by the rarefaction wave from the open end of the shock tube. Therefore, the subject within the test section, if not placed appropriately, will be subjected to a blast wave that does not simulate a field blast. This problem can be resolved by two methods: either having a reflector plate attached to the exit or placing the test section deep inside the driven section. In the case of a reflector plate, the venting gases when impinging on the plate creates a compression wave, which essentially nullifies the rarefaction wave generated from venting (Coulter et al., 1983). In the second case, by having the specimen deep inside the driven section the exit rarefaction wave enters the test section only after the passage of the actual shock-blast wave.

18.1.11 Effects of Placing Specimen Outside the Shock Tube

Studies on the evolution of the shock wave at the exit or open end have attracted researchers over the years because of numerous flow phenomena occurring at the exit (Arakeri

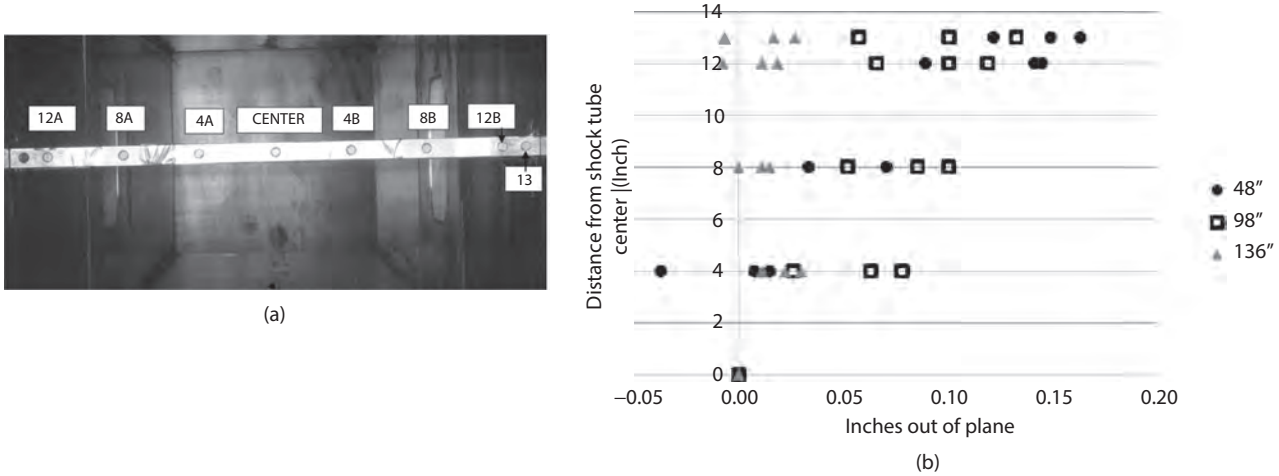


FIGURE 18.7 (a) Sensor bar used for planarity testing in 28-inch shock tube. (b) Shock wave planarity measurements in 28-inch tube taken at 48, 98, and 136 inches from the exit of the transition for 18-psi overpressure shock waves.

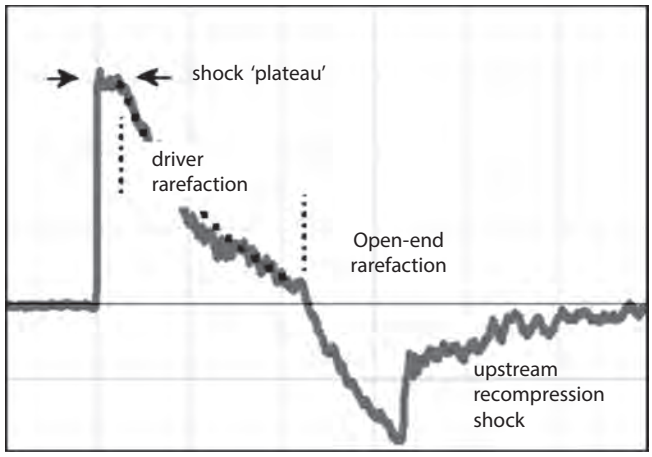


FIGURE 18.8 Untailored shock blast wave profile. (From Ritzel, D. et al., Proceedings HFM-207 NATO Symposium on a Survey of Blast Injury Across the Full Landscape of Military Science, 2011.)

et al., 2004; Honma et al., 2003; Jiang et al., 1999, 2003; Kashimura et al., 2000; Onodera et al., 1998; Setoguchi et al., 1993). It is shown in these studies that at the exit of the shock tube, the shock wave evolves from planar to three-dimensional (3D) spherical with other effects like vortex formation, secondary shock formation, Mach disc, subsonic jet flow, shock-vortex interaction, and impulsive noise. All of these effects may or may not be present depending on the shock wave strength and geometry of the exit. Most of these studies, however, have focused on the flow dynamics aspects with no emphasis on qualitative or quantitative analysis of shock/blast-wave profiles (e.g., *p-t* profiles). This becomes particularly important as many researchers do primary blasting testing using animal model and surrogates outside the shock tube. Therefore, to understand the evolution of the shock-blast wave outside the shock tube, and whether it truly represents all aspects of the field blast, a detailed study of the blast wave exiting the shock tube was conducted using numerical simulations. Furthermore, an experimental study was conducted using a cylindrical model as well as animal model comparing the mechanical responses from outside with the responses obtained inside the shock tube (Chandra et al., 2012; Sundaramurthy et al., 2012)

18.1.11.1 Evolution of Shock-Blast Wave Outside the Shock Tube

Flow field at the exit of the shock tube is studied using numerical simulations. Figure 18.7 shows the pressure and velocity (vector) fields at the exit of the shock tube without a cylinder. As the blast wave exits the shock tube, the flow changes from planar to 3D spherical (Figure 18.7a). Rarefaction wave and vorticities at the corners mix with blast and remaining air ejects as subsonic jet wind; which is evident from velocity vector field of Figure 18.9b. This jet wind effect is not present deep inside tube. Further, to clearly demonstrate this, Figure 18.10a shows the nodal velocities at various locations inside and outside the shock tube. Because fixed Eulerian mesh is used for modeling, velocity at a given mesh node corresponds to the instantaneous velocity of the material point coincident at given time '*t*' with the considered node. High-velocity jet wind is recorded in nodal history for locations outside the shock tube. Particle velocity associated with this jet is higher than particle velocity associated with the shock (Figure 18.10b). Locations inside the shock tube that are closer to the exit also show a second peak in velocity because of rarefaction waves moving into the tube, but magnitude of this second peak is lower than particle velocity associated with the jet for outside locations. In addition, magnitude of this second peak gradually reduces as we move inside the shock tube away from the exit (open end). Deep inside the shock tube ($x = -3048$ mm), a second peak is completely absent.

To clearly exhibit transition of blast wave from planar to 3D spherical, Figure 18.11 shows the pressure distribution at the exit of the shock tube for sequence of times. The black arrows indicate the (velocity) vector field. In each figure outer surrogate contour indicate the primary shock wave and inner green portion indicates primary vortex loop. The primary shock wave at first appears to be square shape with rounded corners as shown in Figure 18.11i. These corners become AQ1
significantly rounded and straight parts at the shock tube walls are shortened (Figure 18.11ii–iv). This indicates that the primary shock wave is planar at the exit (open end) of the shock tube and evolves three dimensionally into a spherical one as time elapses. This process is called a shock wave diffraction and affects the flow expansion behind it (Jiang et al., 2003). Similar arguments can be used to show the 3D nature of primary vortex loop that is evident from green color of Figure 18.11.

18.1.11.2 Comparison of Mechanical Response Between Outside Versus Inside

18.1.11.2.1 Animal Model

In this experiment, five male Sprague-Dawley rats of 320–360 g weight were sacrificed and instrumented with a surface mount Kulite sensor (LE-080-250A) on the nose to measure the reflected pressure, and two Kulite probe sensors (XCL-072-500A, diameter: 1.9 mm, length: 9.5 mm) were implanted in the thoracic cavity and in the brain, respectively. For the brain sensor implantation, the tip of the sensor was backfilled with water to ensure good contact with tissue, and the sensor was inserted through the foramen magnum 4–5 mm into the brain tissue. Then the instrumented rat was placed at four different locations twice inside the shock tube and twice outside. Complete details on the experimental setup can be found elsewhere (Sundaramurthy et al., 2012).

Figure 18.12 shows incident pressure, pressure in the brain and thoracic cavity corresponding to various locations along the length of the shock tube. At placement locations a and b, incident pressure profiles follow the Friedlander waveform (Figure 18.4) fairly well. Pressure profiles in the brain and thoracic cavity also have similar profiles (the shape is almost identical) to that of the incident pressure profiles. At these locations, peak pressures recorded in the brain is higher than

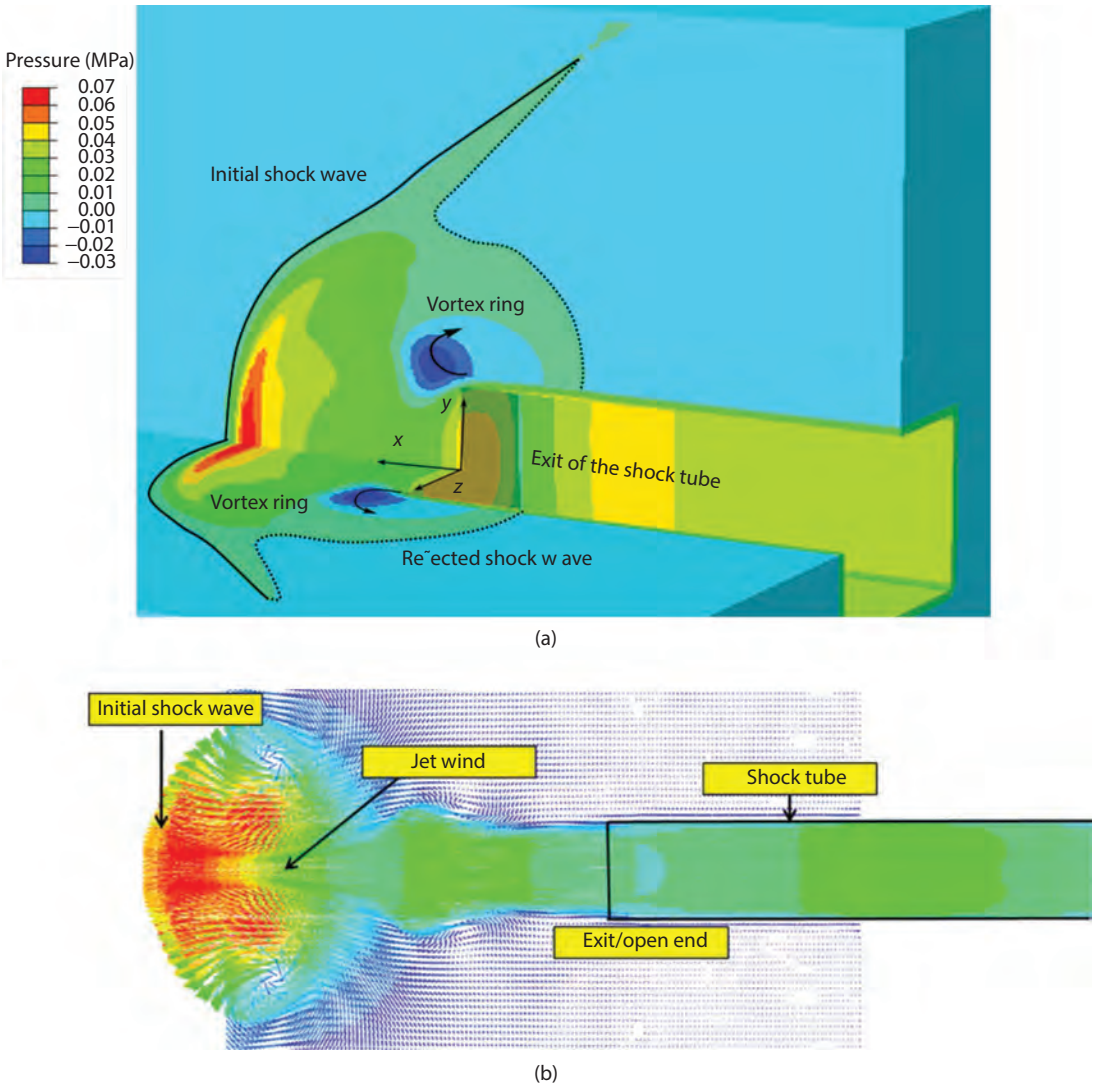


FIGURE 18.9 (a) Pressure field near the exit of the shock tube. Three-dimensional expansion of shock wave along with vortex formation is seen at the exit. (b) Velocity vector field near the exit of the shock tube. Jet wind is clearly visible in velocity vector field. Representative vector field is shown; jet is also observed at other locations close to the exit at earlier times. (From Chandra, N. et al., *Shock Waves*. 22:403–415, 2012.)

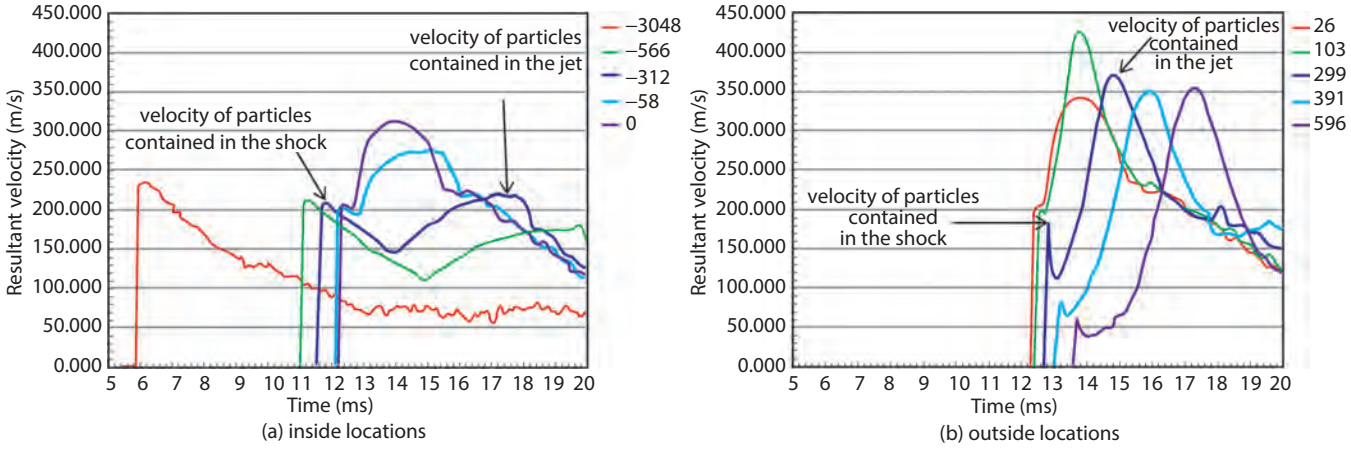


FIGURE 18.10 Nodal velocities at various locations inside and outside the shock tube. Because a fixed Eulerian mesh is used for modeling, velocity at a given mesh node corresponds to the instantaneous velocity of the material point coincident at given time '*t*' with the considered node. (From Chandra, N. et al., *Shock Waves*. 22:403–415, 2012.)

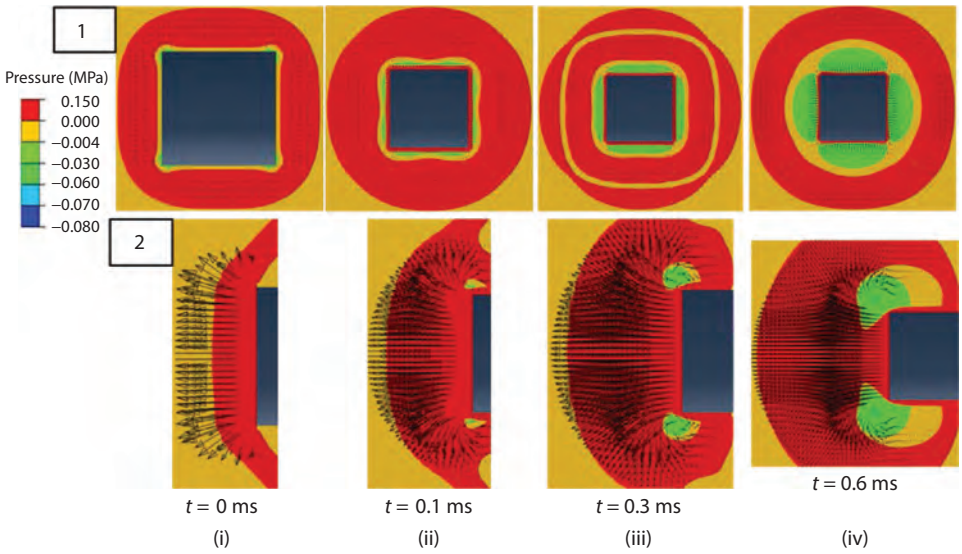


FIGURE 18.11 Flow fields illustrating physics of shock wave diffraction. Row 1 shows the axial view and row 2 shows the top view. Arrival of shock wave at the exit is marked as $t = 0$. (From Chandra, N. et al., *Shock Waves*. 22:403–415, 2012.)

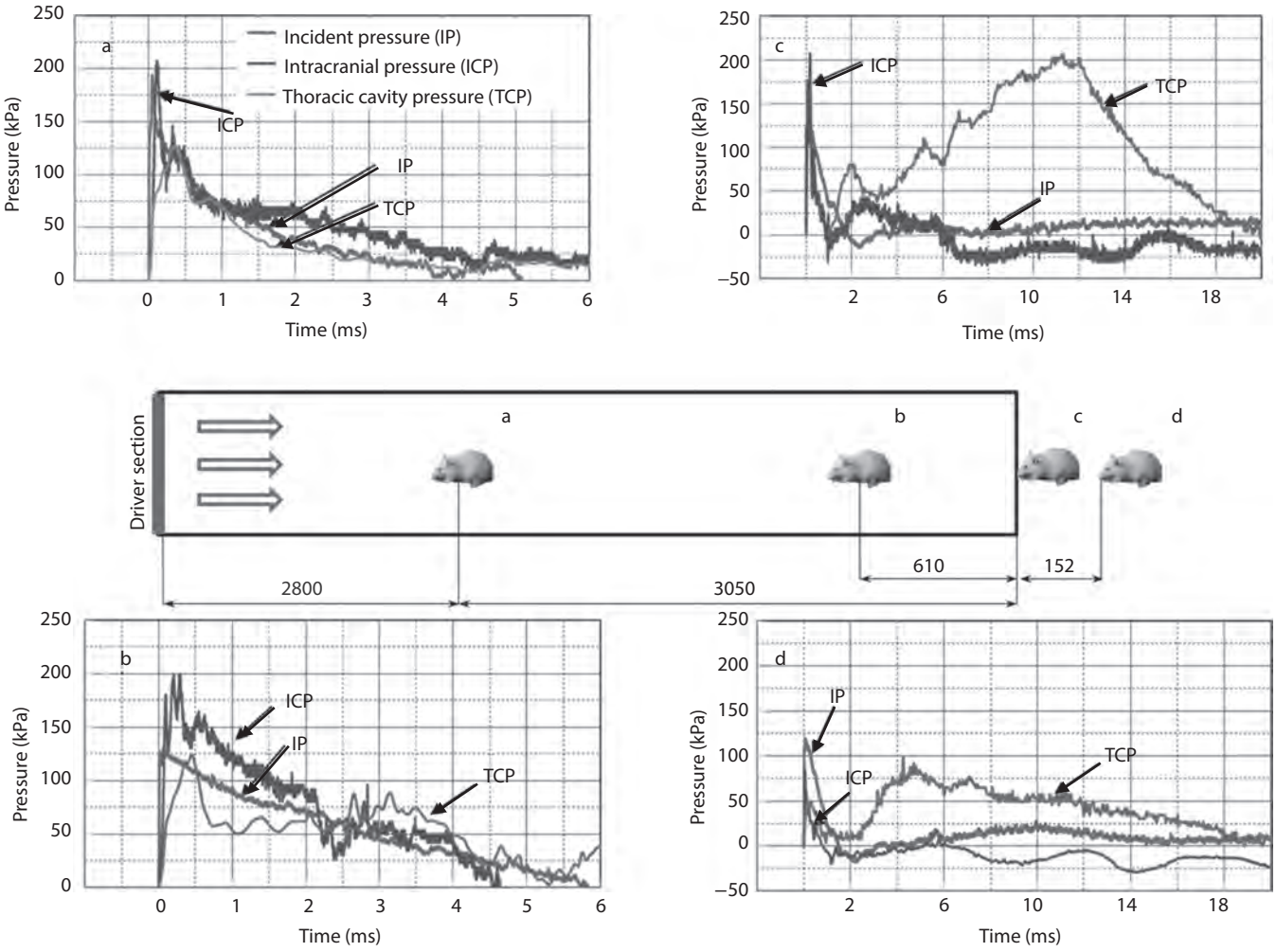


FIGURE 18.12 Measured pressure-time profile in the brain and thoracic cavity with their corresponding incident pressures at all APLs. At APL (a) and (b), both intracranial and thoracic pressures follow the same behavior as incident pressure; however, in APL (c) and (d) (outside the shock tube), the positive time duration in the brain is reduced drastically and the lung experiences a secondary loading. In this figure, all the dimensions shown are in millimeters. (From Sundaramurthy, A. et al. 2012. *Journal of Neurotrauma*. 29:2352, 2012.)

the incident peak pressure and the peak pressure recorded in the thoracic cavity is equivalent to the incident peak pressure. It is clear, at location c, the incident pressure profile differs significantly from the ideal Friedlander waveform, the overpressure decay is rapid and the positive phase duration is reduced from 5 ms at a to 2 ms at c (Fig. 18.12a and c, respectively). Pressure profile in the brain shows a similar trend. Pressure profile in the thoracic cavity shows a secondary loading with higher pressure and longer duration. Pressure profile in d is similar to the pressure profile recorded in c, except the value of the peak pressure reported in the brain is lower than the incident peak pressure.

The biomechanical response of the animal significantly varies with the placement location. Inside the shock tube (a, b, Figure 18.12), the load is due to of the pure blast wave, which is evident from the *p-t* profiles (Friedlander type) recorded in thoracic cavity and brain. For animal placement locations (APLs) at the exit, c and d, *p-t* profiles show sharp decay in pressure after the initial shock front. This decay is due to the interaction between the rarefaction wave from the exit of the shock tube, eliminating the exponentially decaying blast wave, which occurs in a and b. This has two consequences: first, the positive blast impulse (area under the curve) reduces drastically. Second, because the total energy at the exit is conserved, most of the blast energy is converted from supersonic blast wave to subsonic jet wind (Haselbacher et al., 2007). This expansion of blast wave at the exit (subsonic jet) produces an entirely different biomechanical loading effect compared with the blast wave. Consequently, the thoracic cavity experiences secondary loading (i.e., higher pressure and longer positive phase duration). When the animal is constrained, this high-velocity subsonic jet wind exerts severe compression on the tissues in the frontal area (head and neck) that in turn causes pressure increase in the thoracic cavity (lungs, heart). To further illustrate the effect of subsonic jet wind on the rat, experiments a and c without any constraint was performed. Figure 18.13 shows the displacement (motion) of the rat at various time points starting from the moment the blast wave interacts with the animal. At a, the displacement is minimal; however, at c, the rat is tossed away from the bed (motion) because of jet wind. This clearly illustrates the effect of high-velocity subsonic jet wind on the rat when placed outside the shock tube. Consequently, the animal is subjected to extreme compression loading when constrained and subjected to high-velocity (subsonic) wind when free, both of which are not typical of an IED blast. This in turn changes not only the injury type (e.g., brain vs. lung injury) but also the injury severity, outcome (e.g., live vs. dead), and mechanism (e.g., stress wave vs. acceleration).

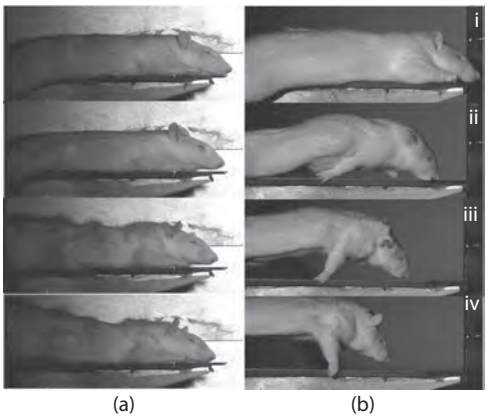


FIGURE 18.13 Motion of unconstrained rat under blast wave loading (a) inside; (b) outside. (i–iv Time points t = 0, 20, 40, and 60 msec, respectively; the rat is thrown out of the bed when placed outside. (From Sundaramurthy, A. et al. 2012. *Journal of Neurotrauma*. 29:2352, 2012.)

18.1.11.2.2 Cylindrical Model

The evolution of the shock-blast wave along the length of the shock tube was measured using an aluminum cylinder (length 230 mm, diameter 41.3 mm). In this case, a cylinder was placed along the longitudinal axis of the shock tube at various offset distances from the exit (open end) both outside (+x) and inside (−x) (Figure 18.14). Seven holes were drilled and tapped to locate seven Dytran model 2300V1 piezoelectric pressure sensors used in conjunction with Dytran model 6502 mounting adapters. The location labeled t0 was centered between the two end surfaces of the cylinder, and the rest of the holes were evenly spaced for a total span of 84 mm. The cylinder was mounted (i.e., firmly secured) using brackets made out of flat steel bar. In addition to the gauges mounted on the cylinder, there were set of gauges (PCB pressure sensor model 134A24) mounted at various locations on the shock tube (along the length) that measure the incident (side-on) pressures. The experiment was repeated three times at each location along the length of the shock tube (N = 3).

Figure 18.15a and b shows the reflected pressure profiles for cylinder placement locations inside and outside of the shock tube. The reflected pressure measures total pressure (both kinetic and potential energy components) at a given point. The reflected pressure profiles for placement locations inside the shock tube show gradual decay in pressure and pressure profiles follow the Friedlander waveform. A small secondary peak in pressure profiles is due to reflection from the walls of the shock tube; however, these wall reflections do not significantly affect pressure profiles. The reflected pressure profiles for placement locations outside the shock tube show rapid pressure decay that do not conform to the Friedlander waveform; shock front and pressure decay rather looks like delta function. This is followed by a long-duration, relatively constant low-pressure regime (starting points of which are demarcated by cross symbols). This long duration, relatively constant low-pressure regime is referred as subsonic jet wind in this work. This jet wind is an artifact of the shock tube exit effect and does not occur in free field blast conditions.

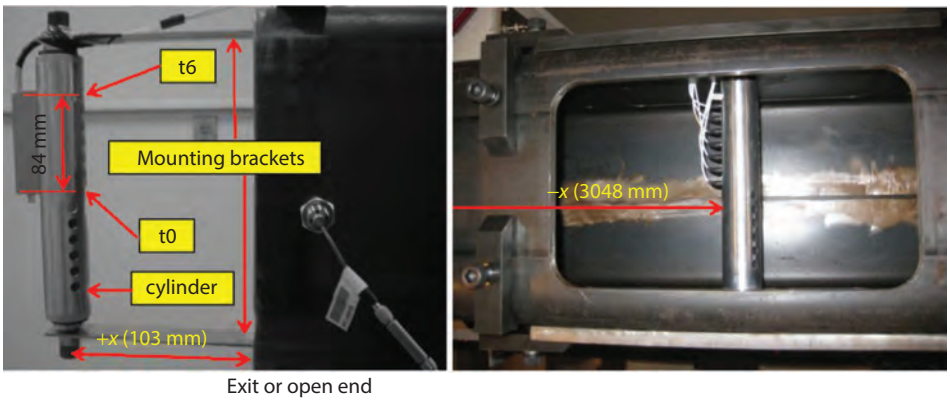


FIGURE 18.14 Experimental setup to measure evolution of the shock wave along the length of the shock tube. Placement of the cylinder at two representative locations along the length of the shock tube is shown. (From Chandra, N. et al., *Shock Waves.* 22:403–415, 2012.)

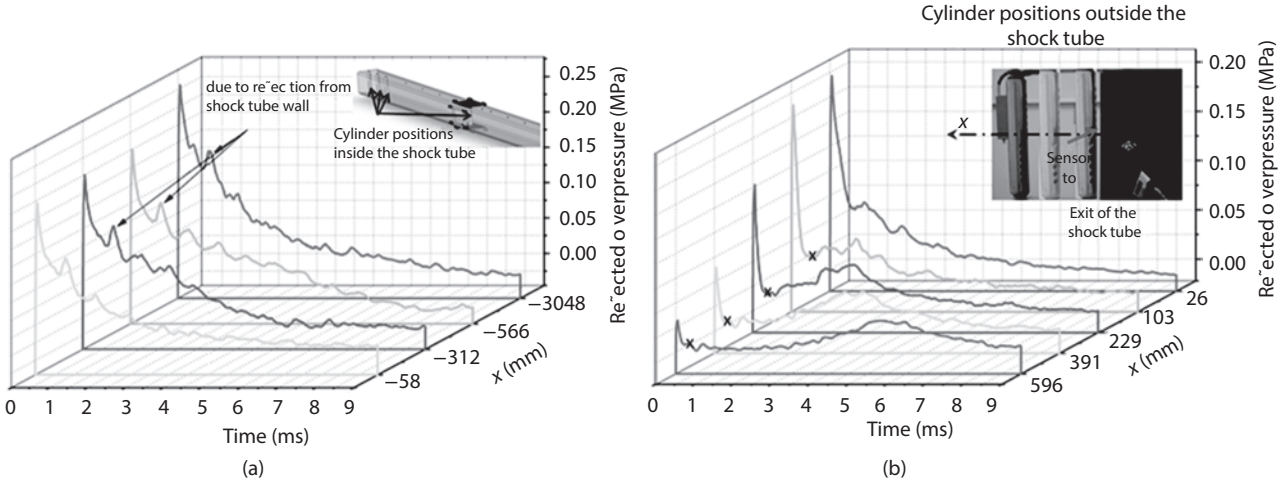


FIGURE 18.15 (a) Experimentally measured *p-t* profiles at various x locations inside the shock tube. *p-t* profiles follow Friedlander waveform fairly well. (b) Experimentally measured *p-t* profiles at various x locations outside the shock tube. In these profiles, the trends do not follow Friedlander waveform and peak overpressure drastically reduces as we move away from the exit. The starting points of subsonic jet wind are demarcated by cross symbols. (From Chandra, N. et al., *Shock Waves.* 22:403–415, 2012.)

Figure 18.16a and b shows the impulse profiles for cylinder placement locations inside and outside of the shock tube. The total impulse is reduced significantly for outside placement locations when compared with inside placement locations. The shape of impulse profiles for placement locations inside the shock tube is relatively constant (i.e., gradual increase) as opposed to nongradual (i.e., with slope changes) for outside placement locations. The contribution of subsonic jet wind to the impulse is high starting points of which are demarcated by cross symbols.

18.1.12 Tailoring the Shock-Blast Wave Profile

In previous sections, we learned about the design, theory, and working of a compressed gas shock tube and then critically analyzed the factors that influence the test section locations for simulating primary shock-blast wave. In the following sections, we will study the methods to tailor a shock-blast wave profile. To attain this goal, an extensive experimental analysis was carried out to show the methods in which the blast wave profile can be tailored to replicate the field conditions. We study the effects of shock tube–adjustable parameters (SAPs) such as breech length, type of gas, membrane thickness, and measurement location on the SWPs. Furthermore, we characterize the flat top or plateau wave and determine the influence driver gas and breech length has on this phenomenon. Finally, we compare the shock-blast wave profile from the shock tube with the field explosion profiles generated in ConWep.

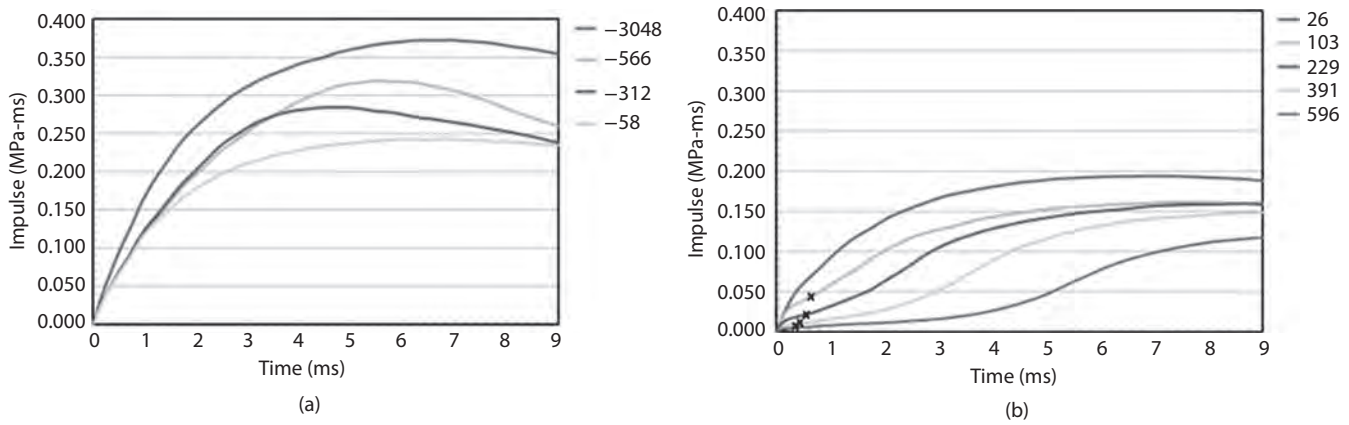


FIGURE 18.16 (a) Impulse profiles at various x locations inside the shock tube obtained by integration of experimentally measured *p-t* profiles. (b) Impulse profiles at various x locations outside the shock tube obtained by integration of experimentally measured *p-t* profiles. Contribution of the subsonic jet wind to the impulse is demarcated by cross symbols. (From Chandra, N. et al., *Shock Waves*. 22:403–415, 2012.)

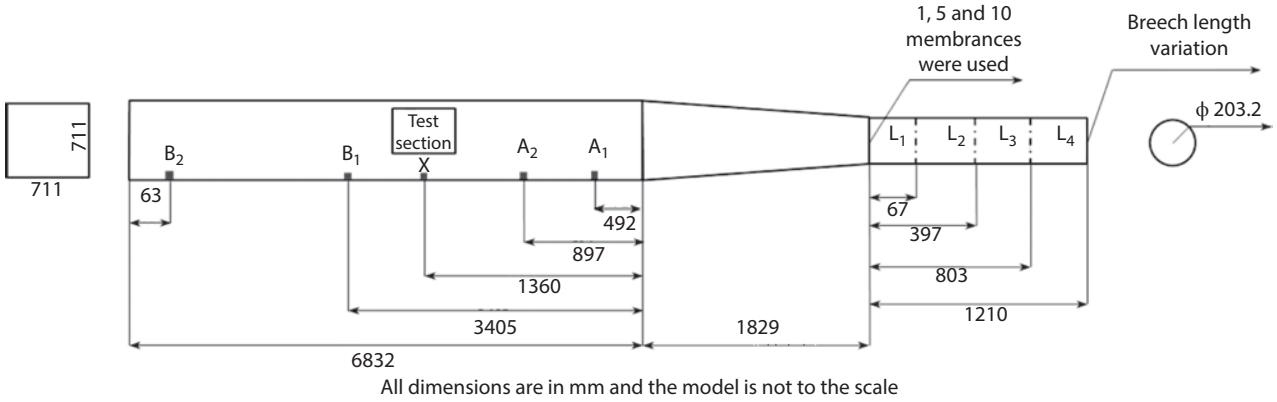


FIGURE 18.17 (a) Experimental variables and sensor location; here A1, A2, X, B1, and B2 are the side-on pressure sensors. (b) Impulse profiles at various x locations outside the shock tube obtained by integration of experimentally measured *p-t* profiles. Contribution of the subsonic jet wind to the impulse is demarcated by cross symbols. (From Sundaramurthy, A. et al. 2012. *Journal of Neurotrauma*. 29:2352, 2012.)

Figure 18.17 shows the experimental variables and the sensor locations. The length of the breech is varied between 67 and 1,210 mm. The membrane thickness is varied by varying the number of membranes between one, five, and 10 (each membrane is 0.254 mm thick). In this work, both nitrogen and helium were used as the driver gas, and the driven gas was air at ambient laboratory conditions (temperature range of 23 ± 20°C). The evolution of the blast wave along the length of the shock tube was measured using a PCB pressure gauges (model 134A24) mounted on the wall of the shock tube at locations A1, A2, X, B1, and B2 (Figure 18.17). Burst pressure in driver just before the rupture of the membranes was also recorded.

18.1.12.1 Burst Pressure

Burst pressure is the pressure in the driver section (breech) during the membrane rupture. This highly compressed gas when allowed to expand compresses atmospheric air in the transition section generating a shock front. Burst pressure for different membrane thicknesses and breech lengths were noted and presented in Figure 18.18a. From Figure 18.18a, it can be seen that the burst pressure increases with an increase in the membrane thickness. Furthermore, there is no discernible difference in the burst pressure with respect to increase in breech length for any of the three membrane thicknesses. This is because the membrane rupture is pressure-dependent, and this critical pressure is not influenced by breech volume (i.e., burst pressure that can be achieved at a minimum breech length L_1 can also be achieved at L_2, L_3, or L_4). Therefore, the quantity of membranes used and its thickness is directly proportional to the burst. This result corroborates with the findings from the study conducted by Payman and Shepherd in which they used copper as their membrane. They determined that for the same thickness, the burst pressure does not vary more than ±3%. Similarly, they also determined that membrane thickness has a linear relationship with burst pressure (Payman and Shepherd, 1946).

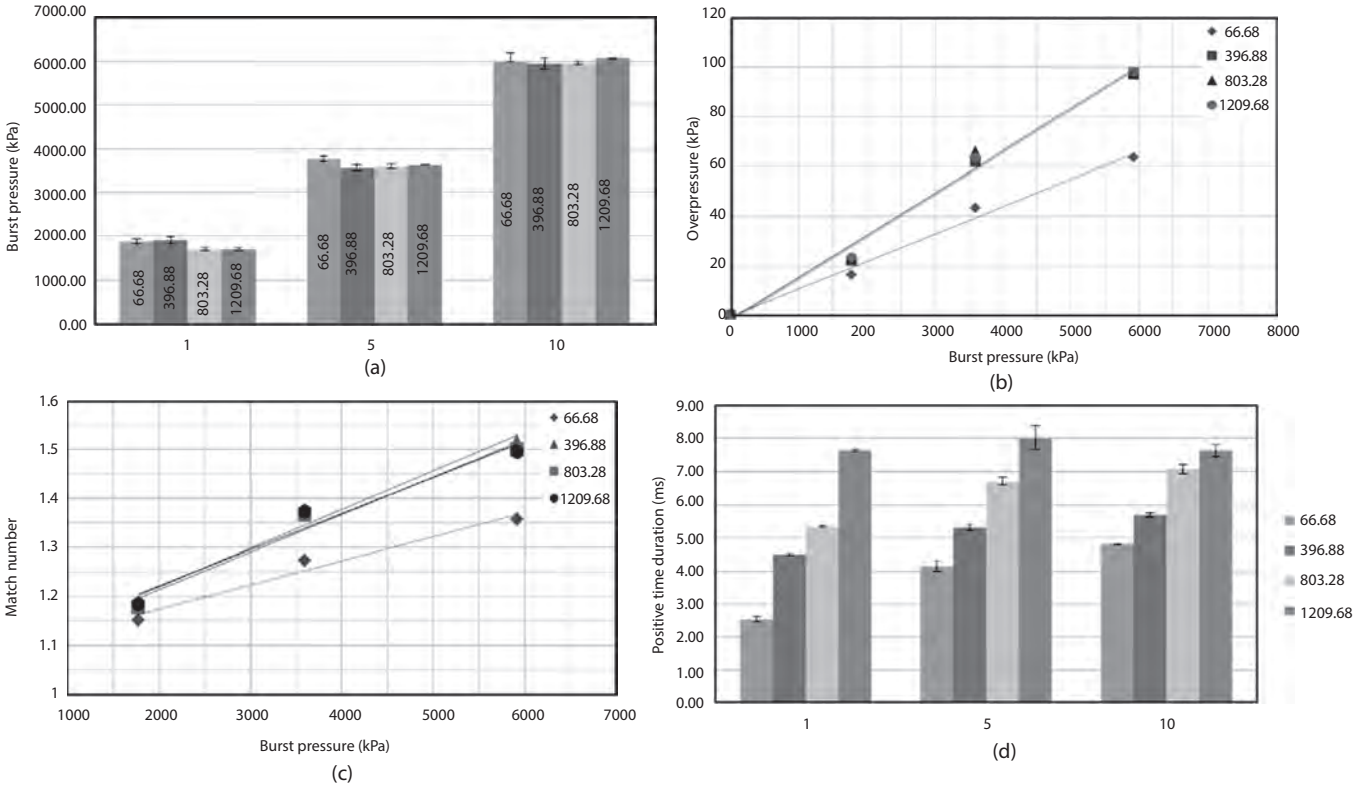


FIGURE 18.18 (a) Relationship between the number of membrane used and burst pressure produced with respect to different breech lengths. (b) Relationship between shock front Mach number and burst pressure, there is linear relationship between Mach number and burst pressure (with strength of linearity R^2 between 0.96 and 0.98). (c) The relationship between shock tube parameter burst pressure with overpressure measured in the test section for different breech lengths. (d) Relationship between PTD and membrane thickness used for different breech lengths. (From Sundaramurthy, A. et al. 2012. *Journal of Neurotrauma*. 29:2352, 2012.)

18.1.12.2 SAPs and Their Influence on the SWPs in the Test Section

By changing the SAPs such as membrane thickness (burst pressure) and breech length, we were able to determine the effect on SWPs such as Mach number, overpressure and positive time duration (PTD) in the test section. Figure 18.18b and c shows the relationship between overpressure, Mach number, and burst pressure for different breech lengths. Both of these variables have a strong positive relationship with the burst. Furthermore, with increase in the burst pressure both Mach number and overpressure for $L_{2,}$ L_3, and L_4 increases with a higher rate than L_1.

PTD is the period within which the shock overpressure reaches the atmospheric pressure. Figure 18.2.18c shows the relationship between PTD and membrane thickness for different breech lengths. For a given membrane thickness, PTD increases with an increase in the breech length. Furthermore, there is an increase in PTD between membrane thicknesses 1 and 5 for breech lengths L_1, L_2, and L_3; however, such an apparent difference is not observed between membrane thicknesses 5 and 10. Finally, for breech length L_4, there is no apparent difference in PTD for different membrane thicknesses.

Controlling overpressure and PTD is essential when replicating a field blast. It is possible in a laboratory shock tube to control aforementioned variables by manipulating breech length, burst pressure (membrane thickness), type of gas, and test section location (by varying the test section within expansion section). It can be seen that within the test section that, with an increase in burst pressure, both the overpressure and the Mach number (strength of shock wave) increases, which implies that both these variables can be increased by increasing the membrane thickness. Similarly, PTD increases with increase in breech length for any given burst pressure. However, at lower breech lengths, both overpressure and PTD is affected by expansion waves (also known as rarefaction waves) that arise from the end of the breech. Furthermore, type of driver gas used also plays a role in the PTD and overpressure. Effect expansion waves and driver gas has on the overpressure and PTD is explained in detail in the following section.

Figure 18.19 shows the x-t wave propagation diagram with shock front, rarefaction head, and tail for two breech lengths. When membranes burst, the driver gas expansion initiates a family of infinite expansion waves toward the closed end. Once the expansion head encounters the closed end, it travels backwards toward the transition. Because of increased temperature from the traverse of the shock front, the expansion head accelerates further and catches the shock front. However, because of the expansion, the temperature and pressure in

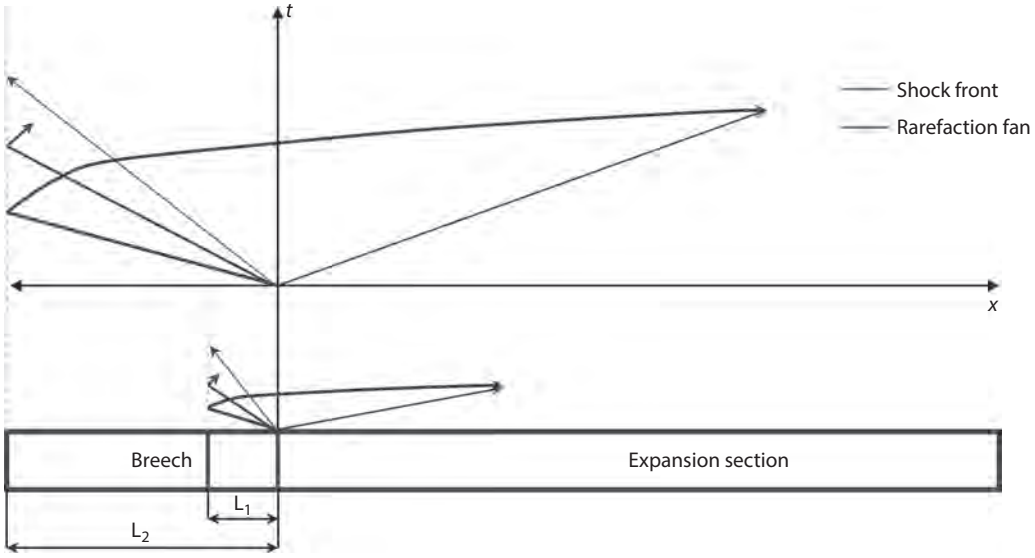


FIGURE 18.19 Ideal breech length x-t diagram for explosive shock wave replication. (From Sundaramurthy, A. et al. 2012. *Journal of Neurotrauma*. 29:2352, 2012.)

breech reduces, which reduces the velocity of the successive expansion waves, resulting in a series of waves, which yields the nonlinear decay and ultimately shaping the shock-blast wave (Ritzel et al., 2011). Once the waveform attains the shape shown in the Figure 18.4, expansion waves start to deplete the overpressure and PTD. Similarly, the breech length and driver gas also play major roles in the evolution and interaction of the expansion wave. The expansion wave while traveling toward the closed end of the driver section travels with the velocity of sound in that medium, which is the driver gas (helium $C_{He} = 972$ m/s and nitrogen $C_N = 353$ m/s). Therefore, for a given breech length and membrane thickness, having helium as a drives gas increases the expansion wave velocity resulting in Friedlander type wave at an earlier point compared with nitrogen gas. Consequently, by varying the length of the breech in conjunction with using the appropriate driver gas, we can optimize PTD and overpressure.

18.1.12.3 Evolution of the Shock-Blast Wave Along the Expansion Section

Figure 18.20(a–c) shows the evolution of the overpressure along the length of the expansion section. From Figure 18.20a, it can be seen that, for one membrane there is no discernible change in overpressure for breech lengths L_2, L_3, and L_4. For all cases with breech length L_1, there is a continuous decay in the overpressure downstream of the shock tube. For all the other breech lengths, unique points of overpressure decays are identified along the expansion section, which is illustrated in the following section.

For L_1 (66.68 mm), L_2 (396.88 mm), L_3 (803.28 mm), and L_4 (1,209.68 mm), we observe the following: (1) for any membrane thicknesses, an obvious difference in overpressure is observed between L_1 and other breech lengths (Figure 18.20a–c); (2) beyond 3,000 mm from the breech, for 5 and 10 membranes and breech length L_2, overpressure starts to decay (Figure 18.20b, c); and (3) beyond 5,000 mm from the breech, for 10 membranes and breech lengths L3, the overpressure starts to decay (Figure 18.20c). Finally, for L_4, there is no unique decay point, which implies a flat top wave throughout the expansion section.

In a typical free field blast, the overpressure decreases rapidly with respect to increase in distance from the blast epicenter (Mott et al., 2008). However, overpressure in a shock tube does not show a drastic reduction because of its constant cross section. There is a considerable difference between the overpressures for L_1 and all the other breech lengths. As discussed earlier, this difference arises from the interaction of expansion waves that comes from the breech. This suggests that the expansion waves from the breech for breech length L_1 arrives earlier than all other breech lengths. With an increase in the breech length and burst pressure, distinct points at which the shock blast starts to decay are shown in Figure 18.20b and c, which implies that beyond this point shock-blast wave has a Friedlander form. Consequently, longer breech lengths that tend to produce a flat top wave in the test section will produce a Friedlander type wave at some point beyond the test section. As discussed in the Mild/Moderate Blast TBI section, when moving closer to the exit, the rarefaction waves from the exit starts to interact with blast wave creating artifacts, which results in inaccurate blast simulation.

Figure 18.20d–f shows the evolution of the PTD along the length of the shock tube expansion section. For any given breech length and membrane thickness, the PTD remains reasonably constant along the length; however, it decreases drastically toward the exit of the shock tube. Positive impulse (PI) is the area under the shock-blast wave profile. Figure 18.20g–i shows the evolution of the PI along the length of the shock tube expansions section. PI is a function of both overpressure and PTD; hence, it increases with an increase in both membrane thickness and breech length. Because of its relationship with the PTD, the impulse drastically reduces near the exit of the shock tube.

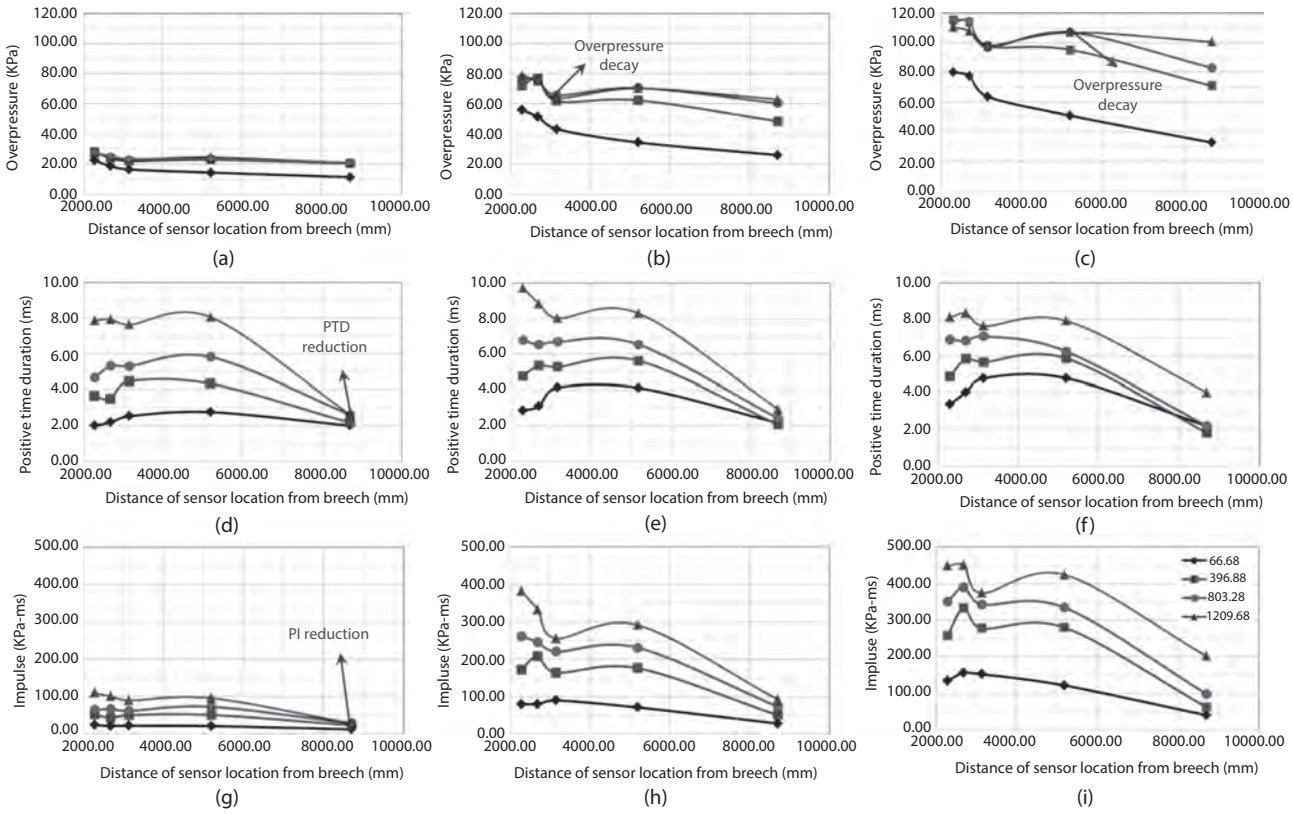


FIGURE 18.20 Describes the variation of shock-blast profile parameters along the length of the shock tube expansion section. All of these experiments were performed for breech lengths 66.68 (black), 396.88 (red), 803.28 (blue), and 1,209.68 (green) mm; (a–c) show the variation of overpressure along the length of the expansion section for burst pressures corresponding to 1, 5, and 10 membranes, respectively; (d–f) show the positive time duration along the expansion section for burst pressures corresponding to 1, 5, and 10 membranes, respectively. (From Sundaramurthy, A. et al. 2012. *Journal of Neurotrauma*. 29:2352, 2012.)

As a result, PTD reduces drastically near the exit of the shock tube because of the interaction between shock front and exit expansion waves. This has two consequences: first, the PI (energy of blast wave) reduces drastically (Figure 18.20g–i). Second, because the total energy at the exit is conserved, all the blast energy is converted from supersonic blast wave to subsonic jet wind, which produces erroneous results. The effect of jet wind and specimen placement location along the expansion section for blast simulation using shock tube is illustrated in the Blunt section.

18.1.12.4 Flattop or Plateau Wave

A flattop or plateau wave is usually witnessed in a gas-driven shock tube (Reneer et al., 2011). In this case, the shock-blast wave profile, once reaching the peak overpressure, maintains its peak value for a certain period before decay. Longer breech lengths in combination with the use of nitrogen as a driver gas seem to have a strong influence on this phenomenon. Figure 18.21 shows the comparison between the shock-blast wave profile with nitrogen and helium as driver gas. In both cases, 10 membranes with a breech length of 1,209.68 mm were used. It can be seen that only in the case of nitrogen as driver gas flat top wave is observed, whereas, in the case of helium, a pure Friedlander wave is witnessed.

There is an inherent relationship between SAPs, such that an optimization of one variable might have a deviating effect on the other variables resulting in having an nonoptimal shock blast wave (in this case a flattop wave).This particular problem arises depending on: (1) breech length and (2) type of driver gas. In the current study, the breech length L_1 is low enough for the expansion waves to reach the shock front and create a Friedlander type wave somewhere before the test section. Therefore, when it arrives at the test section, it has already gone through some overpressure and PTD reduction. Once the breech length is increased, the time taken by the expansion wave to reach the shock front increases. Consequently, for breech lengths L_2, L_3, and L_4, there is no change in the overpressure and PTD at the test section, which implies that it is a flattop wave.

Although nitrogen, because of its low sound speed, has a tendency to produce a longer PTD, using a longer breech length results in a flattop wave. Conversely, helium produces a lower PTD compared with nitrogen but has a sharp decay to the atmospheric pressure. Similar findings are reported by Reneer and Bass in their separate works comparing the wave profiles generated from air (which has speed of sound close to nitrogen) and helium. They found that using air as a driver gas produces a flattop wave (Bass et al., 2012; Reneer et al., 2011).

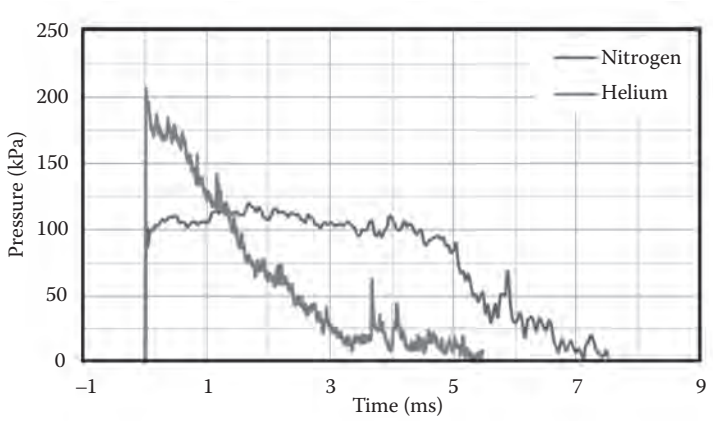


FIGURE 18.21 Comparison of the shock-blast profile for helium and nitrogen with 10 membranes and breech length of 1,209.68 mm; clearly, the wave profile corresponding to helium gas is a Friedlander wave and wave profile corresponding to nitrogen is a flattop wave. (From Sundaramurthy, A. et al. 2012. *Journal of Neurotrauma*. 29:2352, 2012.)

One technique used for avoiding a flattop wave when using long breech length is to place the test section downstream of the expansion section, so that the expansion waves would eventually catch up and produces a Friedlander type wave; nevertheless, this method has its own limitations.

18.1.12.5 Comparison Between Field and Laboratory Profiles

Table 18.1 shows the range of IEDs and mines typically used in the field; their explosive capacity expressed as TNT strength (AEP-55, 2006; Department of Homeland Security, 2009). An important requirement for studying BINT is the ability to produce accurate and repeatable blast loading, which can be related to strengths mentioned in Table 18.1. Using ConWep, we were able to determine the pressure profiles for TNT explosives within the range of strengths described in Table 18.1. A comparison was made between the profiles generated from ConWep with those generated from a shock tube device (Figure 18.22 (a–c, d). Clearly, there is good match in the results, which indicates that the wave profile generated by compressed gas shock tube is directly related to relevant field conditions.

18.2 PMHS BLAST TESTING

In this section, the intracranial and surface pressures along with skull strain response of PMHS heads are studied by subjecting them to primary blast of varying peak incident intensities or overpressures (70, 140, and 200 kPa).

18.2.1 Experiments

18.2.1.1 PMHS Testing in the 28-inch Shock Tube

The PMHS heads were used in conjunction with the Hybrid III neck in these experiments. The head assembly was placed in the test section of the shock tube, as shown in Figure 18.23, and was subjected to frontal blast loading. Experiments were also conducted with the helmets mounted on PMHS heads. The shape, overpressure, and duration of the incident blast wave at a given location are known a priori. This is achieved through sample trials in the shock tube, conducted without the surrogate head and the neck.

18.2.1.1.1 PMHS Preparation

Three PMHS heads were used for this purpose. The specimens had no record of osseous disease and preexisting fractures were not present as confirmed by computed tomography (CT) imaging. The age, gender, and basic anthropometry of the specimen are listed in Table 18.2.

PMHS that are kept frozen for a substantial period tends to have severe tissue degradation after thawing. Thus, the brain was removed from each PMHS head and intracranial space was backfilled with ballistic gelatin. The brain tissue and dura mater were removed through foramen magnum using flat head screwdriver. Twenty percent ballistic gelatin (ballistic gel, from here on) was prepared by dissolving 2 parts of 250 bloom gelatin into 9 parts of warm (40°C) water (by mass), stirring the mixture while pouring in the powdered gelatin. The gelatin was obtained from Gelita USA Inc. (Sioux, IA) in the bloom form. The ballistic gel was poured in the intracranial cavity through foramen magnum and allowed to settle at room temperature. After the ballistic gel had settled, the entire head was put inside the plastic bags and air bubbles were removed using vacuum cleaner. The foramen magnum was sealed using filler material (Bondo). Hybrid III neck was attached to the head using base plate. A base plate was screwed to the bottom of the head.

18.2.1.1.2 Instrumentation

Each PMHS head was instrumented to measure surface pressures, surface strains, and ICPs. Eleven sensor measurements were made on each PMHS head. Surface pressures were measured at two locations, surface strains were measured at four locations, and ICPs were measured at five locations within the head, as shown in Figure 18.23b. CT images of the instrumented head were also taken. CT images were used to verify

TABLE 18.1
Explosive Capacity of the Currently Used IEDs and Mines in the Field

Threat	Explosive Capacity (TNT Equivalent in kg)	Reference
Pipe bomb	2.28	Department of Homeland Security (27)
Suicide bomber	9	
Briefcase bomb	22.70	
Antipersonnel fragmentation device	0.55	AEP-55 (28)
Antivehicular blast landmine	6–10	

Explosive capacity of these IEDs are given in terms of TNT equivalents in kilograms.

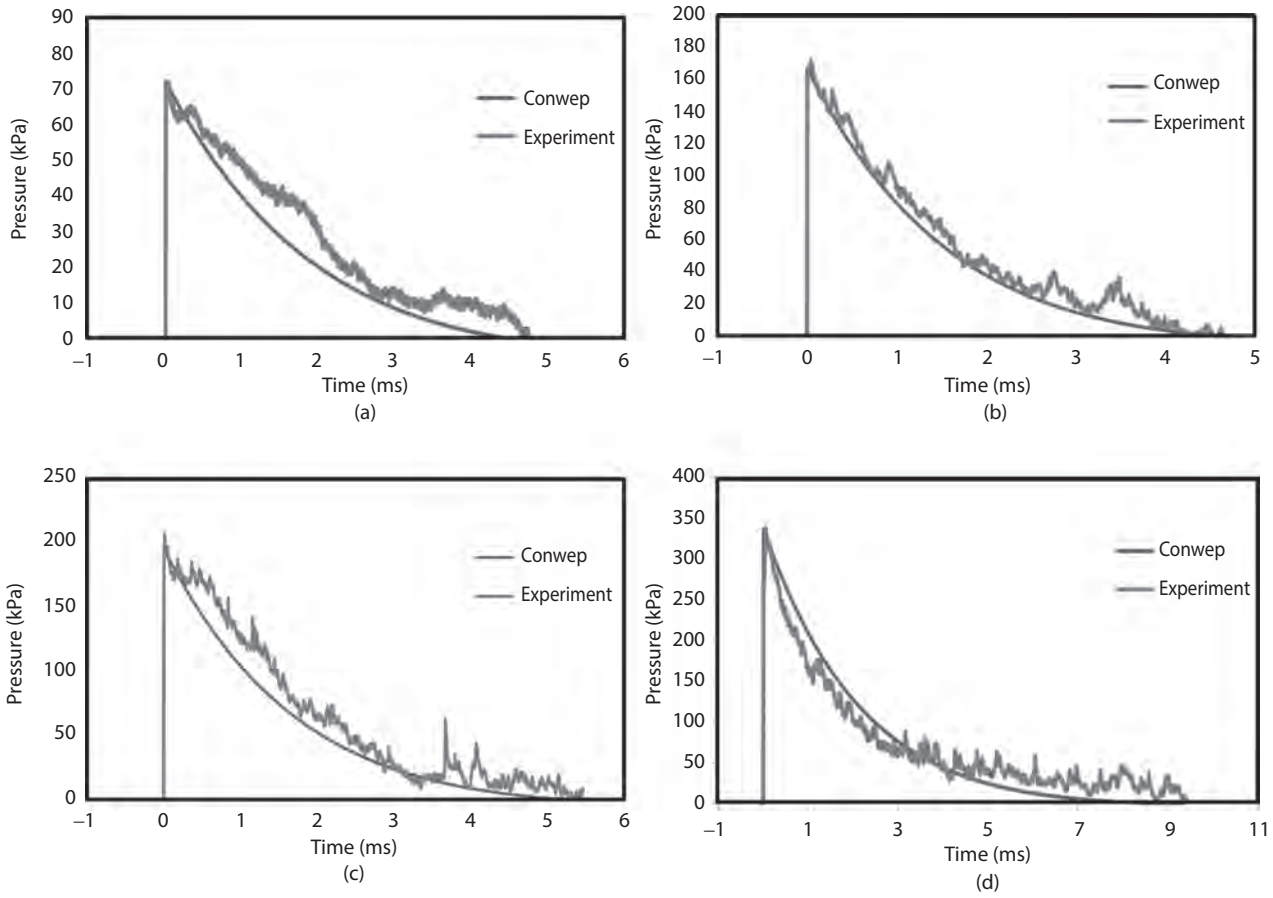


FIGURE 18.22 Comparison of the shock blast profiles from a UNL shock tube device and ConWep simulation software. (a) Comparison between shock blast profile from a 10-membrane, 66.68-mm breech length shot with nitrogen as driver gas ,and 2.56 kg of TNT at 5.18 m. (b) Comparison between shock blast profile from an eight-membrane, 752.48-mm breech length shot with helium as driver gas, and 7.68 kg of TNT at 5 m. (c) Comparison between shock blast profile from a 10-membrane, 1,209.68-mm breech length shot with helium as driver gas, and 14.08 kg of TNT at 5.7 m. (d) Comparison between shock blast profile from 15-membrane, 1,209.68-mm breech length shot with helium as driver gas, and 96 kg of TNT at 8.5 m. (From Sundaramurthy, A. et al. 2012. *Journal of Neurotrauma*. 29:2352, 2012.)

locations of the sensors inside the head (Figure 18.23c). In addition, CT images were also useful in identifying precise geometry of skull and the face in the vicinity of the sensor; by geometry, we implied anatomical features such as air sinus, eye socket, and nasal cavity. For example, a huge air sinus was present in front of certain sensors (see Figure 18.23c, nose ICP). Surface pressures were measured using Kulite surface mount sensors (model LE-080-250A) and ICPs are measured using Kulite probe sensor (XCL-072-500A). Surface strains were measured using Vishay strain gauges (model CEA-13-250UN-350). In addition to these sensors, a PCB pressure gauge (model 134A24) was used to measure incident (side-on) pressure of the blast wave. Incident pressure was measured just before (distance = 200 mm) blast wave encounters the PMHS head. Incident pressure gauge was mounted on the wall of the shock tube.

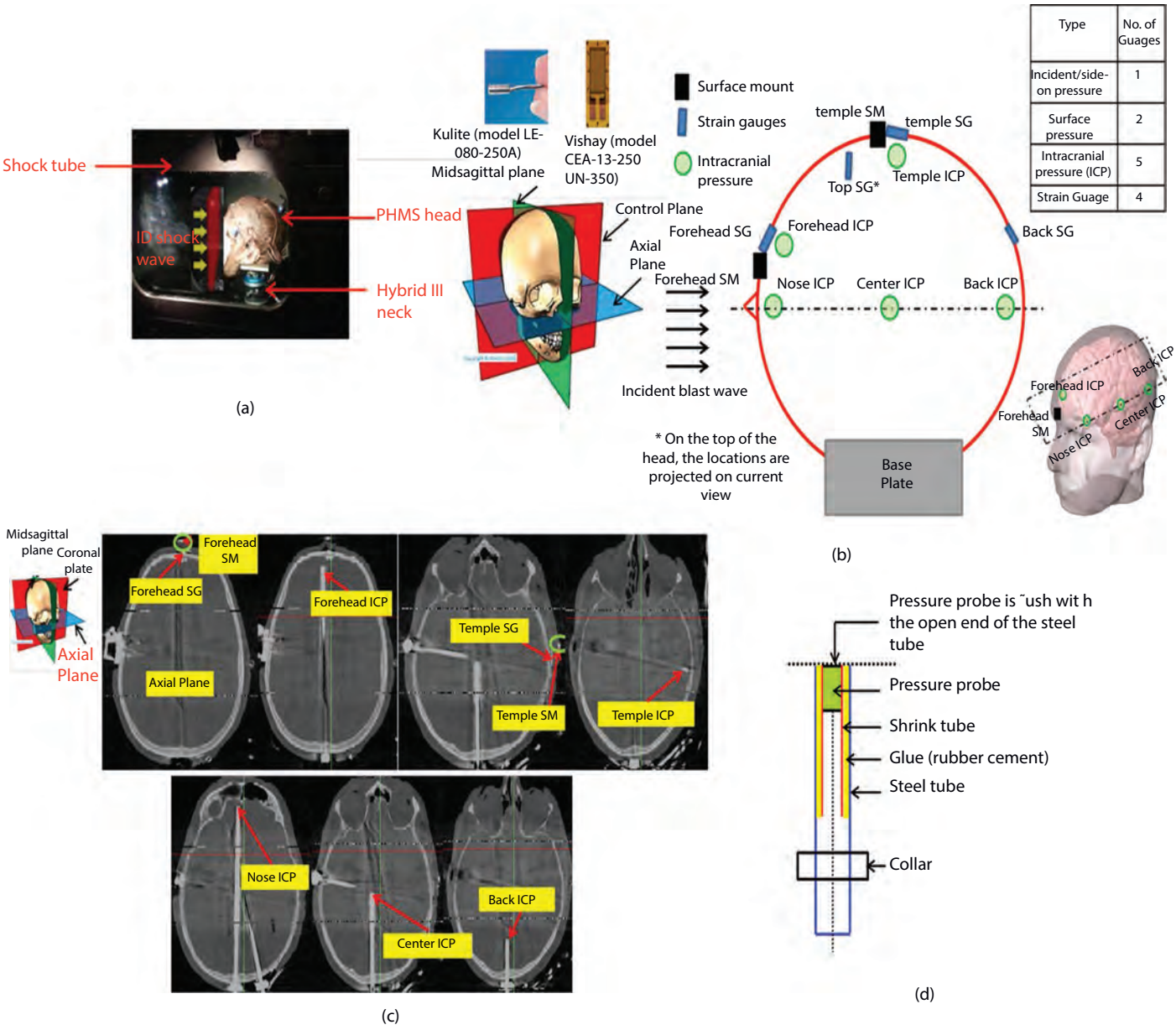


FIGURE 18.23 (a) PMHS heads with hybrid III neck placed in the test section of the shock tube. (b) Schematic showing sensor locations on PMHS head. (c) CT images of instrumented PMHS showing sensor locations. Anthropometric data were also obtained from these CT images. (d) Preparation of pressure probes that are used for ICP measurements.

TABLE 18.2
Characteristics of the Three PMHS Heads Tested in this Study

PMHS No.	PMHS Identification	Sex	Age	Height (cm)	Weight (kg)	Cause of Death
1	421	M	72	175	68	Prostate cancer, diabetes
2	476	M	75	173	79	Cardiovascular disease
3	513	M	65	175	73	Prostate cancer

18.2.1.2 Blast Wave Exposure

All PMHS heads were subjected to blast waves of three different incident intensities or overpressures (70, 140, and 200 kPa). This was achieved by changing number of membranes, which resulted in different burst pressures. The head was oriented in frontal direction to the blast. Each intensity was repeated three times for each head, so there were a total of 27 (3 × 3 × 3) shots. The PMHS head was placed in the test section of the shock tube located approximately 2,502 mm from the driver end; the total length of the shock tube was 12,319 mm.

18.2.1.2.1 Sample Pressure-Time Profiles

Figure 18.24a–h shows sample incident pressure (a), surface (reflected) pressure (b, c), and ICP (d–h), respectively. Sample pressure-time profiles presented here are based on the mean of three shots (experiments) for head 1. While presenting sample pressure-time profiles, the time axis was shifted so that arrival of blast wave at a given sensor location corresponded to t = 0. Incident blast intensity for these profiles was 200 kPa. Raw (pressure) data showed oscillations; thus, the profile was smoothed by performing simple moving average (Kraus et al., 2007). The number of data points selected for moving average varied from five to 20.

Figure 18.24a shows incident pressure profile. The incident pressure was measured at 200 mm (upstream) from the PMHS head. The incident profile showed a sudden rise in pressure (rise time is 10 μs) followed by nonlinear decay; the peak pressure and positive phase duration were 190 kPa and 5.4 ms, respectively. Secondary peaks were also seen in the incident profile. Incident pressure profile was highly repeatable; shot-to-shot variations in the pressure profile were less than 5%.

Figure 18.24b, c shows pressure profiles on the surface of the head. Surface pressures were measured at the forehead and temple locations. The profile for forehead location showed a sudden rise in pressure (rise time was 30 μs) followed by nonlinear decay. The rate of decay was much faster than that observed in incident pressure profile. The peak pressure and positive phase duration for this profile were 592 kPa and 5 ms, respectively. The peak pressure was amplified 3.11 times the peak incident pressure but the positive phase duration remained approximately similar at 5 ms. The pressure profile for temple location also showed a sudden rise in pressure (rise time was 30 μs) followed by another spike. This was followed by a sudden (instantaneous) decay in pressure with huge oscillations (from t = 0.25 to t = 0.5). The oscillating profile with much smaller peaks was observed after this time. The peak pressure and positive phase duration for this profile were 295 kPa and 5 ms, respectively. The ratio of peak pressure to peak incident pressure was 1.55.

The shape and positive phase duration of the surface pressure profile at the forehead location was similar to that of incident pressure profile. However, peak overpressure was significantly higher because of aerodynamic effects and the rate of decay is much faster compared with the incident pressure profile. Temple location had much a smaller peak pressure (50% decrease) compared with the forehead location.

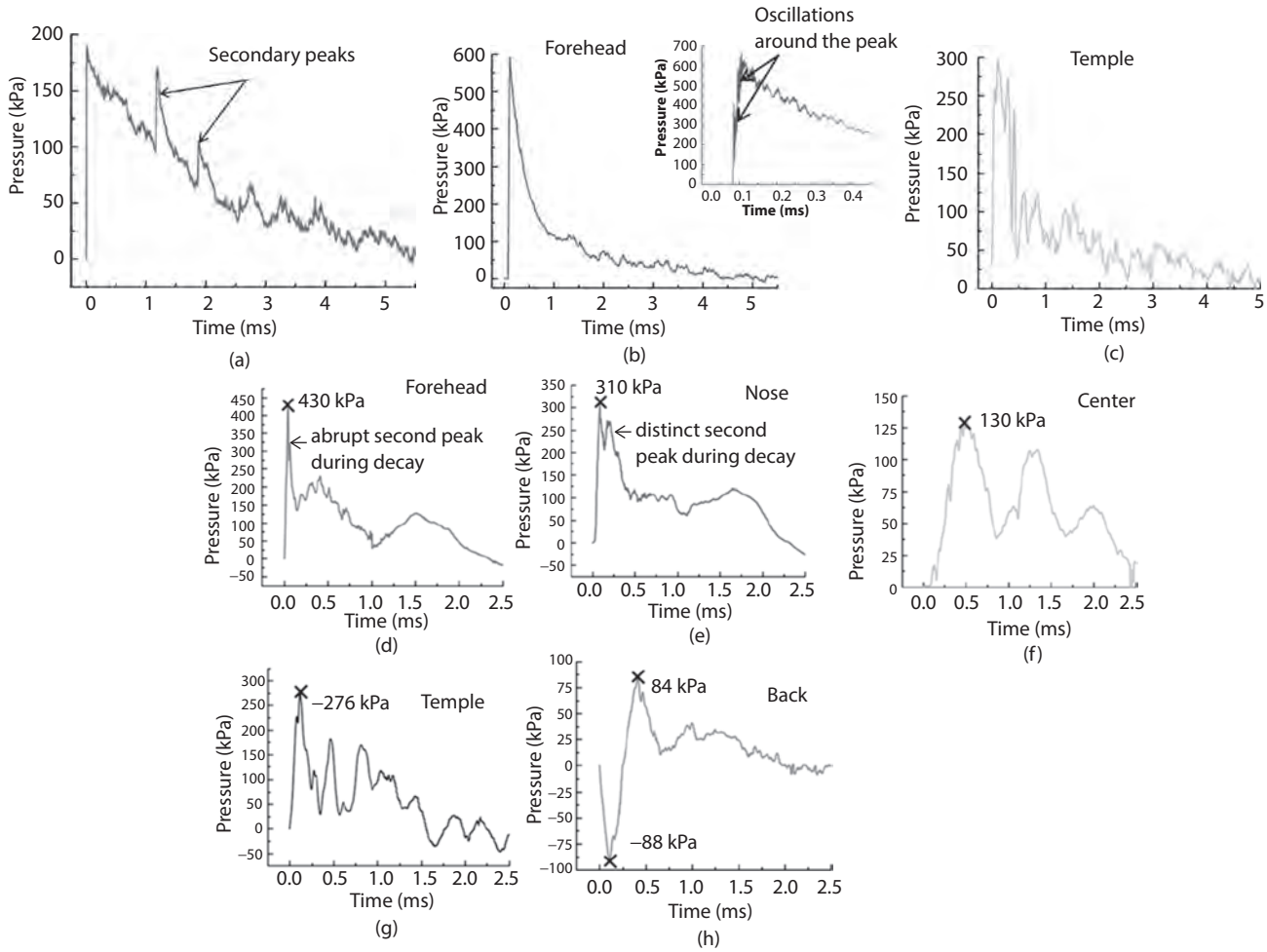


FIGURE 18.24 (a) Incident pressure profile. Incident pressure profile is measured 200 mm (upstream) from the PMHS head. (b, c) Sample pressure profiles on the surface of the head. (d–h) ICP profiles: (d) forehead ICP, (e) nose ICP (e), center ICP, (f) temple ICP, and (g) back ICP.

These effects can be explained by studying blast wave–head interactions. The flow field around the head is illustrated using numerical simulations. At the beginning of the interaction, as the shock front impinges on the forehead at its most upstream region, a reflected shock propagating in the opposite direction starts to develop. The incident shock starts to propagate around the surface of the head. At the same time, regular reflections occur that propagate radially both in upstream and downstream direction. These reflections continuously interact with the incoming tail part of the blast wave. The reflections are tensile in nature and hence a compressive pattern of decreasing strength develops as a result of the incident shock reflection over the surface and the forward motion of the shock tail (also known as blast wind) as shown in Figure 18.25a. Thus, the forehead surface gauge recorded a faster decay compared with incident pressure profile. As the shock wave traversed the head, shock wave diffractions occurred and as a result geometry-induced flow separation took place (Figure 18.25b). This geometry-induced flow separation increased as we moved away from the leading edge (or incident blast site) toward downstream. Because of this flow separation, the temple location showed a decrease in peak pressure with respect to the forehead location. A similar phenomenon of shock wave diffractions and flow separation over cylindrical objects was seen in studies involving shock wave propagation over cylindrical objects (Bass et al., 2012; Brun, 2009; Gould and Tempo, 1981).

Figure 18.24d–h shows the ICP profiles for sensor locations shown in Figure 18.23b. For ICP profiles, wave action (dynamic events) played out in very short time. Positive phase duration was 2.5 ms with initial (or majority of) intracranial dynamics playing out within 0.5 ms. Sensor forehead (FH) ICP (Figure 18.24d) showed a sharp rise (rise time = 40 μs) in pressure profile. This was followed by a decay in pressure until t = 0.15 ms; an abrupt pressure increase was also seen during this decay at t = 0.07 ms. The decay was not sustained and there was another rise in the pressure. A secondary (loading) pulse, which was similar to a pulse observed in impact loading, was seen after 1.0 ms. Sensor nose ICP (Figure 18.24e) also showed a sharp rise (rise time = 70 μs) in the pressure profile. This was followed by decay in pressure until t = 0.5 ms; during this decay, a distinct pressure increase (like another peak) was seen at t = 0.2 ms. After this decay, the pressure remains approximately constant with small oscillations until t = 1 ms. Secondary pulse, which is similar to pulse observed in the FH ICP profile, was seen after 1 ms. Figure 18.24f shows the pressure profile for center ICP. The pressure rise (rise time = 390 μs) is not as sharp compared with FH and nose ICP profiles. Pressure pulse seemed to repeat itself with damping until the pressure equilibrates. Figure 18.24g shows the pressure profile for temple ICP. The profile has similar features as that of center ICP. It appears that center and temple ICPs experience several waves that are emanating from different sources during the rise. Rise time for temple ICP was 115 μs. Figure 18.24h showed the pressure profile for back ICP. Back ICP showed the negative phase followed by the positive phase. The negative phase had a rise time of 100 μs and duration of 0.25 ms. A positive phase of back ICP has features similar to FH and nose ICP profiles. This is followed by decay in pressure after which pressure equilibrates.

Analysis of the peak pressures of ICP profiles has led to some interesting observations. Peak pressures are marked with black cross on each ICP profile. The highest peak pressure is observed behind the forehead. The peak pressures were decreased as we move away from the coup (impact) site toward contrecoup (opposite to impact) site. It should also be noted that significant difference in peak pressure is observed for FH (430 kPa) and nose (310 kPa) ICPs that are in same coronal plane.

The pressure profiles in the brain drastically deviated from surface pressure profiles. ICP dynamics play out in much shorter duration compared with incident or surface pressure profiles. For ICP profiles, positive phase duration was 2.5 ms with initial (or the majority of) intracranial dynamics playing out within 0.5 ms; this was due to wave propagation in skin–skull–brain parenchyma. The impedance mismatch of the layered system (skin–skull–brain) was such that the magnitude of the pressure wave (or input signal) in the skin–skull–brain parenchyma was either amplified or attenuated as it reflected and transmitted through these layers. The wave traversal times through the skin and the skull were 52.9 μs and 3.62 μs assuming 10-mm thickness for both skin and skull. Within 506 μs (i.e., 0.506 ms) two wave traversals occurred in the skin and 29 wave traversals were possible in the skull. Thus, wave action (reflections and transmissions) happens at a much shorter time scale, and a sharp decay in ICP profiles was seen for FH and nose ICPs. This aspect is further elaborated using one-dimensional model of skin–skull–brain parenchyma as shown in Figure 18.25c, d. Figure 18.25c shows response of the skull–brain parenchyma when a loading pulse (Heaviside function) of intensity P is applied to the skull. Pressure in the brain was 0.62 (transmission coefficient) times the applied pressure after first transmission from the skull into the brain. Transmission coefficient increased with each transmission and pressure in the brain equilibrated after the fifth transmission from the skull into the brain. Figure 18.25d shows response of the skin–skull–brain parenchyma when a loading pulse of intensity P was applied to the skin. In this setup (or model), thickness of the skull and skin were designed such that (t_{skull} = 14 t_{skin}) reflection/transmission occurs at same time for skin–skull and skull–brain interfaces. Transmission coefficient was 1.16 after the first transmission from the skull into the brain. However, transmission coefficient drastically decreased to 0.15 after the second transmission. Subsequent transmissions had transmission coefficients of 1.39, 0.42, 1.32, and 0.7. In reality, the thickness of the skin and the skull were almost similar and hence the wave traversal in the skull was ~14 times faster than the skin based on the wave speeds. The transmitted wave from the skull into the brain equilibrated after the fifth transmission (Figure 18.25c). Hence, for wave propagation through skin–skull–brain parenchyma in real scenarios skull (thickness) should not play major role in the wave amplification

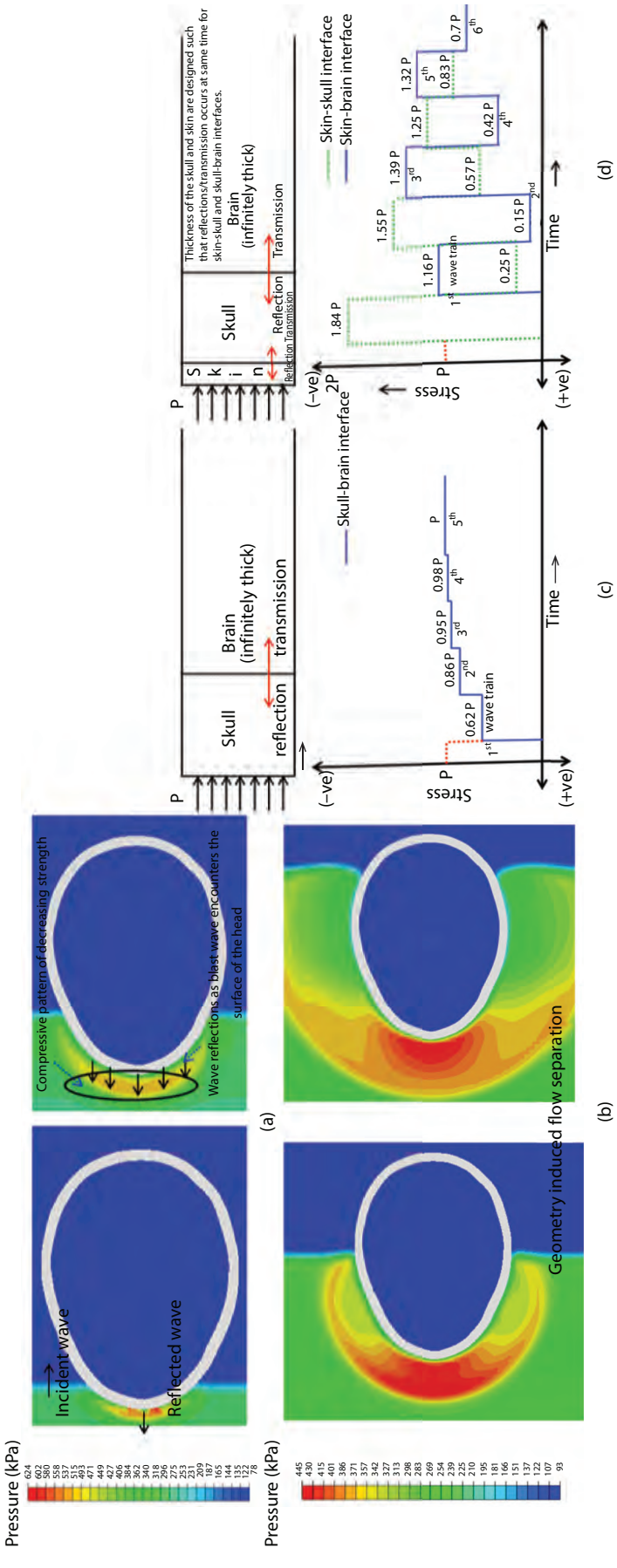


FIGURE 18.25 Blast wave–head interactions as blast wave traverses the head. (a) Blast wave–head interaction at leading edge or incident blast site. (b) Illustration of Mach reflection and flow separation as blast wave traverses the head. In all figures, cuts are made along the axial plane. Wave propagation in skin–skull–brain parenchyma using one-dimensional model. (a) Response of the skull–brain parenchyma to the applied loading pulse of intensity P. (b) Response of the skin–skull–brain parenchyma to the applied loading pulse of intensity P.

or attenuation and brain should ideally see the pressure that is seen by the skull at the skin–skull interface. Even in that case, the transmission coefficient in the brain after the second transmission was 0.25. This explains the sharp decay in ICP profiles for FH and nose ICPs that were closest to incident blast site wherein initial wave propagation obeys one-dimensional theory fairly well (at least in terms of qualitative trends). For FH ICP, the pressure decreased from 430 kPa (first transmission) to 138 kPa (second transmission) in 117 μs; the ratio of these pressures is 0.32, which is consistent with the one-dimensional theory.

The FH and nose ICPs showed a second peak during the initial decay; the second peak was abrupt in the FH ICP and distinct in the nose ICP. This second peak was due to a delayed wave transmission from the eye socket/eyebrow region as illustrated in Figure 18.26. After these initial phases, wave reflections from the head boundaries dominated the response and it was not possible to delineate these effects because of the complex and highly dynamic nature of the problem. The center and temple ICPs, which are probably located deep inside the brain, experienced many waves emanating from different sources. By the time the wave reached center ICP, the pressure was attenuated. This attenuation could be due to material damping, wave dispersion over larger area, and reflections from geometric boundaries and material interfaces. The pressure pattern of the center ICP can be best described as follows. At any given point, the brain experiences a complex set of direct and indirect loadings emanating from different sources (e.g., blast wave transmission, reflections from tissue interfaces, skull deformation) at different time points. These disturbances continuously propagate into the brain as waves. Constructive and destructive interferences of these waves control the pressure history deep inside the brain. Back ICP shows the contrecoup effect (negative pressure) initially because the wave velocity in the skull is higher than the wave velocity in the ballistic gel. Because

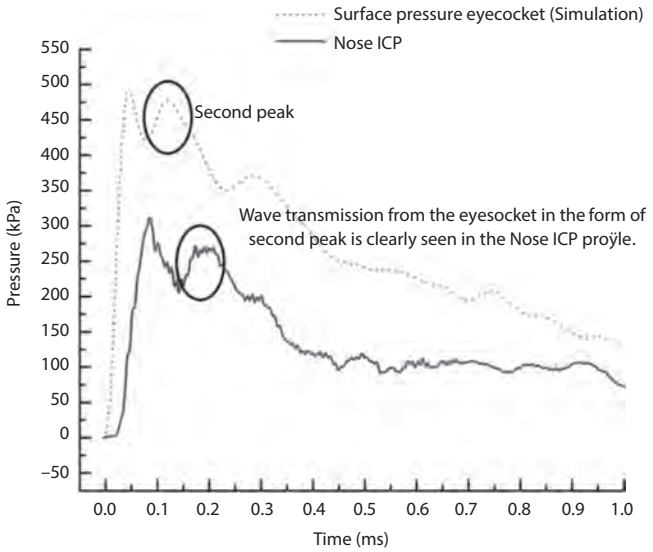


FIGURE 18.26 Comparison of Surace and ICP profiles near the eye socket regions.

of this, the skull moves forward; displacement of the brain lags displacement of the skull and hence tension or negative pressure is generated in the brain. If tensile loads/forces are not allowed to transfer, then separation will take place at the skull–brain interface.

18.2.1.2.2 Pressure Response as a Function of Incident Blast Intensity

Figure 18.27 shows the positive phase impulse for various sensors as a function of intensity. The positive phase impulse increased as the incident blast intensity increased. The differences were statistically significant ($p < 0.05$) at all sensor locations except back ICP sensor for all heads and temple ICP for head 1. Head-to-head variations in the positive phase impulse were also significant; impulse variations up to 77% were observed between the heads.

As mentioned earlier, one of the lingering questions facing the medical and scientific communities is whether blast waves cause TBI. We exposed PMHS heads to pure primary blast of varying intensities and observed statistically significant differences in the peak ICP and total impulse. This finding supported our hypothesis that intracranial response change with change in incident blast intensity. Thus it is clear that primary blast waves acting alone can cause mechanical insult to the brain. The potential of this mechanical insult in causing the BINT will be assessed in the following section. Over the past few years, several mechanisms (see the previous section) have been proposed based on numerical simulation without experimental backup. Our experimental measurements categorically indicated that the blast wave transmission through the cranium induced mechanical insult to the brain of varying degrees that changed with variations in incident intensity. Thus we propose direct transmission of blast wave into the intracranial cavity as essential loading pathway to the brain.

18.2.1.2.3 Sample Strain Profiles

Figure 18.28 shows sample (circumferential) strain profiles for strain gauge locations shown in Figure 18.23b. Incident blast intensity for these profiles was 200 kPa. Negative strain indicated compression and positive strain indicated tension. Front strain gauge showed compressive phase up to 1 ms; this was followed by small (equilibrium) oscillations for 0.2 ms, followed by another compressive pulse. The right temple strain gauge showed initial tension followed by compression. This compressive phase was sustained for 0.2 ms only. This was followed by a tension-compression phase with higher magnitudes and longer durations. Top and back strain gauges showed several compressive phases; each compressive phase was followed by equilibrium oscillations (i.e., small oscillations around zero). Highest circumferential strain was observed for the front location at 0.06%. The shape of the strain profiles was not consistent across the heads and incident intensities or in some cases, even from experiment to experiment for a given head. The magnitude of the strain however was on the same order of magnitude. Head-to-head variation of ±40% was observed in the peak strain.

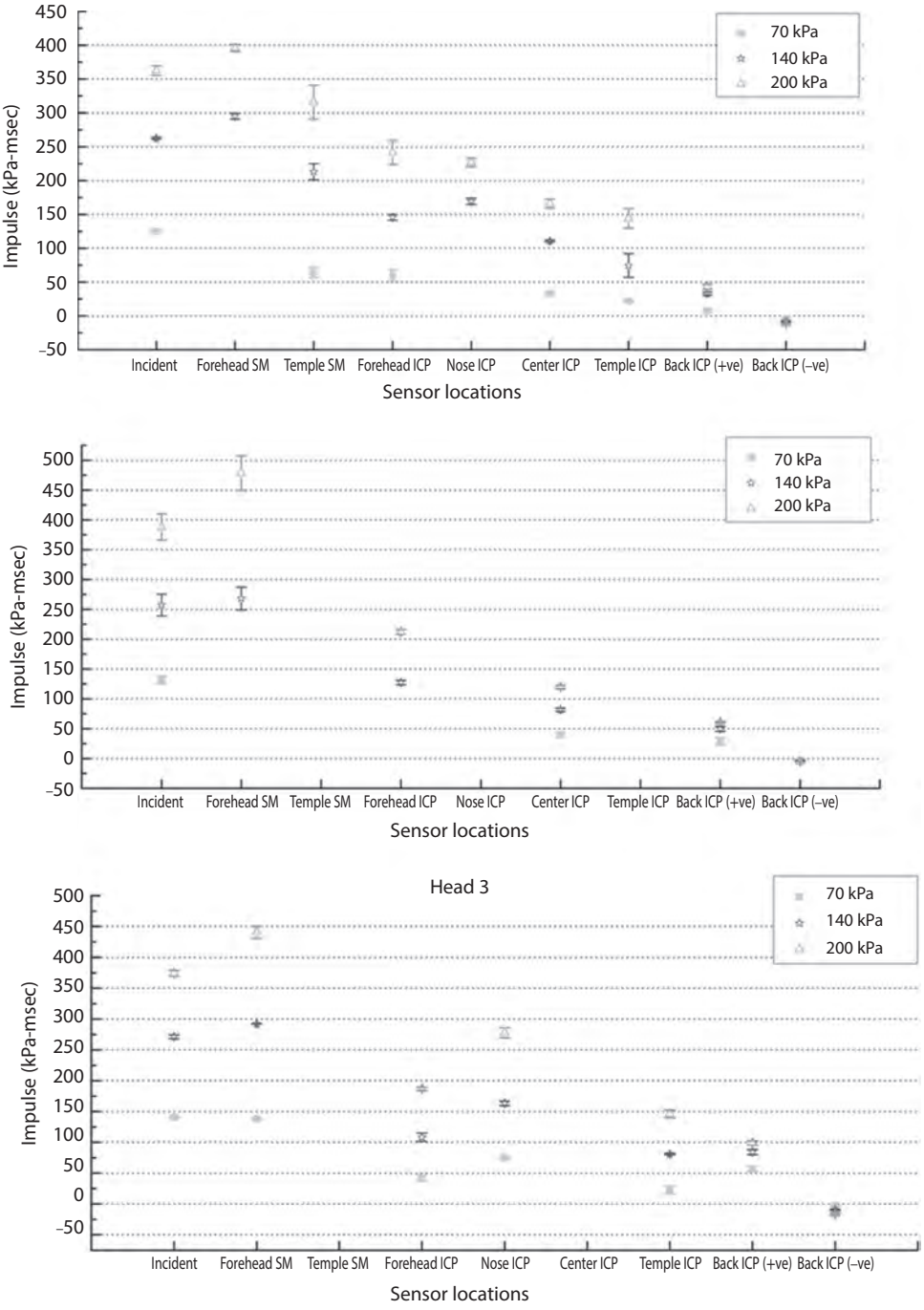


FIGURE 18.27 Positive phase impulse for various sensors as a function of intensity.

18.3 ANIMAL MODEL BLAST TESTING

This section focuses on characterization of biomechanical response and selected pathologies associated with primary blast exposure in vivo animal model (rat), in the acute phase (up to 24 hours postexposure). The first part of this study is the evaluation of mortality rates in the rodent model at five discrete blast intensities. Concurrently, the primary blast biomechanical loading experienced by the body was studied; that is, a correlation between external load (incident and reflected pressures) and biomechanical response (intracranial and intrathoracic pressures) was established. Furthermore, corresponding response at systemic and organ levels (lung injury, heart rate decrease, and body weight loss) was also studied. Finally, to understand the effect of primary blast exposure on brain, selected pathologies were studied (blood–brain barrier [BBB] damage, immunoglobulin G [IgG] extravasation).

18.3.1 Experiment

Adult 10-week-old male Sprague-Dawley rats weighing 320–360 g were used in all studies. Three studies with

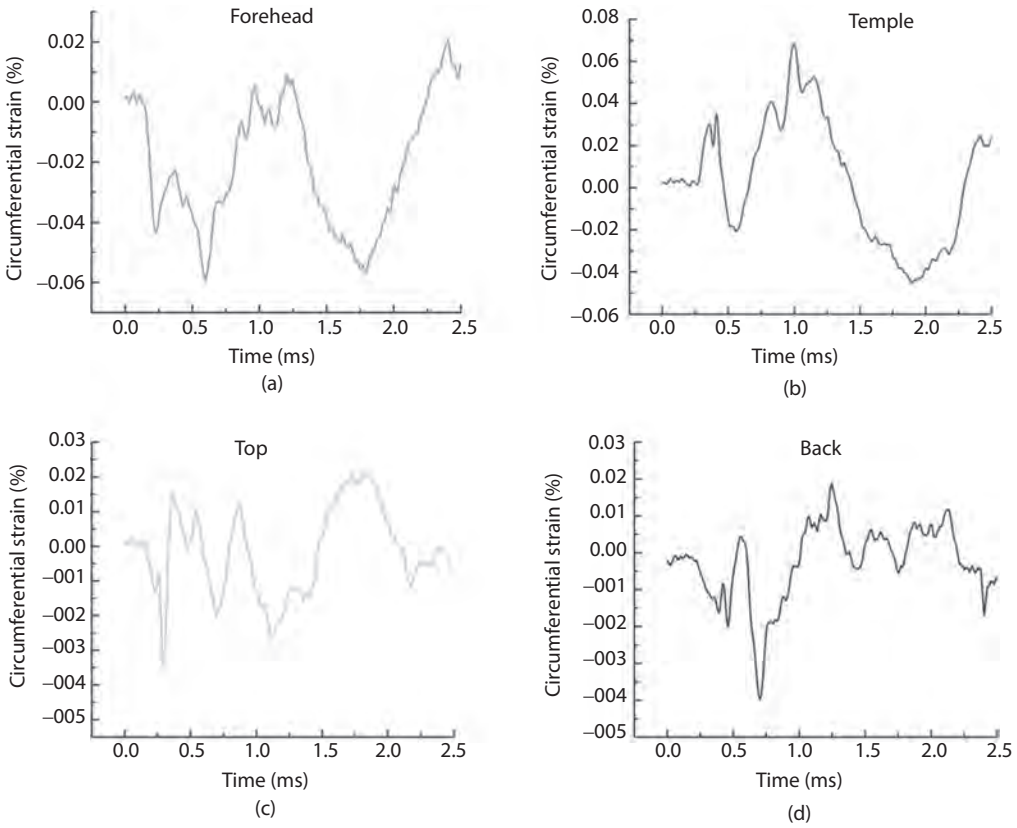


FIGURE 18.28 Strain profiles for various strain gauge locations.

TABLE 18.3
The Peak Overpressure and Impulse Average Values Measured by side-on Sensor (Incident Pressure)

Rat No.	Group Alias	Peak Overpressure kPa[a]	Impulse (pa.s)[a,b]	Survival (%)	No. of Animals[c]	Lung Injury Score	Number of Animals[d5]
1	130[e]	127 ± 8	184 ± 19	100	18	1.8 ± 0.7	5
2	190	195 ± 19	335 ± 25	70	20	8.5 ± 2.9	6
3	230	223 ± 20	393 ± 44	100	10	10.8 ± 3.0	5
4	250	243 ± 21	437 ± 31	76	17	14.4 ± 2.4	5
5	290[f]	288 ± 17	452 ± 45	0	6	13.5 ± 4.0	6

separate groups of rats were performed. In the first study, five cadaver rats were used to record the pressure on the surface of the nose (reflected pressure), in the lungs, and in the brain. In the second study, rats were anesthetized and exposed to the blast and were sacrificed immediately after blast exposure for gross lung pathology and histology evaluation (27 rats). In the third study, monitoring of physiological vitals such as heart rate, blood oxygen saturation, and perfusion index was performed for two periods of 30 minutes, before and after the blast injury (50 animals). The 14 rats in this group were transcardially perfused 24 hours after the blast exposure, and the brain sections were evaluated by histological and immunohistological methods.

The rats were anesthetized with mixture of ketamine and xylazine (10:1 [100 mg/10 mg/kg], 0.1 mL/100 g) administered via intraperitoneal injection. Rats were exposed to the blast wave in the test section located inside of the shock tube (i.e. 2,800 mm from the breech). The tests were performed at five discrete incident peak overpressures detailed in Table 18.3. The incident pressure was controlled by adjusting the number of Mylar membrane, and keeping the breech length constant at 447.7 mm. An aluminum bed was designed and fabricated for holding the rat during the application of blast wave. The aerodynamic riser is attached to the bed to hold the sample in the center of the shock tube. Typically, rats are tested in a prone position and are strapped securely to the bed with a thin cotton cloth wrapped around the body (Fig. 18.29a). Sham control rats received anesthesia and noise exposure, but without blast exposure, and naive control rats were given anesthesia only.

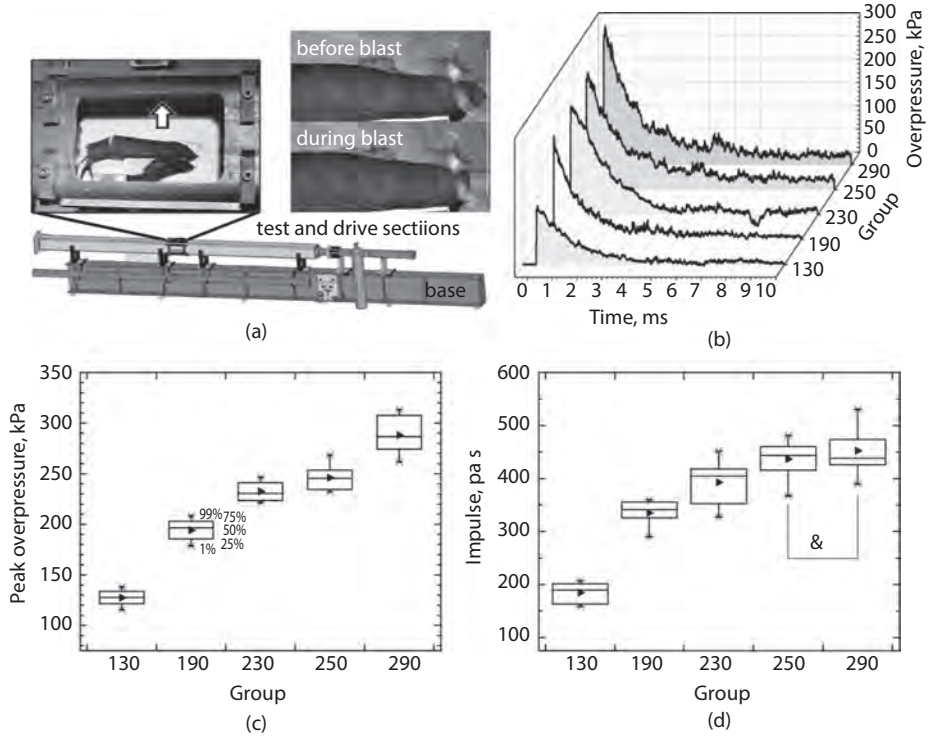


FIGURE 18.29 Schematic representation of the shock tube facility (a): left inset illustrates the side-on pressure sensor location (arrow) and the position and strapping of the animal in the holder; right inset: close-up high-speed video still images demonstrate the typical head displacement during the blast exposure in our model. Representative overpressure profiles (b), side-on overpressure (c), and impulse values (d) of five blast waves with increasing intensities used in our experiments. These data show significant difference in both overpressure values and impulse, except there was no significance between impulse values of groups 250 and 290 kPa ($p > 0.05$, marked with ampersand). Box range: 25%–75%; whisker range: 1%–99% (median: 50%; mean: ►). (From Skotak, M. et al., *Journal of Neurotrauma*. 30:1147–1160, 2013.)

18.3.1.1 Biomechanical Loading Evaluation in Cadaver Rats

Five male Sprague-Dawley rats were sacrificed using carbon dioxide exposure. After the sacrifice, they were instrumented in the same manner as discussed in previously (Figure 18.30a). Cadaver rats were exposed to five shots per animal at: 130 kPa (two rats) and 190, 230, 250, and 290 kPa (two rats). One rat with lungs filled with ballistic gel to ameliorate inconsistent pressure readings was exposed at five blast overpressures (130–290 kPa). To study the harmonic effects in the ICP signal, fast Fourier transformation (FFT) analysis was used.

18.3.1.2 Live Animal Testing

18.3.1.2.1 Mortality Evaluation

To study the mortality, the anesthetized animals were subjected to various levels of blast, characterized by the peak overpressure ranging from 130 to 290 kPa (Table 18.3). No resuscitation was performed after trauma.

18.3.1.2.2 Physiological Evaluation

Body weight measurements were performed before and 24 hours postexposure. Multiple vital signs were measured noninvasively using clinically validated MouseSTAT, a rodent physiological monitoring system (Kent Scientific Corp., Torrington, CT). Briefly, the anesthetized rat was placed in a supine position on the warming pad attached to the control unit to maintain natural body temperature and prevent hypothermia. The temperature was measured rectally at a rate of 1 Hz over the 30-minute period before and after the blast exposure. Simultaneously, heart rate, blood oxygen saturation, and perfusion index were recorded by a y-clip sensor clamped to the back paws of the rat.

18.3.1.2.3 Injury Evaluation

Immediately after the blast exposure, the lungs were extracted from the thoracic cavity, placed in 30–40 mL of freshly prepared solution of 10% formalin, and stored at 4°C for further evaluation. Lung injury severity associated with the primary blast exposure was performed using the Pathology Scoring System for Blast Injuries developed by Yelverton (Yelverton, 1996). The extent of injury is defined by the Elements of the IS according to the equation: AQ2

$$IS = (E + G + ST)\,(SD) \tag{18.2}$$

where E is the extent of injury to the lungs (range 0–5); G is the injury grade including the surface area of the lesions (range, 0–4); ST, severity type elements, which classify the type of the worst-case lesions (range, 0–4); and SD is the severity depth element, indicating the depth or the degree of disruption of the worst-case lesion (range, 1–4).

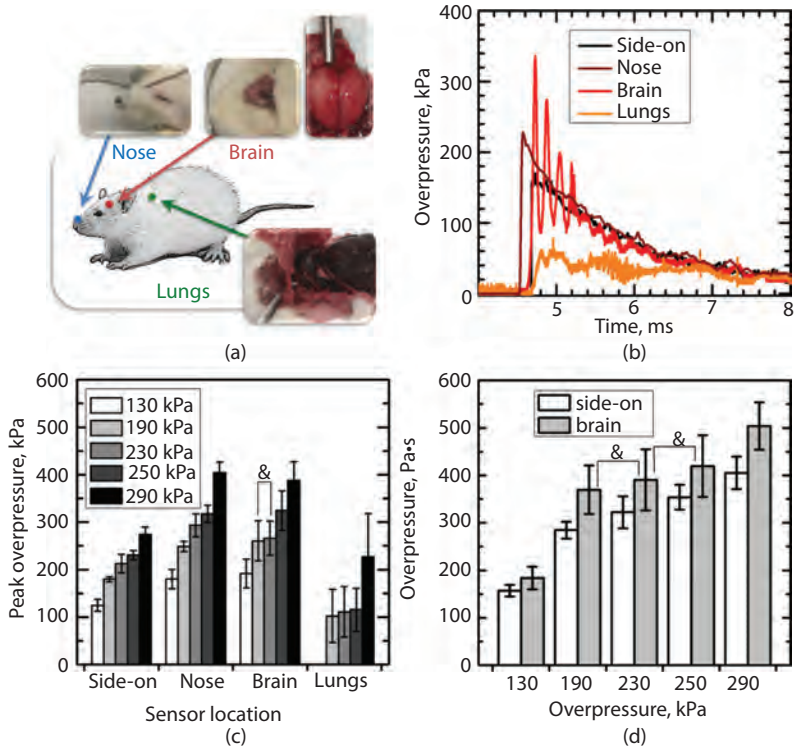


FIGURE 18.30 The diagram of sensor locations (a) used in the cadaver rat experiments. The rightmost inset shows the brain remains intact after the experiments. Representative pressure profiles of the 190-kPa group (b), and average peak overpressures recorded by side-on, nose (reflected pressure), brain, and lungs pressure sensors (c) are presented (no statistically significant differences are noted for 190- and 230-kPa groups; marked with an ampersand). There are no statistical differences between ICP impulse of the 230-kPa group (100% survival, Table 18.1) and ICP impulses of the two lethal groups (190 and 250 kPa) (d). (From Skotak, M. et al., *Journal of Neurotrauma*. 30:1147–1160, 2013.)

18.3.1.2.4 Transcardial Perfusion and Histological Procedures

At 24 hours postexposure, rats were anesthetized with ketamine/xylazine mixture and transcardially perfused with wash solution (0.8% NaCl, 0.4% dextrose, 0.8% sucrose, 0.023% CaCl2, and 0.034% sodium cacodylate), followed by fresh fix solution (4% paraformaldehyde solution supplemented with 4% of sucrose in 1.4% sodium cacodylate buffer, pH = 7.3). Immediately, after perfusion, heads were decapitated and stored for additional 16–18 hours in the excess of fix solution. The brains were subsequently extracted the following day, and stored refrigerated (4°C) in a sodium cacodylate storage buffer. Brains were shipped in phosphate-buffered saline (pH = 7.2) to Neuroscience Associates (Knoxville, TN) for sectioning and staining.

The brains were embedded into one gelatin matrix block using MultiBrain Technology. The block was then allowed to cure and subsequently rapidly frozen in isopentane chilled with crushed dry ice (–70°C). The block was mounted on a freezing stage of a sliding microtome and coronal sections with a thickness of 40 μm were prepared. All sections were collected sequentially into an array of 4 × 6-inch containers that were filled with antigen preserve (buffered 50% ethylene glycol). At the completion of sectioning, each container held a serial set of one of every twelfth sections, i.e., single section at every 480-μm intervals). These sections were stained with an antibody against rat IgG to assess the BBB damage, and with amino cupric silver staining to detect neurodegeneration.

18.3.2 Results and Discussion

18.3.2.1 Biomechanical Loading Evaluation and ICP Analysis

Typical pressure profiles for all four sensors used (denoted as side-on, nose, brain, and lung) are presented in Figure 18.30b. The intensity of the reflected pressure measured on the rat's nose was higher than the intensity of side-on pressure, and both were characterized by gradually increasing values (Figure 18.30c). The reflected (nose sensor) and ICPs were higher than the incident pressure ($p < 0.001$) as observed in Figure 18.30c, but there are no clear differences between reflected pressure and ICP. Moreover, the ICP not only was higher than the incident pressure, but also showed an oscillatory tendency. Although the reflected pressure showed a monotonic increase with side-on pressure for all of the pressure groups (130, 190, 230, 250, and 290), the same cannot be said for the ICP: there were no statistically significant differences between the 190- and 230-kPa groups ($p = 0.70$) (Figure 18.30c). The impulse values for brain sensor indicated there were statistically significant correlations between the nonlethal group at 230 kPa and the two lethal groups (i.e., 190 and 250 kPa). This indicates the outcome

(mortality) is not a function of the total energy transferred to the brain, but depends on the specific response of the cranium. The mortality rates among animals exposed to different levels of blast overpressures are shown in Table 18.3. Exposure to 130 kPa (n = 18) and 230 kPa (n = 10) resulted in no animal death, whereas exposure to 190 kPa (n = 20), 250 kPa (n = 17), and 290 kPa (n = 6) peak overpressure resulted in 30%, 24%, and 100% mortality, respectively.

To elucidate various modes of blast loading, we performed a set of analyses on the data reported by the brain pressure sensor. Using peak-trough analysis, we correlated biomechanical loading at the early, the most violent stages of blast wave–cranium interactions (initial 0.4 ms, Fig. 18.31a, b), with the blast-induced mortality (Table 18.3). The monotonically increasing peak overpressure and impulse values measured outside (side-on sensor) or inside of the cranium did not follow the same trend as mortality data in the Table 18.3. However, there is a strong correlation between the sum of the first two peak-to-peak amplitudes and mortality (Fig. 18.31c). The ICP data subjected to FFT analysis indicated the oscillations have harmonic characteristics, and the high frequency component (10–20 kHz) is present exclusively in the case of the lethal groups (190, 250, and 290 kPa, Fig. 18.31d). Moreover, the maximum ICP frequency increases with increasing blast intensity: peaks at 12.6 kHz (190 kPa), 16.4 kHz (250 kPa), and 19.3 kHz (290 kPa) marked with arrows in Figure 18.31d. In the 290-kPa group, two characteristic frequencies are noted (16.4 and 19.3 kHz). The ICP pressure oscillations are caused by the specific material response of the rat skull, which was also demonstrated in a simplified numerical model of in vivo response to blast proposed by Moss (Moss et al., 2009).

The intrathoracic pressures (lungs) were substantially lower than the incident overpressure and ICPs. However, there were considerable difficulties during pressure measurements in lungs caused by uncontrolled interactions between

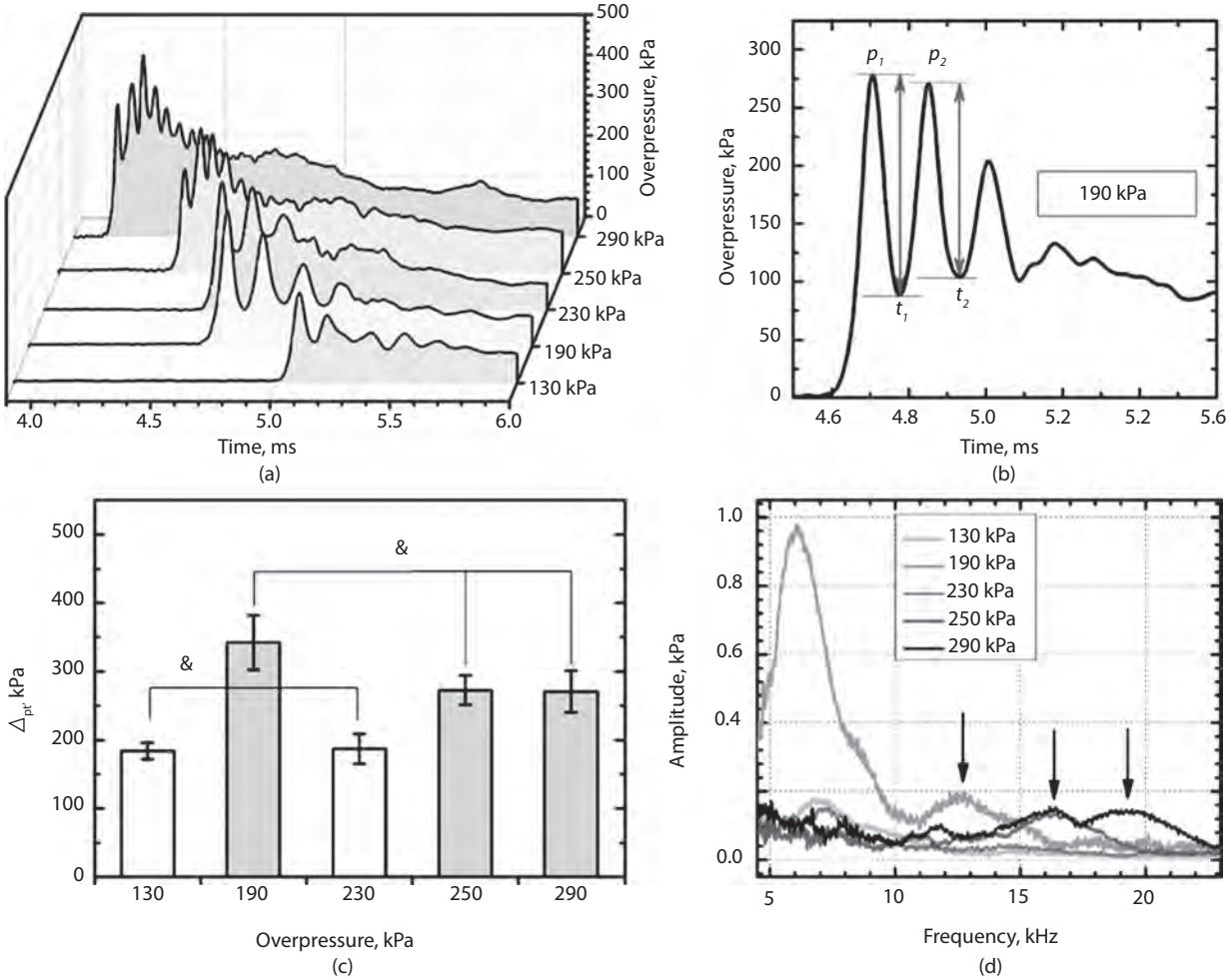


FIGURE 18.31 Representative pressure traces for five exposure groups (a). The signal was smoothed using a FFT band-pass filter for the clarity of presentation. (b) Schematic representation of peak–trough analysis on overpressure recorded by brain sensor: Δpt is a sum of the first two peak-to-peak amplitudes. Results of peak–trough analysis: (c) Lethal groups (190, 250, and 290 kPa) have significantly higher Δpt ($p < 0.05$) compared with nonlethal groups (130 and 230 kPa). There are no statistically significant differences between Δpt in respective nonlethal and lethal groups ($p > 0.05$, marked with ampersand). (d) FFT analysis of the ICP profiles recorded by sensor implanted in the brain. The high frequency component (peaks marked with arrows, >10 kHz) is present in the signal of lethal groups (190, 250, and 290 kPa). (From Skotak, M. et al., *Journal of Neurotrauma*. 30:1147–1160, 2013.)

the pressure sensor and walls of internal organs in the abdomen. It is clearly seen in the experimental data as high variability of peak overpressure values between data sets and a relatively high experimental errors (Fig. 18.30c). In an attempt to mitigate these issues, we filled up lungs with ballistic gel (20% gelatin), but the recorded pressure profiles in this configuration were of much higher magnitude (i.e., comparable with pressures recorded in the brain).

18.3.2.2 Physiological Parameters

We noted statistically significant weight loss in both 190-kPa and 250-kPa injury groups 24 hours after blast exposure (Fig. 18.32). Body weight loss proportional to the blast intensity was reported in mice (Cernak et al., 2011; Wang et al., 2011), and this is typically a manifestation of impairment of neuroendocrine system (hypothalamic-pituitary-target organ axes) (Brown et al., 1993) associated with the damage to the hypothalamic region of the brain.

Heart rate monitoring was performed over the 30-minute period before and after the blast exposure (Fig. 18.33a, b).

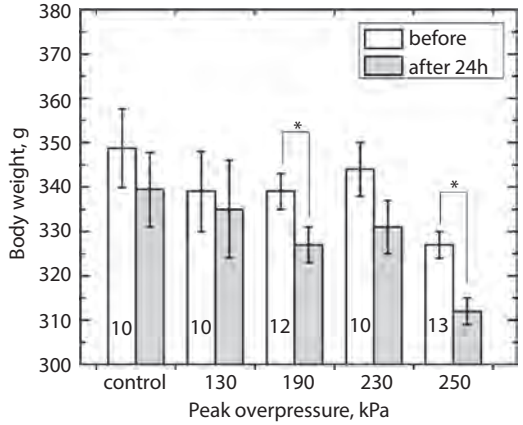


FIGURE 18.32 Exposure to different intensity of primary blast results in the body weight decrease in groups 190 and 250 kPa. In these groups, statistically significant differences (marked with asterisk) were established immediately before and 24 hours after the exposure ($p < 0.05$). Numbers of animals used in respective tests are provided in the bars corresponding to each group. (From Skotak, M. et al., *Journal of Neurotrauma*. 30:1147–1160, 2013.)

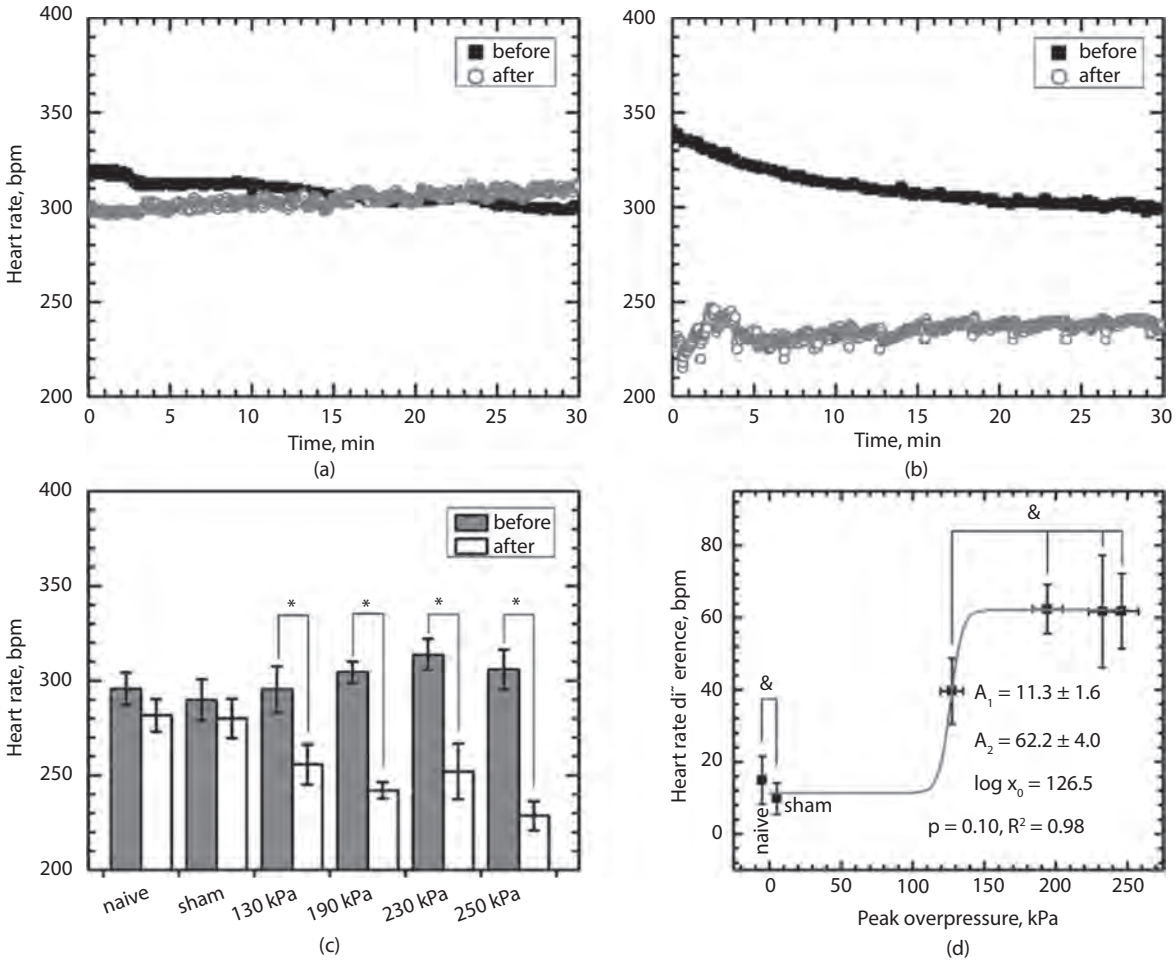


FIGURE 18.33 Representative experimental data demonstrating blast-related bradycardia in the rat model: (a) naive control, (b) rat exposed to 190-kPa peak overpressure (sampling rate 1 Hz in both cases). (c) The heart rate monitoring in the acute phase postexposure revealed the average heartbeat decrease was statistically significant ($p < 0.05$) in animals exposed to blast at peak overpressure of 130 kPa ($\Delta HR = 40 \pm 9$ bpm) and higher (average $\Delta HR = 62 \pm 11$ bpm for 190-, 230-, and 250-kPa groups). (d) The heart rate difference is not statistically significant between two control and four exposed groups ($p > 0.05$, marked with ampersand) and follows dose response model in the acute phase postexposure. (From Skotak, M. et al., *Journal of Neurotrauma*. 30:1147–1160, 2013.)

Observed changes in the heart rate difference between control groups were nonsignificant (Fig. 18.33c, $p > 0.05$). The blast groups, as expected, showed an onset of bradycardia occurring immediately after the blast exposure (Figure 18.5c, $p < 0.05$): the heart rates decreased by 40 ± 9 (130 kPa), 62 ± 7 (190 kPa), 62 ± 15 (230 kPa), and 62 ± 10 (250 kPa) bpm. It appears that blast-induced bradycardia (i.e., expressed as the difference of average heart rate measured during 30-minute intervals before and after exposure) follows a simple dose-response model, with upper value of 62 ± 4 bpm, and inflection point at 126 kPa (Figure 18.33d). However, all the groups of rats exposed to blast are correlated, with 130- and 190-kPa groups being borderline correlated (p = 0.065). Animals surviving blast exposure had a significantly decreased heart rate, compared with control (Fig. 8.33). At high peak overpressure values (i.e., 190 kPa or higher), the heart rate is independent of the blast intensity (Figure 18.33c, d). The blast-induced bradycardia in the current model is similar to reported in other studies using rats (Guy et al., 1998; Irwin et al., 1999; Knöferl et al., 2003). However, in blast trauma mouse models, the opposite relationship was observed: exposure to the mild blast resulted in the heart rate increase immediately after the blast (Cernak et al., 2011). Bilateral cervical vagotomy and intraperitoneal injection of atropine methyl-bromide completely prevented the bradycardia, thus confirming the vasovagal reflex is responsible for bradycardia in the acute phase after the blast exposure (Irwin et al., 1999).

18.3.2.3 Shock Wave–Induced Acute Lung Injury

No animals showed external signs of trauma. At necropsy (performed immediately after the blast exposure), animals subjected to a blast wave showed typical evidence of moderate pulmonary hemorrhage (Figure 18.34), associated with vascular damage, direct alveolar injury, and edema, and generally described as "blast lung" (Brown et al., 1993; Pizov et al., 1999; Sasser et al., 2006; Tsokos et al., 2003). As illustrated in Figure 18.34, animals subjected to a higher blast overpressure (190–290 kPa) were found to have statistically significant pulmonary hemorrhage compared with sham control. The onset of injury in our model takes place at 130 kPa peak overpressure. Modeling of the pulmonary injury as a function of peak overpressure with dose-response function revealed inflection point is located at 184.2 ± 15.7 kPa, with a plateau (the highest score) at 14.32 ± 1.85 (Figure 18.34g). This value is rather low: the maximum possible value in the Yelverton's blast injury index for lungs is 64 (Yelverton, 1996). Interestingly, pathological evaluation of pulmonary injuries in one rat from the 290-kPa group (100% acute mortality) revealed virtually no signs of lung injury. In the areas most severely affected by hemorrhage, approximately 15%–60% of the alveoli were filled with acute pools of hemorrhage (data not shown). Near these pools, there were respiratory bronchioles, which contained small amounts of edema fluid. The more normal sections of lung have moderate atelectasis and very sparse to absent emphysema.

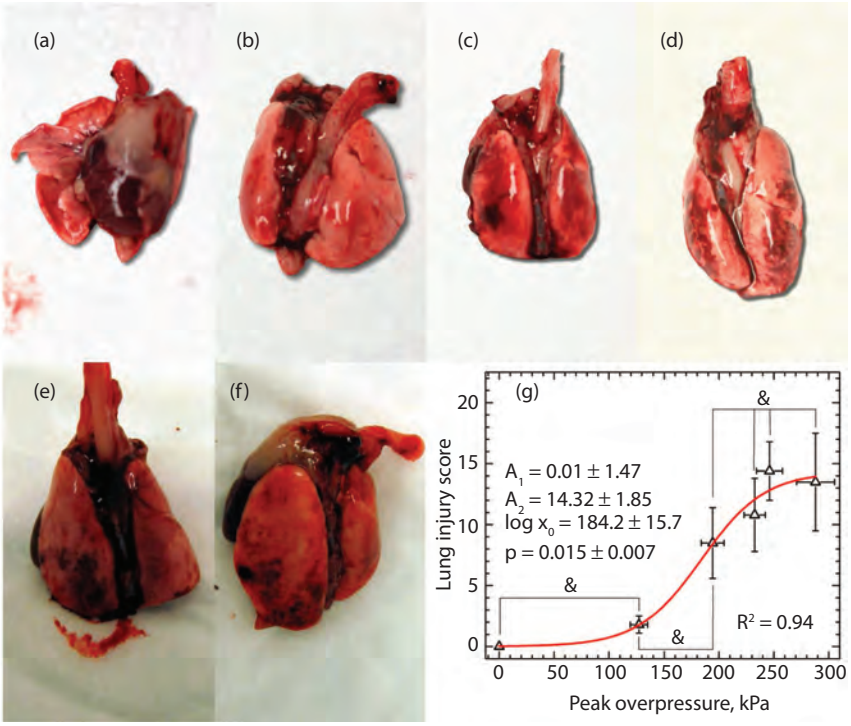


FIGURE 18.34 Blast-induced lung injury immediately postexposure: (a) Control, (b) 130 kPa, (c) 190 kPa, (d) 230 kPa, (e) 250 kPa, and (f) 290 kPa. The extent of injury was quantified using the Pathology Scoring System for Blast Injuries.36 The extent of injury is defined by the Elements of the IS according to equation 18.1 and was modeled with dose-response function (g). Groups with no statistically significant differences ($p > 0.05$) are marked with an ampersand. (From Skotak, M. et al., *Journal of Neurotrauma*. 30:1147–1160, 2013.) AQ3

18.3.2.4 BBB Damage and IgG Uptake by Neurons

Staining to reveal IgG in the brain parenchyma was performed for every twelfth section (each section was 40 μm thick) equally spaced across the entire rat brain (Figure 18.35). The purpose of this staining was twofold: (1) to measure the extent of BBB damage and (2) to visualize the accumulation of IgG in the intracellular space of neurons. Figure 18.35a presents coronal sections where elevated levels of IgG with respect to control samples are obvious. The slides with mounted sections were first digitized, and then we integrated the staining intensity to quantify of the amount of IgG. The olfactory bulb region (initial 12 sections, 5.76 mm from the brain anterior, see inset in Figure 18.35b) was omitted in this analysis. The optical density (OD) of each section was divided by average OD of three control samples resulting in relative OD (ROD). Figure 18.35b presents RODs of 40 sections as a function of section number for a single rat from the 190-kPa group. At lower blast intensities (190 and 230 kPa), in some rats the ROD had a higher value in the rostral than in the dorsal brain region (Figure 18.35). The ROD gradient was not a general pattern and typically the variations were not substantial. However, in one rat exposed at 250-kPa blast intensity, the highest RODs (2.3–2.7) are noted in slide numbers 28–35 (not shown). The RODs pertain to the same brain were averaged and expressed as average ROD. The results for rats exposed at three different blast intensities are presented in Figure 18.35c. At 190 kPa group, two rats have higher average ROD than the control group (average ROD > 1), but two others are comparable. Similar results are noted for the 230-kPa group, but only one rat had a higher average intensity of IgG staining than the rats in the 190-kPa group. The level of BBB damage appears to be correlated with the blast intensity (Figure 18.35c). In animals with compromised BBB, numerous IgG-positive cells of neuronal morphology were noted across brain parenchyma. The IgG accumulated predominantly in the cells localized in various parts of the cerebral cortex (Figure 18.36) and the hippocampus (Fig. 18.37). We have also evaluated brain sections of rats exposed to 190-, 230-, and 250-kPa blast intensity using amino cupric silver staining. These tests gave negative results, indicating 24 hours is insufficient period to induce neuro-degeneration.

18.4 COMPUTER MODELS

In this section, we describe the development of CT/magnetic resonance imaging (MRI)-based finite element model of human and rat heads. In addition, the computational framework for blast simulations is described.

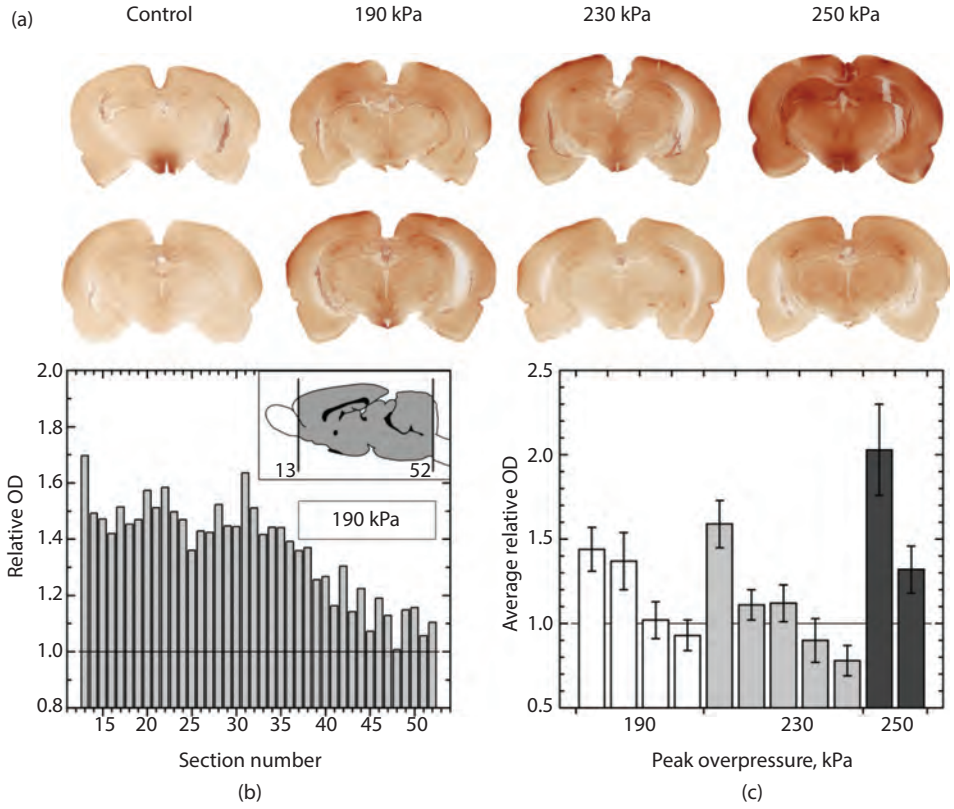


FIGURE 18.35 (a) Immunostaining for rat IgG as an indicator for a compromised BBB. (b) Relative OD of full coronal sections from the brain of a single rat exposed at 190 kPa. The OD of each section was divided by average OD of three controls (two naive and one sham). Inset illustrates brain region covered in this study. (c) Average relative OD of IgG across the brain parenchyma for rats exposed to primary blast and sacrificed 24 hours postexposure. Error bars are standard deviation. (From Skotak, M. et al., *Journal of Neurotrauma*. 30:1147–1160, 2013.)

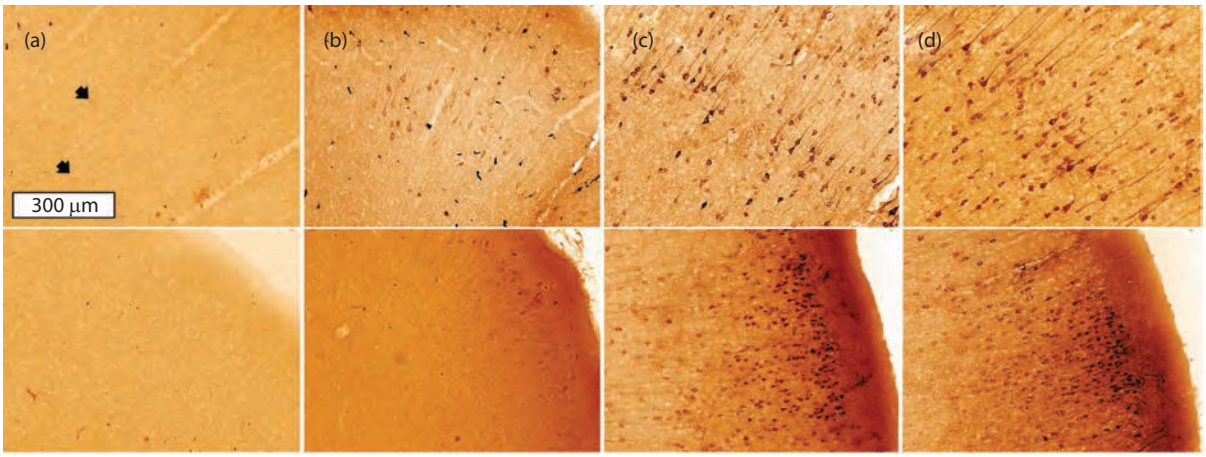


FIGURE 18.36 The IgG uptake in cortical neurons 24 hours after the blast. Coronal sections of the brain were collected from brains of sham control (a) and surviving rats exposed to blast with: (b) 190-kPa, (c) 230-kPa, and (d) 250-kPa peak overpressure. The scale bar (300 µm) is the same for all samples. Arrows indicate faintly stained neurons. (From Skotak, M. et al., *Journal of Neurotrauma*. 30:1147–1160, 2013.)

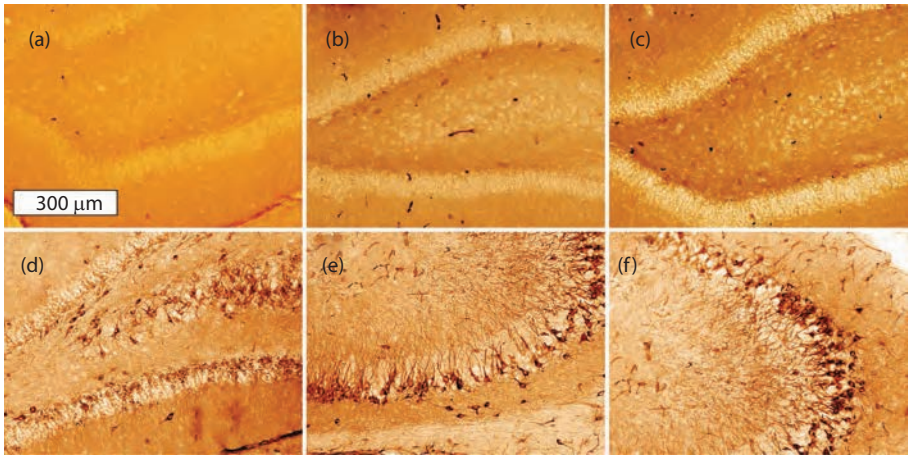


FIGURE 18.37 The IgG-positive cells in hippocampus of sham control (a) and in rats exposed to blast overpressure of 190 (b), 230 (c), and 250 kPa (d–f). The scale bar (300 µm) is the same for all samples. (From Skotak, M. et al., *Journal of Neurotrauma*. 30:1147–1160, 2013.)

18.4.1 Development of Human Head Model

The 3D human head model was generated from segmentation of high-resolution MRI data obtained from the Visible Human Project (2009). The MRI data consisted of 192 T1-weighted slices of 256 × 256 pixels taken at 1-mm intervals in a human male head. The image data are segmented into four different tissue types: (1) skin, (2) skull, (3) subarachnoid space (Sasser et al., 2006) and (4) brain (for which material properties are available). Brain included all important sections: frontal, parietal, temporal, and occipital lobes, cerebrum, cerebellum, corpus callosum, thalamus, midbrain, and brain stem. It was not possible to separately segment cerebrospinal fluid and structures such as membranes and bridging veins because of the resolution of the MRI data; as such, they are considered a part of the SAS. The segmentation uses 3D image analysis algorithms (voxel recognition algorithms) implemented in Avizo. The segmented 3D head model was imported into the meshing software HyperMesh and was meshed as a triangulated surface mesh. The volume mesh was generated from this surface mesh to generate 10-noded tetrahedrons. Tetrahedron meshing algorithms are more robust than hexahedral meshing algorithms and can model complex head volumes like brain and SAS faster and easier (Baker, 2005; Bourdin et al., 2007; Schneiders, 2000). The modified quadratic tetrahedral element (C3D10M) available in Abaqus is very robust and is as good as hexahedral elements (Abaqus user's manual) as far as accuracy of results is concerned (Cifuentes and Kalbag, 1992; Ramos and Simões, 2006; Wieding et al., 2012). In addition, hexahedral elements can suffer from the problem of volumetric locking for highly incompressible materials like brain. The problem of volumetric locking is not present for modified quadratic tetrahedral element (C3D10M) (Abaqus user's manual). For these reasons, we chose the modified quadratic tetrahedral element. The use of specialized 3D image processing (Avizo) and meshing software (HyperMesh) allowed for the development of a geometrically accurate finite element (FE) model. FE discretization is schematically shown in Figure 18.38.

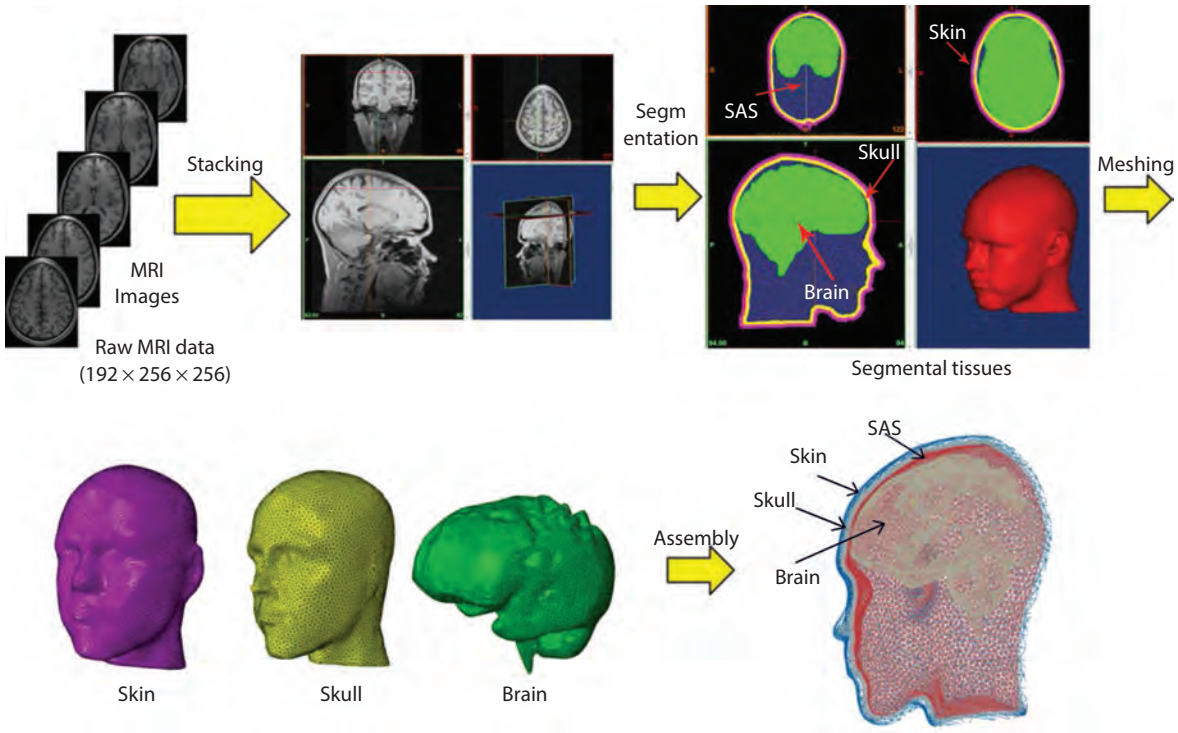


FIGURE 18.38 FE discretization.

18.4.2 Development of Animal Head Model

A very similar approach as described in the human head model was used for developing a 3D rat head model. For development of this model, MRI/CT of a Sprague-Dawley rat was used. Two different T2-weighted MRI scans (one for the muscle skin and other for the brain), and one CT scan (for the skull and the bones) were used. These three different scans were necessary to achieve proper contrast and segmentation of various tissues (i.e., muscle, skin, brain and skull, and bones). The brain MRI has an isotropic resolution of 256 × 256 × 256 pixels, for a field of view of 30 mm in all three directions. The MRI for muscle and skin has an anisotropic resolution, with a pixel size of 512 × 512 × 256, for a field of view of 30, 30, and 50 mm. The three data sets were overlapped, registered, segmented, and triangulated using software Avizo 6.2. The triangulated mesh (i.e., surface mesh) is imported into HyperMesh and a volume mesh is generated from this surface mesh to generate 10-noded tetrahedrons (C3D10M). The skull, skin, and brain share the node across the interface. These elements are treated as Lagrangian elements.

18.4.3 General Theory of Material Models and Material Parameters Used in the Head Models

In both human and animal models, skin and skull are modeled as linear, elastic, isotropic materials with properties adopted from the literature. Similarly, SAS in the human model is considered elastic. In general, elastic properties are sufficient to capture the wave propagation characteristics for these tissue types and this approach is consistent with other published works (Chafi et al., 2010; Chen and Ostoja-Starzewski, 2010; Grujicic et al., 2011; Moore et al., 2009; Moss et al., 2009; Nyein et al., 2010). For elastic material, stress is related to strain as:

$$\sigma_{ij} = \lambda E_{kk}\delta_{ij} + 2\mu E_{ij} \tag{18.3}$$

where σ is a Cauchy stress, E is a Green strain (also known as Green-Lagrange strain), λ and μ are Lame constants, and δ is a Kronecker delta.

The brain is modeled with an elastic volumetric response and viscoelastic shear response. Viscoelastic response is modeled using the Maxwell model. The associated Cauchy stress is computed through:

$$\sigma_{ij} = J^{-1}F_{ik} \cdot S_{km} \cdot F^{T}_{mj} \tag{18.4}$$

where F is a deformation gradient, J is a Jacobian, and S is the second Piola-Kirchhoff stress, which is estimated using following integral:

$$S_{ij} = \int_0^t G_{ijkl}(t-\tau)\frac{\partial E_{kl}}{\partial \tau}d\tau \tag{18.5}$$

where E is the Green strain and G_{ijkl} is the tensorial stress relaxation function. The relaxation modulus for an isotropic material can be represented using Prony series:

$$G(t) = G_\infty + \sum_{i=1}^{n} G_i e^{-\beta_i t} \tag{18.6}$$

where G_∞ is the long-term modulus and β is the decay constant.

18.4.3.1 Material Models for Human Head Model

For material parameters of the brain tissue, the widely accepted bulk modulus value of 2.19 GPa is used in this work. This value is motivated from the works of Stalnaker (Stalnaker, 1969) and McElhaney (McElhaney et al., 1973). The shear properties of the brain tissue are adopted from Zhang et al. (Zhang et al., 2001), who derived shear modulus from the experimental work of Shuck and Advani (Shuck and Advani, 1972) on human white and gray matter. For material parameters, we relied on widely accepted values in the literature for base simulations. In addition, parametric studies are conducted to account for reported variations in the brain material properties. The material properties of the human head model are summarized in Table 18.4.

18.4.3.2 Material Models for Rat Head Model

Skin and skull are modeled as a homogenous linear elastic isotropic material with properties adopted from the literature (Willinger et al., 1999). Brain tissue is modeled as elastic volumetric response and viscoelastic shear response with properties adopted from previous work (Zhang et al., 2001). Air is modeled as an ideal gas equation of state (EOS). The Mach number of the shock front calculated from our experiments is approximately 1.4 and hence the ideal gas EOS assumption is acceptable; the ratio of specific heats does not change drastically at this Mach number value. The material properties along with longitudinal wave speeds are summarized in Table 18.5.

18.4.4 Computational Framework for Blast Simulations

18.4.4.1 Numerical Approach for Shock Tube

In this section, a detailed description of the computational framework for blast simulations using the Euler-Lagrangian coupling method is discussed. In this method, an Eulerian mesh is used to model shock wave propagation inside the shock tube and a Lagrangian mesh for the head. This computational environment allows accurate concurrent simulations of the formation and propagation of blast wave in air, the fluid–structure interactions between the blast wave and the head models, and the stress wave propagation within the head. Computational framework is shown in Figure 18.39.

TABLE 18.4
Material Properties
(a) Elastic Material Properties

Tissue Type	Density (kg/m^3)	Young's Modulus (MPa)	Poisson's Ratio
Skin	1,200	16.7	0.42
Skull	1,710	5,370	0.19
SAS	1,000	10	0.49
Neck	2,500	354	0.3

(b) Viscoelastic Material Properties

	Instantaneous Shear Modulus (kPa)	Long-term Shear Modulus (kPa)	Decay Constant (sec^{-1})
Brain	41.0	7.8	700

TABLE 18.5
Material Properties for Rat Head
(a) Elastic Material Properties

Material	Young's Modulus (MPa)	Poisson's Ratio
Skin	8	0.42
Skull	100	0.3
Brain	0.123	0.49

(b) Viscoelastic Material Properties

Material	Instantaneous Shear Modulus (kPa)	Long-term Shear Modulus (kPa)	Decay Constants^{-1}
Brain	41	7.8	700

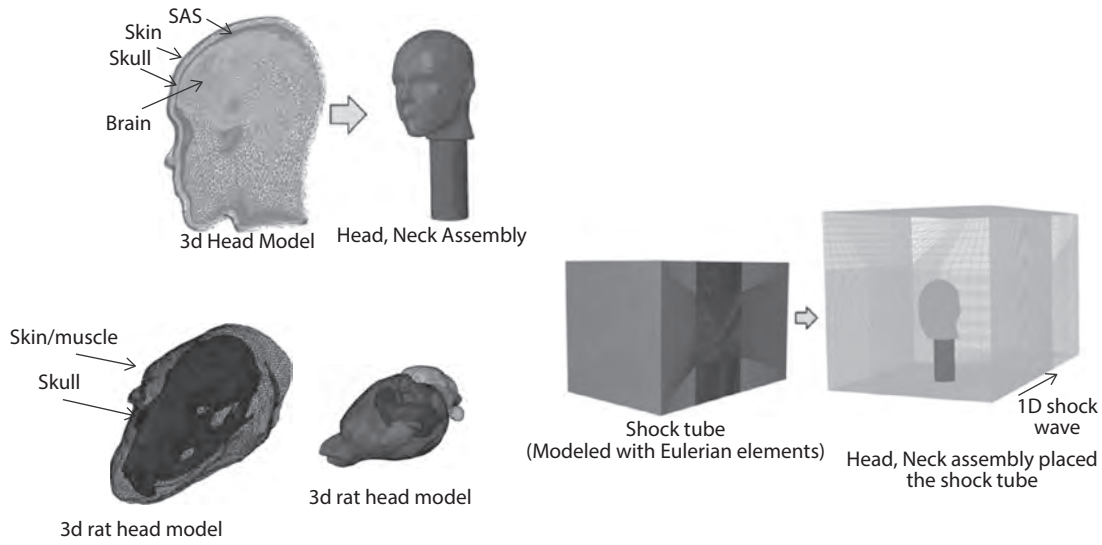


FIGURE 18.39 Computational framework for blast simulations.

The shock tube used in the modeling is based on our experimental shock tube. The head is placed inside the shock tube and subjected to blast wave profile of interest. The Eulerian domain (air inside the shock tube) is meshed with eight-noded brick elements, with appropriate mesh refinement near the regions of solid bodies to capture fluid–structure interaction effects. Parametric studies on mesh size have been performed and it has been found that mesh size of 3 mm is appropriate to capture flow field around the head (i.e., pressures, velocities) and fluid–structure interaction effects. For Eulerian elements, mesh convergence is achieved at this element size; thus element size of 3 mm is used near the regions of solid bodies and along the direction of blast wave propagation. Air is modeled as an ideal gas EOS (see equation 18.7) with following parameters: density, 1.1607 kg/m^3; gas constant, 287.05 J/(kg-K); and temperature 27°C.

$$P = (\gamma - 1)\frac{\rho}{\rho_0}e \tag{18.7}$$

Where P is the pressure, γ is the constant-pressure to constant-volume specific heat ratio (= 1.4 for air), ρ_0 is the initial air mass density, ρ is the current mass density, and e is the internal volumetric energy density. The Mach number of the shock front from our experiments is approximately 1.4, and hence the ideal gas EOS assumption is acceptable because the ratio of specific heats do not change drastically at this Mach number.

18.4.4.2 Loading, Interface, and Boundary Conditions

To numerically reproduce primary blast loading, there are two possible techniques to impose the boundary conditions: Technique 1 models the entire shock tube, in which driver, transition, and extension sections are included in the model so that events of burst, expansion, and development of a planar of the blast wave are reproduced. Technique 2 is a partial model with experimentally measured (*p-t*) history is used as the pressure boundary condition, where the numerical model comprises the downstream flow field containing the test specimen. Technique 1 is computationally very expensive. For example, a full scale simulation of 711 mm × 711 mm cross section, 9,880 mm long shock tube (excluding catch tank) with cylindrical to square transition requires about 5 million eight-noded brick Eulerian elements and takes about 147 CPU hours on a dedicated 48 processors. These simulations reach the limits of computing power in terms of memory and simulation time. On the other hand, technique 2 requires about 1.26 million elements with 10 CPU hours. The pressure, velocity and temperature profiles obtained using technique 2 match well with the profiles that are obtained using full-scale model (technique 1) at the boundary and downstream locations. Hence technique 2 is capable of capturing the pressure, momentum, and energy of the shock wave. An approach similar to technique 2 has been widely used in shock dynamics studies using shock tubes (Honma et al., 2003; Jiang et al., 2003; Kashimura et al., 2000).

The velocity perpendicular to each face of Eulerian domain (shock tube) is kept at zero to avoid escaping/leaking of air through these faces. This will maintain a planar shock front traveling in the longitudinal direction with no lateral flow. The bottom of the neck is constrained in all six degrees of freedom to avoid rigid body motion. An enhanced immersed boundary method is used to provide the coupling between the Eulerian and the Lagrangian domains. Here, the Lagrangian region resides fully or partially within the Eulerian region and provides *no-flow* boundary conditions to the fluid in the direction normal to the local surface. Further, the Eulerian region provides the pressure boundary conditions to the Lagrangian region. Thus, a combination of fixed Eulerian mesh and solid–fluid interface modeling through the enhanced immersed boundary method allows for the concurrent simulations of the formation and propagation of a primary blast wave in a fluid medium and accounts for the effects of both fluid–structure interaction and structural deformations once the blast wave encounters a solid. The

interactions (contact conditions) between Eulerian (containing air and a propagating blast wave) and Lagrangian regions are defined using "general contact" feature (card) in Abaqus. In general contact, contact constraints are enforced through the penalty method with finite sliding contact formulation. Various contact property models are available in general contact. In the present work, frictionless tangential sliding with hard contact is used as contact property model.

18.4.5 Solution Scheme

The finite element model is solved using the nonlinear transient dynamic procedure with the Euler-Lagrangian coupling method (Abaqus). In this procedure, the governing partial differential equations for the conservation of momentum, mass and energy (equations 18.8 through 18.10) along with the material constitutive equations (equations 18.3 through 18.6) and the equations defining the initial and boundary conditions are solved simultaneously.

Conservation of mass (continuity equation):

$$\rho\frac{\partial v_i}{\partial x_i}+\frac{\partial \rho}{\partial t}+v\bullet\nabla\rho=0 \tag{18.8}$$

Conservation of momentum (equation of motion):

$$\frac{\partial \sigma_{ij}}{\partial x_j}+\rho b_i=\rho a_i \tag{18.9}$$

Conservation of energy (energy equation):

$$\rho\frac{\partial e}{\partial t}+v\bullet\nabla e=\sigma_{ij}\frac{\partial v_i}{\partial x_j}-\frac{\partial q_i}{\partial x_i}+\rho q_S \tag{18.10}$$

where ρ is a density; x, v, and a are displacement, velocity, and acceleration of a particle, respectively; σ is a Cauchy stress; b is a body force; e is an internal energy per unit mass; q is a heat flow per unit area; and q_S is a rate of heat input per unit mass by external sources.

In the Eulerian-Lagrangian method, we are actually solving the whole model (i.e., both the Eulerian and Lagrangian domains) with the same Lagrangian equations. The notion of a material (solid or fluid) is introduced when specific constitutive assumptions are made. The choice of a constitutive law for a solid or a fluid reduces the equation of motion appropriately (e.g., compressible Navier-Stokes equation, Euler equations). For the Eulerian part/domain in the model, the results are simply mapped back to the original mesh with extensions to allow multiple materials and to support the Eulerian transport phase for Eulerian elements. Eulerian framework allows for the modeling of highly dynamic events (e.g., shock) which would otherwise induce heavy mesh distortion. In Abaqus, the Eulerian time incrementation algorithm is based on an operator split of the governing equations, resulting in a traditional Lagrangian phase followed by an Eulerian, or transport phase. This formulation is known as "Lagrange-plus-remap." During the Lagrangian phase of the time increment, nodes are assumed to be temporarily fixed within the material, and elements deform with the material. During the Eulerian phase of the time increment, deformation is suspended, elements with significant deformation are automatically remeshed, and the corresponding material flow between neighboring elements is computed. As material flows through an Eulerian mesh, state variables are transferred between elements by advection. Second-order advection is used in the current analysis. The Lagrangian (solid) body can be a deformable body and can deform based on the forces acting on it and the deformation of the Lagrangian solid influences the Eulerian part/domain.

A typical 3D simulation requires about 7 hours of CPU time on 48 dedicated Opteron parallel processors (processor speed 2.2 GHz, 2 GB memory per processor), for an integration time of 2.5 msec. The simulation time is selected such that the peaks resulting from stress wave action have been established. A time step of the order of 5×10^{-7} seconds is used to resolve and capture wave disturbances of the order of 1 MHz, which increases the overall computational effort for the total simulation time of interest.

18.4.6 Model Validations

In this section, both human and animal models will be validated against the experimental blast results. This is a necessary step in developing a finite element model to show that the model mimics the reality to as close as possible.

18.4.6.1 Validation of the MRI-Based Human Head Model Against Blast Experiments

The head model is validated against PMHS experiments, which were previously discussed in this chapter. PMHS specimens (N = 3) were subjected to primary blast of incident intensities 70, 140, and 200 kPa, respectively. The numerical model is validated against surface (reflected) pressures, surface/skull strains and ICPs obtained from these experiments. In the PMHS experiments, dura, subarachnoidal spaces and brain were removed and intracranial contents were backfilled with ballistic gel whose wave speed is calculated at 1,583 ± 118 m/s, which was close to the longitudinal wave speed of water. Thus for head model validation purposes only, SAS and brain were assigned same bulk modulus value of 2.19 GPa. The validation results are presented for incident intensity of 200 kPa, but similar agreement in the simulation and experimental results are seen for other intensities. The arrival time of the experiment at each sensor location is shifted to match the arrival time of the numerical simulation for ease of comparison of the different features of the *p-t* profile. The experimental profiles are based on average of three shots (experiments) for head 1.

Figure 18.40a shows a comparison of the surface pressure profile for front location. For front location (i.e., FH SM), good agreement is seen between the experiment and the simulation both in terms of peak pressure and nonlinear decay. Figure 18.40b shows the comparison of ICP profiles between the experiment and the simulation. Both experimental and simulation

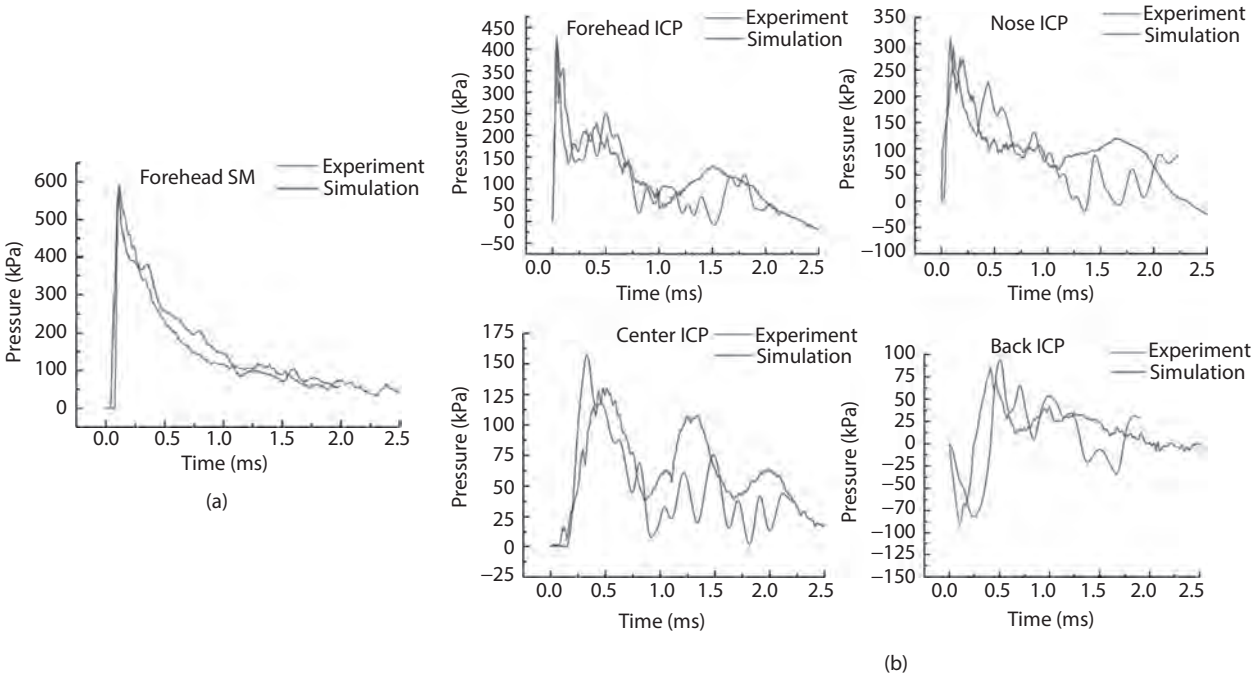


FIGURE 18.40 (a) Comparison of surface pressure profile between experiment and simulation for FH location. (b) Comparison of ICP profiles between experiment and simulation.

data are filtered using a 10-kHz four-pole Butterworth filter. From the figure, it can be seen that there is a reasonably good agreement between the experiment and numerical ICP profiles both in terms of peak values (maximum% difference in peak ICP value is 17%) and shape of the profiles. In general, simulation ICP profiles show more oscillatory behavior than experimental ICP profiles. This can be attributed to following: (1) lack of material characterization for ballistic gel. It is possible that the response of ballistic gel to shock loading is much more complex (because of heterogeneity, rate dependent behavior, effect of curing, wave propagation, and dispersion in 3D setting) than assumed here and (2) frequency response of ICP pressure probes (gauges) embedded in the ballistic gel is not known; it is possible that frequency response of the gauge is slower because of which behavior is less oscillatory in the experiments. Because of these artifacts, discrepancies in the oscillatory pattern are to be expected between the simulation and the experiment. It is also common that the repeated experiments will show small variations in the oscillatory pulse patterns from shot to shot. For these reasons, it is improbable if not impossible to match every aspect of experiment with the computational simulation. With these considerations in mind, some aspects of comparison between experimental and simulation ICP profiles are discussed.

For FH ICP, simulation is able to capture major trends including initial sharp rise (rise time = 40 μs) associated with the shock front, initial decay (till t = 0.15 msec), abrupt pressure increase (second peak) during initial decay (at t = 0.07 msec) and subsequent pressure pattern. Secondary (loading) pulse seen in the experiment after 1.0 ms is not seen in the simulation profile for FH ICP. For nose ICP, fair agreement is seen between the experiment and the simulation. The distinct secondary peak seen during the decay (at t = 0.25 msec) is delayed in the simulation. This secondary peak is due to wave transmission from the eye socket. The delay in this transmission between simulation and experiment is attributed to difference in geometry of the eye socket between the simulation and the experiments. Center ICP also shows fair agreement between the simulation and experiment. The rise time is shaper in the simulation than the experiments. In addition peak ICP value is slightly higher (20% difference) in the simulation. These discrepancies are expected considering complex set of direct and indirect loadings experienced by the center location. The center location experiences complex set of direct and indirect loadings emanating from different sources (e.g., blast wave transmission, reflections from tissue interfaces, skull deformation) at different points of time. These disturbances continuously propagate into the brain as waves. Constructive and deconstructive interferences of these waves control the pressure history deep inside the brain. We believe the obtained match between experiment and simulation for center ICP is reasonable considering these complexities. Back ICP also shows reasonably good agreement between experiment and simulation. The contrecoup phase seen in the experiments is replicated in the simulation.

During PMHS experiments (circumferential) skull strains were also measured at four locations front, temple, top, and back as shown in figure. Table 18.6 compares the peak skull strains obtained from the simulation with that of experimentally measured skull strains at various locations. The maximum peak strain is seen at front location and the strain value at this location is less than 0.1%. It should be noted that the standard deviations in experimentally obtained skull strain values are huge. Standard deviations up to 100% of mean values are seen certain strain measurements. Such standard deviations are normal during strain measurements, especially when strain values are very small. Obtained strain values

TABLE 18.6
Comparison of Peak Circumferential Strains at Various Skull Locations

	Peak Strain (%)	
Location	**Experiment (Mean ± S.D.)**	**Simulation**
Front (compressive)	0.09 ± 0.04	0.06
Front (tensile)	0.01 ± 0.01	0.018
Right temple (compressive)	0.04 ± 0.03	0.045
Right temple (tensile)	0.04 ± 0.02	0.028
Top (compressive)	0.04 ± 0.03	0.042
Top (tensile)	0.035 ± 0.02	0.02
Back (compressive)	0.04 ± 0.02	0.03
Back (tensile)	0.02 ± 0.02	0.03

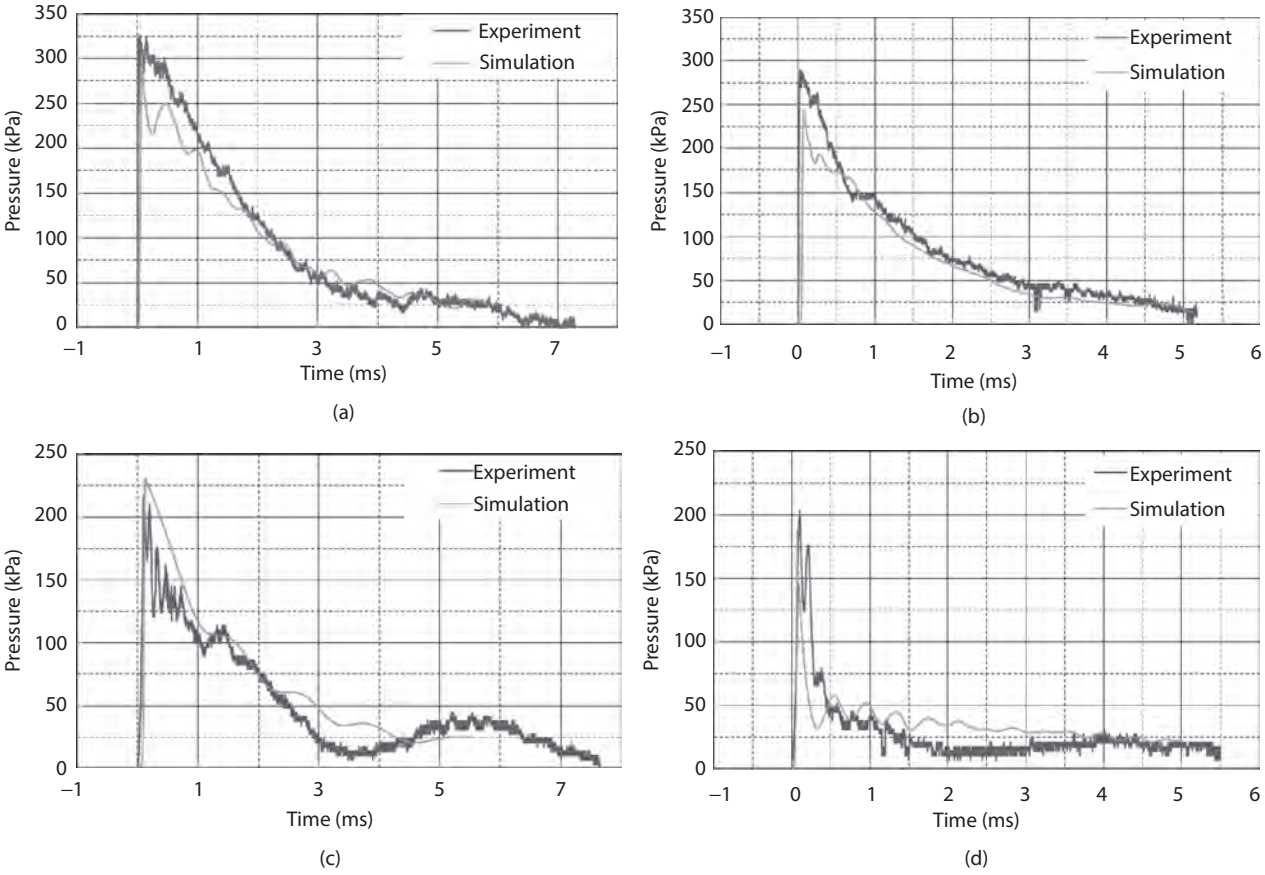


FIGURE 18.41 Comparison between experiments and numerical models both inside and outside the shock tube. (a) Surface pressure measured on the nose. (b) Surface pressure measured on the nose. (c) ICP inside the brain. (d) ICP inside the brain. (From Sundaramurthy, A. et al. 2012. *Journal of Neurotrauma*. 29:2352, 2012.)

from the simulations fall within the range of experimentally obtained strain values. The experimental and numerical strain–time profiles are not compared, as the obtained profiles were not highly repeatable during the experiments.

18.4.6.2 Validation of the MRI-Based Rat Head Model Against Blast Experiments

The rat head model is validated against rat head experiments, which was previously discussed. In this experiment, five male Sprague-Dawley rats of 320–360 g weight were sacrificed and instrumented with a pressure sensor on the nose to measure reflected pressure, and two additional sensors were implanted in thoracic cavity and brain, respectively. To test the robustness of the model it was validated against experiments both inside and outside of the shock tube. Input loading is simulated using partial model technique in the Loading, Interface, and Boundary Conditions section.

Figure 18.41a, b shows comparisons of *p-t* profiles for the surface mount sensor on the nose inside and outside of the shock tube, respectively. Overpressure and the subsequent decay recorded within 1 msec is slightly lower in the case of simulation in the simulation is slightly lower than that of the overpressure recorded in the experiment. Beyond 1ms there is an almost perfect match between experiment and simulation.

This deviation in the initial part of the pressure profile is due to a coarse Eulerian mesh relative to the size of the Lagrangian body (rat head). Tradeoff was made to get reasonably accurate results for higher model efficiency (time for model simulation) and this did not affect the intracranial measurement drastically which will be seen in the following section.

Figure 18.41c, d show the ICP comparisons between experiment and simulation for inside and outside respectively. There is a good agreement between experiment and simulation. Both experimental and simulation data are filtered using a 10-kHz four-pole Butterworth filter. In general, the simulation inside has a less oscillations while outside has more oscillations after 0.5 msec. This model also predicts the effect of exit rarefaction depleting a overpressure and resulting in a low-pressure, high-velocity wind (after 0.5 msec)

18.5 MECHANICS OF BLAST WAVE–HUMAN HEAD INTERACTIONS WITH HELMETS

18.5.1 Flow Field on the Surface of the Head with the Helmet

Figure 18.42 shows the pressure-time history on the surface of the head with and without the helmets. In general, rise time and time to peak is increased and rate of pressure decay is decreased with the helmet. Peak pressures are reduced with the padded helmet at all locations compared with no helmet case. For the suspension helmet, peak pressure is reduced at the incident blast site (sensor FH); on the contrary, peak pressures are increased on the side away from the incident blast side compared with no helmet case. The positive phase impulse either remained equivalent or increased with the suspension and padded helmets as time to peak is increased and rate of pressure decay is decreased with the helmets.

18.5.2 Comparison of Experiments and Numerical Simulations for Helmeted Cases

Numerical simulations are used to understand mechanics of flow field around the head with the helmet. Before using the numerical simulations for this purpose, numerical results are compared and validated against helmeted experiments. Figure 18.43a, b shows a comparison of surface pressures on the surrogate head with suspension and padded helmet, respectively. For the suspension helmet, there is a reasonably good agreement between the experiment and numerical simulation, in terms of peak pressures (maximum difference 26%, minimum difference 0.3%) and nonlinear decay. The simulation is able

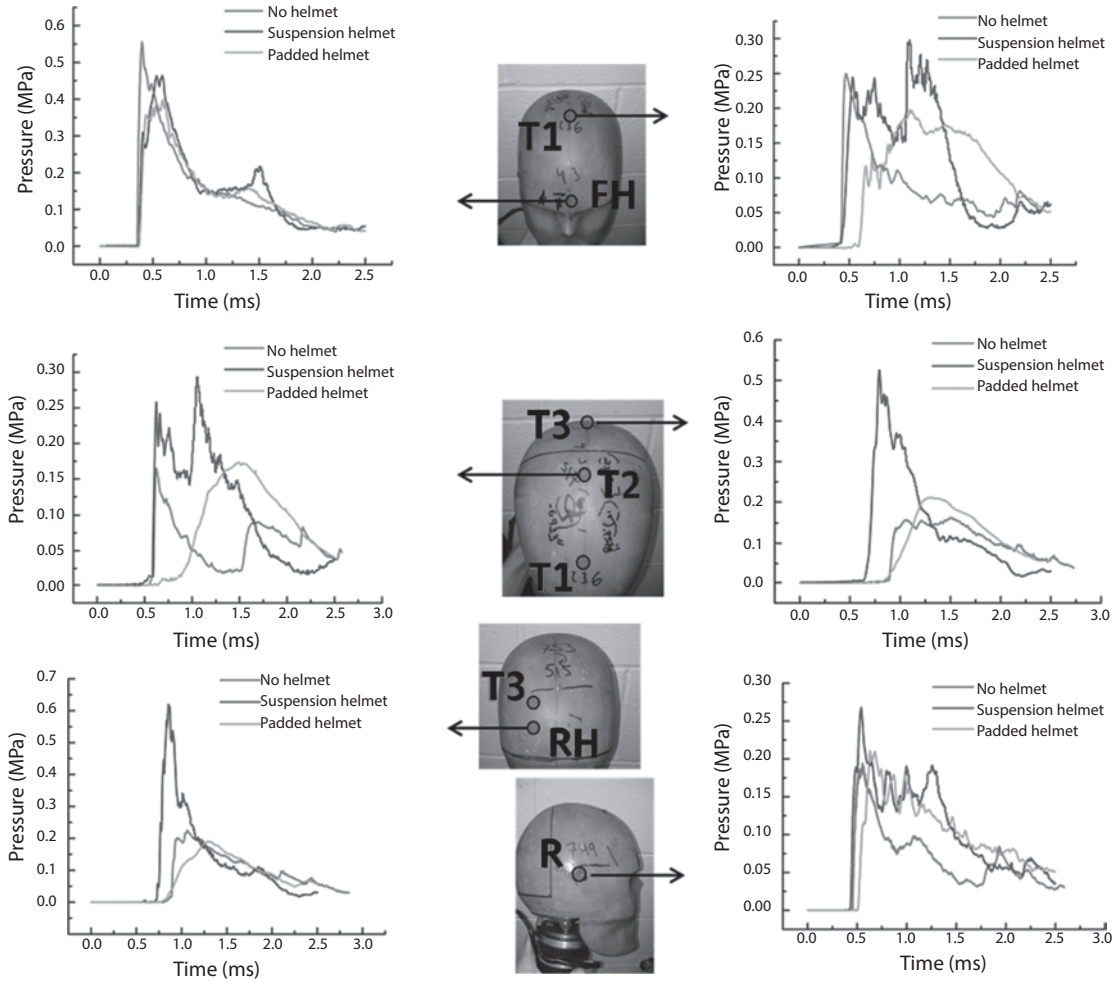


FIGURE 18.42 Pressure-time history on the surface of the head with and without the helmets.

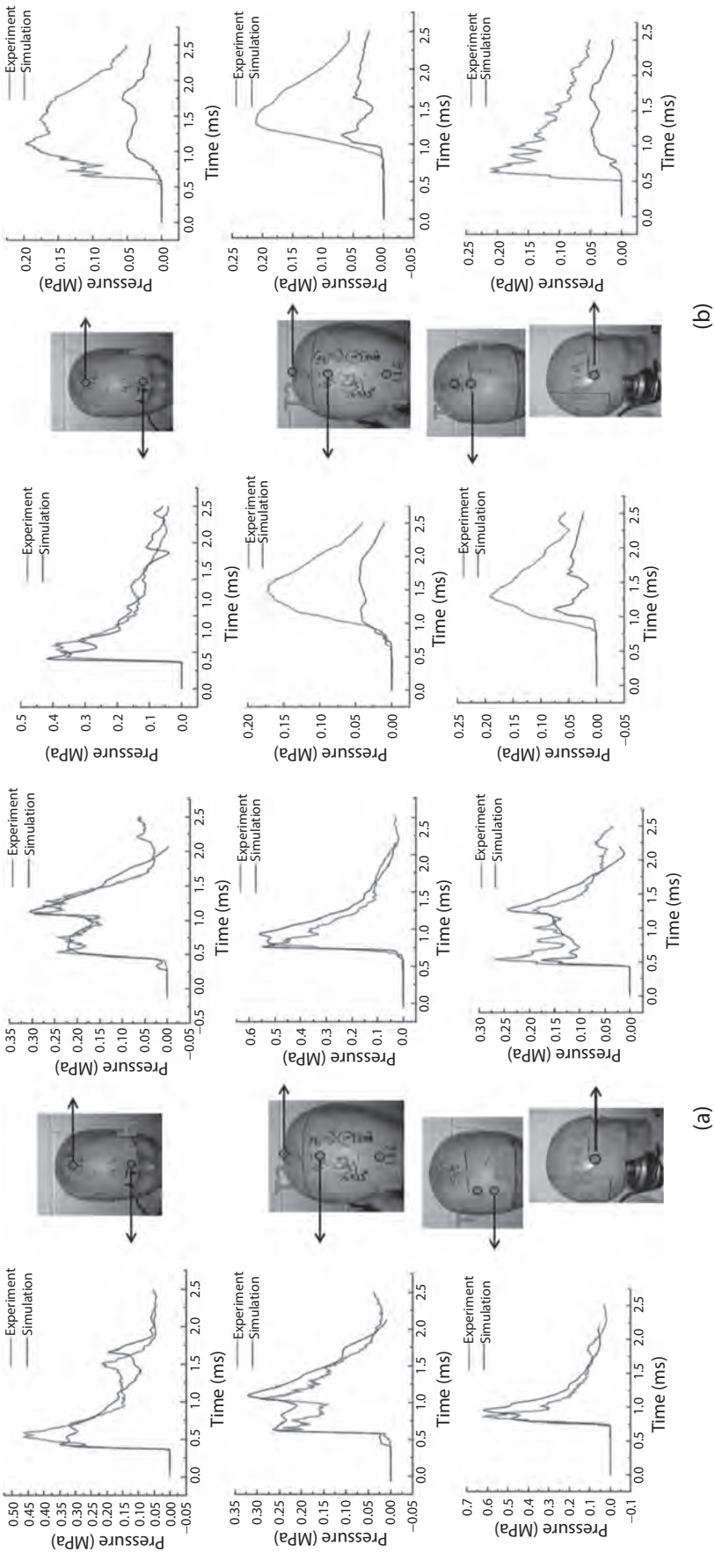


FIGURE 18.43 Comparison of surface pressures from experiments and numerical simulations on the RED head with (a) suspension and (b) padded helmet respectively.

AQ5

to capture majority of the features well, including the arrival of blast wave at a given location, shock front rise time, and underwash (explained in detail in the next section) beneath the helmet. For the padded helmet, fair agreement is obtained between the experiment and simulation. The huge difference is seen in the values of peak pressure and total impulse. This is because it is very difficult if not impossible to know precise placement of padded helmet on the surrogate head in the experiments. Blast wave can enter through small gaps, if any, during the mounting of padded helmet on the surrogate head. In addition, porosity of the foam pads is not modeled in the simulations, which may contribute to the surface pressures.

18.5.3 Underwash Effect of the Helmet

As indicated in previous sections, surface pressures are increased under the suspension helmet on the side away from incident blast side. This is due to the underwash effect of the helmet. This effect is illustrated using numerical simulations (Figure 18.44). The blast front after encountering the head–helmet assembly divides into two fronts: one front travels around the outer perimeter of the helmet whereas the other front penetrates the gap between the head and the helmet (i.e., head–helmet subspace) and travels underneath the helmet toward the back of the head as shown in the Figure 18.44a. The blast front traveling outside the helmet reaches the rear of the helmet before the blast front traversing through the gap (Figure 18.44b-i), and eventually when these two blast fronts meet they focus at a region on the back side of the head (Figure 18.44b-ii). This focusing produces higher pressures on the head, away from the incident blast side when the location is shielded by the helmet. After this high pressure is generated, the high pressure air in the head-helmet subspace expands in all the directions (Figure 18.44b-iii).

To understand how the underwash influences both the local peak pressure and the impulse, it is postulated that the pressure intensification depends on the shape of the helmet (curvature) and the head–helmet subspace gap size with respect to the oncoming pressure wave and its characteristics (e.g., pressure, velocity, rise/fall time). These aspects are studied in the following section using simplified two-dimensional head models. It should be noted that local peak pressures in the head-helmet subspace and impulse transmitted to the head are analyzed because these quantities determine the effective load on the head.

18.5.3.1 Effect of Curvature, Head–Helmet Gap Size, and Incident Peak Pressure Intensity

To examine the effect of geometry, three different cases are considered. In the first case, the head and the helmet are modeled as cylinders, in the second case the head is cylindrical and the helmet flat, and in the third case both the helmet and the head are flat (Figure 18.45a). In all these cases, there is constant gap of 13 mm between the helmet and the head. Figure 18.45b-i and b-ii shows the pressure and impulse profiles at the back of the head–helmet subspace where the

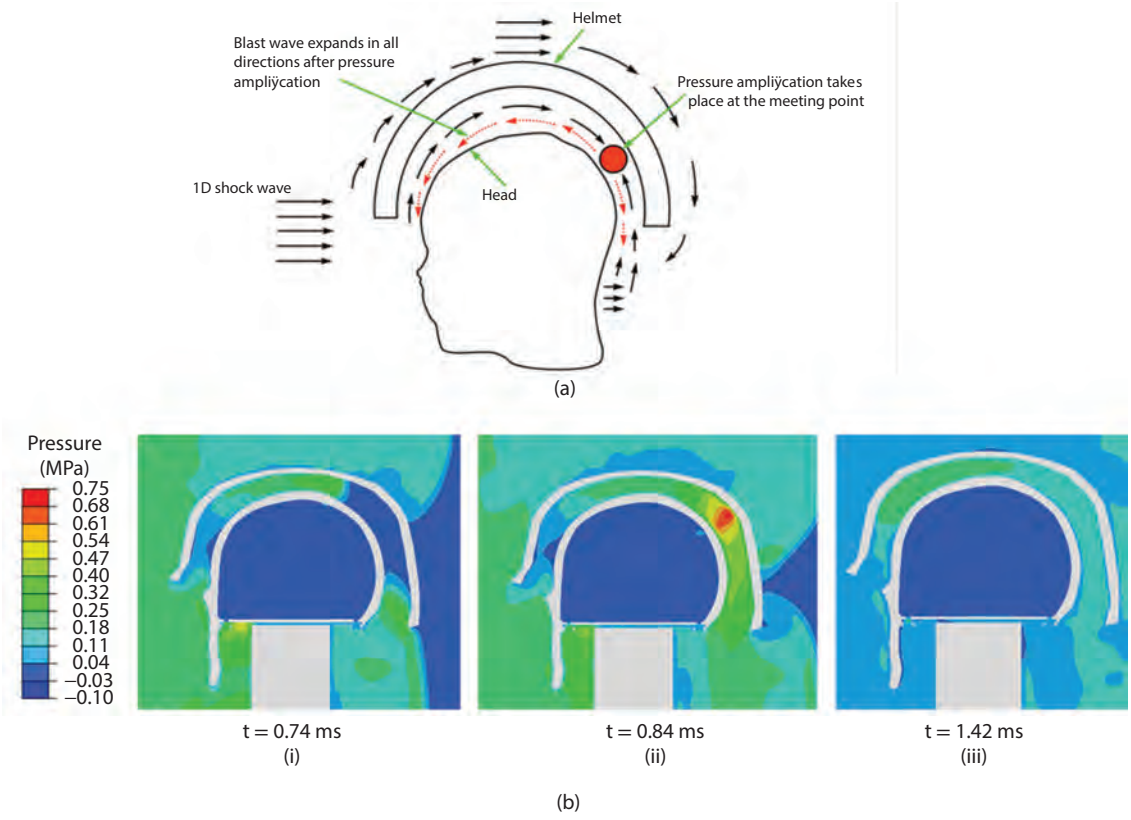


FIGURE 18.44 Underwash effect of the suspension helmet: (a) schematic explaining underwash effect of the helmet; (b) flow field inside and outside of the head–helmet subspace.

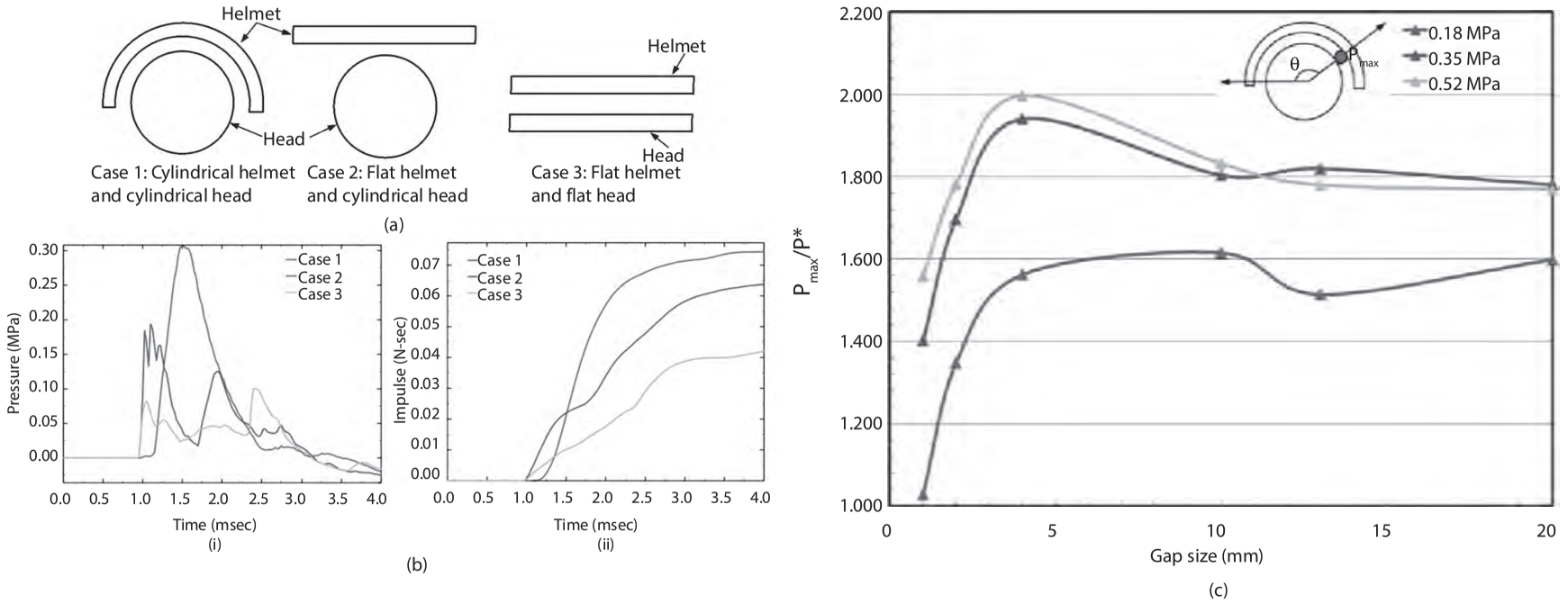


FIGURE 18.45 Effect of curvature of the helmet and the head. (a) Modeling setup for studying curvature effect of the helmet and the head. (b-i) Average pressure in the back region of the head–helmet subspace and (ii) total impulse transmitted to the back region of the head. Incident blast intensity 0.52 Mpa. (c) Normalized maximum peak overpressure in the head–helmet subspace (P_{max}/P^*) as a function of gap size for different incident blast intensities P*. (From Ganpule, S. et al., *Computer Methods in Biomechanics and Biomedical Engineering.* 15:1233–1244, 2011.)

focusing occurs. It is clear from Figure 18.45b that the pressure and impulse are increased when both the shapes are cylindrical in comparison with the other two cases. This trend is the same when the incident overpressure is increased from 0.18 MPa to 0.52 MPa.

Having identified that the cylindrical case offers the most severe loading conditions, this case is used to study the effect of head–helmet gap size and incident peak pressure intensity on the underwash. Figure 18.45c shows the P_{max}/P^* (normalized peak maximum overpressure) in the head–helmet subspace as a function of gap size for different incident peak pressure intensities P*. As the gap is reduced, pressure in the gap increases ($P \alpha 1/V$, V-volume). Thus, the P_{max}/P^* ratio increases as the gap size is reduced until a certain critical gap size. Thereafter, the boundary effects become dominant and P_{max}/P^* ratio decreases because of these boundary effects. The P_{max}/P^* ratio increases as incident peak pressure intensity P* increases. Numerical simulations indicate for the ranges tested, the angle θ at which P_{max} occurs is between 140 and 155°.

Another quantity of interest is the transmitted impulse, *I*, and depends on the maximum peak pressure, P_{max} and rate of pressure decay (i.e., rate of expansion) once P_{max} is established. The higher the P_{max} and lower the rate of pressure decay, the higher is the impulse transmitted. As shown earlier, the P_{max} increases as the gap size is reduced until a critical gap size. The rate of pressure decay, however, decreases continuously (no critical gap size) as the gap size is decreased as shown in Figure 18.46a. This is because as the gap size is reduced, there is not enough space for expansion and boundary reflection effects become dominant. Similar observations are reported by Rafaels et al. (2010) from their blast experiments on a helmeted head. From our simulations it was found that, for a given incident peak pressure intensity P*, rate of pressure decay contributes more to impulse transmitted to the head than P_{max}. Hence, for a given incident peak pressure intensity P*, impulse transmitted to the head continuously increases as the gap size is reduced as shown in Figure 18.46b.

18.5.4 Effect of Orientation on Blast Wave–Head Interactions With and Without Head Protection

As mentioned earlier, to study the effect of orientation on blast wave–head interactions experiments were conducted on the surrogate head with four different orientations to the blast. These orientations are: front, back, side, and 45°. The experiments are conducted with and without the helmets and each scenario was repeated three times. Blast wave–head interactions are studied by monitoring surface pressures on the surrogate head and experimental observations are elucidated with the help of validated numerical models. Role of the head orientations is studied by understanding the mechanics of the blast wave head interactions for no helmet, suspension helmet, and padded helmet cases.

18.5.4.1 No Helmet Case

Figure 18.47a shows the experimentally measured peak pressures for the no helmet case for each head orientation. Pressure at the incident blast site is amplified ($\Lambda = p_R / p_I$) by 2.40, 2.79, 2.38, and 1.39 times the incident pressure for front, back, side, and 45° orientations, respectively, because of aerodynamic effects. This amplification factor (Λ) is based on the mean values of the incident and reflected pressures for each orientation.

For front orientation, pressure gradually decreases from sensor FH to T1 to T2. Sensors T2 and T3 record equivalent pressures. There is a slight increase in pressure from sensor T3 to sensor RH, which is located on the side opposite to the incident blast side. A similar trend is observed for back orientation but in reverse order (i.e., from sensor RH to sensor FH). For these orientations, sensor R records pressure equivalent (within ±2%) to sensor T2. For side orientation, sensor R (i.e., the sensor facing the blast) records the highest pressure; and all sensors in the midsagittal plane record equivalent pressures. Sensor L (i.e. the sensor opposite to the blast side) records marginal pressure. For the 45° orientation,

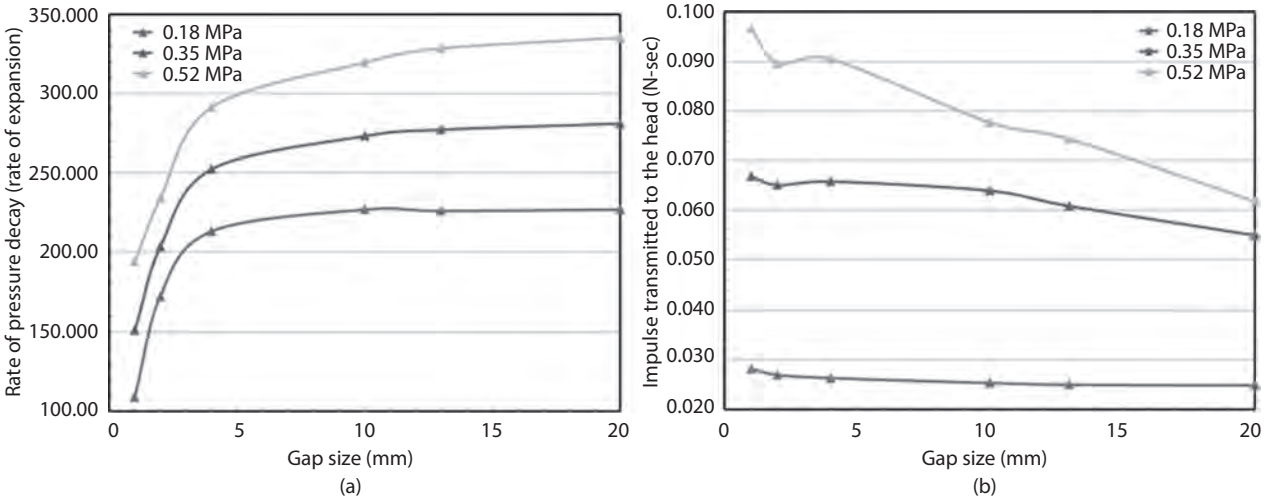


FIGURE 18.46 (a) Rate of pressure decay in head–helmet subspace. (b) Impulse transmitted to the head as a function of gap size for different incident blast intensities P*. (From Skotak, M. et al., *Journal of Neurotrauma*. 30:1147–1160, 2013.)

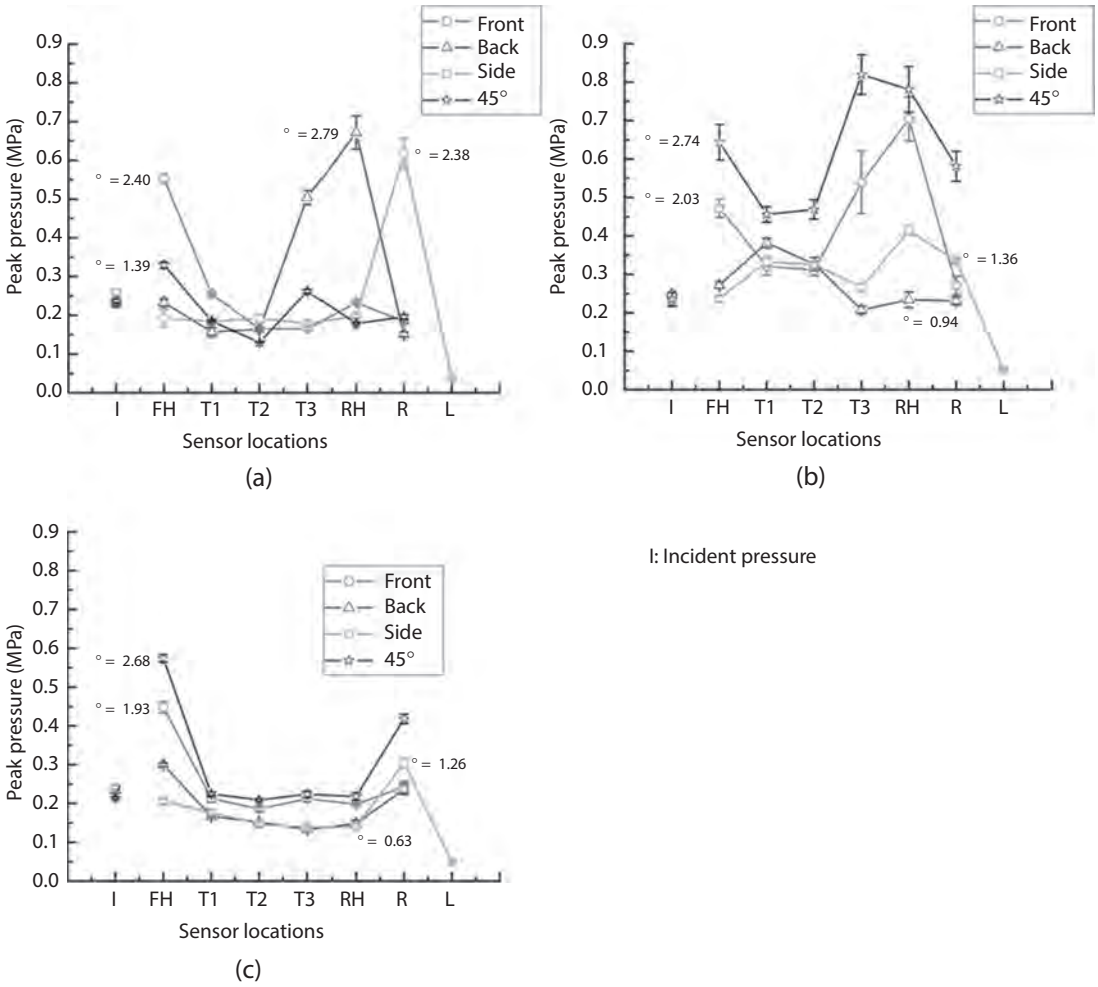


FIGURE 18.47 Peak pressures recorded by the sensors for various orientations: (a) no helmet, (b) suspension helmet, and (c) padded helmet. (Experiment).

trend similar to the front orientation is observed, but the flow reunion takes place near sensor T3 (as indicated by increase in pressure) because of tilt.

18.5.4.2 Suspension Helmet Case

Figure 18.47b shows experimentally measured peak pressures for the suspension helmet case for each head orientation. With the suspension helmet, pressure at the incident blast site is amplified by 2.03, 0.94, 1.36, and 2.74 times the incident pressure for front, back, side, and 45° orientations respectively. The pressure field around the head is complex and does not follow any fixed pattern of variation. In general, pressures are increased on the side away from the incident blast side.

18.5.4.3 Padded Helmet Case

Figure 18.47c shows experimentally measured peak pressures for the padded helmet case for each head orientation. With the padded helmet, pressure at the incident blast site is amplified by 1.93, 0.63, 1.26, and 2.68 times the incident pressure for front, back, side, and 45° orientations respectively. Sensors FH and R record higher pressures compared with the other sensors irrespective of the orientation because these sensors are not fully covered by the foam pads. All other sensors record equivalent pressures for a given orientation.

18.5.5 Total Impulse Around the Head for Various Head–Helmet Configurations

Total impulse (positive phase, I^+) is obtained by integrating pressure over time ($\int P\,dt$). Total impulse shows similar trends as peak surface pressures for all head helmet configurations and for all orientations. Total impulse plots are not shown for brevity.

18.5.6 Results from Numerical Simulations

Numerical simulations are conducted to understand and explain some of the experimental observations. Figure 18.48 shows the flow (pressure) field around the head for various head orientations for no helmet case. The flow field around the head is complex. Orientation of the head to the blast wave governs the flow mechanics around the head.

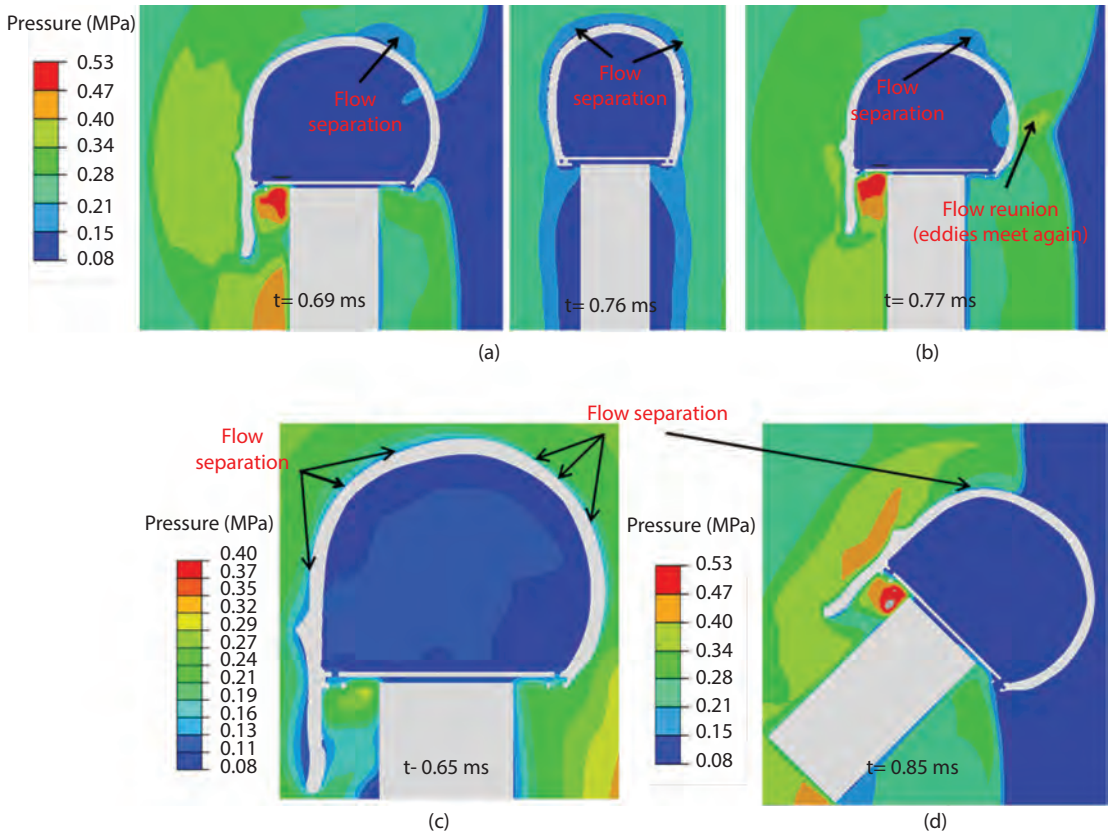


FIGURE 18.48 Flow mechanics around the head. (a) Flow separation on the top and sides of the head for front orientation. (b) Flow reunion on the back of the head for front orientation. (c) Flow separation along the midsagittal plane for side orientation. (d) Flow separation near the face for 45° orientation.

Figure 18.49 shows the pressure field in helmet–head subspace (at incident blast site) for each orientation for suspension helmet case. Least pressures in the helmet–head subspace at incident blast site are observed for back orientation.

Figure 18.50 shows pressure field in the head helmet subspace (away from incident blast site) for each orientation for suspension helmet case. From the pressure field it can be seen that pressures are increased under the suspension helmet on the side away from the incident blast side. This also confirms the presence of underwash effect for back and side orientations. Varying degrees of pressure intensification are observed depending upon the orientation of the head and the helmet to the blast wave. The simulation results are consistent with experimental observations.

18.5.7 Discussion on Orientation-Dependent Blast Wave–Head Interactions

The present results validate both the hypotheses postulated: (1) external pressure field on the surface of the head depends on whether the wearer has suspension, padded or no helmet and (2) orientation of the head to the blast wave governs the pressure field experienced by the head, for a given head helmet configuration. In this section, the results are discussed in the context of these hypotheses.

The blast wave–head interactions are quite complex, as evident from the surface pressure patterns and the values of Λ at the incident blast site for various orientations for various head helmet configurations (Figure 18.47). For no helmet case (Figure 18.47a), statistically similar amplification at the incident blast site is observed for front and side orientations ($p = 0.81$) and a higher amplification for back orientation ($p_{max} = 0.019$). The amplification for 45° orientation is lower ($p_{max} = 0.006$) because of flow separation at the face and as sensor is not present at exact incident site due to 45° tilt (Figure 18.48d). The Λ depends on the incident blast intensity, the angle of incidence, the mass and the geometry of the target, and boundary conditions, and can vary from 2 to 8 (Anderson, 2001; Ganpule et al., 2011). By geometry, we imply geometrical features, such as topology and area of exposure. At the plane of specimen blast wave interaction, the different geometrical features have different effects. For suspension and padded helmet cases (Figure 18.47b, c), Λ at the incident blast site for each orientation is statistically different. For these cases, Λ is governed by the geometry of the helmet, the head helmet configuration, and its orientation to the blast.

To better understand surface pressure patterns and hence the flow fields around the head, numerical simulations are used. First, the flow field around the head for no helmet

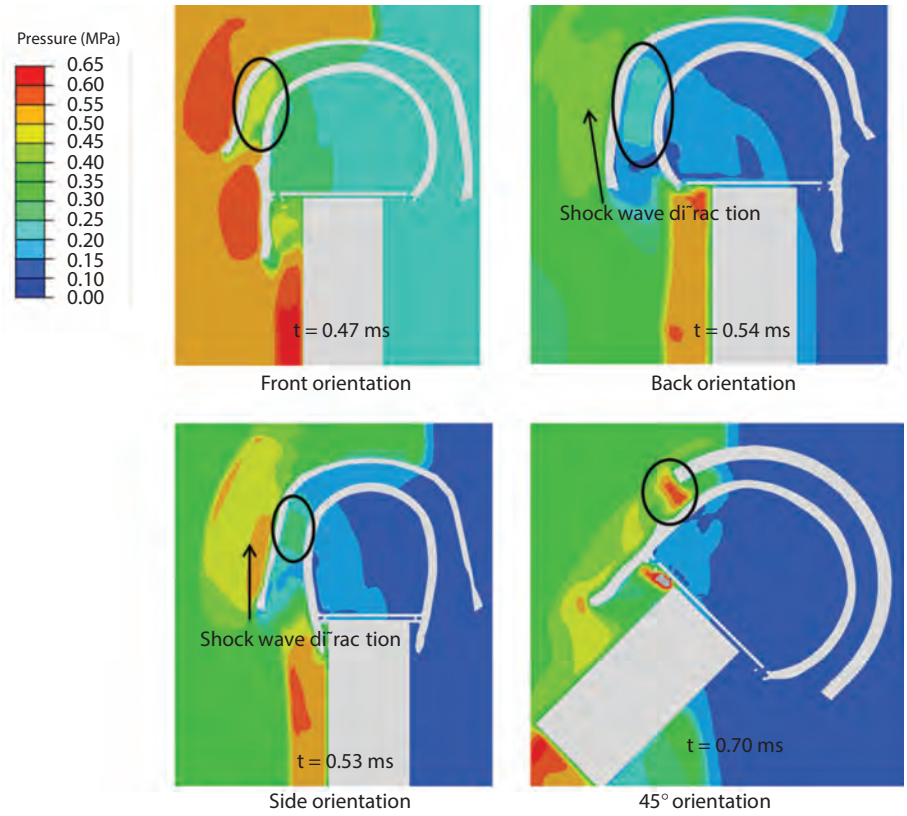


FIGURE 18.49 Pressure contours in helmet head subspace at incident blast site for each orientation. The lowest pressures in the helmet head subspace at incident blast site are observed for back orientation because of shock wave diffraction around outer surface of the helmet. Suspension helmet case is used for illustration.

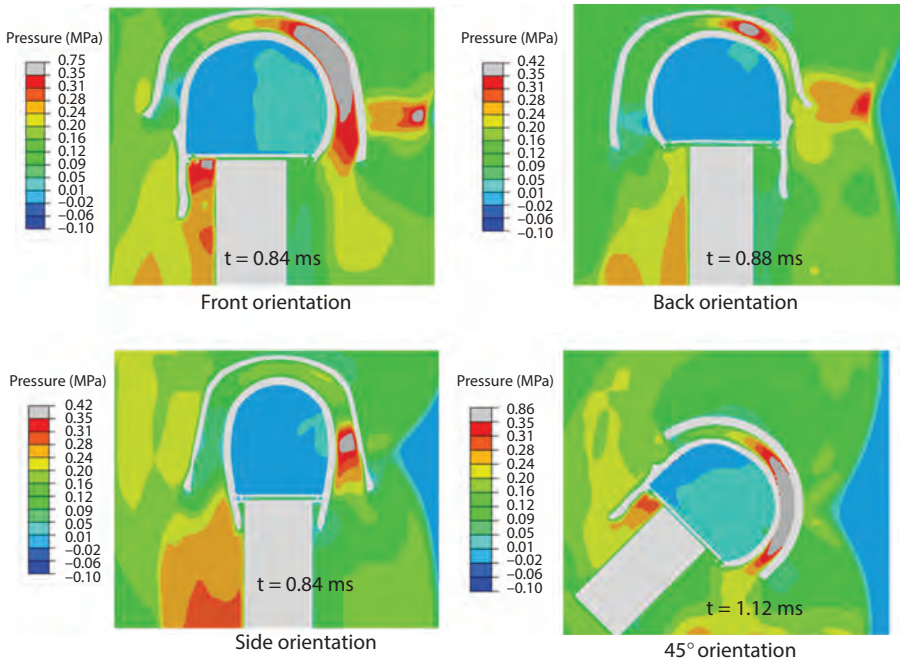


FIGURE 18.50 Pressure intensification on the side away from incident blast side for the suspension helmet. Varying degrees of intensification are observed for various orientations from the geometric effects that govern flow field within the head–helmet subspace. Maximum intensification is observed for 45° orientation.

case is presented. Once the blast wave impinges the head, flow separation occurs, as is evident from the values of the recorded pressure for the senor next to the incident blast site (Figure 18.47a). For example, pressure reduction of 53.89%, 25%, 67.91%, and 43.94% are observed for front, back, side, and 45° orientations respectively for the sensor next to the incident blast site. Flow separation causes low-pressure zones (e.g., top and sides of the head [Figure 18.48a]); thus, pressures are further reduced as we move away from the incident blast side (Figure 18.48a). Blast wave traversing the head and blast wave traversing the neck reunite on the side opposite to the incident blast side (Figure 18.48b). This flow reunion causes an increase in pressure (e.g., sensor RH for front orientation, sensor FH for back orientation, sensor T3 for 45° orientation) (Figure 18.47a). For the side orientation, flow separation occurs before the blast wave reaches the midsagittal plane (Figure 18.48c), thus all the sensors on the midsagittal plane record similar pressures (Figure 18.48a). This flow separation is further enhanced as the blast wave reaches the side opposite to the incident blast side; hence, the corresponding sensor (sensor L) records very low pressure. Flow separation for the side orientation is attributed to a larger area facing the blast. Numerical simulations clearly show that the surface pressures and the flow field around the head are strongly governed by the geometry of the head. Several other studies (Chavko et al., 2010; Ganpule et al., 2011; Mott DR, 2008; Taylor and Ford, 2009; Zhu et al., 2012) have also shown that the geometry of the head plays an important role in the blast wave head interactions and hence in the biomechanical loading of the brain.

Figure 18.51 shows peak pressure plots for no-helmet, suspension helmet, and padded helmet cases superimposed on each other for each head orientation. Table 18.7 shows the percentage reduction in peak pressures at the incident blast site for suspension and padded helmet cases compared with the no-helmet case. By comparing the values of peak pressures (Figure 18.51 and Table 18.7) at the incident blast site, it can be seen that varying degrees of pressure reduction at incident blast site are observed for suspension and padded cases compared with the no-helmet case. Back and side orientations show statistically significant reduction ($p < 0.05$) in pressure under the helmet, but only marginal reduction are seen under the helmet for front orientation ($p > 0.05$). For front orientation, part of the oncoming blast wave contributes

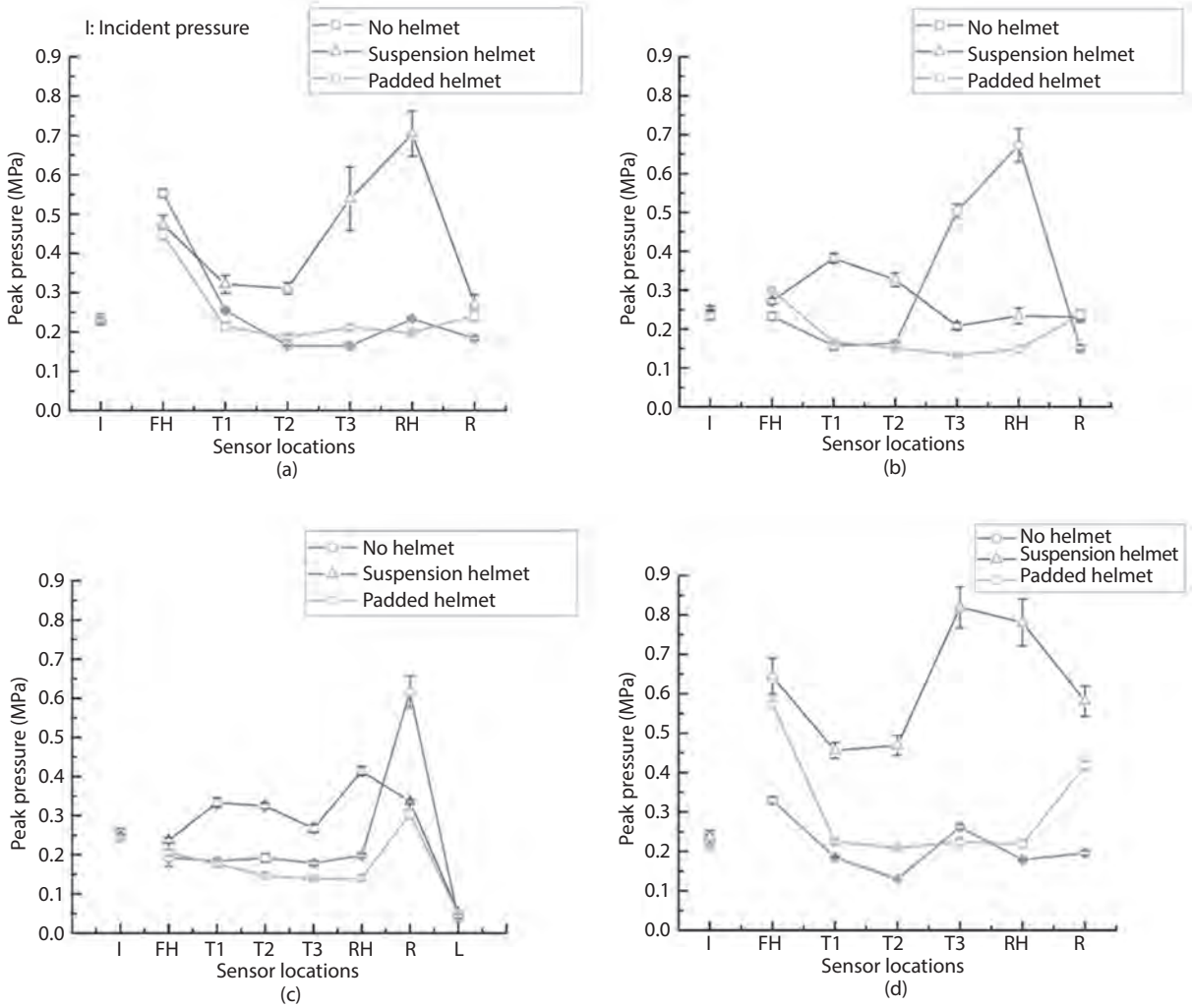


FIGURE 18.51 Peak pressures for no helmet, suspension helmet, and padded helmet cases superimposed on each other for various orientations: (a) front, (b) back, (c) side, and (d) 45°.

TABLE 18.7
Percent Reduction in Peak Pressures at Incident Blast Site for Suspension and Padded Helmet Cases a Compared With a No-Helmet Case

	Peak Pressure Incident Blast Site (MPa)			Percent Reduction in Peak Pressure	
Orientation	No Helmet	Suspension Helmet	Padded Helmet	Suspension Helmet	Padded Helmet
Front	0.55	0.47	0.45	14.47	18.99
Back	0.67	0.23	0.15	65.18	77.98
Side	0.62	0.34	0.30	45.54	50.73
45°	0.33	0.64	0.57	–95.13*	–73.94[a]

Peak pressures are based on mean values.
* Negative number suggests increase in pressure compared with a no-helmet case.

to the pressure as the helmet does not cover the forehead completely (Figure 18.49). A 45° orientation does not show reduction in peak pressure at the incident blast side (i.e., sensor FH). In contrast, for 45° orientation, peak pressures are increased by 95.13% and 73.94% for the suspension and padded helmet cases respectively compared with the no helmet case. This is because (1) flow separation at the face for the no helmet case (Figure 6.17d) and (2) in contrast to flow separation for no helmet case, blast wave is directed in the head–helmet subspace for the suspension and padded helmet cases (Figure 18.49). Of all orientations, maximum reduction in pressure (65.18% and 77.98%, respectively, for suspension and padded helmet cases) at the incident blast site compared with no helmet case is observed for the back orientation (Figure 18.51 and Table 18.7). The helmet has a larger area and height on the back than the front or the side. Thus helmet diffracts and blocks the oncoming blast wave, offering maximum protection as shown in Figure 18.49. Zhang and Makwana (2011) have also found maximum reduction in peak ICP for the back orientation from their numerical simulations.

Pressures are increased under the suspension helmet on the side away from the incident blast side (Figure 18.51). This is due to the underwash effect of the helmet. For orientations studied, maximum underwash (i.e., pressure intensification) under the suspension helmet is observed for the 45° orientation followed by the front orientation (see sensor RH, Figure 18.51). This is mainly for two reasons: (1) orientation of the head–helmet configuration to the blast and (2) the geometry of the helmet. For the 45° orientation, the blast wave penetrates the head–helmet subspace (i.e., gap) more effectively from both sides (Figure 18.50). The blast wave is continuously directed in the head–helmet subspace from the face because of tilt. As mentioned earlier, the back of the helmet has a larger area and height than the front. Thus, for the front orientation, blast wave traversing the neck and blast wave traversing outside the helmet, after reaching the head–helmet subspace, engulfs the head–helmet subspace (due to geometric effects) and causes higher intensification. For other orientations, this engulfment is less intense (Figure 18.50) because of the shorter height of the helmet in the corresponding regions. It should be noted that, for front and 45° scenarios, the maximum surface pressure recorded by the surrogate head with the suspension helmet (P_{max} = 0.76 and 0.87 for front and 45° orientations, respectively) exceeds the maximum surface pressure recorded in the no-helmet case (P_{max} = 0.56 and 0.34 for front and 45° orientations, respectively).

Underwash effect is not seen for the padded helmet case, as evident from Figure 18.51. However, equivalent pressures are seen on the top region of the head (sensors T1–T3) compared with the no-helmet case (Figure 18.51). This indicates that additional pathways/modes of energy transfer exist under the padded helmet. Thus, performance of the foam pads under the blast-loading conditions needs further investigation to identify these pathways/modes.

18.5.8 Role of Helmet in Mechanics of the Blast Wave–Head Interactions: Effect on ICP Response

In published work (Ganpule et al., 2011; Ropper, 2011), the role of the helmet in mechanics of the blast wave–head interactions has been studied in terms of pressure field experienced on the surface of the surrogate dummy head. From the previous study done on surrogates, it was shown that peak surface pressures were reduced at incident blast site (i.e., site closest to impact) for both padded and suspension helmet configurations and these reduction were statistically significant. At other locations, surface pressures were marginally reduced for padded helmet configuration and increased for suspension helmet configuration. Increase in surface pressures under the suspension helmet were due to focusing of blast wave under the suspension helmet. Impulse values were either equivalent or were marginally reduced for both padded and suspension helmet configurations. In addition, for suspension helmet, statistically significant increase in impulse was seen for locations that were directly below focused region. How the external pressure field measured on the surface of the head translates to the intracranial contents is currently not known. Some of the interesting questions are: what dose increase in surface pressures under suspension helmet imply in terms of brain injury? Does blast wave focusing

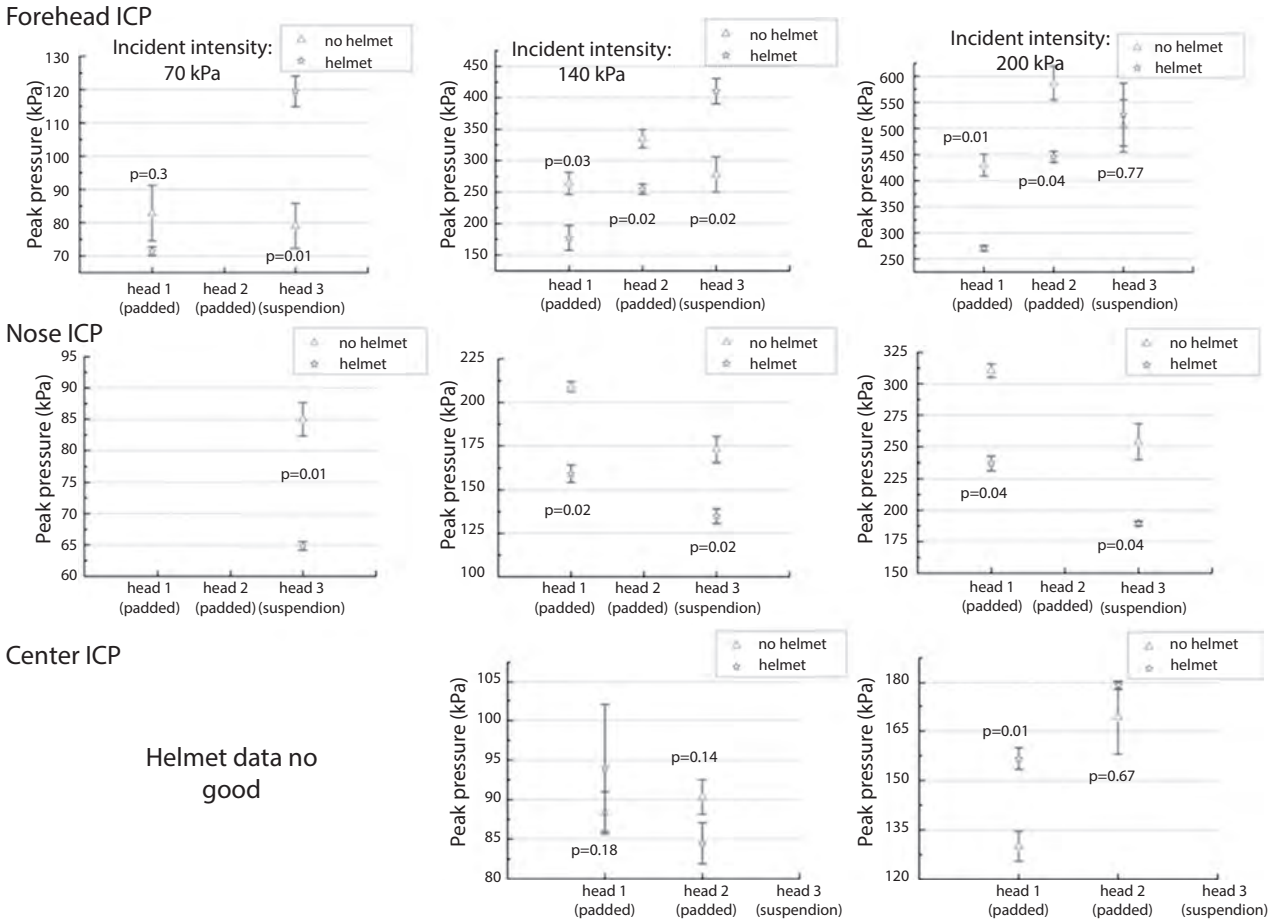


FIGURE 18.52 Comparison of peak ICPs between no helmet, padded helmet, and suspension helmet cases.

affect injury outcome and injury severity? In this section, an attempt is made to address these questions by studying ICP response with and without helmets.

For these experiments, the cadaver heads used in the PMHS Blast Testing section were used with the same array of instrumentation used for the bare head tests. Padded helmets were used for heads 1 and 2 and a suspension helmet was used for head 3. Figure 18.51 shows the comparison of peak ICPs between no-helmet and helmeted cases for FH, nose, and center ICP. Peak ICP values are reduced with the padded helmet for FH and nose locations compared with the no-helmet case; these reductions are statistically significant for most of the cases ($p < 0.05$). Center and back (not shown) locations show equivalent peak ICP values with the padded helmet, compared with the no-helmet case. With the suspension helmet, peak ICP value were increased (statistically significant increase) for the FH location at incident blast intensities of 70 kPa and 140 kPa and remained equivalent for incident blast intensity of 200 kPa. With the suspension helmet, statistically significant reduction in peak nose ICP is seen at all intensities. Center and back locations show equivalent peak ICP values with the suspension helmet.

Figure 18.53 shows the ICP impulse comparison between the no-helmet and helmeted cases for FH, nose, and center ICP. Equivalent ICP impulse values are seen with the padded helmet at all locations compared with no helmet, but there is no fixed pattern of variation across the heads and/or intensities, making it difficult to draw any concrete conclusions. Increased ICP impulse values are seen with the suspension helmet at all locations compared with no helmet scenarios. This increase in impulse under suspension helmet is statistically significant for most of the scenarios.

For the padded helmet, peak ICP values at the FH, nose, and temple locations are reduced and these reductions are statistically significant; center and back locations do not show significant reduction in peak ICP values. ICP impulse values are either equivalent or marginally reduced with the padded helmet (Figure 18.54a). This suggests that the face is important pathway of load transfer to the brain. The area of face is ~25%–30% as that of the area of the forehead. Thus, significant amount of impulse/energy is transferred through the face; this is further confirmed using numerical simulations. The face has been identified as an important pathway of load transfer by Nyein et al. (2010) and a face shield has been proposed for blast mitigation; peak pressure reduction up to 80% were proposed with the face shield. However, some of the major limitations of the Nyein et al.'s study were total simulation time and military/field relevance of their input data. Authors simulated entire blast event for 0.76 msec only; this time period is not sufficient to truly evaluate role of face

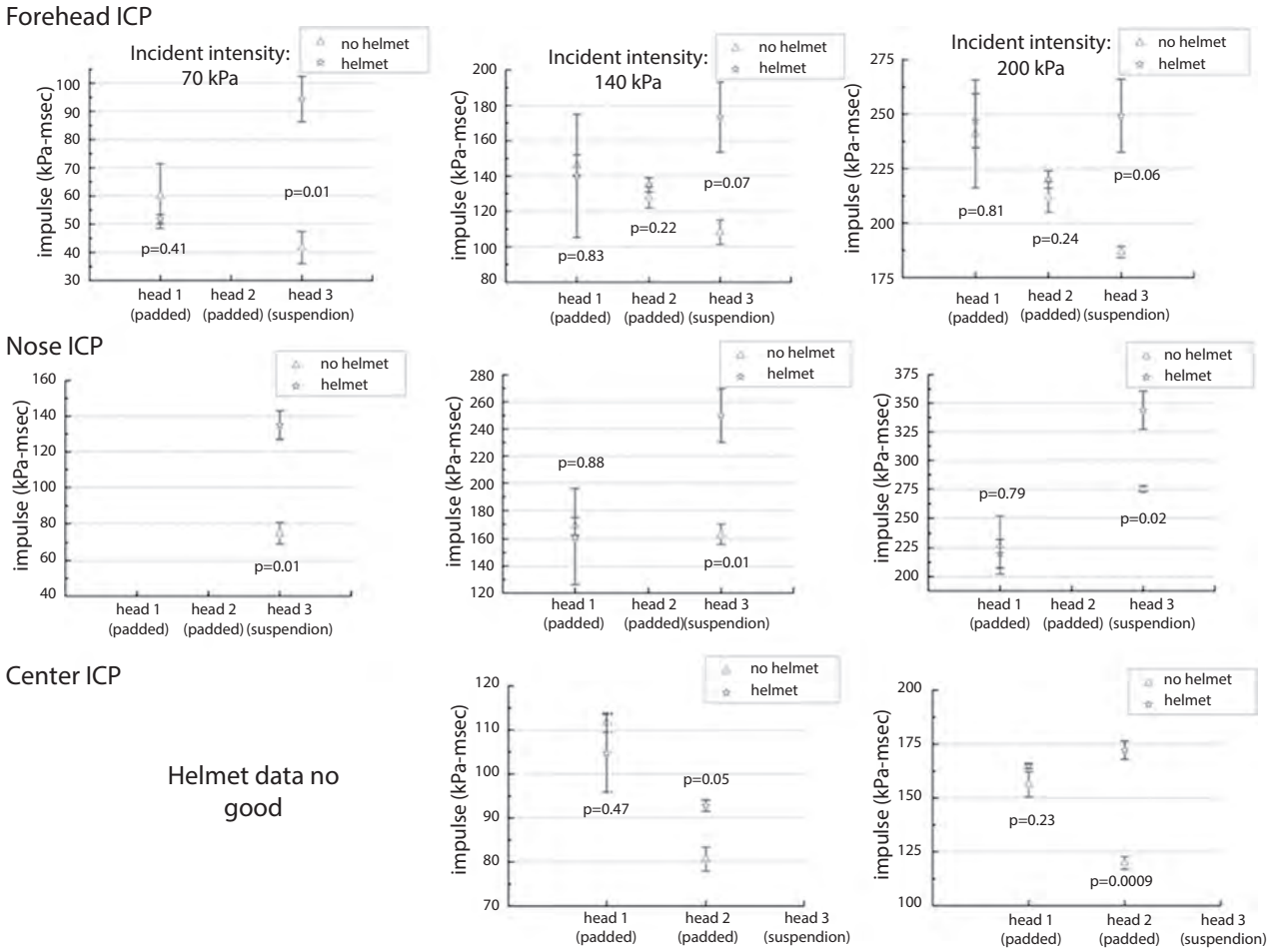


FIGURE 18.53 Comparison of peak ICPs between no helmet, padded helmet, and suspension helmet cases.

shield in blast mitigation as face shield delays the blast wave transmission into intracranial cavity. In addition, incident blast pressures and durations used as an input for numerical simulations were not representative of realistic blast. In addition to the role the face plays in blast wave transmission, marginal impulse reduction seen with the padded helmet from our experiments also highlight the role that structure/geometry of the head plays in governing the ICP response.

With the suspension helmet, peak ICP values are reduced for nose ICP, and these reductions are statistically significant. On the contrary, peak values are increased for FH ICP at incident blast intensities of 70 and 140 kPa and remained equivalent for blast intensity of 200 kPa because of focusing/underwash effect as shown in Figure 18.54b, c. In addition, temple, center, and back locations show equivalent peak ICP values with the suspension helmet. Statistically significant increases in impulse values are seen with the suspension helmet at all locations compared with no helmet scenarios. Thus it is clear that the focusing effect seen under the suspension helmet translates to the intracranial contents and adversely affects the ICP response (Figure 18.55). This does imply that for suspension helmet configuration, wearing a helmet can be worse than not wearing the helmet for primary blasts in which blast waves can potentially focus under the helmet. However, this does not preclude the use of helmets that provide critical protection against blunt and penetrating conditions.

18.6 CONCLUSION

In this chapter, a comprehensive review of current state of the art in BINT research is presented. From the field data, it is very clear that BINT, especially mild bTBIs, is a serious concern to defense personnel during and beyond their service. Although the mechanics of BINT is different from that of blunt and ballistic injuries, pathophysiological and neurobiological aspects of mild TBI are possibly related. BINT in general and mild bTBI in particular have been the subject of investigations by many groups around the world using a variety of models and we are still far away in having a clear understanding of the problem and hence their solution.

In this chapter, we have addressed a few of those challenges including: (1) issues in replication of primary blast in laboratory and methods used for accurate simulation of the primary blasts using compressed gas driven shock tube, (2) loading mechanisms on head that have to be considered during a blast event, (3) injury mechanisms associated with primary blast, (4) procedure for developing anatomically accurate human and animal models, and finally (5) the role

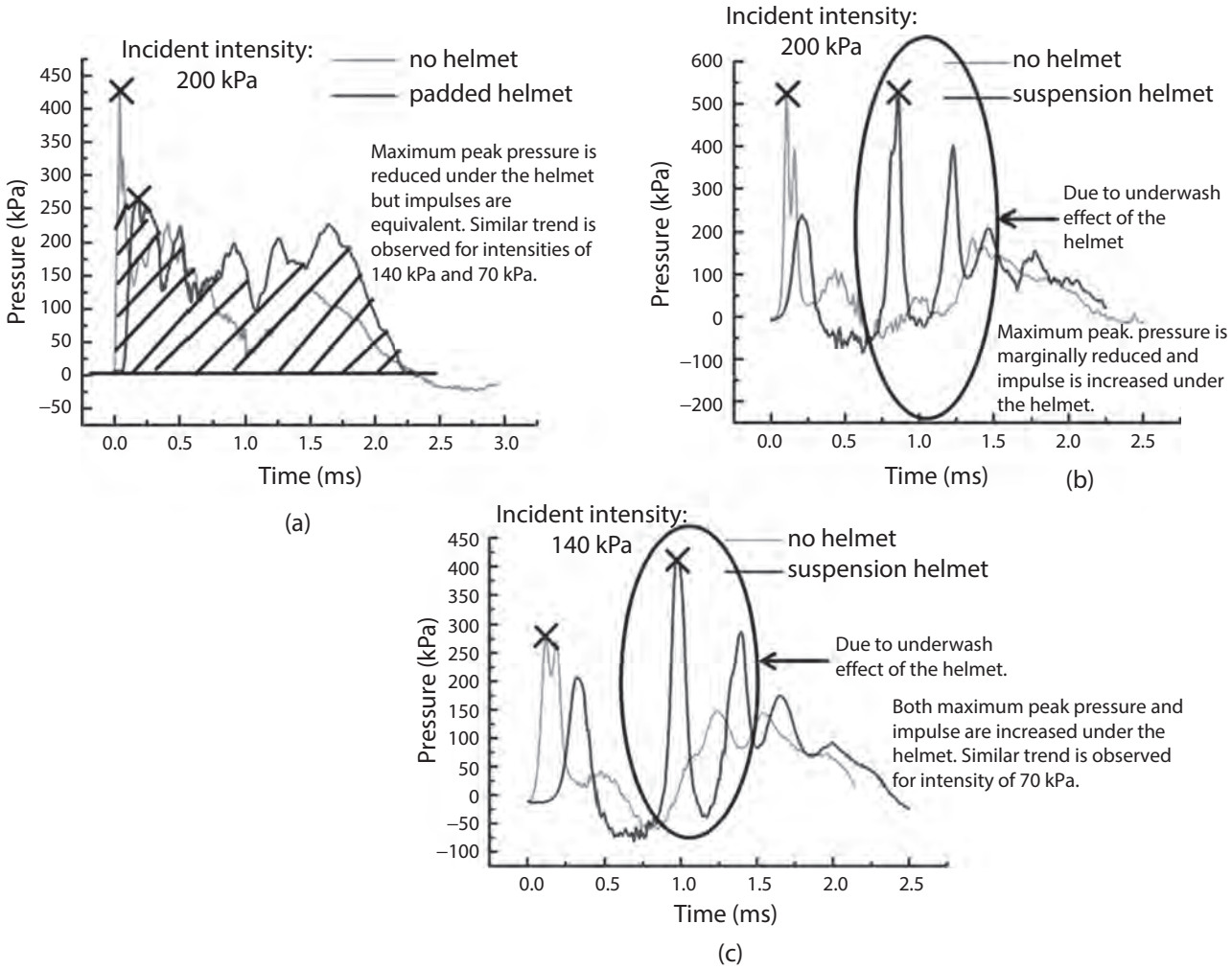


FIGURE 18.54 Pressure time histories with and without the helmet. (a) Padded helmet at incident intensity of 200 kPa. A similar trend is seen for intensities of 70 kPa and 140 kPa. (b) Suspension helmet at incident intensity of 200 kPa. (c) Suspension helmet at incident intensity of 140 kPa. A similar trend is seen at incident intensity of 70 kPa.

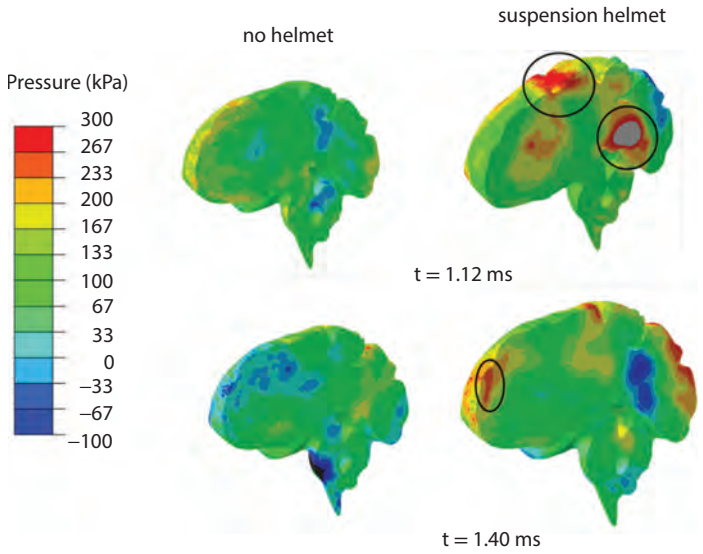


FIGURE 18.55 Focusing effect seen under the suspension helmet translates to the intracranial contents. Intracranial regions with increased pressure with respect to no helmet counterpart are highlighted with an ellipse.

of protective equipment in mitigation of the primary blast. Some of the key points of this chapter are:

- Before performing experiments with a shock tube, it is essential to tune the location of the test section. If located too close to the breach, it will not produce a Friedlander wave and instead will have a flattop wave; if located too close to the exit, it will interact with vorticities or jet winds that are also not representative of a field blast. In any case, it is critical to measure the blast overpressure and impulse impacting the specimen using surrogates. Further, it is necessary to relate these parameters to field relevant values because otherwise we will be exploring injuries in the wrong loading domains.
- Through PMHS testing, we were able to determine that two important loading mechanisms of BINT are: (1) direct transmission of pressure, which was evident from the increase in the ICP and (2) indirect transmission through skull flexure, which was evident from the strain data recorded in the skull.

- Through an animal model, we were able to determine the mortality as well as gross pathology and BBB damage from blast exposure. Furthermore, we also determined that within 24 hours of blast exposure, there was no significant neurodegeneration.
- Methods for developing anatomically accurate human and rat model along with validations are shown.
- Finally, the role of helmet in mitigation of blast is discussed. It was shown through numerical model and experimental testing that use of a suspension helmet, though it works well against ballistic impact, actually aggravates the blast injury.

ACKNOWLEDGEMENTS

The majority of the work reported by the authors was carried out when the senior author was a faculty member at University of Nebraska-Lincoln and was the director of an Army Center on Trauma Mechanics. A number of faculty and students were involved during that period. Among them, we wish to acknowledge the work of and discussions with Ruqiang Feng, Shailesh Ganpule, Maciej Skotak, Fang Wang, Aaron Holmberg, Nick Kleinschmit, Veera Selvan, Aaron Alai, and James Haorah. Financial support was provided by US Army (project monitors: Bruce Lamattina and Larry Russell).

REFERENCES

The Visible Human Project. 2009. U.S. National Library of Medicine, Washington, DC.

Defense and Veterans Brain Injury Center. 2007. Operation Iraqi Freedom (OIF)/Operation Enduring Freedom (OEF) Fact Sheet.

AEP-55. 2006. Procedures for evaluating the protection level of logistic and light armoured vehicle: for mine threat, volume 2. NATO/Partnership for Peace.

Alexander, M.P. 1995. Mild traumatic brain injury: pathophysiology, natural history, and clinical management. *Neurology*. 45:1253–60.

Anderson, J. 2001. *Fundamentals of Aerodynamics*. McGraw-Hill, New York.

Arakeri, J.H., D. Das, A. Krothapalli, and L. Lourenco. 2004. Vortex ring formation at the open end of a shock tube: a particle image velocimetry study. *Physics of Fluids*. 16:1008–1019.

Baker, T.J. 2005. Mesh generation: art or science? *Progress in Aerospace Sciences*. 41:29–63.

Bass, C.R., M.B. Panzer, K.A. Rafaels, G. Wood, J. Shridharani, and B. Capehart. 2012. Brain injuries from blast. *Annals of Biomedical Engineering*.40:1–18.

Benzinger, T.L., D. Brody, S. Cardin, K.C. Curley, M.A. Mintun, S.K. Mun, K.H. Wong, and J.R. Wrathall. 2009. Blast-related brain injury: imaging for clinical and research applications: report of the 2008 St. Louis workshop. *Journal of Neurotrauma*. 26:2127–2144.

Bolander, R., B. Mathie, C. Bir, D. Ritzel, and P. VandeVord. 2011. Skull flexure as a contributing factor in the mechanism of injury in the rat when exposed to a shock wave. *Annals of Biomedical Engineering*. 39:1–10.

Bourdin, X., P. Beillas, P. Petit, and X. Troseille. 2007. Comparison of tetrahedral and hexahedral meshes for human finite element modelling: an application to kidney impact. Paper No. 07-0424-W. In: 20th Enhanced Safety of Vehicles Conference: Innovations for safety: opportunities and challenges. Lyon, France.

Brown, R., G. Cooper, and R.L. Maynard. 1993. The ultrastructure of rat lung following acute primary blast injury. *International Journal of Experimental Pathology*. 74:151.

Brun, R. 2009. Shock Tubes and Shock Tunnels: Design and Experiments. *In* NATO-OTAN. Vol. RTO-EN-AVT-162.

Cengel, Y.A., M.A. Boles, and M. Kanoğlu. 2011. *Thermodynamics: An Engineering Approach.* McGraw-Hill, New York.

Cernak, I., A.C. Merkle, V.E. Koliatsos, J.M. Bilik, Q.T. Luong, T.M. Mahota et al. 2011. The pathobiology of blast injuries and blast-induced neurotrauma as identified using a new experimental model of injury in mice. *Neurobiology of Disease*. 41:538–551.

Cernak, I., J. Savic, and J. Lazarov. 1997. Relations among plasma prolactin, testosterone, and injury severity in war casualties. *World Journal of Surgery*. 21:240–246.

Cernak, I., Z.G. Wang, J.X. Jiang, X.W. Bian, and J. Savic. 2001. Ultrastructural and functional characteristics of blast injury-induced neurotrauma. *Journal of Trauma-Injury Infection and Critical Care*. 50:695–706.

Chafi, M., G. Karami, and M. Ziejewski. 2010. Biomechanical assessment of brain dynamic responses due to blast pressure waves. *Annals of Biomedical Engineering*. 38:490–504.

Chandra, N., S. Ganpule, N. Kleinschmit, R. Feng, A. Holmberg, A. Sundaramurthy, V. Selvan, and A. Alai. 2012. Evolution of blast wave profiles in simulated air blasts: experiment and computational modeling. *Shock Waves*. 22:403–415.

Chavko, M., T. Watanabe, S. Adeeb, J. Lankasky, S.T. Ahlers, and R.M. McCarron. 2010. Relationship between orientation to a blast and pressure wave propagation inside the rat brain. *Journal of Neuroscience Methods*. 195:61–66.

Chen, Y., and M. Ostoja-Starzewski. 2010. MRI-based finite element modeling of head trauma: spherically focusing shear waves. *Acta Mechanica*. 213:155–167.

Cifuentes, A.O., and A. Kalbag. 1992. A performance study of tetrahedral and hexahedral elements in 3-D finite element structural analysis. *Finite Elements in Analysis and Design*. 12:313–318.

Clark, M.E., M.J. Bair, C. Buckenmaier, R.J. Gironda, and R.L. Walker. 2007. Pain and combat injuries in soldiers returning from Operations Enduring Freedom and Iraqi Freedom: Implications for research and practice. *Journal of Rehabilitation Research and Development*. 44:179.

Clemedson, C., and C. Criborn. 1955. A detonation chamber for physiological blast research. *The Journal of Aviation Medicine*. 26:373.

Coulter, G.A., G. Bulmash, and C.N. Kingery. 1983. Experimental and Computational Modeling of Rarefaction Wave Eliminators Suitable for the BRL 2.44 m Shock Tube. DTIC Document.

Courtney, A.C., L.P. Andrusiv, and M.W. Courtney. 2012. Oxy-acetylene driven laboratory scale shock tubes for studying blast wave effects. *Review of Scientific Instruments*. 83:045111–045111–7.

Courtney, A.C., and M.W. Courtney. 2009. A thoracic mechanism of mild traumatic brain injury due to blast pressure waves. *Medical Hypotheses*. 72:76–83.

DePalma, R.G., D.G. Burris, H.R. Champion, and M.J. Hodgson. 2005. Blast Injuries. *New England Journal of Medicine*. 352:1335–1342.

Department of Homeland Security. 2009. Bomb threat stand-off chart, from https://www.llis.dhs.gov/sites/default/files/DHS-BombThreatChart-6-5-09.pdf.

Dewey, J.M. 1971. The properties of a blast wave obtained from an analysis of the particle trajectories. *Proceedings of the Royal Society of London. Series A, Mathematical and Physical Sciences*. 324:275–299.

Ganpule, S., A. Alai, E. Plougonven, and N. Chandra. 2012. Mechanics of blast loading on the head models in the study of traumatic brain injury using experimental and computational approaches. *Biomechanics and Modeling in Mechanobiology*. 12:511–531.

Ganpule, S., L. Gu, A. Alai, and N. Chandra. 2011. Role of helmet in the mechanics of shock wave propagation under blast loading conditions. *Computer Methods in Biomechanics and Biomedical Engineering*. 15:1233–1244.

Ganpule, S.G. 2013. Mechanics of blast loading on post-mortem human and surrogate heads in the study of Traumatic Brain Injury (TBI) using experimental and computational approaches. *In* Mechanical engineering. University of Nebraska Lincoln, Lincoln.

Gould, K.E., and K. Tempo. 1981. High-Explosive Field Tests, Explosion Phenomena and Environmental Impacts. DTIC Document.

Grujicic, M., W. Bell, B. Pandurangan, and P. Glomski. 2011. Fluid/structure interaction computational investigation of blast-wave mitigation efficacy of the advanced combat helmet. *Journal of Materials Engineering and Performance*. 20:877–893.

Guy, R.J., E. Kirkman, P.E. Watkins, and G.J. Cooper. 1998. Physiologic responses to primary blast. *The Journal of Trauma and Acute Care Surgery*. 45:983–987.

Haselbacher, A., S. Balachandar, and S.W. Kieffer. 2007. Open-ended shock tube flows: influence of pressure ratio and diaphragm position. *AIAA Journal*. 45:1917–1929.

Heitger, M.H., R.D. Jones, A.D. Macleod, D.L. Snell, C.M. Frampton, and T.J. Anderson. 2009. Impaired eye movements in post-concussion syndrome indicate suboptimal brain function beyond the influence of depression, malingering or intellectual ability. *Brain*. 132:2850–2870.

Honma, H., M. Ishihara, T. Yoshimura, K. Maeno, and T. Morioka. 2003. Interferometric CT measurement of three-dimensional flow phenomena on shock waves and vortices discharged from open ends. *Shock Waves*. 13:179–190.

Irwin, R.J., M.R. Lerner, J.F. Bealer, P.C. Mantor, D.J. Brackett, and D.W. Tuggle. 1999. Shock after blast wave injury is caused by a vagally mediated reflex. *The Journal of Trauma and Acute Care Surgery*. 47:105–110.

Jiang, Z., O. Onodera, and K. Takayama. 1999. Evolution of shock waves and the primary vortex loop discharged from a square cross-sectional tube. *Shock Waves*. 9:1–10.

Jiang, Z., C. Wang, Y. Miura, and K. Takayama. 2003. Three-dimensional propagation of the transmitted shock wave in a square cross-sectional chamber. *Shock Waves*. 13:103–111.

Jones, E., N.T. Fear, and S. Wessely. 2007. Shell shock and mild traumatic brain injury: a historical review. *American Journal of Psychiatry*. 164:1641–1645.

Kashimura, H., T. Yasunobu, H. Nakayama, T. Setoguchi, and K. Matsuo. 2000. Discharge of a shock wave from an open end of a tube. *Journal of Thermal Science*. 9:30–36.

Kennedy, J.E., M.S. Jaffee, G.A. Leskin, J.W. Stokes, F.O. Leal, and P.J. Fitzpatrick. 2007. Posttraumatic stress disorder and posttraumatic stress disorder-like symptoms and mild traumatic brain injury. *J Rehabil Res Dev*. 44:895–920.

Kinney, G.F., and K.J. Graham. 1985. *Explosive Shocks in Air.* Springer-Verlag, New York.

Kleinschmit, N.N. 2011. A shock tube technique for blast wave simulation and studies of flow structure interactions in shock tube blast experiments, from http://digitalcommons.unl.edu/cgi/viewcontent.cgi?article=1022&context=engmechdiss.

Knöferl, M.W., U.C. Liener, D.H. Seitz, M. Perl, U.B. Brückner, L. Kinzl, and F. Gebhard. 2003. Cardiopulmonary, histological, and inflammatory alterations after lung contusion in a novel mouse model of blunt chest trauma. *Shock*. 19:519–525.

Kobeissy, F.H., S. Mondello, N. Tumer, H.Z. Toklu, M.A. Whidden, N. Kirichenko et al. 2013. Assessing neuro-systemic & behavioral components in the pathophysiology of blast-related brain injury. *Frontiers in Neurology*. 4:186.

Kraus, M.F., T. Susmaras, B.P. Caughlin, C.J. Walker, J.A. Sweeney, and D.M. Little. 2007. White matter integrity and cognition in chronic traumatic brain injury: a diffusion tensor imaging study. *Brain*. 130:2508–2519.

Langlois, J.A., W. Rutland-Brown, and K.E. Thomas. 2004. Traumatic brain injury in the United States: emergency department visits, hospitalizations, and deaths. Department of Health and Human Services, Centers for Disease Control and Prevention, Division of Acute Care, Rehabilitation Research and Disability Prevention, National Center for Injury Prevention and Control.

Leonardi, A.D.C., C.A. Bir, D.V. Ritzel, and P.J. VandeVord. 2011. Intracranial pressure increases during exposure to a shock wave. *Journal of Neurotrauma*. 28:85–94.

Ling, G., F. Bandak, R. Armonda, G. Grant, and J. Ecklund. 2009. Explosive blast neurotrauma. *Journal of Neurotrauma*. 26:815–825.

Lockhart, P.A. 2010. Primary Blast Injury of the Head: Numerical prediction and evaluation of protection. *In* Mechanical Engineering. University of Waterloo Waterloo, Ontario, Canada, p. 136.

Long, J.B., T.L. Bentley, K.A. Wessner, C. Cerone, S. Sweeney, and R.A. Bauman. 2009. Blast overpressure in rats: recreating a battlefield injury in the laboratory. *Journal of Neurotrauma*. 26:827–840.

McElhaney, J., J.W. Melvin, V.L. Roberts, and H.D. Portnoy. 1973. Dynamic characteristics of the tissues of the head. In: Kenedi, R.M. (ed.). *Perspectives in Biomedical Engineering*. Baltimore: University Park Press; pp. 215–222.

Moore, D.F., A. Jerusalem, M. Nyein, L. Noels, M.S. Jaffee, and R.A. Radovitzky. 2009. Computational biology - modeling of primary blast effects on the central nervous system. *Neuroimage*. 47:T10–T20.

Moss, W.C., M.J. King, and E.G. Blackman. 2009. Skull flexure from blast waves: a mechanism for brain injury with implications for helmet design. *Physical Review Letters*. 103:108702.

Mott, D., D. Schwer, T. Young, J. Levine, J.-P. Dionne, A. Makris, and G. Hubler. 2008. Blast-induced pressure fields beneath a military helmet for non-lethal threats. *Bulletin of the American Physical Society*. 53.

Mott DR, S.D., Young TR, Levine J, Dionne JP, Makris A, Hubler G. 2008. Blast-induced pressure fields beneath a military helmet. 20th international symposium on military aspects of blast and shock. September 1–5, 2008. Oslo, Norway.

N.Kleinschmit. 2011. A shock tube technique for blast wave simulation and studies of flow structure interactions in shock tube blast experiments. Master's thesis. Department of Engineering Mechanics, University of Nebraska Lincoln, Lincoln.

Nyein, M.K., A.M. Jason, L. Yu, C.M. Pita, J.D. Joannopoulos, D.F. Moore, and R.A. Radovitzky. 2010. In silico investigation of intracranial blast mitigation with relevance to military traumatic brain injury. *Proceedings of the National Academy of Sciences*. 107:20703–20708.

Okie, S. 2005. Traumatic brain injury in the war zone. *New England Journal of Medicine*. 352:2043–2047.

Onodera, O., Z.L. Jiang, and K. Takayama. 1998. Holographic interferometric observation of shock waves discharged from an open-end of a square cross-sectional shock tube. *JSME International Journal Series B-Fluids and Thermal Engineering*. 41:408–415.

Panzer, M.B., B.S. Myers, B.P. Capehart, and C.R. Bass. 2012. Development of a finite element model for blast brain injury and the effects of CSF cavitation. *Ann Biomed Eng*. 40:1530–1544.

Payman, W., and W.C.F. Shepherd. 1946. Explosion waves and shock waves. VI. The disturbance produced by bursting diaphragms with compressed air. *Proceedings of the Royal Society of London. Series A. Mathematical and Physical Sciences*. 186:293–321.

Pizov, R., A. Oppenheim-Eden, I. Matot, Y.G. Weiss, L.A. Eidelman, A.I. Rivkind, and C.L. Sprung. 1999. Blast lung injury from an explosion on a civilian bus. *CHEST Journal*. 115:165–172.

Ramos, A., and J.A. Simões. 2006. Tetrahedral versus hexahedral finite elements in numerical modelling of the proximal femur. *Medical Engineering & Physics*. 28:916–924.

Reneer, D.V., R.D. Hisel, J.M. Hoffman, R.J. Kryscio, B.T. Lusk, and J.W. Geddes. 2011. A multi-mode shock tube for investigation of blast-induced traumatic brain injury. *Journal of Neurotrauma*. 28:95–104.

Reynolds, G.T. 1998. Walker Bleakney February 8, 1901–January 15, 1992. *Biographical Memoirs*. 73:87.

Risling, M., S. Plantman, M. Angeria, E. Rostami, B.-M. Bellander, M. Kirkegaard, U. et al. 2011. Mechanisms of blast induced brain injuries, experimental studies in rats. *Neuroimage*. 54:S89–S97.

Ritzel, D., S. Parks, J. Roseveare, G. Rude, and T. Sawyer. 2011. Experimental blast simulation for injury studies. Proceedings HFM-207 NATO Symposium on a Survey of Blast Injury Across the Full Landscape of Military Science.

Ropper, A. 2011. Brain injuries from blasts. *New England Journal of Medicine*. 364:2156–2157.

Säljö, A., F. Bao, K.G. Haglid, and H.-A. Hansson. 2000. Blast exposure causes redistribution of phosphorylated neurofilament subunits in neurons of the adult rat brain. *Journal of Neurotrauma*. 17:719–726.

Sasser, S.M., R.W. Sattin, R.C. Hunt, and J. Krohmer. 2006. Blast lung injury. *Prehospital Emergency Care*. 10:165–172.

Schneiders, R. 2000. Algorithms for quadrilateral and hexahedral mesh generation. Proceedings of the VKI Lecture Series on Computational Fluid Dynamics.

Setoguchi, T., K. Matsuo, F. Hidaka, and K. Kaneko. 1993. Impulsive noise induced by a weak shock wave discharged from an open end of a tube: acoustic characteristics and its passive control. Proceedings of the 1993 ASME Winter Meeting, November 28, 1993–December 3, 1993. Vol. 170. New Orleans, ASME; pp. 57–64.

Shuck, L.Z., and S.H. Advani. 1972. Rheological response of human brain-tissue in shear. *Journal of Basic Engineering*. 94:905–911.

Skotak, M., F. Wang, A. Alai, A. Holmberg, S. Harris, I. Switzer, Robert C, and N. Chandra. 2013. Rat injury model under controlled field-relevant primary blast conditions: acute response to a wide range of peak overpressures. *Journal of Neurotrauma*. 30:1147–1160.

Sogbesan, E.A. 2011. Design and Analysis of Blast Induced Traumatic Brain Injury Mechanism Using a Surrogate Headform: Instrumentation and Outcomes. DTIC Document.

Stalnaker, R.L. 1969. Mechanical properties of the head. Ph.D. dissertation. West Virginia University.

Sundaramurthy, A., A. Alai, S. Ganpule, A. Holmberg, |E. Plougonven, and N. Chandra. 2012. Blast-induced biomechanical loading of the rat: an experimental and anatomically accurate computational blast injury model. *Journal of Neurotrauma*. 29:2352.

Tanielian, T., and Jaycox, L.H. 2008. Invisible wounds of war. RAND Corporation, Santa Monica, CA.

Taylor, P.A., and C.C. Ford. 2009. Simulation of blast-induced early-time intracranial wave physics leading to traumatic brain injury. *Journal of Biomechanical Engineering-Transactions of the ASME*. 131:061007.

Teasdale, G., and B. Jennett. 1974. Assessment of coma and impaired consciousness: a practical scale. *The Lancet*. 304:81–84.

Terrio, H., L.A. Brenner, B.J. Ivins, J.M. Cho, K. Helmick, K. Schwab et al. 2009. Traumatic brain injury screening: preliminary findings in a US Army Brigade Combat Team. *Journal of Head Trauma Rehabilitation*. 24:14–23.

Thurman, D.J., C. Alverson, K.A. Dunn, J. Guerrero, and J.E. Sniezek. 1999. Traumatic brain injury in the United States: a public health perspective. *Journal of Head Trauma Rehabilitation*. 14:602–615.

Thurman, D.J., J.E. Sniezek, and D. Johnson. 1995. Guidelines for Surveillance of Central Nervous System Injury. Centers for Disease Control and Prevention, Atlanta.

Tsokos, M., F. Paulsen, S. Petri, B. Madea, K. Puschel, and E.E. Turk. 2003. Histologic, immunohistochemical, and ultrastructural findings in human blast lung injury. *American Journal of Respiratory and Critical Care Medicine*. 168:549–555.

Wang, Y., Y. Wei, S. Oguntayo, W. Wilkins, P. Arun, M. Valiyaveettil, J. Song, J.B. Long, and M.P. Nambiar. 2011. Tightly coupled repetitive blast-induced traumatic brain injury: development and characterization in mice. *Journal of Neurotrauma*. 28:2171–2183.

Warden, D. 2006. Military TBI during the Iraq and Afghanistan wars. *The Journal of Head Trauma Rehabilitation*. 21:398–402.

Wieding, J., R. Souffrant, A. Fritsche, W. Mittelmeier, and R. Bader. 2012. Finite element analysis of osteosynthesis screw fixation in the bone stock: an appropriate method for automatic screw modelling. *PLoS ONE*. 7:e33776.

Willinger, R., H.-S. Kang, and B. Diaw. 1999. Three-dimensional human head finite-element model validation against two experimental impacts. *Annals of Biomedical Engineering*. 27:403–410.

Wojcik, B.E., C.R. Stein, K. Bagg, R.J. Humphrey, and J. Orosco. 2010. Traumatic brain injury hospitalizations of US army soldiers deployed to Afghanistan and Iraq. *American Journal of Preventive Medicine*. 38:S108–S116.

Xiong, Y., A. Mahmood, and M. Chopp. 2013. Animal models of traumatic brain injury. *Nature Reviews Neuroscience*. 14:128–142.

Yelverton, J.T. 1996. Pathology scoring system for blast injuries. *The Journal of Trauma and Acute Care Surgery*. 40:111S–115S.

Zhang, L., and R. Makwana. 2011. Comparison of the head response in blast insult with and without combat helmet. RTO Human Factors and Medicine Panel (HFM) Symposium Halifax, Canada.

Zhang, L.Y., K.H. Yang, and A.I. King. 2001. Comparison of brain responses between frontal and lateral impacts by finite element modeling. *Journal of Neurotrauma*. 18:21–30.

Zhu, F., H. Mao, A. Dal Cengio Leonardi, C. Wagner, C. Chou, X. Jin et al. 2010. Development of an FE model of the rat head subjected to air shock loading. *Stapp Car Crash Journal*. 54:211–25.

Zhu, F., C. Wagner, A. Dal Cengio Leonardi, X. Jin, P. VandeVord, C. Chou et al. 2012. Using a gel/plastic surrogate to study the biomechanical response of the head under air shock loading: a combined experimental and numerical investigation. *Biomechanics and Modeling in Mechanobiology*. 11:341–353.

Author Queries

AQ1 on page 207: please confirm that “i” is correct here (that it is a lowercase one, not the letter i). Please also check “ii–iv” in the next sentence to confirm that these are the correct locants.
AQ2 on page 225: Please clarify what “Elements of the IS” means. What does IS stand for, and should “Elements” be “elements”?
AQ3 on page 229: In the Figure 18.34 legend, please change the reference number 36 to the author-date system.
AQ4 on page 231: Please define SAS on first use.
AQ5 on page 239: In the Figure 18.43 legend, please spell out RED.
AQ6 on page 247: Is Figure 18-48 meant here? Please clarify which figure you are citing here; no Figure 6.17 was provided.

Appendix B – Book Chapter
2019

Authors: M. Skotak, M.T. Townsend, E. Alay and N. Chandra

Title: "*The effect of geometrical factors on the surface pressure distribution on a human phantom model following shock exposure*"

Journal Publication: A computational and experimental study, An online publication, DOI: 10.5772/intechopen.88809, (2019), [19-B2]s

Author Queries	
[AQ1]	Please provide publisher location for Refs. [14, 16].
[AQ2]	Please provide page range for Refs. [17, 20, 27, 38].
[AQ3]	Please provide complete details for Refs. [24, 40, 46, 48].
[AQ4]	Please provide publisher details for Ref. [37].
[AQ5]	Please provide volume number for Ref. [49].

Chapter

The Effect of Geometrical Factors on the Surface Pressure Distribution on a Human Phantom Model Following Shock Exposure: A Computational and Experimental Study

Maciej Skotak, Molly T. Townsend, Eren Alay and Namas Chandra

Abstract

Experimental data and finite element simulations of an anthropometric surrogate headform was used to evaluate the effect of specimen location and orientation on surface pressures following shock exposures of varying intensity. It was found that surface pressure distributions changed with local flow field disturbances, making it necessary to use data reduction strategies to facilitate comparisons between test locations, shock wave intensities and headform orientations. Non-dimensional parameters, termed amplification factors, were developed to permit direct comparisons of pressure waveform characteristics between incident shock waves differing in intensity, irrespective of headform location and orientation. This approach proved to be a sensitive metric, highlighting the flow field disturbances which exist in different locations and indicating how geometric factors strongly influence the flow field and surface pressure distribution.

Keywords: shock wave, shock tube, pressure measurements, human phantom, end effect, numerical simulations, impulse effect, dynamic pressure

1. Introduction

The shock tube is a convenient way to generate the shock waves in a controlled fashion, and it has been employed in various research areas for more than a century [1–6]. The design of a compressed gas driven shock tube includes three standard components: driver (breech) and driven sections with an optional end wave eliminator [7, 8]. The differences in the dimensions (volume of the breech, breech-to-test section diameter ratio, length of the driven section) and operation of the tube (type of driven gas, mechanism of driver gas release) have significant impact on the resulting pressure history measured inside of the tube [9]. The classical design of

IntechOpen

the shock tube employs the plastic or metal membranes, which is used to confine the driver gas from entering the driven test section. The driver section pressure is gradually increased until the point of mechanical failure of the membrane upon which the driver gas is entering the test section, pressurizing the ambient gas and resulting in the formation of the shock wave. Alternative designs employ membraneless drivers where the piston [10–13], or fast acting valve [14–16], are used eliminating the need for membrane replacement between consecutive tests. Both designs have been demonstrated to allow generation of shock waves with diverse magnitudes and characteristics. It is worth mentioning various instrumental factors, discussed in detail in our recent contribution [17], can affect the quality of recorded pressure waveforms and impact the interpretation of the experimental data.

In the biomedical field, research utilizing shock tubes to investigate mechanisms of blast TBI (bTBI) was invigorated only 20 years ago [18, 19]. The primary goal in this area of research is to replicate conditions associated with field explosions, particularly the primary blast injuries caused exclusively by the interaction of a shock wave with the brain are of interest [20]. Simulation of explosive blast implies that a shock wave closely resembling the Friedlander waveform should be produced and it has become a standard in contemporary bTBI models [7, 21]. Two experimental parameters of paramount importance are the specimen restraint and the location of the test section, where the specimen is exposed to a shock wave. For the inanimate specimen the method of restraint is usually not an issue, however, human phantom models are frequently mounted on a biofidelic neck, e.g., Hybrid III, and when subjected to a shock wave loading rapid acceleration can result in the specimen displacement affecting the pressure loading on the surface. When the animal models are used the head restraint becomes extremely important, particularly for rodents with relatively small body dimensions and low weight. If the proper head restraint measures are not included in the experimental design, it might result in the development of erroneous injury modalities. It's been demonstrated that head acceleration might lead to the development of tertiary blast injuries, which have different injury characteristics than those resulting from shock wave loading [22, 23]. The importance of the test location in the shock tube was a subject of the experimental evaluation in the past by our group [24–26]. These results illustrate significant differences between testing the specimen inside of the shock tube, i.e., at the distance from the exit enough to eliminate influence of any end-effects, versus at the end and outside. Testing outside is undoubtedly more convenient, but carries a number of unwanted drawbacks: (1) the shock wave profile is eroded and typically only short duration waveforms are achievable, (2) there is large dynamic pressure component which might contribute to a variety of errors [27], (3) the loading of the specimen strongly depends on the location with respect to the shock tube exit and diameter due to highly heterogeneous conditions [28, 29]. Testing inside provides much higher level of control over the shock wave profile with the dynamic components resembling these encountered in the field explosions.

Numerical simulations are invaluable tools for mechanistic investigation of short lived phenomena like shock wave interaction with complex biological structures. The numerical models in bTBI research area provide insight into: (1) the transmission and propagation of the blast waves in the brain [8, 30, 31], and (2) mitigation of blast effects by helmets [32–40] or other PPE designed to safeguard the craniofacial area [36]. However, the accuracy of the numerical simulations relies on the validation using high-quality experimental data, e.g., the pressure measured on the surface of the helmet or phantom [8, 35, 39], or intracranial pressure [31, 40]. A related branch of experimental work which is yet to be explored to its full potential for numerical model validation is the use of post-mortem human specimens (PMHSs)

[37, 41, 42], instrumented with surface and intracranial pressure sensors. Existing studies in this area are rare and hindered by the experimental difficulties, not to mention complete impracticalities for the evaluation of PPE performance. It only leaves the use of anthropometric phantoms as the only alternative, which, made of non-biological materials, replicate the geometry to a high degree [8, 31, 39, 43, 44].

In this contribution we performed a comprehensive experimental characterization of the human phantom model instrumented with 10 pressure sensors to measure the response to a shock wave loading. The specimen was tested using large cross-sectional area shock tube using three locations with characterized by divergent flow characteristics. The loading of the specimen was administered via a single shock wave with three nominal intensities (70, 140 and 210 kPa), and surface pressure was probed in three headform orientations with respect to the incident shock wave, i.e., 0, 90 and 180°.

2. Methods

2.1 The shock tube

The 7 m long square (0.71 × 0.71 m) cross section shock tube was used in all experiments. This device was previously characterized in detail [24, 26]. The driver gas was compressed helium (ultra-high purity, 99.99%, Airgas, Oakland, NJ), which was allowed to flow into the breech separated from the driven section of the shock tube with membranes made of Mylar (Grafix, Cleveland, OH). Upon the rupture of membranes, the driver gas enters the driven section and compresses the ambient air, which in turn generates a shock wave. Three discrete Friedlander waveform shock waves with nominal intensities of approximately 70, 140 and 210 kPa peak overpressure in the test section (T5 sensor, **Figure 1**) were used. All tests were performed at ambient conditions.

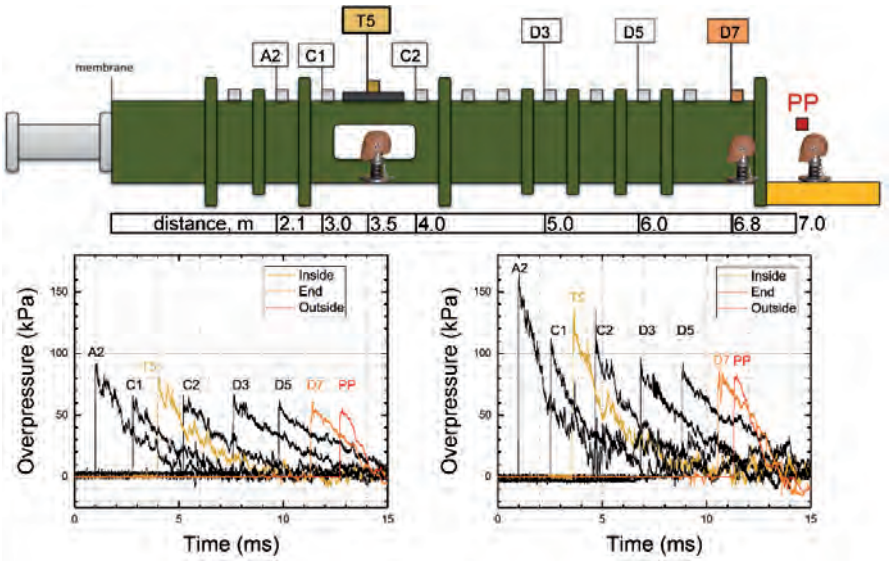
2.2 Pressure measurement, headform preparation, and instrumentation

The temporal evolution of the incident shock wave waveforms was recorded using seven high frequency response pressure sensors model 134A24 (PCB Piezotronics, Inc., Depew, NY, USA), distributed along the shock tube (**Figure 1**). The pencil probe model ICP® 137B24B (PCB Piezotronics Inc., Depew, NY, USA) was used to measure the incident pressure on the outside (PP location, **Figure 1**).

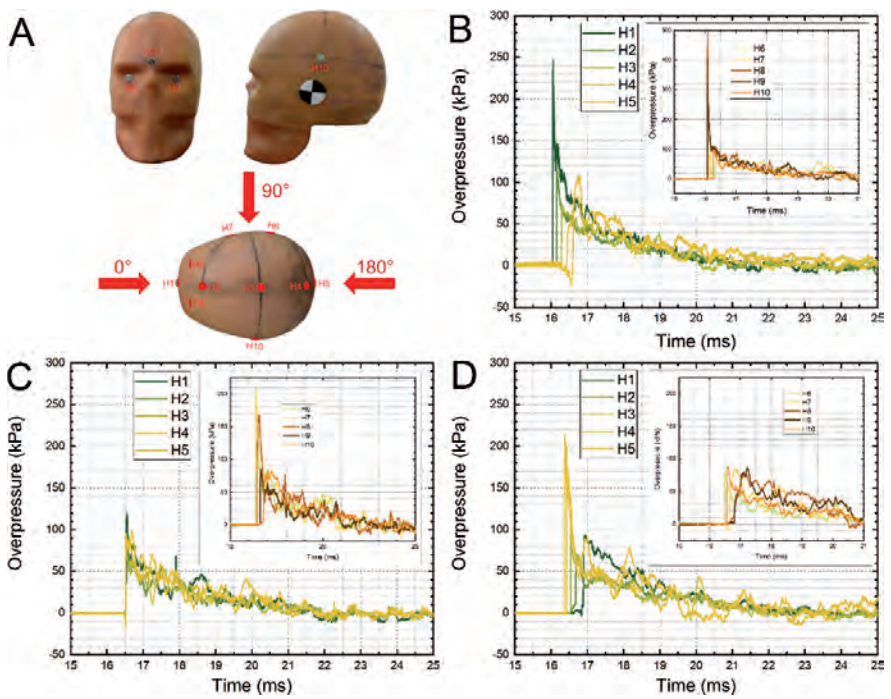
The phantom headform [45], was instrumented with 10 PCB Piezotronics model 102B06 pressure sensors as illustrated in **Figure 2A**. Five medial sensors are located along midline anterior–posterior (H1–H5), and five circumferential sensors: two on the right parietal side (H6 and H7), two in eye sockets (H8 and H9, **Figure 2A**) and one on the left parietal side (H10). These sensors were mounted flush to the surface using tapped holes. The headform was mounted on the Hybrid III neck (Humanetics, Plymouth, MI) [46], in a rigid configuration to eliminate the motion of the headform during shock wave impact. The FOCUS headform-Hybrid III neck the assembly was attached to the adapter plate and bolted to the bottom of the shock tube in the test section in three different locations (**Figure 1**).

A custom LabView program was used to record the pressure waveforms. The data acquisition system is based on PXIe-1082 PCI Express chassis and PXI-6133 S Series multifunction DAQ modules (National Instruments, Austin, TX, USA). The signal of pressure sensors was filtered using 8-channel signal conditioners model 483C05 (PCB Piezotronics Inc., Depew, NY, USA). The pressure waveforms were recorded at 1.0 MHz sampling frequency with an acquisition time of 50 ms.

01



02 **Figure 1.**
Evolution of the shock wave profile traveling in the 28-inch square cross section shock tube. Top panel: schematics of the pressure sensor distribution along the shock tube. The headform is placed in three locations marked as: T5 (inside), D7 (end) and PP (outside). Bottom panels: Pressure profiles of the incident shock wave with nominal BOP of 70 kPa (left) and 140 kPa (right) recorded by sensors distributed along the shock tube as schematically depicted by the top diagram. The shock wave profiles recorded at T5, D7 and PP were used for experimental data normalization. This image was taken from reference [26] (distributed under creative commons attribution (CC BY) license).



03 **Figure 2.**
The schematic representation of the pressure sensor distribution on the headform (A). The direction of the shock wave propagation in experiments where the headform was rotated in 90° intervals is illustrated. The experimental pressure waveforms collected at 70 kPa nominal shock wave intensity by the surface sensors to three headform orientations: (B) 0°, (C) 90°, and (D) 180° with respect to the direction of the shock wave propagation.

2.3 Experimental design, data reduction and statistical analysis

The study was designed as three-factor experimental design, 3 × 3 × 3. The three experimental variables investigated are: (1) the headform location (three levels: inside, end and outside, **Figure 1**), (2) the headform orientation (three levels: 0, 90, and 180°), and (3) shock wave intensity (three levels: 70, 140 and 210 kPa).

All pressure waveforms were processed and quantified in Origin 2018 software (OriginLab Corp., Northampton, MA). All data are presented as mean and standard deviation (n = 4).

The data normalization and reduction were performed as follows. The four pressure waveform characteristics were tabulated. These include (1) the peak overpressure, the increase in pressure observed at arrival of the shock front, (2) the rise time, or the time required for the pressure to increase from 10 to 90% of the peak overpressure, (3) the positive phase duration, or the time required to return to ambient pressure, and (4) the impulse, or the area under the pressure–time curve during the positive phase duration. Each pressure waveform characteristic value was divided by the incident shock wave equivalent (Eq. (1)):

$$x_{\text{non}} = \frac{x_{\text{p}}}{x_{\text{i}}}(1)) \tag{1}$$

where, x_{p}—peak overpressure, rise time, duration or impulse of the resulting pressure waveform on the headform, x_{i}—peak overpressure, rise time, duration or impulse of the incident shock wave, at the headform location (T5, D7 or PP, **Figure 1**). As a result, a set of normalized non-dimensional peak overpressure, rise time, duration and impulse values is generated for each test location, headform orientation and shock wave intensity.

2.4 Flow-field simulations

Finite element models were used to identify the influence the three experimental variables on the flow-field around the specimen. The flow-field around the headform was simulated using a coupled Eulerian-Lagrangian approach to fluid-structure interaction. This solution technique is ideal for the simulation of large deformation finite element analyses and has been used extensively in the simulation of shock-structure interaction physics [8, 47, 48]. The shock wave is modeled in a Eulerian mesh of air and interacts with the headform, modeled using a Lagrangian mesh. The interaction of the two domains results in a solution which depicts the air flow around the headform.

The headform Lagrangian model was generated from a 3D geometrical model generated from the FOCUS headform and the Hybrid III neck using Autodesk Recap Pro 2018 (Autodesk, Inc.). The three-dimensional geometry was meshed using linear tetrahedrons (Simpleware, Synopsys) at a converged mesh density with an average minimum edge length of 8.73 mm (**Figure 3A**). The headform was assumed to be a linear elastic material with a density of 2700 kg/m^3, an elastic modulus of 6.89 GPa, and a Poisson's ratio of 0.33.

A pre-existing, validated model of a shock tube was enhanced for use as the Eulerian domain [49]. This model used a biased linear hexahedral mesh which converged at a minimum edge length of 14 mm at the region of interest. Two shock tube meshes were used, designed to best model the inside specimen placement and to model the exit and outside specimen placements. The model used to simulate the inside of the shock tube was 5.9 m in length and over 580 thousand elements (**Figure 3B**). The model used to simulate the end and outside specimen placements was 2.9 m in length and over 2.24 million elements (**Figure 3C**). The Eulerian mesh

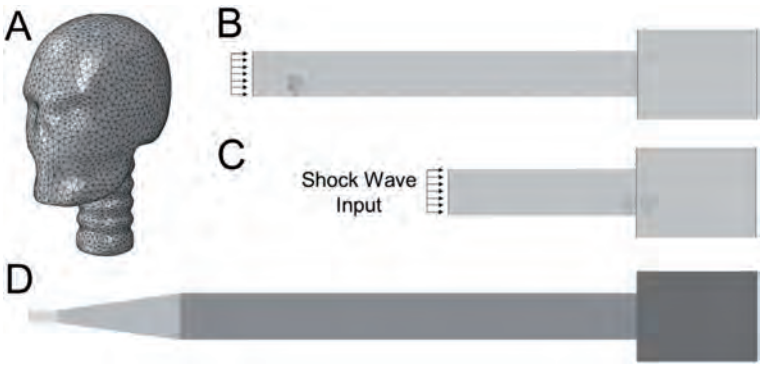


Figure 3.
The finite element models used in the calculation of the flow-fields around the headform. (A) The Lagrangian domain of the FOCUS headform was meshed using linear tetrahedral elements. The Eulerian domains were of two different lengths: (B) a 5.9 m length section downstream of the A2 sensor ***(Figure 1)*** *to model the inside specimen location and (C) a 2.9 m length section downstream of the D5 sensor* ***(Figure 1)*** *to model the end and outside specimen locations. (D) The full shock tube size is shown, depicting the breech, expansion cone, driven region, and catch tank.*

was assumed to be filled with air, approximated using the ideal gas equation of state at 296 K, a density of 1.2 kg/m^3, and a specific heat ratio of 1.4.

Twenty-seven simulated configurations were conducted, mirroring the experimental configurations of three specimen placement locations (inside, at the exit of, and outside the shock tube), three specimen orientations (0, 90, and 180°), and three blast overpressures (70, 140, and 210 kPa). The shock was simulated as a planar pressure wave, applied to a surface upstream from the headform. For each configuration, pressure measurements taken at the sensor coincident with the loading surface were averaged for the four repeated exposures to create an input incident pressure pulse. The pressure pulse for a 210 kPa exposure with the headform located at the exit was used as the pressure pulse for the untested configuration of 210 kPa with the headform outside of the shock tube. All nodes coincident to the walls of the Eulerian domain and the base of the Lagrangian headform were constrained against all translational and rotational degrees of freedom. The enhanced immersed boundary method allowed for the Lagrangian mesh to occupy void regions within the Eulerian mesh, enabling the computation of the interfacial surface. Interaction between the two domains was defined as hard general contact in the direction normal to the interacting surfaces and a frictionless contact in the tangential direction.

All simulations were conducted in Abaqus 6.13-4 on two Intel Xeon 2.10 GHz processors (Dassault Systèmes). For each configuration, the pressure in each element along the vertical longitudinal plane was mapped to plot the blast overpressure (BOP), impulse, and rise time amplification factors (MATLAB R2019a, Mathworks). Element-wise values for the peak BOP were defined as the maximum simulated pressures, the impulses were calculated as the area under the pressure-time curves, and the rise times were calculated as the time required for the signal to increase from 10 to 90% of the peak value. Element-wise values were normalized with values of the incident waveform at that location, resulting in unitless amplification factors.

3. Results

3.1 Experimental surface pressures on the headform

Representative pressure profiles recorded by the surface sensors mounted on the headform are presented in **Figure 2B-D**. These data were recorded at a nominal

shock wave intensity of 70 kPa, and general trends in pressure waveforms distribution are similar for the other two incident shock wave intensities (140 and 210 kPa). The effect of the headform rotation on the surface loading is illustrated in **Figure 2** for the inside test location. In general, on the face exposed to the shock wave the recorded peak overpressures are the highest: 245 kPa (H1 sensor) for the 0° orientation (**Figure 2B**, H8 and H9 sensors are a special case, considering the sensors are located in the concave "eye sockets" which results in the pressure entrapment, and extremely high peak overpressure values), 220 kPa (H7 sensor) for 90° orientation (**Figure 2C**, inset), and 225 kPa (H5 sensor) for 180° orientation (**Figure 2D**). It is obvious that the same trends are observed for the other two test locations and headform orientations (**Figure 4A–C**). It appears that the rise time is a sensitive metrics for the headform loading (**Figure 4D–F**). In general, the rise time is shortened on the front face exposed to the shock wave (H1 at 0° orientation, **Figure 4D**, H6 and H7 at 90° orientation, **Figure 4E**, and H5 at 180° orientation, **Figure 4F**) or it is extended on the converse side of the headform (H4 and H5 at 0° orientation in **Figure 4D**, H10 at 90° orientation in Figure 4E, and H1 and H2 at 180° orientation in **Figure 4F**), compared to the rise time of the incident shock wave. This effect is seen regardless of the headform test location. For the duration and impulse, a different kind of relationship is noticeable. It is expected considering both peak overpressure and the rise time are describing the behavior of the front face of the waveform, while the duration and the impulse are related to the properties of the entire waveform. In general, the duration and impulse values decrease with distance from the breech, corresponding with the test location in the order: inside > end > outside. This is associated with the erosion of the incident wave tail by the end effect. The shock wave exiting the shock tube creates a region of underpressure

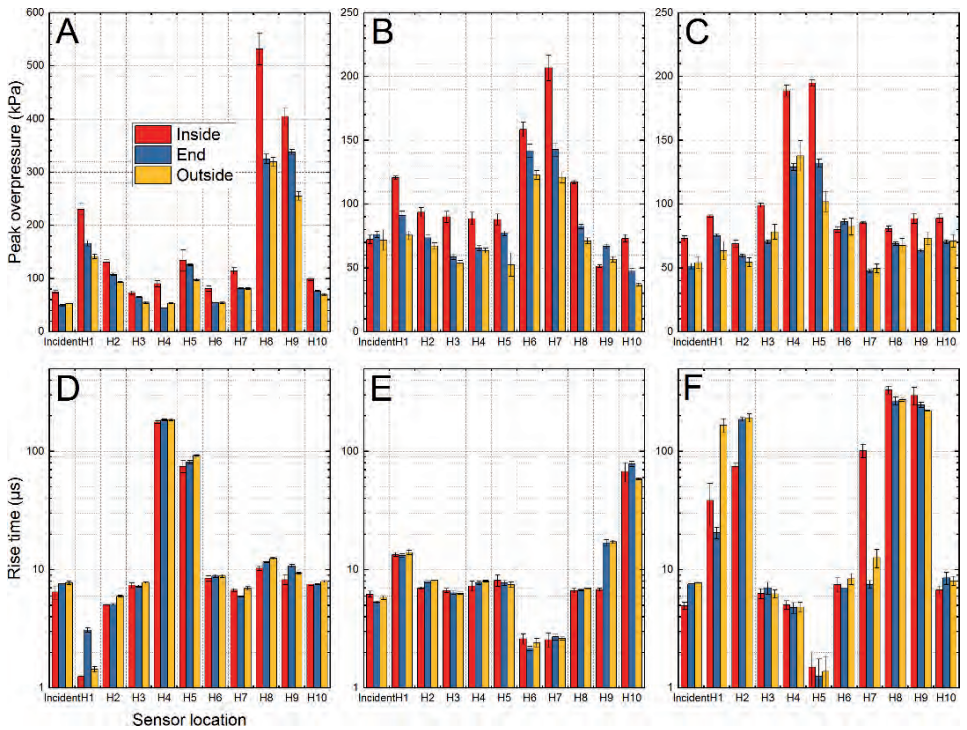


Figure 4.
The results of the pressure waveforms characteristics quantification. The peak overpressure and the rise time for the incident and surface mount sensors collected at three different test locations (inside, end and outside) are presented (n = *4). The headform orientation in these experiments was 0° (A, C), 90° (B, E), and 180° (C, F).*

which travels back into the shock tube [7], and unconfined conditions on the outside allow for free expansion of the previously constrained shock front, resulting in a conversion of the static pressure to 'jet wind', resulting in a shorter durations and lower impulse values at the end and outside locations (**Figure 5**).

3.2 Experimental data normalization

It is thus obvious a further data reduction is necessary in order to compare data collected at three different intensities and three different headform locations. The simplest and most natural approach is to take the characteristic parameters of the incident shock wave waveform (input) recorded by a sensor mounted at specific test location, i.e., T5 for inside, D7 for end and PP for outside location, and compare them with waveforms recorded by pressure sensors on the headform (output). The resulting dimensionless parameters (calculated using Eq. (1)) are a measure of the disturbance caused by introduction of headform into the flow field of the shock wave traveling in the shock tube. The values other than 1 indicate divergence from the waveform characteristics at specific test location in or outside of the shock tube and on the specific location on the headform, compared to the incident shock wave. These can be attributed to geometric factors, changes in shock wave characteristics and presence of additional high velocity flows which are below the detection levels of small cross section sensors sparsely distributed on the surface of the headform. However, if the shock wave properties were only gradually evolving while traveling in the shock tube, it is reasonable to expect similar distribution of non-dimensional parameters as a function of their physical location on the headform which becomes the only defining parameter of the system.

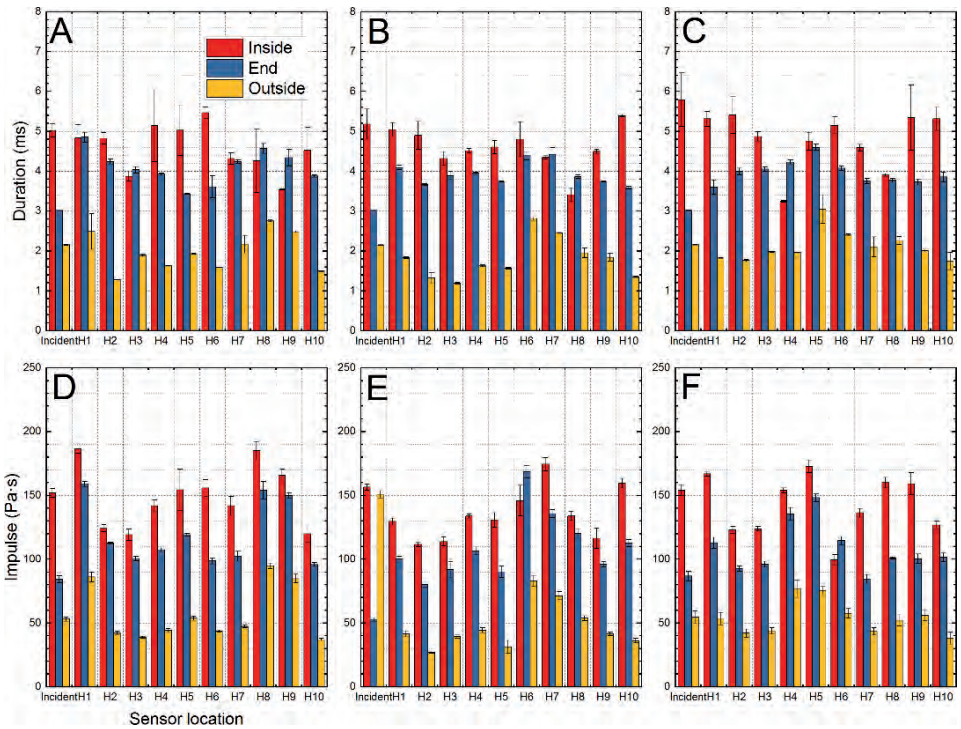


Figure 5.
The results of the pressure waveforms characteristics quantification. The peak duration and the impulse for the incident and surface mount sensors collected at three different test locations (inside, end and outside) are presented (n = *4). The headform orientation in these experiments was 0° (A, C), 90° (B, E), and 180° (C, F).*

The non-dimensional parameters (or amplification factors) allow for direct comparison of pressure waveform characteristic parameters generated by a range of incident shock waves differing in intensity. Using this concept in mind we performed further data reduction for peak overpressures, rise time, impulse and durations in all datasets. The representative bar plot for the amplification factors for the peak overpressure, rise time, duration and impulse for the headform in the 90° orientation and exposed to a shock wave with three nominal intensities (70, 140 and 210 kPa) in three different locations (inside, end and outside) is presented in **Figure 6**. This figure illustrates that indeed the normalization is an effective strategy to compare the data obtained from a variety of exposure conditions. The normalized peak overpressure and rise time follow well defined trends, and the largest divergence is observed for the normalized duration and impulse at the end test location (**Figure 6C** and **D**). It is expected considering duration and impulse values for the end and outside locations vary more significantly than these reported by the headform sensors in the inside location (**Figure 5**).

We previously reported similar trends for the headform tested in the 0° orientation (see Figure 7 in Ref. [26]), and this work expands upon these results by incorporation of two additional orientations (90 and 180°). The data are presented as a function of the sensor distance of the 2D projection of the headform (for details refer to Figure 7B in Ref. [26]). The best results were noted for amplification factors of peak overpressure recorded on the headform at 0° orientation (**Figures 7, 8** and **Table 1**): the data collected in all three test locations has narrow distribution and follows well defined trend. Front sensor H1 has increased values in the range of 2.4–3.6, which gradually decrease along the headform reaching minimum values

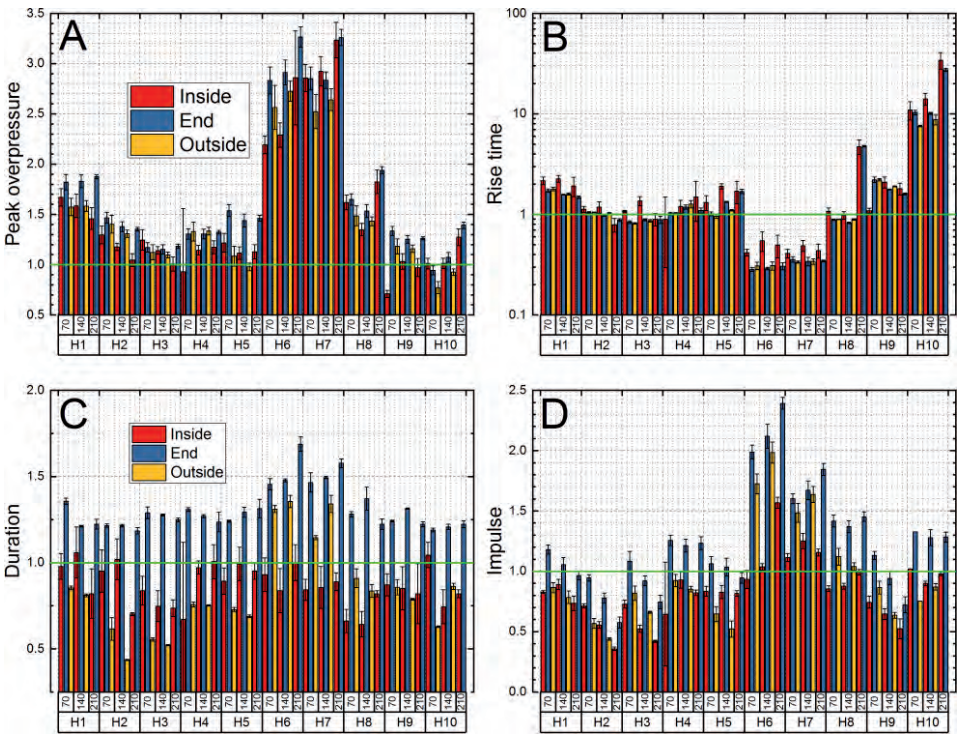


Figure 6.
The results of the pressure waveform characteristics quantification for headform mounted sensors. The normalized peak overpressure (A), rise time (B), duration (C) and impulse (D) are presented (n = 4) *for experiments where the headform was mounted at 90° orientation. The normalization allows comparison of the data quantified for three nominal shock wave intensities: 70, 140 and 210 kPa.*

of about 1 for the H4 and H6 sensors on the back of the headform, and reaching a value of 2 for the H5 sensor at the very end of the headform. This increase is purely due to combined effect of the shock wave wrapping around the headform and its two streams joining together at the back. This is accompanied by increased values for the rise time for H5 sensor by a factor of 10 compared to incident shock wave, which is markedly increased compared to all other sensors, where the rise time amplification factor never exceeds the value of 2 (**Figure 7**). Amplification factors for sensors mounted in the eye sockets are extremely high (in the range of 5–8),

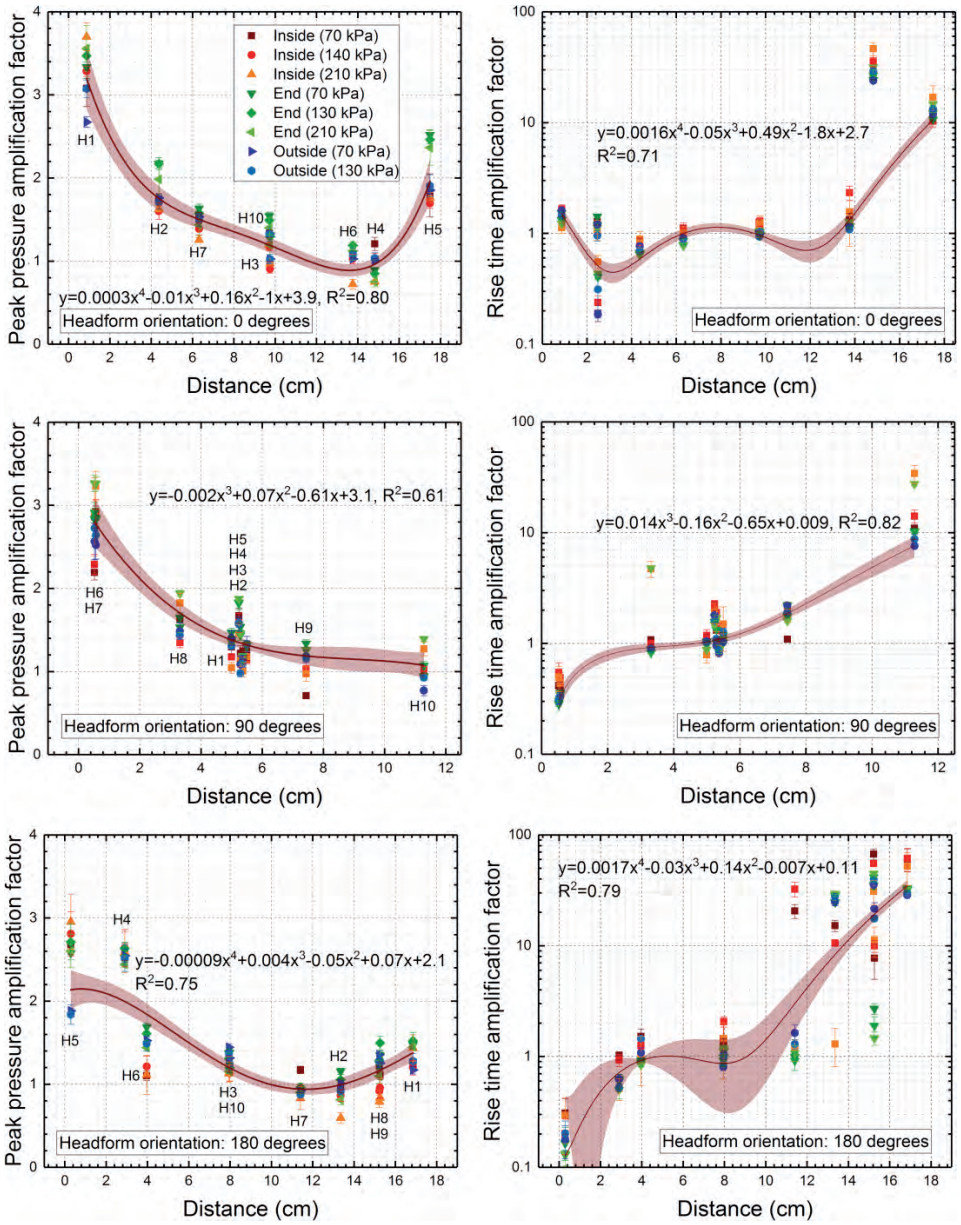


Figure 7.
Amplification factors for peak overpressure and rise time as a function of the headform sensor distance. Polynomial fit performed on normalized data collected for three headform orientations of 0, 90 and 180° at three different test locations (inside, end and outside), three shock wave intensities (as indicated in the figure legend: 70, 140 and 210 kPa) and repeated four times. Adjusted R^2 *values vary from 0.82 (good fit) to 0.59 (mediocre fit) due to broad data distributions. Data are presented as average and standard deviation.*

and they do not follow the same trend as sensors mounted on the flat surface of the headform. The concave geometry of eye sockets is responsible for the compressed air entrapment and momentary stagnation during shock wave exposure, which results in extreme pressures, compared to other locations on the headform. Similar trends are also noticeable for the 90 and 180° orientations, with differences related to the geometrical factors. The amplification factors on the face exposed to the shock wave (H6, H7 for the 90°, and H5 for 180° orientation) have lower values (<3) compared to 0° orientation. The rise time for these two orientations have much

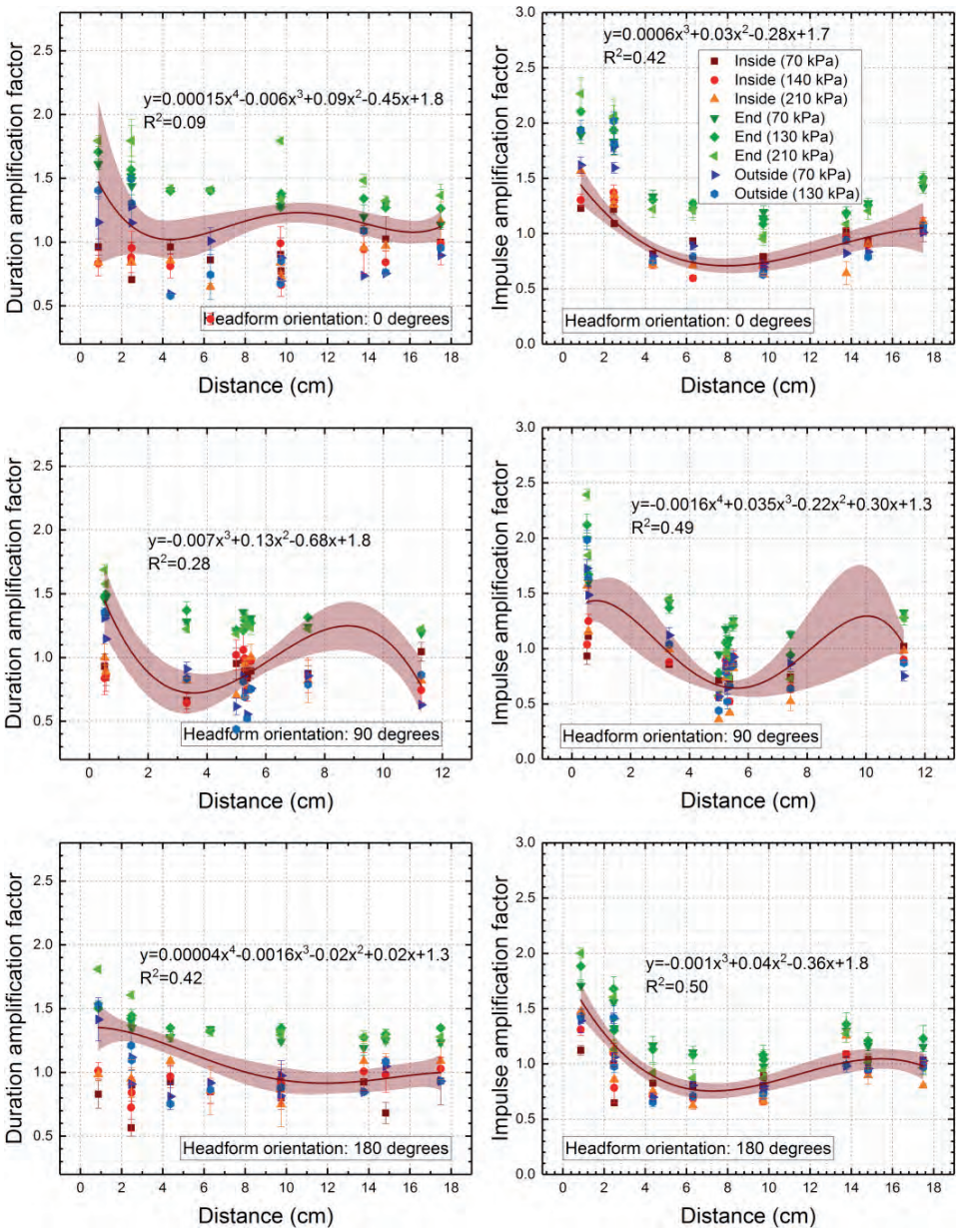


Figure 8.
Amplification factors for the duration and impulse as a function of the sensor distance on the headform. Polynomial fit performed on normalized data collected for three headform orientations of 0, 90 and 180° at three different test locations (inside, end and outside), three shock wave intensities (as indicated in the figure legend: 70, 140 and 210 kPa) and repeated 4 times. Adjusted R^2 values vary from 0.82 (good fit) to 0.04 (bad fit) due to broad data distributions. Data are presented as average and standard deviation.

lower values (<1 μs) and rise time values gradually increase with increased distance (**Figure 7**). Far less consistent results are obtained for the duration and impulse values (**Figure 8**). The spread of amplification factor values in all six cases is 1.0 or more, which indicates that the loading conditions at specific test location plays an important role. These variations are expressed in the goodness of fit parameters (adjusted R^2) which are presented in **Table 1**. It is clear fit parameters for peak overpressure and rise time indicate good fit, while for duration and impulse the parameters are below 0.5, which is indicative of poor-quality fit. The dispersion of the data points is the main reason, and respective data sets appear to follow stochastic distribution pattern rather than a single well-defined function.

3.3 Numerical simulation data normalization

The trends observed experimentally were confirmed using the numerical simulations. Normalized results for the spatial distribution of peak overpressures

Headform orientation	0°	90°	180°
Peak overpressure	0.80	0.61	0.75
Rise time	0.71	0.82[1]	0.79[1]
Impulse	0.42	0.49	0.50
Duration	0.09	0.28	0.42

[1]*Large spread of the data for 90 and 180° orientations.*

Table 1.
Adjusted R^2 *values for fits to different datasets presented in* ***Figures 6*** *and* ***7****.*

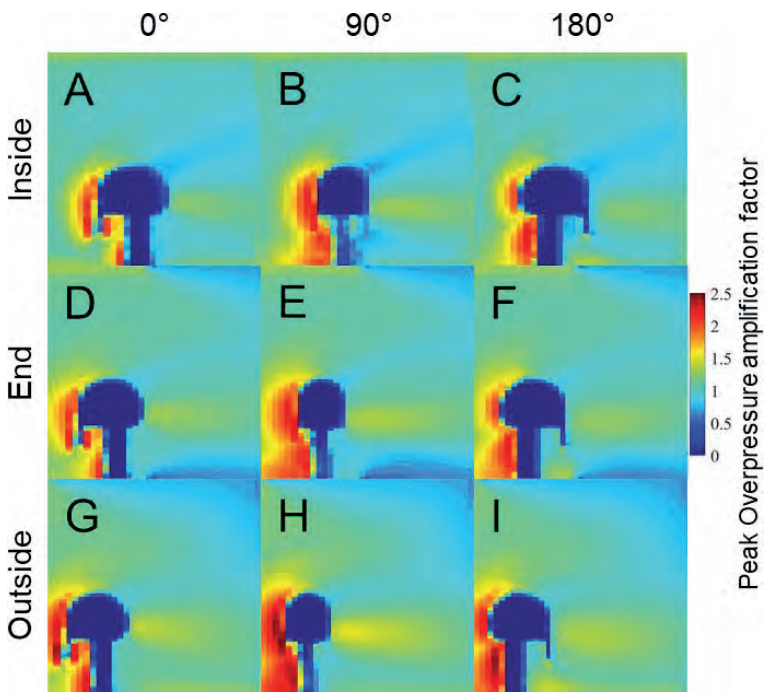


Figure 9.
Spatial distribution of the peak overpressure amplification factors for the 140 kPa exposures in the region surrounding the headform for three specimen locations and for three headform orientations.

confirmed that the highest peak overpressures are seen at the front face of the headform (**Figure 9**). Following data normalization, trends were found to be common between the three shock wave intensities, 70, 140, and 210 kPa, and, therefore, only results for 140 kPa exposures are shown. The area of stagnation is largest in the 90° orientation, followed by the 180° orientation. Additionally, for similar headform orientations, the area of stagnation increased with increasing distance from the breech, with the largest area of stagnations observed in the outside test locations and the smallest area observed at the inside location. A region of increased peak overpressures is observed behind the headform, regardless of the headform orientation or the testing location. This region indicates the area affected after the shock front wraps around the headform. Above and below that area of elevated peak overpressures, the lowest pressures are observed. This phenomenon is most apparent in the inside test location (**Figure 9A–C**), as a fan radiating behind the headform. These results corroborate the observed trends reported in **Figure 7**. The rise time was highest around the posterior face of the headform in all headform orientations and underneath the chin of the headform in the 0° orientation (**Figure 10**). In the area around the headform, the rise time was higher than that of the incident waveform. These trends were observed regardless of specimen location.

Spatial maps of the impulse amplification factors highlight the importance of testing location on specimen loading (**Figure 11**). The end location exhibited the largest impulse amplification factors and the inside location exhibited the smallest. This finding corroborates the wide spread of impulse and duration values reported in **Figure 8**. Furthermore, the impulse was highest in the 90° headform orientation, followed by the 180° orientation. The spatial distribution of the increased impulse was similar among specimen orientations and testing locations, differing in magnitudes only. A region of high impulse is seen on the front face of the headform and a region of low impulse, lower than the impulse of the incident wave, is seen behind the headform.

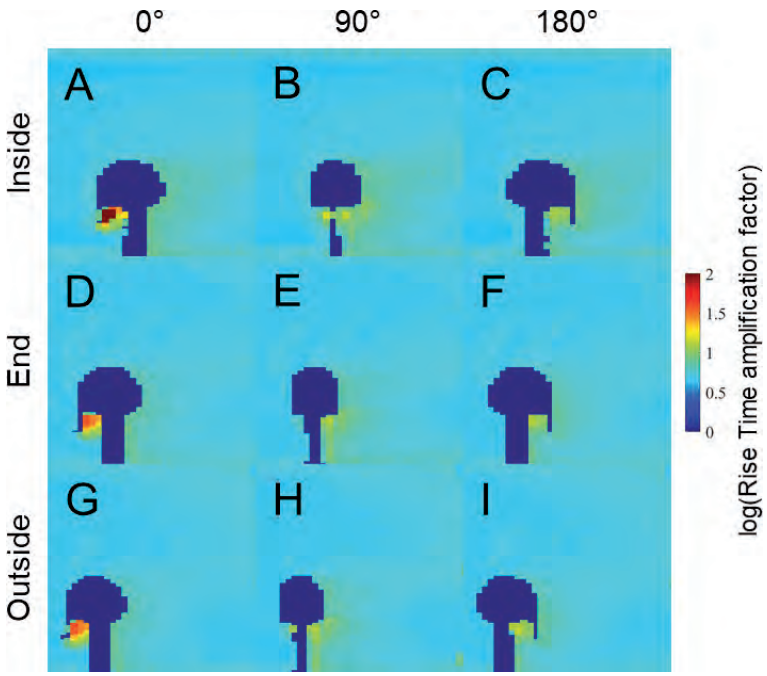


Figure 10.
Spatial distribution of the rise time amplification factors for the 140 kPa exposures in the region surrounding the headform for three specimen locations and for three headform orientations. Data are reported as the log of the rise time amplification factor, indicated the order of magnitude of the change.

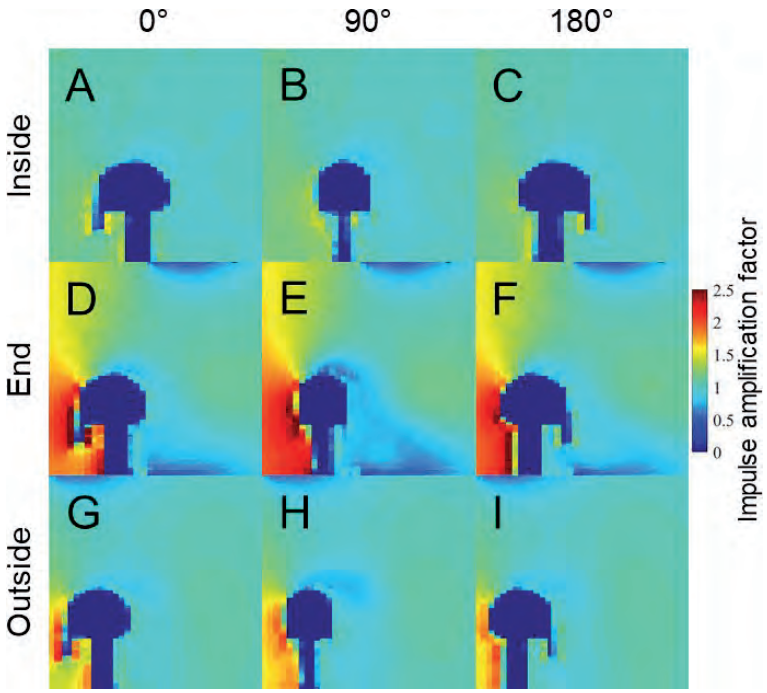


Figure 11.
Spatial distribution of the impulse amplification factors for the 140 kPa exposures in the region surrounding the headform for three specimen locations and for three headform orientations. As the duration and impulse amplification factors showed similar results, only data for the impulse are presented here.

4. Conclusions

Headform instrumented with 10 pressure sensors (mounted to measure surface pressure) was exposed to a single shock wave with three nominal intensities: 70, 140, and 210 kPa. The headform was mounted in three different orientations: 0, 90 and 180° with respect to the direction of the shock wave propagation. The effect of the headform location was evaluated by positioning it inside of the shock tube, at the end and outside of the shock tube. The headform was mounted using Hybrid III biofidelic surrogate neck, which was tightened to eliminate the inertial motion of the headform caused by blast exposure.

Comparison of the test results at three different shock wave intensities complicates data analysis even further. To resolve these issues, we developed a simple strategy of data reduction: the respective pressure parameters recorded by headform sensors are divided by equivalent parameters of the incident shock wave as defined in Eq. (1). As a result, a comprehensive set of non-dimensional parameters is generated. These non-dimensional parameters (or amplification factors) allow for direct comparison of pressure waveform characteristic parameters generated by a range of incident shock waves differing in intensity and for the headform located in different locations.

Using this approach, we found there is a correlation function which allows prediction of the peak pressure on the headform which depends only on the peak pressure of the incident shock wave (for specific sensor location on the headform), and it's independent on the headform location, and to a certain degree the orientation. Similar relationship exists also for the rise time. However, for the duration and impulse similar correlation functions do not exist.

We demonstrated via comprehensive experimental and numerical studies that three different testing locations are characterized by non-equivalent loading

conditions. While it was possible to devise the transfer function for normalized peak overpressure and rise time at 0° orientation, the dispersion and clustering of data points indicates the surface pressure distribution is a function of the headform orientation where geometrical factors play important role.

Acknowledgements

This work was supported by PEO Soldier award no. W91CRB-16-C-0025.

Conflict of interest

The authors declare no conflict of interest.

Author details

Maciej Skotak, Molly T. Townsend, Eren Alay and Namas Chandra*
Department of Biomedical Engineering, Center for Injury Biomechanics, Materials, and Medicine, New Jersey Institute of Technology, Newark, NJ, USA

*Address all correspondence to: namas.chandra@njit.edu

IntechOpen

© 2019 The Author(s). Licensee IntechOpen. This chapter is distributed under the terms of the Creative Commons Attribution License (http://creativecommons.org/licenses/by/3.0), which permits unrestricted use, distribution, and reproduction in any medium, provided the original work is properly cited. CC BY

References

[1] Vieille P. Sur les discontinuités produites par la détente brusque de gaz comprimes. Comptes Rendus de l'Académie des Sciences. 1899; **A 129**:1228-1230

[2] Celander H, Clemedson C-J, Ericsson UA, Hultman HI. The use of a compressed air operated shock tube for physiological blast research. Acta Physiologica Scandinavica. 1955;**33**(1):6-13

[3] Dryer M, Merritt DL, Aronson PM. Interaction of a plasma cloud with the Earth's magnetosphere. Journal of Geophysical Research. 1967;**72**(11):2955-2962

[4] Hooker WJ, Millikan RC. Shock-tube study of vibrational relaxation in carbon monoxide for the fundamental and first overtone. The Journal of Chemical Physics. 1963;**38**(1):214-220

[5] Kiefer J, Mizerka L, Patel M, Wei H. A shock tube investigation of major pathways in the high-temperature pyrolysis of benzene. The Journal of Physical Chemistry. 1985;**89**(10):2013-2019

[6] Park C, Appleton JP. Shock-tube measurements of soot oxidation rates. Combustion and Flame. 1973;**20**(3):369-379

[7] Kuriakose M, Skotak M, Misistia A, Kahali S, Sundaramurthy A, Chandra N. Tailoring the blast exposure conditions in the shock tube for generating pure, primary shock waves: The end plate facilitates elimination of secondary loading of the specimen. PLoS One. 2016;**11**(9):e0161597

[8] Ganpule S, Alai A, Plougonven E, Chandra N. Mechanics of blast loading on the head models in the study of traumatic brain injury using experimental and computational approaches. Biomechanics and Modeling in Mechanobiology. 2013;**12**(3):511-531

[9] Sundaramurthy A, Chandra NA. Parametric approach to shape field-relevant blast wave profiles in compressed-gas-driven shock tube. Frontiers in Neurology. 2014;**5**(253)

[10] Mejia-AlvarezR,WilsonB,LeftwichM, Martinez A, Prestridge K. Design of a fast diaphragmless shock tube driver. Shock Waves. 2015;**25**(6):635-650

[11] Tranter RS, Giri BR. A diaphragmless shock tube for high temperature kinetic studies. The Review of Scientific Instruments. 2008;**79**(9):094103

[12] Takano Y, Akamatsu T. A diaphragmless shock tube. Journal of Physics E: Scientific Instruments. 1984;**17**(8):644

[13] Swietek B, Skotak M, Chandra N, Pfister BJ. Characterization of a controlled shock wave delivered by a pneumatic table-top gas driven shock tube. Review of Scientific Instruments. 2019 (accepted)

[14] Heufer K, Olivier H, Drumm S, Murrenhoff H, editors. A new fast acting valve for diaphragmless shock tubes. In: 28th International Symposium on Shock Waves. Springer; 2012

[15] Downey M, Cloete T, Yates A. A rapid opening sleeve valve for a diaphragmless shock tube. Shock Waves. 2011;**21**(4):315-319

[16] Gageik M, Weiss A, Klioutchnikov I, Olivier H, editors. A numerical investigation of the flow through a new fast acting valve for diaphragmless

AQ1

shock tubes. In: 29th International Symposium on Shock Waves. Vol. 1. Springer; 2015

[17] Skotak M, Alay E, Chandra N. On the accurate determination of shock wave time-pressure profile in the experimental models of blast-induced neurotrauma. Frontiers in Neurology. 2018;**9**(52)

[18] Cernak I, Savic VJ, Kotur J, Prokic V, Veljovic M, Grbovic D. Characterization of plasma magnesium concentration and oxidative stress following graded traumatic brain injury in humans. Journal of Neurotrauma. 2000;**17**(1):53-68

[19] Cernak I, Wang Z, Jiang J, Bian X, Savic J. Cognitive deficits following blast injury-induced neurotrauma: Possible involvement of nitric oxide. Brain Injury. 2001;**15**(7):593-612

[20] Kobeissy F, Mondello S, Tumer N, Toklu H, Whidden M, Kirichenko N, et al. Assessing neuro-systemic & behavioral components in the pathophysiology of blast-related brain injury. Frontiers in Neurology. 2013;**4**(186)

[21] Chandra N, Sundaramurthy A, Gupta RK. Validation of laboratory animal and surrogate human models in primary blast injury studies. Military Medicine. 2017;**182**:105-113

[22] Goldstein LE, Fisher AM, Tagge CA, Zhang X-L, Velisek L, Sullivan JA, et al. Chronic traumatic encephalopathy in blast-exposed military veterans and a blast neurotrauma mouse model. Science Translational Medicine. 2012;**4**(134):134ra60-134ra60

[23] Gullotti DM, Beamer M, Panzer MB, Chia Chen Y, Patel TP, Yu A, et al. Significant head accelerations can influence immediate neurological impairments in a murine model of blast-induced traumatic brain injury. Journal of Biomechanical Engineering. 2014;**136**(9):091004-091011

[24] Alay E, Skotak M, Misistia A, Chandra N. Dynamic loads on human and animal surrogates at different test locations in compressed-gas-driven shock tubes. Shock Waves. 2017

[25] Sundaramurthy A, Alai A, Ganpule S, Holmberg A, Plougonven E, Chandra N. Blast-induced biomechanical loading of the rat: An experimental and anatomically accurate computational blast injury model. Journal of Neurotrauma. 2012;**29**(13):2352-2364

[26] Skotak M, Alay E, Zheng JQ, Halls V, Chandra N. Effective testing of personal protective equipment in blast loading conditions in shock tube: Comparison of three different testing locations. PLoS One. 2018;**13**(6):e0198968

[27] Needham CE, Ritzel D, Rule GT, Wiri S, Young L. Blast testing issues and TBI: Experimental models that lead to wrong conclusions. Frontiers in Neurology. 2015;**6**(72)

[28] Abate G, Shyy W. Dynamic structure of confined shocks undergoing sudden expansion. Progress in Aerospace Sciences. 2002;**38**(1):23-42

[29] Arakeri J, Das D, Krothapalli A, Lourenco L. Vortex ring formation at the open end of a shock tube: A particle image velocimetry study. Physics of Fluids. 2004;**16**(4):1008-1019

[30] Moore DF, Jérusalem A, Nyein M, Noels L, Jaffee MS, Radovitzky RA. Computational biology—Modeling of primary blast effects on the central nervous system. NeuroImage. 2009;**47**:T10-T20

[31] Roberts J, Harrigan T, Ward E, Taylor T, Annett M, Merkle A. Human

head–neck computational model for assessing blast injury. Journal of Biomechanics. 2012;**45**(16):2899-2906

[32] Grujicic M, Bell WC, Pandurangan B, Glomski PS. Fluid/structure interaction computational investigation of blast-wave mitigation efficacy of the advanced combat helmet. Journal of Materials Engineering and Performance. 2010;**20**(6):877-893

[33] Grujicic M, Bell WC, Pandurangan B, He T. Blast-wave impact-mitigation capability of polyurea when used as helmet suspension-pad material. Materials & Design. 2010;**31**(9):4050-4065

[34] Merkle AC, Wing ID, Roberts JC. Human surrogate head response to dynamic overpressure loading in protected and unprotected conditions. In: Herold KE, Vossoughi J, Bentley WE, editors. 26th Southern Biomedical Engineering Conference SBEC 2010, April 30–May 2, 2010, College Park, Maryland, USA. Berlin, Heidelberg: Springer; 2010. pp. 22-25

[35] Ganpule S, Gu L, Alai A, Chandra N. Role of helmet in the mechanics of shock wave propagation under blast loading conditions. Computer Methods in Biomechanics and Biomedical Engineering. 2012;**15**(11):1233-1244

[36] Nyein MK, Jason AM, Yu L, Pita CM, Joannopoulos JD, Moore DF, et al. In silico investigation of intracranial blast mitigation with relevance to military traumatic brain injury. Proceedings of the National Academy of Sciences. 2010;**107**(48):20703-20708

AQ4

[37] Ott K, Voo L, Merkle A, Iwaskiw A, Wickwire A, Wester B, et al., editors. Experimental determination of pressure wave transmission to the brain during head-neck blast tests. In: Proceedings of the ASME 2013 Summer Bioengineering Conference 2013 June 26-29, 2013; Sunriver, Oregon, USA, Abdominal Aortic Aneurysms; Active and Reactive Soft Matter; Atherosclerosis; BioFluid Mechanics; Education; Biotransport Phenomena; Bone, Joint and Spine Mechanics; Brain Injury; Cardiac Mechanics; Cardiovascular Devices, Fluids and Imaging; Cartilage and Disc Mechanics; Cell and Tissue Engineering; Cerebral Aneurysms; Computational Biofluid Dynamics; Device Design, Human Dynamics, and Rehabilitation; Drug Delivery and Disease Treatment; Engineered Cellular Environments. Vol. 1A.

[38] Zhang L, Makwana R, Sharma S. Brain response to primary blast wave using validated finite element models of human head and advanced combat helmet. Frontiers in Neurology. 2013;**4**

[39] Przekwas A, Tan XG, Harrand V, Reeves D, Chen ZJ, S K, et al. Integrated experimental and computational framework for the development and validation of blast wave brain biomechanics and helmet protection. In: Proc HFM-207 NATO Symposium on a Survey of Blast Injury Across the Full Landscape of Military Science; Oct. 3-5, 2011; Halifax NS, Canada. 2011. pp. 34-1-34-20

[40] Grujicic M, Ramaswami S, Snipes J, Dudt P. Potential improvement in helmet blast-protection via the use of a polyurea external coating: Combined experimental/computational analyses. Proceedings of the Institution of Mechanical Engineers, Part L: Journal of Materials: Design and Applications. DOI: 10.1177/1464420716644472

[41] Ouellet S, Bir C, Bouamoul A. Direct Comparison of the Primary Blast Response of a Physical Head Model with Post-Mortem Human Subjects. QC Canada: Defence Research and Development Canada-Valcartier Research Center Quebec; 2014

[42] Ganpule S, Salzar R, Perry B, Chandra N. Role of helmets in blast mitigation: Insights from experiments on PMHS surrogate. International Journal of Experimental and Computational Biomechanics. 2016;**4**(1):13-31

[43] Zhu F, Wagner C, Dal Cengio Leonardi A, Jin X, VandeVord P, Chou C, et al. Using a gel/plastic surrogate to study the biomechanical response of the head under air shock loading: A combined experimental and numerical investigation. Biomechanics and Modeling in Mechanobiology. 2012;**11**(3):341-353

[44] Banton R, Piehler T, Zander N, Benjamin R, Duckworth J. Comparison of numerical simulations with experiments of blast-induced pressure wave impact on a surrogate head model. In: Kimberley J, Lamberson L, Mates S, editors. Proceedings of the 2017 Annual Conference on Experimental and Applied Mechanics, Dynamic Behavior of Materials. Vol. 1. Cham: Springer International Publishing; 2018. pp. 181-187

[45] Crowley JS, Brozoski FT, Duma SM, Kennedy EA. Development of the facial and ocular countermeasures safety (FOCUS) headform. Aviation, Space, and Environmental Medicine. 2009;**80**(9):831

[46] Foster JK, Kortge JO, Wolanin MJ. Hybrid III-A biomechanically-based crash test dummy. SAE International. 1977

[47] Mougeotte C, Carlucci P, Recchia S, Ji H. Novel approach to conducting blast load analyses using Abaqus/explicit-CEL. In: Center AARDE, editor. Picatinny Arsenal. NJ: Defense Technical Information Center; 2010

[48] Tan XG, Przekwas AJ, Gupta RK. Computational modeling of blast wave interaction with a human body and assessment of traumatic brain injury. Shock Waves. 2017

[49] Townsend MT, Alay E, Skotak M, Chandra N. Effect of tissue material properties in blast loading: Coupled experimentation and finite element simulation. Annals of Biomedical Engineering. 2018:1-14

AQ5